



atmosphere

Air Pollution in China

Edited by
Duanyang Liu, Kai Qin and Honglei Wang
Printed Edition of the Special Issue Published in *Atmosphere*

Air Pollution in China

Air Pollution in China

Editors

Duanyang Liu

Kai Qin

Honglei Wang

MDPI • Basel • Beijing • Wuhan • Barcelona • Belgrade • Manchester • Tokyo • Cluj • Tianjin



Editors

Duanyang Liu
Key Laboratory of
Transportation Meteorology
of China Meteorological
Administration
Nanjing Joint Institute For
Atmospheric Sciences
Nanjing
China

Kai Qin
School of Environment and
Spatial Informatics
China University of Mining
and Technology
Xuzhou
China

Honglei Wang
School of Atmospheric
Physics
Nanjing University of
Information Science and
Technology
Nanjing
China

Editorial Office

MDPI
St. Alban-Anlage 66
4052 Basel, Switzerland

This is a reprint of articles from the Special Issue published online in the open access journal *Atmosphere* (ISSN 2073-4433) (available at: www.mdpi.com/journal/atmosphere/special-issues/Air_Pollution_in_China).

For citation purposes, cite each article independently as indicated on the article page online and as indicated below:

LastName, A.A.; LastName, B.B.; LastName, C.C. Article Title. *Journal Name* **Year**, Volume Number, Page Range.

ISBN 978-3-0365-6605-4 (Hbk)

ISBN 978-3-0365-6604-7 (PDF)

© 2023 by the authors. Articles in this book are Open Access and distributed under the Creative Commons Attribution (CC BY) license, which allows users to download, copy and build upon published articles, as long as the author and publisher are properly credited, which ensures maximum dissemination and a wider impact of our publications.

The book as a whole is distributed by MDPI under the terms and conditions of the Creative Commons license CC BY-NC-ND.

Contents

Ruilian Yu, Yiling Lin, Jiahui Zou, Yangbin Dan and Chen Cheng Review on Atmospheric Ozone Pollution in China: Formation, Spatiotemporal Distribution, Precursors and Affecting Factors Reprinted from: <i>Atmosphere</i> 2021 , 12, 1675, doi:10.3390/atmos12121675	1
Wei Chong, Wenhua Lyu, Jian Zhang, Jing Liang, Xiaotong Yang and Guoyu Zhang Effects of Air Pollution on Sunshine Duration Trends in Typical Chinese Cities Reprinted from: <i>Atmosphere</i> 2022 , 13, 950, doi:10.3390/atmos13060950	19
Enwei Sun, Chuanbo Fu, Wei Yu, Ying Xie, Yiwen Lu and Chunsong Lu Variation and Driving Factor of Aerosol Optical Depth over the South China Sea from 1980 to 2020 Reprinted from: <i>Atmosphere</i> 2022 , 13, 372, doi:10.3390/atmos13030372	33
Qi Jiang, Hengde Zhang, Fei Wang and Fei Wang Research on the Growth Mechanism of PM _{2.5} in Central and Eastern China during Autumn and Winter from 2013–2020 Reprinted from: <i>Atmosphere</i> 2022 , 13, 134, doi:10.3390/atmos13010134	47
Xinyu Wang, Wenhui Zhao, Tianyue Zhang, Yun Qiu, Pengfei Ma and Lingjun Li et al. Analysis of the Characteristics of Ozone Pollution in the North China Plain from 2016 to 2020 Reprinted from: <i>Atmosphere</i> 2022 , 13, 715, doi:10.3390/atmos13050715	65
Ju Wang, Ran Li, Kexin Xue and Chunsheng Fang Analysis of Spatio-Temporal Heterogeneity and Socioeconomic driving Factors of PM _{2.5} in Beijing–Tianjin–Hebei and Its Surrounding Areas Reprinted from: <i>Atmosphere</i> 2021 , 12, 1324, doi:10.3390/atmos12101324	83
Lirong Yin, Lei Wang, Weizheng Huang, Shan Liu, Bo Yang and Wenfeng Zheng Spatiotemporal Analysis of Haze in Beijing Based on the Multi-Convolution Model Reprinted from: <i>Atmosphere</i> 2021 , 12, 1408, doi:10.3390/atmos12111408	97
Shah Zaib, Jianjiang Lu and Muhammad Bilal Spatio-Temporal Characteristics of Air Quality Index (AQI) over Northwest China Reprinted from: <i>Atmosphere</i> 2022 , 13, 375, doi:10.3390/atmos13030375	113
Xing Xiang, Guangming Shi, Xiaodong Wu and Fumo Yang The Extraordinary Trend of the Spatial Distribution of PM _{2.5} Concentration and Its Meteorological Causes in Sichuan Basin Reprinted from: <i>Atmosphere</i> 2022 , 13, 853, doi:10.3390/atmos13060853	135
Chunsheng Fang, Hanbo Gao, Zhuoqiong Li and Ju Wang Regional Air Pollutant Characteristics and Health Risk Assessment of Large Cities in Northeast China Reprinted from: <i>Atmosphere</i> 2021 , 12, 1519, doi:10.3390/atmos12111519	153
Ningwei Liu, Xiaolan Li, Wanhui Ren, Liguang Li, Congcong Su and Chuang Wang Concentration Characteristics and Photochemical Reactivities of VOCs in Shenyang, China Reprinted from: <i>Atmosphere</i> 2021 , 12, 1240, doi:10.3390/atmos12101240	167
Yulu Tian, Lingnan Zhang, Yang Wang, Jinxi Song and Haotian Sun Temporal and Spatial Trends in Particulate Matter and the Responses to Meteorological Conditions and Environmental Management in Xi'an, China Reprinted from: <i>Atmosphere</i> 2021 , 12, 1112, doi:10.3390/atmos12091112	181

Wen Wei, Bingliang Zhuang, Huijuan Lin, Yu Shu, Tijian Wang and Huimin Chen et al. Analysis of the Interactions between the 200 hPa Jet and Air Pollutants in the Near-Surface Layer over East Asia in Summer Reprinted from: <i>Atmosphere</i> 2021 , 12, 886, doi:10.3390/atmos12070886	193
Bin Zhou, Duanyang Liu and Wenlian Yan A Simple New Method for Calculating Precipitation Scavenging Effect on Particulate Matter: Based on Five-Year Data in Eastern China Reprinted from: <i>Atmosphere</i> 2021 , 12, 759, doi:10.3390/atmos12060759	213
Weifu Ding and Xueping Qie Prediction of Air Pollutant Concentrations via RANDOM Forest Regressor Coupled with Uncertainty Analysis—A Case Study in Ningxia Reprinted from: <i>Atmosphere</i> 2022 , 13, 960, doi:10.3390/atmos13060960	225
Lirong Yin, Lei Wang, Weizheng Huang, Jiawei Tian, Shan Liu and Bo Yang et al. Haze Grading Using the Convolutional Neural Networks Reprinted from: <i>Atmosphere</i> 2022 , 13, 522, doi:10.3390/atmos13040522	245
Xinyi Wu, Zhixin Liu, Lirong Yin, Wenfeng Zheng, Lihong Song and Jiawei Tian et al. A Haze Prediction Model in Chengdu Based on LSTM Reprinted from: <i>Atmosphere</i> 2021 , 12, 1479, doi:10.3390/atmos12111479	261
Saidur Rahaman, Selim Jahangir, Ruishan Chen and Pankaj Kumar Restricted Anthropogenic Activities and Improved Urban Air Quality in China: Evidence from Real-Time and Remotely Sensed Datasets Using Air Quality Zonal Modeling Reprinted from: <i>Atmosphere</i> 2022 , 13, 961, doi:10.3390/atmos13060961	273
Bingbo Huang, Minjun Deng, Qingxian Gao, Zhanyun Ma and Mindong Chen Study on Improving the Air Quality with Emission Enhanced Control Measures in Beijing during a National Parade Event Reprinted from: <i>Atmosphere</i> 2022 , 13, 1019, doi:10.3390/atmos13071019	295
Jingran Zhang, Wukui Wang, Lei Gao, Zhenzhu Deng and Yu Tian Can the Coal-to-Gas/Electricity Policy Improve Air Quality in the Beijing–Tianjin–Hebei Region?—Empirical Analysis Based on the PSM-DID Reprinted from: <i>Atmosphere</i> 2022 , 13, 879, doi:10.3390/atmos13060879	311
Yang Yu and Tianchang Wang New Urbanization, Energy-Intensive Industries Agglomeration and Analysis of Nitrogen Oxides Emissions Reduction Mechanisms Reprinted from: <i>Atmosphere</i> 2021 , 12, 1244, doi:10.3390/atmos12101244	325
Jianwu Shi, Yuzhai Bao, Feng Xiang, Zhijun Wang, Liang Ren and Xiaochen Pang et al. Pollution Characteristics and Health Risk Assessment of VOCs in Jinghong Reprinted from: <i>Atmosphere</i> 2022 , 13, 613, doi:10.3390/atmos13040613	339
Hao Wu, Pulong Chen, Tijian Wang, Min Xie, Bingliang Zhuang and Shu Li et al. Characteristics and Source Apportionment of Size-Fractionated Particulate Matter at Ground and above the Urban Canopy (380 m) in Nanjing, China Reprinted from: <i>Atmosphere</i> 2022 , 13, 883, doi:10.3390/atmos13060883	355
Wenwen Ai, Xixi Yang, Duanyang Liu, Min Zhang, Yan Sun and Boni Wang et al. Impact of the Levels of COVID-19 Pandemic Prevention and Control Measures on Air Quality: A Case Study of Jiangsu Province, China Reprinted from: <i>Atmosphere</i> 2022 , 13, 640, doi:10.3390/atmos13050640	373

Shiye Wang, Jundong Zhang and Li Yao Effect of Combustion Boundary Conditions and n-Butanol on Surrogate Diesel Fuel HCCI Combustion and Emission Based on Two-Stroke Diesel Engine Reprinted from: <i>Atmosphere</i> 2022 , 13, 303, doi:10.3390/atmos13020303	391
Peihao Zhang, Haomiao Cheng, Zhiwen Jiang and Fanding Xiang How Sensitive Morphological Parameters Influence on the PM _{2.5} Diffusion: An Empirical Study of Two Neighborhoods in Central Beijing Reprinted from: <i>Atmosphere</i> 2022 , 13, 921, doi:10.3390/atmos13060921	407
Ming Chen and Fei Dai PCA-Based Identification of Built Environment Factors Reducing PM _{2.5} Pollution in Neighborhoods of Five Chinese Megacities Reprinted from: <i>Atmosphere</i> 2022 , 13, 115, doi:10.3390/atmos13010115	423
Kamsang Woo, Changqing Lin, Yuehui Yin, Dongshuang Guo, Ping Chook and Timothy C. Y. Kwok et al. The Impact of Air Pollution (PM _{2.5}) on Atherogenesis in Modernizing Southern versus Northern China Reprinted from: <i>Atmosphere</i> 2021 , 12, 1552, doi:10.3390/atmos12121552	437
Jianwu Shi, Yinchuan Feng, Liang Ren, Xiuqing Lu, Yaoqian Zhong and Xinyu Han et al. Mass Concentration, Chemical Composition, and Source Characteristics of PM _{2.5} in a Plateau Slope City in Southwest China Reprinted from: <i>Atmosphere</i> 2021 , 12, 611, doi:10.3390/atmos12050611	447
Chunsheng Fang, Xiaodong Tan, Yue Zhong and Ju Wang Research on the Temporal and Spatial Characteristics of Air Pollutants in Sichuan Basin Reprinted from: <i>Atmosphere</i> 2021 , 12, 1504, doi:10.3390/atmos12111504	463
Maogang Tang, Silu Cheng, Wenqing Guo, Weibiao Ma and Fengxia Hu Effects of Carbon Emission Trading on Companies' Market Value: Evidence from Listed Companies in China Reprinted from: <i>Atmosphere</i> 2022 , 13, 240, doi:10.3390/atmos13020240	481

Review

Review on Atmospheric Ozone Pollution in China: Formation, Spatiotemporal Distribution, Precursors and Affecting Factors

Ruilian Yu *, Yiling Lin, Jiahui Zou, Yangbin Dan and Chen Cheng

College of Chemical Engineering, Huaqiao University, Xiamen 361021, China; 20013087048@stu.hqu.edu.cn (Y.L.); zoujh9@mail2.sysu.edu.cn (J.Z.); dyb@njuae.cn (Y.D.); 19013087047@stu.hqu.edu.cn (C.C.)

* Correspondence: ruiliany@hqu.edu.cn

Abstract: In recent years, atmospheric ozone pollution has become more and more serious in many areas of China due to the rapid development of industrialization and urbanization. The increase in atmospheric ozone concentration will not only cause harm to the human respiratory tract, nervous system and immune system, but also cause obvious harm to crops, which will lead to reductions in crop production. Therefore, the study of atmospheric ozone pollution should not be ignored in research on the atmospheric environment. In this paper, we summarized the formation mechanisms of atmospheric ozone, the spatiotemporal distribution characteristics of atmospheric ozone in some areas of China, the relationship between atmospheric ozone and its precursors, and the main factors affecting the concentration of atmospheric ozone. Then, the control countermeasures against atmospheric ozone pollution were put forward in combination with the actual situation in China.

Keywords: atmospheric ozone pollution; spatiotemporal characteristics; precursors; influencing factors; prevention and control countermeasures

Citation: Yu, R.; Lin, Y.; Zou, J.; Dan, Y.; Cheng, C. Review on Atmospheric Ozone Pollution in China: Formation, Spatiotemporal Distribution, Precursors and Affecting Factors. *Atmosphere* **2021**, *12*, 1675. <https://doi.org/10.3390/atmos12121675>

Academic Editors: Duanyang Liu, Kai Qin and Honglei Wang

Received: 31 October 2021

Accepted: 7 December 2021

Published: 13 December 2021

Publisher's Note: MDPI stays neutral with regard to jurisdictional claims in published maps and institutional affiliations.



Copyright: © 2021 by the authors. Licensee MDPI, Basel, Switzerland. This article is an open access article distributed under the terms and conditions of the Creative Commons Attribution (CC BY) license (<https://creativecommons.org/licenses/by/4.0/>).

1. Introduction

Ozone (O₃) is one of the gas components in the atmosphere. More than 90% of all O₃ is concentrated in the stratosphere, and less than 10% is distributed in the troposphere [1]. As is known, the ozone layer in the stratosphere can protect life on Earth by absorbing most of ultraviolet radiation from the sun. However, O₃ in the troposphere is a secondary pollutant, which is the main driving force of atmospheric photochemical reactions and is one of the key factors in controlling atmospheric pollution [2]. As a characteristic product of photochemical smog, O₃ is a strong oxidant that can threaten human health and vegetation. Excessive inhalation of O₃ may cause respiratory infections, neurotoxic reactions or directly damage the human immune system [3]. High concentrations of O₃ can inhibit the growth of plants, resulting in a reduction in crop yields [4]. Furthermore, tropospheric O₃ is one of the most important greenhouse gases, and it may contribute to climate change. Therefore, tropospheric ozone pollution has attracted more and more attention, especially in recent years.

There are two main sources of tropospheric O₃. One is from stratosphere through the stratospheric–tropospheric exchange. In the stratosphere, oxygen molecules may absorb ultraviolet radiation with a wavelength of less than 240 nm and decompose into oxygen atoms, which can combine with oxygen molecules to form O₃, and this O₃ may be transmitted down to the troposphere and become the source of tropospheric O₃ [5]. The prospective O₃ transmission from stratosphere to troposphere was studied using the most advanced chemical–climate model, and the results showed that the global average annual mass fluxes of stratospheric O₃ into the troposphere were expected to increase by 53% from 2000 to 2100 [6]. It was reported that O₃ in the mid-latitude stratosphere would intrude into the lower troposphere due to the convective activities over the tropical Pacific [7]. Similar stratosphere–troposphere interactions have been observed over the

eastern Mediterranean [8,9]. Recent model studies and some studies based on observational constraints indicate that more than 10% of the ozone in the troposphere is transmitted from the stratosphere, while the rest is photochemically formed in the troposphere [10]. Previous observations indicate that the spring maximum in the lower troposphere over East Asia is contributed by stratospheric-to-tropospheric transport and regional photochemical O_3 production [11]. That is, the tropospheric O_3 can be generated by the photochemical reactions of primary pollutants such as volatile organic compounds (VOCs) and nitrogen oxides (NO_x , mainly including NO and NO_2). The main sources of NO_x in the troposphere are the combustion of coal, vehicle exhausts and the burning of other fossil fuels. VOCs come from a wide range of sources, including natural sources such as plant emissions, and anthropogenic sources such as biomass combustion, coal combustion, solvent usage, and the chemical industry [12]. Under strong sunlight, NO_2 may photolyze to generate atomic oxygen, which can react with oxygen molecules to generate ozone. The existence of massive VOCs in the air will hinder the decomposition of O_3 , resulting in tropospheric O_3 accumulation [13]. Primary pollutants such as NO_x and VOCs, as the precursors of O_3 , are closely related to the generation and change of tropospheric O_3 . Therefore, studying the correlation between O_3 and its precursors is helpful to understand the changing pattern of tropospheric O_3 pollution and to provide a scientific basis for creating effective measures to control the composite atmospheric pollution.

With the development of urbanization, industrialization, and traffic, tropospheric O_3 pollution has become increasingly serious in many areas of China. According to ozone observation data from 74 Chinese cities, the mean daily maximum 8 h average mass concentration of O_3 (O_3 -max-8 h) increased from $149 \mu g \cdot m^{-3}$ in 2013 to $161 \mu g \cdot m^{-3}$ in 2015 [14]. The atmospheric O_3 concentration has the characteristics of spatiotemporal distribution, and can be affected by factors such as the precursors and meteorological factors. In recent years, the frequency of photochemical smog and the concentration of atmospheric O_3 have been increasing year by year, which has increased the complexity of air pollution and the urgency of improving air quality. As a result, much attention has been paid to the formation mechanism of atmospheric O_3 , the pollution status and the influencing factors of tropospheric O_3 , and the sensitivity relationship between O_3 and its precursors, which has become one of the research topics of current atmospheric environmental science [15]. Therefore, the formation mechanism of tropospheric O_3 , the spatiotemporal distribution characteristics of tropospheric O_3 in some regions of China, the relationship between O_3 and its precursors, and the factors affecting tropospheric O_3 levels, were reviewed in this paper. Furthermore, some countermeasures for controlling tropospheric O_3 pollution were put forward based on the actual situation in China.

2. Photochemical Formation Mechanism of Tropospheric O_3

Most of the tropospheric O_3 is generated due to the photochemical reactions of some primary pollutants, such as NO_x and VOCs, under the strong sunlight in the troposphere. Some main reactions of the formation and loss mechanisms of tropospheric ozone are summarized in Table 1.

In the reactions in Table 1, R and M stand for organic group and other matters in the atmosphere, respectively. Tropospheric O_3 is formed by the photolysis of NO_2 , with the reactions R1 and R2 [16]. The three reactions from R1 to R3 constitute a rapid cyclic process, which can reach a dynamic equilibrium under certain conditions without causing an increase in the total amount of O_3 when no other chemical species are involved. However, in the atmosphere polluted by organic matter, peroxy radicals (such as $RO_2 \cdot$ and $HO_2 \cdot$) can replace the O_3 in reaction R3, so the conversion of NO to NO_2 does not need to consume O_3 , but the continuous reactions of R1 and R2 occur subsequently, thereby destroying the photochemical reaction cycle of NO_2 -NO- O_3 , resulting in the accumulation of O_3 . The rate of photochemical O_3 production is primarily determined by the reaction of NO with peroxy radicals such as $RO_2 \cdot$ and $HO_2 \cdot$, with the reactions of R4 and R5. Peroxy radicals

RO₂ and HO₂· can be produced by the reactions of ·OH with hydrocarbon (abbreviated as RH) and CO, with the reactions from R6 to R9.

Table 1. Main reactions of the formation and loss mechanisms of tropospheric ozone.

Reaction	Reaction Number
NO ₂ + hν (λ < 420 nm) → NO + O(³ P)	(R1)
O(³ P) + O ₂ + M → O ₃ + M	(R2)
NO + O ₃ → NO ₂ + O ₂	(R3)
RO ₂ + NO → RO + NO ₂	(R4)
HO ₂ + NO → NO ₂ + OH	(R5)
OH + RH → R + H ₂ O	(R6)
R + O ₂ + M → RO ₂ + M	(R7)
OH + CO → H + CO ₂	(R8)
H + O ₂ + M → HO ₂ + M	(R9)
O ₃ + hν → O ₂ + O(¹ D)	(R10)
O(¹ D) + H ₂ O → 2OH	(R11)
HONO + hν → OH + NO	(R12)
O ₃ + Olefins → products	(R13)
O ₃ + OH → HO ₂ + O ₂	(R14)
O ₃ + HO ₂ → OH + 2O ₂	(R15)

There is a series of chain reactions centered on various free radicals, resulting in the accumulation of O₃ [17]. In the clean troposphere, the ·OH radicals are mainly derived from the reaction of water vapor with O(¹D) atoms, which are usually produced by the photolysis of O₃, with the reactions R10–R11. In the polluted troposphere, the OH radicals are mainly formed from the photolysis of HONO, with reaction R12. At the same time, O₃ can be removed from the atmosphere by some reactions such as R3, R10 and R13–R15. Hence, the net generation rate of O₃ is equal to the total generation rate minus the removal rate. It was reported that the destruction of O₃ could occur in many ways, and the most important pathway is the surface deposition [18]. For example, O₃ consumption pathways can be achieved by oxidation of SO₂ in the liquid phase reaction. The rates of these reactions vary greatly depending on the meteorological and photolysis conditions, in addition to the rate of competitive transport and removal processes.

3. Spatiotemporal Distribution of Tropospheric Ozone in China

Tropospheric O₃ exhibits different characteristics in different regions. Understanding the spatiotemporal characteristics of O₃ concentration is essential for controlling atmospheric O₃ pollution. Since 2012, the Chinese government has included atmospheric O₃ as a regular pollutant monitoring indicator, and the national monitoring network has brought convenience to the study of the spatial and temporal characteristics of atmospheric O₃.

Most of Chinese population lives in the east of China, especially in the three most developed regions of Jing-Jin-Ji (JJJ, including Beijing, Tianjin, and Hebei province), Yangtze River Delta (YRD, including Shanghai, Zhejiang, Jiangsu, and Anhui provinces), and Pearl River Delta (PRD, including nine cities in south-central of Guangdong province). These regions are also the areas with the highest emissions of anthropogenic NO_x and VOCs, thus leading to serious regional atmospheric ozone pollution. Therefore, these regions are the key areas for preventing and controlling air pollution. Figure 1 shows the spatial distribution of annual average O₃-max-8 h in China from 2013 to 2018 [19]. The overall O₃ concentration presented a spatial distribution pattern of higher in the east and lower in the west. The high-value areas of O₃-max-8 h were mainly concentrated in the North China Plain in the east, such as Hebei province and Shandong province, where O₃-max-8 h was higher than 180 µg·m⁻³; followed by the Yangtze River Delta and its nearby areas with an O₃-max-8 h ranging from 120 to 160 µg·m⁻³. The O₃-max-8 h in the southern Pearl River Delta region was also in the range of 120 to 160 µg·m⁻³, but the high-value area was smaller than the Yangtze River Delta area. The O₃-max-8 h was lower in the western

region, ranging from 70 to 100 $\mu\text{g}\cdot\text{m}^{-3}$, and reaching as low as 62 $\mu\text{g}\cdot\text{m}^{-3}$ in the Hami area. The spatial distribution of O_3 -max-8 h was consistent with the distribution pattern of its precursor emissions. The NO_x emission intensity was higher in the east than that in the west, with the highest values distributing in the Beijing–Tianjin–Hebei region, Yangtze River Delta and Pearl River Delta. From 2013 to 2018, the 90th percentile of O_3 -max-8 h concentration in China gradually increased with an annual growth rate of 2.6 $\mu\text{g}\cdot\text{m}^{-3}$ per year. The highest O_3 -max-8 h ($\geq 180 \mu\text{g}\cdot\text{m}^{-3}$) zone mainly occurred in the North China and Yangtze River Plains, which gradually expanded in the North China Plain (NCP) while shrinking in the YRD and PRD.

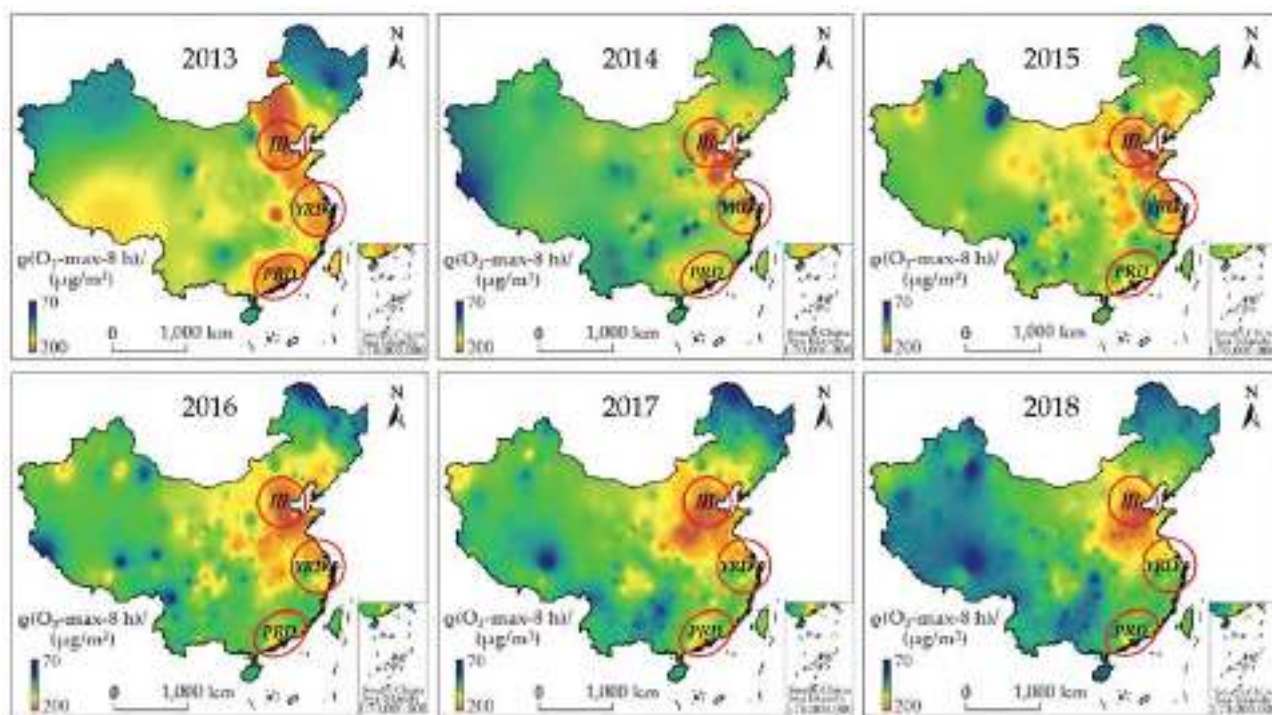


Figure 1. Spatial distribution of annual average O_3 -max-8 h in China from 2013 to 2018. Reprinted with a permission from ref. [19]. Copyright 2021 Li Ze Yuan.

Based on the data of ozone monitoring instruments (OMI) from 2005 to 2014, the tropospheric ozone trend in mid-eastern China (including 10 major cities) was studied [20]. The results showed that the mixing ratios of tropospheric ozone column were fairly stable, but those of ground-level clearly increased, by 12.38%. The concentration of ground-level ozone reached the maximum value from May to June, while the minimum value was from November to December. The concentrations of ground-level ozone increased with the cumulative increments of 6.3, 6.6, and 10.2 ppbv (parts per billion by volume) in Beijing, Shijiazhuang and Tianjin, respectively, from 2005 to 2014. Additionally, the concentration of ground-level ozone increased rapidly in Tianjin during 2012–2014, showing an increase of 13.25% compared with 2010–2011, which might be due to the more rubber and chemical companies around Tianjin. In contrast, the concentration of ground-surface O_3 in the Beijing area showed a slower rising trend from 2005 to 2014. According to previous studies, atmospheric O_3 pollution often appeared in the region of Beijing–Tianjin–Hebei, among which Beijing and Baoding were more polluted [21,22].

The temporal and spatial distribution characteristics of atmospheric O_3 in the Beijing–Tianjin–Hebei region during 2013–2015 indicated that O_3 concentration presented obvious seasonal variation, with the highest concentration in late spring and summer, and showed a single peak distribution during daytime, with the maximum value appearing around 15:00. In contrast, the concentration was lower and had little fluctuation throughout the

day in autumn and winter. The higher values of O₃-max-8 h were mainly distributed in north-central Beijing, Chengde and Hengshui [23]. The seasonal variations of tropospheric O₃ concentration distribution in Beijing, Shanghai, Guangzhou and Chengdu were similar, with the highest value generally occurring in summer and the lowest value generally appearing in winter [24]. Table 2 summarizes the tropospheric ozone concentrations in some regions of China.

Table 2. Summary of tropospheric ozone concentrations in some regions of China.

Region	Period	Maximum Value or Range (ppbv)	Precursors	Reference
Jing-Jin-Ji Urban Agglomeration	2013–2015	(O ₃ -8 h) 77.5–81 *		[23]
Jing-Jin-Ji region	January–December 2017	(O ₃ -1 h) 139.5		[22]
Chang Ping, Beijing	21 June–31 July 2005	(O ₃ -1 h) 286	VOCs (Alkenes, aromatics)	[25]
Beijing	2014–2017	(O ₃ -8 h) 98–103 *		[24]
Nantong, Jiangsu	2013–2015	(O ₃ -8 h) 83.5 *	CO, VOCs (propene, ethane, xylene, acetylene)	[26]
Taicang, Shanghai	4 May–1 June 2005	(O ₃ -1 h) 127	VOCs (Alkenes, aromatics)	[25]
Shanghai	2014–2017	(O ₃ -8 h) 76–94 *		[24]
Jiaxing, Zhejiang	27 June–31 August 2013	(O ₃ -1 h) 84 *	CO, NO ₂	[27]
Shouxian, Anhui	January 2015–December 2018	(Monthly mean) 51.3		[28]
Wan Qing Sha, Guangzhou	20 April–26 May 2004	(O ₃ -1 h) 178	VOCs (aromatics)	[25]
Guangzhou	2014–2017	(O ₃ -8 h) 76–85 *		[24]
Renshou Shan Park, Lanzhou	19 June–16 July 2006	(O ₃ -1 h) 143	VOCs (alkenes)	[25]
Shenyang, Liaoning	2013–2015	(O ₃ -8 h) 77 *	NO ₂ , CO	[29]
Jiangxi	January 2015–August 2017	(O ₃ -1 h) 40.5–70 *		[30]
Chengdu, Sichuan	January 2014–December 2016	(O ₃ -8 h) 2.5–146.5 *		[31]
Chengdu	2014–2017	(O ₃ -8 h) 68–94 *		[24]
Sichuan	July 2017	(O ₃ -8 h) 141.3 *	VOCs	[32]
NCP	June 2017	(O ₃ -1 h) 91 *		[33]

1. O₃-1 h: Maximum 1 h average; O₃-8 h: Maximum 8 h average. 2. Note: * For rough estimates from the literature.

The summer–winter differences are due to the general meteorological conditions including the variability of irradiation levels affecting free-tropospheric and boundary-layer photochemistry, which is also one of the main sources of the high background O₃ on the surface [9]. From 2013 to 2019, the weather in the North China Plain (NCP) drove an increase in surface O₃ [34]. The hot weather in the NCP in summer is usually driven by a wide range of anticyclone conditions, which is regarded as a typical climate pattern for the number of days of O₃ pollution [33]. The influence of the boundary layer on ozone in the summer afternoon cannot be ignored. Under the conditions of free convection, the stronger the ultraviolet radiation (UV), the higher the temperature, the lower the relative humidity (RH) and the higher the boundary-layer height (BLH), the more serious the ozone pollution was in Shijiazhuang in summer of 2018–2019 [35]. The increase in radiation during the day may cause the boundary layer to rise, and the accumulated O₃ may mix down to the boundary layer, affecting the near-surface ozone concentration. The history of the air mass is an important factor in determining the magnitude and potential signs of the impact of entrainment on surface O₃ through atmospheric boundary-layer growth [36]. As the height of the boundary layer increases, the O₃ in the residual layer (RL) is transported to the boundary layer. Some studies have found that the mixed ozone from the RL contributes 50–70% of the maximum concentration near the surface for the next day, and the rest comes from chemical production and possible advection [37,38].

Based on the tropospheric O₃ concentration data of 16 urban monitoring stations from June 2013 to May 2014, the spatiotemporal distribution characteristics of atmospheric O₃ in the Yangtze River Delta region were studied [27]. The results showed that the annual

average O₃ concentration was higher in the cities near the sea and lower in the cities that are inland. The concentration of atmospheric O₃ showed a seasonal variation, with higher concentration in summer and lower concentration in winter. The higher O₃ pollution area was located in the north of Hangzhou Bay in summer, while the higher O₃ pollution area was located in the eastern coastal zone in winter. The diurnal variation of O₃ concentration in the Yangtze River Delta was unimodal throughout the four seasons. The daily minimum O₃ concentration appeared around 06:00 in summer, and was delayed by about one hour in the other seasons, and the daily maximum O₃ concentration appeared around 15:00 in all seasons. Based on the OMI data, the spatiotemporal distribution of the tropospheric O₃ in the Yangtze River Delta region showed a significant zonal difference, increasing with latitude [39]. According to the monitoring data of 72 state-controlled stations in Jiangsu province from 2013 to 2015, the spatiotemporal distribution characteristics of tropospheric O₃ were studied [26]. The results indicated that the annual mean value of atmospheric O₃ in Jiangsu province showed a significant spatial difference, with the concentration gradually decreasing from coast to inland. Tropospheric O₃ showed the highest concentration in Yancheng city, while it was lower in Changzhou, eastern Wuxi and Xuzhou cities. The 90th percentile concentrations of O₃-8 h were significantly different from north to south. The atmospheric O₃ concentration was relatively higher in the cities of Nanjing, Yangzhou and Zhenjiang, while the lower concentrations were found in the cities of Xuzhou and Suqian. It was reported that the atmospheric O₃ peak occurred in the afternoon in Shanghai from 2006 to 2016 [2]. The areas with O₃ concentration exceeding the limit of Chinese national ambient air quality standards were mainly in the southwest suburbs of Shanghai, and the atmospheric O₃ concentration decreased from the southwest suburb to the northeast urban areas. It was reported that the tropospheric O₃ pollution in the Yangtze River Delta region was more serious in Shanghai, Ningbo and other cities [28]. It should be noted that the concentrations of near-ground-surface O₃ in Shanghai, Hangzhou, Hefei and Nanjing in the Yangtze River Delta region have increased slightly during the past 10 years (from 2005 to 2014), but the increase degree was smaller than that in the Beijing–Tianjin–Hebei region. The distribution of atmospheric O₃ pollution in the Yangtze River Delta showed relatively obvious flaky distribution characteristics, and the higher emissions from motor vehicles in the Yangtze River Delta urban cities were the main sources of atmospheric O₃ in this region [20].

The average near-ground-surface O₃ concentration in the Pearl River Delta region was slightly lower than those in the Beijing–Tianjin–Hebei region and the Yangtze River Delta region during 2013–2018 [19]. The characteristics of atmospheric O₃ pollution in the Pearl River Delta region and Guangdong province were reported based on the large-scale and long-term continuous O₃ monitoring data of recent years [40]. The results showed that the atmospheric O₃ concentration in the Pearl River Delta region was higher than that in the northwest of Guangdong province. Outside of the Pearl River Delta region, the eastern area of Guangdong province has the highest atmospheric O₃ level. The O₃ concentration was higher in the central southern part of the Pearl River Delta and the eastern part of Guangdong, while it was lower in the west. The concentration of atmospheric O₃ was higher in summer and autumn, and lower in winter and spring. Due to the large differences of the climate between the Pearl River Delta region and the Beijing–Tianjin–Hebei region and the Yangtze River Delta region, the better atmospheric diffusion conditions made it difficult for atmospheric O₃ to accumulate in the Pearl River Delta region.

In addition to the regions of Beijing–Tianjin–Hebei, the Yangtze River Delta and the Pearl River Delta, other regions in China have also been conducted research on local atmospheric O₃ pollution. The spatial and temporal distribution of atmospheric O₃ pollution in the Bohai Rim region of Liaoning province was reported [41]. The results showed that the atmospheric O₃ pollution presented obvious seasonal variation characteristics, and the main months in which the O₃ concentration exceeded the limit of Chinese national ambient air quality standards were from May to August. The diurnal variation of atmospheric O₃ was unimodal, and the peak concentration appeared in the afternoon. The higher O₃

concentration areas were mainly located in Yingkou in the central Bohai Sea Economic Rim of Liaoning, while the O₃ level was relatively lower in Dalian and Huludao. The investigation of atmospheric O₃ pollution in Shenyang area from 2013 to 2015 showed that the concentration of O₃ in the periphery of the city was higher than that in the center of the city [29]. Compared with the periphery of the city, the concentration of NO emissions is higher in urban centers. The increase in NO emissions leads to an increase in the titration of O₃, which inhibits the accumulation of O₃. The variation of O₃ concentration showed obvious seasonal characteristics, with the highest being in summer and the lowest in winter. The diurnal variation showed a unimodal distribution, with the trough value at 06:00 and the peak value at 14:00. Over continental sites, important nocturnal ozone destruction is observed due to dry deposition and NO titration [42]. The tropospheric O₃ concentrations showed significant “weekend effects”, with higher O₃ concentrations in weekends than in weekdays during the daytime while little difference at night. The spatiotemporal distribution characteristics of surface O₃ concentrations in Fujian province in 2016 was studied [43]. The results showed that the O₃ concentration was higher in spring and autumn, whereas it was lower in winter. The O₃ concentrations in the coastal cities were higher than those in the inland cities. The monthly changes in O₃ concentration presented a bimodal pattern, with peaks generally appearing in May and September. The diurnal variation curve of O₃ concentration was a single peak, which usually appeared at about 14:00. The spatiotemporal distribution characteristics of the atmospheric O₃ concentrations in Jiangxi province during 2015–2017 showed that the higher values of atmospheric O₃ were mainly distributed in the northeast areas such as Nanchang city and Jiujiang city, while the lower values were mainly distributed in the western areas such as Xinyu city and Yichun city [30]. The monthly variation of atmospheric O₃ concentration showed a double-peak pattern with higher values in May and September, while the daily variation showed a single-peak pattern with higher values at 14:00–16:00. The temporal characteristics of atmospheric O₃ pollution and the meteorological factors in Chengdu during 2014–2016 were reported, and the results showed that the situation of atmospheric O₃ pollution in Chengdu became worse in recent years [31]. The concentrations of atmospheric O₃ showed obvious seasonal variation characteristics—higher in summer and spring, while lower in winter and autumn. The diurnal variation of O₃ concentration showed a unimodal distribution, with the peak appearing at around 15:00, which was consistent with the diurnal variation of air temperature and solar irradiance. The distribution of surface O₃ in Chongqing city in 2018 showed that the O₃ concentration in spring to autumn exceeded the limit of Chinese national ambient air quality standards [44]. It was pointed out that the concentration of atmospheric O₃ was the highest and the pollution lasted for a long time in summer. Severe O₃ pollution in the Sichuan basin in summer was also reported [32].

For most urban stations, the potential ozone ($Ox = O_3 + NO_2$) is a conservative amount over a short time scale. When the freshly emitted NO reacts with O₃, NO₂ is formed in a few minutes, so some local NO₂ in the troposphere is produced at the expense of O₃ [45,46]. Generally, the surface ozone production is controlled by NO_x. The diurnal patterns of O₃ and nitrogen dioxide were opposite in Chengdu, indicating that the O₃ sensitivity was VOC-limited [32]. The relationship between atmospheric O₃ with non-methane hydrocarbons (NMHCs) and NO_x in Guangzhou in 2011 was discussed, and the results showed that controlling highly reactive NMHCs and NO_x could effectively reduce O₃ concentration [47]. It should be noted that the reduction in NO_x may have positive or negative impact on local ozone production. Ozone sensitivity was different at different stages, and reducing NO_x emissions had a negative impact on Shenzhen’s ozone pollution control from 2015 to 2018 [48].

4. Relationship between Tropospheric Ozone and Its Precursors

As mentioned before, tropospheric O₃ can be produced by photochemical reactions of VOCs, NO_x and other primary pollutants under solar radiation. Theoretically, the content of O₃ in the troposphere can be controlled by controlling the emission of VOCs

and NO_x. However, the execution difficulty is that the relationship between the generation of O₃ with VOCs and NO_x is nonlinear. An investigation into the relationship between the atmospheric O₃ with NO_x and VOCs showed that the formation of O₃ depended on NO_x in rural areas, while it depended on both NO_x and VOCs in urban areas [49]. A study on the formation of tropospheric O₃ and the effect of VOCs in Shanghai found that alkanes and aromatic hydrocarbons were the dominant VOCs, and aromatic hydrocarbons contributed most to the chemical production of atmospheric O₃ [50]. Similar results were found in Guangzhou, where aromatics accounted for 70% of the atmospheric O₃ formation potential (OFP) [51].

A numerical simulation control of atmospheric O₃ pollution was carried out in Shenzhen city based on the two-dimensional air-quality model [52]. The results showed that the generation of atmospheric O₃ was the product of the interaction between NO_x and VOCs, and the emission of VOCs was more important. The co-emission reduction in the precursors might effectively reduce the atmospheric O₃ pollution. As one of the major species of VOCs emitted from biogenic sources, isoprene is highly reactive and plays an important role in the generation of oxidants for a range of photochemical reactions. A study on the contribution of isoprene emissions to the ground-level O₃ formation in Beijing showed that isoprene emissions accounted for almost half (49.5%) of OFP at 13:00 in August of 2010, suggesting that isoprene played an important role in the ozone formation [53]. According to the results of field sampling, the most influential substances related to OFP in Zhengzhou urban area were ethanol, 2-hexanone, o-trimethylbenzene, and the industrial VOCs were a source of O₃ pollution in Zhengzhou [54]. It is reported that fire can affect NO_x, CO and VOCs, which will significantly affect the background value of O₃ [55].

Therefore, the prevention and control of atmospheric O₃ pollution cannot be simply through a programmed control of primary pollutants. The influence of VOCs and NO_x on atmospheric O₃ production can be characterized by a VOCs-sensitive zone and NO_x-sensitive zone [56]. In general, the oxidation of VOCs with high concentrations of VOCs can produce higher concentrations of RO₂·, and the emission of NO can lead to reaction R4 enhancement. Therefore, the amount of O₃ production increases with the increase in NO_x, and this type of O₃ generation mechanism is described as the NO_x-sensitive (limiting) type. When the concentration of NO_x is high and the concentration of VOCs is low, the reaction rate of NO + O₃ is faster than that of NO + RO₂·. In this case, the cumulative amount of O₃ may decrease with the increase in NO_x, and may increase with the increase in VOCs, hence this mechanism is described as VOC-sensitive (limiting) or NO_x saturation. When the generation of O₃ is restricted by VOCs, the O₃ generation can be controlled by reducing the emission of VOCs. Similarly, when the formation mechanism of O₃ is NO_x-limiting type, the O₃ content can be controlled by reducing the emission of NO_x. The sensitivity of summer O₃ in Beijing during 2010–2015 was studied [57]. The results showed that when VOCs/NO_x was 2.0, the urban areas were more sensitive to VOCs and high concentrations of VOCs persisted in western and northern rural areas. When VOCs/NO_x was 3.0–5.0, O₃ precursors aged, and lower VOCs concentrations appeared in the northern and southern suburbs. A comprehensive investigation into O₃ and its precursors and low tropospheric aerosols over a survey site located at the University of Chinese Academy of Sciences in Beijing showed that the photochemical generation of O₃ in the boundary layer was restricted by VOCs in hazy weather, while the photochemical reaction of O₃ became VOCs–NO_x-limiting in the clean weather [58]. According to the sensitivity analysis, the atmospheric O₃ generation was largely determined by VOCs when air masses came from the polluted areas in the south. Therefore, reducing VOCs emissions from the industrial areas and urbanized areas could help to reduce the ozone pollution at this site.

Currently, there are a variety of methods that can be used to study the sensitivity of atmospheric ozone generation. Some commonly used methods are as follows.

- (1) Ozone production efficiency (OPE, defined as the number of ozone molecules produced for each NO_x molecule oxidized). A lower OPE value (<4) indicates that the free radical cycling efficiency is lower, so VOCs are the limiting factor, and the

formation of O₃ is controlled by VOCs. Conversely, a higher OPE value (>7) indicates that the free radical cycling is efficient and the formation of O₃ is limited by NO_x. When the OPE value is medium (4–7), O₃ generation is controlled by both VOCs and NO_x. The OPE values in rural and suburban areas of Beijing were measured during the 2008 Olympics [59]. The results showed that higher OPE values corresponded to NO_x limiting under low NO_x conditions, whereas OPE values were lower under high NO_x conditions.

- (2) Relative incremental reactivity (RIR, defined as the ratio of the decrease in O₃ production rate to a given reduction in the precursor concentration) is a measure of the sensitivity of a single precursor. Cardelino et al. [60] first used a scenario test calculated by a box model to simulate the response of ozone to changes in precursors. The calculation result can be expressed by the following formula.

$$\text{RIR}(X) = \frac{\Delta\text{O}_3(X)/\text{O}_3}{\Delta C(X)/C(X)}$$

where X represents a group of major pollutants, and O₃ represents the modelled O₃ concentration. $\Delta C(X)/C(X)$ gives the relative change in the primary pollutants in one of the sensitivity tests, and the relative change in modelled ozone concentration is given by $\Delta\text{O}_3(X)/\text{O}_3$. In the study on atmospheric ozone pollution conducted in Chengdu in September 2016, the anthropogenic variation of the main pollutant in the sensitivity test was chosen as 20% in the RIR analysis, because when the variation value was greater than 20%, the RIR value deviated due to the significant change in the simulated free radical concentration [61]. The RIR results demonstrated that anthropogenic VOCs reduction is the most efficient way to mitigate ozone pollution, of which alkenes dominated more than 50% of the ozone production [61].

- (3) H₂O₂/HNO₃ ratio method. A ratio of 0.8–1.2 is used to separate NO_x-sensitive and VOC-sensitive regions. If the ratio is small, it can be considered as a sensitive area of VOCs, otherwise it is a sensitive area of NO_x. Based on this method, the urban areas were sensitive to VOCs while the rural areas were sensitive to NO_x in Hong Kong [62].
- (4) Empirical kinetic modelling approach (EKMA). The EKMA model can give the iso-line of O₃ maxima under different NO_x and VOCs due to photochemical reactions. The initial design was to simulate the maximum O₃ concentrations under different precursor emission scenarios to develop O₃-polluting precursor emission mitigation strategies [48]. The EKMA diagram illustrates the sensitivity of O₃ to VOCs and NO_x and how the ratio of VOCs/NO_x affects the production of O₃. The ridge line of the EKMA curve is formed by connecting the convex points of each curve. EKMA is divided into two parts: when the VOCs/NO_x ratio is located in the left of the ridge line, the O₃ formation is limited by VOCs, otherwise the O₃ formation is limited by NO_x [63]. The advantages of the EKMA curve method are as follows: Firstly, it can provide both a qualitative and quantitative basis for O₃ prevention and control; Secondly, it is a link between secondary and primary pollutants, which can better express the relationship between the two types of pollutants; Thirdly, the shape of EKMA will change under different conditions, which can better reflect the specific local conditions. For example, a Chinese EKMA was developed by following the traditional approach of constructing EKMA curves to explore the cost-effective emission reduction strategies for both O₃ and PM_{2.5}, suggesting that a strategy of “focusing on VOCs first, then NO_x” could be effective in controlling PM_{2.5} and O₃ pollution mitigation in the long term [64].

According to current research on atmospheric ozone formation regimes, most of the urban areas in China are in VOCs-limited zones, with anthropogenic VOCs (especially reactive aromatics and alkenes) playing a dominant role. However, some variations were found in the chemistry regime of atmospheric ozone formation in different regions.

5. Factors Affecting Atmospheric Ozone Level

5.1. Precursors

Photochemical reactions are the main source of tropospheric O_3 , whose concentration is closely related to the concentrations of NO_x and VOCs. Generally, the ozone concentration in urban and suburban areas is mainly affected by photochemistry. The transmission of the “aging” urban plume has resulted in extremely high O_3 levels (up to 286 ppbv) in rural sites downwind of Beijing, which are most affected by local photochemistry. In the suburbs of Shanghai, Guangzhou, and Lanzhou, strong in situ photochemical production is the main focus [25]. The characteristics of VOCs pollution and its contribution to atmospheric O_3 formation in Wuhan city was studied [65]. The results showed that the local pollution source was the main source of VOCs pollution, and olefins had the highest chemical activity and the biggest contribution to atmospheric O_3 . Based on the observed data of atmospheric O_3 and its precursors in Beijing in autumn 2004, the O_3 generation efficiency in the region near the main traffic lines was calculated, and the results suggested that the reduction in VOCs emission was beneficial to the reduction in atmospheric O_3 concentration [66]. Carbonyl compounds are important members of the VOCs family and are important precursors of secondary organic aerosols (SOA); alkenes, aromatics, and isoprene are primarily secondary products of carbonyl compounds; carbonyl groups are usually dominant in the formation of atmospheric O_3 in rural areas [67]. Biovolatile organic compounds (BVOCs) played an important role in the formation of tropospheric O_3 , especially in urban areas [68]. The effects of BVOCs emission on the formation of tropospheric O_3 and SOA were studied by using a WRF-CMAQ simulation system, and the results showed that the biogenic emission peaked in summer and decreased gradually from south China to north China [69]. High BVOCs emissions in eastern and southwestern China increased the ground-level ozone, particularly in the Beijing–Tianjin–Hebei region, Sichuan Basin, Yangtze River Delta and the central Pearl River Delta. The ozone isolines in the summer of 2013 showed that the O_3 concentrations were controlled by NO_x in most areas of China, and the effect of VOCs reduction on O_3 concentration was less, except in the urban areas of Shanghai and Guangzhou [70]. An investigation into the O_3 exposure indices and the source contributions in the forests of China throughout the entire year of 2013 suggested that the O_3 production was much more due to NO_x than due to VOCs [71].

5.2. Meteorological Factors

Tropospheric O_3 concentration was found to be positively correlated with ambient air temperature, and negatively correlated with wind speed and relative humidity. On the contrary, NO_x was positively correlated with relative humidity, and negatively correlated with temperature [72]. Under normal conditions, temperature can affect the concentration of O_3 by influencing the reaction rate, while wind speed can affect the dilution and diffusion of pollutants. Relative humidity has some influence on photochemical reaction processes, and higher relative humidity can cause wet deposition and even lead to the erosion of pollutants by rainwater. It was reported that aerosol could change the photolysis rate of trace gases [73]. Absorption of aerosols can reduce UV flux throughout the troposphere, resulting in a reduction in near-surface O_3 . Based on the analysis of the meteorological effect on atmospheric O_3 in Tianjin from 2009 to 2015, it was concluded that the tropospheric O_3 level was more dependent on temperature in the afternoon than in the morning since the daily maximum temperature usually occurred in the afternoon [74]. In spring and summer, the maximum daily O_3 was less dependent on the solar radiation than the ambient temperature. In autumn and winter, solar radiation played a more important role in determining O_3 level. The concentration of atmospheric O_3 had a weak negative correlation with the wind speed in spring, summer, and autumn, but a weak positive correlation with the wind speed in winter. Moisture in spring and autumn also had an effect on atmospheric O_3 concentration due to the compensation between water vapor and O_3 . Air with high humidity raised $\cdot OH$ radicals and produced higher O_3 concentration in the areas with high NO_x . At the same time, a rise in water vapor also consumed excited

oxygen atoms and increased the loss of O_3 . The relationship between heat waves and the concentration of atmospheric O_3 in the Yangtze River Delta was discussed [75]. The results showed that under the action of heat waves, the water vapor content and the cloud cover of the Yangtze River Delta were reduced because of the anticyclone controlled by the downdraft, which increased the concentration of atmospheric O_3 in the presence of intense solar radiation. In the case of climate warming, the chemical reaction may cause the atmospheric O_3 content to increase significantly, and the high temperature can also promote vertical turbulence and horizontal advection to some extent, which is beneficial to the removal of O_3 , but the extent is much less than that of the chemical action. Relevant studies have shown that the heat-island effect was directly or indirectly related to the increase in the emission of atmospheric O_3 and its precursors. The pollution of atmospheric O_3 in the Yangtze River Delta is becoming more and more serious, and the heat-island effect is the key factor affecting the atmospheric O_3 level. There was a positive correlation between heat-island effect and the atmospheric O_3 concentration in the Yangtze River Delta. The factors influencing the urban heat-island effect and atmospheric O_3 include landscape, topography and population, but land surface temperature and vegetation index are the most important [76]. It was reported that the structure and evolution of weather was of great significance to the atmospheric photochemical pollution [77]. The level of ozone concentration affected by the surface and the boundary layer depends on the main weather conditions that are conducive to large-scale subsidence [78]. The eastern and central basins of the Mediterranean have obvious top-down ozone deposition, which is caused by adiabatic convection over the Persian Gulf during the Indian monsoon season [79]. The influence of Asian continental outflow on the regional background ozone level in the northern South China Sea was studied, and the results indicated that the Asian continental outflows brought about by the winter monsoon could be immense, and intense enough to affect regions from far south, at latitudes similar to Antarctica [80].

5.3. Atmospheric Particulates

Aerosols are small particles suspended in the atmosphere and play an important role in the earth's radiation balance, air quality and cloud microphysics. They directly affect the regional and global climate by absorbing and scattering solar and terrestrial radiation, and indirectly affect the global climate by altering cloud formation characteristics. Ambient aerosol particles are mainly derived from anthropogenic activities and natural sources, such as residential heating, automobile exhausts, open-air combustion and volcanic activities [81]. The Asian monsoon brought in aerosols from biomass burning in southeast Asia, which were mixed with moist air particles in southern China, eventually reaching high aerosol concentrations in the spring, which reached the lowest concentration in winter [82]. There was a significant negative correlation between O_3 and particulate matter in the margin of Tarim Basin, indicating that the effect of dust on solar transmittance in the atmosphere lead to a decrease in net O_3 productivity [83]. The concentration of O_3 was influenced by the nonuniform chemical processes occurring on the surface of particles, so increasing the concentration of $PM_{2.5}$ could weaken the atmospheric radiation. This would allow the O_3 level to be suppressed by eliminating ultraviolet light, which was consistent with the conclusions of Wang et al. [22] and Qu et al. [84]. In 2017, 338 main cities in China were selected to sample ambient air for 365 days to compare the concentrations of O_3 , NO_2 , SO_2 , particulate matter and CO in the atmosphere [85]. The results showed that O_3 concentrations were significantly correlated with PM_{10} in 238 cities, among which, the coefficients in 142 cities were positive whereas those in 96 cities were negative. Most cities with positive correlations were mainly located in the south and northeast, while most cities with negative correlations were mainly located in the north of China. There was no significant correlation between O_3 concentration and PM_{10} concentration in 100 cities. O_3 concentrations were significantly correlated with $PM_{2.5}$ in 250 cities, among which, the coefficients in 117 cities were positive and those in 133 cities were negative. Most cities with positive correlations were mainly located in the south, while most cities with

negative correlations were mainly located in the north. There was no significant correlation between O_3 concentration and $PM_{2.5}$ concentration in 88 cities. The possible reason for the above results was that NO_x and VOCs would simultaneously increase significantly on the particulate matter (PM) pollution days in many cities, and the increase in these precursors influences the atmospheric O_3 concentration more than the particulates. Atmospheric O_3 was usually used as a tracer for photochemical reactions. A large amount of O_3 was used as an oxidant to enrich the secondary components of $PM_{2.5}$ through a secondary photochemical process, so higher $PM_{2.5}/PM_{10}$ usually indicated the existence of more active photochemical reactions. To some extent, $PM_{2.5}/PM_{10}$ could be used as a reference index for the types of air pollution, that is, higher or lower $PM_{2.5}/PM_{10}$ indicated the complicated pollution types related to photochemical reaction [86].

The main fixed sources of $PM_{2.5}$ and PM_{10} are smoke and dust produced by fuel combustion and gas oil during heating in industrial enterprises, such as power generation, oil and printing. The main moving source is exhaust gas emitted by road traffic vehicles into the atmosphere. The temporal characteristics of $PM_{2.5}$ in Anhui province showed that $PM_{2.5}$ decreased from January to July, and increased from July to December, that is, the concentrations of $PM_{2.5}$ were lower in summer and higher in winter [87]. Some studies showed that $PM_{2.5}$ and PM_{10} were positively correlated with NO_2 and CO, and weakly correlated with O_3 . The high concentration of O_3 in highly oxidized air in high-temperature seasons promoted the formation of secondary particulate matter, which made $PM_{2.5}$ positively correlated with O_3 [88]. Several studies have found that reducing $PM_{2.5}$ might lead to an increase in atmospheric O_3 , and reducing emissions of NO_x and VOCs is required to overcome this effect. A more important factor affecting O_3 trends in the North China Plain (NCP) from 2013 to 2017 was the reduction in $PM_{2.5}$, which slowed down the sink of hydroperoxy radicals, thus speeding up O_3 production [89]. In addition, atmospheric particles could directly affect the scattering and absorption of radiation, consequently changing the intensity of incident ultraviolet radiation, and affecting the production of O_3 . The formation of O_3 decreased with the decrease in UV radiation or light scattering associated with $PM_{2.5}$ [90].

5.4. Weekend Effect

The weekend effect refers to the phenomenon of different atmospheric pollutants concentration between weekends and weekdays, mainly caused by human activities. On weekdays, the main anthropogenic precursor emissions are due to commuting driving, especially during the day. However, on the weekends, the main anthropogenic precursors might come from family-related recreational activities. The difference in vehicle emissions between weekdays and weekends is mainly related to fuel combustion products, fuel consumption, and the traffic patterns of gasoline and diesel vehicles. Heavy-duty diesel vehicles are the main source of NO_x and black carbon (BC), while light-duty gasoline vehicles are the main source of CO_2 . In general, the diesel-fueled vehicles showed a significant reduction during weekends, resulting in a significant reduction in NO_x and BC emissions. If the atmospheric system was at nitrogen oxide saturation in urban areas, the reduction in NO_x emission on weekends may lead to a reduction in O_3 titrations, which can reduce the inhibition of O_3 formation, resulting in an increased O_3 concentration on weekends. The “ozone quenching hypothesis” and “ NO_x reduction hypothesis” in the weekend effect prove that NO_x plays a complex role in ozone production and termination [16]. The concentration of atmospheric O_3 increased from weekdays to weekends for a number of sites in the Northern Front Range metropolitan area (NFRMA) of Colorado, with weekend reductions in NO_2 at two sites in downtown Denver between 2000 and 2015, indicating that the region was in a NO_x -saturated ozone production regime [91]. Similar results were found in Shenyang city from 2013 to 2015 [29]. Koo et al. [92] investigated the weekend effect in the Midwest (north-central and northeast) of the United States in the summer of 2005, and the results showed that the reduction in O_3 on weekends depends on the increase in NO_x emissions leading to an increase in O_3 titration. The investigation of the

weekend effect on O₃ in Beijing in 2014 showed that the O₃ concentration at weekends was overall higher than that on weekdays, especially in urban centers [93]. The atmospheric O₃ generation might be limited by VOCs during summer, autumn and winter. However, the weekend O₃ concentration was lower than on the working days in spring, suggesting that O₃ production might be limited by NO_x in this season. On the urban scale, the weekend effect in the central area of the city was larger than that in the suburb, but on the local scale, the weekend effect showed a downward trend, with an increase in urbanization. Weekend O₃ changes depend on the intensity of the sunshine and the ratio of VOCs to NO_x emissions [94].

6. Prevention and Control Measures for Tropospheric Ozone Pollution

In a particular region, the level of tropospheric O₃ depends on meteorology and the interaction between O₃ precursors. The distinction of these impacts is important for evaluating the effectiveness of past emission reduction measures and clarifying the direction of future control plans [95]. In order to effectively reduce the tropospheric O₃ pollution, it is necessary to strengthen the prevention and control of corresponding pollutants.

- (1) The technology and energy structures should be improved, and the emissions of NO_x and highly reactive VOCs should be controlled. Pollution can be reduced by closing high-polluting factories, setting up coal-free zones, restricting vehicles, installing tailpipe cleaners and promoting the use of “three-way” catalytic converters. In addition, improving the fuel, changing the composition of gasoline, or using alternative fuels can reduce the pollution of tail gas.
- (2) The monitoring and management should be strengthened. Measures should be taken to avoid the occurrence of photochemical smog by using warnings issued from monitoring equipment. When oxidant concentrations reach dangerous levels, authorities should prohibit garbage incineration, reduce road vehicles or shut down some factories temporarily. Emissions from oil refineries, petrochemical plants and nitrogen fertilizer plants should be severely restricted by regulations. The VOCs from landfills have been reported to contribute to the formation of O₃ and photochemical smog [96]. Therefore, there is a need for integrated waste management policies, including source reduction and waste recovery, to reduce VOCs emissions.
- (3) The prevention and control of VOCs and NO_x pollution should be strengthened. The control measures should focus on the industries with relatively serious pollution, such as petrochemicals and printing. The comprehensive treatments for the waste gas produced by these processes should be strengthened. The waste-gas-containing pollutants should be centralized processing, and the treated tail gas should be recycled. The use of raw and auxiliary materials with low VOCs content and low reactivity should be promoted, and the production processes should be optimized as much as possible. The implementation of urban forest measures for O₃ should be undertaken in noncompliant areas, that is, the gradual replacement of high-BVOC-emission species with low-emission species, which can effectively control the emission of VOCs to reduce O₃ production [97]. Some regions have been effective in curbing O₃ pollution through synergistic control of VOCs and NO_x, but O₃ remains a problem in most places, especially in areas with high ozone pollution such as Beijing–Tianjin–Hebei, the Yangtze River Delta and the Pearl River Delta. Xiang et al. [64] pointed out that equally reducing NO_x and VOCs emissions in the initial stage may have the least benefit for air pollution improvement in Beijing–Tianjin–Hebei and the surrounding areas because the NO_x-focused strategies may exacerbate O₃ pollution. Emission reduction programs should be optimized in conjunction with short-term or long-term targets to control VOCs and NO_x emissions more scientifically.
- (4) O₃ pollution should be controlled in coordination with PM_{2.5}/PM₁₀. O₃ and PM_{2.5} co-pollution conditions occur under meteorological conditions of high relative humidity, high surface air temperature and low wind speed [98]. When PM_{2.5} and O₃ interact under different ambient meteorological conditions, it depends on the domi-

nant party. Tropospheric O₃ and particulate matter interact through aerosol formation, nonhomogeneous reactions on the surface of the particulate matter and changes in the aerosol-induced photolysis rate. The relationship between PM_{2.5}/PM₁₀ and the atmospheric ozone is therefore complex. High PM_{2.5}/PM₁₀ concentrations can affect the aerosol radiative effects and the surface inhomogeneous reactions, which are also influenced by different regions and meteorology, with long-range transport of air masses bringing about cross-regional pollution of PM_{2.5} and O₃ [99]. Long-term mitigation of PM_{2.5} and O₃ pollution control should be addressed by optimizing the zoning of prevention and control areas and implementing local and targeted measures. Predictive simulation models and representative regional monitoring networks should be developed, and synergistic mitigation strategies for PM_{2.5} and O₃ pollution should be explored. The effective synergistic control measures remain a difficult area for future research.

7. Summary and Recommendations

High ozone concentrations are harmful to humans and the ecological environment, and atmospheric ozone pollution is becoming a major environmental problem that has been plaguing the economic development in China. There are significant regional differences in the distribution of O₃-max-8 h in China. The overall level of O₃-max-8 h in the NCP is higher than that of other regions. Due to economic development and dense population, the eastern region has a higher level of O₃-max-8 h, and the high-value areas are distributed in flakes and bands. The high O₃-max-8 h areas are mainly concentrated in the Beijing–Tianjin–Hebei region, the Yangtze River Delta and the Pearl River Delta. In general, the tropospheric ozone concentration is higher in summer while lower in winter, and higher in coastal areas and lower inland. The concentration of tropospheric O₃ is related to its precursors, air temperature, solar radiation, air humidity, wind speed and the boundary-layer height. There is a highly nonlinear relationship between O₃ and its precursors (NO_x and VOCs), and the influencing mechanisms of NO_x and VOCs in different regions are quite different. Generally speaking, the rural area is controlled by NO_x and the urban area is controlled by VOCs. In addition, the influence of meteorological factors on tropospheric ozone concentration also has large regional differences. The control of atmospheric O₃ should, first of all, be at a specific location. Secondly, the control of atmospheric O₃ should be time-dependent, and largely depends on the meteorological conditions. Finally, in all cases, the optimal VOCs/NO_x ratio for controlling emissions should be studied in detail. Through the coordinated control of O₃ and other air pollution, such as PM_{2.5}/PM₁₀, we can realize people's high expectations of the air environment.

Author Contributions: Conceptualization, R.Y.; writing—original draft preparation, Y.L., J.Z.; writing—review and editing, R.Y., Y.L., C.C. and Y.D.; supervision, R.Y.; project administration, R.Y. All authors have read and agreed to the published version of the manuscript.

Funding: This research was funded by the National Natural Science Foundation of China (No. 21777049) and the Graduate Tutor Team Project in Fujian Province, China (418-50300012). The APC was funded by both of the projects.

Institutional Review Board Statement: Not applicable.

Informed Consent Statement: Not applicable.

Acknowledgments: We acknowledge Gongren Hu and Yu Yan for some comments on the manuscript as well as the anonymous reviewers and editors for helpful comments on the manuscript.

Conflicts of Interest: The authors declare no conflict of interest.

References

- Wang, Y.; Jiang, H.; Xiao, Z.; Zhang, X.; Zhou, G.; Yu, S. Extracting temporal and spatial distribution information about total ozone amount in China based on OMI satellite data. *Environ. Sci. Technol.* **2009**, *32*, 177–181. (In Chinese)
- Lin, Y.; Wang, Q.; Fu, Q.; Duan, Y.; Xu, J.; Liu, Q.; Li, F.; Huang, K. Temporal-spatial characteristics and impact factors of ozone pollution in Shanghai. *Environ. Monit. China* **2017**, *33*, 60–67. (In Chinese)
- Ou, H. Prevention and control of ozone pollution in ambient air. *Guangdong Chem. Ind.* **2019**, *46*, 113–114. (In Chinese)
- Cao, J.; Zhu, J.; Zeng, Q.; Li, C. Research advance in the effect of elevated O₃ on characteristics of photosynthesis. *J. Biol.* **2012**, *29*, 66–70. (In Chinese)
- Geng, F.; Liu, Q.; Chen, Y. Discussion on the research of Surface Ozone. *Desert Oasis Meteor.* **2012**, *6*, 8–14. (In Chinese)
- Meul, S.; Langematz, U.; Kröger, P.; Oberländer-Hayn, S.; Jöckel, P. Future changes in the stratosphere-to-troposphere ozone mass flux and the contribution from climate change and ozone recovery. *Atmos. Chem. Phys.* **2018**, *18*, 721–7738. [CrossRef]
- Lin, C.; Chang, C.; Chan, C.; Kuo, C.; Chen, W.; Chu, D.; Liu, S. Characteristics of springtime profiles and sources of ozone in the low troposphere over northern Taiwan. *Atmos. Environ.* **2010**, *44*, 182–193. [CrossRef]
- Gaudel, A.; Cooper, O.R.; Ancellet, G.; Barret, B.; Boynard, A.; Burrows, J.P.; Clerbaux, C.; Coheur, P.-F.; Cuesta, J.; Cuevas, E.; et al. Tropospheric Ozone Assessment Report: Present-day distribution and trends of tropospheric ozone relevant to climate and global atmospheric chemistry model evaluation. *Elem. Sci. Anth.* **2018**, *6*, 2–58. [CrossRef]
- Kalabokas, P.D.; Thouret, V.; Cammas, J.-P.; Volz-Thomas, A.; Boulanger, D.; Repapis, C.C. The geographical distribution of meteorological parameters associated with high and low summer ozone levels in the lower troposphere and the boundary layer over the eastern Mediterranean (Cairo case). *Tellus B* **2015**, *67*, 1–24. [CrossRef]
- Monks, P.S.; Archibald, A.T.; Colette, A.; Cooper, O.; Coyle, M.; Derwent, R.; Fowler, D.; Granier, C.; Law, K.S.; Mills, G.E.; et al. Tropospheric ozone and its precursors from the urban to the global scale from air quality to short-lived climate forcer. *Atmos. Chem. Phys.* **2015**, *15*, 8889–8973. [CrossRef]
- Dufour, G.; Eremenko, M.; Cuesta, J.; Doche, C.; Foret, G.; Beekmann, M.; Cheiney, A.; Wang, Y.; Cai, Z.; Liu, Y.; et al. Springtime daily variations in lower-tropospheric ozone over east Asia: The role of cyclonic activity and pollution as observed from space with IASI. *Atmos. Chem. Phys.* **2015**, *15*, 10839–10856. [CrossRef]
- Zheng, L.; Xu, T.; Chen, Z.; Wang, H. Characteristics and influencing factors of ozone pollution in summer in Chengdu. *J. Meteor. Environ.* **2019**, *35*, 78–84. (In Chinese)
- Liu, F.; Xu, Y. Review of surface ozone modeling system. *Environ. Monit. China* **2017**, *33*, 1–15. (In Chinese)
- Wang, T.; Xue, L.; Brimblecombe, P.; Lam, Y.F.; Li, L.; Zhang, L. Ozone pollution in China: A review of concentrations, meteorological influences, chemical precursors, and effects. *Sci. Total Environ.* **2017**, *575*, 1582–1596. [CrossRef] [PubMed]
- Duan, Y.; Zhang, Y.; Wang, D.; Xu, J.; Wei, H.; Cui, H. Spatial-temporal patterns analysis of ozone pollution in several cities of China. *Admin. Tech. Environ. Monit.* **2011**, *23*, 34–39. (In Chinese)
- Sadanaga, Y.; Sengen, M.; Takenaka, N.; Bandow, H. Analyses of the ozone weekend effect in Tokyo, Japan: Regime of oxidant (O₃ + NO₂) production. *Aerosol Air Qual. Res.* **2012**, *12*, 161–168. [CrossRef]
- Bowman, F.M.; Seinfeld, J.H. Ozone productivity of atmospheric organics. *J. Geophys. Res.* **1994**, *99*, 5309–5324. [CrossRef]
- Abdul-Wahab, S.A.; Bakheit, C.S.; Al-Alawi, S.M. Principal component and multiple regression analysis in modelling of ground-level ozone and factors affecting its concentrations. *Environ. Model. Softw.* **2005**, *20*, 1263–1271. [CrossRef]
- Li, Z.; Yang, L.; Hua, D.; Fang, J.; Huang, W.; Sun, L.; Wang, C. Spatial pattern of surface ozone and its relation with meteorological variables in China during 2013–2018. *Res. Environ. Sci.* **2021**, *34*, 2094–2104. Available online: <https://doi.org/10.13198/j.issn.1001-6929.2021.06.16> (accessed on 28 November 2021). (In Chinese).
- Liu, X.; Lou, S.; Chen, Y.; Liu, Q.; Wang, J.; Shan, Y.; Huang, S.; Du, H. Spatiotemporal distribution of ground-level ozone in mid-east China based on OMI observations. *Acta Sci. Circumstantiae* **2016**, *36*, 2811–2818. (In Chinese)
- Jiang, L.; Bai, L. Spatio-temporal characteristics of urban air pollutions and their causal relationships: Evidence from Beijing and its neighboring cities. *Sci. Rep.* **2018**, *8*, 1279. [CrossRef] [PubMed]
- Wang, Z.; Li, J.; Liang, L. Spatio-temporal evolution of ozone pollution and its influencing factors in the Beijing-Tianjin-Hebei urban agglomeration. *Environ. Pollut.* **2020**, *256*, 113419. [CrossRef] [PubMed]
- Cheng, L.; Wang, S.; Gong, Z.; Yang, Q.; Wang, Y. Pollution trends of ozone and its characteristics of temporal and spatial distribution in Beijing-Tianjin-Hebei region. *Environ. Monit. China* **2017**, *33*, 14–21. (In Chinese)
- Zhang, Q.; Zhang, X. Ozone spatial-temporal distribution and trend over China since 2013: Insight from satellite and surface observation. *Environ. Sci.* **2019**, *40*, 1132–1142. (In Chinese)
- Xue, L.; Wang, T.; Gao, J.; Ding, A.; Zhou, X.; Blake, D.R.; Wang, X.; Saunders, S.M.; Fan, S.; Zuo, H.; et al. Ground-level ozone in four Chinese cities: Precursors, regional transport and heterogeneous processes. *Atmos. Chem. Phys.* **2014**, *14*, 13175–13188. [CrossRef]
- Xia, S.; Zhao, Q.; Liu, Q. Pollution characteristics of ozone and impacts of its precursors in Jiangsu Province. *Environ. Sci. Technol.* **2018**, *41*, 96–100. (In Chinese)
- Liu, Z.; Xie, X.; Xie, M.; Wang, T.; Zhu, X.; Ouyang, Y.; Feng, W.; Zhun, K.; Shu, L. Spatial-temporal distribution of ozone pollution over Yangtze River Delta region. *J. Ecol. Rural Environ.* **2016**, *32*, 445–450. (In Chinese)


28. Duan, Z.; Yang, Y.; Wang, L.; Liu, C.; Fan, S.; Chen, C.; Tong, Y.; Lin, X.; Gao, Z. Temporal characteristics of carbon dioxide and ozone over a rural-cropland area in the Yangtze River Delta of eastern China. *Sci. Total Environ.* **2021**, *757*, 143750. [CrossRef] [PubMed]
29. Liu, M.; Wang, C.; Hou, L.; Yu, X.; Lin, H. Spatial-temporal patterns and variation trend of ozone pollution in Shenyang. *Environ. Monit. China* **2017**, *33*, 126–131. (In Chinese)
30. Chai, M.; Luo, Y.; Shang, J.; Wang, F.; Liu, M. Pollution status of ozone and its characteristics of temporal and spatial distribution in the cities of Jiangxi province. *Jiangxi Sci.* **2018**, *36*, 95–100. (In Chinese)
31. Wu, K.; Kang, P.; Wang, Z.; Gu, S.; Tie, X.; Zhang, Y.; Wen, X.; Wang, S.; Chen, Y.; Wang, Y.; et al. Ozone temporal variation and its meteorological factors over Chengdu City. *Acta Sci. Circumstantiae* **2017**, *37*, 4241–4252. (In Chinese)
32. Yang, X.; Wu, K.; Wang, H.; Liu, Y.; Gu, S.; Lu, Y.; Zhang, X.; Hu, Y.; Ou, Y.; Wang, S.; et al. Summertime ozone pollution in Sichuan Basin, China: Meteorological conditions, sources and process analysis. *Atmos. Environ.* **2020**, *226*, 117392. [CrossRef]
33. Gong, C.; Liao, H. A typical weather pattern for ozone pollution events in North China. *Atmos. Chem. Phys.* **2019**, *19*, 13725–13740. [CrossRef]
34. Li, K.; Jacob, D.J.; Shen, L.; Lu, X.; De Smedt, I.; Liao, H. Increases in surface ozone pollution in China from 2013 to 2019: Anthropogenic and meteorological influences. *Atmos. Chem. Phys.* **2020**, *20*, 11423–11433. [CrossRef]
35. Tang, G.; Liu, Y.; Huang, X.; Wang, Y.; Hu, B.; Zhang, Y.; Song, T.; Li, X.; Wu, S.; Li, Q.; et al. Aggravated ozone pollution in the strong free convection boundary layer. *Sci. Total Environ.* **2021**, *788*, 147740. [CrossRef]
36. Kaser, L.; Patton, E.G.; Pfister, G.G.; Weinheimer, A.J.; Montzka, D.D.; Flocke, F.; Thompson, A.M.; Stauffer, R.M.; Halliday, H.S. The effect of entrainment through atmospheric boundary layer growth on observed and modeled surface ozone in the Colorado Front Range. *J. Geophys. Res.* **2017**, *122*, 6075–6093. [CrossRef]
37. Neu, U.; Künzle, T.; Wanner, H. On the relation between ozone storage in the residual layer and daily variation in near-surface ozone concentration—A case study. *Bound. Layer Meteorol.* **1994**, *69*, 221–247. [CrossRef]
38. Zhao, W.; Tang, G.; Yu, H.; Yang, Y.; Wang, Y.; Wang, L.; An, J.; Gao, W.; Hu, B.; Cheng, M.; et al. Evolution of boundary layer ozone in Shijiazhuang, suburban site on the North China plain. *J. Environ. Sci.* **2019**, *83*, 152–160. [CrossRef]
39. Shan, Y.; Li, L.; Liu, Q.; Qin, Y.; Chen, Y.; Shi, Y.; Liu, X.; Wang, H.; Ling, Y. Spatial-temporal distribution of ozone and its precursors in typical cities in the Yangtze River Delta. *Desert Oasis Meteor.* **2016**, *10*, 72–78. (In Chinese)
40. Shen, J.; Huang, X.; Wang, Y.; Ye, S.; Pan, Y.; Chen, D.; Chen, H.; Ou, Y.; Lv, X.; Wang, Z. Study on ozone pollution characteristics and source apportionment in Guangdong Province. *Acta Sci. Circumstantiae* **2017**, *37*, 4449–4457. (In Chinese)
41. Liu, S.; Wang, D.; Chen, Z.; Bai, L.; Zhang, J.; Huang, Y. Analysis on the characteristics and trend of ozone pollution in Circum-Bohai-Sea zone. *Environ. Sci. Technol.* **2018**, *41*, 257–262. (In Chinese)
42. Ding, A.; Wang, T.; Thouret, V.; Cammas, J.-P.; Nédélec, P. Tropospheric ozone climatology over Beijing: Analysis of aircraft data from the MOZAIC program. *Atmos. Chem. Phys.* **2008**, *8*, 1–13. [CrossRef]
43. Wang, H.; Jiang, D.; Xie, Z.; Zheng, Q.; Yang, Y. The Spatial and temporal distribution and synoptic causes of surface layer ozone in Fujian province. *Mid-Low Latit. Mt. Meteorol.* **2018**, *142*, 1–6. (In Chinese)
44. He, T.; He, S.; Kuang, S.; Jia, J. Design of temporal-spatial distribution feature extraction system for ozone pollution in different seasons. *Environ. Sci. Manag.* **2019**, *44*, 110–115. (In Chinese)
45. Kley, D.; Geiss, H.; Mohnen, V.A. Tropospheric ozone at elevated sites and precursor emissions in the United States and Europe. *Atmos. Environ.* **1994**, *28*, 140–158. [CrossRef]
46. Kalabokas, P.D.; Viras, L.G.; Bartzis, J.G.; Repapis, C.C. Mediterranean rural ozone characteristics around the urban area of Athens. *Atmos. Environ.* **2000**, *34*, 5199–5208. [CrossRef]
47. Zou, Y.; Charlesworth, E.; Yin, C.; Yan, X.; Deng, X.; Li, F. The weekday/weekend ozone differences induced by the emissions change during summer and autumn in Guangzhou, China. *Atmos. Environ.* **2019**, *199*, 114–126. [CrossRef]
48. Yu, D.; Tan, Z.; Lu, K.; Ma, X.; Li, X.; Chen, S.; Zhu, B.; Lin, L.; Li, Y.; Qiu, P.; et al. An explicit study of local ozone budget and NO_x-VOCs sensitivity in Shenzhen China. *Atmos. Environ.* **2020**, *224*, 117304. [CrossRef]
49. Sillman, S.; Logan, J.A.; Wofsy, S.C. The sensitivity of ozone to nitrogen oxides and hydrocarbons in regional ozone episodes. *J. Geophys. Res.* **1990**, *95*, 1837–1851. [CrossRef]
50. Geng, F.; Zhao, C.; Tang, X.; Lu, G.; Tie, X. Analysis of ozone and VOCs measured in Shanghai: A case study. *Atmos. Environ.* **2007**, *41*, 989–1001. [CrossRef]
51. Tan, Z.; Lu, K.; Jiang, M.; Su, R.; Wang, H.; Lou, S.; Fu, Q.; Zhai, C.; Tan, Q.; Yue, D.; et al. Daytime atmospheric oxidation capacity in four Chinese megacities during the photochemically polluted season: A case study based on box model simulation. *Atmos. Chem. Phys.* **2019**, *19*, 3493–3513. [CrossRef]
52. Yan, M.; Yin, K.; Liang, Y.; Zhuang, Y.; Liu, B.; Li, J.; Liu, Z. Ozone Pollution in Summer in Shenzhen City. *Res. Environ. Sci.* **2012**, *25*, 411–418. (In Chinese)
53. Mo, Z.; Shao, M.; Wang, W.; Liu, Y.; Wang, M.; Lu, S. Evaluation of biogenic isoprene emissions and their contribution to ozone formation by ground-based measurements in Beijing, China. *Sci. Total Environ.* **2018**, *627*, 1485–1494. [CrossRef]
54. Zhang, Y.; Li, C.; Yan, Q.; Han, S.; Zhao, Q.; Yang, L.; Liu, Y.; Zhang, R. Typical industrial sector-based volatile organic compounds source profiles and ozone formation potentials in Zhengzhou, China. *Atmos. Pollut. Res.* **2020**, *11*, 841–850. [CrossRef]
55. Lapina, K.; Honrath, R.E.; Owen, R.C.; Martín, M.V.; Pfister, G. Evidence of significant large-scale impacts of boreal fires on ozone levels in the midlatitude Northern Hemisphere free troposphere. *Geophys. Res. Lett.* **2006**, *33*, L10815. [CrossRef]

56. Walaszek, K.; Kryza, M.; Werner, M. The role of precursor emissions on ground level ozone concentration during summer season in Poland. *J. Atmos. Chem.* **2018**, *75*, 181–204. [CrossRef]
57. Wei, W.; Li, Y.; Ren, Y.; Cheng, S.; Han, L. Sensitivity of summer ozone to precursor emission change over Beijing during 2010–2015: A WRF-Chem modeling study. *Atmos. Environ.* **2019**, *218*, 116984. [CrossRef]
58. Chi, X.; Liu, C.; Xie, Z.; Fan, G.; Wang, Y.; He, P.; Fan, S.; Hong, Q.; Wang, Z.; Yu, X.; et al. Observations of ozone vertical profiles and corresponding precursors in the low troposphere in Beijing, China. *Atmos. Res.* **2018**, *213*, 224–235. [CrossRef]
59. Wang, T.; Nie, W.; Gao, J.; Xue, L.; Gao, X.; Wang, X.; Qiu, J.; Poon, C.; Meinardi, S.; Blake, D.; et al. Air quality during the 2008 Beijing Olympics: Secondary pollutants and regional impact. *Atmos. Chem. Phys.* **2010**, *10*, 7603–7615. [CrossRef]
60. Cardelino, C.A.; Chameides, W.L. An observation-based model for analyzing ozone precursor relationships in the urban atmosphere. *J. Air Waste Manag. Assoc.* **1995**, *45*, 161–180. [CrossRef]
61. Tan, Z.; Lu, K.; Jiang, M.; Su, R.; Dong, H.; Zeng, L.; Xie, S.; Tan, Q.; Zhang, Y. Exploring ozone pollution in Chengdu, southwestern China: A case study from radical chemistry to O₃-VOC-NO_x sensitivity. *Sci. Total Environ.* **2018**, *636*, 775–786. [CrossRef]
62. Lam, K.; Wang, T.; Wu, C.; Li, Y. Study on an ozone episode in hot season in Hong Kong and transboundary air pollution over Pearl River Delta region of China. *Atmos. Environ.* **2005**, *39*, 1967–1977. [CrossRef]
63. Jiang, M.; Lu, K.; Su, R.; Tan, Z.; Wang, H.; Li, L.; Fu, Q.; Zhai, C.; Tan, Q.; Yue, D.; et al. Ozone formation and key VOCs in typical Chinese city clusters. *Chin. Sci. Bull.* **2018**, *63*, 1130–1141. (In Chinese) [CrossRef]
64. Xiang, S.; Liu, J.; Tao, W.; Yi, K.; Xu, J.; Hu, X.; Liu, H.; Wang, Y.; Zhang, Y.; Yang, H.; et al. Control of both PM_{2.5} and O₃ in Beijing-Tianjin-Hebei and the surrounding areas. *Atmos. Environ.* **2020**, *224*, 117259. [CrossRef]
65. Hui, L.; Liu, X.; Tan, Q.; Feng, M.; An, J.; Qu, Y.; Zhang, Y.; Jiang, M. Characteristics, source apportionment and contribution of VOCs to ozone formation in Wuhan, central China. *Atmos. Environ.* **2018**, *192*, 55–71. [CrossRef]
66. An, J. Ozone production efficiency in Beijing area with high NO_x emissions. *Acta Sci. Circumstantiae* **2006**, *26*, 652–657. (In Chinese)
67. Zhang, Y.; Xue, L.; Dong, C.; Wang, T.; Mellouki, A.; Zhang, Q.; Wang, W. Gaseous carbonyls in China's atmosphere: Tempo-spatial distributions, sources, photochemical formation, and impact on air quality. *Atmos. Environ.* **2019**, *214*, 116863. [CrossRef]
68. Liu, Y.; Li, L.; An, J.; Huang, L.; Yan, R.; Huang, C.; Wang, H.; Wang, Q.; Wang, M.; Zhang, W. Estimation of biogenic VOC emissions and its impact on ozone formation over the Yangtze River Delta region, China. *Atmos. Environ.* **2018**, *186*, 113–128. [CrossRef]
69. Wu, K.; Yang, X.; Chen, D.; Gu, S.; Lu, Y.; Jiang, Q.; Wang, K.; Ou, Y.; Qian, Y.; Shao, P.; et al. Estimation of biogenic VOC emissions and their corresponding impact on ozone and secondary organic aerosol formation in China. *Atmos. Res.* **2020**, *231*, 104656. [CrossRef]
70. Guo, H.; Chen, K.; Wang, P.; Hu, J.; Ying, Q.; Gao, A.; Zhang, H. Simulation of summer ozone and its sensitivity to emission changes in China. *Atmos. Pollut. Res.* **2019**, *10*, 1543–1552. [CrossRef]
71. Qiao, X.; Wang, P.; Zhang, J.; Zhang, H.; Tang, Y.; Hu, J.; Ying, Q. Spatial-temporal variations and source contributions to forest ozone exposure in China. *Sci. Total Environ.* **2019**, *674*, 189–199. [CrossRef]
72. Reddy, B.S.K.; Kumar, K.R.; Balakrishnaiah, G.; Gopal, K.R.; Reddy, R.R.; Sivakumar, V.; Lingaswamy, A.P.; Arafath, S.M.; Umadevi, K.; Kumari, S.P.; et al. Analysis of diurnal and seasonal behavior of surface ozone and its precursor (NO_x) at a semi-arid rural site in Southern India. *Aerosol Air Qual. Res.* **2012**, *12*, 1081–1094. [CrossRef]
73. Nishanth, T.; Prasad, K.M.; Satheesh, K.M.K.; Valsaraj, K.T. Influence of ozone precursors and PM₁₀ on the variation of surface O₃ over Kannur, India. *Atmos. Res.* **2014**, *138*, 112–124. [CrossRef]
74. Yang, J.; Liu, J.; Han, S.; Yao, Q.; Cai, Z. Study of the meteorological influence on ozone in urban areas and their use in assessing ozone trends in all seasons from 2009 to 2015 in Tianjin, China. *Meteorol. Atmos. Phys.* **2019**, *131*, 1661–1675. [CrossRef]
75. Pu, X.; Wang, T.; Huang, X.; Melas, D.; Zanis, P.; Papanastasiou, D.K.; Poupkou, A. Enhanced surface ozone during the heat wave of 2013 in Yangtze River Delta region, China. *Sci. Total Environ.* **2017**, *603–604*, 807–816. [CrossRef]
76. Wang, Y.; Du, H.; Xu, Y.; Lu, D.; Wang, X.; Guo, Z. Temporal and spatial variation relationship and influence factors on surface urban heat island and ozone pollution in the Yangtze River Delta, China. *Sci. Total Environ.* **2018**, *631–632*, 921–933. [CrossRef] [PubMed]
77. Tang, G.; Li, X.; Wang, X.; Xin, J.; Hu, B.; Wang, L.; Ren, Y.; Wang, Y. Effect of synoptic type on surface ozone pollution in Beijing. *Environ. Sci.* **2010**, *31*, 73–578. (In Chinese)
78. Kalabokas, P.D.; Cammas, J.-P.; Thouret, V.; Volz-Thomas, A.; Boulanger, D.; Repapis, C.C. Examination of the atmospheric conditions associated with high and low summer ozone levels in the lower troposphere over the Eastern Mediterranean. *Atmos. Chem. Phys.* **2013**, *13*, 10339–10352. [CrossRef]
79. Doche, C.; Dufour, G.; Foret, G.; Eremenko, M.; Cuesta, J.; Beekmann, M.; Kalabokas, P. Summertime tropospheric-ozone variability over the Mediterranean basin observed with IASI. *Atmos. Chem. Phys.* **2014**, *14*, 10589–10600. [CrossRef]
80. Ou-Yang, C.; Hsieh, H.; Wang, S.; Lin, N.; Lee, C.; Sheu, G.; Wang, J. Influence of Asian continental outflow on the regional background ozone level in northern South China Sea. *Atmos. Environ.* **2013**, *78*, 144–153. [CrossRef]
81. Li, Y.; Xue, Y.; Guang, J.; Leeuw, G.; Self, R.; She, L.; Fan, C.; Xie, Y.; Chen, G. Spatial and temporal distribution characteristics of haze days and associated factors in China from 1973 to 2017. *Atmos. Environ.* **2019**, *214*, 116862. [CrossRef]
82. Zhang, M.; Wang, Y.; Ma, Y.; Wang, L.; Gong, W.; Liu, B. Spatial distribution and temporal variation of aerosol optical depth and radiative effect in South China and its adjacent area. *Atmos. Environ.* **2018**, *188*, 120–128. [CrossRef]

83. Yu, H.; Yang, W.; Wang, X.; Yin, B.; Zhang, X.; Wang, J.; Gu, C.; Ming, J.; Geng, C.; Bai, Z. A seriously sand storm mixed air-polluted area in the margin of Tarim Basin: Temporal-spatial distribution and potential sources. *Sci. Total Environ.* **2019**, *676*, 436–446. [CrossRef] [PubMed]
84. Qu, Y.; Wang, T.; Wu, H.; Shu, L.; Li, M.; Chen, P.; Zhao, M.; Li, S.; Xie, M.; Zhang, B.; et al. Vertical structure and interaction of ozone and fine particulate matter in spring at Nanjing, China: The role of aerosol's radiation feedback. *Atmos. Environ.* **2020**, *222*, 117162. [CrossRef]
85. Wang, Z.; Lv, J.; Tan, Y.; Guo, M.; Gu, Y.; Xu, S.; Zhou, Y. Temporospatial variations and Spearman correlation analysis of ozone concentrations to nitrogen dioxide, sulfur dioxide, particulate matters and carbon monoxide in ambient air, China. *Atmos. Pollut. Res.* **2019**, *10*, 1203–1210. [CrossRef]
86. Fang, X.; Fan, Q.; Liao, Z.; Xie, J.; Xu, X.; Fan, S. Spatial-temporal characteristics of the air quality in the Guangdong-Hong Kong-Macau Greater Bay Area of China during 2015–2017. *Atmos. Environ.* **2019**, *210*, 14–34. [CrossRef]
87. Qiu, Y.; Wang, J.; Hu, S. Spatial and temporal distribution of PM_{2.5} and PM_{10-2.5} in Anhui province, 2015–2016. *J. Hefei Univ. Technol. Nat. Sci.* **2020**, *43*, 113–118. (In Chinese)
88. Jia, M.; Zhao, T.; Cheng, X.; Gong, S.; Zhang, X.; Tang, L.; Liu, D.; Wu, X.; Wang, L.; Chen, Y. Inverse relations of PM_{2.5} and O₃ in air compound pollution between cold and hot seasons over an urban area of East China. *Atmosphere* **2017**, *8*, 59. [CrossRef]
89. Li, K.; Jacob, D.J.; Liao, H.; Shen, L.; Zhang, Q.; Bates, K.H. Anthropogenic drivers of 2013–2017 trends in summer surface ozone in China. *Proc. Natl. Acad. Sci. USA* **2019**, *116*, 422–427. [CrossRef]
90. Dickerson, R.R.; Kondragunta, S.; Stenchikov, G.; Civerolo, K.L.; Doddridge, B.G.; Holben, B.N. The impact of aerosols on solar ultraviolet radiation and photochemical smog. *Science* **1997**, *278*, 827–830. [CrossRef]
91. Andrew, J.A.; Farmer, D.K. Summer ozone in the northern Front Range metropolitan area: Weekend–weekday effects, temperature dependences, and the impact of drought. *Atmos. Chem. Phys.* **2017**, *17*, 6517–6529. [CrossRef]
92. Koo, B.; Jung, J.; Pollack, A.K.; Lindhjem, C.; Jimenez, M.; Yarwood, G. Impact of meteorology and anthropogenic emissions on the local and regional ozone weekend effect in Midwestern US. *Atmos. Environ.* **2012**, *57*, 13–21. [CrossRef]
93. Zhao, X.; Zhou, W.; Han, L. Human activities and urban air pollution in Chinese mega city: An insight of ozone weekend effect in Beijing. *Phys. Chem. Earth* **2019**, *110*, 109–116. [CrossRef]
94. Kannari, A.; Ohara, T. Theoretical implication of reversals of the ozone weekend effect systematically observed in Japan. *Atmos. Chem. Phys.* **2010**, *10*, 6765–6776. [CrossRef]
95. Fadnavis, S.; Chakraborty, T.; Beig, G. Seasonal stratospheric intrusion of ozone in the upper troposphere over India. *Ann. Geophys.* **2010**, *28*, 2149–2159. [CrossRef]
96. Ding, Y.; Cai, C.; Hu, B.; Xu, Y.; Zheng, X.; Chen, Y.; Wu, W. Characterization and control of odorous gases at a landfill site: A case study in Hangzhou, China. *Waste Manag.* **2012**, *32*, 317–326. [CrossRef]
97. Taha, H.; Wilkinson, J.; Bornstein, R.; Xiao, Q.; McPherson, G.; Simpson, J.; Anderson, C.; Lau, S.; Lam, J.; Blain, C. An urban-forest control measure for ozone in the Sacramento, CA Federal Non-Attainment Area (SFNA). *Sustain. Cities Soc.* **2016**, *21*, 51–65. [CrossRef]
98. Dai, H.; Zhu, J.; Liao, H.; Li, J.; Liang, M.; Yang, Y.; Yue, X. Co-occurrence of ozone and PM_{2.5} pollution in the Yangtze River Delta over 2013–2019: Spatiotemporal distribution and meteorological conditions. *Atmos. Res.* **2021**, *249*, 105363. [CrossRef]
99. Li, H.; Peng, L.; Bi, F.; Li, L.; Bao, J.; Li, J.; Zhang, H.; Chai, F. Strategy of coordinated control of PM_{2.5} and ozone in China. *Res. Environ. Sci.* **2019**, *32*, 1763–1778. (In Chinese)

Article

Effects of Air Pollution on Sunshine Duration Trends in Typical Chinese Cities

Wei Chong^{1,2,*} , Wenhua Lyu^{1,2,*}, Jian Zhang^{1,3,4}, Jing Liang¹, Xiaotong Yang¹ and Guoyu Zhang^{1,3,4}

¹ School of Opto-Electronic Engineering, Changchun University of Science and Technology, Changchun 130022, China; zhangjian_nr@126.com (J.Z.); 15652926744@163.com (J.L.); apuy697@gmail.com (X.Y.); zh_guoyu@163.com (G.Z.)

² Meteorological Observation Center, China Meteorological Administration, Beijing 100081, China

³ Key Laboratory of Opto-Electronic Measurement and Optical Information Transmission Technology, Ministry of Education, Changchun 130022, China

⁴ Jilin Province Engineering Research Center of Opto-Electronic Measurement and Control Instrumentation, Changchun 130022, China

* Correspondence: chongwei@cma.gov.cn (W.C.); lwhaoc@cma.gov.cn (W.L.)

Abstract: Long-term trends in sunshine duration in Chinese cities have been closely linked to factors caused by air pollution. To understand this impact on sunshine duration (SD), surface solar radiation from 1981 to 2020, annual PM_{2.5} concentration from 2012 to 2020 and air pollution index (API) data from 2013 to 2020 collected in ten representative cities in China were investigated, and the long-term relationship of SD with diffuse fraction (DF), aerosol optical depth (AOD), annual PM_{2.5} concentration and API were analyzed. The results indicated that trends in SD varied across cities. SD decreased in seven of the ten selected cities' stations in the past 40 years, and the annual mean SD decreased from -0.03 h d^{-1} per decade to -0.36 h d^{-1} per decade—particularly in the Beijing North China Plain, Shanghai and Wuhan stations in the Yangtze River delta, where the trend coefficients were lower than -0.5 . Conversely, increases in varying degrees of SD were found in Kunming (0.38 h d^{-1} per decade), Guangzhou and Shenyang in Southwest, South and Northeast China, respectively—with the biggest trend coefficient of 0.54 in Kunming. In addition to the SD variation, the DF in the ten city stations increased continuously from 1981 to 2010 and then declined after 2010, which is closely related to decreases in the annual PM_{2.5} concentration after 2012. The correlation coefficients between DF and SD ranged from -0.04 to -0.62 , validating their negative relationship and the slight increasing trend in SD in recent ten years. The annual averages for SD and the DF plateaued in the 2010s due to the stringent pollution controls established by the Chinese government after 2010. Furthermore, the correlation coefficients between SD and the API ranged from -0.12 to -0.58 , demonstrating a negative relationship between SD and the API.

Keywords: air pollution index; diffuse fraction; sunshine duration; clearness index

Citation: Chong, W.; Lyu, W.; Zhang, J.; Liang, J.; Yang, X.; Zhang, G.

Effects of Air Pollution on Sunshine Duration Trends in Typical Chinese Cities. *Atmosphere* **2022**, *13*, 950.

<https://doi.org/10.3390/atmos13060950>

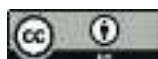
Academic Editors: Duanyang Liu, Kai Qin and Honglei Wang

Received: 13 May 2022

Accepted: 6 June 2022

Published: 10 June 2022

Publisher's Note: MDPI stays neutral with regard to jurisdictional claims in published maps and institutional affiliations.



Copyright: © 2022 by the authors. Licensee MDPI, Basel, Switzerland. This article is an open access article distributed under the terms and conditions of the Creative Commons Attribution (CC BY) license (<https://creativecommons.org/licenses/by/4.0/>).

1. Introduction

Over the past decades, China has become one of the most rapidly industrialized and urbanized countries worldwide. The growing population and intensified anthropogenic activities have led to the continuous increase in anthropogenic pollutant emissions in China. Moreover, the exacerbation of air pollution through aerosol radiative forcing has highly affected the radiation balance of the surface-atmosphere system. As an important indicator of solar radiation, sunshine duration (SD)—defined by the World Meteorological Organization (WMO) in 1989—is “the sum of the time for which the direct solar irradiance exceeds $120 \text{ W} \cdot \text{m}^{-2}$ ” [1]. As SD reflects the solar energy absorbed from the sun, it has become an important thermodynamic factor for large-scale atmospheric movements [2,3]. Small changes in SD may have a tremendous impact on weather and climate [4–6]. However, with the increase of anthropogenic aerosol loading in the atmosphere, the absorption

and scattering of solar radiation by aerosols intensifies the reduction of surface solar radiation [7]. In addition, acting as cloud condensation nuclei, aerosol particles enhance the longevity of clouds and their reflection of extraterrestrial radiation, further reducing SD [8]. Therefore, it is of great significance to study the effect of air pollution on SD.

Several studies have focused on the impact of air pollution on long-term trends in sunshine duration and solar radiation. Fu et al. found that in large cities and medium-sized cities throughout China, due to extensive anthropogenic activities and the air pollution represented by aerosol optical depth (AOD) and tropospheric column NO_2 (TroNO_2), sunny SD presented with a decrease of -0.13 h d^{-1} per decade from 1960 to 2005 [9,10]. Bartoszek et al. researched the relationships between cloudiness, aerosol optical thickness, and sunshine duration in Poland from 1980 to 2018; they found a growing trend in area-average values of relative sunshine duration in each season of the year with reductions in aerosol optical thickness [11]. Wang et al. analyzed the spatiotemporal changes of surface solar radiation over East China during 2000–2016, pointing out that aerosol-induced radiation reduction could result in about a mean 6.74% reduction in rice yield over East China [12]. Chen et al. analyzed trends in global radiation and sunshine hours at 51 stations during 1961–1998 in mainland China and found decreasing trends in global radiation at 47 stations, with 42 stations showing a reduced trend in sunshine hours [13]. Song et al. reported that SD in eastern China decreased throughout the year at an annual rate of -0.132 h d^{-1} per decade during 1961–2014, suggesting that urbanization and industrialization may be responsible [14]. Kaiser and Qian reported an average decrease of approximately 1% per decade in possible SD in China from 1954 to 1998 and proposed that the increased atmospheric anthropogenic aerosol loading due to growing fossil fuel combustion accounted for the decline in SD [15]. Liao et al. pointed out that the attenuation of visibility and SD was consistent during 1980–2012 in South China and suggested that increases in pollutants are responsible for sunlight obstruction and reductions in visibility [16]. Wang et al. investigated the long-term trends in surface solar radiation from 1960 to 2000 in China and found that surface solar radiation in most regions of China began to increase after 1990, which was attributed to decreases in cirrus and cirrostratus clouds [17]. Qi et al. reported that the interannual trends and variations of surface solar radiation decreased in both East and West China during 1961–2010, and suggested that aerosol pollutants were the main factor causing the reduction of surface solar radiation in East China [18]. Furthermore, they determined that an abrupt change occurring in the early 1990s, followed by a sustained increase—possibly due to the Chinese government’s environmental protection plans [18]. The abovementioned studies improve our understanding of air pollution related to changes in SD. However, most of these studies have focused on the influence of air pollution on trends in solar radiation separately, rather than combined with SD, or the impacts have only covered limited land areas or weather conditions. Discussion of the influence of air pollution on long-term SD trends in representative cities of China under all weather conditions are rare in previous studies.

In this study, we examined SD and related solar radiation data from ten typical cities in different climate regions over China from 1981 to 2020, mainly focusing on the long-term trends in and associations between SD, the diffuse fraction (DF), annual $\text{PM}_{2.5}$ concentration and the air pollution index (API)—which is related to increases in anthropogenic aerosols. This paper aims to provide an improved understanding of SD changes influenced by severe environmental issues that have occurred during the industrialization and urbanization caused by China’s reform and opening policy of 1980. The present article is organized as follows: Section 2 introduces the data source and the methods. Section 3 presents interannual SD trends and seasonal SD trends from 1981 to 2020, followed by discussions of the relationships between SD changes and the DF and API. The main conclusions are presented in Section 4.

2. Methodology

2.1. Data

The SD and solar radiation data were collected from ten China Meteorological Radiation Data International Exchange Stations located in seven climate regions in mainland China [19] (Figure 1), with station information shown in Table 1. Daily SD, global solar radiation and diffuse radiation were measured simultaneously from 1981 to 2020—except for Shanghai, from 1991 to 2020. SD was measured using a Jordan Sunshine Recorder with an absolute error of ± 0.1 h and global solar radiation and diffuse radiation were measured horizontally using a thermopile-based pyranometer with a relative error of $\pm 2\%$. The daily data were archived at the National Meteorological Information Center of China Meteorological Administration (<http://data.cma.cn/>, accessed on 31 August 2021). The annual and seasonal averages of SD and solar radiation deduced from daily data were analyzed. In this study, spring, summer, autumn and winter corresponded to March–May, June–August, September–November and December–February, respectively.

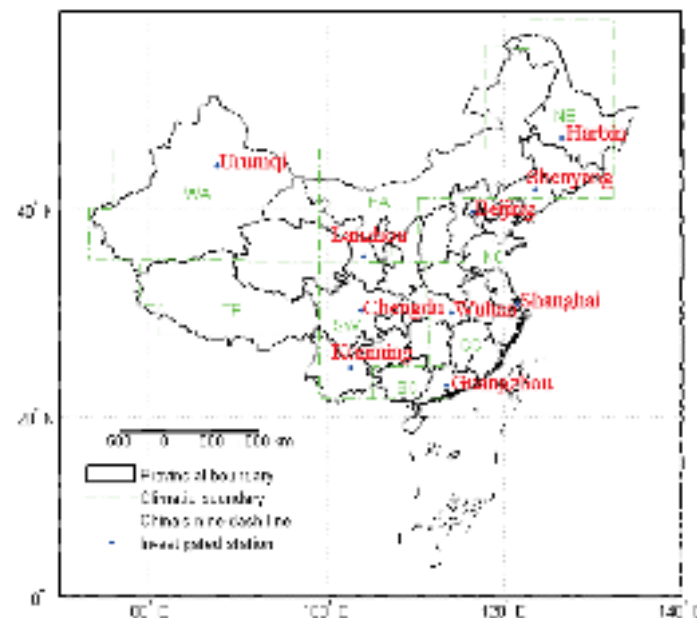


Figure 1. Locations of the ten investigated stations and their climate conditions. NC for North China, NE for Northeast China, CC for Central China, SC for South China, SW for Southwest China, EA for Eastern arid regions, WA for Western arid/semi-arid regions, TP for the Tibetan plateau.

Table 1. Geographical information of the investigated stations used in this study.

Station Name	Longitude/E°	Latitude/N°	Altitude/m asl.	Climate Regions
Beijing	116.47	39.81	32.8	NC
Shenyang	123.51	41.73	51.0	NE
Harbin	126.57	45.93	118.3	NE
Shanghai	121.44	31.39	5.5	CC
Wuhan	114.05	30.60	23.6	CC
Guangzhou	113.48	23.21	70.7	SC
Chengdu	103.86	30.75	547.7	SW
Kunming	102.65	25.01	1888.1	SW
Urumqi	87.65	43.78	935.0	WA
Lanzhou	104.14	35.87	1874.4	EA

The DF and clearness index (CI) are introduced in this article. The DF is defined as the ratio of diffuse radiation to global solar radiation and is an important indicator of the global transmissivity of the atmosphere. The clearness index, which varies primarily due to

cloud cover and cloud type, is the ratio of global solar radiation to extraterrestrial radiation. To obtain the clearness index, the equation for calculating the extraterrestrial radiation (MJ/m^2) on a horizontal surface, H_0 , is as follows [20,21]:

$$H_0 = \frac{24 \times 3600 \times I_{sc}}{\pi} \left[1 + 0.033 \cos \left(\frac{360n}{365} \right) \right] \times \left[\cos \varphi \cos \delta \sin w_s + \frac{\pi w_s}{180^\circ} \sin \varphi \sin \delta \right] \quad (1)$$

where I_{sc} is the solar constant (1367 W m^{-2}), n is the day number of the year—starting from January 1— φ is the latitude of the station in degrees, δ is the declination of the sun in degrees and w_s is the sunrise hour angle in degrees. δ and w_s can be obtained by Equations (2) and (3) [20,21]:

$$\delta = 23.45 \sin \left[\frac{360(n + 284)}{365} \right] \quad (2)$$

$$w_s = \arccos[-\tan \delta \tan \varphi] \quad (3)$$

To ensure the quality of the SD and solar radiation data, some quality control criteria were applied to the daily data. The criteria included: (1) daily collections were rejected if either SD or solar radiation was missing; (2) only daily collections meeting $0 < \text{DF} < 1$ and $0 < \text{CI} < 1$ simultaneously were used; (3) the month was rejected if more than ten days of SD or solar radiation were missing in that month.

API is a dimensionless parameter describing the comprehensive conditions of urban environmental air quality. The higher the API, the more serious the comprehensive pollution. API includes six pollutants: SO_2 , NO_2 , PM_{10} , $\text{PM}_{2.5}$, CO and O_3 ; it is calculated using the sub-index of the six pollutants derived from daily or monthly average concentrations. The equations are as follows:

$$I_i = \frac{C_i}{S_i} \quad (4)$$

$$\text{API} = \sum_{i=1}^6 I_i \quad (5)$$

where I_i is the sub-index of the i th pollutant of the six pollutants, C_i is the concentration of the i th pollutant of the six pollutants; when the i th pollutant is either SO_2 , NO_2 , PM_{10} or $\text{PM}_{2.5}$, C_i is the monthly mean concentration; when the i th pollutant is either CO or O_3 , C_i is the concentration at a specific percentile. S_i is the secondary standard of the i th pollutant; when the i th pollutant is either SO_2 , NO_2 , PM_{10} or $\text{PM}_{2.5}$, S_i is the secondary standard for the annual mean; when the i th pollutant is CO, S_i is the secondary standard for the daily mean; and when the i th pollutant is O_3 , S_i is the secondary standard for the 8 h mean.

The monthly API data used in this study were obtained from the China National Environmental Monitoring Centre (<http://www.cnemc.cn/jcbg/kqzlkzkg/>, accessed on 31 August 2021); however, the data consistent with the SD and global solar radiation stations are only available from January 2013 to August 2020 because the observation starting time and data were unavailable for this study. In addition, the annual $\text{PM}_{2.5}$ concentration data from 2012 to 2020 were used in this study, which were obtained from the Tracking Air Pollution in China website: <http://tapdata.org.cn/> (accessed on 11 May 2022).

2.2. Methods

The linear regression method was used to analyze the inclination of climatic elements over a long time scale. To evaluate inclination, we established the unary linear regression equation $y = a + bx$ between the SD (y) and time series (x , year), where a is the regression constant and b is the regression coefficient—namely, the inclination rate. Both a and b can be calculated using the least square method. $b > 0$ indicates that y increases with an increase in time x ; on the contrary, $b < 0$ means y decreases as time x increases.

A moving average was introduced to investigate the SD trends in this study. For a climate element series, its moving average series can be depicted using Equation (6):

$$\bar{y}_j = \frac{1}{k} \sum_{i=1}^k y_{i+j-1} \quad (j = 1, 2, \dots, n - k + 1) \quad (6)$$

where n stands for the number of years, \bar{y}_j is the j th moving average of SD, k is the step length and i th is the sequence of the step length. From the curve of the moving average, we can see whether the climate variable is increasing or decreasing, which helps determine the turning point of the climate variable.

We also analyzed the trend coefficient r_{yx} , which is defined as a correlation coefficient between the climatic element series and the time series, and can be expressed as in Equation (7) [10]:

$$r_{yx} = \frac{\sum_{i=1}^n (y_i - \bar{y})(i - \bar{x})}{\sqrt{\sum_{i=1}^n (y_i - \bar{y})^2 \sum_{i=1}^n (i - \bar{x})^2}} \quad (7)$$

where n denotes the number of years, i is the year sequence, y_i is the element value in the i th year, \bar{y} represents the mean of all the element values in n years and \bar{x} is equal to $(n + 1)/2$. If $r_{yx} > 0$, the element increases during n years, whereas if $r_{yx} < 0$, the trend in the element declines during n years; $r_{yx} = 0$ means no change. Furthermore, correlation and fitting analyses were used in our study.

3. Results and Discussion

3.1. Trends in Sunshine Duration from 1981 to 2020

Figure 2 shows the spatial distribution of the trend coefficients of SD for the ten stations over China from 1981 to 2020. SD trend coefficients are presented in Table 2. There was a clear decline in SD at seven stations, but not in Kunming, Guangzhou and Shenyang—located in Southwest, South and Northeast China, respectively. Owing to its environment and high altitude, Kunming showed a significant increase in SD, with a trend coefficient greater than 0.5. Guangzhou, thanks to its being an inshore region in southeast China and its advanced technology and tertiary industry, had a positive trend coefficient of 0.21. The trend coefficient of Shenyang was 0.03; hence, the increase in SD in this region was minimal. In contrast, stations in the other representative cities in China showed a decreasing trend in SD. The Beijing, Shanghai and Wuhan stations had trend coefficients lower than -0.5 . Notably, in Beijing and Shanghai, the trend coefficients were both less than -0.6 , which were attributed to their larger population densities and levels of anthropogenic pollution due to urbanization.

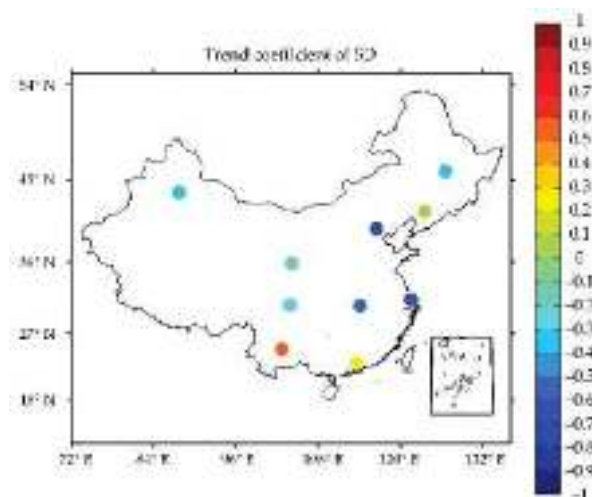


Figure 2. Trend coefficients of SD from 1981 to 2020 for the ten selected stations.

Table 2. Statistical summary of SD.

Station	Mean (h d ^{−1})	Std. (h d ^{−1})	Trend Coefficient	Regression Equation	Correlation Coefficients of SD vs. DF
Beijing	6.93	0.44	−0.62	$y = -0.023x + 7.40$	−0.41
Shenyang	6.62	0.41	0.03	$y = 0.001x + 6.60$	−0.30
Harbin	6.50	0.74	−0.34	$y = -0.022x + 6.95$	−0.40
Shanghai	5.05	0.48	−0.70	$y = -0.036x + 5.64$	−0.44
Wuhan	4.98	0.48	−0.51	$y = -0.021x + 5.41$	−0.59
Guangzhou	4.28	0.39	0.21	$y = 0.007x + 4.14$	−0.48
Chengdu	2.71	0.36	−0.27	$y = -0.008x + 2.89$	−0.35
Kunming	6.13	0.81	0.54	$y = 0.038x + 5.36$	−0.53
Urumqi	7.77	0.53	−0.39	$y = -0.018x + 8.14$	−0.04
Lanzhou	7.08	0.31	−0.10	$y = -0.003x + 7.14$	−0.62

Through a regression analysis of the daily average SD, a ranking of the cities with decreasing SD trends can be obtained: Lanzhou < Chengdu < Urumqi < Wuhan < Harbin < Beijing < Shanghai, ranging from -0.03 h d^{-1} per decade to -0.36 h d^{-1} per decade. Increasing trends in SD were found in Kunming, Guangzhou and Shenyang, with the biggest increasing trend of 0.38 h d^{-1} per decade in Kunming. The regression equations are listed in Table 2.

Setting the step length k as 5 years, the moving average curves of the annual daily mean SD of the ten stations are shown in Figure 3. Except for obvious upward trends in Kunming and Guangzhou and a weak upward trend in Shenyang, downward trends in the SD of the other seven stations can be observed from Figure 3—which is consistent with the results of the linear analysis and trend analysis. Moreover, except for the turning points of Urumqi and Harbin in 2015 and Shenyang in 2006, inflection points in the SD of most stations could be identified at around 2010.

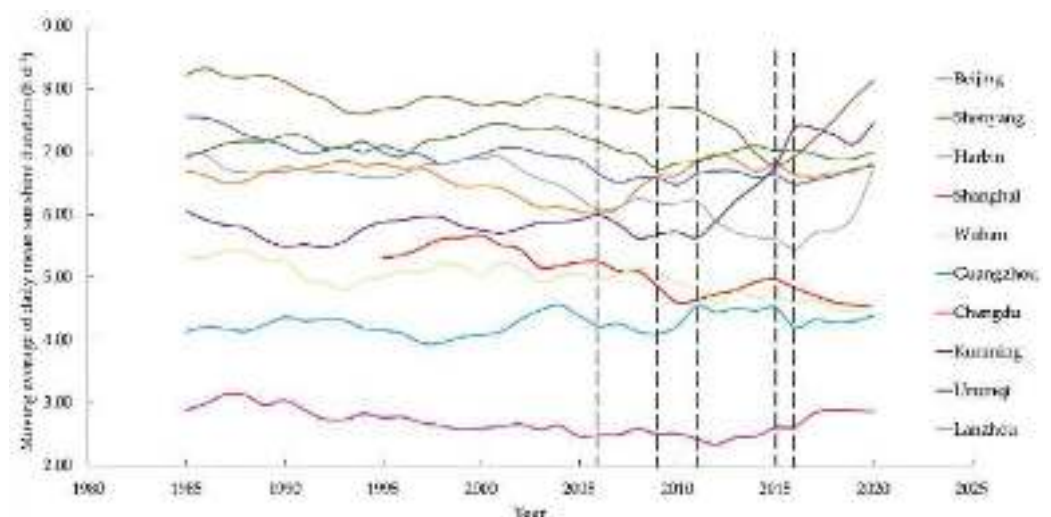
**Figure 3.** Moving average of the daily mean sunshine duration per year.

Figure 4 shows the seasonal trends in SD from 1981 to 2020. Consistently, the changes in SD in the studied cities exhibited a similar variation. The overall SD decreased in 1981–2010 and started increasing after 2010. This fall–rise trend might be due to environmental protection measures taken by the Chinese government over the past decade. In Shanghai, Wuhan and Chengdu, SD trends seasonally varied in fall–rise and rise–fall patterns. This was primarily due to the climate characteristics of spring and winter in these areas, which are not conducive to the diffusion of pollutants, further reducing the solar radiation reaching the ground, and consequently reducing SD.

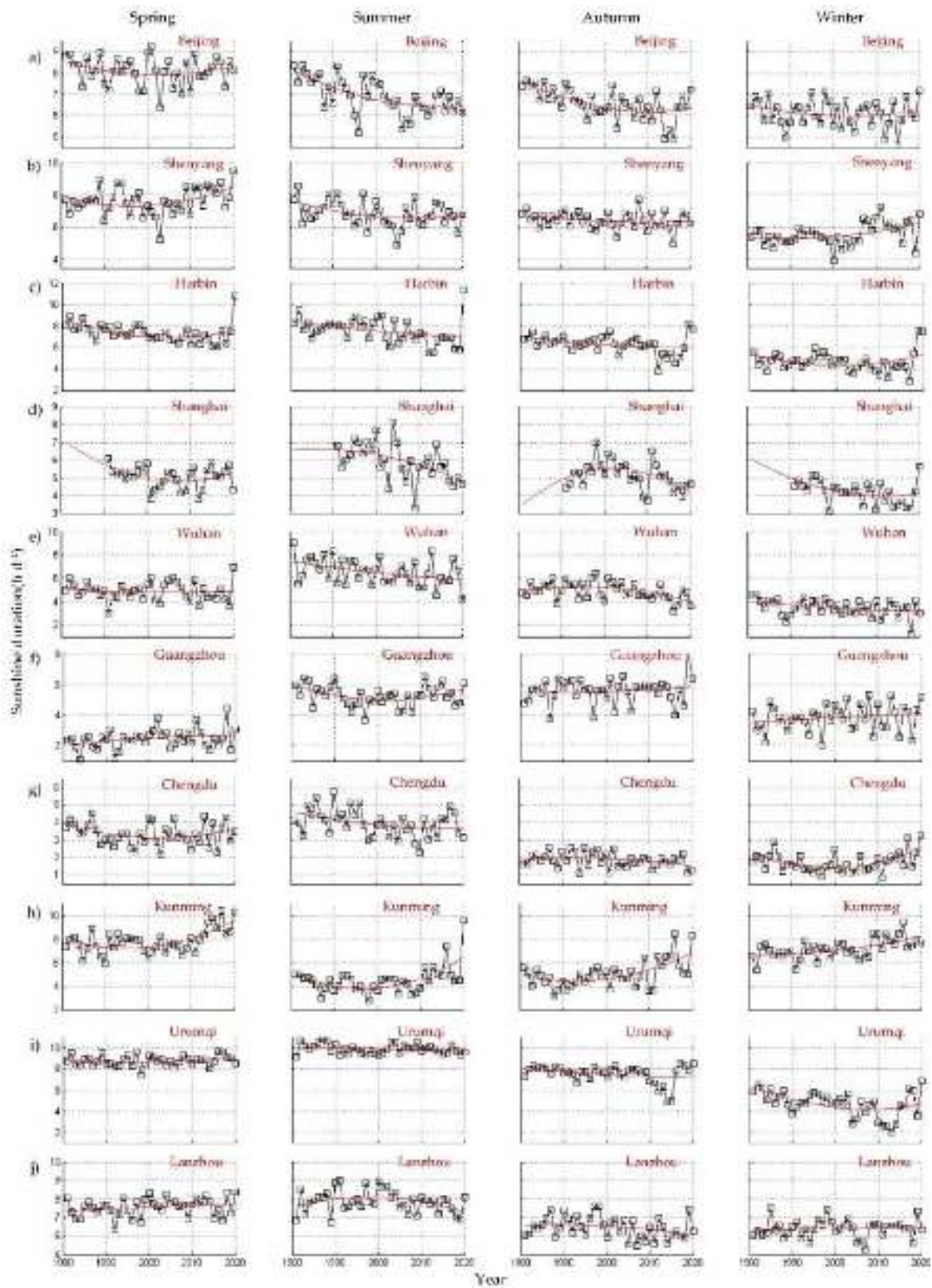


Figure 4. Seasonal trends in SD from 1981 to 2020 for the ten selected stations. (a) Seasonal trends in SD for Beijing; (b) Seasonal trends in SD for Shenyang; (c) Seasonal trends in SD for Harbin; (d) Seasonal trends in SD for Shanghai; (e) Seasonal trends in SD for Wuhan; (f) Seasonal trends in SD for Guangzhou; (g) Seasonal trends in SD for Chengdu; (h) Seasonal trends in SD for Kunming; (i) Seasonal trends in SD for Urumqi; (j) Seasonal trends in SD for Lanzhou.

3.2. DF and SD Trends

Generally, DF is an important indicator of levels of diffuse radiation, which are closely related to the aerosol content in the air, and can uncover the effects of pollutants on SD measurements. The correlation coefficients between DF and SD, listed in Table 2, ranged from -0.04 to -0.62 , indicating that there was a negative relationship between the DF and SD. Therefore, sunshine duration decreased when diffuse radiation increased, and vice versa.

However, the bar graph of the DF trend coefficients shown in Figure 5 provides a different perspective. Long-term trend coefficients of DF during 1981 to 2020 were both positive and negative, with no distinct relationship between SD and the DF. According to the previous analysis on seasonal trends in SD, most SD trends took 2010 as the node—first decreasing and then increasing. We recalculated the trend coefficients of DF according to the 2010 node. From Figure 5, the DF trend coefficients of all the studied stations were positive before 2010 and negative from 2011 to 2020. This indicates that the diffuse radiation component increased continuously from 1981 to 2010, and began to decrease after 2010, just contrary to the seasonal trends in SD depicted in Section 3.1.

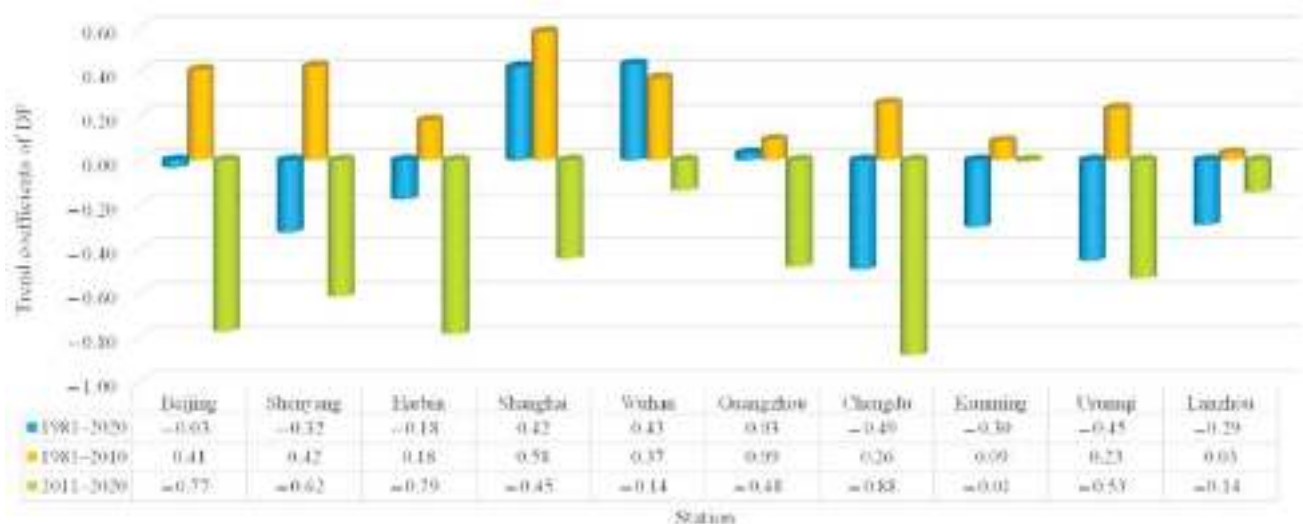


Figure 5. Trend coefficients of DF from 1981 to 2020 for the ten selected stations.

The opposite trend observed between SD and DF might be closely related to anthropogenic emissions. To understand the impact of the anthropogenic emissions on the relationship between SD and DF, AOD, as an important physical property of particle pollutants, is introduced to validate the negative correlation. The spatial-temporal variation and trends in MERRA-2 AOD over China from 1980 to 2017 have been analyzed by Sun et al. [22]. High AOD values mainly appeared in agglomerations such as the North China Plain (the city cluster of Beijing–Tianjin–Hebei), Pearl River Delta (the city cluster of Guangzhou–Shenzhen–Zhuhai), Yangtze River delta (the city cluster of Shanghai–Nanjing–Wuhan) and part of the Sichuan Basin (the city cluster of Chengdu), while low AOD values mainly appeared in western China. The annual Mean MERRA-2 AOD of the whole of China showed a slight increase from the 1980s to the 1990s, a sharp increase from 2001 to 2010 and a decrease from 2010 to 2017—which is almost identical to the trends and turning points of the DF and SD. Furthermore, He et al. [23] investigated the AOD spatial-temporal distribution during 2003 to 2016 throughout China. Their statistical results showed that high AOD values mainly occurred in developed agglomerations; the overall annual mean AOD showed a declining trend of -0.0018 per year from 2004 to 2016 over the whole of China. A remarkable upward trend of 0.012 year^{-1} from 2003 to 2008 and a significant decrease from 2008 to 2016 could be found; the turnaround appeared in 2008, which is adjacent to the inflection point of the SD and DF at around 2010. Obviously, the variation

in AOD had a good positive correlation with the DF, and an evident negative correlation with SD. The possible reason for this might be that the surged anthropogenic emissions could lead to an increase in aerosols and AOD; through scattering and absorbing, a large number of aerosols will increase the diffuse radiation in the atmosphere and reduce the direct radiation reaching the ground—thus reducing the SD. Regarding the turning point shown in the SD, DF and AOD trends, this is most likely due to the Chinese government taking a series of stringent pollution controls from around 2010.

In this study, we took annual $PM_{2.5}$ concentration as an example to investigate the influence of anthropogenic emissions on the relationship between SD and DF. As the particle concentration data from throughout China before 2012 are not available, we could only illustrate the spatial distributions in annual $PM_{2.5}$ concentrations during 2012 to 2020 in Figure 6—which correlate well with the trends in SD and DF after 2010 and are consistent with previous studies [22,23]. From 2012, high concentrations of $PM_{2.5}$ have been distributed over the North China Plain (the city cluster of Beijing–Tianjin–Hebei), Yangtze River delta (the city cluster of Shanghai–Nanjing–Wuhan), Northeast Plain (the city cluster of Shenyang–Jilin–Harbin), Northwest Plateau (the city cluster of Xi’an–Lanzhou–Urumqi) and Sichuan Basin (the city cluster of Chengdu). All these regions are the fastest developing areas in China. However, the interannual trend in $PM_{2.5}$ concentration is getting better year by year. This is likely to be closely related to the Air Pollution Prevention and Control Action Plan (2013–2017) and the Blue Sky Protection Campaign (2018–2020), implemented since 2013. According to statistical studies, the Air Pollution Prevention and Control Action Plan reduced the annual population-weighted mean $PM_{2.5}$ from $62.5 \mu\text{g}/\text{m}^3$ in 2013 to $44.4 \mu\text{g}/\text{m}^3$ in 2017, and the Blue Sky Protection Campaign further reduced $PM_{2.5}$ concentrations to $33.1 \mu\text{g}/\text{m}^3$ in 2020 [24–26]. The decrease in anthropogenic aerosols resulted in a decrease in the DF, which further increased the solar radiation reaching the ground and raised SD. Correspondingly, except for Urumqi—which had a decreasing trend of SD before 2015—the other nine cities had an overall decrease before 2010; after that, the SD trends of the cities rose gradually, which is consistent with the analysis results in Figure 5, validating the negative relationship between SD and DF related to the concentrations of aerosol particles.

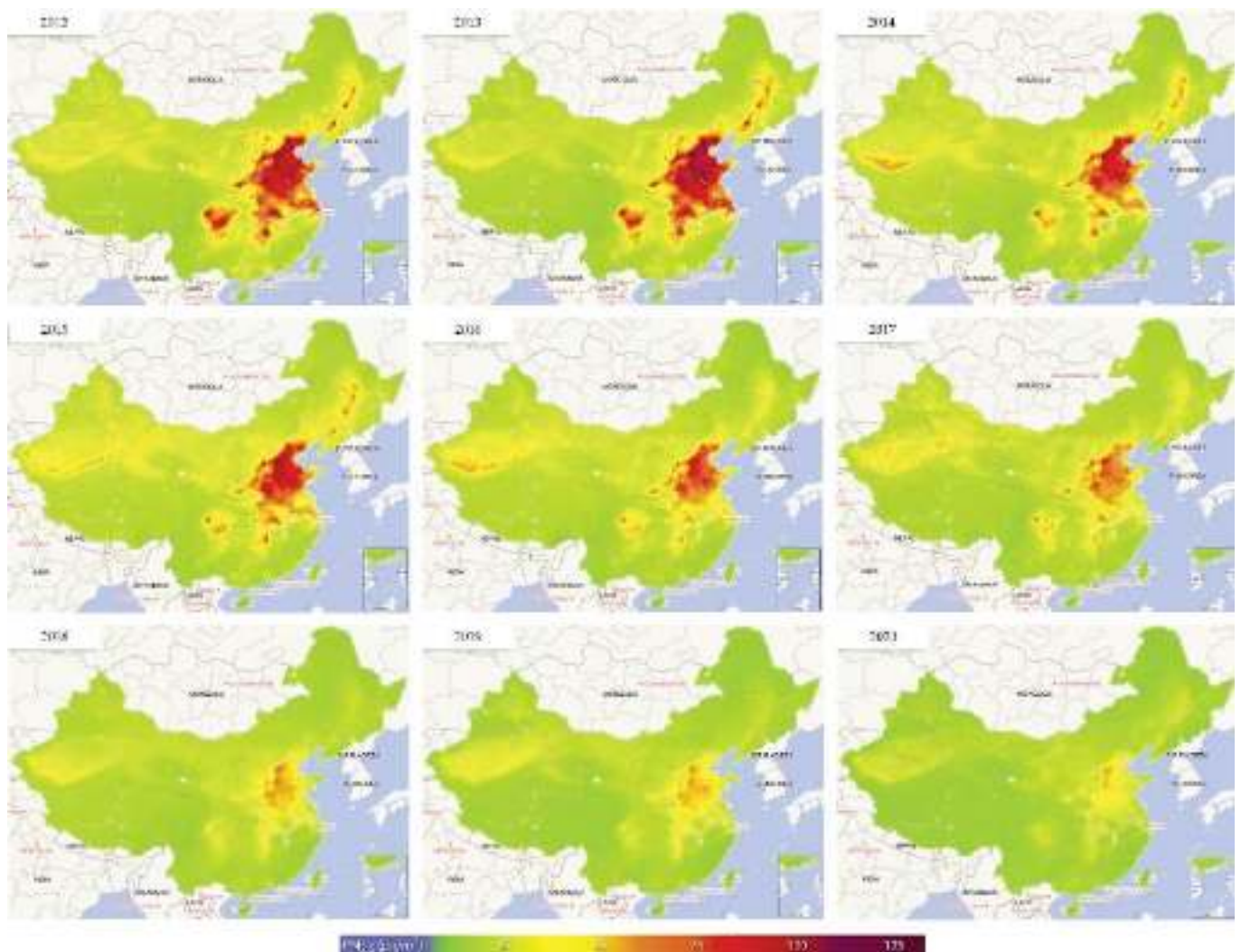
3.3. Connections between API and SD Trends

Figure 7 displays the time series of the annual mean API from 2013 to 2020. A negative correlation was observed between SD and API, which confirms that light pollution will result in high SD. Furthermore, sharp decreases in API were observed after 2015 for all stations, along with a slight improvement in SD during this period. This might correlate with pollution controls such as supersessions in polluting industrial equipment and enterprises, and reductions in emissions of sulfur and nitrogen oxides from large plants.

Using only the available API data, the correlation coefficients between SD and the API were calculated and listed in Table 3, ranging from -0.12 to -0.58 . Correlation coefficients of less than -0.3 could be found in the urban agglomerations in North China Plain, Yangtze River delta, Northeast Plain, and Northwest Plateau, this is supported by the distribution of annual $PM_{2.5}$ concentration across China.

Table 3. The correlation coefficients between SD and API.

Station	Correlation Coefficients of SD vs. API
Beijing	−0.55
Shenyang	−0.39
Harbin	−0.33
Shanghai	−0.32
Wuhan	−0.37
Guangzhou	−0.22
Chengdu	−0.12
Kunming	−0.17
Urumqi	−0.33
Lanzhou	−0.58

**Figure 6.** The spatial distributions of annual PM_{2.5} concentrations from 2012 to 2020 (Source: <http://tapdata.org.cn>, accessed on 11 May 2022).

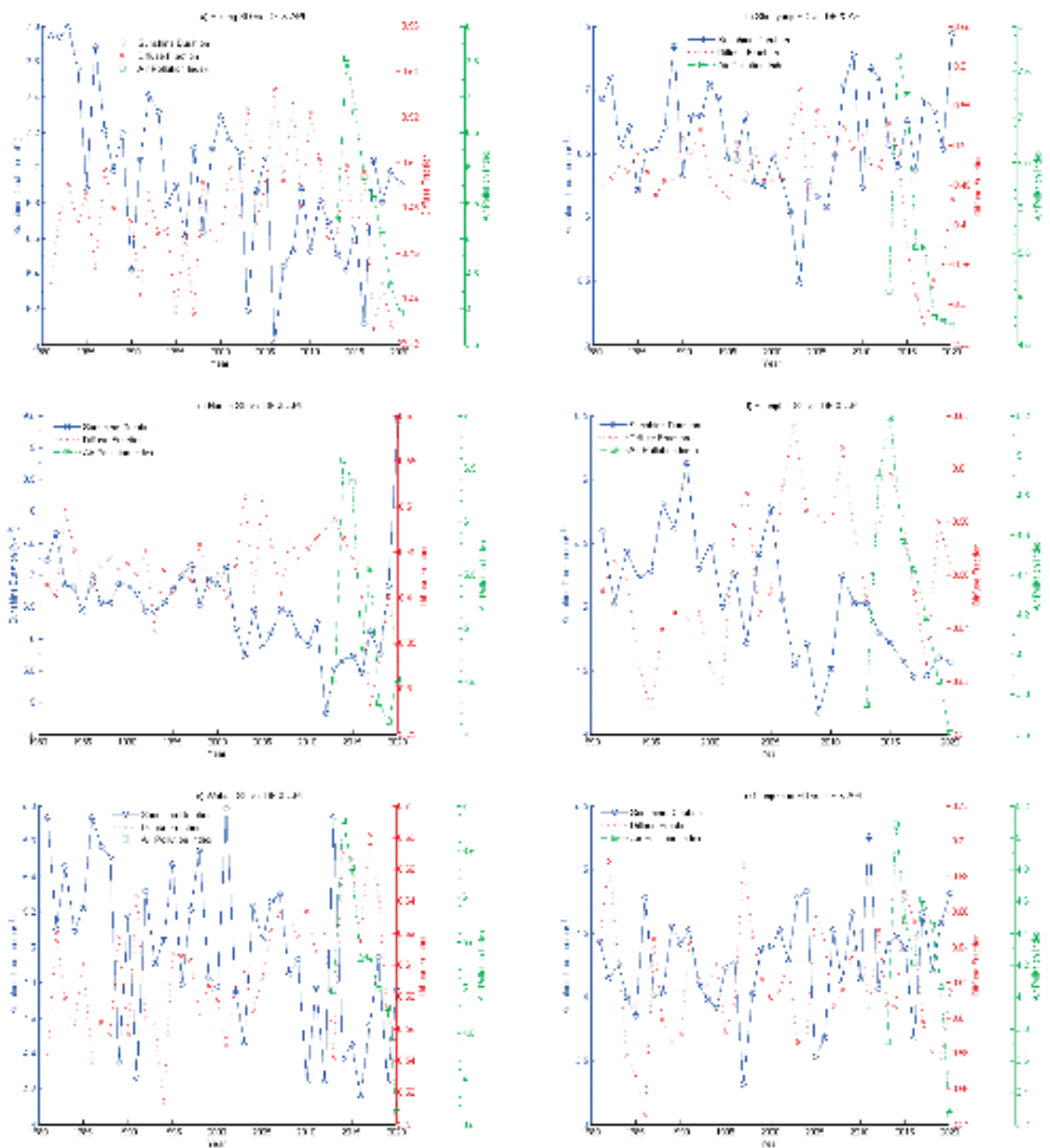


Figure 7. Cont.

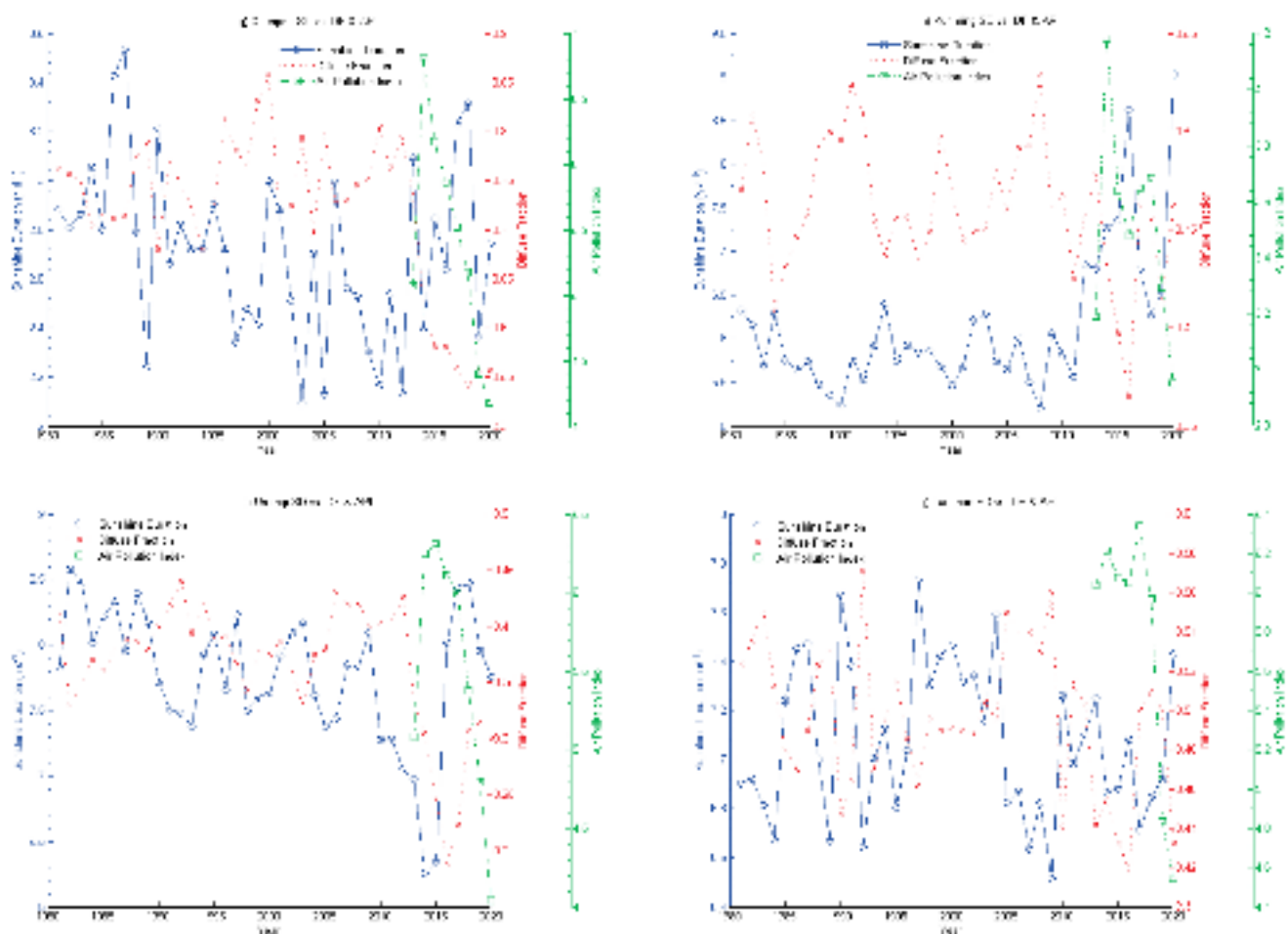


Figure 7. Interannual changes in averaged SD, DF and API for the ten cities from 1981 to 2020. (a) For Beijing; (b) For Shenyang; (c) For Harbin; (d) For Shanghai; (e) For Wuhan; (f) For Guangzhou; (g) For Chengdu; (h) For Kunming; (i) For Urumqi; (j) For Lanzhou.

4. Conclusions

In this study, the SD, surface solar radiation, $PM_{2.5}$ concentration and API data from ten China Meteorological Radiation Data International Exchange Stations in ten representative cities were collected to examine the trends between DF and SD from 1981 to 2020, $PM_{2.5}$ concentration and SD from 2012–2020, and API and SD from 2013–2020. Our analysis indicates that solar radiation and SD are associated closely with aerosol pollutants due to urbanization and industrialization.

Overall, SD decreased in seven of the ten selected cities' stations from 1981 to 2020, with a decreasing rate of -0.03 h d^{-1} per decade to -0.36 h d^{-1} per decade—notable in Beijing, Shanghai and Wuhan, where trend coefficients were lower than -0.5 . By contrast, SD increased in Kunming, Guangzhou and Shenyang, with the largest trend coefficient of 0.54 and the largest increasing rate of 0.38 h d^{-1} per decade in Kunming. Seasonal trends in SD showed a fluctuating decrease in SD from 1981 to 2010 and increases from 2011 to 2020. In contrast to the seasonal trends in SD, the DF trend coefficients suggested that diffuse radiation increased continuously from 1981 to 2010, peaking in the 2010s and decreasing after 2010. The correlation coefficients between DF and SD ranged from -0.04 to -0.62 , validating the negative relationship between DF and SD—this was supported by the improvement in annual $PM_{2.5}$ concentrations due to the stringent pollution controls in place since 2013 throughout China. Furthermore, the correlation coefficients ranging from -0.12 to -0.58 demonstrated a negative relationship between SD and API; sharp decreases in API were observed after 2015 for the ten typical cities' stations and slight improvements

in SD during this period were found which accounted for the pollution impact on SD trends from the other side.

Because many factors can affect the transmission of solar radiation in the atmosphere, some factors might not have been accounted for in this study. SD and diffuse radiation are not only affected by air pollution, but also by clouds. As cloud coverage data are not available for this study, we only adopted the clearness index related to the cloud cover, without analyzing the relationship between SD and cloud cover. We will further explore the influence of clouds on SD in subsequent studies.

Author Contributions: Conceptualization, W.C.; methodology, W.C.; software, W.C.; validation, W.L. and G.Z.; investigation, X.Y.; resources, J.L.; data curation, W.C.; writing—original draft, W.C.; writing—review and editing, J.Z.; supervision, W.L.; project administration, W.L.; funding acquisition, J.Z. and G.Z. All authors have read and agreed to the published version of the manuscript.

Funding: This research was funded by the Youth Fund of the National Natural Science Foundation of China, grant number 61805027; the Jilin Scientific and Technological Development Program, grant number 20190302124GX; and the Innovation Fund of the Changchun University of Science and Technology, grant number XJLLG-2018-02.

Institutional Review Board Statement: Not applicable.

Informed Consent Statement: Not applicable.

Data Availability Statement: The daily SD and solar radiation data were collected from ten China Meteorological Radiation Data International Exchange Stations, located in Mainland China; the data were archived at the National Meteorological Information Center of China Meteorological Administration (<http://data.cma.cn/>, accessed on 31 August 2021); The monthly API data used in this study were provided openly and freely by the China National Environmental Monitoring Centre (<http://www.cnemc.cn/jcbg/kqzlkbg/>, accessed on 31 August 2021). The annual PM_{2.5} concentration data were obtained from Tracking Air Pollution in China (<http://tapdata.org.cn/>, accessed on 11 May 2022).

Acknowledgments: The authors are grateful to the staff at the investigated stations for collecting the sunshine duration and air pollution data used in our research, and the National Meteorological Information Centre of China Meteorological Administration and National Environmental Monitoring Centre of China for providing these archived data. Figure 6 is cited from <http://tapdata.org.cn>, accessed on 11 May 2022; the authors also appreciate the support of the TAP team (Tracking Air Pollution in China) for producing Figure 6.

Conflicts of Interest: The authors declare no conflict of interest.

References

1. World Meteorological Organization (WMO). *Guide to Instruments and Methods of Observation*, 2018th ed.; Part I. WMO-No. 8; World Meteorological Organization: Geneva, Switzerland, 2018; pp. 299–310.
2. Meehl, G.A.; Arblaster, J.M.; Matthes, K.; Sassi, F.; van Loon, H. Amplifying the pacific climate system response to a small 11-year solar cycle forcing. *Science* **2009**, *325*, 1114–1118. [CrossRef] [PubMed]
3. Yu, L.; Zhang, M.; Wang, L.C.; Qin, W.; Lu, Y.; Li, J. Clear-sky solar radiation changes over arid and semi-arid areas in China and their determining factors during 2001–2015. *Atmos. Environ.* **2020**, *223*, 117198. [CrossRef]
4. Qi, Y.; Fang, S.B.; Zhou, W.Z. Correlative analysis between the changes of surface solar radiation and its relationship with air pollution, as well as meteorological factor in East and West China in recent 50 years. *Acta Physiol. Sin.* **2015**, *64*, 089201. [CrossRef]
5. Richard, A. Climate change. Joining forces to pump up a variable sun's climate effects. *Science* **2009**, *325*, 1058–1059. [CrossRef]
6. Makade, R.G.; Jamil, B. Statistical analysis of sunshine based global solar radiation (GSR) models for tropical wet and dry climatic Region in Nagpur, India: A case study. *Renew. Sustain. Energy Rev.* **2018**, *87*, 22–43. [CrossRef]
7. Zhao, J.F.; Kong, X.N.; He, K.J.; Xu, H.; Mu, J. Assessment of the radiation effect of aerosols on maize production in China. *Sci. Total Environ.* **2020**, *720*, 137567. [CrossRef]
8. Fan, J.L.; Wu, L.F.; Zhang, F.C.; Cai, H.; Wang, X.; Lu, X.; Xiang, Y. Evaluating the effect of air pollution on global and diffuse solar radiation prediction using support vector machine modeling based on sunshine duration and air temperature. *Renew. Sustain. Energy Rev.* **2018**, *94*, 732–747. [CrossRef]
9. Fu, C.B.; Dan, L. Influence of intensified air pollution on the sunny diffuse radiation fraction in China. *Chin. Sci. Bull.* **2018**, *63*, 2655–2665. [CrossRef]

10. Fu, C.B.; Dan, L.; Chen, Y.L.; Tang, J. Trends of the sunshine duration and diffuse radiation percentage on sunny days in urban agglomerations of China during 1960–2005. *J. Environ. Sci.* **2015**, *34*, 206–211. [CrossRef]
11. Bartoszek, K.; Matuszko, D.; Soroka, J. Relationships between cloudiness, aerosol optical thickness, and sunshine duration in Poland. *Atmos. Res.* **2020**, *245*, 105097. [CrossRef]
12. Wang, Y.Y.; Meng, Z.; Lyu, R.; Huang, G.; He, Q.; Cheng, T. Spatiotemporal changes of surface solar radiation: Implication for air pollution and rice yield in East China. *Sci. Total Environ.* **2020**, *739*, 140361. [CrossRef] [PubMed]
13. Chen, R.S.; Kang, E.S.; Ji, X.B.; Yang, J.; Zhang, Z. Trends of the global radiation and sunshine hours in 1961–1998 and their relationships in China. *Energy Convers. Manag.* **2006**, *47*, 2859–2866. [CrossRef]
14. Song, Z.Y.; Chen, L.T.; Wang, Y.J.; Liu, X.; Lin, L.; Luo, M. Effects of urbanization on the decrease in sunshine duration over eastern China. *Urban Clim.* **2019**, *28*, 100471. [CrossRef]
15. Kaiser, D.P.; Qian, Y. Decreasing trends in sunshine duration over China for 1954–1998: Indication of increased haze pollution? *Geophys. Res. Lett.* **2002**, *29*, 2042. [CrossRef]
16. Liao, W.H.; Wang, X.M.; Fan, Q.; Zhou, S.; Chang, M.; Wang, Z.; Wang, Y.; Tu, Q. Long-term atmospheric visibility, sunshine duration and precipitation trends in South China. *Atmos. Environ.* **2015**, *107*, 204–216. [CrossRef]
17. Wang, C.H.; Zhang, Z.F.; Tian, W.S. Factors affecting the surface radiation trends over China between 1960 and 2000. *Atmos. Environ.* **2011**, *45*, 2379–2385. [CrossRef]
18. Qi, Y.; Fang, S.B.; Zhou, W.Z. Variation and spatial distribution of surface solar radiation in China over recent 50 years. *Acta Ecol. Sin.* **2014**, *34*, 7444–7453.
19. Zhang, J.; Lin, Z. *Climate in China*; Technology Publishing Company: Shanghai, China, 1985; pp. 467–506. (In Chinese)
20. Duffie, J.A.; Beckman, W.A. *Solar Engineering of Thermal Processes*, 3rd ed.; John Wiley & Sons, Inc.: New Jersey, NJ, USA, 2006; pp. 9–45.
21. Li, H.; Ma, W.; Lian, Y.; Wang, X.; Zhao, L. Global solar radiation estimation with sunshine duration in Tibet, China. *Renew. Energy* **2011**, *36*, 3141–3145. [CrossRef]
22. Sun, E.; Xu, X.; Che, H.; Tang, Z.; Gui, K.; An, L.; Lu, C.; Shi, G. Variation in MERRA-2 aerosol optical depth and absorption aerosol optical depth over China from 1980 to 2017. *J. Atmos. Solar-Terr. Phys.* **2019**, *186*, 8–19. [CrossRef]
23. He, Q.; Gu, Y.; Zhang, M. Spatiotemporal patterns of aerosol optical depth throughout China from 2003 to 2016. *Sci. Total Environ.* **2019**, *653*, 23–35. [CrossRef]
24. Geng, G.; Xiao, Q.; Liu, S.; Liu, X.; Cheng, J.; Zheng, Y.; Xue, T.; Tong, D.; Zheng, B.; Peng, Y.; et al. Tracking Air Pollution in China: Near Real-Time PM_{2.5} Retrievals from Multisource Data Fusion. *Environ. Sci. Technol.* **2021**, *55*, 12106–12115. [CrossRef] [PubMed]
25. Xiao, Q.; Zheng, Y.; Geng, G.; Chen, C.; Huang, X.; Che, H.; Zhang, X.; He, K.; Zhang, Q. Separating emission and meteorological contribution to PM_{2.5} trends over East China during 2000–2018. *Atmos. Chem. Phys.* **2021**, *21*, 9475–9496. [CrossRef]
26. Xiao, Q.; Geng, G.; Cheng, J.; Liang, F.; Li, R.; Meng, X.; Xue, T.; Huang, X.; Kan, H.; Zhang, Q.; et al. Evaluation of gap-filling approaches in satellite-based daily PM_{2.5} prediction models. *Atmos. Environ.* **2021**, *244*, 117921. [CrossRef]

Article

Variation and Driving Factor of Aerosol Optical Depth over the South China Sea from 1980 to 2020

Enwei Sun ^{1,2,*}, Chuanbo Fu ², Wei Yu ¹, Ying Xie ¹, Yiwen Lu ¹ and Chunsong Lu ³

- ¹ Shanghai Ecological Forecasting and Remote Sensing Center, Shanghai Meteorological Service, Shanghai 200030, China; wyu16@fudan.edu.com (W.Y.); xiey@shnwp.org (Y.X.); ywlu9129@163.com (Y.L.)
² Key Laboratory of South China Sea Meteorological Disaster Prevention and Mitigation of Hainan Province, Haikou 570203, China; hnfuchuanbo@163.com
³ Key Laboratory for Aerosol-Cloud-Precipitation of China Meteorological Administration, Nanjing University of Information Science and Technology, Nanjing 210044, China; luchunsong110@163.com
* Correspondence: sunenwei@aliyun.com

Citation: Sun, E.; Fu, C.; Yu, W.; Xie, Y.; Lu, Y.; Lu, C. Variation and Driving Factor of Aerosol Optical Depth over the South China Sea from 1980 to 2020. *Atmosphere* **2022**, *13*, 372. <https://doi.org/10.3390/atmos13030372>

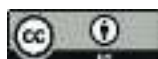
Academic Editors: Duanyang Liu, Kai Qin and Honglei Wang

Received: 20 January 2022

Accepted: 21 February 2022

Published: 23 February 2022

Publisher's Note: MDPI stays neutral with regard to jurisdictional claims in published maps and institutional affiliations.



Copyright: © 2022 by the authors. Licensee MDPI, Basel, Switzerland. This article is an open access article distributed under the terms and conditions of the Creative Commons Attribution (CC BY) license (<https://creativecommons.org/licenses/by/4.0/>).

Abstract: Spatial and temporal variation of aerosol optical depth (AOD) and optical depth of different aerosol types derived from the second Modern-Era Retrospective analysis for Research and Applications (MERRA-2) over the South China Sea (SCS) between 1980 and 2020 were studied. AOD distribution showed different characteristics throughout the entire SCS. Sulfate Aerosol Optical Depth (SO₄AOD) and Sea Salt Aerosol Optical Depth (SSAOD) mainly contributed to the spatial and temporal variation of AOD over the SCS. A significant increasing trend followed by a decreasing trend of AOD could be observed in the north of the SCS from 1980 to 2020. Mean MERRA-2 AOD between 1980 and 2020 showed that AOD was high in the north and low in the south and that AOD gradually decreased from north to south over the SCS. AOD after 2000 was obviously higher than that of the 1980s and 1990s. Higher AOD appeared in the spring and winter, and low AOD appeared in the summer. The spatial distribution of scattering aerosol optical depth (SAOD) was similar to AOD distribution over the SCS. SO₄AOD and SSAOD were obviously higher than black carbon aerosol optical depth (BCAOD), organic carbon aerosol optical depth (OCAOD), and dust aerosol optical depth (DUAOD) over the SCS. SO₄AOD accounted for over 50% of total AOD (TAOD) over the north of the SCS, while BCAOD and DUAOD accounted for less than 10% of TAOD over the entire SCS. An obvious annual mean TAOD increase between 1980 and 2007 could be observed over the northern part of the SCS (NSCS), while a TAOD decrease happened from 2008 to 2020 in this region. The correlation coefficient between TAOD and SO₄AOD over NSCS from 1980 to 2020 was about 0.93, indicating SO₄AOD was the driving factor of TAOD variation in this area. Different AOD variation trends over the different areas of the SCS could be observed during the two periods including 1980–2007 and 2008–2020. AOD increase appeared over most of the SCS during the period from 1980 to 2007, while AOD decrease could be observed over most of the SCS from 2008 to 2020.

Keywords: aerosol optical depth; MERRA-2; South China Sea; climate

1. Introduction

Aerosol is an important constituent of the atmosphere, and plays a key role in the radiation balance, regional and global climate change, and human health [1–11]. Aerosol is released to the atmosphere through both natural and anthropogenic processes. To have a better understanding of aerosol, a large number of studies about aerosol have been conducted by researchers around the world [12–25]. However, at present, aerosol optical property is still one of the largest sources of uncertainty in estimating climate change. AOD represents extinction of light over the vertical column of atmosphere. As an important measure of aerosol loading, AOD is a crucial metric in assessment of global climate change and the impact of aerosol on precipitation, radiation, and clouds [26]. Ground-based

measurement with high accuracy is an effective method to obtain AOD, and is always used to validate satellite and reanalysis data.

Ground-based observation networks mainly include AERONET, China Aerosol Remote Sensing Network (CARSNET), and Sky Radiometer Network (SKYNET). AERONET could provide consistent measurements of aerosol optical properties, and was known as a global sun-photometer network [27–31]. Established by the China Meteorological Administration (CMA) in 2002, CARSNET is an independent aerosol monitoring network with the same type of sun-photometer as AERONET [32–35]. SKYNET equipped with pyranometer and sun/sky photometer is a radiation network [36]. Ground-based observation has high accuracy, but it offers limited temporal and spatial coverage. Compared with sparse ground-based observation, satellite remote sensing can provide measurements covering large areas. For example, the Moderate Resolution Imaging Spectroradiometer (MODIS) aerosol products are usually used in aerosol analysis. Although MODIS data can cover a large area, the study period is only about 20 years. In addition, there are limitations under cloudy conditions for satellite data. Reanalysis product plays an important role in the areas which lack measurements or only have short-term observations. MERRA-2 aerosol products not only can cover large areas, but also provide long-term aerosol data from 1980 to present. Moreover, MERRA-2 also can offer aerosol data under cloudy conditions.

Due to rapid industrial development, air pollution has become a serious problem in the regions where people live. A lot of researchers have carried out studies about aerosol characteristics over land. Yu et al. [37] did research about aerosol optical properties in Beijing with AERONET measurements between 2002 and 2007, finding an obvious seasonal variation with higher AOD values in spring and summer. Kang et al. [38] conducted research about aerosol optical property in Nanjing through ground-based measurements from September 2007 to August 2008, and arrived at the conclusion that aerosol over Nanjing mainly contained the mixed type, urban-industrial type, and biomass burning type. Che et al. [39] studied aerosol pollution in eastern China with ground-based measurements between 2011 and 2015 from seven observation sites, pointing out that—different from northern China—AOD in the Yangtze River Delta during July and August is lower than in January and February because of particle dispersion. Due to air mass transport, natural and anthropogenic aerosol can spread through the atmosphere over a large spatial scale. The transport of atmospheric aerosol from continental areas to oceans leads to the spatiotemporal heterogeneity of the atmospheric aerosol characteristics over oceans, which can influence the regional climate [40]. Therefore, aerosol study over the oceans is also important.

As a low-latitude sea, the South China Sea (SCS) is located in the south of China and is adjacent to several Asian countries. The SCS is a major sea route which connects the Pacific Ocean and the Indian Ocean. With abundant marine resources, the SCS is the largest marginal sea of China. Large amounts of atmospheric aerosols from these surrounding regions transport to the SCS [41]. The deposition of aerosol over sea has an important impact on the seawater. In order to comprehensively understand the significant role of aerosol in climate change and the biogeochemical cycle, variation of aerosol properties over sea needs to be studied. At present, much attention has been given to the SCS. Sun et al. [42] conducted research about variability of AOD in the SCS and concluded that AOD had an obvious dependence on the wind speed. Zhang et al. [43] investigated the aerosol properties over the SCS with ground-based observations in two sites, including Taiping and Dongsha. The study found that AOD in Taiping is less than 0.2 and that AOD in Dongsha was between 0 and 0.6. Li et al. [44] studied the aerosol properties over the northern area of the SCS between 9 August and 7 September 2016 with a shipborne micro-pulse lidar, finding that AOD was lower over the southwest side than the northeast side of the cruise region.

Although investigations about aerosol properties over the SCS have been conducted, the study period of most studies is not long enough. It is essential to conduct investigation on the long-term variation of aerosol loadings over the SCS. In this study, variations of

MERRA-2 AOD, BCAOD, OCAOD, SO₄AOD, DUAOD, and SSAOD from 1980 to 2020 were analyzed to offer a better understanding of aerosol property over the SCS.

2. Materials and Methods

MERRA-2 is a NASA reanalysis product from 1980 onward. With a $0.625^\circ \times 0.5^\circ$ longitude-by-latitude grid, MERRA-2 offers data collections including AOD products, radiation diagnostics, and so on. The resolution of MERRA-2 is approximately 50×50 km. In this study, monthly MERRA-2 AOD, BCAOD, OCAOD, SO₄AOD, DUAOD, and SSAOD were used to study the long-term variation of aerosol over the SCS. Three regions of interest over the SCS were chosen for a better analysis of the aerosol variation. In addition, linear regression method was used to calculate the MERRA-2 AOD variation trend over the SCS in two periods, including 1980–2007 and 2008–2020.

Figure 1 showed the map of the SCS and the locations of the northern part of the South China Sea (NSCS), the middle part of the South China Sea (MSCS), and the southern part of the South China Sea (SSCS).

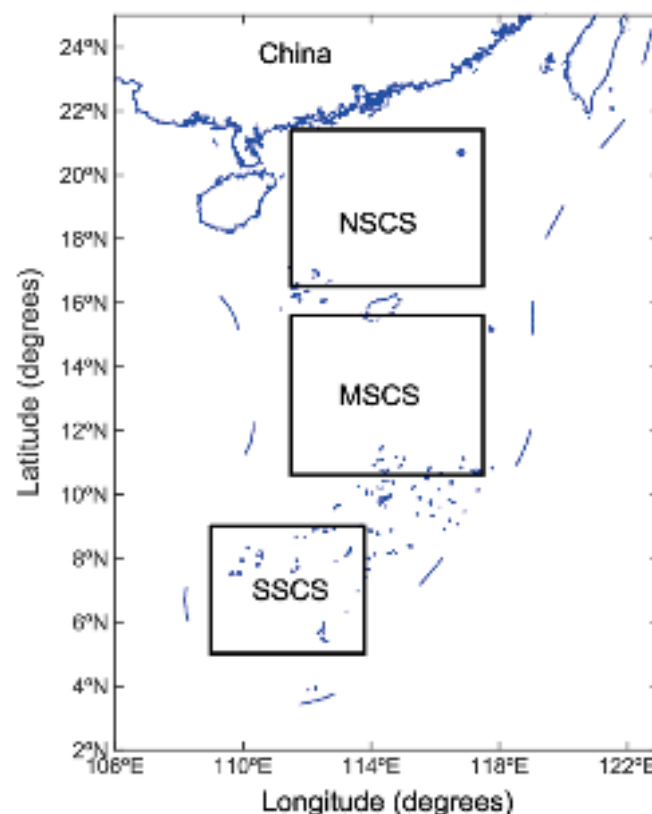


Figure 1. Map of the South China Sea (SCS). The black boxes represent the three selected regions of interest: the northern part of the South China Sea (NSCS), the middle part of the South China Sea (MSCS), and the southern part of the South China Sea (SSCS).

3. Results and Discussion

3.1. Accuracy of MERRA-2 AOD

As AOD are retrieved and assimilated from AERONET, MISR, MODIS, and AVHRR, MERRA-2 AOD agreed well with the ground-based measurements [45]. The correlation coefficients between AERONET and MERRA-2 AOD were 0.84, 0.88, and 0.90 in Xianghe, Beijing, and the Yangtze River Basin [46]. MERRA-2 AOD was compared with ground-based AOD from 29 CARSNET stations throughout China during 2002–2014, and good agreement was also obtained [47]. The good agreement between MERRA-2 and ground-based AOD offered an important theoretical basis for the following study of temporal and spatial distributions of MERRA-2 AOD over the SCS from 1980 to 2020.

3.2. Spatial Distribution and Temporal Variation of MERRA-2 AOD

There are 41 years from 1980 to 2020, totalling 492 months. With the monthly MERRA-2 AOD data, we obtained the mean value of MERRA-2 AOD during the period between 1980 and 2020. In Figure 2, the four-decade-long mean MERRA-2 AOD over the SCS was obviously high in the north and low in the south, and gradually decreased from the north to south. More obvious AOD variation could be seen in the north of the SCS. The highest AOD between 0.35 and 0.40 is over China's offshore region. This is due to the aerosol transport from land with higher AOD (over 0.40) to the ocean. The aerosol over the offshore region can be easily affected by the aerosol over land because of the short distance. The lowest AOD appeared in the southern part of the SCS where AOD was less than 0.15. In the middle of the SCS, AOD value was between 0.15 and 0.20. The mean MERRA-2 AOD value over Dongsha was between 0.275 and 0.30, while the AOD value over Taiping was between 0.15 and 0.175. AOD over Dongsha was higher than AOD over Taiping, which was consistent with the conclusion by Zhang et al. [43].

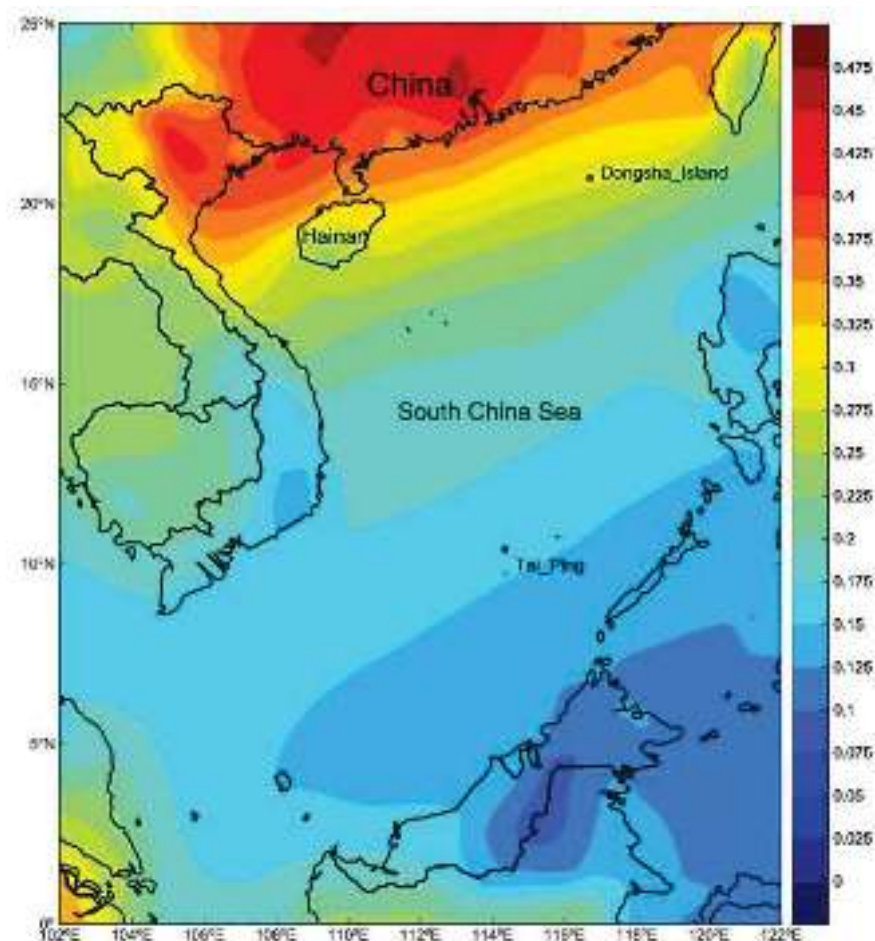


Figure 2. Spatial distribution of mean values of the 550 nm MERRA-2 AOD over the SCS in the period of 1980–2020.

As shown in Figure 3, the spatial distributions of mean MERRA-2 AOD over the SCS in eight 5-year periods showed similar distribution from 1980 to 2020. High AOD appeared in the north of the SCS, and low AOD appeared in the south of the SCS in the eight 5-year periods. In the period of 1980–1985, AOD in the north of the SCS was between 0.20 and 0.30, and AOD in the majority of the southern region of the SCS was between 0.15 and 0.20. In the period of 1986–1990, AOD in the south of the SCS was only between 0.10 and 0.15, which was obviously lower than that in 1980–1985. This could be due to the eruption of the El Chichon volcano in 1982 [48], which caused relatively higher AOD in 1980–1985.

Because of the eruption of Pinatubo volcano in 1991 in the Philippines [49], AOD rose obviously in the period of 1991–1995, and was higher than that in 1986–1990 over the entire SCS. With the gradual deposition of volcanic pollutants, an obvious AOD decrease could be observed in 1996–2000. During 1996–2000, AOD was again below 0.15 in the south of the SCS. After 2000, rapid industrial development of China and the aerosol transport from the land to ocean contributed to the AOD increase over the SCS. AOD over the offshore region of China in the north of the SCS after 2000 was obviously higher than that before 2000. Affected by the high AOD over land, AOD over the offshore region of China could exceed 0.35 after 2000. The sea area to the west of Hainan Island, whose location could be seen in Figure 2, is about 0.40 in the period of 2001–2005. The AOD of this sea area exceeded 0.50 in 2006–2010 and 2011–2015, and then decreased to about 0.40 in 2016–2020.

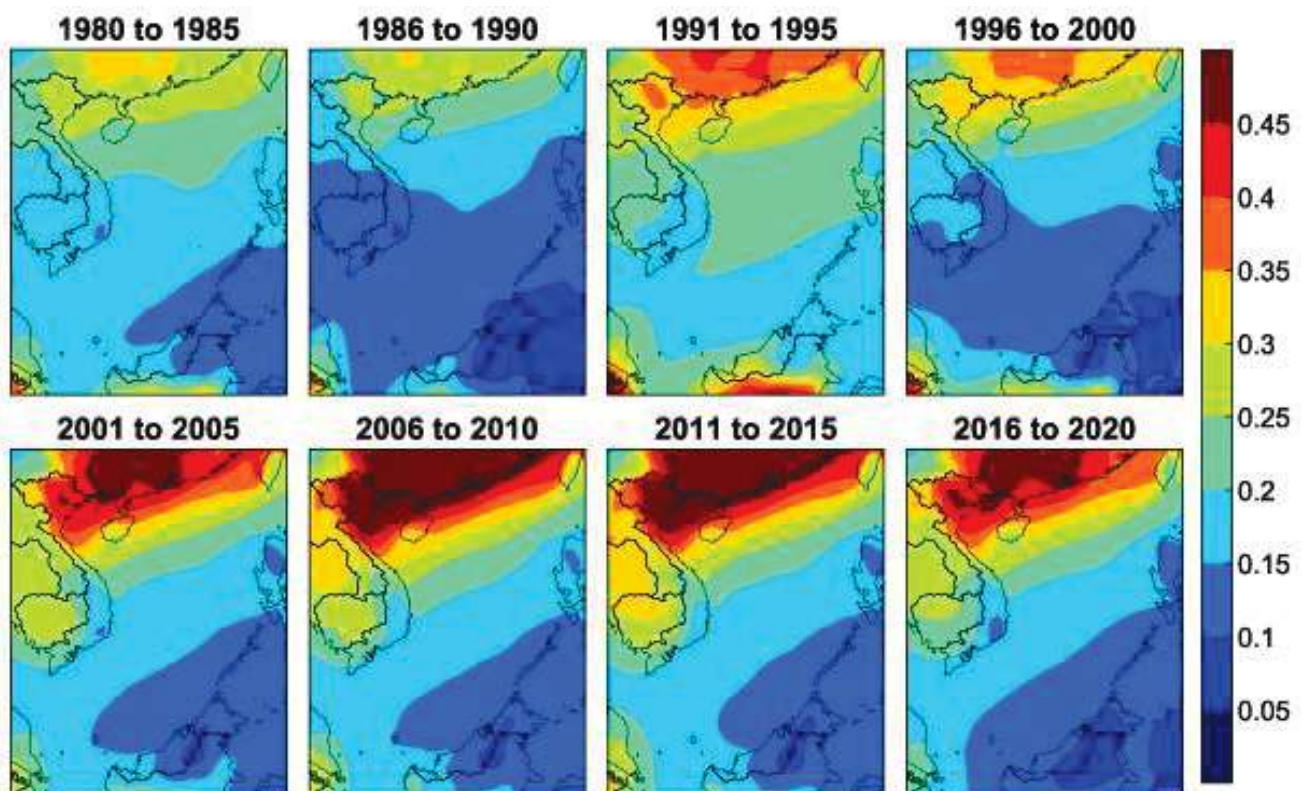


Figure 3. Variation of MERRA-2 AOD in 5-year intervals in the period of 1980–2020.

Figure 4 illustrated the mean AOD in each month over the SCS between 1980 and 2020. In most months, similar spatial distribution could be observed. High AOD appeared in the north and low AOD occurred in the south. In addition, high AOD could be observed in spring and winter, while low AOD occurred in summer. In March and April, AOD over the north of the SCS exceeded 0.50, while in June and July AOD over the north of the SCS was only about 0.20. In September, higher AOD could be observed in the south than in the middle of the SCS. These could be explained by the following facts. With a monsoon climate, the SCS has a northeast monsoon in winter and spring, and a southwest monsoon in summer and autumn. In winter and spring, dust and pollution transported from mainland China and Japan in the northeast, while during summer and autumn, the SCS received biomass burning pollutants from Malaysia and Indonesia from the southwest [41].

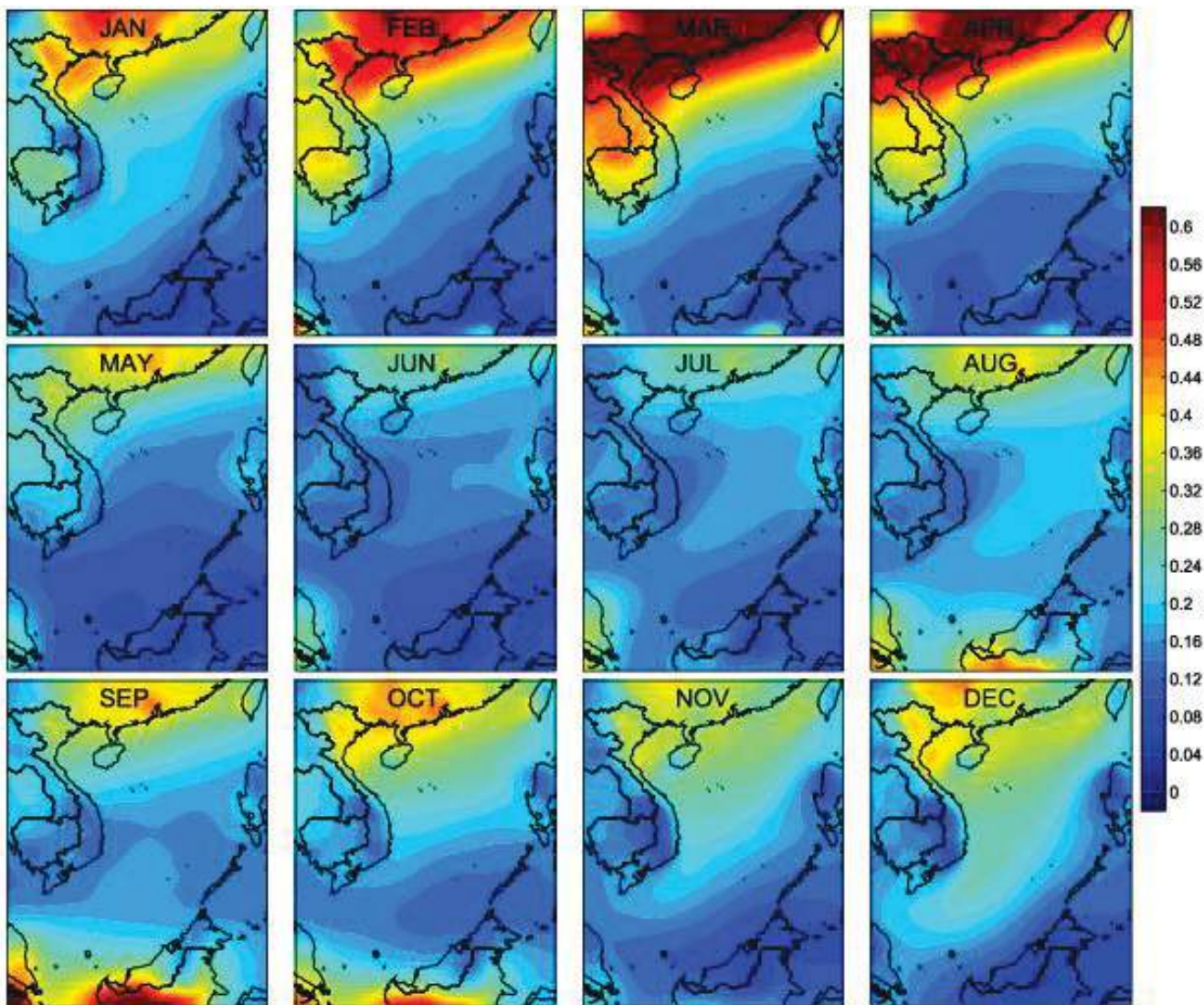


Figure 4. Spatial distribution of mean MERRA-2 AOD in each month in the period of 1980–2020.

3.3. Spatial Distribution of MERRA-2 SAOD and AAOD

Scattering aerosol optical depth (SAOD) could be obtained by subtracting absorption aerosol optical depth (AAOD) from the total aerosol optical depth (TAOD) [50]. Mean values of MERRA-2 SAOD and AAOD between 1980 and 2020 over the SCS were shown in Figure 5. In Figure 5a, the spatial distribution of SAOD was similar to AOD distribution in Figure 2. SAOD was high in the north and low in the south, and gradually decreased from the north to south over the SCS. On the whole, SAOD was a little lower than AOD over the SCS. The north of the SCS showed more obvious SAOD variation. The highest SAOD between 0.325 and 0.375 occurred in the offshore area of China, while the lowest SAOD between 0.125 and 0.15 could be observed in the south of the SCS. In the middle of the SCS, SAOD was between 0.15 and 0.175. As shown in Figure 5b, high AAOD (0.015–0.0175) appeared in the north and low AAOD (0.0025–0.005) was in the south of the SCS. AAOD gradually decreased from the north to the south. More obvious AAOD variation could be observed in the north of the SCS. In the middle of the SCS, AAOD was between 0.005 and 0.0075. Over the entire SCS, AAOD was much lower than SAOD, indicating scattering extinction played a major role in this area.

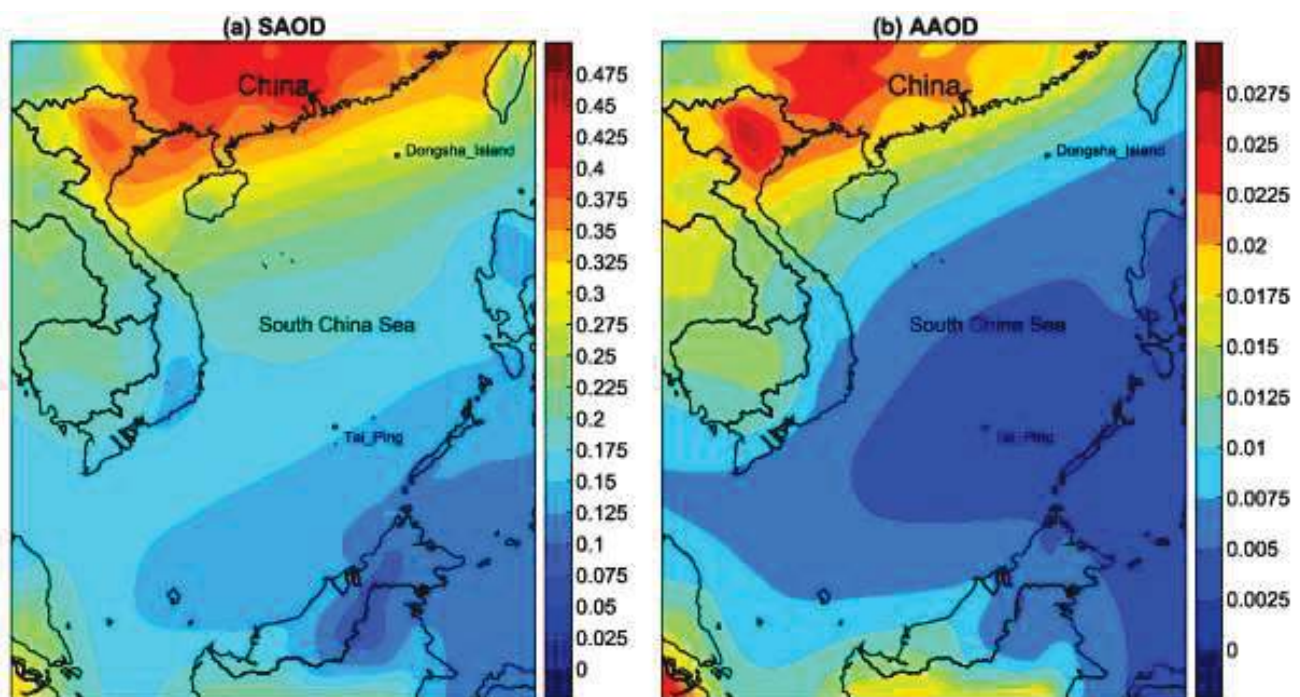


Figure 5. Spatial distribution of mean values of (a) scattering aerosol optical depth (SAOD) and (b) absorption aerosol optical depth (AAOD) over the SCS in the period of 1980–2020.

3.4. Spatial Distribution and Temporal Variation of MERRA-2 AOD of Different Aerosol Compositions

Black carbon, organic carbon, dust, sulfate, and sea salt aerosol are the main components in the aerosol. MERRA-2 AOD is the sum of SO_4AOD , BCAOD , OCAOD , DUAOD , and SSAOD . As shown in Figure 6, the mean BCAOD , OCAOD , DUAOD , SO_4AOD , and SSAOD during 1980 and 2020 showed different characteristics over the SCS. SO_4AOD and SSAOD had higher values than BCAOD , OCAOD , and DUAOD . BCAOD and DUAOD had the lowest values which were less than 0.02 over the entire SCS. OCAOD was also low, and was under 0.04 over most part of the SCS. Only in the north of the SCS, OCAOD exceeded 0.04. SO_4AOD showed similar spatial distribution to the total AOD mentioned above, while the spatial distribution of BCAOD and DUAOD was completely different from that of total AOD. The spatial distribution of BCAOD over the SCS showed almost no difference, and so did DUAOD . The spatial distribution with most obvious difference over the SCS was SO_4AOD . SO_4AOD was high in the north and relatively low in the south, and gradually decreased from the north to south over the SCS. More obvious SO_4AOD variation appeared in the north of the SCS. The highest SO_4AOD (over 0.20) appeared in the north of the SCS, and the lowest SO_4AOD (under 0.06) occurred in the south of the SCS. SO_4AOD in the middle of the SCS was mainly between 0.06 and 0.08. The SSAOD was between 0.06 and 0.10 over most part of the SCS, and the highest SSAOD values were mainly between 0.08 and 0.10. Total AOD over SCS was mainly affected by SO_4AOD and SSAOD .

The contribution of SO_4AOD , BCAOD , OCAOD , DUAOD , and SSAOD to AOD was obtained through the equations

$$\text{SO}_4\text{AOD Percent} = \text{SO}_4\text{AOD} / \text{AOD} \quad (1)$$

$$\text{BCAOD Percent} = \text{BCAOD} / \text{AOD} \quad (2)$$

$$\text{OCAOD Percent} = \text{OCAOD} / \text{AOD} \quad (3)$$

$$\text{DUAOD Percent} = \text{DUAOD} / \text{AOD} \quad (4)$$

$$\text{SSAOD Percent} = \text{SSAOD} / \text{AOD} \quad (5)$$

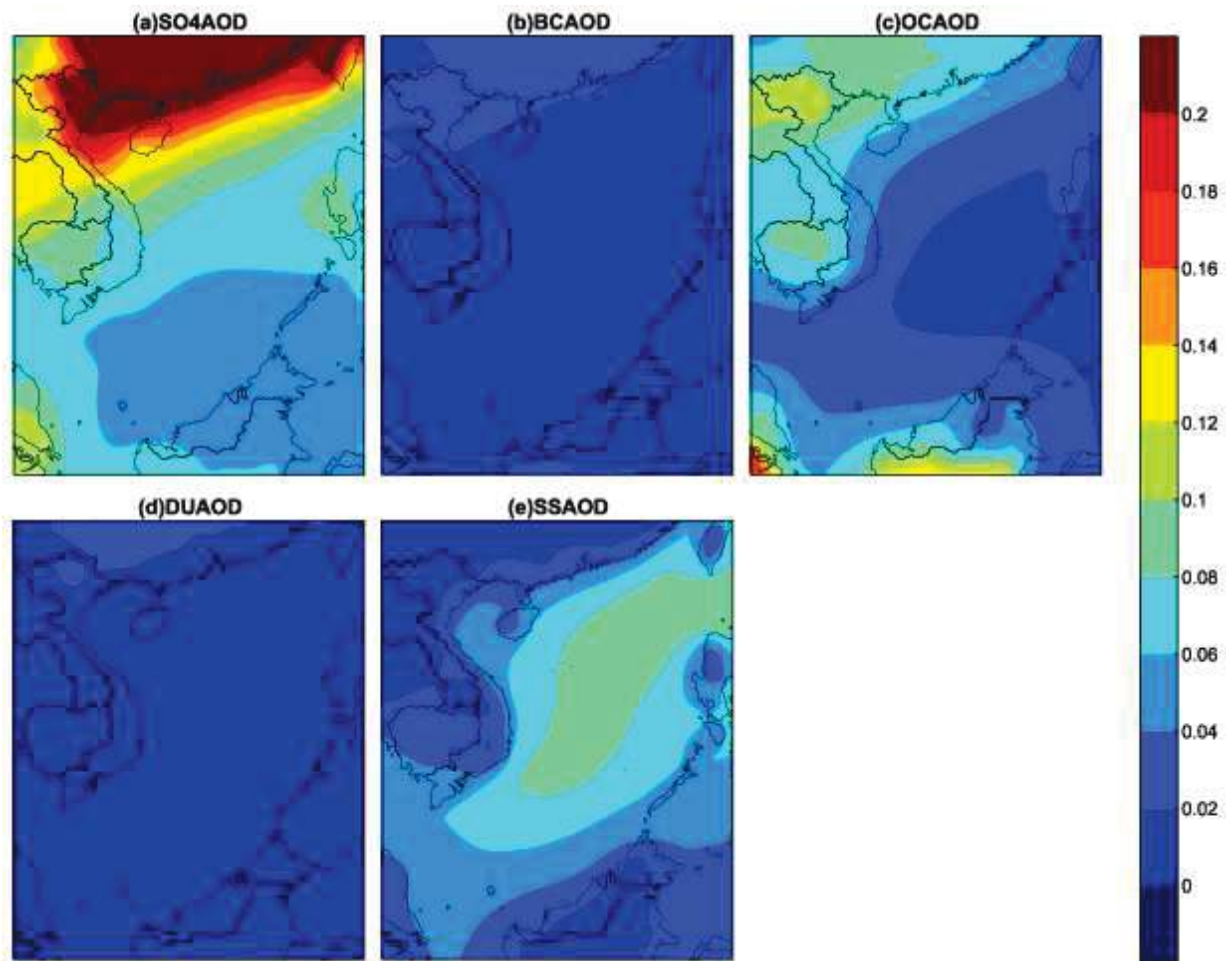


Figure 6. Spatial distribution of mean MERRA-2 values of (a) SO_4AOD , (b) BCAOD , (c) OCAOD , (d) DUAOD , and (e) SSAOD over the SCS during the period of 1980–2020.

Figure 7 showed the contributions of SO_4AOD , BCAOD , OCAOD , DUAOD , and SSAOD to the total AOD over the SCS, respectively. SO_4AOD Percent and SSAOD Percent were obviously higher than BCAOD Percent, OCAOD Percent, and DUAOD Percent. BCAOD Percent and DUAOD Percent had the lowest values which were less than 10% over the entire SCS. OCAOD Percent was mainly between 10% and 20%, and only a small part in the middle of the SCS was under 10%. SO_4AOD Percent decreased from north to the south over the SCS. The highest values of SO_4AOD Percent appeared in the north of the SCS, which were between 50% and 60%. Relatively lower values of SO_4AOD Percent, between 30% and 40%, occurred in the middle and south of the SCS. Different from SO_4AOD Percent, SSAOD Percent was low in the north, and higher in the middle and south of the SCS. In the north of the SCS, SSAOD Percent was between 10% and 20%, which was the lowest over the SCS. Most SSAOD Percent values over the SCS were between 30% and 50%. The highest SSAOD Percent values (between 50% and 60%) appeared in a small part in the middle of the SCS.

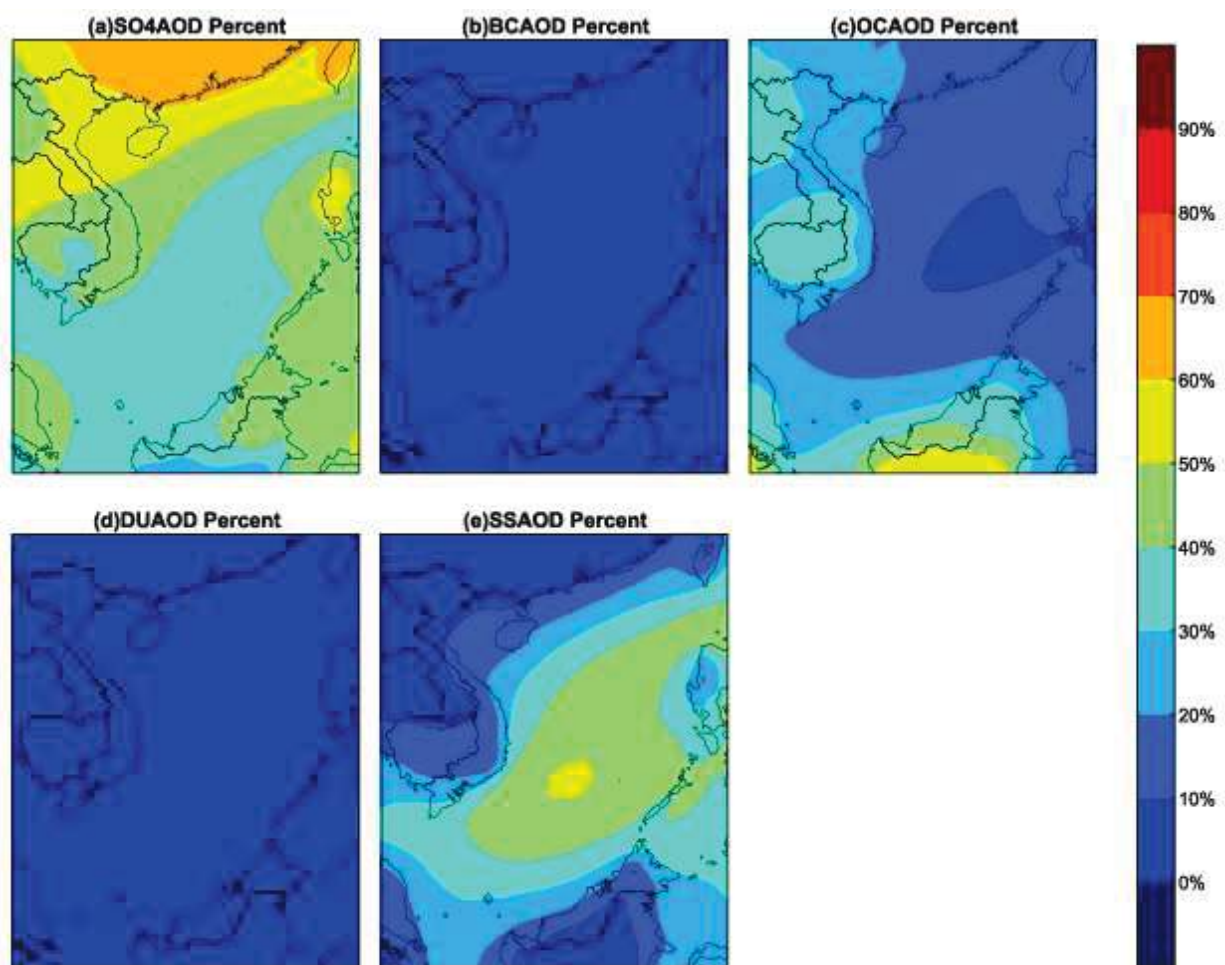


Figure 7. Spatial distribution of (a) SO_4AOD Percent, (b) BCAOD Percent, (c) OCAOD Percent, (d) DUAOD Percent, and (e) SSAOD Percent over the SCS during the period of 1980–2020.

As shown in Figure 8a, an obvious annual mean TAOD increase followed by a decrease could be observed over NSCS during the period of 1980–2020, and the same was for SO_4AOD which was higher than BCAOD , OCAOD , DUAOD , and SSAOD in this region. The TAOD maxima at the beginning of the 1980s and 1990s was due to the El Chichon eruption in Mexico in 1982 [48] and the Pinatubo eruption in the Philippines in 1991 [49]. With the deposition of the pollutants, TAOD gradually decreased after 1982 and 1991, respectively. He et al. [51] studied the MODIS AOD over the entire area of mainland China between 2002 and 2015, and found an upward tendency pre-2008 due to booming economy and a downward tendency post-2008 as a result of the Chinese government's environmental protection policy which lead to emission reduction. In this study, the increase of TAOD (SO_4AOD) during the period of 1980–2007 was 0.0029 (0.0013) per year, while the decrease of TAOD (SO_4AOD) from 2008 to 2020 was -0.0033 (-0.0029) per year over NSCS. The mean value of SO_4AOD during the period of 1980–2020 accounted for 47.9% of TAOD over NSCS. The R between TAOD and SO_4AOD from 1980 to 2020 was about 0.93, indicating that the variation of TAOD was mainly due to the variation of SO_4AOD in this area. In Figure 8b,c, no significant variation trend of TAOD and SO_4AOD could be observed from 1980 to 2020. This could be due to the far distance of MSCS and SSCS from mainland China. SSAOD was higher than SO_4AOD in MSCS and SSCS. SSAOD accounted for 46.5% and 41.7%, while SO_4AOD accounted for 37.9% and 35.6% in MSCS and SSCS, respectively.

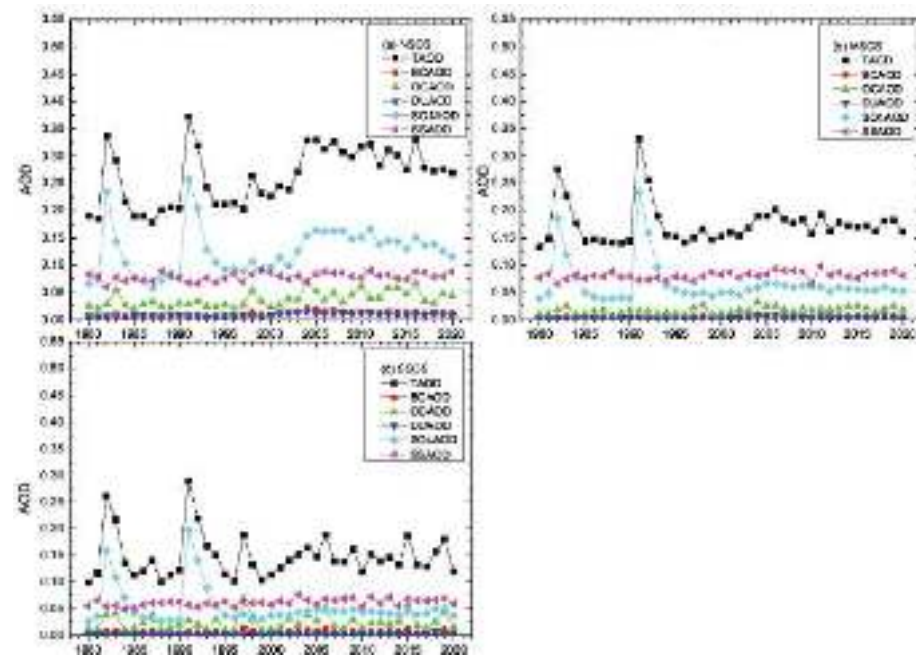


Figure 8. Variation of annual mean values of TAOD, BCAOD, OCAOD, DUAOD, SO_4AOD , and SSAOD over (a) NSCS, (b) MSCS, and (c) SSCS during the period of 1980–2020.

3.5. Variation Trend of MERRA-2 AOD

In Figure 9a, an AOD increase could be observed over most part of the SCS from 1980 to 2007. In this period, highest AOD increase (between 0.005 and 0.01 per year) could be seen in the north of the SCS, and the AOD increase (between 0 and 0.005 per year) occurred in the north and middle of the SCS. p -values of less than 0.05 mainly appeared in the north of the SCS. Hse et al. [52] studied the global trends of AOD over ocean with SeaWiFS data, and also found annual AOD increase trend over ocean from 1998 to 2010. In Figure 9b, AOD decreased over most of the SCS. AOD decrease (between -0.01 and -0.005 per year) appeared over the north of the SCS, and AOD decrease (between -0.005 and 0 per year) was over the north and middle of the SCS. p -values of less than 0.05 mainly occurred in the north of the SCS and a small part in the middle of the SCS. The AOD increase or decrease was more significant over the coastal region of mainland China due to the aerosol transport from land to ocean.

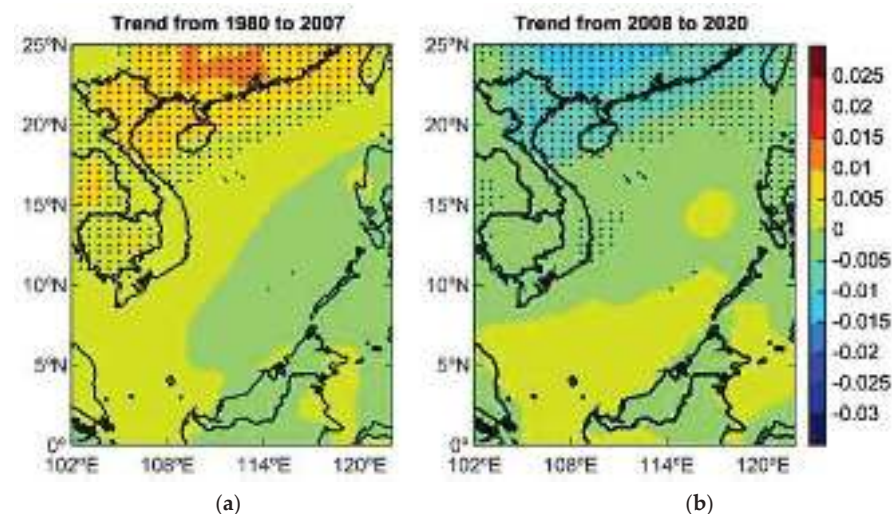


Figure 9. Variation trend of MERRA-2 AOD over the SCS during the period (a) 1980–2007 and (b) 2008–2020 (the small black dot represents $p < 0.05$).

4. Conclusions

We analyzed spatial and temporal variation of AOD and optical depth of different aerosol types during the period of 1980–2020 with MERRA-2 dataset, and the difference of spatial and temporal distribution of AOD was obtained. SO_4 AOD and SSAOD dominated the variation of AOD over the SCS. An AOD upward trend followed by a downward trend occurred in the north of the SCS in this period. Mean MERRA-2 AOD from 1980 to 2020 was high in the north and low in the south over the SCS, and gradually decreased from the north to the south in this region. Due to rapid economic development, AOD after 2000 reached a higher value than that in 1980s and 1990s. Mean AOD in each month from 1980 to 2020 was analyzed. Higher AOD was in spring and winter, and low AOD appeared in summer. Similar spatial distribution could be observed between SAOD and AOD over the SCS, and AAOD was much lower than SAOD in this region. SO_4 AOD and SSAOD had higher values than BCAOD, OCAOD, and DUAOD over the SCS. Over the north of the SCS, SO_4 AOD accounted for more than 50% of TAOD, while BCAOD and DUAOD accounted for only less than 10% of TAOD all over the SCS. TAOD over NSCS showed an upward trend from 1980 to 2007 and a downward trend from 2008 to 2020. Similar annual variation between TAOD and SO_4 AOD over NSCS from 1980 to 2020 could be observed, and the R between them reached 0.93. This indicated that variation of the SO_4 AOD was the driving force of the variation of TAOD over NSCS from 1980 to 2020. The spatial distribution of AOD variation trend over the SCS in two periods was also analyzed. Different AOD variation trends over the different areas of the SCS appeared during the two periods including 1980–2007 and 2008–2020. AOD increase could be observed over most of the SCS between 1980 and 2007, while AOD decrease was observed over most of the SCS from 2008 to 2020.

Author Contributions: Conceptualization, E.S.; Software, E.S., W.Y. and C.F.; Methodology, C.F. and C.L.; Writing—original draft, E.S.; Investigation, W.Y. and Y.X.; Supervision, Y.L.; Writing—reviewing and editing, C.L. All authors have read and agreed to the published version of the manuscript.

Funding: This research was supported by the Key Laboratory of South China Sea Meteorological Disaster Prevention and Mitigation of Hainan Province (SCSF202010).

Institutional Review Board Statement: Not applicable.

Informed Consent Statement: Not applicable.

Data Availability Statement: MERRA-2 aerosol optical property data used in this study is from https://goldsmr4.gesdisc.eosdis.nasa.gov/data/MERRA2_MONTHLY/M2TMNXAER.5.12.4/2020/, accessed on 19 January 2022.

Acknowledgments: We thank NASA for making the MERRA-2 aerosol reanalysis publicly accessible. Thanks are also extended to the anonymous reviewers for their useful comments and suggestions.

Conflicts of Interest: The authors declare no conflict of interest.

References

1. Filip, L.; Stefan, S. Study of the correlation between the near-ground PM10 mass concentration and the aerosol optical depth. *J. Atmos. Sol. Terr. Phys.* **2011**, *73*, 1883–1889. [CrossRef]
2. Charlson, R.J.; Schwartz, S.E.; Hales, J.M.; Cess, R.D.; Coakley, J.A.; Hansen, J.E.; Hofmann, D.J. Climate forcing by anthropogenic aerosols. *Science* **1992**, *255*, 423–430. [CrossRef] [PubMed]
3. Deng, X.; Shi, C.; Wu, B.; Chen, Z.; Nie, S.; He, D.; Zhang, H. Analysis of aerosol characteristics and their relationships with meteorological parameters over Anhui province in China. *Atmos. Res.* **2012**, *109–110*, 52–63. [CrossRef]
4. Zhao, H.; Che, H.; Zhang, X.; Ma, Y.; Wang, Y.; Wang, X.; Liu, C.; Hou, B.; Che, H. Aerosol optical properties over urban and industrial region of Northeast China by using ground-based sun-photometer measurement. *Atmos. Environ.* **2013**, *75*, 270–278. [CrossRef]
5. Liu, X.; Chen, Q.; Che, H.; Zhang, R.; Gui, K.; Zhang, H.; Zhao, T. Spatial distribution and temporal variation of aerosol optical depth in the Sichuan basin, China, the recent ten years. *Atmos. Environ.* **2016**, *147*, 434–445. [CrossRef]

6. Gopal, K.; Reddy, K.; Balakrishnaiah, G.; Arafath, S.; Reddy, N.; Rao, T.; Reddy, T.; Reddy, R. Regional trends of aerosol optical depth and their impact on cloud properties over southern India using MODIS data. *J. Atmos. Sol. Terr. Phys.* **2016**, *146*, 38–48. [CrossRef]
7. Gui, K.; Che, H.; Wang, Y.; Wang, H.; Zhang, L.; Zhao, H.; Zheng, Y.; Sun, T.; Zhang, X. Satellite-derived PM_{2.5} concentration trends over Eastern China from 1998 to 2016: Relationships to emissions and meteorological parameters. *Environ. Pollut.* **2019**, *247*, 1125–1133. [CrossRef]
8. Jin, Q.; Crippa, P.; Pryor, S. Spatial characteristics and temporal evolution of the relationship between PM_{2.5} and aerosol optical depth over the eastern USA during 2003–2017. *Atmos. Environ.* **2020**, *239*, 117718. [CrossRef]
9. Yao, W.; Che, H.; Gui, K.; Wang, Y.; Zhang, X. Can MERRA-2 Reanalysis Data Reproduce the Three-Dimensional Evolution Characteristics of a Typical Dust Process in East Asia? A Case Study of the Dust Event in May 2017. *Remote Sens.* **2020**, *12*, 902. [CrossRef]
10. Yousefi, R.; Wang, F.; Ge, Q.; Lelieveld, J.; Shaheen, A. Aerosol Trends during the Dusty Season over Iran. *Remote Sens.* **2021**, *13*, 1045. [CrossRef]
11. Jin, Y.; Hao, Z.; Chen, J.; He, D.; Tian, Q.; Mao, Z.; Pan, D. Retrieval of Urban Aerosol Optical Depth from Landsat 8 OLI in Nanjing, China. *Remote Sens.* **2021**, *13*, 415. [CrossRef]
12. Chaubey, J.; Moorthy, K.; Babu, S.; Gogoi, M. Spatio-temporal variations in aerosol properties over the oceanic regions between coastal India and Antarctica. *J. Atmos. Sol. Terr. Phys.* **2013**, *104*, 18–28. [CrossRef]
13. Grandey, B.; Stier, P.; Wagner, T. Investigating relationships between aerosol optical depth and cloud fraction using satellite, aerosol reanalysis and general circulation model data. *Atmos. Chem. Phys.* **2013**, *13*, 3177–3184. [CrossRef]
14. Che, H.; Zhang, X.; Xia, X.; Goloub, P.; Holben, B.; Zhao, H.; Wang, Y.; Zhang, X.; Wang, H.; Blarel, L.; et al. Ground-based aerosol climatology of China: Aerosol optical depths from the China Aerosol Remote Sensing Network (CARSNET) 2002–2013. *Atmos. Chem. Phys.* **2015**, *15*, 7619–7652. [CrossRef]
15. He, Q.; Zhang, M.; Huang, B.; Tong, X. MODIS 3 km and 10 km aerosol optical depth for China: Evaluation and comparison. *Atmos. Environ.* **2017**, *153*, 150–162. [CrossRef]
16. Zhang, M.; Wang, Y.; Ma, Y.; Wang, L.; Gong, W.; Liu, B. Spatial distribution and temporal variation of aerosol optical depth and radiative effect in South China and its adjacent area. *Atmos. Environ.* **2018**, *188*, 120–128. [CrossRef]
17. Ali, G.; Bao, Y.; Boiyo, R.; Tang, W.; Lu, Q.; Min, J. Evaluating MODIS and MISR Aerosol Optical Depth Retrievals over Environmentally Distinct Sites in Pakistan. *J. Atmos. Sol. Terr. Phys.* **2019**, *183*, 19–35. [CrossRef]
18. Liu, D.; Zhao, T.; Boiyo, R.; Chen, S.; Lu, Z.; Wu, Y.; Zhao, Y. Vertical Structures of Dust Aerosols over East Asia Based on CALIPSO Retrievals. *Remote Sens.* **2019**, *11*, 701. [CrossRef]
19. Yang, Q.; Yuan, Q.; Yue, L.; Li, T.; Shen, H.; Zhang, L. The relationships between PM_{2.5} and aerosol optical depth (AOD) in mainland China: About and behind the spatio-temporal variations. *Environ. Pollut.* **2019**, *248*, 526–535. [CrossRef]
20. Luo, H.; Han, Y.; Lu, C.; Yang, J.; Wu, Y. Characteristics of Surface Solar Radiation under Different Air Pollution Conditions over Nanjing, China: Observation and Simulation. *Adv. Atmos. Sci.* **2019**, *36*, 1047–1059. [CrossRef]
21. Gupta, P.; Remer, L.; Patadia, F.; Levy, R.; Christopher, S. High-Resolution Gridded Level 3 Aerosol Optical Depth Data from MODIS. *Remote Sens.* **2020**, *12*, 2847. [CrossRef]
22. Liu, Q.; Cheng, N.; He, Q.; Chen, Y.; Liu, T.; Liu, X.; Zhang, H.; Li, J.; Zhan, Q. Meteorological conditions and their effects on the relationship between aerosol optical depth and macro-physical properties of warm clouds over Shanghai based on MODIS. *Atmos. Pollut. Res.* **2020**, *11*, 1637–1644. [CrossRef]
23. Bali, K.; Dey, S.; Ganguly, D. Diurnal patterns in ambient PM_{2.5} exposure over India using MERRA-2 reanalysis data. *Atmos. Environ.* **2021**, *248*, 118180. [CrossRef]
24. Luo, H.; Han, Y.; Cheng, X.; Lu, C.; Wu, Y. Spatiotemporal Variations in Particulate Matter and Air Quality over China: National, Regional and Urban Scales. *Atmosphere* **2021**, *12*, 43. [CrossRef]
25. Huang, J.; Arnott, W.; Barnard, J.; Holmes, H. Theoretical Uncertainty Analysis of Satellite Retrieved Aerosol Optical Depth Associated with Surface Albedo and Aerosol Optical Properties. *Remote Sens.* **2021**, *13*, 344. [CrossRef]
26. Zhao, B.; Jiang, J.; Diner, D.; Su, H.; Gu, Y.; Liou, K.; Jiang, Z.; Huang, L.; Takano, Y.; Fan, X.; et al. Intra-annual variations of regional aerosol optical depth, vertical distribution, and particle types from multiple satellite and ground-based observational datasets. *Atmos. Chem. Phys.* **2018**, *18*, 11247–11260. [CrossRef]
27. Li, J.; Carlson, B.; Dubovik, O.; Lacis, A. Recent trends in aerosol optical properties derived from AERONET measurements. *Atmos. Chem. Phys.* **2014**, *14*, 12271–12289. [CrossRef]
28. Almazroui, M. A comparison study between AOD data from MODIS deep blue collections 51 and 06 and from AERONET over Saudi Arabia. *Atmos. Environ.* **2019**, *225*, 88–95. [CrossRef]
29. McPhetres, A.; Aggarwal, S. An Evaluation of MODIS-Retrieved Aerosol Optical Depth over AERONET Sites in Alaska. *Remote Sens.* **2018**, *10*, 1384. [CrossRef]
30. Fan, A.; Chen, W.; Liang, L.; Sun, W.; Lin, Y.; Che, H.; Zhao, X. Evaluation and Comparison of Long-Term MODIS C5.1 and C6 Products against AERONET Observations over China. *Remote Sens.* **2017**, *9*, 1269. [CrossRef]
31. Merino, C.; Mateos, D.; Toledano, C.; Prospero, J.; Molinie, J.; Clotilde, L.; Gonzalez, R.; Cachorro, V.E.; Calle, A.; de Frutos, A.M. Impact of long-range transport over the Atlantic Ocean on Saharan dust optical and microphysical properties based on AERONET data. *Atmos. Chem. Phys.* **2018**, *18*, 9411–9424. [CrossRef]

32. Xie, Y.; Zhang, Y.; Xiong, X.; Qu, J.J.; Che, H. Validation of MODIS aerosol optical depth product over China using CARSNET measurements. *Atmos. Environ.* **2011**, *45*, 5970–5978. [CrossRef]
33. Gui, K.; Che, H.; Chen, Q.; Yu, J.; Zheng, Y.; Lu, S.; Wang, H.; Wang, Y.; Zhang, X.; Shi, G. Analysis of the Error in Retrievals of Aerosol Optical Properties from Sun photometer Measurements of CARSNET Due to a Variety of Objective Factors. *Atmosphere* **2016**, *7*, 9. [CrossRef]
34. Che, H.; Zhao, H.; Wu, Y.; Xia, X.; Zhu, J.; Dubovik, O.; Estelles, V.; Ma, Y.; Wang, Y.; Wang, H.; et al. Application of aerosol optical properties to estimate aerosol type from ground-based remote sensing observation at urban area of northeastern China. *J. Atmos. Sol. Terr. Phys.* **2015**, *132*, 37–47. [CrossRef]
35. Che, H.; Yang, L.; Liu, C.; Xia, X.; Wang, Y.; Wang, H.; Wang, H.; Lu, X.; Zhang, X. Long-term validation of MODIS C6 and C6.1 Dark Target aerosol products over China using CARSNET and AERONET. *Chemosphere* **2019**, *236*, 124268. [CrossRef]
36. Nakajima, T.; Uno, I.; Higurashi, A.; Sohn, B.J.; Oh, S.; Ohta, S.; Takamura, T.; Sekiguchi, M.; Takemura, T.; Kim, H.; et al. Significance of direct and indirect radiative forcings of aerosols in the East China Sea region. *J. Geophys. Res.* **2003**, *108*, 8658. [CrossRef]
37. Yu, X.; Zhu, B.; Zhang, M. Seasonal variability of aerosol optical properties over Beijing. *Atmos. Environ.* **2009**, *43*, 4095–4101. [CrossRef]
38. Kang, N.; Kumar, K.; Yu, X.; Yin, Y. Column-integrated aerosol optical properties and direct radiative forcing over the urban-industrial megacity Nanjing in the Yangtze River Delta, China. *Environ. Sci. Pollut. Res.* **2016**, *23*, 17532–17552. [CrossRef]
39. Che, H.; Qi, B.; Zhao, H.; Xia, X.; Eck, T.F.; Goloub, P.; Dubovik, O.; Estelles, V.; Cuevas-Agulló, E.; Blarel, L.; et al. Aerosol optical properties and direct radiative forcing based on measurements from the China Aerosol Remote Sensing Network (CARSNET) in eastern China. *Atmos. Chem. Phys.* **2018**, *18*, 405–425. [CrossRef]
40. Pani, S.; Wang, S.; Lin, N.; Tsay, S.; Lolli, S.; Chuang, M.; Lee, C.; Chantara, S.; Yu, J. Assessment of aerosol optical property and radiative effect for the layer decoupling cases over the northern South China Sea during the 7-SEAS/Dongsha Experiment. *J. Geophys. Res. Atmos.* **2016**, *121*, 4894–4906. [CrossRef]
41. Xiao, H.; Xiao, H.; Luo, L.; Shen, C.; Long, A.; Chen, L.; Long, Z.; Li, D. Atmospheric aerosol compositions over the South China Sea: Temporal variability and source apportionment. *Atmos. Chem. Phys.* **2017**, *17*, 3199–3214. [CrossRef]
42. Sun, Q.; Tang, D.; Levy, G.; Shi, P. Variability of aerosol optical thickness in the tropical Indian Ocean and South China Sea during spring inter monsoon season. *Int. J. Remote Sens.* **2018**, *39*, 4531–4549. [CrossRef]
43. Zhang, C.; Xu, H.; Li, Z.; Xie, Y.; Li, D. Maritime Aerosol Optical and Microphysical Properties in the South China Sea Under Multi-source Influence. *Sci. Rep.* **2019**, *9*, 17796. [CrossRef]
44. Li, Y.; Wang, B.; Lee, S.; Zhang, Z.; Wang, Y.; Dong, W. Micro-Pulse Lidar Cruising Measurements in Northern South China Sea. *Remote Sens.* **2020**, *12*, 1695. [CrossRef]
45. Randles, C.; Silva, A.; Buchard, V.; Colarco, P.; Darmenov, A.; Govindaraju, R.; Smirnov, A.; Ferrare, R.; Hair, J.; Shinozuka, Y.; et al. The MERRA-2 Aerosol Reanalysis, 1980-onward, Part I: System Description and Data Assimilation Evaluation. *J. Clim.* **2017**, *30*, 6823–6850. [CrossRef] [PubMed]
46. He, L.; Wang, L.; Huang, B.; Wei, J.; Zhou, Z.; Zhong, Y. Anthropogenic and meteorological drivers of 1980–2016 trend in aerosol optical and radiative properties over the Yangtze River Basin. *Atmos. Environ.* **2020**, *223*, 117188. [CrossRef]
47. Qin, W.; Liu, Y.; Wang, L.; Lin, A.; Xia, X.; Che, H.; Bilal, M.; Zhang, M. Characteristic and Driving Factors of Aerosol Optical Depth over Mainland China during 1980–2017. *Remote Sens.* **2018**, *10*, 1064. [CrossRef]
48. Hirono, M.; Shibata, T. Enormous increase of stratospheric aerosols over Fukuoka due to volcanic eruption of El Chichon in 1982. *Geophys. Res. Lett.* **1983**, *10*, 152–154. [CrossRef]
49. Tupper, A.; Oswalt, J.S.; Rosenfeld, D. Satellite and radar analysis of the volcanic-cumulonimbus at Mount Pinatubo, Philippines, 1991. *J. Geophys. Res.* **2005**, *110*, D09204. [CrossRef]
50. Prijith, S.; Rao, P.; Mohan, M.; Sai, M.; Ramana, M. Trends of absorption, scattering and total aerosol optical depths over India and surrounding oceanic regions from satellite observations: Role of local production, transport and atmospheric dynamics. *Environ. Sci. Pollut. Res.* **2018**, *25*, 18147–18160. [CrossRef]
51. He, Q.; Zhang, M.; Huang, B. Spatio-temporal variation and impact factors analysis of satellite-based aerosol optical depth over China from 2002 to 2015. *Atmos. Environ.* **2016**, *129*, 79–90. [CrossRef]
52. Hsu, N.; Gautam, R.; Sayer, A.; Bettenhausen, C.; Li, C.; Jeong, M.; Tsay, S.; Holben, B. Global and regional trends of aerosol optical depth over land and ocean using SeaWiFS measurements from 1997 to 2010. *Atmos. Chem. Phys.* **2012**, *12*, 8037–8053. [CrossRef]

Article

Research on the Growth Mechanism of PM_{2.5} in Central and Eastern China during Autumn and Winter from 2013–2020

Qi Jiang ¹, Hengde Zhang ^{1,*}, Fei Wang ² and Fei Wang ³

¹ National Meteorological Centre, Beijing 100081, China; Jiangqi89@163.com

² Chinese Academy of Meteorological Sciences, Beijing 100081, China; feiawang@cma.gov.cn

³ Beijing Municipal Weather Modification Office, Beijing 100089, China; wfnk@foxmail.com

* Correspondence: zhanghengde1977@163.com

Abstract: Haze is a majorly disastrous type of weather in China, especially central and eastern of China. The development of haze is mainly caused by highly concentrated fine particles (PM_{2.5}) on a regional scale. Here, we present the results from an autumn and winter study conducted from 2013 to 2020 in seven highly polluted areas (27 representative stations) in central and eastern China to analyze the growth mechanism of PM_{2.5}. At the same time, taking Beijing Station as an example, the characteristics of aerosol composition and particle size in the growth phase are analyzed. Taking into account the regional and inter-annual differences of fine particles (PM_{2.5}) distribution, the local average PM_{2.5} growth value of the year is used as the boundary value for dividing slow, rapid, and explosive growth (only focuses on the hourly growth rate greater than 0). The average value of PM_{2.5} in the autumn and winter of each regional representative station shows a decreasing trend as a whole, especially after 2017, whereby the decreasing trend was significant. The distribution value of +ΔPM_{2.5} (PM_{2.5} hourly growth rate) in the north of the Huai River is lower than that in the south of the Huai River, and both of the +ΔPM_{2.5} after 2017 showed a significant decreasing trend. The average PM_{2.5} threshold before the explosive growth is 70.8 μg m⁻³, and the threshold that is extremely prone to explosive growth is 156 μg m⁻³ to 277 μg m⁻³ in north of the Huai River. For the area south of the Huai River, the threshold for PM_{2.5} explosive growth is relatively low, as a more stringent threshold also puts forward stricter requirements on atmospheric environmental governance. For example, in Beijing, the peak diameters gradually shift to larger sizes when the growth rate increases. The number concentration increasing mainly distributed in Aitken mode (AIM) and Accumulation mode (ACM) during explosive growth. Among the various components of submicron particulate matter (PM₁), organic aerosol (OA), especially primary OA (POA), have become one of the most critical components for the PM_{2.5} explosive growth in Beijing. During the growth period, the contribution of secondary particulate matter (SPM) to the accumulated pollutants is significantly higher than that of primary particulate matter (PPM). However, the proportion of SPM gradually decreases when the growth rate increases. The contribution of the PPM can reach 48% in explosive growth. Compared to slow and rapid growth, explosive growth mainly occurs in the stable atmosphere of higher humidity, lower pressure, lower temperature, small winds, and low mixed layers.

Keywords: PM_{2.5}; explosive growth; chemical compositions; diameter; threshold

Citation: Jiang, Q.; Zhang, H.; Wang, F.; Wang, F. Research on the Growth Mechanism of PM_{2.5} in Central and Eastern China during Autumn and Winter from 2013–2020. *Atmosphere* **2022**, *13*, 134. <https://doi.org/10.3390/atmos13010134>

Academic Editors: Duanyang Liu, Kai Qin and Honglei Wang

Received: 24 November 2021

Accepted: 10 January 2022

Published: 14 January 2022

Publisher's Note: MDPI stays neutral with regard to jurisdictional claims in published maps and institutional affiliations.



Copyright: © 2022 by the authors. Licensee MDPI, Basel, Switzerland. This article is an open access article distributed under the terms and conditions of the Creative Commons Attribution (CC BY) license (<https://creativecommons.org/licenses/by/4.0/>).

1. Introduction

Regional-scale, high-concentration aerosols are important causes of haze in central and eastern China [1,2]. Among a variety of pollutants, high concentrations of PM_{2.5} are still the most important aerosol pollutant, as well as the main cause of haze [3–5]. Elevated PM_{2.5} affects human health, the environment, and even climate [6,7]. The main causes that affect the production and consumption of PM_{2.5} include chemical reaction processes, meteorological factors, and emission sources [8–10]. When the emission source is stable, the temporal and spatial characteristics of air pollution mainly depend on meteorological

factors [11]. The meteorology can influence the particulate matter (PM) evolution through many ways, e.g., secondary formation, accumulation or dilution, liquid-phase and heterogeneous reactions to secondary aerosols, etc. [12,13]. Under adverse atmospheric diffusion conditions, generally characterized by weak wind speeds, high relative humidity (RH), and low planetary boundary layer height, PM_{2.5} can quickly accumulate to a very high concentration [8]. The study by Zhang et al. [14] shows that the unfavorable weather elements in the winter of Beijing-Tianjin-Hebei can cause the PM_{2.5} concentration to increase by about 40% to 100% compared with other seasons. In light of single meteorological elements, Sun et al. revealed that, at low RH levels (<50%), PM increases linearly as a function of RH, among which OAs present the largest mass increase rate at 11.4 mg m⁻³/10% RH during wintertime in Beijing. In addition, the secondary formation is also one of the most important factors for the occurrence and development of haze weather [15]. Quan et al. [16] found that the conversion from NO_x and SO₂ to nitrate and sulfate was likely accelerated, and that both significantly increased in haze events. The secondary formation also promotes the formation of organic aerosols under certain conditions, and the rapid formation of secondary OA (SOA) under strong photochemical reactions can lead to more serious air pollution [17,18].

As a result of large reductions in anthropogenic emissions, the air pollution has been significantly improved with the successful implementation of “Action Plan on Prevention and Control of Air Pollution” in 2013 in China [19]. However, severe haze episodes still happen in some areas of central and eastern China (including Beijing-Tianjin-Hebei [10], Yangtze River Delta [20], Sichuan-Chongqing area [21], Fenwei Plain [22], Central China [23], etc.) in autumn and winter. For example, the rapidly spread coronavirus disease limited people’s outdoor activities and, hence, caused substantial reductions in anthropogenic emissions in 2020; however, there are still two persistent heavy pollution incidents from January 25 to 28 and February 8 to 14 in Beijing [24].

In heavy haze pollution, pollutants exhibit different growth rates at various stages of accumulation. Under different meteorological conditions, they may exhibit slow growth or rapid growth, and may increase by tens or even hundreds in one hour or several hours called “explosive growth” in the later stage of pollution. There is no qualitative conclusion about the cause of the rapid and even explosive growth of PM_{2.5}. Zheng et al. [25] highlight that the trans-regional transportation of pollutants has led to a rapid increase in pollution. Wang et al. [26] believed that the secondary transformation and nucleation effect of aerosols played a more important role through simulation studies. The study by Zhong et al. [13] attributed the rapid increase in pollution more to the effect of meteorological factors, and their study concluded that more than 70% of the increase in PM_{2.5} can be attributed to the feedback effect after the persistent deterioration of the boundary layer meteorological conditions. Zhong et al. [27] conducted a study of 28 pollution episodes in Beijing from 2013 to 2017 and concluded that a threshold value for PM_{2.5} explosive growth is 100 µg m⁻³ in Beijing. Above this threshold, the positive feedback from aerosols to near-ground radiative cooling to anomalous inversion is effectively triggered. However, faced with the decreasing PM_{2.5} concentration year by year, this threshold may change over time and show some geographical differences. Regional emission controls were effective in reducing the PM_{2.5} mass concentration. However, the changes in SOA and inorganic aerosol were comparably small and even had slight increases [24]. Therefore, exploring the chemical component contribution and particle size evolution of aerosol particles is of great significance for further understanding the growth characteristics and physicochemical mechanism of PM_{2.5}. In this study, ground-based PM_{2.5} observation data and meteorological element data are used to discuss the thresholds and year-on-year changes of PM_{2.5} in several major polluted areas in China from 2013 to 2020 under three growth mechanisms (slow, rapid, and explosive). The correlation between meteorological elements and the accumulation rate of pollutants is also discussed. At the same time, using the PM chemical composition and particle size distribution data, the contribution of PM composition and size distribution at different rates of pollutant cumulative stage is analyzed.

2. Materials and Methods

The following data are used in this study. (1) Hourly PM_{2.5} mass concentration from 2013 to 2020 in autumn and winter (October of the current year to February of the following year) is obtained by controlled stations of the Ministry of Environmental Protection in Northeast China (including Harbin (HEB), Changchun (CC) and Shenyang (SY)), Beijing-Tianjin-Hebei and surrounding areas (including Beijing (BJ), Tangshan (TS), Shijiazhuang (SJZ), Xingtai (XT), Jinan (JN) and Zhengzhou (ZZ)), Feiwei Plain (LinFen (LF), Baoji (BaJ), XiAn (XA)), Yangtze River Delta (Nanjing (NJ), Hefei (HF), Shanghai (SH), Hangzhou (HZ)), Sichuan-Chongqing (Chengdu (CD) and Chongqing (CQ)), Central China (Wuhan (WH), Huangshi (HS), Nanchang (NC) and Changsha (CS)) and Pearl River Delta (Guangzhou (GZ), Shenzhen (SZ), and Zhuhai (ZH)). The data used were the mean values of urban observation stations. The geographical location of the relevant stations is shown in Figure 1. (2) To match the above area, the hourly conventional meteorological element data, including wind speed, relative humidity, wind direction, pressure, temperature etc., are provided by National Meteorological Information Center of the China Meteorological Administration (urban stations average). The time resolution of meteorological elements is 1 h. In order to more intuitively show the growth periods of PM_{2.5}, taking Beijing as an example, Figure A1 in Appendix A shows the time series of PM_{2.5} and meteorological elements in January 2015 in Beijing. Furthermore, the average diurnal of PM_{2.5} and meteorological variables from 2013 to 2020 in autumn and winter in Beijing is shown in Figure A2. (3) The chemical composition data of submicron PM (PM₁) were sampled from Institute of Atmospheric Physics (IAP, 39°58'28'' N, 116°22'16'' E), an urban site located between the north 3rd and 4th ring road in Beijing (Jiang et al., 2015). The sampling time was October 2012 to February 2013. The sampling instrument was the Aerosol Chemical Speciation Monitor (ACSM), with a time resolution of ~15 min. ACSM mainly detects particles below 1 µm, which can realize real-time online determination of OA, sulfate (SO₄²⁻), nitrate (NO₃⁻), ammonium salt (NH₄⁺), and chloride (Cl). The detailed description of the relevant instrument principles and parameters of the ACSMs have been to the references of Sun et al. [28] and Ng et al. [29]. At vaporizer temperature of ~600 °C, the ACSM cannot detect refractory materials, e.g., mineral dust and black carbon (BC). Thus, an aethalometer (Model AE22, Magee Scientific Corporation, Berkeley CA, USA) is used to simultaneously measure BC in PM_{2.5}. The PM_{2.5} and gaseous species (including CO, SO₂, NO, NO_x, and O_x) were measured by a heated Tapered Element Oscillating Microbalance (1400a, Thermo Scientific, Waltham, MA, USA) and various gas analyzers (Thermo Scientific). (4) The data of aerosol number spectrum from 27 November 2014 to 28 February 2015, with a time resolution of 3 min and a measurement range of 14.6 nm to 661.2 nm, were measured by an scanning mobility particle sizer (SMPS), provided by the Beijing Meteorological Bureau, China. (5) The PM_{2.5} grid distribution data come from a 1-km-resolution PM_{2.5} dataset, called China High Air Pollutants (CHAP, <https://weijing-rs.github.io/product.html> (accessed on 18 September 2021)) from 2013 to 2020 across China, generated by the Moderate Resolution Imaging Spectroradiometer (MODIS, MODIS Collection 6 MAIAC AOD product (MCD19A2)) and multi-angle implementation of the atmospheric correction (MAIAC) algorithm (Wei et al., 2021). The inversion method is the space-time extra-trees (STET) model with high accuracies (i.e., cross-validation coefficient of determination, CV-R² = 0.86–0.90) and strong predictive powers (i.e., R² = 0.80–0.82) [30].

The Roche method is used to calculate the height of the atmospheric mixing layer height (MLH). It is a method proposed by Nozaki et al. [31] in 1973 to estimate the height of the mixed layer using ground meteorological data. This method takes into account that the atmospheric mixing layer is the result of the combined action of thermal and dynamic turbulence. Moreover, the movement of the atmosphere in the upper boundary layer often interconnect and feedback with ground meteorological elements, so ground meteorological parameters can be used to estimate the height of the mixed layer. In addition, positive matrix factorization (PMF) [32] was preformed to resolve distinct OA factors from specific sources on ACSM mass spectra. The related principles and steps of this method are

detailed in Ulbrich et al. [33] and Decarlo et al. [34]. In this study, we limit PMF analysis to m/z 12–125 considering the low contribution of m/z 125–150 to the total signal. An Igor Pro-based PMF evaluation tool (PET, v 2.04) is used to further evaluated the results of PMF.

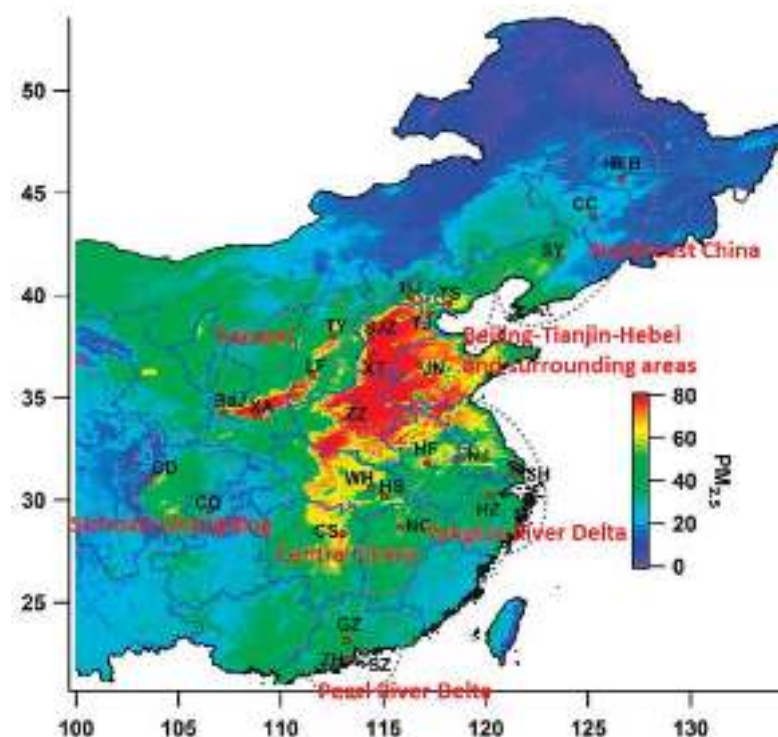


Figure 1. Average $PM_{2.5}$ mass concentration distribution during the autumn and winter of 2013–2020 in the central and eastern of China. The circle is the approximate position of the region.

3. Results and Discussion

3.1. Average Distribution of $PM_{2.5}$ in Autumn and Winter of China from 2013 to 2020

Figure 1 shows the average distribution of $PM_{2.5}$ mass concentration in the autumn and winter (October of the current year to February of the following year) of 2013–2020 based on satellite inversion in the central and eastern of China. On average, Northeast China, Beijing-Tianjin-Hebei, and surrounding areas (Fenwei, Yangtze River Delta, Sichuan-Chongqing, Central China, and Pearl River Delta (seven regions)) are the major areas where $PM_{2.5}$ concentration is relatively high in China. The following research on the growth law of $PM_{2.5}$ is also mainly carried out for the above-mentioned regions and representative cities.

We carried out annual statistics on the average concentration of $PM_{2.5}$ in autumn and winter (Hereinafter refers to as average $PM_{2.5}$ concentration) of selected representative stations since 2013. As shown in Figure 2, from the perspective of the evolution of the time series, since 2013, the $PM_{2.5}$ of the seven regional representative stations shows an overall decreasing trend. For the three regional representative stations of Northeast China, Beijing-Tianjin-Hebei and surrounding areas and Fenwei (north of the Huai River in China), the pollution of $PM_{2.5}$ in autumn and winter is significantly lower after 2016 than before. From 2013 to 2016, 30% of the representative stations in the above three regions had an average $PM_{2.5}$ mass concentration more than $115 \mu\text{g m}^{-3}$ ($115 \mu\text{g m}^{-3}$ is the limit concentration of average daily moderate pollution stipulated by the Ministry of Environmental Protection of the People's Republic of China), and 87% of statistical values exceed $75 \mu\text{g m}^{-3}$ (the second grade of NAAQS released in 2012 by the Ministry of Environmental Protection of the People's Republic of China, <http://kjs.mep.gov.cn/hjbhbz/bzwb/dqhjbh/dqhjlzlbz/201203/t20120302224165.htm> (accessed on 7 September 2021)). The highest average value of $PM_{2.5}$ exceeds $200 \mu\text{g m}^{-3}$ (Shijiazhuang in 2013). However, in the autumn and winter from 2017 to 2020, the average $PM_{2.5}$ concentration is lower than $115 \mu\text{g m}^{-3}$, and only 30%

of sites have an average $\text{PM}_{2.5}$ more than $75 \mu\text{g m}^{-3}$ north of the Huai River. Especially by 2020, the statistics of all sites in the three regions are lower than $75 \mu\text{g m}^{-3}$.

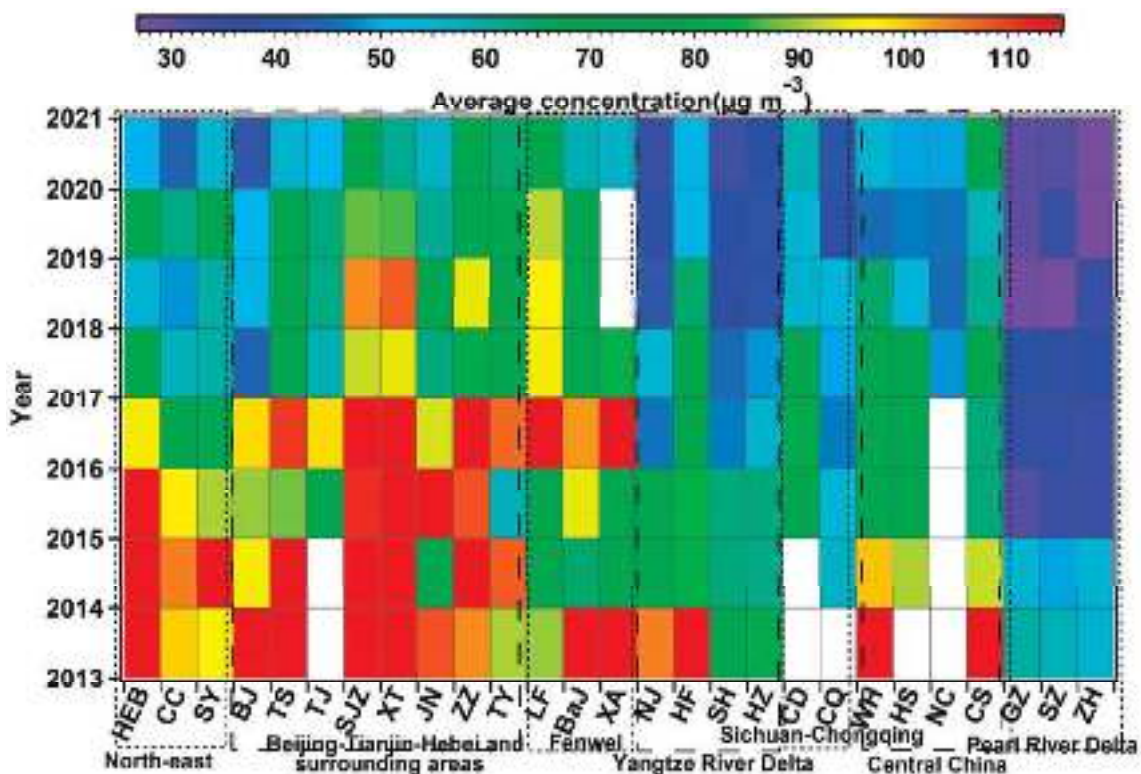


Figure 2. Statistics of $\text{PM}_{2.5}$ mean values of 7 regional representative stations in central and eastern China from 2013 to 2020 in autumn and winter.

The other four areas with a lower latitude south of the Huai River in China (Yangtze River Delta, Sichuan-Chongqing, Central China, and Pearl River Delta) have significantly less fine particulate pollution than the three areas north of the Huai River (Northeast, Beijing-Tianjin-Hebei and surrounding areas, and Fenwei). Among the valid data, except for HF and WH in 2013, which average $\text{PM}_{2.5}$ concentration exceeded $115 \mu\text{g m}^{-3}$, other statistical values are all lower than $115 \mu\text{g m}^{-3}$. For the Pearl River Delta region, after 2015, the average $\text{PM}_{2.5}$ value was lower than $35 \mu\text{g m}^{-3}$ (24-h NAAQS of US EPA). Among sites south of the Huai River, the proportion of average $\text{PM}_{2.5}$ concentration exceeds $75 \mu\text{g m}^{-3}$, which accounts for 26% from 2013 to 2017. However, from 2018 to 2020, the average of $\text{PM}_{2.5}$ is all below $75 \mu\text{g m}^{-3}$. A number of studies showed that the main reason for the gradual decrease in the concentration of $\text{PM}_{2.5}$ in central and eastern China is the decrease in the concentration of gaseous precursors under the joint emission controls and, hence, the suppression of secondary growth and formation [35,36]. However, many studies have also pointed out the importance of meteorological conditions, which can help to explain the reduction in $\text{PM}_{2.5}$ concentration of over 50% [14]. The combined effect of meteorological factors and anthropogenic emissions makes the cause of air quality improvement still uncertain [37]. The main reason that the $\text{PM}_{2.5}$ concentration in the north of Huaihe River is higher than that in the south of the Huaihe River is the comprehensive effect of industrial layout, industrial structure, meteorological factors (precipitation, atmospheric diffusion conditions), and topography, etc.

3.2. Classification of $\text{PM}_{2.5}$ Growth Periods in Central and Eastern China from 2013 to 2020

To explore the growth mechanism of $\text{PM}_{2.5}$ in autumn and winter, the data of $\text{PM}_{2.5}$ growth periods (GP, hourly growth rate > 0) from 2013 to 2020 were selected year by year. Unless otherwise specified, the following research only focuses on the hourly growth rate

greater than 0, that is, the data during the positive GP. The hourly growth rate of $PM_{2.5}$ (unit: $\mu g\ m^{-3}/h$) is expressed as $+\Delta PM_{2.5}$. Figure 3 shows the statistical value of $+\Delta PM_{2.5}$ at different representative stations in autumn and winter year by year. Similar to the average $PM_{2.5}$ concentration, with the Huai River as the boundary, the $+\Delta PM_{2.5}$ of the representative station in the southerly latitude area is lower than that of the northerly latitude station (autumn and winter). In terms of average value, the mean range of $+\Delta PM_{2.5}$ north of the Huai River is $10.7\text{--}40.9\ \mu g\ m^{-3}/h$ between 2013 to 2017 (on the left side of the dotted line). Among them, the maximum value of $40.9\ \mu g\ m^{-3}/h$ appeared in the Harbin (Northeast China) in 2013. Except for Shijiazhuang and Changchun, the average $+\Delta PM_{2.5}$ of 12 of the 14 sites (north of Huai river) in 2015–2016 was lower than that in 2013 and 2014. However, the $+\Delta PM_{2.5}$ of eight sites rebounded in 2016 comparing to 2015. After 2017, $+\Delta PM_{2.5}$ has a stepwise decline. Except for Linfen (Fenwei) and Harbin (Northeast China), whose $+\Delta PM_{2.5}$ is 27.2 and $21.5\ \mu g\ m^{-3}/h$, respectively, all other stations decreased by less than $19\ \mu g\ m^{-3}/h$. Especially in 2021, the maximum value of $+\Delta PM_{2.5}$ is only $15.3\ \mu g\ m^{-3}/h$ with a relatively concentrated distribution range of each site between $15.3\ \mu g\ m^{-3}/h$ and $9.4\ \mu g\ m^{-3}/h$. For the representative stations south of the Huai River (on the right side of the dotted line), the average of $+\Delta PM_{2.5}$ is less than $20\ \mu g\ m^{-3}/h$ except for Hefei in 2013, which was $21.6\ \mu g\ m^{-3}/h$. After 2017, all stations of $+\Delta PM_{2.5}$ reduce to within $15\ \mu g\ m^{-3}/h$ and within $10\ \mu g\ m^{-3}/h$ in 2020.

The statistical results of the 25th, 50th, and 75th percentiles of $+\Delta PM_{2.5}$ are similar to the average overall. The distribution value of $+\Delta PM_{2.5}$ in the north of the Huai River is lower than that in the south of the Huai River, and the $+\Delta PM_{2.5}$ after 2017 also showed a significant decreasing trend compared with that before 2017. In the statistical results, the value of the 50th (median value) of the $+\Delta PM_{2.5}$ is significantly lower than that of the average, indicating that values greater than the 50th deviate are higher than those less than the 50th.

The $PM_{2.5}$ concentration before the start of growth is classified with $75\ \mu g\ m^{-3}$ as the boundary, divided into clean and pollution, of which pollution is further divided into light ($75\text{--}115\ \mu g\ m^{-3}$), moderate ($115\text{--}150\ \mu g\ m^{-3}$), and heavy pollution ($>150\ \mu g\ m^{-3}$). The $+\Delta PM_{2.5}$ is compared based on the $PM_{2.5}$ background mass concentration (clean, lightly polluted, moderately polluted, and severely polluted) before the start of the growth. At the same time, the proportions of pollution background, as well as the proportions of light, moderate, and severe pollution (under pollution background) before the start of growth, are shown in Figure 4. Still using the Huai River as the division, the proportion of $PM_{2.5}$ growth occurring in the pollution background in south of the Huai River is significantly lower than that of the sites north of the Huai River. Among the representative stations in the Pearl River Delta, only 7–8% of $PM_{2.5}$ growth occurred in pollution. Among other representative stations south of the Huai River, the highest probability of $PM_{2.5}$ growth occurring in the pollution is Wuhan (42.0%), followed by Nanjing (40.0%) and Changsha (40.1%). Other sites are all below 40%. For the 14 representative stations north of the Huai River, the proportion of the $PM_{2.5}$ increase in pollution is higher than 33%, and 78.6% of the stations are higher than 40%. For the stations of Shijiazhuang and Xingtai, in particular, the proportion of pollution background is as high as 55.5% and 56.8%, respectively. Further classifying pollution into light, moderate, severely pollution, as indicated in Figure 4, in the pollution background, the sites south of the Huai River are dominated by light pollution, with the lowest being 55% (Hefei) and an average of 71.2%. In contrast, more than 50% of the $PM_{2.5}$ growth occurs in moderate and heavy pollution in the pollution background of the stations north of the Huai River. It is noteworthy that the proportion of heavy pollution is significantly higher than that of moderate, especially for Shijiazhuang and Xingtai, where the proportion of the $PM_{2.5}$ growth occurs in heavy pollution (53.7% and 48.0%, respectively) once the light pollution is exceeded.

The average of $+\Delta PM_{2.5}$ corresponding to clean, light pollution, moderate pollution, and heavy pollution background was calculated before growth in GP (Figure 4 below). It can be seen from Figure 4 that, among all representative stations, the average of $+\Delta PM_{2.5}$

corresponding to the clean background before GP is the lowest, followed by light, moderate, and heavy pollution. Among them, the average of $+\Delta\text{PM}_{2.5}$ under a clean background generally less than $15\text{ }\mu\text{g m}^{-3}$ and the increase value is generally under $10\text{ }\mu\text{g m}^{-3}\text{ h}^{-1}$ in most areas south of the Huai River. Under the background of light pollution, the distribution range of the average $+\Delta\text{PM}_{2.5}$ at stations north of the Huai River is between $11.2\text{ }\mu\text{g m}^{-3}\text{ h}^{-1}$ and $24\text{ }\mu\text{g m}^{-3}\text{ h}^{-1}$, with an average of $16.1\text{ }\mu\text{g m}^{-3}\text{ h}^{-1}$. South of the Huai River is slightly lower, with an average of $10.2\text{ }\mu\text{g m}^{-3}\text{ h}^{-1}$ of $+\Delta\text{PM}_{2.5}$ under a light pollution background. Under moderate and severe backgrounds, the average $+\Delta\text{PM}_{2.5}$ at stations north of the Huai River were $19.0\text{ }\mu\text{g m}^{-3}\text{ h}^{-1}$ and $26.6\text{ }\mu\text{g m}^{-3}\text{ h}^{-1}$, respectively. The average $+\Delta\text{PM}_{2.5}$ south of the Huai River (moderate: $12.3\text{ }\mu\text{g m}^{-3}\text{ h}^{-1}$, severe: $15.1\text{ }\mu\text{g m}^{-3}\text{ h}^{-1}$) is significantly lower than that in the north of the Huai River, but still higher than the average $+\Delta\text{PM}_{2.5}$ under the background of clean and light pollution of the site. Therefore, in each regional representative site, the background concentration of $\text{PM}_{2.5}$ before GP has an important impact on the $\text{PM}_{2.5}$ growth rate. Overall, a higher degree of air pollution before the growth leads to a faster average growth rate of the $\text{PM}_{2.5}$.

The PM_{2.5} shows different growth rates during GP ($+\Delta\text{PM}_{2.5} > 0$). According to the value of $+\Delta\text{PM}_{2.5}$, we divided GP into three categories as slow growth (SLG), rapid growth (RAG), and explosive growth (EXG). The atmosphere aerosol background concentration and the growth rate of PM_{2.5} both show obvious regional and inter-annual differences (Figures 2–4). We define the average annual $+\Delta\text{PM}_{2.5}$ from 2013 to 2020 as the threshold $A_{k,\text{year}}$ (K represents the region) for determining the type of growth (SLG, RAG, or EXG) of the stations in that year. Figure 3a shows the value of $A_{k,\text{year}}$. Slow growth ($\text{SLG}_{k,\text{year}}$), defined as the $+\Delta\text{PM}_{2.5}$, is less than $A_{k,\text{year}}$, i.e., $\text{SLG}_{k,\text{year}} < A_{k,\text{year}}$; the interval of rapid growth ($\text{RAG}_{k,\text{year}}$) is between 1 and 2 times of $A_{k,\text{year}}$, i.e., $A_{k,\text{year}} \leq \text{RAG}_{k,\text{year}} \leq 2 * A_{k,\text{year}}$; and the $+\Delta\text{PM}_{2.5}$ of explosive growth ($\text{EXG}_{k,\text{year}}$) is more than double that of the threshold, i.e., $\text{EXG}_{k,\text{year}} > 2 * A_{k,\text{year}}$.

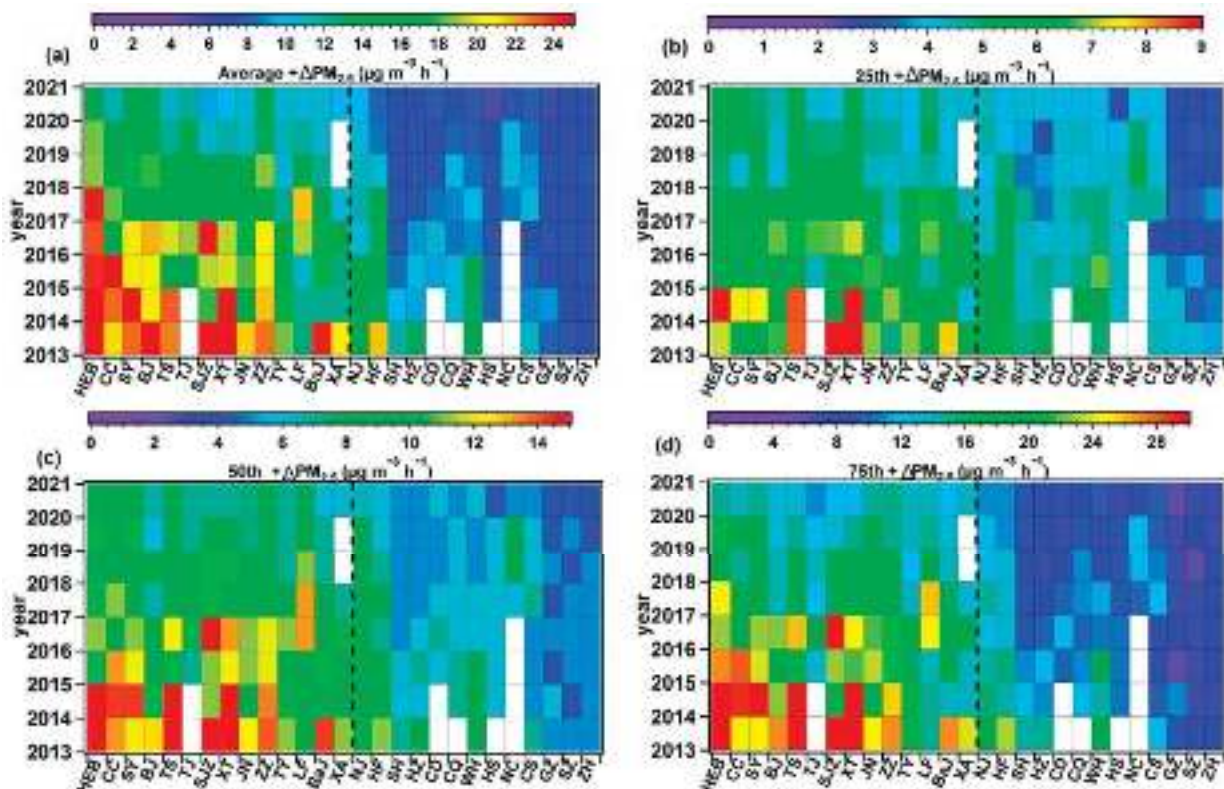


Figure 3. Statistical graph of annual average (a), 25th (b), 50th (c), and 75th (d) percentile value of $+\Delta\text{PM}_{2.5}$ in representative stations of each region in central and eastern China from 2013 to 2020 in autumn and winter.

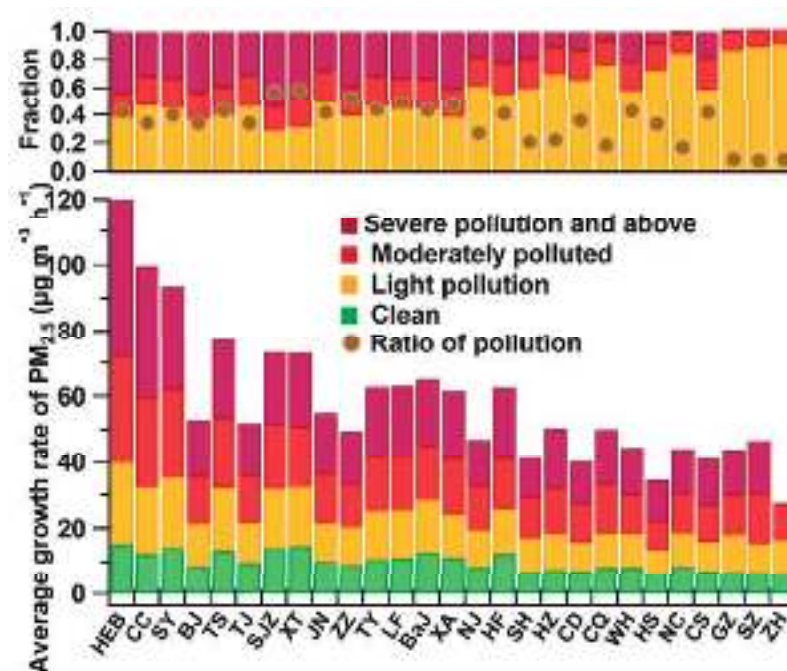


Figure 4. The average growth rate of PM_{2.5} (+ΔPM_{2.5}) at each representative station during clean, light pollution, moderate pollution and heavy pollution before growth (**below**) and the proportion of PM_{2.5} above 75 μg m⁻³ before the growth and the proportion of light, moderate, and heavy pollution (**upper**).

Since the +ΔPM_{2.5} in GP is closely related to the initial PM_{2.5} concentration, there should be a certain PM_{2.5} concentration threshold to judge the rapid or even explosive growth of PM_{2.5}. Zhong et al. [13] found that, when PM_{2.5} reached a certain threshold, the positive feedback from aerosols to near-ground radiative cooling to anomalous inversion is effectively triggered, which subsequently results in explosive rising of PM_{2.5}. In each representative station, the proportion of EXG in GP is 6.2–13.8%, with an average of 10.3% (Figure 5). Among them, the EXG of Tangshan (Beijing-Tianjin-Hebei and surrounding areas) accounted for more than 20% of the GP, which was the highest among all representative stations. Although the proportion of the EXG is lower than the RAG and the SLG, the EXG played a vital role in the occurrence and development of the heavy pollution process. It is necessary to quantify the relevant threshold of the EXG.

Figure 5 presents the average PM_{2.5} concentration thresholds before EXG in representative stations in each region during autumn and winter from 2013 to 2020. The statistical value of the lower quartile (25th) of PM_{2.5} before EXG can be used as the reference threshold of PM_{2.5} concentration for EXG, and the upper quartile (75th) characterizes that exceeding this critical value is extremely prone to EXG [13,27]. In the relatively heavily polluted stations north of the Huai River, the average PM_{2.5} threshold before the EXG is 70.8 μg m⁻³. Among them, the threshold in Beijing is 68.3 μg m⁻³, which is slightly lower than the strict threshold (71 μg m⁻³) proposed by Zhong et al. [13] for the EXG of PM_{2.5} in Beijing. The stations with the highest EXG threshold is Shijiazhuang (91.0 μg m⁻³), followed by Harbin (89.1 μg m⁻³) and Zhengzhou (88.9 μg m⁻³). Although the PM_{2.5} concentration threshold is the highest, the probability of EXG in these three cities (Shijiazhuang, Harbin and Zhengzhou) is still higher than the average proportion in the north of the Huai River (11.5%). For the area south of the Huai River, air pollution is relatively light, but at the same time, the threshold for PM_{2.5} explosive growth is relatively low, and a more stringent threshold also puts forward stricter requirements for atmospheric environmental governance. The upper quartile of the initial PM_{2.5} mass concentration values is much higher than the lower quartile (threshold) with the distribution interval from 156 μg m⁻³ to 277 μg m⁻³ for the

area north of the Huai River. Beijing's upper quartile value is $156 \mu\text{g m}^{-3}$, which indicates that an explosive growth of $\text{PM}_{2.5}$ will likely occur once it is higher than this value.

As a comparison, the statistical values of SLG and RAG are lower than that of EXG, while the relevant thresholds can also be used as a stage indicator of prevention and control measures.

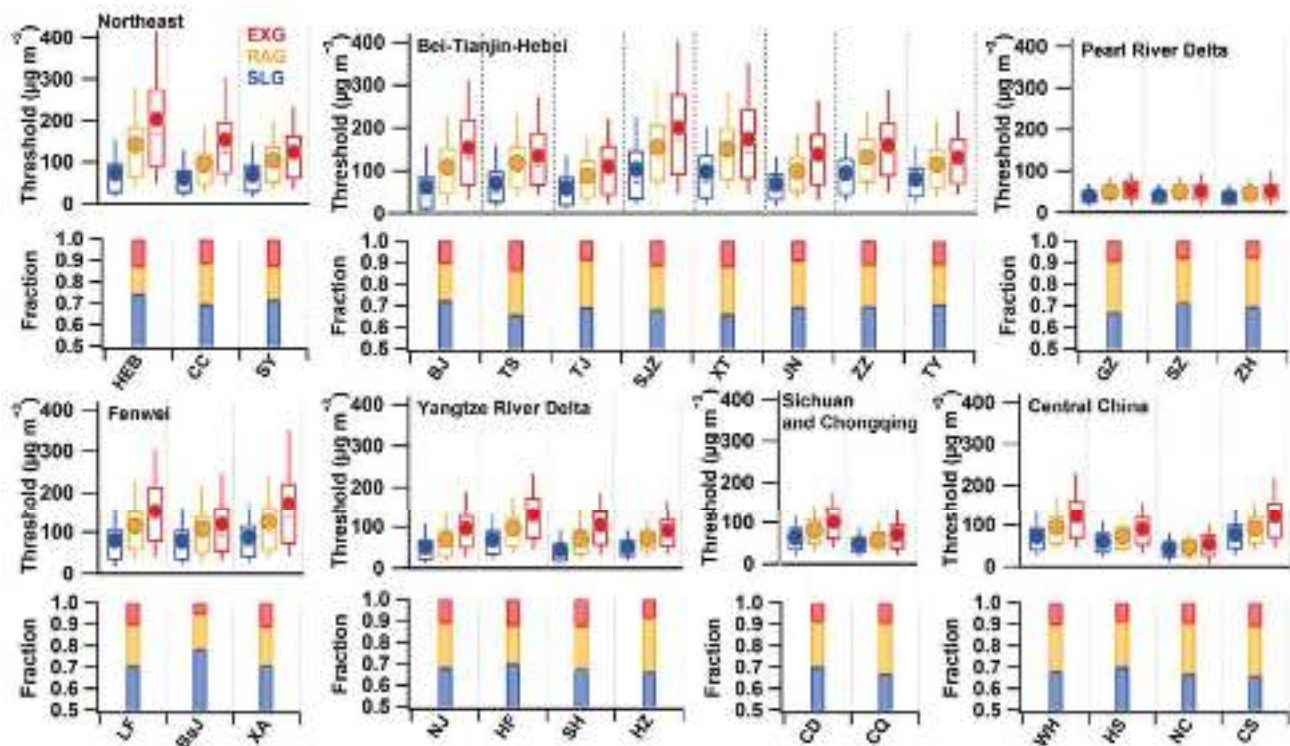


Figure 5. Thresholds for slow growth (SLG), rapid growth (RAG), and explosive growth (EXG) of each region and its representative stations, and the fraction of three growth methods. The dot is the average; the vertical line is the 10th percentile (**bottom**) and the 90th percentile (**top**); and the horizontal line is the 25th, 50th, and 75th percentile from top to bottom (the picture below is the same).

3.3. Size Distribution

Figure 6 shows a comparison of average size distributions before and after GP, SLG, RAG, and EXG in Beijing (27 November 2014 to 28 February 2015). As indicated in Figure 6, from SLG, RAG, to EXG, the peak number concentration gradually increasing. The peak number concentration spectrum distribution of GP is between SLG and RAG. After the growth started, the peak number concentration of the three growth rates all increased significantly. However, there is no significant difference in the peak number concentration particle size before and after the growth of the three growth ways. According to the definition of Hussein et al. (2004), different particle sizes could be divided into four modes: the nucleation mode ($0.01\sim 0.02 \mu\text{m}$), the Aitken mode ($0.02\sim 0.1 \mu\text{m}$), the accumulation mode ($0.1\sim 1 \mu\text{m}$), and the coarse mode ($1\sim 10 \mu\text{m}$) [38]. Limited by the measuring range of the instrument, the coarse mode is not studied in this article. In terms of the number of concentrations, before and after the three growth ways, the number concentration of the nucleation mode (NUM), the Aitken mode (AIM), and the accumulation mode (ACM) all show varying degrees of growth (Table 1). Among RAG and EXG, the increasing number concentration of AIM and ACM is more significant. Calculated from Table 1, during the SLG, the particles' concentration growth rate of the NUM, AIM, and ACM are $1691/\text{cm}^{-3} \text{ h}^{-1}$, $586/\text{cm}^{-3} \text{ h}^{-1}$, and $325/\text{cm}^{-3} \text{ h}^{-1}$, respectively. However, the growth rate of the number concentration of NUM decreases to $941/\text{cm}^{-3} \text{ h}^{-1}$ and $668/\text{cm}^{-3} \text{ h}^{-1}$ in the RAG and EXG, respectively. Simultaneously, the growth rate of AIM in the RAG and EXG

is 3.5 times and 7.7 times higher than that of SLG, respectively. For the ACM, in particular, the growth rate in the EXG can reach $4483/\text{cm}^{-3} \text{ h}^{-1}$ in Beijing during autumn and winter.

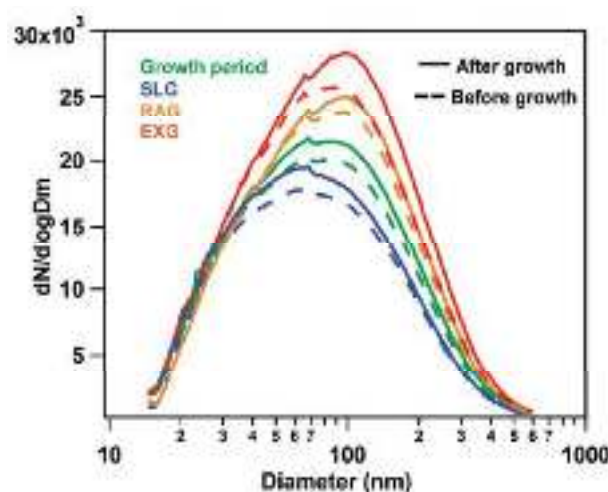


Figure 6. Average size distribution of aerosol particle before and after slow growth (SLG), rapid growth (RAG), explosive growth (EXG), and all growth period (GP) in Beijing.

Table 1. Statistical values of particle number concentration in each mode before and after (1-h interval) slow, rapid, and explosive growth in Beijing.

	Particle Size Mode	Before Growth/ cm^{-3}	After Growth/ cm^{-3}	Number of Samples
SLG	Nucleation mode	1241	2932	425
	Aitken mode	9687	10,273	
	Accumulation mode	5529	5854	
RAG	Nucleation mode	2190	3131	201
	Aitken mode	11,696	13,760	
	Accumulation mode	7098	9838	
EXG	Nucleation mode	3601	4269	115
	Aitken mode	13,451	17,972	
	Accumulation mode	9252	13,735	

Comparing with the three growth rates, the peak diameters gradually shift to larger sizes with the growth rate increasing. The particle diameters corresponding to the peak concentration of SLG is ~ 65 nm, and the peak particle diameters of RAG and EXG grow to ~ 94 nm and ~ 103 nm, respectively. Since the growth rate of $\text{PM}_{2.5}$ is closely related to the degree of air pollution, the average growth rate under pollution background is, on average, higher than that of clean conditions, which is similar to the results of Guo et al. [39], who showed that the average particle diameters of aerosols in Beijing gradually increase from cleaning to pollution with an average daily mass growth of $50\text{--}110 \mu\text{g m}^{-3}$. The study by Xu et al. [40] showed that the increased particle size of OA mainly corresponds to SOA, while the particle size of POA hardly changes. At the same time, the hygroscopicity parameter of OA increased substantially with particle size and has played a further role in promoting the increase in pollution.

Figure 7 shows the number concentration spectrum distribution of 12 times $\text{PM}_{2.5}$ episodes in 2014 and 2015 during autumn and winter. In the cumulative phase of the pollution process, slow, rapid, and explosive growth alternately occur. Before reaching the peak concentration in most heavy pollution episodes (especially the peak concentration of

$\text{PM}_{2.5}$ exceeding $200 \mu\text{g m}^{-3}$), it is accompanied by an obvious explosive increase in $\text{PM}_{2.5}$. Consistent with the above conclusions, when the EXG occurs, the number concentration of NUM does not increase significantly, and the particle size with increased concentration is mainly distributed in AIM and ACM. Since the growth rate of pollution is related to the mass concentration of $\text{PM}_{2.5}$ (Section 3.2), the rapid and explosive growth usually occurs in severe air pollution. On the one hand, there is a noticeable absence of new particle formation as the pollution episode develops. On the other hand, with the stable atmospheric situation, small particles keep growing by collision and hygroscopic growth. While the NUM particles contribute negligibly to the particle mass concentration, the severe pollution episodes (high growth rate) are attributable to the presence of numerous large particles.

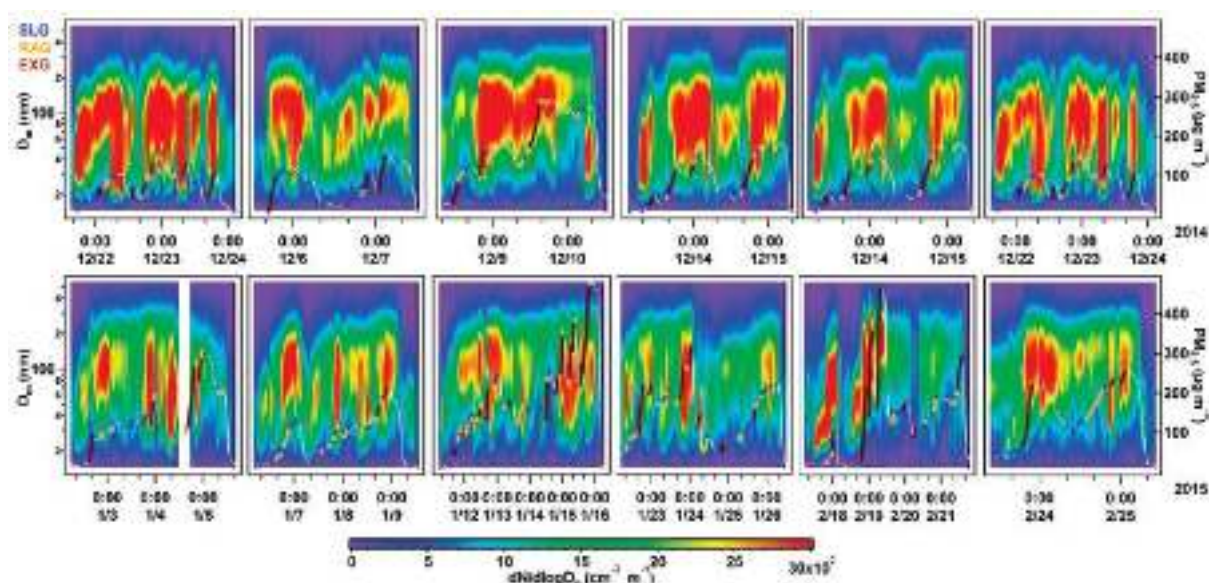


Figure 7. The number concentration spectrum distribution and temporal evolution of $\text{PM}_{2.5}$ mass concentration (right axis) during $\text{PM}_{2.5}$ episodes in 2014 (**top**) and 2015 (**bottom**) in Beijing. The colors of $\text{PM}_{2.5}$ mass concentration represent slow, rapid, and explosive growth. The white line indicates the concentration drop phase.

3.4. Chemical Composition

To explore the contribution of aerosol components in SLG, RAG, and EXG during autumn and winter in Beijing (October 2012 to February 2013), Figure 8a shows the average contribution of PM_1 species ($\text{PM}_1 = \text{OA} + \text{SO}_4^{2-} + \text{NO}_3^- + \text{NH}_4^+ + \text{Chl} + \text{BC}$) to the increasing mass concentration in GP. Among the growing concentration of PM_1 , the contribution of OA exceeds 50% on average (discuss only in the increased concentration, same below). With the increase in $+\Delta\text{PM}_{2.5}$, in particular, the proportion of OA gradually increases. The contribution of OA to the EXG reaches 57.3%, which is significantly higher than the RAG (52.1%) and SLG (54.3%). Among the inorganic components ($\text{SO}_4^{2-} + \text{NO}_3^- + \text{NH}_4^+ + \text{Chl}$), in addition to the EXG, NO_3^- contributes the most in SLG and RAG, followed by NH_4^+ and SO_4^{2-} . However, when the growth rate increases, the contribution of NO_3^- gradually decreases, while the contribution of SO_4^{2-} is the opposite. In the EXG, the contribution of SO_4^{2-} is slightly higher than that of NO_3^- , becoming the largest contributor to the inorganic components. Sun et al. [41] concluded that with the increase in relative humidity in autumn and winter, SO_4^{2-} increased rapidly through liquid phase chemical reactions, while NO_3^- mainly existed in the form of particulate matter, gas-particle transformation was inhibited. Photochemical reactions during the day become the main production mechanism of NO_3^- . It can be seen from Figure 9 that the relative humidity (RH) before the EXG is significantly higher than that of RAG and SLG. Higher RH accelerated the growth rate of

SO_4^{2-} , resulting in a significant increase in the proportion of SO_4^{2-} in the accumulated pollutants.

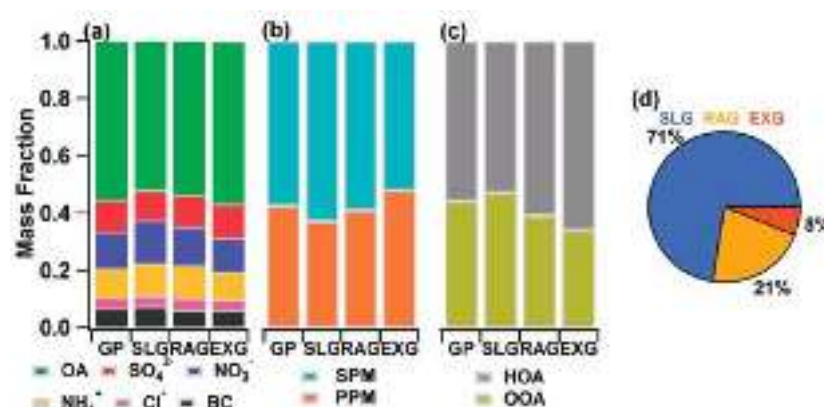


Figure 8. Average mass fractions of PM species ((a): Org, SO_4^{2-} , NO_3^- , NH_4^+ , Chl, and BC) ((b): SPM and PPM) and OA factors ((c): HOA and OOA) in increasing concentration during GP, SLG, RAG, and EXG and the proportion of the three growth methods in the total growth (d) in Beijing.

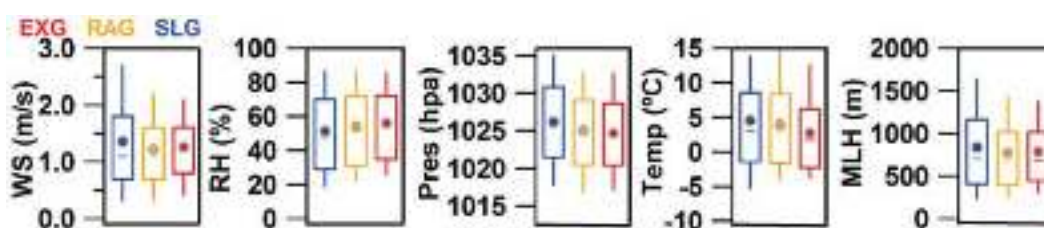


Figure 9. Statistic graphs of temperature (Temp), pressure (Pres), wind speed (WS), humidity (RH), and mixed layer height (MLH) before the explosive, fast, and slow growth in Beijing.

PMF analysis of ACSM mass spectra of OA identified two components, i.e., hydrocarbon-like OA (HOA) and oxygenated OA (OOA), as compared to the simultaneous observation of gas components (O_3 , SO_2 , NO_x , and CO, etc.), and various organic source spectra. In this study, HOA is closely related to BC (a tracer for combustion emissions, $r^2 = \sim 0.63$) and NO_x ($r^2 = \sim 0.57$), indicating the important contribution of vehicle sources. OOA has a high correlation with SO_4^{2-} ($r^2 = \sim 0.68$) and NO_3^- ($r^2 = \sim 0.77$), which are both secondary inorganic species, indicating that OOA is driven by regional production mostly. In the RAG and EXG, POA (in this study = HOA) contributes more than 60% to the growth concentration of OA on average, which is significantly higher than the average proportion of POA in all growth periods ($\sim 55.8\%$) (Figure 8c). The high proportion of HOA is also reflected the important contribution of traffic sources to the accumulation of pollutants in the RAG and EXG. Contrary to the change in humidity, the average temperature before the EXG is the lowest among the three growth rates, followed by RAG (Figure 10b). Studies have shown that the decrease in temperature is conducive to the increase in POA mass concentration [42], which also partly explains the higher proportion of POA in the accumulated OA during the EXG. Therefore, among the various components of PM_{10} , OA, especially POA, have become one of the most critical components for the EXG in Beijing during autumn and winter. In the GP, SOA (in this study = OOA) contributed 47.1% of OA in SLG. Furthermore, in the RAG and EXG, the contribution of SOA decreased to 39% and 34% on average. Figure 10 shows the mass spectra of average OA before and after GP and three growth ways. As illustrated, the intensities of hydrocarbon ion series of m/z 55 (mainly $\text{C}_3\text{H}_3\text{O}^+$, C_4H_7^+), m/z 57 (mainly $\text{C}_3\text{H}_5\text{O}^+$, C_4H_9^+), and m/z 43, characterized by a mass spectral pattern of HOA, show a significant increase after three growth ways. Among them, the growth intensity of EXG is higher than that of SLG and RAG. OOA is characterized by the prominent peak of m/z 44 (CO_2^+). Before and after growth, the intensities of m/z

44 decreased significantly. In the EXG, the intensity of m/z 44 decreases from 11.3% to 10.2% of the total OA signals. Although the proportion of SOA is significantly lower than that of POA in GP, the proportion of SOA in GP is significantly higher than the average observed throughout the autumn and winter (31%). The research of Xu et al. [40] also showed that SOA plays an enhanced role during more severely polluted days. Therefore, in the process of pollution accumulation, SOA also plays a vital role in the increase in OA.

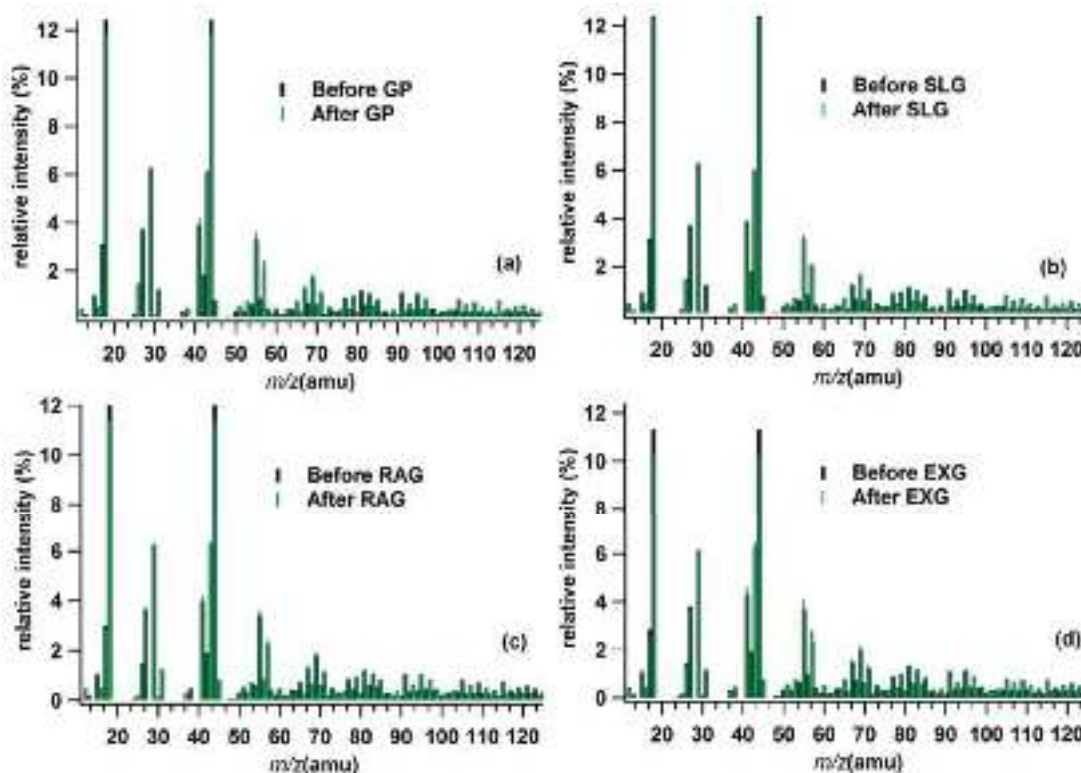


Figure 10. Mass spectra of average OA before and after GP (a), SLG (b), RAG (c), and EXG (d).

Secondary aerosol ($\text{SPM} = \text{SO}_4^{2-} + \text{NO}_3^- + \text{NH}_4^+ + \text{OOA}$) is the most important component of PM_{10} , accounting for ~71% of PM_{10} in autumn and winter in Beijing on average, and has a significant impact on atmospheric extinction [43]. During the GP, the contribution of SPM to the accumulated pollutants is still significantly higher than that of PPM (Chl + BC + HOA). However, from slow to rapid to explosive growth, the proportion of SPM in the increased PM gradually decreases (63% to 59% to 52%) (Figure 8b). During the EXG, the contribution of the PPM can reach to 48% in the increasing concentration of pollutants. PPM mainly comes from local biomass combustion, traffic and catering emissions, and its contribution to pollution accumulation cannot be underestimated. Figure 8d shows that, during the observation period, the proportions of SLG, RAG, and EXG are 71%, 21%, and 8%, respectively, in Beijing during observation. Compared to SLG and RAG, EXG mainly occurs in the quiet and stable atmosphere of higher humidity, lower pressure, lower temperature, small winds, and low MLH (Figure 10).

4. Conclusions

We select a total of 27 representative stations in seven areas (Northeast China, Beijing-Tianjin-Hebei and surrounding areas, Feiwei Plain, Yangtze River Delta, Sichuan-Chongqing, Central China and Pearl River Delta) in central and eastern China to analyze the year-on-year evolution trend of $\text{PM}_{2.5}$ pollution in the autumn and winter from 2013 to 2020. The increased stage of pollutants is divided into SLG, RAG, and EXG, according to the different accumulation rate of pollution. Taking Beijing as an example, a comparative study is conducted on the distribution characteristics of aerosol particle size, the contribution of

chemical components, and the differences in meteorological conditions in three growth rates. The average value of $PM_{2.5}$ in the autumn and winter of each regional representative station shows a decreasing trend as a whole, especially after 2017, where the decreasing trend was significant. The $+\Delta PM_{2.5}$ in the north of the Huai River is lower than that in the south of the Huai River, and the $+\Delta PM_{2.5}$ after 2017 also showed a significant decreasing trend compared with that before 2017. The average $PM_{2.5}$ threshold before the EXG is $70.8 \mu g m^{-3}$, and the threshold that is extremely prone to EXG ranges from $156 \mu g m^{-3}$ to $277 \mu g m^{-3}$ in the stations north of the Huai River. For the area south of the Huai River, the threshold for $PM_{2.5}$ EXG is relatively low, while a more stringent threshold also puts forward stricter requirements for atmospheric environmental governance. With the growth rate increase, the peak number concentration diameters gradually shift to a larger size in Beijing. The number concentration increasing mainly distributed in AIM and ACM during EXG. Among the various components of PM_1 , OAs, especially POA, have become one of the most critical components for the EXG of pollutants in Beijing. During the GP, the contribution of SPM to the accumulated pollutants is significantly higher than that of PPM. However, with the increase in growth rate, the proportion of SPM gradually decrease. In the EXG, the contribution of the PPM can reach up to 48%. Compared to SLG and RAG, EXG mainly occurs in the stable atmosphere of higher humidity, lower pressure, lower temperature, small winds, and low MLH.

Author Contributions: Conceptualization, Q.J. and H.Z.; methodology, F.W. (Fei Wang, feiwang@cma.gov.cn); formal analysis, F.W. (Fei Wang, wfnk@foxmail.com). All authors have read and agreed to the published version of the manuscript.

Funding: National Key Research Program of China (Grant No. 2019YFC0214602) and National Key Research and Development Plan Project (2016YFC0203301).

Institutional Review Board Statement: Not applicable.

Informed Consent Statement: Not applicable.

Data Availability Statement: Not applicable.

Acknowledgments: All individuals included in this section have consented to the acknowledgement.

Conflicts of Interest: The authors declare no conflict of interest.

Appendix A

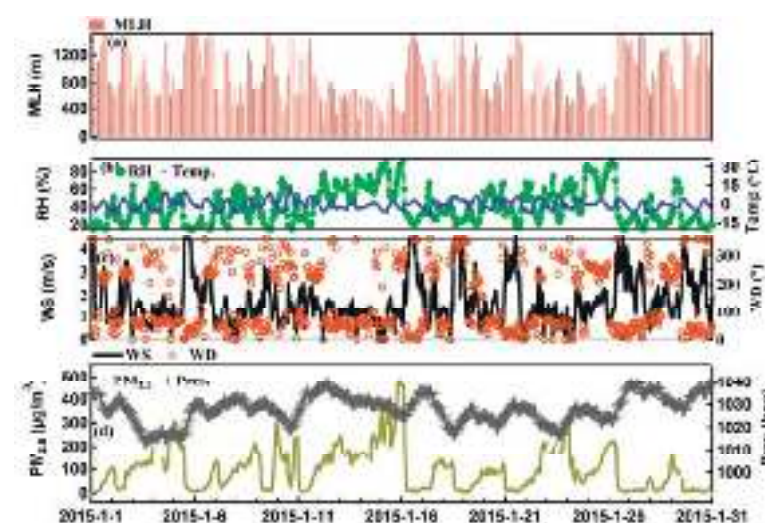


Figure A1. Time series of (a) Mixed layer height (MLH); (b) relative humidity (RH) and temperature (Temp); (c) wind speed (WS) and wind direction (WD); (d) $PM_{2.5}$ and pressure (Pres.) during January 2015 in Beijing.

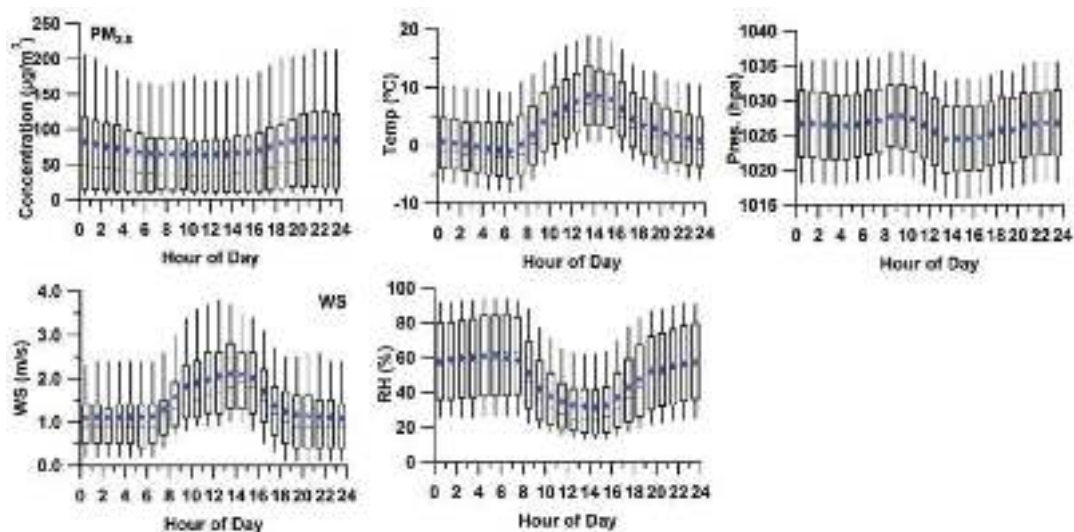


Figure A2. Diurnal of $PM_{2.5}$ and meteorological variables for the entire study.

References

1. Liu, C.; Guo, J.; Zhang, B.; Zhang, H.; Guan, P.; Xu, R. A Reliability Assessment of the NCEP/FNL Reanalysis Data in Depicting Key Meteorological Factors on Clean Days and Polluted Days in Beijing. *Atmosphere* **2021**, *12*, 481. [CrossRef]
2. Fang, C.; Tan, X.; Zhong, Y.; Wang, J. Research on the Temporal and Spatial Characteristics of Air Pollutants in Sichuan Basin. *Atmosphere* **2021**, *12*, 1504. [CrossRef]
3. Cheng, Z.; Wang, S.X.; Fu, X.; Watson, J.G.; Jiang, J.; Fu, Q.; Chen, C.; Xu, B.; Yu, J.; Chow, J.; et al. Impact of biomass burning on haze pollution in the Yangtze River delta, China: A case study in summer 2011. *Atmos. Chem. Phys.* **2014**, *14*, 4573–4585. [CrossRef]
4. Wang, H.; Li, J. Dual effects of environmental regulation on $PM_{2.5}$ pollution: Evidence from 280 cities in China. *Environ. Sci. Pollut. Res.* **2021**, *28*, 47213–47226. [CrossRef] [PubMed]
5. Zhang, Q.H.; Zhang, J.P.; Xue, H.W. The challenge of improving visibility in Beijing. *Atmos. Chem. Phys.* **2010**, *10*, 7821–7827. [CrossRef]
6. Fu, H.; Chen, J. Formation, features and controlling strategies of severe haze-fog pollutions in China. *Sci. Total Environ.* **2017**, *578*, 121–138. [CrossRef] [PubMed]
7. Zhang, L.; Sun, J.Y.; Shen, X.J.; Zhang, Y.M.; Che, H.; Ma, Q.L.; Zhang, Y.W.; Zhang, X.Y.; Ogren, J.A. Observations of relative humidity effects on aerosol light scattering in the Yangtze River Delta of China. *Atmos. Chem. Phys.* **2015**, *15*, 8439–8454. [CrossRef]
8. Liu, X.H.; Zhu, B.; Kang, H.Q.; Hou, X.W.; Gao, J.H. Stable and transport indices applied to winter air pollution over the Yangtze River Delta, China. *Environ. Pollut.* **2020**, *272*, 115954. [CrossRef]
9. Tie, X.; Huang, R.J.; Cao, J.; Zhang, Q.; Cheng, Y.; Su, H. Severe Pollution in China Amplified by Atmospheric Moisture. *Sci. Rep.* **2017**, *7*, 15760. [CrossRef]
10. Xu, W.Q.; Chen, C.; Qiu, Y.M.; Li, Y.; Sun, Y.L. Organic aerosol volatility and viscosity in the North China Plain: Contrast between summer and winter. *Atmos. Chem. Phys.* **2021**, *21*, 5463–5476. [CrossRef]
11. Liu, L.; Zhang, X.; Zhong, J.; Wang, J.; Yang, Y. The ‘two-way feedback mechanism’ between unfavorable meteorological conditions and cumulative $PM_{2.5}$ mass existing in polluted areas south of Beijing. *Atmos. Environ.* **2019**, *208*, 1–9. [CrossRef]
12. Li, J.; Han, Z. A modeling study of severe winter haze events in Beijing and its neighboring regions. *Atmos. Res.* **2016**, *170*, 87–97. [CrossRef]
13. Zhong, J.; Zhang, X.; Wang, Y. Reflections on the threshold for $PM_{2.5}$ explosive growth in the cumulative stage of winter heavy aerosol pollution episodes (HPEs) in Beijing. *Tellus B Chem. Phys. Meteorol.* **2019**, *71*, 1528134. [CrossRef]
14. Zhang, X.Y.; Xu, X.D.; Ding, Y.H.; Liu, Y.J.; Zhang, H.D.; Wang, Y.Q.; Zhong, J.T. The impact of meteorological changes from 2013 to 2017 on $PM_{2.5}$ mass reduction in key regions in China. *Sci. China Earth Sci.* **2019**, *4*, 483–500. (In Chinese) [CrossRef]
15. Lei, L.; Xie, C.H.; Wang, D.W.; He, Y.; Sun, Y.L. Fine particle characterization in a coastal city in China: Composition, sources, and impacts of industrial emissions. *Atmos. Chem. Phys.* **2020**, *20*, 2877–2890. [CrossRef]
16. Quan, J.; Liu, Q.; Li, X.; Gao, Y.; Jia, X.; Sheng, J.; Liu, Y. Effect of heterogeneous aqueous reactions on the secondary formation of inorganic aerosols during haze events. *Atmos. Environ.* **2015**, *122*, 306–312. [CrossRef]
17. Wang, D.; Zhou, B.; Fu, Q.; Zhao, Q.; Qi, Z.; Chen, J.; Xin, Y.; Duan, Y.; Li, J. Intense secondary aerosol formation due to strong atmospheric photochemical reactions in summer: Observations at a rural site in eastern Yangtze River Delta of China. *Sci. Total Environ.* **2016**, *571*, 1454–1466. [CrossRef] [PubMed]

18. Yu, Q.; Chen, J.; Qin, W.; Cheng, S.; Zhang, Y.; Ahmad, M.; Ouyang, W. Characteristics and secondary formation of water-soluble organic acids in PM₁, PM_{2.5} and PM₁₀ in Beijing during haze episodes. *Sci. Total Environ.* **2019**, *669*, 175–184. [CrossRef] [PubMed]
19. China State Council. Action Plan on Prevention and Control of Air Pollution. China State Council, Beijing, China. 2013. Available online: http://www.gov.cn/zwggk/2013-09/12/content_2486773.htm (accessed on 1 January 2018).
20. Sulaymon, I.D.; Zhang, Y.; Hu, J.; Hopke, P.K.; Zhang, Y.; Zhao, B.; Xing, J.; Li, L.; Mei, X. Evaluation of regional transport of PM_{2.5} during severe atmospheric pollution episodes in the western Yangtze River Delta, China. *J. Environ. Manag.* **2021**, *293*, 112827. [CrossRef]
21. Ning, G.; Wang, S.; Ma, M.; Ni, C.; Shang, Z.; Wang, J.; Li, J. Characteristics of air pollution in different zones of Sichuan Basin, China. *Sci. Total Environ.* **2018**, *612*, 975–984. [CrossRef]
22. Cao, J.; Cui, L. Current Status, Characteristics and Causes of Particulate Air Pollution in the Fenwei Plain, China: A Review. *J. Geophys. Res. Atmos.* **2021**, *126*, e2020JD034472. [CrossRef]
23. Li, Z.; Lei, L.; Li, Y.; Chen, C.; Wang, Q.; Zhou, W.; Sun, J.; Xie, C.; Sun, Y. Aerosol characterization in a city in central China plain and implications for emission control. *J. Environ. Sci.* **2021**, *104*, 242–252. [CrossRef]
24. Zheng, G.J.; Duan, F.K.; Su, H.; Ma, Y.L.; Cheng, Y.; Zheng, B.; Zhang, Q.; Huang, T.; Kimoto, T.; Chang, D.; et al. Exploring the severe winter haze in Beijing: The impact of synoptic weather, regional transport and heterogeneous reactions. *Atmos. Chem. Phys.* **2015**, *15*, 2969–2983. [CrossRef]
25. Wang, Z.F.; Li, J.; Wang, Z.; Yang, W.Y.; Tang, X.; Ge, B.Z.; Yan, P.Z. Modeling study of regional severe hazes over mid-eastern China in January 2013 and its implications on pollution prevention and control. *Sci. China Earth Sci.* **2014**, *57*, 3–13. [CrossRef]
26. Zhong, J.T.; Zhang, X.Y.; Dong, Y.S.; Wang, Y.Q. Feedback effects of boundary-layer meteorological factors on cumulative explosive growth of PM_{2.5} during winter heavy pollution episodes in Beijing from 2013 to 2016. *Atmos. Chem. Phys.* **2018**, *18*, 247–258. [CrossRef]
27. Sun, Y.; Lei, L.; Zhou, W.; Chen, C.; Worsnop, D.R. A chemical cocktail during the COVID-19 outbreak in Beijing, China: Insights from six-year aerosol particle composition measurements during the Chinese New Year holiday. *Sci. Total Environ.* **2020**, *742*, 140739. [CrossRef]
28. Sun, Y.; Wang, Z.; Dong, H.; Yang, T.; Li, J.; Pan, X.; Chen, P.; Jayne, J.T. Characterization of summer organic and inorganic aerosols in Beijing, China with an Aerosol Chemical Speciation Monitor. *Atmos. Environ.* **2012**, *51*, 250–259. [CrossRef]
29. Ng, N.L.; Canagaratna, M.R.; Jimenez, J.L.; Chhabra, P.S.; Seinfeld, J.H.; Worsnop, D.R. Changes in organic aerosol composition with aging inferred from aerosol mass spectra. *Atmos. Chem. Phys.* **2011**, *11*, 6465–6474. [CrossRef]
30. Wei, J.; Li, Z.; Lyapustin, A.; Sun, L.; Peng, Y.; Xue, W.; Su, T.; Cribb, M. Reconstructing 1-km-resolution high-quality PM_{2.5} data records from 2000 to 2018 in China: Spatiotemporal variations and policy implications. *Remote Sens. Environ.* **2021**, *252*, 112136. [CrossRef]
31. Nozaki, K.Y. *Mixing Depth Model Using Hourly Surface Observations*; Report 7053; USAF Environmental Technical Applications Center: Patrick Space Force Base, FL, USA, 1973.
32. Paatero, P.; Tapper, U. Positive Matrix Factorization: A non-negative factor model with optimal utilization of error estimates of data values. *Environmetrics* **1994**, *5*, 111–126. [CrossRef]
33. Ulbrich, I.M.; Canagaratna, M.R.; Zhang, Q.; Worsnop, D.R.; Jimenez, J.L. Interpretation of organic components from Positive Matrix Factorization of aerosol mass spectrometric data. *Atmos. Chem. Phys.* **2009**, *9*, 2891–2918. [CrossRef]
34. DeCarlo, P.F.; Ulbrich, I.M.; Crounse, J.; de Foy, B.; Dunlea, E.J.; Aiken, A.C.; Knapp, D.; Weinheimer, A.J.; Campos, T.; Wennberg, P.O.; et al. Investigation of the sources and processing of organic aerosol over the Central Mexican Plateau from aircraft measurements during MILAGRO. *Atmos. Chem. Phys.* **2010**, *10*, 5257–5280. [CrossRef]
35. Sun, Y.L.; Wang, Z.F.; Wild, O.; Xu, W.Q.; Chen, C.; Fu, P.Q.; Du, W.; Zhou, L.B. “APEC Blue”: Secondary Aerosol Reductions from Emission Controls in Beijing. *Sci. Rep.* **2016**, *6*, 20668. [CrossRef] [PubMed]
36. Zhao, J.; Du, W.; Zhang, Y.J.; Wang, Q.Q.; Chen, C.; Xu, W.Q.; Han, T.T.; Wang, Y.; Fu, P.Q.; Wang, Z.F. Insights into aerosol chemistry during the 2015 China Victory Day parade: Results from simultaneous measurements at ground level and 260 m in Beijing. *Atmos. Chem. Phys.* **2017**, *17*, 3215–3232. [CrossRef]
37. Ansari, T.U.; Wild, O.; Li, J.; Yang, T.; Xu, W.Q.; Sun, Y.L.; Wang, Z.F. Effectiveness of short-term air quality emission controls: A high-resolution model study of Beijing during the Asia-Pacific Economic Cooperation (APEC) summit period. *Atmos. Chem. Phys.* **2019**, *19*, 8651–8668. [CrossRef]
38. Hussein, T.; Hämeri, K.; Aalto, P.; Asmi, A.; Kakko, L.; Kulmala, M. Particle size characterization and the indoor-to-outdoor relationship of atmospheric aerosols in Helsinki. *Scand. J. Work Environ. Health* **2004**, *30* (Suppl. 2), 54–62.
39. Guo, S.; Hu, M.; Zamora, M.L.; Peng, J.; Shang, D.; Zheng, J.; Du, Z.; Wu, Z.; Shao, M.; Zeng, L. Elucidating severe urban haze formation in China. *Proc. Natl. Acad. Sci. USA* **2014**, *111*, 17373. [CrossRef]
40. Xu, W.; Chen, C.; Qiu, Y.M.; Xie, C.H.; Chen, Y.L.; Ma, N.; Xu, W.Y.; Fu, P.Q. Size-resolved characterization of organic aerosol in the North China Plain: New insights from high resolution spectral analysis. *Environ. Sci. Atmos.* **2021**, *1*, 346–358. [CrossRef]
41. Sun, Y.L.; Wei, D.; Fu, P.Q.; Wang, Q.Q.; Jie, L.; Ge, X.L.; Zhang, Q.; Zhu, C.; Ren, L.J.; Xu, W.Q. Primary and secondary aerosols in Beijing in winter: Sources, variations and processes. *Atmos. Chem. Phys.* **2016**, *16*, 8309–8329. [CrossRef]

42. Sun, Y.L.; Jiang, Q.; Wang, Z.F.; Fu, P.Q.; Li, J.; Yang, T.; Yin, Y. Investigation of the sources and evolution processes of severe haze pollution in Beijing in January 2013. *J. Geophys. Res. Atmos.* **2014**, *119*, 4380–4398. [CrossRef]
43. Jiang, Q.; Sun, Y.L.; Wang, Z.F.; Yin, Y. Aerosol composition and sources during the Chinese Spring Festival: Fireworks, secondary aerosol, and holiday effects. *Atmos. Chem. Phys.* **2015**, *15*, 6023–6034. [CrossRef]

Article

Analysis of the Characteristics of Ozone Pollution in the North China Plain from 2016 to 2020

Xinyu Wang ¹ , Wenhui Zhao ², Tianyue Zhang ¹, Yun Qiu ², Pengfei Ma ³, Lingjun Li ², Lili Wang ¹, Mi Wang ¹, Dongyang Zheng ¹ and Wenji Zhao ^{1,*}

¹ College of Resource Environment and Tourism, Capital Normal University, Beijing 100048, China; wxywxyeah@163.com (X.W.); zty19930212@163.com (T.Z.); wll_0423@163.com (L.W.); minimii@163.com (M.W.); zdy_cnu@163.com (D.Z.)

² Beijing Municipal Ecological and Environmental Monitoring Center, Beijing 100048, China; wenhuidiandian@163.com (W.Z.); qiuyun@bjmemc.com (Y.Q.); lilingjun@bjmemc.com (L.L.)

³ Satellite Application Center for Ecology and Environment, Beijing 100048, China; mapf@secmep.cn

* Correspondence: 4973@cnu.edu.cn

Abstract: As a major gaseous pollutant, ozone (O₃) adversely affects human health and ecosystems. In recent years, ozone pollution in China has gradually become a prominent issue, especially in the North China Plain (NCP). To study the long-term spatio-temporal variation patterns of O₃ in the NCP, this study selected 230 monitoring stations in the NCP from 2016 to 2020 as research objects, used the Kriging interpolation method and global Moran's index to discuss the spatial-temporal distribution of O₃, combining meteorological and social statistical data to analyze the causes underlying regional differences. The temporal analysis demonstrated that the O₃-8h average concentrations increased annually from 2016 to 2018 and decreased from 2019 to 2020. The O₃ concentrations were higher in spring and summer (117.89–154.20 µg/m³) and lower in autumn and winter (53.81–92.95 µg/m³). The spatial analysis revealed that O₃ concentrations were low in the north and south of the NCP but high in the central area. The spatial distribution of O₃ exhibited considerable cross-seasonal variability. Both meteorological conditions of high temperature and low pressure increased O₃ concentrations. The spatial distribution of O₃ varied depending on the period. However, the central and western regions of the Shandong Province were constantly characterized by high O₃ concentrations. This pattern has been likely formed by heavy industry in the Shandong Province, as large-scale industrial production and frequent traffic flows produce a large amount of precursors, thereby exacerbating regional O₃ pollution. These characteristics were attributed to emission reduction policies, meteorological conditions, the emission intensity of anthropogenic sources, and regional transport in the NCP. Overall, for cities with heavy industrial facilities in the central NCP, a timely adjustment of the energy and industrial structure, effectively controlling the emission of precursors, promoting new clean energy, and strengthening regional joint prevention and control are effective ways to alleviate O₃ pollution.

Citation: Wang, X.; Zhao, W.; Zhang, T.; Qiu, Y.; Ma, P.; Li, L.; Wang, L.; Wang, M.; Zheng, D.; Zhao, W. Analysis of the Characteristics of Ozone Pollution in the North China Plain from 2016 to 2020. *Atmosphere* **2022**, *13*, 715. <https://doi.org/10.3390/atmos13050715>

Academic Editors: Duanyang Liu, Kai Qin, Honglei Wang and Begoña Artíñano

Received: 19 April 2022

Accepted: 27 April 2022

Published: 30 April 2022

Publisher's Note: MDPI stays neutral with regard to jurisdictional claims in published maps and institutional affiliations.

Keywords: North China Plain; ozone; temporal and spatial distribution; pollution analysis



Copyright: © 2022 by the authors. Licensee MDPI, Basel, Switzerland. This article is an open access article distributed under the terms and conditions of the Creative Commons Attribution (CC BY) license (<https://creativecommons.org/licenses/by/4.0/>).

1. Introduction

Photochemical pollution is one of the major types of atmospheric environmental pollution in China. With rapid urbanization and industrialization, the problem of ozone pollution has recently become acute, thereby attracting the attention of atmospheric and environmental researchers [1,2]. As a secondary photochemical pollutant, near-ground ozone (O₃) is mainly formed by photochemical reactions of precursors such as nitrogen oxides (NO_x) and volatile organic compounds (VOCs) [3,4]. Unlike particulate pollution (e.g., aerosol pollution), O₃ pollution is insidious; it occurs even in sunny weather, and its detection and quantification are challenging. These challenges must be alleviated as near-ground O₃ concentrations, exceeding a certain threshold, can cause a series of

adverse effects on human health, the ecological environment and crops [5,6]. At present, O₃ has replaced fine particulate matter as the primary pollutant, inherently affecting the number of good air days in spring and summer [7,8]. O₃ concentrations have already directly affected the ranking of cities based on urban air quality. Therefore, identifying the pollution characteristics and the related drivers is quintessential for formulating air pollution prevention and control strategies.

In the past, scholars usually studied O₃ based on satellite data due to the lack of large-scale and long-term monitoring networks. For instance, Liu et al. [9] used OMI satellite data to analyze the trend of O₃ changes in east-central China from 2005 to 2014. Zhang et al. [10] used satellite observations of tropospheric O₃ data to assess the spatial distribution of O₃ in China. Since 2013, the Ministry of Environmental Protection has been monitoring the pollutant on a large scale in China. Many studies are exploring O₃ concentrations and distribution in various regions of China based on O₃ data from monitoring stations, yielding a multitude of results. For instance, Meng [11] conducted O₃ monitoring in 74 Chinese cities over 3 consecutive years. In particular, it has been previously reported that O₃ concentrations had been increasing annually, and O₃ pollution exhibited distinct regional patterns. Zhang et al. [12] obtained O₃ concentrations data for the Chengdu-Chongqing urban agglomeration from 2015 to 2019 using monitoring station data to discuss the spatio-temporal variation patterns of O₃ in the study region. In addition, the chemical transport model has been implemented to analyze O₃ formation and transport. For instance, Li et al. [13] used the WRF/CMAQ model to simulate the response of PM_{2.5} and O₃ to emission reduction policies in the Yangtze River Delta region. Guo et al. [14] examined the characteristics of O₃ pollution, elucidating its sensitivity to emissions using isolines. They showed that NO_x drives O₃ concentrations in most areas of China, hinting that a reduction in NO_x can substantially reduce the concentration of O₃. Fundamentally, O₃ pollution is not only affected by anthropogenic emissions but also by meteorological factors. On a meteorological scale, Wang et al. [15] argued that O₃ concentrations were closely associated with meteorological conditions. High concentrations of O₃ pollution were usually observed under strong solar radiation and low wind speed. Li et al. [16] concluded that O₃ concentrations negatively correlated with relative humidity by analyzing the correlation between O₃ and meteorological factors in 74 Chinese cities. Cui et al. [17] integrated O₃ concentrations with dynamic meteorological factors in the Beijing–Tianjin–Hebei region and found that the O₃ concentrations positively correlated with temperature and evaporation; however, there was a distinct regional difference in the wind direction and the wind speed.

The NCP is one of the most densely populated areas in the world. The Beijing–Tianjin–Hebei region has a large population and represents China's political and cultural center, where the air pollution issue has become increasingly urgent [18]. The Jiangsu–Anhui–Shandong–Henan region in the southern part of the NCP is the connecting belt of air pollution in the Beijing–Tianjin–Hebei region and the Yangtze River Delta [19]. Only a few studies described the O₃ pollution in the above areas, and the progress toward improving air quality is slow. With its rapid economic development, the NCP suffers from severe air pollution due to anthropogenic emissions, accumulation, and regional transmission [20]. Thus far, the lack of long-term research on the spatio-temporal characteristics of O₃ constrains the progress in this regard. To address this gap, this study investigated the spatio-temporal distribution and drivers of O₃ pollution in the NCP using data on O₃ concentrations (from 230 air monitoring stations), meteorology (from 54 meteorological stations), and social factors between 2016 and 2020 to provide a reference for the management of O₃ pollution.

2. Materials and Methods

2.1. Study Area

As shown in Figure 1, the North China Plain (NCP) is located between 32°–40° N and 114°–121° E along the east coast of China. It represents 1 of the 3 major plains in China,

including Beijing, Tianjin, 9 cities in the Hebei Province, 15 cities in the Henan Province, 16 cities in the Shandong Province, 6 cities in the Anhui Province, and 5 cities in the Jiangsu Province. The names and abbreviations of all cities are shown in Table S1. The study area extends from the south foot of Yanshan Mountain in the north, Taihang Mountain and Funiu Mountain in the west, Dabie Mountain in the south, and the Bohai and Yellow Seas in the east. The total area of the study region is 300,000 km². The topography is flat and low in altitude, with numerous rivers and lakes and a dense population. Most cities in the study area are characterized by a temperate monsoon climate, whereas a few provinces (such as Jiangsu and Anhui) have a subtropical monsoon climate. The four seasons of the study region have been changing significantly, driven by the monsoon climate. The region is characterized by hot and rainy summers, while winters are cold and dry. The precipitation mostly occurs between June and September. Notably, the region stands out with exceptional natural conditions, rendering it an important grain base and geographical space in China [21–23].

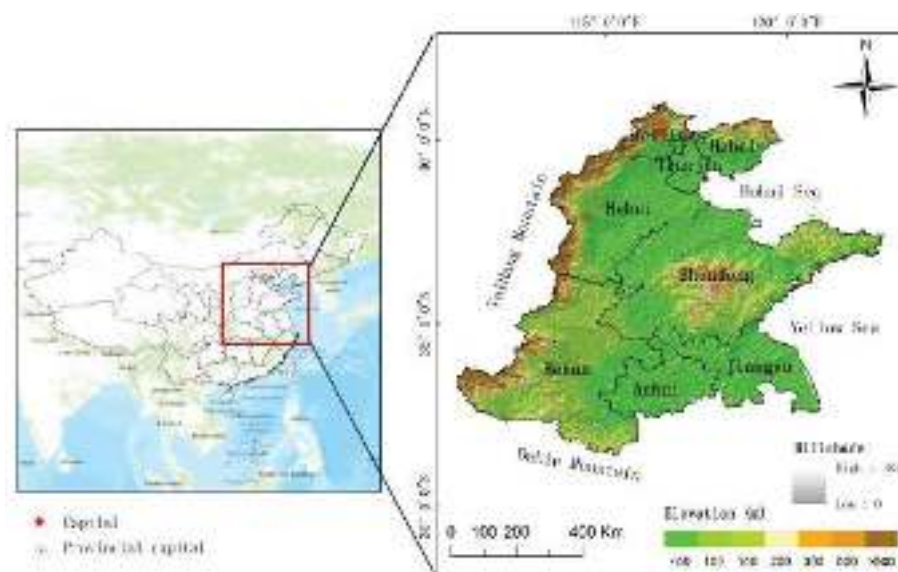


Figure 1. The geographical location of the study area.

2.2. Data Source and Processing

The O₃ data used in this study were obtained from the national urban air quality real-time release platform of the China National Environmental Monitoring Centre (<http://106.37.208.233:20035/>) (accessed on 6 May 2021). The daily surface monitoring data of O₃ in the NCP from 2016 to 2020 were used. This study analyzed data from 230 sites within the study area. The selection was performed after removing the inactive sites and those with incomplete data. According to Ambient Air Quality Standards (GB 3095-2012), the daily maximum 8-h moving average of O₃ is considered the actual O₃ concentration (hereafter referred to as O₃-8h). In addition, the daily arithmetic average of O₃-8h in a calendar month is taken as the monthly average concentration. Note that it is implied that spring lasts from March to May, summer lasts from June to August, autumn lasts from September to November, and winter lasts from December to February of the following year. The quarterly average concentrations were calculated from the arithmetic average of the daily O₃-8h concentrations. The arithmetic average of daily O₃-8h concentrations in a calendar year was taken as the annual average concentration. The meteorological data were obtained from the China Meteorological Data Service Centre (<http://data.cma.cn>) (accessed on 12 May 2021). More specifically, temperature (TEM, °C) and air pressure (Pa, hPa) from 54 meteorological stations in the NCP from 2016–2020 were selected. The point of interest data for the plants were obtained from AutoNavi (<https://amap.com/>) (accessed on 1 August 2021). The administrative boundary vector data and the digital elevation model (DEM 500 m) data were obtained from the Institute of Geographical

Sciences and Natural Resources Research, CAS (<https://www.resdc.cn/>) (accessed on 12 May 2021). To this end, the statistical data for 2016–2020 were obtained from the China Statistical Yearbook, China Urban Statistical Yearbook, China Environmental Statistical Yearbook, and the Local Statistical Bulletin of National Economic and Social Development (<http://www.stats.gov.cn/tjsj/ndsj/>, <https://data.cnki.net/NewHome/Index>) (accessed on 2 December 2021). The time described in this study is Chinese Standard Time (CST).

2.3. Statistical Methods

2.3.1. Kriging Interpolation

Kriging interpolation is fundamentally based on the variogram and basic assumption of a spatially related prior model. Given the dual characteristics of randomness and the structure of natural phenomena in space, the Kriging method can be utilized to quantitatively analyze environmental parameters [24,25]. It has been extensively used in numerous fields such as geology, meteorology, and remote sensing [26]. The Kriging interpolation method was utilized in this study to predict the spatial-temporal distribution of O₃.

2.3.2. Spatial Autocorrelation Test

The first law of geography stipulates that the closer things are in space, the stronger their correlation, also referred to as “spatial autocorrelation” [27]. To elucidate the spatial distribution of O₃, global Moran’s index I was utilized according to Equation (1):

$$I = \frac{N \sum_i \sum_j W_{ij} (X_i - \bar{X})(X_j - \bar{X})}{(\sum_i \sum_j W_{ij}) \sum_i (X_i - \bar{X})^2} \quad (1)$$

where N represents the number of municipal administrative divisions, X_i and X_j represent the average value of O₃ concentrations in administrative regions i and j , respectively; \bar{X} represents the mean value of O₃ concentrations in all administrative regions; and W_{ij} represents the spatial weight matrix. The value range of I was considered $[-1, 1]$. Note that $I < 0$, $I = 0$, and $I > 0$ indicate a spatially negative correlation, the absence of correlation, and positive spatial correlation, respectively, whereas the closer I is to 1, the stronger the spatial correlation is.

To facilitate the interpretation, I is usually transformed into a standardized statistic, $Z(I)$, using Equation (2):

$$Z(I) = \frac{[I - E(I)]}{\sqrt{Var(I)}} \quad (2)$$

where $Z(I)$ represents the significance level of the global Moran’s index, $E(I)$ represents the expected value, and $Var(I)$ represents the variance. In particular, $Z < -2.58$ indicates that O₃ concentrations have a negative spatial correlation, and $-2.58 < Z < 2.58$ indicates that the spatial correlation is not significant. Finally, $Z > 2.58$ indicates the positive spatial autocorrelation of O₃ concentrations [28,29].

3. Results

3.1. Characteristics of Ozone Time Variation

3.1.1. Interannual Variation Characteristics

According to the Ambient Air Quality Standard (GB 3095-2012), the first-level standard limit of the maximum 8-h average concentrations of O₃ per day is 100 µg/m³, while the secondary level standard is 160 µg/m³. On this basis, our study considered the secondary standard limit concentrations as the threshold, implying that when O₃-8h is >160 µg/m³, the standard is exceeded. The annual statistics for O₃-8h are provided in Table 1. As seen, the annual average concentrations of O₃ from 2016 to 2020 were 97.84 ± 4.55 , 107.96 ± 5.40 , 110.28 ± 5.82 , 108.05 ± 4.94 , and 104.04 ± 8.87 µg/m³, respectively.

Table 1. Statistics of O₃-8h data in the NCP from 2016 to 2020. (Mean ± sd).

Date/year	Mean ($\mu\text{g}/\text{m}^3$)	Minimum ($\mu\text{g}/\text{m}^3$)	Maximum ($\mu\text{g}/\text{m}^3$)
2020	104.04 ± 8.87	25.63	203.56
2019	108.05 ± 4.94	19.77	216.30
2018	110.28 ± 5.82	25.83	219.83
2017	107.96 ± 5.40	24.81	223.70
2016	97.84 ± 4.55	19.54	190.23

By ranking the average O₃ concentrations in the NCP, the following order was identified: 2018 > 2019 > 2017 > 2020 > 2016. O₃ concentrations exhibited an increasing trend since 2016, peaked in 2018, and then gradually decreased. We suggest that the change in O₃ concentrations after 2018 is closely related to the following environmental policies. In 2017, China issued “The 2017 work plan for air pollution prevention and control in Beijing, Tianjin, Hebei, and surrounding areas”, which urged Beijing–Tianjin–Hebei and surrounding cities to adjust their industrial structure; banned small, scattered polluting enterprises; and actively promoted the substitution of clean energy, such as electricity and natural gas, for coal. These measures bolstered the efficiency of treatment of industrial air pollution, strengthened the control of motor vehicle emissions, and tightened NO_x emissions control.

The analysis of the statistical yearbook data indicated that the total NO_x emissions in the study area remarkably decreased in 2018. Namely, the total NO_x emissions decreased by 21.34% compared with 2017. The total NO_x emissions in 2019 and 2020 also exhibited a downward trend, with decreases of 26.57% and 48.14%, respectively, compared with 2017. In 2018, China also issued “The Action Plan for Comprehensive Treatment of Air Pollution in Autumn and Winter from 2018 to 2019 in Beijing, Tianjin, Hebei, and surrounding areas”, which put forward special treatment of VOCs in key industries for the first time and achieved its first tangible results by 2019 [30]. Given the efficient control of the emissions of O₃ precursors, the average O₃ concentrations decreased. Notably, O₃ concentrations declined in 2020. We argue that this concurrent reduction was attributed to the reduction in industrial production and anthropogenic activities under the measures enforced to control and prevent the spread of COVID-19 in China in 2020 [31].

3.1.2. Seasonal Variations

The seasonal variations in the O₃ concentrations from 2016 to 2020 are shown in Figure 2. As shown, the variation trend of O₃ average concentrations was approximately the same in different years in the NCP. Moreover, O₃ concentrations gradually increased during spring, peaked in summer (132.53–154.20 $\mu\text{g}/\text{m}^3$), and decreased gradually in autumn and winter, reaching the lowest value in winter (53.81–61.75 $\mu\text{g}/\text{m}^3$). The seasonal variation characteristics of O₃ concentrations were ranked in the following order: summer > spring > autumn > winter. Overall, O₃ pollution mainly developed in summer, as higher concentrations were identified in spring and summer, while lower concentrations were observed in autumn and winter.

The changes in O₃ concentrations are fundamentally closely related to meteorological conditions. The photochemical reaction process can be formalized by Equations (3)–(5) (see below) [32,33]. The main process is NO oxidation by atmospheric oxidants to generate NO₂, whose photolysis generates O₃. Temperature and solar radiation play important roles in the formation and transport of O₃. For instance, Xu, et al. [34] reported that O₃ concentrations positively correlated with temperature and the intensity of solar radiation because intense solar radiation and high temperature promoted the photochemical reaction process. We found that the temperature in the NCP gradually increased from spring, while summer was characterized by the strongest solar radiation and highest temperature throughout the year. Therefore, this period was the most conducive for O₃ formation, whose concentrations reached the highest level. In autumn and winter, the solar radiation

intensity and irradiation time gradually weakened. Thus, O₃ concentrations gradually dwindled, reaching the lowest value in winter. We identified only a slight difference in temperature between spring and autumn. However, O₃ concentrations in spring were significantly higher compared with those in autumn due to the influence of more precursors, drought, and less precipitation in spring:

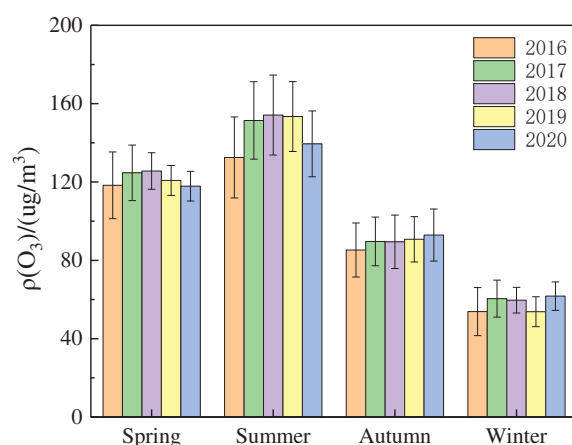


Figure 2. Seasonal changes in O₃ concentrations in the NCP from 2016 to 2020.

3.2. Spatial Distribution Characteristics of O₃

3.2.1. Spatial Aggregation Characteristics

To analyze the spatial aggregation and trends of O₃, we performed a global spatial autocorrelation analysis of the average annual O₃ concentrations. As a result, we obtained Moran's *I* and *Z* values. Table 2 demonstrates that Moran's *I* from 2016 to 2020 were 0.17, 0.36, 0.45, 0.45, and 0.51, respectively, while *Z* values were all >2.58 with an upward trend ($p < 0.01$). This indicates that the administrative units with high O₃ concentrations or those with low O₃ concentrations were significantly clustered in space (e.g., they are spatially positive). The O₃ spatial aggregation increased annually in recent years. We noted a strong spatial autocorrelation and possible spatial aggregation.

Table 2. Spatial autocorrelation test results.

Index	2016	2017	2018	2019	2020
Moran's <i>I</i>	0.17	0.36	0.45	0.45	0.51
<i>Z</i> -score	5.03	10.14	12.65	12.66	14.36
<i>p</i> -value	<0.01	<0.01	<0.01	<0.01	<0.01

To further discuss the spatial aggregation of O₃ concentrations, this study analyzed the cold hotspot map for O₃ concentrations in the NCP; the results are shown in Figure 3. As shown in the figure, the hotspots in the NCP in 2016–2017 were mainly concentrated in the southwestern area of Shandong bordering Henan and Anhui Province. Jiangsu Province was also relatively concentrated. From 2018 to 2020, hotspots were concentrated in the western part of Shandong Province and the junction area of Henan Province and Hebei. From 2016–2020, cold spots were concentrated in Beijing, Tianjin, and surrounding areas, while the agglomeration in other areas was not prominent. Furthermore, after 2016, the spatial correlation of O₃ in the western part of Shandong became increasingly more pronounced, and the aggregation characteristics were the most prominent in 2018, showing

the clustering characteristics of the Hebei–Henan–Shandong–Anhui region. Overall, the comprehensive 2016–2020 trends of O₃ spatial aggregation changes show that the western area of Shandong bordering other provinces forms a stable high-value aggregation feature, whereas Beijing, Tianjin, and the surrounding areas form a stable low-value aggregation. These two parts of the regional spatial correlation of O₃ concentrations were substantial and not easily influenced by other regions.

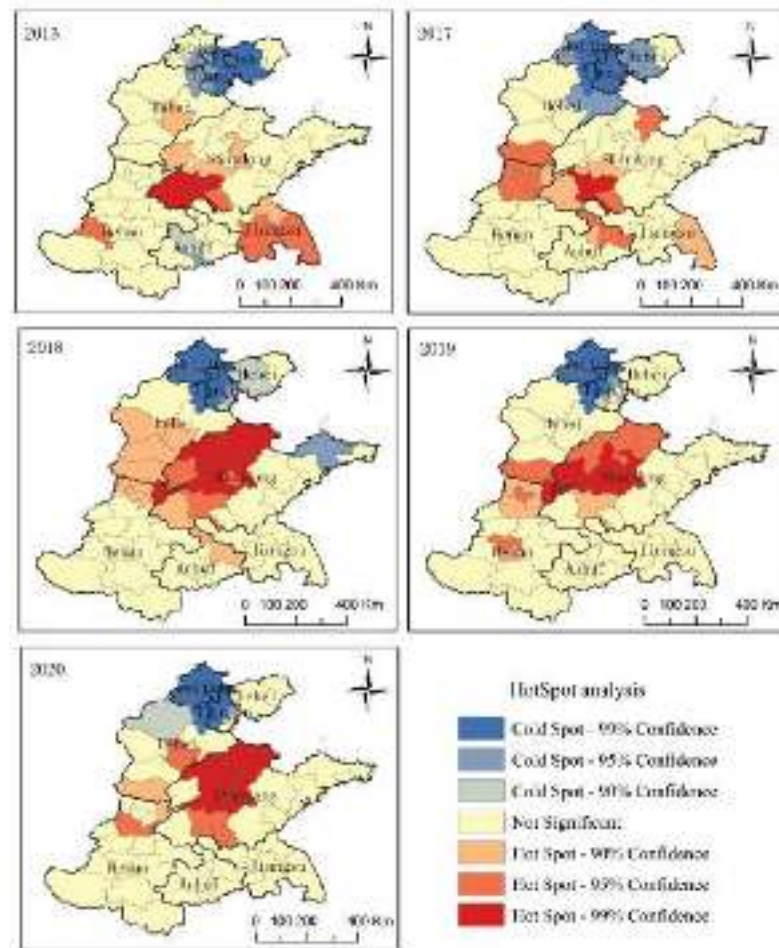


Figure 3. Spatial aggregation characteristics of O₃ concentrations in the NCP from 2016–2020.

3.2.2. Annual Variation of the Spatial Distribution of O₃

The spatial distribution of O₃ in the NCP is shown in Figure 4. As shown, the spatial distribution of O₃ was approximately the same and consistent with the spatial aggregation trend (Figure 3) from 2016 to 2020. Overall, the study area exhibited a spatial variation trend characterized by low O₃ concentrations in the north and south and high concentrations in the central area. Among these, O₃ concentrations in the west of the Shandong Province and the junction of the Jiangsu, Shandong, Hebei, Henan, and Anhui provinces were high, with a maximum value of 120.79 µg/m³. This area was characterized by high O₃ concentrations, which are related to the presence of industrialized cities in the region. Meanwhile, the O₃ concentrations in Beijing, southern cities of Henan Province, Anhui Province, Jiangsu Province, and coastal areas of Shandong Peninsula were low, with the lowest value being 85.58 µg/m³. Furthermore, O₃ concentrations in the study area significantly increased from 2016 to 2018, while the high-value area of O₃ concentrations gradually expanded. In 2019, O₃ concentrations in Jiangsu Province and some surrounding cities in the south of the NCP decreased. In 2020, the pattern changed, and the overall O₃ concentrations in the study area decreased. In previous years, O₃ concentrations in Henan and Hebei

Provinces with higher O₃ concentrations significantly decreased, while some areas with high concentrations persisted in the central and western regions of the Shandong Province.

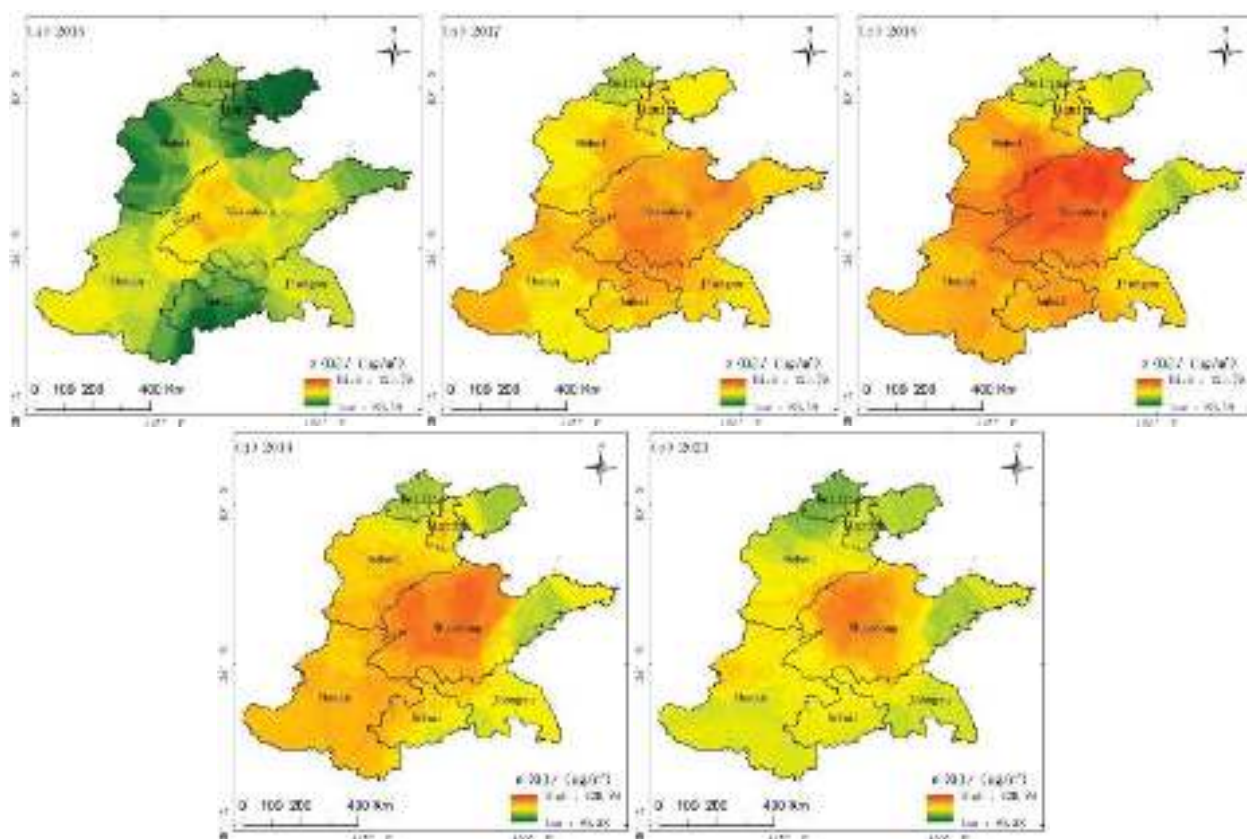


Figure 4. Annual spatial distribution map of O₃ in the NCP from 2016 to 2020: (a) Spatial distribution of O₃ in 2016, (b) Spatial distribution of O₃ in 2017, (c) Spatial distribution of O₃ in 2018, (d) Spatial distribution of O₃ in 2019, (e) Spatial distribution of O₃ in 2020.

Precursors are essential for O₃ formation. The sources of O₃ precursors can be fundamentally divided into natural and anthropogenic sources. Natural sources include soil, lightning, and plant emissions, while anthropogenic sources include motor vehicle exhaust, coal combustion, and industrial and power plant emissions [35]. As the compilation of the VOC source emission inventory was delayed and underwent changes every year, no latest VOC source emission data were available for 2020. Due to this, the NO_x emissions data were taken as the measurement index of precursors. Note that, as a precursor of O₃, the NO_x concentration is closely related to that of O₃ [36,37]. The total NO_x emissions comprise industrial, motor vehicle, and domestic emissions. According to data from the China Environmental Statistics Yearbook (2019), industrial and motor vehicle emissions account for more than 90% of the total emissions in China. Since municipal-level data on NO_x emitted by motor vehicles were not available, industrial NO_x emissions and civil vehicle ownership were selected as relevant indicators to measure the change in O₃ concentrations. Given the lack of statistical data for some years, we considered the data of industrial NO_x emissions in 2017 and civil vehicle ownership in 2019 as examples to shed light on the impact of O₃ precursors on the spatial distribution of O₃. The results are shown in Figure 5.

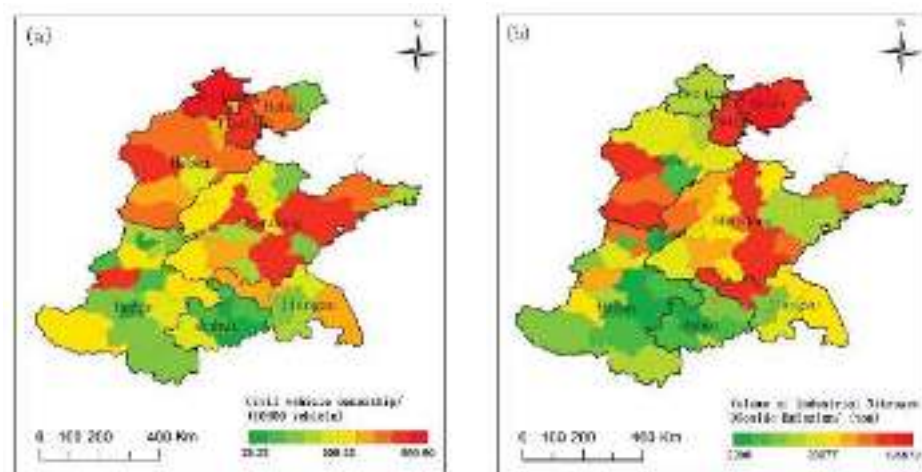


Figure 5. (a) Spatial distribution of civil vehicle ownership in the NCP in 2019; (b) Spatial distribution of industrial NO_x emissions in the NCP in 2017.

Figure 5a shows the civilian car ownership map. As seen, the car ownership in Beijing–Tianjin–Hebei is generally high. The capital city of Beijing, being the political and cultural center of China, is characterized by the highest car ownership of 5.908 million, followed by Zhengzhou (Henan Province), with car ownership of 3.814 million. Jinan, Linyi and the Shandong Peninsula are also characterized by high car ownership. This pattern is driven by the population density of the Beijing–Tianjin–Hebei urban agglomeration. The area is large, and the degree of social and economic development is also high. As a highly populated province, the Shandong Province had a population of >100 million people in 2017 (Chinese Statistic Year, 2018), and motor vehicles were used extensively. As a result, these regions are characterized by the largest car ownership, whereas car ownership in most regions of the Henan and Anhui Provinces is low (the lowest car ownership is equal to 282,300 in the Hebi City of the Henan Province). The distribution map of industrial NO_x emissions (Figure 5b) indicated that Tianjin, Tangshan, Qinhuangdao, southern Hebei Province, and central Shandong Province, such as Binzhou and Zibo, and other cities had higher industrial NO_x emissions. Of these administrative units, Tangshan was characterized by the strongest annual emissions (196,572 tons/year), followed by Tianjin (73,249 tons/year). These cities are heavily industrialized with an economy focused on structure, metallurgy, chemical industry, building materials, and high-energy consuming industries, causing emissions of large amounts of pollutants. However, in the southern part of the study area (the Henan and Anhui Provinces), the emissions of industrial NO_x were relatively low, with the lowest value being 2296 tons. Moreover, the emissions of industrial NO_x in Beijing and the Shandong Peninsula were also relatively low. We combined the number of heavy industrial plants in each province in the study area, shown in Figure 6, and showed that Shandong Province had the largest number of heavy industrial plants, followed by Hebei Province. We argue that this is a manifestation of the convergence of the industrial structure between the provinces and the cities in Beijing–Tianjin–Hebei and the surrounding areas.

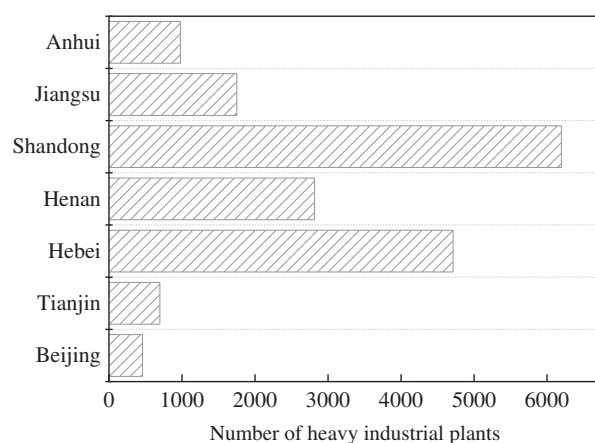


Figure 6. Number of heavy industrial plants in each province of the NCP.

Combined with the analysis results in Figure 4, the areas with high O_3 concentrations were mainly clustered in the central and western regions of Shandong Province, the southern part of Hebei Province, and the junction of Jiangsu, Shandong, Henan, and Anhui Provinces. This finding is in line with the regions characterized by a large number of motor vehicles and large industrial NO_x emissions. However, although Beijing and Tianjin were characterized by a large number of motor vehicles, the O_3 concentrations in the area remained low. This pattern was driven by the strict motor vehicle emission reduction policies implemented by key cities such as Beijing and Tianjin, which effectively controlled the pollution of motor vehicle emissions [38]. Generally, precursor emissions are closely related to O_3 concentrations [39]. Large-scale industrial production and massive traffic flow lead to larger NO_x emissions. Namely, the greater the NO_x emissions in the region, the more conducive the photochemical reaction conditions are and the greater the O_3 concentration. However, the Qinhuangdao City (Hebei Province) was characterized by a large amount of industrial NO_x emissions, and the Shandong Peninsula had a large number of motor vehicles. Thus, one could anticipate that more emissions of precursors could emerge in these areas, and O_3 concentrations would inevitably increase. Nevertheless, O_3 concentrations remained at a moderately low level. As these cities are close to the ocean and experience good atmospheric diffusion conditions, clean ocean air masses moderately exert a dilution effect on local pollution sources.

3.2.3. Seasonal Variation of O_3 Spatial Distribution

The O_3 concentrations in the NCP significantly changed during all seasons from 2016 to 2020. Furthermore, the seasonal-scale spatial distribution of O_3 is shown in Figure 7. In spring, the cities in the northern part of the NCP (such as Beijing and Tianjin) were characterized by the lowest O_3 concentrations, with the lowest value of $111.43 \mu\text{g}/\text{m}^3$. O_3 concentrations in the southern Anhui Province were also low. The high O_3 concentrations areas were mainly concentrated in the southwest part of the Shandong Province, junction cities between the west of Shandong Province and the southeast of Hebei Province, with a maximum of $134.83 \mu\text{g}/\text{m}^3$. In summer, O_3 concentrations in the study area were high, with widely distributed high-concentration areas. The high-value areas of O_3 were mainly clustered in the Beijing–Tianjin–Hebei urban agglomeration, western Shandong Province, and northern Henan Province, with a maximum of $169.90 \mu\text{g}/\text{m}^3$. O_3 concentrations in the Shandong Peninsula, Anhui, and Jiangsu provinces to the south of the NCP were relatively low, with the lowest value of $97.55 \mu\text{g}/\text{m}^3$. In autumn, O_3 concentrations distribution exhibited the low concentrations pattern in the north and the high concentrations in the south. O_3 concentrations in the Beijing–Tianjin–Hebei urban agglomeration were the lowest, with the lowest value of $64.13 \mu\text{g}/\text{m}^3$, while in southern Shandong Province and Anhui Province, they were higher, with a maximum of $116.90 \mu\text{g}/\text{m}^3$. In winter, O_3 concentrations in the study area were lower than those in other seasons. Moreover, O_3 concentration

generally exhibited a trend of low concentrations in the north and high concentrations in the south. From a regional perspective, O_3 concentrations in eastern coastal cities were the highest, with a maximum of $75.63 \mu\text{g}/\text{m}^3$, while O_3 concentrations in the Beijing–Tianjin–Hebei urban agglomeration were low, with the lowest value of $44.78 \mu\text{g}/\text{m}^3$. Overall, although the regional distribution range of high O_3 concentrations exhibited a certain degree of seasonal variability, the central and western parts of Shandong Province were always characterized by high concentrations. This pattern is attributed to the developed industrial structure of the heavy industry in Shandong Province.

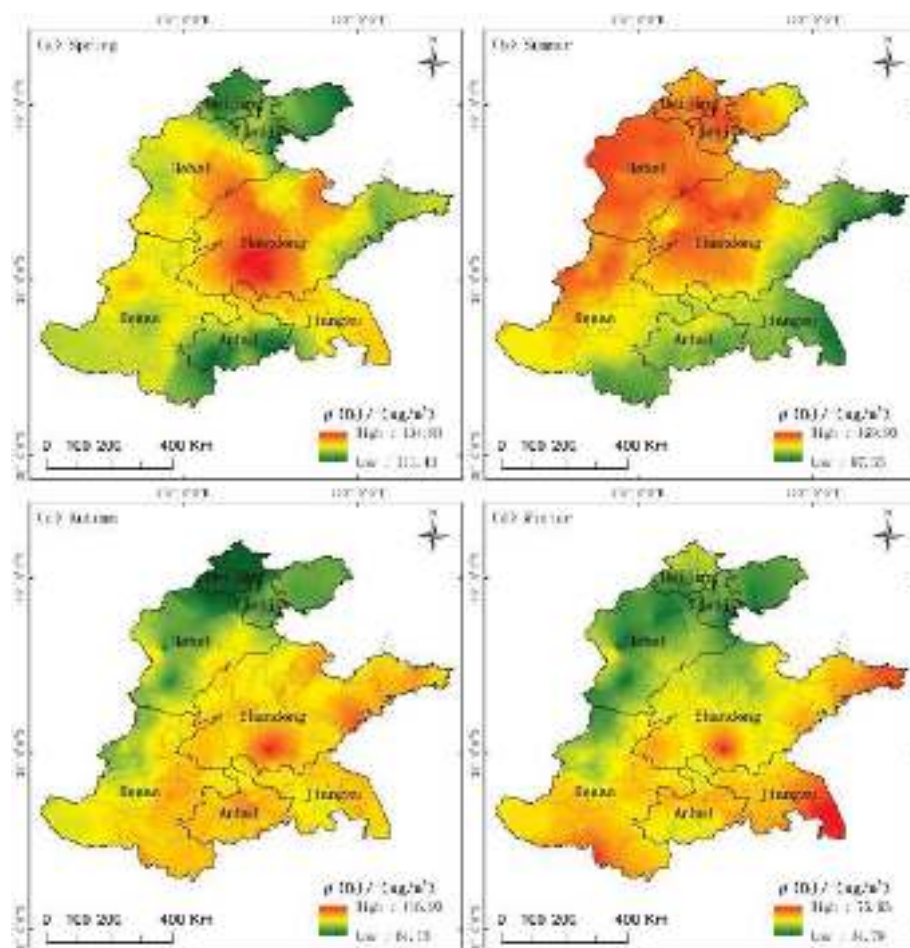


Figure 7. Seasonal spatial distribution map of O_3 in the NCP from 2016 to 2020: (a) Spatial distribution of O_3 in spring, (b) Spatial distribution of O_3 in summer, (c) Spatial distribution of O_3 in autumn, (d) Spatial distribution of O_3 in winter.

If we consider only the impact of precursor emissions, the spatial distribution of O_3 in different seasons reveals the same trend. However, due to the differences in the spatial distribution of O_3 in the four seasons, meteorological conditions must be considered to analyze their impact on the regional differences in O_3 . The variations in O_3 concentrations and meteorological conditions are shown in Figure 8. As shown, the annual variation trends in O_3 concentrations, average temperature, and average air pressure in the NCP were nearly the same from 2016 to 2020. To study the relationship between meteorological conditions and O_3 , the daily O_3 concentrations and excessive rate were statistically analyzed under different meteorological conditions using 2020 as a typical study year. As shown in Figure 9, when the temperature was greater than 30°C , O_3 concentrations were the highest, and the excessive rate reached 32%; when the temperature was less than 0°C , O_3 concentrations were $54.47 \mu\text{g}/\text{m}^3$, and the excessive rate was 0%. Particularly, the higher the temperature, the greater the O_3 concentration and the excessive rate. When the air pressure was in

the range of 1000–1013.25 hPa, O_3 concentrations were high, with a maximum value of $116.52 \mu\text{g}/\text{m}^3$, and the excessive rate reached 15%. When the air pressure was greater than 1020 hPa and less than 990 hPa, the O_3 concentrations were lower, and the excessive rate was 0% at this time. In general, the O_3 concentrations and excessive rate were rather higher under low air pressure meteorological conditions ($\text{Pa} < 1013.25$ hpa standard atmospheric pressure). This trend was driven by the following phenomenon: When the near-ground air pressure is low, O_3 is horizontally transported from the surroundings to the low-pressure area. The O_3 and its precursors converge in the low-pressure area, increasing the O_3 concentration. At the high pressure near the ground, O_3 diffuses into the surroundings. Moreover, the lower the air pressure, the higher the O_3 concentration [40] and vice versa.

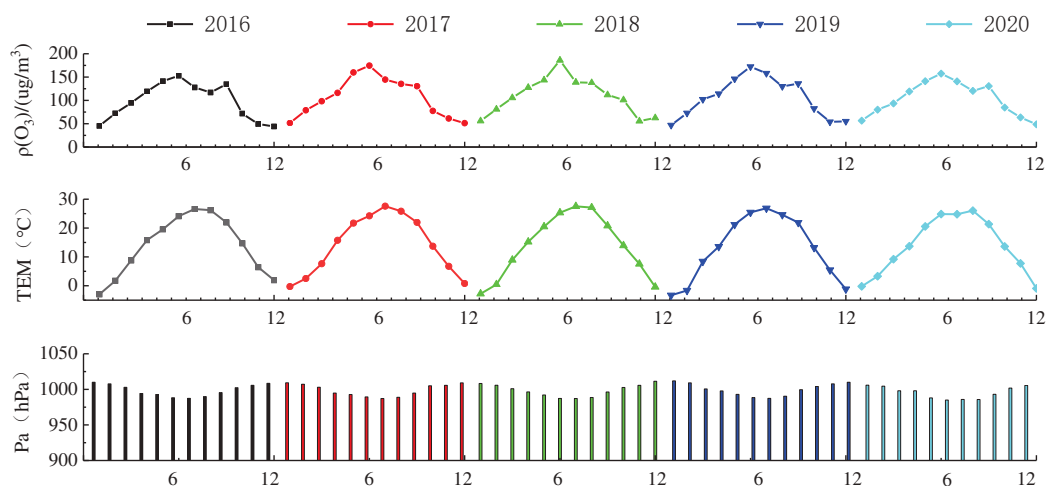


Figure 8. Variation in O_3 concentrations and meteorological conditions in the NCP from 2016 to 2020.

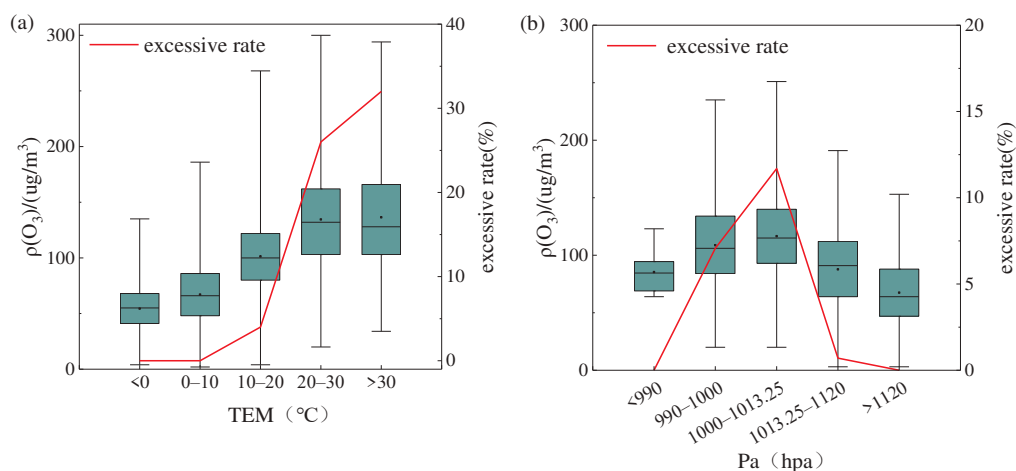


Figure 9. (a) O_3 concentrations and excessive rate under different temperature conditions, (b) O_3 concentrations and excessive rate under different air pressure conditions.

To this end, we analyzed the meteorological conditions in the study area to elucidate the drivers behind the regional differences in O_3 concentrations in different seasons. We found that, in spring, O_3 concentrations were low in large areas, particularly in the northern, southern, and eastern coastal cities of the NCP. However, O_3 concentrations were high in the central and western cities of the Shandong Province. At this time, there was only a minor difference in the average temperature and other meteorological conditions between the provinces in the study area. The regional difference was driven by abundant heavy industrial cities in central and southwest Shandong and due to large energy consumption.

This, in turn, enhanced the emission of pollutants. At the same time, the central area of Shandong is a mountainous and hilly area, where the complex terrain is conducive to the accumulation of pollutants. Therefore, being affected by the industrial structure and topography of this region, O₃ pollution has been more severe compared to other cities [41].

We found that, in summer, the concentration of O₃ in the Beijing–Tianjin–Hebei urban agglomeration and its surrounding areas was high. On the one hand, as the core economic zone of China, the Beijing–Tianjin–Hebei urban agglomeration stands out with a large population density, rapid industrial development, high economic development [42,43], strong urban heat island effect, and higher temperature compared with other regions. Note that high temperatures are conducive to the generation of O₃. On the other hand, some previous studies [44,45] argued that given the complex and regional characteristics of the Beijing–Tianjin–Hebei region, the regional transport of pollutants is prevented. In summer, the O₃ concentrations in the Beijing–Tianjin–Hebei region and cities such as Jinan, Zibo, and Liaocheng in western Shandong Province are relatively high. At the same time, the southeast wind prevails in the northern cities, and the high O₃ concentrations areas are more likely to spread to the northwest, which may lead to the formation of a high O₃ concentrations cluster northwest of the NCP.

In autumn, given the difference in latitude, cities in the southern part of the study area experienced strong solar radiation and high temperatures, which provided favorable conditions for the generation of O₃. The concentrations of O₃ were generally high in the south and low in the north. In winter, the northern part of the study area was closer to the high-pressure center in Asia, and the weather conditions were stable. O₃ generation is affected by the latitude and heat; the temperature and O₃ generation rate in the northern part were lower than those in the southern region, and the O₃ concentrations reached their lowest in a year. However, similar spatial distribution characteristics (low in the north and high in the south) were still evident. Geographically, the coastal areas of the Shandong Peninsula and the Yancheng City of the Jiangsu Province were characterized by the highest O₃ concentrations, possibly caused by external transport and ship-driven pollution [46].

4. Discussion

Previous studies have mostly discussed the spatial and temporal distribution characteristics of O₃ in major urban groups in China, but there are fewer studies on long-term O₃ monitoring and regional causal analysis in the NCP. Therefore, we used the ground monitoring station data to make spatial-temporal distribution maps of O₃, combined with the statistical data of each administrative unit, and discussed the influencing factors of O₃ pollution in a comprehensive manner. This study can provide a reference for O₃ prevention and control in the NCP.

The annual variation in O₃ showed that, compared with the previous two years, O₃ concentrations moderately decreased by 2020, but O₃ pollution was still severe compared with that in 2016. We argue that this pattern is related to high emission intensity of anthropogenic sources. The NCP is rich in mineral resources and coal, but the proportion of energy consumption is unbalanced. Due to this, the industrial structure is unreasonably unsustainable, being characterized by high energy consumption and highly polluting industries, such as metallurgy and building materials, which are common in the region. Moreover, heavily polluting enterprises are highly concentrated in the border areas of the Hebei, Shandong, and Henan provinces. Industrial production inevitably triggers the emission of pollutants, except in Beijing, where the industrial structure, similar to other cities, is low [30]. Figure 10 shows the number of civilian vehicles from 2016 to 2020. It can be seen that the number of civilian vehicles in seven provinces in the study area annually increased from 2016 to 2020. Compared to 2016, the number of civilian vehicles increased by 9.47% in Beijing, 20.36% in Tianjin, 40.24% in Hebei, 58.59% in Henan, 47.22% in Shandong, 64.20% in Anhui, and 42.73% in Jiangsu. In 2020, the number of vehicles in Shandong Province reached 25.524 million. Moreover, there is a large freight volume in the study area, and the transportation structure is mainly represented by highways. The O₃ precursors

such as CO and NO_x, produced by a large number of heavy diesel vehicles and other motor vehicles, exacerbate O₃ pollution. The data of China's anthropogenic emission inventory in 2020 [47] indicates that the anthropogenic source emissions of VOCs and NO_x in Shandong Province were the largest, while the Jiangsu and Hebei Provinces were also characterized by large emissions. The increase in precursor emissions facilitates the secondary conversion to generate O₃. Therefore, anthropogenic emissions are one of the main factors affecting regional air quality.

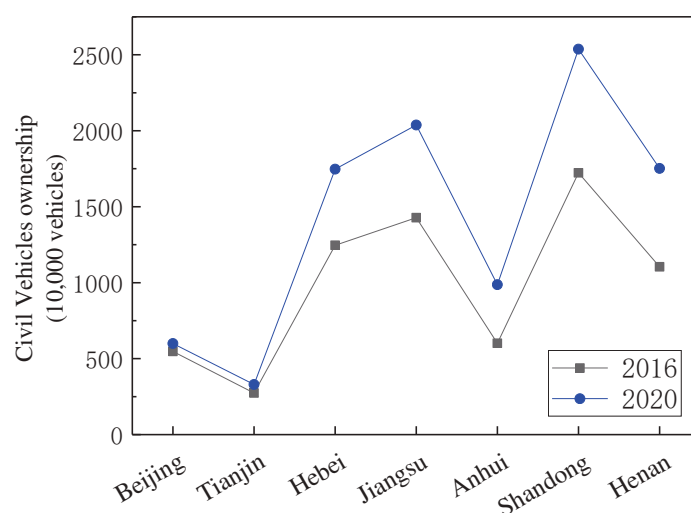


Figure 10. Changes in Civil Vehicle Ownership from 2016 to 2020.

In addition to precursor-related factors, meteorological factors can also affect O₃ concentrations through a series of reaction processes. Adverse meteorological conditions and high-intensity precursor emissions are often the preconditions for O₃ pollution. Generally, O₃ pollution events occur under high-temperature conditions, strong solar radiation, low pressure, low relative humidity, and weak winds [15,16]. Figure 11 shows the change in mean annual average temperature (MAAT) in China from 2011 to 2020, showing that the annual average temperature in China has increased significantly in the past decade, with the highest temperature in the past decade being recorded in 2015, rising by 0.94 °C compared to the average temperature from 1981 to 2010 (9.55 °C). The frequency of extreme weather in China has recently intensified and is currently higher than usual. Moreover, extreme weather conditions such as high temperatures and heavy precipitation have also intensified in China. According to the “Blue book on climate change in China 2021”, released by the Climate Change Center of the China Meteorological Administration, the warming rate in China has been higher than the global trend during the same period, and the climate warming continues. Climate warming bolsters atmospheric stability, weakening the regional atmospheric convection and diffusion. In turn, the change in air quality caused by climate change is also one of the drivers behind the increase in near-ground O₃ concentrations.

The external transmission somewhat affects the urban atmosphere. For instance, Jia et al. [48] utilized Ozone Source Apportionment Technology (OSAT) technology to analyze O₃ pollution in the summer of 2015. The simulation of the O₃ sources in Beijing and its surrounding areas indicated that Beijing was mainly affected by external transportation in the Hebei Province, followed by the Shandong Province and the Henan Province, while Tianjin was mainly affected by the Hebei and Shandong Provinces. Liu et al. [49] studied the transport pathways of atmospheric pollutants in Henan Province in 2017 using the WRF/CAMQ model. Their results showed that O₃ concentrations in Henan Province were influenced by a combination of regional transport and natural sources, with the border between Henan Province and neighboring provinces being more significantly influenced by regional transport. Furthermore, Xing et al. [50] used the extended response surface modeling (ERSMv2.0) technique to quantify the contribution of multi-regional sources to

PM_{2.5} and O₃ in the Beijing–Tianjin–Hebei region. The results showed that PM_{2.5} was more influenced by local than regional transport in most regions, while O₃ showed the opposite trend, being more heavily influenced by regional transport. Through relevant articles, we know that regional transport fundamentally affects O₃ pollution. The central areas in the NCP have serious O₃ pollution, thereby exacerbating the pressure on the ambient air quality of the transmitted cities. Thus, joint prevention and control measures are essential for mitigating O₃ pollution in the NCP.

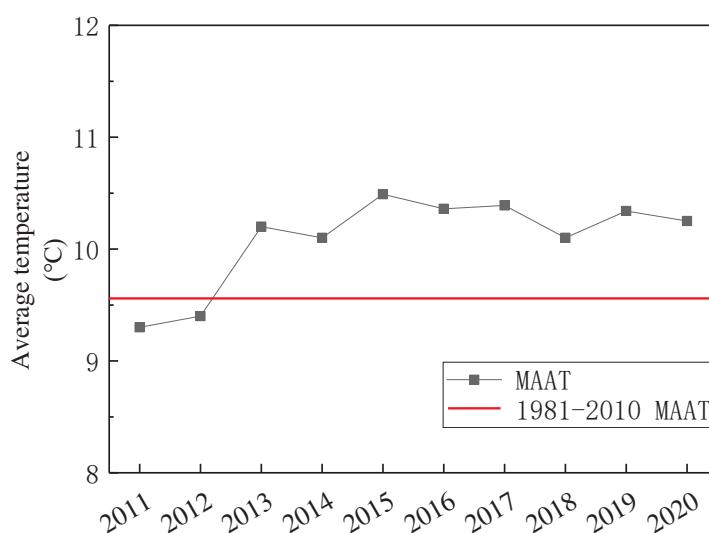


Figure 11. National mean annual average temperature changes over the years.

In general, O₃ pollution is the result of the combined influence of natural conditions and human factors. As the natural conditions are fundamentally unaffected by human being, the anthropogenic sources of pollutants should be primarily addressed. The key to controlling O₃ pollution is to reduce the emissions of precursors. Cities in the central part of the NCP are seriously polluted by O₃; we should manage the core cities with heavy industrial structures in the region, timely adjust the energy structure, promote clean energy, and adopt a long-term control strategy for NO_x and VOCs. At the same time, the NCP region needs to strengthen regional cooperation to form joint prevention and control of air management mechanisms to effectively solve the problem of O₃ transmission across regions. Moreover, as individuals, we should privilege green travel, which is an effective way to alleviate O₃ pollution. However, due to the unavailability of detailed O₃ precursor emission data for recent years, there are some methodological shortcomings in the analysis of O₃ causation correlation, and the correlation between precursors and O₃ should be discussed in detail in future studies.

5. Conclusions

This study investigated the characteristics, spatio-temporal distribution, and drivers of O₃ pollution in the NCP from 2016 to 2020, providing an effective management reference for O₃ pollution control policies. It was proven that O₃ pollution in the NCP was severe from 2016 to 2018, but after 2018, O₃ concentrations gradually decreased. The seasonal variation of O₃ concentrations was found to be regular. The O₃ concentrations were higher in spring and summer (117.89–154.20 µg/m³) and lower in autumn and winter (53.81–92.95 µg/m³). The spatial analysis revealed that O₃ exhibited distinct spatial patterns from 2016 to 2020. On an interannual scale, the overall concentrations of O₃ exhibited a spatial distribution trend of low concentrations in the north and south and high concentrations in the central area. This pattern was attributed to the characteristics of the regional industrial structure and the pollutants discharged by motor vehicles. Fundamentally, large-scale industrial production and frequent traffic flow trigger strong precursor emissions. In addition, the

greater the number of precursors, the worse the O₃ pollution. The analysis showed that the spatial distribution of O₃ exhibited certain differences being affected by precursor emissions and meteorological conditions in different seasons. Of note, high temperature and low pressure can increase O₃ concentrations, and high emissions of precursors also contribute to O₃ pollution. This calls for further decreasing the emissions of precursors to alleviate O₃ pollution.

Supplementary Materials: The following supporting information can be downloaded at: <https://www.mdpi.com/article/10.3390/atmos13050715/s1>, Table S1: Names and abbreviations of cities in the study area.

Author Contributions: Conceptualization, X.W. and W.Z. (Wenhui Zhao); methodology, L.L.; software, X.W. and T.Z. and L.W. and D.Z.; resources, M.W.; writing—original draft preparation, X.W.; writing—review and editing, W.Z. (Wenji Zhao) and P.M. and Y.Q.; supervision, W.Z. (Wenji Zhao) All authors have read and agreed to the published version of the manuscript.

Funding: This research was funded by National Key Research and Development Program of China (2018YFC0706004) and National Natural Science Foundation (42071422).

Institutional Review Board Statement: Not applicable.

Informed Consent Statement: Not applicable.

Data Availability Statement: The atmospheric O₃ data used in this study are available at <http://106.37.208.233:20035/>. Meteorological data are available at <http://data.cma.cn>. Vector data and DEM data are available at <https://www.resdc.cn/>. The statistical data from 2016 to 2020 are available at <http://www.stats.gov.cn/tjsj/ndsj/> and <https://data.cnki.net/NewHome/Index>. The POI data are available at <https://amap.com/> (accessed on 18 April 2022).

Conflicts of Interest: The authors declare no conflict of interest.

References

1. Yu, R.; Lin, Y.; Zou, J.; Dan, Y.; Cheng, C. Review on Atmospheric Ozone Pollution in China: Formation, Spatiotemporal Distribution, Precursors and Affection Factors. *Atmosphere* **2021**, *12*, 1675. [CrossRef]
2. Wang, X.; Li, J.; Zhang, Y.; Xie, S.; Tang, X. Ozone source attribution during a severe photochemical smog episode in Beijing, China. *Sci. China Ser. B Chem.* **2009**, *52*, 1270–1280. [CrossRef]
3. Toro, A.R.; Seguel, R.; Morales, S.R.; Leiva, G.M. Ozone, nitrogen oxides, and volatile organic compounds in a central zone of Chile. *Air Qual. Atmosphere Health* **2014**, *8*, 545–557. [CrossRef]
4. Shao, P.; An, J.; Xin, J.; Wu, F.; Wang, J.; Ji, D.; Wang, Y.S. Source apportionment of VOCs and the contribution to photochemical ozone formation during summer in the typical industrial area in the Yangtze River Delta, China. *Atmos. Res.* **2016**, *176*, 64–74. [CrossRef]
5. Lehman, J.; Swinton, K.; Bortnick, S.; Hamilton, C.; Baldridge, E.; Eder, B.; Cox, B. Spatio-temporal characterization of tropospheric ozone across the eastern United States. *Atmos. Environ.* **2004**, *38*, 4357–4369. [CrossRef]
6. Wang, X.; Lu, W.; Wang, W.; Leung, A.Y. A study of ozone variation trend within area of affecting human health in Hong Kong. *Chemosphere* **2003**, *52*, 1405–1410. [CrossRef]
7. Yi, R.; Wang, Y.; Zhang, Y.; Shi, Y.; Li, M. Pollution characteristics and influence factors of ozone in Yangtze River Delta. *Acta Sci. Circumstantiae* **2015**, *35*, 2370–2377. [CrossRef]
8. Zhang, P.; Wang, X.; Pan, B.; Guo, C. A Preliminary Study on the Distribution Characteristics and Sources of O₃ Concentration in the Central Plains Urban Agglomeration. *Environ. Monit. China* **2017**, *33*, 132–139. [CrossRef]
9. Liu, X.; Lou, S.; Chen, Y.; Liu, Q.; Wang, J.; Shan, Y.; Huang, S.; Du, H. Spatiotemporal distribution of ground-level ozone in mid-east China based on OMI observations. *Acta Sci. Circumstantiae* **2016**, *36*, 2811–2818. [CrossRef]
10. Zhang, Q.-Q.; Zhang, X.-Y. Ozone Spatial-temporal Distribution and Trend over China Since 2013: Insight from Satellite and Surface Observation. *Environ. Sci.* **2019**, *40*, 1132–1142. [CrossRef]
11. Meng, X.; Gong, Z.; Ye, C.; Wang, S.; Sun, H.; Zhang, X. Characteristics of Ozone concentration variation in 74 cities from 2013 to 2016. *Environ. Monit. China* **2017**, *33*, 101–108. [CrossRef]
12. Zhang, T.; Shen, N.; Zhao, X.; Wang, X.; Zhao, W. Spatiotemporal variation characteristics of ozone and its population exposure risk assessment in Chengdu-Chongqing urban agglomeration during 2015 to 2019. *Acta Sci. Circumstantiae* **2021**, *41*, 4188–4199. [CrossRef]
13. Li, Z.; Yu, S.; Li, M.; Chen, X.; Zhang, Y.; Song, Z.; Li, J.; Jiang, Y.; Liu, W.; Li, P.; et al. The Modeling Study about Impacts of Emission Control Policies for Chinese 14th Five-Year Plan on PM_{2.5} and O₃ in Yangtze River Delta, China. *Atmosphere* **2022**, *13*, 26. [CrossRef]

14. Guo, H.; Chen, K.; Wang, P.; Hu, J.; Ying, Q.; Gao, A.; Zhang, H. Simulation of summer ozone and its sensitivity to emission changes in China. *Atmos. Pollut. Res.* **2019**, *10*, 1543–1552. [CrossRef]
15. Wang, T.; Wu, Y.; Cheung, T.; Lam, K. A study of surface ozone and the relation to complex wind flow in Hong Kong. *Atmospheric Environ.* **2001**, *35*, 3203–3215. [CrossRef]
16. Li, M.; Yu, S.; Chen, X.; Li, Z.; Zhang, Y.; Wang, L.; Liu, W.; Li, P.; Lichtfouse, E.; Rosenfeld, D.; et al. Large scale control of surface ozone by relative humidity observed during warm seasons in China. *Environ. Chem. Lett.* **2021**, *19*, 3981–3989. [CrossRef]
17. Cui, M.; Bai, Y.; Feng, J.; Lin, X.; Li, H.; Gao, W.; Li, Z. Analysis of temporal and spatial variations of ozone coupling with dynamics of meteorological factors in the Beijing-Tianjin-Tangshan region. *Acta Sci. Circumstantiae* **2021**, *41*, 373–385. [CrossRef]
18. Jia, M.; Zhao, T.; Cheng, X.; Gong, S.; Zhang, X.; Tang, L.; Liu, D.; Wu, X.; Wang, L.; Chen, Y. Inverse Relations of PM_{2.5} and O₃ in Air Compound Pollution between Cold and Hot Seasons over an Urban Area of East China. *Atmosphere* **2017**, *8*, 59. [CrossRef]
19. Wang, X.; Yan, G.; Lei, Y.; Ning, M. The Status and Problems of Air Pollution of the Border Area of Jiangsu, Anhui, Shandong and Henan. *Environ. Prot.* **2020**, *48*, 45–48. [CrossRef]
20. Dong, Y.; Li, J.; Guo, J.; Jiang, Z.; Chu, Y.; Chang, L.; Yang, Y.; Liao, H. The impact of synoptic patterns on summertime ozone pollution in the North China Plain. *Sci. Total Environ.* **2020**, *735*, 139559. [CrossRef]
21. Zhao, S.; Gong, Z.; Liu, X. Correlation analysis between vegetation coverage and climate drought conditions in North China during 2001–2013. *J. Geogr. Sci.* **2015**, *70*, 717–729. [CrossRef]
22. Wang, H. Spatial-Temporal Dynamics of Regional Economic Disparity in Jiangsu-Shandong-Henan-Anhui Provinces. Master's Thesis, Henan University, Kaifeng, China, 2016.
23. Duo, A.; Zhao, W.; Gong, Z.; Zhang, M.; Fan, Y. Temporal analysis of climate change and its relationship with vegetation cover on the north China plain from 1981 to 2013. *Acta Ecol. Sin.* **2017**, *37*, 576–592. [CrossRef]
24. Qin, T.; Fu, Z. Comparison of several interpolation methods in Arcgis. *Comput. Tech. Geophys. Geochem. Explor.* **2007**, *29*, 72–75. [CrossRef]
25. Goovaerts, P. Geostatistical approaches for incorporating elevation into the spatial interpolation of rainfall. *J. Hydrol.* **2000**, *228*, 113–129. [CrossRef]
26. Wu, X.; Yan, L. Setting Parameters and Choosing Optimum Semivariogram Models of Ordinary Kriging Interpolation—A case study of spatial interpolation to January average temperature of Fujian province. *Geo-Inf. Sci.* **2007**, *9*, 104–108. [CrossRef]
27. Tobler, W.R. A Computer movie simulating urban growth in the detroit region. *Econ. Geogr.* **1970**, *46*, 234–240. [CrossRef]
28. Li, X.; Li, S.; Liu, P.; Kong, Y.; Song, H. Spatial and temporal variations of ozone concentrations in China in 2016. *Acta Sci. Circumstantiae* **2018**, *38*, 1263–1274. [CrossRef]
29. Han, G.; Xu, J.; Wang, W.; Ma, J. The spatial statistic analysis of Air Pollutants in Chongqing city. *Res. Environ. Sci.* **2006**, *19*, 30–35. [CrossRef]
30. Li, H.; Wang, S.; Zhang, W.; Wang, H.; Wang, H.; Wang, S.; Li, H. Characteristics and influencing factors of urban air quality in Beijing-Tianjin-Hebei and its surrounding areas ('2 + 26' cities). *Res. Environ. Sci.* **2021**, *34*, 172–184. [CrossRef]
31. Yue, X.; Lei, Y.; Zhou, H.; Liu, Z.; Hu, S.; Cai, Z.; Lin, J.; Jiang, Z.; Liao, H. Changes of anthropogenic carbon emissions and air pollutants during the COVID-19 epidemic in China. *Trans. Atmos. Sci.* **2020**, *43*, 265–274. [CrossRef]
32. Cui, M. Characteristics of ozone pollution and the sensitivity of its formation to precursors in Beijing. Master's Thesis, Chengdu University of Information Technology, Chengdu, China, 2019.
33. Zou, Y.; Charlesworth, E.; Yin, C.; Yan, X.; Deng, X.; Li, F. The weekday/weekend ozone differences induced by the emissions change during summer and autumn in Guangzhou, China. *Atmos. Environ.* **2019**, *199*, 114–126. [CrossRef]
34. Xu, W.Y.; Zhao, C.S.; Ran, L.; Deng, Z.Z.; Liu, P.F.; Ma, N.; Lin, W.L.; Xu, X.B.; Yan, P.; He, X.; et al. Characteristics of pollutants and their correlation to meteorological conditions at a suburban site in the North China Plain. *Atmos. Chem. Phys.* **2011**, *11*, 4353–4369. [CrossRef]
35. Fu, C.; Zhou, H. Research progress on the formation mechanism and impact factors of urban ozone pollution in China. *Environ. Monit. China* **2021**, *37*, 33–43. [CrossRef]
36. Kajino, M.; Hayashida, S.; Sekiyama, T.T.; Deushi, M.; Ito, K.; Liu, X. Detectability assessment of a satellite sensor for lower tropospheric ozone responses to its precursors emission changes in East Asian summer. *Sci. Rep.* **2019**, *9*, 19629. [CrossRef]
37. Yu, Y.-J.; Wang, Z.; He, T.; Meng, X.-Y.; Xie, S.-Y.; Yu, H.-X. Driving factors of the significant increase in surface ozone in the Yangtze River Delta, China, during 2013–2017. *Atmos. Pollut. Res.* **2019**, *10*, 1357–1364. [CrossRef]
38. Guo, Y.; Wang, Z.; Xu, C. Spatio-temporal evolution and influencing factors of total particulate matter emissions of vehicles in China. *Acta Ecol. Sin.* **2021**, *41*, 4406–4417. [CrossRef]
39. Jhun, I.; Coull, B.A.; Zanutti, A.; Koutrakis, P. The impact of nitrogen oxides concentration decreases on ozone trends in the USA. *Air Qual. Atmos. Health* **2015**, *8*, 283–292. [CrossRef]
40. Ke, B.; He, C.; Yang, L.; Ye, Z.; Yi, J.; Tian, Y.; Mu, H.; Tu, P.; Han, C.; Hong, S. Study on the spatiotemporal variation of surface ozone and the main driving factors in North China. *China Environ. Sci.* **2021**, *42*, 1–13. [CrossRef]
41. Liu, X. Analysis on Variation Characteristics of Air Pollution in Shandong Province during 2000–2005. Master's Thesis, Shandong University, Jinan, China, 2008.
42. Wang, S.; Fang, C.; Wang, Y. Quantitative investigation of the interactive coupling relationship between urbanization and eco-environment. *Acta Ecol. Sin.* **2015**, *35*, 2244–2254. [CrossRef]

43. Lu, D. Function orientation and coordinating development of subregions within the Jing-Jin-Ji Urban Agglomeration. *Prog. Geogr.* **2015**, *34*, 265–270. [CrossRef]
44. Wang, Y.; Xue, W.; Lei, Y.; Wu, W. Model-derived source apportionment and regional transport matrix study of ozone in Jingjinji. *China Environ. Sci.* **2017**, *37*, 3684–3691. [CrossRef]
45. Shao, P.; Wang, L.-L.; An, J.-L.; Zhou, Y.-L.; Wang, Y.-S. Observation and Analysis of Air Pollution in Zhangjiakou, Hebei. *Environ. Sci.* **2012**, *33*, 2538–2550. [CrossRef]
46. Wu, J. Study on Ozone generation sensitivity and Source Analysis in Typical Coastal Cities in Summer. Master's Thesis, Shandong Normal University, Jinan, China, 2019.
47. Zheng, B.; Zhang, Q.; Geng, G.; Chen, C.; Shi, Q.; Cui, M.; Lei, Y.; He, K. Changes in China's anthropogenic emissions and air quality during the COVID-19 pandemic in 2020. *Earth Syst. Sci. Data* **2021**, *13*, 2895–2907. [CrossRef]
48. Jia, H.; Yin, T.; Qu, X.; Cheng, N.; Cheng, B.; Wang, J.; Tang, W.; Meng, F.; Chai, F. Characteristics and source simulation of ozone in Beijing and its surrounding areas in 2015. *China Environ. Sci.* **2017**, *37*, 1231–1238. [CrossRef]
49. Liu, G.; Su, F.; Xu, Q.; Zhang, R.; Wang, K. One-year Simulation of Air Pollutions in Central China, Characteristic, Distribution, Inner Region Cross-transmission, and Path Way Research in 18 Cities. *Environ. Sci.* **2022**, 1–17. [CrossRef]
50. Xing, J.; Wang, S.; Zhao, B.; Wu, W.; Ding, D.; Jang, C.; Zhu, Y.; Chang, X.; Wang, J.; Zhang, F.; et al. Quantifying Nonlinear Multiregional Contributions to Ozone and Fine Particles Using an Updated Response Surface Modeling Technique. *Environ. Sci. Technol.* **2017**, *51*, 11788–11798. [CrossRef]

Article

Analysis of Spatio-Temporal Heterogeneity and Socioeconomic driving Factors of PM_{2.5} in Beijing–Tianjin–Hebei and Its Surrounding Areas

Ju Wang *, Ran Li, Kexin Xue and Chunsheng Fang

College of New Energy and Environment, Jilin University, Changchun 130012, China; liran19@mails.jlu.edu.cn (R.L.); xuekx20@mails.jlu.edu.cn (K.X.); fangcs@jlu.edu.cn (C.F.)

* Correspondence: wangju@jlu.edu.cn

Citation: Wang, J.; Li, R.; Xue, K.; Fang, C. Analysis of Spatio-Temporal Heterogeneity and Socioeconomic driving Factors of PM_{2.5} in Beijing–Tianjin–Hebei and Its Surrounding Areas. *Atmosphere* **2021**, *12*, 1324. <https://doi.org/10.3390/atmos12101324>

Academic Editors: Duanyang Liu, Kai Qin and Honglei Wang

Received: 15 September 2021

Accepted: 8 October 2021

Published: 10 October 2021

Publisher's Note: MDPI stays neutral with regard to jurisdictional claims in published maps and institutional affiliations.

Abstract: Due to rapid urbanization and socio-economic development, fine particulate matter (PM_{2.5}) pollution has drawn very wide concern, especially in the Beijing–Tianjin–Hebei region, as well as in its surrounding areas. Different socio-economic developments shape the unique characteristics of each city, which may contribute to the spatial heterogeneity of pollution levels. Based on ground fine particulate matter (PM_{2.5}) monitoring data and socioeconomic panel data from 2015 to 2019, the Beijing–Tianjin–Hebei region, and its surrounding provinces, were selected as a case study area to explore the spatio-temporal heterogeneity of PM_{2.5} pollution, and the driving effect of socioeconomic factors on local air pollution. The spatio-temporal heterogeneity analysis showed that PM_{2.5} concentration in the study area expressed a downward trend from 2015 to 2019. Specifically, the concentration in Beijing–Tianjin–Hebei and Henan Province had decreased, but in Shanxi Province and Shandong Province, the concentration showed an inverted U-shaped and U-shaped variation trend, respectively. From the perspective of spatial distribution, PM_{2.5} concentrations in the study area had an obvious spatial positive correlation, with agglomeration characteristics of “high–high” and “low–low”. The high-value area was mainly distributed in the junction area of Henan, Shandong, and Hebei Provinces, which had been gradually moving to the southwest. The low values were mainly concentrated in the northern parts of Shanxi and Hebei Provinces, and the eastern part of Shandong Province. The results of the spatial lag model showed that Total Population (POP), Proportion of Urban Population (UP), Output of Second Industry (SI), and Roads Density (RD) had positive driving effects on PM_{2.5} concentration, which were opposite of the Gross Domestic Product (GDP). In addition, the spatial spillover effect of the PM_{2.5} concentrations in surrounding areas has a positive driving effect on local pollution levels. Although the PM_{2.5} levels in the study area have been decreasing, air pollution is still a serious problem. In the future, studies on the spatial and temporal heterogeneity of PM_{2.5} caused by unbalanced social development will help to better understand the interaction between urban development and environmental stress. These findings can contribute to the development of effective policies to mitigate and reduce PM_{2.5} pollutions from a socio-economic perspective.

Keywords: PM_{2.5}; spatio-temporal heterogeneity; socio-economic driving factors



Copyright: © 2021 by the authors. Licensee MDPI, Basel, Switzerland. This article is an open access article distributed under the terms and conditions of the Creative Commons Attribution (CC BY) license (<https://creativecommons.org/licenses/by/4.0/>).

1. Introduction

With the advancement of industrialization and urbanization, many cities around the world are experiencing severe air pollution, especially particulate matter pollution. On a global scale, China, India, and South Asia have the most severe particulate matter pollution in the world [1]. In China, since 2011, Beijing–Tianjin–Hebei [2], the Yangtze River Delta [3], and other regions have experienced frequent smog, and air pollution has caused widespread concern. High concentrations of PM_{2.5} can, not only accelerate the formation of haze but also significantly affect people's health [4]. It has been proved that long-term exposure to high PM levels can easily cause a variety of diseases [5] and increase

the risk of death [6]. In 2017, the State Ministry of Environmental Protection issued the “Beijing–Tianjin–Hebei and Surrounding Area Air Pollution Prevention and Control Work Plan in 2017”, which first proposed the concept of “2 + 26 cities” and implemented a large number of pollution control measures in these cities to alleviate air pollution in North China. Therefore, strengthening scientific understanding of the regulations of regional air particulate pollution will help to formulate urbanization policies and ensure that targeted air pollution control measures are properly implemented.

At present, research on $PM_{2.5}$ pollutions mainly focuses on temporal and spatial distribution rules [7], influencing factor analyses [8], source analyses [9], and health risk assessments [10] along with other aspects. Among them, influencing factors mainly include meteorological factors and socio-economic factors. Meteorological factors affect $PM_{2.5}$ concentration by changing its diffusion and chemical reaction conditions. Chen et al. [11] summarized the methods to quantify the impact of meteorological factors on $PM_{2.5}$ and comprehensively reviewed their impact mechanisms. Xu et al. [12] conducted a study on the temporal and spatial distributions of the influence of meteorological conditions on $PM_{2.5}$ concentration in China from 2000 to 2017, which showed an overall downward trend in $PM_{2.5}$ concentration, and the influence of meteorology varied greatly between different provinces. The socio-economic factors that directly or indirectly affect $PM_{2.5}$ concentration in the process of urbanization and economic development, include the national economy, industrial structure, population density, transportation, and other factors [13]. These factors mainly represent the impact of human activities on $PM_{2.5}$. The average urban $PM_{2.5}$ level is mainly affected by anthropogenic emissions of local air pollutants and the surrounding ecological level. Cheng et al. [14] used a dynamic spatial panel model to analyze the impact of foreign direct investment (FDI) on China’s $PM_{2.5}$ pollutions, and the results showed that FDI significantly aggravated China’s urban $PM_{2.5}$ pollutions. The study of Yan et al. [15] expressed that there was a heterogeneous relationship between $PM_{2.5}$ concentration and economic growth, urbanization, industrialization, and FDI and that population density had the greatest positive impact on $PM_{2.5}$ pollution. Zhang et al. [16] noted that $PM_{2.5}$ pollution was positively correlated with urbanization and road density, and negatively correlated with the proportion of tertiary industries.

Although many studies have been conducted on the temporal and spatial distributions of $PM_{2.5}$ and its influencing factors, the study areas of most studies mainly concentrate on the level of countries, urban agglomerations, and cities, while comparisons between regions are relatively rare. In addition, with rapid economic development, the North China region has been experiencing severe $PM_{2.5}$ pollution. Shanxi Province is located in the central region and has a decreasing economic development. Therefore, this study selects Beijing City, Tianjin City, Hebei Province, Henan Province, and Shanxi Province as the study areas. There are significant distinctions of $PM_{2.5}$ and economic development levels between the different cities, which provides advantages for studying the impact of socio-economic factors and spatial spillover effects on the $PM_{2.5}$ level. The aims of this study are: (1) explore the temporal and spatial distribution characteristics of $PM_{2.5}$ levels; (2) compare the spatial heterogeneity of $PM_{2.5}$ distribution characteristics in different regions, and (3) determine the influence of socio-economic factors and spatial spillover effects on $PM_{2.5}$ levels.

2. Materials and Methods

2.1. Study Area

This study selects Beijing City, Tianjin City, Hebei Province, Henan Province, and Shanxi Province as the study areas, which contains 56 cities in four provinces and two municipalities, as shown in Figure 1. Among them, Hebei Province, Shandong Province, Shanxi Province, and Henan Province have 11, 16, 11, and 18 prefecture-level cities, respectively. The names and abbreviations of all cities are shown in Table S1. The study area is located between 31°23′ N–42°40′ N and 110°14′ E–122°42.3′ E in China, with the Loess Plateau in the west and the North China Plain in the east. With its rapid economic

development and rapid consumption of energy, the air quality in North China is not better and haze pollution incidents occur frequently; this area is considered one of the most polluted areas of China. In addition, the study area includes, not only the eastern regions with their rapid economic development, such as the Beijing–Tianjin–Hebei urban agglomeration and Shandong Province but also the central regions with slower economic development speeds, such as Shanxi Province. The socio-economic development of the study area is very unbalanced, which provides favorable conditions for analyzing the influence of socio-economic factors on $PM_{2.5}$ concentration. Therefore, this paper selects four provinces and two municipalities as the study areas to explore the temporal and spatial heterogeneity of $PM_{2.5}$ and the influence of socioeconomic factors on $PM_{2.5}$ concentrations in 2015–2019.

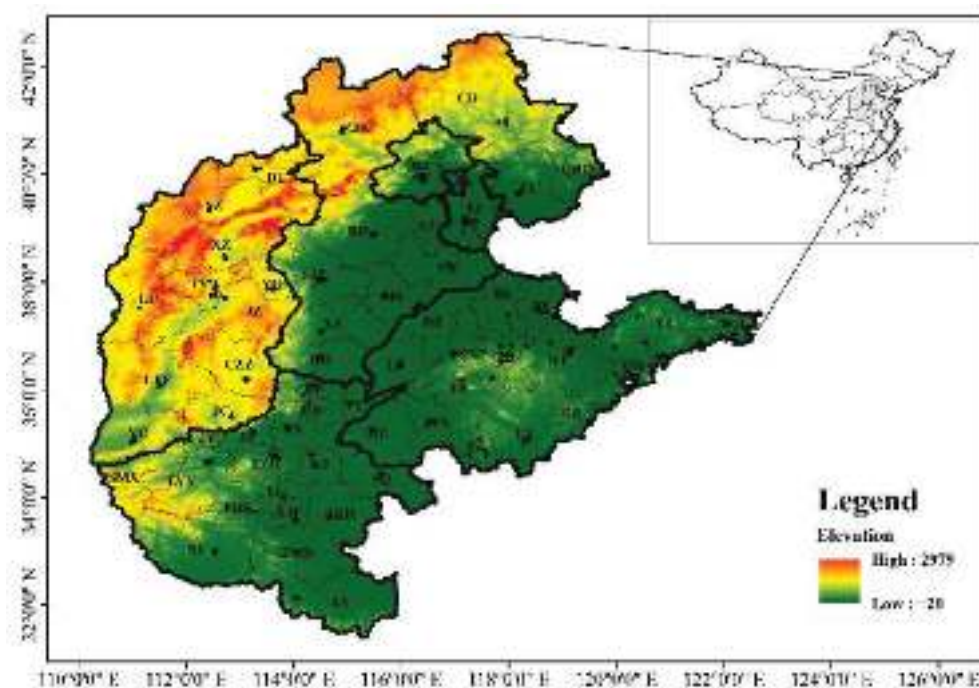


Figure 1. Study area.

2.2. Data Sources and Validity

This study collected hourly $PM_{2.5}$ concentration data from 347 automatic air quality monitoring stations in the study area, from 1 January 2015, to 31 December 2019. This set of data was obtained from the Urban Air Quality Distribution platform of the National Environmental Monitoring Center (<http://www.mec.cma.gov.cn>, accessed on 9 October 2021). Based on the hourly $PM_{2.5}$ data, the arithmetic mean method was used to calculate the annual $PM_{2.5}$ concentration in each city, from 2015 to 2019. To improve the validity of the data, we processed the missing values according to the provisions of the Ambient Air Quality Standard (GB3095–2012). When calculating the daily average concentrations, we required that the number of hourly average concentrations or the sampling time should be more than 20, otherwise the daily average concentration was considered invalid. In calculating the average monthly concentrations, we required at least 27 (February: 25) daily average concentration values, otherwise, the monthly mean concentration was considered invalid. At least 324 daily average concentrations were required to calculate the annual average concentration, otherwise, the annual average concentration was considered invalid.

The potential impact of socioeconomic indicators on $PM_{2.5}$ pollution has been widely discussed. Based on previous studies and the availability of socioeconomic data, we selected seven indicators (Table 1): Population (POP), Gross Domestic Product (GDP), Green Ratio of Built-up Area (GR), Output of Second Industry (SI), Proportion of Urban Population (UP), Roads Density (RD), and Proportion of Built-up Area (BA). Among them, POP, GDP, and GR, respectively, represent population size, economic development level,

and urban greening; SI and RD express industrial structure and traffic factors, respectively; UP and BA represent population urbanization and spatial urbanization. The annual statistical data of POP, GDP, SI, and RD were acquired from the Social and Economic Development Bulletin and Statistical Yearbook of each city in the study area, while those of GR and BA were obtained from the China Urban Statistical Yearbook. The time span of all socioeconomic indicators was consistent with that of PM_{2.5} data in this study. Figure S4 provides detailed statistical information on these socioeconomic factors, for each city.

Table 1. Socioeconomic indicators and the abbreviations and units.

Category	Variable	Abbreviation	Units
Independent variable	PM _{2.5} concentration	PM _{2.5}	µg/m ³
Dependent variable	Total Population	POP	10 ⁴ persons
	Gross Domestic Product	GDP	10 ⁴ CNY
	Green Ratio of Built-up Area	GR	%
	Output of Second Industry	SI	10 ⁴ CNY
	Proportion of Urban Population	UP	%
	Roads Density	RD	km/km ²
	Proportion of Built-up Area	BA	%

2.3. Statistical Methods

2.3.1. Moran's I Test

Air pollution usually has obvious spatial distribution characteristics with regional aggregation. Many researchers usually use Moran's I to test the spatial correlation of variables. In this study, we used the Global Moran's I to test the overall spatial effect of PM_{2.5} concentrations in 58 cities, from 2015 to 2019. The Global Moran's I model can be explained as follows [17]:

$$\text{Global Moran's } I_i = \frac{n \sum_{i=1}^n \sum_{j=1}^n w_{ij} (y_i - \bar{y})(y_j - \bar{y})}{S_0 \sum_{i=1}^n (y_i - \bar{y})^2} \quad (1)$$

$$Z = \frac{1 - E(I)}{\sqrt{\text{Var}(I)}} \quad (2)$$

$$E[I] = -1/(n - 1) \quad (3)$$

$$V[I] = E[I^2] - E[I]^2 \quad (4)$$

where y_i is the PM_{2.5} concentration of city i , y_j is the PM_{2.5} concentration of city j , and \bar{y} is the average PM_{2.5} concentration of the study area. w_{ij} is the spatial weight matrix; if two cities share a common boundary, the weight is 1, otherwise, it is 0; $S_0 = \sum_{i=1}^n \sum_{j=1}^n w_{ij}$ is the aggregation of all spatial weights; $n = 56$ is the number of cities. Z score and p values used to judge the Moran's I significance level; when the $|Z| > 1.96$ or $p < 0.05$, the result is considered significant at the 95% confidence level; when the $|Z| > 2.58$ or $p < 0.01$, the result is considered significant at the 99% confidence level. In this paper, the Global Moran's I was calculated using ArcGIS software.

2.3.2. Hot Spot Analysis

Hot Spot Analysis is often used to identify potential spatial agglomeration characteristics of PM_{2.5} pollution, and PM_{2.5} levels are divided into cold spots, insignificant points, and hot spots. The Getis-Ord G_i^* of ArcGIS was used to calculate the G_i^* of each city in the study area. The principle formulae are as follows [18]:

$$G_i^* = \frac{\sum_{j=1}^n w_{ij} x_j - \bar{x} \sum_{j=1}^n w_{ij}}{S \sqrt{\frac{n \sum_{j=1}^n w_{ij}^2 - \left(\sum_{j=1}^n w_{ij}\right)^2}{n-1}}} \quad (5)$$

$$S = \sqrt{\frac{\sum_{j=1}^n x_j^2}{n} - (\bar{x})^2} \quad (6)$$

where x_j is the annual $PM_{2.5}$ concentration of city j ; ω_{ij} is the spatial weight between city i and city j , and $n = 56$ represents the number of cities in the study area.

2.3.3. Spatial Lag Model

Socioeconomic variables, such as GDP, population size, and traffic, greatly affect local $PM_{2.5}$ concentrations. In this study, the Spatial Lag Model (SLM) was used to determine the influence of different socio-economic factors on $PM_{2.5}$ concentration, which could be explained by Formula (7):

$$Y = \rho WY + X\beta + \varepsilon, \varepsilon \sim N[0, \sigma^2 I] \quad (7)$$

where Y indicates the $PM_{2.5}$ concentration; X expresses the independent variables, including all introduced socioeconomic factors; ρ is the spatial effect coefficient, and its value ranges from 0 to 1. The spatial matrix is represented by W , which indicates whether two spatial elements have a common boundary; β represents the regression coefficient of explanatory variables; and ε is the error term.

3. Results and Discussion

3.1. Temporal Variation Characteristics of $PM_{2.5}$

3.1.1. Temporal Variation Trend of $PM_{2.5}$ Concentration

The variation trend of $PM_{2.5}$ concentration in the study area was determined by calculating the Probability Density Functions (PDFs) and annual average concentrations of $PM_{2.5}$ in the study area, from 2015 to 2019. As shown in Figure 2, the $PM_{2.5}$ concentration in the study area expressed a downward trend from 2015 to 2019, which decreased by 27.17%, from $73.23 \mu\text{g}/\text{m}^3$ in 2015 to $53.34 \mu\text{g}/\text{m}^3$ in 2019. Although the annual $PM_{2.5}$ concentration decreased, it still exceeded the Grade II standard of $PM_{2.5}$ ($35 \mu\text{g}/\text{m}^3$) in the Ambient Air Quality Standard (GB3095-2012) in 2019, which indicated that $PM_{2.5}$ pollution in the study area was still severe. The frequency distribution of $PM_{2.5}$ can be found in the PDF graph. From 2015 to 2019, the probability density curve moved to the left as a whole, indicating that $PM_{2.5}$ concentration had decreased in all concentration intervals. The curves of 2015 and 2016 are similar, while those of 2017, 2018, and 2019 are similar. Compared with 2016, the occurrence probability of high concentration decreased significantly in 2017, resulting in a significant increase in probability in the low concentration intervals, and then remained stable. This sudden change may be related to the stricter air pollution control measures that were implemented in 2017.

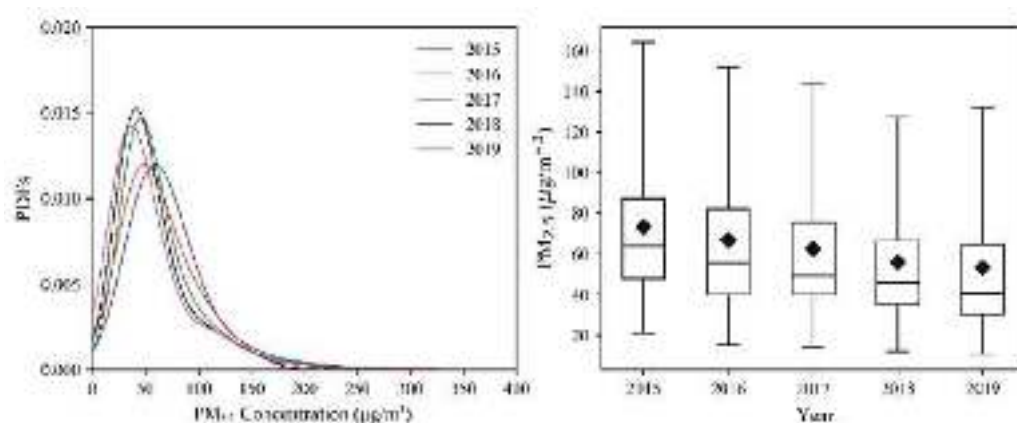


Figure 2. Probability density function (PDFs) and annual concentration of $PM_{2.5}$ from 2015 to 2019.

The mitigation trend was more significant in the context of concentration levels. In 2015, the average annual concentration of PM_{2.5} in all cities ranged from 34.6 to 106.42 µg/m³, but was 26.52–72.39 µg/m³ in 2019. We can find that there was a large difference between different cities, with the maximum concentration being about three times that of the minimum. During the period of 2015–2019, the maximum concentration occurred in BD in 2015 and the minimum concentration occurred in WH in 2018. In addition, we also determined the statistics on the percentage of exceeding standard days in each city, from 2015 to 2019, as shown in Figure S1. In 2015, the average percentage of exceeding standard days in the study area was 37.45%, but it dropped to 15.66% in 2019. This apparent mitigation of PM_{2.5} pollution did not just start in 2015, it had been going on for a long time. Some studies on the long-term variation trends of PM_{2.5} concentrations have shown that it had been increasing since 2000 until reaching a peak in 2008, and then it fluctuated continuously and reached another peak in 2014 before decreasing since then [19]. It fluctuated after 2008 as the harm of PM_{2.5} pollution was widely known after the Beijing Olympic Games and China gradually entered the stage of economic restructuring [20]. China's government began to implement strict pollution control measures and regarded PM_{2.5} as a routine monitoring pollutant after issuing the Action Plan for Air Pollution Prevention and Control in 2013, which may be why PM_{2.5} concentration continued to decrease after 2014 [21]. As a large number of emission reduction measures have already been implemented, the reduction in PM_{2.5} will gradually reduce in the future. Therefore, the speed of pollution mitigation may be slowed down, and the spatial difference between cities would become narrower. From this aspect, Jiang et al. [22] reported that there was a spatial convergence trend for PM_{2.5} concentrations in the Beijing–Tianjin–Hebei region.

3.1.2. The Spatial Heterogeneity of Temporal Variations

Although PM_{2.5} concentrations in the study area have been decreasing on the whole, they express different temporal regulations in various areas. As shown in Figure S2, Beijing, Tianjin, and most cities in Hebei and Henan Provinces decreased from 2015 to 2019, while a few cities showed different patterns. The average concentrations in Hebei Province and Henan Province also had the same patterns as most of the cities under their jurisdictions. However, the patterns of cities in Shanxi Province and Shandong Province were quite different from the others. To be more specific, PM_{2.5} concentrations in Shanxi Province first went up but then decreased, and reached their highest level in 2017, presenting an inverted U-shaped trend. In Shandong Province, it first went down, and then it went up, reaching the lowest level in 2018 and showing a U-shaped trend. The patterns of most cities in the two provinces were consistent with their corresponding provinces. This heterogeneity may be related to differences in economic development, environmental protection policies, geographical differences, and other factors between the different provinces. The regions with the highest PM_{2.5} concentration in 2015 were Beijing and Henan Provinces, and Henan Province exhibited the highest PM_{2.5} concentration for the period of 2016–2019. After five years of decline, Beijing ranked last among the four provinces and two municipalities in 2019.

Specific to the urban level, the discrepancies in the reduction rates among different regions were more obvious, as shown in Figure S3. Specifically, BJ, BD, LF, DZ, and LC exhibited the highest reduction rate if more than 40%. Those of TY, YQ, JC, YC, and LFF were slightly less than 10%. The former was mainly concentrated in the Beijing–Tianjin–Hebei region, while the latter was under the jurisdiction of Shanxi Province. To further explore the differences in temporal variations, we plotted the PDFs of PM_{2.5} in each province or municipality from 2015 to 2019, as shown in Figure 3. To facilitate comparison, we divided the study area into the Beijing–Tianjin–Hebei region and its surrounding regions (Shandong, Hebei, Shanxi Province). In 2015, the PDFs of each province varied greatly. Shanxi Province had the highest peak value, while Beijing had the lowest. Although the concentration ranges of the two peak areas were similar, the occurrence probability of high PM_{2.5} concentration in Beijing was high, indicating that Beijing was prone to PM_{2.5} pollution events. On the whole, the peaks in the Beijing–Tianjin–Hebei region were lower, while those

in the surrounding region were higher, indicating that PM_{2.5} pollution in the Beijing–Tianjin–Hebei region was more serious than in its surrounding areas. From the temporal point of view, the curve variation of the Beijing–Tianjin–Hebei region is very significant, especially in terms of BJ. The Shandong, Henan, and Shanxi regions also showed a trend of pollution alleviation. It is worth noting that the PDFs curve of Henan Province was always at the bottom, indicating that it had higher PM_{2.5} pollution. After five years of improvement, the PDFs curves of the six regions showed a tendency to gradually coincide. Until 2019, the curves were quite similar, showing that the spatial differences of PM_{2.5} concentration were narrowing, which is similar to the research results of Jiang, He, and Zhou [22].

3.2. Spatial Variation Trend of PM_{2.5}

To determine the spatial distribution characteristics of PM_{2.5} concentrations in the study areas, we calculated the Global Moran's I during 2015–2019. As shown in Table 2, with p -values < 0.01 and Z-score > 2.58, the Global Moran's I was acceptable. From 2015 to 2019, the PM_{2.5} concentrations in the study areas showed a significant positive spatial correlation, which indicated that the diffusion of PM_{2.5} concentrations between cities was not random, and rather showed similar spatial connections and tended to aggregate. This spatial correlation has been gradually increasing since 2016. To better exhibit the agglomeration characteristics of the study area, we drew a Moran scatter diagram, as shown in Figure 4. Most cities are concentrated in the first and third quadrants, and only a few cities appear in the second and fourth quadrants which indicate that PM_{2.5} pollution in the study areas presented obvious “high–high” and “low–low” agglomeration. This spatial characteristic is caused by the unbalanced economic development in the earlier period. With the sustainable development of the economy and the transformation of urban planning and layout, it would change.

Table 2. Global Moran's I from 2015 to 2019.

Year	I	p -Value	Z-Score
2015	0.372501	0.000001	4.855292
2016	0.344208	0.000006	4.532812
2017	0.363731	0.000002	4.796205
2018	0.389324	0.000000	5.123085
2019	0.414598	0.000000	5.429379

To clearly determine the high and low concentration areas of PM_{2.5} pollution, we drew a Getis-Ord Gi* statistical graph for the study area during 2015–2019, as shown in Figure 5. On the whole, the cold spots in the study area were mainly distributed in the north of Shanxi and Hebei Provinces, and the eastern coastal areas of Shandong Province and the hot spots were mainly concentrated in the junction area of Hebei, Shandong, and Henan Provinces. In terms of temporal change, the cold spots gradually shifted from the northwest to the north of the study area, while those in the eastern coastal region of Shandong Province were composed of YT, QD, and WH with no change. Additionally, the hot spot moved to the southwest gradually from 2015 to 2019. This moving of the PM_{2.5} pollution center does not mean that the air quality in hot spots city were getting worse. In fact, almost all cities had been experiencing PM_{2.5} pollution alleviation at different levels. The PM_{2.5} concentration in some cities, such as SJZ, JN, and DZ, decreased sharply from hot spots to insignificant spots; some cities, such as JY, LYY, and PDS, declined slowly from insignificant spots to hot spots. This conversion of hot and cold spots is essentially determined by the transformation of the local industrial structure and the implementation of environmental protection policies. In fact, the upgrading and relocation of heavily polluting enterprises in the Beijing–Hebei–Tianjin region may also be one of the reasons for the moving of the pollution centroid. XT, HD, LC, AY, KF, PY, HB, XX, and other cities had always been hot spot cities during 2015–2019, indicating that the pollution in these cities was relatively serious and that control measures still needed to be taken for reducing the PM_{2.5} pollution risk level.

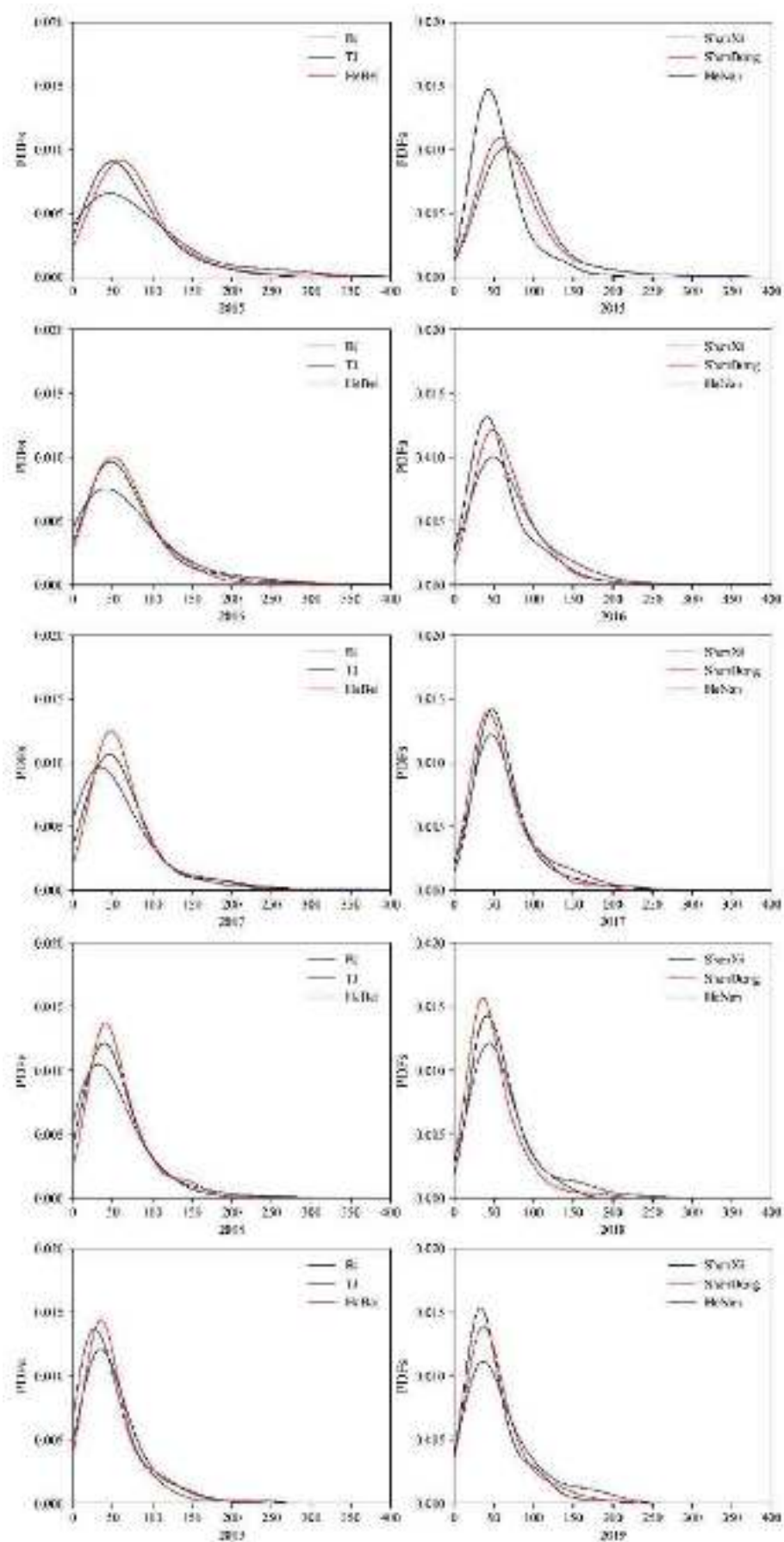


Figure 3. Probability density functions of each province during 2015–2019.

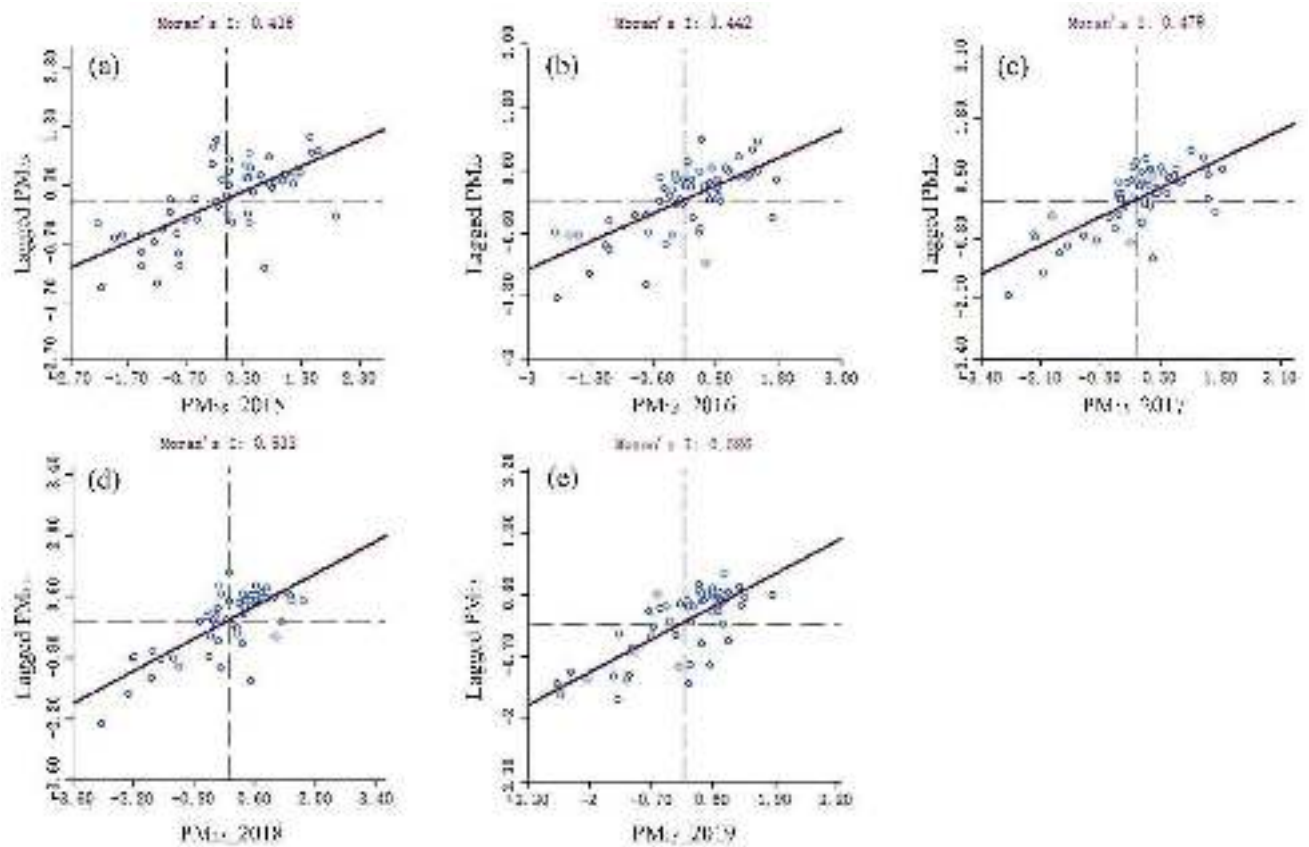


Figure 4. Moran scatter diagram from 2015 to 2019. (a) 2015; (b) 2016; (c) 2017; (d) 2018; (e) 2019.

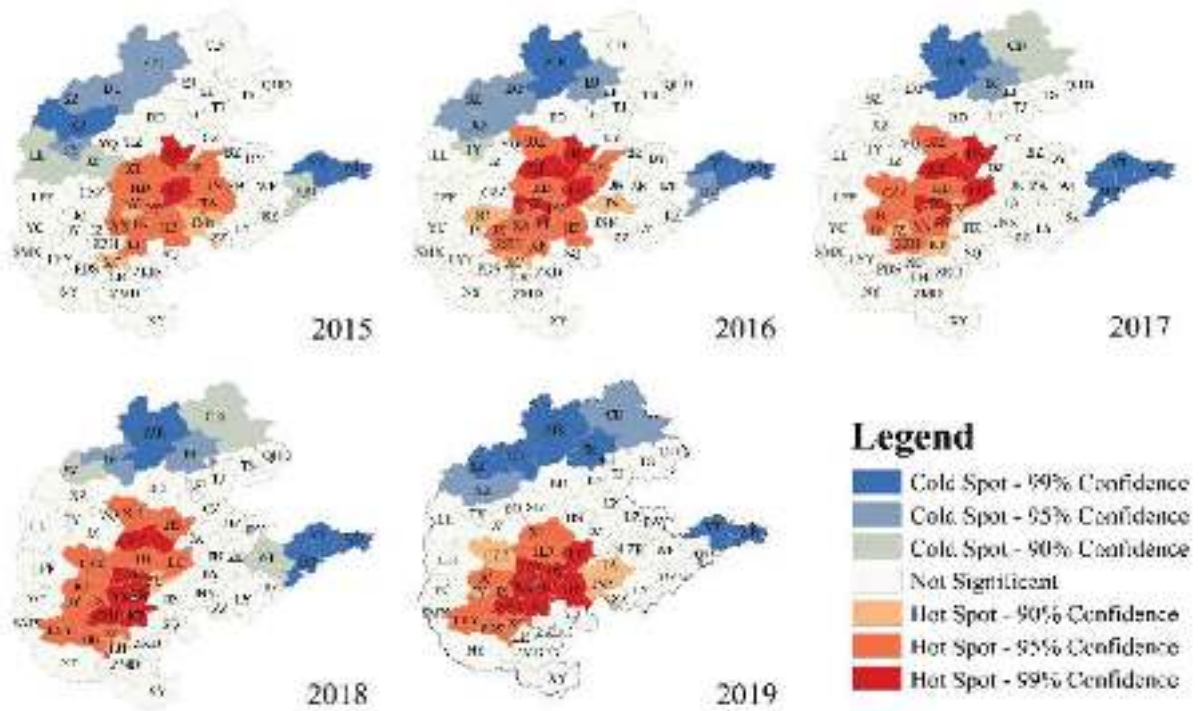


Figure 5. Cold-hot spot diagram of $PM_{2.5}$ concentration from 2015 to 2019.

3.3. Analysis of Socioeconomic Influence Factors

Different socioeconomic indicators reflect different human activities, which could affect the spatial and temporal heterogeneity of PM_{2.5} concentrations to various degrees. In this study, we used a spatial lag model (SLM) to determine the impact of various socioeconomic factors on PM_{2.5} concentrations. To ensure the data conformed to the normal distribution, a logarithmic transformation was performed on the socioeconomic data and PM_{2.5} concentrations before using SLM. Table 3 shows the quantified results of the SLM model from 2015 to 2019.

Table 3. Results of spatial lag model.

Variable	2015		2016		2017		2018		2019	
	Coefficient	Probability	Coefficient	Probability	Coefficient	Probability	Coefficient	Probability	Coefficient	Probability
ρ	0.560	0.000 **	0.583	0.000 **	0.739	0.000 **	0.724	0.000 **	0.574	0.000 **
GDP	−0.405	0.005 **	−0.328	0.088	−0.489	0.001 **	−0.364	0.012 *	−0.415	0.002 **
POP	0.222	0.001 **	0.195	0.047 *	0.289	0.000 **	0.244	0.003 **	0.243	0.002 **
UP	0.085	0.010 *	0.225	0.317	0.422	0.039 *	0.351	0.091	0.339	0.080
SI	0.375	0.007 **	0.238	0.110	0.323	0.005 **	0.202	0.062	0.248	0.018 *
RD	0.337	0.000 **	0.271	0.000 **	0.163	0.011 *	0.146	0.020 *	0.218	0.001 **
BA	−0.036	0.199	−0.020	0.480	−0.029	0.193	−0.005	0.831	0.015	0.533
GR	0.217	0.332	−0.112	0.560	−0.132	0.631	−0.166	0.582	−0.163	0.595

** : Significant at 0.01 levels; * : significant at 0.05 levels.

The spatial lag model introduced the spatial effect coefficient ρ to characterize the influence of PM_{2.5} levels from the surrounding areas on the local area. From 2015 to 2019, there was a positive relationship between PM_{2.5} concentration in local and surrounding regions, indicating that local PM_{2.5} levels were significantly influenced by surrounding areas. This is consistent with the “high–high” and “low–low” agglomeration characteristics of PM_{2.5} concentrations in the study area. Local PM_{2.5} pollution was not only related to local pollutant emissions but was also affected by pollution transport from other regions. Dong et al. [23] studied the pollution transmission contribution in the Beijing–Tianjin–Hebei region and the results showed 32.5% to 68.4% contribution of PM_{2.5} transmission in 2017. Local emission sources remain important contributors to the Beijing–Tianjin–Hebei region but the interactions between cities are also strong.

GDP represents the local economic development level. Except for 2016, GDP showed a significant negative correlation with the PM_{2.5} level, indicating that economic development had a certain inhibitory effect on PM_{2.5} pollution in the study area. As an economy grows, local investment in air pollution control will also increase. In addition, a relatively developed economy is conducive to effective integration and utilization of resources, affecting the local industrial structure and urban layout. Dong et al. [24] found that economic development and industrial upgrading were the main driving forces for haze pollution improvement in China’s regions, while the transportation industry and construction industry were the two major sources of PM_{2.5} pollution. This is consistent with our findings, but other studies have shown different results. Yan, Kong, Jiang, Huang, and Ye [13] observed that the impacts of economic development on PM_{2.5} pollution varied with the degree of development. Economic development can alleviate PM_{2.5} pollution in developed areas, while it can promote PM_{2.5} pollution in underdeveloped areas. As noted by the theory of the Environmental Kuznets Curve (EKC), a later stage of urbanization is ultimately conducive to alleviating the pollution caused by the early stage of urbanization, and there is a threshold of an inflection point in the middle. Wang et al. [25] explained this in detail and obtained similar results to us.

Over 2015–2019, POP and PM_{2.5} levels showed a positive correlation, passing the significance test, indicating that population growth contributed to the formation of urban PM_{2.5} pollution. The increase in the population size resulted in growing demands for employment, housing, transportation, and energy consumption; thus, promoting the emission of pollutants. Han et al. [26] analyzed the relationship between population variations and PM_{2.5} levels, and the results showed that there was a positive trend between population and PM_{2.5} in most cities in China and that the contribution rate of megacities

was $5.40 \pm 4.80 \mu\text{g}/\text{m}^3$ per million people. However, there was also a negative trend between population size and $\text{PM}_{2.5}$ in some regions [13], because megacities with dense populations help to integrate resources and improve the utilization efficiency of urban infrastructure and natural resources, thus reducing $\text{PM}_{2.5}$ pollution.

UP refers to the proportion of the urban population in the total population, which is usually used to represent the level of urbanization. The results of Table 3 indicate that UP had a positive impact on $\text{PM}_{2.5}$ pollution in 2015 and 2017, but did not pass the significance test in other years. The growth or aggregation of an urban population usually leads to an increase in automobiles, housing and energy consumption, industrial production, and construction activities, which would have an impact on the increase in $\text{PM}_{2.5}$ concentrations. Relevant studies [27] showed that the relationship between the proportion of the urban population and ecological environment pressures in the Beijing–Tianjin–Hebei region also conformed to the EKC theory, and it could effectively alleviate ecological environment pressure until it reached 80%, which was the turning point in EKC for most cities. By 2019, the proportion of the urban population in BJ and TJ exceeded 80%, while others were within the scope of 40–60%, below the threshold, indicating that we still have a long way to go in the urbanization process.

SI is the value-added of Secondary Industry and is used to represent the industrial structure. There was a significant positive correlation between SI and $\text{PM}_{2.5}$ concentrations in 2015, 2017, and 2019. According to the statistical results of the output of the secondary industry, as shown in Figure S4, it had been decreasing or first increasing and then decreasing in AY, BJ, BD, LC, JNN, LF, PY, SJZ, TJ, and TA during 2015–2019, while it increased in other cities. These cities were often accompanied by severe $\text{PM}_{2.5}$ pollution, which indicated that these cities may have already carried out the elimination of backward production capacity or the transfer of secondary industry to alleviate local $\text{PM}_{2.5}$ pollution. The national development strategy has significantly increased the proportion of tertiary industries in the Beijing–Tianjin–Hebei region through the relocation and replacement of traditional secondary industries, which is consistent with our results. The results of Hao and Liu [28] are similar to ours, and they believe that $\text{PM}_{2.5}$ concentrations in Chinese cities are also strongly influenced by secondary industry. In 2019, the average ratio of secondary industry to GDP in the study area was 41.97 percent. In addition, energy-intensive industries characterized by high emissions have a large-scale base, and the effect of industrial transformation and upgrading is not obvious in the short term. Therefore, to effectively reduce the level of urban $\text{PM}_{2.5}$, it is necessary to accelerate the transformation of economic structures and reduce the dependence on secondary industries, especially heavy industries.

RD, road length per unit area, is often used to represent the impact of traffic factors on $\text{PM}_{2.5}$. During the study period, there was a significant positive relationship between $\text{PM}_{2.5}$ concentration and RD. According to the statistical results, as shown in Figure S4, the road length of most cities in the study area kept increasing in 2015–2019, except for BJ and TJ. A dense urban road traffic network promotes the increase in vehicle ownership, and pollutants from vehicle exhaust, such as NO_x , are important sources of $\text{PM}_{2.5}$ [29,30]. In addition, the increase in roads also enhances road dust, which is also a source of $\text{PM}_{2.5}$ [31]. In this regard, traffic will continue to have an impact on continuing $\text{PM}_{2.5}$ levels. There are also related studies [24] that use other indicators to characterize the influence of traffic factors and obtain similar results. Ding et al. [32] used per capita vehicle ownership to characterize traffic impacts, which determined that this factor had a driving effect on $\text{PM}_{2.5}$ pollution and that it fluctuated during the study period.

In this study, BA and GR did not pass the significance test and were not statistically significant, so the results were not credible. BA is the ratio of the built-up area to the area of the municipal district. Due to the jurisdiction of the county, BA cannot completely represent the overall situation of cities in the research region. The GR of all cities was about 40% with slight distinctions. This may be why the results were not statistically significant. In addition, some studies used related indicators to explore the influence on $\text{PM}_{2.5}$. For example, Wang, Yao, Xu, Sun, and Li [25] found an inverted U-shaped relationship between

built-up area and PM_{2.5} levels but lacked in-depth discussions. Qin et al. [33] simulated the impact of urban greening on atmospheric particulate matter, and the results showed that reasonable tree cover could reduce PM by 30%. In addition, there are still many deficiencies in this study. First, in addition to socio-economic factors, PM_{2.5} is also affected by topography, meteorology, pollution emissions, and other factors, which are not involved in this study. Secondly, the social and economic data used in this study are from various statistical yearbooks and bulletins, which may have certain deviations and bring certain uncertainties. In future studies, more factors should be considered to ensure the accuracy of the results.

4. Conclusions

This study used PDFs to analyze the temporal variation trends and spatial distribution differences of PM_{2.5} concentrations in the Beijing–Tianjin–Hebei region and its surrounding provinces from 2015 to 2019. Then, the spatial distribution characteristics of PM_{2.5} concentrations were analyzed using Moran's I and Getis-Ord-Gi*. Finally, SLM was adopted to quantify the driving effect of socioeconomic factors on PM_{2.5} levels. The main results were as follows:

(1) From 2015 to 2019, PM_{2.5} in the study area showed an overall downward trend. The Beijing–Tianjin–Hebei region and Henan Province decreased for the period of 2015 to 2019; Shanxi and Shandong Provinces expressed a variation trend of an inverted U-shape and U-shape, respectively. In a word, air quality in the study area had been improving from 2015 to 2019.

(2) From the perspective of spatial distributions, PM_{2.5} concentrations in the study area indicated an obvious positive spatial correlation with “high–high” and “low–low” agglomeration characteristics. The high-value area of PM_{2.5} was mainly concentrated in the junction of Henan, Shandong, and Hebei Provinces, which had a characteristic of moving to the southwest. The low values were mainly distributed in the northern part of Shanxi and Hebei Provinces, and the eastern part of Shandong Province.

(3) Socio-economic factor analysis showed that POP, UP, SI, and RD had a positive effect on PM_{2.5} concentration, while GDP had a negative driving effect. In addition, PM_{2.5} was also affected by PM_{2.5} pollution levels in surrounding areas.

Although PM_{2.5} levels in the study area decreased, PM_{2.5} pollution was still a serious problem until 2019. The significance of this study is to highlight the spatio-temporal heterogeneity of PM_{2.5} concentration distributions and the driving role of socioeconomic factors on PM_{2.5} pollution in the Beijing–Tianjin–Hebei region and its surrounding areas. Identifying the differences in PM_{2.5} concentration caused by socioeconomic development is helpful to better understand the interaction between urbanization and ecological environmental problems.

Supplementary Materials: The following are available online at <https://www.mdpi.com/article/10.3390/atmos12101324/s1>, Table S1: Names and abbreviations of cities in the study region, Figure S1: the percentage of exceeding standard days in each city from 2015 to 2019, Figure S2: PM_{2.5} concentration in each city and province from 2015 to 2019, Figure S3: Decreasing rate of PM_{2.5} concentration in 2019 compared with 2015, Figure S4: Statistics of social and economic factors in each city from 2015 to 2019.

Author Contributions: Data curation, C.F.; formal analysis, K.X.; investigation, J.W.; methodology, R.L.; project administration, J.W.; software, R.L.; visualization, K.X.; writing—original draft, R.L.; writing—review and editing, C.F. All authors have read and agreed to the published version of the manuscript.

Funding: This research was funded by the Ecology and Environment Department of Jilin Province. The project numbers are 2018-19 and 2019-08.

Institutional Review Board Statement: Not applicable.

Informed Consent Statement: Not applicable.

Data Availability Statement: The datasets supporting the conclusions of this article are included within the article and its additional file.

Conflicts of Interest: The authors declare no conflict of interest.

References

1. Zhang, L.; Wilson, J.P.; MacDonald, B.; Zhang, W.; Yu, T. The changing PM_{2.5} dynamics of global megacities based on long-term remotely sensed observations. *Environ. Int.* **2020**, *142*, 105862. [CrossRef]
2. Wang, L.; Xiong, Q.; Wu, G.; Gautam, A.; Jiang, J.; Liu, S.; Zhao, W.; Guan, H. Spatio-Temporal Variation Characteristics of PM_{2.5} in the Beijing-Tianjin-Hebei Region, China, from 2013 to 2018. *Int. J. Environ. Res. Public Health* **2019**, *16*, 4276. [CrossRef] [PubMed]
3. Lou, C.R.; Liu, H.Y.; Li, Y.F.; Li, Y.L. Socioeconomic Drivers of PM_{2.5} in the Accumulation Phase of Air Pollution Episodes in the Yangtze River Delta of China. *Int. J. Environ. Res. Public Health* **2016**, *13*, 928. [CrossRef] [PubMed]
4. Pala, K.; Aykac, N.; Yasin, Y. Premature deaths attributable to long-term exposure to PM_{2.5} in Turkey. *Environ. Sci. Pollut. Res. Int.* **2021**, *37*, 51940–51947. [CrossRef] [PubMed]
5. Liu, M.; Saari, R.K.; Zhou, G.; Li, J.; Han, L.; Liu, X. Recent trends in premature mortality and health disparities attributable to ambient PM_{2.5} exposure in China: 2005–2017. *Environ. Pollut.* **2021**, *279*, 116882. [CrossRef] [PubMed]
6. Yap, C.C.; Jie, Y.; Jun, H.; Xiaogang, Y.; Richard, H.; Dongsheng, J. An investigation into the impact of variations of ambient air pollution and meteorological factors on lung cancer mortality in Yangtze River Delta. *Sci. Total. Environ.* **2021**, *779*, 146427. [CrossRef]
7. Tian, J.; Fang, C.; Qiu, J.; Wang, J. Analysis of Pollution Characteristics and Influencing Factors of Main Pollutants in the Atmosphere of Shenyang City. *Atmosphere* **2020**, *11*, 766. [CrossRef]
8. Wang, Y.; Liu, C.; Wang, Q.; Qin, Q.; Ren, H.; Cao, J. Impacts of natural and socioeconomic factors on PM_{2.5} from 2014 to 2017. *J. Environ. Manag.* **2021**, *284*, 112071. [CrossRef]
9. Meng, F.; Wang, J.; Li, T.; Fang, C. Pollution Characteristics, Transport Pathways, and Potential Source Regions of PM_{2.5} and PM₁₀ in Changchun City in 2018. *Int. J. Environ. Res. Public Health* **2020**, *17*, 6585. [CrossRef]
10. Liu, J.; Yin, H.; Tang, X.; Zhu, T.; Zhang, Q.; Liu, Z.; Tang, X.; Yi, H. Transition in air pollution, disease burden and health cost in China: A comparative study of long-term and short-term exposure. *Environ. Pollut.* **2021**, *277*, 116770. [CrossRef]
11. Chen, Z.; Chen, D.; Zhao, C.; Kwan, M.P.; Cai, J.; Zhuang, Y.; Zhao, B.; Wang, X.; Chen, B.; Yang, J.; et al. Influence of meteorological conditions on PM_{2.5} concentrations across China: A review of methodology and mechanism. *Environ. Int.* **2020**, *139*, 105558. [CrossRef] [PubMed]
12. Xu, Y.; Xue, W.; Lei, Y.; Huang, Q.; Zhao, Y.; Cheng, S.; Ren, Z.; Wang, J. Spatiotemporal variation in the impact of meteorological conditions on PM_{2.5} pollution in China from 2000 to 2017. *Atmos. Environ.* **2020**, *223*, 117215. [CrossRef]
13. Yan, D.; Kong, Y.; Jiang, P.; Huang, R.; Ye, B. How do socioeconomic factors influence urban PM_{2.5} pollution in China? Empirical analysis from the perspective of spatiotemporal disequilibrium. *Sci. Total. Environ.* **2021**, *761*, 143266. [CrossRef] [PubMed]
14. Cheng, Z.; Li, L.; Liu, J. The impact of foreign direct investment on urban PM_{2.5} pollution in China. *J. Environ. Manag.* **2020**, *265*, 110532. [CrossRef]
15. Yan, D.; Ren, X.; Kong, Y.; Ye, B.; Liao, Z. The heterogeneous effects of socioeconomic determinants on PM_{2.5} concentrations using a two-step panel quantile regression. *Appl. Energy* **2020**, *272*, 115246. [CrossRef]
16. Zhang, X.; Gu, X.; Cheng, C.; Yang, D. Spatiotemporal heterogeneity of PM_{2.5} and its relationship with urbanization in North China from 2000 to 2017. *Sci. Total. Environ.* **2020**, *744*, 140925. [CrossRef]
17. Getis, A.; Ord, J.K. The Analysis of Spatial Association by Use of Distance Statistics. *Geogr. Anal.* **1992**, *24*, 189–206. [CrossRef]
18. Ord, J.K.; Getis, A. Local Spatial Autocorrelation Statistics—Distributional Issues and an Application. *Geogr. Anal.* **1995**, *27*, 286–306. [CrossRef]
19. Bai, K.; Ma, M.; Chang, N.B.; Gao, W. Spatiotemporal trend analysis for fine particulate matter concentrations in China using high-resolution satellite-derived and ground-measured PM_{2.5} data. *J. Environ. Manag.* **2019**, *233*, 530–542. [CrossRef] [PubMed]
20. Liu, L.; Silva, E.A.; Liu, J. A decade of battle against PM_{2.5} in Beijing. *Environ. Plan. A Econ. Space* **2018**, *50*, 1549–1552. [CrossRef]
21. Xia, X.-S.; Wang, J.-H.; Song, W.-D.; Cheng, X.-F. Spatio-temporal Evolution of PM_{2.5} Concentration During 2000–2019 in China. *Environ. Sci.* **2020**, *41*, 4832–4843. [CrossRef]
22. Jiang, L.; He, S.; Zhou, H. Spatio-temporal characteristics and convergence trends of PM_{2.5} pollution: A case study of cities of air pollution transmission channel in Beijing-Tianjin-Hebei region, China. *J. Clean. Prod.* **2020**, *256*, 120631. [CrossRef]
23. Dong, Z.; Wang, S.; Xing, J.; Chang, X.; Ding, D.; Zheng, H. Regional transport in Beijing-Tianjin-Hebei region and its changes during 2014–2017: The impacts of meteorology and emission reduction. *Sci. Total. Environ.* **2020**, *737*, 139792. [CrossRef] [PubMed]
24. Dong, F.; Zhang, S.; Long, R.; Zhang, X.; Sun, Z. Determinants of haze pollution: An analysis from the perspective of spatiotemporal heterogeneity. *J. Clean. Prod.* **2019**, *222*, 768–783. [CrossRef]
25. Wang, Y.; Yao, L.; Xu, Y.; Sun, S.; Li, T. Potential heterogeneity in the relationship between urbanization and air pollution, from the perspective of urban agglomeration. *J. Clean. Prod.* **2021**, *298*. [CrossRef]
26. Han, L.; Zhou, W.; Li, W. Growing Urbanization and the Impact on Fine Particulate Matter (PM_{2.5}) Dynamics. *Sustainability* **2018**, *10*, 1696. [CrossRef]
27. Wang, S.; Ma, H.; Zhao, Y. Exploring the relationship between urbanization and the eco-environment—A case study of Beijing-Tianjin-Hebei region. *Ecol. Indic.* **2014**, *45*, 171–183. [CrossRef]
28. Hao, Y.; Liu, Y.-M. The influential factors of urban PM_{2.5} concentrations in China: A spatial econometric analysis. *J. Clean. Prod.* **2016**, *112*, 1443–1453. [CrossRef]

29. Jeong, C.-H.; Wang, J.M.; Hilker, N.; Debosz, J.; Sofowote, U.; Su, Y.; Noble, M.; Healy, R.M.; Munoz, T.; Dabek-Zlotorzynska, E.; et al. Temporal and spatial variability of traffic-related PM_{2.5} sources: Comparison of exhaust and non-exhaust emissions. *Atmos. Environ.* **2019**, *198*, 55–69. [CrossRef]
30. Pui, D.Y.H.; Chen, S.-C.; Zuo, Z. PM_{2.5} in China: Measurements, sources, visibility and health effects, and mitigation. *Particuology* **2014**, *13*, 1–26. [CrossRef]
31. Wang, S.-B.; Ji, Y.-Q.; Li, S.-L.; Zhang, W.; Zhang, L. Characteristics of Elements in PM_{2.5} and PM₁₀ in Road Dust Fall During Spring in Tianjin. *Environ. Sci.* **2018**, *39*, 39–990. [CrossRef]
32. Ding, Y.; Zhang, M.; Qian, X.; Li, C.; Chen, S.; Wang, W. Using the geographical detector technique to explore the impact of socioeconomic factors on PM_{2.5} concentrations in China. *J. Clean. Prod.* **2019**, *211*, 1480–1490. [CrossRef]
33. Qin, H.; Hong, B.; Jiang, R.; Yan, S.; Zhou, Y. The Effect of Vegetation Enhancement on Particulate Pollution Reduction: CFD Simulations in an Urban Park. *Forests* **2019**, *10*, 373. [CrossRef]

Article

Spatiotemporal Analysis of Haze in Beijing Based on the Multi-Convolution Model

Lirong Yin ¹, Lei Wang ¹ , Weizheng Huang ², Shan Liu ² , Bo Yang ² and Wenfeng Zheng ^{2,*} 

¹ Department of Geography and Anthropology, Louisiana State University, Baton Rouge, LA 70803, USA; lyin5@lsu.edu (L.Y.); leiwang@lsu.edu (L.W.)

² School of Automation, University of Electronic Science and Technology of China, Chengdu 610054, China; huangwz12@163.com (W.H.); shanliu@uestc.edu.cn (S.L.); boyang@uestc.edu.cn (B.Y.)

* Correspondence: winfirms@uestc.edu.cn or wenfeng.zheng.cn@gmail.com

Abstract: As a kind of air pollution, haze has complex temporal and spatial characteristics. From the perspective of time, haze has different causes and levels of pollution in different seasons. From the perspective of space, the concentration of haze in adjacent areas will affect each other, showing some correlation. In this paper, we construct a multi-convolution haze-level prediction model for predicting haze levels in different areas of Beijing, which uses the remote sensing satellite image of the Beijing divided into nine regions as input and the haze pollution level as output. We categorize the predictions into four seasons in chronological order and use frequency histograms to analyze haze levels in different regions in different seasons. The results show that the haze pollution in the southern regions is significantly different from that in the northern regions. In addition, the haze tends to be clustered in adjacent areas. We use Global Moran's *I* to analyze the predictions and find that haze is related to the geographical location in summer and autumn. We also use Local Moran's *I*, Moran scatter plot, and Local Indicators of Spatial Association (LISA) to study the spatial characteristics of haze in adjacent areas. The results show, for the spatial distribution of haze in Beijing, that the southern regions present a high-high agglomeration, while the northern regions exhibit a 'low-low agglomeration. The temporal evolution of haze on the seasonal scale, according to the chronological order of winter, spring, and summer to autumn, shows that the haze gradually becomes agglomerated. The main finding is that the haze pollution in southern Beijing is significantly different from that of northern regions, and haze tends to be clustered in adjacent areas.

Citation: Yin, L.; Wang, L.; Huang, W.; Liu, S.; Yang, B.; Zheng, W. Spatiotemporal Analysis of Haze in Beijing Based on the Multi-Convolution Model. *Atmosphere* **2021**, *12*, 1408. <https://doi.org/10.3390/atmos12111408>

Academic Editors: Duanyang Liu, Kai Qin and Honglei Wang

Received: 1 September 2021

Accepted: 21 October 2021

Published: 26 October 2021

Keywords: convolution neural network; Moran's *I*; LISA aggregation graph; haze; spatial autocorrelation

Publisher's Note: MDPI stays neutral with regard to jurisdictional claims in published maps and institutional affiliations.



Copyright: © 2021 by the authors. Licensee MDPI, Basel, Switzerland. This article is an open access article distributed under the terms and conditions of the Creative Commons Attribution (CC BY) license (<https://creativecommons.org/licenses/by/4.0/>).

1. Introduction

In recent years, haze has attracted the media's attention, and that of the government and population of various countries. It has triggered a wide-ranging discussion on how to coordinate economic development and environmental protection. However, this started a public panic about air pollution and how this affected the physical health of people. Moreover, haze predicts human damage from air pollution [1,2]. For these reasons, haze has aroused the concern of researchers. Therefore, a large amount of experimental data and theoretical reasoning are focused on the cause of haze [3–8], the scope of pollution [9–16], the hazards [2,11,17–22], spatial and temporal distribution, and prevention measures.

With the establishment of many ground detection stations, the detection data of PM_{2.5} and PM₁₀, which are the primary pollutants of haze, gradually increase, which facilitates the study of its spatial and temporal characteristics [8,14,15,20,22–25]. Researchers have performed analyses of the spatial and temporal evolution of haze in different areas based on satellite images [4,14,26–28]. Gehrig et al. [29] studied the long-term observations of PM_{2.5} and PM₁₀ in seven regions of Switzerland and obtained the range of PM_{2.5} concentrations in different regions. Although there were different haze concentrations in different regions,

the correlation between daily PM_{2.5} and PM₁₀ concentrations was very high in all regions. In terms of time characteristics, the haze pollution in the Swiss region in winter is the most severe of the four seasons, and the haze pollution in the spring is the lightest. Zhang et al. [30] analyzed the PM_{2.5} concentration data of 190 cities in China. They found that the significant seasonal variation of PM_{2.5} occurred in winter and the lowest in summer on the time scale. In terms of the geographical distribution, the PM_{2.5} concentrations in the northern region are generally higher than in the south. Zhao et al. [27] collected PM_{2.5} and PM₁₀ concentrations from 30 ground detection stations in Beijing and analyzed haze concentrations' temporal and spatial distribution in winter and spring. The results showed that the concentration of haze in the northern mountains area is lower than that in the south of Beijing, and the haze pollution in urban and rural areas is quite different. The time characteristics of haze showed that there is serious pollution in winter and slight pollution in spring, the highest concentration of PM_{2.5} and PM₁₀ appears in January, and the lowest concentration appears in April. Zhao et al. [31] compared the time characteristics of urban and rural areas in Beijing.

The concentration prediction of PM_{2.5} and PM₁₀ as the primary pollutants of haze is also one of the most concerning areas, and researchers have proposed many different prediction models. In the early days of haze prediction, Fuller et al. [32] used empirical models to predict the daily average concentrations of PM_{2.5} and PM₁₀ in some regions of the U.K., but the scalability was poor due to the model being based on observations in local areas. Dong et al. [33] proposed a hidden Markov-based prediction model to predict PM_{2.5} concentration. After training, the hidden Markov model can finally predict the PM_{2.5} concentration value in the next 24 h. Lee et al. [34] combined the MODIS aerosol optical depth (AOD) over England with ground monitoring data to predict haze concentrations in specific areas. As neural networks began to show solid complex-fitting capabilities, researchers began to apply different neural networks to predict haze. Ordieres et al. [35] compared the performance of three neural network structures—multilayer perceptron, radial basis function neural network, and squared multilayer perceptron—with classic predictive models in daily average PM_{2.5} concentration predictions. The neural networks are significantly better than the classic approaches. Marzano et al. [36] established a recurrent neural network to predict climate phenomena with input from remote sensing satellite imagery.

Unlike previous prediction models, which mainly predict PM_{2.5}/PM₁₀ concentration in a single area [37], this paper proposed a multi-convolution haze-level prediction model to simultaneously predict PM_{2.5} concentration levels in multiple adjacent areas. This paper used remote sensing satellite images from Beijing as the model's input. The images are cut into nine blocks of the same size and applied in various data processing methods, including radiation correction, geometric correction, area extraction and synthesis, RGB image synthesis, and image cutting. This paper then uses the daily PM_{2.5} level of nine blocks as output.

In addition to predicting the haze levels in different blocks in Beijing, we also analyzed haze's temporal and spatial characteristics in different areas. Previous researchers have focused on the temporal and spatial characteristics of haze in one area while ignoring the haze correlation between areas bordering each other. Therefore, this paper divided the predicted results into four seasons in chronological order and used frequency histograms to analyze the haze levels in different regions. Furthermore, this paper used the Global Moran's *I* to obtain the correlation between haze in different seasons and geographic locations. It used the Local Moran's *I*, Moran scatter plot, and Local Indicators of Spatial Association (LISA) to study the spatial characteristics of haze in adjacent regions.

2. Data Processing and Calibration

2.1. Remote Sensing Image Processing

In the haze spatial evolution, the haze in the immediate vicinity will be highly correlated to the appropriate length of time. In order to analyze the temporal and spatial

evolution characteristics of haze, the input of the model needs to involve different regions. Therefore, we chose Beijing as the research object according to the administrative division. Beijing is the capital of China and has severe haze pollution [28]. There are 36 air pollutant monitoring stations relatively evenly distributed in different parts of Beijing, which provide us with historical haze concentration data for different regions [1]. Based on the available data from the ground stations, the time span is chosen as 2013 to 2015.

In this paper, we collect two types of dataset:

- (1) Real-time PM_{2.5} concentration was released by ground monitoring stations in Beijing in 2013 and 2014. The data in 2014 are converted into haze levels according to the correspondence table of haze concentration and haze level, which formed a training set of multi-convolution combined haze-level prediction models. The data in 2015 is also converted to haze levels to test model accuracy.
- (2) MOD02_1km data for the Beijing area in 2013 and 2014. The MOD02_1km data is a remote sensing satellite image containing latitude and longitude information in the Beijing area and is the model input.

We preprocess the remote sensing satellite images in Beijing to improve the model's classification prediction accuracy and data consistency. We use ENVI 5.0 software (L3Harris Geospatial, Boulder, CO, USA) to process satellite images: radiation correction, geometric correction, area extraction and synthesis, RGB image synthesis, and image cutting.

- (1) Radiation correction. We use ENVI 5.0 to automate the radiation correction of MOD02_1km data.
- (2) Geometric correction. We use the MODIS data processing tool, Georeference MODIS in the ENVI software, to geometrically correct the data of the emissivity channel. In the calibration, we select the Beijing coordinate system in World Geodetic System 1984 (WGS-84) standard to geometrically correct the emissivity file and establish Ground Control Points (GCPs) as the standard for other channels to maintain consistent geometric correction results. Then we use GCPs generated by the emissivity to correct the reflectance file. After reading the GCPs, the Triangulation correction method and the Bilinear resampling method are selected so that the correction result of the reflectance can match the emissivity.
- (3) Area extraction and synthesis. According to the administrative area of Beijing: 39.4° N–41.1° N; 115.4° E–117.4° E, we cut the administrative regional geographic files in ENVI software to obtain satellite images of the Beijing area. Next, we use the same method to cut the emissivity file and reflectivity file of the satellite image, then place the file of the emissivity channel on the top, and the reflectivity channel file on the bottom. Finally, we synthesize the image to obtain the full channel satellite image with the same administrative scope and uniform size.
- (4) RGB image synthesis. The processed satellite image contains multiple channels, where channels 1–7 monitor the edge of the land and cloud. The wavelength and spatial resolution of each channel are shown in Table 1. We want to convert satellite images into three-channel RGB images by combining multiple suitable channels. The wavelength range of red light is between 622 and 780; green light is between 492 and 577; blue light is between 455 and 470. Comparing the visible light and satellite channel information, we synthesize the satellite's channel 1, channel 4, and channel 3, and the synthesized results are shown in Figure 1a,b.
- (5) Image cutting: We cut the satellite image into nine equally sized blocks, as shown in Figure 1c. Every block of the image contains an actual region of Beijing. Thus, different blocks are adjacent from spatial relationships, which helps us study the haze's spatial evolution.

After the synthesized RGB satellite image Figure 1b is cut, Figure 1c contains nine blocks of the same size, and we sort them from left to right and from top to bottom in Block 1 to Block 9. The administrative divisions contained in different blocks are shown in Table 2.

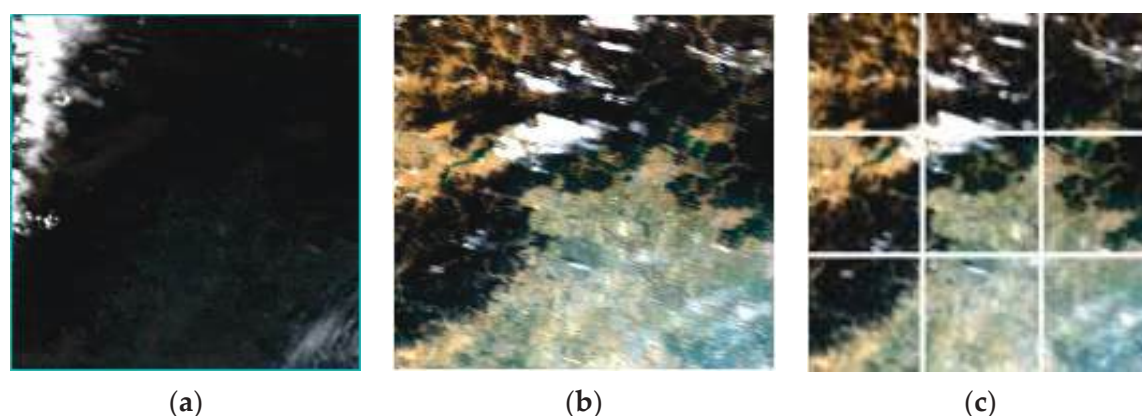


Figure 1. (a) is the satellite image with full channel information, and (b) is the synthesized RGB image. (c) is cut into nine equally sized blocks based on (b).

Table 1. Spatial resolution and wavelength interval of each channel in MOD021KM.

Channel	Wavelength Interval (nm)	Spatial Resolution (m)
1	620–670	250
2	841–876	250
3	459–479	500
4	545–565	500
5	1230–1250	500
6	1628–1652	500
7	2105–2155	500

Table 2. Correspondence between block and administrative divisions.

Block	Administrative Divisions
1	Yanqing
2	Huairou
3	Miyun
4	Changping + Haidian (Metropolitan Area)
5	Shunyi + Chaoyang (Metropolitan Area)
6	Pinggu
7	Mentougou + Fangshan
8	Metropolitan Area + Daxing
9	Tongzhou

2.2. Haze Level Transformation

The haze-level prediction model outputs haze levels in different regions. Therefore, we divide the collected PM_{2.5} concentration in Beijing into 10 levels. Level 1: 0–35 $\mu\text{g}/\text{m}^3$, air quality is good, basically no pollution; level 2: 36–70 $\mu\text{g}/\text{m}^3$, acceptable; level 3: 71–105 $\mu\text{g}/\text{m}^3$, mild pollution; level 4: 106–140 $\mu\text{g}/\text{m}^3$, moderate pollution; level 5–7: 141–245 $\mu\text{g}/\text{m}^3$, severe pollution; level 8–10: 245–500 $\mu\text{g}/\text{m}^3$, severe pollution. We use the one-hot vector to label the training set, as in (1).

$$y_i = [p, c_1, c_2, \dots, c_n] \quad (1)$$

The p -bit of the first element in the vector indicates whether there is a cloud layer effect and whether haze characteristics can be extracted. If $p = 1$, it means that haze characteristics are undetectable. In this case, the parameter optimization is to ignore the subsequent elements so that the adjustment of the parameters will not be affected in training; if $p = 0$, it means that the haze characteristics can be detected. When n represents the number of haze level, the subsequent c_n represent the corresponding haze level. If the number of c_4 is 1, it

indicates the corresponding haze level of the input data is 4. i indicates the serial number of the region where the PM_{2.5} concentration is located, and i ranges from 1 to 9. Hence, the ground truth corresponding to each satellite image is as shown in (2).

$$y = [p^1 \ c_1^1 \ \dots \ c_{10}^1 \ \dots \ p^9 \ c_1^9 \ \dots \ c_{10}^9] \quad (2)$$

3. Method

3.1. Joint Structure of Multi-Convolution Neural Networks

In order to identify haze grades for finer spatial scales and study the temporal and spatial evolution of haze in different regions of Beijing, we use a multi-convolution network structure to segment the haze data and then classify it. The multi-convolution neural network structure includes an input layer, block layer, convolution layer, pooling layer, local full connection layer, and classification layer [37], as shown in Figure 2. In this network, we use unified input and unified output.

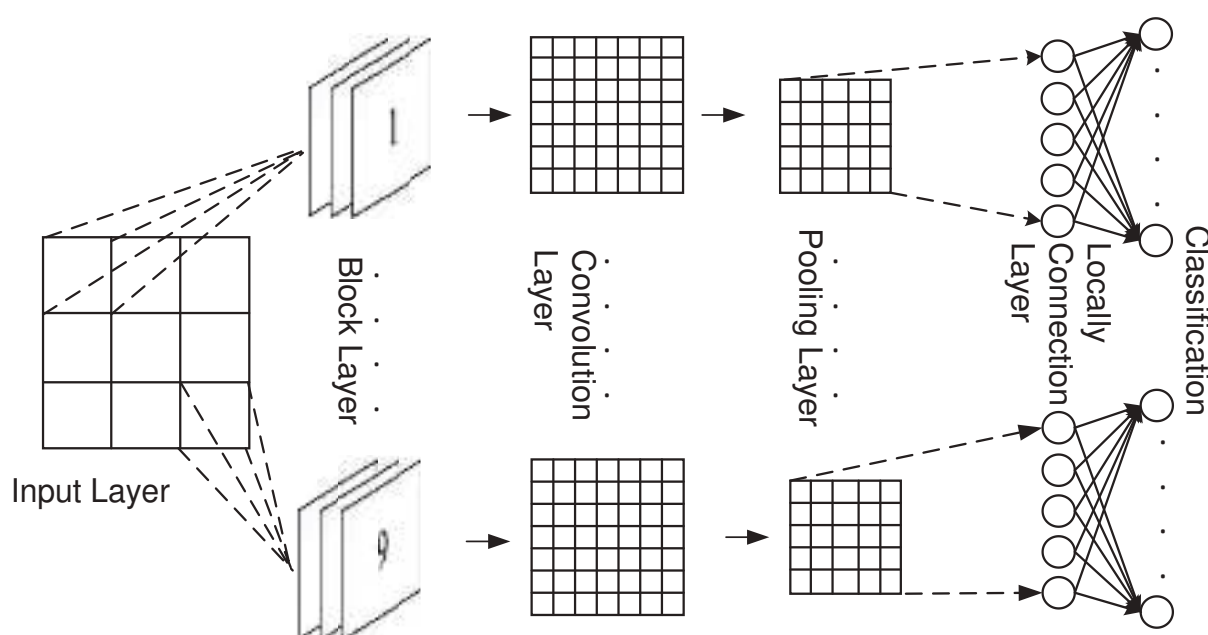


Figure 2. The structure of the multi-convolution neural network.

The input layer accepts the processed satellite images in the Section 2 as inputs to obtain more spatio-temporal data.

The block layer is a sliding window, whose size is $60 \times 60 \times 3$. The sliding step is 60, so the original $180 \times 180 \times 3$ images can be divided into 9 blocks from the upper to the lower, from left to right, and then input into the different convolution neural networks.

Nine convolution layers acquire image features of nine different regions. Because different regions have different background information, such as geographical environment, the separated convolution layer can distinguish the fine-grained differences of different regions and provide the haze levels of different regions.

The pooling layer can help reduce the size of the model and increase the speed of the operation. First, we set padding with 0 and choose the maximum pooling function. Max pooling uses the maximum value of the region to replace all the elements in the region.

The locally full connection layer prevents cross-contamination of the different layer outputs at the fully connected layer, preserving the characteristics of each region. Each locally full connection corresponds to a soft-max classification layer. The classification layer consists of 99 nodes corresponding to nine regions. The marking and representation of data is the same as in Equation (2).

3.2. Spatial Autocorrelation Analysis of Haze Concentration

Global spatial autocorrelation analysis can reflect the relationship between haze concentration and spatial distribution. Suppose a piece of data is related to geographic location. In that case, the distribution of the data in geographic space is also correlated, and the degree of correlation is inversely proportional to the region's distance. Its distribution methods are clustering, random distribution, and regular distribution. Through the spatial autocorrelation analysis of haze, this phenomenon can be better understood. Its essence is to analyze haze distribution in different geographic spaces and the correlation between different regions. In this section, the specific forms of using the matrix notation method to mark the data of the nine blocks are from top to bottom, and from left to right are Block 1 to Block 9.

3.2.1. Global Moran's I

We use the Global Moran's I to study the overall spatial characteristics of haze, indicating whether the haze is related to space, as in (3).

$$I = \frac{n \sum_{i=1}^n \sum_{j=1}^n w_{ij} (p_i - \bar{p})(p_j - \bar{p})}{\sum_{i=1}^n \sum_{j=1}^n w_{ij} \cdot \sum_{i=1}^n (p_i - \bar{p})^2} \quad (3)$$

This paper cuts the satellite image into nine sub-regions of the same size, so $n = 9$ in the Equation. p_i, p_j denote the average levels for Block i and Block j in one of the seasons. \bar{p} denotes the average haze level for all blocks in a given season. w_{ij} represents the weight between Block i and Block j . Since the image is equally divided, the areas on the diagonal are not considered to be adjacent. Then its spatial adjacency graph is as shown in Figure 3 below:

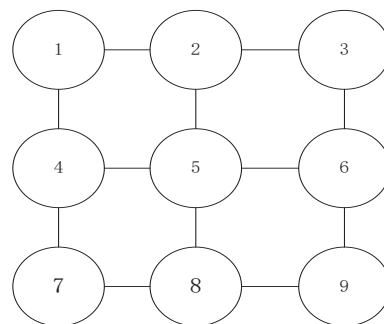


Figure 3. Spatial adjacency diagram.

From the adjacency relationship in the above figure, we can obtain its spatial adjacency matrix, the weight matrix in this section. We set each side to be 1, and the weight between two blocks is 1, as in Equation (4), and the weight matrix is as shown in Equation (5).

$$w_{ij} = \begin{cases} 1 & \text{if Block } i \text{ is adjacent to Block } j \\ 0 & \text{other} \end{cases} \quad (4)$$

$$W = \begin{bmatrix} 0 & 1 & 0 & 1 & 0 & 0 & 0 & 0 & 0 \\ 1 & 0 & 1 & 0 & 1 & 0 & 0 & 0 & 0 \\ 0 & 1 & 0 & 0 & 0 & 1 & 0 & 0 & 0 \\ 1 & 0 & 0 & 0 & 1 & 0 & 1 & 0 & 0 \\ 0 & 1 & 0 & 1 & 0 & 1 & 0 & 1 & 0 \\ 0 & 0 & 1 & 0 & 1 & 0 & 0 & 0 & 1 \\ 0 & 0 & 0 & 1 & 0 & 0 & 0 & 1 & 0 \\ 0 & 0 & 0 & 0 & 1 & 0 & 1 & 0 & 1 \\ 0 & 0 & 0 & 0 & 0 & 1 & 0 & 1 & 0 \end{bmatrix} \quad (5)$$

In this section, the essential reason for using the Moran's I is to analyze and indirectly reflect the correlation between the two spatially adjacent areas of the haze concentration level. In order to facilitate the analysis and use of the Moran's I , we use (6)–(8) to simplify (3).

$$S_0 = \sum_{i=1}^n \sum_{j=1}^n w_{ij} \quad (6)$$

$$z_i = (p_i - \bar{p}) \quad (7)$$

$$z^T = [z_1, z_2, \dots, z_n] \quad (8)$$

The simplified global Moran's I is given by (9).

$$I = \frac{n}{S_0} \frac{\sum_{i=1}^n \sum_{j=1}^n w_{ij} z_i z_j}{\sum_{i=1}^n z_i^2} = \frac{n}{S_0} \frac{z^T W z}{z^T z} \quad (9)$$

The range of the global Moran's I is between $[-1, 1]$. If $I > 0$, the haze has a positive correlation with the space and, the closer the value is to 1, the stronger the correlation, and there is a strong positive correlation between haze and space. Conversely, if $I < 0$, the haze is negatively correlated with space, and the closer the value is to -1 , the stronger the negative correlation.

The analysis methods of spatial autocorrelation generally consist of the following three types: 1. Local Indicators of Spatial Association (LISA); 2. G statistics; 3. Moran scatter plot; the first is the method of local spatial analysis, which will be used in the following experiment. In the global analysis, the Moran scatter diagram is adopted as the analysis method, and its four quadrants respectively represent the spatial relationship between the four blocks and their neighboring blocks, and the corresponding relationships are as follows:

As shown in Figure 4, the Moran scatter plot consists of four quadrants representing four different spatial association types. The relationship of the first quadrant is high–high, indicating that the haze concentration level of the area and the surrounding area are both high, and the spatial difference is slight. The spatial relationship is a positive correlation. The relationship of the second quadrant is low–high, indicating that the haze level of the area and the surrounding area differs significantly. The level of the area is low, and the haze level around it is high. The spatial relationship is now negatively correlated. The relationship of the third quadrant is low–low, indicating the haze concentration in this area is low, and the spatial relationship is positive. The relationship between the fourth quadrant is high–low, indicating that the haze level in the area is high. However, the haze concentration level in the surrounding area is low. The spatial relationship is negatively correlated. Quadrant 1 and quadrant 3 reveal positive local spatial autocorrelation, and quadrant 2 and quadrant 4 reveal negative local spatial autocorrelation.

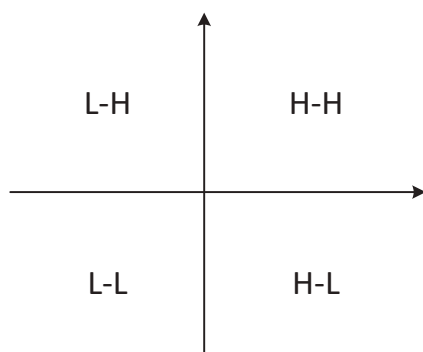


Figure 4. Moran scatter image limit relationship.

3.2.2. Local Moran's I

Like the global Moran's I , the local Moran's I focuses on a specific block to describe the similarity between Block i and its adjacent areas, as shown in (10).

$$I_i = \frac{n(p_i - \bar{p}) \sum_{j=1}^n w_{i,j}(p_j - \bar{p})}{\sum_{i=1}^n (p_i - \bar{p})^2} = \frac{nz_i \sum_{j=1}^n w_{i,j}z_j}{z^T z} \quad (10)$$

The standardized statistics for local Moran's I monitoring are specified in the following form:

$$Z(I_i) = \frac{I_i - E(I_i)}{\sqrt{\text{Var}(I_i)}} \quad (11)$$

This formula can be used to study the spatial heterogeneity of each region, and can also study and analyze the relative spatial relationship and its changes, where $E(I_i)$ represents the mathematical expectation of the Local Moran's I of the i -th Block under the condition of no spatial autocorrelation, and its formula is expressed as:

$$E(I) = -\frac{1}{n-1} \quad (12)$$

$\sqrt{\text{Var}(I_i)}$ represents the standard deviation of the Local Moran's I in the region. Since the LISA method is relatively intuitive, in the local analysis the Local Moran's I of LISA is used for spatial analysis.

By comparing the sign of $Z(I_i)$ and the value of the local correlation coefficient I_i , the spatial units whose local correlation index reaches a certain threshold can be divided into four types of spatial autocorrelation relationships, as shown in the following Table 3.

Table 3. Corresponding values of time–space relationship.

I_i	$Z(I_i) < 0$	$Z(I_i) > 0$
Positive	low-high	high-high
negative	low-low	high-low

Among these, the local Moran's I , whose significance level reaches a certain threshold, indicates a positive correlation in the spatial relationship. If it is significantly negative, it indicates a negative correlation between the two research areas in the space–time relationship. Combined with the standardized measurement Z , the time–space relationship can be analyzed. The high–high type indicates that the haze density level of area i and its neighboring blocks are relatively high. This area is a point where haze occurs frequently. The low–low type indicates that the haze concentration levels of the research block i and the surrounding adjacent blocks are relatively low. It indicates an area with lighter haze pollution. The other two types, low–high and high–low respectively, indicate that the high-pollution area surrounds the polluted area, and the high-pollution area is surrounded by the low-pollution area, showing a negative correlation. Compared with the spatial analysis obtained by general actual monitoring sites, the research in this section has the advantage that the research areas are distributed in equal blocks in time and space, and the distances are equal. Therefore, the accuracy of the weight matrix is higher.

4. Results

4.1. Analysis of Output Multi-Convolutional Neural Network

We divide the haze prediction results of Beijing in 2014 into nine regions. Further, to visually observe the spatial distribution of haze and the temporal evolution characteristics at the seasonal scale, we divide the results into four seasons and plot the frequency histograms of the haze level. We analyze the overall frequency of haze, some areas with obvious haze characteristics in different seasons and the similarity between different re-

gions. The frequency histograms of haze levels in winter, spring, summer, and autumn are respectively shown in Figure 5a–d.

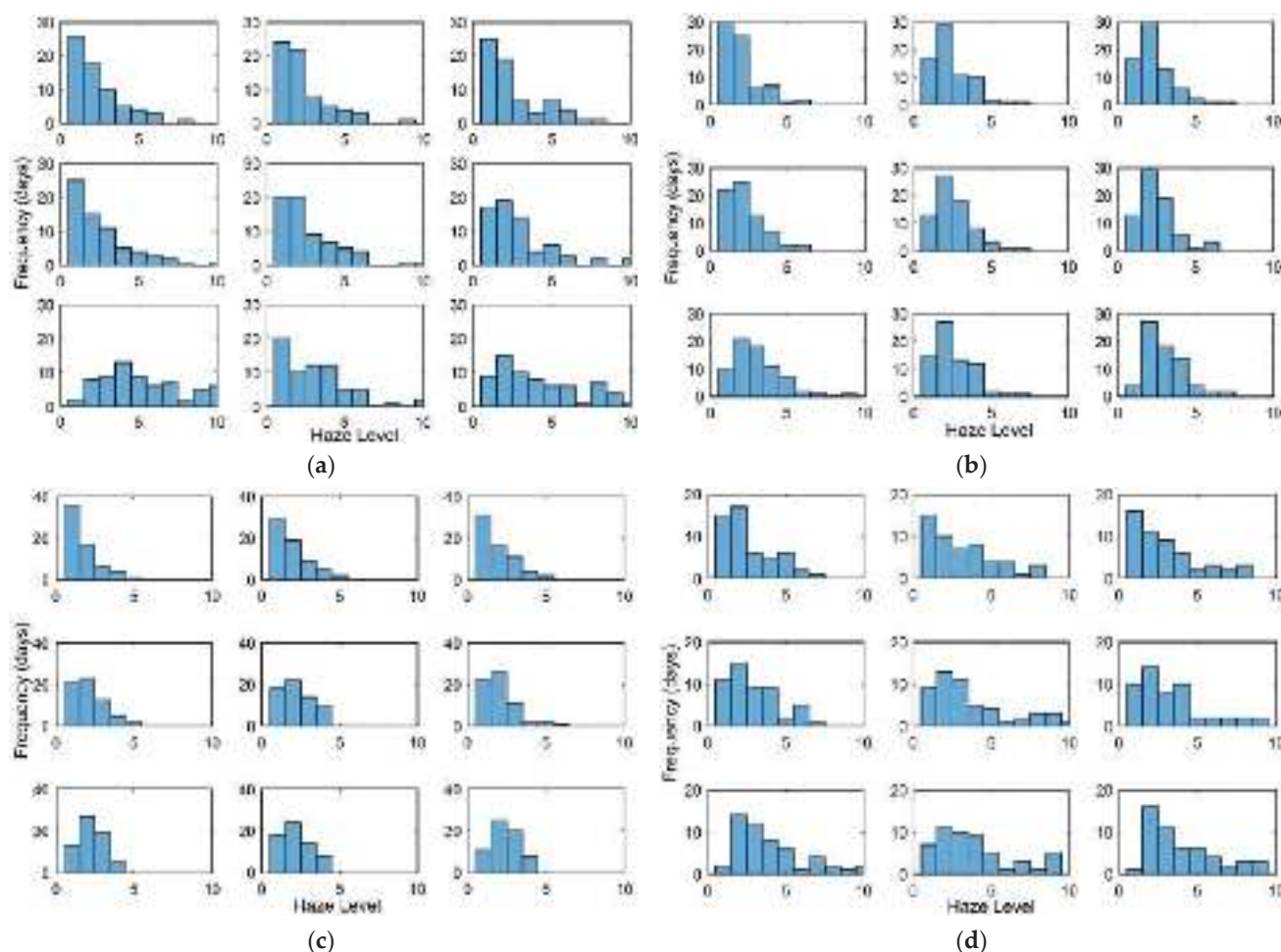


Figure 5. The frequency histograms of haze levels in (a) winter. (b) spring. (c) summer. (d) autumn.

Then the results are analyzed in three aspects:

- (1) Frequency of overall haze; (2) Analysis of the highest and lowest grade areas;
- (3) Similarity between blocks.

Figure 5a shows that:

1. The concentration of haze in winter is generally high, especially in Block 7, Block 8, and Block 9. Block 7 is average in different levels and has the most severe haze pollution.
2. There is a high similarity among Block 3, Block 4 and Block 5, and they have the lowest average of haze levels.
3. There is a haze with super-high concentration levels in the middle and southern regions, and these areas have more daily pollution such as that from vehicle emission and urban construction due to high population density.

The frequency histograms of haze levels in spring show:

1. Overall haze levels in spring are low. Block 1 has the lowest haze level, mainly concentrated between level 1 and level 2. The concentration in the blocks adjacent to Block 1 is low, and the trend of increasing concentration follows the increasing speed of distance.
2. The most extensive average haze level among the nine blocks occurs in Block 7, whose haze levels are concentrated at levels 3 and 4. Block 7 also has severe haze and has low similarity to the surrounding area.

- Block 1 and Block 4 have high similarities. Likewise, block 2 is similar to Block 3, and there is a high similarity between Block 5 and Block 8 and Block 9.

Figure 5c shows:

- Summer is the season with the weakest pollution in a year. In haze distribution, the pollution in the central region is more severe than in the upper region and weaker than in the lower region. The lower region has the most polluted air and the pollution decreases towards the upper region.
- All the haze levels in summer are under level 5. The Block with the lowest average concentration is still Block 1. Block 7 and Block 9 have the highest average concentration.
- Blocks 4, 7, 8, and 9 exhibit a high correlation, and Blocks 1, 2, and 3 show a high similarity.

Analyzing the frequency histograms in autumn, we can draw the following conclusions:

- The concentration of haze in autumn is generally high with decreasing low levels and increasing severe haze pollution.
- Blocks 1, 2, and 4 have mainly low levels, while other blocks have higher haze levels, such as level 8 or level 9.
- Block 1 and Block 4 have high similarity, Block 2 and Block 3 have high similarity, Block 5 is similar to Block 6, and the three blocks in the south have high similarity.

From the degree of haze pollution at a seasonal scale, Beijing's pollution intensity is in the order: autumn > winter > spring > summer.

If the generation of data is related to the geographical location, the spatial distribution of the data is also location-dependent, and the correlation is positive to the distance. There are three distribution forms: clustering, random distribution, and rule distribution. Haze is a kind of data related to location. We conducted a spatial autocorrelation analysis of the prediction results to analyze the distribution of haze in different geographies and the correlation between different regions. We used Global Moran's I and Local Moran's I to analyze the global and local spatial characteristics of haze, respectively.

4.2. Results of Spatial Autocorrelation Experiment

In this experiment, Moran scatter plot and the LISA plot were used to analyze and study the spatial relationship of haze in different seasons. Then, the total spatial autocorrelation during the period was analyzed. The global Moran's I result are shown in Table 4:

Table 4. Global Moran Index Table.

Season	Winter	Spring	Summer	Autumn
global Moran's I	0.071	0.052	0.375	0.349

The Moran's I of the haze of Beijing in winter, spring, summer, and autumn is 0.071, 0.052, 0.375, and 0.349. It shows that the haze concentration in the four seasons is positively correlated with the geographical area. This relationship is the strongest in summer and autumn, indicating that the spatial correlation in these two seasons is more prominent. Moran's I in winter and spring is very close to zero, indicating that the haze randomly occurs in nine blocks in these two seasons, while in summer and autumn, the haze has the characteristics of regional accumulation.

4.2.1. Moran Scatter Plot Results and Analysis

The point in the Moran scatter plot represents an area, and the slope of a linearly fitted curve is equal to the global Moran's I . According to the global Moran's I results, there is a high correlation between haze and spatial position in summer and autumn, and the correlation in spring and winter is low. Moran scatter plots for summer, autumn, winter, and spring are shown in Figure 6a–d.

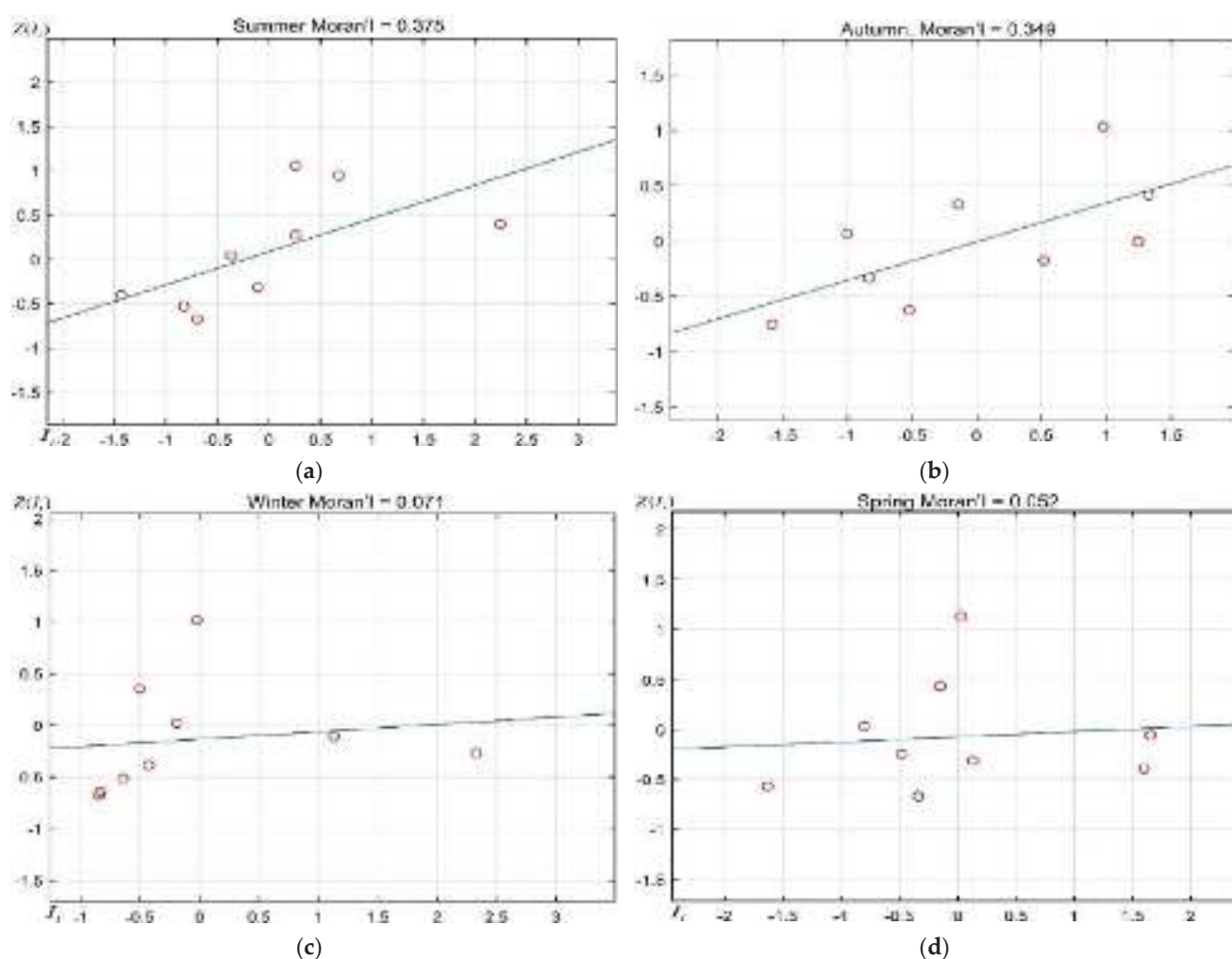


Figure 6. The Moran scatter plot in and respectively. (a) summer, (b) autumn, (c) winter, and (d) spring.

Figure 6a shows that four blocks are in the first quadrant, one block is in the second quadrant, and four blocks are in the third quadrant, and there are generally positive correlation characteristics. Blocks 5, 7, 8, and 9 are in the first quadrant, exhibiting the characteristics of high–high, which means that the haze levels in these four blocks are high, and there is a high positive correlation. Block 4 is in the second quadrant and has a characteristic of low–high. Blocks 1, 2, 3, and 6 are located in the third quadrant, exhibiting a low–low characteristic, and the haze levels of the four blocks are low. In general, the overall characteristics of haze in summer are aggregation type, including high concentration aggregation and low concentration aggregation.

Figure 6b shows two blocks in the first quadrant, two blocks in the second quadrant, three blocks in the third quadrant, and two blocks in the fourth quadrant, which generally show a positive correlation. Blocks 8 and 9 located in the first quadrant exhibit high–high characteristics. Block 4 and Block 6 are in the second quadrant, exhibiting the characteristics of low–high. Blocks 1, 2, and 3 are in the third quadrant, exhibiting low–low characteristics. Finally, Blocks 5 and 7 are in the fourth quadrant exhibiting a ‘high–low’ characteristic. In general, the haze aggregation in autumn is worse than in summer, but there are fewer isolated points, and the overall appearance is aggregated.

The global Moran’s I is small in spring and winter, and the correlation between haze and geographic location is generally weak. There is no block with ‘high–high’ characteristics in the spring, and the other three characteristics are evenly distributed. The coefficient of positive correlation of the overall haze is also low, and the distribution is discrete. There is no high–high characteristic in winter, but there are more low–low

blocks, and the correlation is better than in spring. The remaining low-concentration areas surround two high-concentration areas, and the overall distribution shows low concentration aggregation.

4.2.2. Results and Analysis of LISA Cluster Map

We also use the LISA to visualize the haze aggregation characteristics of the nine blocks. The autoregressive analysis of the local space of nine blocks, combined with the block information table in Table 1, explains the specific spatial location and the saliency of agglomeration. The saliency is the Z value used in the theoretical introduction. In the experiment of this section, the Geoda tool is used for LISA analysis. We use red for H-H, blue for L-L, pink for H-L, and purple for L-H. The LISA maps of winter, spring, summer, and autumn are shown in Figure 7a–d.

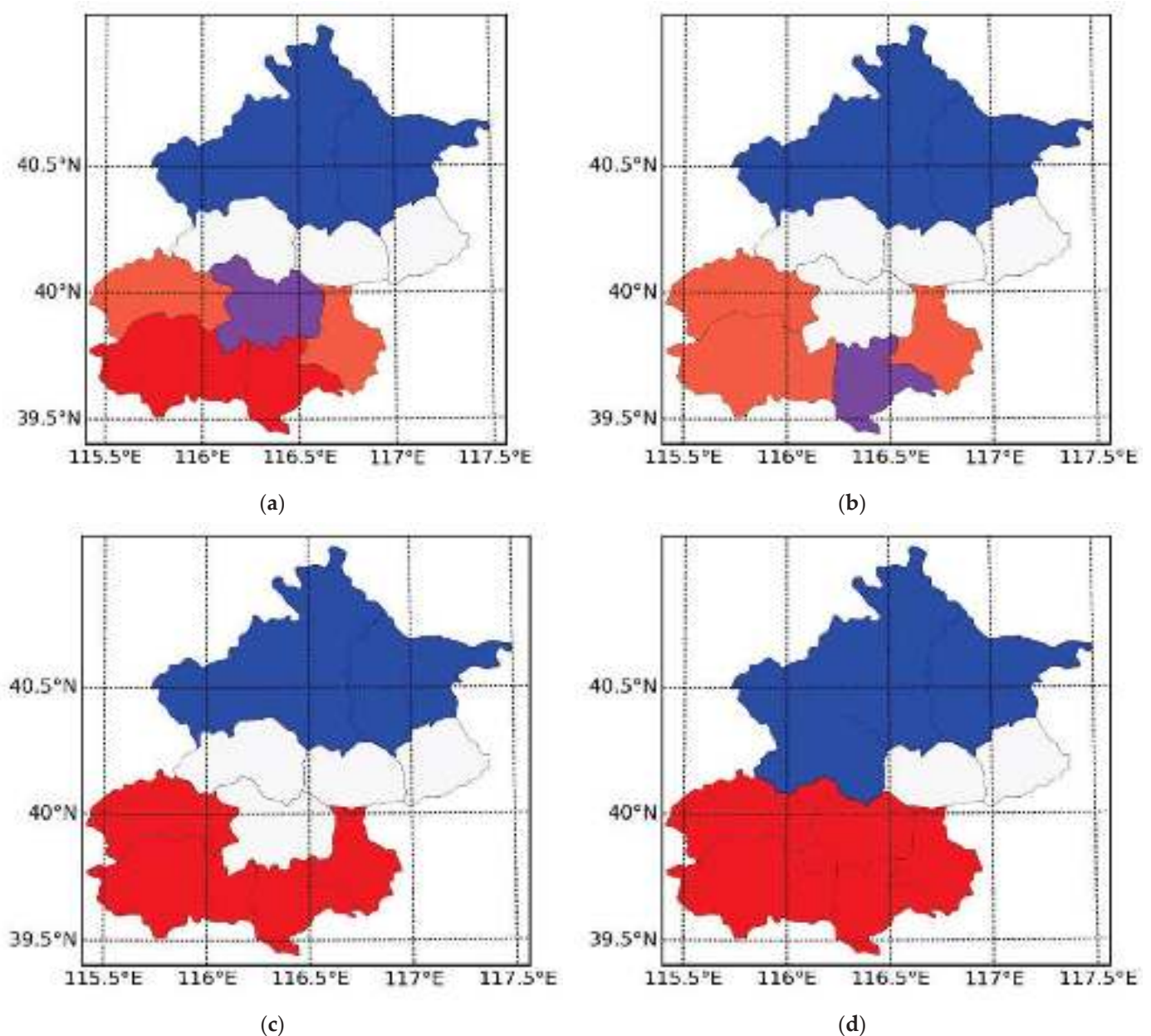


Figure 7. LISA map of the nine regions in (a) winter. (b) spring. (c) summer. (d) autumn.

From the LISA map of Figure 7a, the low agglomeration area is in northern Beijing in winter, and the high agglomeration area is in the south of Beijing. The low agglomeration area is larger than the high agglomeration area. Thus, the central area of Beijing is the L-H type, where the haze concentration in the winter is far lower than the haze concentration of the surrounding area.

Compared with the winter, the concentration in Block 8 becomes the 'L-H' type, and the 'Fangshan' in Block 7 becomes the 'H-L' type. As a result, the haze pollution in the middle part of the high-concentration area in spring is degraded, so that the 'H-H' agglomeration area disappears in the spring, and the 'L-L' low-concentration area is the same as the winter consisting of the four areas of the northern area.

As shown in Figure 7c, the agglomeration characteristics in summer are apparent, and the northern blocks are still low-concentration areas. However, the haze concentration in southern Beijing begins to rise, forming an H-H agglomeration area.

Figure 7d shows that the central area of Beijing has become a high-aggregation pattern, which further expands into the south. In contrast, the haze concentration in the north has been in the 'L-L' agglomeration type.

The LISA maps for the above four seasons all pass the 5% significance level test, and spatial correlation types of regions in different seasons are shown in Table 5.

Table 5. Spatial correlation types of regions in different seasons.

Seasons	H-H	H-L	L-L	L-H
Winter	Fangshan, Daxing	Mentougou, Tongzhou	Yanqing, Huairou, Miyun, Changping	Metropolitan Area
Spring	-	Mentougou, Fangshan, Tongzhou	Yanqing, Huairou, Miyun, Changping	Daxing
Summer	Mentougou, Fangshan, Daxing, Tongzhou	-	Yanqing, Huairou, Miyun	-
Autumn	Mentougou, Fangshan, Daxing, Tongzhou, Metropolitan Area	-	Yanqing, Huairou, Miyun, Changping	-

The results in Table 5 are arranged in chronological order from top to bottom. Thus, we can analyze the temporal evolution of haze at the seasonal scale.

- (1) The Yanqing, Huairou, and Miyun in the north of Beijing are stable low-concentration areas. As a result, the overall pollution level is low, and the seasonal impact is small. Changping is also relatively stable and only becomes a non-aggregation zone in summer.
- (2) Fangshan in winter is the 'H-H' agglomeration area, which became the 'H-L' agglomeration area in the spring, indicating the concentration of haze in the vicinity of Fangshan has decreased in the spring.
- (3) Mentougou and Tongzhou have high haze concentrations in summer and autumn, affecting the haze level of the surrounding areas, forming a high concentration area in southern Beijing and the Fangshan and Daxing.
- (4) The areas belonging to 'H-L' and 'L-H' are easily affected by the haze around them and become high or low accumulation areas in summer and autumn, improving spatial autocorrelation.

5. Discussion

In this paper, we propose a multi-convolution haze-prediction model to predict the daily haze pollution level in different areas of Beijing. We divide the predictions into nine regions and four seasons to study the fine-grained haze pollution and time characteristics. We use the haze level frequency histograms to present the results. From the degree of haze pollution at the seasonal scale, the intensity of haze pollution in Beijing is in the order:

autumn > winter > spring > summer. From the distribution of the pollution, the overall pollution in northern Beijing is weak, and the seasonal changes are also small. On the other hand, the haze pollution in the southern regions is intense and shows an aggregation trend.

Moreover, we use the global Moran's I to measure the correlation between haze and geographical location. The results show that, in general, haze in summer and autumn has regional aggregation characteristics, while in winter and spring the haze distribution is relatively random.

Since the global Moran's I can only reflect the overall correlation between the haze and the geographical location, we use the local Moran's I , the Moran scatter plot and the Local Indicators of Spatial Association (LISA) to study the spatial characteristics of haze in the vicinity. The results show that there are obvious agglomeration areas in summer and autumn, while the aggregation effects in spring and winter were relatively weak. Thus, the spatial distribution of haze in Beijing is as follows: the southern region presents a high-high agglomeration, while the northern region exhibits a low-low agglomeration. The temporal evolution of haze on the seasonal scale is according to the chronological order of winter, spring, and summer to autumn, the haze gradually becoming agglomerated.

6. Conclusions

Inspired by the idea of YOLO and other object detection convolutional neural networks, this paper cuts the remote sensing image, analyzes the haze concentration in different areas qualitatively and quantitatively, and derives the spatial laws of different seasons to predict and analyze the haze in a finer time dimension. This paper first proposes the structure of the multi-convolution joint neural network, classifies the spatio-temporal data of haze in the Beijing area by block level, and carries out the frequency statistical analysis method on the output results of the multi-convolution joint neural network. First, the frequency of occurrence of haze levels was displayed and analyzed accordingly. Then, to analyze the results more finely, the Moran's I of spatial autocorrelation analysis was used in subsequent research to analyze the spatial relationship between each block. Then, to analyze the haze's temporal and spatial evolution more intuitively, the spatial variation of the haze is analyzed in the LISA cluster map on the time unit of the seasonal scale. Finally, it is concluded that the temporal and spatial distribution of haze in the Beijing area is high in the south and low in the north. Moreover, its temporal and spatial evolution characteristics on a seasonal scale are that, according to the time changes from winter, spring, summer to autumn, the relationship of the haze concentration between each sub-region gradually changes from a discrete state to a concentrated state.

Author Contributions: Conceptualization, W.Z. and L.W.; methodology, L.Y. and S.L.; software, W.H.; formal analysis, B.Y. and L.W.; data curation, W.H.; writing—original draft preparation, L.Y. and W.H.; writing—review and editing, L.Y. and W.Z.; funding acquisition, W.Z. and B.Y. All authors have read and agreed to the published version of the manuscript.

Funding: This work was jointly supported by the Sichuan Science and Technology Program (Grant:2021YFQ0003, 2019YJ0189).

Institutional Review Board Statement: Not Applicable.

Informed Consent Statement: Not Applicable.

Data Availability Statement: The haze level data used in this paper is an open-resource data provided by UCI Center for Machine Learning and Intelligent System at <https://archive.ics.uci.edu/ml/datasets/Beijing+Multi-Site+Air-Quality+Data>. The MODIS data is also an open-resource data provided by NASA at <https://modis.gsfc.nasa.gov/data/>.

Conflicts of Interest: The authors declare no conflict of interest.


References

1. Zhang, M.; Song, Y.; Cai, X. A health-based assessment of particulate air pollution in urban areas of Beijing in 2000–2004. *Sci. Total Environ.* **2007**, *376*, 100–108. [CrossRef]
2. Boldo, E.; Medina, S.; Le Tertre, A.; Hurley, F.; Mücke, H.-G.; Ballester, F.; Aguilera, I. Apheis: Health impact assessment of long-term exposure to PM 2.5 in 23 European cities. *Eur. J. Epidemiol.* **2006**, *21*, 449–458. [CrossRef]
3. Zhang, R.; Jing, J.; Tao, J.; Hsu, S.-C.; Wang, G.; Cao, J.; Lee, C.S.L.; Zhu, L.; Chen, Z.; Zhao, Y. Chemical characterization and source apportionment of PM 2.5 in Beijing: Seasonal perspective. *Atmos. Chem. Phys.* **2013**, *13*, 7053–7074. [CrossRef]
4. Prospero, J.M.; Olmez, I.; Ames, M. Al and Fe in PM 2.5 and PM 10 suspended particles in south-central Florida: The impact of the long range transport of African mineral dust. *Water Air Soil Pollut.* **2001**, *125*, 291–317. [CrossRef]
5. Chen, X.; Yin, L.; Fan, Y.; Song, L.; Ji, T.; Liu, Y.; Tian, J.; Zheng, W. Temporal evolution characteristics of PM2.5 concentration based on continuous wavelet transform. *Sci. Total Environ.* **2020**, *699*, 134244. [CrossRef]
6. Dankwa, S.; Zheng, W.; Gao, B.; Li, X. Terrestrial Water Storage (TWS) Patterns Monitoring in the Amazon Basin Using Grace Observed: Its Trends and Characteristics. In Proceedings of the IGARSS 2018—2018 IEEE International Geoscience and Remote Sensing Symposium, Valencia, Spain, 22–27 July 2018; pp. 768–771.
7. Ding, Y.; Tian, X.; Yin, L.; Chen, X.; Liu, S.; Yang, B.; Zheng, W. Multi-scale Relation Network for Few-Shot Learning Based on Meta-learning. In Proceedings of the International Conference on Computer Vision System (2019), Thessaloniki, Greece, 23–25 September 2019; pp. 343–352.
8. Zhou, Y.; Zheng, W.; Shen, Z. A New Algorithm for Distributed Control Problem with Shortest-Distance Constraints. *Math. Probl. Eng.* **2016**, *2016*, 1604824. [CrossRef]
9. Pandolfi, M.; Gonzalez-Castanedo, Y.; Alastuey, A.; Jesus, D.; Mantilla, E.; De La Campa, A.S.; Querol, X.; Pey, J.; Amato, F.; Moreno, T. Source apportionment of PM 10 and PM 2.5 at multiple sites in the strait of Gibraltar by PMF: Impact of shipping emissions. *Environ. Sci. Pollut. Res.* **2011**, *18*, 260–269. [CrossRef]
10. Li, X.; Zheng, W.; Yin, L.; Yin, Z.; Song, L.; Tian, X. Influence of social-economic activities on air pollutants in Beijing, China. *Open Geosci.* **2017**, *9*, 314–321. [CrossRef]
11. Liu, S.; Gao, Y.; Zheng, W.; Li, X. Performance of two neural network models in bathymetry. *Remote Sens. Lett.* **2015**, *6*, 321–330. [CrossRef]
12. Ni, X.; Yin, L.; Chen, X.; Liu, S.; Yang, B.; Zheng, W. Semantic representation for visual reasoning. *MATEC Web Conf.* **2019**, *277*, 02006. [CrossRef]
13. Tang, Y.; Liu, S.; Deng, Y.; Zhang, Y.; Yin, L.; Zheng, W. Construction of force haptic reappearance system based on Geomagic Touch haptic device. *Comput. Methods Programs Biomed.* **2020**, *190*, 105344. [CrossRef] [PubMed]
14. Zheng, W.; Li, X.; Xie, J.; Yin, L.; Wang, Y. Impact of human activities on haze in Beijing based on grey relational analysis. *Rend. Lincei* **2015**, *26*, 187–192. [CrossRef]
15. Zheng, W.; Li, X.; Yin, L.; Wang, Y. The retrieved urban LST in Beijing based on TM, HJ-1B and MODIS. *Arab. J. Sci. Eng.* **2016**, *41*, 2325–2332. [CrossRef]
16. Yin, L.; Li, X.; Zheng, W.; Yin, Z.; Song, L.; Ge, L.; Zeng, Q. Fractal dimension analysis for seismicity spatial and temporal distribution in the circum-Pacific seismic belt. *J. Earth Syst. Sci.* **2019**, *128*, 22. [CrossRef]
17. Schwartz, J.; Laden, F.; Zanobetti, A. The concentration-response relation between PM (2.5) and daily deaths. *Environ. Health Perspect.* **2002**, *110*, 1025–1029. [CrossRef]
18. Franklin, M.; Zeka, A.; Schwartz, J. Association between PM 2.5 and all-cause and specific-cause mortality in 27 US communities. *J. Expo. Sci. Environ. Epidemiol.* **2007**, *17*, 279–287. [CrossRef]
19. Tucker, W.G. An overview of PM2.5 sources and control strategies. *Fuel Process. Technol.* **2000**, *65*, 379–392. [CrossRef]
20. Liu, S.; Wang, L.; Liu, H.; Su, H.; Li, X.; Zheng, W. Deriving bathymetry from optical images with a localized neural network algorithm. *IEEE Trans. Geosci. Remote Sens.* **2018**, *56*, 5334–5342. [CrossRef]
21. Ma, Z.; Zheng, W.; Chen, X.; Yin, L. Joint embedding VQA model based on dynamic word vector. *PeerJ Comput. Sci.* **2021**, *7*, e353. [CrossRef] [PubMed]
22. Zheng, W.; Li, X.; Yin, L.; Wang, Y. Spatiotemporal heterogeneity of urban air pollution in China based on spatial analysis. *Rend. Lincei* **2016**, *27*, 351–356. [CrossRef]
23. Zheng, W.; Liu, X.; Yin, L. Research on image classification method based on improved multi-scale relational network. *PeerJ Comput. Sci.* **2021**, *7*, e613. [CrossRef]
24. Zheng, W.; Yin, L.; Chen, X.; Ma, Z.; Liu, S.; Yang, B. Knowledge base graph embedding module design for Visual question answering model. *Pattern Recognit.* **2021**, *120*, 108153. [CrossRef]
25. Zheng, W.; Liu, X.; Ni, X.; Yin, L.; Yang, B. Improving Visual Reasoning Through Semantic Representation. *IEEE Access* **2021**, *9*, 91476–91486. [CrossRef]
26. Zheng, W.; Liu, X.; Yin, L. Sentence Representation Method Based on Multi-Layer Semantic Network. *Appl. Sci.* **2021**, *11*, 1316. [CrossRef]
27. Zhao, C.-X.; Wang, Y.-Q.; Wang, Y.-J.; Zhang, H.-L.; Zhao, B.-Q. Temporal and spatial distribution of PM2.5 and PM10 pollution status and the correlation of particulate matters and meteorological factors during winter and spring in Beijing. *Huan Jing Ke Xue Huanjing Kexue* **2014**, *35*, 418–427. [PubMed]

28. Ando, M.; Katagiri, K.; Tamura, K.; Yamamoto, S.; Matsumoto, M.; Li, Y.; Cao, S.; Ji, R.; Liang, C. Indoor and outdoor air pollution in Tokyo and Beijing supercities. *Atmos. Environ.* **1996**, *30*, 695–702. [CrossRef]
29. Gehrig, R.; Buchmann, B. Characterising seasonal variations and spatial distribution of ambient PM10 and PM2.5 concentrations based on long-term Swiss monitoring data. *Atmos. Environ.* **2003**, *37*, 2571–2580. [CrossRef]
30. Zhang, Y.-L.; Cao, F. Fine particulate matter (PM 2.5) in China at a city level. *Sci. Rep.* **2015**, *5*, 14884. [CrossRef]
31. Zhao, X.; Zhang, X.; Xu, X.; Xu, J.; Meng, W.; Pu, W. Seasonal and diurnal variations of ambient PM2.5 concentration in urban and rural environments in Beijing. *Atmos. Environ.* **2009**, *43*, 2893–2900. [CrossRef]
32. Fuller, G.W.; Carslaw, D.C.; Lodge, H.W. An empirical approach for the prediction of daily mean PM10 concentrations. *Atmos. Environ.* **2002**, *36*, 1431–1441. [CrossRef]
33. Dong, M.; Yang, D.; Kuang, Y.; He, D.; Erdal, S.; Kenski, D. PM2.5 concentration prediction using hidden semi-Markov model-based times series data mining. *Expert Syst. Appl.* **2009**, *36*, 9046–9055. [CrossRef]
34. Lee, H.; Liu, Y.; Coull, B.; Schwartz, J.; Koutrakis, P. A novel calibration approach of MODIS AOD data to predict PM2.5 concentrations. *Atmos. Chem. Phys.* **2011**, *11*, 7991–8002. [CrossRef]
35. Ordieres, J.; Vergara, E.; Capuz, R.; Salazar, R. Neural network prediction model for fine particulate matter (PM2.5) on the US–Mexico border in El Paso (Texas) and Ciudad Juárez (Chihuahua). *Environ. Model. Softw.* **2005**, *20*, 547–559. [CrossRef]
36. Reid, C.E.; Jerrett, M.; Petersen, M.L.; Pfister, G.G.; Morefield, P.E.; Tager, I.B.; Raffuse, S.M.; Balmes, J.R. Spatiotemporal prediction of fine particulate matter during the 2008 Northern California wildfires using machine learning. *Environ. Sci. Technol.* **2015**, *49*, 3887–3896. [CrossRef] [PubMed]
37. He, L.; Li, H.; Liu, F.; Liu, N.; Sun, Z.; He, Z. Multi-patch convolution neural network for iris liveness detection. In Proceedings of the 2016 IEEE 8th International Conference on Biometrics Theory, Applications and Systems (BTAS), Niagara Falls, NY, USA, 6–9 September 2016; pp. 1–7.

Article

Spatio-Temporal Characteristics of Air Quality Index (AQI) over Northwest China

Shah Zaib ¹, Jianjiang Lu ^{1,*} and Muhammad Bilal ² 

¹ Key Laboratory of Environmental Monitoring and Pollution Control of Xinjiang Bingtuan, School of Chemistry and Chemical Engineering, Shihezi University, Shihezi 832003, China; shah@stu.shzu.edu.cn

² School of Marine Sciences, Nanjing University of Information Science and Technology, Nanjing 210044, China; muhammad.bilal@connect.polyu.hk

* Correspondence: lujj@shzu.edu.cn

Abstract: In recent years, air pollution has become a serious threat, causing adverse health effects and millions of premature deaths in China. This study examines the spatial-temporal characteristics of ambient air quality in five provinces (Shaanxi (SN), Xinjiang (XJ), Gansu (GS), Ningxia (NX), and Qinghai (QH)) of northwest China (NWC) from January 2015 to December 2018. For this purpose, surface-level aerosol pollutants, including particulate matter (PM_x, x = 2.5 and 10) and gaseous pollutants (sulfur dioxide (SO₂), nitrogen dioxide (NO₂), carbon monoxide (CO), and ozone (O₃)) were obtained from China National Environmental Monitoring Center (CNEMC). The results showed that fine particulate matter (PM_{2.5}), coarse particulate matter (PM₁₀), SO₂, NO₂, and CO decreased by 28.2%, 32.7%, 41.9%, 6.2%, and 27.3%, respectively, while O₃ increased by 3.96% in NWC during 2018 as compared with 2015. The particulate matter (PM_{2.5} and PM₁₀) levels exceeded the Chinese Ambient Air Quality Standards (CAAQS) Grade II standards as well as the WHO recommended Air Quality Guidelines, while SO₂ and NO₂ complied with the CAAQS Grade II standards in NWC. In addition, the average air quality index (AQI), calculated from ground-based data, improved by 21.3%, the proportion of air quality Class I (0–50) improved by 114.1%, and the number of pollution days decreased by 61.8% in NWC. All the pollutants' (except ozone) AQI and PM_{2.5}/PM₁₀ ratios showed the highest pollution levels in winter and lowest in summer. AQI was strongly positively correlated with PM_{2.5}, PM₁₀, SO₂, NO₂, and CO, while negatively correlated with O₃. PM₁₀ was the primary pollutant, followed by O₃, PM_{2.5}, NO₂, CO, and SO₂, with different spatial and temporal variations. The proportion of days with PM_{2.5}, PM₁₀, SO₂, and CO as the primary pollutants decreased but increased for NO₂ and O₃. This study provides useful information and a valuable reference for future research on air quality in northwest China.

Keywords: northwest China; AQI; primary pollutant; CNEMC; Pearson correlation

Citation: Zaib, S.; Lu, J.; Bilal, M. Spatio-Temporal Characteristics of Air Quality Index (AQI) over Northwest China. *Atmosphere* **2022**, *13*, 375. <https://doi.org/10.3390/atmos13030375>

Academic Editors: Célia Alves, Duanyang Liu, Kai Qin and Honglei Wang

Received: 23 December 2021

Accepted: 17 February 2022

Published: 23 February 2022

Publisher's Note: MDPI stays neutral with regard to jurisdictional claims in published maps and institutional affiliations.



Copyright: © 2022 by the authors. Licensee MDPI, Basel, Switzerland. This article is an open access article distributed under the terms and conditions of the Creative Commons Attribution (CC BY) license (<https://creativecommons.org/licenses/by/4.0/>).

1. Introduction

Unprecedented economic activity, urbanization, industrialization, and motorization have deteriorated the ambient air quality in China [1–6]. China is the manufacturing hub of the world, with the majority of the industries in northwest China (NWC). Several studies have reported higher pollution levels in NWC due to increased industry, coal consumption, distinct topography, and adverse meteorology [2,5,7–11]. Increased pollution levels have attracted the attention of the general public, the scientific community, and relevant authorities because of their detrimental health effects [4,12–16]. To combat increasing pollution levels, China has made significant efforts, e.g., establishing Chinese ambient air quality standards (CAAQS) for six criteria pollutants [17], implementing the Atmospheric Pollution Prevention and Control Action Plan 2013 (APPCAP) [18], technical regulation on ambient air quality index (HJ 633–2012) [19], nationwide air quality monitoring, online data-sharing networks, etc. [20,21]. These measures have helped to reduce pollution to

some extent; e.g., from Ref. [22], a 12.3% reduction in fine particulate matter ($PM_{2.5}$) was observed in China between 2013 and 2015, while other authors [23] observed a one-third reduction in $PM_{2.5}$ from 2013 to 2017 due to APPCAP in China. In Ref. [24], it was observed that the annual average concentration ($PM_{2.5}$), coarse particulate matter (PM_{10}), sulfur dioxide (SO_2), nitrogen dioxide (NO_2), and carbon monoxide (CO) decreased by 27.9%, 23.8%, 51.2%, 10.6%, and 25.3%, respectively, in China from 2015 to 2019. Even after strict environmental regulations, the air pollution in some areas of NWC is beyond certain limits and causes serious health effects [25–28].

Most of the spatio-temporal studies in China focused on central China, north China, considered few parameters, fewer cities, mostly provincial capitals, and lacked detailed assessment, with few exceptions. Multiple studies, e.g., [3,29], observed higher $PM_{2.5}$ pollution in northern China, western China, northwestern China, etc. due to increased industrial emissions, coal combustion, stagnant meteorology, etc. Similarly, other researchers [30,31] carried out a more detailed assessment, covered six criteria pollutants in provincial capitals, and observed higher pollution levels in the north and northwestern region. In Ref. [1], they analyzed the criteria pollutants ($PM_{2.5}$, PM_{10} , SO_2 , NO_2 , CO, and O_3) in 336 cities of China, while other researchers [31] analyzed the criteria pollutants in 367 cities of China and observed higher pollution in industrialized areas of north China. Further, Ref. [2] thoroughly assessed the air pollution in NWC by analyzing the criteria pollutants in six cities of Gansu province in NWC and observed higher pollution in Lanzhou, the provincial capital, with increased energy consumption and industrial activity and facing serious health concerns [25].

$PM_{2.5}$ is more dangerous than PM_{10} and is ranked as the first leading risk factor for disease in China, causing more than 1.1 million premature deaths, with the highest share being stroke, ischemic heart disease (IHD), lung cancer, lower respiratory infections, chronic obstructive pulmonary disease (COPD), etc. [32–34]. Other criteria pollutants, e.g., PM_{10} , CO, O_3 , SO_2 , and NO_2 , cause multiple health disorders, e.g., headaches, dizziness, nausea, respiratory disorders, inflammatory reactions, reduced lung function, hampered neurological function, etc. [35–37]. Apart from jeopardizing human health, air pollution is also responsible for visibility reduction, economic losses, and climate change [13]. $PM_{2.5}$ and O_3 can cause gross domestic production (GDP) losses of 2.09% in health expenditure [38].

In view of such circumstances, we examined the spatial and temporal distribution of $PM_{2.5}$, PM_{10} , SO_2 , NO_2 , CO, and O_3 in 53 cities located in five provinces of NWC for a period of four years (2015 to 2018). Besides the criteria pollutants, we also examined the $PM_{2.5}/PM_{10}$ ratio, Air Quality Index (AQI), AQI class distributions, major pollutant on a representative day, number of pollution days, and correlations among different pollutants to explicate the pollution status, spatial, and temporal distribution of air quality in NWC over time. This study provides useful information and a valuable reference for future research on air quality in NWC and is of considerable significance to environmental protection and human health.

2. Materials and Methods

2.1. Site Selection

In this study, we examined the ambient air quality in the northern and western parts of China, known as northwest China (NWC), from January 2015 to December 2018 to understand the spatio-temporal variation across NWC better. NWC is a mixture of agricultural areas, deserts, mountains, etc. with significant coal reserves, industrial activity, covering an area of 3.1 million sq. km area (32.4% of China), having a population of more than 96.65 million, and experiencing degraded air quality. NWC consists of five provinces, namely Shaanxi (SN), Xinjiang (XJ), Gansu (GS), Ningxia (NX), and Qinghai (QH) (Supplementary Material Figure S1). Table 1 gives detailed information about 5 provinces and 53 cities.

Table 1. Description of cities under observation in five provinces (Shaanxi (SN), Xinjiang (XJ), Gansu (GS), Ningxia (NX), and Qinghai (QH)) of northwest China (NWC).

Province	City	Population (million)	Area (km ²)	Monitoring Stations	Attainment (%)			
					2015	2016	2017	2018
Shaanxi (SX)	Ankang	2.63	23,536	3	20.27	17.49	13.70	8.49
	Baoji	3.717	18,712	8	23.56	36.61	33.42	21.64
	Hanzhong	3.84	27,246	4	20.82	25.68	27.12	14.25
	Shanglou	2.34	19,587	2	15.34	15.85	7.67	3.29
	Tongchuan	0.83	3882	4	24.93	44.54	31.51	21.37
	Weinan	5.52	13,134	4	27.40	54.10	54.52	33.42
	Xian	12	10,097	13	30.14	47.54	50.14	36.16
	Xianyang	5.096	10,213	4	27.12	53.55	55.89	24.93
	Yannan	2.198	37,000	4	22.47	21.04	13.97	3.29
	Yulin	3.38	43,578	4	19.73	19.67	22.74	9.32
Xinjiang (XJ)	Aksu	2.37	127,144.91	2	52.60	72.68	23.56	18.63
	Altay	0.526	117,699.01	2	0.27	0.00	0.00	0.00
	Bortala	0.443	24,934.33	2	9.32	9.56	10.68	6.30
	Crete	0.525	72,468.08	1	49.32	50.27	21.64	16.99
	Changji	1.428	73,139.75	3	18.63	26.78	29.32	24.66
	Hami	0.572	142,094.88	2	16.99	12.57	5.48	1.37
	Hotan	2.014	249,146.59	2	75.07	73.77	19.18	12.05
	Ili	2.482	56,381.53	3	14.79	16.94	23.56	20.55
	Karamy	0.39	8654.08	5	8.49	9.02	11.78	8.22
	Korla	1.278	470,954.25	3	31.51	44.26	34.79	8.77
	Kashgar	3.979	137,578.51	3	71.51	77.32	40.82	30.96
	Shihezi	0.635	456.84	2	21.92	25.41	37.53	25.75
	Tacheng	1.219	94,698.18	1	0.00	0.27	0.27	0.27
	Turpan	0.622	67,562.91	2	36.16	55.19	32.33	21.64
	Urumqi	3.11	13,787.90	7	33.97	31.69	33.15	23.56
	Wujiaqu	0.09	742	1	23.84	33.33	32.60	25.75
Gansu (GS)	Dingxi	3.031	19,609	2	16.71	12.84	8.22	3.29
	Gannan	0.689	40,898	1	18.36	15.03	8.77	2.74
	Jiayuguan	0.231	2935	2	18.08	17.76	4.38	1.92
	Jinchang	0.228	8896	3	20.55	20.77	7.67	2.74
	Jiuquan	1.096	191,342	2	26.58	35.52	31.78	21.10
	Lanzhou	3.61	13,300	5	21.64	15.30	15.89	4.66
	Linxia	0.25	88.6	2	7.12	7.10	6.03	2.47
	Longnan	2.567	27,000	2	18.08	10.66	3.56	0.27
	Pinglian	2.068	11,196	2	21.64	14.75	6.03	2.74
	Qingyang	2.21	27,119	3	15.07	12.30	7.95	1.92
	Silver City	1.708	21,200	2	24.38	17.49	7.95	3.29
	Tianshui	3.262	14,300	3	15.34	16.12	7.40	6.03
	Wuwei	1.815	33,000	2	17.53	15.85	6.85	1.92
	Zhangye	1.2	42,000	2	23.29	14.48	5.48	0.27
Ningxia (NX)	Guyuan	1.45	14,413	3	12.88	13.11	4.38	1.10
	Shizuishan	0.73	5208.13	4	38.08	33.33	24.38	9.86
	Yinchuan	2.293	8874.61	3	25.75	23.50	13.70	4.93
	Wuzhong	1.3	16,758	6	26.03	29.23	30.68	9.59
	Zhongwei	1.041	16,986	3	24.66	21.04	16.16	2.74
Qinghai (QH)	Guoluo/Golog	0.181	76,312	1	8.22	4.10	5.48	1.92
	Haibei	0.273	39,354	1	19.73	15.57	2.47	0.82
	Haidong	1.396	12,810	1	27.67	21.86	12.60	7.40
	Hainan	0.441	45,895	1	16.99	9.29	4.11	1.37
	Haixi	0.515	325,785	1	14.79	6.83	2.19	0.00
	Huanggnan	0.256	17,921	1	33.97	30.33	27.40	21.64
	Xinning	2.208	7372	4	18.90	25.68	13.15	4.66
	Yushu/Gyegu	0.12	13,462	1	5.48	1.91	1.10	0.27

2.2. Data Collection

To meet the objectives of the study, we analyzed the ambient air quality in 53 cities located in five provinces (SN, XJ, GS, NX, and QH) of NWC (Table 1) for a period of four years (2015–2018). The hourly concentration of PM_{2.5}, PM₁₀, SO₂, NO₂, CO, and O₃ was collected from China National Environmental Monitoring Center (CNEMC). The online data-sharing platform covers 367 cities of China, and dispatch/publish information according to the Technical Guideline on Environmental Monitoring Quality Management (HJ 630-2011) [39].

2.3. Air Quality Index (AQI)

The air quality index (AQI) includes 24-h average measurement of PM_{2.5}, PM₁₀, NO₂, SO₂, CO, and 8-h average concentration of O₃ and reflects the overall air quality [8,28,40]. Individual air quality index (IAQI) for six criteria pollutants is determined by using Equation (1), and the overall AQI is calculated based on the highest IAQI by using Equation (2) according to the instruction given in technical regulation on ambient air quality index (on trial) (HJ-633-2012) [19].

$$IAQI_p = \frac{I_{high} - I_{low}}{C_{high} - C_{low}} \times (C_p - C_{low}) + I_{low} \quad (1)$$

IAQI_p = individual sub air quality index of the pollutant p

C_p = concentration of the pollutant p

C_{high} = concentration breakpoint that is $\geq C_p$

C_{low} = concentration breakpoint that is $\leq C_p$

I_{high} = index breakpoint corresponding to C_{high}

I_{low} = index breakpoint corresponding to C_{low}

$$AQI = \max(I_1, I_2, \dots, I_n) \quad (2)$$

In Equation (2), “n” indicates the number of criteria pollutants. When AQI is higher than 50, the highest IAQI is considered as a major pollutant for that given day [23,28,41–44]. Air Quality Index (AQI) has the following six categories:

Class I: 0–50 (Green), Good

Class II: 51–100 (Yellow), Moderate

Class III: 101–150 (Orange), Unhealthy for Sensitive Groups

Class IV: 151–200 (Red), Unhealthy

Class V: 201–300 (Purple), Very unhealthy

Class VI: 300–500 (Maroon), Hazardous

2.4. Quality Assurance and Quality Control (QA&AR)

Quality assurance and control procedures for ambient air quality data were strictly in accordance with Chinese Ambient Air Quality Standards (CAAQS) (GB-3095-2012) [17]. The daily average value was calculated when we have valid data for more than 16 h of that day (except for ozone, minimum 6-h value for 8-h ozone value); the monthly average was calculated only when we have 27 daily mean values; an annual value was calculated only when we have 324 daily mean values. Besides this, manual inspection was carried out to remove abnormal values, e.g., PM_{2.5} values higher than PM₁₀ values.

2.5. Inverse Distance Weighted (IDW) Spatial Interpolation

Many spatial interpolation methods, such as kriging (universal or ordinary) and inverse distance weighted (IDW) spatial interpolation, have been used in different studies [45,46]. IDW geospatial interpolation is a type of deterministic method for multivariate interpolation with a known scattered set of points. IDW assigns values to unknown points according to the weighted average of the values of the known points and is more suitable

for regional interpolation [47]. In this study, we used IDW spatial interpolation technique to interpolate spatial distribution of PM_{2.5}, PM₁₀, SO₂, NO₂, CO, O₃, AQI, and PM_{2.5}/PM₁₀ ratio in NWC. Equation (3) describes the interpolation analysis.

$$Zp = \frac{\sum_i^n = 1 \frac{z_i}{dip}}{\sum_i^n = 1 \frac{1}{dip}} \quad (3)$$

where Zp refers to the value of unknown point, Zi is the value observed at the point of I ; I represents the nearest neighborhood of interpolated point produced; p is the weighting absolute value, and p is equal to inverse distance weight, respectively.

2.6. Statistical Analysis

In this study, we used Statistical Package for Social Sciences (SPSS) for Windows (IBM SPSS Statistics, Version 25) to find the Pearson's correlation coefficient for criteria pollutants on an annual and seasonal basis [48], and used RStudio for graphical representation [49]. The high (low) value of the Pearson's correlation represents the same (different) variations in one criteria pollutant with respect to another pollutant. The effect of a certain variable was considered statistically significant for P (0.01, and 0.05) (two-tailed). Annual mean values, mean absolute deviation (MAD), mean square error (MSE), root mean square error (RMSE), mean absolute percentage error (MAPE), and mean percentage error (MPE) of six criteria pollutants between 2015 and 2018 were calculated by Microsoft Excel 2016.

3. Results

3.1. Spatial and Temporal Variation of Six Criteria Pollutants

During the study period (2015–2018), the average concentration of PM_{2.5}, PM₁₀, SO₂, NO₂, and CO decreased by 28.2% (14.2%, 25.8%, 31.1%, 34.4%, 47.1%) (Figure 1a), 32.7% (18.5%, 32.5%, 31.8%, 32.7%, 46.3%) (Figure 1b), 41.9% (30.6%, 43.8%, 46.8%, 48.7%, 32.3%) (Figure 1c), 6.2% (+3.59%, 4.44%, 18.8%, +3.72%, 8.45%) (Figure 1d), and 27.3% (32.7%, 21%, 38.4%, 17.2%, 16%) (Figure 1e), respectively, in NWC (SN, XJ, GS, NX, QH). In contrast to the other pollutants, the ozone levels increased by 3.69% (5.4%, 6.04%, 1.32%, 19.3%, 5.66%) in NWC (SN, XJ, GS, NX, QH) between 2015 and 2018 (Figure 1f). The annual average concentration of PM_{2.5} and PM₁₀ failed to comply with CAAQS Grade II standards (35 µg/m³ and 70 µg/m³, annual mean) and exceeded them by 25% and 31.9%, respectively, and exceeded them by 3.37 and 3.61 times, respectively, for the WHO air quality guidelines (10 µg/m³ and 20 µg/m³, annual mean) in NWC. PM_{2.5} and PM₁₀ failed to comply with CAAQS Grade II standards in SN, XJ, GS, NX, and NWC (Figure 1a,b), while SO₂ and NO₂ complied with CAAQS Grade II standards (60 µg/m³ and 40 µg/m³, annual mean) in SN, XJ, GS, NX, QH, and NWC (Figure 1c,d). CO and O₃ do not have annual standards under CAAQS; CO decreased in SN, XJ, GS, NX, QH, and NWC, while O₃ decreased in GS and QH during 2018 as compared with 2015 (Figure 1e,f). During the study period, the highest concentration of PM_{2.5}, PM₁₀, SO₂, NO₂, CO, and O₃ occurred in SN, XJ, NX, SN, SN, and QH, respectively. Figure 2 explains the spatial distribution of the criteria pollutants in 53 cities of NWC during 2015 to 2018, obtained by the inverse distance weighted (IDW) interpolation technique. The obtained results from spatial interpolation were quite similar to the actual values. In the case of spatial distribution, 92.5%, 96.2%, 92.5%, 64.5%, 88.7%, and 11.3% of the cities of NWC experienced a reduction in PM_{2.5} (Figure 2a–d), PM₁₀ (Figure 2e–h), SO₂ (Figure 2i–l), NO₂ (Figure 2m–p), CO (Figure 2q–t), and O₃ (Figure 2u–x), respectively, during 2018 as compared 2015. Similarly, 66%, 72.5%, and 13.2% of the cities failed to meet the CAAQS Grade II for PM_{2.5}, PM₁₀, and NO₂ (35 µg/m³, 70 µg/m³, 40 µg/m³, annual mean), respectively (Table S1). Most of the cities that were not complying with the CAAQS are cities with a larger population and increased industrial activities.

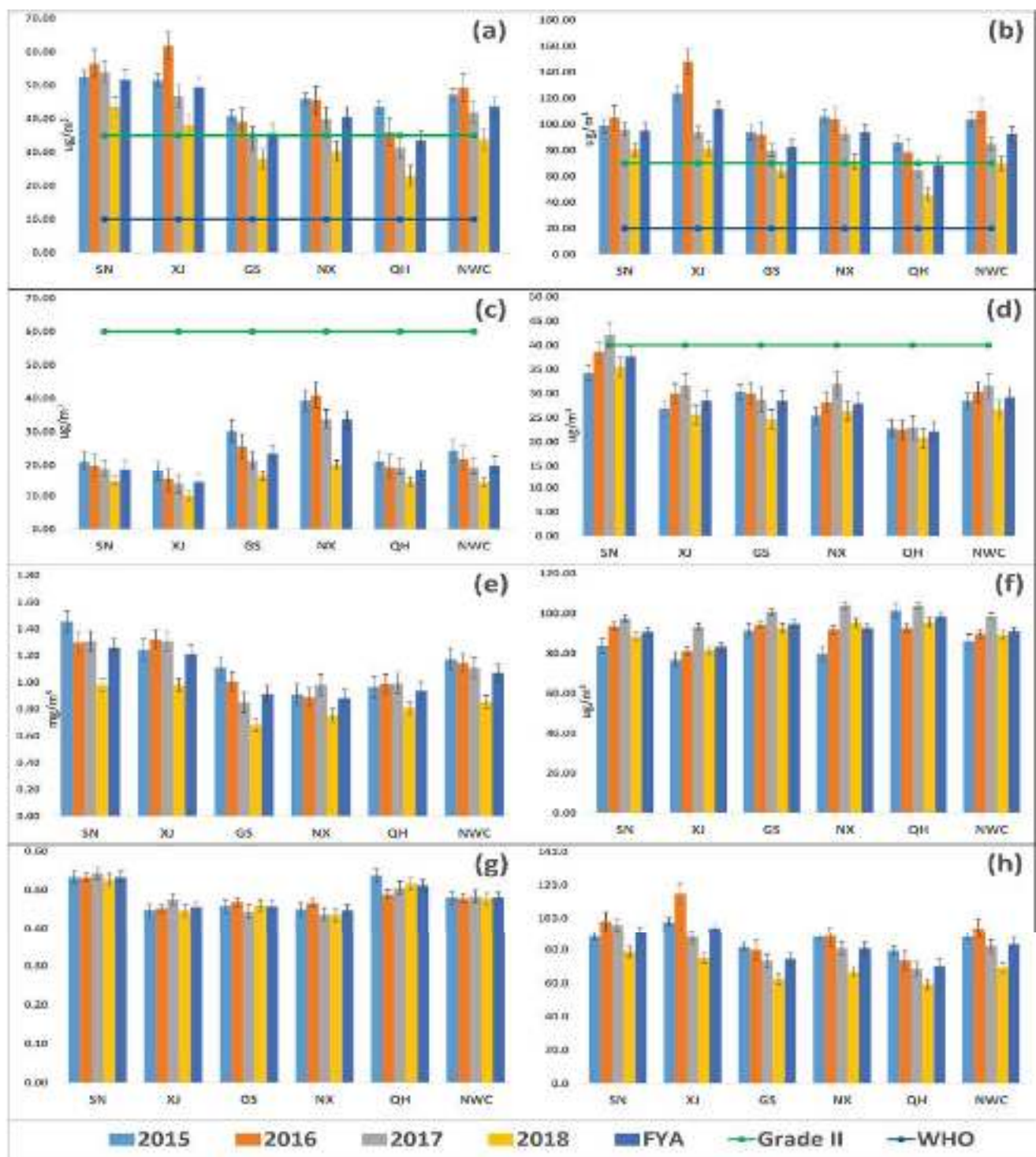


Figure 1. Annual variation of $PM_{2.5}$ (a), PM_{10} (b), SO_2 (c), NO_2 (d), CO (e), O_3 (f), $PM_{2.5}/PM_{10}$ (g), and AQI (h) in five provinces (Shaanxi (SN), Xinjiang (XJ), Gansu (GS), Ningxia (NX), and Qinghai (QH)) of northwest China (NWC) and NWC as a whole between 2015 and 2018. Descriptions are as follows: light blue bar (2015), orange bar (2016), grey bar (2017), yellow bar (2018), blue bar (four-year average (FYA)), parrot line with dots (CAAQS Grade II standards, annual mean), and dark blue with dots (WHO standards). The abbreviations are as follows: $PM_{2.5}$ (fine particulate matter), PM_{10} (coarse particulate matter), SO_2 (sulfur dioxide), NO_2 (nitrogen dioxide), CO (carbon monoxide), O_3 (ozone), $PM_{2.5}/PM_{10}$ (ratio of $PM_{2.5}$ with PM_{10}), and AQI (air quality index).

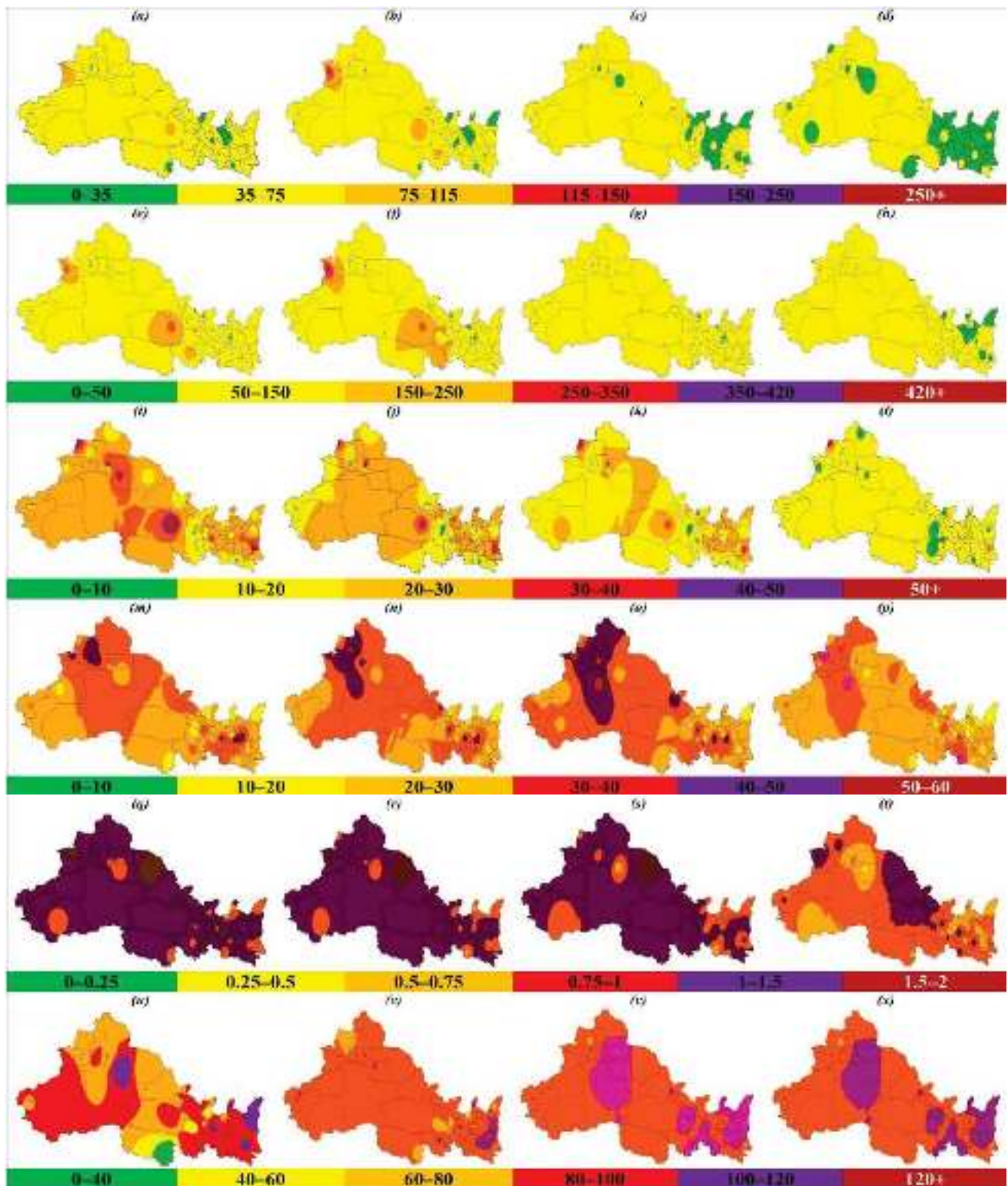


Figure 2. The spatial distribution of PM_{2.5} (a–d), PM₁₀ (e–h), SO₂ (i–l), NO₂ (m–p), CO (q–t), and O₃ (u–x) between 2015 and 2018 in northwest China (NWC). Color represents the different pollution levels, e.g., green (good), yellow (moderate), orange (unhealthy for the sensitive group), red (unhealthy for all), purple (very unhealthy), and maroon (hazardous). The abbreviations are as follows: PM_{2.5} (fine particulate matter), PM₁₀ (coarse particulate matter), SO₂ (sulfur dioxide), NO₂ (nitrogen dioxide), CO (carbon monoxide), and O₃ (ozone).

3.2. Seasonal Variation of Six Criteria Pollutants

In terms of seasonality, all the pollutants ($PM_{2.5}$, PM_{10} , SO_2 , NO_2 , and CO) observed the highest concentration in winter and the lowest occurred in summer except O_3 (vice versa) between 2015 and 2018 (Figure 3). $PM_{2.5}$ exceeded CAAQS Grade II ($75 \mu g/m^3$, daily mean) in SN, and XJ during winter (Figure 3a), while PM_{10} , SO_2 , NO_2 , CO, and O_3 complied with CAAQS Grade II ($150 \mu g/m^3$, $150 \mu g/m^3$, $80 \mu g/m^3$, $4 mg/m^3$, and $160 \mu g/m^3$, daily mean) in SN, XJ, GS, NX, QH, and NWC during spring, summer, autumn, and winter (Figure 3b–f). The average concentration of $PM_{2.5}$, PM_{10} , SO_2 , NO_2 , and CO decreased in all seasons, e.g., spring, summer, autumn, and winter, while the average concentration of O_3 increased in all seasons between 2015 and 2018. Figure S2 explains the spatial distribution of the criteria pollutants in 53 cities of NWC during different seasons. $PM_{2.5}$ exceeded CAAQS Grade II standards (daily mean) in 1.89%, 5.56%, and 32.1% of the cities during spring, summer, and winter, respectively (Figure S2a). Similarly, PM_{10} exceeded the daily standard in 5.66%, 7.55%, 1.89%, and 26.4% of the cities in spring, summer, autumn, and winter, respectively (Figure S2b), while, SO_2 , NO_2 , CO, and O_3 complied with CAAQS Grade II standards (daily mean) in all the cities of NWC during all seasons (Figure S2c–f).

Figure 4 illustrates the monthly variation in the criteria pollutants, $PM_{2.5}/PM_{10}$ ratio, and AQI in NWC between 2015 and 2018. $PM_{2.5}$, PM_{10} , NO_2 , SO_2 , and CO explicated “U” shaped curves, with the highest concentration in winter (October to January) due to increased coal combustion for civil heating and stagnant meteorological conditions, e.g., lower wind speed, low temperature, etc., while the lowest concentration occurred in summer (June to August) due to seasonal rains and favorable atmospheric conditions that help in pollution dispersion. In the case of PM_{10} , higher pollution levels also occurred in spring (March to May) due to haze events. In contrast to other pollutants, the O_3 levels were higher in June to August (summer) and lower in winter.

3.3. $PM_{2.5}/PM_{10}$ Ratio

The $PM_{2.5}/PM_{10}$ ratio normally reflects the composition and quality of air, e.g., a higher $PM_{2.5}/PM_{10}$ ratio indicates the increased proportion of $PM_{2.5}$ and a lower $PM_{2.5}/PM_{10}$ ratio indicates a higher concentration of PM_{10} in the atmosphere. The annual average $PM_{2.5}/PM_{10}$ ratio in NWC during 2015 to 2018 was 0.480 ± 0.08 , 0.478 ± 0.07 , 0.483 ± 0.08 , and 0.478 ± 0.07 , respectively, and experienced a reduction of 0.43% over time (Figure 1g). The highest $PM_{2.5}/PM_{10}$ ratio occurred in SN followed by QH, GS, XJ, and NX. In terms of seasonality, the highest $PM_{2.5}/PM_{10}$ ratio occurred in winter, followed by autumn, spring, and summer, and experienced an average change of -2.77% , -4.98% , 1.82% , and 5.31% , respectively (Figure 3g). In the case of monthly variation, a “U” shaped curve was observed with the highest value in winter and the lowest value in the summer Figure 4g. Figure 5 illustrates the annual (a–d) and seasonal (spring (e–h), summer (i–l), autumn (m–p), and winter (q–t)) spatial distribution of $PM_{2.5}/PM_{10}$ ratio in NWC during 2015 to 2018. In 2018, 49.1% of the cities of NWC experienced an increase in the $PM_{2.5}/PM_{10}$ ratio as compared with 2015. Similarly, 49.1%, 62.3%, 35.9%, and 39.6% of the cities of NWC experienced increased $PM_{2.5}/PM_{10}$ ratio in spring, summer, autumn, and winter, respectively, in 2018 against 2015. From 2015 to 2018, approximately 1.89%, 1.89%, 3.74%, and 26.4% of the cities experienced $PM_{2.5}/PM_{10}$ ratio higher than 0.60 in spring, summer, autumn, and winter, respectively, in NWC.

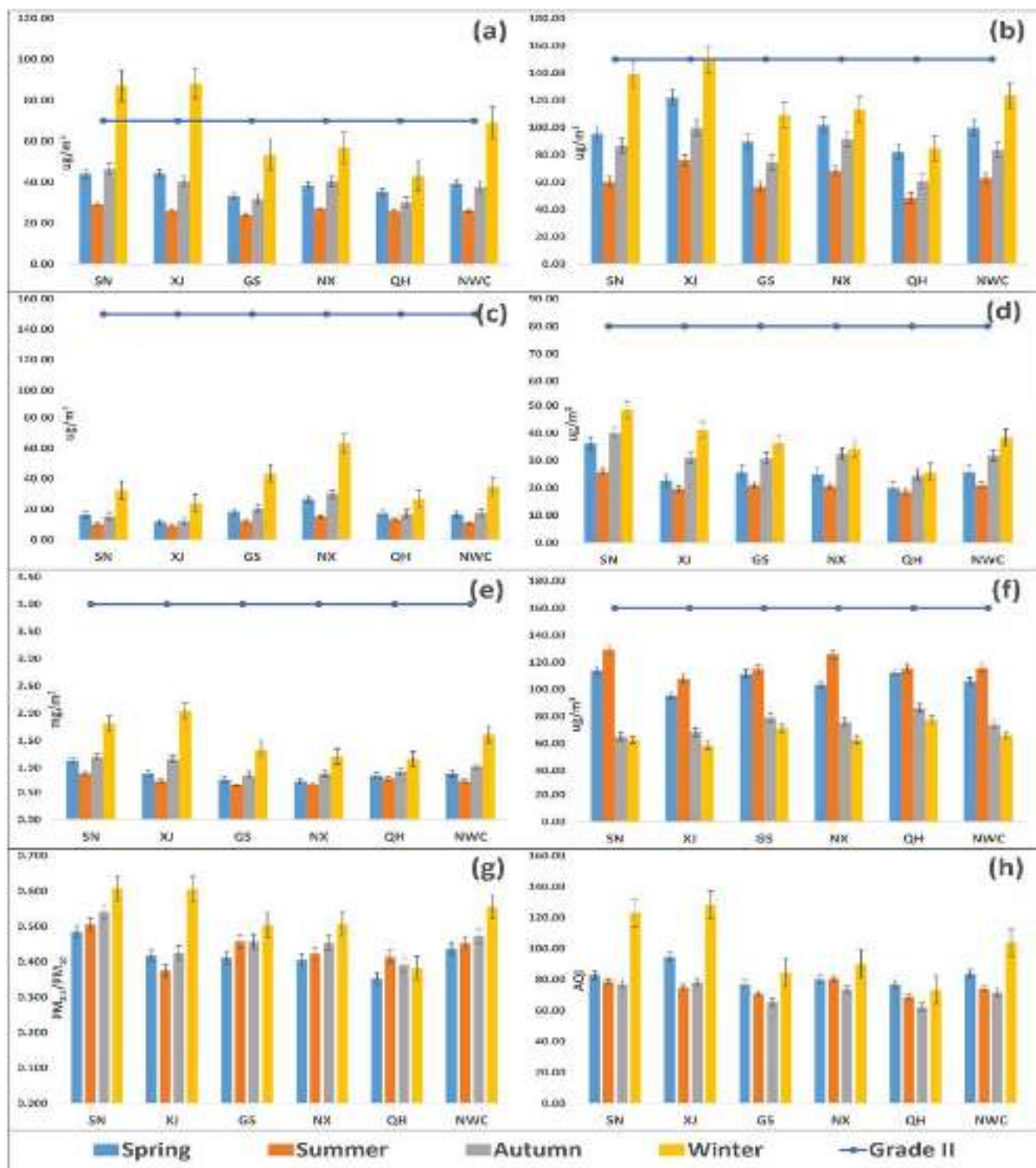


Figure 3. Seasonal variation of PM_{2.5} (a), PM₁₀ (b), SO₂ (c), NO₂ (d), CO (e), O₃ (f), PM_{2.5}/PM₁₀ ratio (g), and AQI (h) in five provinces (Shaanxi (SN), Xinjiang (XJ), Gansu (GS), Ningxia (NX), and Qinghai (QH)) of northwest China (NWC) and NWC as a whole between 2015 and 2018. Descriptions are as follows: light blue bar (spring), orange bar (summer), grey bar (autumn), yellow bar (winter), and blue line with dots (CAAQS Grade II standards, daily mean). The abbreviations are as follows: PM_{2.5} (fine particulate matter), PM₁₀ (coarse particulate matter), SO₂ (sulfur dioxide), NO₂ (nitrogen dioxide), CO (carbon monoxide), O₃ (ozone), PM_{2.5}/PM₁₀ (ratio of PM_{2.5} with PM₁₀), and AQI (air quality index).

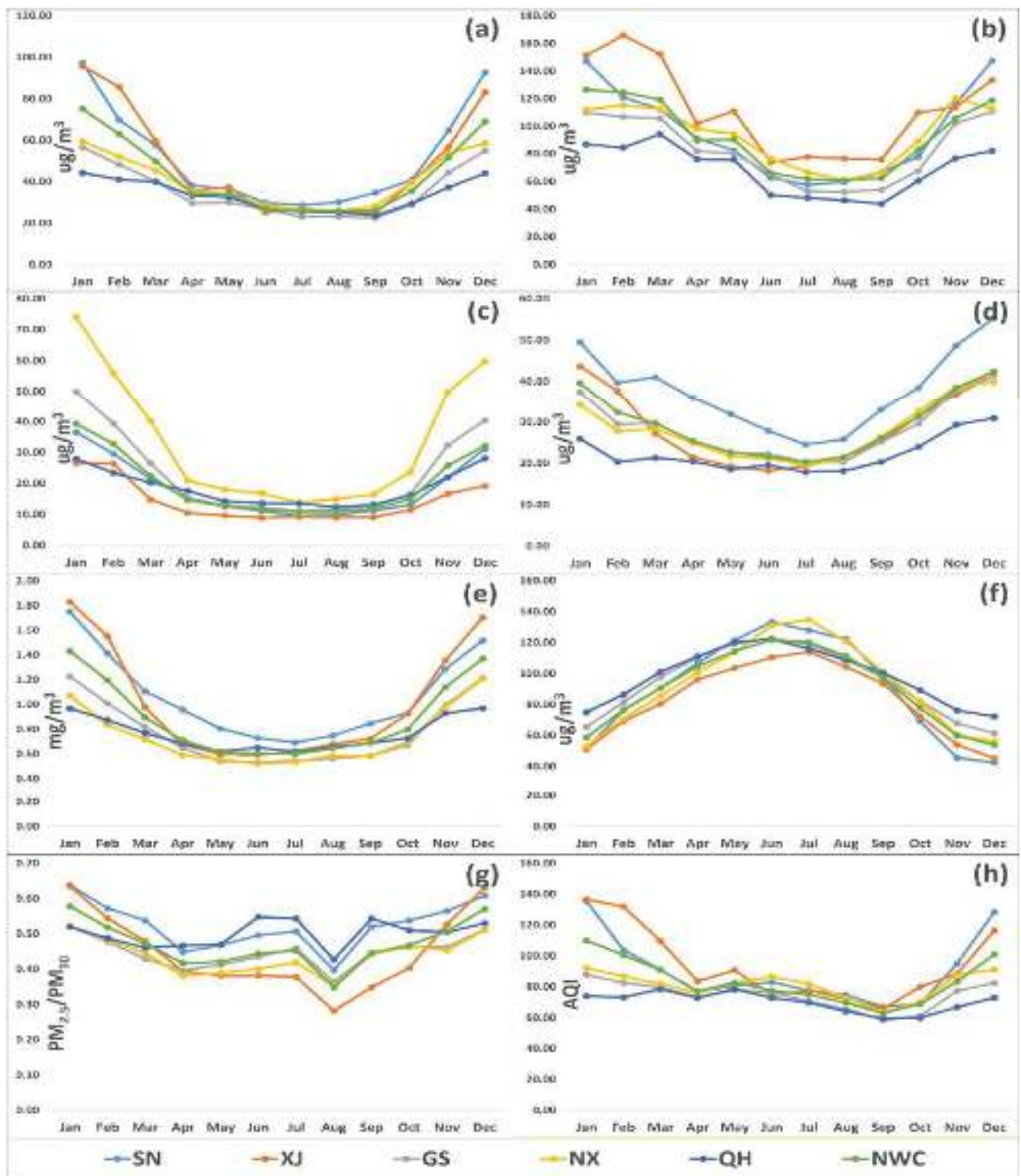


Figure 4. The monthly average concentration of PM_{2.5} (a), PM₁₀ (b), SO₂ (c), NO₂ (d), CO (e), O₃ (f), PM_{2.5}/PM₁₀ (g), and AQI (h) in five provinces (Shaanxi (SN), Xinjiang (XJ), Gansu (GS), Ningxia (NX), and Qinghai (QH)) of northwest China (NWC) between 2015 and 2018. Descriptions are as follows: light blue line with dots (SN), orange line with dots (XJ), grey line with dots (GS), yellow line with dots (NX), blue line with dots (QH), and parrot line with dots (NWC). The abbreviations are as follows: PM_{2.5} (fine particulate matter), PM₁₀ (coarse particulate matter), SO₂ (sulfur dioxide), NO₂ (nitrogen dioxide), CO (carbon monoxide), and O₃ (ozone).

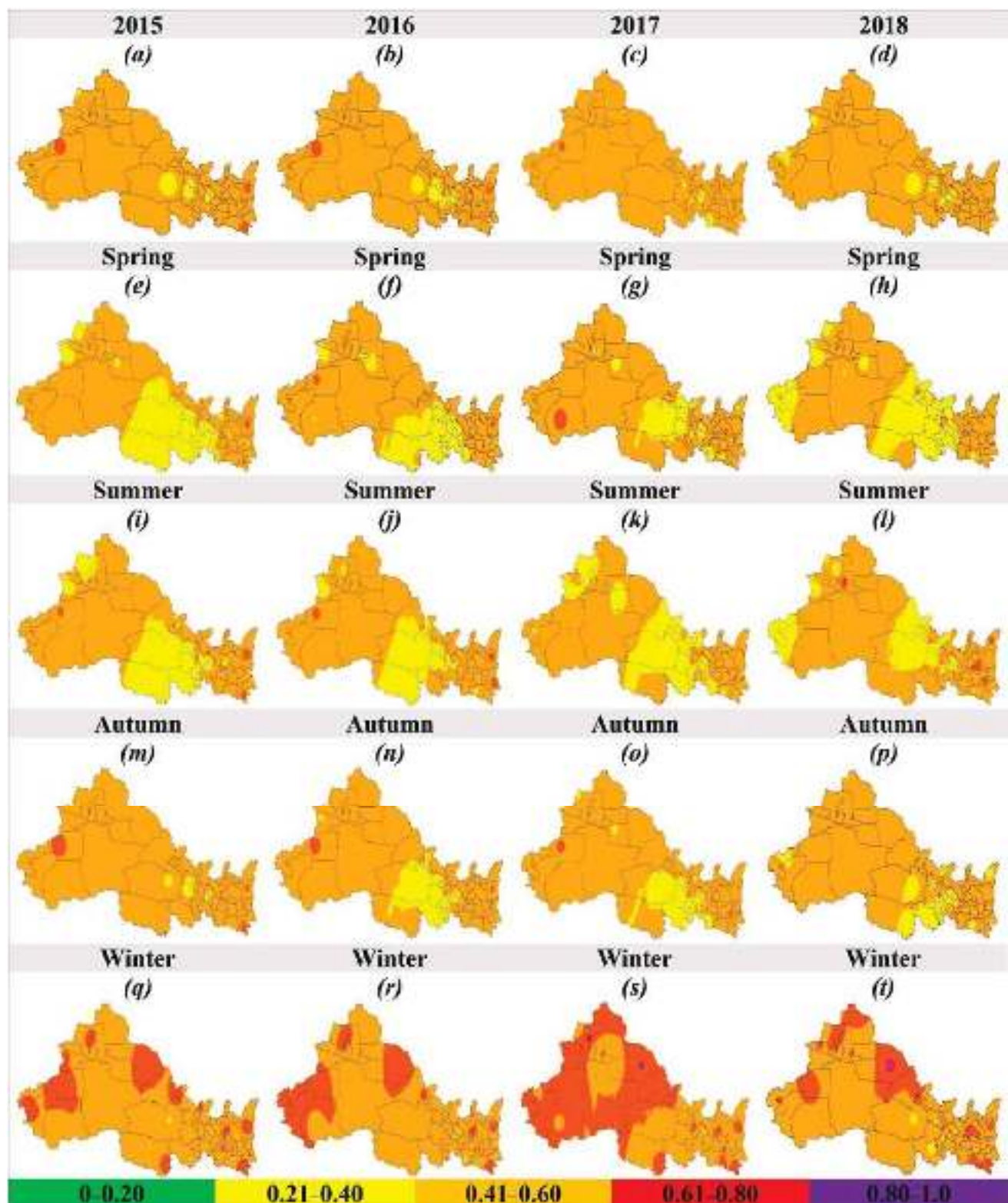


Figure 5. Annual (a–d) and seasonal (spring (e–h), summer (i–l), autumn (m–p), and winter (q–t)) spatial distribution of $PM_{2.5}/PM_{10}$ in 53 cities of northwest China (NWC) between 2015 and 2018. Color represents the different pollution levels, e.g., green (good), yellow (moderate), orange (unhealthy for a sensitive group), red (unhealthy for all), purple (very unhealthy), and maroon (hazardous).

3.4. Air Quality Index (AQI)

Air quality index (AQI) is a color-coded scale that simplifies different pollutants concentrations into a single numerical value that reflects overall air quality, health effects, sensitive groups, and required precautionary measures. During the study period (2015–2018), the annual average AQI in NWC was 88.1 ± 24.1 , 93.5 ± 36.3 , and 82 ± 18.7 , 69.2 ± 14.8 , respectively, and improved by 21.3% (Figure 1h). The highest AQI occurred in XJ, followed by SN, NX, GS, and QH. The AQI improved in all the cities except a few cities in SN (Weinan, Xian), and XJ (Changji, Ili, Shihezi, Tacheng, Wujiaqu). In 2018, the average AQI was under the threshold value of 100 in all the cities except Shihezi and Wujiaqu in Xinjiang (Figure 6d).

In the case of seasonal variation, the highest AQI occurred in winter, followed by spring, summer, and autumn, respectively, and improved by 17.5%, 30.8%, 18.7%, 17.4%, respectively, in NWC during 2018 as compared with 2015. The seasonal variation was consistent throughout NWC, e.g., highest AQI in winter and lowest in autumn, except XJ (Figure 3h). Figure 6 illustrates the seasonal (spring (e–h), summer (i–l), autumn (m–p), and winter (q–t)) spatial distribution of AQI in NWC between 2015 and 2018. In different seasons, e.g., spring, summer, autumn, and winter, the number of cities exceeding the AQI threshold value of 100 decreased from 24.5% to 0% (Figure 6e–h), 7.55% to 0% (Figure 6i–l), 7.55% to 0% (Figure 6m–p), and 50.9% to 22.6% (Figure 6q–t), respectively, in NWC. In the case of the monthly variation, a “U” shaped curve was observed with the highest value in winter and the lowest value in summer Figure 4h.

3.5. Proportion of Six Air Quality Index (AQI) Classes

Figure 7 explains the annual (a–d) and seasonal (spring (e–h), summer (i–l), autumn (m–p), and winter (q–t)) proportion of AQI classes in NWC during 2015 to 2018. During the study period, the average proportion of Class I, Class II, Class III, Class IV, Class V, and Class VI accounted for 17.2%, 63.1%, 13.1%, 3.01%, 2.14%, and 1.03% of the days, respectively. In NWC, the proportion of Class I, Class II, Class III, Class IV, Class V, and Class VI experienced an average change of 114.1%, -1.08% , -55.2% , -29.5% , -69.2% , and -58.3% , respectively, in 2018, with respect to 2015. The combined proportion of Class I and II increased by 18.5%, with the highest increase in spring (28.73%), followed by winter (27.2%), autumn (11.2%), and summer (10.9%), indicating significant improvement in air quality over the time span.

3.6. The Major Pollutants/Primary Pollutants

During the study period, PM_{10} was a major pollutant, accounting for more than 32.9% of the days, followed by O_3 (25.9%), $PM_{2.5}$ (16.4%), NO_2 (3.52%), CO (1.43%), and SO_2 (1.01%) in NWC (Figure 8). In 2018, the number of days with PM_{10} , $PM_{2.5}$, SO_2 , and CO as major pollutants decreased by 35%, 38%, 52%, and 90%, respectively, and increased by 46% and 11% for O_3 and NO_2 , respectively. PM_{10} was a major pollutant in autumn (41.3%), spring (39.1%), and a second major pollutant in winter (34.3%), while $PM_{2.5}$ was a major pollutant in winter (42.1%), and O_3 was a major pollutant (59.7%) in summer. The number of days with O_3 as a major pollutant was higher in the hotter months March–September), and, for $PM_{2.5}$, it was higher in the colder months (November–February). During the study period, the number of days with PM_{10} as a major pollutant decreased by 47.2%, 76.3%, and 19.7% in spring, summer, and autumn, respectively, and increased by 4.58% in winter 2018 as compared with 2015. Similarly, the number of days with $PM_{2.5}$ as a major pollutant decreased by 62.3%, 90.8%, 42.9%, and 24.6% in spring, summer, autumn, and winter, respectively. The number of days with SO_2 as a major pollutant decreased in all the seasons except summer, NO_2 decreased in summer and winter, CO decreased in spring, summer, autumn, and winter, while O_3 increased in all the seasons, e.g., in spring, summer, autumn, and winter 2018 as compared with 2015.

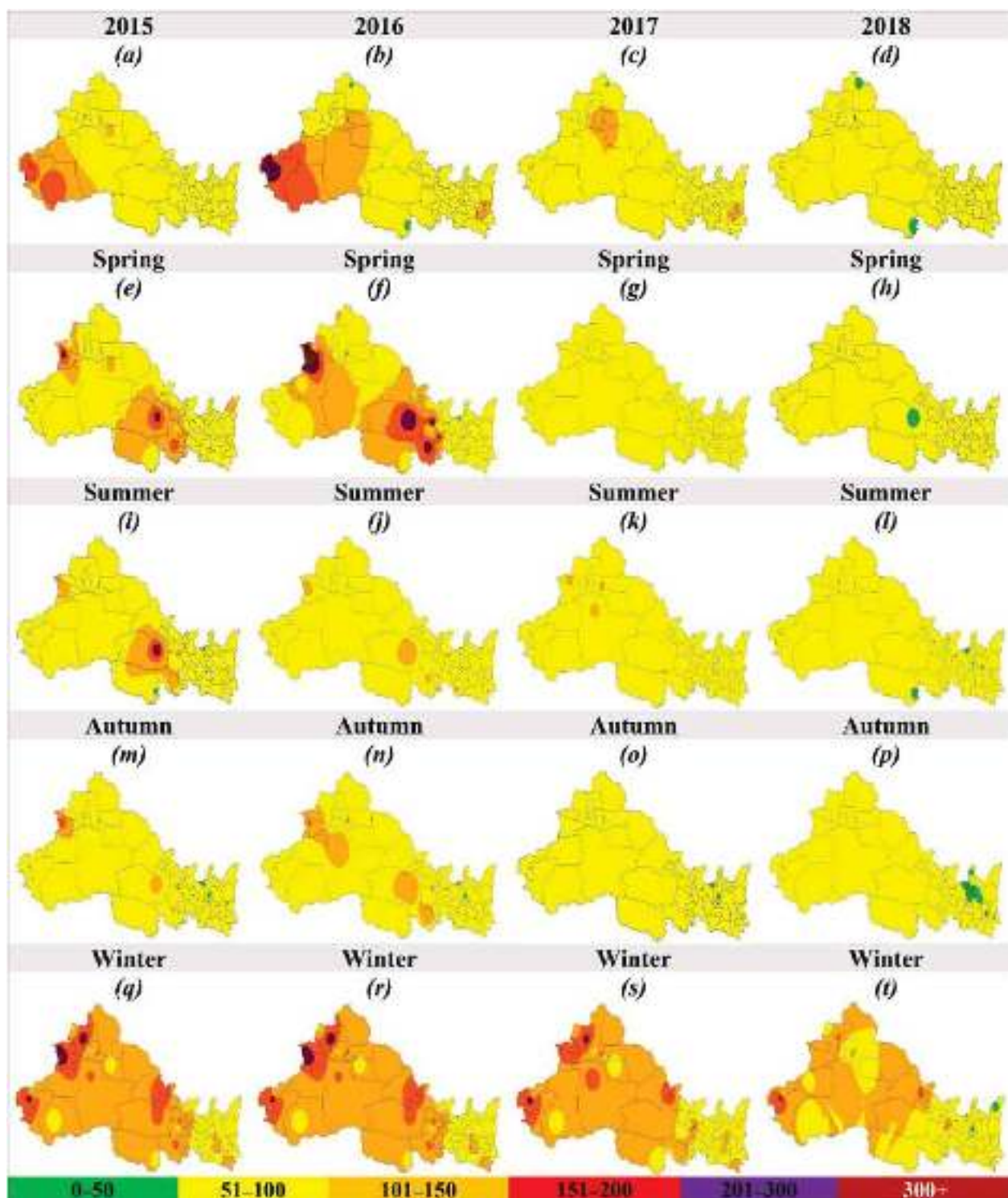


Figure 6. Annual (a–d) and seasonal (spring (e–h), summer (i–l), autumn (m–p), and winter (q–t)) spatial distribution of AQI between 2015 and 2018 in 53 cities of northwest China (NWC). Color represents the different classes of air quality index, e.g., green (0–50, good), yellow (51–100, moderate), orange (101–150, unhealthy for the sensitive group), red (151–200, unhealthy for all), purple (201–300, very unhealthy), and maroon (300+, hazardous).

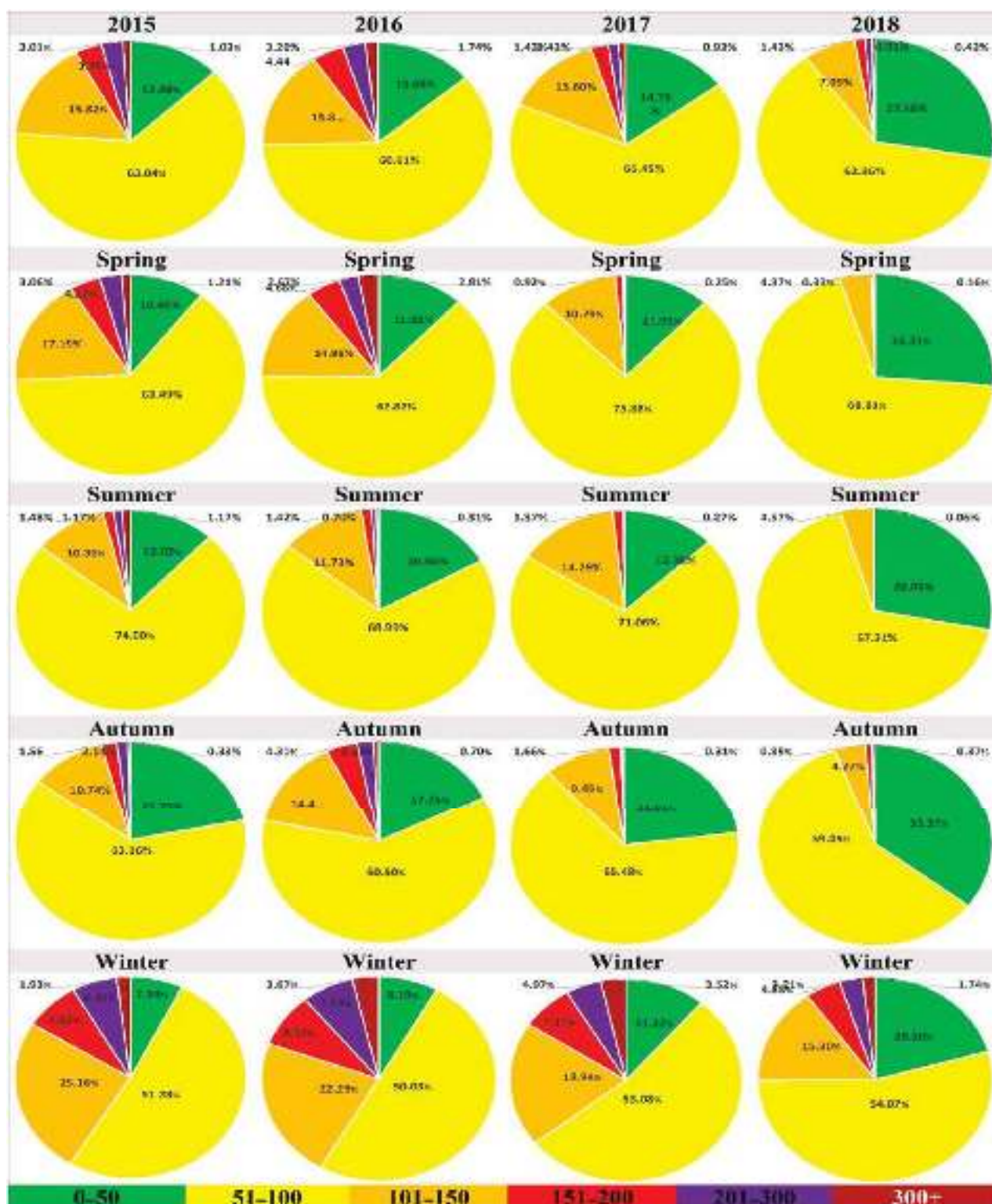


Figure 7. The annual (1st row) and seasonal (spring (2nd row), summer (3rd row), autumn (4th row), and winter (5th row)) distribution of AQ class, e.g., Class I (0–50, good, green), Class II (51–100, moderate, yellow), Class III (101–150, unhealthy for a sensitive group, orange), Class IV (151–200, unhealthy for all, red), Class V (201–300, very unhealthy, purple), and Class VI (300+, hazardous, maroon) in northwest China (NWC) between 2015 and 2018.

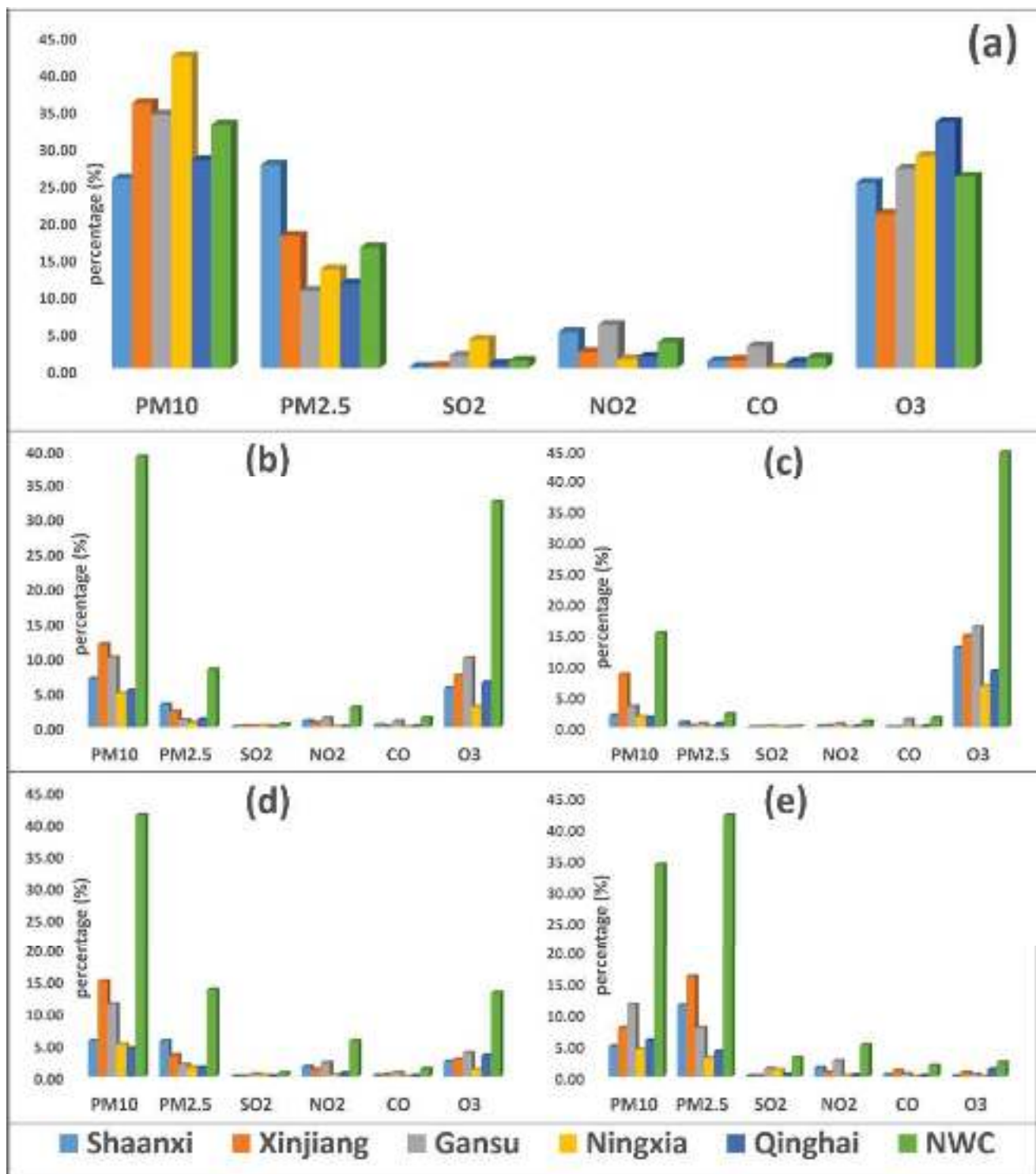


Figure 8. The annual (a) and seasonal (spring (b), summer (c), autumn (d), winter (e)) percentage of days with different primary pollutants (PM_{2.5}, PM₁₀, SO₂, NO₂, CO, and O₃) in five provinces (Shaanxi (SN), Xinjiang (XJ), Gansu (GS), Ningxia (NX), and Qinghai (QH)) of northwest China (NWC) between 2015 and 2018. Descriptions are as follows: light blue bar (Shaanxi), orange bar (Xinjiang), grey bar (Gansu), yellow bar (Ningxia), blue bar (Qinghai), and parrot bar (NWC). The abbreviations are as follows: PM_{2.5} (fine particulate matter), PM₁₀ (coarse particulate matter), SO₂ (sulfur dioxide), NO₂ (nitrogen dioxide), CO (carbon monoxide), and O₃ (ozone).

3.7. Pollution Days/Non-Attainment Days

Any day with one or more pollutants exceeding CAAQS (Grade II) standards is considered as a non-attainment/pollution day. In NWC, the proportion of non-attainment days were 23.3%, 23.9%, 16.2%, and 8.9% during 2015 to 2018, respectively. The proportion of non-attainment days decreased by 61.77% (24%, 47.1%, 79.1%, 77.9%, and 73.9%) in NWC (SN, XJ, GS, NX, and QH) during 2015 to 2018 (Table 1). The highest reduction in the proportion of non-attainment days occurred in spring (79.6%), summer (63.1%), autumn (60.4%), and winter (37.6%), respectively.

3.8. Statistical Analysis

The result of Pearson's correlation (Table S2) indicated that AQI was strongly positively correlated ($R > 0.5$) with $PM_{2.5}$, PM_{10} , SO_2 , NO_2 , and CO on an annual basis and strongly anti-correlated ($R > -0.5$) with O_3 in the NWC (Figure S3a). The seasonal variation in the correlation between AQI and different pollutants was evident (Figure S3b–e). In spring, AQI was strongly correlated ($R > -0.5$) with $PM_{2.5}$, PM_{10} , SO_2 , and CO, moderately correlated ($R > -0.3$) with NO_2 , while strongly anti-correlated ($R > -0.5$) with O_3 (Figure S3b). In summer, AQI was strongly correlated ($R > 0.5$) with $PM_{2.5}$, PM_{10} , and O_3 , weakly correlated ($R > 0.2$) with SO_2 , weakly anti-correlated ($R > -0.1$) with CO, and strongly anti-correlated ($R > -0.5$) with NO_2 (Figure S3c). In autumn, AQI was strongly correlated ($R > 0.5$) with $PM_{2.5}$, PM_{10} , SO_2 , NO_2 , and CO, while strongly anti-correlated ($R > -0.5$) with O_3 (Figure S3d). In winter, AQI was strongly correlated ($R > 0.5$) with $PM_{2.5}$, PM_{10} , SO_2 , and CO, moderately correlated ($R > 0.3$) with NO_2 , and moderately anti-correlated ($R > -0.3$) with O_3 (Figure S3e). Throughout the study period, all the pollutants were positively correlated with each other except O_3 (Table S2).

4. Discussion

During the study period, the average concentrations of $PM_{2.5}$, PM_{10} , SO_2 , NO_2 , CO, and O_3 , decreased in 92.5%, 96.2%, 92.5%, 64.5%, 88.7%, and 11.3% of the 53 cities in NWC. Based on the results above, we concluded that strict environmental regulations have significantly improved the air quality in NWC between 2015 and 2018 [3,20–23]. $PM_{2.5}$ mainly originates from industrial activities, coal consumption, power generation, biomass burning, automobile exhausts, construction activities, road dust, etc. [28–30,50–52]. From 2015 to 2018, the average concentration of $PM_{2.5}$ decreased in all the cities except a few cities (Changji, Ili, Shihezi, Wujiaqu) in the northern part of XJ. Higher pollution in XJ, SN, and GS, $PM_{2.5}$ hotspots [53,54], is because of increased coal-based industry, vehicular emission, civil heating, construction activities, natural sources (dust storms), and adverse meteorology [55–60]. PM_{10} mainly originates from natural sources, e.g., sand storms, haze events, etc., as well as from anthropogenic sources, e.g., developmental activities, industrial emissions, traffic emissions, road dust, etc. [15,26–28]. The highest pollution levels occurred in XJ, followed by SN, NX, GS, and QH. Elevated pollution levels in southern Xinjiang (Kashgar) indicate the influences of emissions from natural sources, e.g., Taklimakan deserts, dust storms, haze events, etc. [61–64]. Similarly, higher particulate pollution in Shaanxi (FWP region) is associated with increased anthropogenic emissions, e.g., industrial activities, construction activities, etc. [55]. All the cities of NWC experienced a reduction in PM_{10} except Shihezi and Wujiaqu in northern XJ, indicating the influence of both manmade and natural emission sources. This decrease is associated with strict environmental regulations, e.g., Chinese Ambient Air Quality Standards (CAAQS) (GB 3095–2012) [17], Atmospheric Pollution Prevention and Control Action Plan (APPCAP, 2013) [18], technical regulation on ambient air quality index (HJ 633–2012) [19], the establishment of nationwide air quality monitoring stations, etc. [3,20–23].

In the case of gaseous pollutants, the average concentration of SO_2 , NO_2 , and CO decreased by 41.9%, 6.19%, and 27.3%, respectively, in NWC. Industrial emissions, coal burning, fossil fuel burning, power generation, traffic exhausts, etc. are major sources of SO_2 , NO_2 , and CO [65–69]. The concentration of SO_2 decreased in all the cities except

Ili, Hami (XJ), Jiuquan (GS), and Yushu (QH), indicating the influence of increased coal combustion, vehicular exhaust, and industrial emission [27,28,57,70]. In the case of NO_2 , the average concentration decreased in 71.7% of the cities of NWC between 2015 and 2018. The highest pollution level occurred in the provincial capitals, e.g., Xi'an (SN), Urumqi (XJ), Lanzhou (GS), etc., and major cities (Ili, Hami, Jiuquan, Yushu, etc.), indicating increased fossil fuel combustion, e.g., automobile exhaust, industrial emission, etc. [34,63,65–69]. Similarly, the highest concentration of CO occurred in SN, followed by XJ, QH, GS, and NX. Higher CO indicates incomplete combustion of fossil fuels, biomass burning, industrial emission, and causes multiple health disorders, e.g., hypoxia, major heart and neural disorders [28,67,68]. In contrast to other pollutants, O_3 increased by 3.69% in NWC during the study period. All the cities experienced an increase in O_3 concentration except Ankang, Shanglou, Longnan, Haibei, Hainan, and Haixi. This increase in O_3 is associated with a decrease in $\text{PM}_{2.5}$ and other pollutants, which slows down the sink of hydroperoxy radicals and helps in the accumulation of ozone [55].

In terms of seasonality, $\text{PM}_{2.5}$, PM_{10} , SO_2 , NO_2 , and CO experienced the same seasonal variation, e.g., highest in winter and lowest in summer. Higher pollution in winter is associated with increased coal combustion, civil heating, power generation, fossil fuel burning, industrial activity, vehicular exhausts, and adverse/stagnant meteorology [13–15,26–30,50–52,71–75]. In the case of PM_{10} , higher pollution levels also occurred from March to May (spring) due to haze events [76,77]. In contrast to other pollutants, the concentration of O_3 was highest in summer and lowest in winter [14,28,30,78]. Ozone is a secondary pollutant, formed due to a photochemical reaction between VOCs and NO_x [43,44,79]. The concentration of ozone in the summer was approximately twice that in winter due to lower NO_x levels in winter as NO_x levels decrease the O_3 depletion and enhance the accumulation of O_3 [80]. Similarly, higher temperatures, e.g., in summer, favor the accumulation of ozone [81–83].

The $\text{PM}_{2.5}/\text{PM}_{10}$ ratio reflects air quality, pollution sources, and origin, e.g., a higher $\text{PM}_{2.5}/\text{PM}_{10}$ ratio indicates the increased proportion of $\text{PM}_{2.5}$, mainly emitted from anthropogenic activities, and a lower ratio indicates an increased proportion of PM_{10} , mainly from natural activities [28,61–64]. During the study period (2015–2018), the $\text{PM}_{2.5}/\text{PM}_{10}$ ratio slightly decreased by 0.43% and in 50.9% of the cities of NWC. This decrease is associated with a reduction in $\text{PM}_{2.5}$ over time. In general, the $\text{PM}_{2.5}/\text{PM}_{10}$ ratio was higher in winter (low temperature) as compared with summer (high temperature) due to increased anthropogenic activities that release a significant amount of $\text{PM}_{2.5}$ and stable atmospheric conditions that help the accumulation of pollution [26–29,53,54,84].

During the study period (2015–2018), the AQI improved by 21.3%, and 86.8% of the cities of NWC experienced AQI improvement. This improvement is associated with a reduction in the criteria pollutants over time. AQI crossed the threshold value of 100 in 10 cities, out of which seven cities are in Xinjiang (Kashgar, Hotan, Aksu, Wujiaqu, Crete, Urumqi, Turpan) and three cities are in Shaanxi (Xiangyang, Xi'an, Weinan) (Table S1). The higher AQI values in Xinjiang and Shaanxi are associated with the increased coal-based industry, civil heating, and vehicular exhaust [3,14,30,51,52,56,69,85]. In the case of seasonal variations, the highest AQI occurred in winter due to increased anthropogenic emissions and stable atmospheric conditions [15,58,84]. In NWC, the proportion of AQI “Class I” improved by 114.1%, while the proportion of Class II, Class III, Class IV, Class V, and Class VI decreased by 1.08%, 55.2%, 29.5%, 69.2%, and 58.3%, respectively, during 2015 to 2018. The proportion of AQI “Class I” improved from 12.9% in 2015 to 27.6% in 2018. Similarly, the proportion of AQI “Class I” improved in all the provinces, e.g., SN, XJ, GS, NX, and QH, in all the seasons, and improved by 2.53 times, 2.33 times, 1.63 times, and 2.79 times in spring, summer, autumn, and winter in 2018 as compared with 2015, which indicates improvement in air quality [28,57].

During the study period (2015–2018), the proportion of days with PM_{10} , $\text{PM}_{2.5}$, SO_2 , and CO as a major pollutant decreased by 35%, 38%, 52%, and 90%, respectively, due to strict environmental legislation [20–23]. $\text{PM}_{2.5}$ was a major pollutant in winter (42%), indicating

anthropogenic emissions, e.g., coal burning, civil heat, industrial emissions, and vehicular emissions [28,56–58]. Similarly, O_3 was a major pollutant (44.7%) in summer due to lower NO_x levels as lower NO_x levels prevent ozone depletion and the higher temperature in summer favors ozone generation and accumulation [78,80,82,83,86–88], while PM_{10} was a major pollutant in autumn (41.3%), spring (39.1%), and the second major pollutant in winter (34.3%). The number of days with PM_{10} as a major pollutant was higher in southern Xinjiang due to emissions from natural sources, e.g., the Taklimakan desert, sand storms [61–64,89]. Any day with one or more pollutants exceeding CAAQS (Grade II) is considered as a non-attainment/pollution day [2,30]. During the study period, the proportion of non-attainment days decreased by 61.8% in NWC. Similarly, the proportion of non-attainment days decreased in all the provinces, e.g., SN, XJ, GS, NX, and QH, and experienced a reduction of 79.6%, 63.1%, 60.4%, and 37.6% in spring, summer, autumn, and winter, respectively, which clearly indicates that the ambient air quality improved significantly.

Rapid economic development, industrialization, haze events, dust storms, and adverse meteorological conditions play a crucial role in air quality deterioration [2,4–10]. The Chinese government is working proactively to combat the pollution levels by revising and implementing strict environmental regulations [3,20,21]. According to this study, the concentration of $PM_{2.5}$, PM_{10} , SO_2 , NO_2 , and CO, AQI, the proportion of AQI “Class I”, and pollution days decreased significantly in NWC between 2015 and 2018.

5. Conclusions

In this study, we examined the spatial and temporal variation of ambient air quality in northwest China (NWC) for a period of four years (2015–2018). During the study period, the average concentration of $PM_{2.5}$, PM_{10} , SO_2 , NO_2 , CO, and O_3 decreased in 92.5%, 96.2%, 92.5%, 64.5%, 88.7%, and 11.3% of the cities in NWC. The annual average concentration of particulate matter ($PM_{2.5}$ and PM_{10}) exceeded the CAAQS Grade II standards and WHO recommended air quality guidelines in NWC, while the annual average concentration of SO_2 and NO_2 complied with the CAAQS Grade II standards in NWC. In the case of seasonality, the highest pollution level occurred in winter except for ozone, with varying degrees of spatial distribution. The AQI, the proportion of AQI Class I, and the number of pollution days improved by 21.3%, 114.1%, and 61.8%, respectively, in NWC. The AQI improved in all the seasons, with the maximum improvement in spring followed by summer, winter, and autumn. In NWC, PM_{10} was a major pollutant for most of the days, followed by O_3 , $PM_{2.5}$, NO_2 , CO, and SO_2 with different spatial and temporal variations. A strong correlation occurred between AQI and all the pollutants except O_3 . Stricter regulations, e.g., a three-year action plan to win the blue sky defense war, sector-specific guidelines, and strict enforcement of environmental legislation, are the keys to pollution-free and breathable air. This paper comprehensively discussed the spatio-temporal characteristics of the ambient air quality in NWC and calls for future detailed assessment focusing on source apportionment, health risk assessment, the impact of meteorology, dispersion modeling, and impact of the chemical processes that influence the air quality.

Supplementary Materials: The following are available online at <https://www.mdpi.com/article/10.3390/atmos13030375/s1>, Figure S1: The locations of 53 cities in five provinces (Shaanxi (SN), Xinjiang (XJ), Gansu (GS), Ningxia (NX), and Qinghai (QH)) northwest China (NWC). Color represents the different classes of air quality index, e.g., green (0–50, good), yellow (51–100, moderate), orange (101–150, unhealthy for a sensitive group), red (151–200, unhealthy for all), purple (201–300, very unhealthy), and maroon (300+, hazardous); Figure S2: The seasonal (spring (light blue line), summer (orange line), autumn (grey line), and winter (yellow line)) spatial distribution of $PM_{2.5}$ (a), PM_{10} (b), SO_2 (c), NO_2 (d), CO (e), and O_3 (f) in 53 cities of northwest China between 2015 and 2018. Descriptions are as follows: light blue line with dots (spring), orange line with dots (summer), grey line with dots (autumn), yellow line with dots (winter), and the blue line (CAAQS, daily mean). The abbreviations are as follows: $PM_{2.5}$ (fine particulate matter), PM_{10} (coarse particulate matter), SO_2 (sulfur dioxide), NO_2 (nitrogen dioxide), CO (carbon monoxide), and O_3 (ozone); Figure S3: Annual

(a) and seasonal (spring (b), summer (c), autumn (d), winter (e)) relationship between air quality index (AQI) and criteria pollutants (PM_{2.5}, PM₁₀, SO₂, NO₂, CO, and O₃). The abbreviations are as follows: AQI (air quality index), PM_{2.5} (fine particulate matter), PM₁₀ (coarse particulate matter), SO₂ (sulfur dioxide), NO₂ (nitrogen dioxide), CO (carbon monoxide), and O₃ (ozone); Table S1: Lists of cities, their rankings in five provinces (Shaanxi (SN), Xinjiang (XJ), Gansu (GS), Ningxia (NX), and Qinghai (QH)) of northwest China (NWC) between 2015 and 2018; Table S2: Pearson correlation between AQI and six criteria pollutants (PM_{2.5}, PM₁₀, SO₂, NO₂, CO, and O₃) in northwest China (NWC) between 2015 and 2018. The abbreviations are as follows: AQI (air quality index), PM_{2.5} (fine particulate matter), PM₁₀ (coarse particulate matter), SO₂ (sulfur dioxide), NO₂ (nitrogen dioxide), CO (carbon monoxide), and O₃ (ozone).

Author Contributions: Conceptualization, S.Z.; data curation/accumulation, S.Z.; investigation and data validation, J.L. and M.B.; methodology, S.Z.; data modelling, S.Z.; GIS mapping, S.Z.; writing—original draft preparation, S.Z.; review and editing, J.L. and M.B.; supervision, J.L.; funding acquisition, J.L. All authors have read and agreed to the published version of the manuscript.

Funding: This research work is supported by the National Natural Science Foundation of China (No. 21667026), the Social Science Foundation of Xinjiang Production and Construction Corps (No. 18YB13), and the Startup Foundation for Introduction Talent of NUIST (2017r107).

Institutional Review Board Statement: Not applicable.

Informed Consent Statement: Not applicable.

Data Availability Statement: The data presented in this study are available upon request from the corresponding author.

Acknowledgments: I would like to acknowledge the China National Environmental Monitoring Center (CNEMC) for the provision of air quality data. I am also very thankful to Jianjiang Lu and research scholar Anam Arshad from the School of Chemistry and Chemical Engineering, Shihezi University for helping and guiding me throughout the preparation of this paper.

Conflicts of Interest: The authors declare no conflict of interest.

References

- Li, R.; Wang, Z.; Cui, L.; Fu, H.; Zhang, L.; Kong, L.; Chen, J. Air pollution characteristics in China during 2015–2016: Spatiotemporal variations and key meteorological factors. *Sci. Total Environ.* **2019**, *648*, 902–915. [CrossRef] [PubMed]
- Luo, H.; Guan, Q.; Lin, J.; Wang, Q.; Yang, L.; Tan, Z.; Wang, N. Air pollution characteristics and human health risks in key cities of northwest China. *J. Environ. Manage.* **2020**, *269*, 110791. [CrossRef] [PubMed]
- Maji, K.J. Substantial changes in PM_{2.5} pollution and corresponding premature deaths across China during 2015–2019: A model prospective. *Sci. Total Environ.* **2020**, *729*, 138838. [CrossRef] [PubMed]
- Qiu, Y.; Yang, T.; Seyler, B.C.; Wang, X.; Wang, Y.; Jiang, M.; Li, F. Ambient air pollution and male fecundity: A retrospective analysis of longitudinal data from a Chinese human sperm bank (2013–2018). *Environ. Res.* **2020**, *186*, 109528. [CrossRef] [PubMed]
- Yang, J.; Ji, Z.; Kang, S.; Zhang, Q.; Chen, X.; Lee, S.Y. Spatiotemporal variations of air pollutants in western China and their relationship to meteorological factors and emission sources. *Environ. Pollut.* **2019**, *254*, 112952. [CrossRef]
- Zhao, S.; Yin, D.; Yu, Y.; Kang, S.; Qin, D.; Dong, L. PM_{2.5} and O₃ pollution during 2015–2019 over 367 Chinese cities: Spatiotemporal variations, meteorological and topographical impacts. *Environ. Pollut.* **2020**, *264*, 114694. [CrossRef]
- Pu, H.; Luo, K.; Wang, P.; Wang, S.; Kang, S. Spatial variation of air quality index and urban driving factors linkages: Evidence from Chinese cities. *Environ. Sci. Pollut. Res.* **2017**, *24*, 4457–4468. [CrossRef]
- Wang, W.; Cui, K.; Zhao, R.; Hsieh, L.T.; Lee, W.J. Characterization of the air quality index for Wuhu and Bengbu cities, China. *Aerosol Air Qual. Res.* **2018**, *18*, 1198–1220. [CrossRef]
- Shao, Z.; Jia, X.; Zhong, X.; Wang, D.; Wei, J.; Wang, Y.; Chen, L. Detection, extinguishing, and monitoring of a coal fire in Xinjiang, China. *Environ. Sci. Pollut. Res.* **2018**, *25*, 26603–26616. [CrossRef]
- Soleimani, M.; Amini, N.; Sadeghian, B.; Wang, D.; Fang, L. Heavy metals and their source identification in particulate matter (PM_{2.5}) in Isfahan City, Iran. *J. Environ. Sci.* **2018**, *72*, 166–175. [CrossRef]
- Zhao, S.; Yu, Y.; Yin, D.; He, J.; Liu, N.; Qu, J.; Xiao, J. Annual and diurnal variations of gaseous and particulate pollutants in 31 provincial capital cities based on in situ air quality monitoring data from China National Environmental Monitoring Center. *Environ. Int.* **2016**, *86*, 92–106. [CrossRef] [PubMed]
- Fan, H.; Zhao, C.; Yang, Y. A comprehensive analysis of the spatio-temporal variation of urban air pollution in China during 2014–2018. *Atmos. Environ.* **2020**, *220*, 117066. [CrossRef]

13. Feng, J.; Yu, H.; Mi, K.; Su, X.; Li, Y.; Li, Q.; Sun, J. One-year study of PM_{2.5} in Xinxiang city, North China: Seasonal characteristics, climate impact and source. *Ecotoxicol. Environ. Saf.* **2018**, *154*, 75–83. [CrossRef] [PubMed]
14. Liu, B.; Wu, J.; Zhang, J.; Wang, L.; Yang, J.; Liang, D.; Zhang, Q. Characterization and source apportionment of PM_{2.5} based on error estimation from EPA PMF 5.0 model at a medium city in China. *Environ. Pollut.* **2017**, *222*, 10–22. [CrossRef]
15. Turap, Y.; Rekefu, S.; Wang, G.; Talifu, D.; Gao, B.; Aierken, T.; Nuerla, A. Chemical Characteristics and Source Apportionment of PM_{2.5} during winter in the Southern Part of Urumqi, China. *Aerosol Air Qual. Res.* **2019**, *19*, 1325–1337. [CrossRef]
16. Wang, H.; Chen, H. Understanding the recent trend of haze pollution in eastern China: Roles of climate change. *Atmos. Chem. Phys.* **2016**, *16*, 4205–4211. [CrossRef]
17. GB 3095-2012. *Chinese Ambient Air Quality Standards (CAAQS)*; Ministry of Environmental Protection of the Peoples Republic of China (MEP): Beijing, China, 2012.
18. Zhu, J.; Chen, L.; Liao, H. Multi-pollutant air pollution and associated health risks in China from 2014 to 2020. *Atmos. Environ.* **2022**, *268*, 118829. [CrossRef]
19. HJ 633-2012. *Technical Regulation on Ambient Air Quality Index (on Trial)*; Ministry of Environmental Protection of the Peoples Republic of China (MEP): Beijing, China, 2012.
20. Ye, W.F.; Ma, Z.Y.; Ha, X.Z. Spatial-temporal patterns of PM_{2.5} concentrations for 338 Chinese cities. *Sci. Total Environ.* **2018**, *631*, 524–533. [CrossRef]
21. Song, C.; Wu, L.; Xie, Y.; He, J.; Chen, X.; Wang, T.; Dai, Q. Air pollution in China: Status and spatiotemporal variations. *Environ. Pollut.* **2017**, *227*, 334–347. [CrossRef]
22. Guo, H.; Cheng, T.; Gu, X.; Wang, Y.; Chen, H.; Bao, F.; Meng, C. Assessment of PM_{2.5} concentrations and exposure throughout China using ground observations. *Sci. Total Environ.* **2017**, *601*, 1024–1030. [CrossRef]
23. Shen, Y.; Zhang, L.; Fang, X.; Ji, H.; Li, X.; Zhao, Z. Spatiotemporal patterns of recent PM_{2.5} concentrations over typical urban agglomerations in China. *Sci. Total Environ.* **2019**, *655*, 13–26. [CrossRef] [PubMed]
24. Guo, P.; Umarova, A.B.; Luan, Y. The spatiotemporal characteristics of the air pollutants in China from 2015 to 2019. *PLoS ONE* **2020**, *15*, e0227469. [CrossRef] [PubMed]
25. Li, T.; Guo, Y.; Liu, Y.; Wang, J.; Wang, Q.; Sun, Z.; He, M.Z.; Shi, X. Estimating mortality burden attributable to short-term PM_{2.5} exposure: A national observational study in China. *Environ. Intl.* **2019**, *125*, 245–251. [CrossRef]
26. Turap, Y.; Talifu, D.; Wang, X.; Abulizi, A.; Maihemuti, M.; Tursun, Y.; Rekefu, S. Temporal distribution and source apportionment of PM_{2.5} chemical composition in Xinjiang, NW-China. *Atmos. Res.* **2019**, *218*, 257–268. [CrossRef]
27. Chen, J.; Lu, J.; Ning, J.; Yan, Y.; Li, S.; Zhou, L. Characteristics and sources analysis of PM_{2.5} in a major industrial city of northern Xinjiang, China. *SN Appl. Sci.* **2020**, *2*, 1–9. [CrossRef]
28. Yin, Z.; Cui, K.; Chen, S.; Zhao, Y.; Chao, H.R.; Chang-Chien, G.P. Characterization of the air quality index for Urumqi and Turfan cities, China. *Aerosol Air Qual. Res.* **2019**, *19*, 282–306. [CrossRef]
29. Zhao, X.; Zhou, W.; Han, L.; Locke, D. Spatiotemporal variation in PM_{2.5} concentrations and their relationship with socioeconomic factors in China's major cities. *Environ. Intl.* **2019**, *133*, 105145. [CrossRef]
30. Wang, Y.; Ying, Q.; Hu, J.; Zhang, H. Spatial and temporal variations of six criteria air pollutants in 31 provincial capital cities in China during 2013–2014. *Environ. Intl.* **2014**, *73*, 413–422. [CrossRef]
31. Kuerban, M.; Waili, Y.; Fan, F.; Liu, Y.; Qin, W.; Dore, A.J.; Zhang, F. Spatio-temporal patterns of air pollution in China from 2015 to 2018 and implications for health risks. *Environ. Pollut.* **2020**, *258*, 113659. [CrossRef]
32. Cohen, A.J.; Brauer, M.; Burnett, R.; Anderson, H.R.; Frostad, J.; Estep, K.; Feigin, V. Estimates and 25-year trends of the global burden of disease attributable to ambient air pollution: An analysis of data from the Global Burden of Diseases Study 2015. *Lancet.* **2017**, *389*, 1907–1918. [CrossRef]
33. Zhu, G.; Hu, W.; Liu, Y.; Cao, J.; Ma, Z.; Deng, Y.; Wang, H. Health burdens of ambient PM_{2.5} pollution across Chinese cities during 2006–2015. *J. Environ. Manage.* **2019**, *24*, 250–256. [CrossRef] [PubMed]
34. Wang, Q.; Wang, J.; Zhou, J.; Ban, J.; Li, T. Estimation of PM_{2.5} associated disease burden in China in 2020 and 2030 using population and air quality scenarios: A modelling study. *Lancet Planet. Health.* **2019**, *3*, 71–80. [CrossRef]
35. Li, R.; Kou, X.; Geng, H.; Xie, J.; Tian, J.; Cai, Z.; Dong, C. Mitochondrial damage: An important mechanism of ambient PM_{2.5} exposure-induced acute heart injury in rats. *J. Hazard. Mater.* **2015**, *287*, 392–401. [CrossRef]
36. Mannucci, P.M.; Franchini, M. Health effects of ambient air pollution in developing countries. *Int. J. Environ. Res. Public Health* **2017**, *14*, 1048. [CrossRef] [PubMed]
37. Zhang, J.; Liu, Y.; Cui, L.L.; Liu, S.Q.; Yin, X.X.; Li, H.C. Ambient air pollution, smog episodes and mortality in Jinan, China. *Sci. Rep.* **2017**, *7*, 1–8. [CrossRef]
38. Xie, Y.; Dai, H.; Zhang, Y.; Wu, Y.; Hanaoka, T.; Masui, T. Comparison of health and economic impacts of PM_{2.5} and ozone pollution in China. *Environ. Int.* **2019**, *130*, 104881. [CrossRef]
39. HJ 630-2011. *Technical Guideline on Environmental Monitoring Quality Management*; Ministry of Environmental Protection of the People Republic of China (MEP): Beijing, China, 2011.
40. Thach, T.Q.; Tsang, H.; Cao, P.; Ho, L.M. A novel method to construct an air quality index based on air pollution profiles. *Int. J. Hyg. Environ. Health.* **2018**, *221*, 17–26. [CrossRef]
41. Cheng, W.L.; Chen, Y.S.; Zhang, J.; Lyons, T.J.; Pai, J.L.; Chang, S.H. Comparison of the revised air quality index with the PSI and AQI indices. *Sci. Total Environ.* **2007**, *382*, 191–198. [CrossRef]

42. She, Q.N.; Peng, X.; Xu, Q.; Long, L.B.; Wei, N.; Liu, M.; Jia, W.X. Air quality and its response to satellite-derived urban form in the Yangtze River Delta, China. *Intl. J. Environ. Res. Public Health*. **2017**, *75*, 297–306. [CrossRef]
43. Xu, K.; Cui, K.; Young, L.H.; Hsieh, Y.K.; Wang, Y.F.; Zhang, J.; Wan, S. Impact of the COVID-19 Event on Air Quality in Central China. *Aerosol Air Qual. Res.* **2020**, *20*, 915–929. [CrossRef]
44. Xu, K.; Cui, K.; Young, L.H.; Wang, Y.F.; Hsieh, Y.K.; Wan, S.; Zhang, J. Air Quality Index, Indicator Air Pollutants and Impact of COVID-19 Event on the Air Quality near Central China. *Aerosol Air Qual. Res.* **2020**, *20*, 1204–1221. [CrossRef]
45. Apak, S.; Atay, E. Industrial Policy and Climate Change Management of Turkey as an EU candidate country. *Procedia-Soc. Behav. Sci.* **2013**, *75*, 246–254. [CrossRef]
46. Das, M.; Das, A.; Ghosh, S.; Sarkar, R.; Saha, S. Spatio-temporal concentration of atmospheric particulate matter (PM_{2.5}) during pandemic: A study on most polluted cities of indo-gangetic plain. *Urban. Climate* **2021**, *35*, 100758. [CrossRef]
47. Zhang, H.; Tripathi, N.K. Geospatial hot spot analysis of lung cancer patients correlated to fine particulate matter (PM_{2.5}) and industrial wind in Eastern Thailand. *J. Clean. Prod.* **2018**, *170*, 407–424. [CrossRef]
48. Zaib, S.; Lu, J.; Shahid, M.Z.; Ahmar, S.; Shahid, I. Impact of SARS-CoV-2 on Ambient Air Quality in Northwest China (NWC). *Atmosphere* **2021**, *12*, 518. [CrossRef]
49. RStudio Team. RStudio: Integrated Development for R. R Studio, PBC, Boston, MA 2020. Available online: <http://www.rstudio.com> (accessed on 28 January 2022).
50. Chen, J.; Lu, J.; Ning, J.; Yan, Y.; Li, S.; Zhou, L. Pollution characteristics, sources, and risk assessment of heavy metals and per fluorinated compounds in PM_{2.5} in the major industrial city of northern Xinjiang, China. *Air Qual. Atmos. Health*. **2019**, *12*, 909–918. [CrossRef]
51. Liu, T.; Zhuang, G.; Huang, K.; Lin, J.; Wang, Q.; Deng, C.; Fu, J.S. A Typical Formation Mechanism of Heavy Haze-Fog Induced by Coal Combustion in an Inland City in North-Western China. *Aerosol Air Qual. Res.* **2017**, *17*, 98–107. [CrossRef]
52. Du, W.; Zhang, Y.; Chen, Y.; Xu, L.; Chen, J.; Deng, J.; Xiao, H. Chemical characterization and source apportionment of PM_{2.5} during spring and winter in the Yangtze River Delta, China. *Aerosol Air Qual. Res.* **2017**, *17*, 2165–2180. [CrossRef]
53. Zhao, Z.; Lv, S.; Zhang, Y.; Zhao, Q.; Shen, L.; Xu, S.; Jin, C. Characteristics and source apportionment of PM_{2.5} in Jiaying, China. *Environ. Sci. Pollut. Res.* **2019**, *26*, 7497–7511. [CrossRef]
54. Zhao, D.; Chen, H.; Yu, E.; Luo, T. PM_{2.5}/PM₁₀ Ratios in Eight Economic Regions and Their Relationship with Meteorology in China. *Adv. Meteorol.* **2019**. [CrossRef]
55. Shen, F.; Zhang, L.; Jiang, L.; Tang, M.; Gai, X.; Chen, M.; Ge, X. Temporal variations of six ambient criteria air pollutants from 2015 to 2018, their spatial distributions, health risks and relationships with socioeconomic factors during 2018 in China. *Environ. Int.* **2020**, *137*, 105556. [CrossRef] [PubMed]
56. Da, Y.L.M.A.B.; Limu, D.L.N.T.L.; Miti, A.B.L.Y.; Wang, X.; Ding, X. Autumn and wintertime polycyclic aromatic hydrocarbons in PM_{2.5} and PM_{2.5–10} from Urumqi, China. *Aerosol Air Qual. Res.* **2013**, *13*, 407–414. [CrossRef]
57. Ding, Y.; Lu, J.; Liu, Z.; Li, W.; Chen, J. Volatile organic compounds in Shihezi, China, during the heating season: Pollution characteristics, source apportionment, and health risk assessment. *Environ. Sci. Pollut. Res.* **2020**, *27*, 16439–16450. [CrossRef] [PubMed]
58. Xu, G.; Jiao, L.; Zhang, B.; Zhao, S.; Yuan, M.; Gu, Y.; Tang, X. Spatial and temporal variability of the PM_{2.5}/PM₁₀ ratio in Wuhan, Central China. *Aerosol Air Qual. Res.* **2016**, *17*, 741–751. [CrossRef]
59. Zhang, Q.; Streets, D.G.; Carmichael, G.R.; He, K.B.; Huo, H.; Kannari, A.; Chen, D. Asian emissions in 2006 for the NASA INTEX-B mission. *Atmos. Chem. Phys.* **2009**, *9*, 5131–5153. [CrossRef]
60. Zhao, Y.; Nielsen, C.P.; Lei, Y.; McElroy, M.B.; Hao, J. Quantifying the uncertainties of a bottom-up emission inventory of anthropogenic atmospheric pollutants in China. *Atmos. Chem. Phys.* **2011**, *10*, 29075–29111. [CrossRef]
61. Pey, J.; Querol, X.; Alastuey, A.; Forastiere, F.; Stafoggia, M. African dust outbreaks over the Mediterranean Basin during 2001–2011: PM₁₀ concentrations, phenomenology and trends, and its relation with synoptic and mesoscale meteorology. *Atmos. Chem. Phys.* **2013**, *13*, 1395–1410. [CrossRef]
62. Wang, S.; Zhang, M.; Minguillón, M.C.; Zhang, X.; Feng, F.; Qiu, X. PM₁₀ concentration in urban atmosphere around the eastern Tien Shan, Central Asia during 2007–2013. *Environ. Sci. Pollut. Res.* **2015**, *22*, 6864–6876. [CrossRef]
63. Wang, Y.; Zhang, J.; Bai, Z.; Yang, W.; Zhang, H.; Mao, J.; Chen, L. Background concentrations of PMs in Xinjiang, West China: An estimation based on meteorological filter method and Eckhardt algorithm. *Atmos. Res.* **2019**, *215*, 141–148. [CrossRef]
64. Wang, W.; Samat, A.; Abuduwaali, J.; Ge, Y. Spatio-Temporal Variations of Satellite-Based PM_{2.5} Concentrations and Its Determinants in Xinjiang, Northwest of China. *Int. J. Environ. Res. Public Health*. **2020**, *17*, 2157. [CrossRef]
65. Ashraf, A.; Butt, A.; Khalid, I.; Alam, R.U.; Ahmad, S.R. Smog analysis and its effect on reported ocular surface diseases: A case study of 2016 smog event of Lahore. *Atmos. Environ.* **2019**, *198*, 257–264. [CrossRef]
66. Bourdrel, T.; Bind, M.A.; Béjot, Y.; Morel, O.; Argacha, J.F. Cardiovascular effects of air pollution. *Arch. Cardiovasc. Dis.* **2017**, *110*, 634–642. [CrossRef] [PubMed]
67. Guo, H.; Wang, T.; Simpson, I.J.; Blake, D.R.; Yu, X.M.; Kwok, Y.H.; Li, Y.S. Source contributions to ambient VOCs and CO at a rural site in eastern China. *Atmos. Environ.* **2004**, *38*, 4551–4560. [CrossRef]
68. Kato, S.; Shiobara, Y.; Uchiyama, K.; Miura, K.; Okochi, H.; Kobayashi, H.; Hatakeyama, S. Atmospheric CO, O₃, and SO₂ measurements at the summit of Mt. Fuji during the summer of 2013. *Aerosol Air Qual. Res.* **2016**, *16*, 2368–2377. [CrossRef]

69. Wang, Y.; Jia, C.; Tao, J.; Zhang, L.; Liang, X.; Ma, J.; Zhang, K. Chemical characterization and source apportionment of PM_{2.5} in a semi-arid and petrochemical-industrialized city, Northwest China. *Sci. Total Environ.* **2016**, *573*, 1031–1040. [CrossRef]
70. Wang, M.; Zheng, S.; Nie, Y.; Weng, J.; Cheng, N.; Hu, X.; Bai, Y. Association between short-term exposure to air pollution and dyslipidemias among type 2 diabetic patients in northwest China: A population-based study. *Intl. J. Environ. Res. Public Health*. **2018**, *15*, 631. [CrossRef]
71. Ma, X.; Xiao, Z.; He, L.; Shi, Z.; Cao, Y.; Tian, Z.; Liu, J. Chemical Composition and Source Apportionment of PM_{2.5} in Urban Areas of Xiangtan, Central South China. *Int. J. Environ. Res. Public Health* **2019**, *16*, 539. [CrossRef]
72. Tao, J.; Gao, J.; Zhang, L.; Zhang, R.; Che, H.; Zhang, Z.; Hsu, S.C. PM_{2.5} pollution in a megacity of southwest China: Source apportionment and implication. *Atmos. Chem. Phys.* **2014**, *14*, 8679–8699. [CrossRef]
73. Alam, K.; Mukhtar, A.; Shahid, I.; Blaschke, T.; Majid, H.; Rahman, S.; Rahman, N. Source Apportionment and Characterization of Particulate Matter (PM₁₀) in Urban Environment of Lahore. *Aerosol Air Qual. Res.* **2014**, *14*, 1851–1861. [CrossRef]
74. Chatterjee, A.; Sarkar, C.; Adak, A.; Mukherjee, U.; Ghosh, S.K.; Raha, S. Ambient air quality during Diwali festival over Kolkata—a mega-city in India. *Aerosol Air Qual. Res.* **2013**, *13*, 1133–1144. [CrossRef]
75. Bilal, M.; Mhawish, A.; Nichol, J.E.; Qiu, Z.; Nazeer, M.; Ali, M.A.; Ke, S. Air pollution scenario over Pakistan: Characterization and ranking of extremely polluted cities using long-term concentrations of aerosols and trace gases. *Remote Sens. Environ.* **2021**, *264*, 112617. [CrossRef]
76. Huang, X.; Zhang, J.; Luo, B.; Wang, L.; Tang, G.; Liu, Z.; Wang, Y. Water-soluble ions in PM_{2.5} during spring haze and dust periods in Chengdu, China: Variations, nitrate formation and potential source areas. *Environ. Pollut.* **2018**, *243*, 1740–1749. [CrossRef] [PubMed]
77. Li, H.; Duan, F.; Ma, Y.; He, K.; Zhu, L.; Ma, T.; Kimoto, T. Case study of spring haze in Beijing: Characteristics, formation processes, secondary transition, and regional transportation. *Environ. Pollut.* **2018**, *242*, 544–554. [CrossRef] [PubMed]
78. Chai, F.; Gao, J.; Chen, Z.; Wang, S.; Zhang, Y.; Zhang, J.; Ren, C. Spatial and temporal variation of particulate matter and gaseous pollutants in 26 cities in China. *J. Environ. Sci.* **2014**, *26*, 75–82. [CrossRef]
79. Zhang, H.; Ying, Q. Contributions of local and regional sources of NO_x to ozone concentrations in Southeast Texas. *Atmos. Environ.* **2011**, *45*, 2877–2887. [CrossRef]
80. Chameides, W.L.; Fehsenfeld, F.; Rodgers, M.O.; Cardelino, C.; Martinez, J.; Parrish, D.; Wang, T. Ozone precursor relationships in the ambient atmosphere. *J. Geophys. Res. Atmos.* **1992**, *97*, 6037–6055. [CrossRef]
81. Zhao, R.; Cui, K.P.; Wang, W.W.; Wang, L.C.; Yan, P. Atmospheric PM_{2.5} and total PCDD/FsWHO2005-TEQ level: A case of Handan and Kaifeng cities, China. *Aerosol Air Qual. Res.* **2018**, *18*, 994–1007. [CrossRef]
82. Biswas, M.S.; Ghude, S.D.; Gurnale, D.; Prabhakaran, T.; Mahajan, A.S. Simultaneous Observations of Nitrogen Dioxide, Formaldehyde and Ozone in the Indo- Gangetic Plain. *Aerosol Air Qual. Res.* **2019**, *19*, 1749–1764. [CrossRef]
83. Rasheed, A.; Aneja, V.P.; Aiyer, A.; Rafique, U. Measurements and analysis of air quality in Islamabad, Pakistan. *Earth's Future* **2014**, *2*, 303–314. [CrossRef]
84. Huang, W.; Long, E.; Wang, J.; Huang, R.; Ma, L. Characterizing spatial distribution and temporal variation of PM₁₀ and PM_{2.5} mass concentrations in an urban area of southwest China. *Atmos. Pollut. Res.* **2015**, *6*, 842–848. [CrossRef]
85. Shen, F.Z.; Ge, X.L.; Hu, J.L.; Nie, D.Y.; Tian, L.; Chen, M.D. Air pollution characteristics and health risks in Henan Province, China. *Environ. Res.* **2017**, *156*, 625–634. [CrossRef] [PubMed]
86. Filonchyk, M.; Peterson, M. Air quality changes in Shanghai, China, and the surrounding urban agglomeration during the COVID-19 lockdown. *J. Geovis. Spat. Anal.* **2020**, *4*, 1–7. [CrossRef]
87. Ghauri, B.; Lodhi, A.; Mansha, M. Development of baseline (air quality) data in Pakistan. *Environ. Monit. Assess.* **2007**, *127*, 237–252. [CrossRef]
88. Sharma, A.; Sharma, S.K.; Mandal, T.K. Influence of ozone precursors and particulate matter on the variation of surface ozone at an urban site of Delhi, India. *Sustain. Environ. Res.* **2016**, *26*, 76–83. [CrossRef]
89. Sugimoto, N.; Shimizu, A.; Matsui, I.; Nishikawa, M. A method for estimating the fraction of mineral dust in particulate matter using PM_{2.5}-to- PM₁₀ ratios. *Particuology* **2016**, *28*, 114–120. [CrossRef]

Article

The Extraordinary Trend of the Spatial Distribution of PM_{2.5} Concentration and Its Meteorological Causes in Sichuan Basin

Xing Xiang¹, Guangming Shi^{1,2,*} , Xiaodong Wu¹ and Fumo Yang^{1,2}

¹ Department of Environmental Science and Engineering, Sichuan University, Chengdu 610065, China; xiangxing@stu.scu.edu.cn (X.X.); wuxiaodong@stu.scu.edu.cn (X.W.); fmyang@scu.edu.cn (F.Y.)

² National Engineering Research Center on Flue Gas Desulfurization, Chengdu 610065, China

* Correspondence: shigm@scu.edu.cn

Abstract: Sichuan Basin is an area with some of the most serious PM_{2.5} pollution, and it is also a key area for joint prevention and control of air pollution in China. Therefore, it is necessary to clarify the temporal and spatial distribution characteristics of PM_{2.5} concentration in Sichuan Basin (SCB) and study the influence of meteorological conditions. In this study, the spatial disparity of PM_{2.5} concentration in SCB and its variation trend from 1 December 2015 to 30 November 2019 were analyzed. The results showed that the spatial disparity of SCB was decreasing and distinct variation trends of PM_{2.5} concentration were observed in different areas. The PM_{2.5} concentrations declined rapidly in the western and southern basin (most severely polluted areas), decreased at a slower rate in the central and eastern basin, but unexpectedly increased slightly in the northern and northeastern basin. From the perspective of relative spatial anomalies (RAs), the decreasing (increasing) trend of RAs of PM_{2.5} concentrations in the western and southern (northern and northeastern) parts of SCB were also prominent. The reduction in spatial disparity and the regionally extraordinary increasing trend could be partly explained by the variations in synoptic circulations. Specifically, the reasons for the decrease in wintertime spatial disparity and the increase in RAs in the northern basin were the reduction in synoptic pattern Type 2 (weak high-pressure system and uniform pressure fields) and Type 3 (high-pressure system to the north) and the growth of Type 6 (weak low-pressure system with high-pressure system to the north). In spring, the reasons were the reduction in Type 1 (weak low-pressure system) and Type 5 (weak low-pressure system to the southwest) and the growth of Type 2. The reduction in Type 2 and the growth in Type 4 (weak high-pressure system to the east) could explain the variation in PM_{2.5} distribution in autumn. This study showed the importance of implementing more precise and effective emission control measures, especially in relatively cleaner areas, in which the impacts of meteorological conditions might cause fluctuation (even rebounding) in the PM_{2.5} concentration.

Citation: Xiang, X.; Shi, G.; Wu, X.; Yang, F. The Extraordinary Trend of the Spatial Distribution of PM_{2.5} Concentration and Its Meteorological Causes in Sichuan Basin. *Atmosphere* **2022**, *13*, 853. <https://doi.org/10.3390/atmos13060853>

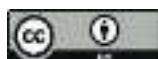
Academic Editors: Duanyang Liu, Kai Qin and Honglei Wang

Received: 10 April 2022

Accepted: 23 May 2022

Published: 24 May 2022

Publisher's Note: MDPI stays neutral with regard to jurisdictional claims in published maps and institutional affiliations.



Copyright: © 2022 by the authors. Licensee MDPI, Basel, Switzerland. This article is an open access article distributed under the terms and conditions of the Creative Commons Attribution (CC BY) license (<https://creativecommons.org/licenses/by/4.0/>).

Keywords: PM_{2.5}; Sichuan Basin; spatial distribution; spatial disparity; synoptic patterns; meteorological conditions

1. Introduction

Haze pollution has occurred frequently in the past few decades due to the rapidly developing economy and accelerating urbanization in China. As the major cause of haze, PM_{2.5} (particles with aerodynamic equivalent diameter less than 2.5 µm) was one of the most concerned air pollutants because of its harm to human health and impact on global climate [1–3]. For example, it was found that long-term exposure to high PM_{2.5} concentration could lead to cardiovascular diseases, respiratory diseases and even premature deaths [4,5]. PM_{2.5} could change the climate on both global and local scales through directly scattering incident solar radiation or indirectly influencing clouds and precipitation [6–8]. This made the collocation between PM_{2.5}, population and ecosystem of considerable interest. Therefore, the temporal and spatial characteristics of PM_{2.5} concentration and its causes were the most discussed topics in previous studies.

Excessive anthropogenic pollutant emissions and adverse meteorological conditions were the determinant factors causing frequent and severe PM_{2.5} pollution events [9–12]. A series of controlling measures were implemented aiming to reduce the anthropogenic emissions of air pollutants, which led to a significant decrease in PM_{2.5} concentration across China [13,14]. However, the impact of meteorological conditions on PM_{2.5} concentration was complicated. Generally, wind is one of the most important meteorological factors. High wind speeds facilitate the diffusion of pollutants and the transport of pollutants is related to both the direction and speed of prevailing wind [15,16]. The vertical diffusion capability, characterized by temperature inversion or planetary boundary layer height (PBLH), limits the space for pollutant mixing and, hence, affects the accumulation process [17–20]. Relative humidity (RH) is also important for the secondary formation and hygroscopic growth of atmospheric particles [21,22]. On the synoptic scale, the relevant meteorological parameters are affected by atmospheric circulation. Therefore, the classification of atmospheric circulation is of great significance to examine the relationship between meteorology and air pollution [23–25].

Sichuan Basin (SCB), located in Southwest China and surrounded by plateaus to the west and south and high mountains to the north and east, is one of the most polluted areas in China [12,26]. The complex topography led to special meteorological conditions with extremely calm winds and stagnation in the basin area [27]. The average occurrence frequency of air stagnation in winter, from 2013 to 2016, exceeded 76% in SCB [28]. The RH in SCB was high, which was conducive to the hygroscopic growth of particles [29,30]. The circulation in SCB was also important, as previously revealed, as southerly warm flows favored the PM_{2.5} pollution and northerly cold flows were conducive to the dissipation of PM_{2.5} [17,30]. Moreover, the complicated topography modulated the distribution of PM_{2.5} from both the horizontal and vertical perspective. Ning et al. found that there was a nonlinear relationship between urban PM concentration and altitude in SCB [11]. Shu et al. found that there was a higher PM_{2.5} layer at a height of 1.5–3 km in the basin, and the PM_{2.5} concentration between this layer and the ground was relatively low [31].

Although many studies on the distribution characteristics of PM_{2.5} concentration and their relationship with meteorological conditions were conducted in SCB [28,30,32], few focused on the trend of spatial distribution of PM_{2.5} concentration. In this study, we examined the variations in PM_{2.5} distribution from 2016 to 2019 and found extraordinary trends in the northeastern basin. The possible meteorological causes of these regional characteristics were explored from the perspective of synoptic classification. The results could provide potential reference for joint prevention and control measures of PM_{2.5} pollution in SCB.

2. Materials and Methods

2.1. Study Area

This study covered the 18 prefecture-level cities in SCB, which were Chengdu (CD), Chongqing (CQ), Deyang (DY), Mianyang (MY), Meishan (MS), Leshan (LS), Ya'an (YA), Yibin (YB), Zigong (ZG), Luzhou (LZ), Neijiang (NJ), Ziyang (ZY), Suining (SN), Guangyuan (GY), Bazhong (BZ), Nanchong (NC), Dazhou (DZ) and Guang'an (GA). As shown in Figure 1, these cities were in the basin area confined by Tibetan Plateau to the west, Yunnan-Guizhou Plateau to the south, Wuling Mountain to the east and Daba Mountain to the North. The average altitude in the basin is about 400 m above sea level, while the altitudes of the plateaus and mountains are above 4000 m and 2000 m, respectively. The huge height drop creates lee-side calm area in the basin. Besides, the topography in the basin is also complicated, which could be divided into Chengdu Plain in the west, Hilly Area in the central basin and Ridge Valley area in the east by Longquan Mountain and Huaying Mountain.

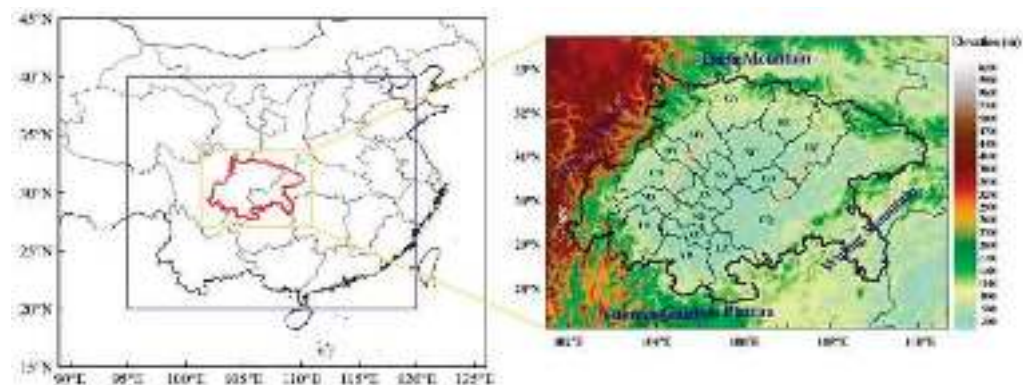


Figure 1. The location (left panel) and topography (right panel) of the Sichuan Basin. In the left panel, the blue square presents the region where the synoptic classification was conducted and the red polylines presents the location of SCB.

2.2. $PM_{2.5}$ Concentration Data and Spatial Characterization Method

The hourly $PM_{2.5}$ concentration data of the state-controlled air-quality-monitoring sites in SCB from December 2015 to November 2019 were obtained from China National Environmental Monitoring Centre (<https://air.cnemc.cn:18007/> (accessed on 1 December 2019)). The concentrations of all the sites in the same city were averaged to represent the urban $PM_{2.5}$ concentration in this city. The annual $PM_{2.5}$ concentration of a certain city was calculated by averaging the hourly data from January to November of the current year and December of the previous year. Correspondingly, winter was defined as January and February in the current year and December in the previous year in this study. Spring, summer and autumn were defined as March to May, June to August and September to November, respectively.

Two metrics were used to analyze the characteristics of spatial distribution of $PM_{2.5}$ concentration in SCB. The first one was the coefficient of variation (CV) used to quantify the spatial disparity of $PM_{2.5}$ concentration between 18 cities [12]. The CV was defined as $CV = \sigma / C_m$, in which σ and C_m were the standard deviation and the average of $PM_{2.5}$ concentrations in 18 cities, respectively. During a certain period, the CV represented how uniformly the $PM_{2.5}$ concentration distributed in the cities of SCB. Smaller CV indicated more obvious regional characteristics of $PM_{2.5}$ pollution. The CV can characterize the variations in $PM_{2.5}$ homogeneity but cannot reveal how these variations evolved. Hence, the relative spatial anomalies (RA) of average $PM_{2.5}$ concentration for each city were used. RA for a certain city was calculated by $RA = (C_i - C_m) / C_m$, in which C_i and C_m were average $PM_{2.5}$ concentration in this city and all cities, respectively. Therefore, larger RA meant relatively higher $PM_{2.5}$ concentration in the relevant city compared to other cities. The inter-annual variation in CVs could provide the change in $PM_{2.5}$ spatial disparity and the RAs could better show the spatial distribution of $PM_{2.5}$ varying trend.

2.3. ERA5 Reanalysis Data and Objective Synoptic Classification

ERA5 dataset contains the fifth-generation atmospheric reanalysis data released by the European Center for Medium-Range Weather Forecasting (ECMWF). These data were obtained based on the 4D-Var data assimilation and model prediction of CY41R2 in the Integrated Forecasting System (IFS). Compared with its previous generation, namely ERA-interim, the horizontal and vertical resolutions of ERA5 were significantly improved, and the performance of ERA5 was better in the evaluation of tropospheric temperature, wind and humidity. Since the first release, ERA5 was widely used in research fields of atmospheric sciences, environmental issues [33–36], etc. ERA5 data at both upper-level isobaric surfaces and several single levels from December 1st 2015 to November 30th 2019 were collected. The data at 850 hPa, including potential height, relative humidity, temperature, vertical velocity and horizontal wind speed and direction, were used in this study. Besides, data at single levels, including surface pressure, 2 m temperature, 10 m

horizontal wind speed and direction at ground level and PBLH, were used too. The data in full horizontal resolution ($0.25^\circ \times 0.25^\circ$) and temporal resolution (1 h) were used.

The synoptic classification was conducted to explore the possible meteorological causes of the variation in $PM_{2.5}$ spatial distribution. Synoptic classification could be carried out by subjective and objective methods, among which the subjective methods were mainly based on artificially defined a priori criteria and had great uncertainties [37]. On the contrary, objective methods were based on the maximization of similarity and variance; hence, these methods were appropriate for processing mass data without relying on a priori experiences [38]. The Cost733class package, a software jointly developed by Earth System Science and Environmental Management (ESSEM) and European Cooperation in Science and Technology (COST), focused on creating and evaluating weather and circulation-type classifications utilizing various different methods, including PCT (t-mode principal component analysis using oblique rotation), PTT (t-mode principal component analysis using orthogonal rotation), SOM (self-organizing maps) [39,40], etc. In this study, the PTT method was used to classify the synoptic patterns in SCB and its surrounding areas. The input data were the daily average geopotential heights at 850 hPa isobaric surface from ERA5 reanalysis data of ECMWF with a spatial resolution of $0.25^\circ \times 0.25^\circ$. The region implementing the synoptic classification was the area in 95° E– 120° E and 20° N– 40° N (Figure 1).

3. Results and Discussion

3.1. Variations in $PM_{2.5}$ Spatial Disparity

The CVs of annual and seasonal $PM_{2.5}$ concentrations are shown in Figure 2. The annual CVs showed a general decreasing trend from 2016 to 2019, except for slightly rebounding in 2017. This indicated that the differences in annual $PM_{2.5}$ concentrations between 18 cities in SCB were narrowing. Similar variation trends were observed in other regions in China, such as North China Plain [41] and Northeastern China [42]. From the seasonal perspective, the CVs were the largest in summer among the four seasons, followed by spring and winter. This was partly due to the low average concentrations in summer (Table 1). The CVs in spring and summer decreased gradually from 2016 to 2019. The CV was 0.16 in the winter of 2016, but increased to 0.21 in 2017 and then gradually decreased to 0.13 in 2019. The spatial disparity varied more obviously in autumn than in other seasons. In the autumn of 2016 and 2017, the CVs were 0.25 and 0.26, respectively, and decreased to around 0.16 in 2018 and 2019. The smallest CV in 2018 was 38% lower than the largest value in 2017. In general, the spatial disparity of $PM_{2.5}$ concentration in SCB decreased from 2016 to 2019, whether in terms of annual or seasonal average $PM_{2.5}$ concentrations. In addition, it is worth noting that the CVs of the wintertime average $PM_{2.5}$ concentration were close to those of annual averages. This revealed that the variation in $PM_{2.5}$ distribution was dominated by wintertime $PM_{2.5}$ distribution in SCB.

Table 1. The annual and seasonal averages and standard deviations of $PM_{2.5}$ concentrations ($\mu\text{g}/\text{m}^3$) in SCB from 2016 to 2019.

Year	Annual	Winter	Spring	Summer	Autumn
2016	51 ± 10	74 ± 12	51 ± 11	31 ± 8	48 ± 11
2017	46 ± 10	85 ± 18	41 ± 9	27 ± 6	35 ± 9
2018	46 ± 8	76 ± 14	42 ± 8	24 ± 5	37 ± 6
2019	41 ± 6	69 ± 9	41 ± 7	24 ± 4	32 ± 5

To explore the in-depth details about the variations in $PM_{2.5}$ spatial disparity in SCB, the $PM_{2.5}$ concentrations of 18 cities in SCB at annual and seasonal scales from 2016 to 2019 are shown in Figure 3. From the perspective of annual average $PM_{2.5}$ concentrations, a rapid $PM_{2.5}$ concentration decrease of $23 \mu\text{g}/\text{m}^3$, $15 \mu\text{g}/\text{m}^3$, $18 \mu\text{g}/\text{m}^3$ and $20 \mu\text{g}/\text{m}^3$ from 2016 to 2019 was observed in ZG, CD, LZ and MS, the most polluted cities in SCB. The $PM_{2.5}$ concentrations of moderately polluted cities decreased more slowly. For example,

the concentrations of CQ fell by $12 \mu\text{g}/\text{m}^3$ during these four years. However, the $\text{PM}_{2.5}$ concentrations in GY and BZ, representing relatively lightly polluted cities, showed an increasing trend of $4 \mu\text{g}/\text{m}^3$ and $1 \mu\text{g}/\text{m}^3$, respectively. Hence, the decrease in $\text{PM}_{2.5}$ concentrations in severely polluted cities and the maintaining (even increasing) of concentrations in moderately and lightly polluted cities together made the spatial disparity of $\text{PM}_{2.5}$ concentration gradually decrease in SCB.

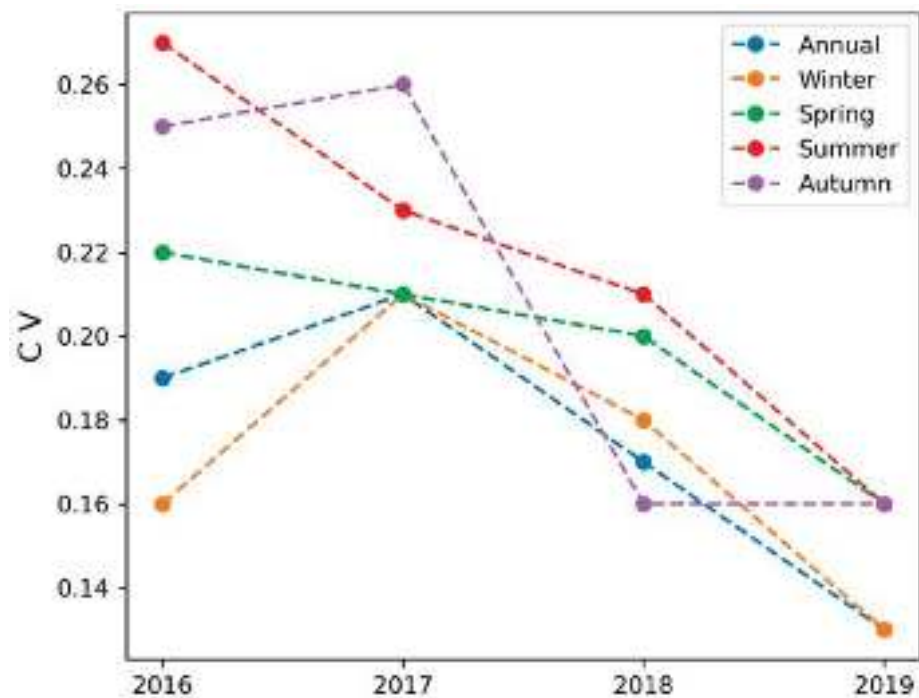


Figure 2. The CVs of annual and seasonal average concentrations of $\text{PM}_{2.5}$ in SCB from 2016 to 2019.

The inter-annual variations in wintertime $\text{PM}_{2.5}$ concentrations presented a similar trend to the annual concentrations from 2017 to 2019, except before 2017. The $\text{PM}_{2.5}$ concentrations in most cities increased from 2016 to 2017 and severely polluted cities showed a larger increase. The rising amount was $18 \mu\text{g}/\text{m}^3$, $29 \mu\text{g}/\text{m}^3$ and $19 \mu\text{g}/\text{m}^3$ in ZG, CD and MS, respectively. In the representative cities of moderately polluted cities, CQ, and lightly polluted cities, GY increased by $7 \mu\text{g}/\text{m}^3$ and decreased by $3 \mu\text{g}/\text{m}^3$, respectively. As a result, the range of concentrations in 18 cities became wider and wintertime CV increased significantly in 2017. From then to 2019, $\text{PM}_{2.5}$ concentrations in ZG, CD and MS decreased significantly, by $40 \mu\text{g}/\text{m}^3$, $39 \mu\text{g}/\text{m}^3$ and $39 \mu\text{g}/\text{m}^3$, respectively. The concentration in CQ decreased only by $12 \mu\text{g}/\text{m}^3$ and the concentrations in GY and BZ rose by $5 \mu\text{g}/\text{m}^3$ and $2 \mu\text{g}/\text{m}^3$, respectively.

The inter-annual variations in $\text{PM}_{2.5}$ concentrations in spring and summer were consistent with the annual trend. In autumn, the concentrations decreased in all cities at a similar rate from 2016 to 2017. However, much more obvious increasing trends were observed in moderately and lightly polluted cities from 2017 to 2018. The autumntime $\text{PM}_{2.5}$ concentrations in BZ, GA, and GY increased by more than $10 \mu\text{g}/\text{m}^3$. Even the concentrations in CQ increased slightly as well. The reductions in autumntime concentrations in severely polluted cities, such as ZG, LZ and MS, were smaller than those in other seasons. This led to a significant reduction in spatial disparity in autumn of 2018 in SCB. From 2018 to 2019, the autumntime concentrations in most cities decreased at similar rates, hence, the spatial disparity remained stable, as shown in Figure 2.

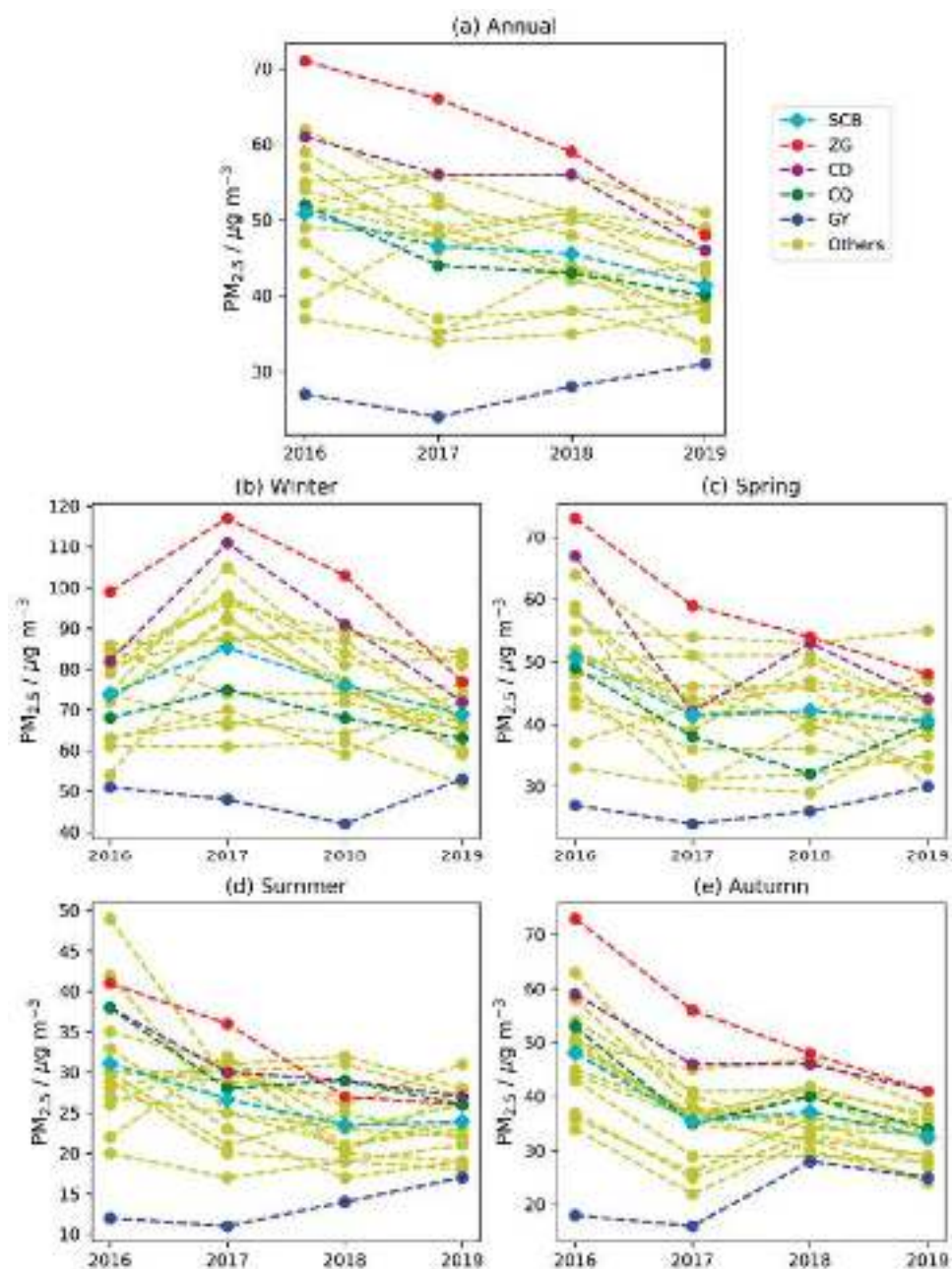


Figure 3. Inter-annual variations in (a) annual, (b) wintertime, (c) springtime, (d) summertime and (e) autumntime average $PM_{2.5}$ concentrations of 18 cities in SCB from 2016 to 2019.

3.2. Variations in $PM_{2.5}$ Spatial Distribution

The spatial distribution of RAs in annual average concentrations can be found in Figure 4. In 2016, the $PM_{2.5}$ concentrations of most cities in the western (CD, MS and LS) and south parts (ZG, YB and LZ) of SCB were highest, inferred from the distribution of positive RAs in these areas. The RAs of cities in the northeast part of SCB were slightly positive (DZ and NC) or negative (GY, BZ, GA), revealing relatively lower concentrations in this area. In 2017, in total, 10 cities held positive RAs, among which 9 cities were located in the western and southern parts of SCB, except DZ in the northeast part, including CD, DY, MY, MS, YA, LS, ZG, YB and LZ. Moreover, the RAs of these cities were higher than those in 2016, resulting in larger spatial disparity in annual average concentrations in 2017, as shown in Figure 2. In 2018 and 2019, cities with positive RAs were distributed in the south (ZG, YB and LS), the northwest (CD, DY and MY) and the northeast (DZ and NC) parts of SCB. Another feature was that the RA in MS (LZ) decreased (increased)

significantly from 2018 to 2019. The variations in RA distribution further suggested that spatial disparity of annual average $PM_{2.5}$ concentrations was declining in SCB because the maximum RA decreased from 2016 to 2019 and the variations in RAs showed obvious regional characteristics, decreasing in the western and southern basin and increasing in the northern basin.

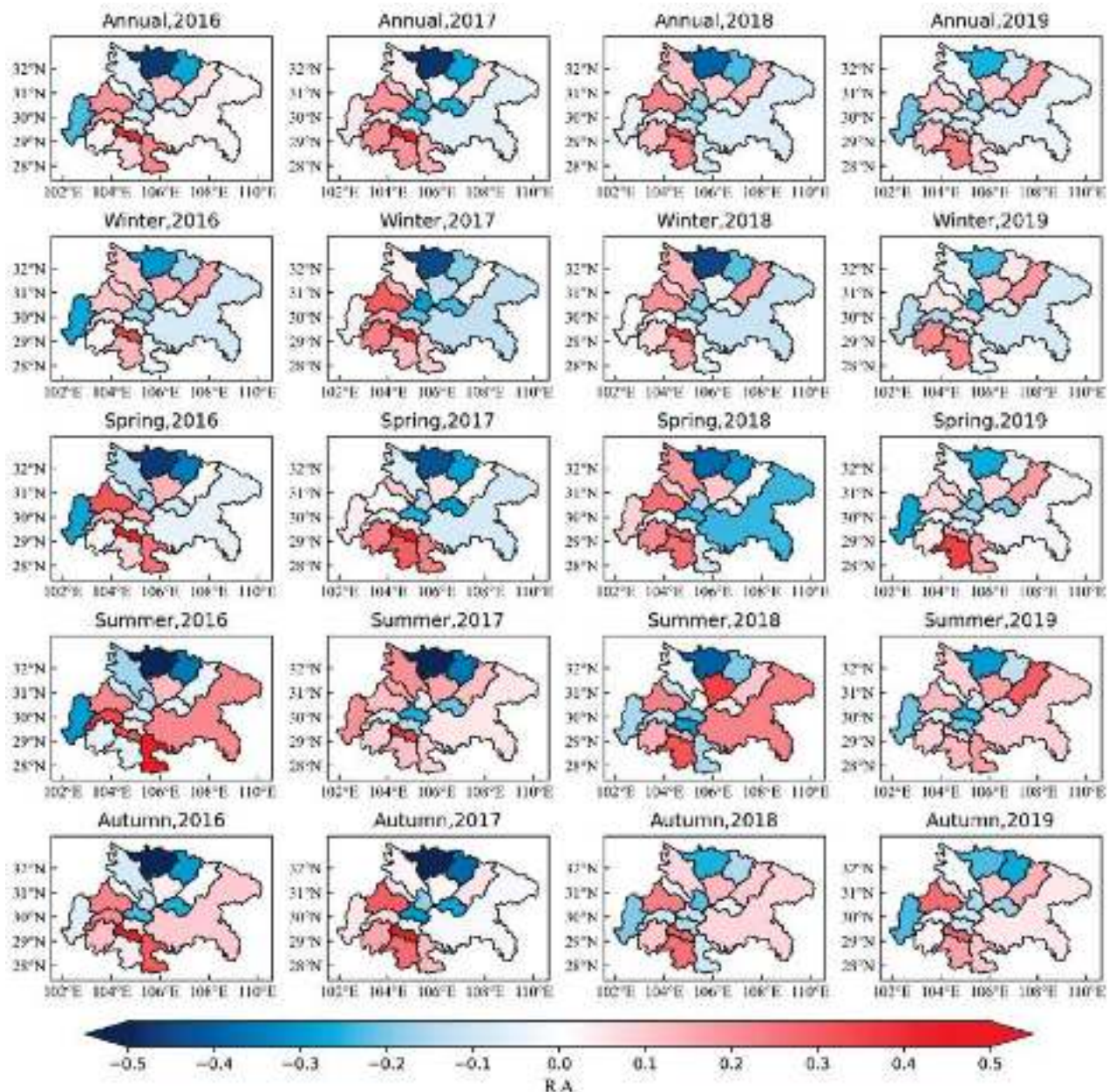


Figure 4. The distribution of RAs in annual and seasonal average $PM_{2.5}$ concentrations from 2016 to 2019 in SCB.

Generally, the variation features of RAs in seasonal average $PM_{2.5}$ concentrations were coincident with those of the annual averages. In winter, the RAs in the western and southern parts of SCB were much higher than those in other parts and kept decreasing from 2016 to 2019. The lowest RAs were found in the northern part of SCB, such as GY and BZ and the RAs in this area increased significantly from 2016 to 2019, especially in 2019. In spring and autumn, the RAs in GY and BZ increased more significantly than in winter, while the RAs in the western and southern parts of SCB were decreasing. In summer,

the RA in CQ was higher than that in other seasons, and the RAs in the northern part of SCB maintained the values in other seasons.

In summary, the spatial disparity of PM_{2.5} concentrations of 18 cities in SCB narrowed and the variations in concentrations showed prominent regional characteristics, namely decreasing in the western and southern basin, maintaining in the central and eastern basin, and slightly increasing in the northern basin. These regional characteristics suggested that the meteorological conditions might be important causes, especially the increase in concentrations in the northern basin, despite strict emission control measures. Therefore, in the next section, the synoptic patterns were identified and their impacts on the distribution of atmospheric diffusion conditions were analyzed, aiming to explain the regional maintaining or increasing trends of PM_{2.5} concentration in the northeastern basin.

3.3. Synoptic Patterns and Their Impacts on PM_{2.5} Spatial Distribution

3.3.1. Identified Synoptic Patterns

By implementing the PTT classification method, the synoptic patterns in SCB and the surrounding area were classified into nine types in total, according to the daily average geopotential heights at 850 hPa, from 1 December 2015 to 30 November 2019. Among these patterns, the last three types occurred in less than 10 days and the first six types occurred in more than 98.8% of the days accumulatively. Hence, only the first six patterns were analyzed in this study, and their occurring days are shown in Table 2.

Table 2. The occurring days of 6 synoptic patterns in four seasons from 2016 to 2019.

Type	Season	2016	2017	2018	2019	Type	Season	2016	2017	2018	2019
Type 1	Winter	22	33	21	28	Type 2	Winter	17	16	22	9
	Spring	40	35	36	26		Spring	17	23	28	28
	Summer	30	38	29	22		Summer	18	15	9	16
	Autumn	17	18	18	19		Autumn	14	19	24	11
Type 3	Winter	42	31	38	20	Type 4	Winter	0	0	0	1
	Spring	9	17	5	16		Spring	5	1	5	4
	Summer	1	2	0	0		Summer	27	16	41	26
	Autumn	15	18	21	17		Autumn	37	25	18	36
Type 5	Winter	5	1	4	6	Type 6	Winter	5	9	5	26
	Spring	18	16	15	15		Spring	3	0	3	2
	Summer	14	18	12	23		Summer	0	0	0	0
	Autumn	7	7	7	4		Autumn	1	1	2	2

The first synoptic pattern occurred in 432 days, out of 1443 days in total, which was much more than other types. The occurring days of Types 2–6 were 286, 252, 242, 172 and 59 days, respectively. Seasonally, Type 1 and Type 2 almost evenly occurred throughout the four seasons. The occurrence frequencies of Type 3 were highest in winter, followed by autumn and spring, but only occurred on 3 days in summer. On the contrary, the occurrence frequencies of Type 4 were relatively higher in summer and autumn, and close to zero in winter and autumn. Type 5 occurred more frequently in spring and summer than the other two seasons, while Type 6 almost occurred only in winter. Therefore, we mainly discussed Type 1, Type 2, Type 3 and Type 6 in winter, Type 1, Type 2, Type 3 and Type 5 in spring, Type 1, Type 2, Type 4 and Type 5 in summer, and Type 1, Type 2, Type 3 and Type 4 in autumn.

The spatial distribution characteristics of 850 hPa potential heights for six synoptic patterns are shown in Figure 5. In Type 1, the SCB was controlled by a weak low-pressure system, noted as weak low-pressure type. When Type 2 occurred, the SCB was under the control of a weak high-pressure system and uniform pressure fields (weak high-uniform-pressure type). In Type 3, there was a strong high-pressure center to the north of SCB, noted as northern high-pressure type. Type 4 could be summarized as eastern weak high-pressure type for the existence of a weak high-pressure center to the east of SCB. Similarly, Type

5 could be named as southwestern weak low-pressure type for the existence of a weak low-pressure center to the southwest. Type 6 was also characterized with the control of a weak low-pressure system, just as Type 1, but collocating a high-pressure system to the north of SCB, noted as weak low-pressure with northern high-pressure type.

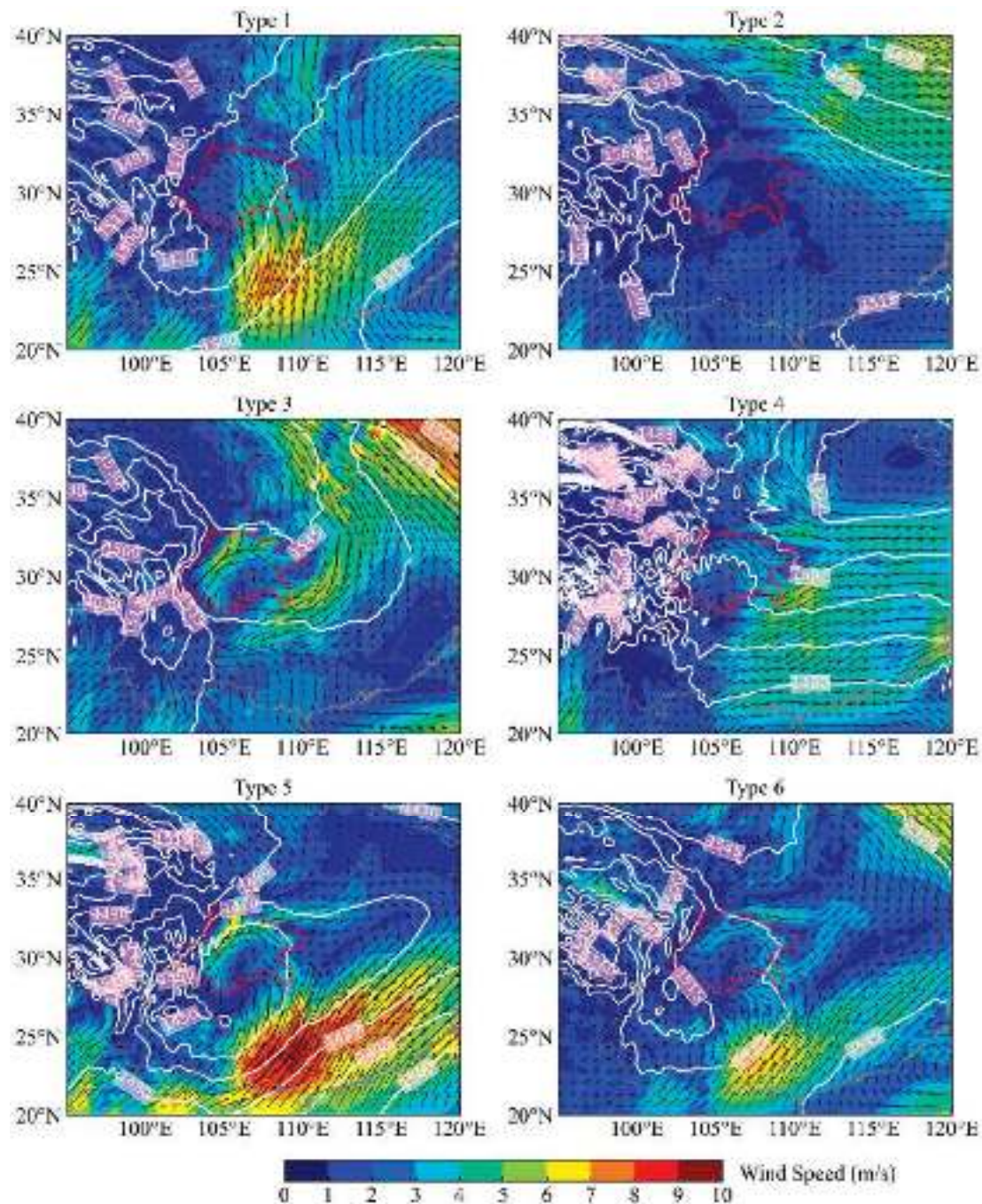


Figure 5. The distribution of geopotential heights at 850 hPa (white isolines) and the horizontal wind fields at 850 hPa (colored shadings and black vectors) for the six synoptic patterns in SCB.

Figure 5 presents the wind fields at 850 hPa for the six synoptic patterns in SCB. In Type 1, the regions to the east of SCB prevailed southerly winds. Air masses originated in southern China, such as Guangxi and Guangdong provinces, and entered the SCB through the southeastern edge of the basin (the south part of CQ). This air flows towards the north through the central and eastern basin, and turns west in the western basin. Affected by the topography, the wind speeds in the western basin were relatively low. In Type 2,

the uniform pressure fields led to extremely calm winds in the basin. The northeast part of the basin was controlled by the westerly or northwesterly air flows. Type 3 presented prevailing strong northerly winds in the areas to the east of SCB. These strong northerly winds entered SCB through the high mountains in the north and caused a relatively strong wind zone in the northern basin and western basin. The cyclonic circulation converged in the southeastern basin and led to a calm wind zone there. In Type 4, easterly winds invaded SCB through the eastern part of the basin area and turned south in the western part of the basin. This circulation pattern made the wind velocity in the southern part of the basin extremely low. In Type 5, although southerly winds prevailed in the area to the southeast of SCB, the air masses from the south could not cross over the mountains in the southeastern edge of the basin. Hence, the basin was mainly affected by the northerly air flows and created similar circulations as Type 3. The circulation features in Type 6 were similar to those in Type 5 but the wind speeds were relatively lower.

3.3.2. The Impacts of Synoptic Patterns on PM_{2.5} Spatial Distribution

Figure 6 shows the average PM_{2.5} concentrations and their CVs in SCB for six synoptic patterns. The PM_{2.5} concentrations of different synoptic patterns were almost the same in summer, around 26 $\mu\text{g}/\text{m}^3$. In other three seasons, the concentrations of Type 1 and Type 2 were relatively higher than those of Type 3. In winter, PM_{2.5} concentrations exceeded 80 $\mu\text{g}/\text{m}^3$ in Type 1 and Type 2 and only 64 $\mu\text{g}/\text{m}^3$ in Type 3. The PM_{2.5} concentrations of Type 1, Type 2 and Type 3 were 50 $\mu\text{g}/\text{m}^3$, 43 $\mu\text{g}/\text{m}^3$ and 36 $\mu\text{g}/\text{m}^3$ in spring, and 44 $\mu\text{g}/\text{m}^3$, 45 $\mu\text{g}/\text{m}^3$ and 33 $\mu\text{g}/\text{m}^3$ in autumn, respectively. In addition, the concentration of Type 6 also exceeded 80 $\mu\text{g}/\text{m}^3$ in winter and the concentrations of Type 5 in spring and Type 4 in autumn were relatively low, about 38 $\mu\text{g}/\text{m}^3$ and 32 $\mu\text{g}/\text{m}^3$, respectively. Therefore, Type 1, Type 2 and Type 6 were more conducive to the formation of PM_{2.5} pollution, and the air quality was relatively better in Type 3, Type 4 and Type 5. From the perspective of the spatial disparity, the largest CVs were 0.18 (in Type 2), 0.20 (in Type 5), 0.21 (in Type 4) and 0.22 (in Type 1) in winter, spring, summer and autumn, respectively. This indicated that the CVs were not related to concentrations.

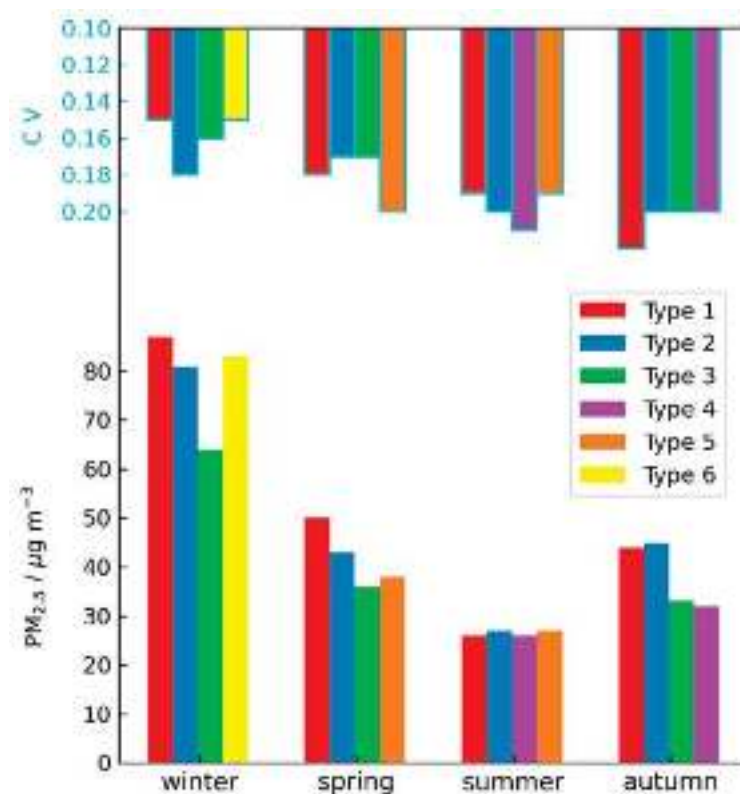


Figure 6. Seasonal average PM_{2.5} concentrations and their CVs for six synoptic patterns in SCB.

The spatial distribution of RAs in four seasons for different synoptic patterns is shown in Figure 7. In winter, the distribution of RAs for Type 1, Type 3 and Type 6 was consistent to the average feature, as shown in Figure 4. However, in Type 2, the RAs in the northwestern basin (CD, DY and MY) were higher than those in the southern basin and the RA in GY showed a relatively low value compared with the other types. The ranges in wintertime RAs were relatively large in Type 2 and small in Type 6. In spring, Type 1 and Type 5 presented more prominent regional characteristics, with higher (lower) RAs in the western and southern (northern) basin. Comparatively, Type 2 and Type 3 showed relatively higher RAs in the northern basin and lower RAs in the western and southern basin. The largest and smallest variation ranges of RAs occurred in Type 5 and Type 2, respectively. In summer, Type 1 showed a similar RA distribution to Type 1 in spring. Type 2 presented a distinct distribution feature with lower RAs in the southern basin and higher RAs in the eastern and northeastern basin. The RA was only 0.08 in ZG and actually negative in YB and LS. The highest RAs were distributed in CQ, DZ and NC. Type 4 and Type 5 showed similar RA distribution characteristics but with higher (lower) RAs in the southern (northern) basin compared with Type 2. In autumn, the RA distribution feature of Type 1 was similar to that of Type 5 in spring, and the distribution features of Type 3 and Type 4 were similar to that of Type 5 in summer. Type 2 showed a different distribution. The RA of ZG was the largest, exceeding 0.40, but the RAs of other southern cities were lower than 0.10. RAs in the western basin were larger than the remaining regions, but the difference was small compared with other types in autumn.

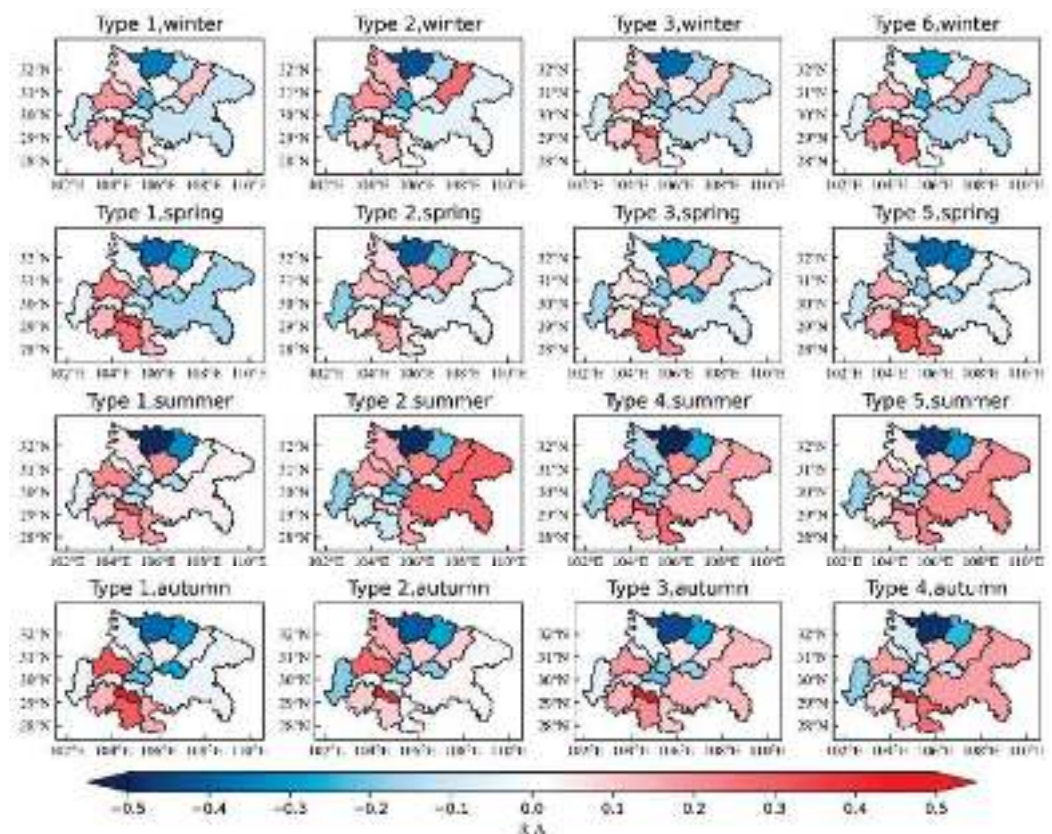


Figure 7. The distribution of RAs of seasonal average $PM_{2.5}$ concentrations for different synoptic patterns in SCB.

3.3.3. The Mechanisms of the Impacts of Synoptic Patterns on $PM_{2.5}$ Spatial Distribution

PBLH and horizontal wind were key meteorological factors to measure the vertical and horizontal diffusion ability of air pollutants [43]. Hence, the PBLH and 10 m wind fields over SCB in four seasons were extracted from ERA5 reanalysis data and these

fields for different synoptic patterns are presented in Figures 8–11. In winter (Figure 8), the main meteorological feature was the relatively high PBLH area covering the central basin, including the eastern parts of MY, DY, CD and MS, the western parts of ZY and SN, and the southern part of GY. The covering regions and PBLH values, collocating with horizontal wind fields and emissions, determined the distribution of $PM_{2.5}$. Type 3 presented the highest PBLH and strongest winds, and correspondingly, the average $PM_{2.5}$ concentration was the lowest. In Type 2, the low PBLH and calm winds were conducive to the accumulation of pollutants. Hence, the distribution of emissions was the dominant factor influencing $PM_{2.5}$ distribution, which made the RAs vary in relatively larger ranges in Type 2. In Type 1 and Type 6, the regions with massive emissions, such as the western and southern basin, were controlled by the high-PBLH area and relatively strong winds. This made the diffusion condition in higher emission areas better than other areas. As a result, the spatial disparity of $PM_{2.5}$ concentrations in Type 1 and Type 6 was lower.

In spring, the PBLH in the basin was significantly higher than those in winter. Hence, the wind-induced transportation of air pollutants might be the main factor determining $PM_{2.5}$ distribution. In Type 5 and Type 3, northerly winds invaded the basin from GY, BZ and DZ, blew straight southwards and converged in the southern and southeastern basin. This flow field could transport air pollutants to the south and aggravate the pollution in the southern basin. Meanwhile, the downwind regions confronted low-PBLH conditions. Consequently, these factors led to the relatively high RAs in the southern basin. In Type 2, the wind speeds were the lowest and pollutant transport was limited. Additionally, the relatively high PBLH in the western and southern basin promoted the diffusion of pollutants in massive emission areas. Therefore, the difference in $PM_{2.5}$ concentrations in SCB was relatively low. The winds in Type 1 blew from east to west and turned south near the western edge of the basin, which caused higher RAs in the western and southern basin.

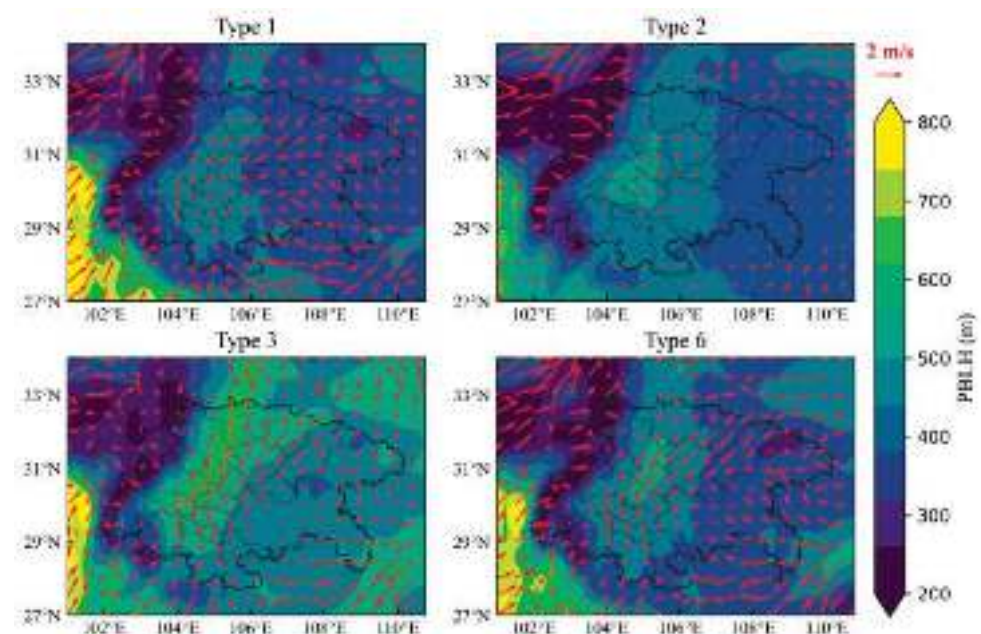


Figure 8. The PBLH and 10 m wind fields of different synoptic patterns in winter.

In summer, the wind fields were also the dominant factors influencing $PM_{2.5}$ distribution because of the relatively uniformly distributed PBLH. Similar wind fields were observed in Type 1 compared to those of Type 1 in spring, and resulted in higher RAs in the western and southern basin. The weak southerly winds prevailed in Type 2, with relatively larger velocities in the northeastern basin (CD, DY and MY) and the low PBLH controlled the eastern and southern basin. These made the higher RAs distribute in the northeastern basin (CD, DY, MY) and eastern basin (DZ and CQ). Type 4 and Type 5 presented similar

cyclonic circulation in SCB, which led to calm winds in the southern and eastern basin and resulted in higher RAs in these regions. Furthermore, the air masses from north entered SCB through western pathways and the northerly winds in the western basin were stronger in Type 5. Hence, the RAs in the western basin were lower in Type 5 than those in Type 4.

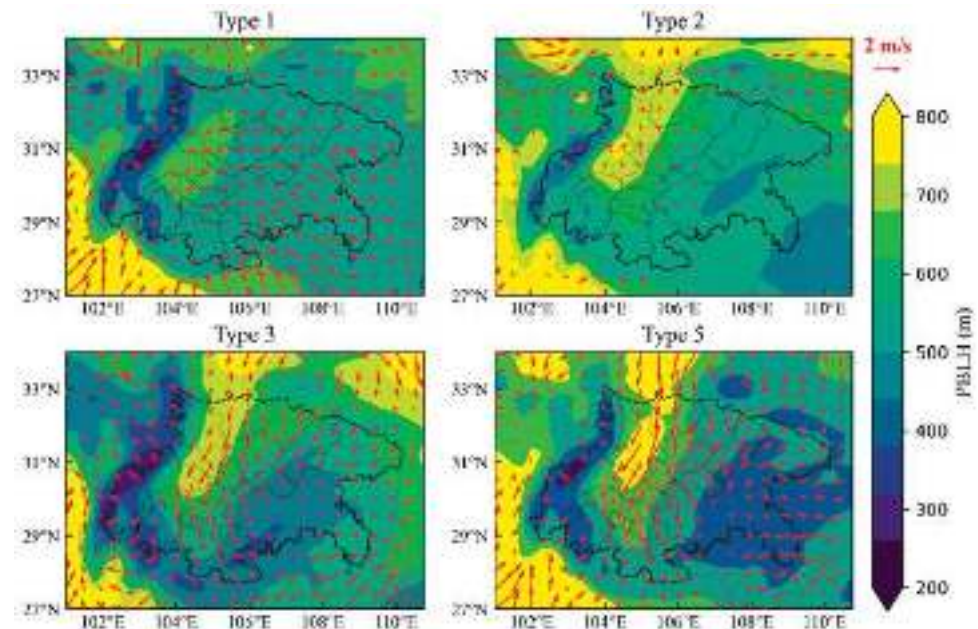


Figure 9. The PBLH and 10 m wind fields of different synoptic patterns in spring.

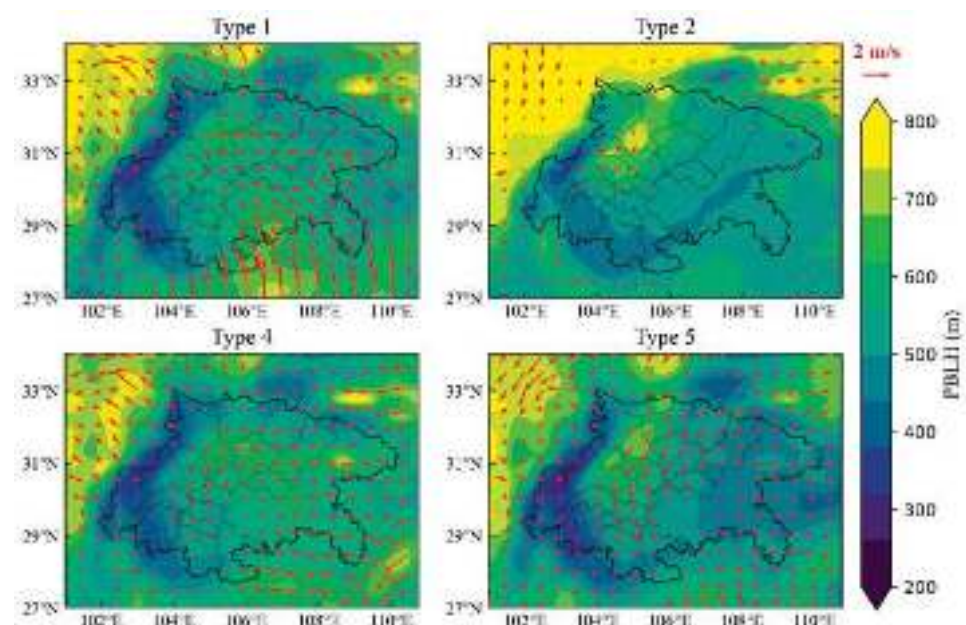


Figure 10. The PBLH and 10 m wind fields of different synoptic patterns in summer.

The wind fields were the dominant factors in autumn due to the relatively low and uniformly distributed PBLH. In Type 1, easterly winds invaded SCB from the northeast basin corner and caused prevailing northwesterly winds in the basin. The transport of air pollutants caused the relatively higher RAs in the western and southern basin. Extreme stagnation conditions occurred in Type 2 and made the high RAs distribute in massive emission areas. Type 3 and Type 4 presented similar northerly invasion air flows and caused cyclonic circulation, converging in the eastern basin. The pollutant transport and calm-wind-induced stagnation led the higher RAs in the southern basin and eastern basin,

respectively. The relatively stronger winds in Type 4 more thoroughly transported the pollutants to the downwind areas, so lower RAs were observed in LS and YB compared with those in Type 3.

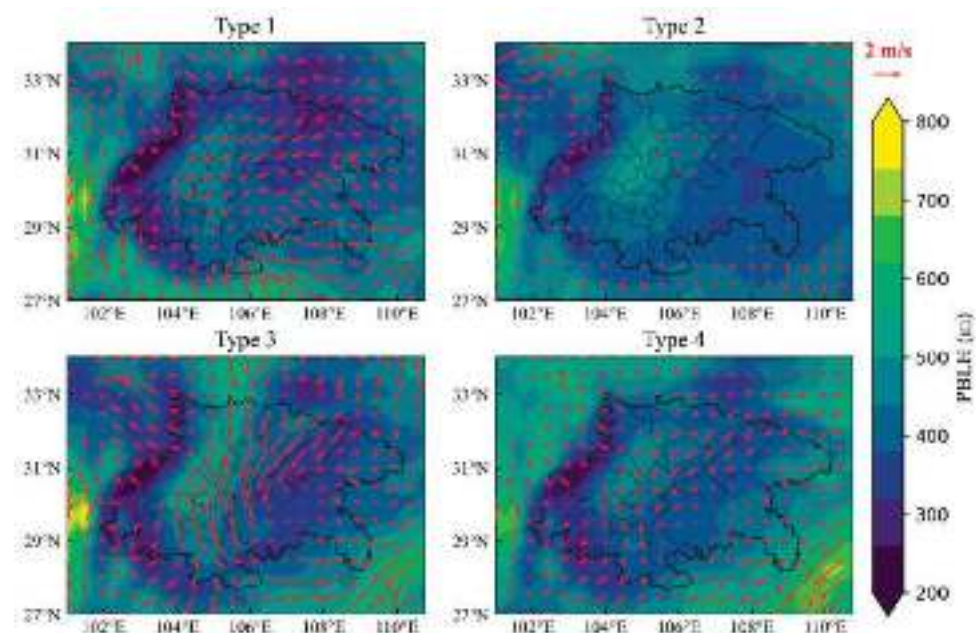


Figure 11. The PBLH and 10 m wind fields of different synoptic patterns in autumn.

3.3.4. The Synoptic Causes of PM_{2.5} Distribution Variations

From previous analysis, we could conclude that the spatial disparity of PM_{2.5} concentration was gradually decreasing in SCB and presented prominent regional characteristics of declining in the western and southern basin, maintaining in other regions and even increasing in the northern and northeastern basin. In this section, possible synoptic causes of this phenomenon are analyzed. Because the PM_{2.5} concentrations in summer were relatively low (Figure 6) and the occurrence frequencies of identified summertime synoptic patterns varied slightly, except in Type 1, as shown in Table 2, the synoptic causes in summer were not analyzed.

In winter, the two synoptic patterns with the two largest CVs, Type 2 and Type 3, occurred in declining frequencies. As shown in Table 2, the occurrence days of Type 2 and Type 3 decreased from 17 days and 42 days to 9 days and 20 days, respectively, during 2016–2019. On the contrary, the synoptic patterns with the smallest CV (Type 6) occurred more frequently, from 5 days to 26 days. Along with the metric of CV, the average PM_{2.5} concentration in the northern basin (GY, BZ, NC and DZ) was largest in Type 6, reaching 79 µg/m³, and smallest in Type 3, only 58 µg/m³. Therefore, the growth in Type 6 and the reduction in Type 3 and Type 2 could be the reasons for the decrease in spatial disparity in SCB and the increase in RAs in the northern basin in winter.

In spring, the synoptic patterns with higher CVs, Type 5 and Type 1, were increasing and the synoptic patterns with lower CVs, Type 3 and Type 2, were decreasing. Type 1 occurred in 40 days in 2016 and 26 days in 2019. The occurrence days slightly declined from 18 days to 15 days, while Type 2 and Type 3 grew from 17 days and 9 days to 28 days and 16 days, respectively. Specifically, the RAs in the northern basin (NC, DZ and BZ) for Type 2 and Type 3 were relatively larger than those for Type 1 and Type 5. Hence, the reduction in Type 1 and Type 5 and the growth in Type 2 and Type 3 could reduce the spatial disparity of PM_{2.5} in SCB, and explain the increasing RAs in the northern basin in spring.

In autumn, the occurrence frequencies of all synoptic patterns in 2019 remained almost the same as those in 2016. This was consistent with the fact that the distribution in RAs varied slightly, as shown in Figure 4. In detail, the difference in RAs between the western and northern basin began narrowing from 2017. Correspondingly, Type 2, in which the

RAs in the northwestern basin (CD, DY and MY) were higher than other cities, occurred in more days, and Type 3 and Type 4, in which RAs in the northwestern basin were lower, occurred in fewer days.

4. Conclusions

In this study, the spatial disparity of PM_{2.5} concentrations in SCB and its variation characteristics were explored, and the possible synoptic causes of these variations were analyzed. It was found that the spatial disparity of PM_{2.5} concentrations in SCB narrowed from 2016 to 2019. This tendency towards conformity of PM_{2.5} distribution was the result of a decreasing trend in cities with high concentrations, maintaining trend in cities with moderate concentrations and increasing trend in cities with low concentrations. Spatially, the main feature was that PM_{2.5} pollution was improved in the western and southern basin and deteriorated in the northern basin, especially in GY and BZ.

The regional characteristics of PM_{2.5} distribution variations could be partly interpreted by the occurrence frequencies of typical synoptic patterns, including weak low-pressure type (Type 1), weak high-pressure system and uniform pressure fields (Type 2), northern high-pressure type (Type 3), eastern weak high-pressure type (Type 4), southwest weak low-pressure type (Type 5), and weak low-pressure with northern high-pressure type (Type 6). Type 1, Type 2 and Type 6 were related to more polluted weather and Type 2, Type 3 and Type 5 were linked to cleaner days. The synoptic patterns influenced the PM_{2.5} distribution by modulating the diffusion conditions through PBLH and wind fields. The reduction in Type 2 and Type 3 (Type 1 and Type 5) and the growth of Type 6 (Type 2) led to a decrease in spatial disparity in winter (spring). Moreover, diffusion conditions (PBLH and wind) were the most important meteorological conditions affecting PM_{2.5} concentration and spatial distribution in SCB.

It was worth noting that the emission control measures were key factors that led to an improvement in air quality, although the impacts of synoptic patterns were manifested in this study. Specifically, the fact that PM_{2.5} concentration declined at a faster rate in more polluted cities might be the result of easier and more effective emission reduction in these areas. However, the regional maintaining, even rebounding, of PM_{2.5} concentration in the northern and northeastern basin could not be easily explained by emission variation alone, because a continuous reduction in emissions was expected, considering the implemented policies. Hence, the results of this study provide rational interpretation to this extraordinary trend on one hand. On the other hand, the fluctuation in PM_{2.5} concentration caused by synoptic circulation implied that the emissions in these areas might be close to the atmospheric capacity already. Implementing more precise and effective emission control measures is urgent to continuously improve the air quality.

Author Contributions: Conceptualization, G.S.; methodology, X.X.; investigation, X.X. and X.W.; writing—original draft preparation, X.X.; writing—review and editing, G.S. and F.Y.; supervision, F.Y. All authors have read and agreed to the published version of the manuscript.

Funding: This research was funded by the National Key R&D Program of China, grant number 2018YFC0214002 and 2018YFC0214001; the Key S&T Program of Sichuan Province, grant number 2018SZDZX0023; the National Natural Science Foundation of China, grant number 22076129; the Fundamental Research Funds for the Central Universities, grant number 41875162 and 22076129; the Young Talent Team Science and Technology Innovation Project of Sichuan Province, grant number 2020JDTD0005.

Institutional Review Board Statement: Not applicable.

Informed Consent Statement: Not applicable.

Conflicts of Interest: The authors declare no conflict of interest.

References

- Green, M.C.; Chen, L.W.A.; DuBois, D.W.; Molenar, J.V. Fine particulate matter and visibility in the Lake Tahoe Basin: Chemical characterization, trends, and source apportionment. *J. Air Waste Manag. Assoc.* **2012**, *62*, 953–965. [CrossRef]
- Silva, R.A.; Adelman, Z.; Fry, M.M.; West, J.J. The Impact of Individual Anthropogenic Emissions Sectors on the Global Burden of Human Mortality due to Ambient Air Pollution. *Environ. Health Perspect.* **2016**, *124*, 1776–1784. [CrossRef]
- Wang, Y.G.; Ying, Q.; Hu, J.L.; Zhang, H.L. Spatial and temporal variations of six criteria air pollutants in 31 provincial capital cities in China during 2013–2014. *Environ. Int.* **2014**, *73*, 413–422. [CrossRef] [PubMed]
- Guo, Y.M.; Zeng, H.M.; Zheng, R.S.; Li, S.S.; Barnett, A.G.; Zhang, S.W.; Zou, X.N.; Huxley, R.; Chen, W.Q.; Williams, G. The association between lung cancer incidence and ambient air pollution in China: A spatiotemporal analysis. *Environ. Res.* **2016**, *144*, 60–65. [CrossRef] [PubMed]
- Cohen, A.J.; Brauer, M.; Burnett, R.; Anderson, H.R.; Frostad, J.; Estep, K.; Balakrishnan, K.; Brunekreef, B.; Dandona, L.; Dandona, R.; et al. Estimates and 25-year trends of the global burden of disease attributable to ambient air pollution: An analysis of data from the Global Burden of Diseases Study 2015. *Lancet* **2017**, *389*, 1907–1918. [CrossRef]
- Albrecht, B.A. Aerosols, Cloud Microphysics, and Fractional Cloudiness. *Science* **1989**, *245*, 1227–1230. [CrossRef]
- Guo, J.P.; Liu, H.; Li, Z.Q.; Rosenfeld, D.; Jiang, M.J.; Xu, W.X.; Jiang, J.H.; He, J.; Chen, D.D.; Min, M.; et al. Aerosol-induced changes in the vertical structure of precipitation: A perspective of TRMM precipitation radar. *Atmos. Chem. Phys.* **2018**, *18*, 13329–13343. [CrossRef]
- Yang, X.; Zhao, C.F.; Guo, J.P.; Wang, Y. Intensification of aerosol pollution associated with its feedback with surface solar radiation and winds in Beijing. *J. Geophys. Res.-Atmos.* **2016**, *121*, 4093–4099. [CrossRef]
- Mu, M.; Zhang, R.H. Addressing the issue of fog and haze: A promising perspective from meteorological science and technology. *Sci. China-Earth Sci.* **2014**, *57*, 1–2. [CrossRef]
- Wang, H.J.; Chen, H.P. Understanding the recent trend of haze pollution in eastern China: Roles of climate change. *Atmos. Chem. Phys.* **2016**, *16*, 4205–4211. [CrossRef]
- Ning, G.C.; Wang, S.G.; Ma, M.J.; Ni, C.J.; Shang, Z.W.; Wang, J.X.; Li, J.X. Characteristics of air pollution in different zones of Sichuan Basin, China. *Sci. Total Environ.* **2018**, *612*, 975–984. [CrossRef] [PubMed]
- He, J.J.; Gong, S.L.; Yu, Y.; Yu, L.J.; Wu, L.; Mao, H.J.; Song, C.B.; Zhao, S.P.; Liu, H.L.; Li, X.Y.; et al. Air pollution characteristics and their relation to meteorological conditions during 2014–2015 in major Chinese cities. *Environ. Pollut.* **2017**, *223*, 484–496. [CrossRef] [PubMed]
- Su, F.C.; Xu, Q.X.; Wang, K.; Yin, S.S.; Wang, S.B.; Zhang, R.Q.; Tang, X.Y.; Ying, Q. On the effectiveness of short-term intensive emission controls on ozone and particulate matter in a heavily polluted megacity in central China. *Atmos. Environ.* **2021**, *246*, 118111. [CrossRef]
- Wang, J.D.; Zhao, B.; Wang, S.X.; Yang, F.M.; Xing, J.; Morawska, L.; Ding, A.J.; Kulmala, M.; Kerminen, V.M.; Kujansuu, J.; et al. Particulate matter pollution over China and the effects of control policies. *Sci. Total Environ.* **2017**, *584*, 426–447. [CrossRef]
- Li, X.; Feng, Y.J.; Liang, H.Y.; Iop. The Impact of Meteorological Factors on PM_{2.5} Variations in Hong Kong. In Proceedings of the 8th International Conference on Environmental Science and Technology (ICEST), Technical University of Madrid, Computer Science School, Madrid, Spain, 12–14 June 2017.
- Xu, J.M.; Chang, L.Y.; Qu, Y.H.; Yan, F.X.; Wang, F.Y.; Fu, Q.Y. The meteorological modulation on PM_{2.5} interannual oscillation during 2013 to 2015 in Shanghai, China. *Sci. Total Environ.* **2016**, *572*, 1138–1149. [CrossRef] [PubMed]
- Ning, G.C.; Wang, S.G.; Yim, S.H.L.; Li, J.X.; Hu, Y.L.; Shang, Z.W.; Wang, J.Y.; Wang, J.X. Impact of low-pressure systems on winter heavy air pollution in the northwest Sichuan Basin, China. *Atmos. Chem. Phys.* **2018**, *18*, 13601–13615. [CrossRef]
- Li, Z.Q.; Guo, J.P.; Ding, A.J.; Liao, H.; Liu, J.J.; Sun, Y.L.; Wang, T.J.; Xue, H.W.; Zhang, H.S.; Zhu, B. Aerosol and boundary-layer interactions and impact on air quality. *Natl. Sci. Rev.* **2017**, *4*, 810–833. [CrossRef]
- Miao, Y.C.; Liu, S.H. Linkages between aerosol pollution and planetary boundary layer structure in China. *Sci. Total Environ.* **2019**, *650*, 288–296. [CrossRef]
- Miao, Y.C.; Che, H.Z.; Zhang, X.Y.; Liu, S.H. Integrated impacts of synoptic forcing and aerosol radiative effect on boundary layer and pollution in the Beijing-Tianjin-Hebei region, China. *Atmos. Chem. Phys.* **2020**, *20*, 5899–5909. [CrossRef]
- Ding, Y.H.; Liu, Y.J. Analysis of long-term variations of fog and haze in China in recent 50 years and their relations with atmospheric humidity. *Sci. China-Earth Sci.* **2014**, *57*, 36–46. [CrossRef]
- Sun, Y.L.; Wang, Z.F.; Fu, P.Q.; Jiang, Q.; Yang, T.; Li, J.; Ge, X.L. The impact of relative humidity on aerosol composition and evolution processes during wintertime in Beijing, China. *Atmos. Environ.* **2013**, *77*, 927–934. [CrossRef]
- Li, J.D.; Hao, X.; Liao, H.; Hu, J.L.; Chen, H.S. Meteorological Impact on Winter PM_{2.5} Pollution in Delhi: Present and Future Projection under a Warming Climate. *Geophys. Res. Lett.* **2021**, *48*, 10. [CrossRef]
- Zhang, J.P.; Zhu, T.; Zhang, Q.H.; Li, C.C.; Shu, H.L.; Ying, Y.; Dai, Z.P.; Wang, X.; Liu, X.Y.; Liang, A.M.; et al. The impact of circulation patterns on regional transport pathways and air quality over Beijing and its surroundings. *Atmos. Chem. Phys.* **2012**, *12*, 5031–5053. [CrossRef]
- Miao, Y.C.; Guo, J.P.; Liu, S.H.; Liu, H.; Li, Z.Q.; Zhang, W.C.; Zhai, P.M. Classification of summertime synoptic patterns in Beijing and their associations with boundary layer structure affecting aerosol pollution. *Atmos. Chem. Phys.* **2017**, *17*, 3097–3110. [CrossRef]

26. Miao, Y.C.; Liu, S.H.; Guo, J.P.; Huang, S.X.; Yan, Y.; Lou, M.Y. Unraveling the relationships between boundary layer height and PM_{2.5} pollution in China based on four-year radiosonde measurements. *Environ. Pollut.* **2018**, *243*, 1186–1195. [CrossRef] [PubMed]
27. Zhan, C.C.; Xie, M.; Fang, D.X.; Wang, T.J.; Wu, Z.; Lu, H.; Li, M.M.; Chen, P.L.; Zhuang, B.L.; Li, S.; et al. Synoptic weather patterns and their impacts on regional particle pollution in the city cluster of the Sichuan Basin, China. *Atmos. Environ.* **2019**, *208*, 34–47. [CrossRef]
28. Liao, T.T.; Gui, K.; Jiang, W.T.; Wang, S.G.; Wang, B.H.; Zeng, Z.L.; Che, H.Z.; Wang, Y.Q.; Sun, Y. Air stagnation and its impact on air quality during winter in Sichuan and Chongqing, southwestern China. *Sci. Total Environ.* **2018**, *635*, 576–585. [CrossRef]
29. Wang, H.B.; Shi, G.M.; Tian, M.; Zhang, L.M.; Chen, Y.; Yang, F.M.; Cao, X.Y. Aerosol optical properties and chemical composition apportionment in Sichuan Basin, China. *Sci. Total Environ.* **2017**, *577*, 245–257. [CrossRef]
30. Zhao, S.Y.; Feng, T.; Tie, X.X.; Wang, Z.B. The warming Tibetan Plateau improves winter air quality in the Sichuan Basin, China. *Atmos. Chem. Phys.* **2020**, *20*, 14873–14887. [CrossRef]
31. Shu, Z.Z.; Liu, Y.B.; Zhao, T.L.; Xia, J.R.; Wang, C.G.; Cao, L.; Wang, H.L.; Zhang, L.; Zheng, Y.; Shen, L.J.; et al. Elevated 3D structures of PM_{2.5} and impact of complex terrain-forcing circulations on heavy haze pollution over Sichuan Basin, China. *Atmos. Chem. Phys.* **2021**, *21*, 9253–9268. [CrossRef]
32. Zhao, S.P.; Yu, Y.; Yin, D.Y.; Qin, D.H.; He, J.J.; Li, J.L.; Dong, L.X. Two winter PM_{2.5} pollution types and the causes in the city clusters of Sichuan Basin, Western China. *Sci. Total Environ.* **2018**, *636*, 1228–1240. [CrossRef] [PubMed]
33. Hersbach, H.; Bell, B.; Berrisford, P.; Hirahara, S.; Horanyi, A.; Muñoz-Sabater, J.; Nicolas, J.; Peubey, C.; Radu, R.; Schepers, D.; et al. The ERA5 global reanalysis. *Q. J. R. Meteorol. Soc.* **2020**, *146*, 1999–2049. [CrossRef]
34. Kuma, P.; Bender, F.A.M.; Schuddeboom, A.; McDonald, A.J.; Seland, Ø. Machine learning of cloud types shows higher climate sensitivity is associated with lower cloud biases. *Atmos. Chem. Phys. Discuss.* **2022**, *2022*, 184. [CrossRef]
35. Dekhtyareva, A.; Hermanson, M.; Nikulina, A.; Hermansen, O.; Svendby, T.; Holmén, K.; Graversen, R. Springtime nitrogen oxides and tropospheric ozone in Svalbard: Results from the measurement station network. *Atmos. Chem. Phys. Discuss.* **2021**, *2021*, 770. [CrossRef]
36. Barten, J.G.M.; Ganzeveld, L.N.; Steeneveld, G.J.; Krol, M.C. Role of oceanic ozone deposition in explaining temporal variability in surface ozone at High Arctic sites. *Atmos. Chem. Phys.* **2021**, *21*, 10229–10248. [CrossRef]
37. Huth, R.; Beck, C.; Philipp, A.; Demuzere, M.; Ustrnul, Z.; Cahynova, M.; Kysely, J.; Tveito, O.E. Classifications of Atmospheric Circulation Patterns Recent Advances and Applications. In *Trends and Directions in Climate Research*; Gimeno, L., GarciaHerrera, R., Trigo, R.M., Eds.; Annals of the New York Academy of Sciences, Wiley-Blackwell: Hoboken, NJ, USA, 2008; Volume 1146, pp. 105–152.
38. Philipp, A.; Beck, C.; Huth, R.; Jacobeit, J. Development and comparison of circulation type classifications using the COST 733 dataset and software. *Int. J. Climatol.* **2016**, *36*, 2673–2691. [CrossRef]
39. Philipp, A.; Beck, C.; Esteban, P.; Kreienkamp, F.; Krennert, T.; Lochbihler, K.; Lykoudis, S.P.; Pianko-Kluczynska, K.; Post, P.; Alvarez, D.R.; et al. *Cost733Class-1.2 User Guide*; University of Augsburg: Augsburg, Germany, 2014.
40. Philipp, A.; Bartholy, J.; Beck, C.; Erpicum, M.; Esteban, P.; Fettweis, X.; Huth, R.; James, P.; Jourdain, S.; Kreienkamp, F.; et al. Cost733cat—A database of weather and circulation type classifications. *Phys. Chem. Earth* **2010**, *35*, 360–373. [CrossRef]
41. Wang, Y.; Li, H.; Feng, J.; Wang, W.; Liu, Z.; Huang, L.; Yaluk, E.; Lu, G.; Manomaiphiboon, K.; Gong, Y.; et al. Spatial Characteristics of PM_{2.5} Pollution among Cities and Policy Implication in the Northern Part of the North China Plain. *Atmosphere* **2021**, *12*, 77. [CrossRef]
42. Wang, Y.; Sun, Y.; Zhang, Z.; Cheng, Y. Spatiotemporal variation and source analysis of air pollutants in the Harbin-Changchun (HC) region of China during 2014–2020. *Environ. Sci. Ecotech.* **2021**, *8*, 100126. [CrossRef]
43. Wang, G.; Leng, W.; Jiang, S.; Cao, B. Long-Term Variation in Wintertime Atmospheric Diffusion Conditions over the Sichuan Basin. *Front. Environ. Sci.* **2021**, *9*, 763504. [CrossRef]

Article

Regional Air Pollutant Characteristics and Health Risk Assessment of Large Cities in Northeast China

Chunsheng Fang, Hanbo Gao, Zhuoqiong Li and Ju Wang *

College of New Energy and Environment, Jilin University, Changchun 130012, China; fangcs@jlu.edu.cn (C.F.); gaohb19@mails.jlu.edu.cn (H.G.); zhuoqiong21@mails.jlu.edu.cn (Z.L.)

* Correspondence: wangju@jlu.edu.cn; Tel.: +86-131-0431-7228

Abstract: This study systematically investigated the pollution characteristics of atmospheric O₃ and PM_{2.5}, regional transport, and their health risks in three provincial capitals in northeast China during 2016–2020. The results show that O₃ concentrations showed a trend of high summer and low winter, while PM_{2.5} concentrations showed a trend of high winter and low summer during these five years. The results of the correlation analysis indicate that external sources contribute more O₃, while PM_{2.5} is more from local sources. The backward trajectory clustering analysis results showed that Changchun had the highest share of northwest trajectory with a five-year average value of 67.89%, and the city with the highest percentage of southwest trajectory was Shenyang with a five-year average value of 23.95%. The backward trajectory clustering analysis results showed that the share of the northwest trajectory decreased and the share of the southwest trajectory increased for all three cities in 2020 compared to 2016. The results of the potential source contribution function (PSCF) and concentration weighting trajectory (CWT) analysis showed that the main potential source areas and high concentration contribution areas for PM_{2.5} in the northeast were concentrated in Mongolia, Inner Mongolia, Shandong Province, and the northeast, and for O₃ were mainly located in Shandong, Anhui, and Jiangsu Provinces, and the Yellow Sea and Bohai Sea. The non-carcinogenic risk of PM_{2.5} in Harbin was high with a HQ of 2.04, while the other cities were at acceptable levels (HQ < 0.69) and the non-carcinogenic risk of O₃ was acceptable in all three cities (HQ < 0.22). However, PM_{2.5} had a high carcinogenic risk ($4 \times 10^{-4} < CR < 0.44$) and further treatment is needed to reduce the risk.

Keywords: PM_{2.5}; ozone; cluster analysis; health risk

Citation: Fang, C.; Gao, H.; Li, Z.; Wang, J. Regional Air Pollutant Characteristics and Health Risk Assessment of Large Cities in Northeast China. *Atmosphere* **2021**, *12*, 1519. <https://doi.org/10.3390/atmos12111519>

Academic Editors: Duanyang Liu, Kai Qin and Honglei Wang

Received: 14 October 2021

Accepted: 16 November 2021

Published: 18 November 2021

Publisher's Note: MDPI stays neutral with regard to jurisdictional claims in published maps and institutional affiliations.



Copyright: © 2021 by the authors. Licensee MDPI, Basel, Switzerland. This article is an open access article distributed under the terms and conditions of the Creative Commons Attribution (CC BY) license (<https://creativecommons.org/licenses/by/4.0/>).

1. Introduction

With the rapid economic growth and urbanization in China and the world, there is a growing concern in the international community and in China about the relationship between air pollution and public health [1]. Long-term exposure to PM_{2.5} and O₃ can lead to cardiovascular disease [2], ophthalmic disease [3], and premature birth [4]. The combination of chronic and acute exposures leads to a high global and regional burden of mortality and morbidity [5–7]. The research by Edlund et al. [8] showed that air pollution is the biggest environmental contributor to disease, with a disproportionate impact on low and middle income countries. Furthermore, high levels of PM_{2.5} in the outdoor environment can also be exposure to indoors, affecting the health of people who are exposed to indoor rest and work for long periods of time [9]. Thus, both PM_{2.5} and O₃ have attracted widespread public and scientific attention.

To improve air quality in China, in 2013, the Chinese State Council issued the Air Pollution Prevention and Control Action Plan (APPCAP) to reduce the number of PM_{2.5} and associated haze days. Through the implementation of the APPCAP measures, PM_{2.5} concentrations have decreased significantly across the country since 2013. The improvement in air quality was reported by Yue et al. [10] and was mainly associated with strengthening industrial emission standards, upgrading industrial boilers, phasing out obsolete industrial capacity, and promoting cleaner fuels in the residential sector. A decrease in NO_x

and SO₂ accompanied the reduction in PM_{2.5}. However, O₃ concentrations showed an increasing trend. Fan et al. [11] found that the daily average maximum concentration of O₃ (MDA8-O₃) in summer increased from 91.6 µg/m³ in 2015 to 103.1 µg/m³ in 2018, with an annual growth rate of 4.4 µg/m³. The annual average PM_{2.5} concentrations in 2017 in key city groups such as Beijing–Tianjin–Hebei, Yangtze River Delta, and Pearl River Delta compared to 2013 decreased by 39.6%, 34.3%, and 27.7%, respectively, but the 90% quantile of the maximum ozone 8-h sliding average (MDA8-O₃) instead increased by 19.1%, 10.4%, and 5.8%, respectively, compared to 2013 [12–15]. The increase in ozone has triggered a discussion among scholars about the synergistic management of O₃ and PM_{2.5}, and it is necessary and correct to study O₃ and PM_{2.5} under the same perspective. In this study, for the 2016–2020 O₃ and PM_{2.5} pollution phenomena in three provincial capitals in northeast China, we used time series, meteorological factor analysis, and correlation analysis to characterize the pollutants' pollution characteristics. Various methods based on backward trajectories including trajectory clustering, potential source contribution functions (PSCF), and concentration weight trajectories (CWT) were used to analyze the regional transport trends of pollutants. Health risks were assessed using methods recommended by the United States Environmental Protection Agency (USEPA).

2. Materials and Methods

2.1. Study Area and Data Selection

Northeast China spans the middle temperate and cold temperate zones from south to north, and has a temperate monsoon climate with four distinct seasons, warm and rainy in summer and cold and dry in winter. From the southeast to the northwest, the annual precipitation drops from 1000 mm to less than 300 mm, transitioning from the humid and semi-humid zones to the semi-arid zone.

Considering the meteorological conditions and the current urban development situation in northeast China, three typical large cities in northeast China were selected as the subjects of this study. A total of 27 automatic air quality monitoring stations in the above three cities were selected for this study, as shown in Figure 1, and the hourly PM_{2.5} and O₃ concentration data for 2016–2020 were obtained from the China Environmental Quality Monitoring Platform, with 10 stations selected in Harbin, nine in Changchun, and eight in Shenyang (<https://www.aqistudy.cn/historydata/>) (accessed on 25 June 2021). The meteorological data were obtained from city stations in each city and are available on the China Meteorological Data Network (<http://data.cma.cn/>) (accessed on 16 June 2021).

2.2. Backward Trajectory Clustering Analysis

This study used the HYSPLIT (Hybrid Single Particle Lagrangian Integrated Trajectory) model developed by the National Oceanic Atmospheric Center (NOAA) and the Australian Bureau of Meteorology (BOM) (<http://ready.arl.noaa.gov/HYSPLIT.php>) (accessed on 21 June 2021) simulates the 72 h backward trajectory at 500 m height in the central city of three provincial capitals to analyze the atmospheric pollutant transport and dispersion trajectory, and other scholars have also conducted similar studies using this model in different areas [16–18].

To facilitate the analysis of pollutant migration paths, we used the stepwise cluster analysis (SCA) algorithm to cluster the backward trajectories with some optimization [19,20]. The clustering analysis process is shown by Equations (1)–(3):

$$D = \sqrt{\sum_{j=0}^t d_j^2} \quad (1)$$

$$\text{SPVAR} = \sum_{i=1}^X \sum_{j=0}^t D_{ij}^2 \quad (2)$$

$$\text{TSV} = \sum \text{SPVAR} \quad (3)$$

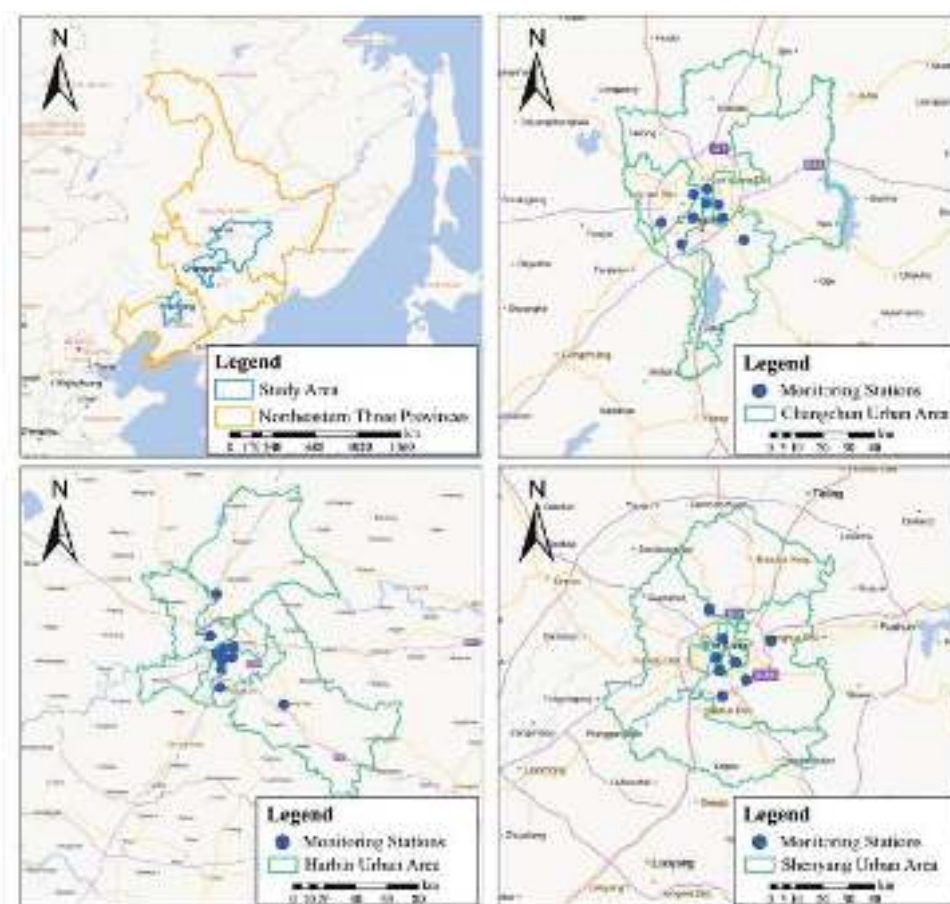


Figure 1. Geographical location and site distribution in the study area.

In the above equation, i is the number of trajectories; j is the number of passing points; t is the movement time of airflow; d_j is the distance between the j th point of two trajectories; X is the number of trajectories in the cluster; D is the distance between trajectories, so D_{ij} indicates the distance from the j th passing point in the i th trajectory to the corresponding point on the average trajectory; SPVAR is the spatial variation of each group of trajectories; and TSV is the total spatial variation. The stepwise cluster analysis method can group the adjacent points into one category in a large number of statistical samples, and then select the trajectories with higher similarity for classification. The more classifications, the closer the situation is to the real situation, and the smaller the error of the results.

Cluster analysis was performed on 8760 or 8784 trajectories for each year throughout the study period to identify the transport pathways of pollutants in different periods. In this study, the clustering was set to result in eight trajectories.

2.3. Potential Source Contribution Function (PSCF) and Concentration Weighting Trajectory (CWT) Analysis

2.3.1. PSCF Analysis

In this study, PSCF analysis was used to locate the pollution sources. The weighting factor W_{ij} used in this study reduced the uncertainty of the PSCF results, called WPSCF, and analyzed the potential source contribution areas of $PM_{2.5}$ and O_3 in the capital cities of northeast China for the years 2016–2020 overall and for single years 2016 and 2020 [21]. In order to calculate the PSCF, the area through which the trajectory passes should first be gridded, and the grid resolution was set to 0.5×0.5 in this study [22,23].

For the PSCF analysis of trajectories, we combined the pollution of $PM_{2.5}$ and O_3 in northeast China to mark trajectories with O_3 concentrations more significant than the 75th percentile and $PM_{2.5}$ concentrations greater than $75 \mu g/m^3$ as exceedance trajectories, where the $PM_{2.5}$ limit value was the limit value of the secondary standard of the National

Ambient Air Quality Standard (NAAQS) set by the Ministry of Ecology and Environment of China. A weighting factor W_{ij} was introduced. Its value will depend on the relationship between the sum of the transmission time of all trajectories in a particular grid and the average residence time of each grid. In this study, W_{ij} is expressed by Equation (4):

$$W_{ij} = \begin{cases} 1.0 & n_{ij} > 90 \\ 0.8 & 30 < n_{ij} \leq 90 \\ 0.45 & 20 < n_{ij} \leq 30 \\ 0.10 & 0 < n_{ij} \leq 20 \end{cases} \quad (4)$$

2.3.2. CWT Analysis

The CWT method can quantify the concentration contribution level of external transport by taking the average value of the concentration of samples corresponding to all trajectories passing through a single grid during the study period [24]. The CWT analysis method can obtain the difference in the pollution level of contaminated trajectories by calculating the weighted degree. In the CWT analysis method, each grid point is assigned a degree of weight. By introducing the same numerical correction from W_{ij} in the PSCF method, the weighted average concentration value (WCWT value) can be used to distinguish the source intensity of potential sources [25,26].

A higher WCWT value in the grid indicates that the air mass passing through the grid results in a high receiving point concentration, and the area corresponding to this grid can be considered as a potential area of high concentration contribution to the external transport of pollutants from the receiving area.

2.4. Health Risk Assessment

In this study, health risks associated with O_3 and $PM_{2.5}$ via the inhalation route were calculated according to the recommended methods of the U.S. EPA and previously reported studies [27,28]. Exposure concentrations (EC) of O_3 and $PM_{2.5}$ were calculated according to Equation (5).

$$EC = (CA \times EF \times ET \times ED) / AT \quad (5)$$

In this expression, CA is the concentration of O_3 and $PM_{2.5}$; ET is the exposure time (3 h/day); EF is the exposure frequency (300 d/year); ED is the exposure duration (25 years); and AT is the average time (non-carcinogenic risk: $ED \times 365 \text{ d/year} \times 24 \text{ h/day}$, carcinogenic risk: $70 \text{ years} \times 365 \text{ d/year} \times 24 \text{ h/day}$). The hazard quotient (HQ) method was used to estimate the non-carcinogenic risk. The carcinogenic risk CR was calculated from the Inhalation Unit Risk (IUR). The HQ and CRs are expressed by Equations (6) and (7).

$$HQ = EC / REL \quad (6)$$

$$CR = EC \times IUR \quad (7)$$

In the above equation, REL is the reference exposure level. According to the NAAQS, the second upper limit standards for O_3 and $PM_{2.5}$ were $160 \mu\text{g}/\text{m}^3$ and $75 \mu\text{g}/\text{m}^3$, respectively. The IUR value per $\mu\text{g}/\text{m}^3$ of $PM_{2.5}$ was 0.008 [29]. The non-carcinogenic and carcinogenic risks of $PM_{2.5}$ were calculated. In contrast, due to the lack of available data on exposure parameters, only non-carcinogenic risks were determined for O_3 exposure. An HQ value less than 1 indicates no significant risk. A CR value less than 1×10^{-6} indicates a negligible cancer risk, a CR value between 1×10^{-6} and 1×10^{-4} indicates a potential cancer risk, and a CR value greater than 1×10^{-4} indicates a high potential cancer risk.

3. Results and Discussion

3.1. Pollution Characteristics of Major Cities in the Three Eastern Provinces

3.1.1. Annual Variation of $PM_{2.5}$ and O_3 Concentrations

As shown in Figure 2, the five-year time series of O_3 and $PM_{2.5}$ shows that, in general, $PM_{2.5}$ shows a high concentration in winter and a low concentration in summer in these five

years, which is basically consistent with the results of other studies [30], mainly because there is a heating period in northeast China, which generally reaches about five months, so it shows a trend of high $\text{PM}_{2.5}$ in roughly late October–early April [31,32]. The overall trend of $\text{PM}_{2.5}$ is high. For O_3 , concentrations are higher in the late spring, throughout the summer, and early autumn in the three major cities in the northeast than in the winter, that is, they are higher in May–September, mainly because of the high temperature in summer and low temperature in winter, and O_3 has a certain sensitivity to temperature [33]. It is also noteworthy that in winter, all three cities experience pollution events with different degrees of high concentrations, with Harbin having the highest frequency, with varying degrees of high $\text{PM}_{2.5}$ concentration days ($>300 \mu\text{g}/\text{m}^3$) in each of the years 2016–2020, Changchun in 2020, and Shenyang without, with Harbin reaching a maximum daily average concentration of $487.8 \mu\text{g}/\text{m}^3$, while Changchun reached a maximum of $508.4 \mu\text{g}/\text{m}^3$, which was the highest value among the three cities, and Shenyang was $266.9 \mu\text{g}/\text{m}^3$.

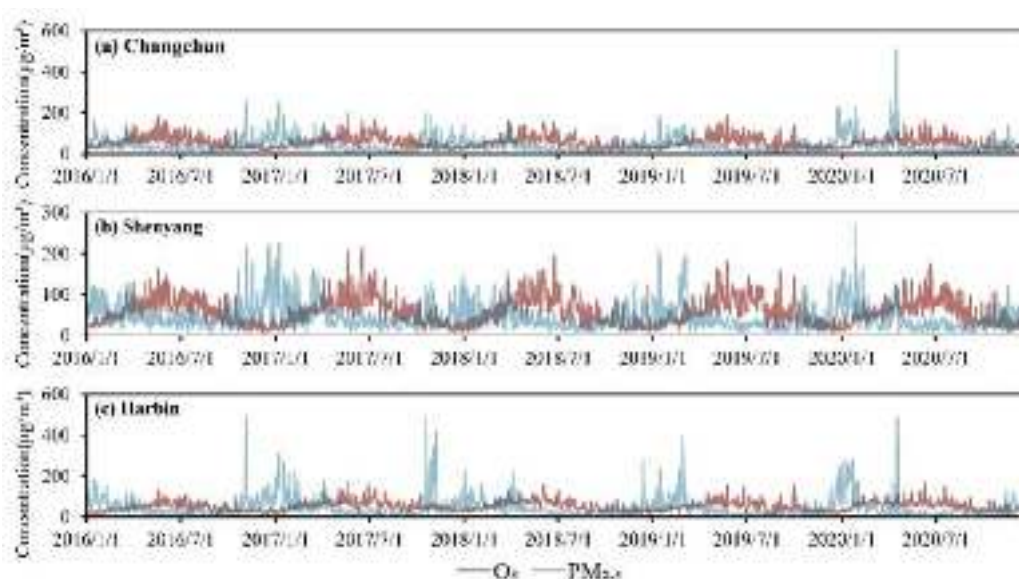


Figure 2. Five-year time series of $\text{PM}_{2.5}$ and O_3 concentrations in the capital cities of northeast China ((a) Changchun; (b) Shenyang; (c) Harbin. Red and blue lines are O_3 and $\text{PM}_{2.5}$ concentrations, respectively).

3.1.2. Relationship between Meteorological Factors and $\text{PM}_{2.5}$ and O_3

The distribution of $\text{PM}_{2.5}$ and O_3 in 2016–2020 in the three provincial capitals in each wind direction is shown in Figure 3. The dominant wind direction in Changchun and Harbin is southwest followed by northwest, and the dominant wind direction in Shenyang is southward followed by northeast. The results show that one of the influential factors causing pollution in the northeast region may be the transfer of pollutants from other surrounding areas to the downwind region due to atmospheric flow, while higher wind speeds on clean days may also serve to disperse pollutants, which may also reduce pollutant concentrations in the northeast region [20].

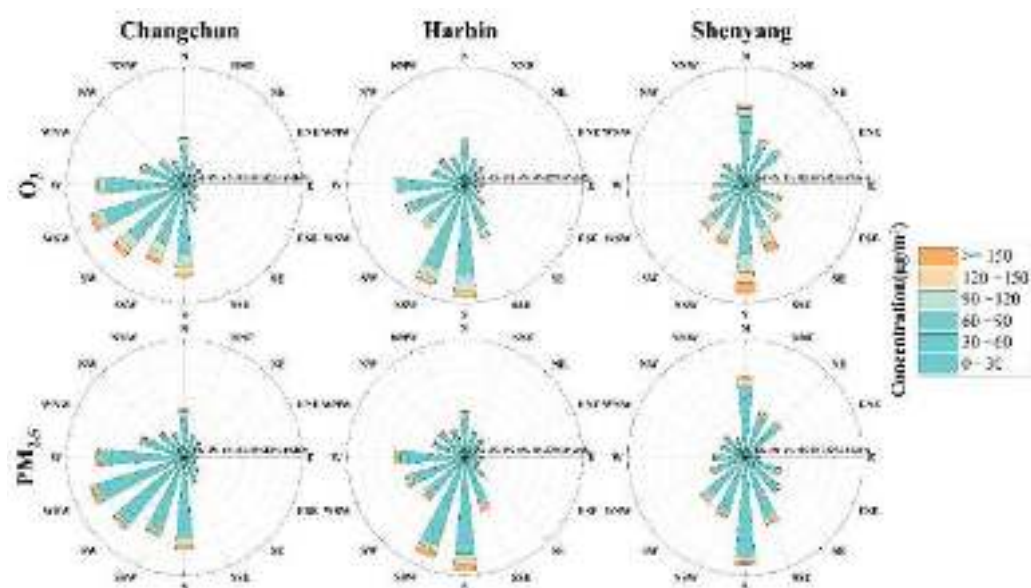


Figure 3. Distribution of $PM_{2.5}$ and O_3 concentrations in Changchun, Shenyang, and Harbin in each wind direction.

As shown in Figure 4, the correlations between $PM_{2.5}$ and O_3 and other meteorological factors were most significant in the studied cities. $PM_{2.5}$ was positively correlated with atmospheric pressure and relative humidity and negatively correlated with temperature and wind speed in all cities. The highest correlation coefficients of $PM_{2.5}$ with atmospheric pressure and temperature were in Harbin, -0.36 and 0.28 , respectively, and the highest correlation coefficients with relative humidity and wind speed were in Shenyang, 0.1 and -0.17 , respectively. It is worth noting that $PM_{2.5}$ was not significantly correlated with wind direction, but O_3 was negatively correlated with wind direction; this result indicates that in the large cities in the northeast region, $PM_{2.5}$ from regional transmission $PM_{2.5}$ concentrations do not account for a high proportion, mostly from local sources, while O_3 is influenced by regional transport, which leads to an increase in local O_3 concentrations.

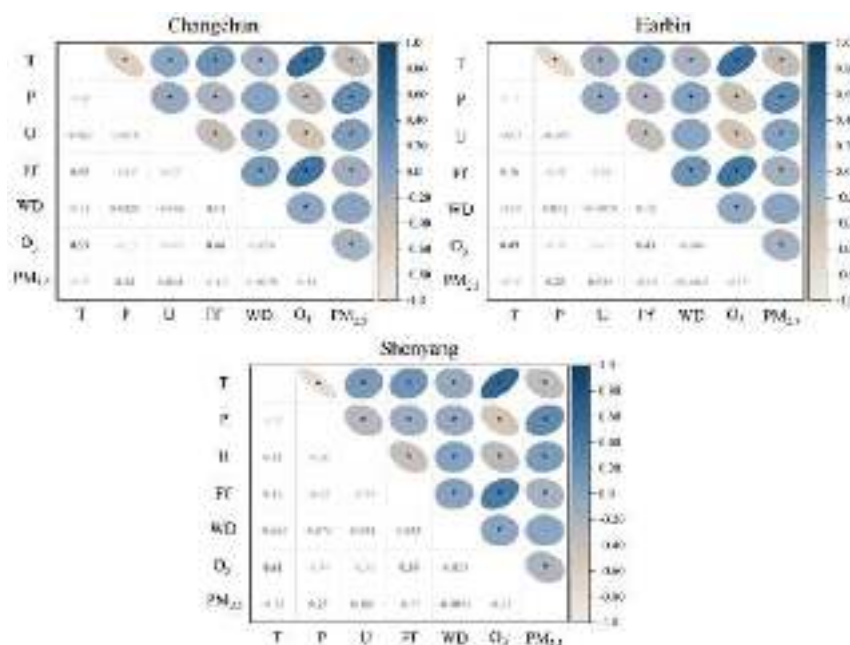


Figure 4. Correlation between $PM_{2.5}$ and O_3 and each meteorological factor in the capital cities of northeast China ($p < 0.05$).

O₃ is positively correlated with temperature and wind speed in each city and negatively correlated with atmospheric pressure and relative humidity. The highest correlation coefficients with temperature and atmospheric pressure were in Shenyang with 0.61 and −0.49, respectively; relative humidity and wind direction in Harbin with −0.47 and −0.046, respectively; and wind speed in Changchun with 0.46. Notably, the correlation results of O₃ and PM_{2.5} with each meteorological factor were the opposite, especially with wind direction and wind speed. This indicates that external sources contribute more O₃, while PM_{2.5} is more from local sources.

3.2. Backward Trajectory-Based PSCF and CWT Analysis

3.2.1. Backward Trajectory Clustering Analysis

As shown in Figure 5, Changchun, Harbin, and Shenyang are all dominated by the northwest direction trajectory, followed by the southwest direction, and the trajectory with the longest transmission distance also tends to appear in the northwest direction. For Changchun, the proportion of northwest trajectories was 77.43% in 2016, while it decreased to 64.33% in 2020, while the proportion of southwest trajectories increased from 14.32% in 2016 to 27.94% in 2020. For Harbin, the northwest trajectory accounted for 64.34% in 2016, while it decreased to 56.41% in 2020, and the southwest trajectory increased from 19.73% in 2016 to 23.11% in 2020. For Shenyang, the percentage of northwest trajectory was 65.91% in 2016, while it dropped to 60.33% in 2020, and the percentage of southwest trajectory increased from 22.79% in 2016 to 26.09% in 2020.

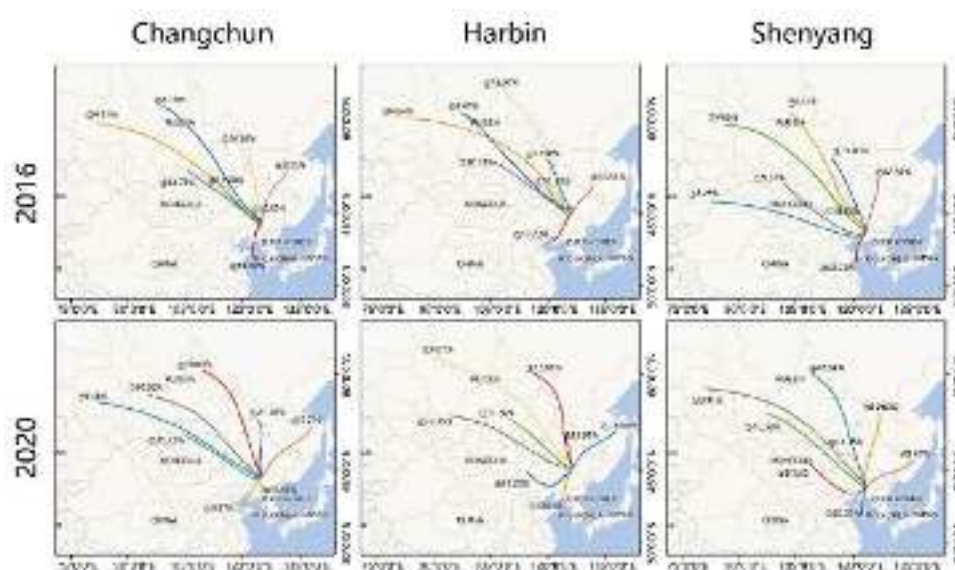


Figure 5. Backward trajectory clustering results for the northeast provincial capitals, 2016 and 2020 (trajectory simulation time interval was 1 h, simulation time was 72 h).

Overall, the city with the most northwest-oriented trajectory was Changchun, which is located in the central part of the northeast region, with the Changbai Mountains in the west, so the air masses transmitted from Russia and Japan in the east are small, while too many mountains do not block Harbin and Shenyang, so the air masses transmitted in the east share part of the percentage. The city with the most southwestern trajectories was Shenyang, which is due to the different altitudes of the three cities. Shenyang, which has the lowest latitude, was most strongly influenced by the southward Bohai anticyclone, so the total percentage of trajectories was the highest, while Harbin, which has the highest latitude, was the least influenced by the Bohai anticyclone, so the percentage of trajectories was the lowest. It can also be found that compared with 2016, the trajectory share of the southwest direction in all three cities increased in 2020, while the trajectory share of the

northwest direction decreased, which was related to the annual meteorological conditions in the year.

3.2.2. PSCF Analysis

As shown in Figure 6, the potential source areas for $PM_{2.5}$ in Harbin were mainly in Mongolia, Inner Mongolia, and Hebei in 2016, with the addition of Henan in 2020, and the potential source areas in Changchun were mainly in Mongolia, Shandong, and Jiangsu in 2016, with Shandong and eastern Russia in 2020. The potential source areas of $PM_{2.5}$ in Shenyang were mainly located in Mongolia, Inner Mongolia, and Shanxi as well as the border between Heilongjiang and Jilin and the East China Sea, which will be reduced to Mongolia, Jilin Province and Heilongjiang Province in 2020. The above results show that the northwestern countries and provinces are the main contributors to the external sources of $PM_{2.5}$ in these three large cities. The reason is that the dust aerosols from Mongolia, Russia, and Inner Mongolia and the anthropogenic particulate emissions from the passing areas arrive in northeastern China along with the northwestern winds, thus contributing to a certain $PM_{2.5}$ concentration, indicating that the long-distance transmission of particulate matter is noteworthy.

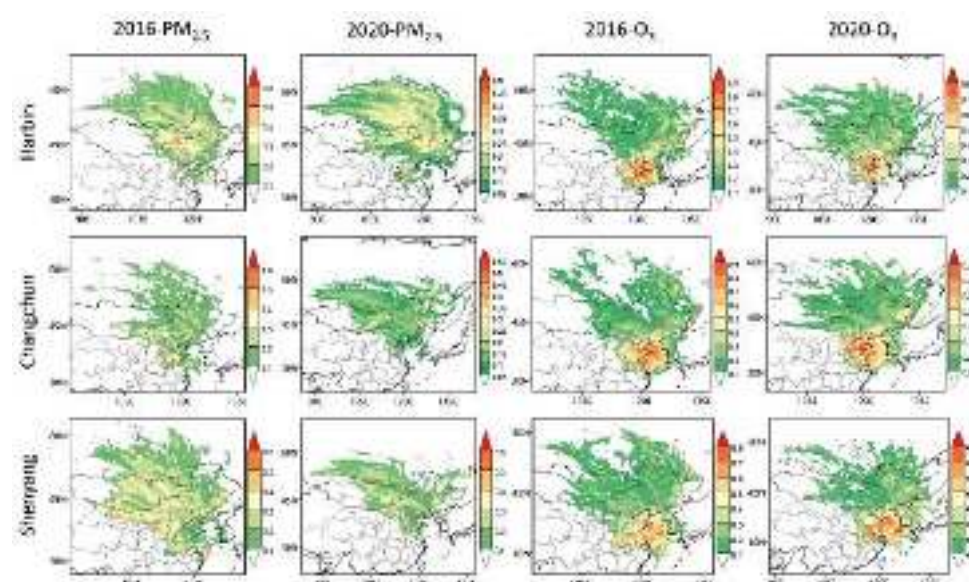


Figure 6. Potential source areas of $PM_{2.5}$ and O_3 in the capital cities of northeast China.

The potential source areas of O_3 in Harbin in 2016 were mainly distributed in Shandong Province, Jiangsu Province, and the Yellow Sea and Bohai Sea, and remain unchanged in 2020. The potential source areas of O_3 in Changchun in 2016 were mainly distributed in the same way as Harbin in 2016, and some areas in Anhui Province were added in 2020. The potential source areas of O_3 in Shenyang in 2016 were mainly distributed in Anhui, Jiangsu, and the Yellow Sea and Bohai Sea, and remain unchanged in 2020. The distribution of potential source areas for O_3 in Shenyang in 2016 was mainly in Anhui, Jiangsu, and the Yellow Sea and Bohai Sea, and remained the same in 2020. In summary, the potential source areas of O_3 in these three cities were generally concentrated in Shandong, Anhui, Jiangsu, and the Yellow Sea and Bohai Sea, among which the WPSCF values were generally higher in the Yangtze River Delta region, which emits NO_x and VOC plus photochemical pollution due to the developed shipbuilding industry, petrochemical industry, and industry, which play an obvious role in promoting the generation of O_3 and will further influence the atmospheric oxidation through regional transmission. This affects the atmospheric oxidation in the northeast, resulting in high WPSCF values in these areas. The O_3 generated from the refraction of sunlight by marine droplets in the Yellow Sea and Bohai Sea reaches

the northeast region through regional transport, which is also the reason for the high WPSCF values in the Yellow Sea and Bohai Sea region.

3.2.3. CWT Analysis

The CWT distribution characteristics of $PM_{2.5}$ and O_3 in the capital cities of northeast China in 2016–2020 are shown in Figure 7. For $PM_{2.5}$, in the results for Harbin, the high contributing regions are mainly concentrated in Mongolia, Russia, and Inner Mongolia in 2016 and 2020. In Changchun's results, the high contributing regions were concentrated in Heilongjiang, Inner Mongolia, Shandong, and Hebei Provinces in 2016, and changed to Russia, Mongolia, Jilin, and Shandong Provinces in 2020. For Shenyang, the high contributing regions were concentrated in Russia, Mongolia, Inner Mongolia, Shanxi, Hebei, and northeast China in 2016 and reduced to Shanxi and Hebei in 2020. For O_3 , in the results for Harbin, the high contributing regions in 2016 were mainly in Shandong, Jiangsu, and the Yellow and Bohai Seas, with the addition of Liaoning in 2020. For Changchun, the high contributing regions were mainly located in Hebei, Shandong, and the Yellow and Bohai Seas in 2016, with the addition of Jiangsu and Liaoning in 2020. In the results for Shenyang, the high contributing areas were mainly located in Shandong, Jiangsu, Anhui, and the Yellow Sea and Bohai Sea in 2016, and remain unchanged in 2020.

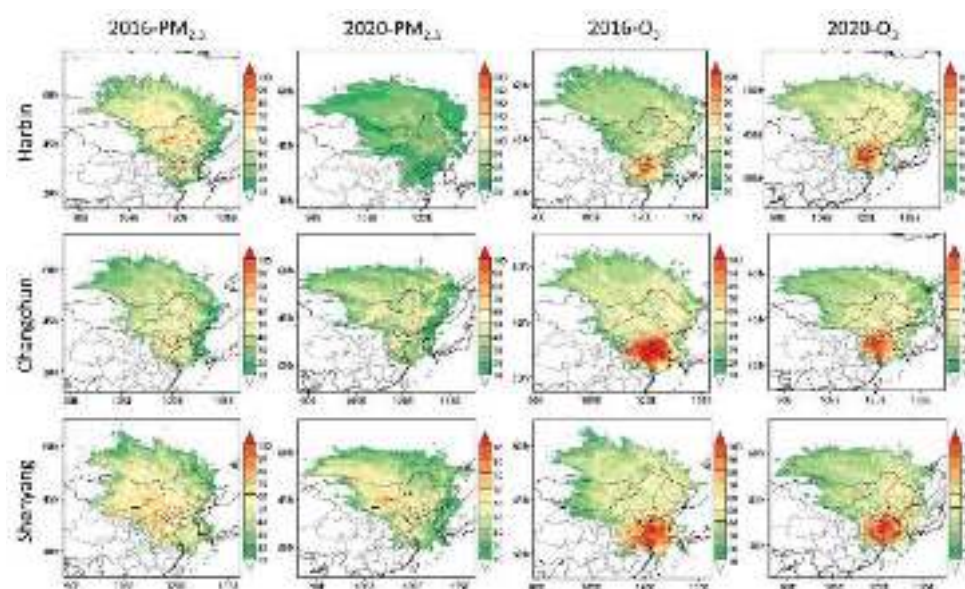


Figure 7. Results of CWT analysis of $PM_{2.5}$ and O_3 in the capital cities of northeast China.

In summary, it can be concluded that the $PM_{2.5}$ concentrations contributed by neighboring cities are essentially the contribution of local emissions in northeast China, while long-range transport also contributes a high $PM_{2.5}$ concentration. Compared with O_3 , the concentration contribution of $PM_{2.5}$ through regional transport comes more from the northwest, which is consistent with the cluster analysis results. In contrast, O_3 is more influenced by air masses transmitted from the south, which also confirms that O_3 pollution south of northeastern China is serious and even affects the air quality in the north, as pointed out by other studies [34].

3.3. Health Risk Assessment

The characteristics of potential non-carcinogenic risk hazard quotient (HQ) and carcinogenic risk (CR) for O_3 and $PM_{2.5}$ in Harbin, Shenyang, and Changchun are shown in Figure 8 and Tables 1–3. At all sites, the HQ values of $PM_{2.5}$ and O_3 and the sum of both were below the acceptable limit of 1.0 most of the time, indicating an acceptable risk. However, at most stations in Harbin, the maximum value of HQ for $PM_{2.5}$ was more significant than 1, reaching a maximum of 2.044, indicating some non-carcinogenic risk

on a few heavy pollution days. However, the CR values of PM_{2.5} were all greater than 1.0×10^{-4} , which had a high carcinogenic risk. In other countries, the same results were obtained by Othman et al. [26] in Selangor, Peninsular Malaysia, and in China, similar results were obtained by Wang et al. [25] in Yancheng, Jiangsu, China.

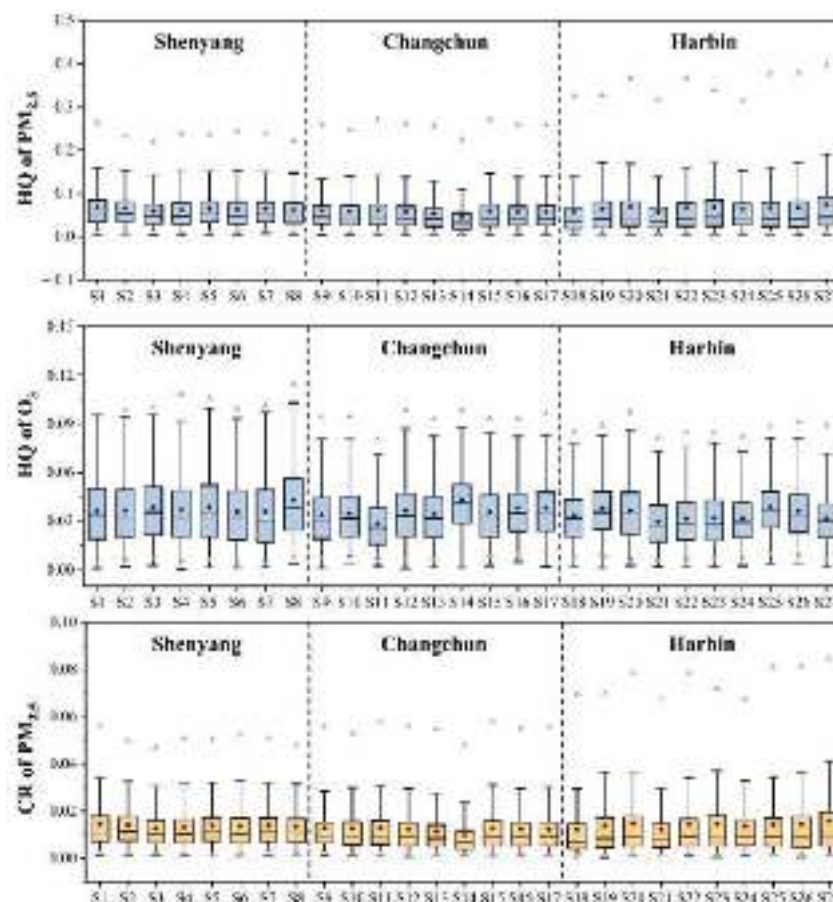


Figure 8. Distribution of hazard quotient (HQ) values of PM_{2.5} and O₃ with carcinogenic risk (CR) values of PM_{2.5} at each monitoring station (S1–S27 are the numbers of automatic air quality monitoring stations).

Table 1. Non-carcinogenic risks, estimated as HQ, and the carcinogenic risks, estimated as CR, from exposure to O₃ and PM_{2.5} in Shenyang.

Pollutants		S1	S2	S3	S4	S5	S6	S7	S8
Non-carcinogenic risks									
O ₃	Min	0.0011	0.0023	0.0027	0.0006	0.0018	0.0013	0.0018	0.0037
	Max	0.1388	0.1391	0.1511	0.1493	0.1304	0.1392	0.1391	0.1535
	Median	0.0340	0.0322	0.0354	0.0322	0.0342	0.0321	0.0308	0.0384
	Mean	0.0365	0.0364	0.0386	0.0370	0.0384	0.0358	0.0358	0.0427
PM _{2.5}	Min	0.0051	0.0056	0.0046	0.0043	0.0027	0.0026	0.0068	0.0041
	Max	0.4353	0.4114	0.3349	0.3148	0.3755	0.4594	0.4357	0.3101
	Median	0.0513	0.0521	0.0462	0.0472	0.0515	0.0478	0.0515	0.0504
	Mean	0.0675	0.0659	0.0591	0.0614	0.0645	0.0629	0.0644	0.0621
Carcinogenic risks									
PM _{2.5}	Min	0.0011	0.0012	0.0010	0.0009	0.0006	0.0006	0.0015	0.0009
	Max	0.0933	0.0882	0.0718	0.0675	0.0805	0.0984	0.0934	0.0665
	Median	0.0110	0.0112	0.0099	0.0101	0.0110	0.0102	0.0110	0.0108
	Mean	0.0145	0.0141	0.0127	0.0132	0.0138	0.0135	0.0138	0.0133

Table 2. Non-carcinogenic risks, estimated as HQ, and the carcinogenic risks, estimated as CR, from exposure to O₃ and PM_{2.5} in Changchun.

Pollutants		S9	S10	S11	S12	S13	S14	S15	S16	S17
Non-carcinogenic risks										
O ₃	Min	0.0013	0.0044	0.0026	0.0010	0.0019	0.0013	0.0026	0.0046	0.0021
	Max	0.1164	0.1156	0.1054	0.1277	0.1193	0.1312	0.1200	0.1235	0.1311
	Median	0.0306	0.0317	0.0259	0.0334	0.0316	0.0411	0.0322	0.0350	0.0344
	Mean	0.0337	0.0348	0.0286	0.0365	0.0344	0.0429	0.0354	0.0378	0.0380
PM _{2.5}	Min	0.0048	0.0043	0.0040	0.0021	0.0038	0.0030	0.0024	0.0032	0.0028
	Max	0.6070	0.4541	0.4771	0.5710	0.5801	0.6858	0.6086	0.5257	0.4754
	Median	0.0450	0.0436	0.0440	0.0416	0.0390	0.0320	0.0416	0.0415	0.0412
	Mean	0.0596	0.0586	0.0605	0.0573	0.0533	0.0446	0.0590	0.0577	0.0575
Carcinogenic risks										
PM _{2.5}	Min	0.0010	0.0009	0.0009	0.0004	0.0008	0.0007	0.0005	0.0007	0.0006
	Max	0.1301	0.0973	0.1022	0.1224	0.1243	0.1470	0.1304	0.1126	0.1019
	Median	0.0096	0.0094	0.0094	0.0089	0.0084	0.0068	0.0089	0.0089	0.0088
	Mean	0.0128	0.0126	0.0130	0.0123	0.0114	0.0096	0.0126	0.0124	0.0123

Table 3. Non-carcinogenic risks, estimated as HQ, and the carcinogenic risks, estimated as CR, from exposure to O₃ and PM_{2.5} in Harbin.

Pollutants		S18	S19	S20	S21	S22	S23	S24	S25	S26	S27
Non-carcinogenic risks											
O ₃	Min	0.0019	0.0013	0.0028	0.0021	0.0019	0.0024	0.0026	0.0039	0.0039	0.0019
	Max	0.1092	0.1209	0.1320	0.1059	0.1294	0.2202	0.1131	0.1223	0.1285	0.1170
	Median	0.0319	0.0354	0.0343	0.0264	0.0289	0.0288	0.0293	0.0372	0.0326	0.0296
	Mean	0.0335	0.0380	0.0365	0.0296	0.0314	0.0319	0.0318	0.0387	0.0361	0.0318
PM _{2.5}	Min	0.0037	0.0018	0.0039	0.0037	0.0050	0.0020	0.0052	0.0041	0.0021	0.0040
	Max	0.9925	1.4299	1.4414	1.1773	2.0438	1.2372	0.8054	1.2463	1.5295	0.9394
	Median	0.0332	0.0394	0.0429	0.0363	0.0410	0.0446	0.0418	0.0413	0.0400	0.0448
	Mean	0.0569	0.0639	0.0687	0.0573	0.0672	0.0678	0.0633	0.0662	0.0670	0.0739
Carcinogenic risks											
PM _{2.5}	Min	0.0008	0.0004	0.0008	0.0008	0.0011	0.0004	0.0011	0.0009	0.0005	0.0009
	Max	0.2127	0.3064	0.3089	0.2523	0.4380	0.2651	0.1726	0.2671	0.3278	0.2013
	Median	0.0071	0.0085	0.0092	0.0078	0.0088	0.0096	0.0090	0.0088	0.0086	0.0096
	Mean	0.0122	0.0137	0.0147	0.0123	0.0144	0.0145	0.0136	0.0142	0.0144	0.0158

In Shenyang, the site with the highest HQ mean for O₃ was S8, reaching 0.0427; the site with the highest HQ mean for PM_{2.5} was S1, reaching 0.0675; the site with the highest CR mean for PM_{2.5} was S1, reaching 0.0145. In Changchun, the site with the highest HQ mean for O₃ was S14, reaching 0.0429, and the site with the highest HQ mean for PM_{2.5}. In Harbin, the highest HQ mean for O₃ was S25, reaching 0.0387, the highest HQ mean for PM_{2.5} was S27, reaching 0.0739, and the highest CR mean for PM_{2.5} was S27 at 0.0158.

In summary, among the three cities, the highest non-carcinogenic risk for O₃ was Changchun and the lowest was Harbin. The highest non-carcinogenic risk for PM_{2.5} was Harbin and the lowest was Changchun, and the results for the carcinogenic risk for PM_{2.5} were the same as those for the non-carcinogenic risk, and the carcinogenic risk for PM_{2.5} was high in all three eastern provinces, with the highest Harbin urgently needing to control the pollution of PM_{2.5}, while for O₃, even though the HQ values of all three cities were exceeded, Changchun, which had the highest HQ, needed to be prevented.

4. Conclusions

Despite the implementation of boiler renovation projects and straw burning bans in China as well as policies and laws that have effectively reduced the concentrations of

various air pollutants, there is still a gap in the cleanliness of the atmosphere in the northeast compared to other developed regions and developed countries. In 2016–2020, three provincial capitals in northeast China also experienced more severe pollution ($>300 \mu\text{g}/\text{m}^3$) due to high $\text{PM}_{2.5}$ concentrations caused by coal-fired heating in winter, with Harbin experiencing the highest frequency of severe pollution. The correlation between meteorological factors and $\text{PM}_{2.5}$ and O_3 corroborates that the external sources of O_3 contribute more and the local sources contribute more of $\text{PM}_{2.5}$.

The cluster analysis results show that the highest proportion of northwest-oriented trajectories was in Changchun and the lowest was in Shenyang, influenced by the surrounding topography. The city with the highest percentage of southwest trajectories was Shenyang and the lowest was Harbin, which is influenced by the Bohai Sea anticyclone and its latitude. The results of the PSCF analysis showed that the main potential source areas of $\text{PM}_{2.5}$ in northeast China were concentrated in Mongolia and Inner Mongolia, and the main potential source areas of O_3 were concentrated in Shandong, Jiangsu, Anhui, and the Yellow Sea and Bohai Sea. The results of the CWT analysis showed that the high concentration of $\text{PM}_{2.5}$ in the northeast China contribution areas were mainly concentrated in Russia, Mongolia, Inner Mongolia, Hebei, and northeast China, and the high concentration contribution areas of O_3 were mainly concentrated in Shandong Province, Jiangsu Province, and the Yellow Sea and Bohai Sea.

The results of the health risk evaluation showed that the mean HQ values of O_3 and $\text{PM}_{2.5}$ in all cities were below the limit values, which indicated that the non-carcinogenic risk of both air pollutants was at an acceptable level. However, the carcinogenic risk of exposure to $\text{PM}_{2.5}$ was relatively high, especially in Harbin, where the highest CR value reached 0.438, indicating that $\text{PM}_{2.5}$ pollution in the northeast still needs further in-depth treatment. Implementing a more stringent regional control of $\text{PM}_{2.5}$ pollution in the northeast and other regions to obtain better air quality is required to implement stricter regional control of pollutants. This study can also provide some basis for future studies of atmospheric pollution characteristics, and in the future, coupled analysis can also be performed using computer techniques based on time decomposition [35], neural-based ensembles [36], nonlinear combinations method [37], and phase adjustment [38] to obtain more accurate, diverse, and informative conclusions.

Author Contributions: Data curation and validation, Z.L.; Methodology and directors, C.F.; Supervision, J.W.; Conceptualization, original draft writing, review and editing, H.G. All authors have read and agreed to the published version of the manuscript.

Funding: This research was funded by the Ecology and Environment Department of Jilin Province. The project numbers are 2018-19 and 2019-08.

Institutional Review Board Statement: Not applicable.

Informed Consent Statement: Not applicable.

Data Availability Statement: Publicly available datasets were analyzed in this study. This data can be found here: [<http://www.cnemc.cn/>] accessed on 17 November 2021.

Acknowledgments: The authors would like to thank the Ecological Environment Monitoring Center of Changchun, Jilin Province, for providing the data on pollutants. Additionally, the authors would like to thank the group members of Laboratories 537 and 142 of Jilin University.

Conflicts of Interest: The authors declare no conflict of interest.

References

1. Zhang, Q.; Jiang, X.; Tong, D.; Davis, S.J.; Zhao, H.; Geng, G.; Feng, T.; Zheng, B.; Lu, Z.; Streets, D.G.; et al. Transboundary health impacts of transported global air pollution and international trade. *Nature* **2017**, *543*, 705–709. [CrossRef]
2. Lelieveld, J.; Pozzer, A.; Poschl, U.; Fnaiss, M.; Haines, A.; Munzel, T. Loss of life expectancy from air pollution compared to other risk factors: A worldwide perspective. *Cardiovasc. Res.* **2020**, *116*, 1910–1917. [CrossRef]
3. Kim, Y.; Choi, Y.H.; Kim, M.K.; Paik, H.J.; Kim, D.H. Different adverse effects of air pollutants on dry eye disease: Ozone, $\text{PM}_{2.5}$, and PM_{10} . *Environ. Pollut.* **2020**, *265*, 115039. [CrossRef]

4. Smith, R.B.; Beevers, S.D.; Gulliver, J.; Dajnak, D.; Fecht, D.; Blangiardo, M.; Douglass, M.; Hansell, A.L.; Anderson, H.R.; Kelly, F.J.; et al. Impacts of air pollution and noise on risk of preterm birth and stillbirth in London. *Environ. Int.* **2020**, *134*, 105290. [CrossRef]
5. Dedoussi, I.C.; Eastham, S.D.; Monier, E.; Barrett, S.R.H. Premature mortality related to United States cross-state air pollution. *Nature* **2020**, *578*, 261–265. [CrossRef]
6. Pope, C.A., III; Coleman, N.; Pond, Z.A.; Burnett, R.T. Fine particulate air pollution and human mortality: 25+ years of cohort studies. *Environ. Res.* **2020**, *183*, 108924. [CrossRef]
7. Zhu, Y.; Wang, Y.; Xu, H.; Luo, B.; Zhang, W.; Guo, B.; Chen, S.; Zhao, X.; Li, W. Joint effect of multiple air pollutants on daily emergency department visits in Chengdu, China. *Environ. Pollut.* **2020**, *257*, 113548. [CrossRef]
8. Edlund, K.K.; Killman, F.; Molnár, P.; Boman, J.; Stockfelt, L.; Wichmann, J. Health Risk Assessment of PM_{2.5} and PM_{2.5}-Bound Trace Elements in Thohoyandou, South Africa. *Int. J. Environ. Res. Public Health* **2021**, *18*, 1359. [CrossRef]
9. Jones, E.R.; Cedeño Laurent, J.G.; Young, A.S.; MacNaughton, P.; Coull, B.A.; Spengler, J.D.; Allen, J.G. The effects of ventilation and filtration on indoor PM_{2.5} in office buildings in four countries. *Build. Environ.* **2021**, *200*, 107975. [CrossRef]
10. Yue, H.; He, C.; Huang, Q.; Yin, D.; Bryan, B.A. Stronger policy required to substantially reduce deaths from PM_{2.5} pollution in China. *Nat. Commun.* **2020**, *11*, 1462. [CrossRef]
11. Fan, H.; Zhao, C.; Yang, Y. A comprehensive analysis of the spatio-temporal variation of urban air pollution in China during 2014–2018. *Atmos. Environ.* **2020**, *220*. [CrossRef]
12. Li, K.; Jacob, D.J.; Liao, H.; Shen, L.; Zhang, Q.; Bates, K.H. Anthropogenic drivers of 2013–2017 trends in summer surface ozone in China. *Proc. Natl. Acad. Sci. USA* **2019**, *116*, 422. [CrossRef] [PubMed]
13. Sicard, P.; De Marco, A.; Agathokleous, E.; Feng, Z.; Xu, X.; Paoletti, E.; Rodriguez, J.J.D.; Calatayud, V. Amplified ozone pollution in cities during the COVID-19 lockdown. *Sci. Total Environ.* **2020**, *735*, 139542. [CrossRef]
14. Wang, Y.; Liao, H. Effect of emission control measures on ozone concentrations in Hangzhou during G20 meeting in 2016. *Chemosphere* **2020**, *261*, 127729. [CrossRef] [PubMed]
15. Wang, Z.; Li, Y.; Chen, T.; Li, L.; Liu, B.; Zhang, D.; Sun, F.; Wei, Q.; Jiang, L.; Pan, L. Changes in atmospheric composition during the 2014 APEC conference in Beijing. *J. Geophys. Res.* **2015**, *120*, 12695–12707. [CrossRef]
16. Park, E.H.; Heo, J.; Kim, H.; Yi, S.-M. The major chemical constituents of PM_{2.5} and airborne bacterial community phyla in Beijing, Seoul, and Nagasaki. *Chemosphere* **2020**, *254*, 126870. [CrossRef]
17. Salmabadi, H.; Khalidy, R.; Saeedi, M. Transport routes and potential source regions of the Middle Eastern dust over Ahvaz during 2005–2017. *Atmos. Res.* **2020**, *241*, 104947. [CrossRef]
18. Xia, L.; Zhang, G.; Zhan, M.; Li, B.; Kong, P. Seasonal variations of atmospheric CH₄ at Jingdezhen station in Central China: Understanding the regional transport and its correlation with CO₂ and CO. *Atmos. Res.* **2020**, *241*, 104982. [CrossRef]
19. Fang, C.; Gao, J.; Wang, D.; Wang, D.; Wang, J. Optimization of stepwise clustering algorithm in backward trajectory analysis. *Neural Comput. Appl.* **2020**, *32*, 109–115. [CrossRef]
20. Wang, L.; Wang, J.; Fang, C. Assessing the Impact of Lockdown on Atmospheric Ozone Pollution Amid the First Half of 2020 in Shenyang, China. *Int. J. Environ. Res. Public Health* **2020**, *17*, 9004. [CrossRef]
21. Polissar, A.V.; Hopke, P.K.; Paatero, P.; Kaufmann, Y.J.; Hall, D.K.; Bodhaine, B.A.; Dutton, E.G. The aerosol at Barrow, Alaska: Long-term trends and source locations. *Atmos. Environ.* **1999**, *33*, 18. [CrossRef]
22. Dimitriou, K.; Kassomenos, P. Combining AOT, Angstrom Exponent and PM concentration data, with PSCF model, to distinguish fine and coarse aerosol intrusions in Southern France. *Atmos. Res.* **2016**, *172*, 74–82. [CrossRef]
23. Dimitriou, K.; Kassomenos, P. Indicators reflecting local and transboundary sources of PM_{2.5} and PMCOARSE in Rome—Impacts in air quality. *Atmos. Environ.* **2014**, *96*, 154–162. [CrossRef]
24. Stohl, A. Trajectory statistics-A new method to establish source-receptor relationships of air pollutants and its application to the transport of particulate sulfate in Europe. *Atmos. Environ.* **1996**, *30*, 579–587. [CrossRef]
25. Li, L.; Yan, D.; Xu, S.; Huang, M.; Wang, X.; Xie, S. Characteristics and source distribution of air pollution in winter in Qingdao, eastern China. *Environ. Pollut.* **2017**, *224*, 44–53. [CrossRef]
26. Zhao, Q.; He, Q.; Jin, L.; Wang, J.; Donato, A. Potential Source Regions and Transportation Pathways of Reactive Gases at a Regional Background Site in Northwestern China. *Adv. Meteorol.* **2021**, *2021*, 1–20. [CrossRef]
27. Wang, L.; Xing, L.; Wu, X.; Sun, J.; Kong, M. Spatiotemporal variations and risk assessment of ambient air O₃, PM₁₀ and PM_{2.5} in a coastal city of China. *Ecotoxicology* **2021**, *30*, 1333–1342. [CrossRef] [PubMed]
28. Othman, M.; Latif, M.T.; Yee, C.Z.; Norshariffudin, L.K.; Azhari, A.; Halim, N.D.A.; Alias, A.; Sofwan, N.M.; Hamid, H.H.A.; Matsumi, Y. PM_{2.5} and ozone in office environments and their potential impact on human health. *Ecotox. Environ. Saf.* **2020**, *194*, 110432. [CrossRef]
29. Othman, M.; Latif, M.T. Air pollution impacts from COVID-19 pandemic control strategies in Malaysia. *J. Clean. Prod.* **2021**, *291*, 125992. [CrossRef]
30. Li, B.; Shi, X.; Liu, Y.; Lu, L.; Wang, G.; Thapa, S.; Sun, X.; Fu, D.; Wang, K.; Qi, H. Long-term characteristics of criteria air pollutants in megacities of Harbin-Changchun megalopolis, Northeast China: Spatiotemporal variations, source analysis, and meteorological effects. *Environ. Pollut.* **2020**, *267*, 115441. [CrossRef]

31. Li, W.; Duan, F.; Zhao, Q.; Song, W.; Cheng, Y.; Wang, X.; Li, L.; He, K. Investigating the effect of sources and meteorological conditions on wintertime haze formation in Northeast China: A case study in Harbin. *Sci. Total Environ.* **2021**, *801*, 149631. [CrossRef] [PubMed]
32. Ma, Y.; Wang, M.; Wang, S.; Wang, Y.; Feng, L.; Wu, K. Air pollutant emission characteristics and HYSPLIT model analysis during heating period in Shenyang, China. *Environ. Monit. Assess.* **2020**, *193*, 9. [CrossRef] [PubMed]
33. Raoufi, S.S.; Goharnejad, H.; Niri, M.Z. Air Pollution Effects on Climate and Air Temperature of Tehran City Using Remote Sensing Data. *Asian J. Water Environ. Pollut.* **2018**, *15*, 79–87. [CrossRef]
34. Liu, N.; Lin, W.; Ma, J.; Xu, W.; Xu, X. Seasonal variation in surface ozone and its regional characteristics at global atmosphere watch stations in China. *J. Environ. Sci.* **2019**, *77*, 291–302. [CrossRef] [PubMed]
35. Neto, P.S.G.D.M.; Marinho, M.H.N.; Siqueira, H.; de Souza Tadano, Y.; Machado, V.; Antonini Alves, T.; de Oliveira, J.F.L.; Madeiro, F. A Methodology to Increase the Accuracy of Particulate Matter Predictors Based on Time Decomposition. *Sustainability* **2020**, *12*, 7310. [CrossRef]
36. Neto, P.S.G.D.M.; Firmino, P.R.A.; Siqueira, H.; Tadano, Y.D.S.; Alves, T.A.; Oliveira, J.F.L.D.; Marinho, M.H.D.N.; Madeiro, F. Neural-Based Ensembles for Particulate Matter Forecasting. *IEEE Access* **2021**, *9*, 14470–14490. [CrossRef]
37. Neto, P.S.G.D.M.; Cavalcanti, G.D.C.; Madeiro, F. Nonlinear combination method of forecasters applied to PM time series. *Pattern Recogn. Lett.* **2017**, *95*, 65–72. [CrossRef]
38. Neto, P.S.G.D.M.; Madeiro, F.; Ferreira, T.A.E.; Cavalcanti, G.D.C. Hybrid intelligent system for air quality forecasting using phase adjustment. *Eng. Appl. Artif. Intell.* **2014**, *32*, 185–191. [CrossRef]

Article

Concentration Characteristics and Photochemical Reactivities of VOCs in Shenyang, China

Ningwei Liu ^{1,*}, Xiaolan Li ¹, Wanhui Ren ², Liguang Li ¹, Congcong Su ² and Chuang Wang ²

¹ Institute of Atmospheric Environment, China Meteorological Administration, Shenyang 110166, China; leexl@iaesy.cn (X.L.); liliguang@iaesy.cn (L.L.)

² Shenyang Ecological Environment Monitoring Center of Liaoning Province, Shenyang 110169, China; rwhui2000@163.com (W.R.); sy23935117@163.com (C.S.); clover310@163.com (C.W.)

* Correspondence: liunw@iaesy.cn

Abstract: We investigated the seasonal and diurnal characteristics of volatile organic compound (VOC) concentrations in Shenyang, China, using the whole-year hourly data of 52 types of VOC at three sites over the year 2019. The photochemical reactivities of VOCs were also studied by analyzing the influence of VOCs on ozone and secondary organic aerosol (SOA) formation potential and the hydroxyl radical consumption rate. It is shown that the order of VOC concentrations from high to low is alkanes, alkynes, alkenes, and aromatic hydrocarbons. For various types of VOCs, the maximum appeared in the morning and at night, whereas the minimum appeared in the afternoon. The contributions of VOCs to ozone formation potential are highest for aromatic hydrocarbons with a value of 78%, followed by alkenes and alkanes, among which toluene and isoprene contributed the most. The contributions of VOCs to SOA formation potential are also highest for aromatic hydrocarbons with a value of 94%, followed by alkanes and alkenes, among which the contributions of toluene and benzene add up to over 70%. Being the most active type of VOCs in atmospheric chemical reactions, aromatic hydrocarbons are the dominant contributor to the formation of both ozone and SOA, and therefore being able to control of the use of a large number of solvents and vehicle exhaust emissions would be an effective way to regulate the formation of ozone and SOA in Shenyang.

Keywords: VOCs; photochemical reactivities; ozone; SOA

Citation: Liu, N.; Li, X.; Ren, W.; Li, L.; Su, C.; Wang, C. Concentration Characteristics and Photochemical Reactivities of VOCs in Shenyang, China. *Atmosphere* **2021**, *12*, 1240. <https://doi.org/10.3390/atmos12101240>

Academic Editors: Duanyang Liu, Kai Qin and Honglei Wang

Received: 12 August 2021

Accepted: 20 September 2021

Published: 23 September 2021

Publisher's Note: MDPI stays neutral with regard to jurisdictional claims in published maps and institutional affiliations.



Copyright: © 2021 by the authors. Licensee MDPI, Basel, Switzerland. This article is an open access article distributed under the terms and conditions of the Creative Commons Attribution (CC BY) license (<https://creativecommons.org/licenses/by/4.0/>).

1. Introduction

The significant role of volatile organic compounds (VOCs) in the process of atmospheric photochemical reactions was first recognized by Haagen-Smit [1]. Since then, the formation of photochemical pollutants such as ozone (O₃) and secondary organic aerosols (SOAs) by VOCs and NO_x via solar radiation has been widely recognized [2–4]. Studying the impact of VOCs and their atmospheric chemical reactions on the formation of atmospheric secondary pollutants is of great significance, and is essential for the sake of not only controlling air pollution, but for revealing the mechanism of atmospheric photochemical reactions.

Factors determining the influence of VOCs on ozone formation in the atmosphere include the levels of hydroxyl radical and NO_x, the proportions of various reaction processes and the efficiencies of NO transforming into NO₂ during these processes, as well as the reaction rates of various VOCs and hydroxyl radicals. The complexity of VOC components results in an uncertain relationship between them and ozone formation. In the early 1990s, the United States Environmental Protection Agency produced a set of standard methods for the analysis of environmental atmospheric VOCs through research, with the intention of not only reducing NO_x, but also of controlling the active VOC components in order to effectively solve the problem of ozone pollution [5,6]. Compared with foreign countries, the study of VOC–NO_x–ozone in China started late, and the concentration limit and measurement specification of VOCs in the atmosphere have not been clearly defined until now

(Ambient Air Quality Standard (GB3095-2012) [7]). Furthermore, the research is mainly focused on the three major polluted areas in China, namely, the Beijing-Tianjin-Hebei region, Pearl River Delta, and Yangtze River Delta, where VOCs play very different roles in the process of ozone formation [8–16]. At present, studies of the VOC-NO_x-ozone relationship and the interactions of VOCs in atmospheric chemical reactions are still urgently needed.

In the formation of urban haze pollution in China, the secondary generated aerosol components account for 51%–77%, of which organic aerosol is the most significant component [17,18]. Observations from 37 sites around the world show that SOA accounts for more than 90% in remote areas and more than 60% in urban areas, despite a relatively high proportion of primary aerosol [16]. In recent years, a set of aerosol formation coefficients (fractional aerosol coefficients, or FACs) were proposed by Grosjean and Seinfeld [19] based on a large number of smoke chamber experimental data and atmospheric chemical kinetics data. Several studies conducted by scholars inside and outside China on SOA formation potential, combining VOCs' observation data and FACs, have consistently shown that aromatic hydrocarbons contribute the most to SOA formation potential [19–22]. Wang et al. [23] studied the SOA formation potential of all aromatic hydrocarbons and isoprene in Shenzhen using the FAC method, and found that toluene contributed the most to SOA formation. In addition, the reactions between VOCs and hydroxyl radicals are the main chemical processes for the transformation of organic compounds, in which the consumption rate of hydroxyl radical is used to evaluate the chemical activity of various VOC species [24].

As the largest city in northeast China, Shenyang's atmospheric environmental problems have hardly been solved in the recent two decades. Despite strong governance, the urbanization trend, leading to a current population of over 9.1 million and an urban area that has rapidly grown to 3500 km² (within the total area of Shenyang of 13,000 km²), makes air pollution a continuing and significant problem in this metropolis. Since 2007, most of the original heavy industry enterprises in downtown Shenyang have been relocated to a new economic development zone approximately 20 km away to the west of the urban center; thus, it is not industrial emissions but traffic emissions that directly affect the ambient air quality over the Shenyang urban area with a total of 2.65 million automobiles, which increase at the rate of 800 per day. Although a number of studies have analyzed the mechanism of pollution formation in Shenyang and its ambient areas [25], few of them have focused on VOCs. In this study, using the whole-year hourly data of 52 types of VOC at each of the three sites over the year 2019, photochemical reactivities of VOCs were revealed, and the prior VOC species were further selected to provide theoretical support for local pollution management.

2. Materials and Methods

2.1. Data Sources

Hourly VOCs and ozone concentration observation data throughout 2019 were from the Shenyang ecological environment monitoring center of Liaoning Province. VOCs' monitoring is based on a GC5000 online gas chromatograph produced by the AMA Instrument Company (Ulm, Germany). The instrument consists of two subsystems (a GC5000 VOC analyzer and a GC5000 BTX analyzer), a calibration module (a DIM200 VOC calibration instrument) and other auxiliary equipment. A type 49i ozone analyzer produced by Thermo Fisher China Co., Ltd. (Shanghai, China) was used for ozone monitoring. The monitoring data of wind direction and speed used to analyze the distribution of wind roses in Shenyang are from the Shenyang National Basic Meteorological Station (NBMS).

The three VOC environmental monitoring sites in Shenyang are Huagongyuan (HGY), Danan Street (DNS), and Tianzhushan Road (TZSR), and the 11 state-controlled ambient air quality monitoring sites are Dongling Road (DLR), Hunnan East Road (HNR), Jingshen Street (JSS), Dongling Street (LDS), Senlin Road (SLR), Shenliao West Road (SLXR), Taiyuan Street (TYS), Wenhua Road (WHR), Xiaoheyuan (XHY), Xinxiu Street (XXS), and Yunong Road (YNR). The locations of each air quality monitoring site and Shenyang NBMS are shown in Figure 1. The characteristics and levels of ozone, NO_x , and $\text{PM}_{2.5}$ are listed in Table 1. HGY, DNS, LDS, TYS, WHR, XHY, and NBMS are urban sites; TZSR, DLR, HNR, XXS, YNR, SLXR, and JSS are suburban sites; and SLR is a rural site due to its remote location. The land-use at the suburban sites is a mixture of city and cropland, whereas the rural site, SLR, is primarily covered by forest and a reservoir. HGY is located in an economic-technical development zone with many enterprises, including chemical, electrical, and pharmaceutical factories, etc., which leads to a large number of industrial source emissions, while the transport of freight vehicles also emits vehicle exhaust. In addition, HNR and XXS are accessible via a highway around the city area of Shenyang.

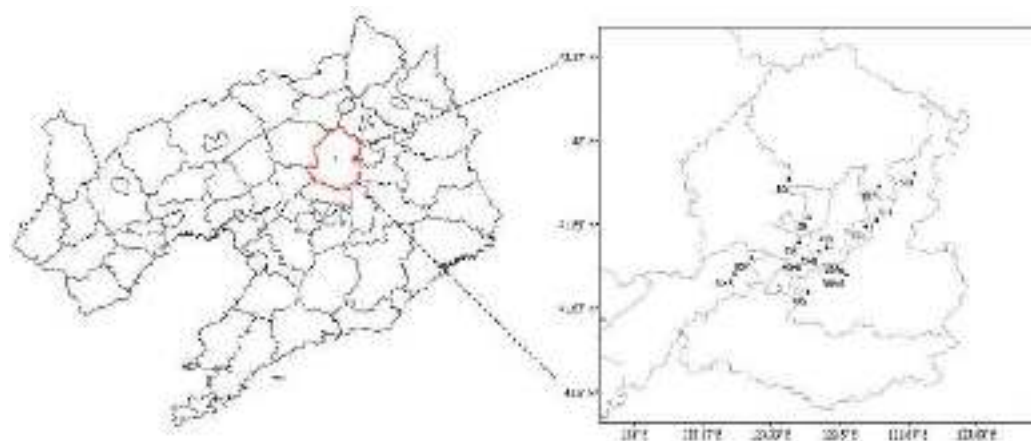


Figure 1. Map of Liaoning Province and locations of the ambient air quality monitoring sites in Shenyang.

Regarding the key pollutants, the ozone level at the suburban sites is higher than that at the urban sites in general, among which the maximum appears at YNR, a downwind suburban site located in the direction of the prevailing wind from Shenyang. Spatial variation in Shenyang has been reported based on the observations from 2013 to 2015 as well [25]. However, the levels in NO_x and $\text{PM}_{2.5}$ are significantly higher at urban sites than at suburban sites, with a peak level in NO_x appearing at HGY and high levels at the other two VOC environmental monitoring sites. Compared to pollutant levels in Beijing in 2016 [26], $\text{PM}_{2.5}$ in Shenyang during 2019 was relatively close, whereas NO_x in Shenyang was around 10 ppbv higher, meaning that the current high-level of NO_x in Shenyang still cannot be negligible.

Table 1. Characteristics and levels of ozone, NO_x (ppbv) and PM_{2.5} (µg/m³).

Information of Each Site	VOCs' Environmental Monitoring Site					State-Controlled Ambient Air Quality Monitoring Site										NBMS
Site	HGY	DNS	TZSR	LDS	TYS	WHR	XHY	DLR	HNR	XXS	YNR	SLXR	JSS	SLR	NBMS	
Latitude	41.77° N	41.78° N	41.83° N	41.85° N	41.80° N	41.77° N	41.79° N	41.84° N	41.74° N	41.70° N	41.91° N	41.73° N	41.92° N	41.93° N	41.73	
Longitude	123.29° E	123.45° E	123.57° E	123.43° E	123.40° E	123.41° E	123.47° E	123.59° E	123.51° E	123.42° E	123.60° E	123.24° E	123.38° E	123.68° E	123.52	
Location	Urban	Urban	Suburbs	Urban	Urban	Urban	Urban	Suburbs	Suburbs	Suburbs	Suburbs	Suburbs	Suburbs	Rural	Urban	
Land-use	City	City	City/ cropland	City	City	City	City	City/ cropland	City/ cropland	City/ cropland	City/ cropland	City/ cropland	City/ cropland	Forest / reservoir	City	
Ozone—mean	26	29	29	29	28	30	27	29	27	30	32	31	31	31		
Ozone—max	479	54	52	52	52	53	48	50	47	52	51	51	52	47		
Ozone—min	9	10	11	12	10	12	10	12	10	13	14	13	14	16		
NO _x —mean	51	34	25	37	33	30	30	22	31	36	20	30	28	15		
NO _x —max	78	49	28	60	53	52	49	35	53	55	33	46	44	21		
NO _x —min	26	19	14	16	15	11	14	12	17	19	13	12	15	10		
PM _{2.5} —mean	48	50	44	40	44	44	42	41	49	45	37	47	39	41		
PM _{2.5} —max	76	82	70	63	70	73	71	71	83	78	59	81	68	66		
PM _{2.5} —min	22	22	22	18	21	21	17	16	20	18	17	20	19	20		

2.2. Data Analysis Methods

In 2019, 27 types of alkanes, 14 types of aromatic hydrocarbons, 10 types of alkenes and one type of alkyne were detected at the three VOCs environmental monitoring sites in Shenyang, with a total of 52 VOC species. The original concentration unit of each VOC species was $\mu\text{g}/\text{m}^3$. First, according to the method of Liu et al. [25], the VOC concentrations were converted into volume mixture ratios (with the units of ppbv) at a standard temperature and pressure. Then, the diurnal and seasonal variation characteristics of VOC concentrations in Shenyang were analyzed using the mean hourly concentrations of the three monitoring sites.

2.2.1. Aerosol Formation

Based on the smokebox experiment of Grosjean and Seinfeld [19], this study used FAC, the fraction of VOC converted into aerosol, called aerosol yield, whereby the change in the amount of SOA formed is divided by the change of emissions of individual VOCs in order to estimate the SOA formation potential of atmospheric VOCs. According to Grosjean's hypothesis, the formation of SOA only takes place during the day (from 8 a.m. to 5 p.m. Beijing time), and VOCs only react with hydroxyl radicals to form SOA. The FAC and FVOCr (the fraction of VOC consumed by gas-phase chemical reactions with the unit of %) used in the formula are obtained by the smokebox experiment [27]. According to Grosjean [27], the estimations of FVOCr for each VOC were completed for a number of scenarios that specify the concentrations of the electrophiles, e.g., ozone, hydroxyl radicals, and NO_3 , as well as the air mass transportation time. The daytime scenario selected here was relevant to southern Californian smog episodes, which was set at $\text{O}_3 = 100$ ppbv, $\text{OH} = 1.0 \times 10^6$ molecules cm^{-3} , and $\text{NO}_3 = 0$, with a chemical reaction time of 6 h. For this scenario, Grosjean calculated for each alkene the fraction that was consumed by its reaction with ozone and by its reaction with hydroxyl radicals, respectively (these calculations were not necessary for alkanes, aromatics, and saturated oxygenates, which reacted only with hydroxyl radicals). He also assumed that aerosol production from alkene was via their reaction with ozone. The assumption was supported by results from a number of experimental studies on cyclic alkene, which was shown to produce aerosol by reaction with ozone and little or no aerosol by reaction with hydroxyl radicals [19,28].

Components that can form an SOA can be defined as:

$$\text{FAC}_i = \text{SOAp} / \text{VOCs}_0 \quad (1)$$

In the formula, FAC_i is the FAC of the i th VOC as a dimensionless quantity. SOAp is the formation potential of SOA with the unit of ppbv. VOCs_0 should have been the initial emission amount quantified in mass, moles, or flux units for a given region or for a unit area. However, due to the limited technology, it was almost impossible to obtain flux data for so many VOC components until now. Therefore, here, an "approximate initial concentration" of VOCs_0 is used to represent the levels of emission source with the unit of ppbv. The FACs are used to calculate the SOA formation potential:

$$\text{SOAp} = \text{VOCs}_0 \times \text{FAC} \quad (2)$$

Considering that the VOCs measured at the receptor point (VOCs_t) are usually the concentrations after oxidation, the relationship between VOCs_t and the initial concentration of VOCs_0 can be expressed by the following formula:

$$\text{VOCs}_t = \text{VOCs}_0 \times (1 - \text{FVOCr}/100) \quad (3)$$

2.2.2. Ozone Formation

The types of VOC in the atmosphere are very complex, with the resulting amount of ozone generated from the reaction dependent on the levels, rates of oxidation, oxidation mechanism, and concentrations of NO_x . The MIR method considers the impacts of different

reaction mechanisms and VOC/NO_x ratios on ozone formation. Incremental reactivity (IR) is the change in ozone divided by the change in the emissions of individual VOCs. It is a quantity term used to calculate the OFP (ozone formation potential) of an individual VOC compound, and MIR explains the maximum reactivity condition of individual VOC species in a high NO_x environment, in which ozone formation is most sensitive to VOCs. The calculation formula of OFP_i is as follows:

$$\text{OFP}_i = \text{VOC}_{s0} \times \text{MIR}_i \quad (4)$$

In the formula, OFP_i is the OFP of the *i*th VOC with the unit of ppbv. MIR_i is the maximum incremental reactivity of the *i*th VOC in ozone as a dimensionless quantity. Similarly, the relationship between VOC_{s_t} and VOC_{s₀} can refer to formula (3), which converts measured concentrations into the approximate initial concentrations [29].

2.2.3. Hydroxyl Radical Consumption Rate

Hydroxyl radical is the most significant oxidant in the troposphere. The photooxidation reactions of various VOCs often start with their reaction with hydroxyl radicals, during which new hydroxyl radicals are constantly formed in O₂ and NO_x, with light degradation leading to chain reactions. All VOC species are compared on the same standard to evaluate the reactivity of hydroxyl radical. The hydroxyl radical consumption rate is often used to measure the ability of VOCs to participate in atmospheric autooxidation reactions to form peroxy radicals, which can also be used to estimate the impact of a specific VOC species on the ozone formation rate in a polluted atmosphere [29]. Its calculation formula is as follows:

$$L^{\text{OH}}_i = C_i \times K^{\text{OH}}_i \quad (5)$$

In the formula, L^{OH}_i is the hydroxyl radical consumption rate of the *i*th VOC with the unit of s^{−1}. C_i is the observed concentration of the *i*th VOCs with the unit of ppbv. K^{OH}_i is the hydroxyl radical consumption rate constant corresponding to the *i*th VOC at the temperature of 298 K [30]. However, it should be pointed out that their reaction with hydroxyl radical is not the only way VOCs can react in the atmosphere, since many VOCs are also consumed to a significant extent by reaction with ozone or (at night) with NO₃, and some also with photolyze.

3. Concentration Characteristics of VOCs

3.1. Seasonal Variations

In Shenyang, the total concentration of the 52 types of VOCs (TVOC) from high to low appears in winter, autumn, spring, and summer, whereas the concentration of ozone from high to low appears in summer, spring, autumn, and winter. The TVOC reaches a maximum in January, with a value of a little more than 33 ppbv, and reaches a minimum in June. The concentration of ozone reaches a maximum in May and July, with a value of near 50 ppbv in July, and a minimum in December (Figure 2). For various types of VOCs, the concentrations of alkanes, alkenes, and alkynes generally appear highest in winter and lowest in summer, but the concentrations of aromatic hydrocarbons were highest in autumn and lowest in summer. Alkanes appear with the highest concentration, followed by alkynes, alkenes, and aromatic hydrocarbons (Figure 3). In general, seasonal variations of VOC concentrations are mainly influenced by three factors, namely, the variations of VOC source strength, the various degrees of photochemical reaction due to the seasonal levels of hydroxyl radical and the variations of the atmospheric mixing state. The higher values of TVOC and its components in autumn and winter over Shenyang are mainly due to the large amount of emission of primary pollutants from heating in autumn and winter, which directly or indirectly influences the source strength of VOCs. In addition, the atmospheric photochemical reaction is hardly active enough to remove VOCs due to the lower temperatures in autumn and winter. Moreover, the relatively stable atmospheric and temperature inversion at night are not conducive to the diffusion and dilution of

pollutants [31]. The fact that aromatic hydrocarbons appear higher in autumn than in winter was also found in the study of Baoji, Shanxi, with the process here related to the combustion emissions of petrochemical, pharmaceutical, pesticide, paint, and other industries and fossil fuels [32].

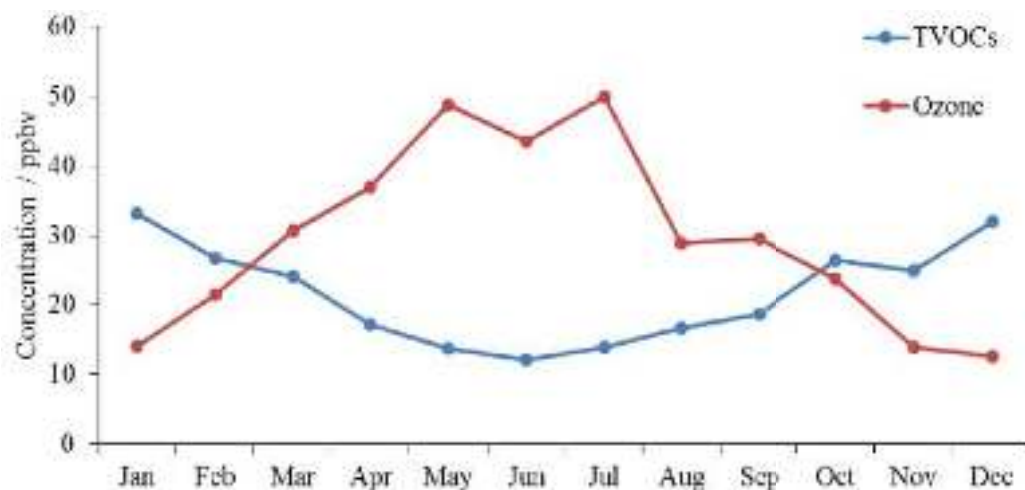


Figure 2. Monthly variation of concentrations for total VOCs and ozone in Shenyang.

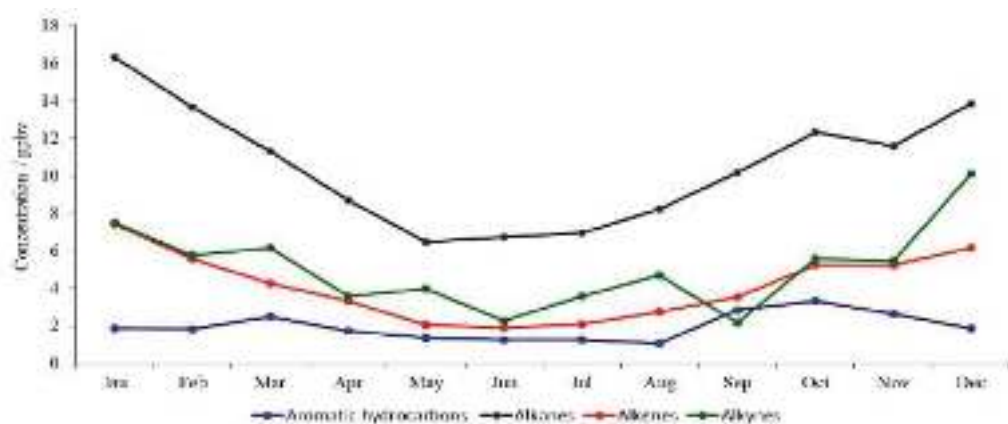


Figure 3. Monthly variation of concentrations for various types of VOCs in Shenyang.

The highest concentration component is acetylene, with a mean annual concentration of a little more than 5 ppbv. Ethane has the highest concentration among alkanes, with a mean annual concentration of just less than 5 ppbv. Ethylene has the highest concentration among alkenes, with a mean annual concentration of somewhat below 3 ppbv. Benzene has the highest concentration among aromatic hydrocarbons, with a mean annual concentration of around 1 ppbv. Compared with the northern suburbs of Nanjing, the concentrations of ethane, ethylene, and benzene are all lower, but the concentration of acetylene is slightly higher in Shenyang [8], which is significantly related to the emissions from traffic sources and industrial sources in both places. During 2019 in Shenyang, industrial emissions of NO_x and VOCs are 31,603.05 tons and 6475.59 tons, respectively, whereas town emissions of NO_x and VOCs are 3916.15 tons and 1172.63 tons, respectively [33].

For the three VOC environmental monitoring sites in Shenyang, the annual mean VOC concentrations from high to low appear at HGY, DNS, and TZSR, whereas the annual mean ozone concentration from high to low appears at DNS, TZSR (with the same level as DNS), and HGY. The concentration of each VOC component is the highest in HGY, which is located in an industrial area, whereas the concentration of ozone is lower than those at DNS and TZSR, which are located to its east and northeast (Figure 4). The reason is that the dominant wind direction in Shenyang is southwesterly on average throughout the year,

while the wind speed is over 3 m/s, which is faster than those of other directions (Figure 5). Driven by the dominant wind, ozone formed locally and VOCs at the site located in the upwind direction (e.g., HGY) are transported to the east and northeast, with the further formation of ozone due to photochemical reaction during this process [25]. Elevated ozone then appears in the downwind direction (e.g., at DNS and TZSR sites).

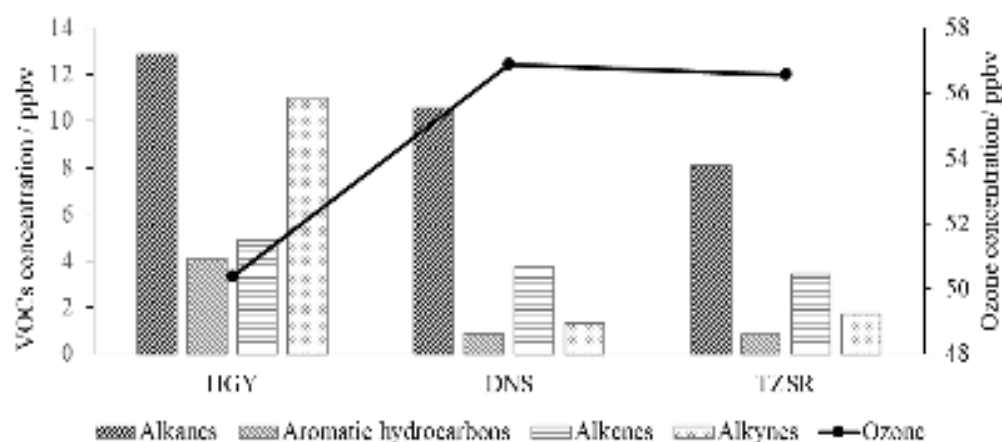


Figure 4. Concentrations for various types of VOCs and ozone at each site in Shenyang.

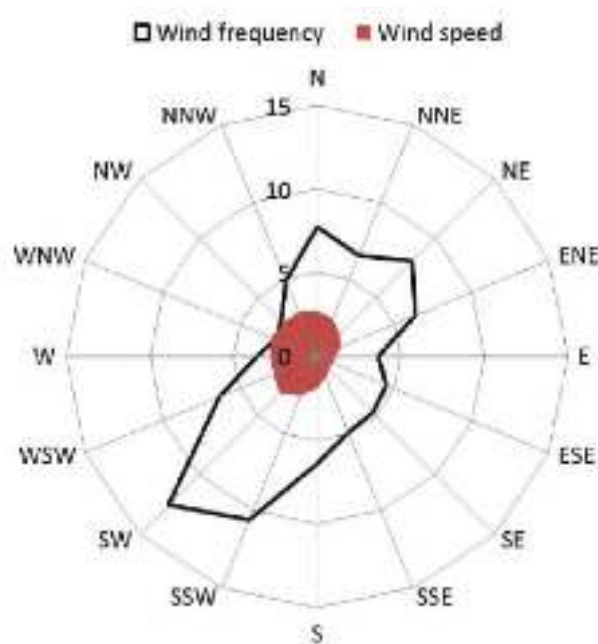


Figure 5. Wind frequency (%) and wind speed (m/s) roses in Shenyang.

3.2. Diurnal Variation

Diurnal variations in each type of VOC show rather similar bimodal patterns, with the peaks mainly appearing in the morning and evening. Alkanes and alkenes reach their maximum at 7:00 (Beijing time, the same below), whereas alkyne and aromatic hydrocarbons reach their maximum at 22:00 and 21:00, respectively, which is basically consistent with the peak hours of traffic. The concentration of each type of VOC reaches a minimum in the afternoon (13:00–14:00) (Figure 6). In the morning rush hours, human activities, such as traffic and industry, become frequent, rapidly increasing the concentration of VOCs to reach the first peak. Then, with the gradual significance of solar radiation and turbulence, VOC levels keep decreasing until they reach a minimum in the afternoon. At night, the suspension of photochemical reactions due to solar radiation decreases, along with the

accumulated contribution of the evening traffic peak, results in the second peak of VOCs. The concentration of each type of VOC is higher at night and lower in the daytime, which is significantly related to the lack of photochemical reaction consumption at night, and the lower atmospheric boundary layer height hardly being conducive to pollutant diffusion.

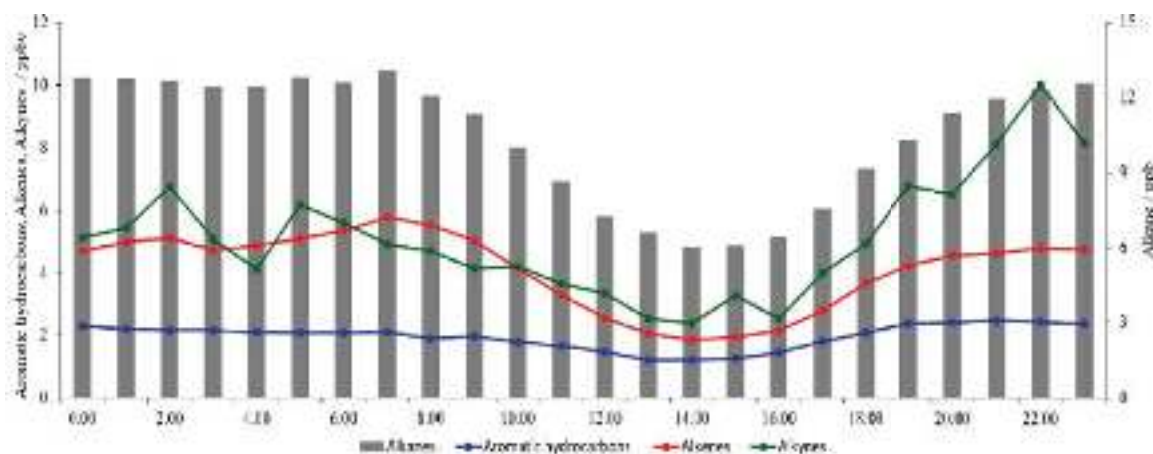


Figure 6. Diurnal variations of concentrations for various types of VOCs in Shenyang.

4. Photochemical Reactivities of VOCs

4.1. SOA Formation Potential in VOCs

Figure 7 shows the chemical reactivities of various types of VOCs. Contributions to the formation potential of SOA from large to small are aromatic hydrocarbons (94%), alkanes (4%), and alkenes (2%). Despite the lower level of aromatic hydrocarbons compared with other types of VOCs, they play an absolutely dominant role in the contribution to the formation of SOA, which is demonstrated in the results of the northern suburbs of Nanjing [8,22], which show a similar percentage, indicating that the formation of SOA is significantly influenced by aromatic hydrocarbons. The dominant contributions of aromatic hydrocarbons to the formation potential of SOA appear in various seasons, with the percentage from high to low in autumn, spring, winter, and summer (Table 2).

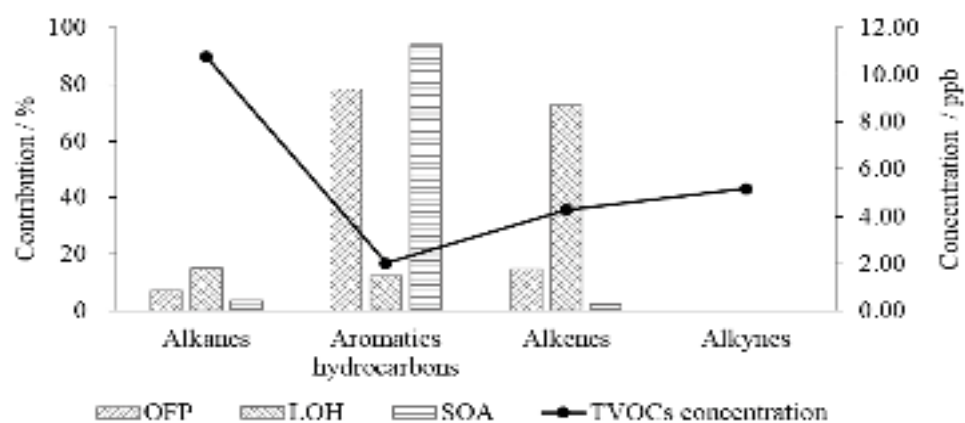


Figure 7. Photochemical reactivities for various types of VOCs in Shenyang.

Table 2. Seasonal variations of the contribution of VOCs to ozone and SOA formation potential and hydroxyl radical consumption rate.

Season	Photochemical Reactivities	VOC (ppbv)	Alkanes (%)	Aromatic Hydrocarbons (%)	Alkenes (%)
Spring	OFP	5.09	7	79	14
	L ^{OH}	82.68	15	12	73
	SOAp	7.46	3	95	2
Summer	OFP	4.99	6	61	33
	L ^{OH}	64.42	18	13	69
	SOAp	5.40	4	89	7
Autumn	OFP	6.46	7	86	7
	L ^{OH}	114.67	15	14	71
	SOAp	10.40	3	96	1
Winter	OFP	6.84	8	82	10
	L ^{OH}	136.13	13	11	76
	SOAp	8.79	4	94	2

The total formation potential of SOA in each VOC component is around 8.04 ppbv, while the 10 VOC components with the highest contributions in 2019 were toluene (39.21%), benzene (31.07%), o-xylene (5.93%), ethylbenzene (5.52%), isoprene (2.33%), 1,3,5-trimethylbenzene (2.12%), m-ethyltoluene (2.09%), methylcyclohexane (1.80%), p-diethylbenzene (1.51%), and 1,2,3-trimethylbenzene (1.47%) (Table 3). Similar to the results in the northern suburbs of Nanjing [8], the contribution percentages of toluene appear the highest in Shenyang as well, where the percentage is higher than that in the northern suburbs of Nanjing (27.28%). The contribution of benzene is next, and, along with the contribution of toluene, the total percentage add up to over 70%. Benzene and toluene, including other benzene series which contribute significantly to the formation of SOA, are both key raw materials of the organic chemical industry that can be used as solvents [34]. Furthermore, they are among the important products of flow sources [35]. Therefore, VOC components that contribute more to SOA formation in Shenyang come significantly from solvents and vehicle emissions, meaning that control of the use of a large number of solvents and vehicle emissions is an effective method to suppress SOA formation.

Table 3. 10 VOC components with the highest contributions to SOA formation potential.

Units/ppbv.	Mean Level (ppbv)	FAC (%)	FVOCr (%)	SOAp (ppbv)	SOAp (%)
toluene	0.55	5.40	12.00	3.15	39.21
benzene	1.12	2.00	10.00	2.50	31.07
o-xylene	0.07	5.00	26.00	0.48	5.93
ethylbenzene	0.07	5.40	15.00	0.44	5.52
isoprene	0.09	2.00	0.00	0.19	2.33
1,3,5-trimethylbenzene	0.02	2.90	74.00	0.17	2.12
m-ethyltoluene	0.02	6.30	31.00	0.17	2.09
methylcyclohexane	0.04	2.70	20.00	0.14	1.80
p-diethylbenzene	0.01	6.30	47.00	0.12	1.51
1,2,3-trimethylbenzene	0.02	3.60	51.00	0.12	1.47

4.2. Ozone Formation Potential in VOCs

Contributions to the formation potential of ozone from large to small are aromatic hydrocarbons (78%), alkene (15%), and alkane (7%). Contributions of aromatic hydrocarbons to the potential of ozone formation are much more significant than those of the three other types of VOCs (Figure 7), meaning that it is the most active type of VOC in atmospheric chemical reactions, in accord with the results from an examination of the urban area of Guangzhou [15]. The main discrepancy between the two regions is that the percentage

of alkenes contributing to ozone formation in Shenyang appears two times higher than that in Guangzhou (38%). Thus, it is shown that aromatic hydrocarbons are the dominant contributor to the formation of ozone and SOA, rather than alkanes, although alkanes are the chief VOC component in the atmospheric environment of Shenyang. The contributions of aromatic hydrocarbons to the potential of ozone formation appear the most significant throughout the year, with the percentages from high to low in autumn, winter, spring, and summer (Table 2). In contrast, the results of the northern suburbs of Nanjing [8] show that alkenes contribute the most to ozone formation, which is probably due to the different estimation method.

As is shown in Table 4, the total formation potential of ozone in each VOC component is about 5.74 ppbv, and the 10 VOC components with the highest contributions in 2019 were toluene (29.64%), isoprene (14.83%), o-xylene (10.79%), 1,3,5-trimethylbenzene (10.36%), benzene (9.13%), 1,2,4-trimethylbenzene (8.32%), 1,2,3-trimethylbenzene (5.09%), ethylbenzene (3.87%), methylcyclopentane (2.06%), and methylcyclohexane (1.68%). In accordance with the observations in Guangzhou [15,36], toluene contributes the most to ozone formation, while the contribution of isoprene is not ignorable. In general, isoprene originates not only from biological emissions throughout the year at times other than in winter [37], but also from anthropogenic emissions, especially traffic emissions [38], meaning that control of the use of a large number of solvents and vehicle emissions is also an effective way to control ozone pollution in Shenyang. Moreover, exploring solutions to control isoprene emission from broad-leaved forests and shrubs [37] might also be factors worth considering.

Table 4. 10 VOC components with the highest contributions to ozone formation potential.

Units/ppbv.	Mean Level (ppbv)	MIR	FVOCr (%)	OFP (ppbv)	OFP (%)
toluene	0.55	2.70	12.00	1.70	29.64
isoprene	0.09	9.10	0.00	0.85	14.83
o-xylene	0.07	6.50	26.00	0.62	10.79
1,3,5-trimethylbenzene	0.02	10.10	74.00	0.59	10.36
benzene	1.12	0.42	10.00	0.52	9.13
1,2,4-trimethylbenzene	0.02	8.80	58.00	0.48	8.32
1,2,3-trimethylbenzene	0.02	8.90	51.00	0.29	5.09
ethylbenzene	0.07	2.70	15.00	0.22	3.87
methylcyclopentane	0.04	2.80	10.00	0.12	2.06
methylcyclohexane	0.04	1.80	20.00	0.10	1.68

4.3. Influence of VOCs on the Consumption Rate of Hydroxyl Radicals

Contributions to the consumption rate of hydroxyl radicals from large to small are alkenes (73%), alkanes (15%), and aromatic hydrocarbons (12%). Here, the contribution of alkenes is far more significant (Figure 7). The contribution of alkenes to the consumption rate of hydroxyl radicals in Shenyang, which is a bit higher than that in Guangzhou (64%) [15], appears dominant throughout the year with the percentages from high to low in winter, spring, autumn, and summer (Table 2).

As is shown in Table 5, the total consumption rate of VOCs on the consumption rate of hydroxyl radicals is around 99.49 ppbv, and the 10 VOC components with the highest contributions are ethylene (24.64%), propylene (16.16%), 1-hexene (9.93%), 1-butene (5.17%), trans-2-butene (4.98%), cis-2-butene (3.62%), propane (3.47%), toluene (3.32%), cis-2-pentene (3.16%), and styrene (3.15%). It is significantly different from the results in Guangzhou, where the contribution of trans-2-pentene appears the largest with a percentage of 19.14% [15].

Table 5. 10 VOC components with the highest contributions to the consumption rate of hydroxyl radical.

Units/ppbv.	Mean Level (ppbv)	K ^{OH}	L ^{OH} (ppbv)	L ^{OH} (%)
ethylene	2.88	8.52	24.51	24.64
propylene	0.61	26.30	16.07	16.16
1-hexene	0.27	37.00	9.88	9.93
1-butene	0.16	31.40	5.14	5.17
trans-2-butene	0.08	64.00	4.95	4.98
cis-2-butene	0.06	56.40	3.60	3.62
propane	3.17	1.09	3.46	3.47
toluene	0.55	5.96	3.31	3.32
trans-2-pentene	0.05	65.00	3.14	3.16
styrene	0.05	58.00	3.13	3.15

5. Conclusions

In Shenyang, the concentrations of TVOCs from high to low appear in winter, autumn, spring, and summer. For various types of VOCs, the concentrations of alkanes, alkenes, and alkynes appear generally the highest in winter and the lowest in summer, whereas the concentrations of aromatic hydrocarbons appear the highest in autumn and the lowest in summer. Alkanes appear with the highest concentration, followed by alkynes, alkenes, and aromatic hydrocarbons. Diurnal variations in each type of VOC experience peaks mainly in the morning and evening, among which alkanes and alkenes reach the maximum at 7:00, whereas alkyne and aromatic hydrocarbons reach a maximum in traffic peak hours of 22:00 and 21:00, respectively. The concentration of each type of VOC reaches a minimum in the afternoon (13:00–14:00).

As they are the most active type of VOC in atmospheric chemical reactions, aromatic hydrocarbons are the dominant contributor to the formation of both ozone and SOA. Contributions to the formation potential of SOA from large to small are aromatic hydrocarbons (94%), alkanes, and alkenes, which is similar with the results of the northern suburbs of Nanjing. The dominant contributions of aromatic hydrocarbons to the formation potential of SOA appear in various seasons, with the percentage from high to low in autumn, spring, winter, and summer. The 10 VOC components with the highest contributions are toluene, benzene, o-xylene, ethylbenzene, isoprene, 1,3,5-trimethylbenzene, m-ethyltoluene, methylcyclohexane, p-diethylbenzene, and 1,2,3-trimethylbenzene, while the contributions of toluene and benzene add up to over 70%, meaning that control of the use of a large number of solvents and vehicle emissions would be an effective method to suppress SOA formation in the Shenyang area.

Contributions to the formation potential of ozone from large to small are aromatic hydrocarbons (78%), alkene, and alkane. The contribution of aromatic hydrocarbons to the potential of ozone formation is much more significant than that of the three other types of VOCs, in accordance with the results of the urban area of Guangzhou. The discrepancy is that the contribution percentage of alkenes to ozone formation in Shenyang appears twice as high. The contributions of aromatic hydrocarbons to the potential of ozone formation appear the most significant throughout the year, with the percentages from high to low in autumn, winter, spring, and summer. In contrast, most likely due to the different estimation method, the results of the northern suburbs of Nanjing show that alkenes contribute the most to ozone formation. The 10 VOC components with the highest contributions are toluene, isoprene, o-xylene, 1,3,5-trimethylbenzene, benzene, 1,2,4-trimethylbenzene, 1,2,3-trimethylbenzene, ethylbenzene, methylcyclopentane, and methylcyclohexane. Similar to SOA, control of the use of a large number of solvents and vehicle emissions would be an effective way to control ozone pollution in Shenyang. Moreover, exploring solutions to control isoprene emission from broad-leaved forests and shrubs also might be factors worth considering.

Contributions to the consumption rate of hydroxyl radicals from large to small are alkenes (73%), alkanes, and aromatic hydrocarbons, while the contribution of alkenes is

far more significant, and is a bit higher than that in Guangzhou. The 10 VOC components with the highest contributions are ethylene, propylene, 1-hexene, 1-butene, trans-2-butene, cis-2-butene, propane, toluene, cis-2-pentene, and styrene.

Author Contributions: Conceptualization, N.L.; methodology, N.L. and X.L.; software, N.L.; validation, L.L. and C.W.; formal analysis, N.L. and L.L.; investigation, N.L.; resources, N.L.; data curation, W.R. and C.S.; writing—original draft preparation, N.L.; writing—review and editing, N.L. and X.L.; visualization, N.L.; project administration, N.L. All authors have read and agreed to the published version of the manuscript.

Funding: This research was funded by the Basic Research Funds of Central Public Welfare Research Institutes, grant number 2020SYIAEZD1, the Science & Technology Project of Liaoning Province, grant number 2019JH8/10300095, and the Key program of science foundation of Liao-ning Meteorological Office, grant number D202101.

Institutional Review Board Statement: Not applicable.

Informed Consent Statement: Not applicable.

Data Availability Statement: Informed consent was obtained from all subjects involved in the study.

Conflicts of Interest: The authors declare no conflict of interest.

References

1. Haagen-Smit, A.J. Chemistry and physiology of Los Angeles Smog. *Ind. Eng. Chem.* **1952**, *44*, 1342–1346. [CrossRef]
2. Seinfeld, J.H. Urban air pollution: State of the science. *Science* **1989**, *243*, 745–752. [CrossRef] [PubMed]
3. Seinfeld, J.H.; Pandis, S.N. *Atmospheric Chemistry and Physics: From Air Pollution to Climate Change*; Wiley Interscience: Hoboken, NJ, USA, 1998.
4. Sillman, S. The relation between ozone, NO_x and hydrocarbons in urban and polluted rural environment. *Atmos. Environ.* **1999**, *33*, 1821–1845. [CrossRef]
5. Cooper, O.R.; Gao, R.S.; Tarasick, D.; Leblanc, T.; Sweeney, C. Long-term ozone trends at rural ozone monitoring sites across the United States, 1990–2010. *J. Geophys. Res. Atmos.* **2012**, *117*, D22307. [CrossRef]
6. Simon, H.; Reff, A.; Wells, B.; Xing, J.; Frank, N. Ozone trends across the United States over a period of decreasing NO_x and VOC emissions. *Environ. Sci. Technol.* **2015**, *49*, 186–195. [CrossRef] [PubMed]
7. China's Ministry of Environmental Protection. *China's Ambient Air Quality Standard*; Ministry of Environmental Protection: Beijing, China, 2012.
8. Lin, X.; Zhu, B.; An, J.L.; Yang, H. Potential contribution of secondary organic aerosols and ozone of VOCs in the Northern Suburb of Nanjing. *China Environ. Sci.* **2015**, *35*, 976–986.
9. Lyu, X.P.; Chen, N.; Guo, H.; Zhang, W.H.; Wang, N.; Wang, Y.; Liu, M. Ambient volatile organic compounds and their effect on ozone production in Wuhan, central China. *Sci. Total. Environ.* **2016**, *541*, 200–209. [CrossRef]
10. Ran, L.; Zhao, C.S.; Xu, W.Y.; Lu, X.Q.; Han, M.; Lin, W.L.; Yan, P.; Xu, X.B.; Deng, Z.Z.; Ma, N.; et al. VOC reactivity and its effect on ozone production during the HaChi summer campaign. *Atmos. Chem. Phys.* **2011**, *11*, 4657–4667. [CrossRef]
11. Shao, M.; Zhang, Y.; Zeng, L.; Tang, X.; Zhang, J.; Zhong, L.; Wang, B. Ground-level ozone in the Pearl River Delta and the roles of VOC and NO_x in its production. *J. Environ. Manag.* **2009**, *90*, 512–518. [CrossRef]
12. Tang, X.Y.; Zhang, Y.H.; Shao, M. *Atmospheric Environmental Chemistry*, 2nd ed.; Higher Education Press: Beijing, China, 2006.
13. Xue, L.K.; Wang, T.; Gao, J.; Ding, A.J.; Zhou, X.H.; Blake, D.R.; Wang, X.F.; Saunders, S.M.; Fan, S.J.; Zuo, H.C.; et al. Ground-level ozone in four Chinese cities: Precursors, regional transport and heterogeneous processes. *Atmos. Chem. Phys.* **2014**, *14*, 13175–13188. [CrossRef]
14. Yang, X.X.; Tang, L.L.; Zhang, Y.J.; Mu, Y.F.; Wang, M.; Chen, W.T.; Zhou, H.C.; Hua, Y.; Jiang, R.X. Correlation analysis between characteristics of VOCs and ozone formation potential in summer in Nanjing urban district. *Environ. Sci.* **2016**, *37*, 443–451.
15. Yu, X.F.; Cheng, P.; Gu, Y.G.; Li, M.; Tian, Z. Formation potential of ozone and secondary organic aerosol from VOCs oxidation in summer in Guangzhou, China. *China Environ. Sci.* **2018**, *38*, 830–837.
16. Zhang, J.; Wang, T.; Chameides, W.L.; Cardelino, C.; Kwok, J.; Blake, D.R.; Ding, A.; So, K.L. Ozone production and hydrocarbon reactivity in Hongkong, Southern China. *Atmos. Chem. Phys.* **2007**, *7*, 557–573. [CrossRef]
17. Huang, R.J.; Zhang, Y.L.; Carlo, B.; Ho, K.F.; Cao, J.J.; Han, Y.; Daellenbach, K.R.; Slowik, J.G.; Platt, S.M.; Canonaco, F.; et al. High secondary aerosol contribution to particulate pollution during haze events in China. *Nature* **2014**, *514*, 218–222. [CrossRef] [PubMed]
18. Sun, Y.L.; Wang, Z.F.; Fu, P.Q.; Yang, T.; Jiang, Q.; Dong, H.B.; Li, J.; Jia, J.J. Aerosol composition, sources and processes during wintertime in Beijing, China. *Atmos. Chem. Phys.* **2013**, *13*, 4577–4592. [CrossRef]
19. Grosjean, D.; Seinfeld, J.H. Parameterization of the formation potential of secondary organic aerosols. *Atmos. Environ.* **1989**, *23*, 1733–1747. [CrossRef]

20. Barthelmie, R.J.; Pryor, S.C. Secondary organic aerosols: Formation potential and ambient data. *Sci. Total. Environ.* **1997**, *205*, 167–178. [CrossRef]
21. Lv, Z.F.; Hao, J.M.; Duan, J.C.; Li, J.H. Estimate of the Formation Potential of Secondary Organic Aerosol in Beijing Summertime. *Environ. Sci.* **2009**, *34*, 424–433.
22. Wang, Q.; Chen, C.H.; Wang, H.L.; Zhou, M.; Lou, S.R.; Qiao, L.P.; Huang, C.; Li, L.; Su, L.Y.; Mu, Y.Y.; et al. Forming potential of secondary organic aerosols and sources apportionment of VOCs in autumn of Shanghai, China. *Environ. Sci.* **2013**, *30*, 969–975.
23. Wang, F.P.; Zhu, Q.; Feng, N.; Liu, R.L.; Huang, X.F.; He, L.Y. The generation potential of secondary organic aerosol of atmospheric VOCs in Shenzhen. *China Environ. Sci.* **2014**, *34*, 2449–2457.
24. Qi, A.A.; Zhou, X.P.; Lei, C.N.; Ma, X.; Xie, Y.S.; Pang, W.Q.; Hao, L.L. Key active components and sources of volatile organic compounds in ambient air of Lanzhou city. *Environ. Chem.* **2020**, *39*, 3083–3093.
25. Liu, N.W.; Ren, W.H.; Li, X.L.; Ma, X.; Zhang, Y.; Li, B. Distribution and urban–suburban differences in ground-level ozone and its precursors over Shenyang, China. *Meteorol. Atmos. Phys.* **2019**, *131*, 669–679. [CrossRef]
26. Shao, M.; Wang, W.J.; Yuan, B.; Parrish, D.D.; Li, X.; Lu, K.; Wu, L.; Wang, X.; Mo, Z.; Yang, S.; et al. Quantifying the role of PM_{2.5} dropping in variations of ground-level ozone: Inter-comparison between Beijing and Los Angeles. *Sci. Total. Environ.* **2021**, *788*, 147712. [CrossRef]
27. Grosjean, D. In situ organic aerosol formation during a smog episode: Estimated production and chemical functionality. *Atmos. Environ.* **1992**, *24A*, 953–963. [CrossRef]
28. Izumi, K.; Fukuyama, T. Photochemical aerosol formation from aromatic hydrocarbons in the presence of NO_x. *Atmos. Environ.* **1990**, *24A*, 1433–1441. [CrossRef]
29. Carter, W.P.L. Development of ozone reactivity scales for volatile Organic compounds. *Air Waste* **1994**, *44*, 881–899. [CrossRef]
30. Atkinson, R.; Arey, J. Atmospheric degradation of volatile organic compounds. *Chem. Rev.* **2003**, *103*, 4605–4638. [CrossRef]
31. Liu, N.; Ma, J.Z. Seasonal relationships between tropospheric ozone and its precursors over East Asia. *J. Appl. Meteorol. Sci.* **2017**, *28*, 427–435.
32. Zhang, R.X.; Liu, H.W.; Deng, S.X. Characteristics of VOCs and formation potential of O₃ and SOA in autumn and winter in Baoji, China. *China Environ. Sci.* **2020**, *40*, 983–996.
33. Shenyang Ecological Environment Bureau. *Shenyang Ecological Environment Quality Report in 2016 to 2020*; Shenyang Ecological Environment Bureau: Shenyang, China, 2021.
34. Guo, H.; Wang, T.; Louie, P.K.K. Source apportionment of ambient non-methane hydrocarbons in Hong Kong: Application of a principal component analysis (PCA)/absolute principal component scores (APCS) receptor model. *Environ. Pollut.* **2004**, *129*, 489–498. [CrossRef]
35. Ye, W.H.; Sun, X.H.; Liu, J.S.; Pan, H.F.; Pang, X.L. Study on air pollution of VOC in arterial traffic. *Environ. Monit. China* **2009**, *25*, 85–89.
36. Zou, Y.; Deng, X.J.; Zhu, D.; Gong, D.C.; Wang, H.; Li, F.; Tan, H.B.; Deng, T.; Mai, B.R.; Liu, X.T.; et al. Characteristics of 1 year of observational data of VOCs, NO_x and O₃ at a suburban site in Guangzhou, China. *Atmos. Chem. Phys.* **2015**, *15*, 6625–6636. [CrossRef]
37. Xu, Z.N. *Observation Based Study of VOCs and Their Influence on Ozone and Secondary Organic Formation in the Western YRD Region, China*; Nanjing University: Nanjing, China, 2019.
38. Liu, Y.; Shao, M.; Lu, S. Volatile organic compound (VOC) measurements in the Pearl River Delta (PRD) region, China. *Atmos. Chem. Phys.* **2008**, *8*, 1531–1545. [CrossRef]

Article

Temporal and Spatial Trends in Particulate Matter and the Responses to Meteorological Conditions and Environmental Management in Xi'an, China

Yulu Tian ^{1,2}, Lingnan Zhang ³, Yang Wang ⁴, Jinxi Song ^{1,*}  and Haotian Sun ^{1,*}

¹ Shaanxi Key Laboratory of Earth Surface System and Environmental Carrying Capacity, College of Urban and Environmental Sciences, Northwest University, Xi'an 710127, China; tianyulu@nwnu.edu.cn

² Key Laboratory for Ecology and Environment of River Wetlands in Shaanxi Province, Weinan 714099, China

³ School of Geography and Tourism, Shaanxi Normal University, Xi'an 710119, China; zhangln@snnu.edu.cn

⁴ College of Life Science and Technology, Inner Mongolia Normal University, Hohhot 010022, China; ywang@imnu.edu.cn

* Correspondence: jinxisong@nwnu.edu.cn (J.S.); sunhaotian@nwnu.edu.cn (H.S.)

Citation: Tian, Y.; Zhang, L.; Wang, Y.; Song, J.; Sun, H. Temporal and Spatial Trends in Particulate Matter and the Responses to Meteorological Conditions and Environmental Management in Xi'an, China. *Atmosphere* **2021**, *12*, 1112. <https://doi.org/10.3390/atmos12091112>

Academic Editors: Duanyang Liu, Honglei Wang and Kai Qin

Received: 19 August 2021

Accepted: 27 August 2021

Published: 30 August 2021

Publisher's Note: MDPI stays neutral with regard to jurisdictional claims in published maps and institutional affiliations.



Copyright: © 2021 by the authors. Licensee MDPI, Basel, Switzerland. This article is an open access article distributed under the terms and conditions of the Creative Commons Attribution (CC BY) license (<https://creativecommons.org/licenses/by/4.0/>).

Abstract: Particulate matter contributes much to the haze pollution in China. Meteorological conditions and environmental management significantly influenced the accumulation, deposition, transportation, diffusion, and emission intensity of particulate matter. In this study, temporal and spatial variations of PM₁₀ and PM_{2.5}—and the responses to meteorological factors and environmental regulation intensity—were explored in Xi'an, China. The concentrations of PM₁₀ were higher than those of PM_{2.5}, especially in spring and winter. The mean annual concentrations of PM₁₀ and PM_{2.5} markedly decreased from 2013 to 2017, but the decreasing trend has plateaued since 2015. The concentrations of PM₁₀ and PM_{2.5} exhibited seasonal differences, with winter being the highest and summer the lowest. Air quality monitoring stations did not reveal significant spatial variability in PM₁₀ and PM_{2.5} concentrations. The concentrations of PM₁₀ and PM_{2.5} were significantly influenced by precipitation, relative humidity, and atmospheric temperature. The impact of wind speed was prominent in autumn and winter, while in spring and summer the impact of wind direction was obvious. Additionally, the emission intensity of SO₂, smoke and dust could be effectively decreased with the increasing environmental regulation intensity, but not the concentrations of particulate matter. This study could provide a scientific framework for atmospheric pollution management.

Keywords: particulate matter; emission intensity; meteorological conditions; environmental management; Xi'an

1. Introduction

With rapid urbanization and industrialization, air quality has been deteriorating in many cities in China, resulting in major environmental problems [1–3]. Particulate matter, such as PM_{2.5} (particles with diameter less than 2.5 µm) and PM₁₀ (particles with diameter less than 10 µm), are regarded as the dominant pollutants influencing air quality [4]. PM_{2.5} components are complex, predominantly generated by human activities and natural release, and the former is more harmful. PM_{2.5} are mainly chemically formed, or condensed from hot vapor (i.e., diesel exhaust) and coagulated into fine particles. PM₁₀, mainly derived from natural processes and imperfect combustion, and commonly affected by the suspension and transport of sand and soil particles [5,6]. Given the negative effects of particulate matter on human health, governments have implemented strict pollutant reduction measures, which were deemed as an effective way for air quality improvement [7]. The concentrations of particulate matter across timescales can provide insight into the myriad causes of observed variations in air pollution [8]. Data at the annual scale can reflect the effects of mitigation strategies implemented by the government [9]. Seasonal variations of air quality are conducive to parsing the contribution of meteorological conditions, and the

intensity of emissions [10,11]. Studies have shown that particulate matter exerts a serious impact on the air quality in spring and winter [12]. In addition, the spatial heterogeneity of air quality can reveal the effectiveness of environmental regulation practices [13,14]. Though local emissions contribute to the air pollution, the meteorological conditions are also at play, affecting the accumulation, deposition, transportation, and diffusion of air pollutants [2,15]. The meteorological factors showed a non-linear relationship with the concentrations of particulate matter [16]. Therefore, the temporal and spatial characteristics captured by air quality and the relationship with meteorological conditions and environmental management also deserve further investigation.

Unregulated local emissions elevate the concentrations of particulate matter, especially in developing regions [17]. For example, in China, the large-scale emission sources of PM₁₀ and PM_{2.5} include coal combustion, traffic engine exhausts, biomass burning, industrial activities, fugitive dust from construction activities and sandstorms [18,19]. Particulate matter as the primary pollutant (i.e., the concentration is higher than other atmospheric pollutants) with a higher proportion [12], its improvement plays a key role in improving air quality, especially in cities of the semi-arid and arid regions in western and northwestern China, where fugitive dust is the major component of aerosol particles.

Xi'an, the capital city of Shaanxi province, with an area of 10,108 km² and a population of 13.0 million, is the most urbanized region in northwestern China. Due to the topography, meteorological conditions, and tremendous amount of atmospheric pollutants emissions derived from urbanization and industrialization, Xi'an has been plagued by severe air pollution over the last decade [6,20]. PM₁₀ and PM_{2.5} contribute more than 90% of all air pollutants, which are regarded as the dominant controller of air quality in this region [12,21]. In recent years, atmosphere environment protection policies have been vigorously implemented in Xi'an, but few studies have assessed the effectiveness of environmental management in improving atmospheric pollution. The atmospheric pollution in Xi'an exhibits seasonal dependence. Bare surface and strong wind in spring, and biomass burning and coal combustion from intensive heating demand in winter—accompanied with meteorological factors closely related to atmospheric pollution—all promote an abundance of particulate matter and visibility impairment [1,6,22]. Evaluation and improvement of air quality in the context of changes in energy consumption and rapid urbanization is conducive to the future development and sustainability of other megacities in northwest China.

In this study, PM₁₀ and PM_{2.5} from 13 air monitoring stations in Xi'an from 2013 to 2017 were analyzed. We aimed to: (1) characterize the temporal and spatial variations of PM₁₀ and PM_{2.5} in Xi'an; (2) analyze the relationships between particulate matter and meteorological conditions; and (3) explore the response of the concentration and emission intensity of atmospheric pollutants to the environmental management. This study aims to provide a scientific framework for atmospheric pollution management.

2. Materials and Methods

2.1. Study Area

Xi'an, the capital of Shaanxi Province, is a megacity in western China, located at the central part of the Guanzhong Plain, with the Loess Plateau to the north, and the Qingling Mountains to the south. Xi'an is situated in a sub-humid and warm temperate region under the influence of the East Asian monsoon with hot and humid summers, and cold winters. During the warm period (May–October), winds blow in from southern China; during the cold period (November–April), winds from the desert regions of north-western and western China are dominant. Over the period of 2001–2017, the average annual temperature was 13.6 °C, and the annual precipitation was 558.2 mm (<http://data.cma.cn/>, accessed on 1 March 2020).

2.2. Particulate Matter Datasets

The atmospheric environment monitoring network in Xi'an is composed of 13 national air quality real-time monitoring stations: the Voltage Switchgear Factory (VS), the Xingqing Community (XQ), Textile City (TC), Xiaozhai (XZ), People's Stadium (PS), High-tech District (HT), the Economic Development District (ED), Chang'an District (CA), Yanliang District (YL), Lintong District (LT), Caotan (CT), Qujiang (QJ), and Guangyun Lake (GY) (Figure 1). The daily mean concentrations of particulate matter (PM₁₀ and PM_{2.5}) at each station, from 1 January 2013 to 31 December 2017, were used in the analysis. These data are publicly available at the Xi'an Ecology and Environment Bureau (<http://xaepb.xa.gov.cn/>, accessed on 9 July 2021).

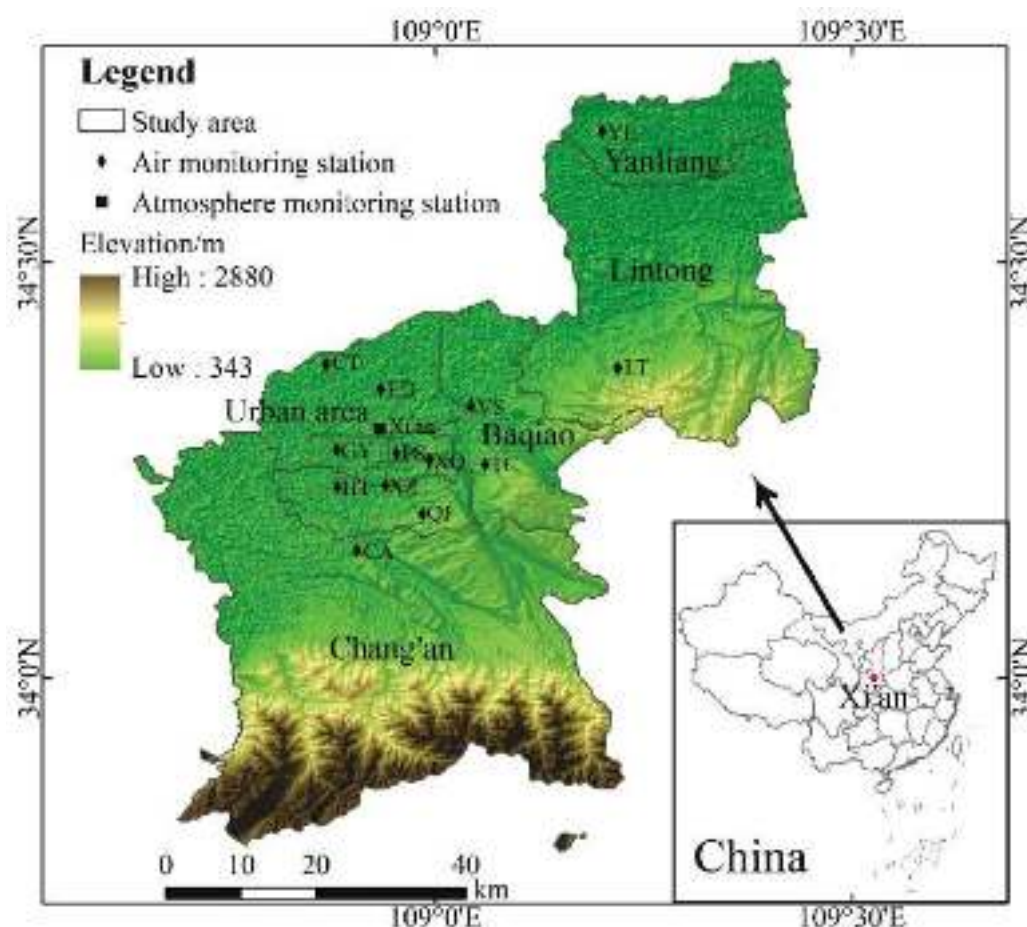


Figure 1. Distribution of air monitoring stations and atmosphere monitoring station.

According to the emissions standards of air pollutants from the Ambient Air Quality Standard (GB 3095-2012) [23]. Grade 1 concentration limits (24 h average) of PM₁₀ and PM_{2.5} are 50 $\mu\text{g}/\text{m}^3$ and 35 $\mu\text{g}/\text{m}^3$, which are the maximum concentrations healthy for humans. Grade 3 concentration limits of PM₁₀ and PM_{2.5} are 150 $\mu\text{g}/\text{m}^3$ and 75 $\mu\text{g}/\text{m}^3$, which are unhealthy for humans.

2.3. Meteorological Datasets

The meteorological datasets for Xi'an covers 5 years from 2013 to 2017, obtained from the National Meteorological Information Centre (<http://data.cma.cn/>, accessed on 8 June 2019). Six meteorological indices were selected to study the influence of meteorological conditions on atmospheric pollutants, including mean daily total precipitation, atmospheric pressure, relative humidity, atmospheric temperature, wind speed, and wind direction.

2.4. Environmental Management

Environmental management in this study refers to the calculated emission intensity, environmental regulation intensity. The emission intensity is targeted at Xi'an, based on the ratio of the SO₂, soot, and dust emissions to GDP. The environmental regulation intensity is targeted at Shaanxi province, based on the emissions and environmental investment.

The environmental regulation intensity is measured by environmental governance investment per unit of atmospheric pollutant emissions. The calculation formula is

$$ERI = Inv./Pollu. \quad (1)$$

where *ERI* represents the strength of environmental regulations; *Inv.* represents the investment in atmospheric environmental improvement; *Pollu.* represents the concentrations of atmospheric pollutants.

Environmental management datasets were obtained from the Statistical Yearbook (<http://www.stats.gov.cn/>, accessed on 6 May 2020), including the emission intensity (t/10⁴ RMB) and the environmental regulation investment (10⁸ RMB) in Xi'an, Shaanxi province.

2.5. Statistical Analysis

The Kolmogorov–Smirnov test was used to confirm that the datasets followed a normal distribution, and the analysis method was dependent on the results of the K-S test. Spearman correlation analysis was carried out between the concentrations of PM₁₀ and PM_{2.5}. Spearman correlation coefficients were also calculated for the relationships between atmospheric pollutants and the meteorological factors, environmental regulation intensity. One-way ANOVA and t-pair test were conducted to analyze differences at different monitoring sites and time scales (annual, seasonal, and monthly). All data analyses and figure drawings were performed in SPSS 20.0 and MATLAB R2019a.

3. Results

3.1. Temporal Variations in the Concentrations of PM₁₀ and PM_{2.5}

The mean annual, seasonal, and monthly concentrations of PM₁₀ were all higher than those of PM_{2.5} (Figure 2). Intra-annual variations in the concentrations of PM₁₀ and PM_{2.5} exhibited similar characteristics during 2013–2017. From 2013 to 2017, the mean annual concentration of PM₁₀ in Xi'an declined from 186.3 µg/m³ to 131.7 µg/m³, with the lowest value in 2015 (128.0 µg/m³). The highest inter-annual decline rate was 19.2%, which occurred during 2013–2014. There was no significant difference ($p > 0.05$) between the mean annual concentrations of PM₁₀ in 2015, 2016, and 2017 (Figure 2A). Similarly, the mean annual concentration of PM_{2.5} in Xi'an declined from 107.4 µg/m³ in 2013 to 73.7 µg/m³ in 2017, and the lowest value occurred in 2015 (58.1 µg/m³). The highest inter-annual decline rate was 27.9%, which occurred during 2013–2014. The differences between 2015, 2016, and 2017 were also nonsignificant ($p > 0.05$) (Figure 2B).

The maximum seasonal concentrations of PM₁₀ (218.5 µg/m³) and PM_{2.5} (137.2 µg/m³) were recorded in winter, and the minimum (86.7 and 40.0 µg/m³) in summer. The seasonal concentrations of PM₁₀ in spring were higher than those in autumn, while the concentrations of PM_{2.5} in spring were lower than those in autumn, and the differences were all nonsignificant ($p > 0.05$) (Figure 2C,D). The maximum monthly concentrations of both PM₁₀ (239.2 µg/m³) and PM_{2.5} (151.9 µg/m³) occurred in January. The monthly concentrations of PM₁₀ and PM_{2.5} decreased from January to June, with the lowest concentrations recorded in June (85.0 and 38.5 µg/m³). Concentrations then increased from June to December. The maximum inter-monthly decrease rate of PM₁₀ and PM_{2.5} occurred during March–April (26.7% and 30.6%), while the maximum inter-monthly increase rates of PM₁₀ and PM_{2.5} occurred during November–December (36.3% and 52.1%).

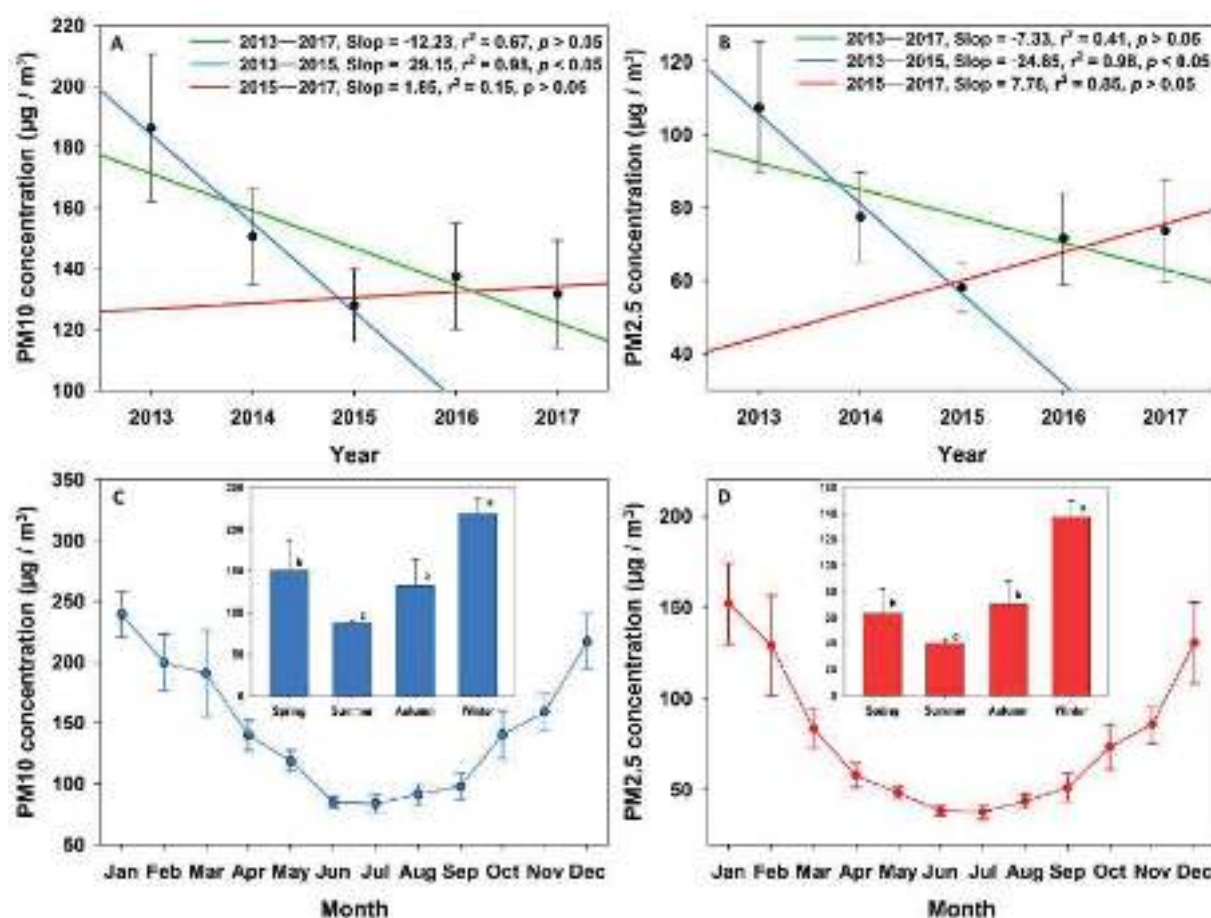


Figure 2. Annual, seasonal, and monthly variations in the concentrations of PM10 and PM2.5. (A): interannual variation of PM10; (B): interannual variation of PM2.5; (C): intraannual variation of PM10; (D): intraannual variation of PM2.5.

3.2. The Concentrations of PM10 and PM2.5 at Different Air Monitoring Stations in Xi'an

As a whole, the concentrations of PM10 and PM2.5 exhibited positive correlations ($p < 0.05$) during the days that exceeded the Grade 3 concentration limits (24 h average); and negative correlations ($p < 0.05$) during the days with Grade 1 concentration limits (24 h average) or lower (Table 1 and Figure 3).

Table 1. Spearman correlation coefficients between concentrations of PM10 and PM2.5 and the days that $\text{PM}_{10} > 150 \mu\text{g}/\text{m}^3$, $\text{PM}_{10} < 50 \mu\text{g}/\text{m}^3$, $\text{PM}_{2.5} > 75 \mu\text{g}/\text{m}^3$, $\text{PM}_{2.5} < 35 \mu\text{g}/\text{m}^3$.

Time Period	PM10 > 150	PM10 < 50	PM2.5 > 75	PM2.5 < 35
Spring	0.868 ** (n = 182)	−0.637 * (n = 54)	0.913 ** (n = 127)	−0.866 ** (n = 84)
Summer	0.861 ** (n = 21)	−0.900 ** (n = 171)	0.794 ** (n = 25)	−0.984 ** (n = 213)
Autumn	0.894 ** (n = 149)	−0.676 * (n = 101)	0.930 ** (n = 154)	−0.851 ** (n = 89)
Winter	0.663 * (n = 278)	−0.552 (n = 17)	0.740 ** (n = 288)	−0.450 (n = 27)
Annual	0.934 ** (n = 630)	−0.731 ** (n = 343)	0.951 ** (n = 594)	−0.846 ** (n = 413)

* indicates a significance level of 0.05, ** indicates a significance level of 0.01.

The concentrations of PM10 and PM2.5 from all 13 of the air monitoring stations were involved to analyze the spatial differences in Xi'an. The concentrations of PM10, as well as PM2.5, among the 13 air monitoring stations were nonsignificant ($p > 0.05$), exhibiting similar characteristics of annual and seasonal concentrations (Figure 3).

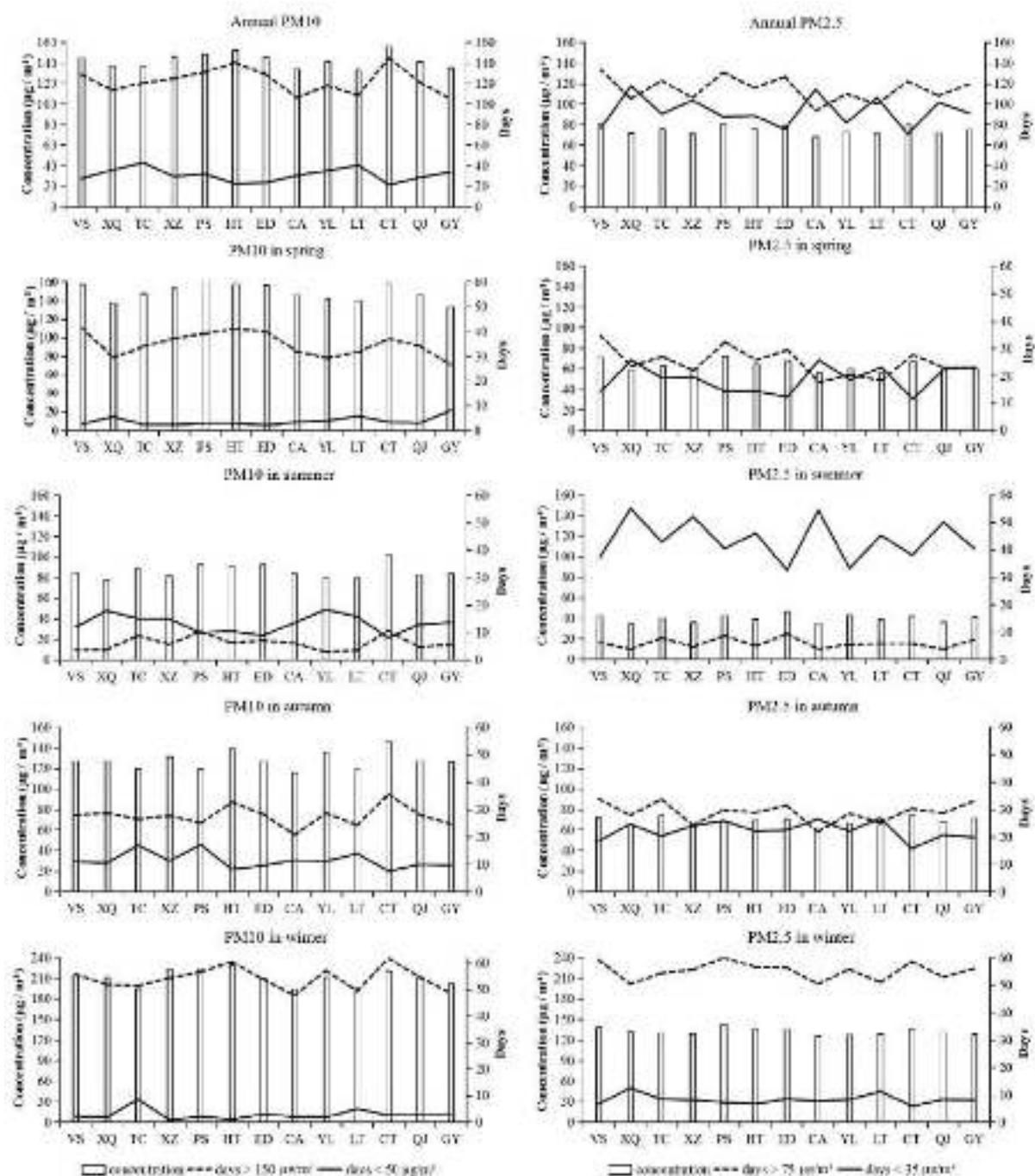


Figure 3. Annual and seasonal concentrations of PM10 and PM2.5 and the days that the concentrations lower than Grade 1 and higher than Grade 3 at different monitoring stations in Xi'an.

The concentrations of PM10 and PM2.5 among monitoring stations varied across temporal scales (Table 2). Annually, PM10 concentrations in Caotan (CT, $156.4 \mu\text{g}/\text{m}^3$) and High-Tech District (HT, $156.4 \mu\text{g}/\text{m}^3$) exceeded the Grade 3 concentration limit ($>150 \mu\text{g}/\text{m}^3$); while PM2.5 concentrations in Voltage Switchgear Factory (VS, $80.2 \mu\text{g}/\text{m}^3$) (TC, $76.0 \mu\text{g}/\text{m}^3$), People's Stadium (PS, $80.6 \mu\text{g}/\text{m}^3$), High-Tech District (HT, $76.4 \mu\text{g}/\text{m}^3$), Economic development District (ED, $79.2 \mu\text{g}/\text{m}^3$), and Caotan (CT, $76.9 \mu\text{g}/\text{m}^3$) exceeded the Grade 3 concentration limit ($>75 \mu\text{g}/\text{m}^3$). Seasonally, in spring, PM10 concentrations in Voltage Switchgear Factory (VS, $157.1 \mu\text{g}/\text{m}^3$), Xiaozhai (XZ, $152.5 \mu\text{g}/\text{m}^3$), People's Stadium (PS, $161.2 \mu\text{g}/\text{m}^3$), High-Tech District (HT, $157.3 \mu\text{g}/\text{m}^3$), Economic development District (ED, $156.4 \mu\text{g}/\text{m}^3$), and Caotan (CT, $158.3 \mu\text{g}/\text{m}^3$) exceeded the Grade 3 concentra-

tion limit; for PM_{2.5} concentrations, no station exceeded the Grade 3 concentration limit. In summer and autumn, neither the PM₁₀ nor the PM_{2.5} exceeded the Grade 3 concentration limit. Whereas in winter, both PM₁₀ and PM_{2.5} exceeded the Grade 3 concentration limit, with no monitoring station reaching the Grade 1 concentration limit for PM₁₀ ($<50 \mu\text{g}/\text{m}^3$). However, Xingqing Community (XQ, $34.5 \mu\text{g}/\text{m}^3$) and Chang'an District (CA, $35.0 \mu\text{g}/\text{m}^3$) meet the Grade 1 PM_{2.5} concentration limit ($<35 \mu\text{g}/\text{m}^3$) in summer. The maximum PM₁₀ concentration difference between seasons was identified in Xiaozhai (XZ, $142.1 \mu\text{g}/\text{m}^3$), the minimum in Textile City (TC, $106.0 \mu\text{g}/\text{m}^3$). The maximum PM_{2.5} concentration difference was found in People's Stadium (PS, $100.4 \mu\text{g}/\text{m}^3$), the minimum in Yanliang District (YL, $84.5 \mu\text{g}/\text{m}^3$).

Table 2. The concentrations of PM₁₀ and PM_{2.5} among monitoring stations in Xi'an annually and seasonally.

Types	Stations	Annual (n = 1080)	Spring (n = 460)	Summer (n = 458)	Autumn (n = 450)	Winter (n = 432)	Max-Min
PM ₁₀	VS	145.0	157.1	85.1	127.4	214.5	129.4
	XQ	137.6	137.7	78.0	127.5	211.4	133.4
	TC	136.7	147.3	88.6	120.0	194.6	106.0
	XZ	146.3	152.5	81.4	131.4	223.5	142.1
	PS	148.4	161.2	92.5	119.8	223.9	131.4
	HT	153.0	157.3	90.8	138.8	228.8	138.0
	ED	145.8	156.4	92.6	127.1	210.4	117.8
	CA	134.0	145.4	84.2	115.5	193.8	109.6
	YL	141.5	142.3	80.5	135.6	211.6	131.1
	LT	132.8	139.5	79.5	119.2	195.9	116.4
	CT	156.4	158.3	102.6	146.6	220.8	118.2
	QJ	141.2	145.8	83.0	127.7	212.1	129.1
	GY	135.9	133.0	83.9	126.3	203.0	119.1
PM _{2.5}	VS	80.2	70.8	42.8	72.1	138.7	95.9
	XQ	71.9	59.3	34.5	65.6	131.6	97.1
	TC	76.0	62.7	40.6	73.9	130.5	89.9
	XZ	71.5	60.3	36.0	63.4	129.3	93.3
	PS	80.6	71.8	42.5	68.1	142.9	100.4
	HT	76.4	64.8	38.8	69.1	135.7	96.9
	ED	79.2	68.3	46.4	70.6	134.6	88.2
	CA	68.1	55.9	35.0	59.2	125.3	90.3
	YL	73.7	60.2	43.2	66.4	127.7	84.5
	LT	71.4	56.1	39.0	64.8	128.5	89.5
	CT	79.6	67.1	41.8	74.2	136.9	95.1
	QJ	72.9	59.8	36.1	68.1	130.9	94.8
	GY	74.9	60.3	41.7	71.2	128.8	87.1

Notes: Max-Min was the maximum difference between the seasons. Units: $\mu\text{g}/\text{m}^3$.

Overall, the concentrations of PM₁₀ and PM_{2.5} were highest in People's Stadium (PS) and Caotan (CT), and lowest in the Xingqing Community (XQ), the Chang'an District (CA), the Lintong District (LT), and Guangyun Lake (GY).

3.3. Relationships between the Concentrations of Particulate Matter and Meteorological Factors

Spearman correlation coefficients between PM₁₀ (and PM_{2.5}) and meteorological factors varied across seasons, indicating that the dominant meteorological factors and their influence on PM₁₀ and PM_{2.5} vary over time (Tables 3 and 4).

Table 3. Spearman correlations and multivariate progressive linear regression between PM10 and meteorological factors in Xi'an.

Temporal Scales	Precipitation	Atmospheric Pressure	Relative Humidity	Atmospheric Temperature	Wind Speed	Wind Direction
Spring (n = 460)	−0.332 **	−0.040	−0.394 **	−0.134 **	−0.015	−0.142 **
Summer (n = 458)	−0.307 **	−0.149 **	−0.281 **	0.238 **	0.004	−0.171 **
Autumn (n = 450)	−0.480 **	0.008	−0.350 **	−0.168 **	−0.291 **	−0.036
Winter (n = 432)	−0.154 **	−0.343 **	0.388 **	0.108 *	−0.381 **	−0.256 **
Annual (n = 1080)	−0.358 **	0.335 **	−0.191 **	−0.478 **	−0.243 **	−0.100 **

* indicates a significance level of 0.05; ** indicates a significance level of 0.01.

Table 4. Spearman correlations and multivariate progressive linear regression between PM2.5 and meteorological factors in Xi'an.

Temporal Scales	Precipitation	Atmospheric Pressure	Relative Humidity	Atmospheric Temperature	Wind Speed	Wind Direction
Spring (n = 460)	−0.191 **	0.016	−0.111 *	−0.254 **	−0.079	−0.296 **
Summer (n = 458)	−0.200 **	−0.096 *	−0.038	0.161 **	0.035	−0.265 **
Autumn (n = 450)	−0.372 **	0.011	−0.220 **	−0.153 **	−0.309 **	−0.085
Winter (n = 432)	−0.057	−0.334 **	0.521 **	0.067	−0.460 **	−0.294 **
Annual (n = 1080)	−0.260 **	0.368 **	−0.0031	−0.506 **	−0.294 **	−0.178 **

* indicates a significance level of 0.05; ** indicates a significance level of 0.01.

Precipitation was negatively correlated with PM10 and PM2.5 ($p < 0.01$), except for PM2.5 in winter ($p > 0.05$). Atmospheric pressure was negatively correlated with PM10 and PM2.5 in summer and winter ($p < 0.05$), and positively correlated with the annual PM10 and PM2.5 ($p < 0.05$). Relative humidity showed a negative correlation ($p < 0.05$) with the annual and seasonal concentrations of PM10, except in winter. This same correlation with relative humidity was also exhibited for PM2.5 in spring and autumn, though a positive correlation was found with PM10 and PM2.5 in winter. Atmospheric temperature exhibited a negative correlation with PM10 and PM2.5 in spring and autumn, and a positive correlation in summer and winter. Wind speed only exhibited a negative correlation ($p < 0.05$) with PM10 and PM2.5 in autumn and winter. Finally, wind direction exhibited a negative correlation ($p < 0.05$) with PM10 and PM2.5 in all seasons except for autumn.

3.4. Response of Atmospheric Pollutants to the Environmental Management

Figure 4 displayed the emission intensity of SO₂, smoke, and dust, and environmental regulation intensity in 2013–2017 in Xi'an. With the growth of economy, the emission intensity of SO₂, smoke and dust exhibited declining trends during 2013–2017, especially SO₂. In 2015–2016, the emission intensity of these atmospheric pollutants sharply declined from 9.49 to 1.20 t/10⁸ RMB. However, the environmental regulation intensity (ERI) exhibited increasing trends during 2013–2017. In 2015–2016, ERI dramatically increased from 3.27 to 9.98.

ERI was significantly and negatively correlated with the emission intensity of SO₂, smoke and dust ($p < 0.05$), but not significantly correlated with the concentration of PM10 and PM2.5 ($p > 0.05$).

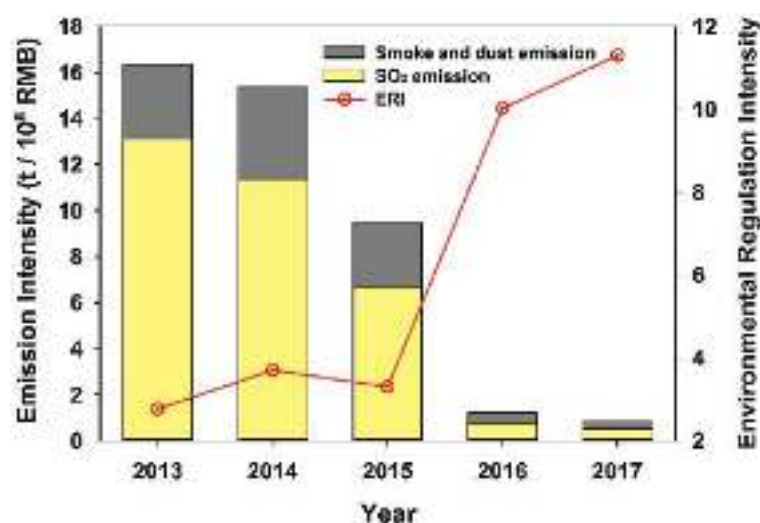


Figure 4. Environmental regulation intensity and the emission intensity of SO₂, smoke, and dust.

4. Discussion

4.1. Temporal and Spatial Variations of PM₁₀ and PM_{2.5}

The mean annual concentrations of PM₁₀ and PM_{2.5} decreased significantly from 2013 to 2017, while concentrations during 2015–2017 did not exhibit any significant variations. Studies have shown that improvements in air quality in megacities are significant in the early stages of governance and then stalled. The improvement of environmental quality rarely accompanies urbanization and industrialization [21]. The inter-annual variation may be attributed to human activities, including auto emissions and steel productions. Additionally, the demand for housing intensified by the expansion of urban land could increase construction dust emissions. The observed variations in the concentrations of PM_{2.5} and PM₁₀ may thus be a result of specific weather conditions, combined with changes in land use and the increased development of urban infrastructure [2,24].

Regarding the seasonal variations in PM₁₀ and PM_{2.5}, both the highest concentrations occurred in winter and the lowest in summer, the second-highest in spring and autumn. This phenomenon might be attributable to frequent sandstorms originating in northwestern China with bare land cover and strong wind, which produced anomalously high concentrations of mineral dust, resulting in a prominent rise of particulate matter in spring [6]. In autumn, straw burning after agricultural harvests results in the rise in particulate matter concentrations. In addition, meteorological factors also play an important role in these processes. Cloudy weather and low wind speed could contribute to the elevated particulate matter concentrations [25]. Many cities seek to alter meteorological conditions to some extent by changing the urban landscape [26]. Wind and turbulence within the urban canopy can play an important role in local measurements of meteorological conditions. This is especially true if pollutants are frequently capped by a statically stable atmospheric layer [2,14]. Such stable conditions may contribute to the lack of spatial variations observed in the downtown area. Our results showed nonsignificant difference for the concentrations of PM₁₀ and PM_{2.5} among the 13 stations. Zhang et al. [27] analyzed the particulate matter at six sites in Xi'an, and also found nonsignificant spatial variations. However, the concentrations of particulate matter were lower in the stations that locate near places with higher tree coverage rates and large water bodies. Meanwhile, the concentrations were higher in the stations surrounded by high energy consumption and bare land. Based on these observations, we believe that the spatial homogeneity of the air quality is also affected by human activities (i.e., pollutant emissions and land use).

4.2. Effects of Meteorological Conditions and Environmental Management on Atmospheric Pollution

Affecting the formation, diffusion, dilution, transformation, transportation, and accumulation of airborne pollutants, meteorological conditions are crucial for establishing air quality levels [11,12]. In this study, the meteorological factors significantly influenced the seasonal variations of particulate matter concentrations. This is partly because of the stable interaction between particulate matter and meteorological factors. Precipitation, for example, can remove particulate matter in the atmosphere and reducing the concentrations across seasons [27,28]. However, there are also some unstable interactions. Within a certain range, the wind can dilute the concentrations of particulate matter, otherwise the effect could be the opposite. In spring, for instance, strong winds from the north-west can easily bring sandstorms from Loess Plateau and increase the concentrations of particulate matter. The increased relative humidity caused by precipitation can reduce the concentrations of particulate matter, whereas high relative humidity can accumulate water-soluble ions, such as NH_4^+ , NO_3^- , and SO_4^{2-} , which are major aerosol components during haze episodes [29,30]. In addition, there may be a combination of other factors, such as vegetation cover, which can adsorb the particulate matter. Vegetation cover is regulated by phenology, such as atmospheric temperature [14]. This may result in the different relationships between particulate matter and atmospheric temperature across seasons.

The environmental management could determine the pollution intensity and the types of pollutants. In this study, we found that the environmental regulation intensity could significantly alleviate the emissions of SO_2 , smoke and dust, neither the particulate matter (Table 5). Compared with SO_2 , smoke and dust, the composition, chemical process, and the influence factors of particulate matter are more complicated [30,31]. It may be ineffective by simply increasing the environmental regulation intensity in a short period. Therefore, further exploration and verification are needed in terms of environmental management.

Table 5. Correlation coefficients between the environmental regulation intensity and the concentration and emission of atmospheric pollutants.

	PM10	PM2.5	SO_2 Emission	Smoke and Dust Emission
ERI	−0.52	−0.30	−0.92 *	0.95 *

*, $p < 0.05$.

Considering the difficulty of artificial control of meteorological conditions, more attention has been paid to the environmental management, which has been confirmed as the effective way to the improvement of atmospheric pollution. A one-size-fits-all management model may also have side effects on the development of socio-economics in a developing region. To reduce atmospheric pollution, effective environmental management should factor in the seasonal meteorological conditions. For instance, increasing relative humidity is an effective measure to reduce airborne pollution in spring and autumn. In winter, it is quite clear that improving ventilation and reducing relative humidity may ameliorate some of the effects of atmospheric pollution [25,32]. It is necessary to implement the intensity of targeted atmospheric governance under specific meteorological conditions to achieve the sustainability of socio-economic development and environmental protection.

4.3. Further Work

Our results suggest that the worsening of air quality in Xi'an is mainly caused by the combination of human activities and natural sources. Many regulators believe that local air quality can be improved by efforts to reduce anthropogenic emissions, and controlling trans-boundary pollutants from the Gobi desert through increasing vegetation cover. It is necessary to investigate the effects of different types of human activities on air quality in the urban environment, and this will form the basis of our future work. Air monitoring stations

that cover different environments are also needed. Further research should involve more monitoring systems by factoring in local land use, while involving both the downtown and suburban areas.

5. Conclusions

In this study, we explored the temporal and spatial trends of the concentrations of PM₁₀ and PM_{2.5} in Xi'an, China, and the response to the meteorological factors and environmental regulation intensity. The concentrations of PM₁₀ were higher than those of PM_{2.5}, especially in spring and winter. The annual, seasonal, and monthly variations of PM₁₀ and PM_{2.5} were striking. In terms of seasonal variations, the air quality is best in summer, and worst in winter. The spatial characteristics of air quality did not reveal any significant spatial differences due to the air monitoring stations being concentrated in the downtown area.

Among the meteorological factors, precipitation, relative humidity, and atmospheric temperature had impacts on atmospheric pollution. Conversely, wind speed affected concentration only in autumn and winter, and wind direction affected them only in spring and summer. In addition, the effects of environmental regulation intensity were prominent (i.e., environmental governance investment per unit of air pollutant emissions).

Author Contributions: Conceptualization, Y.T. and H.S.; methodology, Y.T. and L.Z.; software, Y.T. and Y.W.; validation, Y.T., L.Z. and H.S.; formal analysis, Y.T. and L.Z.; investigation, Y.T. and L.Z.; resources, Y.T., L.Z. and J.S.; data curation, Y.T., L.Z. and Y.W.; writing—original draft preparation, Y.T.; writing—review and editing, Y.T. and H.S.; visualization, Y.T. and L.Z.; supervision, J.S.; project administration, J.S.; funding acquisition, J.S. and H.S. All authors have read and agreed to the published version of the manuscript.

Funding: This work was funded by the Key Research and Development Program of Shaanxi, grant number 2019ZDLSF05-02; the Open Research Fund of Key Laboratory for Ecology and Environment of River Wetlands in Shaanxi Province, grant number SXSD202002.

Institutional Review Board Statement: Not applicable.

Informed Consent Statement: Not applicable.

Data Availability Statement: Not applicable.

Conflicts of Interest: The authors declare no conflict of interest.

References

- Huang, R.; Zhang, Y.L.; Bozzetti, C.; Ho, K.; Cao, J.; Han, Y.M.; Daellenbach, K.R.; Slowik, J.G.; Platt, S.M.; Canonaco, F.; et al. High secondary aerosol contribution to particulate pollution during haze events in China. *Nature* **2014**, *514*, 218–222. [CrossRef]
- Lu, C.; Liu, Y. Effects of China's urban form on urban air quality. *Urban Stud.* **2016**, *53*, 2607–2623. [CrossRef]
- Le, T.H.; Wang, Y.; Liu, L.; Yang, J.N.; Yung, Y.L.; Li, G.H.; Seinfeld, J.H. Unexpected air pollution with marked emission reductions during the COVID-19 outbreak in China. *Science* **2020**, *369*, 702–706. [CrossRef]
- Sbai, S.E.; Li, C.L.; Boreave, A.; Charbonnel, N.; Perrier, S.; Vernoux, P.; Bentayeb, F.; George, C.; Gil, S. Atmospheric photochemistry and secondary aerosol formation of urban air in Lyon, France. *J. Environ. Sci.* **2021**, *99*, 313–325. [CrossRef]
- Tian, G.J.; Qiao, Z.; Xu, X.L. Characteristics of particulate matter (PM₁₀) and its relationship with meteorological factors during 2001–2012 in Beijing. *Environ. Pollut.* **2014**, *192*, 266–274. [CrossRef] [PubMed]
- Yuan, W.; Huang, R.J.; Yang, L.; Ni, H.Y.; Wang, T.; Cao, W.J.; Duan, J.; Guo, J.; Huang, H.B.; Hoffmann, T. Concentrations, optical properties and sources of Humic-Like Substances (HULIS) in fine particulate matter in Xi'an, Northwest China. *Sci. Total Environ.* **2021**, *789*, 147902. [CrossRef]
- Curtis, L.; Rea, W.; Smith-Willis, P.; Fenyves, E.; Pan, Y.Q. Adverse health effects of outdoor air pollutants. *Environ. Int.* **2006**, *32*, 815–830. [CrossRef] [PubMed]
- Huo, Y.Q.; Guo, Z.H.; Li, Q.; Wu, D.; Ding, X.; Liu, A.L.; Huang, D.; Qiu, G.K.; Wu, M.M.; Zhao, Z.J.; et al. Chemical fingerprinting of HULIS in particulate matters emitted from residential coal and biomass combustion. *Environ. Sci. Technol.* **2021**, *55*, 3593–3603. [CrossRef] [PubMed]
- Yan, S.J.; Cao, H.; Chen, Y.; Wu, C.Z.; Tao, H.; Fan, H.L. Spatial and temporal characteristics of air quality and air pollutants in 2013 in Beijing. *Environ. Sci. Pollut. Res.* **2016**, *23*, 13996–14007. [CrossRef] [PubMed]

10. Cao, J.J.; Wu, F.; Chow, J.; Lee, S.C.; Li, Y.; Chen, S.W.; An, Z.S.; Fung, K.K.; Watson, J.G.; Zhu, C.S.; et al. Characterization and source apportionment of atmospheric organic and elemental carbon during fall and winter of 2003 in Xi'an, China. *Atmos. Chem. Phys.* **2005**, *5*, 3127–3137. [CrossRef]
11. Xue, W.H.; Zhang, J.; Qiao, Y.; Wei, J.; Lu, T.W.; Che, Y.F.; Tian, Y.L. Spatiotemporal variations and relationships of aerosol-radiation-ecosystem productivity over China during 2001–2014. *Sci. Total Environ.* **2020**, *741*, 140324. [CrossRef] [PubMed]
12. Tian, Y.L.; Jiang, Y.; Liu, Q.; Xu, D.X.; Zhao, S.D.; He, L.H.; Liu, H.J.; Xu, H. Temporal and spatial trends in air quality in Beijing. *Landsc. Urban Plan.* **2019**, *185*, 35–43. [CrossRef]
13. Hopke, P.K.; Cohen, D.D.; Begum, B.A.; Biswas, S.K.; Ni, B.F.; Pandit, G.G.; Santoso, M.; Chung, Y.; Rahman, S.A.; Hamzah, M.S.; et al. Urban air quality in the Asian region. *Sci. Total Environ.* **2008**, *404*, 103–112. [CrossRef]
14. Chen, A.; Yao, X.A.; Sun, R.H.; Chen, L.D. Effect of urban green patterns on surface urban cool islands and its seasonal variations. *Urban For. Urban Gree.* **2014**, *13*, 646–654. [CrossRef]
15. Landguth, E.L.; Holden, Z.A.; Graham, J.; Stark, B.; Mokhtari, E.B.; Kaleczyc, E.; Anderson, S.; Urbanski, S.; Jolly, M.; Semmens, E.O.; et al. The delayed effect of wildfire season particulate matter on subsequent influenza season in a mountain west region of the USA. *Environ. Int.* **2020**, *139*, 105668. [CrossRef]
16. Wang, P.; Cao, J.J.; Shen, Z.X.; Han, Y.M.; Lee, S.C.; Huang, Y.; Zhu, C.S.; Wang, Q.Y.; Xu, H.M.; Huang, R.J. Spatial and seasonal variations of PM_{2.5} mass and species during 2010 in Xi'an, China. *Sci. Total Environ.* **2015**, *508*, 477–487. [CrossRef]
17. Zhang, R.; Jing, J.; Tao, J.; Hsu, S.C.; Wang, G.; Cao, J.; Lee, C.S.L.; Zhu, L.; Chen, Z.; Zhao, Y.; et al. Chemical characterization and source apportionment of PM_{2.5} in Beijing: Seasonal perspective. *Atmos. Chem. Phys.* **2013**, *13*, 7053–7074. [CrossRef]
18. Cao, Z.Z.; Yang, Y.Y.; Lu, J.L.; Zhang, C.X. Atmospheric particle characterization, distribution, and deposition in Xi'an, Shaanxi Province, Central China. *Environ. Pollut.* **2011**, *159*, 577–584. [CrossRef]
19. Samad, A.; Vogt, U.; Panta, A.; Upreti, D. Vertical distribution of particulate matter, black carbon and ultra-fine particles in Stuttgart, Germany. *Atmos. Pollut. Res.* **2020**, *11*, 1441–1450. [CrossRef]
20. Wang, D.X.; Hu, J.L.; Xu, Y.; Lv, D.; Xie, X.Y.; Kleeman, M.; Xing, J.; Zhang, H.L.; Ying, Q. Source contributions to primary and secondary inorganic particulate matter during a severe wintertime PM_{2.5} pollution episode in Xi'an, China. *Atmos. Environ.* **2014**, *97*, 182–194. [CrossRef]
21. Xue, W.H.; Wei, J.; Zhang, J.; Sun, L.; Che, Y.F.; Yuan, M.; Hu, X. Inferring near-surface PM_{2.5} concentrations from the VIIRS deep blue aerosol product in China: A spatiotemporally weighted random forest model. *Remote Sens.* **2021**, *13*, 505. [CrossRef]
22. Wu, J.; Kong, S.F.; Wu, F.Q.; Cheng, Y.; Zheng, S.R.; Qin, S.; Liu, X.; Yan, Q.; Zheng, H.; Zheng, M.M.; et al. The moving of high emission for biomass burning in China: View from multi-year emission estimation and human-driven forces. *Environ. Int.* **2020**, *142*, 105812. [CrossRef]
23. Ministry of Ecology and Environment of the People's Republic of China. The Ambient Air Quality Standard (GB 3095-2012). 2012. Available online: <http://www.mee.gov.cn/> (accessed on 4 August 2018).
24. Elminir, H.K. Dependence of urban air pollutants on meteorology. *Sci. Total Environ.* **2005**, *350*, 225–237. [CrossRef] [PubMed]
25. Zhou, B.; Liu, D.Y.; Yan, W.L. A Simple new method for calculating precipitation scavenging effect on particulate matter: Based on five-year data in Eastern China. *Atmosphere* **2021**, *12*, 759. [CrossRef]
26. Luan, Q.Z.; Li, B.; Ye, C.H.; Zhang, X.S.; Zhang, Y. Preliminary analysis about impacts of urban 3D landscape pattern on regional meteorological condition in Beijing. *Ecology Environ. Sci.* **2019**, *28*, 514–522. [CrossRef]
27. Zhang, T.; Cao, J.J.; Tie, X.X.; Shen, Z.X.; Liu, S.X.; Ding, H.; Han, Y.M.; Wang, G.H.; Ho, K.F.; Qiang, J.; et al. Water-soluble ions in atmospheric aerosols measured in Xi'an, China: Seasonal variations and sources. *Atmos. Res.* **2011**, *102*, 110–119. [CrossRef]
28. Xu, Z.; Chen, S.X.; Wu, X. Meteorological change and impacts on air pollution: Results from North China. *J. Geophys. Res. Atmos.* **2020**, *125*. [CrossRef]
29. Shen, Z.X.; Cao, J.J.; Arimoto, R.; Han, Z.W.; Zhang, R.J.; Han, Y.M.; Liu, S.X.; Okuda, T.; Nakao, S.; Tanaka, S. Ionic composition of TSP and PM_{2.5} during dust storms and air pollution episodes at Xi'an, China. *Atmos. Environ.* **2009**, *43*, 2911–2918. [CrossRef]
30. Huang, R.; Yang, L.; Shen, J.C.; Yuan, W.; Gong, Y.Q.; Guo, J.; Cao, W.J.; Duan, J.; Ni, H.Y.; Zhu, C.S.; et al. Water-insoluble organics dominate brown carbon in wintertime urban aerosol of China: Chemical characteristics and optical properties. *Environ. Sci. Technol.* **2020**, *54*, 7836–7847. [CrossRef] [PubMed]
31. Li, X.H.; Han, J.Z.; Hopke, P.K.; Hu, J.G.; Shu, Q.; Chang, Q.; Ying, Q. Quantifying primary and secondary humic like substances in urban aerosol based on emission source characterization and a source-oriented air quality model. *Atmos. Chem. Phys.* **2019**, *19*, 2327–2341. [CrossRef]
32. Beaver, S.; Tanrikulu, S.; Palazoglu, A.; Singh, A.; Soong, S.T.; Jia, Y.Q.; Tran, C.; Ainslie, B.; Steyn, D.G. Pattern-based evaluation of coupled meteorological and air quality models. *J. Appl. Meteorol. Clim.* **2010**, *49*, 2077–2091. [CrossRef]

Article

Analysis of the Interactions between the 200 hPa Jet and Air Pollutants in the Near-Surface Layer over East Asia in Summer

Wen Wei ¹, Bingliang Zhuang ^{1,*}, Huijuan Lin ¹, Yu Shu ^{2,*}, Tijian Wang ¹, Huimin Chen ¹ and Yiman Gao ¹

¹ School of Atmospheric Sciences, Nanjing University, Nanjing 210023, China; mg1928050@smail.nju.edu.cn (W.W.); mg1928012@smail.nju.edu.cn (H.L.); tjwang@nju.edu.cn (T.W.); mg1728037@smail.nju.edu.cn (H.C.); mg20280011@smail.nju.edu.cn (Y.G.)
² Nanjing Meteorological Bureau, Nanjing 210019, China
 * Correspondence: blzhuang@nju.edu.cn (B.Z.); njushuyu@sina.com (Y.S.)

Citation: Wei, W.; Zhuang, B.; Lin, H.; Shu, Y.; Wang, T.; Chen, H.; Gao, Y. Analysis of the Interactions between the 200 hPa Jet and Air Pollutants in the Near-Surface Layer over East Asia in Summer. *Atmosphere* **2021**, *12*, 886. <https://doi.org/10.3390/atmos12070886>

Academic Editors: Duanyang Liu, Kai Qin and Honglei Wang

Received: 4 June 2021
 Accepted: 6 July 2021
 Published: 8 July 2021

Publisher's Note: MDPI stays neutral with regard to jurisdictional claims in published maps and institutional affiliations.



Copyright: © 2021 by the authors. Licensee MDPI, Basel, Switzerland. This article is an open access article distributed under the terms and conditions of the Creative Commons Attribution (CC BY) license (<https://creativecommons.org/licenses/by/4.0/>).

Abstract: The rapid economic development in East Asia has led to serious air pollution problems in the near-surface layer. Studies have shown that there is an interaction between air pollution and the East Asian upper-level jet, which is an important weather system controlling the climate in East Asia. Therefore, it is of great significance to study the relationship between the surface layer air pollutants and the upper-level jet stream in East Asia. Based on the daily wind and vertical velocity data provided by the National Centers for Environmental Prediction/National Center for Atmospheric Research as well as the surface pollutant and meteorological variable data provided by the Science Data Bank, we use statistical analysis methods to study the relationship between the East Asian upper-level jet and the high-concentration area of near-surface air pollutants in summer. Meanwhile, the mechanisms of the interaction are preliminarily discussed. The results show that the North China Plain and the Tarim Basin are the high-value areas of the particulate matter (PM) in summer during 2013–2018, and the ozone (O₃) concentration in the near-surface atmospheric layer in the North China Plain is also high. The average concentrations of the PM_{2.5}, PM₁₀ and O₃ in the North China Plain are 45.09, 70.28 and 131.27 µg·m^{−3}, respectively, and the days with the concentration exceeding the standard reach 401, 461 and 488, respectively. During this period, there is an increasing trend in the O₃ concentration and a decreasing trend in the PM concentration. The average ratio of the PM_{2.5} to PM₁₀ is approximately 0.65 with a decreasing trend. The air pollutant concentration in this region has a significant relationship with the location of the East Asian upper-level jet. The low wind speed at the surface level under the control of the upper-level jet is the main reason for the high pollutant concentration besides the pollutant emission. They relate to each other through the surface humidity and the meridional and zonal wind. Meanwhile, the concentrations of the PM_{2.5} and PM₁₀ are high in the near-surface layer in the Tarim Basin, and the average concentrations are 45.19 and 49.08 µg·m^{−3}, respectively. The days with the concentration exceeding the standard are 265 and 193, respectively. The interannual variation in the PM concentration shows an increasing trend first and then a decreasing trend. The average ratio of PM_{2.5} to PM₁₀ in this region reaches approximately 0.9. The ratio reaches the highest in 2013 and 2014 and then decreases to and maintains at approximately 0.85. The concentration of air pollutants in the basin has a significant relationship with the intensity of the upper-level jet in East Asia. The weakening of the upper-level jet will lead to a decrease in the surface humidity in the northern part of the basin, an increase in the surface temperature in the western part of the basin and a decrease in the surface zonal wind in the eastern part of the basin, which will result in a higher PM concentration.

Keywords: East Asian upper-level jet; atmospheric particulate matter; ozone; surface meteorological variables; statistical analysis

1. Introduction

Since the industrial revolution, the increase in human activities has exacerbated climate change in the earth system. At present, observation results have proved that global

climate change has become an unequivocal fact, such as the continuous rise of the global temperature, glacier melting and frequent extreme weather events, which are serious threats to human survival and development [1]. Therefore, the in-depth understanding of climate change is the current hotspot of scientific research, which will provide scientific support for climatic policymaking.

Some studies have pointed out that there is an interaction between climate change and air pollution [2]. Among the influencing factors of climate change, the role of aerosol is the most uncertain [1]. The main component of air pollutants is the atmospheric aerosol. The atmospheric aerosol refers to the particulate matter (PM) suspended in the atmosphere. Aerosol particles can be solid or liquid and can also exist in the mixing form of solid and liquid. In general, the diameters of the atmospheric aerosol particles are several nanometers to tens of microns. The sources of aerosol particles in the atmosphere are different, and different aerosols have different physical, chemical and optical properties, resulting in more complex climatic effects of aerosols. The climatic effects of aerosols can be divided into direct climatic effects, indirect effects and semi-direct effects. Although the three effects are different in their interaction mechanisms, they all essentially lead to the change in the earth climate system by affecting the radiation budget balance of the earth-atmosphere system [3–7]. At the same time, variations in the climate system will cause the variation in relevant meteorological factors, which will have an impact on the distribution of air pollutants [8,9].

The East Asian upper-level jet is a narrow wind belt with a high wind speed above 500 hPa in the East Asia region [10]. Many observational data show that the strongest subtropical westerly wind speed generally exists at 200 hPa [10,11], and the East Asian jet is generally defined as the 200 hPa maximum zonal wind speed zone. The East Asian upper-level jet has significant seasonal variation, and its location and intensity will change accordingly. The jet stream, with its strong shears, plays an important role in forming upper level convergence and divergence. Therefore, it causes variations of the weight of all the air in a column from the ground to the limit of the atmosphere. In other words, The upper level jet stream makes the surface pressure change, which could result in variations in the air flow field at the ground [12]. At present, a large number of studies have shown that the East Asian upper-level jet controls the atmospheric circulation in East Asia and has an extremely important impact on the weather and climate in East Asia [13–15]. Secondary circulations will be generated around the East Asian upper-level jet, leading to the coupling of upper-level and low-level weather systems accompanied by the exchange of the matter, momentum and energy between the upper level and the ground. Therefore, the East Asian upper-level jet, as important weather and climate system in East Asia, may have a certain interaction with the surface pollutants. Studies have shown that surface pollutants have effects on the upper-level jet stream. Song et al. [16] and Chen et al. [17] pointed out that the increase in summer aerosols will cause the southward movement of the upper-level jet stream, which is mainly due to the change in the upper-level temperature gradient caused by the aerosol forcing. Liu et al. [18] pointed out that, in winter, to the north of 30° N, the mid-latitude cooling caused by aerosols leads to the enhancement of the subtropical jet stream and the weakening of the temperate jet stream, which further makes the upper-level jet stream move southward. In other studies, it has been found that the upper-level jet stream can affect the distribution of surface pollutants. Ordóñez et al. [19] found that the location of the North Atlantic jet stream has a greater impact on the concentration distribution of the surface PM₁₀ than on its intensity. Barnes and Fiore [20] have shown that the location of the jet stream in eastern North America in summer is closely related to the surface ozone concentration. Kerr et al. [21] used a model to analyze the position of the upper-level jet stream affecting the transport of the ozone by affecting the surface meridional wind. However, current research mainly focusses on the one-way effect between the upper-level jet stream and surface pollutants and rarely focusses on the interaction between them. In addition, the East Asia region has a wide zonal range, and the distributions of the terrain, coastline and land use are

relatively complex. The region is mainly controlled by the monsoon system, and the seasonal change in the climate is distinctive. In particular, the role of the summer monsoon system is relatively significant. Meanwhile, the population in East Asia accounts for one third of the world's population. On the one hand, the climate change in East Asia has a significant impact on the production and lives of the local people. On the other hand, the climate in East Asia is also strongly affected by human factors related to the rapid economic development of Asian countries. Therefore, the East Asian upper-level jet is one of the main members of the monsoon system that controls the weather and climate in East Asia, and the surface pollutant is an important factor affecting weather and climate changes. It is of great practical significance to study the interaction between them in summer and explore the mechanism.

2. Materials and Methods

2.1. Data

The National Centers for Environmental Prediction/National Center for Atmospheric Research (NCEP/NCAR) daily reanalysis data of the zonal wind and vertical velocity from 1989 to 2018 are used with the horizontal resolution of $2.5^\circ \times 2.5^\circ$ (the number of grid points is 144×73) and the vertical resolution of 17 layers.

The surface pollutant data and the surface meteorological variables including the relative humidity, temperature, surface meridional wind and surface zonal wind data are derived from the second version of the high-resolution air pollution reanalysis dataset in China in the Science Data Bank during 2013–2018. The dataset mainly contains two parts. The first part is the surface concentration reanalysis data of six conventional air pollutants ($PM_{2.5}$, PM_{10} , SO_2 , NO_2 , CO and O_3) in China from 2013 to 2018. These data are obtained by assimilating the surface observation data provided by the China National Environmental Monitoring Center by using the ensemble Kalman filter and the Nested Air Quality Prediction Modeling System. The second part is the Weather Research and Forecasting model simulation data of surface meteorological variables including the wind speed, temperature, air pressure and relative humidity during the same period. The spatio-temporal resolution of the dataset is high with the temporal resolution of 1 h and the spatial resolution of 15 km. By using cross-validation, independent data verification and comparing with similar data at home and abroad, it was found that the dataset is highly accurate [22]. In this study, four surface pollutants of the NO_2 , PM_{10} , $PM_{2.5}$ and O_3 are selected as the main research objects, and the O_3 data are processed into the format of the maximum concentration in 8 h per day.

2.2. Methods

All methods used in this paper were coded and computed in the programming language Python.

2.2.1. Empirical Orthogonal Function Decomposition

The empirical orthogonal function (EOF) is applied to the meteorological variable that changes with time, and the meteorological variable is decomposed into two parts, namely, the function of time and the function of space.

Assuming that the sample size is n and the meteorological variable X contains p spatial points (variables), the anomaly value of any spatial point i at any time point j can be regarded as the linear combination of p spatial functions v_{ik} and p time functions y_{kj} ($k = 1, 2, 3 \dots$ and p). The decomposition is expressed as a matrix form of $X = VY$.

The space vector V is a matrix of n row and n column, which are orthogonal to each other: $V^T \times V = I$ (I is a unit matrix)

The time vectors Y is an n -row and m -column matrix, and Y are also orthogonal:

$Y \times Y^T = \Lambda$ (Λ is a diagonal matrix)

Defining the matrix A as $A = X \times X^T$, and then we have:

$A = V \times \Lambda \times V^T$

V is also the eigenvector of A , Λ 's principal diagonal is the eigenvalue of A and the rest are all 0. Y can be obtained as $Y = V^T \times X$.

This method is used to study the spatio-temporal characteristics of 200 hPa zonal wind. More information about EOF can be found in [23].

2.2.2. Singular Value Decomposition

The singular value decomposition (SVD) method is performed on the covariance matrix of two variables. The anomalies fields of the variables and the normalized variables are commonly used. The decomposition result reveals the spatial correlation of two variable fields within a certain time range to a great extent. The heterogeneous correlation diagrams of the left and right fields explain the correlation between the two variables, and the SVD results are tested by using the Monte-Carlo method to avoid false correlation. The detailed descriptions and application of SVD is given in [24]. This approach is used to test the relationships between upper level jet stream (200 hPa zonal wind) and surface pollutants (PMs and O_3) over East Asia.

2.2.3. Pearson Correlation Coefficient

The Pearson correlation coefficient is a statistic that measures the linear correlation between two variables. It is usually represented by r , and its value ranges between -1 and 1 . The calculation formula of the correlation coefficient between variables $x_1, x_2, x_3 \dots x_n$ and variables $y_1, y_2, y_3 \dots y_n$ is as follows:

$$r = \frac{\sum_{i=1}^n (x_i - \bar{x})(y_i - \bar{y})}{\sqrt{\sum_{i=1}^n (x_i - \bar{x})^2 \sum_{i=1}^n (y_i - \bar{y})^2}} \quad (1)$$

The correlation coefficient in this study is tested by using the Monte Carlo method. That is, the two variables are considered to obey the normal distribution. The H_0 hypothesis is when the correlation coefficient is r , the two variables are not correlated. Given the confidence level α , the corresponding critical value can be determined according to the degree of freedom so that the probability distribution function conforms to $P(|r| > r_{1-\alpha}) = \alpha$. If $|r| > r_{1-\alpha}$, the hypothesis H_0 is rejected, and the correlation between the two variables is significant. Otherwise, the two variables are not correlated. The specific approaches are as follows.

First, a pair of arrays that conform to the normal distribution with sample sizes of n are randomly generated, and the Pearson correlation coefficient between them is calculated.

Second, the first step is repeated 15,000 times, and the obtained correlation coefficients are sorted in descending order. The 5000th correlation coefficient ($1-\alpha$) is found and marked as $r_{1-\alpha}$.

Third, the actual correlation coefficient $|r|$ and the $r_{1-\alpha}$ are compared. If $|r| > r_{1-\alpha}$, the two variables are correlated. Otherwise, they are not correlated.

We used this method to analyze the relationships between jet stream (200 hPa zonal wind) and surface meteorological elements (humidity, temperature, meridional wind and zonal wind), as well as the relationships between surface pollutants (PMs and O_3) and surface meteorological variables (humidity, temperature, meridional wind and zonal wind). The Monte Carlo method is also used to test whether the correlation is significant [25].

2.3. Relevant Definitions of the East Asian Upper-Level Jet

In this study, the area with the westerly wind speed greater than $30 \text{ m} \cdot \text{s}^{-1}$ at 200 hPa in East Asia ($70^\circ\text{--}140^\circ \text{ W}$, $15^\circ\text{--}55^\circ \text{ N}$) is defined as the East Asian upper-level jet. The position of the East Asian upper-level jet is defined as the latitude of the maximum westerly wind speed at 200 hPa in East Asia. The intensity of the East Asian upper-level jet is defined as the average wind speed on the jet stream axis. Figure 1 shows the average climate state of the 200 hPa jet stream axis in summer from 1989 to 2018. The position of the 200 hPa jet stream in summer is around 40° N with relatively large interannual fluctuations.

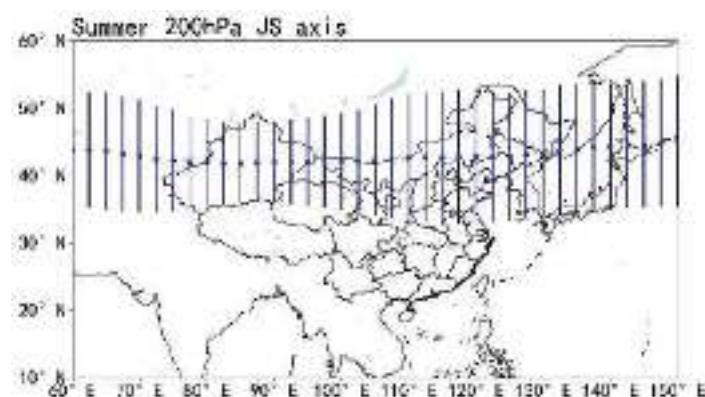


Figure 1. The average climate state of the jet stream axis at 200 hPa in summer from 1989 to 2018 (scatter points and error bars indicate the average position and the variabilities of the jet stream axis, respectively).

3. Results

3.1. Characteristics of the East Asian Upper-Level Jet and Surface Pollutants in Summer

3.1.1. Spatio-Temporal Characteristics of the East Asian Upper-Level Jet in Summer

The monthly average data of 200 hPa zonal wind in summer over East Asia from 2009 to 2018 are selected, and the spatio-temporal decomposition is carried out based on the data. The covariance contribution rates of the first two modes of the EOF (hereafter referred to as EOF1 and EOF2, respectively) decomposition results (Figure 2) are 57.54% and 8.78%, respectively. The spatial distribution of the EOF1 shows that the dividing line of the 200 hPa zonal wind is around 40° N, which is the average position of the upper-level jet stream in summer. The variations in the north and the south are opposite, which shows that the EOF1 represents the position variation in the upper-level jet stream. In the time series corresponding to the EOF1, the time coefficients are all negative in June during 2009–2018, while the time coefficients are both positive in July and August in the same years. This indicates that the position of the jet stream in June in this decade is to the south of that in July and August in the same years. The spatial distribution of the EOF2 of the 200 hPa upper-level zonal wind shows that there is a minimum area centered around 40° N, which is the average position of the upper-level jet stream in summer. Therefore, the EOF2 represents the intensity variation in the upper-level jet stream.

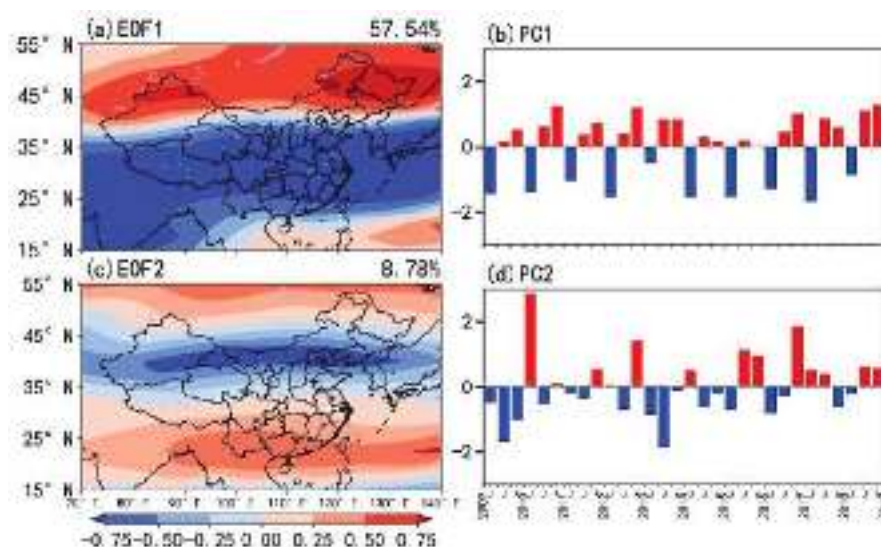


Figure 2. Spatial distributions (a,c) and the time coefficients (b,d) of the EOF1 and EOF2 of the 200 hPa zonal wind in summer from 2009 to 2018.

3.1.2. Distribution Characteristics of Surface Pollutants in East Asia in Summer

The average concentrations of the NO_2 , PM_{10} , O_3 (the maximum concentration in 8 h) and $\text{PM}_{2.5}$ in summer from 2013 to 2018 are shown in Figure 3. Combined with the first-level concentration indices of pollutants in the Ambient Air Quality Standards (GB 3095–2012), it can be seen that the overall NO_2 concentration in summer in China is within the normal standard range. There is relatively serious PM pollution in the Tarim Basin ($37\text{--}42^\circ \text{N}$, $75\text{--}90^\circ \text{E}$) and most parts of northern China. The O_3 concentration is relatively high in northern China and most areas of Qinghai-Tibet. The O_3 pollution in the North China Plain ($35\text{--}40^\circ \text{N}$, $113\text{--}123^\circ \text{E}$) is the most serious. Therefore, the PM_{10} and $\text{PM}_{2.5}$ in the Tarim Basin and the PM_{10} , O_3 , and $\text{PM}_{2.5}$ in the North China Plain are taken as the research objects of summer pollutants in this study.

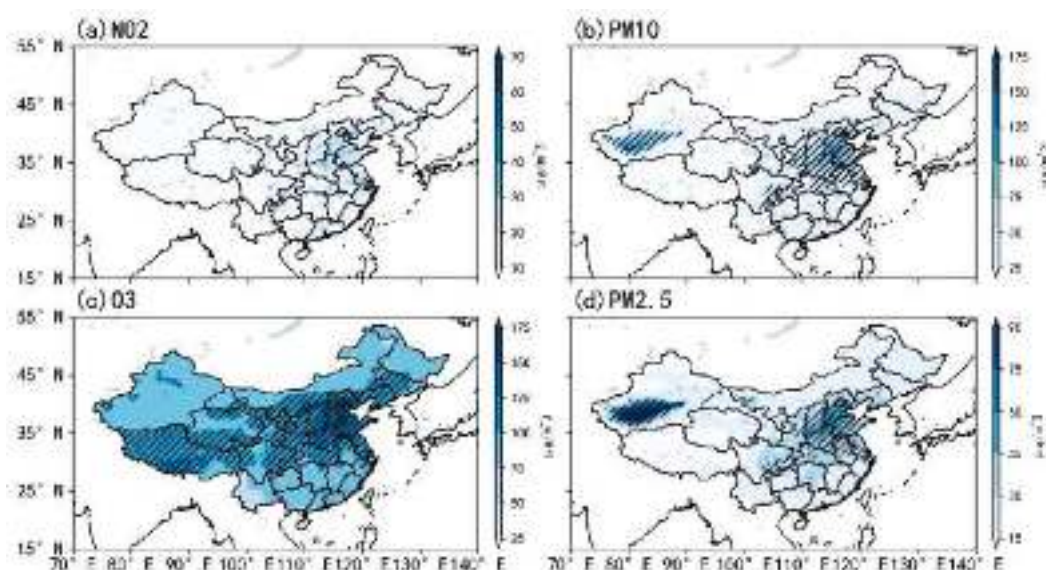


Figure 3. Season mean concentrations of air pollutants (a) NO_2 , (b) PM_{10} , (c) O_3 (8 h maximum concentration) and (d) $\text{PM}_{2.5}$ in China in summer during 2013–2018 (unit: $\mu\text{g}\cdot\text{m}^{-3}$, the slashed area indicates that the pollutant concentration in the area has exceeded the first-level concentration index of the Ambient Air Quality Standards in China).

In summer during 2013–2018, the average concentrations of the $\text{PM}_{2.5}$ and PM_{10} in the Tarim Basin are 45.19 and $49.08 \mu\text{g}\cdot\text{m}^{-3}$ (Table 1), respectively. The interannual variations of the PM concentration increased year by year before 2015 and decreased after 2015. The PM concentration reached the maximum in 2015, and many discrete values in 2018 indicate that severe PM pollution events occurred frequently in that year (Figure 4a,b). In Figure 5a, the days with the $\text{PM}_{2.5}$ exceeding the standard are more than those of the PM_{10} in summer in the Tarim Basin with a total of 265 and 193 days during 2013 to 2018, respectively. The ratio of $\text{PM}_{2.5}$ to PM_{10} in this area is high with an average of approximately 0.9 (Figure 7). The ratio of the $\text{PM}_{2.5}$ to PM_{10} reaches a high value in 2013 and 2014 with the maximum reaching 1, but the ratio declines in subsequent years and maintains at around 0.85 (Figure 6a).

Table 1. Average concentration of pollutants in the Tarim Basin and the North China Plain from 2013 to 2018 (unit: $\mu\text{g}\cdot\text{m}^{-3}$).

Area \ Pollution Kind	$\text{PM}_{2.5}$	PM_{10}	O_3
TB	45.19	49.08	-
NCP	45.09	70.28	131.27

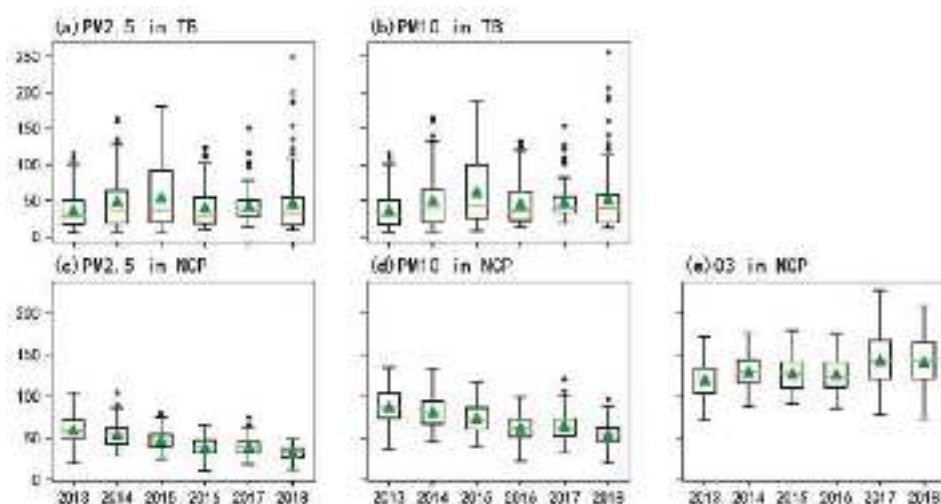


Figure 4. Interannual variation in the average pollutant concentrations in the Tarim Basin (a,b) and the North China Plain (c–e) (unit: $\mu\text{g}\cdot\text{m}^{-3}$, orange lines represent the median, green triangles represent the average value, and hollow dots represent the discrete value).

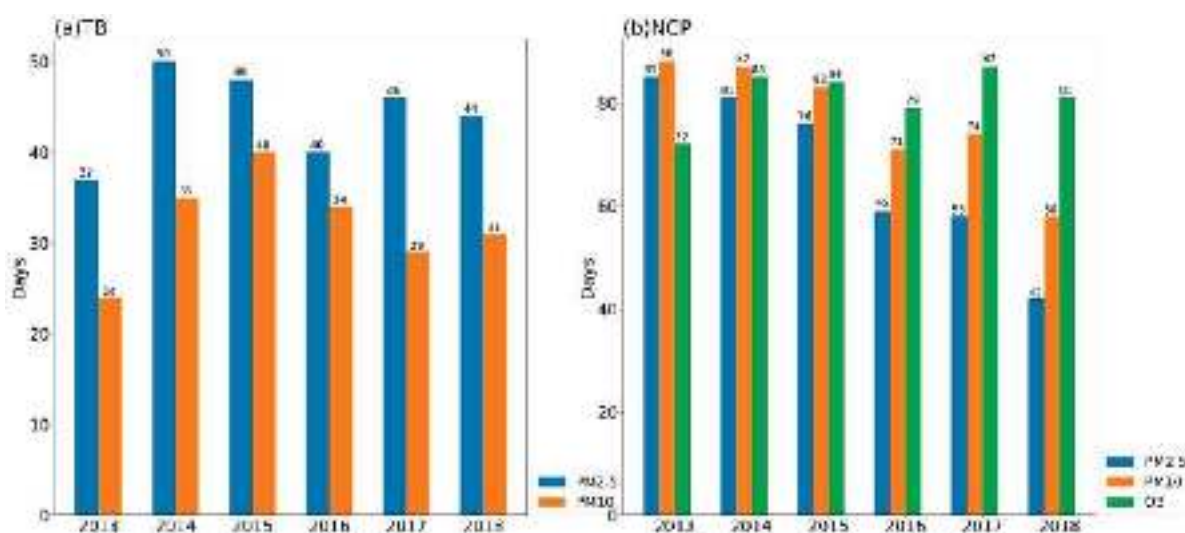


Figure 5. Days with pollutant concentrations exceeding the national first-level environmental standard in the Tarim Basin (a) and the North China Plain (b) in summer from 2013 to 2018.

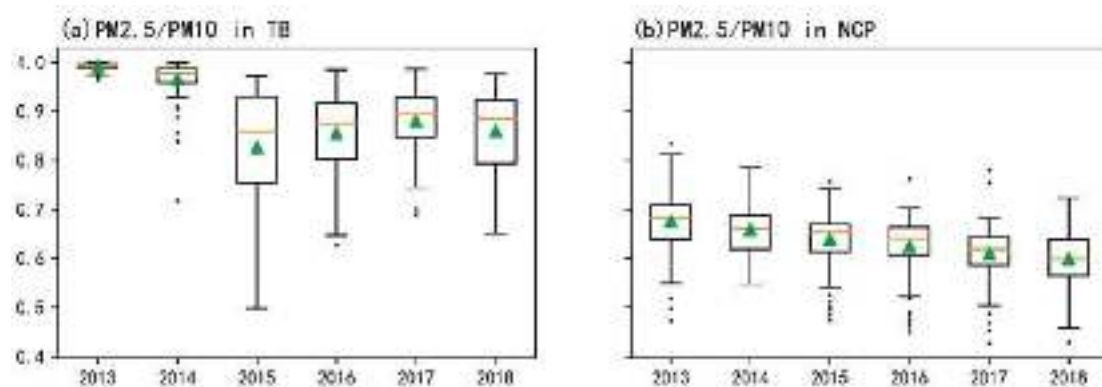


Figure 6. Interannual variation in the ratio of the PM_{2.5} to PM₁₀ concentration in the Tarim Basin (a) and the North China Plain (b) in summer from 2013 to 2018 (orange lines represent the median, green triangles represent the mean value and black dots represent the discrete point).

The average concentrations of the three pollutants of the $PM_{2.5}$, PM_{10} and O_3 in the North China Plain in the summer during 2013–2018 are 45.09, 70.28 and 131.27 $\mu g \cdot m^{-3}$ (Table 1), respectively. The days with concentrations exceeding the standard reach 401, 461 and 488, respectively, and the days with the PM_{10} exceeding the standard are more than those of the $PM_{2.5}$ (Figure 5b). Figure 4c–e show that the PM concentrations in the North China Plain show decreasing trends, while the O_3 concentration shows an increasing trend. The average ratio of the $PM_{2.5}$ to PM_{10} in this area is approximately 0.65, and the ratio shows a decreasing trend (Figures 6 and 7).

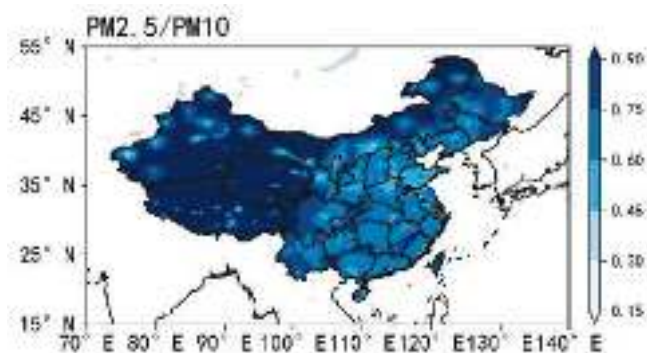


Figure 7. Spatial distribution of the ratio of the $PM_{2.5}$ to PM_{10} in summer from 2013 to 2018.

3.2. Relationship between the East Asian Upper-Level Jet and Surface Pollutants in Summer

3.2.1. Preliminary Analysis of the Relationship between the East Asian Upper-Level Jet and Surface Pollutants in Summer

According to the analysis results in Section 3.1.1, it can be concluded that there is an intraseasonal northward shift of the jet stream position in summer during 2013–2018. Therefore, the impact of the East Asian upper-level jet on pollutants in each month in summer is discussed separately. The temporal average of the monthly 200 hPa zonal wind and the pollutant concentration, including the PM_{10} , O_3 , and $PM_{2.5}$, in the summer during 2013–2018 are calculated. Figure 8 shows that the average position of the upper-level jet stream in June is around 40° N, and the average central wind speed is higher than 39 $m \cdot s^{-1}$. The average positions of the upper-level jet stream in July and August are around 45° N. The average wind speeds of the jet stream centers in July and August are approximately 31 and 35 $m \cdot s^{-1}$, respectively. The above results show that the upper-level jet stream has an obvious northward jump in summer, which is consistent with the EOF analysis result. The intensity of the upper-level jet stream in summer is the strongest in June and the weakest in July.

In addition, the pollutants in the North China Plain in June locate near the left side of the entrance region of the upper-level jet stream (Figure 8a,d). Combined with the atmospheric meridional vertical circulation in June (Figure 9a), it can be seen that the North China Plain, locating near 32–40° N, is dominated by the descending motion in the left side of the entrance region of the upper-level jet stream between 850 and 300 hPa, while there is a weak ascending motion below 850 hPa, the average vertical velocity in North China Plain in June from Table 2 can also prove this. It indicates that the atmospheric stratification over the North China Plain is relatively stable in June, which is conducive to the pollutant accumulation. The 1000 hPa surface wind during the same period (Figure 8g) shows that the pollutants from southern China are transported to the North China Plain due to the large-scale southerly wind. The low wind speed in the North China Plain is not conducive to the pollutant diffusion in the region. Therefore, the pollutant concentrations are high in the North China Plain in June including PM_{10} , O_3 and $PM_{2.5}$.

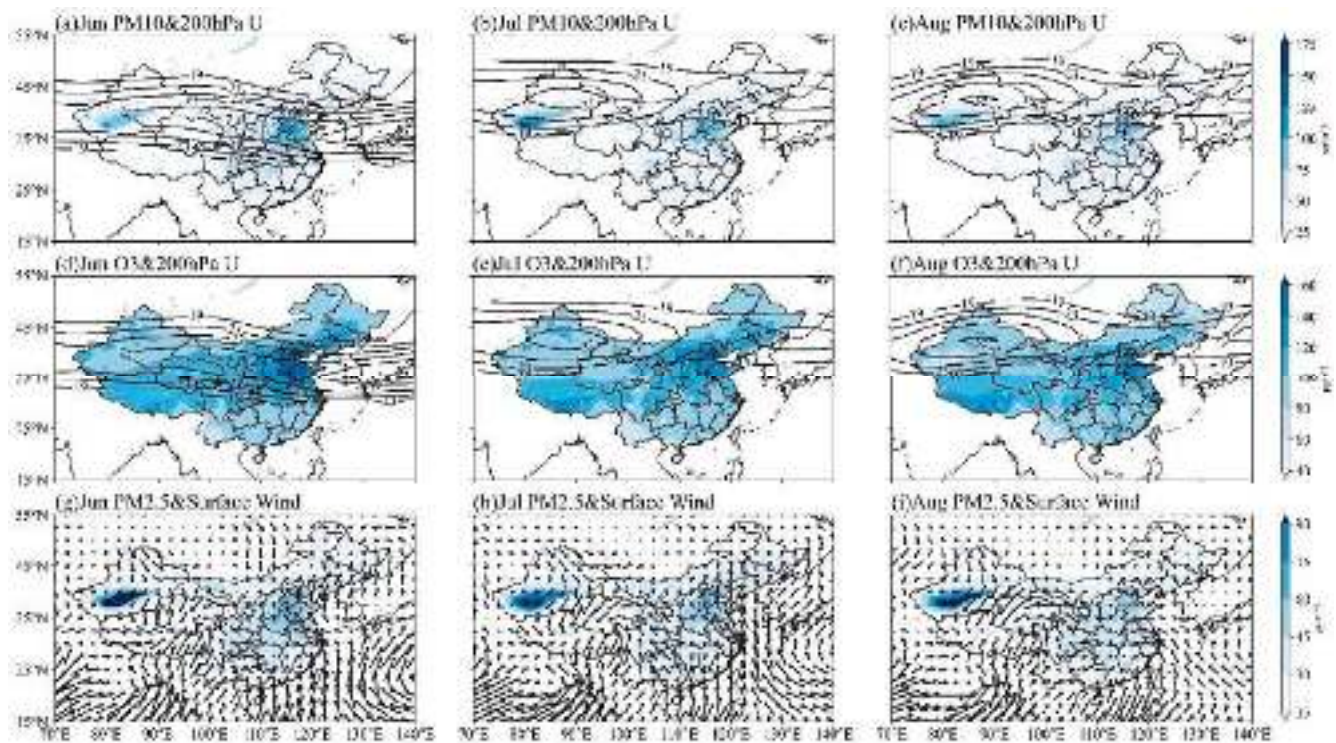


Figure 8. Variations of the 200 hPa westerly jet stream (unit: $\text{m}\cdot\text{s}^{-1}$, a–f, contours), distributions of the monthly mean surface air pollutants (unit: $\mu\text{g}\cdot\text{m}^{-3}$, including PM_{10} , O_3 and $\text{PM}_{2.5}$) and 1000 hPa wind fields (unit: $\text{m}\cdot\text{s}^{-1}$, g–i, vectors) in June, July and August from 2013 to 2018. The PM_{10} , O_3 , $\text{PM}_{2.5}$ are plotted in shaded in a–c, d–f, g–i, respectively.

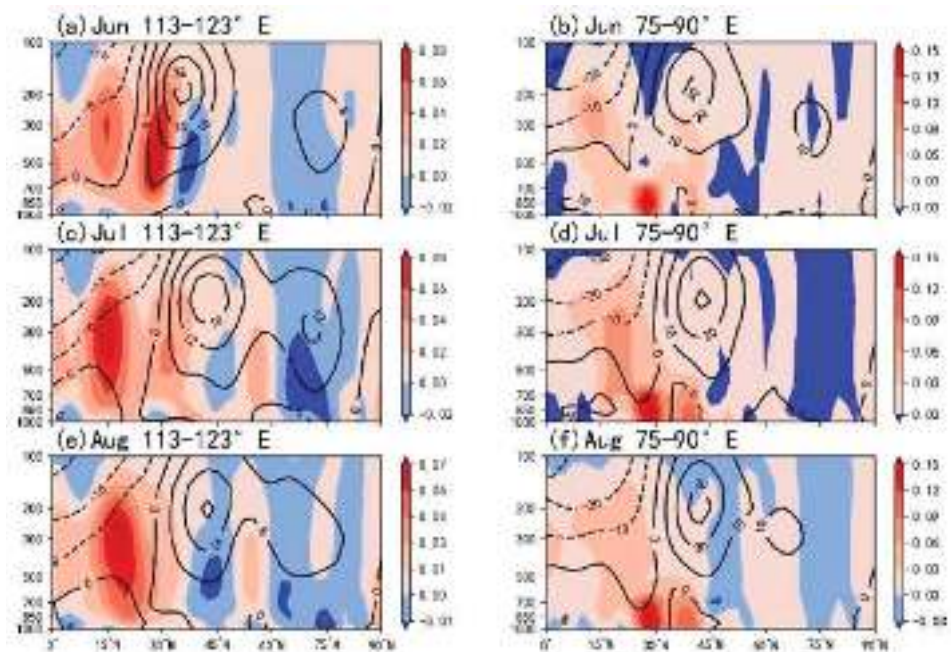


Figure 9. The height-latitude profile of the meridional-averaged zonal wind (unit: $\text{m}\cdot\text{s}^{-1}$, contours) and vertical movement (unit: $\text{pa}\cdot\text{s}^{-1}$, shades: red indicates ascending motion, blue indicates descending motion) in different areas in July and August. (a,c,e) represent the situation in the North China Plain, and (b,d,f) represent the situation in the Tarim Basin.

Table 2. The average value of the meteorological elements and pollutant concentrations in the North China Plain (NCP) and Tarim Basin (TB) in June, July and August.

		Jun	Jul	Aug
NCP	surface wind speed ($\text{m}\cdot\text{s}^{-1}$)	2.48	2.61	1.36
	200 hPa zonal wind speed ($\text{m}\cdot\text{s}^{-1}$)	31.77	17.39	18.60
	vertical velocity($\text{pa}\cdot\text{s}^{-1}$) *	0.009	−0.022	−0.003
	PM _{2.5} ($\mu\text{g}\cdot\text{m}^{-3}$)	48.09	44.09	39.60
	PM ₁₀ ($\mu\text{g}\cdot\text{m}^{-3}$)	75.37	67.21	62.15
	O ₃ ($\mu\text{g}\cdot\text{m}^{-3}$)	141.70	126.13	123.50
TB	surface wind speed ($\text{m}\cdot\text{s}^{-1}$)	1.41	1.76	1.99
	200 hPa zonal wind speed ($\text{m}\cdot\text{s}^{-1}$)	30.29	26.71	29.03
	vertical velocity($\text{pa}\cdot\text{s}^{-1}$) *	−0.037	−0.056	−0.061
	PM _{2.5} ($\mu\text{g}\cdot\text{m}^{-3}$)	35.56	44.51	43.43
	PM ₁₀ ($\mu\text{g}\cdot\text{m}^{-3}$)	39.32	48.21	47.41

* The vertical velocity is the average value of the vertical velocity below the 200 hPa level.

Combined with Table 2, in July and August, the North China Plain is located near the right side of the exit region of the upper-level jet stream over the Sea of Japan. It is dominated by the ascending motion caused by the upper-level jet stream, which makes pollutants, including PM₁₀, O₃ and PM_{2.5}, diffuse in the vertical direction to a certain extent in the North China Plain, and the surface concentration is lower than that in June. However, the surface wind speed in the North China Plain is relatively low, and the horizontal diffusion of pollutants is relatively hard. Therefore, the pollution in the North China Plain in July and August is still serious.

The Tarim Basin has a special topography. Except for the Hexi Corridor to the east, the north, west and south sides are all surrounded by high mountains with an average altitude of more than 5000 m [26,27]. Throughout the summer, the Tarim Basin locates at the right of the entrance region of the upper-level jet stream dominated by the ascending motion caused by the upper-level jet stream (Table 2). However, Figure 9b–e indicate that the ascending motion above 700 hPa is very weak, and the air vertical movement is not enough to carry the surface PM₁₀ and PM_{2.5} away from the basin. Meanwhile, the Tarim Basin is dominated by the easterly wind, and the surface wind speed is relatively low in summer. The horizontal diffusion of pollutants is hindered by the surrounding mountains (Figure 8g–i). Therefore, the pollutant concentrations including PM_{2.5} and PM₁₀ are high in summer in the Tarim Basin.

The above analyses show that there is a connection between the summer jet stream and surface pollutants.

3.2.2. Relationship between the Surface Pollutants and the Position and Intensity of the East Asian Upper-Level Jet in Summer

The SVD method is used to further analyze the relationship between the East Asian upper-level jet and surface pollutants in summer. The sum of the cumulative covariance contribution of the first two modes of the SVD (hereafter referred to as SVD1 and SVD2, respectively) of the surface O₃ concentration and the 200 hPa zonal wind in summer is 88.46%. The sum of the square of the explained total covariance of the SVD1 is 81.35%, and the correlation coefficient of the time series of the left and right fields is 0.96, showing the synchronized variation in the two fields. In Figure 10e,f, when the time coefficients of the left and right fields are both positive, there are positive anomalies of the O₃ concentration in the North China Plain in the left field. The dividing line in the right field is about 40°N, which is the average position of the East Asian upper-level jet axis in summer, and the north and south regions of the 200 hPa zonal wind show positive anomalies and negative anomalies, respectively. That is, the position of the upper-level jet stream is more southward when the surface O₃ concentration is higher in the North China Plain, and vice versa. Moreover, the spatial distribution of the right field heterogeneous correlation of this mode is similar to that of the EOF1 of the 200 hPa zonal wind. Therefore, the SVD1 of the

surface O_3 concentration and 200 hPa zonal wind represents the relationship between the surface O_3 and the position of the East Asian upper-level jet.

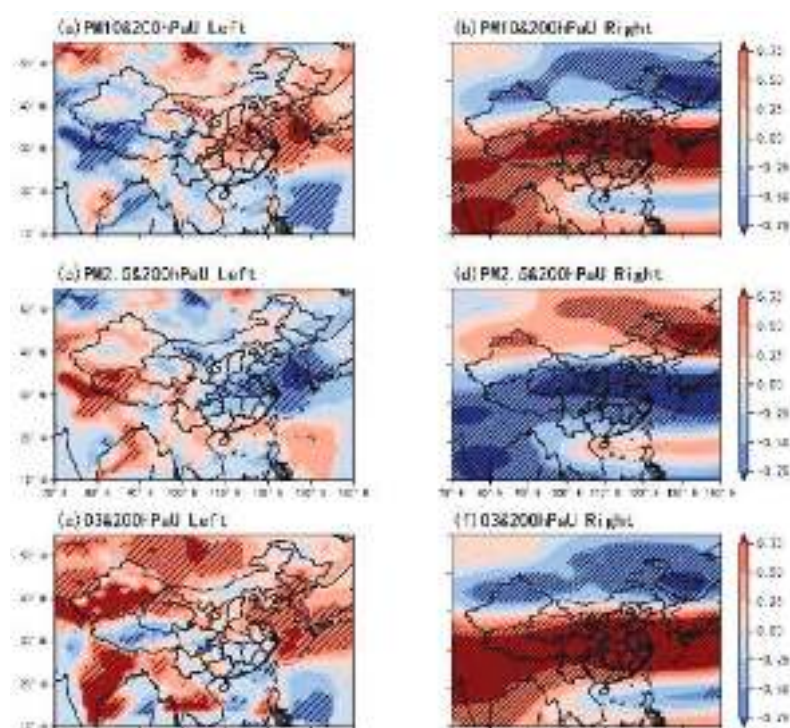


Figure 10. The (a,c,e) left and (b,d,f) right heterogeneous correlation diagrams of the SVD1 of the surface pollutants including the PM_{10} , O_3 and $PM_{2.5}$ (the left field) and the 200 hPa zonal wind field (the right field) in summer from 2013 to 2018. The slashes indicate that the results passed the 95% Monte Carlo correlation test.

For the SVD2 of the O_3 concentration and 200 hPa zonal wind in summer, the sum of the square of the explained total covariance is 7.31%, and the correlation coefficient of the time series of the left and right fields is 0.94, showing the synchronized variation relationship. The spatial distribution of the left field heterogeneous correlation is similar to that of the EOF2 of the 200 hPa zonal wind. Therefore, the left and right fields heterogeneous correlation of the SVD2 represents the relationship between the surface O_3 and the intensity of the East Asian upper-level jet. However, their relationship is not significant in the North China Plain (Figure 11e,f).

Therefore, there may be a certain relationship between the surface O_3 concentration in the North China Plain in summer and the position of the East Asian upper-level jet, but the relationship with the intensity of the upper-level jet stream is not significant.

Since the SVD results of the 200 hPa zonal wind and the surface PM_{10} and $PM_{2.5}$ concentrations are similar in summer, the relationship of the 200 hPa zonal wind with the PM_{10} and that with the $PM_{2.5}$ are discussed together. For the SVD1 and SVD2 of the 200 hPa zonal wind and the PM_{10} and $PM_{2.5}$, the sums of the cumulative covariance contribution are 86.39% and 85.06%, respectively. The sum of squares of the explained total covariance of the SVD1 are 71.13% and 71.76%, respectively. The correlation coefficients of the time series of the left and right fields are 0.96 and 0.84, respectively, showing the synchronized variation relationship. The slashes in Figure 10a–d show that, when the anomalies of the PM_{10} and $PM_{2.5}$ concentrations in the North China Plain in the left field are negative, the dividing line of the 200 hPa zonal wind in the right field is about 40°N, which is the average position of the East Asian upper-level jet axis in summer, and the north and south regions show negative anomalies and positive anomalies, respectively. That is, the position of the East Asian upper-level jet is more northward when the concentrations of the PM_{10} and

PM_{2.5} are low in the North China Plain, and vice versa. Moreover, the spatial distribution of the left-field heterogeneous correlation of this mode is similar to that of the EOF1 of the 200 hPa zonal wind. Therefore, the surface PM₁₀ and PM_{2.5} concentrations are associated with the position of the East Asian upper-level jet.

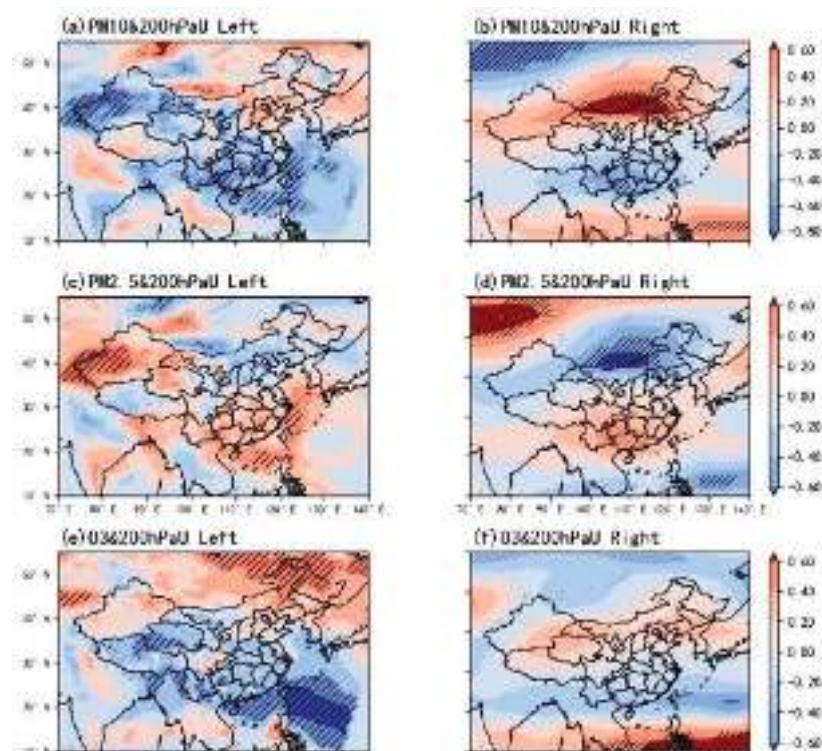


Figure 11. The (a,c,e) left and (b,d,f) right heterogeneous correlation diagrams of the SVD2 of the surface pollutants including the PM₁₀, O₃ and PM_{2.5} (the left field) and the 200 hPa zonal wind field (the right field) in summer from 2013 to 2018. The slashes indicate that the results passed the 95% Monte Carlo correlation test.

For the SVD2 of the 200 hPa zonal wind and the PM₁₀ and PM_{2.5} surface concentration in summer, the sum of squares of the explained total covariance are 15.26% and 13.30%, respectively. The correlation coefficients of the time series of the left and right fields are 0.91 and 0.83, respectively, presenting the synchronized variation relationship. The slashes in Figure 11a–d show that when the anomalies of the PM₁₀ and PM_{2.5} concentrations in the Tarim Basin in China are negative, there is a negative anomalous region of the 200 hPa zonal wind centered around 40° N, which corresponds to the average position of the East Asian upper-level jet in summer. That is, the intensity of the East Asian jet stream is low (high) when the PM₁₀ and PM_{2.5} concentrations are high (low) in the Tarim Basin. The spatial distribution of the right field heterogeneous correlation of this mode is similar to that of the EOF2 of the 200 hPa zonal wind. Therefore, the left and right fields heterogeneous correlation of the SVD2 represents the relationship between the surface concentrations of the PM₁₀ and PM_{2.5} and the intensity of the East Asian upper-level jet.

By comparing the significance of the heterogeneous correlation diagrams of the first and second modes, we found that the anomalous PM₁₀ and PM_{2.5} concentrations in summer over the North China Plain may have a certain relationship with the position variation in the East Asian upper-level jet, but the relationship with the intensity anomaly of the upper-level jet stream is not significant. The anomalous surface PM₁₀ and PM_{2.5} concentrations in the Tarim Basin may have a certain relationship with the intensity anomaly of the East Asian upper-level jet, but the relationship with the position variation in the upper-level jet stream is not significant.

In summary, there is a certain relationship between the movement of the East Asian upper-level jet in summer and the variations of the three pollutants' concentrations, including PM_{10} , $PM_{2.5}$ and O_3 , in the North China Plain. When the position of the East Asian upper-level jet is more northward, the concentrations of the PM_{10} , $PM_{2.5}$ and O_3 in North China Plain are significantly lower, and vice versa. There is a connection between the intensity variation in the East Asian upper-level jet in summer and the concentration variations of the PM_{10} and $PM_{2.5}$ in the Tarim Basin. When the intensity of the East Asian upper-level jet is relatively high, the concentrations of the PM_{10} and $PM_{2.5}$ in the Tarim basin are both low, and vice versa.

3.3. Preliminary Analyses of the Interaction Mechanism between the Summer Jet Stream and Pollutants

The East Asian upper-level jet has a three-dimensional structure, and a series of secondary circulations are generated around the upper-level jet stream, which are associated with surface pollutants. The idea of using statistical methods to study the interaction between them is to find out the medium existing in the interaction between them. That is, to find out the surface meteorological variable that connects to the upper-level jet stream and then interacts with surface pollutants. Due to the exchange of the energy, matter and momentum between the upper-level jet stream and the surface, the surface meteorological variables, such as the humidity, temperature, zonal wind and meridional wind, are selected in the study. The correlation analysis method is used to explore the relationships between the upper-level jet stream and the surface meteorological variables including the humidity, temperature, surface zonal wind and surface meridional wind as well as the relationships between the surface meteorological variables and the surface pollutants.

3.3.1. Relationship between the Summer Jet Stream and Surface Meteorological Variables

According to the analyses in Section 3.1.1, it can be concluded that the EOF1 of the 200 hPa zonal wind in the summer from 2013 to 2018 represents the position variation in the summer jet stream. The correlation analysis between the time series of the EOF1 and the surface meteorological variables in the corresponding period can be regarded as the correlation analysis between the position of the upper-level jet stream and the surface meteorological variables in summer. Figure 12 shows that, in the North China Plain, the position of the East Asian upper-level jet in summer has significant positive correlations with the surface humidity and temperature and negative correlations with the surface meridional and zonal wind. In the Tarim Basin, the position variation in the East Asian upper-level jet in summer is significantly positively correlated with the humidity and temperature and negatively correlated with the surface zonal wind. However, the position variation in the East Asian upper-level jet is positively correlated with the surface meridional wind in a small region in the western part of the Tarim Basin, and there is a negative correlation between them in the eastern part of the Tarim Basin.

Combined with the spatio-temporal distribution of the first mode of the 200 hPa zonal wind, it can be said that when the position of the East Asian upper-level jet is more northward, the surface humidity and temperature in North China Plain are higher, and the surface meridional wind and zonal wind are weaker. The surface humidity and temperature in the Tarim Basin are higher, and the surface zonal wind is weaker. The surface meridional wind in the west part of the Tarim Basin is stronger, and weaker in the east part, and vice versa.

The EOF2 of the 200 hPa zonal wind in summer from 2013 to 2018 represents the intensity variation in the summer jet stream. The correlation analyses between the time series of the EOF2 and the surface meteorological variables in the corresponding period represent the relationship between the intensity of summer upper-level jet stream and the surface meteorological variables. In Figure 13, the intensity of the East Asian jet stream is proportional to the surface temperature in the North China Plain, while it is insignificantly related to the surface humidity, meridional wind and zonal wind. In the Tarim Basin, the intensity of the East Asian upper-level jet has a significantly negative correlation with the

surface humidity in the northern region, a significantly positive correlation with the surface temperature in the whole area and a significantly negative correlation with the surface zonal wind in the eastern region, but its relationship with the surface meridional wind is insignificant.

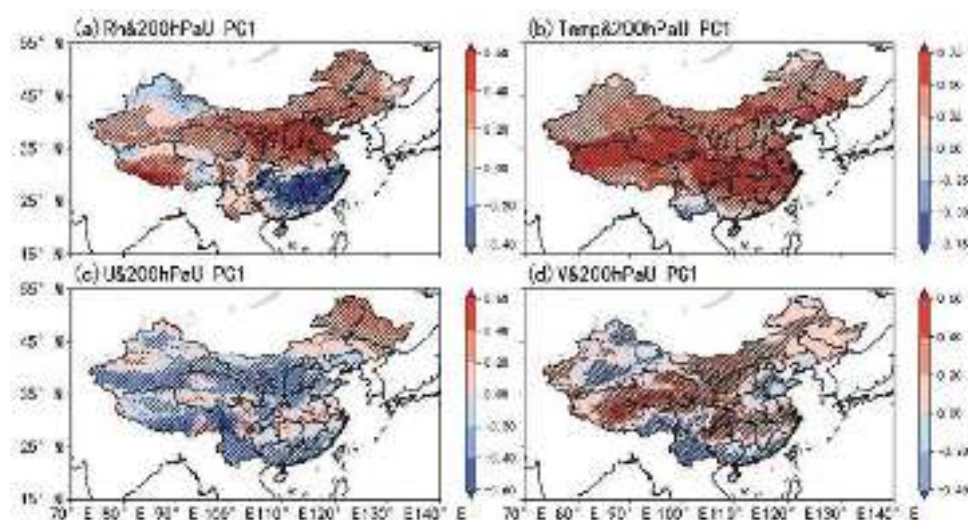


Figure 12. The correlation coefficients between the time series of the EOF1 of the 200 hPa zonal wind and surface meteorological variables of the (a) humidity, (b) temperature, (c) surface zonal wind and (d) surface meridional wind in summer during 2013–2018. The slashes indicate that the results passed the 95% Monte Carlo correlation test.

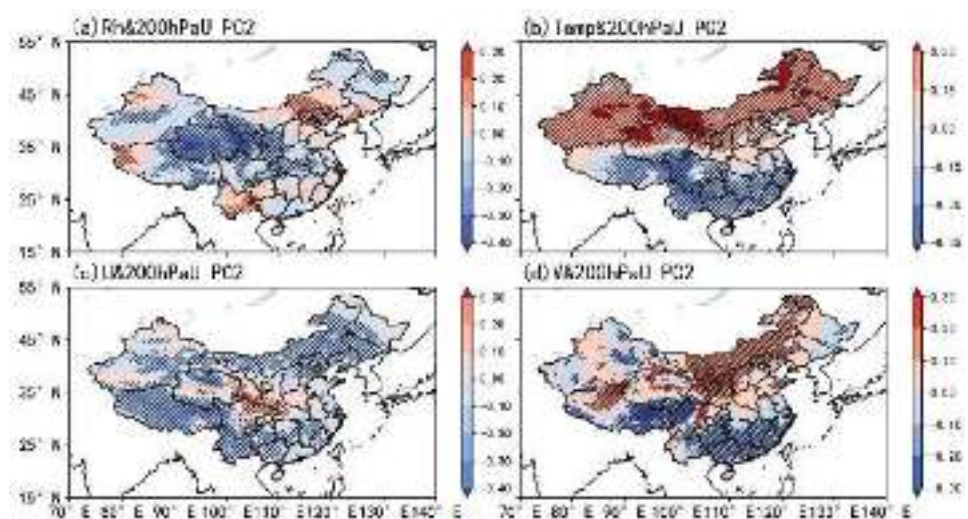


Figure 13. The correlation coefficients between the time series of the EOF2 of the 200 hPa zonal wind and surface meteorological variables of the (a) humidity, (b) temperature, (c) surface zonal wind and (d) surface meridional wind in summer during 2013–2018. The slashes indicate that the results passed the 95% Monte Carlo correlation test.

According to the spatio-temporal distribution of the second mode of the 200 hPa zonal wind, when the intensity of the East Asian upper-level jet is weaker, the surface temperature in the North China Plain is higher, the surface humidity in the northern Tarim Basin is lower, the surface temperature in the region is higher and the surface zonal wind in the eastern part of the basin is weaker, and vice versa.

3.3.2. Relationship between Pollutants and Surface Meteorological Variables in Summer

The correlation coefficients of the surface pollutants including PM_{10} , O_3 and $PM_{2.5}$ with the daily average data of surface meteorological variables in summer from 2013 to 2018 are shown in Figure 14. The PM_{10} , O_3 , and $PM_{2.5}$ in the North China Plain are negatively correlated with the surface humidity and are significantly positively correlated with the surface temperature, zonal wind and meridional wind. However, the significant regions of the correlations between different pollutants and meteorological variables are different. The $PM_{2.5}$ has a significantly negative correlation with the humidity only in the southern part of the North China Plain. The PMs maintain significant positive correlations with the surface temperature only in the northern and southeastern parts of the North China Plain. In addition, these three pollutants are significantly negatively correlated with the surface zonal wind in different areas in the east parts of the North China Plain. That is, when the pollutant concentrations in the North China Plain are higher (lower), the surface humidity in the certain region is lower (higher) correspondingly, the temperature is higher (lower), and the zonal wind and the meridional wind are stronger (weaker).

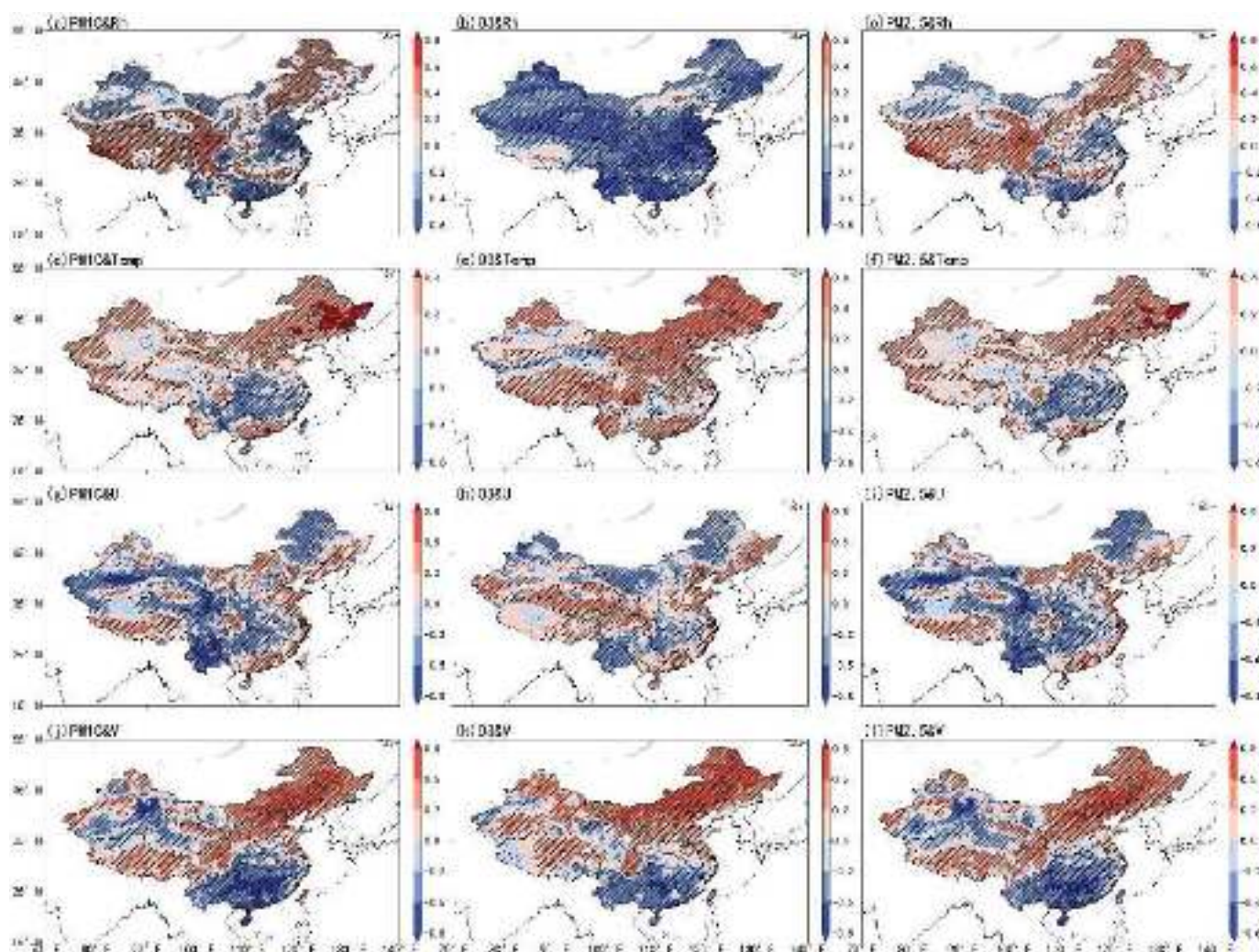


Figure 14. Correlation coefficients between surface pollutants and corresponding surface meteorological variables in summer from 2013 to 2018. (a) PM_{10} and humidity, (d) PM_{10} and temperature, (g) PM_{10} and zonal wind and (j) PM_{10} and meridional wind. (b) O_3 and humidity, (e) O_3 and temperature, (h) O_3 and zonal wind and (k) O_3 and meridional wind. (c) $PM_{2.5}$ and humidity, (f) $PM_{2.5}$ and temperature, (i) $PM_{2.5}$ and zonal wind and (l) $PM_{2.5}$ and meridional wind. The slashes indicate that the results passed the 95% Monte Carlo correlation test.

Both the PM_{10} and $PM_{2.5}$ in the Tarim Basin have good heterocorrelations with the surface humidity and zonal wind, and the PMs are significantly positively correlated with the surface temperature only in the west part of the Tarim Basin and have significant negative correlations with the surface meridional wind in the south part of the Tarim Basin. That is, when the concentrations of the PM_{10} and $PM_{2.5}$ in the Tarim Basin are higher (lower), the surface humidity in the region is lower (higher) and the zonal wind is weaker (stronger). The surface temperature in the west part of the region increases (decreases) and the surface meridional wind in the south part of the region weakens (strengthens).

The summer months of 2013–2018 could be divided into the southerly jet month and the northerly jet month, as well as the stronger and weaker jet months according to the time series of the first and second modes of the 200 hPa zonal wind in summer of 2013–2018. In the light of the four classification results, the pollutant concentrations in different jet months in both the North China Plain and Tarim Basin are calculated as shown in Table 3. It can be seen from Table 3 that the concentrations of $PM_{2.5}$, PM_{10} and O_3 in the North China Plain can reach 48.09, 75.37, and 141.70 $\mu g \cdot m^{-3}$, respectively, when the East Asian jet shifts southward. These loadings are much higher than their seasonal means in summer of 2013–2018. The average concentration of $PM_{2.5}$, PM_{10} and O_3 in the North China Plain can reach 41.54, 64.5 and 125.01 $\mu g \cdot m^{-3}$, respectively, when the East Asian jet shifts northward, which is lower than their seasonal means in summer of 2013–2018.

Table 3. The average concentration of the air pollutants in North China Plain (NCP) and the Tarim Basin (TB) in different East Asian jet periods in summer from 2013–2018. (units: $\mu g \cdot m^{-3}$).

		$PM_{2.5}$	PM_{10}	O_3
NCP	Southward	48.09	75.37	141.70
	Northward	41.54	64.5	125.01
	Average	43.92	68.25	130.44
TB	strong	36.30	38.88	-
	weak	53.24	59.04	-
	Average	41.17	44.98	-

The concentrations of $PM_{2.5}$ PM_{10} in the Tarim Basin can reach 36.30 and 38.88 $\mu g \cdot m^{-3}$, respectively, when the intensity of the East Asian jet is relatively stronger. These loadings are lower than their seasonal means in summer of 2013–2018. The concentrations of $PM_{2.5}$ and PM_{10} in the Tarim Basin can reach 53.24 and 59.04 $\mu g \cdot m^{-3}$, respectively, when the intensity of the East Asian jet is weaker, which are higher than their seasonal means in summer of 2013–2018.

Combined with the analyses in Section 3.2.2, it can be concluded that the position of the upper-level jet stream in summer may be related to the PM_{10} , O_3 and $PM_{2.5}$ due to the effects of the surface humidity and the meridional and zonal wind in the corresponding region of North China Plain. When the position of the upper-level jet stream in summer is more northward, the surface humidity is higher, and the meridional and zonal wind is stronger. At this time, the concentrations of three pollutants in North China are all lower, and vice versa. The intensity of the East Asian upper-level jet in summer may have correlations with the PM_{10} and $PM_{2.5}$ due to the interaction with the surface humidity in the northern part of the Tarim Basin, the surface temperature in the western part, and the surface zonal wind in the eastern part. When the intensity of the East Asian upper-level jet is weaker, the humidity in the northern part of the region is lower, the temperature in the western part is higher, and the zonal wind in the eastern part is weaker. At this time, the concentrations of surface PMs are higher, and vice versa.

4. Conclusions and Discussion

Based on the NCEP/NCAR daily wind and vertical velocity data, as well as the surface pollutants and meteorological variables data derived from the Science Data Bank, statistical analysis methods were used to study the relationships between the East Asian

upper-level jet and the high concentration areas of near-surface air pollutants in summer in this study, and the interaction mechanisms between them are preliminarily discussed. The conclusions are as follows.

- (1) In summer, the average position of the East Asian upper-level jet axis is around 40° N. The EOF1 of the 200 hPa zonal wind in East Asia represents the position variation in the East Asian upper-level jet in summer. The corresponding time coefficient diagrams show that the position of the East Asian upper-level jet has a northward jump in summer. The EOF2 reflects the intensity variation in the East Asian upper-level jet in summer.
- (2) In the summer, pollutants concentrate in the North China Plain and Tarim Basin. The PM_{2.5}, PM₁₀ and O₃ are the main pollutants in the North China Plain with the average concentrations of 45.09, 70.28 and 131.27 $\mu\text{g}\cdot\text{m}^{-3}$, respectively. The days with concentrations exceeding the standard are 401, 461 and 488, respectively. The O₃ concentration has an increasing trend during this period, while the PM concentration has a decreasing trend. The average ratio of the PM_{2.5} to PM₁₀ is approximately 0.65, and the ratio shows a descending trend. The main pollutants in the Tarim Basin are the PM_{2.5} and PM₁₀ with average concentrations of 45.19 and 49.08 $\mu\text{g}\cdot\text{m}^{-3}$, respectively. The days with concentrations exceeding the standard are 265 and 193, respectively. The interannual variation in PM concentration shows an increasing trend at first and then a decreasing trend. The average ratio of PM_{2.5} to PM₁₀ in this region is about 0.9. The ratio reaches the highest in 2013 and 2014 and then decreases to and maintains at about 0.85. In June, the North China Plain locates on the left side of the upper-level jet stream entrance region, which is dominated by descending motions. The surface wind speed is relatively low, which is not conducive to the pollutant diffusion, resulting in high concentrations of pollutants, including the PM₁₀, O₃ and PM_{2.5}. In July and August, the North China Plain locates near the right side of the upper-level jet stream exit region, and there are mainly ascending motions in the vertical direction, which lead to the lower concentrations of pollutants including the PM₁₀, O₃ and PM_{2.5} in July and August than those in June. However, the surface wind speed is low, and the pollutants are not effectively diffused, so the concentrations of the PM₁₀, O₃ and PM_{2.5} are still higher. Throughout the summer, the Tarim Basin locates on the right side of the upper-level jet stream entrance region. There are mainly ascending motions in the vertical direction caused by the upper-level jet stream, and there is mainly easterly wind in the horizontal direction. However, due to the special terrain of the Tarim Basin, the diffusion process of the PM₁₀ and PM_{2.5} in horizontal and vertical directions is blocked, resulting in higher concentrations of the PM₁₀ and PM_{2.5} in this region.
- (3) The analysis results on the relationship between upper-level jet stream and air pollutants in East Asia indicate that the position of the upper-level jet stream in summer may be related to the PM₁₀, O₃ and PM_{2.5} due to the effects of the surface humidity and the meridional and zonal wind in the corresponding region of the North China Plain. When the position of the upper-level jet stream is more northward in summer, the surface humidity is higher and the meridional and zonal wind is weaker. At this time, the concentrations of the three pollutants in North China are all lower, and vice versa. Meanwhile, the intensity of the East Asian upper-level jet may have correlations with the PM₁₀ and PM_{2.5} due to the interaction with the surface humidity in the northern part of the Tarim Basin, the surface temperature in the western part, and the zonal wind in the eastern part. When the intensity of the East Asian upper-level jet is weaker, the humidity in the northern part of the region is lower, the temperature in the western part is lower, the surface zonal wind in the eastern part is weaker and the PM concentration in the Tarim Basin is higher, and vice versa.

Chen et al. [17] used CESM and indicated that the regional anthropogenic aerosol caused the 200 hPa jet stream to weaken and shift southward over East Asia in summer, which is in agreement with our results, despite the different kind of aerosol. Wang et al. [28]

found that the sand-dust weather often occurred in Taklimakan Desert in spring and summer. The dust particle also had an influence on the summer atmospheric boundary layer structure in Taklimakan Desert. This result can imply that the upper level jet stream has a connection with surface pollutants in Tarim Basin to some extent. Results here also show some connections between the jet and surface air pollutants in summer. Kerr et al. [21] used the global model to study the influence of the upper-level jet stream position on the surface zonal wind and meridional wind in the mid-latitude region of the northern hemisphere in summer. Their results showed that the influence of the upper-level jet stream position on the surface zonal wind mainly occurred over the sea, while its impact on the surface meridional wind occurred over both the sea and the land. Their finding is slightly different from the conclusion of this paper. The possible reason might be that the range of the study area is different. Further investigations are needed based on the regional numerical models to identify the difference.

In this study, the interactions between meteorological variables and pollutants in the vicinity of pollutant regions are not considered when analyzing the relationships between the concentrations of near-surface air pollutants and meteorological variables. In addition, the research conclusions are all obtained based on statistical methods. The rules revealed in the conclusions and the complex interaction mechanisms between the East Asian upper-level jet and surface pollutants require further verification and exploration based on the numerical models.

Author Contributions: Conceptualization, W.W., B.Z. and Y.S.; software, W.W., H.L. and Y.G.; validation, W.W., B.Z. and T.W.; formal analysis, W.W. and H.C.; writing—original draft preparation, W.W.; writing—review and editing, B.Z.; supervision, B.Z. All authors have read and agreed to the published version of the manuscript.

Funding: This research was funded by the National Key R&D Program of China, the National Natural Science Foundation of China and the Fundamental Research Funds for the Central Universities (2019YFA0606803, 42075099, 0207-14380169, 41675143, 42077192, 41621005).

Institutional Review Board Statement: Not applicable.

Informed Consent statement: Not applicable.

Data Availability Statement: The high-resolution air pollution and the surface meteorological variables reanalysis dataset in China during 2013–2018 and are available here: [<https://www.scidb.cn/en/detail?dataSetId=696756084735475712&dataSetType=personal>] (accessed on 2 June 2021). The NCEP/NCAR reanalysis data can be found here: [<https://psl.noaa.gov/data/gridded/data.ncep.reanalysis.html>] (accessed on 2 June 2021).

Acknowledgments: We thank Nanjing Hurricane Translation for reviewing the English language quality of this paper. This work was supported by the National Key R&D Program of China, the National Natural Science Foundation of China and the Fundamental Research Funds for the Central Universities (2019YFA0606803, 42075099, 0207-14380169, 41675143, 42077192, 41621005).

Conflicts of Interest: The authors declare that they have no competing interests.


References

1. IPCC. *Climate Change 2013: The Physical Science Basis: Working Group I Contribution to the Fifth Assessment Report of the Intergovernmental Panel on Climate Change*; Cambridge University Press: Cambridge, UK, 2014; ISBN 978-1-107-05799-9.
2. Ding, Y.H.; Li, Q.P.; Liu, Y.J.; Zhang, L.; Song, Y.F.; Zhang, J. Atmospheric Aerosols, Air Pollution and Climate Change. Available online: <http://qxqk.nmc.cn/html/2009/3/20090301.html> (accessed on 30 March 2021).
3. Twomey, S. Pollution and the Planetary Albedo. *Atmos. Environ.* **1974**, *8*, 1251–1256. [CrossRef]
4. Albrecht, B.A. Aerosols, Cloud Microphysics, and Fractional Cloudiness. *Science* **1989**, *245*, 1227–1230. [CrossRef]
5. Pincus, R.; Baker, M.B. Effect of Precipitation on the Albedo Susceptibility of Clouds in the Marine Boundary Layer. *Nature* **1994**, *372*, 250–252. [CrossRef]
6. Haywood, J.; Boucher, O. Estimates of the Direct and Indirect Radiative Forcing Due to Tropospheric Aerosols: A Review. *Rev. Geophys.* **2000**, *38*. [CrossRef]
7. Hansen, J.; Sato, M.; Ruedy, R. Radiative Forcing and Climate Response. *J. Geophys. Res.* **1997**, *102*, 6831–6864. [CrossRef]

8. Zhang, X.Y.; Arimoto, R.; An, Z.S. Dust Emission from Chinese Desert Sources Linked to Variations in Atmospheric Circulation. *J. Geophys. Res.* **1997**, *102*, 28041–28047. [CrossRef]
9. Zhu, J.; Liao, H.; Li, J. Increases in Aerosol Concentrations over Eastern China Due to the Decadal-Scale Weakening of the East Asian Summer Monsoon. *Geophys. Res. Lett.* **2012**, *39*, 9809. [CrossRef]
10. Chambers, E. The Jet Stream. *J. Navig.* **1959**, *12*, 266–288. [CrossRef]
11. Jin, R.; Li, Y.; Long, Q.; Liu, S. The 200-HPa Wind Perturbation in the Subtropical Westerly over East Asia Related to Medium-Range Forecast of Summer Rainfall in China. *J. Meteorol. Res.* **2018**, *32*, 491–502. [CrossRef]
12. Alaka, M.A.-R. *The Jet Stream*; U.S. Navy, Fifth Naval District, Publications and Printing Office: Norfolk 11, VA, USA, 1953.
13. Yang, S. Variations of the East Asian Jet Stream and Asian–Pacific–American Winter Climate Anomalies. *J. Clim.* **2002**, *15*, 20. [CrossRef]
14. Zhongda, L.; Riyu, L. Interannual Meridional Displacement of the East Asian Upper-Tropospheric Jet Stream in Summer. *Adv. Atmos. Sci.* **2005**, *22*, 199–211. [CrossRef]
15. Rui, M.; Daoyi, G.; Qiaomin, F. Influences of the East Asian Jet Stream on Winter Climate in China. Available online: <http://html.rhhz.net/yyqxzb/html/20070226.htm> (accessed on 31 March 2021).
16. Song, F.; Zhou, T.; Qian, Y. Responses of East Asian Summer Monsoon to Natural and Anthropogenic Forcings in the 17 Latest CMIP5 Models: Responses of EASM to External Forcings. *Geophys. Res. Lett.* **2014**, *41*, 596–603. [CrossRef]
17. Chen, G.; Wang, W.-C.; Chen, J.-P. Circulation Responses to Regional Aerosol Climate Forcing in Summer over East Asia. *Clim. Dyn.* **2018**, *51*, 3973–3984. [CrossRef]
18. Liu, Z.; Ming, Y.; Wang, L.; Bollasina, M.; Luo, M.; Lau, N.; Yim, S.H. A Model Investigation of Aerosol-Induced Changes in the East Asian Winter Monsoon. *Geophys. Res. Lett.* **2019**, *46*, 10186–10195. [CrossRef]
19. Ordóñez, C.; Barriopedro, D.; García-Herrera, R. Role of the Position of the North Atlantic Jet in the Variability and Odds of Extreme PM10 in Europe. *Atmos. Environ.* **2019**, *210*, 35–46. [CrossRef]
20. Barnes, E.A.; Fiore, A.M. Surface Ozone Variability and the Jet Position: Implications for Projecting Future Air Quality: Ozone Variability, Jet, and Climate Change. *Geophys. Res. Lett.* **2013**, *40*, 2839–2844. [CrossRef]
21. Kerr, G.H.; Waugh, D.W.; Steenrod, S.D.; Strode, S.A.; Strahan, S.E. Surface Ozone-Meteorology Relationships: Spatial Variations and the Role of the Jet Stream. *Atmos. Sci.* **2020**, *125*, e2020JD032735. [CrossRef]
22. Kong, L.; Tang, X.; Zhu, J.; Wang, Z.; Li, J.; Wu, H.; Wu, Q.; Chen, H.; Zhu, L.; Wang, W.; et al. A 6-Year-Long (2013–2018) High-Resolution Air Quality Reanalysis Dataset in China Based on the Assimilation of Surface Observations from CNEMC. *Earth Syst. Sci. Data* **2021**, *13*, 529–570. [CrossRef]
23. Hannachi, A.; Jolliffe, I.; Stephenson, D. Empirical Orthogonal Functions and Related Techniques in Atmospheric Science: A Review. *Int. J. Climatol.* **2007**, *27*. [CrossRef]
24. Bretherton, C.S.; Smith, C.; Wallace, J.M. An Intercomparison of Methods for Finding Coupled Patterns in Climate Data. *J. Clim.* **1992**, *5*, 541–560. [CrossRef]
25. Wilks, D.S. *Statistical Methods in the Atmospheric Sciences*; Academic Press: Cambridge, MA, USA, 2011; ISBN 978-0-12-385022-5.
26. Sun, J.; Zhang, M.; Liu, T. Spatial and Temporal Characteristics of Dust Storms in China and Its Surrounding Regions, 1960–1999: Relations to Source Area and Climate. *J. Geophys. Res.* **2001**, *106*, 10325–10334. [CrossRef]
27. Chen, S.; Huang, J.; Kang, L.; Wang, H.; Ma, X.; He, Y.; Yuan, T.; Yang, B.; Huang, Z. Emission, Transport and Radiative Effects of Mineral Dust from Taklimakan and Gobi Deserts: Comparison of Measurements and Model Results. *Atmos. Chem. Phys.* **2016**, *17*, 2401–2421. [CrossRef]
28. Wang, M.; Wei, W.; He, Q.; Yang, Y.; Fan, L.; Zhang, J. Summer Atmospheric Boundary Layer Structure in the Hinterland of Taklimakan Desert, China. *J. Arid Land* **2016**, *8*, 846–860. [CrossRef]

Article

A Simple New Method for Calculating Precipitation Scavenging Effect on Particulate Matter: Based on Five-Year Data in Eastern China

Bin Zhou ^{1,2,3}, Duanyang Liu ^{1,3,4,5,*}  and Wenlian Yan ^{1,6}

- ¹ Key Laboratory of Transportation Meteorology, China Meteorological Administration, Nanjing 210008, China; zhoubin2009@163.com (B.Z.); yike-112@163.com (W.Y.)
- ² Wuxi Meteorological Observatory of Jiangsu Province, Wuxi 214101, China
- ³ Collaborative Innovation Center of Atmospheric Environment and Equipment Technology, Jiangsu Key Laboratory of Atmospheric Environment Monitoring and Pollution Control (AEMPC), Nanjing University of Information Science & Technology, Nanjing 210044, China
- ⁴ Key Laboratory for Aerosol-Cloud-Precipitation of China Meteorological Administration, Nanjing University of Information Science and Technology, Nanjing 210044, China
- ⁵ Nanjing Joint Institute for Atmospheric Sciences, China Meteorological Administration, Nanjing 210008, China
- ⁶ Jiangsu Meteorological Observatory, Nanjing 210008, China
- * Correspondence: liudanyang@cma.gov.cn; Tel.: +86-181-6810-0412

Citation: Zhou, B.; Liu, D.; Yan, W. A Simple New Method for Calculating Precipitation Scavenging Effect on Particulate Matter: Based on Five-Year Data in Eastern China. *Atmosphere* **2021**, *12*, 759. <https://doi.org/10.3390/atmos12060759>

Academic Editors: Mihalis Lazaridis and Dongshen Chen

Received: 26 April 2021

Accepted: 7 June 2021

Published: 11 June 2021

Publisher's Note: MDPI stays neutral with regard to jurisdictional claims in published maps and institutional affiliations.



Copyright: © 2021 by the authors. Licensee MDPI, Basel, Switzerland. This article is an open access article distributed under the terms and conditions of the Creative Commons Attribution (CC BY) license (<https://creativecommons.org/licenses/by/4.0/>).

Abstract: A “rain-only” method is proposed to find out the precipitation effect on particle aerosol removal from the atmosphere, and this method is not only unique and novel but also very simple and can be easily adapted to predict aerosol particle scavenging over any region across the world irrespective of the topographical, orographical, and climatic features. By using this simple method, the influences of the rain intensity and particle mass concentration on the aerosol scavenging efficiency are discussed. The results show that a higher concentration, a higher rain intensity, and a larger particle size lead to a higher scavenging efficiency and a higher scavenging rate. The greater the rain intensity, the higher the scavenging efficiency. The scavenging efficiency of PM₁₀ by precipitation is better than that of PM_{2.5}. When the rain intensity is 10 mm h^{−1}, the scavenging efficiency of PM_{2.5} reaches 5.1 μg m^{−3} h^{−1}, and the scavenging efficiency of PM₁₀ reaches 15.8 μg m^{−3} h^{−1}. The scavenging rate increases faster when accumulative precipitation is below 15 mm. The scavenging rate has obvious monthly variation, and the scavenging rate of coastal areas is less than that of inland Jiangsu. The growth of the particle mass concentration after precipitation is divided into two stages: the rapid growth stage after precipitation ends, and the slow growth stage about 24 h after precipitation ends.

Keywords: air pollution; China; particulate matter; precipitation scavenging; scavenging efficiency; scavenging rate

1. Introduction

In our previous article, we discussed the adverse meteorological variables (such as precipitation, wind speed and direction, humidity, inversion, and mixing layer height) that affect air pollution and the surface synoptic situation patterns related to air pollution in eastern China, where the threshold values of meteorological elements are summarized [1]. From the previous article, we found that wind speed, RHs, inversion intensity (ITI), height difference in the temperature inversion (ITK), the lower height of temperature inversion (LHTI), and mixed layer height (MLH) in terms of a 25–75% high-probability range were, respectively, within 0.5–3.6 m s^{−1}, 55–92%, 0.7–4.0 °C 100 m^{−1}, 42–576 m, 3–570 m, and 200–1200 m. The probability of RPHPDs without rain was above 92% with the daily and hourly precipitation of all RPHPDs below 2.1 mm and 0.8 mm [1]. In this article,

we will discuss the precipitation scavenging effect conducive to air pollution removal. Scavenging of atmospheric aerosols by precipitation is a major removal mechanism for airborne particles [2]. Atmospheric aerosol wet scavenging directly affects the air quality by controlling the aerosol mass concentrations, and temporal and spatial distributions [3,4]. The scavenging of atmospheric aerosols also has a large impact on the chemical composition of rainwater [5,6]. Thus, the understanding and quantification of aerosol scavenging processes are very important for air quality and its improvements.

The wet process can be described by a wet scavenging coefficient [7–10]. The wet scavenging of atmospheric pollutants includes in-cloud scavenging processes [11–13] and below-cloud scavenging processes [14–27]. Below-cloud atmospheric particles are removed by raindrops via Brownian diffusion, interception, and impaction [28]. Bae et al. [16] noted that the collection efficiency, terminal velocity of raindrops, raindrop size distribution, and particle size distribution are important factors affecting below-cloud scavenging. In the later period of rainstorms, high concentrations of aerosols improved the precipitation efficiency significantly, resulting in more centralized clusters of intense precipitation [29].

Tai et al. [30] reported that precipitation is strongly negatively correlated with all $PM_{2.5}$ components. The collection efficiency diameter is a function of both terminal velocity and collection mechanisms. When considering Brownian diffusion and interception, the most penetrating particle sizes increase as the drop diameter increases, which shows that the most penetrating particle sizes depend on the collection efficiency mechanism, vertical velocity, and collector diameter [28]. Chate et al. [20] found that the predicted rainwater concentration for a relative humidity (RH) of 50% is about two times larger than that for an RH of 95% in the case of hygroscopic particles. Using field observations and modeling, McLachlan and Sellström [31] found that the differences between ground-level and in-cloud temperatures should be considered when calculating the scavenging ratio.

The air pollution in the eastern part of China is quite serious and has become a serious environmental problem [32]; therefore, natural clearance (dry deposition and wet deposition) is very important, and especially precipitation scavenging is most important. Therefore, the understanding and quantification of aerosol scavenging processes are of extreme importance due to their impact on the physical and chemical characteristics of aerosols as well as precipitations [3].

In most parts of China, raindrop and aerosol particle spectra are not widely observed. However, atmospheric aerosol mass concentrations are widely observed. These common observation data of aerosol mass concentrations are helpful for us to analyze the clearance effect of precipitation on aerosols. In addition, scavenging schemes used by various aerosol transport models follow the theoretical estimation of scavenging and have become a high source of uncertainty for such models [33]. Therefore, it has become necessary to study precipitation scavenging in a more simple and quantitative way with a higher number of samples to analyze the dataset with high statistical significance. This would, in turn, reduce the uncertainties associated with the various chemical transport models used to study precipitation scavenging.

Thus, the present study is an attempt (1) to establish a “rain-only” method on particle aerosol removal from the atmosphere which is not only unique and novel but also very simple, (2) to investigate how aerosol scavenging depends on the precipitation intensity, precipitation duration, particle mass concentrations, and precipitation volumes, (3) to determine the threshold values of the precipitation intensity and duration below and above which aerosol scavenging behaves differently, and (4) to establish whether air pollution can be quantitatively predicted if one holds only the information of the precipitation intensity, precipitation duration, particle mass concentrations, and precipitation volumes for a given pollution level. Such a simple methodology can be easily adapted to predict aerosol particle scavenging over any region across the world irrespective of the topographical, orographical, and climatic features.

We examine aerosol scavenging by precipitation in eastern China. The remainder of this paper is organized as follows: The study area, observations, and analysis methods used

are described in Section 2. We analyze precipitation scavenging on aerosols in Section 3. The conclusions are given in Section 4.

2. Study Area and Methodology

2.1. Study Area

Jiangsu Province is located at the Yangtze River in eastern China. The region has a long coastline of 954 km. We also chose 17 environmental monitoring stations close to these 17 weather stations. The distribution of meteorological stations and state-controlled environmental protection stations (SCEPSs) in Jiangsu is shown in Figure 1.

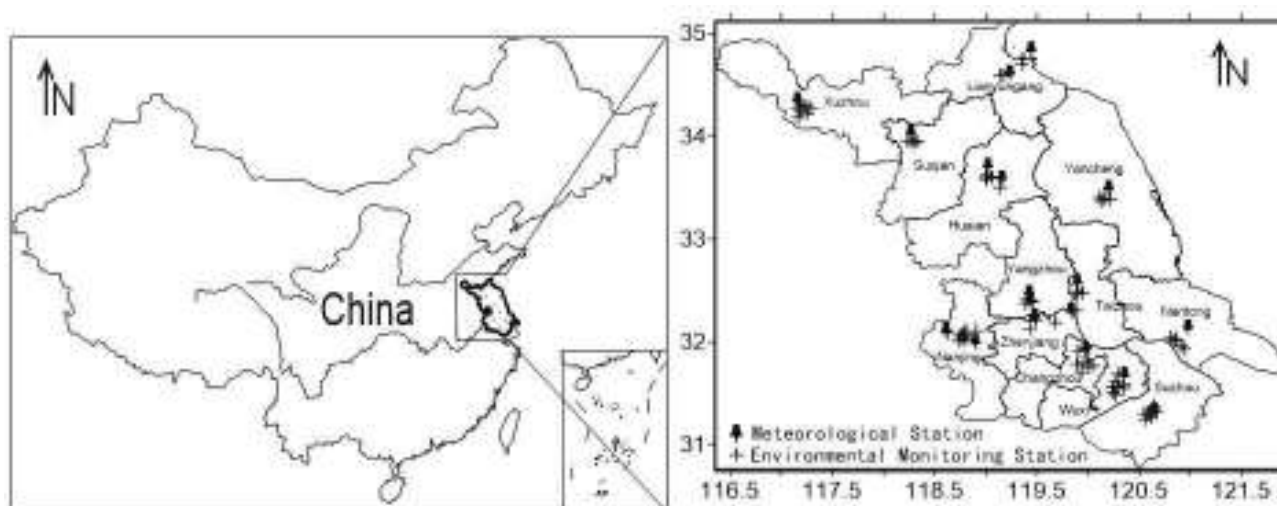


Figure 1. Geographical location of Jiangsu Province, the distribution of environmental monitoring stations, and their nearest weather stations in the study area.

2.2. Observations

The observation period was from 2013 to 2017, including hourly precipitation, wind speed, wind direction, and PM₁₀ and PM_{2.5} particulate concentrations. The PM₁₀ and PM_{2.5} particle monitors used were BAM1020 particle monitors (Met One Instruments INC, Grants Pass, OR, USA) produced by the American company METONE (<https://metone.com/products/bam-1020/>, accessed on 10 June 2021). The BAM-1020, on an hourly basis, automatically measures and records airborne particulate concentration levels (in micrograms per cubic meter) using the industry-proven principle of beta ray attenuation, which can obtain the PM₁₀ and PM_{2.5} mass concentrations in the environment in real time.

2.3. Analysis Methodology

Precipitation event: A precipitation process starts in the first hour when precipitation reaches at least 0.1 mm. If precipitation in an hour was zero after the beginning of the precipitation process, that hour was recorded as an interrupted hour, and the end of the process appeared when three consecutive precipitation interruptions occurred. The hour before the interrupted hour was recorded as the last hour of the precipitation process. As a result, we obtained 27,219 precipitation processes in total.

The effects of concentration and precipitation on the removal rate were analyzed by classifying precipitation processes (0–1 mm, 1–5 mm, 5–10 mm, 10–20 mm, 20–30 mm, 30–50 mm, >50 mm).

Scavenging efficiency (SE): SE is the particle mass concentration change in unit time (t). In an hour with a particle mass concentration CON_{before} before the rain starts and with a particle mass concentration CON_{after} after the rain stops, the SE is expressed as

$$SE = (CON_{after} - CON_{before}) / t$$

Scavenging rate (SR): SR is the percentage change of particle mass concentration changes. For a precipitation process with a particle mass concentration CON_{before} before the rain starts and a particle mass concentration CON_{after} after the rain stops, we defined SR as

$$SR = \frac{CON_{before} - CON_{after}}{CON_{before}} \times 100\% \quad (1)$$

In some cases, the rain did not remove the particles, but the concentration continued to increase. Therefore, we made a rule that if the SR is positive, it is a positive scavenging process, and if the SR is negative, it is a negative scavenging process (which means the precipitation had a very limited scavenge).

3. Results and Discussion

3.1. Relationship between Precipitation, Particle Mass Concentration, and SE

First, we investigated potential size effects on the scavenging efficiencies. The figure shows the relationship between the RI and SE. In the distribution of the precipitation intensity, most precipitation intensities are lower than 5 mm/h. A precipitation intensity above 5 mm/h takes a relatively low proportion in the samples. Therefore, for the segment with rainfall less than 1 mm, a 0.2 mm interval is adopted, while for the segment with rainfall greater than 1 mm, a 2 mm interval is adopted. From Figure 2, we can see that when the rain intensity (RI) is less than 0.4 mm h⁻¹, the SE of PM_{2.5} is almost zero, but the SE of PM₁₀ can reach ~2 µg m⁻³ h⁻¹. The concentration of PM_{2.5} often rises during weak precipitation (RI lower than 0.5 mm h⁻¹); when the RI is 7 mm h⁻¹, the SEs of PM_{2.5} and PM₁₀ are 2.7 and 6.3 µg m⁻³ h⁻¹, respectively. The SE is positively correlated with the RI: the greater the RI, the higher the SE. When the RI is 10 mm h⁻¹, the SE of PM_{2.5} reaches 5.1 µg m⁻³ h⁻¹, and the SE of PM₁₀ reaches 15.8 µg m⁻³ h⁻¹.

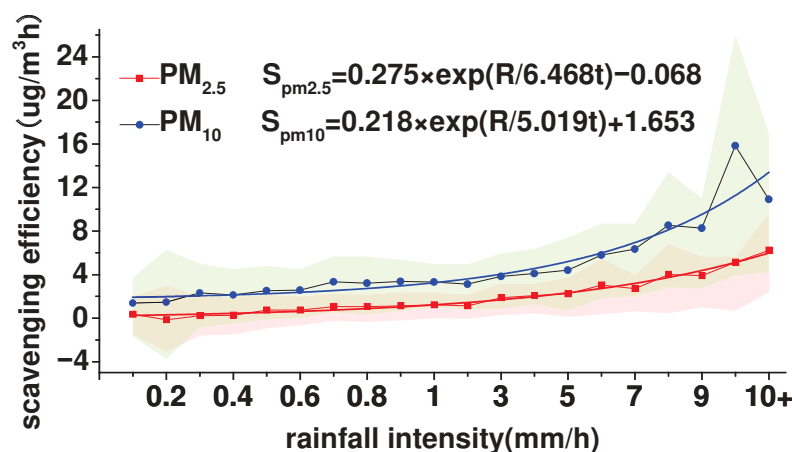


Figure 2. Relationship between precipitation intensity and scavenging efficiency (SE) (the dashed lines are the fitted curves, the green area is the interquartile span of PM₁₀, the red area is the interquartile span of PM_{2.5}, and the gray area is the overlapping region).

By using functions to fit the rainfall intensity and scavenging efficiency, where $SE_{pm2.5}$ and SE_{pm10} are the SEs of precipitation on PM_{2.5} and PM₁₀, respectively, RI is precipitation, and t is the precipitation duration, we relate the RI and SE as follows:

$$SE_{pm2.5} = 0.275 \times \exp\left(\frac{RI}{6.468 \times t}\right) - 0.068 \quad (2)$$

$$SE_{pm10} = 0.218 \times \exp\left(\frac{RI}{5.019 \times t}\right) + 1.653 \quad (3)$$

The changes in $PM_{2.5}$ and PM_{10} caused by precipitation under a stable RI (the precipitation intensity remains unchanged) are as follows:

$$CON_{pm2.5} = \left[0.275 \times \exp\left(\frac{RI}{6.468 \times t}\right) - 0.068 \right] \times t \quad (4)$$

$$CON_{pm10} = \left[0.218 \times \exp\left(\frac{RI}{5.019 \times t}\right) + 1.653 \right] \times t \quad (5)$$

The derivatives of Equations (3) and (4), respectively, are

$$CON'_{pm2.5} = 0.275 \times \exp\left(\frac{RI}{6.468 \times t}\right) \times \left(1 - \frac{RI}{6.468 \times t}\right) - 0.068 \quad (6)$$

$$CON'_{pm10} = 0.218 \times \exp\left(\frac{RI}{5.019 \times t}\right) \times \left(1 - \frac{RI}{5.019 \times t}\right) + 1.653 \quad (7)$$

Therefore, when $CON'_{pm2.5}$ or CON'_{pm10} is equal to zero, changes in $CON_{pm2.5}$ and CON_{pm10} caused by precipitation reach the maximum values; the corresponding RI reaches 5.8 mm/h and 10.1 mm h^{-1} , respectively.

Based on the analysis of the 27,219 precipitation processes from 2013 to 2017 in Jiangsu Province, we find that the effect of precipitation is greater on coarse particles than on smaller particles.

Figure 3 shows the effect of the particle mass concentration on the SE under different RI s when precipitation processes are classified according to the RI . Higher particle mass concentrations under the same RI and heavy rain under the same particle mass concentration all have a higher SE . The precipitation SE on PM_{10} is higher than that of $PM_{2.5}$ for the same RI and the same particle mass concentration. The SE is an increasing function of both the RI and the initial concentration. Precipitation has a limited effect on particulate matter and even has no effective clearance when the particle mass concentration is below the thresholds ($PM_{2.5}$ below $40 \mu\text{g m}^{-3}$ and PM_{10} below $60 \mu\text{g m}^{-3}$). The precipitation SE on the particle is significantly enhanced with the increase in the particle mass concentration. The precipitation SE with an intensity below 0.5 mm h^{-1} can reach more than $15 \mu\text{g m}^{-3} \text{ h}^{-1}$ when the concentration of $PM_{2.5}$ or PM_{10} is above $140 \mu\text{g m}^{-3}$. This also explains why sometimes the particle mass concentration rises after strong precipitation and why sometimes the particle mass concentration decreases after weak precipitation. This is because the SE is not only determined by accumulative precipitation or the RI but also by the two combined. Strong precipitation with a low particle mass concentration may result in a negative clearance effect, and a high particle mass concentration with weak precipitation may lead to a positive SE . This result is similar to the numerical model simulation results, in that the same amount of precipitation may lead to different removal efficiencies of atmospheric aerosols [2]. Jose Nicolás et al. [34] and Yoo et al. [35] also found a higher atmospheric removal efficiency for coarse particles than for fine particles.

3.2. Relationship between SR , Precipitation, and Particle Mass Concentration

The scavenging ratio SR indicates precipitation effects on the particle mass concentration. Figure 4 shows that the SR is positively correlated with accumulative precipitation. The data corresponding to the position of 5 mm on the X-axis are the SR s of the precipitation process between 0 and 5 mm; similarly, the position of 10 mm is the average SR of the precipitation process with precipitation of 5–10 mm in Figure 4. From the figure, we can see that it increases faster when accumulative precipitation is below 15 mm and more slowly when accumulative precipitation is above 15 mm. The SR of PM_{10} is higher than the SR of $PM_{2.5}$ under the same accumulative precipitation, and when accumulative precipitation is above 50 mm, the precipitation SR s of $PM_{2.5}$ and PM_{10} are about 50% and 60%, respectively.

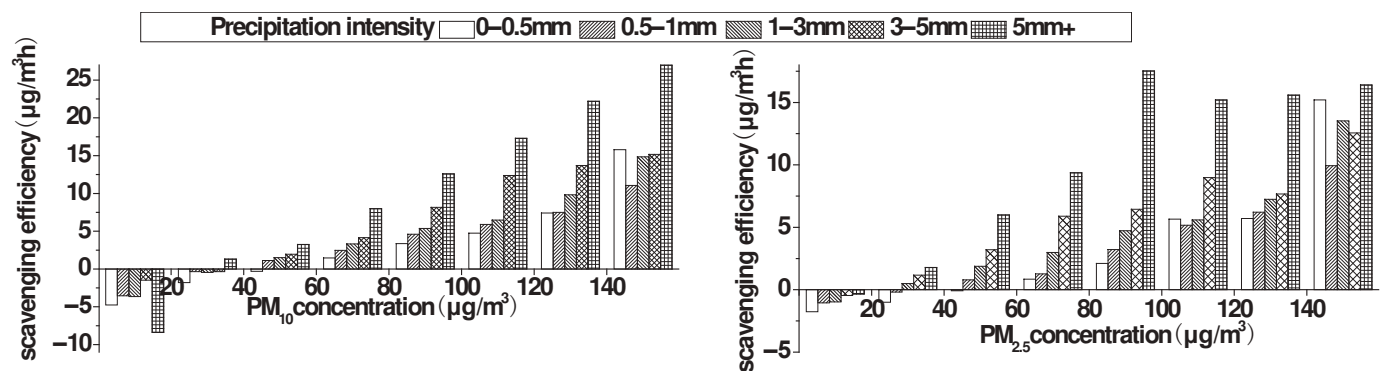


Figure 3. Effects of different rain intensities (RIs) and particle mass concentrations on scavenging efficiency (SE).

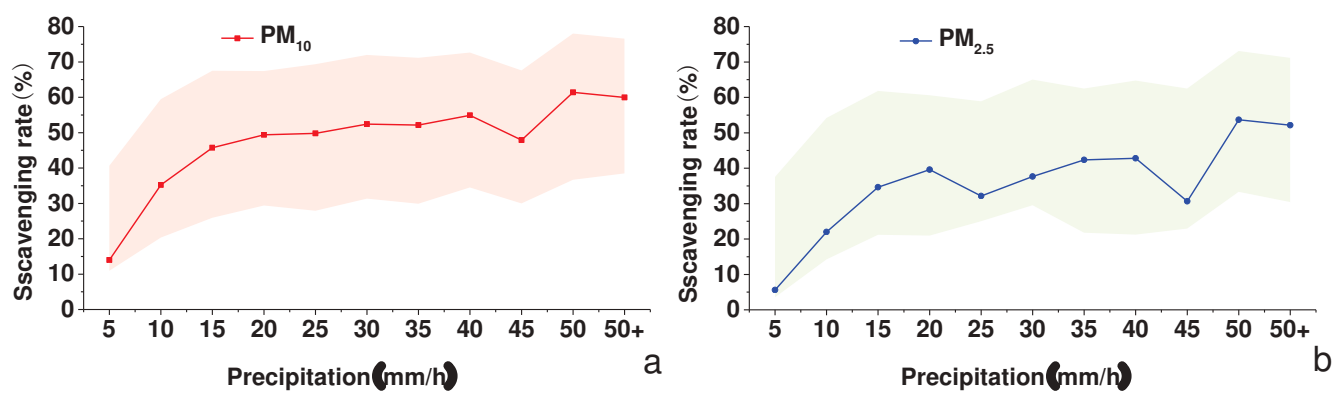


Figure 4. Relationship between precipitation and scavenging rate (SR) about the particle mass concentrations ((a), PM_{10} ; (b), $PM_{2.5}$). (The solid line is the arithmetic mean of the SR, and the shaded area is the 25% and 75% percentile values of all the individual cases).

The precipitation effect on the removal of particles is not only related to precipitation but also related to the particle mass concentration before precipitation starts. Figure 5 shows the effect of the particle mass concentration on the SR under different precipitation volumes. We can see that the SR and particle mass concentration before the rain are positively correlated, the arithmetic mean SR of precipitation at any level is above zero while the $PM_{2.5}$ concentration is higher than $50 \mu\text{g m}^{-3}$, and the average SR of precipitation at almost any level is less than zero while the $PM_{2.5}$ concentration is lower than $20 \mu\text{g m}^{-3}$ (which means precipitation had a very limited scavenge). In addition, the SR increases faster with the increase in the particle mass concentration when the particle mass concentration is below $50 \mu\text{g m}^{-3}$, and it increases more slowly when the particle mass concentration is higher than $50 \mu\text{g m}^{-3}$.

Assuming that the SRs of $PM_{2.5}$ and PM_{10} are, respectively, $SR_{pm2.5}$ and SR_{pm10} , the particulate matter concentration before precipitation is C , and the process of rainfall is P , the quadric surface fitting is performed on the segmentation statistical results in Figure 5 (not for all samples, but for the classification analysis of samples as shown in Figure 5), and the results are as follows:

$$SR_{pm2.5} = -66.6 + 1.4323P + 1.4241C - 0.0148P^2 - 0.0053C^2 + 0.0032P \times C \quad (8)$$

$$SR_{pm10} = -85.04 + 1.2770P + 1.8157C - 0.0126P^2 - 0.0070C^2 + 0.0024P \times C \quad (9)$$

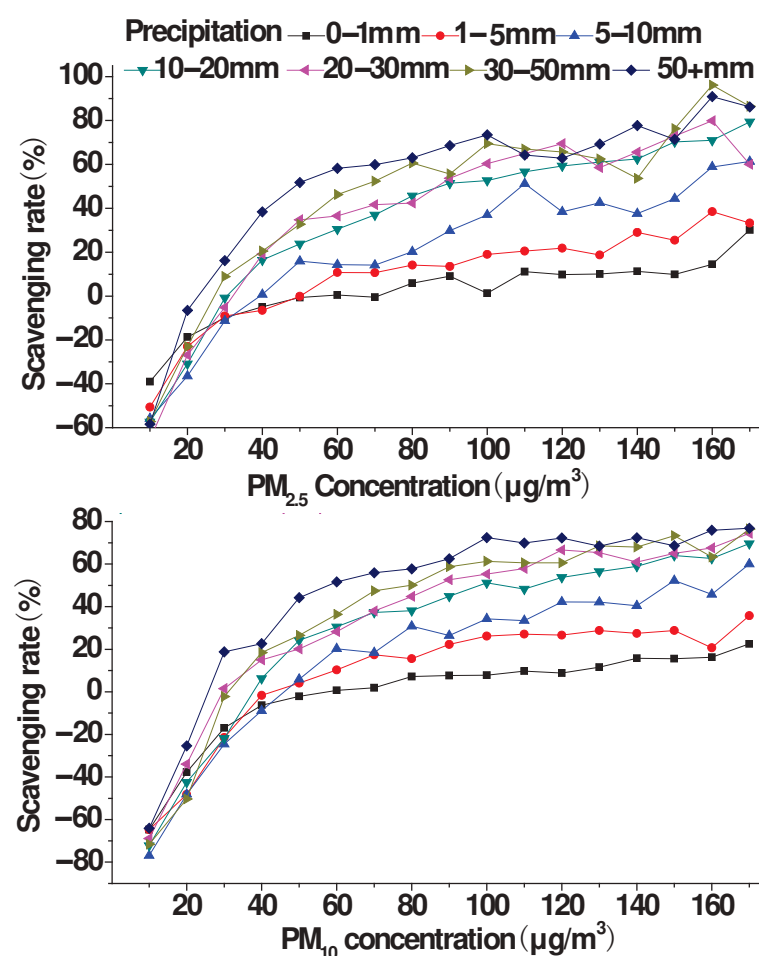


Figure 5. Effect of particle concentration on SR under different precipitation volumes. Rain ranges: 0–1, 1–5, 5–10, 10–20, 20–30, 30–50, >50 mm.

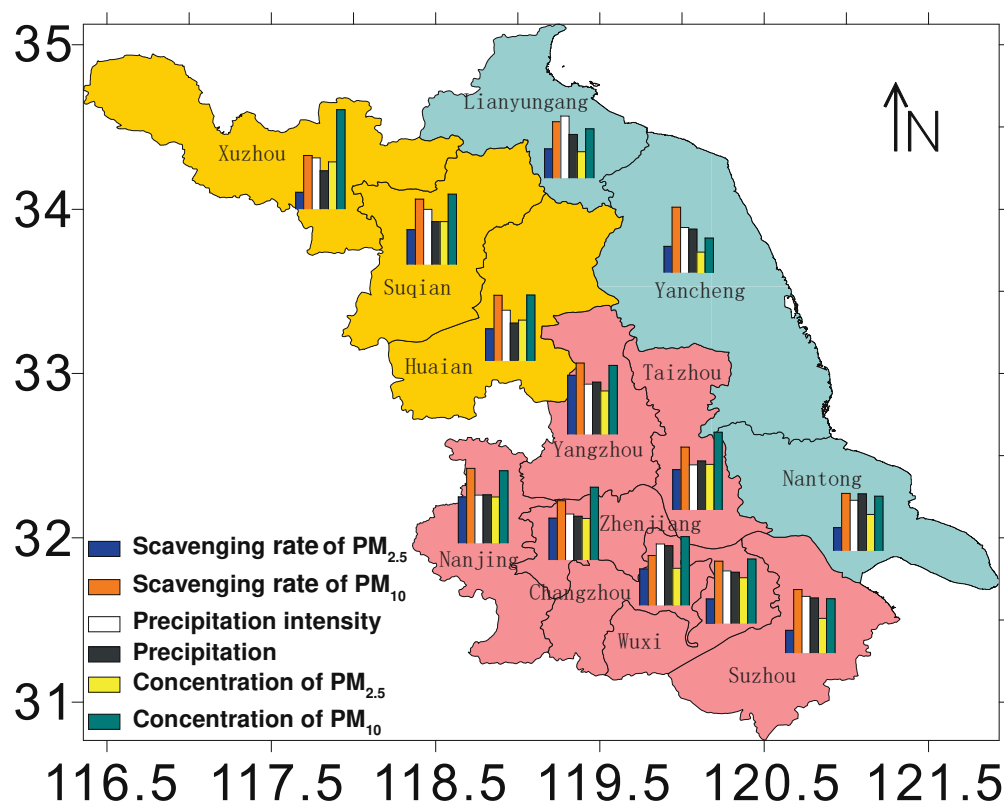
The Adj. R-Square of the two equations is 0.87 and 0.90, respectively, which means that the deviation between the fitting data and the statistical data is small, and the fitting effect is good.

3.3. Region Difference of SR

In this section, it is discussed whether there are any differences between different regions for the precipitation, *RI*, particle mass concentration, and SR in Jiangsu. Figure 6 shows the relationship among precipitation, particle mass concentration, and SR in Jiangsu. The average concentration of $PM_{2.5}$ in the 10 inland cities was $51.0 \mu\text{g m}^{-3}$, and the average concentration of PM_{10} was $80.5 \mu\text{g m}^{-3}$, higher than the average concentration of $PM_{2.5}$ in the coastal areas, which was $40.4 \mu\text{g m}^{-3}$, and the average concentration of PM_{10} , which was $63.0 \mu\text{g m}^{-3}$. The SR of coastal areas is less than the SR of inland Jiangsu, which is consistent with the distribution of the particle mass concentration because the inland concentration is higher than the coastal concentration. However, precipitation is also an important factor. The increase in the *RI* and mean precipitation accumulation was beneficial to the increase in the SR. The SR in coastal areas is relatively low because the concentration of particulate matter is lower than that in inland areas. The higher the precipitation, the higher the SR and SE. Therefore, the precipitation distribution center in south Jiangsu shows the SR is higher in southwest Jiangsu.

Table 1. Relationships between precipitation, *RI*, particle mass concentration, and *SR* in Jiangsu from 2013 to 2017 (data are consistent with Figure 6).

	<i>SR</i>		<i>RI</i>	Precipitation	Concentration	
	PM _{2.5}	PM ₁₀			PM _{2.5}	PM ₁₀
Xuzhou	0.10	0.24	1.16	9.42	54.07	101.08
Changzhou	0.18	0.24	1.31	12.68	47.26	79.98
Zhenjiang	0.20	0.25	1.08	10.45	50.45	79.44
Lianyungang	0.16	0.25	1.3	10.46	39.44	65.65
Nantong	0.13	0.26	1.15	12.03	46.67	70.29
Wuxi	0.14	0.28	1.21	11.54	53.84	77.17
Suzhou	0.13	0.28	1.24	11.95	45.58	69.41
Yancheng	0.15	0.28	1.01	9.64	35.02	53.11
Suqian	0.17	0.28	1.19	10.15	50.63	76.88
Huaian	0.16	0.28	1.19	9.76	49.29	74.35
Taizhou	0.20	0.29	1.04	11.16	53.56	84.3
Yangzhou	0.27	0.31	1.13	11.19	52.08	79.87
Nanjing	0.22	0.32	1.07	10.13	53.63	82.83

**Figure 6.** Relationships between precipitation, *RI*, particle mass concentration, and *SR* in Jiangsu from 2013 to 2017 (the data in Table 1). (The average PM concentration is based on the mean hourly particulate concentration of all stations in each city over a five-year period. The average values of precipitation and the precipitation rate are the average values of all precipitation processes in the region in 5 years. Three colors in the map: red, the southern inland area; blue, coastal areas; and orange, the northern inland area.)

In this section, it is discussed why the *SR* of PM_{2.5} in the northern coastal area of Jiangsu is higher than that in the southern coastal area though the PM_{2.5} concentration and average precipitation in the northern coastal area are less than those in the southern coastal area. This is due to the influence of the *RI*, which is larger in the northern coastal area. The *SR* of PM₁₀ is less affected by the *RI* compared with the *SR* of PM_{2.5}. Therefore, the *SR* of

PM₁₀ in southeast Jiangsu is higher than that in the northeast region in spite of the larger *RI* in the northeast. Therefore, the *SR* of PM_{2.5} is more affected by the *RI*. Precipitation with a low *RI* has almost no *SE* on PM_{2.5}. Therefore, continuous drizzle can cause a large amount of precipitation over a long time period but cannot effectively reduce the concentration of PM_{2.5}. Since low-*RI* precipitation has some *SE* on PM₁₀, more precipitation (meaning high-*RI* precipitation or continuous drizzle) can reduce the PM₁₀ concentration effectively.

3.4. Change in Particle Mass Concentration after Rain

The concentration of particulate matter in the atmosphere depends on the balance between emissions and atmosphere self-cleaning. When the emission source is not changed and the weather system is stable, the particle mass concentration should be around the equilibrium state. In the absence of external transport, the PM concentration in the atmosphere depends on environmental emissions and dry or wet deposition. In a relatively short period of time, it can be considered that environmental emissions before and after precipitation do not change much; therefore, the impact of precipitation on the particle concentration can be analyzed. When the effects of dry deposition and environmental emissions cancel out, the concentration of particulate matter stabilizes, which is the equilibrium state. Then, how does the particle mass concentration approach the equilibrium state after a precipitation process?

The change in the particle mass concentration within 168 h after precipitation ends was analyzed using 6882 processes. The results are shown in Figure 7. The average particle mass concentration is low at the end of precipitation, being about 50 $\mu\text{g m}^{-3}$ for PM_{2.5} and 70 $\mu\text{g m}^{-3}$ for PM₁₀. The particle mass concentration increases gradually after the end of precipitation. The average concentrations of PM_{2.5} and PM₁₀ 168 h after precipitation are more than 65 and 115 $\mu\text{g m}^{-3}$, respectively. The growth of the particle mass concentration after precipitation was divided into two stages: 0–24 h after the end of precipitation is the rapid growth stage, and 24 h after the end of precipitation is the slow growth stage. The concentrations of PM_{2.5} and PM₁₀ increase at 0.46 and 1.35 $\mu\text{g m}^{-3}$ per hour during the rapid growth phase, while they increase at 0.07 and 0.51 $\mu\text{g m}^{-3}$, respectively, in the slow growth stage.

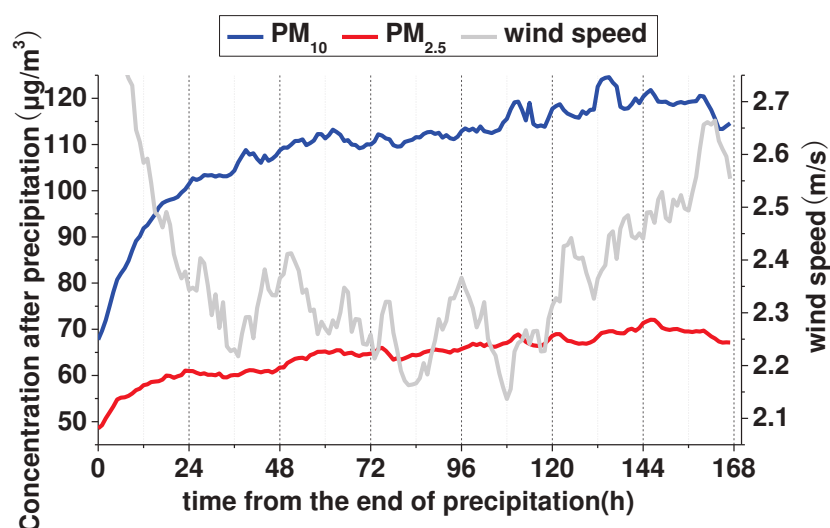


Figure 7. Changes in particle concentrations and wind speeds with time after precipitation ends.

In this section, the reason for the growth rate of the particle mass concentration within 24 h after precipitation being greater than that after 24 h is discussed.

The factors that influence air pollution include internal factors (emission sources) and external factors (such as precipitation, wind speed and direction, humidity, inversion, and mixing layer height [36]) and were discussed in the previous article [1], showing that

the threshold value is one of the criteria of pollution intensity. Analysis of the average wind speed within 168 h after the rain starts shows that the wind speed within 24 h after precipitation is greater than that after 24 h; the high wind is not conducive to the increase in the particle mass concentration. Meanwhile, emission sources are usually stable and can be considered as constant during the precipitation process. For a period of time after the end of precipitation, if the emission source is regarded as constant, the PM concentration change depends on the dry deposition and environmental emissions. When the concentration of particulate matter is high, the dry deposition effect is strong, exceeding the environmental emission, and the PM concentration decreases with time. When the PM concentration is low, the dry deposition effect is lower than that of environmental emissions, and the PM concentration increases with time. When the effects of dry deposition and environmental emissions cancel out, the concentration of particulate matter stabilizes, which is the equilibrium state. When the actual particle concentration is lower than the equilibrium concentration, dry deposition caused by the effect of the particle concentration decreases below the environmental emissions, which could lead to an increase in the particle concentration effect, where the PM concentration will increase to approach the equilibrium concentration. When there is a greater difference between the actual concentration and the equilibrium concentration, dry deposition caused by the effect of the PM concentration decreases below the environmental emissions, which could lead to an increase in the particle concentration effect, causing a greater particle concentration change over time. When the particle mass concentration approaches the equilibrium state, the closer it is to the equilibrium point, the more slowly it moves toward the equilibrium point. The particle mass concentration is far from the equilibrium point at the end of precipitation; therefore, the growth rate is relatively large. In the case of no rain within 168 h after the previous precipitation process, the weather is often sunny, and the particle mass concentration approaches the equilibrium state; therefore, the particle growth rate is slowed down significantly. Here, we choose the cases where there were more than 10 consecutive days without precipitation after the studied precipitation process. Additionally, we analyze particle concentration changes after the precipitation, in order to determine the above equilibrium concentration. According to the results of the 10-day or longer continuous observation, the arithmetic average concentrations of $PM_{2.5}$ and PM_{10} are finally stabilized at about 80 and 120 $\mu g m^{-3}$, which can be considered as the equilibrium points for $PM_{2.5}$ and PM_{10} .

4. Conclusions

Particle air pollution scavenging was jointly affected by the wind diffusion effect and precipitation scavenging effect. Precipitation is the most important factor in the balance of air pollution in ecosystems.

Deducing the threshold values of precipitation scavenging that were conducive to the pollution accumulation was very necessary to achieve better control of air pollution. This study provides a simple and quantitative way to establish a “rain-only” method on particle aerosol removal from the atmosphere. Such a simple methodology can be easily adapted to predict aerosol particle scavenging over any region across the world irrespective of the topographical, orographical, and climatic features. The threshold values of the precipitation intensity and duration below and above which aerosol scavenging behaves differently were developed.

A higher concentration, larger RI , and larger particle size lead to a higher SE . The greater the RI , the higher the SE , meaning the precipitation SE on PM_{10} is better than that on $PM_{2.5}$. $RI = 8.0 mm h^{-1}$ has the best SE on $PM_{2.5}$, and $RI = 11.3 mm h^{-1}$ has the best SE on PM_{10} when the total precipitation is fixed. The SR increases faster when accumulative precipitation is below 15 mm and more slowly when accumulative precipitation is above 15 mm. When accumulative precipitation is above 50 mm, the precipitation SR s of $PM_{2.5}$ and PM_{10} are about 50% and 60%, respectively. The SR of coastal areas is less than that of

inland Jiangsu. In the future, if the regional PM_{2.5} concentrations continue to decrease, the threshold values would remain applicable.

The growth of the particle mass concentration after precipitation was divided into two stages: the slow growth stage about 24 h after the end of precipitation, and the rapid growth stage 24 h after the end of precipitation. The concentrations of PM_{2.5} and PM₁₀ increase at 0.46 and 1.35 $\mu\text{g m}^{-3}$ per hour, respectively, during the rapid growth phase, while they increase at 0.07 and 0.51 $\mu\text{g m}^{-3}$, respectively, in the slow growth stage.

The methods in this study just studied the “rain-only” effect on particle aerosol removal from the atmosphere, and the influence of wind was not discussed. The present long-term and large datasets are able to quantitatively predict aerosol scavenging at any part if only the rain rate and duration are available.

Author Contributions: Conceptualization, D.L.; validation, D.L.; formal analysis, B.Z. and W.Y.; project administration, D.L.; resources, D.L.; writing—original draft preparation, B.Z.; writing—review and editing, D.L. All authors have read and agreed to the published version of the manuscript.

Funding: This work was jointly supported by the National Key Project of MOST (2016YFC0203303, the open fund by the Key Laboratory for Aerosol–Cloud–Precipitation of CMA–NUIST in China (KDW1801), the Open fund by Jiangsu Key Laboratory of Atmospheric Environment Monitoring and Pollution Control (KHK2005), and the Jiangsu Meteorological Bureau General project (KZ201902).

Institutional Review Board Statement: Not applicable.

Informed Consent Statement: Not applicable.

Data Availability Statement: The data are availability from <http://106.37.208.233:20035/> (accessed on 10 June 2021).

Acknowledgments: Thanks to the Chinese Ministry of Environmental Protection for providing the environmental monitoring data.

Conflicts of Interest: The authors declare no conflict of interest.

References

1. Dai, Z.J.; Liu, D.Y.; Yu, K.; Cao, L.; Jiang, Y.S. Meteorological Variables and Synoptic Patterns Associated with Air Pollutions in Eastern China during 2013–2018. *Int. J. Environ. Res. Public Health* **2020**, *17*, 2528. [CrossRef]
2. Hou, P.; Wu, S.; McCarty, J.L.; Gao, Y. Sensitivity of atmospheric aerosol scavenging to precipitation intensity and frequency in the context of global climate change. *Atmos. Chem. Phys.* **2018**, *18*, 8173–8182. [CrossRef]
3. Pruppacher, H.R.; Klett, J.D. *Microphysics of Clouds and Precipitation*; Kluwer Academic Publisher: Dordrecht, The Netherlands, 1997; Volume 17.
4. Ohata, S.; Moteki, N.; Mori, T.; Koike, M.; Kondo, Y. A key process controlling the wet removal of aerosols: New observational evidence. *Sci. Rep.* **2016**, *6*, 34113. [CrossRef] [PubMed]
5. Zhang, G.Z.; Liu, D.Y.; He, X.H.; Yu, D.Y.; Pu, M.J. Acid rain in Jiangsu province, eastern China: Tempo-spatial variations features and analysis. *Atmos. Pollut. Res.* **2017**, *8*, 1031–1043. [CrossRef]
6. Roy, A.; Chatterjee, A.; Ghosh, A.; Das, S.K.; Ghosh, S.K.; Raha, S. Below-cloud scavenging of size-segregated aerosols and its effect on rainwater acidity and nutrient deposition: A long-term (2009–2018) and real-time observation over eastern Himalaya. *Sci. Total Environ.* **2019**, *674*, 223–233. [CrossRef]
7. Aikawa, M.; Hiraki, T. Washout/rainout contribution in wet deposition estimated by 0.5 mm precipitation sampling/analysis. *Atmos. Environ.* **2009**, *43*, 4935–4939. [CrossRef]
8. Andronache, C. Estimates of sulfate aerosol wet scavenging coefficient for locations in the Eastern United States. *Atmos. Environ.* **2004**, *38*, 795–804. [CrossRef]
9. Andronache, C. Estimated variability of below-cloud aerosol removal by rainfall for observed aerosol size distributions. *Atmos. Chem. Phys.* **2003**, *3*, 131–143. [CrossRef]
10. Andronache, C.; Grönholm, T.; Laakso, L.; Phillips, V.; Venäläinen, A. Scavenging of ultrafine particles by rainfall at a boreal site: Observations and model estimations. *Atmos. Chem. Phys.* **2006**, *6*, 4739–4754. [CrossRef]
11. Chatterjee, A.; Jayaraman, A.; Rao, T.N.; Raha, S. In-cloud and below-cloud scavenging of aerosol ionic species over a tropical rural atmosphere in India. *J. Atmos. Chem.* **2011**, *66*, 27–40. [CrossRef]
12. Li, P.H.; Wang, Y.; Li, Y.H.; Yang, M.M.; Sun, M.H.; Guo, J.; Shou, Y.P.; Yi, X.; Wang, L.; Xi, Z.L.; et al. Characterization of polycyclic aromatic hydrocarbons in cloud deposition at Mount Heng in Southern China. *Aerosol Air Qual. Res.* **2016**, *16*, 3164–3174. [CrossRef]

13. Santachiara, G.; Prodi, F.; Belosi, F. Atmospheric aerosol scavenging processes and the role of thermo- and diffusio-phoretic forces. *Atmos. Res.* **2013**, *128*, 46–56. [CrossRef]
14. Bae, S.Y.; Jung, C.H.; Kim, Y.P. Relative contributions of individual phoretic effect in the below-cloud scavenging process. *J. Aerosol Sci.* **2009**, *40*, 621–632. [CrossRef]
15. Bae, S.Y.; Jung, C.H.; Kim, Y.P. Derivation and verification of an aerosol dynamics expression for the below-cloud scavenging process using the moment method. *J. Aerosol Sci.* **2010**, *41*, 266–280. [CrossRef]
16. Bae, S.Y.; Park, R.J.; Kim, Y.P.; Woo, J.H. Effects of below-cloud scavenging on the regional aerosol budget in East Asia. *Atmos. Environ.* **2012**, *58*, 14–22. [CrossRef]
17. Berthet, S.; Leriche, M.; Pinty, J.P.; Cuesta, J.; Pigeon, G. Scavenging of aerosol particles by rain in a cloud resolving model. *Atmos. Res.* **2010**, *96*, 325–336. [CrossRef]
18. Chate, D.M.; Murugavel, P.; Ali, K.; Tiwari, S.; Beig, G. Below-cloud rain scavenging of atmospheric aerosols for aerosol deposition models. *Atmos. Res.* **2011**, *99*, 528–536. [CrossRef]
19. Chate, D.M. Field studies of scavenging of aerosols by rain events. *J. Aerosol Sci.* **2004**, *35*, 695–706. [CrossRef]
20. Chate, D.M.; Rao, P.S.P.; Naik, M.S.; Momin, G.A.; Safai, P.D.; Ali, K. Scavenging of aerosols and their chemical species by rain. *Atmos. Environ.* **2003**, *37*, 2477–2484. [CrossRef]
21. Huang, C.J.; Chen, K.S.; Lai, Y.C.; Wang, L.C.; Chang-Chien, G.P. Wet deposition of polychlorinated dibenzo-p-dioxins/dibenzofuran in a Rural Area of Taiwan. *Aerosol Air Qual. Res.* **2011**, *11*, 732–748. [CrossRef]
22. Li, Y.; Wang, Y.; Ding, A.J.; Liu, X.; Guo, J.; Li, P.; Sun, M.; Ge, F.; Wang, W. Impact of long-range transport and under-cloud scavenging on precipitation chemistry in East China. *Environ. Sci. Pollut. Res. Int.* **2011**, *18*, 1544–1554. [CrossRef]
23. Wang, W.; Cui, K.; Zhao, R.; Lee, W.J.; Yan, P. Sensitivity analyses for atmospheric scavenging ratio of total PCDD/Fs-TEQ wet deposition: Case of Wuhu City, China. *Aerosol Air Qual. Res.* **2018**, *18*, 719–733. [CrossRef]
24. Wang, X.; Zhang, L.; Moran, M.D. Bulk or modal parameterizations for below-cloud scavenging of fine, coarse, and giant particles by both rain and snow. *J. Adv. Modeling Earth Syst.* **2014**, *6*, 1301–1310. [CrossRef]
25. Wiegand, F.; Pereira, F.N.; Teixeira, E.C. Study on wet scavenging of atmospheric pollutants in south Brazil. *Atmos. Environ.* **2011**, *45*, 4770–4776. [CrossRef]
26. Zhao, S.; Yu, Y.; He, J.; Yin, D.; Wang, B. Below-cloud scavenging of aerosol particles by precipitation in a typical valley city, northwestern China. *Atmos. Environ.* **2015**, *102*, 70–78. [CrossRef]
27. Zhao, Y.; Cui, K.; Chen, S.; Yin, Z.; Chao, H.R.; Chang-Chien, G.P. Atmospheric PM_{2.5}, total PCDD/Fs-WHO2005-TEQ level and wet deposition: Cases of Jinan and Weihai Cities, China. *Aerosol Air Qual. Res.* **2018**, *18*, 3081–3095. [CrossRef]
28. Jung, C.H.; Bae, S.Y.; Kim, Y.P. Approximated solution on the properties of the scavenging gap during precipitation using harmonic mean method. *Atmos. Res.* **2011**, *99*, 496–504. [CrossRef]
29. Bai, Y.Q.; Qi, H.X.; Zhao, T.L.; Zhou, Y.; Liu, L.; Xiong, J.; Zhou, Z.M.; Cui, C.G. Simulation of the responses of rainstorm in the Yangtze River Middle Reaches to changes in anthropogenic aerosol emissions. *Atmos. Environ.* **2020**, *220*, 117081. [CrossRef]
30. Tai, A.P.K.; Mickley, L.J.; Jacob, D.J. Correlations between fine particulate matter (PM_{2.5}) and meteorological variables in the United States: Implications for the sensitivity of PM_{2.5} to climate change. *Atmos. Environ.* **2010**, *44*, 3976–3984. [CrossRef]
31. McLachlan, M.S.; Sellström, U. Precipitation scavenging of particle-bound contaminants—A case study of PCDD/Fs. *Atmos. Environ.* **2009**, *43*, 6084–6090. [CrossRef]
32. Nie, D.; Chen, M.; Wu, Y.; Ge, X.; Hu, J.; Zhang, K.; Ge, P. Characterization of Fine Particulate Matter and Associated Health Burden in Nanjing. *Int. J. Environ. Res. Public Health* **2018**, *15*, 602. [CrossRef]
33. Rasch, P.; Feichter, J.; Law, K.; Mahowald, N.; Penner, J.; Benkovitz, C.; Genthon, C.; Giannakopoulos, C.; Kasibhatla, P.; Koch, D.; et al. A comparison of scavenging and deposition processes in global models: Results from the WCRP Cambridge Workshop of 1995. *Tellus B* **2000**, *52*, 1025–1056. [CrossRef]
34. Nicolás, J.F.; Lucarelli, F.; Galindo, N.; Yubero, E.; Crespo, J.; Calzolari, G.; Nava, S. Impact of Traffic Flows and Meteorological Events on the Hourly Elemental Composition of Fine and Coarse Particles at an Urban Site. *Aerosol Air Qual. Res.* **2020**, *20*, 991–1001. [CrossRef]
35. Yoo, J.M.; Lee, Y.R.; Kim, D.; Jeong, M.J.; Stockwell, W.R.; Kundu, P.K.; Oh, S.M.; Shin, D.B.; Lee, S.J. New indices for wet scavenging of air pollutants (O₃, CO, NO₂, SO₂, and PM₁₀) by summertime rain. *Atmos. Environ.* **2014**, *82*, 226–237. [CrossRef]
36. Zhang, Y.; Cao, F. Fine particulate matter (PM_{2.5}) in China at a city level. *Sci. Rep.* **2015**, *5*, 14884. [CrossRef] [PubMed]

Article

Prediction of Air Pollutant Concentrations via RANDOM Forest Regressor Coupled with Uncertainty Analysis—A Case Study in Ningxia

Weifu Ding ¹ and Xueping Qie ^{2,*}
¹ School of Mathematics and Information, North Minzu University, Yinchuan 750021, China; dingweifu@163.com

² School of Education, Ningxia University, Yinchuan 750021, China

* Correspondence: qxp2008@nxu.edu.cn

Abstract: Air pollution has not received much attention until recent years when people started to understand its dreadful impacts on human health. According to air pollution and the meteorological monitoring data from 1 January 2016 to 31 December 2017 in Ningxia, we analyzed the impact of ground surface temperature, air temperature, relative humidity and the power of wind on air pollutant concentrations. Meanwhile, we analyze the relationships between air pollutant concentrations and meteorological variables by using the mathematical model of decision tree regressor (DTR), feedforward artificial neural network with back-propagation algorithm (FFANN-BP) and random forest regressor (RFR) according to air-monitoring station data. For all pollutants, the RFR increases R^2 of FFANN-BP and DTR by up to 0.53 and 0.42 respectively, reduces root mean square error (RMSE) by up to 68.7 and 41.2, and MAE by up to 25.2 and 17. The empirical results show that the proposed RFR displays the best forecasting performance and could provide local authorities with reliable and precise predictions of air pollutant concentrations. The RFR effectively establishes the relationships between the influential factors and air pollutant concentrations, and well suppresses the overfitting problem and improves the accuracy of prediction. Besides, the limitation of machine learning for single site prediction is also overcome.

Keywords: air pollution; random forest; feedforward artificial neural network with back-propagation; decision tree; Ningxia

Citation: Ding, W.; Qie, X. Prediction of Air Pollutant Concentrations via RANDOM Forest Regressor Coupled with Uncertainty Analysis—A Case Study in Ningxia. *Atmosphere* **2022**, *13*, 960. <https://doi.org/10.3390/atmos13060960>

Academic Editors: Duanyang Liu, Kai Qin and Honglei Wang

Received: 24 April 2022

Accepted: 8 June 2022

Published: 14 June 2022

Publisher's Note: MDPI stays neutral with regard to jurisdictional claims in published maps and institutional affiliations.



Copyright: © 2022 by the authors. Licensee MDPI, Basel, Switzerland. This article is an open access article distributed under the terms and conditions of the Creative Commons Attribution (CC BY) license (<https://creativecommons.org/licenses/by/4.0/>).

1. Introduction

With industrialization and urbanization, air pollution in most countries is worsening over the years. Many areas including the north China and south of the Yangtze River have suffered severe and continuous haze weather. High level of air pollutant concentrations plays an important role not only in degrading the environment but also in causing respiratory diseases [1–6]. In order to enable the government to put forward reasonable measures in mitigating air pollution, it is very necessary to accurately predict the concentrations of air pollutants in real time or near real time.

Generally forecasting techniques can be divided into deterministic and stochastic approaches. The deterministic model is suitable for a wide range of trend forecasting, and the stochastic model is suitable for single site prediction. The deterministic air quality models based on numerical models mainly include Chem models, Community Multiscale Air Quality (CMAQ) [7] and Nested Air Quality Prediction Model System (NAQPMS) [8] etc. It mainly uses all kinds of meteorological data and emission source data to estimate the diffusion of air pollutants through the physical and chemical processes. It has a solid theoretical foundation and a relatively transparent model. However, the accuracy of the deterministic model is highly influenced by the boundary condition of the model and the initial conditions. Furthermore, historical data are not be used in the model. At the

same time, the computations of the model are complex and the requirement of computing resources is higher. So it is difficult to fully understand and quantify [9–11].

The stochastic methods mine the relationships between air pollutant concentrations and the influential factors, including the meteorological variables and human activities based on machine learning methods, and then predict air pollutant concentrations in the future [12–14]. Statistical methods are considered more reliable tools to predict air pollutant concentrations than deterministic approaches [15–20], including principle components analysis (PCA), kriging, inverse distance weighting [21,22], land-use regression (LUR) and artificial neural network (ANNs), etc. [23–26]. Regression methods can learn the intrinsic relationships between the influential factors and air pollutant concentrations [27]. Harishkumar [28] proposed to use geographical weighted regression (GWR) method to study the relationships between air pollutant concentration and the influential factors, and achieved good results. LUR is technically simple, easy to fit in calculation and high spatial resolution. Since its emergence in 1997, it has been applied to the predictions of air pollutant concentrations. However, the regression methods do not consider the spatial correlation in the air pollution data and overestimate the importance of covariates. At the same time, because the error does not meet the assumption of independent and identically distributed, the prediction ability of the regression method is low in the space-time domain. The performances of ANNs are generally higher than air quality numerical models CMAQ and NAQPMS. ANNs have the advantages of less sample data, simple modeling, convenient operation, small relative error [17,20]. However, there are generally some disadvantages in ANNs, such as poor generalization ability, over fitting, easy to fall into local optimization.

Geostatistics is based on the principle that the closer the observation value in the space-time domain is more similar than the farther the observation value [29]. There is no the assumption of sample independence in Geostatistics and obeys the constraint of normal distribution to obtain a good fit to the data. However, it results in spatiotemporal heterogeneity after adding time dimension, which makes spatiotemporal data visualization and analysis quite challenging. In addition, spatiotemporal data usually contain a long time series of air pollution [18]. It is necessary to impose strong assumptions on the process [21,22].

In this paper, RFRs have been employed in this work in order to predict air pollutant concentrations. RFRs have the characteristics of adaptive training and tuning and effectively establish the relationships between the meteorological variables and air pollutant concentrations, and well suppress the overfitting problem and improves the accuracy of prediction. Besides the limitation of machine learning for single site prediction is also overcome.

The remainder of our paper is organized as follows: In the next section we present the study area and the data collected. In Section 3 the basic concepts of FFANN-BP, DTR and RFR are presented, and how the validity indices can be used to identify and compare the predicted results. The critical analysis is followed by predicting air pollutant concentrations based on data from 2016–2017. Finally, we conclude our work at the end part after discussing the results of our experiments.

2. Area Description

Study Area

Ningxia is located in the inland area of northwest China, bounded between the latitudes of 35°14' N–39°14' N and the longitudes of 104°17' E–109°39' E, adjacent to Shaanxi in the east, Inner Mongolia in the west and Gansu in the north, with a total area of 66,400 square kilometers, and a permanent population of 6.8179 million. The topography of Ningxia gradually inclines from southwest to northeast. It is divided into three parts: the irrigation area of the Yellow River in the north, the arid zone in the middle and the mountain area in the south. Located within the Yellow River system, Ningxia has a temperate continental arid and semi-arid climate with a high terrain in the south and a low terrain in the north. The southern Liupan Mountains are wet and rainy with low

temperature and short frost-free period. The northern part has abundant sunshine, strong evaporation, large temperature difference between day and night, and the annual sunshine reaching 3000 h.

Ningxia which is located in the western margin of China's monsoon area is affected by southeast monsoon in summer, low precipitation, with July being the hottest month, the average temperature is 24 °C. In winter, it is greatly affected by northwest monsoon, with a large fluctuation in temperature, with an average temperature of −9 °C lowest temperature. The annual precipitation in the whole region ranges from 150 mm to 600 mm. The average annual water surface evaporation in Ningxia is 1250 mm, ranging from 800 to 1600 mm. Furthermore, the prevailing north wind lowers the humidity level [30].

In Ningxia, the extremely hot and dry climatic conditions in the area play an important role in the resuspension of fine particle, both the sand storm and the domestic fuel are the sources of air pollution. According to the Ningxia annual reports on air quality, the O₃ and particulate matter (PM) are the most important air pollutants in the city [31]. There are 15 air monitoring stations of the China National Environmental Protection Agency and 12 meteorological stations in Ningxia.

3. Methods

3.1. Data Preprocessing

The data with concentrations less than 0 µg/m³ and more than 1000 µg/m³ are eliminated. If one item of meteorological data is missing or abnormal, all data of that day will be eliminated. Outliers are data points that are far from other data points. They are problematic for many statistical analyses because they can cause tests to either miss significant findings or distort real results and are defined as values that deviate from the mean by more than 3 times the standard deviation. Outliers strongly influence the output of a machine learning model. In this paper, the mean value of the data is used to replace the abnormal and missing values.

In our experiment, the concentrations and the raw meteorological data were scaled to a fixed range from 0 to 1 by using the min-max normalization method. We standardize the data by using scikit-learn with the StandardScaler class. The normalization formula is as follows [32]:

$$y_i = \frac{x_i - \min_{1 \leq j \leq n} x_j}{\max_{1 \leq j \leq n} x_j - \min_{1 \leq j \leq n} x_j}, i = 1, 2, \dots, n. \quad (1)$$

where y_i is the normalized data, x_i is the data before normalization, n is the number of observations.

3.2. FFANN-BP

It is well known in FFANN-BP the weighted sum of inputs and bias term are passed to the activation level through the transfer function to produce the output. The network is trained in an iterative process. The number of hidden layers is chosen to be only one to reduce the network complexity, and increase the computational efficiency. Figure 1 shows the architecture of the FFANN-BP [33]. The inputs are fed into the input layer and propagate through the activation function, different layers may perform different transformations on their inputs. Then The mean squared error between the outputs and actual target values is backpropagated from the output layer to the input layer. The error is minimized by the adaptation of their connected weights in a supervised way. The most important problem is to decide the number of layers and neurons in the hidden layers.

Without loss of generality, let there be n neurons in the input layer, p neurons in the hidden layer, and q neurons in the output layer. The k -th input vector is $x(k) = (x_1(k), x_2(k), \dots, x_n(k))$. The k -th input vector of the hidden layer is $hi_k = (hi_1(k), hi_2(k), \dots, hi_p(k))$, the k -th output vector of hidden layer is $ho(k) = (ho_1(k), ho_2(k), \dots, ho_p(k))$. The k -th input vector of the output layer is $yi(k) = (yi_1(k), yi_2(k), \dots, yi_q(k))$, the k -th output vector of the output layer is $yo(k) = (yo_1(k), yo_2(k), \dots, yo_q(k))$. The desired output vector is $d_o(k) = (d_1(k), d_2(k), \dots, d_q(k))$. The weights between the i -th neuron in the input layer and h -th neu-

ron in the hidden layer are w_{ih} . The weights between h -th neuron in the hidden layer and o -th neuron in the output layer are w_{ho} , where $i = 1, 2, \dots, n, h = 1, 2, \dots, p, o = 1, 2, \dots, q$. The biases of the hidden layer and the output layer are b_h and b_o respectively. The number of samples is m , and f is the activation function. The commonly used activation function is the sigmoid function:

$$f(x_i) = \frac{1}{1 + e^{-x_i}} \quad (2)$$

Each connection weight is assigned a random number in the interval $(-1, 1)$. E, ε, M are the error function, the calculation accuracy value, and the maximum learning times respectively.

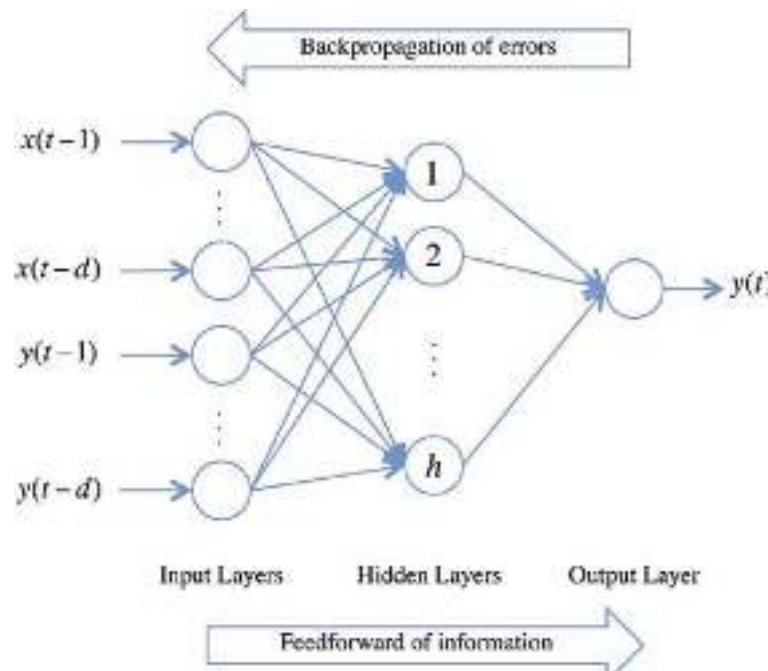


Figure 1. The architecture of the FFANN-BP.

The k -th input sample $x(k) = (x_1(k), x_2(k), \dots, x_n(k))$ is randomly selected, and the corresponding expected output are $d_o(k) = (d_1(k), d_2(k), \dots, d_q(k))$ and calculate the input and output of each neuron in the hidden layer.

$$hi_h(k) = \sum_{i=1}^n w_{ih}x_i(k) - b_h, h = 1, 2, \dots, p \quad (3)$$

$$ho_h(k) = f(hi_h(k)), h = 1, 2, \dots, p \quad (4)$$

$$yi_o(k) = \sum_{i=1}^p w_{ho}ho_i(k) - b_o, o = 1, 2, \dots, q \quad (5)$$

$$yo_o(k) = f(yi_o(k)), o = 1, 2, \dots, q \quad (6)$$

Then the total error is computed,

$$E = \frac{1}{2m} \sum_{k=1}^m \sum_{o=1}^q (d_o(k) - y_o(k))^2 \quad (7)$$

The partial derivatives of the error function to each neuron in the output layer are calculated by using the expected output and the actual output of the network $\delta_o(k)$, then the partial derivative of the error function to each neuron in the hidden layer is calculated

by using the connection weights from the hidden layer to the output layer, $\delta_o(k)$ the output of the output layer and $\delta_h(k)$ the output of the hidden layer [33].

$$\frac{\partial E}{\partial w_{ho}} = \frac{\partial E}{\partial y_{io}} \frac{\partial y_{io}}{\partial w_{ho}} = -ho_h(k)(d_o(k) - y_{o_o}(k))f'(y_{i_o}(k)) = -ho_h\delta_o(k) \quad (8)$$

$$\Delta w_{ho}(k) = -\mu \frac{\partial E}{\partial w_{ho}} = \mu \delta_o(k)ho_h(k) \quad (9)$$

$$w_{ho}^{N+1} = w_{ho}^N + \eta \delta_o(k)ho_h(k) \quad (10)$$

$$\Delta w_{ih}(k) = -\mu \frac{\partial E}{\partial w_{ih}} = -\mu \frac{\partial E}{\partial h_{i_h}(k)} \frac{\partial h_{i_h}(k)}{\partial w_{ih}} = \delta_h(k)x_i(k) \quad (11)$$

$$w_{ih}^{N+1} = w_{ih}^N + \eta \delta_h(k)x_i(k) \quad (12)$$

The algorithm terminates when the error reaches the preset accuracy or the number of learning is greater than the prespecified set maximum number of times. Otherwise, we select the next learning sample and the corresponding expected output and return to enter the next round of learning.

3.3. DTR

A decision tree corresponds to a partition of the feature space and the output value on the partition unit which is constructed by recursive segmentation, and the feature with the highest information gain is split first. The training process consists of feature selection, tree generation and pruning. All values of the feature are traversed and the space is divided until the value of the feature minimizes the loss function, and a partition point is obtained.

The optimal segmentation is used as the node of the decision tree. When generating leaf nodes, the most important thing is to pay attention to whether it is necessary to stop the growth of the tree. The process continues iteratively until we reach a prespecified stopping criterion such as a maximum depth, which only allows a certain number of splits from the root node to the terminal nodes. It breaks down a dataset into smaller and smaller subsets while at the same time an associated decision tree is incrementally developed. The final result is a tree with decision nodes and leaf nodes. The topmost decision node in a tree corresponds to the best predictor called the root node.

A primary advantage of DTR is that it is easy to follow and understand. It does not require any transformation of the features according to nonlinear data. In order to reduce storage requirement, the size of a decision tree is controlled by setting parameters such as maximum depth and minimum number of leaf nodes. At each segmentation, the features are always randomly arranged. Its output value is the average of all leaf node samples. Therefore, even if the same training data set is used, the optimal segmentation may be different. DTRs tend to overfit very easily.

3.4. Random Forest Regression

RFR is one of the most popular algorithms for regression problems because of its simplicity and high accuracy. It is an ensemble technique that combines multiple decision trees with a voting mechanism. Due to randomness it has a better generalization performance than DTR. This helps to decrease the model's variance. It is usually trained by using the bagging method which combines predictions from multiple machine learning algorithms together to make predictions more accurate than an individual model. They are less sensitive to outliers in the dataset and do not require much parameter tuning. The only parameter in RFRs is typically needed to experiment with is the number of trees in the ensemble. The predictions are calculated as the average prediction over all decision trees. The key lies in the fact that there is a low correlation between the individual models.

RFR is regressor, which adopts a voting mechanism to obtain prediction results based on decision tree. RFRs establish multi-decision trees by dividing the training samples. According to the bootstrap sampling method, part of the data is randomly extracted from

the data set as the training sample, and the remaining data is used as the validation sample of each decision tree. When regressing unknown samples, the prediction of each decision tree is output first, and then all the prediction results are synthesized by using the simple voting method to obtain the final prediction.

The most apparent benefit of RFR is its default ability in correcting the overfitting problems of decision trees to their training data sets. By using the bagging method and random feature selection the overfitting problem, which often leads to inaccurate outcomes, is almost completely resolved.

3.5. Statistical Indexes

The performances of DTR, FFANN-BP and RFR are evaluated by using four commonly used statistics indices, which are the coefficient of determination (R^2), root mean square error (RMSE), mean absolute error (MAE), and Mean Absolute Percentage Error (MAPE) between the predicted and observed air pollutant concentrations. The indices are defined as [34].

$$R^2 = \frac{\sum_{i=1}^n (p_i - \bar{o})^2}{\sum_{i=1}^n (o_i - \bar{o})^2} \quad (13)$$

$$RMSE = \sqrt{\frac{1}{n} \sum_{i=1}^n (o_i - p_i)^2}, \quad (14)$$

$$MAE = \frac{1}{n} \sum_{i=1}^n |o_i - p_i|, \quad (15)$$

$$MAPE = \frac{1}{n} \sum_{i=1}^n \left| \frac{o_i - p_i}{o_i} \right|, \quad (16)$$

where o_i , p_i , \bar{o} , \bar{p} and n are the observed, predicted and the mean of observed and predicted concentrations and the number of observations, respectively. The coefficient of determination indicates the closeness between the overall trend of the predicted value of the model and the observed value. The mean absolute error and root mean square error reflect the deviation of the observed value from the predicted value. The higher the value of R^2 , the better the model performance. Correspondingly, the lower the value of the RMSE, MAE and MAPE, the better the model acquired.

4. Results and Discussion

4.1. Data Used

We obtained the air pollutant concentrations from Ministry of Ecology and Environment of the People's Republic of China. Meteorological variables are obtained from China meteorological administration. The concentrations of carbon monoxide (CO), nitrogen dioxide (NO_2), ozone (O_3), particulate matter (PM) and sulfur dioxide (SO_2) are monitored. The data basis consists daily values corresponding to the 2-year period between January 2016 and December 2017.

Furthermore, the air monitoring stations do not monitor the level of meteorological variables. Thus, we select the nearest meteorological stations to represent the levels of the meteorological variables in the air monitoring stations. However, the distances of some air monitoring stations and meteorological stations are too far. Consequently, only three air monitoring stations, Ma Lian Kou, Sha Po Tou and Ma Yuan are selected for this research. Figure 2 and Table 1 showed the geographical regions of Ningxia and the locations of air monitoring stations.



Figure 2. The locations of air monitoring and meteorological stations, where the purple and blue solid point represent the air monitoring stations and meteorological stations in Ningxia, respectively.

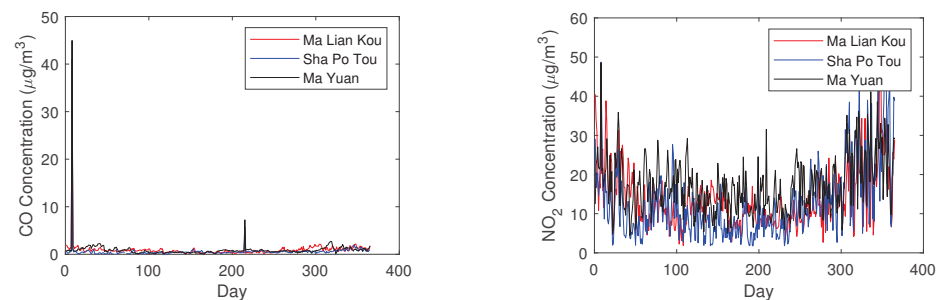
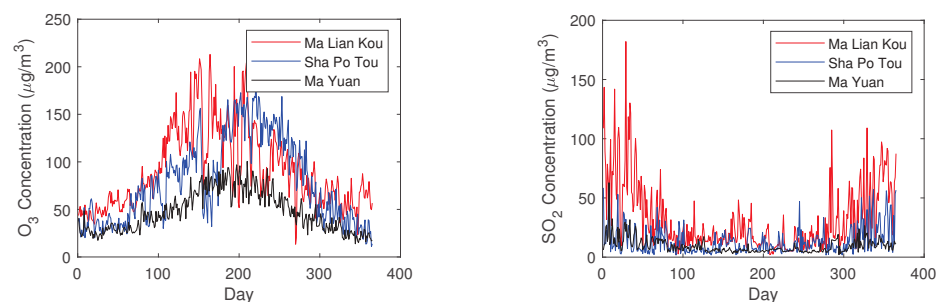
Table 1. Coordinates of the air monitoring stations in Ning Xia.

	Air Stations	Coordinates
1	Ma Lian Kou	105.95, 38.60
2	Sha Po Tou	105.02, 37.45
3	Ma Yuan	106.23, 36.14

Ma Lian Kou is located at the foot of Helan mountain in Yinchuan city and belongs to the northern Yellow river diversion irrigation area. Sha Po Tou is located in the central arid zone, near the Tengger Desert and on the Bank of the Yellow River. Ma Yuan is located in Guyuan city and belongs to the southern mountainous area. A descriptive statistics of these parameters in three monitoring stations for the studied period is presented in Table 2, including minimum, mean, median and maximum levels of the 12 input parameters and the concentrations of air pollutants during 2016–2017. Figures 3–5 show the diurnal variations of air pollutant concentrations in three selected monitoring stations.

Table 2. Basic descriptive statistics of the observed concentrations. Minimum, maximum, mean and standard deviation of six output parameters during 2016–2017 used in this study, all in $\mu\text{g}/\text{m}^3$.

Air Pollutants	Station	Mean	Median	Range	SD
CO	Ma Lian Kou	0.88	0.70	0.67~40.8	2.1
	Sha Po Tou	0.62	0.52	0.01~41.0	1.7
	Ma Yuan	0.91	0.74	0.01~45.0	1.90
NO ₂	Ma Lian Kou	13.8	12.2	1.63~53.6	7.3
	Sha Po Tou	16.6	14.5	1.8~57.0	10.7
	Ma Yuan	21.4	20.3	4.4~60.0	9.3
O ₃	Ma Lian Kou	95.6	90.1	13.4~213	36.2
	Sha Po Tou	79.1	75.5	11.0~189	38.8
	Ma Yuan	57.9	54.8	13.8~137.4	26.8
PM ₁₀	Ma Lian Kou	33.2	27.1	6.1~195.2	22.4
	Sha Po Tou	35.1	28.0	2.1~192.8	27.0
	Ma Yuan	34.3	29.0	2.3~224.5	22.8
PM _{2.5}	Ma Lian Kou	75.4	62.6	3~696	53.1
	Sha Po Tou	100.8	71.7	5.2~1313.3	112.2
	Ma Yuan	86.5	71.9	5.4~874.2	76.3
SO ₂	Ma Lian Kou	31.2	20.3	2.0~182.0	27.0
	Sha Po Tou	15.2	11.0	1.73~91.6	12.1
	Ma Yuan	10.1	9.0	2.1~62.8	5.3

**Figure 3.** The variations of the concentrations for CO and NO₂ at Ma Lian Kou, Sha Po Tou and Ma Yuan in 2016.**Figure 4.** The variations of the concentrations for O₃ and SO₂ at Ma Lian Kou, Sha Po Tou and Ma Yuan in 2016.

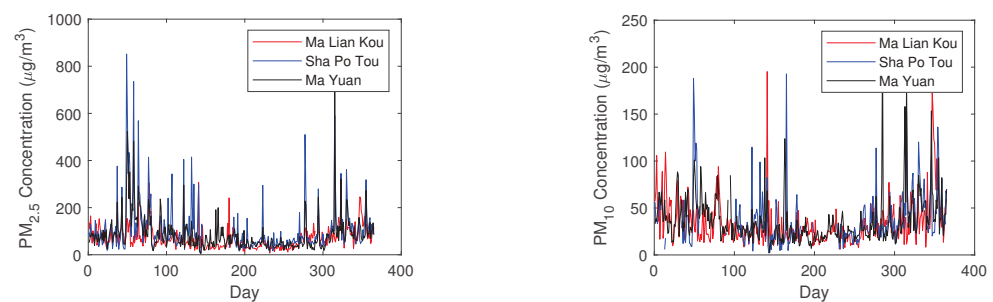


Figure 5. The variations of the concentrations for $PM_{2.5}$ and PM_{10} at Ma Lian Kou, Sha Po Tou and Ma Yuan in 2016.

In Ma Lian Kou, the concentrations of CO fluctuated enormously, with maxima of $38.24 \mu\text{g}/\text{m}^3$ in January 2016, and $4.59 \mu\text{g}/\text{m}^3$ in August 2016, respectively. These maxima correspond to the winter months. Concentration minima of CO took place during the summer months. Its values were $0.0722 \mu\text{g}/\text{m}^3$ and $0.1053 \mu\text{g}/\text{m}^3$ in April and August 2016.

Similarly, the concentrations of NO_2 fluctuated significantly with several maxima of 54 and $51 \mu\text{g}/\text{m}^3$ in December 2016, respectively. These maxima correspond to the days of highest energy consumption in homes due to heating and a greater density of cars on the roads during the winter season. Likewise, the minima in the concentrations corresponded to the spring months.

The concentrations of O_3 also fluctuated considerably, with maxima of $213 \mu\text{g}/\text{m}^3$ in June 2016, and $208 \mu\text{g}/\text{m}^3$ in May 2016, respectively. These maxima corresponded to the summer months. Concentration minima of O_3 took place in September 2016, its values were $13.375 \mu\text{g}/\text{m}^3$ and $20.3 \mu\text{g}/\text{m}^3$ in September. This trend is general throughout the studied years, since the formation of O_3 is associated with photochemical reactions, which requires the presence of strong sunlight as a catalyst.

In a similar way, the concentrations of $PM_{2.5}$ went up and down slightly but remained quite stable at around $70 \mu\text{g}/\text{m}^3$ with two spikes at $307 \mu\text{g}/\text{m}^3$ in May 2016 and March 2016, and a minimum of $6.9 \mu\text{g}/\text{m}^3$ in August 2016 and $11.4 \mu\text{g}/\text{m}^3$ in September 2016.

Similarly, the concentrations of PM_{10} went up and down slightly but remained quite stable at around $33 \mu\text{g}/\text{m}^3$ with two spikes at $195 \mu\text{g}/\text{m}^3$ in May 2016 and September 2016, and a minimum of $6.1 \mu\text{g}/\text{m}^3$ in August 2016. SO_2 went up and down slightly but remained quite stable at around $32 \mu\text{g}/\text{m}^3$ with two spikes at $182 \mu\text{g}/\text{m}^3$ and $143 \mu\text{g}/\text{m}^3$ in January 2016.

It is shown that the trends of air pollutant concentrations at the three monitoring stations are generally different, and the concentrations of air pollutants in Ma Yuan are the lowest. Therefore, the differences of air pollutant concentrations are closely related to geographical locations.

The meteorological variables such as ground surface minimum temperature, maximum and mean temperature, minimum relative humidity and maximum relative humidity, air minimum temperature, maximum and mean temperature, minimum, mean, maximum wind speed, sunshine duration supplied by the China meteorological data service center, their units were $^{\circ}\text{C}$, m/s, and hour, respectively. The meteorological variables were recorded on a daily basis. Table 3 show that the minimum of air temperature (T_{\min}) ranged from -15 in January to 27°C in July, while the maximum of air temperatures (T_{\max}) varied from -10°C in January to 41°C in July. The average sun shine of duration (ssd) was 6.7 h with the minimum and maximum values of 0h and 14 h appearing in November and June, respectively at Ma Lian Kou station.

Table 3. Basic descriptive statistics of the measured meteorological variables at the three stations.

Meteorological Variables	Station	Mean	Median	Range	SD
Mean GST (°C)	Ma Lian Kou	14.2	15.9	−13.4~40.2	14.7
	Sha Po Tou	13.7	15.5	−12.9~39.1	13.1
	Ma Yuan	10.8	10.8	−14.6~34.5	11.2
Max RHU (%)	Ma Lian Kou	48.9	48.0	14.0~94	15.40
	Sha Po Tou	52.6	52	19~91	14.7
	Ma Yuan	53.6	53	12~93	17.3
Mean TEM (°C)	Ma Lian Kou	10.9	12.6	−15.4~30.3	11.4
	Sha Po Tou	10.6	12.7	−17.4~29.8	11.0
	Ma Yuan	8.4	8.8	−18.1~27.5	9.8
Mean WIN (m/s)	Ma Lian Kou	40.4	37	17~116	15.1
	Sha Po Tou	57.1	56	17~150	20.9
	Ma Yuan	55.0	52.5	25~119	15.2
SSD (hr)	Ma Lian Kou	7.9	8.3	0~13.6	3.6
	Sha Po Tou	8.4	8.8	0~13.9	3.5
	Ma Yuan	6.9	7.9	0~13.7	3.9

GST, RHU, TEM, WIN, SSD represent ground surface temperature, relative humidity, air temperature, wind speed and sunshine of duration respectively.

4.2. Selection of the Influential Factors

The selection of input parameters is generally based on the prior knowledge of the formation of the air pollutants and the correlation analysis. Through the descriptive analysis of the air pollutant concentrations and the meteorological variables, we can select the most important input parameters and understand which are the dominant factors for the formation and diffusion of air pollutants. Generally, the levels of air pollutant concentrations are associated with emission sources, the formation of secondary pollutants and wind speed, air temperature and ground surface temperature, etc. It is well known that air pollutants and weather conditions are associated with each other in a complex relationship. With the increase of air temperature, the stronger the atmospheric convection activity, the more unstable the air stratification, which is conducive to the diffusion and dilution of pollutants. The air pollutant concentrations were closely related to the change of meteorological factors. Furthermore, relative humidity shows significant negative effect on the concentrations of O_3 , $PM_{2.5}$ and SO_2 , because precipitation will wash out the atmospheric particles. It can be seen from Table 4 that there is a strong negative correlation between wind speed and air pollutant concentration, significant negative effect demonstrates the fact that low concentrations are linked with high wind speed in Ningxia. It is shown in Figure 4a that the concentration of O_3 was higher in hot summer due to the high radiation and temperature, and lower in winter. The ground surface temperatures have the strongest correlations with the air pollutant concentrations, which is due to the enhancement of ultraviolet radiation, the increase of temperature, the enhancement of the decomposition of oxygen molecules, and the increase of the photochemical reaction rate of O_3 formation, resulting in the increase of air pollutant concentrations. The obtained results show that there are strong relationships between ground surface temperatures have and the concentrations of the majority of pollutants in the region of Ningxia. Moreover, air pollutant concentrations have a close relationship with the concentrations at previous time. There is a high possibility of mutual conversion between $PM_{2.5}$ and other pollutants, especially PM_{10} . $PM_{2.5}$ and PM_{10} are negatively correlated with air temperature. Furthermore, the concentrations of NO_2 may have a notable influence on the concentrations of O_3 . High levels of particulate matter in Ningxia are mostly caused by sand storms and construction activities near the monitoring stations. High temperature can result in enhanced re-suspension of road dust. Meteorological variables are used for the prediction of air pollutant concentrations.

We only consider variables with a coefficient of correlation greater than 0.30 as input dataset [35]. According to the correlation coefficient matrix shown in Table 4, there is a negative relationship between the concentrations of NO_2 and air temperature and wind speed, respectively. Hence the combinations of other air pollutant concentrations, the air pollutant concentrations one day in advance and meteorological variables for each air pollutant concentration are chosen as the input dataset. And we obtained the selected meteorological variables for every pollutant in Table 5.

Table 4. The Pearson correlation coefficients between the meteorological variables and air pollutant concentrations in 2016.

	CO	NO_2	O_3	PM_{10}	$PM_{2.5}$	SO_2
CO^a	0.05	0.13 ***	−0.14 ***	0.15 ***	0.07	0.16 ***
NO_2^a	0.08 **	0.66 ***	−0.40 ***	0.52 ***	0.27 ***	0.56 ***
O_3^a	−0.15 ***	−0.42 ***	0.87 ***	−0.28 ***	−0.18 ***	−0.49 ***
PM_{10}^a	0.05	0.42 ***	−0.32 ***	0.57 ***	0.44 ***	0.39 ***
$PM_{2.5}^a$	0.04	0.19 ***	−0.24 ***	0.42 ***	0.56 ***	0.22 ***
SO_2^a	0.12 ***	0.57 ***	−0.46 ***	0.45 ***	0.28 ***	0.69 ***
GST^a	−0.17 ***	−0.53 ***	0.75 ***	−0.38 ***	−0.28 ***	−0.64 ***
RHU^a	0.04	0.25 ***	−0.20 ***	0.20 ***	−0.09	−0.04
SSD^a	−0.07	−0.31 ***	0.46 ***	−0.30 ***	−0.20 ***	−0.22 ***
TEM^a	−0.17 ***	−0.52 ***	0.73 ***	−0.36 ***	−0.26 ***	−0.64 ***
WIN^a	−0.31	−0.33 ***	0.08	−0.13 ***	0.07	−0.20 ***

*** and ** indicate that the Pearson correlation coefficient test is significant at the level of 1% and 5%, respectively. x^a represents the variable x one day in advance.

Table 5. The selected influential variables for every pollutant, where x^a represent the air pollutant concentration the day in advance.

Air Pollutants	Influential Factors
CO	WIN^a
NO_2	$NO_2^a, O_3^a, PM_{10}^a, SO_2^a, GST^a, TEM^a$
O_3	$NO_2^a, O_3^a, SO_2^a, GST^a, SSD^a, TEM^a$
PM_{10}	$NO_2^a, PM_{10}^a, PM_{2.5}^a, SO_2^a, GST^a, TEM^a$
$PM_{2.5}$	$PM_{10}^a, PM_{2.5}^a$
SO_2	$NO_2^a, O_3^a, PM_{10}^a, SO_2^a, GST^a, TEM^a$

4.3. Experimental Results and Interpretations

For the purposes of comparisons, FFANN-BP, DTR and RFR models are trained in order to predict air pollutant concentrations in the three monitoring stations of Ningxia at a local scale. In this study, DTR, FFANN-BP and RFR were used to evaluate the ability of two-layer random forest model to estimate air pollutant concentrations. The data from 1 January 2016 to 30 June 2017 is used for model training, and the remaining is used for model prediction. It is trained on DTR, FFANN-BP and RFR, and the parameters are fine tuned according to the experimental results. The flowchart of our method is shown in Figure 6.

The initial values of the parameters are set according to the algorithmic characteristics and parameter-adjustment experience of different models, and the grid search provided by scikit learn is used for super parameter optimization. In this paper, the base model of random forest is DTR, and the alternative values of the number of DTRs are set as 10, 20, 30, 40 and 50. Other super parameters such as the maximum number of samples and the minimum number of segmented samples of the leaf nodes use the default minimum value. The final number of DTRs is 20. The stopping criterion is met if there is no improvement in the R^2 after ten iterations, in combination with a maximum number of iterations equal to 500. The optimal parameters of FFANN-BP are that the least mean square error as 0.001, max training time as 1000, and learning rate as 0.15. The size of the network and learning parameters greatly affect prediction performance. The best network structure trained is

5 input nodes and 12 hidden nodes. The output layer has only one neuron, corresponding to the air pollutant concentrations. It has been demonstrated that the BFGS algorithm is the most efficient method to solve the optimization of the object function because of its speed and robustness. Due to space constraints, this paper only shows the experimental results of Ma Lian Kou air monitoring station.

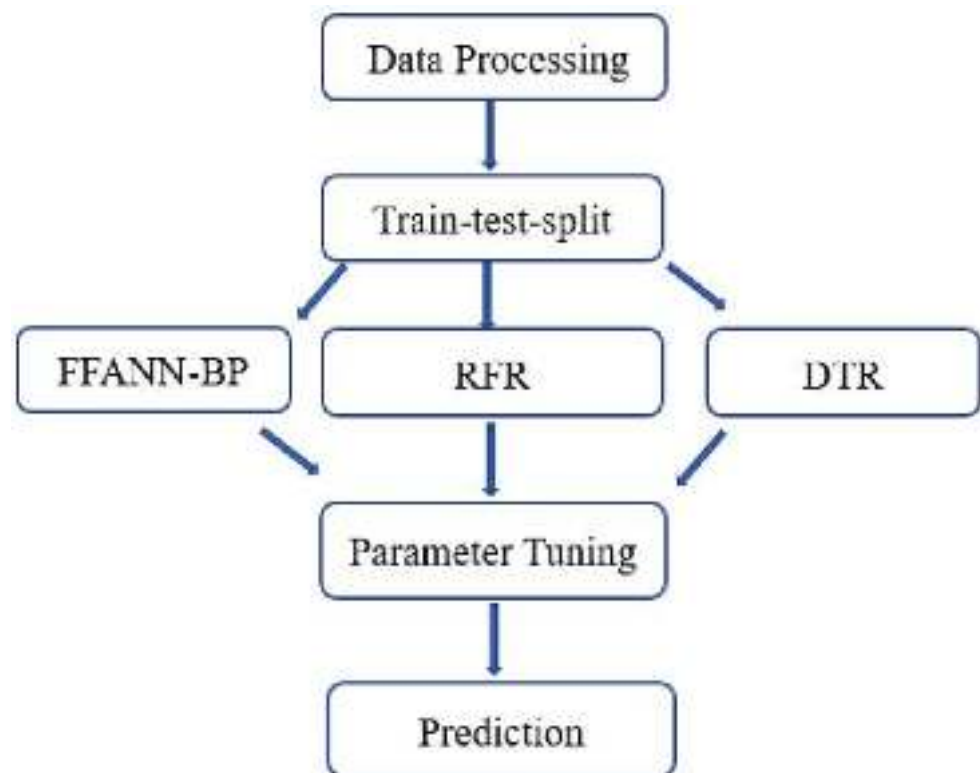


Figure 6. The flowchart of our method.

To verify the performances of the DTR, FFANN-BP and RFR used in this study, Table 6 shows the RMSE, R^2 , MAE and MAPE between the measured and predicted values of air pollutant concentrations of the above three models at Ma Lian Kou, Sha Po Tou and Ma Yuan air monitoring stations. The R^2 of the three machine learning models is between 0.44 and 0.99, it is shown that the values of these statistical parameters for the three models are all within the recommended range. The RMSE of each model is between 0.25 and 126.7, and the RMSE of the RFR model is the lowest. Compared with the MAE, the RFR model has the lowest MAE of 6.93, followed by the FFANN-BP model of 7.74, and the DTR model has the highest MAE of 10.6. For MAPE, the RFR model is also the lowest among the three models of 17.56. It can be found that RFR shows good experimental results. The time series plots are also shown in Figure 7 to depict the relationships between the observed and predicted data. These results indicate the important goodness of fit of the RFR to the observed data. Following the same methodology, fitting were also made for the other air pollutants as dependent variables using DTR, FFANN-BP and RFR with the results as follows. It is shown that RFR is the best model for predicting the concentration of air pollutant concentrations in the three air monitoring stations at a local scale, since the correlation coefficient of RFR equal to 0.99.

The time series plot of the ground measured air pollutant concentrations and the predictions by DTR, FFANN-BP and RFR are shown in Figures 7–9. It can be observed that there is a higher agreement between the observed and predicted data. It is also shown that the predicted concentrations of RFR are closer to the observed data than those of the DTR and FFANN-BP, meaning that the RFR improves the predicted performance of air pollutant concentrations. We also employ the histograms to provide further insight into

the relationship of the predictors with air pollutant concentrations in Figures 10–12. RFR for air pollutant concentrations is very good since the histogram of RMSE is very steep and it is also considerable for the other pollutants in Figures 10–12. At the same time, according to the construction time of the models, RMSE, MAE, MAPE are analyzed to evaluate the model. The prediction accuracy and model construction efficiency of different machine learning models are compared and analyzed. Appropriate variables are selected for the prediction of air pollutant concentrations. In terms of prediction accuracy, the RFR model has the best prediction ability, followed by the FFANN-BP model, and the DTR model. RFRs have stable accuracy and good prediction capability. The results show that RFR not only increases the performance of the prediction of air pollutant concentrations in Ningxia, but also discriminates the influential factors and reduces the dimension of the data, therefore reduces the time complexity of the algorithm.

Table 6. The predicted performance of the DTR, FFANN-BP and RFR model for the concentrations of six air pollutants at Ma Lian Kou, Sha Po Tou and Ma Yuan in 2016.

Air	Statistical	Ma Lian Kou				Sha Po Tou				Ma Yuan			
Pollutants	Index	R^2	RMSE	MAE	MAPE	R^2	RMSE	MAE	MAPE	R^2	RMSE	MAE	MAPE
CO	DTR	0.70	0.25	0.21	0.31	0.61	0.47	0.33	0.38	0.46	0.63	0.51	0.66
	FFANN-BP	0.71	0.24	0.18	0.31	0.70	0.23	0.16	0.19	0.61	0.32	0.24	0.33
	RFR	0.90	0.15	0.12	0.20	0.91	0.14	0.10	0.11	0.62	0.45	0.20	0.21
NO ₂	DTR	0.66	6.2	5.4	0.47	0.51	8.0	6.7	0.28	0.47	7.8	6.4	0.25
	FFANN-BP	0.72	4.5	3.4	0.29	0.76	5.3	4.2	0.17	0.75	5.3	4.4	0.17
	RFR	0.95	1.8	1.4	0.12	0.83	4.3	3.4	0.14	0.87	4.0	3.2	0.13
O ₃	DTR	0.54	23.9	16.1	0.17	0.70	16.3	13.4	0.24	0.52	20.2	16.5	0.37
	FFANN-BP	0.67	20.3	12.2	0.12	0.86	12.1	9.1	0.16	0.89	9.7	7.8	0.16
	RFR	0.89	12.2	8.6	0.09	0.95	7.3	5.6	0.11	0.94	8.4	6.8	0.15
PM _{2.5}	DTR	0.73	21.2	16.3	0.25	0.72	99.1	42.3	0.32	0.67	45.4	23.0	0.23
	FFANN-BP	0.81	18.1	13.9	0.21	0.44	126.7	50.5	0.35	0.76	43.0	22.6	0.23
	RFR	0.96	9.2	6.1	0.09	0.97	57.9	25.3	0.26	0.92	30.4	13.2	0.18
PM ₁₀	DTR	0.82	8.6	6.5	0.22	0.79	17.8	12.4	0.32	0.88	8.6	6.3	0.20
	FFANN-BP	0.64	13.7	9.4	0.30	0.90	12.8	8.8	0.26	0.81	10.6	6.9	0.21
	RFR	0.98	3.5	2.4	0.09	0.94	12.2	7.7	0.23	0.97	4.9	3.9	0.14
SO ₂	DTR	0.81	15.5	10.4	0.42	0.51	23.8	16.3	0.55	0.86	4.2	2.9	0.27
	FFANN-BP	0.76	16.3	11.7	0.55	0.83	14.5	9.6	0.34	0.61	8.8	4.5	0.38
	RFR	0.99	4.5	3.4	0.18	0.92	11.0	5.8	0.17	0.98	1.8	1.3	0.15

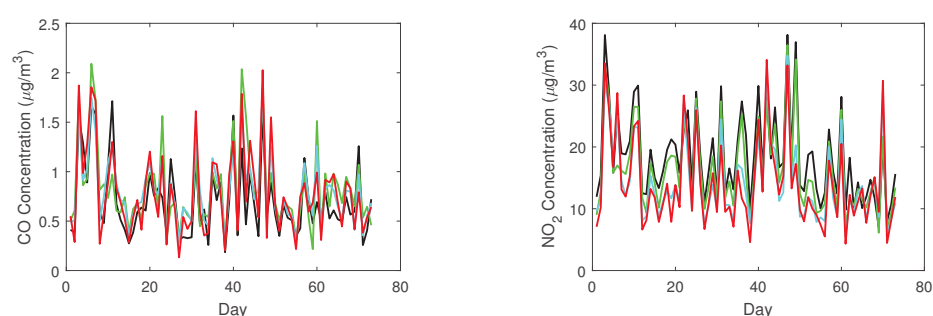


Figure 7. The observed concentrations and the predicted concentrations of DTR, FFANN-BP and RFR for CO and NO₂ at Ma Lian Kou, where the red line and the black, green and lightcyan lines represent the observations, and the predictions of DTR, FFANN-BP and RFR, respectively.

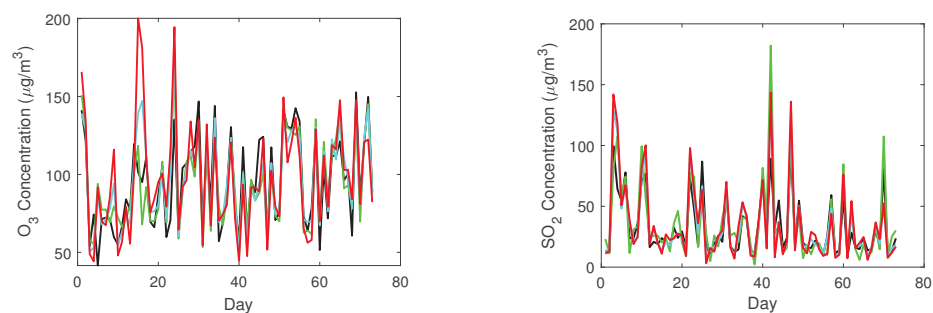


Figure 8. The observed concentrations and the predicted concentrations of DTR, FFANN-BP and RFR for O_3 and SO_2 at Ma Lian Kou, where the red line and the black, green and lightcyan lines represent the observations, and the predictions of DTR, FFANN-BP and RFR, respectively.

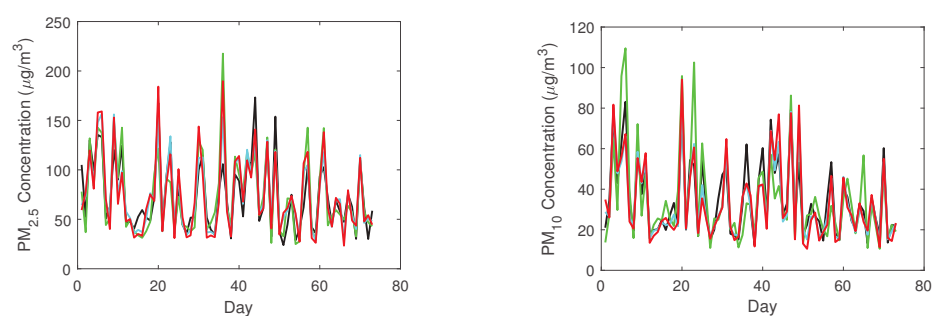


Figure 9. The observed concentrations and the predicted concentrations of DTR, FFANN-BP and RFR for $PM_{2.5}$ and PM_{10} at Ma Lian Kou, where the red line and the black, green and lightcyan lines represent the observations, and the predictions of DTR, FFANN-BP and RFR, respectively.

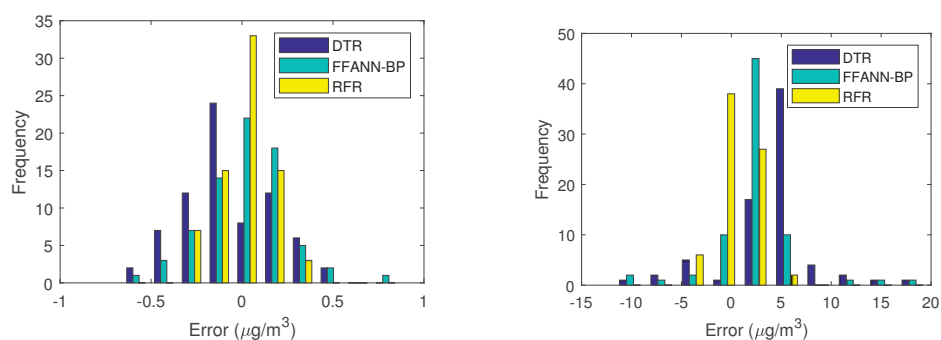


Figure 10. The error histogram of the prediction for CO and NO_2 at Ma Lian Kou.

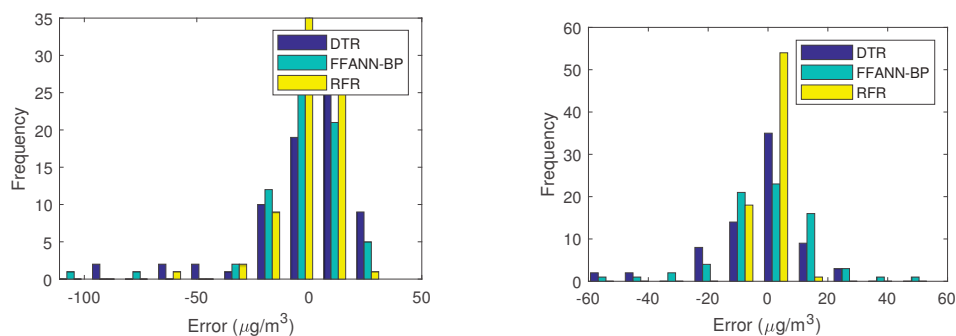


Figure 11. The error histogram of the prediction for O_3 and SO_2 at Ma Lian Kou.

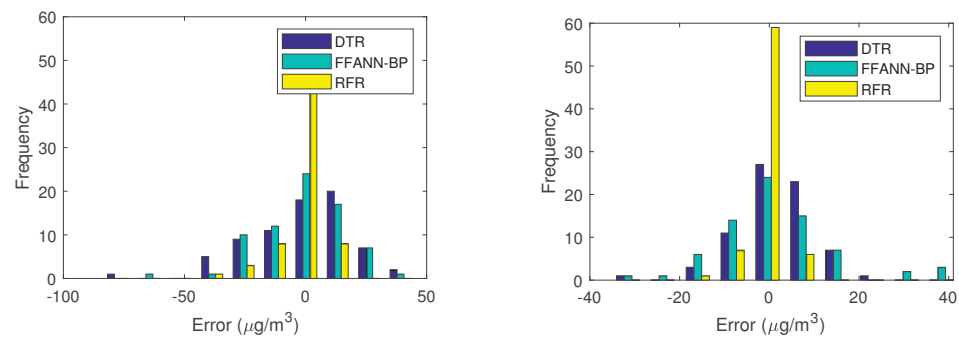


Figure 12. The error histogram of the prediction for $PM_{2.5}$ and PM_{10} at Ma Lian Kou.

RFR uses the average reduction of node impurity to describe the importance of the variables. The greater the reduction of node impurity by a factor, the more important the factor becomes. The importance of variables in the decision tree model is measured in the form of weight. The greater the weight of a factor, the stronger the influence of the factor in affecting the concentration of air pollutants. In this research, the importance of each factor on the prediction of air pollutant concentration is further analyzed. Figures 13–15 and Table 7 show the analysis of the most important features of DTR and RFR for six air pollutant at Ma Lian Kou. The characteristic variables considered include meteorological factors, air pollutant concentrations of the previous day.

For CO , it can be seen that the concentrations of NO_2 rank first and contribute the most. For NO_2 , it can be seen that PM_{10} concentrations rank first and contribute the most. For O_3 , it can be seen that ground surface temperature ranks first and contributes the most. For SO_2 , it can be seen that NO_2 concentration ranks first and contributes the most. For $PM_{2.5}$, it can be seen that PM_{10} concentration ranks first and contributes the most. For PM_{10} , it can be seen that $PM_{2.5}$ concentration ranks first and contributes the most. As shown in Table 5, the weight importance of temperature, relative humidity and air pressure are 14 and 25 in turn, indicating that ground surface temperature and relative humidity have the greatest impact on the concentration of air pollutants predicted by DTR, followed by air pressure and precipitation, and wind speed has the least impact. Figures 13–15 and Table 7 shows the importance analysis of various influencing factors when we use decision tree and random forest algorithm to predict the concentration of various air pollutants in 2016. As shown in Figures 13–15 and Table 7, for CO , NO_2 is the most important factors in both methods. For NO_2 , PM_{10} is the most important factor. For ozone, the ground surface temperature is the most important factor. $PM_{2.5}$ and PM_{10} are the most important influencing factors for each other. NO_2 is the most important factor in the prediction of SO_2 .

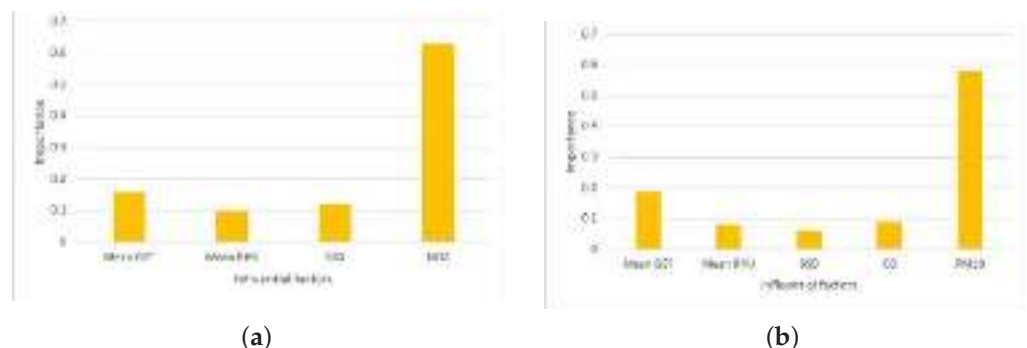


Figure 13. The importance of predictor variables of RFR for (a) CO and (b) NO_2 at Ma Lian Kou.

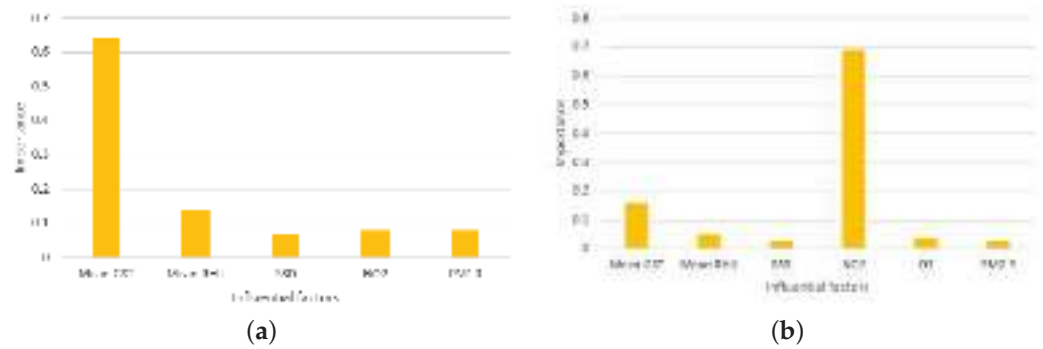


Figure 14. The importance of predictor variables of RFR for (a) O_3 and (b) SO_2 at Ma Lian Kou.

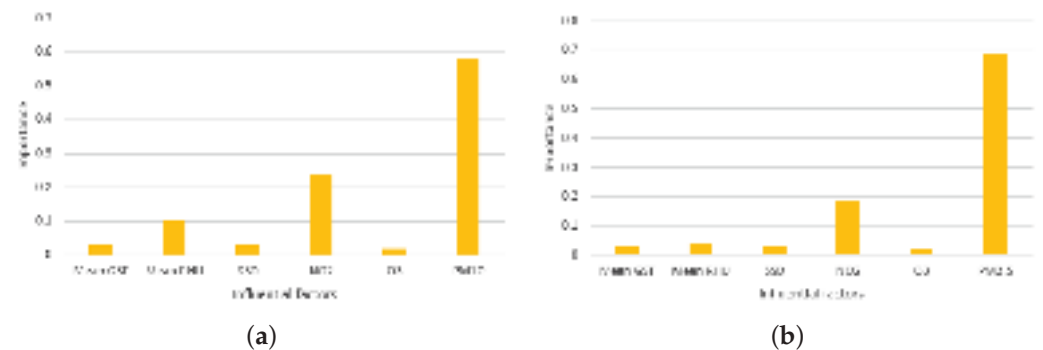


Figure 15. The importance of predictor variables of RFR for (a) $PM_{2.5}$ and (b) PM_{10} at Ma Lian Kou.

Table 7. The importances of influential factor at Ma Lian Kou in 2016.

Pollutants	Index	Mean GST	Mean RHU	SSD	NO_2	O_3	$PM_{2.5}$	PM_{10}
CO	DTR	0.01	0.0	0.0	0.99			
	RFR	0.16	0.1	0.12	0.63			
NO_2	DTR	0.19	0.12	0.07		0.08		0.55
	RFR	0.19	0.08	0.06		0.09		0.58
O_3	DTR	0.61	0.14	0.07	0.09			0.1
	RFR	0.64	0.14	0.07	0.08			0.08
$PM_{2.5}$	DTR	0.03	0.04	0.03	0.33	0.01		0.57
	RFR	0.03	0.1	0.03	0.24	0.02		0.58
PM_{10}	DTR	0.02	0.02	0.02	0.16	0.05	0.73	
	RFR	0.03	0.04	0.03	0.19	0.02	0.69	
SO_2	DTR	0.17	0.06	0.05	0.66	0.04	0.03	
	RFR	0.16	0.05	0.03	0.69	0.04	0.03	

Mean GST, Mean RHU and SSD represent the average ground surface temperature, average relative humidity and sun shine duration, respectively.

Table 8 shows the running time of the three algorithms on the concentrations of six pollutants in Ma Lian Kou in 2016. It can be seen from the Table 8 that the running time of DTR is the shortest due to its simple structure, FFANN-BP model takes the longest time to build, followed by RFR model. The running time of RFR is much lower than that of FFANN-BP. This is enough to reflect that RFR has low time complexity.

Due to the randomness of the three methods, the accuracy of the three methods cannot be evaluated by one experimental result. Therefore, this paper runs 1000 Monte Carlo experiments and takes the average of the running results to evaluate the accuracy of the three methods. The results in Table 9 show that the accuracy and prediction stability of RFR are better than the other two methods.

Table 8. The runtime of the three algorithm at Ma Lian Kou in 2016, all in (s).

	FFANN-BP	DTR	RFR
CO	0.058	0.002	0.032
NO ₂	0.242	0.002	0.034
O ₃	0.303	0.002	0.034
PM _{2.5}	0.349	0.002	0.04
PM ₁₀	0.206	0.002	0.038
SO ₂	0.364	0.002	0.038

Table 9. The mean, variance and the confidence interval of the predicted concentrations for six air pollutants based on 1000 Monte Carlo experiments at Ma Lian Kou in 2016.

	Mean	Variance	CI _l	CI _u
CO	0.65	0.14	0.42	0.85
NO ₂	4.4	0.73	3.1	6.8
O ₃	85.8	11.7	60.7	100.9
PM _{2.5}	33.9	8.5	28.8	34.1
PM ₁₀	135.9	22.8	91.8	156.9
SO ₂	1.9	0.8	1.2	6.6

The performances achieved highlight that for the extreme concentrations of air pollutants, the performance of the DTR is not significant. The reason is that the construction project of this period is particularly high in Ningxia. However, RFR still acceptedly performs even with the sudden occurrence of such event. For the particulate matter, we find the decrease in performance of DTR and FFANN-BP, making the variance of the concentrations of the particulate matter larger. However, RFR is still more adaptable than FFANN-BP and DTR. It shows that the DTR model has poor prediction ability in using the meteorological elements to predict air pollutant concentrations, and it is recommended to use the RFR model to predict air pollutant concentrations.

5. Conclusions

In this study, Ningxia Province, where air pollution has been increasing in recent years, is selected as the research area. It is shown that the concentrations of CO, PM₁₀ and PM_{2.5} were higher in the cold and dry winter than those in summer because of the combustion of fossil fuels for heating purposes. The aim of this study was to propose a modelling procedure that would yield satisfactory results for the prediction of ambient air pollutant concentrations. In this work DT, FFANN-BP and RFR models were proposed for predicting the air pollutant concentrations in Ningxia, China. The levels of air pollutant concentrations were observed in three air monitoring stations, the capital of Ningxia and the rural areas of Ningxia.

The collected data for air pollutant concentrations and meteorological variables were used for the development of DTR, FFANN-BP and RFR. Data was prepared by calculating the average of the air pollutant concentrations for each day of the study period. Compared with DTR and FFANN-BP, it is evident that RFR is superior to the other methods. Furthermore, the proposed method has been successfully applied to the analysis of the importance of the predictors. We conducted an uncertainty analysis based on Monte Carlo experiments. The proposed method has worked well in predicting the air pollutant concentrations and can be effectively utilized for the analysis of the importance of the predictors. It reveals that there is a close relationship between air pollutant concentrations and meteorological variables. Hence, the developed model is capable of generating better forecasting performance for air pollutant concentrations. Because of the generality of the algorithm, it can be applied to other area and databases.

It can be incorporated into the control and management for a cleaner air and a better environment in many cities. Furthermore, we will consider other ways of using the spatial and meteorological conceptions. Our future research work will focus on the improvement and optimization of machine learning models. Multimodal analysis can effectively decompose the time periodic change trend and noise of air pollutant concentration. Therefore, the introduction of multimodal analysis into random forest regression model can effec-

tively improve the prediction accuracy and the prediction of air pollutant concentration in extreme pollution weather, which will be a problem to be solved in the future.

Author Contributions: Funding acquisition, W.D.; Investigation, W.D.; Methodology, X.Q.; Resources, X.Q.; Supervision, X.Q.; Visualization, W.D. All authors have read and agreed to the published version of the manuscript.

Funding: This work was supported by the Ningxia Natural Science Foundation under Grant no. 2021AAC03223, the National Natural Science Foundation of China under Grant no. 11761002, First-Class Disciplines Foundation of Ningxia under Grant NXYLXK2017B09, Western light project of Chinese Academy of Sciences: Application of big data analysis technology in air pollution assessment.

Institutional Review Board Statement: Not applicable.

Informed Consent Statement: Not applicable.

Data Availability Statement: Not applicable.

Conflicts of Interest: The authors declare no conflict of interest.

References

1. Berg, A.; McColl, K.A. No projected global dry lands expansion under greenhouse warming. *Nat. Clim. Chang.* **2021**, *11*, 331–337. [CrossRef]
2. Liao, Z.; Gao, M.; Sun, J.; Fan, S. The impact of synoptic circulation on air quality and pollution-related human health in the Yangtze River Delta region. *Sci. Total Environ.* **2017**, *607*, 838–846. [CrossRef]
3. Pang, Y.; Huang, W.; Luo, X.; Chen, Q.; Zhan, Z.; Tang, M.; Hong, Y.; Chen, J.; Li, H. In-vitro human lung cell injuries induced by urban $PM_{2.5}$ during a severe air pollution episode: Variations associated with particle components. *Ecotoxicol. Environ. Saf.* **2020**, *206*, 111406. [CrossRef]
4. Shang, Y.; Sun, Z.; Cao, J.; Wang, X.; Zhong, L.; Bi, X.; Li, H.; Liu, W.; Zhu, T.; Huang, W. Systematic review of Chinese studies of short-term exposure to air pollution and daily mortality. *Environ. Int.* **2013**, *54*, 100–111. [CrossRef]
5. Shaddick, G.; Thomas, M.L.; Amini, H. Data integration for the assessment of population exposure to ambient air pollution for global burden of disease assessment. *Environ. Sci. Technol.* **2018**, *52*, 9069–9078. [CrossRef]
6. Zhang, J.S.; Ding, W.F. Prediction of air pollutants concentration based on extreme learning machine: The case of Hong Kong. *Int. J. Environ. Sci. Public Health* **2017**, *7*, 114. [CrossRef]
7. Dennis, R.L.; Byun, D.W.; Novak, J.H. The next generation of integrated air quality modeling: EPA's models-3. *Atmos. Environ.* **1996**, *30*, 1925–1938. [CrossRef]
8. Wang, Z.F.; Xie, F.Y.; Wang, X.Q. Development and application of nested air quality prediction modeling system. *Atmos. Sci.* **2006**, *31*, 778–790.
9. Batterman, S.A.; Zhang, K.; Kononowech, R. Prediction and analysis of near-road concentrations using a reduced-form emission/dispersion model. *Environ. Health* **2010**, *9*, 29. [CrossRef]
10. Abal, G.; Aicardi, D.; Suarez, R.A.; Laguarda, A. Performance of empirical models for diffuse fraction in uruguay. *Sol. Energy* **2017**, *141*, 166–181. [CrossRef]
11. Briant, R.; Seigneur, C.; Gadrat, M.; Bugajny, C. Evaluation of roadway gaussian plume models with large-scale measurement campaigns. *Geosci. Model.* **2013**, *6*, 445–456. [CrossRef]
12. Mishra, D.; Goyal, P. Development of artificial intelligence based NO₂ forecasting models at Taj Mahal, Agra centre for atmospheric sciences. *Atmos. Pollut. Res.* **2015**, *6*, 99–106. [CrossRef]
13. Pahlavani, P.; Sheikhan, H.; Bigdeli, B. Assessment of an air pollution monitoring network to generate urban air pollution maps using Shannon information index, fuzzy overlay, and Dempster-Shafer theory, A case study: Tehran, Iran. *Atmos. Environ.* **2017**, *167*, 254–269. [CrossRef]
14. Sayegh, A.S.; Munir, S.; Habeebullah, T.M. Comparing the performance of statistical models for predicting PM_{10} concentrations. *Aerosol. Air Qual. Res.* **2014**, *14*, 653–665. [CrossRef]
15. Chen, Y.; Zheng, W.; Li, W.; Huang, Y. Large group activity security risk assessment and risk early warning based on random forest algorithm. *Pattern Recognit. Lett.* **2021**, *144*, 1–5. [CrossRef]
16. Danesh Yazdi, M.; Kuang, Z.; Dimakopoulou, K.; Barratt, B.; Suel, E.; Amini, H.; Schwartz, J. Predicting fine particulate matter ($PM_{2.5}$) in the greater London area: An ensemble approach using machine learning methods. *Remote Sens.* **2020**, *12*, 914. [CrossRef]
17. Ding, W.F.; Zhang, J.S. Prediction of air pollutant concentration based on sparse response backpropagation training feedforward neural networks. *Environ. Sci. Pollut. Res.* **2016**, *23*, 19481–19494. [CrossRef]
18. Ding, W.; Leung, Y.; Zhang, J.; Fung, T. A hierarchical Bayesian model for the analysis of space-time air pollutant concentrations and an application to air pollution analysis in Northern China. *Stoch. Environ. Res. Risk Assess.* **2021**, *35*, 2237–2271. [CrossRef]

19. Joharestani, M.Z.; Cao, C.; Ni, X.; Bashir, B.; Talebiesfandarani, S. PM_{2.5} Prediction based on random forest, XGBoost, and deep learning using multisource remote sensing data. *Atmosphere* **2019**, *10*, 373. [CrossRef]
20. Sanchez, A.B.; Ordóñez, C.; Lasheras, F.S.; de Cos Juez, F.J.; Roca-Pardias, J. Forecasting SO₂ pollution incidents by means of elman artificial neural networks and ARIMA models. In *Abstract and Applied Analysis*; Hindawi: London, UK, 2013; pp. 1–6.
21. Li, L.; Zhang, J.; Qiu, W.; Wang, J.; Fang, Y. An ensemble spatiotemporal model for predicting PM_{2.5} concentrations. *Int. J. Environ. Res. Public Health* **2017**, *14*, 549. [CrossRef]
22. Liu, N.; Zou, B.; Li, S.; Zhang, H.; Qin, K. Prediction of PM_{2.5} concentrations at unsampled points using multiscale geographically and temporally weighted regression. *Environ. Pollut.* **2021**, *284*, 117116. [CrossRef]
23. Alimissis, A.; Philippopoulos, K.; Tzani, C.G. Spatial estimation of urban air pollution with the use of artificial neural network models. *Atmos. Environ.* **2018**, *191*, 205–213. [CrossRef]
24. Bahari, R.A.; Abbaspour, R.A.; Pahlavani, P. Prediction of PM_{2.5} concentrations using temperature inversion effects based on an artificial neural network. In Proceedings of the ISPRS International Conference of Geospatial Information Research, Tehran, Iran, 15–17 November 2014; Volume 15, p. 17.
25. Feng, X.; Li, Q.; Zhu, Y.; Hou, J.; Jin, L.; Wang, J. Artificial neural networks forecasting of PM_{2.5} pollution using air mass trajectory based geographic model and wavelet transformation. *Atmos. Environ.* **2015**, *107*, 118–128. [CrossRef]
26. Valentini, G. *Ensemble Methods: A Review, in Advances in Machine Learning and Data Mining for Astronomy*; Chapman & Hall Data Mining and Knowledge Discovery Series; CRC Press: London, UK, 2012; Volume 26, pp. 563–594.
27. Calkins, C.; Ge, C.; Wang, J.; Anderson, M.; Yang, K. Effects of meteorological conditions on sulfur dioxide air pollution in the North China plain during winters of 2006–2015. *Atmos. Environ.* **2016**, *147*, 296–309. [CrossRef]
28. Harishkumar, K.; Yogesh, K.; Gad, I. Forecasting air pollution particulate matter (PM_{2.5}) using machine learning regression models. *Procedia Comput. Sci.* **2020**, *171*, 2057–2066.
29. Tobler, W.R. A Computer Movie Simulating Urban Growth in the Detroit Region. *Econ. Geogr.* **1970**, *46* (Supp. 1), 234–240. [CrossRef]
30. Ningxia Government. Overview of Ningxia. Available online: [cn.nxcan.com/index.php?case=archive&&\\$act=show&&\\$aid=55](http://cn.nxcan.com/index.php?case=archive&&$act=show&&$aid=55) (accessed on 6 July 2015).
31. Ningxia Government. Ningxia Meteorology. Available online: <https://sthjt.nx.gov.cn> (accessed on 8 August 2014)
32. Sergey, I.; Christian, S. Batch normalization: Accelerating deep network training by reducing internal covariate shift. In Proceedings of the 32nd International Conference on Machine Learning, Lille, France, 6–11 July 2015; pp. 448–456.
33. Bishop, C. *Neural Networks for Pattern Recognition*, 3rd ed.; Oxford University Press: Oxford, UK, 1995.
34. Scikit-Learn: Machine Learning in Python. Available online: <https://scikit-learn.org/stable/> (accessed on 9 September 2016).
35. Hastie, T.; Tibshirani, R.; Friedman, J. The elements of statistical learning. *J. R. Stat. Soc.* **2004**, *167*, 192.

Article

Haze Grading Using the Convolutional Neural Networks

Lirong Yin ¹, Lei Wang ¹ , Weizheng Huang ², Jiawei Tian ² , Shan Liu ² , Bo Yang ² and Wenfeng Zheng ^{2,*} 

¹ Department of Geography and Anthropology, Louisiana State University, Baton Rouge, LA 70803, USA; lyin5@lsu.edu (L.Y.); leiwang@lsu.edu (L.W.)

² School of Automation, University of Electronic Science and Technology of China, Chengdu 610054, China; huangwz12@163.com (W.H.); jravis.tian23@gmail.com (J.T.); shanliu@uestc.edu.cn (S.L.); boyang@uestc.edu.cn (B.Y.)

* Correspondence: winfirms@uestc.edu.cn or wenfeng.zheng.cn@gmail.com

Abstract: As an air pollution phenomenon, haze has become one of the focuses of social discussion. Research into the causes and concentration prediction of haze is significant, forming the basis of haze prevention. The inversion of Aerosol Optical Depth (AOD) based on remote sensing satellite imagery can provide a reference for the concentration of major pollutants in a haze, such as PM_{2.5} concentration and PM₁₀ concentration. This paper used satellite imagery to study haze problems and chose PM_{2.5}, one of the primary haze pollutants, as the research object. First, we used conventional methods to perform the inversion of AOD on remote sensing images, verifying the correlation between AOD and PM_{2.5}. Subsequently, to simplify the parameter complexity of the traditional inversion method, we proposed using the convolutional neural network instead of the traditional inversion method and constructing a haze level prediction model. Compared with traditional aerosol depth inversion, we found that convolutional neural networks can provide a higher correlation between PM_{2.5} concentration and satellite imagery through a more simplified satellite image processing process. Thus, it offers the possibility of researching and managing haze problems based on neural networks.

Keywords: CNN; MODIS; PM_{2.5}; haze forecast; aerosol optical depth; air pollution

Citation: Yin, L.; Wang, L.; Huang, W.; Tian, J.; Liu, S.; Yang, B.; Zheng, W. Haze Grading Using the Convolutional Neural Networks. *Atmosphere* **2022**, *13*, 522. <https://doi.org/10.3390/atmos13040522>

Academic Editors: Duanyang Liu, Kai Qin, Honglei Wang and Rajasekhar Balasubramanian

Received: 18 January 2022

Accepted: 22 March 2022

Published: 25 March 2022

Publisher's Note: MDPI stays neutral with regard to jurisdictional claims in published maps and institutional affiliations.



Copyright: © 2022 by the authors. Licensee MDPI, Basel, Switzerland. This article is an open access article distributed under the terms and conditions of the Creative Commons Attribution (CC BY) license (<https://creativecommons.org/licenses/by/4.0/>).

1. Introduction

The main component of haze is fine particulate matter (PM_{2.5}), an organic compound of toxic substances such as heavy metals and carcinogens. It is the most harmful air pollution to the human body because it can directly enter the lungs [1–3]. In recent years, more and more people have paid close attention to its environmental damage and influence on the human body in large urban areas [4–6].

With the increased attention on haze, the harm it does to the human body is gradually being revealed. Therefore, the research on haze becomes deeper and more diverse [7–11]. Predominant questions involve the causes of haze, pollution composition, time distribution, regional distribution, and management programs. The research methods also span multiple disciplines such as chemical analysis, biological testing, economic development, and haze data mining.

Because of the improved human aerospace technology and remote sensing satellite technology in recent years, the cost of remote sensing satellite imagery has been reduced. It is more macroscopic than the traditional ground station monitoring data. The satellite images provide the information of the temporal and spatial changes of haze comprehensively and quickly [12–18]; therefore, researchers utilize remote sensing images in the monitoring and analysis of haze. Researchers often use remote sensing satellite images for the inversion of Aerosol Optical Depth (AOD) and further analyze meteorological features based on the correlation between aerosol depth and atmospheric pollutant concentrations. McGowan et al. [19] proposed a PM₁₀ dust concentration of a 500 m vertical

profile measured during a regional dust event in western Queensland, Australia, based on MODIS Terra satellite data and a spatiotemporal analysis. Guo et al. [20] used a correlation analysis between the PM_{2.5} concentration ground haze monitoring stations in China during 2007 and 2008 and the AOD obtained from the satellite remote sensing image. They also discussed the feasibility of satellite remote sensing technology for estimating the haze concentration on the ground. Nordio et al. [21] used MODIS data to study the correlation between aerosol and PM₁₀ concentration in Lombardy, Italy, and successfully used aerosol data to predict the haze concentration. Seo et al. [22] compared the aerosol depth based on ground monitoring stations and MODIS satellite images to PM₁₀ concentrations in Seoul, Korea. It was concluded that MODIS images are more relevant than ground monitoring stations, especially in winter.

Another emerging approach to haze research is machine learning. Machine learning methods, especially the rapid development of neural networks, have shown researchers great potential to fit complex functions. Therefore, some studies have used haze detection data to train neural networks to predict haze concentrations. For example, Pérez et al. [23] used the neural network structure to predict and analyze the average concentration of haze in the San Diego area in the next few hours. Grivas et al. [24] optimized the structure and parameters of the neural network based on the previous Pérez study to predict the concentration of PM₁₀. With the continuous optimization of the network, many scholars have used neural networks to predict and analyze the haze in time series [25–28].

Comparing the two haze analysis methods, estimating the concentration of haze pollutants, such as PM_{2.5} and PM₁₀, using the inversion of AOD on remote sensing satellite images has a broader research background and relative higher precision. However, the data preprocessing for obtaining AOD from satellite images is very complicated and often requires steps such as radiation correction, geometric correction, and processing angle data for satellite images. By contrast, neural networks have powerful feature capture capabilities and flexible adjustment capabilities using these learned features. These characteristics allow neural networks to use simplified data processing compared with traditional inversion methods. Moreover, the neural network excels in complex function fitting, making it easy to fit uncertain function expressions or expressions with complex parameters. In the study of haze, PM_{2.5} concentration prediction is a complex function fitting problem, since the concentration of other major pollutants such as PM_{2.5} depends on many complicated meteorological and human factors.

This paper aims to simplify complex data processing in traditional AOD inversion methods by using the feature capture ability and complex function fitting ability of neural networks by training a haze-level classification network. We directly use remote sensing satellite images as input and use convolutional neural networks as training models to classify the level of haze concentration. This paper compares the results from two methods, one using a traditional AOD inversion method, and the other the proposed neural networks inversion method. Experiments show that the proposed network can reduce the manual inversion work, and also achieves good results in fitting the non-linear relationship between the data and the haze concentration level.

2. Research Area and Dataset

2.1. Research Area

The air pollutant monitoring stations in the Beijing area mainly detect the concentration of various air pollutant gases (such as carbon monoxide, sulfur dioxide, and ozone) and PM₁ and PM_{2.5}. These monitoring stations are distributed in various districts of Beijing, as shown in Figure 1. The data and monitoring records collected by the monitoring points will be published in real-time for easy access and research.

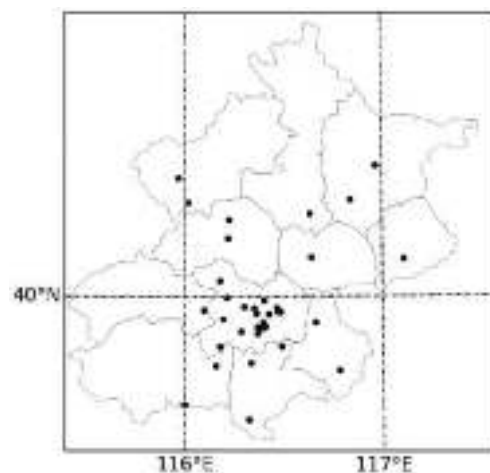


Figure 1. Distribution map of monitoring stations in Beijing.

There are also some objective reasons for selecting the Beijing area for study. The Beijing area is one of the more effective observation points of NASA's meteorological satellites, and it is also the network point of the ground aerosol automatic observation network (AREONET). Therefore, different data can be used for comparison. Moreover, Beijing is the capital of China, with a relatively high population density and frequent haze. Therefore, the significance and feasibility of the research are high.

2.2. Dataset

Satellite remote sensing data has solid spatial coverage. In remote sensing science, researchers invert images to obtain AOD and haze concentrations.

This paper hopes to simplify the data processing and replace the traditional AOD inversion method using the fitting ability of convolutional neural networks, and construct an end-to-end haze level prediction network. Considering the experimental needs, we collect several highly relevant experimental data:

- (1) MOD02-1 km data for the Beijing area in 2013 and 2014. The MOD02-1 km is a satellite remote sensing image product of MODIS. The latitude and longitude are calibrated based on the original data. Subsequently, we will preprocess it and use the preprocessed data as training and testing data for the traditional inversion method of AOD and the haze level prediction network.
- (2) Real-time haze concentration data covering the entire Beijing area in 2013. We will preprocess the dataset to obtain the haze level and use this to mark the satellite imagery of the 2013 Beijing area to build a complete training set.
- (3) Real-time haze concentration data covering the entire Beijing area in 2014. The data include real-time PM_{2.5} concentrations and PM₁₀ concentrations per hour for each day in 2014, and Air Quality Index (AQI) information. The data come from 36 automatic monitoring stations for atmospheric pollutants covering the entire main area of Beijing. The data will verify the correlation between haze concentration and AOD.
- (4) AREONET ground monitoring aerosol data are used to verify the accuracy of aerosol inversion. This observatory will also provide three levels of data: Level 1.0 (un-screened), Level 1.5 (cloud-screened and quality controlled), and Level 2.0 (quality-assured). Among them, the observation accuracy of the AOD of L2 data is the highest.
- (5) Remote sensing image products from AQUA and TERRA satellites equipped with MODIS. The MODIS product models are: MOD02-1 km (MYD-021 km) and MOD04-3 k (MYD04-3 k), secondary satellite products, and processed aerosol products. MOD02-1 km belongs to the L1b product, the original data after the latitude and longitude calibration, while MOD04-3 km is the processed second-level product containing multiple aerosol products.

3. Comparison with Traditional Method

In order to determine the type of data that can provide information regarding the haze concentration and the type of input data of the convolutional neural network, it is necessary to study the data used in the traditional inversion method. Then, from the data processing process used in the traditional method, the data type and processing method required by the convolutional neural network are analyzed and obtained. This section presents the traditional method selected to set up the convolutional neural network in order to obtain the required information. The method will also be used to examine the performance of the proposed neural network method.

The data processing process in the traditional method is as follows:

- (1) Radiation correction: We used ENVI5.0 to read data from MOD02-1 km, and the software automatically radiated and corrected the data.
- (2) Geometric correction: We used the MODIS data processing tool, Georeference MODIS in the ENVI software, to geometrically correct the data of the emissivity channel. In the calibration, we selected the Beijing coordinate system in the World Geodetic System 1984 (WGS-84) standard to geometrically correct the emissivity file and establish Ground Control Points (GCPs) as the standard for other channels to maintain consistent geometric correction results. We used GCPs generated by the emissivity to correct the reflectance file. After reading the GCPs, the triangulation correction method and the bilinear resampling method were selected so that the correction result of the reflectance can match the emissivity.
- (3) Interest area extraction and synthesis: We selected the administrative regional geographic graphic document (shapefile) in the Global Administrator Areas Database (GADM). According to the administrative area of Beijing: 39.4 N~41.1 N; 115.4~117.4 E, we tailored the emissivity and reflectivity file, which kept the consistency of the administrative scope and the size of the processed data. After the region of interest was synthesized, the emissivity channel files were placed at the top, and the reflectivity channel files were placed at the bottom. The result of the image processing is shown in Figure 2.

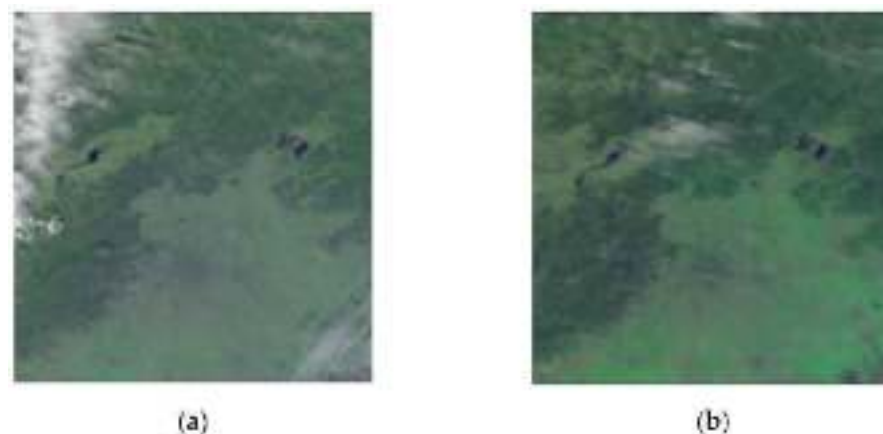


Figure 2. Corrected remote sensing images. Here, (a,b) are two remote sensing images with different haze levels on different dates. The corrected results show that the size and range of the images are the same.

- (4) The processing of angle data: First, we used the ground control point file to correct the angle dataset geometrically and used the shape-file cutting angle data of the Beijing area, and then synthesized the angle data according to the order of the solar zenith angle, the solar azimuth angle, the satellite zenith angle, and the satellite azimuth angle. Finally, the time sequence stored the processed data for subsequent inversion processing.

- (5) AOD inversion: The inversion method was the lookup table method (LUT): the lookup table file is a general-purpose file. Its content is a table of the relationship between radiation reflection, emissivity, angle data, and AOD. This paper used the aerosol inversion tool in ENVI to read the data results processed in steps (3) and (4). Then, it combined the relationship between the corresponding emissivity, reflectivity, angle, and AOD in the lookup table file to perform the aerosol inversion.

Through the operation of the above five parts, the inversion of the AOD was realized.

We can learn from previous researchers that there is a functional mapping between the optical depth of aerosol and the sun's radiation. Holben et al. [29] proposed a radiation transfer formula that combines AOD with radiation. The relationship between them is described as Equation (1).

$$R(x_a, \mu_s, \mu_v, \phi) = R_0(x_a, \mu_s, \mu_v, \phi) + \frac{F_d(x_a, \mu_s)T(x_a, \mu_v)\rho}{1 + s(x_a)\rho} \quad (1)$$

$R(x_a, \mu_s, \mu_v, \phi)$ in the above formula denotes a comprehensive signal of all reflected signals received by satellite, where x_a denotes AOD. μ_s and μ_v denote the solar zenith angle and satellite zenith angle when the satellite passes through the region of interest, respectively. ϕ denotes the corresponding sun azimuth angle and satellite azimuth. $R_0(x_a, \mu_s, \mu_v, \phi)$ denotes the reflected solar radiation by the atmosphere. $F_d(x_a, \mu_s)$ denotes the solar radiation that is not reflected and injected into the atmosphere, and $T(x_a, \mu_v)$ denotes the satellite emission signal that passes through the atmosphere. ρ is the reflectivity of the ground to solar radiation. $s(x_a)$ denotes the reflectivity of the atmosphere to the sun's radiation.

4. CNN Haze Classification Method

The convolutional neural network used in this research adopts an end-to-end idea. Therefore, the final training process is to fit this mapping relationship using a haze satellite remote sensing image as input, and the haze concentration level as output. The specific algorithm flow is shown in Figure 3.

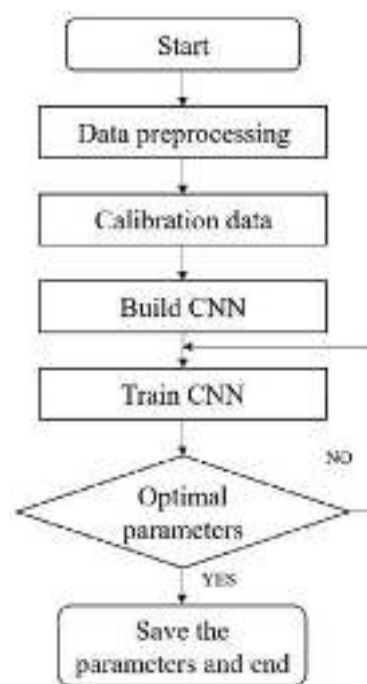


Figure 3. Convolutional neural network (CNN) haze classification flow chart.

4.1. CNN Data Processing

When the traditional method retrieves the AOD and haze concentrations from remote sensing images, the information of these angles needs to be extracted, cut, and synthesized, and this process is relatively cumbersome. After evaluating the zenith and azimuth angles, we decided not to consider their changes since these angles are relatively fixed when the satellite passes through the same area in the same season. Therefore, when preprocessing the remote sensing data, the CNN method only needs to extract, cut, and synthesize the reflectivity and emissivity. After the data are processed as above, they are stored chronologically by season. Then, the convolution neural network is used to fit their non-linear relationship, and finally, the haze level is classified through the classification layer.

According to the channel information, the channels for monitoring the edge and characteristics of the land and cloud are 1–7 channels. The wavelength and spatial resolution of each channel are shown in Table 1. We want to convert the satellite image into a three-channel RGB image to the convolutional neural network. Combining the wavelength range of visible light, as shown in Table 2, the three channels that best fit the three bands of RGB are channel 1, channel 4, and channel 3, so we combine the data of these three channels to get a true-color image. The synthesized image is shown in Figure 4. The correspondence AQI and PM 2.5 concentration of each haze level is shown in Table 3.

Table 1. Spatial resolution and internal wavelength of each channel in MOD02-1 km.

Channel	Internal Wavelength (nm)	Spatial Resolution (m)
1	620–670	250
2	841–876	250
3	459–479	500
4	545–565	500
5	1230–1250	500
6	1628–1652	500
7	2105–2155	500

Table 2. Internal visible light wavelength.

RGB	Internal Wavelength (nm)
Red	622–780
Green	492–577
Blue	455–470



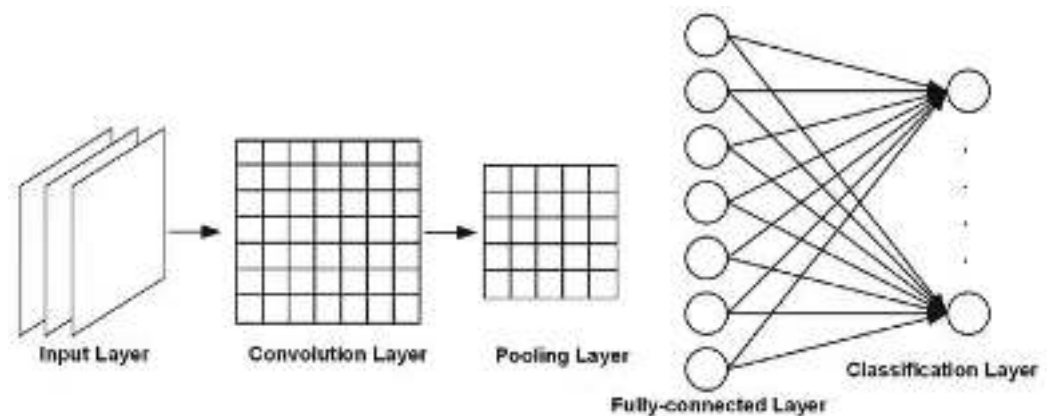
Figure 4. (a) is the satellite image with full channel information, and (b) is the synthesized RGB image.

Table 3. Correspondence table among haze level, air quality index, and PM2.5 concentration.

Haze Level	AQI	Daily Average PM2.5 Concentration
1	0~50	0~35
2	51~100	36~75
3	101~150	76~115
4	151~200	116~150
5	201~300	151~250
6	301~500	251~500

4.2. CNN Structure

The general structure of the CNN network proposed in this article is shown in Figure 5.

**Figure 5.** Structure of convolutional neural network (CNN).

Input layer: If the input data are RGB true-color images, the input data format is: $n_h \times n_w \times 3$; if they are grayscale image data, the input data format is: $n_h \times n_w \times 1$. Moreover, the input data of the input layer should be normalized, and the size of the image and the number of data channels should be consistent.

Convolution layer: The convolution operation is expressed as C , where f represents the length and width of the convolution kernel. The length and width are the same, and the number of channels is the same as the number of input channels. m represents the number of convolution kernels. Then, the process of convolution operation is shown in Equation (2):

$$y_{i,j}^l = \sum_{r=0}^{m-1} \sum_{s=0}^{f-1} \sum_{t=0}^{f-1} W_{s,t}^{(r,l)} x_{i+s,j+t}^{l-1} + b^l \quad (2)$$

The first-level summation formula means that all convolution kernels are traversed once. The second- and third-layer summation formulas indicate that a convolution kernel with a size of $f \times f$ is used to perform a convolution operation on the input, where W is the weight and b is the bias. Where i, j represent the position of the image in the output layer as shown in Equation (3):

$$\begin{aligned} i &= 1, 2, \dots, (n_h - f) \\ j &= 1, 2, \dots, (n_w - f) \end{aligned} \quad (3)$$

Activation function: Use Sigmoid activation function, as shown in Equation (4):

$$\text{Sigmoid}(x) = \frac{1}{1 + e^{-x}} \quad (4)$$

Pooling layer: This is an essential step in a convolutional neural network, also called a down-sampling layer, and the size is generally a square window with the same length and width. The pooling process is shown in Equation (5):

$$y_{i,j}^l = \max_{0 \leq s, t \leq f} \left[\text{ReLU} \left(\sum_{r=0}^{m-1} \sum_{s=0}^{f-1} \sum_{t=0}^{f-1} W_{s,t}^{(r,l)} x_{i+s,j+t}^{l-1} + b^l \right) \right] \quad (5)$$

After the input data are translated and transformed, the output will not change, improving the convolutional network's robustness to extract features. This kind of translation invariance is a very practical property.

Fully connected layer: In the studied model, there are six categories according to the level of haze, and the corresponding labels are: (0 0 0 0 0 1), (0 0 0 0 1 0), ..., (0 1 0 0 0 0). Among them, data that are disturbed by information such as clouds and cannot be identified are marked with p position 1, that is, (1 0 0 0 0 0).

SoftMax classification layer: The classification process is to judge the probability that this vector belongs to each category, and the one with the highest probability is the result of the classification, as shown in Equation (6):

$$h_{\theta}(x_i^{l-1}) = \begin{bmatrix} p(y_i = 1 | x_i^{l-1}; \theta) \\ p(y_i = 2 | x_i^{l-1}; \theta) \\ \vdots \\ p(y_i = n | x_i^{l-1}; \theta) \end{bmatrix} = \frac{1}{\sum_{j=1}^n e^{\theta_j^T x_i}} \begin{bmatrix} e^{\theta_1^T x_1} \\ e^{\theta_2^T x_2} \\ \vdots \\ e^{\theta_n^T x_n} \end{bmatrix} \quad (6)$$

where $p(y_i = n | x_i^{l-1}; \theta)$ represents the probability estimation of the classification function to the data being the n th category, and θ represents the model's parameters. The rightmost formula of the equation represents the normalized form of the probability so that the sum of all the probabilities is 1.

4.3. CNN Parameter Adjustment

We used the stochastic gradient descent method as the parameter adjustment optimization method. Although the convolutional neural network used in this article does not have many layers, its structure belongs to deep learning. Let θ be a parameter in the neural network, the negative conditional log-likelihood of the training data can be expressed by Equation (7):

$$J(\theta) = \frac{1}{m} \sum_{i=1}^m L(x^i, y^i, \theta) \quad (7)$$

where L represents the loss function corresponding to the i -th input, then for these cost functions that you want to add, the gradient descent method needs to be calculated using Equation (8):

$$\nabla_{\theta} J_{\theta} = \frac{1}{m} \sum_{i=1}^m \nabla_{\theta} L(x^i, y^i, \theta) \quad (8)$$

The calculation time complexity of this optimization process is $O(m)$, where m is the amount of data in the training set. As training increases, this complexity will increase. The core of the stochastic gradient descent method is to perform a small-scale sample approximate estimation. A small batch of training (minibatch) was performed in each step, and the sample size at this time was m' , and $m' \ll m$, and then pass. The results obtained in this part were used to estimate the results of the entire sample so that the amount of calculation will be significantly reduced. The gradient estimation, Equation (9), is as follows:

$$g = \frac{1}{m'} \nabla_{\theta} \sum_{i=1}^{m'} L(x^i, y^i, \theta) \quad (9)$$

Use the mini-batch described above to train and estimate the entire sample using the following gradient estimation algorithm as Equation (10):

$$\theta - \alpha g \rightarrow \theta \quad (10)$$

The small-batch gradient descent method solves the shortcomings of the gradient descent method's time complexity and unreliability of the gradient descent method in the parameter optimization process. Finally, we optimized the parameters of the classification layer and used the evaluation function as Equation (11):

$$J(\theta) = -\frac{1}{m} \left[\sum_{i=1}^m \sum_{j=1}^n 1\{y_i = j\} \log \left(\frac{e^{\theta_j^T x_i}}{\sum_{k=1}^n e^{\theta_k^T x_i}} \right) \right] \quad (11)$$

The optimization process is the process of minimizing the evaluation function so that the parameter θ will reach the optimal value.

5. Experiment and Result

5.1. Correlation Analysis between Traditional Method Inversion Results and Haze Concentration

This experiment used traditional methods to analyze the correlation between the inversion data of MOD02-1 km in Beijing in 2014 and the PM_{2.5} concentration of ground monitoring stations in Beijing. The result is shown in Figure 6, where (a–d) represents the results of the four seasons.

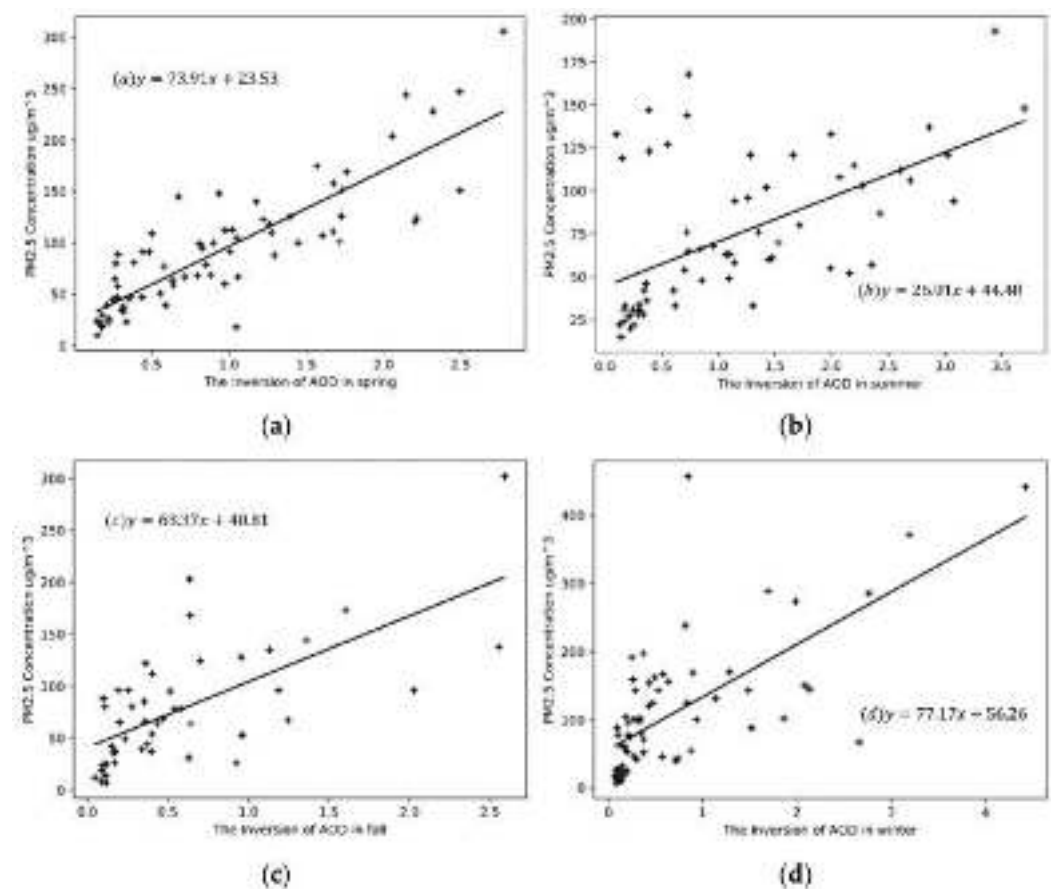


Figure 6. Linear regression between Aerosol Optical Depth (AOD) and PM_{2.5} (a) The inversion in spring; (b) The inversion in summer; (c) The inversion in fall; (d) The inversion in winter.

From the results, the highest correlation coefficient is in the spring inversion, which reaches a high level of 0.86, followed by winter and autumn, and the worst in summer. All

of the correlation coefficients are above 0.5, indicating a strong correlation between AOD and PM2.5 concentration, considering their non-linear relationship and complex dynamics.

We also performed a linear fit to the inversion results of AOD in the whole year of 2014, as shown in Figure 7. The y-intercept a_0 is 45.85, the slope a_1 is 50.79, and the correlation coefficient R is 0.59. Compared with the results of the four seasons, the correlation coefficient of the linear fit for the whole year is 30% lower than that of the spring. We think this is because the four seasons have different factors, such as different climatic characteristics, industrial activities, and gas emissions caused by heating demand, which contribute to the correlation between AOD and PM2.5 concentration. Therefore, we conclude that studying the correlation performance of AOD and PM2.5 according to the season division can provide a more accurate basis for analysis.

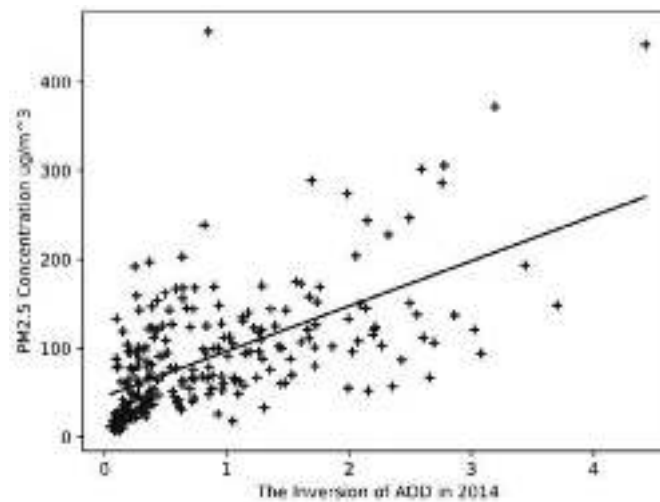


Figure 7. Overall linear regression between AOD and PM2.5 in 2014.

Figure 7 shows that we can train the processed data through the neural network method to approximate the coupling relationship between the mapping relation and the linear relation to achieve the inversion classification method.

5.2. Comparison of CNN Analysis Results

We extracted the image after two 7×7 convolution layers to analyze whether the model can extract the haze characteristics [30–32], as shown in Figure 8.

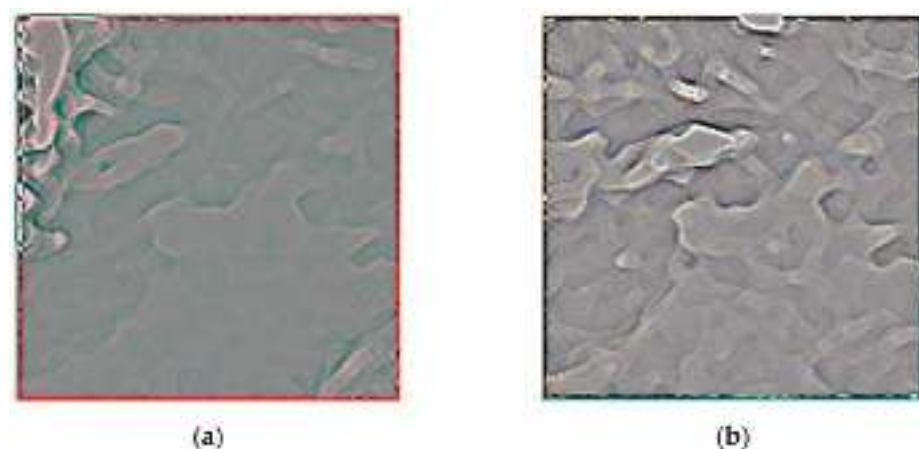


Figure 8. Convolution feature extraction diagram (a) Convolution diagram during severe haze; (b) Convolution diagram with a lower haze level.

Figure 8a is a convolution result diagram when the haze is severe in spring, and the bright block is in the upper left corner of the image. We find a cloud layer in the area comparing it with the original image, which indicates that the cloud layer appears bright in the convolution result. The remaining areas with severe haze are darker, where the difference between emissivity and reflectance is more significant. Figure 8b is a convolution result graph containing minimum cloud information and a lower haze concentration level. The brighter feature in Figure 8 is the area where the AOD is low. The difference between the emissivity and the reflectance is slight. We found that the haze level prediction model can effectively distinguish the image characteristics of different haze concentrations by comparing the results. We labeled the cloud information of the image when marking the dataset, avoiding the mistakes where the cloud was identified as haze.

We used the MOD02-1 km data of the Beijing area in 2013 and 2014 as the training set and test set of the haze level prediction model. We extracted satellite images from the MOD02-1 km data so that the training and test sets contained 730 satellite images. We marked the haze level on the training set.

To verify whether the model can effectively establish the correlation between satellite image and PM2.5 concentration and to compare it with the traditional inversion method, we conducted the same linear regression between the output of the haze level prediction model and the PM2.5 daily average concentration. The results are shown in Figure 9.

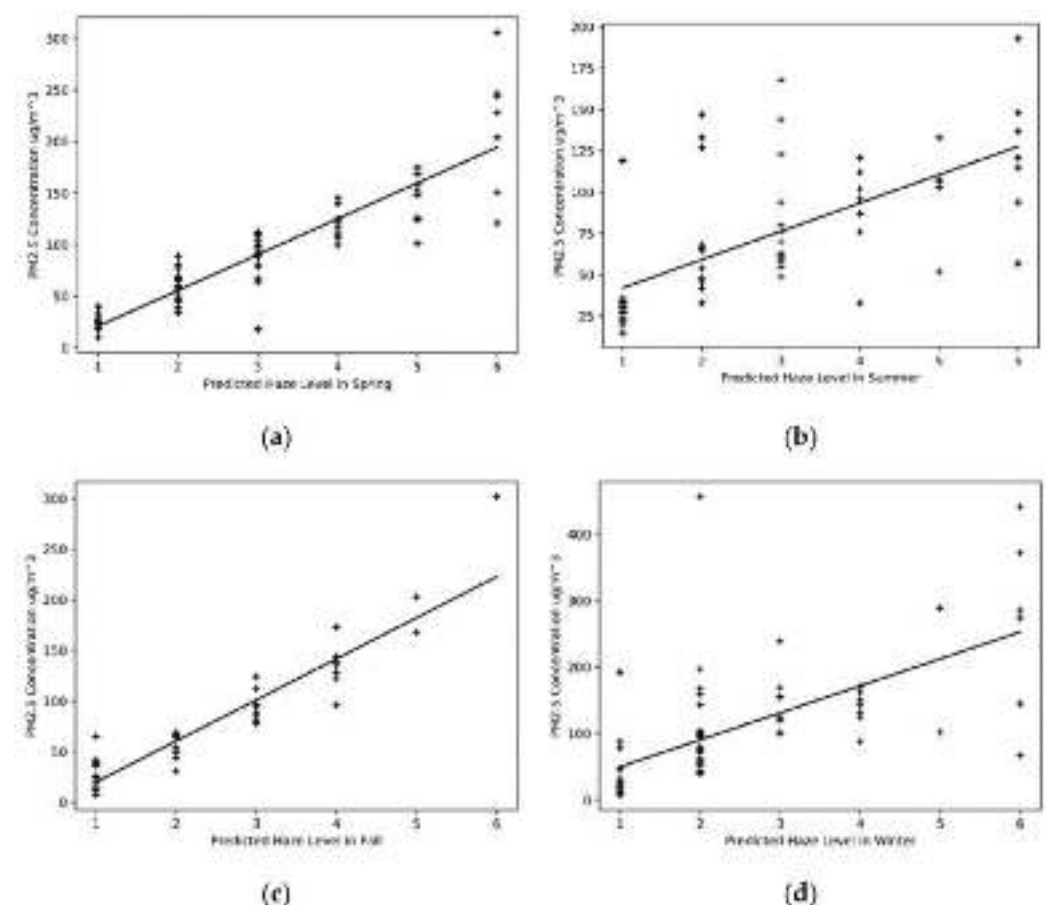


Figure 9. Linear regression between haze level using CNN and PM2.5 (a) Linear regression for CNN and PM2.5 in Spring; (b) Linear regression in Summer; (c) Linear regression in Fall; (d) Linear regression in Winter.

In Figure 9a, the y-intercept a_0 is -13.88 . The slope a_1 is 34.74 . The correlation coefficient R is 0.90 . In Figure 9b, the y-intercept a_0 is 25.07 . The slope a_1 is 17.11 , and the correlation coefficient R is 0.65 . In Figure 9c, the y-intercept a_0 is -20.74 . The slope a_1 is

40.61. The correlation coefficient R is 0.93. In Figure 9d, the y-intercept a_0 is 9.03, and the slope a_1 is 40.67, the correlation coefficient R is 0.65.

A comparison with the traditional inversion method is shown in Table 4.

Table 4. The correlation coefficient between traditional inversion and level prediction.

Season	R (Lookup Table)	R (CNN Model)
Spring	0.86	0.90
Summer	0.57	0.64
Fall	0.67	0.93
Winter	0.68	0.65

From Table 4, the correlation coefficient of the haze level prediction model based on the convolutional neural network is superior to the traditional inversion method in spring, summer, and fall. In particular, the summer and fall results are improved by 12% and 39%, respectively, which indicates that the haze level prediction model can provide a better PM_{2.5} concentration prediction than the traditional inversion method. Furthermore, all correlation coefficients in the haze prediction model are above 0.6, indicating a strong correlation between haze level and PM_{2.5} concentration.

6. Discussion

This study first studied the traditional haze inversion method. After studying the relationship between AOD and haze concentration, we found a non-linear mapping relationship between the two. Therefore, we propose a CNN-based haze classification model to take advantage of CNN's non-linear relationship fitting. Through the experimental comparison between the traditional method and our proposed model, the correlation coefficient of the haze classification model based on the convolutional neural network in spring, summer and fall are better than the traditional inversion method. In particular, the results in summer and fall increased by 12% and 39%, respectively, which indicates that the CNN haze classification model can provide better classification results than traditional inversion methods. In addition, all correlation coefficients in the haze classification model are above 0.6, indicating a strong correlation between the haze level and the PM_{2.5} concentration.

In general, whether it is a traditional inversion method or a CNN-based method, summer has the lowest correlation coefficient, followed by winter. The reason may be that the fog concentration of summer aerosol is higher than that of haze. In winter, there are many days of heavy haze and uneven distribution of time and space, resulting in a low recognition rate of the CNN. On the other hand, the increase in fall is due to the smaller haze level, which is most concentrated in the top four levels, and there is less severe haze weather.

The result shows consistency with other studies [3,5,20]. The winter is the most polluted season in this area of China. The pattern may contribute to the high correlation coefficient in the winter. The result from the CNN shows a better performance in spring, summer, and fall. The feature capture characteristics of the CNN and its ability to fit with complex functions could benefit haze classification and prediction [31,32]. Since the CNN model could improve the inversion results when the haze is less severe, other machine learning methods could be used on a broader range of areas and haze scenarios. After considering the limitations of both the proposed method and the comparison traditional method, the result of both the proposed method and the comparing result is limited. However, the results still show the potential of combining neural networks with time-consuming tasks in atmospheric studies.

7. Conclusions

This research is based on experimental research on convolutional neural networks' classification and prediction of haze levels. We found that a convolutional neural network

uses images to identify haze concentrations, which can sufficiently fit the non-linear relationship between input and output. It proves the feasibility of a convolutional neural network to classify and invert haze. At the same time, the use of trained convolutional neural networks can reduce manual inversion work to a certain extent. Our proposed CNN-based haze level classification model greatly simplifies data processing compared to traditional inversion methods. By comparing the correlation coefficients of traditional inversion methods and CNN-based methods, we prove that the haze prediction network can provide better PM_{2.5} concentration classification than traditional inversion methods. It also proves that the original remote sensing satellite images can provide rich features for analyzing haze problems.

Since this study still contains many limitations, including the limited data and only covering a limited range of the haze problem, this method is only the starting point for further combining machine learning methods with atmospheric problems. Moreover, the recognition rate reached more than 80%. However, due to insufficient data, the accuracy of the recognition result is not high, but it is also feasible. Among them, the accuracy rate and the F1 value of levels 1–4 are higher. However, the values of these three items of grades 5 and 6 all decreased, and the reason is because the concentration span of the latter two grades is larger.

Since the proposed method aims to replace and replicate the traditional process using CNN, the proposed method shares the same limitations as the traditional method. The estimate heavily depends on the satellite image, which contains many other elements that could be falsely claimed as haze. The traditional method uses various calibration processes with satellite parameters including azimuth, zenith, emissivity, and reflectivity to reduce these false results. Some of these calibration processes are removed to fit the network structure and simplify the network process when constructing a neural network to replace the labor-intensive traditional method. Although the proposed method has fewer calibrations and processes than the traditional method, the results are still compatible and even better than those in several situations. This result is likely caused by the nature of neural networks that have an outstanding performance in fitting complex natural processes. This study and previous studies have shown that neural networks have a great capacity and performance in simulating haze progress and in the prediction of haze states [23–26,28,31,32]. Of course, due to all of the simplification processes, this study took some time to construct the network, and the original limitations of the traditional method still remain in the network, there will be many misfits and false claims of haze phenomena. In order to demonstrate the great potential of the neural network on the haze problem, we believe that the following aspects can be further studied to improve the accuracy of haze prediction.

Future studies could further improve the model's ability to interpret images. In order to avoid the influence of clouds on the model's ability to identify polluted areas and pollutant concentrations, this paper manually annotated cloud information on all satellite images. This paper also removed some steps in traditional image processing to reduce complexity and time, which would cause errors in the outcome. In future research, the model's ability to process images can be improved to replace manual marking, which keeps the accuracy and quality. In addition, convolutional neural networks have good recognition performance for images, but they lack the ability to process time-series information. Therefore, to obtain the haze characteristics in the time series, utilizing more network models would benefit future studies.

Author Contributions: Conceptualization, W.Z. and L.W.; methodology, L.Y. and W.H.; software, J.T. and W.H.; formal analysis, B.Y. and S.L.; data curation, W.H.; writing—original draft preparation, L.Y. and W.H.; writing—review and editing, L.Y. and W.Z.; funding acquisition, W.Z. All authors have read and agreed to the published version of the manuscript.

Funding: This work was jointly supported by the Sichuan Science and Technology Program (Grant: 2021YFQ0003).

Institutional Review Board Statement: Not applicable.

Informed Consent Statement: Not applicable.

Data Availability Statement: This study created or analyzed no new data. Data sharing is not applicable to this article.

Conflicts of Interest: The authors declare no conflict of interest.

References

- Chen, X.; Yin, L.; Fan, Y.; Song, L.; Ji, T.; Liu, Y.; Tian, J.; Zheng, W. Temporal evolution characteristics of PM_{2.5} concentration based on continuous wavelet transform. *Sci. Total Environ.* **2020**, *699*, 134244. [PubMed]
- Xu, J.; Liu, Z.; Yin, L.; Liu, Y.; Tian, J.; Gu, Y.; Zheng, W.; Yang, B.; Liu, S. Grey Correlation Analysis of Haze Impact Factor PM_{2.5}. *Atmosphere* **2021**, *12*, 1513.
- Li, X.; Zheng, W.; Yin, L.; Yin, Z.; Song, L.; Tian, X. Influence of social-economic activities on air pollutants in Beijing, China. *Open Geosci.* **2017**, *9*, 314–321.
- Zheng, W.; Li, X.; Xie, J.; Yin, L.; Wang, Y. Impact of human activities on haze in Beijing based on grey relational analysis. *Rend. Lincei* **2015**, *26*, 187–192.
- Zheng, W.; Li, X.; Yin, L.; Wang, Y. The retrieved urban LST in Beijing based on TM, HJ-1B and MODIS. *Arab. J. Sci. Eng.* **2016**, *41*, 2325–2332.
- Zheng, W.; Li, X.; Yin, L.; Wang, Y. Spatiotemporal heterogeneity of urban air pollution in China based on spatial analysis. *Rend. Lincei* **2016**, *27*, 351–356.
- Dankwa, S.; Zheng, W.; Gao, B.; Li, X. Terrestrial Water Storage (TWS) Patterns Monitoring in the Amazon Basin Using Grace Observed: Its Trends and Characteristics. In Proceedings of the IGARSS 2018—2018 IEEE International Geoscience and Remote Sensing Symposium, Valencia, Spain, 22–27 July 2018; pp. 768–771.
- Livieris, I.E.; Pintelas, E.; Pintelas, P. A CNN-LSTM model for gold price time-series forecasting. *Neural Comput. Appl.* **2020**, *32*, 17351–17360.
- Zhao, B.; Lu, H.; Chen, S.; Liu, J.; Wu, D. Convolutional neural networks for time series classification. *J. Syst. Eng. Electron.* **2017**, *28*, 162–169.
- Wu, X.; Liu, Z.; Yin, L.; Zheng, W.; Song, L.; Tian, J.; Yang, B.; Liu, S. A Haze Prediction Model in Chengdu Based on LSTM. *Atmosphere* **2021**, *12*, 1479.
- Shang, K.; Chen, Z.; Liu, Z.; Song, L.; Zheng, W.; Yang, B.; Liu, S.; Yin, L. Haze Prediction Model Using Deep Recurrent Neural Network. *Atmosphere* **2021**, *12*, 1625.
- Ni, X.; Yin, L.; Chen, X.; Liu, S.; Yang, B.; Zheng, W. Semantic representation for visual reasoning. *MATEC Web. Conf.* **2019**, *277*, 02006.
- Rubinstein-Salzedo, S. Big o notation and algorithm efficiency. In *Cryptography*; Springer: Berlin/Heidelberg, Germany, 2018; pp. 75–83.
- Caraka, R.E.; Lee, Y.; Chen, R.-C.; Toharudin, T. Using hierarchical likelihood towards support vector machine: Theory and its application. *IEEE Access* **2020**, *8*, 194795–194807.
- Hernández-Orallo, J. ROC curves for regression. *Pattern Recognit.* **2013**, *46*, 3395–3411.
- Elayaraja, P.; Suganthi, M. Automatic approach for cervical cancer detection and segmentation using neural network classifier. *Asian Pac. J. Cancer Prev. APJCP* **2018**, *19*, 3571.
- Delforge, D.; Watlet, A.; Kaufmann, O.; Van Camp, M.; Vanclooster, M. Time-series clustering approaches for subsurface zonation and hydrofacies detection using a real time-lapse electrical resistivity dataset. *J. Appl. Geophys.* **2021**, *184*, 104203.
- Esling, P.; Agon, C. Time-series data mining. *ACM Comput. Surv. (CSUR)* **2012**, *45*, 1–34.
- McGowan, H.A.; Clark, A. A vertical profile of PM₁₀ dust concentrations measured during a regional dust event identified by MODIS Terra, western Queensland, Australia. *J. Geophys. Res. Earth Surf.* **2008**, *113*, F2.
- Guo, Y.; Feng, N.; Christopher, S.A.; Kang, P.; Zhan, F.B.; Hong, S. Satellite remote sensing of fine particulate matter (PM_{2.5}) air quality over Beijing using MODIS. *Int. J. Remote Sens.* **2014**, *35*, 6522–6544.
- Nordio, F.; Kloog, I.; Coull, B.A.; Chudnovsky, A.; Grillo, P.; Bertazzi, P.A.; Baccarelli, A.A.; Schwartz, J. Estimating spatio-temporal resolved PM₁₀ aerosol mass concentrations using MODIS satellite data and land use regression over Lombardy, Italy. *Atmos. Environ.* **2013**, *74*, 227–236.
- Seo, S.; Kim, J.; Lee, H.; Jeong, U.; Kim, W.; Holben, B.; Kim, S.-W.; Song, C.; Lim, J. Estimation of PM₁₀ concentrations over Seoul using multiple empirical models with AERONET and MODIS data collected during the DRAGON-Asia campaign. *Atmos. Chem. Phys.* **2015**, *15*, 319–334.
- Pérez, P.; Trier, A.; Reyes, J. Prediction of PM_{2.5} concentrations several hours in advance using neural networks in Santiago, Chile. *Atmos. Environ.* **2000**, *34*, 1189–1196.
- Grivas, G.; Chaloulakou, A. Artificial neural network models for prediction of PM₁₀ hourly concentrations, in the Greater Area of Athens, Greece. *Atmos. Environ.* **2006**, *40*, 1216–1229.
- Reid, C.E.; Jerrett, M.; Petersen, M.L.; Pfister, G.G.; Morefield, P.E.; Tager, I.B.; Raffuse, S.M.; Balmes, J.R. Spatiotemporal prediction of fine particulate matter during the 2008 northern California wildfires using machine learning. *Environ. Sci. Technol.* **2015**, *49*, 3887–3896.

26. Marzano, F.S.; Rivolta, G.; Coppola, E.; Tomassetti, B.; Verdecchia, M. Rainfall nowcasting from multisatellite passive-sensor images using a recurrent neural network. *IEEE Trans. Geosci. Remote Sens.* **2007**, *45*, 3800–3812.
27. Slini, T.; Kaprara, A.; Karatzas, K.; Moussiopoulos, N. PM10 forecasting for Thessaloniki, Greece. *Environ. Model. Softw.* **2006**, *21*, 559–565.
28. Bahari, R.; Abbaspour, R.A.; Pahlavani, P. Prediction of PM25 concentrations using temperature inversion effects based on an artificial neural network. In Proceedings of the ISPRS International Conference of Geospatial Information Research, Tehran, Iran, 15–17 November 2014; p. 17.
29. Holben, B.N.; Eck, T.F.; Slutsker, I.A.; Tanre, D.; Buis, J.; Setzer, A.; Vermote, E.; Reagan, J.A.; Kaufman, Y.; Nakajima, T. AERONET—A federated instrument network and data archive for aerosol characterization. *Remote Sens. Environ.* **1998**, *66*, 1–16.
30. Wang, J.; Christopher, S.A. Intercomparison between satellite-derived aerosol optical thickness and PM2.5 mass: Implications for air quality studies. *Geophys. Res. Lett.* **2003**, *30*, 21.
31. Linlin, Y.; Xinxin, L.; Li, S.; Qiang, L. Research on the back propagation neural network haze prediction model based on particle swarm optimization. In Proceedings of the 2020 International Conference on Computer Engineering and Application (ICCEA), Guangzhou, China, 18–20 March 2020; pp. 344–348.
32. Ke, L.; Liao, P.; Zhang, X.; Chen, G.; Zhu, K.; Wang, Q.; Tan, X. Haze removal from a single remote sensing image based on a fully convolutional neural network. *J. Appl. Remote Sens.* **2019**, *13*, 036505.

Article

A Haze Prediction Model in Chengdu Based on LSTM

Xinyi Wu ^{1,*}, Zhixin Liu ^{1,*}, Lirong Yin ^{2,*}, Wenfeng Zheng ^{3,*}, Lihong Song ³, Jiawei Tian ³, Bo Yang ³ and Shan Liu ³

¹ School of Life Science, Shaoxing University, Shaoxing 312000, China; xinyi.wu@gmail.com

² Department of Geography and Anthropology, Louisiana State University, Baton Rouge, LA 70803, USA

³ School of Automation, University of Electronic Science and Technology of China, Chengdu 610054, China; lihong.song.cn@outlook.com (L.S.); jravis.tian23@gmail.com (J.T.); boyang@uestc.edu.cn (B.Y.); shanliu@uestc.edu.cn (S.L.)

* Correspondence: liuzhixin@usx.edu.cn (Z.L.); lyin5@lsu.edu (L.Y.); winfirms@uestc.edu.cn (W.Z.)

Abstract: Air pollution with fluidity can influence a large area for a long time and can be harmful to the ecological environment and human health. Haze, one form of air pollution, has been a critical problem since the industrial revolution. Though the actual cause of haze could be various and complicated, in this paper, we have found out that many gases' distributions and wind power or temperature are related to PM_{2.5}/10's concentration. Thus, based on the correlation between PM_{2.5}/PM₁₀ and other gaseous pollutants and the timing continuity of PM_{2.5}/PM₁₀, we propose a multilayer long short-term memory haze prediction model. This model utilizes the concentration of O₃, CO, NO₂, SO₂, and PM_{2.5}/PM₁₀ in the last 24 h as inputs to predict PM_{2.5}/PM₁₀ concentrations in the future. Besides pre-processing the data, the primary approach to boost the prediction performance is adding layers above a single-layer long short-term memory model. Moreover, it is proved that by doing so, we could let the network make predictions more accurately and efficiently. Furthermore, by comparison, in general, we have obtained a more accurate prediction.

Keywords: haze prediction; multilayer long short-term memory; PM_{2.5}; PM₁₀

Citation: Wu, X.; Liu, Z.; Yin, L.; Zheng, W.; Song, L.; Tian, J.; Yang, B.; Liu, S. A Haze Prediction Model in Chengdu Based on LSTM. *Atmosphere* **2021**, *12*, 1479. <https://doi.org/10.3390/atmos12111479>

Academic Editors: Duanyang Liu, Kai Qin and Honglei Wang

Received: 12 October 2021

Accepted: 4 November 2021

Published: 9 November 2021

Publisher's Note: MDPI stays neutral with regard to jurisdictional claims in published maps and institutional affiliations.



Copyright: © 2021 by the authors. Licensee MDPI, Basel, Switzerland. This article is an open access article distributed under the terms and conditions of the Creative Commons Attribution (CC BY) license (<https://creativecommons.org/licenses/by/4.0/>).

1. Introduction

The air pollution incidents caused by haze have often occurred in metropolises such as Los Angeles and London. Respiratory diseases caused by haze have killed ten thousand people and caused widespread public panic [1,2]. In China, social industrialization and urbanization have brought economic development, while the awareness and measures for environmental protection have lagged [2–5].

Sichuan Basin is an area of severe haze pollution in the western part of China. In the 74 major cities monitored, the average annual concentration of PM_{2.5} ranged from 26 to 160 µg/m³, the average concentration was 72 µg/m³, the proportion of qualified cities was 4.1%, and the average annual concentration of PM₁₀ ranged from 47 to 305 µg/m³, the average concentration was 118 µg/m³, and the proportion of qualified cities was 14.9%. In the following years, haze pollution has been alleviated, but the overall pollution situation is still not optimistic.

The prevention and prediction of haze have become the focus of the public and researchers. The haze research mainly focuses on two aspects: the cause of haze and the prediction of haze. Hinton et al. [6] studied photochemical haze in Los Angeles. They concluded that primary pollutants emitted by motor vehicles and chemical plants and secondary chemical pollutants caused by photochemistry are the primary pollutants. Gupta [7,8] compared the PM₁₀ concentration between the residential and industrial areas in Kolkata, India, and found that soot and motor vehicle emissions had the most significant impact on haze pollution in the area. Minguillón et al. [9] used a positive definite matrix to analyze the main components and formation factors of PM_{2.5} in Switzerland. Ho et al. [10]

collected and tested the chemical composition of PM_{2.5} in the suburbs of Hong Kong, evaluated the relatively enriched factors in the crustal elements, and used multivariate correlation techniques to determine the source of PM_{2.5} and its impact.

In terms of haze prediction, researchers have used many different methods to predict haze pollution in different regions. Haze prediction methods include multivariate statistical methods [11–14], chemical transformation models [15–17], and prediction methods based on remote sensing satellite imagery [3,18–21].

RNN (recurrent neural network) and LSTM (long short-term memory) [22–27] have been gradually applied to haze prediction. Qin et al. [28] proposed the new concentration prediction scheme of urban PM_{2.5} based on CNN (convolutional neural network) and LSTM. Tsai et al. [29] used RNN and LSTM networks to predict air pollution in Taiwan. Li et al. [16] developed a hybrid called the CNN-LSTM model, which is used to predict the concentration of PM_{2.5} in Beijing in the next 24 h. Bai et al. [30] proposed an E-LSTM neural network, which constructs multiple LSTM models in different modes for integrated learning with an hourly PM_{2.5} concentration forecast. Our time series model did show a better result [26,31–33].

In this paper, we applied neural network methods to predict the concentration of haze pollutants, including PM_{2.5} and PM₁₀. First, we argued that the concentration of PM_{2.5}/PM₁₀ is related to other gaseous pollutants, such as O₃, CO, NO₂, SO₂, and the concentration of PM_{2.5}/PM₁₀ has time series continuity, which means that the curve of concentration is smooth. Furthermore, the concentration at different times is correlated within a certain time window. Based on the two assumptions, we collected real-time PM_{2.5}, PM₁₀, O₃, CO, NO₂, and SO₂ concentrations published by six ground monitoring stations in Chengdu from 1 June 2014 to 30 June 2017, and meteorological data, such as wind power and temperature. Then, we analyzed the correlation between the collected data and PM_{2.5}, constructed different datasets for predicting PM_{2.5} and PM₁₀, respectively, and constructed a haze prediction model based on LSTM. The LSTM-based haze prediction model uses the O₃, CO, NO₂, SO₂ concentrations, and PM_{2.5}/PM₁₀ concentrations in the last 24 h as inputs to predict future PM_{2.5}/PM₁₀ concentrations. We also focused on adjusting the haze prediction model's hidden layers to explore the model's best performance.

2. Approach

The long short-term memory [34] neural network (LSTM) is a new deep machine learning network built on RNN. In order to avoid the vanishing gradient issue and the gradient explosion problem, a long-term delay process is added to the network. Thus, the state unit can keep the error stream, which successfully solves the defects that exist in the RNN and has been widely used in many fields.

RNN has only one hidden layer state, so short-term input is compassionate when dealing with time series, while long-term input is relatively slow. Therefore, LSTM adds a cell state based on the RNN network for long-term state preservation. An unrolled LSTM is shown in Figure 1. It represents the input of the LSTM network at t -time, the output, and the LSTM network's cell state of the LSTM network at $T-1$ time. These three data are the input, output, and cell state of the LSTM network at t -time, and X , h , and c are vectors.

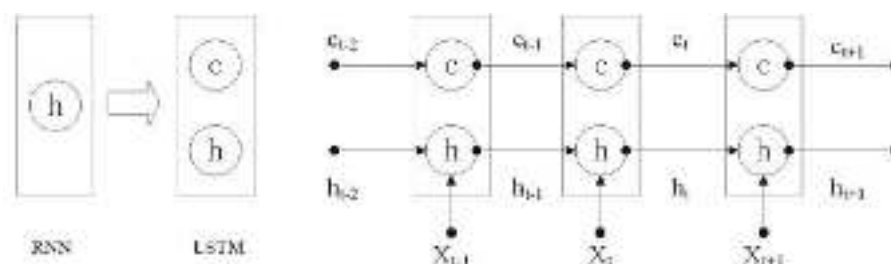


Figure 1. Expanded view of LSTM.

The LSTM implements the preservation, update, and input of long-term state c through the internal forget gate, input, and output gate, as shown in Figure 2. The forget gate and output gate control the cell state of the LSTM. They respectively determine the preserved information of the cell state and the preserved information of the input at the moment of t . The output gate controls the parts of the cell state that we want to include in the output.

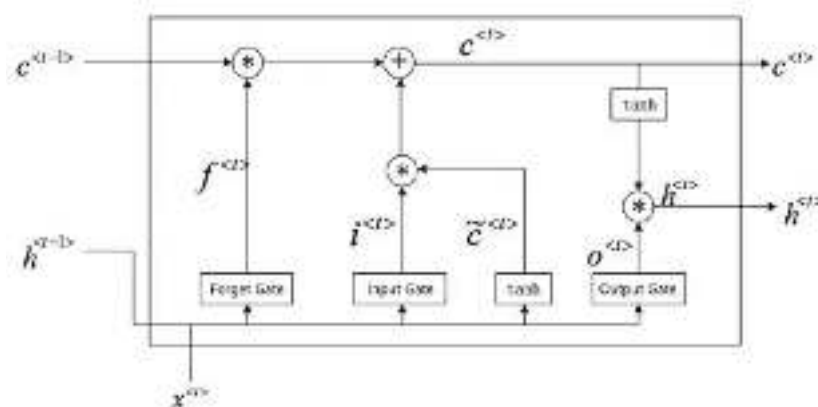


Figure 2. The internal structure of LSTM.

Gates are the full connection layers, and the expression of the gate is as shown in Formula (1), where the input and output are all represented by vectors. The output is the real number vector with a range of $[0, 1]$. Thus, in Formula (1), W denotes the gate's weight matrix, and b represents the error vector. σ is the sigmoid function, whose output ranges from 0 to 1 and determines whether the input can pass through the gate.

$$g(x) = \sigma(Wx + b) \quad (1)$$

The forget gate is shown in Formula (2). It allows the LSTM to forget the memories based on the current input selectively. The input of the forget gates is the input of the current time and the output of the hidden layer node at the previous time. Weight matrix W and error b are used to adjust the input. The sigmoid function is used to filter out outdated information that is useless for the current output.

$$f_t = \sigma(W_f \cdot [h_{t-1}, x_t] + b_f) \quad (2)$$

The calculation of the input gate is shown in (3). The input gate controls input information. W_i represents the weight matrix of the output gate, and b_i represents the bias of the input gate.

$$i_t = \sigma(W_i \cdot [h_{t-1}, x_t] + b_i) \quad (3)$$

The input state unit c'_t at the current time t is calculated through the output of the network at the time $t - 1$ and the input at the time t , as shown in (4).

$$c'_t = \tanh(W_c[h_{t-1}, x_t] + b_c) \quad (4)$$

Therefore, the cell state at the current time c_t can be obtained by the Formula (5), where the symbol \circ denotes the elementwise multiplication.

$$c_t = f_t \circ c_{t-1} + i_t \circ c'_t \quad (5)$$

The output gate can be expressed as (6). Output gate controls the influence of long-term information on the current output. The output of the long-term memory neural network is determined according to the output gate and cell state, as shown in (7).

$$o_t = \sigma(W_o[h_{t-1}, x_t] + b_o) \quad (6)$$

$$h_t = o_t \circ \tanh(c_t) \quad (7)$$

3. Dataset

In order to predict PM_{2.5} and PM₁₀ concentrations, we collected two types of data: gas concentration data and meteorological data [7]. First, we collected the real-time concentration data of PM_{2.5}, PM₁₀, O₃, CO, NO₂, and SO₂ released by six ground monitoring stations in the Chengdu urban area from 1 June 2014 to 30 June 2017. The data update frequency is once an hour. PM_{2.5}, PM₁₀, O₃, and SO₂ units: $\mu\text{g}/\text{m}^3$ and CO, NO₂ units: mg/m^3 . We used the average concentration simultaneously in six ground monitoring stations as gas concentration data in Chengdu. Moreover, we have collected the temperature, humidity, and wind data released by the China Weather Network (WEATHER) as meteorological data (<http://www.cnemc.cn/> (accessed on 16 October 2019)).

The six monitoring stations selected in the study cover the whole urban area of Chengdu and can completely monitor the changes of air quality in Chengdu. The geographical location of the ground monitoring stations in Chengdu is shown in Figure 3.



Figure 3. The geographical location of the ground monitoring stations in Chengdu.

3.1. Correlation Analysis

Since autumn and winter are higher frequency seasons of haze than spring and summer, it can be assumed that haze has different causes in different seasons. When studying the correlation between haze and meteorological conditions, we selected pollutant concentrations such as PM_{2.5}, PM₁₀, O₃, CO, NO₂, and SO₂ and the meteorological data such as temperature, humidity, and wind power in two different time ranges (from 0:00

on 4 July 2016 to 23:00 on 10 July 2016, and from 0:00 on 24 December 2016 to 23:00 on 30 December 2016). The correlation analysis tool in MATLAB was used to complete the correlation analysis between meteorological factors and PM2.5. The results are shown in Table 1.

Table 1. Correlation coefficient value of PM2.5 and meteorological factors.

Correlation Coefficient	Highest Temperature	Lowest Temperature	Humidity	Wind Power	O ₃	CO	NO ₂	PM10	SO ₂
winter	0.29	−0.01	−0.25	−0.35	−0.13	0.49	0.54	0.79	0.48
summer	0.38	−0.05	−0.22	−0.38	−0.56	0.67	0.38	0.95	0.39

The correlation coefficient table shows that in winter, the pollutant most related to PM2.5 is PM10, followed by NO₂, CO, SO₂. O₃, wind power, and temperature have a low correlation. However, in summer, the correlation between meteorological factors and PM2.5 is different. The correlation ranking is $PM10 \geq CO \geq O_3 \geq SO_2 \geq NO_2$. If the $| \text{correlation coefficient} | < 0.4$, it has a low correlation; if $0.4 \leq | \text{correlation coefficient} | < 0.7$, it has a significant linear correlation; if $0.7 \leq | \text{correlation coefficient} | \leq 1$, it is highly correlated. In general, PM2.5 in Chengdu has a low correlation with temperature, humidity, and wind power, a significant correlation with CO, SO₂, NO₂, and O₃, and a high correlation with PM10.

Because PM2.5 and PM10 are both essential factors affecting haze, this paper uses PM2.5 and PM10 concentration to represent haze pollution, which is also the research object of our LSTM-based haze prediction model. According to the correlation analysis results, PM2.5 has a low correlation with temperature, humidity, and wind power in the short term. It is considered that the weather parameters are stable in the short term. Therefore, we selected CO, SO₂, NO₂, O₃, historical PM10, and historical PM2.5 as inputs to train the haze prediction model and achieve the goal of predicting the concentration of PM2.5/PM10.

3.2. Data Completion

The collected PM2.5, PM10, O₃, CO, NO₂, and SO₂ concentration data totaled 26,120. This paper calculates the mean of the previous and next state's concentration data. It completes the time series of missing data, as shown in Formula (8). The final data set contains PM2.5, PM10, O₃, CO, NO₂, and SO₂ concentration adequate data in 27,380 moments.

$$X_t = \frac{1}{2}(X_{t-1} + X_{t+1}) \quad (8)$$

In (8), X_t represents the missing concentration data at the current time, X_{t-1} represents the concentration data at the previous moment, and X_{t+1} represents the concentration data at the next time point. Furthermore, it is for sure that this could add additional noise to the dataset since we are just filling missing points with roughly generated data. We do not need to complete most of the dataset because the final dataset is only 3% greater than the vanilla one, which is tolerable for machine learning tasks.

3.3. Standardized Processing

In the neural network, large-value data tends to increase the proportion of influence on the model and makes the model lose the characteristic properties of the data with low value. Therefore, to avoid errors caused by different numerical ranges, we convert all historical concentration data to $-1 \sim 1$ (9).

$$X' = \frac{X - \bar{X}}{X_{\max} - X_{\min}} \quad (9)$$

X' denotes the concentration data after the standardized processing, X represents the original concentration data, \bar{X} denotes the mean of the concentration data, X_{\max} denotes the maximum value, and X_{\min} represents the minimum value.

In this paper, we base on the assumption that the PM_{2.5} or PM₁₀ concentration at the next moment is related to its short-term historical data and the O₃, CO, NO₂, and SO₂ concentration values at the same moment. Therefore, we reconstructed the dataset and used the PM_{2.5} concentration in the past 24 h. The current PM₁₀, O₃, CO, NO₂, and SO₂ concentration values were training data, and the corresponding ground truth was the current PM_{2.5} concentration. Similarly, we also constructed a dataset for predicting the concentration of PM₁₀. Again, the PM₁₀ concentration in the past 24 h and the PM_{2.5}, O₃, CO, NO₂, and SO₂ concentration values at the current time were used as training data. The ground truth was the current time PM₁₀ concentration. Finally, we divided the reorganized dataset into the training set, verification set, and test set according to 80%, 10%, and 10%.

4. Experiment and Result

4.1. Evaluation

This research is a simulation experiment of realizing the prediction model based on Python-TensorFlow framework.

In order to reflect the prediction accuracy of the haze prediction model at different levels, we used numerical evaluation and hierarchical evaluation. We used the root-mean-square error (RMSE) [35] as a numerical evaluation method to reflect the overall accuracy of the model's haze prediction values, as shown in (10).

$$RMSE = \sqrt{\frac{1}{m} \sum_i^m (T_i - P_i)^2} \quad (10)$$

In (10), i refers to the number of a test sample, m refers to the total number of predicted samples, T_i represents the actual concentration of the test sample, the ground-truth, with the unit: $\mu\text{g}/\text{m}^3$, and P_i represents the predicted concentration value with the unit: $\mu\text{g}/\text{m}^3$.

We divided the PM_{2.5} and PM₁₀ concentrations into six grades based on the Air Quality Index (AQI) to assess the model's error in macroscopic pollution levels, as shown in Table 2. If the prediction result and the result are at the same level, the prediction result is judged to be excellent; if the prediction result and the result are adjacent, the prediction result is determined to be acceptable; if the prediction result is different from the result by two levels or more, the predicted result is unacceptable.

Table 2. PM_{2.5} and PM₁₀ levels.

Level	1	2	3	4	5	6
Level range ($\mu\text{g}/\text{m}^3$)	0–35	36–75	76–115	116–150	151–250	>250

4.2. Result

In this paper, by changing the dataset, we used the LSTM-based haze prediction model to predict the concentration of PM_{2.5} and PM₁₀, respectively. The number of input layer nodes was 29, and the number of output layer nodes was 1. While predicting the PM_{2.5} concentration, the inputs were the PM₁₀, O₃, CO, NO₂, and SO₂ at the n hour and the PM_{2.5} concentration in the last 24 h. The output was the PM_{2.5} concentration at n hour. While predicting the PM₁₀ concentration, the inputs were the PM_{2.5}, O₃, CO, NO₂, and SO₂ at the n time, and the PM₁₀ concentration in the last 24 h. The output was the PM₁₀ concentration at the n hour.

The initialization parameters were as follows: the weight gradient learning rate was set to 0.01, the visible layer node bias was initialized to 0.05, the hidden layer node bias was initialized to 0.1, the target error was set to 0.005, and the iteration number was 5000.

We have also conducted several experiments to study the effect of different hidden layers on prediction accuracy. In order to more directly reflect the prediction result of PM_{2.5}/PM₁₀ and calculate the accuracy of the experiment, we selected the prediction data and actual data of 360 consecutive moments to demonstrate. We performed five

experiments on each model with different hidden layer numbers and selected the best result. The prediction results of PM2.5 concentration in different hidden layers based on the LSTM-based haze prediction model are shown in Table 3.

Table 3. PM2.5 prediction results with different hidden layers.

Hidden Layers	Neuron Distribution	PM2.5 RMSE $\mu\text{g}/\text{m}^3$	Excellent	Acceptable	Unacceptable
1	10	10.95	80.83%	18.89%	0.28%
2	10 9	9.72	81.67%	18.33%	0.00%
3	10 9 8	8.81	84.44%	15.56%	0.00%
4	10 9 8 7	8.41	83.89%	16.11%	0.00%
5	10 9 8 7 6	8.18	85.28%	14.72%	0.00%
6	10 9 8 7 6 5	8.31	84.72%	15.28%	0.00%
7	10 9 8 7 6 5 4	8.11	86.39%	13.61%	0.00%
8	10 9 8 7 6 5 4 3	8.23	85.56%	14.44%	0.00%

The PM2.5 prediction results show that even if the LSTM has only one hidden layer, the RMSE of the prediction result is only 10.95, which is a lower error level. Thus, the prediction level of PM2.5 is generally consistent with the actual situation, which indicates the high correlation between the input data and the concentration of PM2.5.

In fixing the number of hidden layer nodes, the prediction accuracy is related to the number of hidden layers. Therefore, the increase in the number of hidden layers generally improves the prediction accuracy of PM2.5, both at RMSE and level evaluation. However, the accuracy of the prediction result brought by the increase of the hidden layer also has a bottleneck. For example, when the hidden layer is 7, the mean square error is 8.11, the excellent is 86.39%, the acceptable is 13.61%, and the unacceptable is 0%. Figure 4 shows the PM2.5 prediction results of hidden layer 5 and hidden layer 7, respectively.

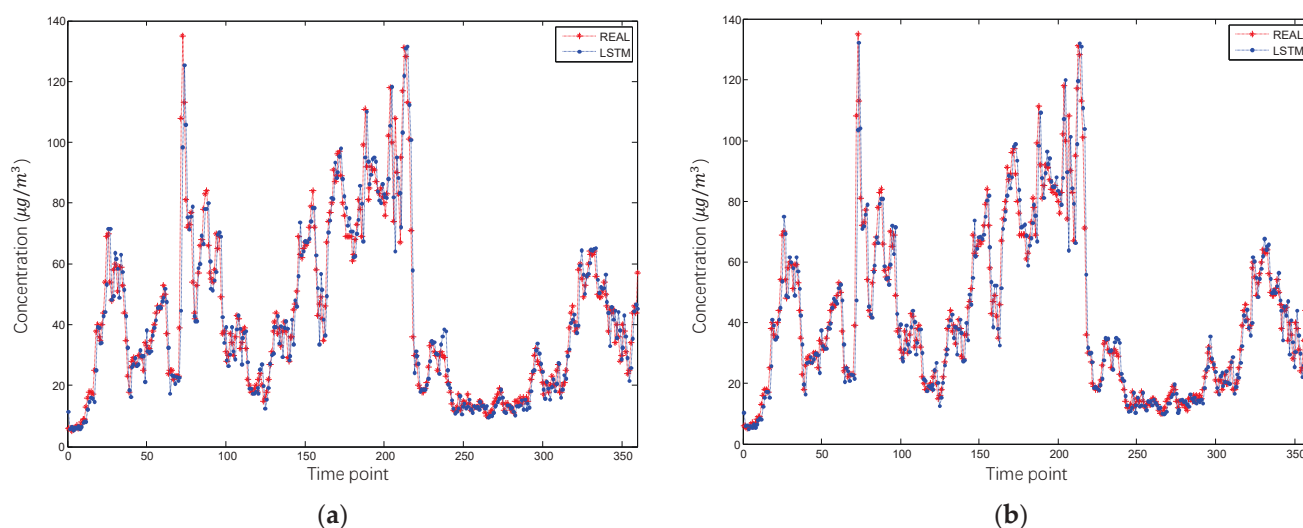


Figure 4. Prediction results of PM2.5 in different hidden layers of the LSTM model: (a) five hidden layers; (b) seven hidden layers.

We used the same method to predict the concentration of PM10. The predicted PM10 concentrations in different hidden layers based on the LSTM-based haze prediction model are shown in Table 4.

Increasing the number of the hidden layer can improve the prediction accuracy of PM10 to a certain extent, reducing the RMSE of the prediction result and improving the acceptability of the level prediction. For example, the haze prediction model with 7 hidden layers has the best result, where the root-mean-square error is 15.41, the excellent is 81.67%, the acceptable is 18.33%, and the unacceptable is 0%. Figure 5 shows the PM10 prediction

results of hidden layer 5 and hidden layer 7, respectively. However, the root-mean-square error value is also very close when the hidden layers are 5, 6, and 8. This shows that the improvement of hidden layers above five can hardly increase the accuracy of the predicted concentration of PM10, which is the limitation imposed by the LSTM model.

Table 4. PM10 prediction results with different hidden layers.

Hidden Layers	Neuron Distribution	PM10 RMSE $\mu\text{g}/\text{m}^3$	Excellent	Acceptable	Unacceptable
1	10	18.95	73.89%	25.28%	0.83%
2	10 9	17.02	78.61%	21.11%	0.28%
3	10 9 8	16.66	79.72%	20.00%	0.28%
4	10 9 8 7	16.05	80.56%	19.17%	0.28%
5	10 9 8 7 6	15.40	81.11%	18.89%	0.00%
6	10 9 8 7 6 5	15.48	81.11%	18.89%	0.00%
7	10 9 8 7 6 5 4	15.41	81.67%	18.33%	0.00%
8	10 9 8 7 6 5 4 3	15.40	81.39%	18.61%	0.00%

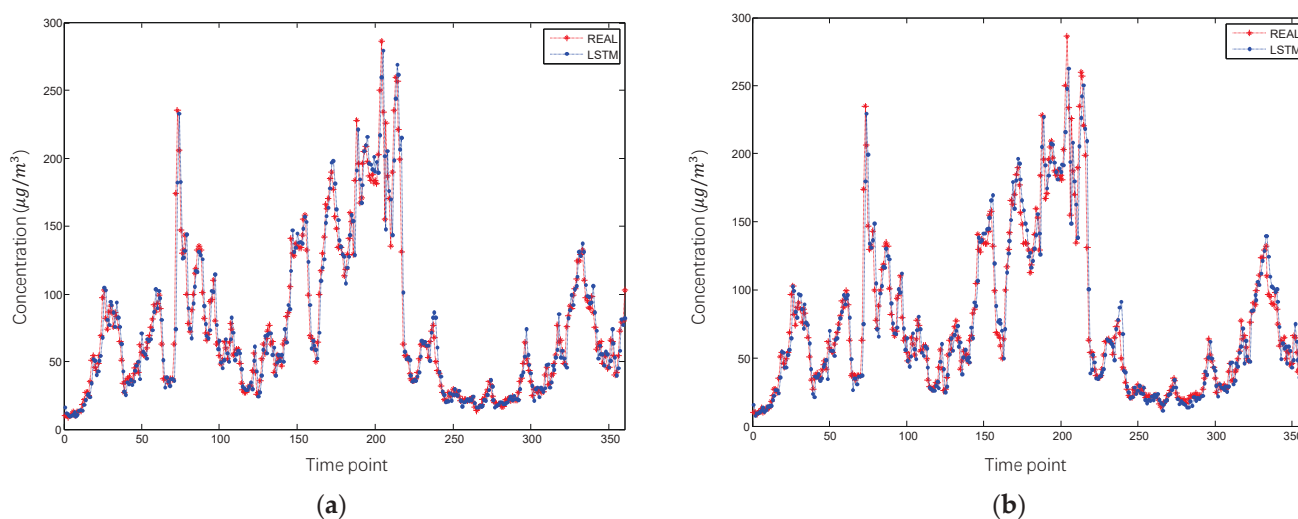


Figure 5. Prediction results of PM10 in different hidden layers of the LSTM model: (a) five hidden layers; (b) seven hidden layers.

Compared with Table 3, the RMSE of PM10 is always more significant than the RMSE of PM2.5. The haze prediction model also produces a more significant deviation in the PM10 level prediction. The excellent and acceptable levels are both reduced by about 5% compared to the PM2.5 level prediction. Analyzing the result accuracy of PM2.5 and PM10, we argue that the model fits well with the correlation between O_3 , CO, NO_2 , SO_2 , and haze pollutants and achieves accurate predictions both on haze concentration and level.

5. Discussion

This paper shows that LSTM with multiple layers stacked could dramatically increase the prediction's accuracy. Moreover, it is correlated to the general rule of deep learning models: a deep structure could better cope with complicated multi-dimension datasets than models with limited depth.

Furthermore, using correlation analysis could let us decide which part of the whole dataset should be included, which prevents us from just pouring all data into the network to waste time and damage the accuracy.

Compared with the CNN+LSTM model in [28], the multilayer LSTM model proposed in this paper can achieve more accurate results. The reason may be that the six monitoring stations selected in this article are all from Chengdu, with even distance intervals. The climate data except for the main pollutants are similar. Therefore, the mutual influence

between the data is small, leading to more accurate results. Compared with [29], its paper mentions that in the past 3, 8, 24, and 72 h forecast results, 72 h is the best forecast accuracy. We used the data of the past 24 h to predict PM_{2.5}, and the result is better than its 72 h forecast accuracy. Compared with [16], the original text uses the previous week's data (7 days) as the input of the data model. This paper uses the data 24 h ago as the input, which reduces the amount of calculation. Compared with [30], our multilayer LSTM shows more accurate and less biased results. We found that our model made more accurate predictions for such prediction tasks.

To keep increasing the model's accuracy and improve its ability to generalize, we are considering the following methods.

1. We could feed the network with more data from areas adjacent to the target area whose haze concentration is what we want to predict. Haze is always a meteorological phenomenon, which indicates that the appearance of haze should be related to what is happening around the target area. For instance, if there is a signal of a powerful wind around the target area yet such signal is not included in our data, we could make a massive error because a powerful wind is likely to take pollutants away. Therefore, including data from adjacent areas could better fit the reality.
2. A combination of different genres of deep learning models could be potentially helpful to increase accuracy. For example, we could consider that using a convolutional neural network to analyze a satellite photo could be helpful to give our sequential model a complete overall view of what is going to happen.
3. Deep learning models always show their abilities when there are so many dimensions of the input. Thus, it is reasonable to add more parameters to the model to generate a prediction. In conclusion, adding extra dimensions should be considered as a way to improve accuracy.
4. Since the GRU cell is generally a suitable replacement for the LSTM cell, since its complexity is lower yet the outcome remains much the same or even better, it is reasonable and worthy to use GRU to make predictions instead of LSTM. However, accuracy-wise speaking, LSTM is sufficient.
5. Network Architecture Search (NAS), for instance, a Bayesian theory-based searching method [36], could help optimize our settings about the hyperparameters so that accuracy could be improved even further.

Since our experiment shows that gas concentration data work when using them as materials to make haze concentration predictions, we are considering the potential of utilizing neural networks to make predictions because neural networks could learn some patterns of meteorological phenomena. However, even if we know much about the mechanics behind many meteorological phenomena, we can hardly predict what will take place a few more days later because there are too many noises and uncertain interferences. We can achieve better accuracy through neural networks because our simulation methods are limited when generating long-term predictions.

Since the volume of meteorological data could be tremendous, it makes sense to use deep learning structures to learn the hidden patterns. Therefore, in future work, besides achieving better performance when using current data to predict the target quantity, there is also a need to develop models for predicting the future since simulation does have its limitations.

6. Conclusions

This paper proposes a multilayer LSTM haze prediction model to predict the PM_{2.5}/PM₁₀ concentration in Chengdu, utilizing O₃, CO, NO₂, SO₂, and PM_{2.5}/PM₁₀ in the last 24 h as inputs. Analyzing the result accuracy of PM_{2.5} and PM₁₀, we argued that the model fits well with the correlation between O₃, CO, NO₂, SO₂, and haze pollutants and achieves accurate predictions both on haze concentration and level. At the same time, the prediction results show that, within a certain range, the greater the number of hidden layers, the higher the prediction accuracy. When a specific value is reached, the accuracy is roughly

equivalent. Under the same network, the prediction accuracy of PM_{2.5} is significantly higher than that of PM₁₀. Besides pre-processing the data, the primary approach to boost the prediction performance is adding layers above a single-layer LSTM model. Moreover, it is proved that by doing so, we could let the network make predictions more accurately and efficiently.

Author Contributions: S.L. and W.Z. contributed to the conception of the paper and supervision; L.Y. performed the formal experiment; W.Z. contributed significantly to analysis and manuscript preparation; J.T., L.S. and X.W. performed the data analyses and wrote the manuscript; B.Y. and Z.L. helped perform the analysis with constructive discussions; S.L. performed the formal analysis and revised the manuscript. All authors have read and agreed to the published version of the manuscript.

Funding: This work was jointly supported by the Sichuan Science and Technology Program (2021YFQ0003).

Institutional Review Board Statement: Not applicable.

Informed Consent Statement: Not applicable.

Data Availability Statement: The data that support the findings of this study are available from China National Environmental Monitoring Centre, but restrictions apply to the availability of these data, which were used under license for the current study, so are not publicly available. Data are, however, available from the authors upon reasonable request and with permission of the China National Environmental Monitoring Centre.

Conflicts of Interest: The authors declare no conflict of interest.

References

1. Lirong, Y.; Zheng, W.; Yin, L.; Yin, Z.; Song, L.; Tian, X. Influence of Social-economic Activities on Air Pollutants in Beijing, China. *Open Geosci.* **2017**, *9*, 314–321. [CrossRef]
2. Zheng, W.; Li, X.; Yin, L.; Wang, Y. Spatiotemporal heterogeneity of urban air pollution in China based on spatial analysis. *Rend. Lincei* **2016**, *27*, 351–356. [CrossRef]
3. Zheng, W.; Li, X.; Yin, L.; Wang, Y. The retrieved urban LST in Beijing based on TM, HJ-1B and MODIS. *Arab. J. Sci. Eng.* **2016**, *41*, 2325–2332. [CrossRef]
4. Li, X.; Lam, N.; Qiang, Y.; Li, K.; Yin, L.; Liu, S.; Zheng, W. Measuring County Resilience After the 2008 Wenchuan Earthquake. *Int. J. Disaster Risk Sci.* **2016**, *7*, 393–412. [CrossRef]
5. Zheng, W.; Li, X.; Xie, J.; Yin, L.; Wang, Y. Impact of human activities on haze in Beijing based on grey relational analysis. *Rend. Lincei* **2015**, *26*, 187–192. [CrossRef]
6. Hinton, G.E.; Salakhutdinov, R.R. Reducing the Dimensionality of Data with Neural Networks. *Science* **2006**, *313*, 504–507. [CrossRef]
7. Zhang, J.; Liu, L.; Wang, Y.; Ren, Y.; Wang, X.; Shi, Z.; Zhang, D.; Che, H.; Zhao, H.; Liu, Y.; et al. Chemical composition, source, and process of urban aerosols during winter haze formation in Northeast China. *Environ. Pollut.* **2017**, *231*, 357–366. [CrossRef]
8. Chaloulakou, A.; Kassomenos, P.; Spyrellis, N.; Demokritou, P.; Koutrakis, P. Measurements of PM₁₀ and PM_{2.5} particle concentrations in Athens, Greece. *Atmos. Environ.* **2003**, *37*, 649–660. [CrossRef]
9. Minguillón, M.; Querol, X.; Baltensperger, U.; Prévôt, A. Fine and coarse PM composition and sources in rural and urban sites in Switzerland: Local or regional pollution? *Sci. Total Environ.* **2012**, *427*, 191–202. [CrossRef]
10. Ho, K.; Cao, J.; Lee, S.; Chan, C.K. Source apportionment of PM_{2.5} in urban area of Hong Kong. *J. Hazard. Mater.* **2006**, *138*, 73–85. [CrossRef]
11. Manly, B.F.; Alberto, J.A.N. *Multivariate Statistical Methods: A Primer*; Chapman and Hall/CRC: Boca Raton, FL, USA, 2016.
12. Yin, L.; Li, X.; Zheng, W.; Yin, Z.; Song, L.; Ge, L.; Zeng, Q. Fractal dimension analysis for seismicity spatial and temporal distribution in the circum-Pacific seismic belt. *J. Earth Syst. Sci.* **2019**, *128*, 22. [CrossRef]
13. Tang, Y.; Liu, S.; Li, X.; Fan, Y.; Deng, Y.; Liu, Y.; Yin, L. Earthquakes spatio-temporal distribution and fractal analysis in the Eurasian seismic belt. *Rend. Lincei* **2020**, *31*, 203–209. [CrossRef]
14. Chen, X.; Yin, L.; Fan, Y.; Song, L.; Ji, T.; Liu, Y.; Tian, J.; Zheng, W. Temporal evolution characteristics of PM_{2.5} concentration based on continuous wavelet transform. *Sci. Total Environ.* **2020**, *699*, 134244. [CrossRef]
15. Elbayoumi, M.; Ramli, N.A.; Yusof, N.F.F.M.; Bin Yahaya, A.S.; Al Madhoun, W.; Ul-Saufie, A.Z. Multivariate methods for indoor PM₁₀ and PM_{2.5} modelling in naturally ventilated schools buildings. *Atmos. Environ.* **2014**, *94*, 11–21. [CrossRef]
16. Li, T.; Hua, M.; Wu, X. A Hybrid CNN-LSTM Model for Forecasting Particulate Matter (PM_{2.5}). *IEEE Access* **2020**, *8*, 26933–26940. [CrossRef]
17. Zheng, W.; Li, X.; Lam, N.; Wang, X.; Liu, S.; Yu, X.; Sun, Z.; Yao, J. Applications of integrated geophysical method in archaeological surveys of the ancient Shu ruins. *J. Archaeol. Sci.* **2013**, *40*, 166–175. [CrossRef]

18. Pérez, P.; Trier, A.; Reyes, J. Prediction of PM_{2.5} concentrations several hours in advance using neural networks in Santiago, Chile. *Atmos. Environ.* **2000**, *34*, 1189–1196. [CrossRef]
19. Liu, S.; Wang, L.; Liu, H.; Su, H.; Li, X.; Zheng, W. Deriving Bathymetry from Optical Images with a Localized Neural Network Algorithm. *IEEE Trans. Geosci. Remote Sens.* **2018**, *56*, 5334–5342. [CrossRef]
20. Deng, Y.; Tang, Y.; Yang, B.; Zheng, W.; Liu, S.; Liu, C. A Review of Bilateral Teleoperation Control Strategies with Soft Environment. In Proceedings of the 2021 6th IEEE International Conference on Advanced Robotics and Mechatronics (ICARM), Chongqing, China, 3–4 July 2021; pp. 459–464.
21. Yin, L.; Wang, L.; Huang, W.; Liu, S.; Yang, B.; Zheng, W. Spatiotemporal Analysis of Haze in Beijing Based on the Multi-Convolution Model. *Atmosphere* **2021**, *12*, 1408. [CrossRef]
22. Sherstinsky, A. Fundamentals of Recurrent Neural Network (RNN) and Long Short-Term Memory (LSTM) network. *Phys. D Nonlinear Phenom.* **2020**, *404*, 132306. [CrossRef]
23. Zheng, W.; Liu, X.; Yin, L. Sentence Representation Method Based on Multi-Layer Semantic Network. *Appl. Sci.* **2021**, *11*, 1316. [CrossRef]
24. Zheng, W.; Liu, X.; Ni, X.; Yin, L.; Yang, B. Improving Visual Reasoning through Semantic Representation. *IEEE Access* **2021**, *9*, 91476–91486. [CrossRef]
25. Zheng, W.; Yin, L.; Chen, X.; Ma, Z.; Liu, S.; Yang, B. Knowledge base graph embedding module design for Visual question answering model. *Pattern Recognit.* **2021**, *120*, 108153. [CrossRef]
26. Zheng, W.; Liu, X.; Yin, L. Research on image classification method based on improved multi-scale relational network. *PeerJ Comput. Sci.* **2021**, *7*, e613. [CrossRef]
27. Li, Y.; Zheng, W.; Liu, X.; Mou, Y.; Yin, L.; Yang, B. Research and improvement of feature detection algorithm based on FAST. *Rend. Lincei* **2021**, 1–15. [CrossRef]
28. Qin, D.; Yu, J.; Zou, G.; Yong, R.; Zhao, Q.; Zhang, B. A novel combined prediction scheme based on CNN and LSTM for urban PM_{2.5} concentration. *IEEE Access* **2019**, *7*, 20050–20059. [CrossRef]
29. Tsai, Y.-T.; Zeng, Y.-R.; Chang, Y.-S. Air pollution forecasting using RNN with LSTM. In Proceedings of the 2018 IEEE 16th International Conference on Dependable, Autonomic and Secure Computing, 16th International Conference on Pervasive Intelligence and Computing, 4th International Conference on Big Data Intelligence and Computing and Cyber Science and Technology Congress (DASC/PiCom/DataCom/CyberSciTech), Athens, Greece, 12–15 August 2018; pp. 1074–1079.
30. Bai, Y.; Zeng, B.; Li, C.; Zhang, J. An ensemble long short-term memory neural network for hourly PM_{2.5} concentration forecasting. *Chemosphere* **2019**, *222*, 286–294. [CrossRef] [PubMed]
31. Tang, Y.; Liu, S.; Deng, Y.; Zhang, Y.; Yin, L.; Zheng, W. An improved method for soft tissue modeling. *Biomed. Signal Process. Control.* **2021**, *65*, 102367. [CrossRef]
32. Ma, Z.; Zheng, W.; Chen, X.; Yin, L. Joint embedding VQA model based on dynamic word vector. *PeerJ Comput. Sci.* **2021**, *7*, e353. [CrossRef] [PubMed]
33. Zhang, Z.; Tian, J.; Huang, W.; Yin, L.; Zheng, W.; Liu, S. A Haze Prediction Method Based on One-Dimensional Convolutional Neural Network. *Atmosphere* **2021**, *12*, 1327. [CrossRef]
34. Gers, F.A.; Schmidhuber, J.; Cummins, F.A. Learning to Forget: Continual Prediction with LSTM. *Neural Comput.* **2000**, *12*, 2451–2471. [CrossRef] [PubMed]
35. Keane, R.D.; Adrian, R.J. Theory of cross-correlation analysis of PIV images. *Flow Turbul. Combust.* **1992**, *49*, 191–215. [CrossRef]
36. Snoek, J.; Larochelle, H.; Adams, R.P. Practical bayesian optimization of machine learning algorithms. *Adv. Neural Inf. Process. Syst.* **2012**, *25*, 2951–2959.

Article

Restricted Anthropogenic Activities and Improved Urban Air Quality in China: Evidence from Real-Time and Remotely Sensed Datasets Using Air Quality Zonal Modeling

Saidur Rahaman ¹ , Selim Jahangir ², Ruishan Chen ^{1,*}  and Pankaj Kumar ³ 

¹ Key Laboratory of Geographic Information Science, School of Geographic Sciences, Ministry of Education, East China Normal University, Shanghai 200241, China; 52183901022@stu.ecnu.edu.cn

² Transdisciplinary Centre for Qualitative Methods, Prasanna School of Public Health, Manipal Academy of Higher Education, Udipi 576104, India; selim.jahangir@learner.manipal.edu

³ Department of Geography, Delhi School of Economics, University of Delhi, New Delhi 110007, India; pankajdsedu@gmail.com

* Correspondence: rschen@geo.ecnu.edu.cn

Abstract: The study aims to examine the major atmospheric air pollutants such as NO₂, CO, O₃, PM_{2.5}, PM₁₀, and SO₂ to assess the overall air quality using air quality zonal modeling of 15 major cities of China before and after the COVID-19 pandemic period. The spatio-temporal changes in NO₂ and other atmospheric pollutants exhibited enormous reduction due to the imposition of a nationwide lockdown. The present study used a 10-day as well as 60-day tropospheric column time-average map of NO₂ with spatial resolution 0.25 × 0.25° obtained from the Global Modeling and Assimilation Office, NASA. The air quality zonal model was employed to assess the total NO₂ load and its change during the pandemic period for each specific region. Ground surface monitoring data for CO, NO₂, O₃, PM₁₀, PM_{2.5}, and SO₂ including Air Quality Index (AQI) were collected from the Ministry of Environmental Protection of China (MEPC). The results from both datasets demonstrated that NO₂ has drastically dropped in all the major cities across China. The concentration of CO, PM₁₀, PM_{2.5}, and SO₂ demonstrated a decreasing trend whereas the concentration of O₃ increased substantially in all cities after the lockdown effect as observed from real-time monitoring data. Because of the complete shutdown of all industrial activities and vehicular movements, the atmosphere experienced a lower concentration of major pollutants that improves the overall air quality. The regulation of anthropogenic activities due to the COVID-19 pandemic has not only contained the spread of the virus but also facilitated the improvement of the overall air quality. Guangzhou (43%), Harbin (42%), Jinan (33%), and Chengdu (32%) have experienced maximum air quality improving rates, whereas Anshan (7%), Lanzhou (17%), and Xian (25%) exhibited less improved AQI among 15 cities of China during the study period. The government needs to establish an environmental policy framework involving central, provincial, and local governments with stringent laws for environmental protection.

Keywords: COVID-19; air pollution; lockdown; air quality zonal modeling; China

Citation: Rahaman, S.; Jahangir, S.; Chen, R.; Kumar, P. Restricted Anthropogenic Activities and Improved Urban Air Quality in China: Evidence from Real-Time and Remotely Sensed Datasets Using Air Quality Zonal Modeling. *Atmosphere* **2022**, *13*, 961. <https://doi.org/10.3390/atmos13060961>

Academic Editors: Duanyang Liu, Kai Qin and Honglei Wang

Received: 7 May 2022

Accepted: 30 May 2022

Published: 14 June 2022

Publisher's Note: MDPI stays neutral with regard to jurisdictional claims in published maps and institutional affiliations.



Copyright: © 2022 by the authors. Licensee MDPI, Basel, Switzerland. This article is an open access article distributed under the terms and conditions of the Creative Commons Attribution (CC BY) license (<https://creativecommons.org/licenses/by/4.0/>).

1. Introduction

Air pollution and its quality in cities are the major concerns worldwide and China is no exception. Air pollution has been a serious environmental issue in China since extensive industrial production and other anthropogenic activities exponentially increased the concentration of major atmospheric pollutants that damaged the environmental quality and harmfully impacted human health [1–5]. The World Health Organization (WHO) reiterates that environmental and health risk factors from outdoor air pollution are substantial. In 2016, 91% of the world population was living in places where the WHO air quality guidelines levels were not met [6]. New estimates in 2018 revealed that 9 out of 10 people breathe air containing high levels of pollutants [7]. Over the last four decades,

rapid economic development, industrialization, and urbanization across China has caused serious air pollution problems [8–10]. China's National Western Development Strategies (the 'Go West' movement) by the Chinese government in 1999 also contributed to the spatial expansion of industrialization and urbanization [11]. This has resulted in the GDP reaching around RMB 8270 billion, to which industrial production contributes 34% as the most significant contributing factor (<http://www.stats.gov.cn/tjsj/ndsj/>, accessed on 18 April 2020). Furthermore, due to rapid industrialization and urbanization air pollution has become the fourth primary health risk factor for all deaths in China after heart attack, dietary risk, and smoking [12]. The recent COVID-19 pandemic at the global and regional level has substantially affected the spatial and temporal characteristics of significant air pollutants, such as NO₂, CO, O₃, PM₁₀, PM_{2.5}, and SO₂ across China [13–15]. In this context, the present study aims to assess the overall air quality from ground-based monitoring and remotely sensed datasets using air quality zonal modeling in 15 major cities of China before and after pandemic lockdown periods. Here, we estimated the changes in pollutant concentration and the spatio-temporal variation characteristics for 60 days before and after the shutting down of the nation. Section 2 discusses data and methods where we mentioned data sources, how we analyzed the data, and what techniques we used. Next are the results in Section 3 where we analyzed the spatio-temporal distribution of NO₂ before and after the pandemic; total NO₂ load over the area using air quality zonal modeling, and trends of air pollutants in China before and after the pandemic. Section 4 presents the discussion where we critically evaluate the results and link our study with other relevant studies with reasons and evidence.

NO₂ is primarily released by anthropogenic emissions, which contain the industrial burning of fossil fuels such as coal, oil, natural gas, vehicle exhaust, biomass burning, and electricity generation [16–18]. Pollutants such as carbon monoxide (CO) and sulphur dioxide (SO₂) are mainly released from industrial plants and heating processes due to anthropogenic activities [19]. SO₂ is regarded as one of the major air pollutants in cities because of its negative effects on human health and the ecosystem [20]. Particulate Matter (PM₁₀, PM_{2.5}) is a common proxy indicator for air pollution and it affects more people than any other pollutant. The major components of PM are sulfate, nitrates, ammonia, sodium chloride, black carbon, mineral dust, and water [6]. Tropospheric O₃ is produced by emissions of nitrogen oxides (NO_x = NO + NO₂) and volatile organic compounds (VOCs) in the presence of sunlight [21]. The distribution of O₃ varies with space and time and is lower in urban polluted areas than elsewhere because it disappears when it reacts with other pollutants [22,23]. Among NO_x elements, NO₂ is the most important precursor and quencher of O₃ through NO_x titration particularly during wintertime [24]. The daytime relationship between NO₂ and O₃ concentration in Northern China demonstrates significant ozone titration. However, this titration effect has been considerably attenuated with increasing PM_{2.5}, which further reduces the incoming solar radiation, during the lockdown period [25]. It is not only harmful to human health but also poses adverse impacts on plants and ecosystems [1,3,26,27].

Various studies have been carried out to investigate the spatial and temporal distribution patterns of NO₂, CO, O₃, PM₁₀, PM_{2.5}, and SO₂ at national, regional, and local levels [2,28–42] along with their driving forces in the recent past [27,43–46]. Numerous studies have shown a strong correlation between level of exposure to atmospheric pollutants and human health [2,4,5]; increased mortality [47–49]; sleeping disorders among elderly [50]; body weight and obesity [51]. To mitigate air pollution, the Chinese government has imposed stringent air quality standards [52] and strengthened emission controls of major atmospheric pollutants [53–57].

The understanding of the spatial distribution of air pollution in China has been recently improved by the application of advanced assessment tools, such as satellite remote sensing. The satellite-retrieved products have many advantages, including global coverage, high spatial-temporal resolution, and historical datasets [41,42,47]. Amid the coronavirus pandemic in China, NASA and European Space Agency (ESA) pollution monitoring satellites

have detected significant decreases in nitrogen dioxide (NO₂) over mainland China [13–15]. There is evidence that the change is at least partly related to the economic slowdown following the outbreak of the COVID-19 virus. According to NASA scientists, the reduction in NO₂ pollution was first apparent near Wuhan, but eventually broke out across the country [58]. In line with the previous studies of holiday effects on pollution [59–62], the main purpose of this work is to quantify spatial and temporal changes in primary pollutants such as NO₂, CO, O₃, PM₁₀, PM_{2.5}, and SO₂ over China's mainland due to shutdown of anthropogenic activities.

2. Data and Methods

2.1. Study Region

This study focuses on COVID-19's footprint on air quality in 15 cities of China's mainland namely Guangzhou, Xiamen, Xian, Wuhan, Beijing, Nanjing, Xinjiang, Lanzhou, Anshan, Shanghai, Jinan, Harbin, Chongqing, Zhengzhou, and Chengdu from where 145 random grid samples were taken for micro-level assessment with the help of air quality zonal modeling (Figures 3 and 6).

2.2. Data Source

The time-average map of NO₂ for consecutive 10- and 60-day average tropospheric columns (molecules/cm²) and time series daily area-average of NO₂ tropospheric columns (30% cloud screened) with spatial resolution $0.25 \times 0.25^\circ$ from 24 November 2019 to 22 March 2020 were collected from Giovanni interface [63–65], Global Modeling and Assimilation Office, NASA. The hourly and daily average concentrations of CO, O₃, NO₂, PM₁₀, PM_{2.5}, SO₂, and AQI data for 50 consecutive days before and 50 days after lockdown were collected from ground monitoring stations provided by the Ministry of Environmental Protection of China (MEPC), China Ministry of Ecology and Environment (<https://aqicn.org/map/china/cn/>, accessed on 20 March 2020) for the same study period.

2.3. OMI Data Retrieval

Nitrogen dioxide (NO₂) is a very important atmospheric gas in both the troposphere where it is a precursor to ozone production and in the stratosphere where it plays the main role in ozone chemistry (https://disc.gsfc.nasa.gov/datasets/OMNO2d_003/summary, accessed on 25 March 2020). NO₂ in the troposphere is produced in various combustion processes and lightning, which is an indicator of poor air quality [66]. NO₂ product (OMNO2d) is a daily global Level-3 gridded data with a spatial resolution of $0.25 \times 0.25^\circ$ [67,68] which contains time-average tropospheric column (30% cloud screened) and area-average total column [31]. We further retrieved the dataset from optional tools (use smoothing, equidistant cylindrical projection system) with linear scaling and a maximum of 65 palettes were used for this study. In this process, we ignored negative values especially for the 10-day average of the NO₂ total column map [31,69].

2.4. Data Analysis Method

As mentioned before, OMI data have been used for detecting the total column of NO₂ levels in the atmosphere [31,70]. Previous studies [31,70–72] have also used time-average OMI tropospheric total column maps and area-average OMI tropospheric total column datasets for assessing the air quality, especially for macro scale. We selected China's mainland for this study and assessed the total column of NO₂ before and after the outbreak of COVID-19. This study divided China's mainland into 145 grids (dimension 255×255 km²) for the micro-level study. While in the process, the work extracted the exact value of NO₂ tropospheric total column of each grid for 15 cities using spatial attribute tools in ArcMap and then we divided 145 grids into 5 equal categories based on the maximum and minimum range. In the last stage, we calculated the total area of each category and compared the extracted datasets with before and after 60- and 10-day area-average columns of NO₂ in total and in percentage.

We calculated the daily mean concentration of CO, O₃, NO₂, PM₁₀, PM_{2.5}, SO₂, and AQI from ground monitoring datasets provided by MEPC. We also calculated the 50 days before and after average concentration of each pollutant in 14 major cities of China obtained from real-time datasets. This study conducted a compound bar graph and trend line analysis for monitoring the change in air quality before and after the lockdown of 14 cities of China, in terms of total and percentage.

Air Quality Zonal Modeling

We conducted air quality zonal modeling for predicting zonal change in air quality. In general, the air quality zonal modeling represents the overall pollution concentration in any specific region based on several pollutant particles obtained from remotely sensed raster datasets [73]. In other words, the air quality zonal model is a compilation of total air pollution load in a particular zone accumulated by various air pollution particles which is represented through individual grids over a specific time period. This spatial and temporal model were created through different phases using various statistical analyses of GES-DISC time-averaged map and area-averaged time-series datasets obtained from MODIS- Terra, MERRA-2, OMI, and AIRS.

For this study, we conducted various sets of statistical analyses for interpreting remotely sensed data. In the first phase, we divided China's mainland into 145 grids, each grid representing 65,025 km². After that, we extracted each pollutant's average concentration from an individual grid using the raster calculator in ArcMap. The Moving Mean (MM) of 10 days total column of NO₂ of 15 cities was interpreted using equation 1. A specific grid value was ranked using exploratory analysis of ranking given by Alvo and Philip [74] (Equation (2)). The average concentration of each air pollutant particle of 145 grids was categorized based on the maximum and minimum range of datasets which is computed in the second phase (Equation (3)). After that, we compiled total pollution concentration in a specific grid using composite indexing and principal component analysis (PCA); subsequently, we conducted Spearman's model for factor analysis for assessing the maximum and minimum reduction [75] in specific air pollutants which is compiled in the third phase (Equations (2) and (3)). The 60-day average total air pollution load was calculated using Equation (4); here, we excluded zero factors of different raster datasets. The sum of the 60-day average concentration of different air pollutants and their percentage change was calculated using Equation (5). Zonal indexing of specific grids was formulated for extracting the exact concentration of air pollution (Equation (6)) and in the last phase, we calculated area/grid-wise total air pollution load (Equations (7) and (8)) through spatial analysis tools in GIS using air quality zonal modeling.

$$mm = \frac{\sum 10}{n} \times 6 \quad (1)$$

where mm = moving mean, $\sum 10$ = sum of 10 days average, n = number, and 6 = number of raster data.

$$m = \sum_{j=1}^{dx} \frac{(n_j v_j) \times i}{n} \quad (2)$$

where m = mean rank, dx = dimension, i = th entry equals, v_j , $j = 1$ represents all possible rankings of the dx , n_j = frequency of ranking, $v_j(i)$ = rank score, and n = number of raster data sets.

$$x = [n_1 F_1 + n_2 F_2 + \dots + n_{mm} F_m + s_m F_m] \quad (3)$$

where x = variation in maximum and minimum range of air pollutants with zero mean, n_1 , n_2 = loading factors of specified air pollutants and n_{mm} = moving mean,

F_1, F_2 = common factors and F_m = moving mean of the common factor with zero mean, and s_m = specific factor of the individual mean.

$$\mu p = \left[\frac{\sum (x_1 + x_2 + x_3 + x_4 + x_5 + x_6)}{6} \right] \cup [na] \quad (4)$$

where μp = 60 days average of pollution load, x = sum of 10 days average of pollution load, 6 = number of datasets, and $\cup [na]$ = excluding factor of zero (data not available).

$$p = \frac{(\sum 60a - \sum 60b)}{\sum 60b} \times 100 \quad (5)$$

where p = change in percentage, $\sum 60$ = sum of 60 days average concentration, a = during lockdown, and b = before.

$$a = \sqrt{\frac{\sum w_i (x_i - x)^2}{\sum w_i}} \quad (6)$$

where a = area of individual cells, w = weights, i = an index over all the data points being averaged, and x_i = individual pollutant variables.

$$t = \sum taop - [na] \quad (7)$$

where t = total pollution counts in individual grids, $taop$ = total air pollution load, $[na]$ = excluding 'data not available' grids.

$$a = n \times dx \quad (8)$$

where a = total area of each category, n = number of countable grids, and dx = dimension of different variables/ grids ($255 \times 255 \text{ km}^2$).

3. Results

3.1. Spatio-Temporal Distribution of NO_2 before and after the Pandemic

The spatial distribution of 10-day time-average maps of NO_2 tropospheric columns before and after the COVID-19 pandemic exhibited that the cities experienced a low concentration of NO_2 and improved quality of air. Among these, the period 2 February to 11 February observed the lowest level of NO_2 in all 15 major cities (Figure 1).

The post-lockdown maps portray that NO_2 concentration has increased from 22 February to 12 March and then again started decreasing from 13 March to 22 March. The 10-day average NO_2 tropospheric column (Figure 2) reveals that the level of NO_2 has tremendously reduced in major cities such as Guangzhou, Beijing, Anshan, Zhengzhou, and Chengdu after the pandemic. The air quality has started improving from the 2nd week of January just after the lockdown throughout the country.

Similarly, the 60-day time-average map (Figure 3) of NO_2 tropospheric column also displayed that the lowest range of NO_2 concentration was 2^{e+14} and the maximum concentration was 3.5^{e+16} before imposition of lockdown whereas the lowest range of NO_2 concentration came down to 1.4^{e+15} and the maximum to 1.8^{e+16} after the lockdown.

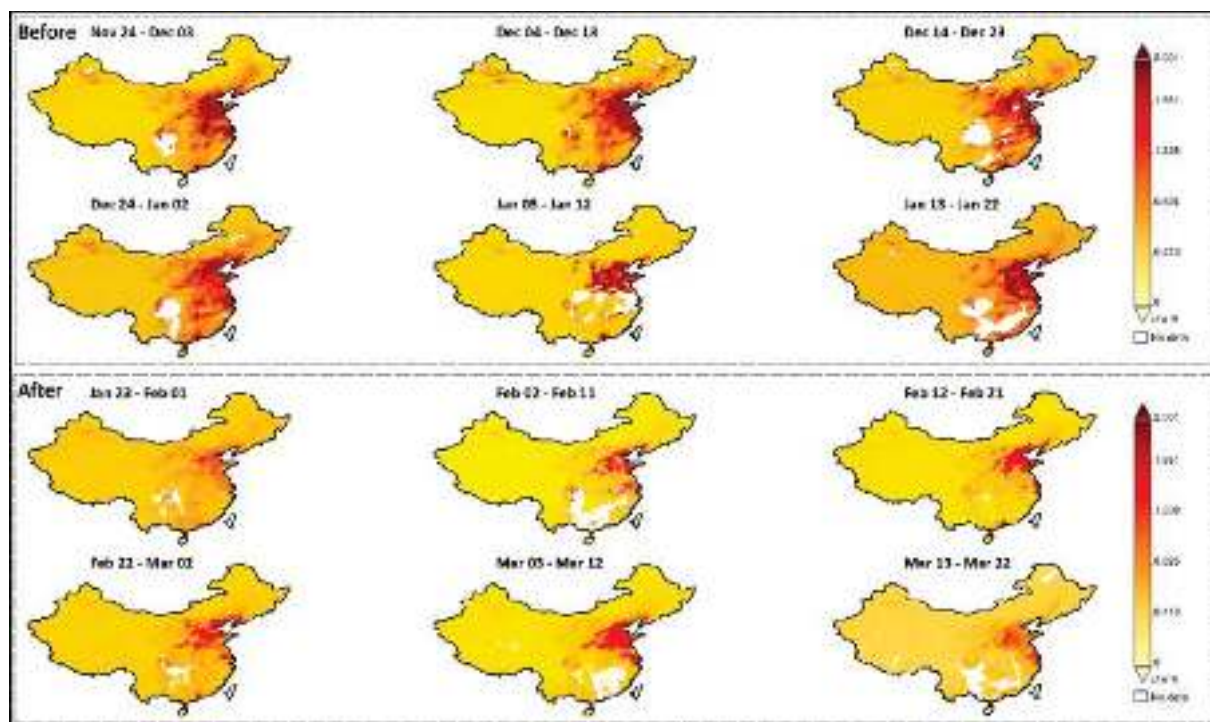


Figure 1. Spatial distribution of 10-day time-average map of NO₂ tropospheric column of China before (24 November 2019 to 22 January 2020) and after the pandemic (23 January to 22 March 2020). Source: OMI, Global Modeling and Assimilation Office, NASA, 2020.

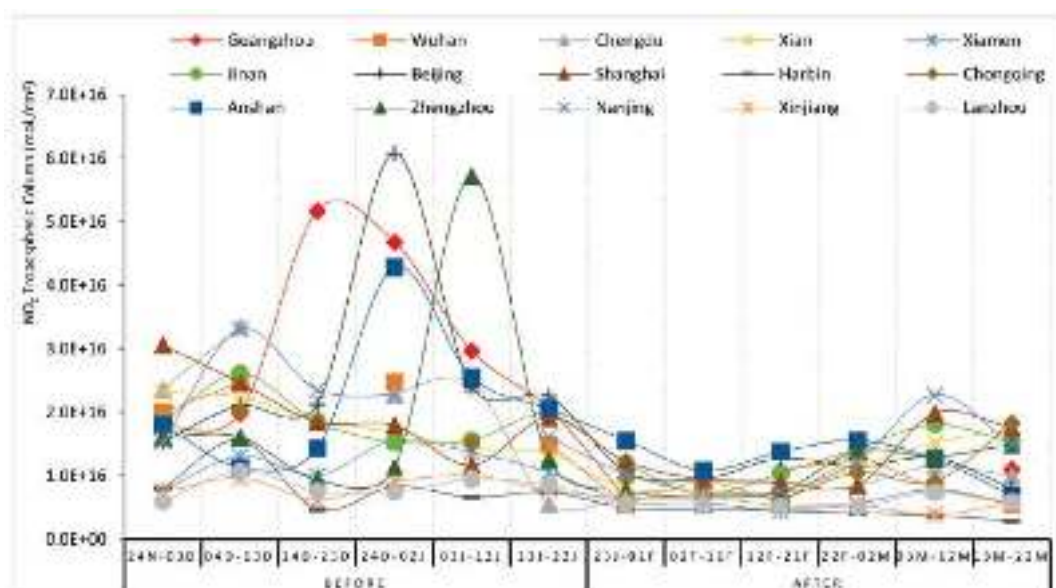


Figure 2. Temporal variation (10 days average) in NO₂ tropospheric column of 15 major cities of China before and after the pandemic. Sources: Calculated by author, 2020.

The absolute concentration of NO₂ tropospheric column (Figure 4) also revealed that all 15 major cities of China experienced lower emissions of NO₂ just after lockdown. The maximum concentration of NO₂ tropospheric column was 2.8×10^{16} before lockdown (24 November–22 January) and the minimum concentration was 1×10^{16} after lockdown (23 January–22 March) (Figure 4a). While we look at the proportion of NO₂ concentration reduction, Guangzhou received only 37% of NO₂ in the atmosphere after the pandemic. Similarly, the air quality of other cities also improved because of low emissions of NO₂ after lockdown. The graph (Figure 4b) revealed that Wuhan received only 35% of NO₂

concentration; whereas, Chengdu received 39%, Beijing 41%, Nanjing 48%, Xiamen 50%, Chongqing 53%, and Harbin 57% after the pandemic outbreak (23 January–22 March). On the other hand, the minimum reduction in NO_2 concentration was found in cities of Anshan (67%), Lanzhou (67%), Jinan (66%), Xinjiang (65%) where NO_2 concentration was comparatively low even before the pandemic in these same regions (Figure 4b).

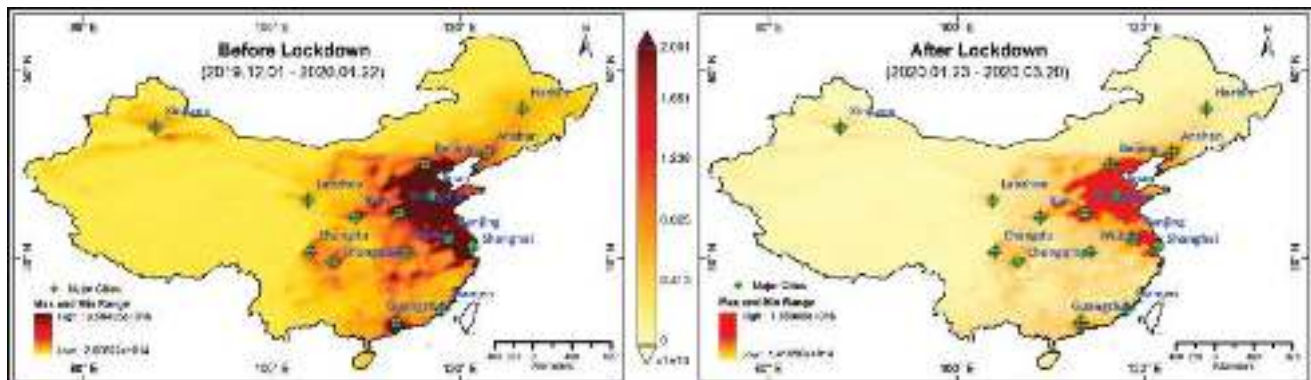


Figure 3. Time-average map of NO_2 tropospheric column (molecules/ cm^2) of 15 major cities of China before and after the pandemic. Source: OMI, Global Modeling and Assimilation Office, NASA, 2020.

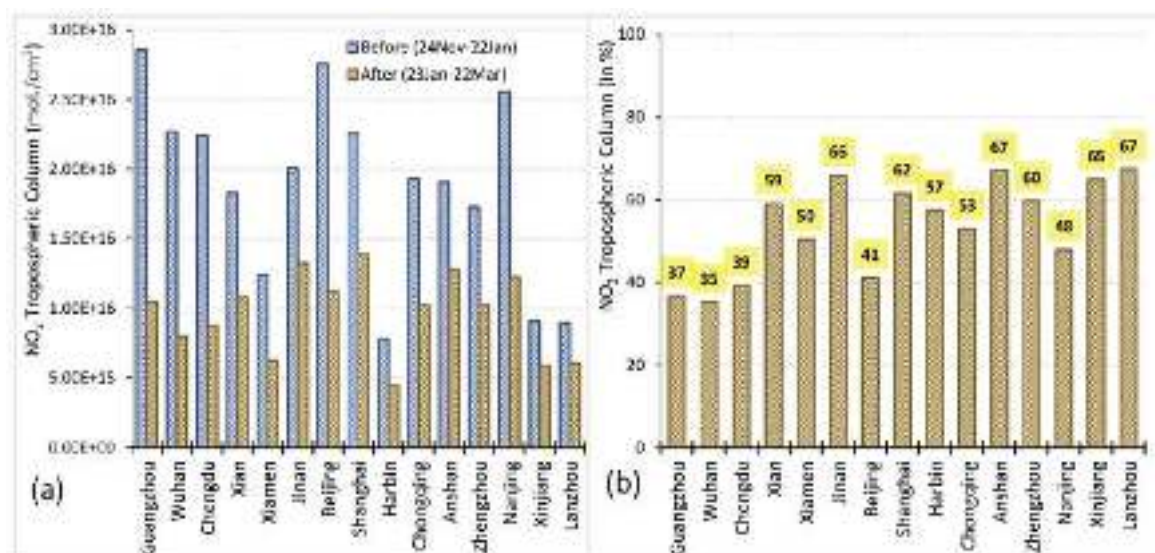


Figure 4. NO_2 tropospheric column of 15 major cities of China before and after the pandemic. (a) Absolute concentration and (b) decline in percentage. Source: Calculated by author, 2020.

The time-series of NO_2 tropospheric column graph (30% cloud screened) displays that the total mass column of NO_2 in China was highest during the first two weeks of December 2019 and remained as high as 4.3×10^{15} till the second week of January. After that, the NO_2 mass column suddenly dropped till March 22 (Figure 5).

3.2. Total NO_2 Load over the Area Using air Quality Zonal Modeling

A total 60-day average NO_2 tropospheric column was demonstrated through the air quality zonal modeling (Figure 6). Here, the whole country was divided into 145 grids ($255 \times 255 \text{ km}^2$) where the spatial distribution of NO_2 (Figure 6a) was displayed for the micro-level understanding of the air quality changes in different regions of the country. The area was also calculated under each grid category. The NO_2 concentration ranges between (1.7×10^{15} – 3.2×10^{15}) had 131 grids and the area was 5.5 million sq.km before the lockdown but the grids have increased to 191 and the area has also increased to 80 million sq.km. Conversely, the areas under the high NO_2 concentration category (5.5×10^{15} – 9.8×10^{15}) have

significantly decreased from 1.1 to 0.2 million sq.km. Moreover, there was a significant decrease in NO₂ concentration in the areas that come under a very high concentration category where the NO₂ tropospheric column ranges between 1.6×10^{16} and 2.6×10^{16} ; 13 grids were accounting for 0.55 million km² before the lockdown but none of the areas were under this very high category after lockdown (Figure 6a).

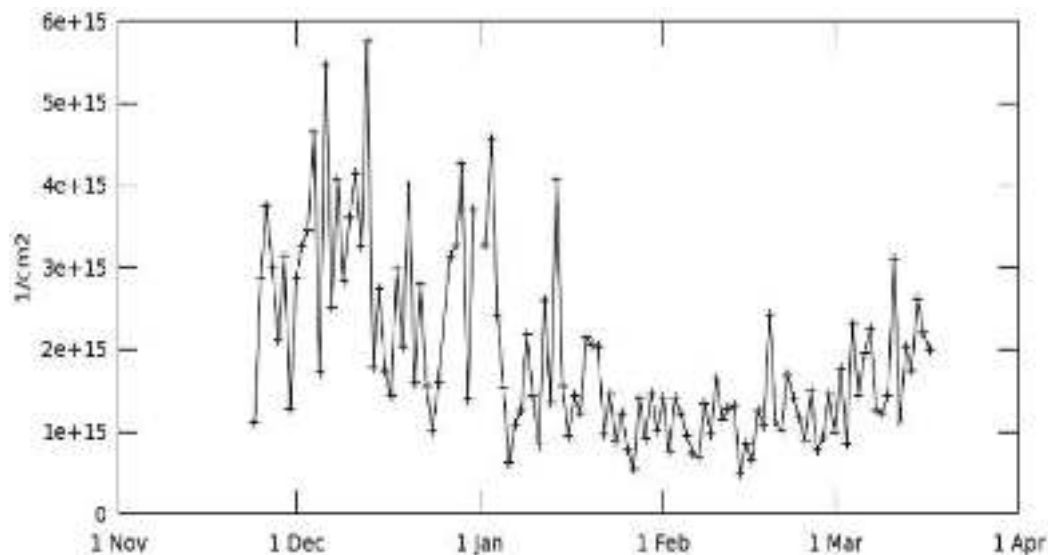


Figure 5. Time series, area-average of NO₂ tropospheric column (30% cloud screened) daily 0.25 deg. [OMI OMNO2d v003] 1/cm² over 24 November 2019–22 March 2020, shape China. Source: OMI, Global Modeling and Assimilation Office, NASA, 2020.

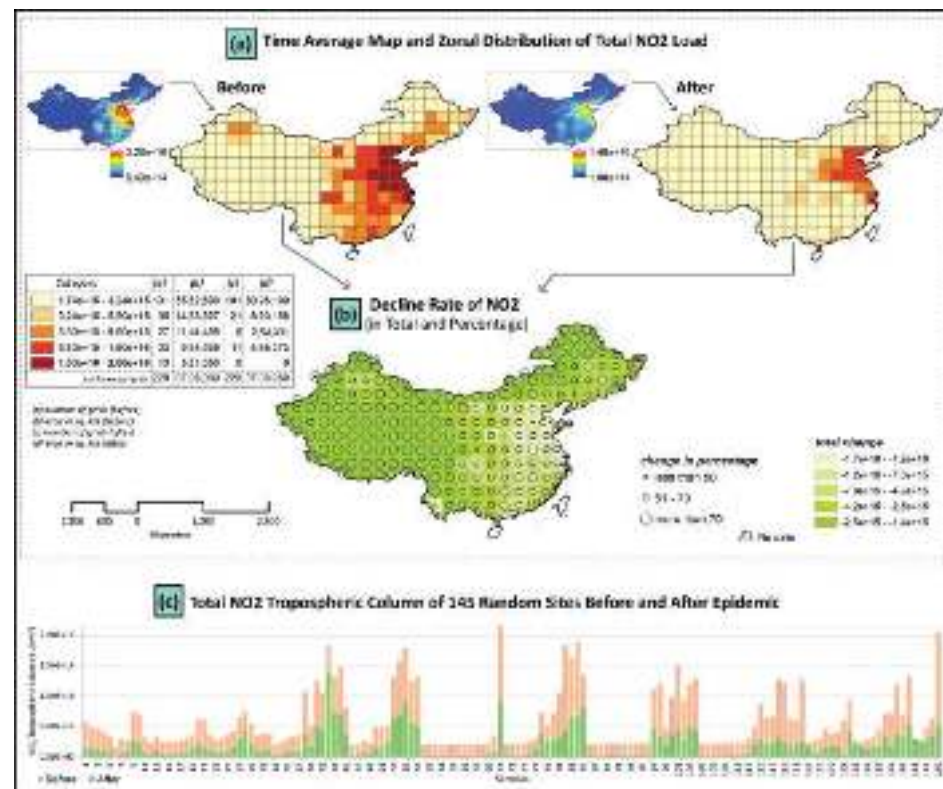


Figure 6. (a) Time average map and zonal distribution of the NO₂ tropospheric column, (b) declining rate (in total and percentage) of NO₂, (c) trend analysis of the total NO₂ tropospheric column of 145 random sites of China's mainland before and after pandemic. Source: OMI, Global Modeling and Assimilation Office, NASA.

The total column of NO₂ decline rate in percentage was grouped into three categories, i.e., less than 50%, 51–70%, and more than 70%. The maximum decline rate (more than 70%) of the NO₂ total column was measured in Guangzhou, Wuhan, and Chengdu city of China before and after the pandemic COVID-19 event (Figure 6b). Figure 6c reveals the trend of the total NO₂ tropospheric column of 145 random sites before and after the pandemic where it is clearly visible that almost all the sample sites have experienced a low concentration of NO₂ in the atmosphere.

In the graphs (Figure 7), steepness of the histogram revealed the degree of reduction in the NO₂ concentration. Guangzhou city showed high steepness of NO₂ reduction after the pandemic. The maximum (almost 60%) declining rate of NO₂ was observed in Guangzhou, Wuhan, Chengdu, and Beijing; whereas the minimum (almost 40%) declining rate of NO₂ total column in the atmosphere was found in Jinan, Shanghai, Anshan, Zhengzhou, Xinjiang, and Lanzhou.

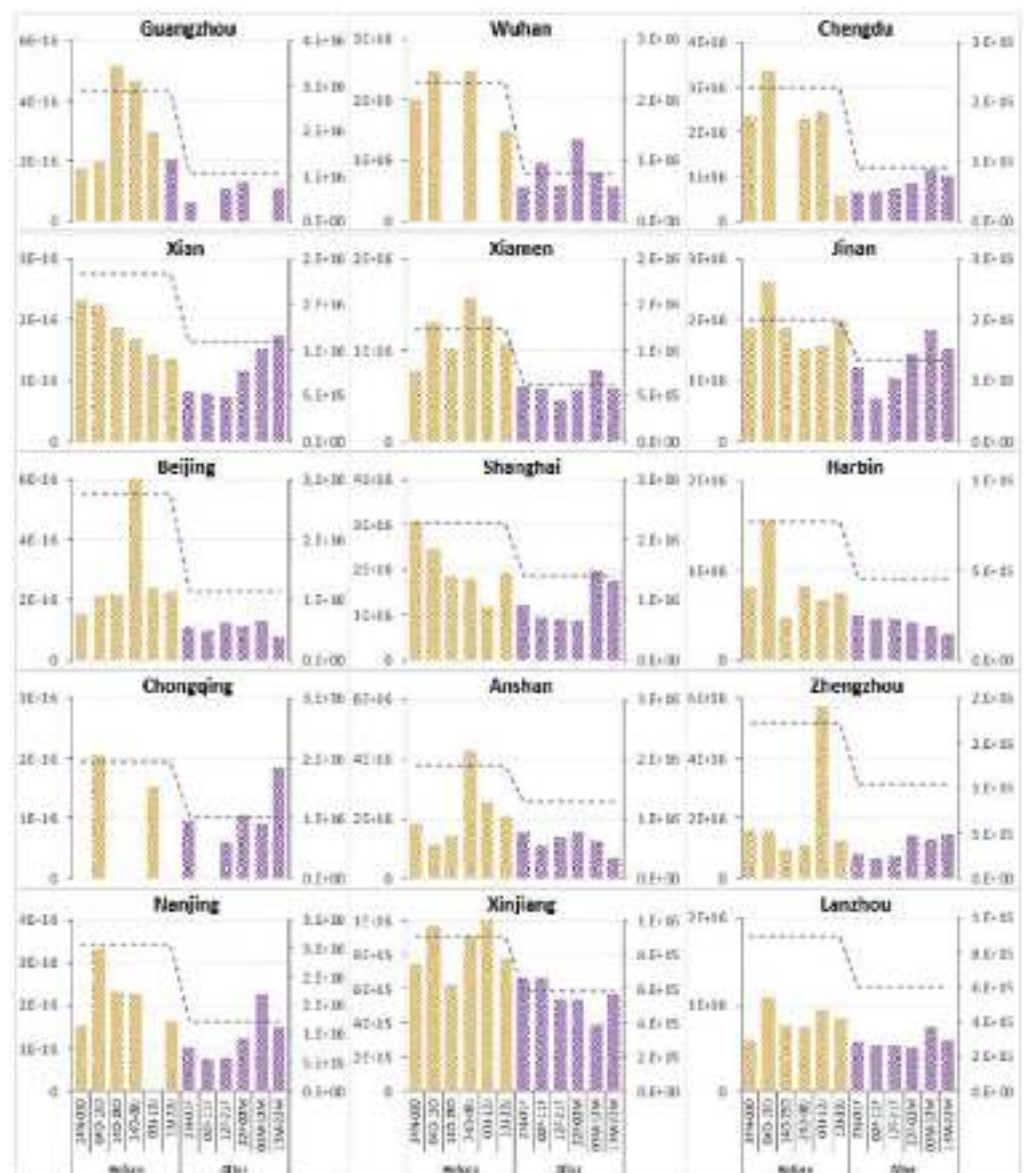


Figure 7. Absolute trend line indicates 60-day average of NO₂ tropospheric column (molecules/cm²), whereas the bar graph represents 10-day average concentration (X-axis) of NO₂ in 15 major cities of China before (yellow) and after (purple) the COVID-19 lockdown period. Source: OMI, Global Modeling and Assimilation Office, NASA, 2020.

3.3. Trends of Air Pollutants in China before and after the Pandemic

The overall air quality change in 50 days (Table 1) reveals that Harbin recorded the highest reduction (43%) in air pollutants followed by Guangzhou (42%), Wuhan (36%), Jinan (33%), Chengdu (32%), Nanjing (31%), Shanghai (30%), Zhengzhou (29%), Xian (25%), Xiamen (23%), Chongqing (23%), Lanzhou (17%), and Anshan (4%). The most interesting fact in this analysis is that when all the cities were experiencing improved air quality, Beijing recorded deteriorating air quality; it recorded a 34% increase in air pollutants during the 50-day study period after lockdown. In this context, it is important to look into the individual pollutants in detail for an insight into understanding their roles in determining air quality.

Table 1. Temporal change in air pollutants of 14 cities of China before (4 December 2019 to 22 January 2020) lockdown and after lockdown (23 January to 12 March 2020). The 100-day daily average concentration in total and change in percentage. Total 6 pollutants NO₂, O₃, PM₁₀, PM_{2.5}, SO₂ (µg/m³), CO (mg/m³) including AQI (change in percentage).

City	Jinan	Guangzhou	Shanghai	Nanjing	Xiamen	Beijing	Zhengzhou	Wuhan	Harbin	Chongqing	Chengdu	Xian	Lanzhou	Anshan
CO	Before	1.46	0.98	0.83	0.97	0.61	0.86	1.28	1.09	1.22	1.02	0.98	1.33	1.87
	After	0.92	0.73	0.65	0.69	0.44	0.86	0.89	0.91	0.85	0.79	0.67	0.95	1.12
	Change	−37	−25	−21	−29	−27	0	−31	−17	−30	−22	−28	−40	−14
NO ₂	Before	56.57	60.86	57.60	53.73	25.75	45.17	54.83	52.73	56.73	46.05	48.70	61.48	65.80
	After	27.02	27.68	27.68	25.91	13.01	26.31	25.83	19.54	28.89	24.51	21.94	32.29	40.40
	Change	−52	−55	−52	−52	−49	−42	−53	−63	−49	−47	−55	−47	−39
O ₃	Before	25.74	43.01	39.73	30.62	64.35	25.44	25.95	23.69	32.37	14.45	23.85	17.08	34.74
	After	64.18	48.69	71.77	68.07	75.40	49.59	66.24	58.47	70.48	35.36	52.35	51.20	62.74
	Change	149	13	81	122	17	95	155	147	118	145	120	200	81
PM ₁₀	Before	141.31	74.48	49.40	80.86	43.07	57.45	121.43	86.54	141.98	83.93	102.22	148.41	107.27
	After	89.01	33.03	34.84	50.75	30.66	59.60	89.67	47.61	77.55	58.11	65.05	107.01	88.11
	Change	−37	−56	−29	−37	−29	4	−26	−45	−45	−31	−36	−28	−18
PM _{2.5}	Before	98.66	38.18	53.15	56.17	30.95	44.69	106.48	63.58	129.74	59.86	75.56	116.60	61.27
	After	62.39	21.92	35.13	36.18	21.22	63.89	72.21	39.08	68.51	44.44	47.27	81.10	40.58
	Change	−37	−43	−34	−36	−31	43	−32	−39	−47	−26	−37	−30	−34
SO ₂	Before	21.52	8.64	7.80	7.80	5.31	4.87	10.24	9.46	36.40	8.96	8.22	14.16	29.77
	After	13.27	5.49	5.66	5.38	4.40	4.53	8.37	7.50	27.25	6.70	6.92	10.51	18.23
	Change	−38	−36	−27	−31	−17	−7	−18	−21	−25	−25	−16	−26	−39
AQI	Before	131.38	164.22	73.80	79.16	48.00	65.71	141.37	88.17	61.70	82.16	102.16	153.66	88.42
	After	88.44	92.98	51.59	54.42	36.95	88.12	101.06	56.58	35.91	63.37	68.98	114.82	73.79
	Change	−33	−43	−30	−31	−23	34	−29	−36	−42	−23	−32	−25	−17

Source: Arranged by author, Ministry of Environmental Protection of China (MEPC), China Ministry of Ecology and Environment, 2020.

During the 50 days of study after lockdown, the concentration of carbon monoxide (mg/m³) reduced by 40% in Lanzhou, 37% in Jinan, 31% in Zhengzhou and Chengdu, 30% in Harbin, 29% in Nanjing, 28% in Xian, 27% in Xiamen, and 25% in Guangzhou (Figure 8b). The temporal changes in NO₂ (Figure 8c) reveal that the more than 50% concentration of NO₂ has reduced in Wuhan (63%), Chengdu and Guangzhou (55%), Zhengzhou (53%), Jinan, Nanjing and Shanghai (52%) while, other cities received below 50% NO₂ concentration (ranging between 20% and 49%).

On the other hand, the results displayed a drastic rise in ozone in the atmosphere in almost all cities after the lockdown. The detailed analysis of O₃ (Figure 8d) explained that Xian experienced a 200% rise in O₃. Moreover, most of cities experienced more than 100% escalation of O₃, for instance, Zhengzhou (155%), Jinan (149%), Wuhan (147%), Chongqing (145%), Nanjing (122%), Chengdu (120%), and Harbin (118%). Interestingly Beijing, the city where the overall quality of air has declined, also experienced a high rise in O₃ (95%). In addition, the concentration of ozone has also increased in Shanghai (81), Lanzhou (81%), and Anshan (57%). Cities such as Xiamen and Guangzhou experienced only 17% and 13% increases in O₃, respectively.

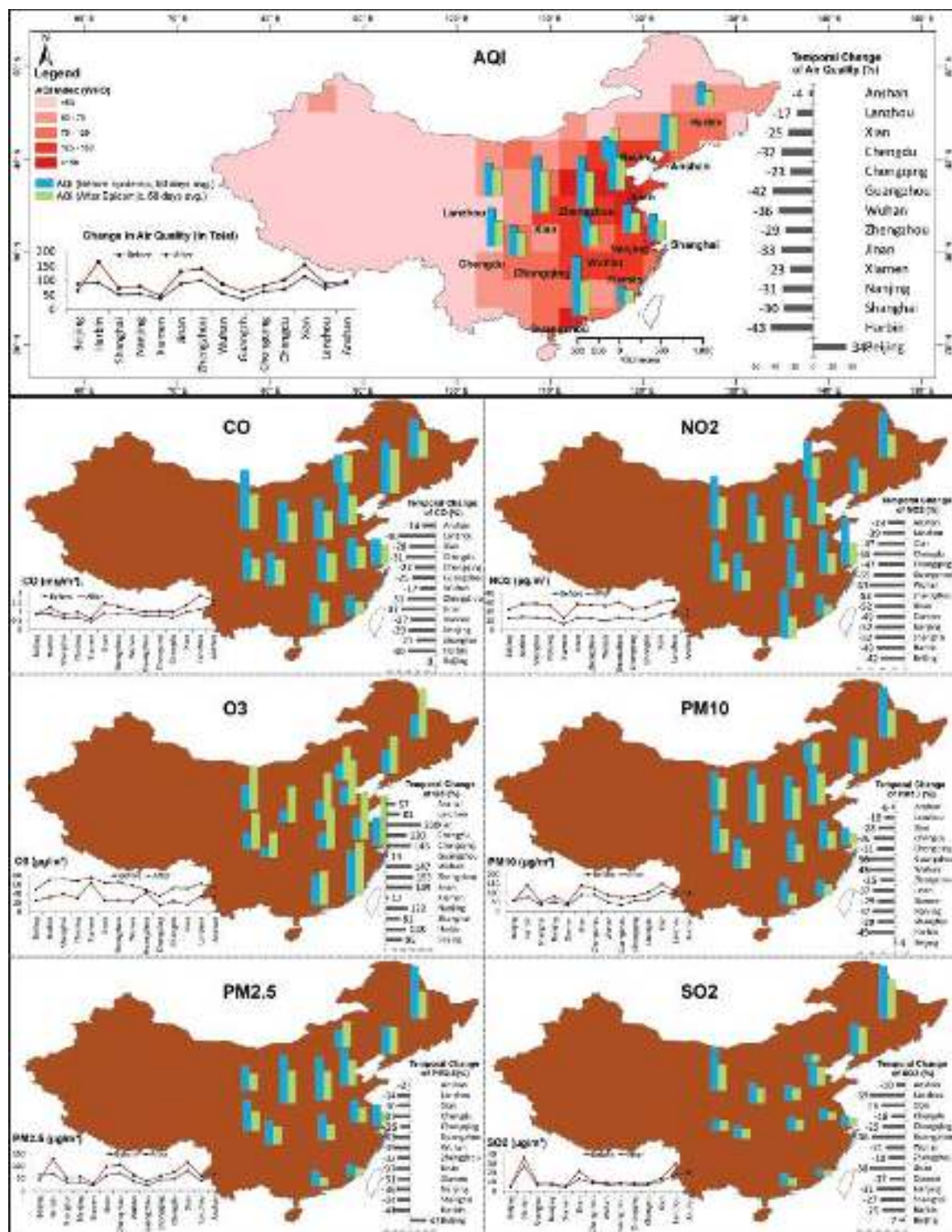


Figure 8. Temporal change in air quality of China before and after lockdown. Total 100-day daily average data, 4 December 2019 to 22 January 2020 (before lockdown) and 23 January to 12 March 2020 (after lockdown). (a) Air Quality Index; (b) CO; (c) NO₂; (d) O₃; (e) PM₁₀; (f) PM_{2.5}; (g) SO₂. Source: Ministry of Environmental Protection of China (MEPC), China Ministry of Ecology and Environment, 2020 and OMI, Global Modeling and Assimilation Office, NASA.

The temporal change in PM₁₀ ($\mu\text{g}/\text{m}^3$) (Figure 8e) reveals its sudden decrease in all cities except Beijing after the lockdown (Table 1). The maximum decrease in PM₁₀ concentration was observed in Guangzhou (56%) followed by Wuhan and Harbin (45%). The other cities that observed a substantial decrease in PM₁₀ are Nanjing and Jinan (37%), Chengdu

(36%), Shanghai and Xiamen (29%), Xian (28%), and Zhengzhou (26%). Conversely, PM_{10} concentration increased by 4% in Beijing after the lockdown. Like PM_{10} , the concentration of $PM_{2.5}$ also considerably decreased after the pandemic lockdown (Figure 8f). The cities which observed low concentrations of $PM_{2.5}$ are Harbin (47%), Guangzhou (43%), Wuhan (39%), Jinan and Chengdu (37%), Nanjing (36%), Shanghai and Lanzhou (34%), Zhengzhou (32%), Xiamen (31%), and Xian (30%). Simultaneously, Beijing experienced a very high concentration of $PM_{2.5}$ (43%) after the lockdown.

Along with other pollutants, the temporal change in SO_2 concentration (Figure 8g) displays a substantial decrease in all cities after the lockdown. The cities that experienced a high proportion decrease in SO_2 concentration are Lanzhou (39%), Jinan (38%), Guangzhou (36%), Nanjing (31%), Shanghai (27%), Xian (26%), and Chongqing and Harbin (25%) (Table 1).

The daily average concentration of air pollutants for 100 days (50 days before lockdown and 50 days after lockdown) of 14 cities (Figure 9) reveals that the air quality has remarkably improved in Guangzhou where 43% of pollutants have declined during this study period. The concentration of PM_{10} and NO_2 has reduced by 56% and 55%, respectively. Similarly, in Shanghai, the overall pollutants in the atmosphere have decreased by 30% (Table 1). In Nanjing, the overall air quality (AQI) has improved by 31%. Moreover, the air quality of Xiamen has improved by 23% and the concentration of NO_2 and $PM_{2.5}$ has declined by 49% and 31%, respectively. In Jinan, the overall air quality has improved by 33% and the NO_2 concentration has decreased by 52%. However, the concentration of O_3 has amplified by 149%. In Zhengzhou, the concentration of NO_2 has reduced by 53% and the concentration of O_3 has grown by 155%. In Wuhan, the major pandemic affected area, the concentration of NO_2 has reduced by 63% and PM_{10} by 45% whereas the concentration of O_3 has increased by 147%. The air quality has also improved in Harbin where the concentration of NO_2 has reduced by 49% and the concentration of O_3 has increased by 118%. In Chongqing, the concentration of NO_2 has reduced by 47% and the concentration of O_3 has improved by 145%. Similarly, in Chengdu, there has been a 55% reduction in NO_2 concentration and a 120% increase in O_3 concentration in the atmosphere. In Xian, there is a 47% change in NO_2 and a 200% increase in O_3 in the atmosphere. In Anshan, the concentration of NO_2 has reduced by 29% whereas the concentration of O_3 has increased by 57%.

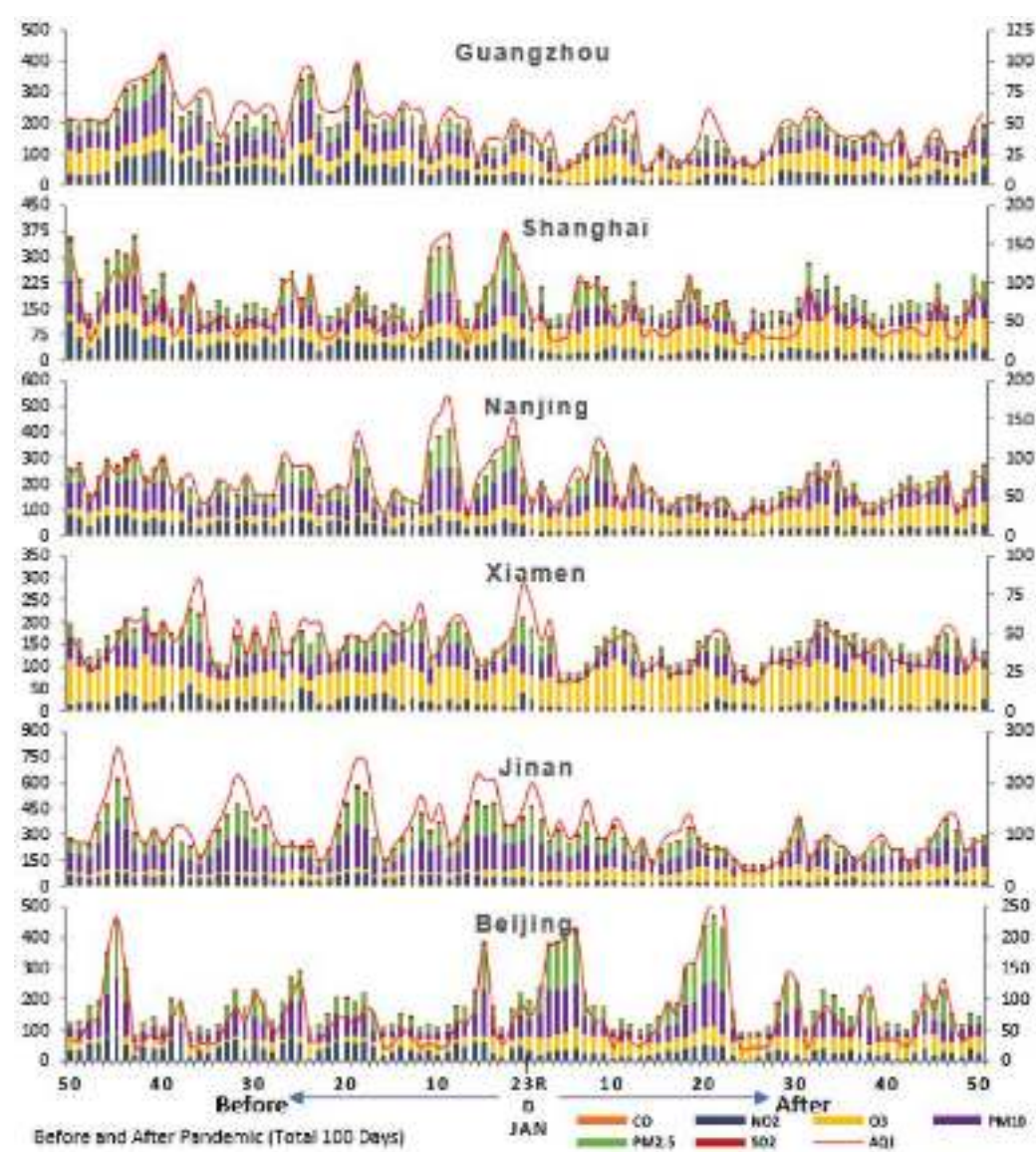


Figure 9. Cont.

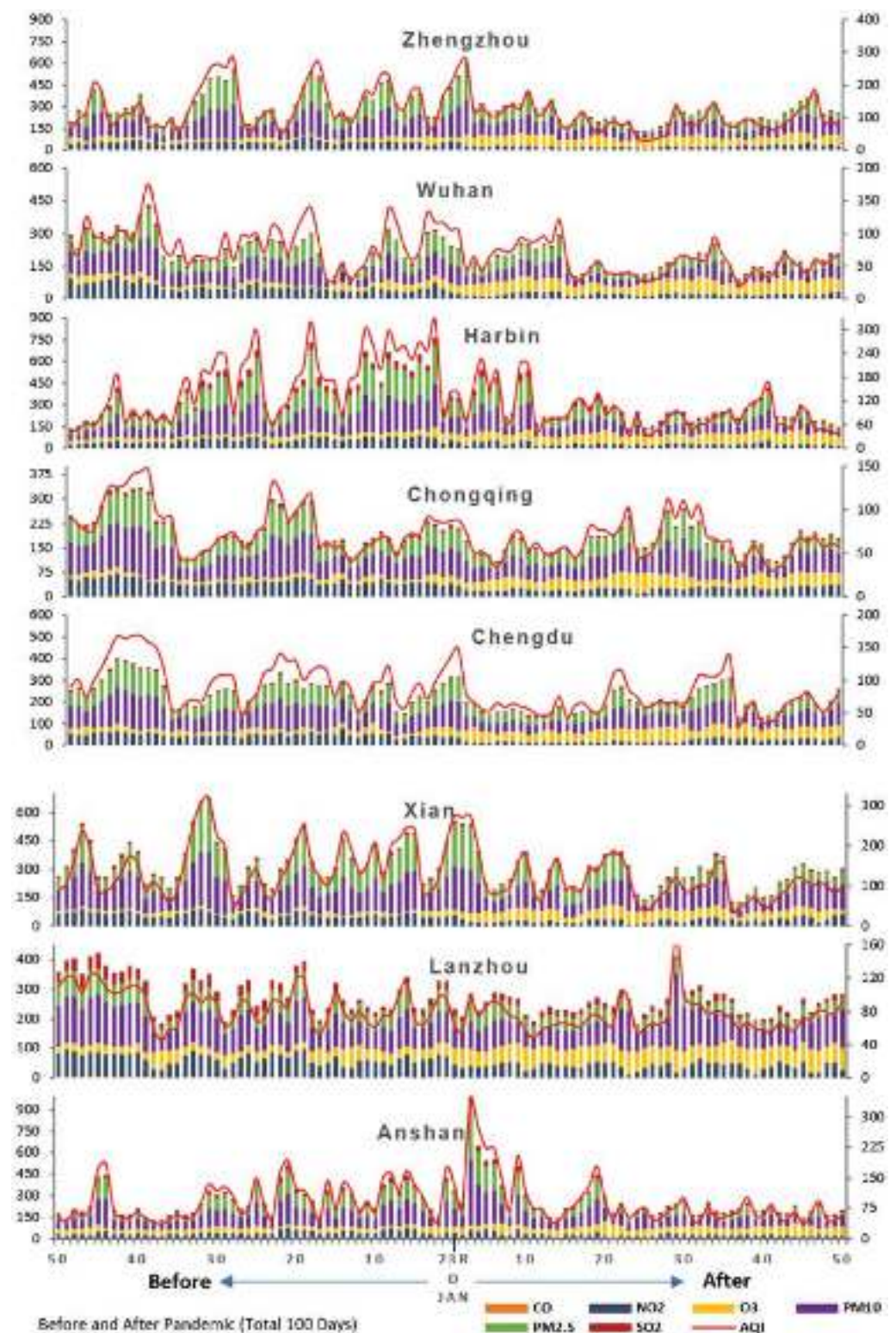


Figure 9. The daily average concentration of air pollutants in 14 cities of China. The 100 days (50 days before lockdown and 50 days after lockdown). NO₂, O₃, PM₁₀, PM_{2.5}, SO₂ (µg/m³), and CO (mg/m³): primary vertical (left) and AQI shown in secondary vertical (right). Source: Ministry of Environmental Protection of China (MEPC), China Ministry of Ecology and Environment, 2020.

4. Discussion

The coronavirus first outbreak started in December 2019 and human-to-human transmission was confirmed on 20 January 2020 [14]. Wuhan city was locked from other regions

of the country to stop the spread of the SARS-CoV virus since 23 January 2020. After a few days, the administrative authorities of Guangzhou and Beijing declared the lockdown. The highest level of public health emergency was announced within a week in a few administrative units [13,15]. The anthropogenic emissions from industrial and manufacturing units were closed after the spreading of coronavirus which caused improvement in overall air quality in China [14].

The present study found that there was a substantial decrease in NO₂ concentration and consequently improvement in air quality. It is noteworthy that NO₂ concentration has tremendously decreased in the cities of Guangzhou, Wuhan, and Chengdu. These cities come under the same category, where NO₂ tropospheric column (molecules/cm²) ranges between 1.6×10^{16} and 3×10^{16} before the pandemic but after the shutdown none of these cities reported high emissions of NO₂. NASA and European Space Agency (ESA) pollution monitoring satellites have also detected a substantial decrease in NO₂ over China due to a complete shutdown. The concentration of nitrogen dioxide was reduced as the sources of this pollutant such as motor vehicles, power plants, and industrial facilities were closed for two months [58]. In addition, the lockdown has coincided with the Lunar New Year celebration which also facilitated to decrease the concentration of NO₂ in all major cities in China's mainland. Some of the preceding studies have also established that many cities such as Guangzhou, Beijing, Chengdu, Shenzhen, Nanjing, Shanghai, Chongqing, etc., have experienced low concentrations of NO₂ and particulate matter in the atmosphere due to regulatory effects in China [76–79].

The study found a substantial decline in CO in all cities except Beijing where it remained static. The maximum declining rate of CO was observed in Lanzhou (40%), Jinan (37%), and Zhengzhou (31%) whereas the minimum declining rate of CO was measured in Anshan (14%), Wuhan (17%), and Shanghai (21%) because of the complete halt of vehicles, wood-burning, and industry. Similar to this line, several studies established that vehicles, wood-burning, and industry are the main sources of CO [80–84]. The reduction in CO in 60 days is a significant indicator for air quality because of its 1–2-month life span in the atmosphere, thereby improved quality of air [85,86].

The particulate pollutants such as PM_{2.5} and PM₁₀ have also decreased substantially during the lockdown period as the sources of these pollutants were restricted. Several previous studies have documented that the primary sources of PM_{2.5} and PM₁₀ are automobile emissions, incomplete combustion, wind-blown soil and dust, construction dust, and biomass burning [82,87,88]. The result displays that the maximum declining rate of PM₁₀ and PM_{2.5} was measured in Guangzhou (56% and 43%), Wuhan (45% and 39%), Jinan (37% and 38%), and Nanjing (37% and 36%). Similarly, some other studies have also found that Beijing, Lanzhou, Tianjin, Nanning, and Chongqing reported lower concentrations of these particulate matters during the regulation effect on certain occasions [89–91]. On the other hand, the concentration of SO₂ has also declined in all cities due to strict regulation and the closing of heavy industrial factories such as iron, steel, and cement industries [92–95]. The major sources of SO₂ are coal combustion of biomass in coal-fired power plants and industry sector [9,96–98] that were completely locked during the pandemic. Some other studies have exhibited that SO₂, combined with volatile organic compounds (VOCs), enhances the formation of new particles, particularly sulphate which is one of the main components of PM_{2.5} [99–102].

Consistent with previous studies, this study [103–105] also found that due to the decrease in all air pollutants including CO, NO₂, PM_{2.5}, PM₁₀, and SO₂ the total concentration of O₃ has increased in all 15 cities in China during the study period. The maximum increasing rate of O₃ was found in Xian (200%), Zhengzhou (155%), Jinan (149%), and Chongqing (145%) whereas the minimum increasing trend was found in Guangzhou (13%), Xiamen (17%), and Anshan (57%). Several reasons have been proposed to explain this complex relation: (a) inverse relation between O₃ and its precursors NO₂, PM_{2.5}, PM₁₀, and SO₂ lower emission of these pollutants results in faster ozone production in nitrogen oxide (NO_x) concentrated areas [106–109]; (b) low concentration of NO_x also causes less

destruction of ozone [88,110]; (c) decreased level of atmospheric pollutants leads to more clear sunshine that also accentuates more ozone production [108,111]. In addition, a pause of vehicles also resulted in a reduction in CO and NO_x including NO and NO₂ facilitating an increase in the level of ozone in the atmosphere [81,112–114]. The production of ozone under the influence of anthropogenic activities in the troposphere and involving catalysis by NO₂ and NO should be significant [22]. Its precursor compounds NO_x and VOC have a wide variety of sources and can exhibit a non-linear effect on ozone production, while its accumulation is strongly influenced by meteorological parameters [115]. Although reductions in atmospheric ozone allow more solar radiation to reach ground level, resulting in higher surface temperatures, a decrease in the downward longwave radiation emitted by CO₂, O₃, and H₂O from a cooler lower stratosphere with less ozone would result in a decrease in surface temperatures [22].

One of the major outcomes of reduced atmospheric pollutants is a substantial improvement in overall air quality except for Beijing. Since most of the industrial production, vehicle movements, and other anthropogenic activities in the cities were closed, the reduced level of NO₂, CO, PM_{2.5}, PM₁₀, and SO₂ improved the air quality in these cities. Similar to this, several previous studies have found that air quality is positively related to the low concentration of atmospheric pollutants [116–118]. Conversely, Beijing has reported a decline in the overall air quality during the study period despite the closure of manufacturing units. The reason may be the increasing level of PM_{2.5} and PM₁₀ during the same period. The concentration of PM_{2.5} has increased manyfold in Beijing because the city experienced a number of severe haze events during the lockdown period. Some of the previous studies [25,31,79] mentioned that complex relationships among changes in relative humidity, near-surface wind speed and direction, planetary boundary layer height, and precipitation have influenced the increasing concentration of PM_{2.5} in Beijing. Climatologically, Beijing has dry air during the wintertime, but a larger than normal amount of moisture accumulated near the surface during the lockdown period. This has facilitated multiphase reactions for aerosol formation and growth [25]. Moreover, wind conditions also facilitate to formation of haze in Beijing as the mean wind speed declined. In addition, the wind direction changed to southerly which usually carries polluted air from Hebei Province's industrial regions. Moreover, the planetary boundary layer height in northern China also declined during the lockdown and this lower height facilitated stagnant air and subsequently resulted in increasing PM_{2.5} in Beijing. Further, during the lockdown period, precipitation mainly occurred in southern China and the Northern part did not receive enough rain to wash out the haze that formed over the region [40].

5. Conclusions

The assessment of major atmospheric pollutants during lockdown due to the COVID-19 pandemic has markedly influenced the air quality in China. The cities such as Guangzhou, Wuhan, and Chengdu that have shown a very high concentration of NO₂ tropospheric column (molecules/cm²) before the pandemic and have experienced a sudden decline after the lockdown. The air quality zonal model has also displayed about 390,150 km² areas that were under the high level of air pollutants have come under low concentration areas. In addition, the spatio-temporal evaluation of the NO₂ and other main pollutants in the major 15 cities of China exhibited a remarkable reduction which in turn, facilitated to improve the overall air quality except in Beijing where the air quality has been degraded due to the overwhelming concentration of PM_{2.5} and PM₁₀.

The overall air quality of eastern coastal and industrial cities such as Jinan, Zhengzhou, Wuhan, Guangzhou, Chengdu, and Xian have recorded low concentrations of air pollutants and such reduction in atmospheric pollutants has improved the air quality. The overall air quality change in 50 days reveals that Harbin has recorded the highest reduction (43%) in air pollutants followed by Guangzhou (42%), Wuhan (36%), Jinan (33%), Chengdu (32%), Nanjing (31%), Shanghai (30%), Zhengzhou (29%), Xian (25%), Xiamen (23%), Chongqing (23%), Lanzhou (17%), and Anshan (4%). Since most of the industrial productions, vehicle

movements, and other anthropogenic activities in the cities were restricted, the study revealed that the levels of NO₂, CO, PM_{2.5}, PM₁₀, and SO₂ have remarkably reduced. It is noteworthy that the reduction in atmospheric pollutants and consequently improved air quality would have a positive impact on the environment and human health. To address the emission of atmospheric pollutants, particularly NO₂, CO, PM_{2.5}, PM₁₀, and SO₂, the government needs to establish an environmental policy framework involving central, provincial, and local governments with stringent laws for environmental protection. The restriction and regulation of all anthropogenic sources of pollutants due to the COVID-19 outbreak was an example of such stringent enforcement of the law to protect human health. Similarly, to protect the environment from atmospheric pollutants strong political commitment, technological development, and policy enforcement are essential to make policies, such as 11th and 12th five-year plans of China, successful towards improving and protecting the environment and human health.

Author Contributions: Data collection, S.R. and R.C.; conceptualization, S.R., S.J., P.K. and R.C.; methodology, S.R.; software, S.R.; validation, S.R. and R.C.; formal analysis, S.J.; investigation, P.K. and R.C.; resources, S.R., S.J., P.K. and R.C.; data curation, S.R.; writing introduction, P.K. and S.J.; writing data source and methodology, S.R.; writing results discussion and conclusion, S.J.; referencing, S.R. and S.J.; review and editing, S.R.; supervision, P.K. and R.C. All authors have read and agreed to the published version of the manuscript.

Funding: This research received no external funding.

Informed Consent Statement: Not applicable.

Data Availability Statement: Data are openly available at Global Modeling and Assimilation Office, NASA. The hourly and daily average concentrations of CO, O₃, NO₂, PM₁₀, PM_{2.5}, SO₂, and AQI data on China Ministry of Ecology and Environment (<https://aqicn.org/map/china/cn/>, accessed on 20 March 2020).

Acknowledgments: We would like to thank the Ministry of Environmental Protection of China (MEPC), Chinese Ministry of Ecology and Environment, 2020 and OMI datasets, Global Modeling and Assimilation Office, NASA for providing data.

Conflicts of Interest: The authors declare no conflict of interest.

Abbreviations

AIRS	Atmospheric Infrared Sounder
AQI	Air Quality Index
CO	Carbon Monoxide
COVID	Coronavirus Disease
ESA	European Space Agency
GES-DISC	Goddard Earth Sciences Data and Information Services Center
GSFC	Goddard Space Flight Center
MEPC	Environmental Protection of China
MERRA-2	Modern Era Retrospective Research and Application
MODIS-terra	Moderate Resolution Imaging Spectroradiometer
NASA	National Aeronautics and Space Administration
NH ₃	Ammonia
NO ₂	Nitrogen Dioxide
NO _x	Nitrogen Oxide
O ₃	Ozone
OMI	Ozone Monitoring Instrument
PCA	Principal Component Analysis
PM ₁₀	Particulate Matter ≤10 µm
PM _{2.5}	Particulate Matter ≤2.5 µm
SO ₂	Sulphur Dioxide
VOCs	Volatile Organic Compounds
WHO	World Health Organization

References

1. Brauer, M.; Freedman, G.; Frostad, J.; Van Donkelaar, A.; Martin, R.V.; Dentener, F.; Dingenen, R.V.; Estep, K.; Amini, H.; Apte, J.S.; et al. Ambient air pollution exposure estimation for the global burden of disease 2013. *Environ. Sci. Technol.* **2016**, *50*, 79–88. [CrossRef]
2. Kuerban, M.; Waili, Y.; Fan, F.; Liu, Y.; Qin, W.; Dore, A.J.; Peng, J.; Xu, W.; Zhang, F. Spatio-temporal patterns of air pollution in China from 2015 to 2018 and implications for health risks. *Environ. Pollut.* **2020**, *258*, 113659. [CrossRef]
3. Lin, Y.; Jiang, F.; Zhao, J.; Zhu, G.; He, X.; Ma, X.; Li, S.; Sabel, C.E.; Wang, H. Impacts of O₃ on premature mortality and crop yield loss across China. *Atmos. Environ.* **2018**, *194*, 41–47. [CrossRef]
4. Liu, W.; Xu, Z.; Yang, T. Health effects of air pollution in China. *Int. J. Environ. Res. Public Health* **2018**, *15*, 1471. [CrossRef] [PubMed]
5. Zou, B.; Li, S.; Lin, Y.; Wang, B.; Cao, S.; Zhao, X.; Peng, F.; Qin, N.; Guo, Q.; Feng, H.; et al. Efforts in reducing air pollution exposure risk in China: State versus individuals. *Environ. Int.* **2020**, *137*, 105504. [CrossRef]
6. WHO. Air Pollution in the Western Pacific. 2016. Available online: <https://www.who.int/data/gho/data/themes/air-pollution/who-air-quality-database#cms> (accessed on 15 April 2020).
7. WHO. Air Pollution in the Western Pacific. 2019. Available online: <https://www.who.int/westernpacific/health-topics/air-pollution> (accessed on 15 April 2020).
8. Richter, A.; Burrows, J.P.; Nüß, H.; Granier, C.; Niemeier, U. Increase in tropospheric nitrogen dioxide over China observed from space. *Nature* **2005**, *437*, 129–132. [CrossRef]
9. Zhang, H.; Li, J.; Ying, Q.; Yu, J.Z.; Wu, D.; Cheng, Y.; He, K.; Jiang, J. Source apportionment of PM_{2.5} nitrate and sulfate in China using a source-oriented chemical transport model. *Atmos. Environ.* **2012**, *62*, 228–242. [CrossRef]
10. Zhao, B.; Wang, S.X.; Liu, H.; Xu, J.Y.; Fu, K.; Klimont, Z.; Hao, J.M.; He, K.B.; Cofala, J.; Amann, M. NO_x emissions in China: Historical trends and future perspectives. *Atmos. Chem. Phys.* **2013**, *13*, 9869–9897. [CrossRef]
11. Deng, X.; Bai, X. Sustainable urbanization in western China. *Environ. Sci. Pol. Sustain. Dev.* **2014**, *56*, 12–24. [CrossRef]
12. Jiang, L.; Bai, L. Spatio-temporal characteristics of urban air pollutions and their causal relationships: Evidence from Beijing and its neighboring cities. *Sci. Rep.* **2018**, *8*, 1279. [CrossRef]
13. Lau, H.; Khosrawipour, V.; Kocbach, P.; Mikolajczyk, A.; Schubert, J.; Bania, J.; Khosrawipour, T. The positive impact of lockdown in Wuhan on containing the COVID-19 outbreak in China. *J. Travel Med.* **2020**, 1–7. [CrossRef]
14. Pei, Z.; Han, G.; Ma, X.; Su, H.; Gong, W. Response of major air pollutants to COVID-19 lockdowns in China. *Sci. Total Environ.* **2020**, *743*, 140879. [CrossRef]
15. He, G.; Pan, Y.; Tanaka, T. The short-term impacts of COVID-19 lockdown on urban air pollution in China. *Nat. Sustain.* **2020**, *3*, 1005–1011. [CrossRef]
16. International Energy Agency (IEA). *Weo-2016 Special Report Energy and Air Pollution*; International Energy Agency: Paris, France, 2016; pp. 1–266. Available online: <https://webstore.iea.org/weo-2016-special-report-energy-and-air-pollution> (accessed on 12 April 2020).
17. World Energy Council. *World Energy Resources 2013 Survey: Summary*; World Energy Council: London, UK, 2013; pp. 1–29. Available online: https://www.worldenergy.org/assets/images/imported/2013/10/WEC_Resources_summary-final_180314_TT.pdf (accessed on 27 April 2020).
18. WHO. Ambient Air Pollution: A Global Assessment of Exposure and Burden of Disease. 2016. Available online: <http://who.int/phe/publications/air-pollution-global-assessment/en/> (accessed on 7 April 2020).
19. Ashraf, A.; Butt, A.; Khalid, I.; Alam, R.U.; Ahmad, S.R. Smog analysis and its effect on reported ocular surface diseases: A case study of 2016 smog event of Lahore. *Atmos. Environ.* **2019**, *198*, 257–264. [CrossRef]
20. Zhu, L.; Gan, Q.; Liu, Y.; Yan, Z. The impact of foreign direct investment on SO₂ emissions in the Beijing-Tianjin-Hebei region: A spatial econometric analysis. *J. Clean. Prod.* **2017**, *166*, 189–196. [CrossRef]
21. Atkinson, R. Atmospheric chemistry of VOCs and NO_x. *Atmos. Environ.* **2000**, *34*, 2063–2101. [CrossRef]
22. Crutzen, P.J. The role of NO and NO₂ in the chemistry of the troposphere and stratosphere. *Annu. Rev. Earth Planet. Sci.* **1979**, *7*, 443–472. [CrossRef]
23. Parra, M.A.; González, L.; Elustondo, D.; Garrigó, J.; Bermejo, R.; Santamaría, J.M. Spatial and temporal trends of volatile organic compounds (VOC) in a rural area of northern Spain. *Sci. Total Environ.* **2006**, *370*, 157–167. [CrossRef] [PubMed]
24. Jhun, I.; Coull, B.A.; Zanobetti, A.; Koutrakis, P. The impact of nitrogen oxides concentration decreases on ozone trends in the USA. *Air Qual. Atmos. Health* **2015**, *8*, 283–293. [CrossRef] [PubMed]
25. Le, T.; Wang, Y.; Liu, L.; Yang, J.; Yung, Y.L.; Li, G.; Seinfeld, J.H. Unexpected air pollution with marked emission reductions during the COVID-19 outbreak in China. *Science* **2020**, *369*, 702–706. [CrossRef] [PubMed]
26. Booker, F.; Muntifering, R.; McGrath, M.; Burkey, K.; Decoteau, D.; Fiscus, E.; Manning, W.; Krupa, S.; Chappelka, A.; Grantz, D. The ozone component of global change: Potential effects on agricultural and horticultural plant yield, product quality and interactions with invasive species. *J. Integr. Plant Biol.* **2009**, *51*, 337–351. [CrossRef] [PubMed]
27. Fann, N.; Lamson, A.D.; Anenberg, S.C.; Wesson, K.; Risley, D.; Hubbell, B.J. Estimating the national public health burden associated with exposure to ambient PM_{2.5} and ozone. *Risk Anal.* **2012**, *32*, 81–95. [CrossRef]
28. Lu, C.; Tian, H. Spatial and temporal patterns of nitrogen deposition in China: Synthesis of observational data. *J. Geophys. Res. Atmos.* **2007**, *112*, D22S05. [CrossRef]

29. Qi, Y. Spatio-temporal distributions of tropospheric NO₂ over oases in Taklimakan Desert, China. *Chin. Geogr. Sci.* **2015**, *25*, 561–568. [CrossRef]
30. Bao, J.; Yang, X.; Zhao, Z.; Wang, Z.; Yu, C.; Li, X. The spatial-temporal characteristics of air pollution in China from 2001–2014. *Int. J. Environ. Res. Public Health* **2015**, *12*, 15875–15887. [CrossRef] [PubMed]
31. Zhang, L.; Lee, C.S.; Zhang, R.; Chen, L. Spatial and temporal evaluation of long-term trend (2005–2014) of OMI retrieved NO₂ and SO₂ concentrations in Henan Province, China. *Atmos. Environ.* **2017**, *154*, 151–166. [CrossRef]
32. Xu, W.; Wu, Q.; Liu, X.; Tang, A.; Dore, A.J.; Heal, M.R. Characteristics of ammonia, acid gases, and PM_{2.5} for three typical land-use types in the NCP. *Environ. Sci. Pollut. R.* **2016**, *23*, 1158–1172. [CrossRef]
33. Cui, Y.; Lin, J.; Song, C.; Liu, M.; Yan, Y.; Xu, Y.; Huang, B. Rapid growth in nitrogen dioxide pollution over Western China, 2005–2013. *Atmos. Chem. Phys.* **2016**, *16*, 6207. [CrossRef]
34. Song, C.; Wu, L.; Xie, Y.; He, J.; Chen, X.; Wang, T.; Lin, Y.; Jin, T.; Wang, A.; Liu, Y.; et al. Air pollution in China: Status and spatiotemporal variations. *Environ. Pollut.* **2017**, *227*, 334–347. [CrossRef]
35. Li, R.; Cui, L.; Li, J.; Zhao, A.; Fu, H.; Wu, Y.; Zhang, L.; Kong, L.; Chen, J. Spatial and temporal variation of particulate matter and gaseous pollutants in China during 2014–2016. *Atmos. Environ.* **2017**, *161*, 235–246. [CrossRef]
36. Chen, G.; Wang, Y.; Li, S.; Cao, W.; Ren, H.; Knibbs, L.D.; Abramson, M.J.; Guo, Y. Spatiotemporal patterns of PM₁₀ concentrations over China during 2005–2016: A satellite-based estimation using the random forests approach. *Environ. Pollut.* **2018**, *242*, 605–613. [CrossRef]
37. Cai, K.; Li, S.; Zheng, F.; Yu, C.; Zhang, X.; Liu, Y.; Li, Y. Spatio-temporal variations in NO₂ and PM_{2.5} over the central plains economic region of China during 2005–2015 based on satellite observations. *Aerosol Air Qual. Res.* **2018**, *18*, 1221–1235. [CrossRef]
38. Fan, H.; Zhao, C.; Yang, Y. A comprehensive analysis of the spatio-temporal variation of urban air pollution in China during 2014–2018. *Atmos. Environ.* **2020**, *220*, 117066. [CrossRef]
39. Xu, W.; Sun, J.; Liu, Y.; Xiao, Y.; Tian, Y.; Zhao, B.; Zhang, X. Spatiotemporal variation and socioeconomic drivers of air pollution in China during 2005–2016. *J. Environ. Manag.* **2019**, *245*, 66–75. [CrossRef] [PubMed]
40. Guo, H.; Gu, X.; Ma, G.; Shi, S.; Wang, W.; Zuo, X.; Zhang, X. Spatial and temporal variations of air quality and six air pollutants in China during 2015–2017. *Sci. Rep.* **2019**, *9*, 15201. [CrossRef] [PubMed]
41. Wang, W.; Samat, A.; Abuduwaili, J.; Ge, Y. Spatio-Temporal Variations of Satellite-Based PM_{2.5} Concentrations and Its Determinants in Xinjiang, Northwest of China. *Int. J. Environ. Res. Pub. Health* **2020**, *17*, 2157. [CrossRef]
42. Li, R.; Mei, X.; Chen, L.; Wang, L.; Wang, Z.; Jing, Y. Long-Term (2005–2017) View of Atmospheric Pollutants in Central China Using Multiple Satellite Observations. *Remote Sens.* **2020**, *12*, 1041. [CrossRef]
43. Rohde, R.A.; Muller, R.A. Air pollution in China: Mapping of concentrations and sources. *PLoS ONE* **2015**, *10*, e0135749. [CrossRef] [PubMed]
44. Karagulian, F.; Belis, C.A.; Dora, C.F.C.; Prüss-Ustün, A.M.; Bonjour, S.; Adair-Rohani, H.; Amann, M. Contributions to cities' ambient particulate matter (PM): A systematic review of local source contributions at global level. *Atmos. Environ.* **2015**, *120*, 475–483. [CrossRef]
45. Lyu, W.; Li, Y.; Guan, D.; Zhao, H.; Zhang, Q.; Liu, Z. Driving forces of Chinese primary air pollution emissions: An index decomposition analysis. *J. Clean. Prod.* **2016**, *133*, 136–144. [CrossRef]
46. Xu, S.; Miao, Y.; Li, Y.; Zhou, Y.; Ma, X.; He, Z.; Zhao, B.; Wang, S. What Factors Drive Air Pollutants in China? An Analysis from the Perspective of Regional Difference Using a Combined Method of Production Decomposition Analysis and Logarithmic Mean Divisia Index. *Sustainability* **2019**, *11*, 4650. [CrossRef]
47. Peng, J.; Chen, S.; Lü, H.; Liu, Y.; Wu, J. Spatiotemporal patterns of remotely sensed PM_{2.5} concentration in China from 1999 to 2011. *Remote Sens. Environ.* **2016**, *174*, 109–121. [CrossRef]
48. Lin, H.; Wang, X.; Liu, T.; Li, X.; Xiao, J.; Zeng, W.; Ma, W. Air pollution and mortality in China. In *Ambient Air Pollution and Health Impact in China*; Dong, G.H., Ed.; Springer: Singapore, 2017; pp. 103–121.
49. Mokoena, K.K.; Ethan, C.J.; Yu, Y.; Shale, K.; Liu, F. Ambient air pollution and respiratory mortality in Xi'an, China: A time-series analysis. *Respir. Res.* **2019**, *20*, 139. [CrossRef] [PubMed]
50. Tang, M.; Li, D.; Liew, Z.; Wei, F.; Wang, J.; Jin, M.; Chen, K.; Ritz, B. The association of short-term effects of air pollution and sleep disorders among elderly residents in China. *Sci. Total Environ.* **2020**, *708*, 134846. [CrossRef] [PubMed]
51. Deschenes, O.; Wang, H.; Wang, S.; Zhang, P. The effect of air pollution on body weight and obesity: Evidence from China. *J. Dev. Econ.* **2020**, *145*, 102461. [CrossRef]
52. Siddiqi, T.A.; Chong-Xian, Z. Ambient air quality standards in China. *Environ. Manag.* **1984**, *8*, 473–479. [CrossRef]
53. Wang, S.; Hao, J. Air quality management in China: Issues, challenges, and options. *J. Environ. Sci.* **2012**, *24*, 2–13. [CrossRef]
54. Jin, Y.; Andersson, H.; Zhang, S. Air pollution control policies in China: A retrospective and prospects. *Int. J. Environ. Res. Public Health* **2016**, *13*, 1219. [CrossRef]
55. Feng, L.; Liao, W. Legislation, plans, and policies for prevention and control of air pollution in China: Achievements, challenges, and improvements. *J. Clean. Prod.* **2016**, *112*, 1549–1558. [CrossRef]
56. Huang, C.; Wang, Q.; Wang, S.; Ren, M.; Ma, R.; He, Y. Air Pollution Prevention and Control Policy in China. In *Ambient Air Pollution and Health Impact in China*; Dong, G.H., Ed.; Springer: Singapore, 2017; pp. 243–261.
57. Zhang, J.; Jiang, H.; Zhang, W.; Ma, G.; Wang, Y.; Lu, Y.; Hu, X.; Zhou, J.; Peng, F.; Bi, J.; et al. Cost-benefit analysis of China's Action Plan for Air Pollution Prevention and Control. *Front. Eng. Manag.* **2019**, *6*, 524–537. [CrossRef]

58. NASA Earth Observatory. Airborne Nitrogen Dioxide Plummets over China. 2020. Available online: <https://earthobservatory.nasa.gov/images/146362/airborne-nitrogen-dioxide-plummets-overchina> (accessed on 17 April 2020).
59. Lin, C.; Huang, R.; Xu, W.; Duan, J.; Zheng, Y.; Chen, Q.; Hu, W.; Li, Y.; Ni, H.; Wu, Y.; et al. Comprehensive Source Apportionment of Submicron Aerosol in Shijiazhuang, China: Secondary Aerosol Formation and Holiday Effects. *ACS Earth Space Chem.* **2020**, *4*, 947–957. [CrossRef]
60. Tan, P.H.; Chou, C.; Liang, J.Y.; Chou, C.C.K.; Shiu, C.J. Air pollution “holiday effect” resulting from the Chinese New Year. *Atmos. Environ.* **2009**, *43*, 2114–2124. [CrossRef]
61. Yang, Y.; Wang, Y.; Yao, D.; Zhao, S.; Yang, S.; Ji, D.; Sun, J.; Wang, Y.; Liu, Z.; Hu, B.; et al. Significant decreases in the volatile organic compound concentration, atmospheric oxidation capacity and photochemical reactivity during the National Day holiday over a suburban site in the North China Plain. *Environ. Pollut.* **2020**, *263*, 114657. [CrossRef]
62. Zhao, X.; Zhou, W.; Han, L. Human activities and urban air pollution in Chinese mega city: An insight of ozone weekend effect in Beijing. *Phys. Chem. Earth* **2019**, *110*, 109–116. [CrossRef]
63. Weblink 1.a. Available online: https://giovanni.gsfc.nasa.gov/giovanni/#service=TmAvMp&starttime=2019-11-24T00:00:00Z&endtime=2020-01-22T23:59:59Z&shape=state_dept_countries/shp_43&&data=OMNO2d_003_ColumnAmountNO2TropCloudScreened&variableFacets=dataFieldMeasurement%3ANO2%3B (accessed on 25 March 2020).
64. Weblink 1.b. Available online: https://giovanni.gsfc.nasa.gov/giovanni/#service=TmAvMp&starttime=2020-01-23T00:00:00Z&endtime=2020-03-22T23:59:59Z&shape=state_dept_countries/shp_43&&data=OMNO2d_003_ColumnAmountNO2TropCloudScreened (accessed on 25 March 2020).
65. Weblink 2. Available online: https://giovanni.gsfc.nasa.gov/giovanni/#service=ArAvTs&starttime=2019-11-24T00:00:00Z&endtime=2020-03-22T23:59:59Z&shape=state_dept_countries/shp_43&&data=OMNO2d_003_ColumnAmountNO2TropCloudScreened (accessed on 25 March 2020).
66. Duncan, B.N.; Prados, A.I.; Lamsal, L.N.; Liu, Y.; Streets, D.G.; Gupta, P.; Hilsenrath, E.; Kahn, R.A.; Nielsen, J.E.; Beyersdorf, A.J.; et al. Satellite data of atmospheric pollution for US air quality applications: Examples of applications, summary of data end-user resources, answers to FAQs, and common mistakes to avoid. *Atmos. Environ.* **2014**, *94*, 647–662. [CrossRef]
67. Lin, J.; Nielsen, C.P.; Zhao, Y.; Lei, Y.; Mcelroy, M.B. Recent changes in particulate air pollution over China observed from space and the ground: Effectiveness of emission control. *Environ. Sci. Technol.* **2010**, *44*, 7771–7776. [CrossRef] [PubMed]
68. Streets, D.G.; Canty, T.; Carmichael, G.R.; de Foy, B.; Dickerson, R.R.; Duncan, B.N.; Edwards, D.P.; Haynes, J.A.; Henze, D.K.; Houyoux, M.R.; et al. Emissions estimation from satellite retrievals: A review of current capability. *Atmos. Environ.* **2013**, *77*, 1011–1042. [CrossRef]
69. Yan, H.H.; Li, X.J.; Zhang, X.Y.; Wang, W.H.; Cheng, L.F.; Zhang, M.G.; Xu, J. Comparison and validation of band residual difference algorithm and principal component analysis algorithm for retrievals of atmospheric SO₂ columns from satellite observations. *Acta Phys. Sin.* **2016**, *65*, 084204. [CrossRef]
70. Krotkov, N.A.; McLinden, C.A.; Li, C.; Lamsal, L.N.; Celarier, E.A.; Marchenko, S.V.; Swartz, W.H.; Bucsela, E.J.; Joiner, J.; Duncan, B.N.; et al. Aura OMI observations of regional SO₂ and NO₂ pollution changes from 2005 to 2015. *Atmos. Chem. Phys.* **2016**, *16*, 4605–4629. [CrossRef]
71. Mallik, C.; Lal, S. Seasonal characteristics of SO₂, NO₂, and CO emissions in and around the Indo-Gangetic Plain. *Environ. Monit. Assess.* **2014**, *186*, 1295–1310. [CrossRef] [PubMed]
72. Duncan, B.N.; Yoshida, Y.; de Foy, B.; Lamsal, L.N.; Streets, D.; Lu, Z.; Pickering, K.E.; Krotkov, N.A. The observed response of the Ozone Monitoring Instrument (OMI) NO₂ column to NO_x emission controls on power plants in the United States: 2005–2011. *Atmos. Environ.* **2013**, *81*, 102–111. [CrossRef]
73. Rahaman, S.; Jahangir, S.; Chen, R.; Kumar, P.; Thakur, S. COVID-19’s lockdown effect on air quality in Indian cities using air quality zonal modeling. *Urban Clim.* **2021**, *36*, 100802. [CrossRef]
74. Alvo, M.; Philip, L.H. *Statistical Methods for Ranking Data*; Springer: New York, NY, USA, 2014; ISBN 978-1-4939-1471-5. [CrossRef]
75. Nardo, M.; Saisana, M.; Saltelli, A.; Tarantola, S. Tools for composite indicators building. *Eur. Com. Ispra* **2005**, *15*, 19–20.
76. Lai, Y.; Brimblecombe, P. Regulatory effects on particulate pollution in the early hours of Chinese New Year, 2015. *Environ. Monit. Assess.* **2017**, *189*, 467. [CrossRef]
77. Mao, X.; Zhou, J.; Corsetti, G. How well have China’s recent Five-Year Plans been implemented for energy conservation and air pollution control? *Environ. Sci. Technol.* **2014**, *48*, 10036–10044. [CrossRef] [PubMed]
78. Cao, J.; Garbaccio, R.; Ho, M.S. China’s 11th Five-Year Plan and the environment: Reducing SO₂ emissions. *Rev. Environ. Econ. Policy* **2009**, *3*, 231–250. [CrossRef]
79. Zhang, S.Q.; Huang, D. Controlling fine particulate pollution and mitigating environmental health damage. *Environ. Prot.* **2011**, *16*, 25–26.
80. Seinfeld, J.H.; Pandis, S.N. *Atmospheric Chemistry and Physics: From Air Pollution to Climate Change*; Wiley: New York, NY, USA, 1998.
81. Morawska, L.; Jayaratne, E.R.; Mengersen, K.; Jamriska, M.; Thomas, S. Difference in airborne particle and gaseous concentrations in urban air between weekdays and weekends. *Atmos. Environ.* **2002**, *36*, 4375–4383. [CrossRef]
82. Streets, D.G.; Bond, T.C.; Carmichael, G.R.; Fernandes, S.D.; Fu, Q.; He, D.; Klimont, Z.; Nelson, S.M.; Tsai, N.Y.; Wang, M.Q.; et al. An inventory of gaseous and primary aerosol emissions in Asia in the year 2000. *J. Geophys. Res.* **2003**, *108*, 8809. [CrossRef]
83. Yang, K.L.; Ting, C.C.; Wang, K.L.; Wingenter, O.W.; Chan, C.C. Diurnal and seasonal cycles of ozone precursors observed from continuous measurement at an urban site in Taiwan. *Atmos. Environ.* **2005**, *39*, 3221–3230. [CrossRef]

84. Kato, N.; Akimoto, H. Anthropogenic emissions of SO₂, and NO_x in Asia: Emission inventories. *Atmos. Environ.* **2007**, *41*, 171–191. [CrossRef]
85. Kato, S.; Kajii, Y.; Itokazu, R.; Hirokawa, J.; Koda, S.; Kinjo, Y. Transport of atmospheric carbon monoxide, ozone, and hydrocarbons from Chinese coast to Okinawa island in the Western Pacific during winter. *Atmos. Environ.* **2004**, *38*, 2975–2981. [CrossRef]
86. Lin, C.Y.; Liu, S.C.; Chou, C.C.K.; Huang, S.J.; Liu, C.M.; Kuo, C.H.; Young, C.Y. Long-range transport of aerosols and the impact on the air quality of Taiwan. *Atmos. Environ.* **2005**, *39*, 6066–6067. [CrossRef]
87. Latha, K.M.; Highwood, E.J. Studies on particulate matter (PM₁₀) and its precursors over urban environment of Reading, UK. *J. Quant. Spectrosc. Radiat. Transfer.* **2006**, *101*, 367–379. [CrossRef]
88. Moreno, T.; Querol, X.; Alastuey, A.; Santos, S.G.; Gibbons, W. Controlling of influences on daily fluctuations of inhalable particles and gas concentrations: Local versus regional and exotic atmospheric pollutants at Puertollano, Spain. *Atmos. Environ.* **2006**, *40*, 3207–3218. [CrossRef]
89. Wang, Y.; Zhuang, G.; Xu, C.; An, Z. The air pollution caused by the burning of fireworks during the lantern festival in Beijing. *Atmos. Environ.* **2007**, *41*, 417–431. [CrossRef]
90. Yang, L.; Gao, X.; Wang, X.; Nie, W.; Wang, J.; Gao, R.; Xu, P.; Shou, Y.; Zhang, Q.; Wang, W. Impacts of firecracker burning on aerosol chemical characteristics and human health risk levels during the Chinese New Year celebration in Jinan, China. *Sci. Total Environ.* **2014**, *476*, 57–64. [CrossRef]
91. Zhao, S.; Yu, Y.; Yin, D.; Liu, N.; He, J. Ambient particulate pollution during Chinese Spring Festival in urban Lanzhou, Northwestern China. *Atmos. Pollut. Res.* **2014**, *5*, 335–343. [CrossRef]
92. Zheng, C.-X.; Liu, B. Speciation analysis of Cd in PM₁₀ and PM_{2.5} during heating period in Urumqi. *Spectrosc. Spect. Anal.* **2012**, *32*, 235–238.
93. Wang, K.; Tian, H.Z.; Hua, S.B.; Zhu, C.Y.; Gao, J.J.; Xue, Y.F.; Hao, J.M. A comprehensive emission inventory of multiple air pollutants from iron and steel industry in China: Temporal trends and spatial variation characteristics. *Sci. Total Environ.* **2016**, *559*, 7–14. [CrossRef]
94. Wang, Q.; Zhuang, G.; Huang, K.; Liu, T.; Lin, Y.; Deng, C.; Fu, Q.; Fu, J.S.; Chen, J.; Zhang, W. Evolution of particulate sulfate and nitrate along the Asian dust pathway: Secondary transformation and primary pollutants via long-range transport. *Atmos. Res.* **2016**, *169*, 86–95. [CrossRef]
95. Hua, S.B.; Tian, H.Z.; Wang, K.; Zhu, C.Y.; Gao, J.J.; Ma, Y.L.; Xue, Y.F.; Wang, Y.; Duan, S.H.; Zhou, J.R. Atmospheric emission inventory of hazardous air pollutants from China's cement plants: Temporal trends, spatial variation characteristics and scenario projections. *Atmos. Environ.* **2016**, *128*, 1–9. [CrossRef]
96. Chai, F.; Gao, J.; Chen, Z.; Wang, S.; Zhang, Y.; Zhang, J.; Zhang, H.; Yun, Y.; Ren, C. Spatial and temporal variation of particulate matter and gaseous pollutants in 26 cities in China. *J. Environ. Sci.* **2014**, *26*, 75–82. [CrossRef]
97. Lu, Z.; Streets, D.G.; Zhang, Q.; Wang, S.; Carmichael, G.R.; Cheng, Y.F.; Wei, C.; Chin, M.; Diehl, T.; Tan, Q. Sulfur dioxide emissions in China and sulphur trends in East Asia since 2000. *Atmos. Chem. Phys.* **2010**, *10*, 6311–6331. [CrossRef]
98. Pui, D.Y.; Chen, S.C.; Zuo, Z. PM_{2.5} in China: Measurements, sources, visibility and health effects, and mitigation. *Particuology* **2014**, *13*, 1–26. [CrossRef]
99. Liu, L.; Yang, X.; Liu, H.; Wang, M.; Welles, S.; Marquez, S.; Frank, A.; Haas, C.N. Spatial-Temporal analysis of air Pollution, climate change, and Total Mortality in 120 cities of China. *Front. Public Health* **2016**, *4*, 2012–2013. [CrossRef]
100. Liu, P.F.; Zhang, C.L.; Mu, Y.J.; Liu, C.T.; Xue, C.Y.; Ye, C. The possible contribution of the periodic emissions from farmers' activities in the NCP to atmospheric water-soluble ions in Beijing. *Atmos. Chem. Phys.* **2016**, *16*, 10097–10109. [CrossRef]
101. Liu, T.; Wang, X.; Hu, Q.; Deng, W.; Zhang, Y.; Ding, X. Formation of secondary aerosols from gasoline vehicle exhaust when mixing with SO₂. *Atmos. Chem. Phys.* **2016**, *16*, 675–689. [CrossRef]
102. Zhao, Y.; Wang, S.; Duan, L.; Lei, Y.; Cao, P.; Hao, J. Primary air pollutant emissions of coal-fired power plants in China: Current status and future prediction. *Atmos. Environ.* **2008**, *42*, 8442–8452. [CrossRef]
103. Rahman, A.; Luo, C.; Khan, M.H.R.; Ke, J.; Thilakanayaka, V.; Kumar, S. Influence of atmospheric PM_{2.5}, PM₁₀, O₃, CO, NO₂, SO₂, and meteorological factors on the concentration of airborne pollen in Guangzhou, China. *Atmos. Environ.* **2019**, *212*, 290–304. [CrossRef]
104. Tian, D.; Fan, J.; Jin, H.; Mao, H.; Geng, D.; Hou, S.; Zhang, P.; Zhang, Y. Characteristic and spatiotemporal variation of air pollution in Northern China based on correlation analysis and clustering analysis of five air pollutants. *J. Geophys. Res. Atmos.* **2020**, *125*, e2019JD031931. [CrossRef]
105. Xiao, K.; Wang, Y.; Wu, G.; Fu, B.; Zhu, Y. Spatiotemporal characteristics of air pollutants (PM₁₀, PM_{2.5}, SO₂, NO₂, O₃, and CO) in the inland basin city of Chengdu, southwest China. *Atmosphere* **2018**, *9*, 74. [CrossRef]
106. Ma, J.Z.; Xu, X.B.; Zhao, C.; Yan, P.A. Review of Atmospheric Chemistry Research in China: Photochemical Smog, Haze Pollution, and Gas-Aerosol Interactions. *Adv. Atmos. Sci.* **2012**, *29*, 1006–1026. [CrossRef]
107. Meng, Z.; Dabdub, D.; Seinfeld, J.H. Chemical coupling between atmospheric ozone and particulate matter. *Science* **1997**, *277*, 116–119. [CrossRef]
108. Murphy, J.G.; Day, D.A.; Cleary, P.A.; Wooldridge, P.J.; Millet, D.B.; Goldstein, A.H.; Cohen, R.C. The weekend effect within and downwind of Sacramento—Part 1: Observations of ozone, nitrogen oxides, and VOC reactivity. *Atmos. Chem. Phys.* **2007**, *7*, 5327–5339. [CrossRef]

109. Qin, Y.; Tonnesen, G.S.; Wang, Z. Weekend/weekday differences of ozone, NO_x, CO, VOCs, PM₁₀ and the light scatter during ozone season in southern California. *Atmos. Environ.* **2004**, *38*, 3069–3087. [CrossRef]
110. Chou, C.C.K.; Liu, S.C.; Lin, C.Y.; Shiu, C.J.; Chang, K.H. The trend of surface ozone in Taipei, Taiwan, and its causes: Implications for ozone control strategies. *Atmos. Environ.* **2006**, *40*, 3898–3908. [CrossRef]
111. California Air Resources Board. *The Ozone Weekend Effect in California*; CARB Planning and Technical Support Division: Sacramento, CA, USA, 2003.
112. Beaney, G.; Gough, W.A. The influence of tropospheric ozone on the air temperature of the city of Toronto, Ontario, Canada. *Atmos. Environ.* **2002**, *36*, 2319–2325. [CrossRef]
113. Beirle, S.; Platt, U.; Wenig, M.; Wagner, T. Weekly cycle of NO₂ by GOME measurements: A signature of anthropogenic sources. *Atmos. Chem. Phys.* **2003**, *3*, 2225–2232. [CrossRef]
114. Riga-Karandinos, A.-N.; Saitanis, C. Comparative assessment of ambient air quality in two typical Mediterranean coastal cities in Greece. *Chemosphere* **2005**, *59*, 1125–1136. [CrossRef]
115. Geddes, J.A.; Murphy, J.G.; Wang, D.K. Long term changes in nitrogen oxides and volatile organic compounds in Toronto and the challenges facing local ozone control. *Atmos. Environ.* **2009**, *43*, 3407–3415. [CrossRef]
116. Fu, X.; Wang, X.; Guo, H.; Cheung, K.; Ding, X.; Zhao, X.; He, Q.; Gao, B.; Zhang, Z.; Liu, T. Trends of ambient fine particles and major chemical components in the Pearl River Delta region: Observation at a regional background site in fall and winter. *Sci. Total Environ.* **2014**, *497*, 274–281. [CrossRef] [PubMed]
117. Liang, X.; Zou, T.; Guo, B.; Li, S.; Zhang, H.; Zhang, S.; Huang, H.; Chen, S.X. Assessing Beijing's PM_{2.5} pollution: Severity, weather impact, APEC and winter heating. *Proc. R. Soc. A* **2015**, *471*, 20150257. [CrossRef]
118. Lyu, X.; Chen, N.; Guo, H.; Zeng, L.; Zhang, W.; Shen, F.; Quan, J.; Wang, N. Chemical characteristics and causes of airborne particulate pollution in warm seasons in Wuhan, central China. *Atmos. Chem. Phys.* **2016**, *16*, 10671–10687. [CrossRef]

Article

Study on Improving the Air Quality with Emission Enhanced Control Measures in Beijing during a National Parade Event

Bingbo Huang ¹, Minjun Deng ², Qingxian Gao ³, Zhanyun Ma ³ and Mindong Chen ^{1,*}

¹ Jiangsu Key Laboratory of Atmospheric Environment Monitoring and Pollution Control, Collaborative Innovation Center of Atmospheric Environment and Equipment Technology, School of Environmental Science and Engineering, Nanjing University of Information Science & Technology, Nanjing 210044, China; 20171102061@nuist.edu.cn

² Ningxia Meteorological Service Center, Yinchuan 750002, China; minjundeng1@163.com

³ Chinese Research Academy of Environmental Sciences, Beijing 100012, China; gaoqx@craes.org.cn (Q.G.); mazy@craes.org.cn (Z.M.)

* Correspondence: chenmd@nuist.edu.cn; Tel.: +86-25-58731089

Abstract: Research on the enhanced control and emission-reduction measures to improve air quality during major events could provide data theory and scientific support for air-quality improvement during non-activities. Based on the air-quality data published by the China Environmental Monitoring Station and the meteorological elements and weather conditions released by the China Meteorological Administration, this paper explored the characteristics of air-quality evolution in Beijing from 5 August to 18 September 2015 and the weather situation during the Military Parade. The results showed that: (1) Emission-reduction measures implemented for air quality by Beijing and its surrounding area were induced, and we explored the contribution of these measures to pollutants or AQI in the locality. (2) During the 2015 Military Parade, Beijing was in the front or lower part of the high-pressure system. Due to the strong effect of North or Northeast winds, the weather situation was conducive to the diffusion of pollutants. When before or after the implementation, once the atmospheric diffusion was poor, the pollutants would accumulate gradually. Thus, it can be seen that the weather situation had a great impact on air quality. (3) During the implementation, PM_{2.5}, PM₁₀, NO₂ and other pollutants decreased significantly, of which the concentration of PM₁₀ decreased the most, from 109 µg·m⁻³ down to 34 µg·m⁻³, and the concentration of PM_{2.5} decreased by 72.73%. According to the changes between before and during the implementation or during and after the implementation, the concentration of PM₁₀ and PM_{2.5} increased when the implementation of the emission-reduction measures had been finished, indicating that the enhanced control measures made a great contribution to the emission reduction in particles. (4) In addition, the annual average of AQI in the three years is 87.49, and the average value of a normal year was the average value of 2013 and 2014. The average value of the normal year during the military parade is 64.63, which was 70.40% lower than the average value of AQI during the military parade. The goal of reaching the secondary standard of GB-3095-2012 was achieved, and there was still a long way to go from the primary standard. In a few words, in order to achieve the goal of better air quality throughout the year, all parties still needed to coordinate control and make joint efforts.

Keywords: military parade; air quality; emission control and reduction measures; weather situation; Olympic Sports Center

Citation: Huang, B.; Deng, M.; Gao, Q.; Ma, Z.; Chen, M. Study on Improving the Air Quality with Emission Enhanced Control Measures in Beijing during a National Parade Event. *Atmosphere* **2022**, *13*, 1019. <https://doi.org/10.3390/atmos13071019>

Academic Editors: Duanyang Liu, Kai Qin and Honglei Wang

Received: 11 May 2022

Accepted: 15 June 2022

Published: 24 June 2022

Publisher's Note: MDPI stays neutral with regard to jurisdictional claims in published maps and institutional affiliations.



Copyright: © 2022 by the authors. Licensee MDPI, Basel, Switzerland. This article is an open access article distributed under the terms and conditions of the Creative Commons Attribution (CC BY) license (<https://creativecommons.org/licenses/by/4.0/>).

1. Introduction

In recent years, a series of temporary emission-reduction measures have been adopted to ensure air quality during some large-scale events at home and abroad, such as the 2002 Busan Asian Games, the 2008 Beijing Olympic Games, the 2010 Guangzhou Asian Games, and the 2014 APEC Meeting in Beijing. Many scholars have studied air quality from the aspect of air quality protection measures. For example, Li L et al. [1] used the WRF-CMAQ

model to simulate the concentration of PM_{2.5} under the condition of no control measures and temporary industrial control measures or carried out the evaluation of effect of control measures on air-quality improvement during the Nanjing Youth Olympic Games based on actual observation data. Wang et al. [2] found that during the APEC meeting in 2014, the overall air quality of Shijiazhuang city was better than that of the same period in 2013, and the mass concentration of all air pollutants except for O₃ decreased significantly. Lee et al. [3] conducted a study on PM₁₀, CO, NO₂, and SO₂ of 13 air sub-stations during the traffic restriction period of the 2002 Busan Asian Games in South Korea and found that the concentrations of these pollutants all decreased significantly. Beig et al. [4] used the WRF-Chem model to evaluate and found that if effective emission-reduction measures were not taken during the event, the air quality improvement effect would be limited. Liu et al. [5] found in their study that the contribution of early progressive emission reduction to SO₂, NO₂, VOC, and other pollutants was greater than that of temporary emission-reduction measures. Li et al. [6] analyzed the improvement in air quality in Beijing during APEC and found that compared with the same period in 2013, the concentration of PM_{2.5} significantly decreased during APEC in 2014, and the air quality was dominated by fine weather, indicating that enhanced emission-reduction measures had a significant effect on the improvement in air quality in Beijing.

Studies showed that different weather situations, different seasons, and different pollution sources have different impacts on pollutant concentrations [7–12]. Therefore, a lot of research has been conducted on weather conditions during major events. For example, Li et al. [13] analyzed the variable characteristics of air quality and pollution meteorological conditions in Guangzhou during the Guangzhou Asian Games and pointed out that the air quality during the Asian Games could be guaranteed under the influence of strong emission-reduction measures implemented by the government and good weather conditions. Yu et al. [14] analyzed the weather conditions during the Asian Youth Games and found that due to the influence of afternoon thundershowers and typhoons, the weather conditions during the Asian Youth Games were good for the diffusion of pollutants, and the air quality was significantly better than that of the same period in 2011 and 2012. Chen et al. [15] studied the impact of meteorological conditions on air quality during the Shanghai World Expo. Although the joint prevention and control measures of air quality during the Shanghai World Expo made pollution emissions lower than in normal years, the transport and diffusion of atmospheric circulation still led to three pollution events during the Shanghai World Expo when the meteorological conditions were unfavorable. The results indicated that meteorological conditions are one of the main factors affecting the air quality during the Shanghai World Expo. In addition, some scholars studied the formation mechanism of pollution under different control measures [16–28].

In honor of the 70th-anniversary victory of the Chinese People's War of Resistance against Japanese Aggression and the World Anti-Fascist, a grand ceremony was held on 3 September 2015 in China. So as to protect Beijing's air quality during the Military Parade, six provinces around Beijing jointly implemented a series of control measures and regional joint prevention, including odd–even license plate restrictions, industrial production and suspension. During this period, Beijing's air quality reached grade one (excellent) weather for 15 consecutive days, and on September 3rd, there were blue skies and white clouds, widely known as "Military Parade blue". At present, scholars have evaluated the effect of emission reduction during the Military Parade [29,30].

Different from previous studies, this study conducted a comparative study on the air quality of Beijing before, during, and after the implementation of the enhanced control measures for the 2015 military parade, as well as during the same period in 2013 and 2014. In addition, a comparative analysis of the improvement effect of air quality between the 2014 APEC and the 2015 Military Parade was also carried out. Meanwhile, emission enhanced control and reduction measures with regard to Beijing or its surrounding area during the 2015 Military Parade were induced. To explore and analyze the contribution of emission-reduction measures and weather conditions to the improvement of air quality in

Beijing, this study can provide data theory for air-quality research before, during, and after the implementation of emission-reduction measures during major activities and scientific support for the implementation of air quality assurance measures during non-activities. The actual mechanism and single-factor research had not been applied in this study, so further study is needed.

Based on the air-quality data of the Beijing Olympic Sports Center released by the China Environmental Monitoring Station, this study compared the changes in Beijing's air quality before, during, and after the implementation of the Military Parade, as well as the same three years in 2013, 2014, and 2015. The discussion of the effect of emission-reduction measures or the influence of weather conditions on Beijing's air quality has important scientific significance and practical value, and at the same time, it could provide scientific and technical support for improving Beijing's air quality.

2. Materials and Methods

2.1. Data

- (1) Air-quality data were collected from the data of various pollutants released by the China Environmental Monitoring Station of the Ministry of Environmental Protection (<https://air.cnemc.cn:18007/>, accessed on 10 May 2022), including the hourly concentration value, daily concentration value, and Air Quality Index (AQI) or various pollutants.
- (2) AQI standards and technical regulations in China: air quality standards in China come from the ambient air quality standards (GB 3095-2012) and the technical regulations for ambient air quality index (AQI) (Trial) (HJ 633-2012) (hereinafter referred to as the regulations) issued by the Ministry of Environmental Protection.
- (3) The weather situation field three times a day was taken from the weather situation of the Central Meteorological Observatory, including the analysis of the surface situation, the high altitude 850 hPa and 500 hPa situation maps, and the wind direction and speed data observed by the national hourly ground automatic stations.
- (4) For the sake of comparing the impact of the enhanced control and emission-reduction measures on air quality, the monitoring station of the Olympic Sports Center was selected as the research object, and the point of time that was picked was 15 days before, during, and after the implementation of the enhanced control and emission-reduction measures, respectively (from 5 August to 18 September, a total of 45 days). Figure 1 shows the location diagram of the research site. The Olympic Sports Center was the emptiest area near the North Fourth Ring Road. The monitoring site was laid in the willows on the south side of the vacant lot. It was about 150 m away from the Olympic Sports Center to the south, 380 m away from the Ding Road to the east, 540 m away from the main road of the North Fourth Ring Road, and 730 m away from Bei Chen Road to the west. There was a large area of open greenbelt in the south of the Olympic Sports Center.
- (5) Emission-reduction measures from the government sites of Beijing and its surrounding area during the 2015 Military Parade.



Figure 1. Location of monitoring sites of the Beijing Olympic Sports Center. Notes: The Chinese characters in the left picture is the meaning of Chinese Geographic Names, which also represents its geographical location. The green circle (a), yellow circle (b), blue circle (c), orange circle (d) in the left picture is the meaning of Urban environmental assessment point, Urban cleanliness control point, Area background transfer point, Traffic pollution monitoring point, respectively. And which the number of this points are 23, 1, 6, 5, respectively.

2.2. Methods

The research method adopted in this study was time series analysis in statistics. Firstly, the enhanced control measures such as traffic restriction and emission reduction adopted in Beijing and its surrounding areas during the Military Parade were summarized and sorted out. Secondly, the air quality before, during, and after the implementation of the enhanced control measures was analyzed. At the same time, the air quality in 2013 and the air quality in 2014 were compared.

Taking into account the calculation of ambient air quality in China, the 1-h concentration air quality sub-index (IAQI) classification concentration limit of particulate matter ($PM_{2.5}$ and PM_{10}) is based on the 24-h concentration AQI classification concentration limit. The study consulted AQI standards and technical regulations from Data (2), and an AQI greater than 150 (corresponding to the daily average concentration limit of $PM_{2.5}$ greater than $115 \mu g \cdot m^{-3}$) is defined as a pollution event, i.e., an event with continuous occurrence of moderate pollution or more is defined as a pollution event. At the same time, it is stipulated that a pollution event is composed of two parts: the pollution accumulation process and the pollution disappearance process. The pollution accumulation process refers to the process in which pollutants rise from the trough (minimum value) to the peak (maximum value). One pollution disappearance process refers to the process in which the pollution drops from the peak value to another valley value. Generally speaking, the accumulation time of the pollution accumulation process will be longer than that of the pollution disappearance process.

Supplemented by sky photos from 08:00 to 08:30 every morning as a reference, it could visually compare the evolution of air quality around the Beijing Olympic Sports Center. The photos were taken from the top floor of the Chinese Academy of Environmental Sciences to the Southwest (the tree of life sightseeing tower). Although the photos were static and instantaneous, they also reflected the actual situation of air quality in Beijing to some extent.

In short, in order to simplify the structure of the article, the implementation of enhanced control and emission-reduction measure was abbreviated as IECERM. The time of

IECERM (during the Military Parade) was from 20 August to 3 September. Among them, 15 days from 5 August to 19 August were chosen as before IECERM (before the Military Parade), and 15 days from 4 September to 18 September were selected as after IECERM (after the Military Parade).

3. Results

For the purpose of ensuring air quality during the Military Parade on 3 September, six provinces and cities around Beijing with Beijing had jointly implemented temporary enhanced control and emission-reduction measures. Among them, motor vehicles, industrial enterprises, coal burning, and dust as the main control objects. The measures would be sustained from midnight on 20 August to 24:00 on 4 September.

3.1. Review of the Implementation of Enhance Control and Emission-Reduction Measures during the Military Parade

In Beijing, including industrial enterprises, coal-fired boilers or construction, and other aspects of enhanced emission-reduction measures were taken. With regard to the industrial source, measures should be taken to suspend or limit the production of workshops and processes that emitted air pollutants in petrochemical, building materials, industrial painting, printing, furniture, and other industries. For the aerial dust source, there were two ways to go. On the one hand, earthwork, road milling, structural demolition, construction waste and residue transportation, painting, and other construction operations were stopped. On the other hand, construction waste and heavy vehicles such as muck trucks and gravel trucks were banned from driving on the road. In terms of the moving source, in addition to public transport, ambulance, fire, sanitation, law enforcement, “green channel”, and other urban operation support vehicles or pure electric buses, odd–even motor vehicles in all regions were implemented; 30% of motor vehicles of the party and government organs at all levels, municipal social organizations, public institutions, and state-owned enterprises would be suspended from driving on account of odd–even license plates, and 80% of official vehicles would be suspended from driving. Moreover, construction waste and muck carriers, concrete tankers, sand and stone carriers, hazardous chemical carriers, and other vehicles were prohibited from driving on Beijing municipal roads all day long, and freight vehicles, low-speed trucks, and tractors were prohibited from driving on roads within the Sixth Ring Road from 06:00 to 24:00 h every day.

In terms of road transportation, measures such as odd–even license plate restrictions and suspension of official vehicles were taken. In the administrative area of Beijing, from 20 August to 4 September, motor vehicles with license plates issued by Beijing and motor vehicles from other provinces, regions, and cities entering Beijing were driven in single and double numbers for one day and two days from 03:00 to 24:00 day by day. In addition, 80% of the day’s motor vehicles affiliated with party and government organs at all levels, social organizations, public institutions, and state-owned enterprises of Beijing stopped driving. Motor vehicles in other provinces were prohibited from driving on roads within Beijing’s Fifth Ring Road (including the Fifth Ring Road) from 07:00 to 09:00 and 17:00 to 20:00 every day. Table 1 lists the specific restrictions.

In addition, from midnight on 28 August to 24:00 on 4 September, six provinces surrounding Beijing, including Tianjin, Hebei, Shanxi, Inner Mongolia Autonomous Region, Shandong, and Henan provinces, implemented temporary enhanced emission-reduction measures in the union to ensure air quality during the Military Parade. Specific measures were as follows.

In Tianjin, there were 285 steel, cooking, cement, glass, and other elevated pollution sources suspended, and 421 enterprises in chemical, printing, industrial painting, furniture, automobile manufacturing, automobile repair, and other industries that produced volatile organic compounds had taken measures to stop production, repairment, and limit production. In order to ensure a discharge standard, all pollutants should be reduced by at least 30 percent as a result of the discharge. To minimize elevated pollution sources and pol-

lutants from key industrial enterprises, all construction work on buildings, roads, and demolition sites; open burning and barbecuing; and fireworks and firecrackers were prohibited in urban and rural areas in Shandong. In Henan, 13 electric power, 48 carbon, 25 cement, and 297 refractory enterprises in Zhengzhou were investigated and rectified; 14 of its 29 coal-fired units were shut down in Pingdingshan; Jiaozuo imposed total coal consumption controls on 28 key coal-consuming enterprises, while Xinxiang and Sanmenxia also adopted corresponding measures. In total, 8587 heavy polluters were investigated, of which 128 enterprises were ordered to stop construction, 304 enterprises to stop production, and 112 enterprises to shut down in Shanxi. According to the climate characteristics of the summer–autumn transition period, pollutant emissions, or pollutant diffusion of the air quality of Beijing, Hebei province could be divided into key control areas—Shijiazhuang, Tangshan, Langfang, Baoding, Hengshui, Xingtai, Handan city, Dingzhou, Xinji, Qianan, Zhuozhou or Ningjin, Jing County, and Wei County—while the others are general control areas. Measures such as reducing production load, burning high-quality coal with low-sulfur, and implementing emission performance management should be taken to reduce pollutant discharge by more than 30% from elevated pollution sources in the area. During the event, the Inner Mongolia Autonomous Region strengthened the monitoring of motor vehicle exhaust emissions, set up 12 security checkpoints in Beijing, strengthened the inspection of vehicles entering Beijing, and required that vehicles do not meet the emission level of national III or above of the driving restriction requirements in time, and the traffic control department of public security denied all vehicles that do not meet the formalities entrance to Beijing. Hohhot, Baotou, Chifeng, the Xilin Gol League, and Ulanqab, which were close to Beijing, were also listed as key control areas. In these areas, carrying earth or muck and vehicles carrying dangerous goods were prohibited, and vehicles with yellow labels, low-speed trucks, and agricultural vehicles were restricted at different times.

Table 1. Arrangement of single and double limit line time for Beijing motor vehicles.

Sunday	Monday	Tuesday	Wednesday	Thursday	Friday	Saturday
						None traffic restriction 1 August
None traffic restriction 2nd	5 and 0 traffic restriction 3rd	1 and 8 traffic restriction 4th	2 and 7 traffic restriction 5th	3 and 6 traffic restriction 6th	4 and 0 traffic restriction 7th	None traffic restriction 8th
None traffic restriction 9th	5 and 0 traffic restriction 10th	1 and 8 traffic restriction 11th	2 and 7 traffic restriction 12th	3 and 6 traffic restriction 13th	4 and 0 traffic restriction 14th	None traffic restriction 15th
None traffic restriction 16th	5 and 0 traffic restriction 17th	1 and 8 traffic restriction 18th	2 and 7 traffic restriction 19th	Double number travel 20th	Single number travel 21st	Double number travel 22nd
Single number travel 23rd	Double number travel 24th	Single number travel 25th	Double number travel 26th	Single number travel 27th	Double number travel 28th	Single number travel 29th
Double number travel 30th	Single number travel 31st	Single number travel Sep.1st	Double number travel 2nd	Single number travel 3rd Holiday	4 and 0 traffic restriction 4th Holiday	None traffic restriction 5th Holiday
None traffic restriction 6th Working	5 and 0 traffic restriction 7th	1 and 8 traffic restriction 8th	2 and 7 traffic restriction 9th	3 and 6 traffic restriction 10th	4 and 0 traffic restriction 11th	None traffic restriction 12th

After the safeguard measures for air quality in seven provinces and cities were implemented in a union, emission-reduction measures such as vehicle restrictions, enterprise suspension, production restriction, and construction site suspension were put in place, which helped Beijing’s air quality remain excellent quickly. From 20 August to

3 September, compared to the air quality with no measures, the concentration of $PM_{2.5}$ at 11 state-controlled air-quality-monitoring stations in Beijing dropped by an average of about 41 percent. If no safeguard measures were taken, the concentration of $PM_{2.5}$ would increase by about 70 percent. The air quality of Tianjin, Hebei, Shanxi, Shandong, Henan, Inner Mongolia, and other neighboring provinces improved significantly, and the average concentration of $PM_{2.5}$ in 70 cities at prefecture-level and above dropped by about 40 percent. In addition to the excellent performance of $PM_{2.5}$, other pollutants also showed a significant decline under the enhanced emission-reduction measures of the city and surrounding provinces. The average concentration of SO_2 , NO_2 , and PM_{10} was $3.2 \mu\text{g}\cdot\text{m}^{-3}$, $22.7 \mu\text{g}\cdot\text{m}^{-3}$, and $25.3 \mu\text{g}\cdot\text{m}^{-3}$, year-on-year declined by 46.7%, 52.1%, and 69.2%, respectively. They both reached the lowest levels in the history of monitoring; during the Military Parade on the morning of 3 September, the average concentration of $PM_{2.5}$ in Beijing was only $8 \mu\text{g}\cdot\text{m}^{-3}$.

The proportion of pollutant emission reduction and $PM_{2.5}$ concentration improvement achieved by the air quality safeguard measures was slightly higher than that achieved by the 2014 APEC air quality safeguard measures. Compared with the same period in 2014, the total emission reduction ratio of SO_2 , NO_2 , PM_{10} , $PM_{2.5}$, and volatile organic compounds in Beijing reached 36.5%, 49.9%, 50.3%, 49.0%, and 32.4%, respectively.

3.2. Air Quality and Weather Background during the Military Military Parade

3.2.1. Hourly Concentration of $PM_{2.5}$

For evaluating the improvement effect of enhanced control and emission-reduction measures on air quality in Beijing, Figure 2 showed the hourly concentration of $PM_{2.5}$ at Beijing Olympic Sports Center monitoring sites combined with photos of the sky from 8:00 a.m. to 08:30 a.m from 5 August to 19 September in 2015. By comparing the sky photos before, during, and after the traffic restriction, it could be seen that a blue sky appeared for 7 days during the traffic restriction and only appeared for 5 days before and after the traffic restriction. Before the restrictions, there were three pollution processes, the longest of which was four days. During the three pollution accumulation processes, the hourly concentration of $PM_{2.5}$ exceeded $100 \mu\text{g}\cdot\text{m}^{-3}$, and the maximum concentration of $PM_{2.5}$ reached $153 \mu\text{g}\cdot\text{m}^{-3}$ during the pollution accumulation process. There were no pollution processes during the traffic restriction. The maximum concentration of $PM_{2.5}$ reached $58 \mu\text{g}\cdot\text{m}^{-3}$ in the pollution accumulation process, and the concentration of $PM_{2.5}$ remained below $100 \mu\text{g}\cdot\text{m}^{-3}$, indicating that fine weather was dominant during the period of traffic restriction, but there were only 7 days with blue skies, which may be related to the weather situation at that time. After the traffic restriction, there was a pollution process. Compared with the traffic restriction, the pollution accumulation time and pollution degree increased, especially from 14 September to 18 September. The pollution accumulation time was most serious for 5 days, and the concentration of $PM_{2.5}$ reached a maximum of $252 \mu\text{g}\cdot\text{m}^{-3}$ during the pollution process. As can be seen from the maximum concentration of $PM_{2.5}$ in the pollution accumulation process, the air quality during the traffic restriction was better than that before or after the traffic restriction. In addition, the average concentration of $PM_{2.5}$ for 15 days before, during, and after the traffic restriction was 66, 18, and 52, respectively. The concentration of $PM_{2.5}$ during the traffic restriction period was significantly lower than the concentration at other times, which showed that the enhanced control and emission-reduction measures significantly improved Beijing's air quality.

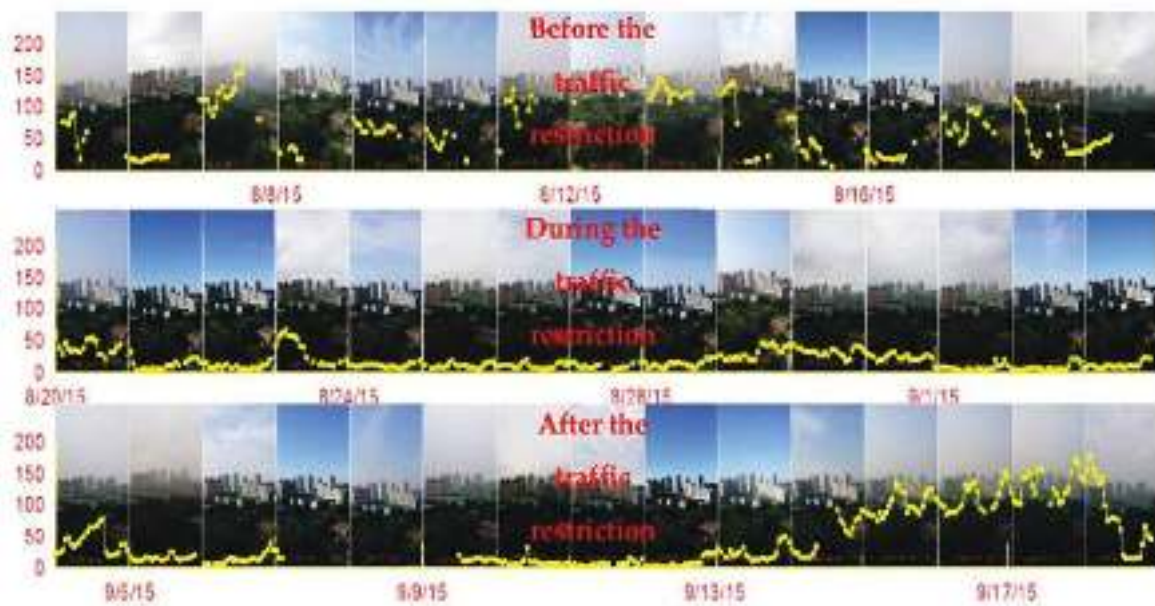


Figure 2. Hourly concentration of PM_{2.5} in Monitoring sites of Beijing Olympic Sports Center. Notes: The yellow line represents the trends of hourly concentration of PM_{2.5} when before, during, and after the restriction (from 5 August to 19 September). The y-axis is the concentration of PM_{2.5}, among the unit is $\mu\text{g}\cdot\text{m}^{-3}$. The x-axis is the date when from 5 August to 19 September. The picture shows the daily weather conditions at 07:00 of the monitoring site from 5 August to 19 September.

3.2.2. Weather Background during the Military Parade

In view of the fine weather during the military parade, the weather background during the military parade period from 1 September to 4 September was analyzed by combining the weather chart three times a day and the one-hour wind field once a day. On this account, the influence of the weather situation on air quality in Beijing was investigated, for details, referred to Figures 3–6.

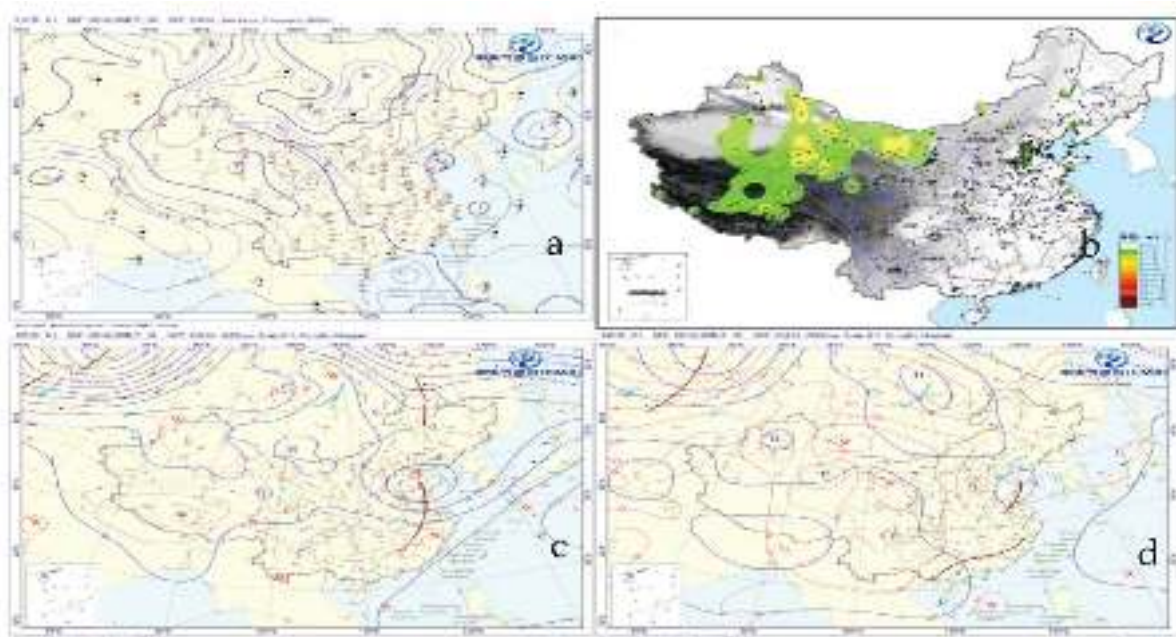


Figure 3. Maps of the weather and AQI situation at 07:00 on 1 September in 2015. Notes: (a,c,d) shows the map of the surface, 500 hPa height, 850 hPa height, respectively. (b) shows the automatic ground observation of 1 h wind field at 07:00 on 1 September in 2015.

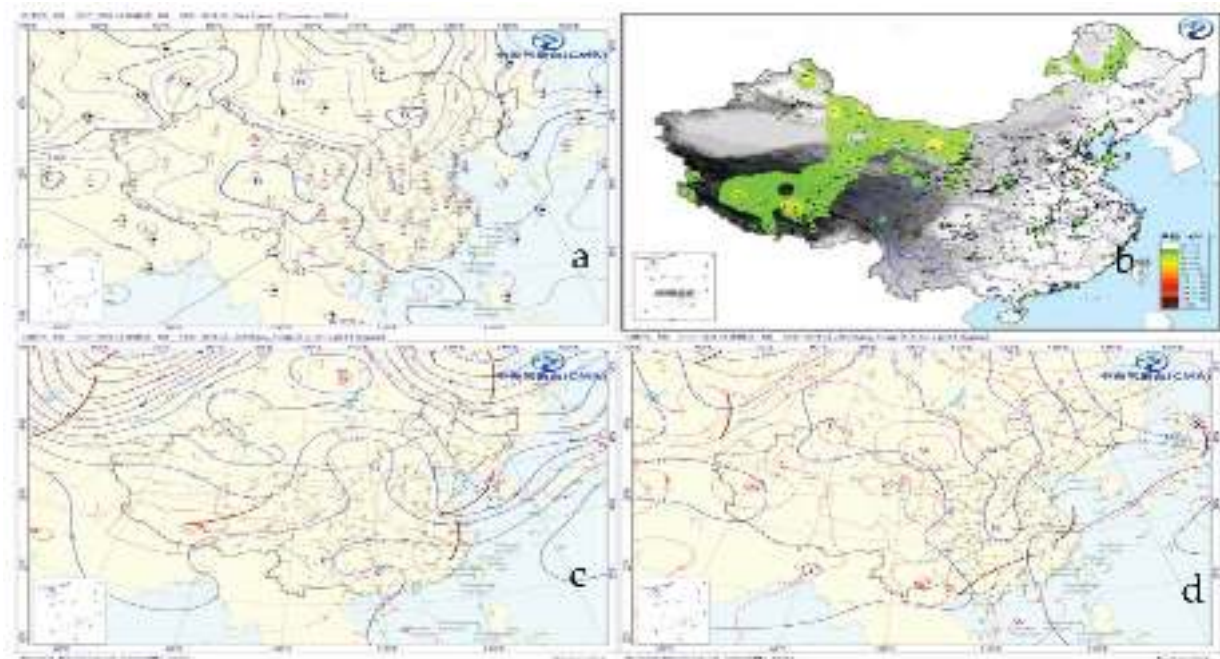


Figure 4. Maps of the weather and AQI situation at 07:00 on 2 September in 2015. Notes: (a,c,d) shows the map of the surface, 500 hPa height, 850 hPa height, respectively. (b) shows the automatic ground observation of 1 h wind field at 07:00 on 2 September in 2015.

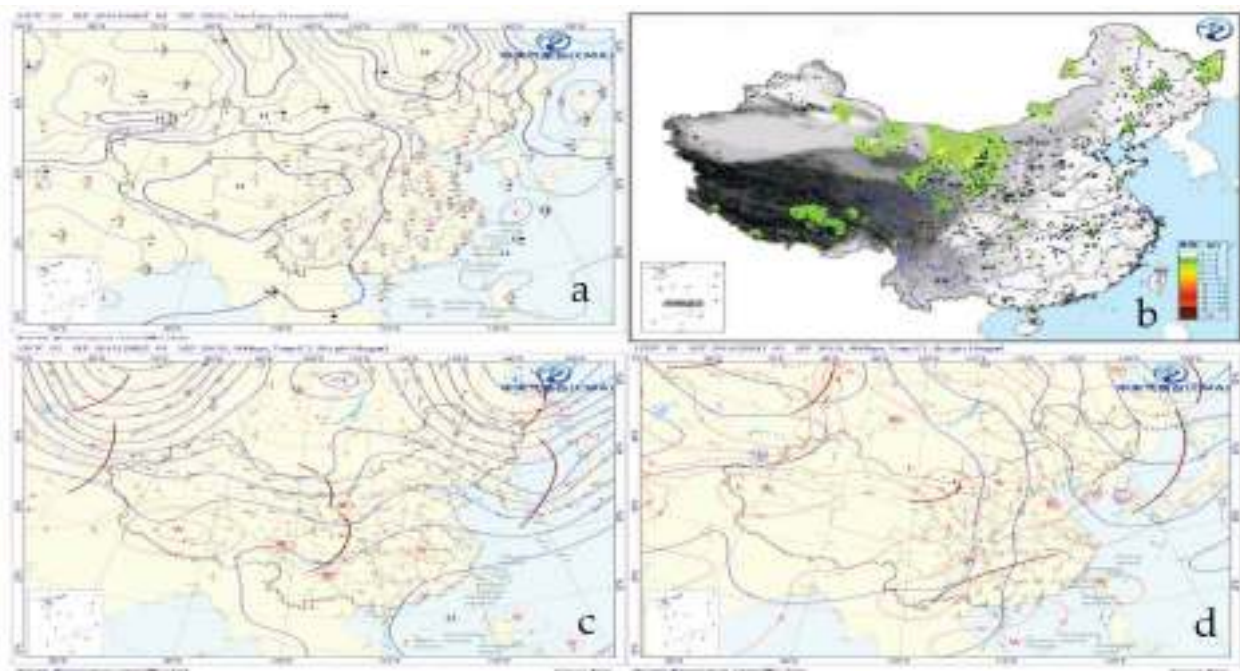


Figure 5. Maps of the weather and AQI situation at 07:00 on 3 September in 2015. Notes: (a,c,d) shows the map of the surface, 500 hPa height, 850 hPa height, respectively. (b) shows the automatic ground observation of 1 h wind field at 07:00 on 3 September in 2015.

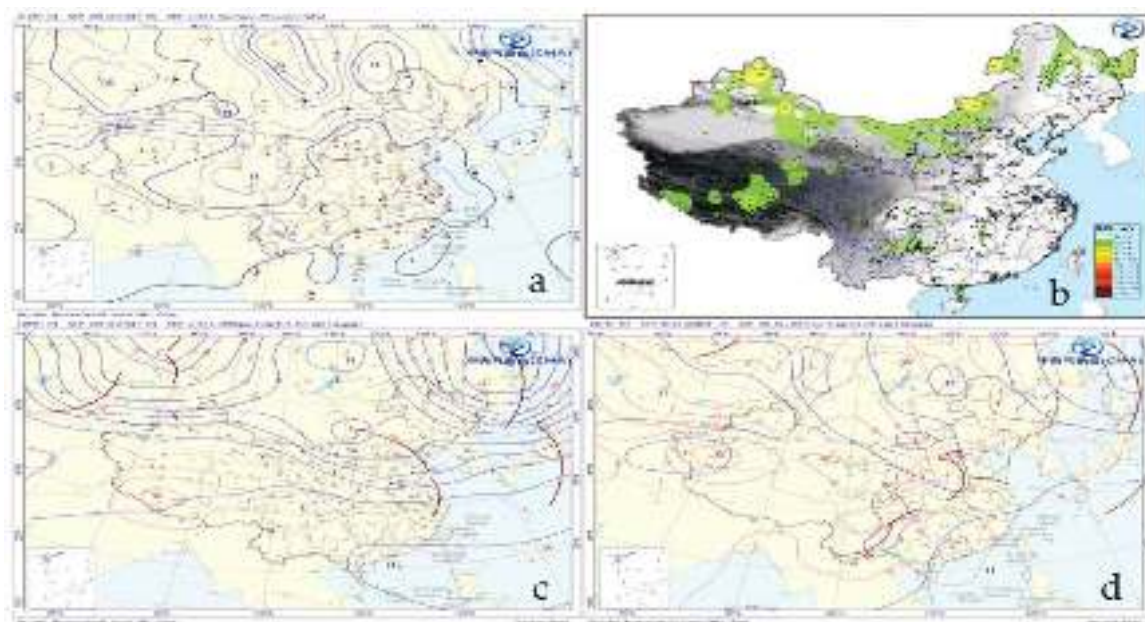


Figure 6. Maps of the weather and AQI situation at 08:00 on 4 September in 2015. Notes: (a,c,d) shows the map of the surface, 500 hPa height, 850 hPa height, respectively. (b) shows the automatic ground observation of 1 h wind field at 08:00 on 4 September in 2015.

At 07:00 on 1 September in 2015, the ground situation chart which can be seen from Figure 3a showed that Beijing was in the lower part of the cold high pressure, which was influenced by the northeast airflow. At altitude, (d) resembled to (c), and Beijing was located on the north side of the North China vortex, which was influenced by the northwest airflow. After that, the vortex continued to move eastward, and the wind speed reached force 3–4 $\text{m}\cdot\text{s}^{-1}$ (b), which was beneficial to the spread of pollutants. The main pollutant on that day was O_3 , with a concentration of $53 \mu\text{g}\cdot\text{m}^{-3}$, while the concentrations of other pollutants, such as $\text{PM}_{2.5}$, PM_{10} , NO_2 , and SO_2 , were 10, 15, 23, and $2 \mu\text{g}\cdot\text{m}^{-3}$, respectively, and the AQI was 21, which indicated the air quality was excellent.

At 07:00 on 2 September in 2015, Figure 4 provided the ground situation map (a), 500 hPa height map (b), 850 hPa height map (c) and automatic ground observation of 1 h wind field, respectively. Among of them, (a) showed that the North China Vortex continues to move eastward, the west was controlled by Hetao high pressure, the east was controlled by low pressure, and all were influenced by northwest airflow. (c) showed that the eastern part of mainland China was mainly influenced by the northwest airflow behind the cold trough, Beijing was located behind the trough, and the wind speed was 2–4 $\text{m}\cdot\text{s}^{-1}$ according to (b). (d) showed that Beijing was in the front of the high-pressure trough and the rear of the low-pressure trough. Under the influence of the northwest airflow, the particulate matter that accumulated in the air could be removed, and the air quality in the whole of North China was improved. The main pollutant was O_3 , and other pollutants were lower. Finally, the AQI was 25. These all indicated the air quality was excellent, which also laid the foundation for the subsequent “Military Parade blue”.

Figure 5 gave the ground situation map (a), 500 hPa height map (b), 850 hPa height map (c) and automatic ground observation of 1 h wind field at 07:00 on 3 September in 2015, respectively. (a) showed that the western part of Mainland China was controlled by Hetao high pressure, while the eastern part was controlled by low pressure. Beijing was in the front of the high center, affected by the northerly airflow, and the wind speed was maintained at force 1–2 $\text{m}\cdot\text{s}^{-1}$ based on (b). The (d) showed that Beijing was in the front of the high-pressure trough and the back of the low-pressure trough, affected by the northerly airflow. (c) showed that North China was behind the cold trough, and “Military Parade blue” appeared in Beijing. Similar to the previous two days, O_3 was still the main pollutant,

and the concentration increased to $81 \mu\text{g}\cdot\text{m}^{-3}$. Additionally, the concentration of PM_{10} increased slightly. The AQI was 36, and the air quality was still excellent, which may be related to the season at that time in Beijing.

Figure 6a showed that the western part of Northern China was controlled by Mongolian low pressure and the eastern part was by high pressure. As could be seen from (c), the entirety of mainland China lied behind the cold trough, mainly by the west airflow and a weak warm advection eastward. Due to the influence of southwest airflow, the water vapor in Beijing was increasing. In addition, on account of the existence of an inversion layer, the pollution diffusion condition became worse, and the pollutants' concentration increased slightly. Among them, the concentration of PM_{10} increased from $31 \mu\text{g}\cdot\text{m}^{-3}$ to $33 \mu\text{g}\cdot\text{m}^{-3}$, which was the main pollutant on that day. NO_2 and $\text{PM}_{2.5}$ increased to $33 \mu\text{g}\cdot\text{m}^{-3}$ and $53 \mu\text{g}\cdot\text{m}^{-3}$, respectively. AQI also increased from 36 to 73, while only O_3 decreased slightly compared with yesterday. These all indicated that the weather situation had a great impact on air quality [16].

It could be seen from the above analysis that due to the influence of the strong cold high-pressure system during the Military Parade, Beijing was in the front or lower part of the high-pressure system. Additionally, the weather situation was conducive to the diffusion of pollutants under the influence of north or northeast winds.

3.3. Comparative Analysis of Beijing's Air Quality before, during, and after the IECERM for the Military Parade

Table 2 and Figure 7 show the changes in various pollutants in the monitoring station of the Olympic Sports Center and the comparison of various pollutants before, during, and after the traffic restriction in 2013, 2014, and 2015, respectively. It can be seen that during the IECERM of the 2015 Military Parade, the concentration of $\text{PM}_{2.5}$, PM_{10} , and NO_2 , significantly decreased, among which the concentration of PM_{10} decreased the most, from $109 \mu\text{g}\cdot\text{m}^{-3}$ to $34 \mu\text{g}\cdot\text{m}^{-3}$, and the concentration of $\text{PM}_{2.5}$ decreased by 72.73%. Combined with the changes before and after the implementation, it could be seen that the concentration of PM_{10} and $\text{PM}_{2.5}$ increased after the implementation of the emission-reduction measures, indicating that enhanced control and emission-reduction measures greatly contribute to the emission reduction in particulate matter. The concentration of NO_2 decreased by 40.82% according to the comparison of during and before the implementation; however, the concentration increased by 51.67% compared to after implementation. For $\text{PM}_{2.5}$ and PM_{10} , after the implementation changed to greater than before the implementation, which may be related to a large amount pollutants' exhaust after the implementation. The concentration of O_3 had been decreasing at any implementation moment, which may be related to the current season in Beijing. In addition, the concentration of SO_2 changed little before, during, and after the implementation of the measures and remained at a low concentration level. Compared with the concentration of various pollutants in the same period of 2013 and 2014, it was found that the concentration of various pollutants in the early period of 2015 had not changed a lot, among which $\text{PM}_{2.5}$ and PM_{10} increased, while NO_2 decreased slightly. During and after the implementation of measures, except for O_3 , $\text{PM}_{2.5}$, PM_{10} , and NO_2 concentrations were lower than those in 2013 and 2014, indicating that IECREM had improved Beijing's air quality to some extent.

Table 2. Changes in pollutants in the Olympic Sports Center monitoring station.

Various Pollutants Concentration ($\mu\text{g}\cdot\text{m}^{-3}$)	Before the Implementation	During the Implementation	After the Implementation	Changes of before and during Implementation (%)	Changes in during and after Implementation (%)
$\text{PM}_{2.5}$	66	18	52	72.73	65.38
PM_{10}	109	34	80	68.81	57.5
NO_2	49	29	60	40.82	51.67
SO_2	6	2	5	66.67	60
O_3	113	79	72	30.09	−9.72

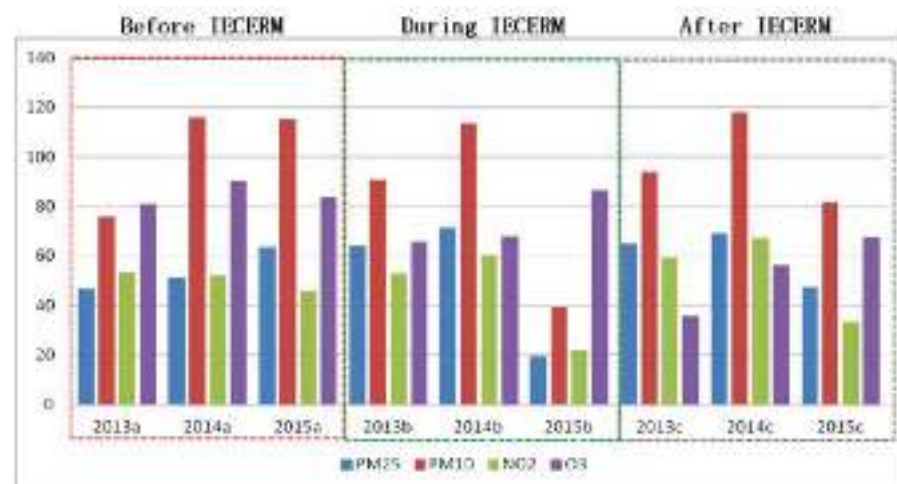


Figure 7. The change trend of pollutants over the same period when before, during, and after the IECERM from 2013 to 2015. Notes: The unit on the y-axis is $\mu\text{g}\cdot\text{m}^{-3}$.

3.4. Evolution Analysis of Air Quality during the Same Period of Military Parade from 2013 to 2015

Figure 8 shows the evolution chart of the daily mean $\text{PM}_{2.5}$ concentration in the monitoring station of the Beijing Olympic Sports Center from 2013 to 2015. It could be seen that the number of days with an average daily concentration below $150 \mu\text{g}\cdot\text{m}^{-3}$ in 2015 was less than that in 2014 and 2013. Although the average daily concentration had exceeded the standard in 2015 and even exceeded $500 \mu\text{g}\cdot\text{m}^{-3}$ in several days, most of the days were decreasing, indicating that the air quality in Beijing was improving year by year. The average daily concentration during the implementation of enhanced control and emission-reduction measures during APEC in 2014 and the 2015 Military Parade was compared with the same period in 2013, and it was found that although the average daily concentration during the 2014 APEC and 2015 Military Parade was below $100 \mu\text{g}\cdot\text{m}^{-3}$, most of the average daily concentrations during the military parade were below $50 \mu\text{g}\cdot\text{m}^{-3}$, which is significantly lower than the average daily concentration during the APEC military parade, indicating that the emission reduction effect during the military parade was better, which may be related to the weather situation at that time. In the same period as the parade in 2014 and 2013 or the same period as APEC in 2013 and 2015, the average daily concentration of the parade was more than $100 \mu\text{g}\cdot\text{m}^{-3}$, especially in the same period as APEC in 2013 and 2015. The average daily concentration on some days was more than $300 \mu\text{g}\cdot\text{m}^{-3}$. It showed that enhanced control and emission-reduction measures greatly contributed to the reduction in $\text{PM}_{2.5}$. In addition, after entering autumn and winter in 2015, the $\text{PM}_{2.5}$ concentration reached its peak, and the average daily concentration even reached $500 \mu\text{g}\cdot\text{m}^{-3}$ on some days, indicating that Beijing's air pollution sources were complex [6], and air quality assurance measures still need to be enhanced.

As can be seen from Table 3, the effective samples from 2013 to 2015 were 344, 362, and 360 days, respectively, and the three-year mean valid sample was 355 days, accounting for 97.3% in the whole year. The annual average of AQI in 2013, 2014, and the three-year period was 88.2, 90.53, and 87.49, respectively, which were all higher than 83.75 in 2015. The average AQI in 2015 during the Military Parade with the IECERM was only 19.27, far less than the average of the other two years and the three-year period. In addition, the enhanced control and emission-reduction measures were implemented during APEC in 2014; however, the annual average AQI in 2014 was higher than the annual average in 2013 and the three-year period, which may be related to the worse weather situation in 2014. The annual average AQI in the three-year period was 87.49. For the purpose of achieving the goal of GB-3095-2012 s-level standard and first-level standard, the annual average of AQI should be reduced by 60.00% and 82.46%, respectively. The average of the normal year is the average of 2013 and 2014. The average of the normal year during the Military

Parade was 64.63, which was reduced by 70.40% compared with the average AQI during the Military Parade. It had achieved the goal of GB-3095-2012 level-2 standard, which was still some distance from the level-1 standard. All these indicated that the enhanced control and emission-reduction measures had made a certain contribution to the improvement of Beijing's air quality, but to achieve the goal of better annual air quality, all parties still needed to coordinate control and joint efforts.

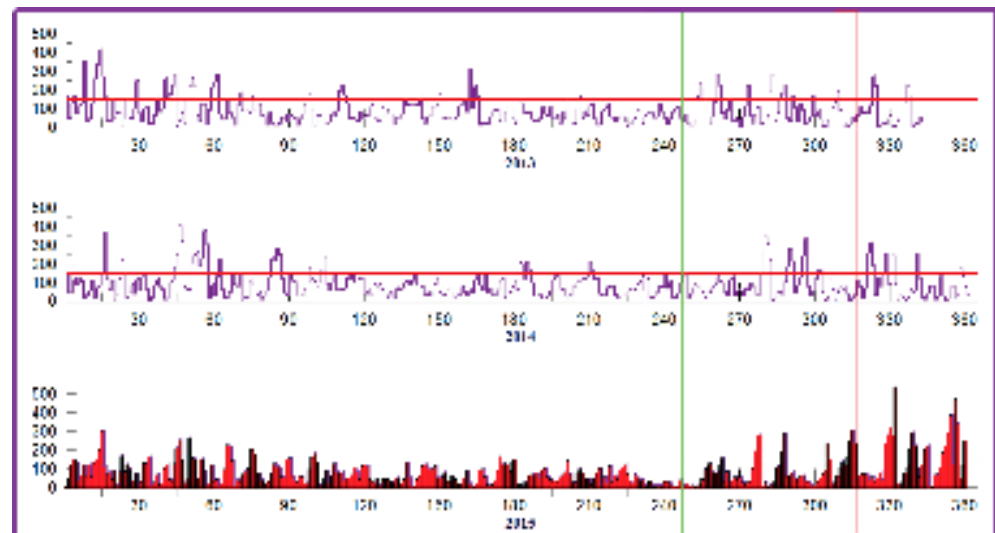


Figure 8. Daily mean value of $PM_{2.5}$ in monitoring sites of the Olympic Center from 2013 to 2015. Notes: The unit on the y -axis is $\mu g \cdot m^{-3}$. The vertical green line and red line show the comparison over the same period when the 2015 Military Parade and 2014 APEC for three years from 2013 to 2015, respectively. The transverse red line shows the concentration of $PM_{2.5}$ is $115 \mu g \cdot m^{-3}$.

Table 3. Changes in AQI over the same period from 2013 to 2015 during the Military Parade.

Data	Effective Sample	AQI Annual Average	AQI Average during the Military Parade
2013	344	88.20	58.20
2014	362	90.53	71.06
2015	360	83.75	19.27
Three-year average	355	87.49	49.51

To compare the changes in the Air Quality Index for the same period of three years during the Military Parade in Beijing, Tables 4 and 5 provide the days with their pollution level and the average value of AQI for the three years before, during, and after the IECERM, respectively, i.e., before the IECERM (5 August to 19 August), during the IECERM (20 August to 3 September), and after the IECERM (4 September to 18 September). It could be seen that the number of good days during the Military Parade in 2015 was 35 days (Table 4), accounting for 77.78% of the effective days, higher than 66.67% and 68.89% in 2013 and 2014, respectively. The number of days with mild and moderate pollution was nine days, less than fourteen and thirteen days in 2013 and 2014, respectively. There was one day of heavy pollution in 2013 and 2014 and none in 2015. According to the average value of AQI, except for mild pollution (AQI between 76 and 115), the average value of AQI in other intervals in 2015 was lower than the average value of AQI in 2013 and 2014. In addition, Table 5 showed the days' pollution levels and the average AQI for the same period in three years during the IECERM. It was found the days in 2015 were all fine which have implemented the measures, with twelve days of excellent and three days of good. In 2013 and 2014, the number of fine days without measures was 11 and 8, accounting for 73.33% and 53.33%, respectively. The results suggested that the IECERM contributes significantly to the improvement of air quality in Beijing [30].

Table 4. Changes in AQI over the same period from 2013 to 2015 before, during, and after the IECERM.

Before, during, and after IECERM AQI	2013		2014		2015	
	Effective Sample	Average	Effective Sample	Average	Effective Sample	Average
<35	11	21.19	12	23.50	23	16.20
36–75	19	56.43	19	55.79	12	48.65
76–115	9	91.88	9	91.65	6	95.78
116–150	5	128.60	4	134.86	3	124.74
151–250	1	163.73	1	157.38		

Table 5. Changes in AQI over the same period from 2013 to 2015 during the IECERM.

During IECERM AQI	2013		2014		2015	
	Effective Sample	Average	Effective Sample	Average	Effective Sample	Average
<35	4	21.54	5	21.52	12	14.78
36–75	7	53.56	3	60.60	3	37.20
76–115	3	96.64	4	94.42		
116–150	1	121.92	3	132.96		
151–250						

4. Conclusions

(1) Seven provinces and cities implemented the emission-reduction measures for air quality in a union. Emission-reduction measures, such as vehicle restrictions, enterprise suspension, production restriction, and construction site suspension, were put in place. As a result, the concentration of PM_{2.5} at 11 state-controlled air quality monitoring stations in Beijing dropped by an average of about 41 percent. Besides the average concentration of SO₂, NO₂ and PM₁₀ reached the lowest levels in the history of monitoring, which made Beijing's air quality excellent in a short time. It suggested that the enhanced emission-reduction measures had made a significant contribution to the improvement of local air quality in Beijing.

(2) During the 2015 Military Parade, Beijing was in the front or lower part of the high-pressure system. Due to the strong effect of north or northeast winds, the weather situation was conducive to the diffusion of pollutants. Before the implementation, Beijing was affected by the southwest airflow, and the adverse atmospheric diffusion conditions had caused the accumulation of pollutants in Beijing. After the implementation, owing to the adverse temperature layer, the pollution diffusion conditions were poor, and the pollutant concentration rose slightly, in which PM₁₀ was increased from 31 $\mu\text{g}\cdot\text{m}^{-3}$ increased to 33 $\mu\text{g}\cdot\text{m}^{-3}$ compared with yesterday, NO₂ and PM_{2.5} increased to 33 $\mu\text{g}\cdot\text{m}^{-3}$ and 53 $\mu\text{g}\cdot\text{m}^{-3}$, respectively. O₃ decreased, and AQI increased from 36 to 73. The air quality changed from excellent to good. Thus, it can be seen that the weather situation had a great impact on air quality.

(3) During the implementation, PM_{2.5}, PM₁₀, NO₂, and other pollutants decreased significantly, of which the concentration of PM₁₀ decreased the most, from 109 $\mu\text{g}\cdot\text{m}^{-3}$ down to 34 $\mu\text{g}\cdot\text{m}^{-3}$, and the concentration of PM_{2.5} decreased by 72.73%. According to the changes before and during the implementation and after the implementation, the concentration of PM₁₀ and PM_{2.5} increased after the implementation of the emission-reduction measures, indicating that the enhanced control measures have made a great contribution to the emission reduction in particles.

(4) The number of good days before, during, and after the Military Parade in 2015 was 35, accounting for 77.78% of the effective days, higher than 66.67% and 68.89% in 2013 and 2014. The number of days with mild pollution was 9, less than 14 and 13 days in 2013 and 2014, respectively. There was one day of heavy pollution in 2013 and 2014,

respectively. In 2015, there were no pollution days. In addition, the annual average of AQI in the three years is 87.49. In order to achieve the objectives of class II standard and class I standard in the GB-3095-2012 ambient air quality standard, the annual average AQI needed to be reduced by 60.00% and 82.46%, respectively. The average value of the normal year was the average value of 2013 and 2014. The average value of the normal year during the military parade is 64.63, which was 70.40% lower than the average value of AQI during the military parade. The goal of reaching the secondary standard of GB-3095-2012 was achieved, and there is still a long way to go from the primary standard. In a few words, the enhanced control and emission-reduction measures had made a certain contribution to the improvement of air quality in Beijing. However, in order to achieve the goal of better air quality throughout the year, all parties still need to coordinate control and make joint efforts.

Author Contributions: Conceptualization, M.C. and B.H.; formal analysis, M.D.; investigation, B.H.; resources, Q.G.; data curation, B.H. and Z.M.; writing—original draft preparation, B.H.; writing—review and editing, B.H.; funding acquisition, M.C. All authors have read and agreed to the published version of the manuscript.

Funding: This research was funded by the National Natural Science Foundation of China (grant number 21976094, 22176100) and the National Key Research and Development Project 9 (grant number 2018YFC0213802).

Institutional Review Board Statement: Not applicable.

Informed Consent Statement: Not applicable.

Data Availability Statement: Not applicable.

Acknowledgments: This study was finally accomplished with the assistance of co-authors. All diagrams in the manuscript, whether drawn by yourself or another author, are permitted. In a word, thanks to the cooperation units for their help in data collection and processing, at the same time, also express sincere thanks to the co-authors for their careful guidance in the chart description and article written.

Conflicts of Interest: The authors declare no conflict of interest.

References

1. Li, L.; Liu, Q.; Li, B. Assessment of air quality benefits from control measures during Nanjing Youth Olympic Games. *Res. Environ. Sci.* **2016**, *29*, 175–182.
2. Wang, H.; Li, Y.; Gao, J.; Wang, S.L.; Chai, F.H.; Wei, J.L. Characteristics of air pollution and evaluation of the effects of air quality assurance measures in Shijiazhuang City during the 2014 APEC Meeting. *Res. Environ. Sci.* **2016**, *29*, 164–174. [CrossRef] [PubMed]
3. Lee, B.K.; Jun, N.Y.; Lee, H.K. Analysis of impacts on urban air quality by restricting the operation of passenger vehicles during Asian Game events in BUSAN, Korea. *Atmos. Environ.* **2005**, *39*, 2323–2338. [CrossRef]
4. Beig, G.; Chate, D.M.; Ghude, S.D.; Mahajan, A.S.; Srinivas, R.; Ali, K.; Sahu, S.K.; Parkhi, N.; Surendran, D.; Trimbake, H.R. Quantifying the effect of air quality control measures during the 2010 commonwealth games at Delhi, India. *Atmos. Environ.* **2013**, *80*, 455–463. [CrossRef]
5. Liu, H.; Wang, X.; Zhang, J.; He, K.; Wu, Y.; Xu, J. Emission controls and changes in air quality in Guangzhou during the Asian Games. *Atmos. Environ.* **2013**, *76*, 81–93. [CrossRef]
6. Li, W.T.; Gao, Q.X.; Liu, J.R.; Li, L.; Gao, W.K.; Su, B.D. Comparative analysis of air quality improvement in Beijing during APEC. *Res. Environ. Sci.* **2015**, *12*, 0250–3301.
7. Zheng, J.; Zhong, L.; Wang, T.; Louie, P.K.; Li, Z. Ground-level ozone in the Pearl River Delta region: Analysis of data from a recently established regional air quality monitoring network. *Atmos. Environ.* **2010**, *44*, 814–823. [CrossRef]
8. Xu, X.D.; Zhou, X.J.; Shi, X.H. Spatial structure and scale characteristics of air pollution impacts in urban communities. *Chin. Sci. Bull. Ser. D* **2006**, *35*, 1–19.
9. Li, L.J.; Wang, Y.; Zhang, Q. Effect of wheat straw incineration on air quality in Beijing. *Chin. Sci. Bull. Ser. D* **2008**, *38*, 232–242.
10. Meng, X.Y.; Yu, Y.; Zhang, Z.F.; Li, G.; Wang, S.; Du, L. Preliminary study on the causes of frequent strong haze in January 2013 in Beijing-Tianjin-Hebei region. *Environ. Sci. Technol.* **2014**, *37*, 190–194.
11. Zheng, M.; Salmon, L.G.; Schauer, J.J.; Zeng, L.; Kiang, C.S.; Zhang, Y.; Cass, G.R. Seasonal trends in PM_{2.5} source contributions in Beijing, China. *Atmos. Environ.* **2005**, *39*, 3967–3976. [CrossRef]

12. Zhang, J.; Lu, Y.; Gui, H.; Liu, J.; Du, P.; Li, D.; Wang, J. Variations of PM_{2.5} pollution and related meteorological factors before and after the 2014 APEC conference in Beijing. *Res. Environ. Sci.* **2016**, *29*, 646–653.
13. Li, T.Y.; Deng, X.J.; Fan, S.J.; Wu, D.; Li, F.; Deng, T.; Tan, H.B.; Jiang, D.H. Analysis of air quality and pollution meteorological conditions during Guangzhou Asian Games in 2010. *Environ. Sci.* **2012**, *33*, 2932–2938.
14. Yu, Y.Y.; Xie, F.J.; Lu, X.B.; Zhu, Z.F.; Shu, Y. Analysis on the air quality and its cause of Nanjing Asian Youth Conference. *Environ. Monit.* **2014**, *6*, 5–9.
15. Chen, M.; Ma, L.M.; Wei, H.P.; Shi, H.; Ma, J.H.; Zhou, G.Q.; Gu, S.Q.; Zhang, G.L. Effects of meteorological conditions on air quality during World Expo in Shanghai. *J. Appl. Meteorol. Sci.* **2013**, *24*, 140–150. [CrossRef]
16. Zhang, X.Y.; Sun, J.Y.; Wang, Y.Q.; Li, W.J.; Zhang, Q.; Wang, W.G.; Quan, J.N.; Cao, G.L.; Wang, J.Z.; Yang, Y.Q.; et al. Reflections on the causes and control of haze in China. *Chin. Sci. Bull.* **2013**, *58*, 1178–1187.
17. Guo, X.R.; Cheng, S.Y.; Chen, D.S.; Zhou, Y.; Wang, H.Y. Estimation of economic costs of particulate air pollution from road transport in China. *Atmos. Environ.* **2010**, *44*, 3369–3377. [CrossRef]
18. Cao, W.H.; Liang, X.D.; Li, Q.C. Analysis of stage characteristics and influencing factors of a persistent haze process in Beijing. *Acta Meteorol. Sin.* **2013**, *71*, 940–951.
19. Wang, H.L.; Chen, C.H.; Huang, H.Y.; Wang, Q.; Chen, Y.R.; Huang, C.; Li, L.; Zhang, G.F.; Chen, M.H.; Lou, X.R.; et al. Study on emission intensity and pollution sources of volatile organic compounds in Shanghai during World Expo. *Environ. Sci.* **2012**, *33*, 4151–4158.
20. Wu, D.; Liao, B.T.; Wu, X.; Chen, H.Z.; Li, F.; Li, H.Y.; Ai, H. Analysis of haze Weather during Guangzhou Asian Games in 2010. *Acta Sci. Circumstantiae* **2012**, *32*, 521–527.
21. Wang, X.; Westerdahl, D.; Chen, L.C.; Wu, Y.; Hao, J.; Pan, X.; Guo, X.; Zhang, K.M. Evaluating the air quality impacts of the 2008 Beijing Olympic Games: On-road emission factors and black carbon profiles. *Atmos. Environ.* **2009**, *43*, 4535–4543. [CrossRef]
22. Wang, Y.; Hao, J.; McElroy, M.B.; Munger, J.W.; Ma, H.; Chen, D.; Nielsen, C.P. Air quality during the 2008 Beijing Olympics: Effectiveness of emission restrictions. *Atmos. Chem. Phys.* **2009**, *9*, 5237–5251. [CrossRef]
23. Wang, W.; Wang, Y.; Wang, L.; Zhu, B.; Wang, Y. Observation and Study on the air quality at the Olympic Village Station during the Beijing Olympic Games. *Res. Environ. Sci.* **2010**, *23*, 48–54.
24. Hu, J.; Cheng, S.Y.; Su, F.Q. Evolution Characteristics and Causes of PM₁₀ Mass Concentration in Beijing During the Olympic Games and Paralympic Games Period. *Res. Environ. Sci.* **2009**, *22*, 1395–1402.
25. Querol, X.; Alastuey, A.; Ruiz, C.R.; Artiñano, B.; Hansson, H.C.; Harrison, R.M.; Buringh, E.T.; Ten Brink, H.M.; Lutz, M.; Bruckmann, P.; et al. Speciation and origin of PM₁₀ and PM_{2.5} in selected European cities. *Atmos. Environ.* **2004**, *38*, 6547–6555. [CrossRef]
26. Wu, Q.M.; Zhang, S.J. Analysis of pollution influence factors in a haze weather process. *J. Meteorol. Environ.* **2010**, *33*, 12–16.
27. Li, J.; Wang, Z.; Zhuang, G.; Luo, G.; Sun, Y.; Wang, Q. Mixing of Asian mineral dust with anthropogenic pollutants over East Asia: A model case study of a super-dust storm in March 2010. *Atmos. Chem. Phys.* **2012**, *12*, 7591–7607. [CrossRef]
28. Yu, H.; Wang, P.C.; Zong, X.M.; Li, X.; Lv, D.R. Satellite monitoring of NO₂ column concentration in Beijing during the Olympic Games. *Chin. Sci. Bull.* **2009**, *54*, 299–304.
29. Cheng, N.L.; Zhang, D.W.; Li, Y.T.; Chen, T.; Sun, F.; Li, L.; Cheng, B. Characteristics of NO_x concentration in Beijing during Athletics Championships and Military Parade in 2015. *J. Univ. Chin. Acad. Sci.* **2016**, *6*, 2095–6134.
30. Wang, W.; Li, J.; Zhu, L.L. *Simulation Analysis of Pollutant Emission Reduction Contribution in Beijing-Tianjin-Hebei Region and Surrounding Areas during the Military Parade on Sep 3th*; Springer Science & Business Media: Berlin/Heidelberg, Germany, 2008.

Article

Can the Coal-to-Gas/Electricity Policy Improve Air Quality in the Beijing–Tianjin–Hebei Region?—Empirical Analysis Based on the PSM-DID

Jingran Zhang ¹, Wukui Wang ^{1,*}, Lei Gao ^{2,*}, Zhenzhu Deng ¹ and Yu Tian ³

¹ School of Economics and Management, Beijing Forestry University, Beijing 100083, China; zjrky@126.com or zjrky@bjfu.edu.cn (J.Z.); dzz_911117@bjfu.edu.cn (Z.D.)

² School of Economics and Management, Yanshan University, Qinhuangdao 066004, China

³ Institute of Ancient Books, Jilin University, Changchun 130012, China; yutian19@mails.jlu.edu.cn

* Correspondence: wangwukui@bjfu.edu.cn (W.W.); gkbmaster@yeah.net or gaolei@ysu.edu.cn (L.G.)

Abstract: Air pollution caused by coal burning not only increases the cost of environmental pollution but also harms human health. It is urgent for China to change the practice of coal-fired central heating. Therefore, the effectiveness and sustainability of the Coal to Gas and Electricity policy have become the focus of all sectors of society. In this paper, eight cities in the Beijing–Tianjin–Hebei region were taken as the experimental groups and the other eleven cities as the control groups. Based on the PSM-DID model and the time-varying DID model, a quasi-natural experimental analysis was conducted to evaluate the effect of the policy of coal to gas and electricity to improve air quality in the Beijing–Tianjin–Hebei region from 2015 to 2020 and to test the sustainability of the policy. Three research conclusions are shown below: First, during the implementation of the policy, especially in 2019, the AQI index decreased significantly. Although there was a rebound thereafter, it was still lower than before. This shows that the Coal to Gas and Electricity policy has indeed improved the air quality in Beijing, Tianjin, and Hebei during its implementation. Second, the policy had a great impact on SO₂ and PM₁₀ but was relatively weak on PM_{2.5} and CO. Therefore, there is an urgent need to formulate scientific and accurate policies to control different air pollutants. Third, the time-varying DID model was used to identify the dynamic sustainability effect of the Coal to Gas and Electricity policy. The results showed that the policy had a strong impact in the initial stage, but its effect was greatly reduced at the end of the implementation or near the end, when it was far less obvious than in the initial stage of the policy. Therefore, in formulating relevant measures to reduce air pollution, it is necessary to fully consider the sustainability of the policy.

Keywords: coal-to-gas/electricity; air quality; PSM-DID model; Beijing–Tianjin–Hebei

Citation: Zhang, J.; Wang, W.; Gao, L.; Deng, Z.; Tian, Y. Can the Coal-to-Gas/Electricity Policy Improve Air Quality in the Beijing–Tianjin–Hebei Region?—Empirical Analysis Based on the PSM-DID. *Atmosphere* **2022**, *13*, 879. <https://doi.org/10.3390/atmos13060879>

Academic Editors: Duanyang Liu, Kai Qin and Honglei Wang

Received: 28 April 2022

Accepted: 27 May 2022

Published: 28 May 2022

Publisher’s Note: MDPI stays neutral with regard to jurisdictional claims in published maps and institutional affiliations.



Copyright: © 2022 by the authors. Licensee MDPI, Basel, Switzerland. This article is an open access article distributed under the terms and conditions of the Creative Commons Attribution (CC BY) license (<https://creativecommons.org/licenses/by/4.0/>).

1. Introduction

As the largest developing country in the world, China is facing great pressure from the international community to reduce emissions [1]. Coal, as a high-carbon energy source, has been burned in China for thousands of years. The burning of coal for heating has led to a significant increase in the TSP (Total Suspended Particle) level in northern China [2], and it is also the main cause of frequent respiratory diseases and skin diseases for urban residents in recent years [3]. Consequently, to improve air quality and show a pragmatic image to the international community, China has formally put forward the “dual-carbon” strategic goal of a “carbon peak in 2030 and carbon neutrality in 2060” [4–7]. Moving from coal to gas and electricity is the main way to reduce coal use and improve air quality in winter [8]. In this way, the effectiveness of the Coal to Gas and Electricity policy, promoted by the state through financial subsidies, especially to Beijing, Tianjin, and Hebei as important cities in northern China, has become the focus of society.

The prevention and control of air pollution have become China's top priority [9], and its governance policies and effects have triggered academic discussions. Research shows burning coal accelerates air deterioration [10,11]. In particular, the emission of air pollutants caused by coal-fired heating in winter is more harmful to air quality and human health than industrial sources with the same emissions [12,13]. Against the background of carbon peak and carbon neutralization, it is urgent to change the practice of coal-fired central heating. Therefore, the state promotes the Coal to Gas and Electricity policy through financial subsidies. At present, academic research on this issue is rare [14]. Li et al. studied the changes in air quality, energy efficiency, and residents' energy consumption before and after the implementation of the Coal to Gas and Electricity policy, based on the panel data of 41 cities in China from 2003 to 2015 [15]. Shi et al. studied the green coordinated development effect of the policy of coal to gas and electricity in Beijing, Tianjin, and Hebei [16]. Liu et al. analyzed the typical problems in the construction of the coal to gas project in Beijing and put forward relevant policy suggestions [17]. Yu et al. evaluated the green net benefit of the coal to gas project in Beijing, Tianjin, and Hebei, and considered that the coal to gas policy could improve green comprehensive efficiency by 0.3%–0.4% [18]. However, some scholars believe that the policies of coal to gas and electricity and "clean coal substitution" increase residents' heating costs [19]. Scholars mainly discuss air pollution control, green development, and the cost subsidies of the Coal to Gas and Electricity policy and rarely use more micro and refined data to analyze the air pollution control effect of the policy. Further research shows that the frequency of severe pollution weather in northern China coincides with the concentration of coal-fired heating in winter [20,21]. China's unique coal-fired heating measures in the north in winter have led to more prominent air pollution problems in northern China than in the south [22]. The air pollution problem of the Beijing–Tianjin–Hebei urban agglomeration in the northern region is particularly serious [23]. Early research found that although Beijing, Tianjin, Hebei, and the surrounding areas account for only 7.2% of the national land area, they consume 33% of the national coal, and the pollutant emission intensity per unit area is about four times the national average [24]. However, the research conclusions on the relationship between the air control effect and pollutant emissions in Beijing, Tianjin, and Hebei are not completely consistent. Some scholars found that environmental regulations can significantly reduce PM_{2.5} and SO₂ concentrations [25]. Based on ecological environmental monitoring and meteorological observation data, Zhu Yuan-yuan et al. analyzed the characteristics of ozone concentrations in the major cities in the Beijing–Tianjin–Hebei region from 2016 to 2020 and found that ozone concentrations in the region increased by 11.6%, showed an overall trend of fluctuation during 2016 to 2019, and then decreased in 2020 [26]. In addition, few studies can clearly point out the clear relationship between the air quality index and specific pollutants in Beijing, Tianjin, and Hebei. Therefore, it is of great significance to use weekly micro panel data to test the effectiveness of the Coal to Gas and Electricity policy in the Beijing–Tianjin–Hebei region and to explore the specific impact of the policy on specific pollutants.

From the urban perspective, a regional joint prevention and control strategy must be adopted for air pollution control to avoid the "leakage effect" and "free-riding behavior" of air pollution control [27]. However, because of the limitations of research data and research methods, it is difficult to determine the dynamic and sustainable effects of air pollution control policies in urban agglomerations [28]. In addition, only a few articles use the policy evaluation method in econometrics [29], and the conclusions are inconsistent. Duwencui et al., using the Single DID method, found that the coordinated control of haze in Beijing, Tianjin, and Hebei had not improved the air quality in this area [30]. Wayi et al. found that the joint action of "2 + 26" cities in Beijing, Tianjin, Hebei and surrounding areas under the guidance of the action plan for comprehensive treatment of air pollution in autumn and winter helped improve the air quality in the region [31]. The Coal to Gas and Electricity policy in Beijing, Tianjin, Hebei, and surrounding areas has an obvious process from pilot to promotion, and the time and intensity of joint prevention and control

in different cities are not completely consistent [29]. Therefore, the estimation results using a single DID model are likely to include errors, resulting in unsolvable endogeneity problems [32]. Using the DID method, the most important premise is that the processing group and control group must meet the common trend assumption, that is, if there were no Coal to Gas and Electricity policy, there would be no systematic difference in the change in the trend of air quality between Beijing, Tianjin and Hebei and other regions over time. But in reality, this assumption of the DID method may not be satisfied. However, the PSM-DID method proposed and developed by Heckman et al. could effectively solve this problem and make the DID method meet the common trend hypothesis [33,34]. In addition, the time-varying DID model can capture the dynamic changes of the policy to measure the effect of the joint prevention and control policy of coal to gas and electricity in Beijing, Tianjin, and Hebei more accurately. Therefore, it is not only necessary to expand the sample number of the Beijing Tianjin Hebei urban agglomeration to improve the integrity of the impact of the Coal to Gas and Electricity policy on air quality, but it is also necessary to adopt the PSM-DID model and the time-varying DID model to evaluate the effectiveness and dynamics of policy implementation.

The purpose of this study is to test the impact of the Coal to Gas and Electricity policy on air quality in Beijing, Tianjin, and Hebei and find possible measures for improvement. Therefore, based on the weekly air quality and meteorological data of nineteen cities in Beijing, Tianjin, Hebei, and surrounding areas from 2015 to 2020, we used the PSM-DID method to evaluate the effectiveness and dynamics of the Coal to Gas and Electricity policy on air quality improvement. This article provides some important insights: First, this study adopts the method of propensity score matching (PSM) for the first time, and “wind speed” and “temperature” were finally obtained as characteristic variables from 6042 original atmospheric data of nine experimental groups and eleven control groups, which overcomes the endogenous problem between explanatory variables. Second, taking the implementation of coal to gas and electricity as a quasi-experiment, differences-in-differences (DID) was used to identify the impact of the policy on air quality and PM_{2.5}, PM₁₀, SO₂, and CO. The results show that the Coal to Gas and Electricity policy has indeed improved the air quality in Beijing, Tianjin, and Hebei during the implementation period. The policy had a great impact on SO₂ and PM₁₀, while the effects on PM_{2.5} and CO were relatively weak. Third, the time-varying DID model was used to identify the dynamic sustainability effect of the Coal to Gas and Electricity policy. It proves that the policy has a strong impact in the initial stage. However, at the end of the implementation or near the end, the effect is greatly reduced, and it is far less obvious than at the beginning of the policy. These results held true after several robustness tests. The above conclusions based on the evaluation of the Coal to Gas and Electricity policy in Beijing, Tianjin, and Hebei may provide relevant references and lessons for air governance in other countries.

The rest of the study presents the data and methodology (Section 2), empirical results (Section 3), and robust tests (Section 4). Finally, we draw three conclusions (Section 5).

2. Data and Methodology

2.1. Data and Variables

The air quality index (AQI) and the concentration of individual pollutants are the air quality indicators that are most widely consulted by the public and highly valued by the national ecological and environmental department. Among them, the AQI is a dimensionless comprehensive index, which is obtained by standardizing the concentration index of each single pollutant, allowing it to be a comprehensive reflection of the daily air quality of the city. The value range is 0–500, and according to the size of the AQI, we divide urban air quality into six levels. The larger the value, the more serious the air pollution [35–37]. In addition, the assessment method of the action plan for air pollution prevention and control clearly points out that the annual average concentration decline ratios of PM_{2.5} and PM₁₀ are used as the assessment index [38]. As one of the important indicators to measure whether SO₂ and CO are polluted in the atmosphere. Therefore, this

paper selects the daily data of the AQI, PM_{2.5}, PM₁₀, SO₂, and CO in Beijing, Tianjin, Hebei and surrounding areas from 2015 to 2020. According to the weighted average calculation, the weekly data were obtained for regression analysis. Relevant data comes from China's air quality online monitoring and analysis platform (<https://www.AQIstudy.cn>, accessed on 15 February 2022).

Research shows that weather conditions can have a significant impact on air quality [39,40]. Therefore, to ensure the accuracy of the study, the control variables selected in this paper include daily average temperature, daily average humidity, and wind level. The weekly data is calculated according to the weighted average of daily average data. Relevant data comes from China's air quality online monitoring and analysis platform (<https://www.AQIstudy.cn>, accessed on 15 February 2022).

2.2. Methodology

The Propensity Score Matching (PSM) and Difference-in-Difference model (DID) method are used to evaluate the effect of policy implementation. The PSM is particularly suitable for studies using non-random data. Computing the average processing effect of the treatment group samples through the common support hypothesis test and balance hypothesis test can obtain basic unbiased estimates, thus obtaining a natural experiment under the condition of using non-random data. The influence of selective bias and confounding factors in the performance evaluation process can be excluded as far as possible by the PSM method, ensuring that the final estimated performance results are an unbiased "net effect". The PSM can solve the problem of sample selection bias, but cannot avoid the endogenous problem caused by variable omission; The DID can solve the endogenous problem through double difference, but cannot solve the problem of sample selection deviation well. Based on this, this paper combines PSM and DID for robustness estimation. At present, there are few articles using the policy evaluation method in econometrics [29]; moreover, even if a single DID model is used, the estimation results are likely to be biased, resulting in endogenous problems that cannot be reasonably solved [32]. Using the DID method, the most important premise is that the processing group and control group must meet the common trend assumption; that is, if there is no Coal to Gas and Electricity policy, there is no systematic difference in the changing trend of air quality between the Beijing–Tianjin–Hebei region and other regions over time. But in reality, this assumption of the DID method may not be satisfied. However, the PSM-DID method that has been proposed and developed can effectively solve this problem [33,34]. In addition, the time-varying DID model can capture the dynamic changes of the policy to measure the effect of the joint prevention and control policy of coal to gas and electricity in Beijing, Tianjin, and Hebei more accurately. Therefore, this study first takes *group* as the grouping variable, speed and temp among the control variables as the characteristic variables, and AQI as the output variable for PSM matching, which solves the problems of deviation and endogeneity between variables. Second, to avoid the problem of multicollinearity, we selected eight cities in the Tianjin Hebei region as the experimental group by using the atmospheric data from 2015 to 2020, and chose another eleven cities with similar geographical locations, similar air pollution, or similar population and economic levels as the control group, using the DID model to identify the effectiveness of the Coal to Gas and Electricity policy in the Beijing–Tianjin–Hebei region. Finally, the time-varying DID model is used to evaluate the effectiveness and dynamics of policy implementation.

2.2.1. Model Construction

This paper first uses the DID model to evaluate the effect of the Coal to Gas and Electricity policy on air pollution control in the Beijing–Tianjin–Hebei region and surrounding areas. The model is as follows:

$$Y_{ct} = \beta_0 + \beta_1 \text{Group}_c \times \text{Policy}_t + \delta X_{ct} + \epsilon_{ct} \quad (1)$$

where Y_{ct} represents the air quality index and single pollutant concentration of city C on date T, and $Group_c$ indicates whether city C is in the experimental group or the control group. If it is the experimental group, the value is 1; otherwise, the value is 0. The dummy variable $Policy_t$ indicates whether the policy is executed. Policy implementation is 0 before implementation and 1 after implementation. The variable $Policy_t$ indicates the change of the air quality of the experimental group after the policy implementation, and the coefficient β_1 can be used to measure the effect of the air pollution prevention and control policy. The control variable X_{ct} indicates other factors affecting air quality, including weather conditions (daily average temperature-*temp*, average daily humidity-*humidity*, and wind level-*speed*). The random perturbation term is represented by ϵ_{ct} .

Although there were reports of “the Coal to Gas and Electricity policy” from 2003 to 2016, the frequency was relatively low. On 5 December 2017, the National Development and Reform Commission and other departments jointly issued the Plan for Clean Heating in Winter in Northern China (2017–2021), proposing for the first time to build a complete clean heating industry system in northern China within 3 to 5 years. According to the evolution time of the policy of coal to gas and electricity and considering the applicability of the model, we defined the period before the implementation of the policy as January 2015–31 December 2017 and the period after the implementation of the policy as January 2018–31 December 2020. The policy involved in this study is mainly concerned with heating. The value is 0 before the policy is implemented and 1 after the policy is implemented. We used weekly data, so the specific implementation date was 1 in the second week of 2018, and 0 in the previous week.

Based on similar geographical location, air pollution, level of economic development, and permanent population, the following choices were made. The experimental group included eight cities in the Beijing–Tianjin–Hebei area: Beijing, Tianjin, Shijiazhuang, Tangshan, Langfang, Baoding, Qinhuangdao, and Zhangjiakou. The control group contained eleven cities: Taiyuan, Yangquan, Changzhi, Jinan, Jining, Hohhot, Baotou, Zhengzhou, Jincheng, Datong, Kaifeng. When the time interaction between a certain city in the experimental group and the policy implementation was equal to 1, it meant that the city was incorporated into the Coal to Gas and Electricity policy at that time point. Before that time point, the interaction term was 0. The geographical location map is shown below (Figure 1).

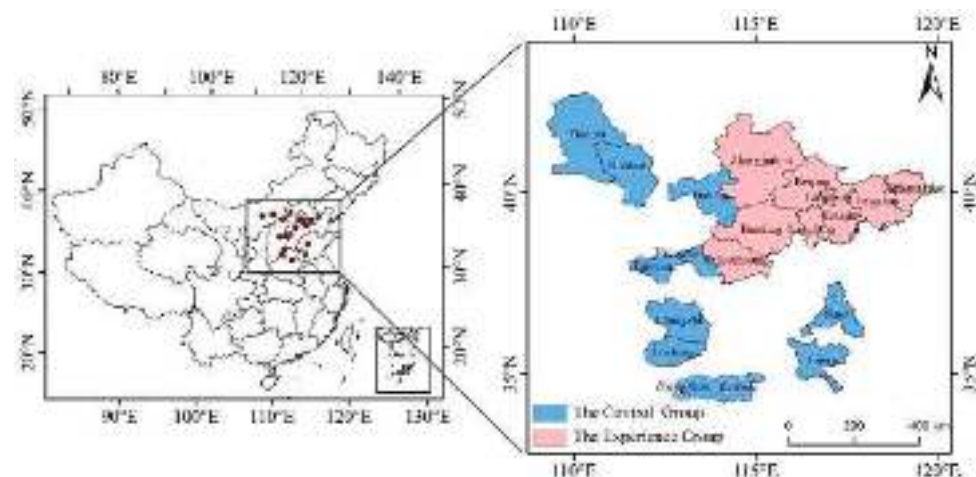


Figure 1. The geographical location map.

2.2.2. Descriptive Statistics

The sample size shown in the following table is the sample size after PSM treatment, and the original sample size is 6042, and the sample size after PSM treatment is 4063, which will be mentioned in the subsequent PSM analysis. From the value range of variables, the value range of each variable is within a reasonable range, and the outlier is not obvious. See Table 1.

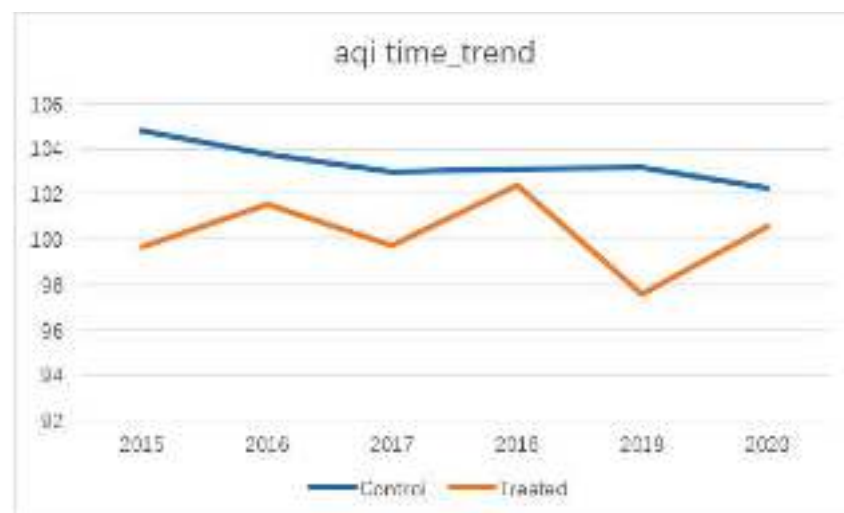
Table 1. Description of variables and data.

Variable	Units Value	Meaning	N	Mean	Median	SD	Max	Min
AQI	-	Air Quality Index	4063	99.8	91.7	41.3	500	0
PM _{2.5}	ug/m ³	fine particulate matter	4063	64.2	53.1	42.4	496	0
PM ₁₀	ug/m ³	Inhalable particles	4063	114	101	60.5	740	0
CO	mg/m ³	carbon monoxide	4063	1.39	1.17	0.751	9.72	0.267
SO ₂	ug/m ³	Sulfur dioxide	4063	25.7	17.9	25.8	328	2
temp	°C	Daily mean temperature	4063	12.2	13.1	10.9	32.1	−19.5
speed	-	Wind scale	4063	1.85	1.74	0.524	4.61	0.726
Humidity	%	Daily mean humidity	4063	55.9	55.9	15.6	99.5	15

3. Result

3.1. Basic Result Analysis

We take the AQI as an example to make the trend change map of environmental indicators (Figure 2). In the long term, the control group has a slight downward trend, but the trend is relatively limited. The experimental group was affected by the policy, so the change range is large, especially in the second year affected by the policy; in 2019, the AQI had a significant decline, reflecting the impact effect of the policy. Despite the subsequent rebound, it was still lower than the 2018 level and also significantly lower than the control sample level of that year.

**Figure 2.** The AQI time-trend.

If the time range is set from 2017–2019, one year before and after the policy occurred, the results of Table 2 are as follows. There was a significant downward trend before the policy, in which the average value of the experimental group was −1.659 and the average value of the control group was 0.820. The range of decline in the experimental group was significantly greater than that of the control group, reaching twice that of the control group, reflecting the impact of the policy implementation.

For the specific impact of policy implementation on the four dependent variables, we used an independent sample *t*-test method. The *t*-test tests whether the variable is significant over all periods. The first was for the whole sample, including the experimental and control groups. From the results of the *t*-test (Table 3), the *p*-value of the four indicators was less than 0.05, and the sample with a group value of 1 after implementation was less than the sample before implementation, which shows that the policy implementation reduced the index value and had significant differences. Secondly, a further *t*-test was performed for the samples from the experimental group (Table 4). For the experimental group samples, the conclusion did not differ from the overall sample, and the samples

after the implementation decreased significantly compared with the samples before the implementation. Moreover, it was more obvious in the first two indicators, with $PM_{2.5}$ decreasing by 11.37 and 14.9 in the experimental group. In the PM_{10} index, the overall sample decreased by 36.44, and the experimental group sample decreased by 41.57. Therefore, the impact of the policy is obvious and significant.

Table 2. The change values of different cities before and after the policies.

City Code	Before	After	Dif
Beijing	107.587	93.402	−14.185
Tianjin	103.593	94.576	−9.017
Shijiazhuang	93.451	98.129	4.678
Tangshan	89.550	96.898	7.348
Langfang	110.230	99.662	−10.568
Baoding	100.368	97.475	−2.893
Qinghuangdao	102.485	107.996	5.511
Zhangjiakou	90.141	96.010	5.869
Taiyuan	101.916	103.289	1.373
Yangquan	116.549	102.741	−13.808
Changzhi	92.112	92.470	0.358
Jinan	103.276	108.419	5.143
Jining	112.995	96.981	−16.014
Huohhot	98.294	100.779	2.485
Baotou	85.334	90.744	5.410
Zhengzhou	107.607	117.145	9.538
Jincheng	106.470	102.405	−4.065
Datong	108.864	102.405	−4.306
Kaifeng	101.924	106.789	4.865

Table 3. *T*-test results for the whole sample.

Variables	Post	Mean \pm sd	T	Sig
$PM_{2.5}$	0	69.63 \pm 47.47	8.70	0.00
	1	58.26 \pm 35.32		
PM_{10}	0	131.38 \pm 68.46	20.45	0.00
	1	94.94 \pm 43.17		
CO	0	1.48 \pm 0.87	8.04	0.00
	1	1.29 \pm 0.58		
SO ₂	0	35.52 \pm 31.46	28.20	0.00
	1	15.21 \pm 9.91		

Table 4. *T* test results of the experimental group.

Variables	Post	Mean \pm sd	T	Sig
$PM_{2.5}$	0	75.88 \pm 52.72	8.09	0.00
	1	60.98 \pm 36.40		
PM_{10}	0	140.31 \pm 76.33	16.23	0.00
	1	98.74 \pm 46.34		
CO	0	1.55 \pm 1.01	6.45	0.00
	1	1.33 \pm 0.63		
SO ₂	0	29.23 \pm 23.08	22.27	0.00
	1	13.64 \pm 8.53		

3.2. PSM Model Results

The role of PSM is to reduce endogeneity problems and reduce the bias between samples. Here we take group as the grouping variable, *speed* and *temp* among the control variables as the characteristic variables, and AQI as the output variable for PSM processing (Table 5).

Table 5. Changes in the sample size before and after PSM.

	Before	After
Control	3498	1683
Treated	2544	2380
Total	6042	4063

One might ask, why is the humidity variable not included? The first reason is that the two grouped samples were so close in *humidity* that the bias itself could be considered small. The second reason was that, after our attempt to add the variable of *humidity*, we found that the bias between samples did not shrink but increased, so joining became meaningless. From the PSM results (Table 6), we used variables *speed* and *temp* as conditions for sample matching, and after the last matching samples, the bias was reduced by 31.8% and 90.5%, respectively, which was successful and effective from the purpose perspective.

Table 6. PSM model result.

Unmatched		Mean		Reduce (%)		T-test	
Variables	Matched	Treated	Control	Bias (%)	bias	T	$p > t$
Speed	U	1.7478	1.9316	−34.3	−13.19	0	0
	M	1.7976	1.923	−23.4	31.8	−7.53	
Temp	U	12.438	11.696	6.7	2.59	0.01	0.84
	M	12.127	12.197	−0.6	90.5	−0.2	

3.3. DID Model Baseline Analysis

The analysis of the DID model was mainly carried out by observing the influence of DID variables. To avoid multicollinearity problems, the grouping variable group and the policy implementation variable post were not used here. We used four models constructed with different dependent variables, and the fit effect of the model was at the normal level, except for Model 2, in which the R^2 was around 0.2 to 0.3. In terms of variable action, the control variables we selected had obvious effects on the dependent variables, in which the variable *temp* and the variable *speed* had stable negative effects—that is, the higher temperature, the faster the speed, and the better the air quality. However, the action mechanism of the variable *humidity* was relatively complex, with significant positive effects on $PM_{2.5}$ and CO , but with negative effects on PM_{10} and SO_2 . However, our core variable DID had significant negative effects in all four models; that is, the implementation of the policy improved the ambient air quality. Considering that the range of values of different indicators varies, it is normal that the coefficient size varies greatly, and it is more meaningful for us to compare the significance of the variables. From the significance level, the policy affected SO_2 and PM_{10} greatly, while the effects on $PM_{2.5}$ and CO were relatively weak. The results are shown in Table 7.

Table 7. DID model result.

	Model 1	Model 2	Model 3	Model 4
Variables	$PM_{2.5}$	PM_{10}	CO	SO_2
DiD	−5.269 *** (−4.03)	−23.602 *** (−11.94)	−0.071 *** (−3.22)	−17.516 *** (−22.45)
Temp	−1.633 *** (−28.83)	−1.691 *** (−19.74)	−0.036 *** (−37.86)	−0.984 *** (−29.11)
Humidity	0.483 *** (11.39)	−0.003 (−0.05)	0.012 *** (17.20)	−0.034 (−1.36)
Speed	−16.369 *** (−13.51)	−18.880 *** (−10.30)	−0.165 *** (−8.06)	−3.069 *** (−4.24)

Table 7. Cont.

	Model 1	Model 2	Model 3	Model 4
Variables	PM _{2.5}	PM ₁₀	CO	SO ₂
Constant	88.748 *** (23.39)	176.039 *** (30.67)	1.462 *** (22.77)	50.181 *** (22.15)
Observations	4063	4063	4063	4063
R ²	0.249	0.154	0.313	0.274
Adj-R ²	0.248	0.153	0.312	0.273
F	336.2	184.7	462.5	382.0

t-statistics in parentheses. *** $p < 0.01$, ** $p < 0.05$, * $p < 0.1$.

4. Robust Test

4.1. Parallel Trend Test

The hypothesis of parallel trends is that there was no significant difference between the control and experimental groups before the policy occurred. After the policy implementation, there were significant differences between the experimental group and the control group. We here constructed the dummy variables using the dates of the first three events and tested them. Because the previous period is too close to the policy, the results of the previous three and two periods prevailed, namely the before_3 and before_2 variables in our results. From the results (Table 8), the before_3 variable had a nonsignificant negative effect in all four models, while the direction of before_2 was positive and negative, but overall, the effect was not significant, so the four dependent variables passed the parallel trend test. From the trend of change (Figure 3), there was indeed a downward trend from before_1 to after 2, which also proves the effectiveness of the policy.

Table 8. Parallel trend test results.

	Model 1	Model 2	Model 3	Model 4
Variables	PM _{2.5}	PM ₁₀	CO	SO ₂
Did	−4.298 *** (−2.89)	−20.756 *** (−9.91)	−0.076 *** (−2.88)	−16.710 *** (−19.33)
Before-3	−12.474 (−1.02)	−24.011 (−1.39)	−0.105 (−0.48)	−6.370 (−0.89)
Before-2	−4.456 (−0.43)	−1.074 (−0.07)	0.161 (0.88)	7.242 (1.21)
Before-1	34.451 *** (3.24)	51.803 *** (3.46)	0.692 *** (3.68)	9.154 (1.48)
Constant	65.277 *** (82.81)	119.494 *** (107.57)	1.404 *** (100.68)	30.346 *** (66.16)
Observations	4063	4063	4063	4063
R ²	0.005	0.027	0.006	0.086
Adj-R ²	0.00408	0.0265	0.00487	0.0853
F	5.159	28.59	5.967	95.67

t-statistics in parentheses. *** $p < 0.01$, ** $p < 0.05$, * $p < 0.1$.

4.2. Placebo Test

The idea for the placebo test in this study was to advance the policy implementation date by one year, until 1 January 2017, and to re-run the DID model (These four models are the did models constructed with the four indicators of PM_{2.5}, PM₁₀, CO and SO₂ as the dependent variables.). Based on the results, the effect of DID was no longer significant in the PM_{2.5} and CO models. However, PM₁₀ still has a significant negative effect in SO₂, which is not much different from the original model (Table 9). This indicates that the two measures of PM_{2.5} and CO passed the placebo test, while PM₁₀ and SO₂ failed the placebo test, but does not mean that the policy has no effect on the latter two. In previous analyses, namely in parallel trend tests and DID models, we concluded that policy does

have a significant impact on environmental indicators. Combined with the analysis results of the trend chart part, we can believe that the ambient air index itself has a downward trend, which is not caused by a separate policy, but the result of a series of relevant policies and institutional provisions. The policy of this study has a relatively more obvious effect on PM_{2.5} and CO, while accelerating and promoting the effect on PM₁₀ and SO₂, that is, accelerating the existing downward trend.

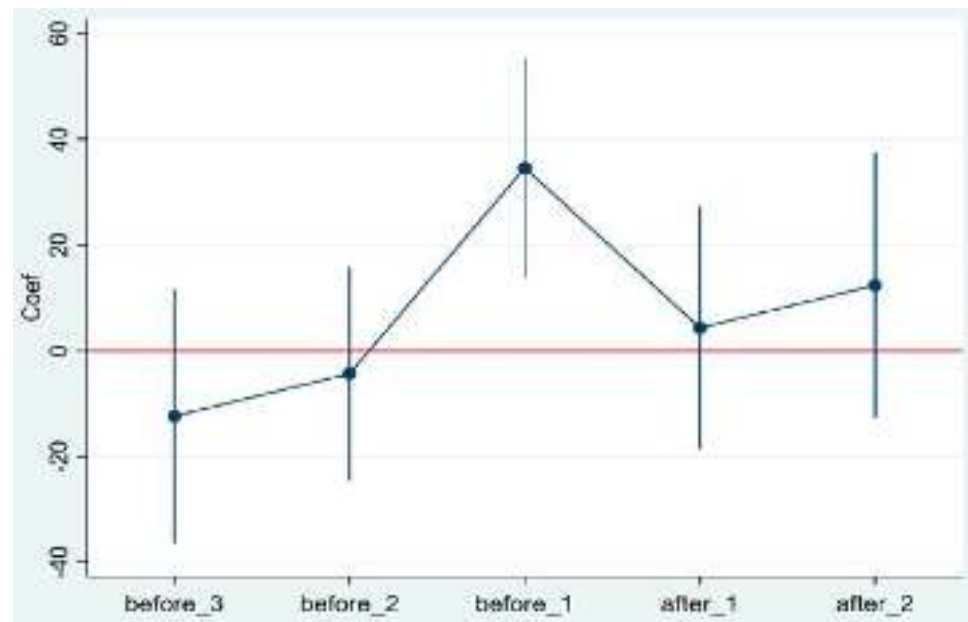


Figure 3. Coefficient trend change.

Table 9. Placebo test results.

	Model 1	Model 2	Model 3	Model 4
Variables	PM _{2.5}	PM ₁₀	CO	SO ₂
Did	−0.251 (−0.21)	−11.256 *** (−6.16)	0.004 (0.17)	−15.704 *** (−21.98)
Temp	−1.643 *** (−28.97)	−1.720 *** (−19.84)	−0.036 *** (−37.99)	−0.994 *** (−29.35)
Humidity	0.506 *** (11.94)	0.061 (0.94)	0.013 *** (17.71)	−0.015 (−0.59)
Speed	−15.677 *** (−13.04)	−18.880 *** (−8.81)	−0.165 *** (−7.65)	−3.069 *** (−1.93)
Constant	84.953 *** (22.63)	165.635 *** (28.86)	1.406 *** (22.15)	47.243 *** (21.07)
Observations	4063	4063	4063	4063
R ²	0.246	0.132	0.311	0.270
Adj-R ²	0.245	0.132	0.311	0.270
F	330.8	154.8	458.8	375.7

t-statistics in parentheses. *** $p < 0.01$, ** $p < 0.05$, * $p < 0.1$.

4.3. Dynamic Effect of the Coal to Gas and Electricity Policy

For the test of dynamic effect, the main design ideas refer to Zhu et al. [29]. The biggest difference is the different data dimensions. This study by Zhu et al. used daily data as the analysis data, while our study used weekly data as the main data. Autumn and winter were also used by Zhu et al. [29]. as the policy implementation cycle, specifically from the fortieth week to the tenth week of the second year. That model is different from the DID model of our subject. The Zhu et al. subject model belongs to the time-invariant DID model, while our model belongs to the time-varying DID model, that is, DID in which the individual's

policy implementation status will change within a year. In terms of test methods, the *DID* variable and dummy variable forms were also used. As shown in Table 10, the *week1*, and *week2* variables represent the first two weeks, and the *week3* and *week4* variables represent the last two weeks.

Table 10. Dynamic test result.

	Model 1	Model 2	Model 3	Model 4
Variables	PM _{2.5}	PM ₁₀	CO	SO ₂
Did2	−0.045 (−0.04)	−10.595 *** (−5.77)	0.013 (0.63)	−15.401 *** (−21.48)
Week1	−20.030 *** (−3.97)	−24.934 *** (−3.23)	−0.292 *** (−3.41)	−6.260 ** (−2.07)
Week2	−8.819 *** (−3.22)	−12.737 *** (−3.04)	−0.184 *** (−3.97)	−4.066 ** (−2.48)
Week3	9.737 * (1.83)	−5.190 (−0.64)	−0.092 (−1.02)	−7.291 ** (−2.29)
Week4	1.185 (0.46)	−4.250 (−1.08)	−0.058 (−1.32)	−2.635 * (−1.71)
Temp	−1.622 *** (−28.49)	−1.718 *** (−19.72)	−0.036 *** (−37.86)	−1.001 *** (−29.42)
Humidity	0.512 *** (12.11)	0.069 (1.07)	0.013 *** (17.91)	−0.012 (−0.47)
Speed	−16.012 *** (−13.34)	−16.641 *** (−9.06)	−0.161 *** (−7.95)	−1.507 ** (−2.10)
Constant	85.202 *** (22.73)	166.478 *** (29.02)	1.418 *** (22.36)	47.614 *** (21.24)
Observations	4063	4063	4063	4063
R ²	0.251	0.137	0.316	0.273
Adj-R ²	0.250	0.135	0.315	0.272
F	170.2	80.30	234.5	190.7

t-statistics in parentheses. *** $p < 0.01$, ** $p < 0.05$, * $p < 0.1$.

From the results (Table 10), the *DID* variable still had a significant negative effect on PM₁₀ and SO₂, while the effect of the other two indicators was not significant. As for the dynamic effect we are concerned about, the dummy variables in the first two weeks all had a significant negative effect, proving that the policy had a strong impact in the initial stage. The effect in the last two weeks was very weak, and only in SO₂ was there still a significant negative effect. This shows that at the end of the implementation of the policy, or near the end of the stage, its effect was greatly reduced, and it was far less obvious than in the initial stage of the policy.

5. Conclusions

To reach the carbon peak and carbon neutrality targets, reducing carbon emissions and reducing particulate matter concentration are important ways to improve atmospheric quality. China has introduced a policy of coal to gas and electricity to combat frequent smog and severe air pollution caused by coal-fired heating. Based on the panel data of nineteen cities in The Beijing–Tianjin–Hebei region and surrounding areas from 2016 to 2020, the PSM-DID model and the time-varying DID model were used to test the effectiveness and dynamic sustainability of the policy of coal to gas and electricity on air pollution. The empirical analysis results show that (1) the propensity score matching method (PSM) can be used to match the influencing factors of air quality in nineteen cities in Beijing–Tianjin–Hebei and surrounding areas and to overcome the endogenous problem among variables. It provides new evidence to study the relationship between the policy of changing coal to gas and electricity and the influencing factors of air pollution, and it enriches the research methods of the existing literature on the influence of coal to gas and electricity. (2) On the whole, the fitting effect of DID model is at a normal level; that is, the air pollution

levels in the Beijing–Tianjin–Hebei urban agglomeration that participated in the Coal to Gas and Electricity policy did decrease, indicating that the coal to gas power policy has indeed achieved the expected effect. One possible reason is that the government plays a leading role in air pollution; the coal to gas policy involves the coordinated development of the Beijing–Tianjin–Hebei city, indicating that the choice of pilot cities is obviously representative. (3) Regarding the significance level, the policy had a relatively large impact on SO_2 and PM_{10} , while the effects on $\text{PM}_{2.5}$ and CO were relatively weak. This result shows the urgent need for more accurate improvement plans for various pollutants. The weak reduction capacity of $\text{PM}_{2.5}$ may be due to the fact that $\text{PM}_{2.5}$ had shown a downward trend before the implementation of the Coal to Gas and Electricity policy in the Beijing–Tianjin–Hebei region; other air joint prevention and control policies had shown a more powerful governance effect. The weak impact on carbon emissions suggests that other precise solutions for carbon emissions are needed to achieve dual-carbon targets. (4) The dynamic sustainability results of the policy of changing coal to gas and electricity show that the virtual variables in the first two weeks have a significant negative effect, proving that the policy has a strong impact in the initial stage. The effect of the last two weeks was very modest, with a significant negative effect only in SO_2 . This shows that the effect of the policy at the end stage or near the end stage of the implementation is greatly reduced and is far less obvious than at the early stage of the policy. It shows that the one-size-fits all policy does not have a good sustainable effect, which may be due to the smaller subsidy intensity in the later stage, the increased cost for residents using gas and electricity, or the inherent living habits resulting in the smaller policy intensity.

In the end, given the current situation in Beijing, Tianjin, and Hebei, we propose the following recommendations to improve air quality: First, during the implementation of the policy, the air quality in Beijing, Tianjin, and Hebei was improved, and specific action arrangements have been planned for the future. However, there are different difficulties and effects between regions, Hebei is regarded as a key area to undertake the transfer industries of Beijing, which can hardly bear the impact of the coal ban on its economy, so as to Tianjin, while the air pollution in Hebei and Tianjin will also infect Beijing. So, establishing a regional joint prevention-and-control mechanism for air pollution; building one picture of the responsibility of replacing coal with gas and electricity in Beijing, Tianjin, and Hebei; promoting the upgrading of regional industrial structure; and balancing the regional central budget are the most crucial missions that should be completed in the following days. Second, although the Coal to Gas and Electricity policy has reduced the AQI index, it only had a large impact on SO_2 and PM_{10} , and was relatively weak on $\text{PM}_{2.5}$ and CO. Therefore, to increase investment in R&D, strategies for reducing individual pollutants are urgently needed. The policy of coal to gas and electricity has had little impact on carbon emissions. To achieve the dual-carbon target, we need to cooperate to achieve a precise emission reduction strategy. Last but not least, we find air quality continues to deteriorate after the end of the policy, which means that a policy that imposes uniformity in all cases is not sustainable. In reality, the implementation of policy is often difficult to accomplish in one stroke. Not only does the policy need to prevent the emergence of a gas shortage under the law of objective economics and slowly promote the policy according to the local economic situation and residents' income and habits, but it also must enhance service guarantees, strive for more subsidies and more alternative energy like biomass fuel, wind energy, and solar energy for the local people. So, we will continue to pay attention to that in our research.

Author Contributions: Conceptualization, J.Z. and L.G.; methodology, J.Z.; software, J.Z. and L.G.; validation, Z.D.; formal analysis, J.Z. and Z.D.; investigation, J.Z.; resources, Z.D.; data curation, Z.D.; writing—original draft preparation, J.Z.; writing—review and editing, J.Z., W.W. and L.G.; visualization, W.W.; supervision, J.Z. and Y.T.; project administration, W.W.; funding acquisition, W.W. All authors have read and agreed to the published version of the manuscript.

Funding: This research is funded by the Annual Project of Philosophy and Social Sciences of Henan Province (Grant No.2021CJJ135); Science and Technology Innovation Project of Beijing Forestry University (Grant No.2021SPS01); The Social Science Foundation Cultivation Program of Yanshan University (Grant No.118/0370044).

Institutional Review Board Statement: Not applicable.

Informed Consent Statement: Not applicable.

Data Availability Statement: All data used during the study are available from the corresponding author by request.

Conflicts of Interest: The authors declare no conflict of interest.

References

1. Zhang, Y.J.; Liu, Z.; Zhang, H.; Tan, T.D. The impact of economic growth, industrial structure and urbanization on carbon emission intensity in China. *Nat. Hazards* **2014**, *73*, 579–595. [CrossRef]
2. Almond, D.; Chen, Y.; Greenstone, M.; Hongbin, L. Winter heating or clean air? Unintended impacts of China’s Huai river policy. *Am. Econ. Rev.* **2009**, *99*, 184–190. [CrossRef]
3. Wang, Y.; Guo, Z.; Han, J. The relationship between urban heat island and air pollutants and them with influencing factors in the Yangtze river delta, China. *Ecol. Indic.* **2021**, *129*, 107976. [CrossRef]
4. Yu, S.W.; Wei, Y.M.; Wang, K. Provincial allocation of carbon emission reduction targets in China: An approach based on improved fuzzy cluster and Shapley value decomposition. *Energy Policy* **2014**, *66*, 630–644. [CrossRef]
5. Yu, S.W.; Wei, Y.M.; Fan, J.L.; Zhang, X.; Wang, K. Exploring the regional characteristics of inter-provincial co2 emissions in Shina: An improved fuzzy clustering analysis based on particle swarm optimization—ScienceDirect. *Appl. Energy* **2012**, *92*, 552–562. [CrossRef]
6. Wang, Q.; Zhao, M.; Li, R.; Su, M. Decomposition and decoupling analysis of carbon emissions from economic growth: A comparative study of China and the United States. *J. Clean. Prod.* **2018**, *197*, 178e184. [CrossRef]
7. The Website of the Central People’s Government of the PRC. Available online: http://www.gov.cn/zhengce/2021-10/24/content_5644.htm (accessed on 12 February 2021).
8. The Website of the Central People’s Government of the PRC. Available online: http://www.gov.cn/zhengce/2018-01/24/content_5260167.htm (accessed on 12 February 2021).
9. Wang, M.; Wang, Y.; Feng, X.; Zhao, M.; Du, X.; Wang, Y.; Wu, L. The effects of intensive supervision mechanism on air quality improvement in China. *J. Air Waste Manag. Assoc.* **2021**, *71*, 1102–1113. [CrossRef]
10. Streets, D.G.; Gupta, S.; Waldhoff, S.T.; Wang, M.Q.; Bo, Y. Black carbon emissions in China. *Atmos. Environ.* **2001**, *35*, 4281–4296. [CrossRef]
11. Sun, Y.; Jiang, Q.; Wang, Z.; Fu, P.; Li, J.; Yang, T.; Yin, Y. Investigation of the sources and evolution processes of severe haze pollution in Beijing in January 2013. *J. Geophys. Res. Atmos.* **2014**, *119*, 4380–4398. [CrossRef]
12. Chen, Y.; Ebenstein, A.; Greenstone, M.; Li, H. Evidence on the impact of sustained exposure to air pollution on life expectancy from China’s Huai River policy. *Proc. Natl. Acad. Sci. USA* **2013**, *110*, 12936–12941. [CrossRef]
13. Zhao, W.H.; Xu, Q.; Li, L.J.; Jiang, L.; Zhang, D.W.; Chen, T. Estimation of Air Pollutant Emissions from Coal Burning in the Semi-Rural Areas of Beijing Plain. *Res. Environ. Sci.* **2015**, *28*, 869–876.
14. Xiong, Y.; Liao, W.J.; Wang, L. A Study on Air Pollution Governance Effect of the “Coal-to-Gas/Electricity” Policy. *Collect. Essays Financ. Econ.* **2021**, *270*, 103–112.
15. Li, S.L.; Chen, M.M. A Study on the impact of “coal to gas” and “coal to electricity” policies on green development. *Res. Financ. Econ. Issues* **2019**, *428*, 49–56.
16. Shi, D.; Li, S.L. The Effect of Green Cooperative Development in Beijing-Tianjin-Hebei Region—A Quasi-Natural Experiment Based on the Policy of “Coal-to-Gas/Electricity”. *Res. Econ. Manag.* **2018**, *39*, 64–77.
17. Liu, H. “Coal to gas” project is feasible and prudent—Based on the investigation and analysis of “coal to gas” project in Beijing. *Macroeconomics* **2015**, *4*, 9–13.
18. Yue, H.F.; Shi, C. Green Net Benefit Evaluation and Policy Optimization Measures of “Coal to Gas” Project. *J. Hebei Univ. Econ. Bus.* **2019**, *40*, 86–91.
19. Xie, L.Y.; Chang, Y.X.; Lan, Y. The Effectiveness and Cost-Benefit Analysis of Clean Heating Program in Beijing. *Chin. J. Environ. Manag.* **2019**, *11*, 87–93.
20. Zhang, J.F.; Smith, K.R. Household air pollution from coal and biomass fuels in China: Measurements, health impacts, and interventions. *Environ. Health Perspect.* **2007**, *115*, 848–855. [CrossRef]
21. Chen, Y.; Shen, H.; Smith, K.R.; Guan, D.; Chen, Y.; Shen, G.; Tao, S. Estimating household air pollution exposures and health impacts from space heating in rural China. *Environ. Int.* **2018**, *119*, 117–124. [CrossRef]
22. Pi, D.Q.; Chen, H.S.; Wei, W.; Wang, W.D.; Xiao, L.H.; Zhang, W.D.; Wu, J.D.; Li, J.J.; Yan, P.Z. The causes and sources of a heavy-polluted event in Beijing-Tianjin-Hebei region. *China Environ. Sci.* **2019**, *39*, 1899–1908.

23. Song, Y.; Li, Z.; Yang, T.; Xia, Q. Does the expansion of the joint prevention and control area improve the air quality?—Evidence from China's Jing-Jin-Ji region and surrounding areas. *Sci. Total Environ.* **2019**, *706*, 136034. [CrossRef] [PubMed]
24. Amann, M.; Bertok, I.; Borken-Kleefeld, J.; Cofala, J.; Heyes, C.; Höglund-Isaksson, L.; Winiwarter, W. Cost-effective control of air quality and greenhouse gases in Europe: Modeling and policy applications. *Environ. Model. Softw.* **2011**, *26*, 1489–1501. [CrossRef]
25. Pan, T.; Xue, Y.F.; Zhong, L.H.; Zhou, Z.; Yan, J. The Methodology for Air Pollutants Emission Inventory from Residential Coal Combustion and Its Application. *Environ. Prot.* **2016**, *6*, 20–24.
26. Zhu, Y.Y.; Liu, B.; Gui, H.L.; Wang, W. Characteristics of Ozone Pollution, Meteorological Impact, and Evaluation of Forecasting Result Based on a Neural Network Model in Beijing-Tianjin-Hebei Region. *Environ. Sci.* **2022**, *4*, 1–15.
27. Lin, F.Q.; Wu, Z.R. Governance of Ecological Environment in Beijing, Tianjin and Hebei: From “fragmentation” to the Holistic. *J. Hebei Univ. Econ. Bus.* **2017**, *38*, 96–103.
28. Wang, X.-C.; Klemes, J.J.; Dong, X.; Fan, W.; Xu, Z.; Wang, Y. Air pollution terrain nexus: A review considering energy generation and consumption. *Renew. Sustain. Energy Rev.* **2019**, *105*, 71–85. [CrossRef]
29. Zhu, Z.Z.; Liao, H. Evaluation on the Effects of Joint Prevention and Control of Air Pollution in Beijing-Tianjin-Hebei Region and Its Surrounding Areas—An Empirical Study Based on Multi-period Difference-in-Difference Model. *J. China Univ. Geosci. Soc. Sci. Ed.* **2022**, *2*, 142–156.
30. Du, W.C.; Xia, Y.M. Did the Measures of Haze Cooperative Governance in Beijing-Tianjin-Hebei Region Work: An Analysis Based on the DID Model. *Contemp. Econ. Manag.* **2018**, *40*, 53–59.
31. Wang, Q.; Zheng, S.L. Impact of joint prevention and control action on atmospheric pollutant concentration in ‘2 + 26’ cities. China Population. *Resour. Environ.* **2019**, *29*, 51–62.
32. Wang, S.; Huang, Q.; Liu, Q.; Sun, D. Can clean heating in winter in northern China reduce air pollution?—empirical analysis based on the psm-did method. *Energies* **2022**, *15*, 1839. [CrossRef]
33. Heckman, J.J.; Ichimura, H.; Todd, P.E. Matching as an Econometric Evaluation Estimator: Evidence from Evaluating a Job Training Program. *Rev. Econ. Stud.* **1997**, *64*, 605–654. [CrossRef]
34. Heckman, J.J.; Ichimura, H.; Todd, P.E. Matching as an Econometric Evaluation Estimator. *Rev. Econ. Stud.* **1998**, *65*, 261–294. [CrossRef]
35. Tong, Z.; Chen, Y.; Malkawi, A.; Liu, Z.; Freeman, R.B. Energy saving potential of natural ventilation in China: The impact of ambient air pollution. *Appl. Energy* **2016**, *179*, 660–668. [CrossRef]
36. Kyrkilis, G.; Chaloulakou, A.; Kassomenos, P.A. Development of an aggregate Air Quality Index for an urban Mediterranean agglomeration: Relation to potential health effects. *Environ. Int.* **2007**, *33*, 670–676. [CrossRef] [PubMed]
37. Lian, X.; Huang, J.; Huang, R.-J.; Liu, C.; Wang, L.; Zhang, T. Impact of city lockdown on the air quality of COVID-19-hit of Wuhan city. *Sci. Total Environ.* **2020**, *742*, 140556. [CrossRef]
38. The Website of the Central People's Government of the PRC. Available online: https://www.gov.cn/zhengce/content/2014-05/27/content_8830.htm (accessed on 12 February 2021).
39. Cao, J.; Wang, X.; Zhong, X.H. Did Driving Restrictions Improve Air Quality in Beijing? *China Econ. Q.* **2014**, *13*, 1091–1126.
40. Shi, Q.L.; Guo, F.; Chen, S.Y. “Political Blue Sky” in Fog and Haze Governance—Evidence from the Local Annual “Two Sessions” in China. *China Ind. Econ.* **2016**, *5*, 40–56.

Article

New Urbanization, Energy-Intensive Industries Agglomeration and Analysis of Nitrogen Oxides Emissions Reduction Mechanisms

Yang Yu * and Tianchang Wang

School of Economics and Management, Beijing University of Chemical Technology, Beijing 100029, China; 2019200891@mail.buct.edu.cn

* Correspondence: yuyang@mail.buct.edu.cn

Abstract: With the deepening of urbanization and industrialization, as well as the exacerbation of energy consumption, China is facing a severe situation in which nitrogen oxide (NO_x) emissions reduction is imperative. In this study, it is aimed to put forward countermeasures and suggestions to reduce NO_x emissions by analyzing the impact and mechanism of new urbanization, the agglomeration of energy-intensive industries and mutual interactions on China's NO_x emissions. By analyzing the data of 30 provinces in China from 2006 to 2017, this paper adopted the system generalized method of moments (SYS-GMM) and intermediary effect model to introduce four variables, such as: energy efficiency, human capital, industrial structure and energy structure, which were for empirical analysis. From the results, it was shown that: (1) NO_x emissions in China have an accumulated effect; (2) new urbanization inhibits NO_x emissions, whilst the agglomeration of energy-intensive industries intensifies NO_x emissions. New urbanization weakens the negative impact of the agglomeration of energy-intensive industries on NO_x emissions reduction and, (3) among the impacts of new urbanization on NO_x emissions, the energy efficiency and human capital reflect the intermediary effect mechanism. At the same time, in the impact of the agglomeration of energy-intensive industries on NO_x emissions, the industrial structure and energy structure show the mechanisms of the intermediary effect and masking effect, respectively.

Keywords: air pollution; new urbanization; energy-intensive industries agglomeration; NO_x emissions; intermediary effect model; transmission mechanism

Citation: Yu, Y.; Wang, T. New Urbanization, Energy-Intensive Industries Agglomeration and Analysis of Nitrogen Oxides Emissions Reduction Mechanisms. *Atmosphere* **2021**, *12*, 1244. <https://doi.org/10.3390/atmos12101244>

Academic Editors: Duanyang Liu, Kai Qin and Honglei Wang

Received: 24 August 2021

Accepted: 18 September 2021

Published: 24 September 2021

Publisher's Note: MDPI stays neutral with regard to jurisdictional claims in published maps and institutional affiliations.



Copyright: © 2021 by the authors. Licensee MDPI, Basel, Switzerland. This article is an open access article distributed under the terms and conditions of the Creative Commons Attribution (CC BY) license (<https://creativecommons.org/licenses/by/4.0/>).

1. Introduction

In the “2030 Agenda for Sustainable Development” formulated by the United Nations, 17 sustainable development goals were put forward; among which, SGD11 and SGD13 describe the requirements for building sustainable cities and solving the problems of climate changes, respectively. A key role has been played by new urbanization in promoting urban and ecological sustainable development. In recent years, China's urban air quality has been continuously improved; despite this, there are still some atmospheric pollutants, such as nitrogen oxides, ozone and other gases, that have been emitted at a high level. The emissions reduction effect of these gases is not obvious and brings huge challenges to the prevention and control of air pollution. Nitrogen oxides (NO_x = NO + NO₂) is one of the most serious air pollutants, and its hazards are reflected in environmental governance and human health. NO_x not only directly affects the concentration of nitrogen dioxides in the air but is also the main source of ozone pollutants. In the research on how these gasses harm human health, scholars have discussed the adverse effects of NO_x on human life expectancy [1], asthma symptoms [2], mental health disorders complicating pregnancy [3,4] and lung function [5] at birth. In 2018, NO_x accounting for the highest proportion of total industrial waste gas emissions, seriously hindering the improvement of China's new urbanization level and the construction of ecological civilization.

In China, NO_x emissions are mainly from transportation sources (using automobile engines) and industrial sources (boiler combustion and cement and steel production). It has been pointed out that 75.34% of the NO_x emissions from industrial sources focus on nonmetallic mineral products, electric power, thermal power production and supply and ferrous metal smelting and rolling processing industries in energy-intensive industries (Bulletin of the second national survey of pollution sources [6]). It is necessary to reduce NO_x emissions from the source, which means that the structure of energy-intensive industries should be upgraded. At present, the view that it is significant to adjust the industrial spatial layout by means of industrial agglomeration give full attention to the technology spillover effect and improve the environment has been recognized by most scholars [7–10]. During the process of actively promoting new urban construction in China, the profound changes are dramatic in the industrial layout. However, it remains to be explored whether the geographical concentration of energy-intensive industries will reduce pollutant emissions. Therefore, it has important guidelines for furthering the construction of new urbanization, optimizing the industrial layout and reducing NO_x emissions to clarify the impact and mechanism of new urbanization and energy-intensive industry agglomerations on NO_x emissions in China.

It is an important guarantee for sustainable social development to make the development of urbanization and the environment harmonious. The relationship between them has been widely explored by scholars. It is concluded from the research on this topic covering: urbanization improving environmental pollution [11,12], urbanization intensifying environmental pollution [13,14] and the nonlinear relationship between urbanization and environmental pollution [15–17]. Based on a nonlinear relationship, in the early stages of urbanization, with the level of urbanization increasing, pollution intensifies. After that, when urbanization reaches a certain level, pollution will be improved. In some scholars' opinions, they attribute the impact of urbanization on the environment to population growth and industrial agglomeration, holding the opinion that population growth and industrial agglomeration brought about by urbanization have a greater impact on the environment. From the perspective of population factors, as early as 1978, Malthus pointed out that a lack of technology and that population growth will reach the limit because of resource shortage; at the same time, the impact of demographic factors on the environment is also universal [18]. Since then, from the research, large number of scholars have also believed the negative impact of population growth on the environment [19–22].

From the perspective of agglomeration, with the development of urbanization, industrial agglomeration is a form of enterprise agglomeration of organizations with close geographical locations and industrial connections. Some scholars believe that industrial agglomeration has a positive effect on the improvement of environmental pollution. First, most industries gather in specific areas based on unique regional resource conditions, thereby reducing transboundary pollution [23]. Second, industrial agglomeration will attract a large amount of labor force. Meanwhile, specialized equipment can be applied on a large scale, thus promoting the development of specialized investments and services [24]. Third, industrial agglomeration will benefit mutual learning among enterprises and promote the spillover of knowledge and technology [10,25]. In contrast, other scholars believe that industrial agglomeration has exacerbated environmental pollution [26–28], expanding the production scale and output [29,30] and causing crowding effects, as well as environmental damage. Furthermore, other scholars have also verified the nonlinear relationship between industrial agglomeration and environmental pollution [31–33].

NO_x is a kind of air pollutant, and manmade NO_x emissions mainly come from energy consumption. Considering the seriousness of NO_x emissions, large number of scholars have confirmed energy-intensive industries such as iron and steel [34], thermal power [35], cement [36,37] and petrochemicals [38] have bad influences on NO_x emissions. After subdividing these industrial sectors, scholars proposed that the emission factors of power generation in the iron and steel industry should be reduced [39], and coal-fired

power plants should implement ultra-low emissions policies [35], strengthen technology research and development [40] and reduce NOx emissions.

By analyzing the literature, it was found as below: firstly, although scholars have conducted deep research into the relationships between urbanization and environmental pollution, industrial agglomeration and environmental pollution, their conclusions are not confirmed. Secondly, the existing literature has covered few researches on the action path of urbanization and industrial agglomeration on the environment, as well as the pollutants rarely involving NOx. Thirdly, with the new urbanization being promoted, the industry has been modified in the original spatial layout; however, few scholars have researched and discussed the relationship between energy-intensive industries and nitrogen oxides from the perspective of agglomeration.

Recently, scholars have paid more attention to evaluating the ecological efficiency [41–44] during the period of measuring the level of urbanization. A new urbanization index system will be constructed, including four dimensions such as population, social development, ecological environment and land, integrating the new urbanization and agglomeration of energy-intensive industries into a unified framework and analyzing their impact on China's NOx emissions by applying the systematic GMM method. In addition, this paper also applied the intermediary effect model to explore the action path of new urbanization and agglomeration of energy-intensive industries on NOx emissions. Finally, some suggestions are put forward to reduce the NOx emissions, in order to provide countermeasures to deal with the air pollution problems during development.

2. Methodology

2.1. Model Setting

2.1.1. Benchmark Regression Model

Liu et al. [28] investigated the relationship between industrial agglomeration and environmental pollution by adding industrial agglomeration into the production function. Zhu and Yan [45] extended the model on this basis and introduced urbanization into the equation. Based on the theories and methods of Zhu and Yan [45], in this paper, a regression equation was constructed, including new urbanization (*nurb*), the agglomeration of energy-intensive industries (*hagg*) and NOx emissions (*NE*). Based on previous studies [46–50], this paper introduced five control variables, such as the industrial structure (*is*), technological innovation (*r&d*), foreign direct investment (*fdi*), environmental regulation (*er*) and economic development (*pgdp*). In order to avoid heteroscedasticity, all variables were treated with a logarithm, and the benchmark regression model was set as below:

$$\ln NE_{it} = \beta + \beta_1 \ln nurb_{it} + \beta_2 \ln hagg_{it} + \beta_3 \ln is_{it} + \beta_4 \ln r\&d_{it} + \beta_5 \ln fdi_{it} + \beta_6 \ln er_{it} + \beta_7 \ln pgdp_{it} + \varepsilon_{it} \quad (1)$$

In Equation (1) and the following equations, ε_{it} is the standard error term.

The new urbanization and agglomeration of energy-intensive industries interact with each other. At the same time, considering a certain dynamic lag of NOx emissions, the interaction term between the new urbanization and agglomeration of energy-intensive industries and the first-order lag term of NOx emissions were introduced to build a dynamic model as follows:

$$\ln NE_{it} = \eta + \eta_0 \ln NE_{i,t-1} + \eta_1 \ln nurb_{it} + \eta_2 \ln hagg_{it} + \eta_3 c \ln nurb_{it} * c \ln hagg_{it} + \eta_4 \ln is_{it} + \eta_5 \ln r\&d_{it} + \eta_6 \ln fdi_{it} + \eta_7 \ln er_{it} + \eta_8 \ln pgdp_{it} + \varepsilon_{it} \quad (2)$$

Among them, thanks to the variable centralization, the multicollinearity problem caused by the introduction of interaction terms can be avoided effectively. $c \ln nurb_{it}$ and $c \ln hagg_{it}$ are the variable representations after being intensively processed.

It makes the model having a dynamic interpretation ability to introduce the first-order lag term of NOx emissions into the regression model, but it will result in endogenous problems of the model. The different generalized methods of moments (DIF-GMM) can

reduce the influence of endogeneity on the model estimation. However, the DIF-GMM has serious problems, such as: weak instrumental variables and poor accuracy of the coefficient estimation results. From this, scholars combined the horizontal equation and the first-order difference equation, as well as proposed the system generalized method of moments (SYS-GMM) [51,52]. Due to limited samples, the system GMM method ensures the accuracy of the estimation. Therefore, Stata 16.0 [53] was used to analyze the model based on the system generalized moment estimation method.

2.1.2. Intermediary Effect Model

To explore the transmission mechanism of new urbanization and energy-intensive industry agglomeration to nitrogen oxides, this paper constructed an intermediary effect model by referring to the method of a stepwise testing regression coefficient proposed by Judd and Kenny [54] and Baron and Kenny [55]:

$$\ln NE_{it} = \theta + \theta_0 \ln NE_{i,t-1} + \theta_1 \ln X_{it} + \theta_2 \ln \pi_{it} + \varepsilon_{it} \quad (3)$$

$$\ln M_{it} = \omega + \omega_0 \ln M_{i,t-1} + \omega_1 \ln X_{it} + \omega_2 \ln \pi_{it} + \varepsilon_{it} \quad (4)$$

$$\ln NE_{it} = \rho + \rho_0 \ln NE_{i,t-1} + \rho_1 \ln X_{it} + \rho_2 \ln M_{it} + \rho_3 \ln \pi_{it} + \varepsilon_{it} \quad (5)$$

In the process of replacing X in the equation with *nurb*, M is regressed with energy efficiency (*ee*) and human capital (*hc*), respectively. In the process of replacing X in the equation with *hagg*, M is regressed with the industrial structure (*is*) and energy structure (*es*), respectively.

Based on the intermediary effect model: (1) if the total effect coefficient θ_1 is significant, it should be the intermediary effect; otherwise, it is the masking effect. (2) If the coefficients ω_1 and ρ_2 are significant, the indirect effect of $\omega_1 \times \rho_2$ is significant. (3) If the coefficient ρ_1 of the direct effect is significant, $\omega_1 \times \rho_2$ and ρ_1 are the same sign, which reflects the intermediary effect, and if $\omega_1 \times \rho_2$ and ρ_1 are different signs, it reflects the masking effect [56,57]. In addition, the mediating effect should satisfy that the coefficient ρ_1 is less than the coefficient θ_1 .

2.2. Index Construction

2.2.1. New Urbanization

Compared with the traditional urbanization measured only by the indicator of population, as for the new urbanization, more attention should be attached to the quality of urban development. From this, referring to the existing research [58–61], this paper constructed a new comprehensive evaluation index system of the urbanization level from 13 indexes and four aspects, including population, social development, ecological environment and land, which are shown in Table 1.

Based on the variation degree of each index, the entropy method determines the index weight, and the evaluation deviation of the human factors is avoided to a certain extent. In this paper, the entropy method is applied to measure the weight for each index in the new urbanization index system. The calculation formula of the weight is as follows:

Step 1: Calculate the proportion of index j :

$$y_{ij} = \frac{X_{ij}}{\sum_{i=1}^n X_{ij}}, \quad i = 1, 2, \dots, n, \quad j = 1, 2, \dots, m \quad (6)$$

Step 2: Calculate the entropy of index j :

$$e_j = -\frac{1}{\ln n} \sum_{i=1}^n y_{ij} \ln y_{ij} \quad (7)$$

Step 3: Calculate the weight of each indicator:

$$\omega_j = \frac{(1 - e_j)}{\sum_{j=1}^m (1 - e_j)} \quad (8)$$

X_{ij} is the result of the standardization of the actual value of the j th index in the i th province, Y_{ij} is the proportion of the actual value of the j th index in the i th province, e_j is the information entropy of the index and ω_j is the entropy weight. Table 1 lists the comprehensive evaluation index system of the new urbanization level.

Table 1. The comprehensive evaluation index system of the new urbanization levels.

Target Layer	Dimension	Index	Polarity
Comprehensive evaluation index of new urbanization	Population urbanization	Proportion of urban population (%)	+
		Urban population density (people/km ²)	+
		Dependency ratio of the elderly population (%)	+
	Social development urbanization	Medical insurance (ten thousand)	+
		Proportion of fixed assets investment (%)	+
		Consumption proportion of urban and rural residents (%)	-
		Number of museums (unit)	+
	Ecological environment urbanization	Pollution-free treatment rate of domestic waste (%)	+
		Per capita green space (m ² /person)	+
		Urban green space area (hectares)	+
		Number of parks (unit)	+
	Land urbanization	Per capita urban road area (m ²)	+
		Construction area (km ²)	+

2.2.2. Energy-Intensive Industries Agglomeration

This paper measures the degree of industrial agglomeration by the number of employees in six energy-intensive industries (chemical raw materials and chemical products manufacturing industry, nonmetallic mineral manufacturing industry, ferrous metal smelting and rolling processing industry, nonferrous metal smelting and rolling processing industry, petroleum processing coking and nuclear fuel processing industry, and power and heat production and supply industry). The calculation formula is as follows:

$$hagg_{ij} = \frac{(m_{ij}/m_j)}{(M_i/M)} \quad (9)$$

where m_{ij} is the employment of industry i in area j , m_j is the employment of all the industries in area j , M_i is the national employment of industry i and M is the employment number of all the industries in the country.

2.3. Data Description

Considering the availability of the data, this paper selected the panel data of 30 provinces in China (excluding Tibet, Hong Kong, Macao and Taiwan) from 2006 to 2017 to verify the relationship between new urbanization, energy-intensive industries agglomeration and NOx emissions and the intermediary effect. The data comes from the China Statistical Yearbook (2007–2018) [62] and China Environment Yearbook (2007–2018) [63,64]. The GDP data used in the variables were calculated at a constant price in 2006 and were processed by using a logarithm. The representation and descriptive statistics of the related variables are shown in Table 2.

Table 2. Variable description statistics.

Variables	Representations of Variable	Mean	Std. Dev.	Min.	Max.
lnNE	Regional NOx emissions	3.8538	0.7655	1.3863	5.1936
lnnurb	—	5.8389	0.4071	4.4776	6.7733
lnhagg	—	0.0691	0.4509	−1.2463	1.6868
lnpgdp	GDP per resident population	10.3004	0.6220	8.6570	11.9360
lnr	Proportion of environmental protection expenditure in fiscal expenditure in the year	−3.5628	0.3617	−4.7732	−2.6992
lnr&d	The proportion of regional research and experiment funds in GDP	−4.7267	0.6613	−8.0286	−3.5696
lnfdi	The proportion of actual foreign direct investment in industrial added value of the year	14.4673	1.5769	9.7361	16.9303
lnis	The proportion of added value of secondary industry in GDP	−0.6907	0.1903	−1.4451	−0.4897
lnce	The ratio of gross regional product to regional energy consumption	−0.0643	0.4942	−1.3816	1.0164
lnhc	The proportion of the number of students in colleges and universities in the total population of the region	4.092	0.8314	1.2809	5.3059
lnes	The ratio of coal consumption to total energy consumption	−0.4733	0.4439	−3.0136	0.4248

3. Results

3.1. Stationary Test and Multicollinearity Test of Variables

Before regression, it is required to test the stationarity of the data to avoid pseudo regression. The unit root test is a common method to test the stationarity of data. For example, Levin, Lin and Chu [65] derived the unit root test (LLC test) from Levin and Lin [66], and it was proposed by IM, Pesaran and Shin [67] that the unit root test considers panel heterogeneity (IPS test). The test results are shown in Table 3. In the LLC test, all the variables deny the original hypothesis of the “existence of a unit root” at the level of 1%, while, in the test of IPS, the variables such as lnNE, lnpgdp, lnr&d, lnis, lnce and lnhc were unstable. After the first-order difference, all the variables rejected the original hypothesis of the “existence of a unit root” at the level of 1%. At the same time, multicollinearity will distort the regression estimation model. The value of the variance inflation factor (VIF) was calculated to judge whether there was multicollinearity between the prediction variables or not. It was found that the VIF values were less than 10. Therefore, from this, it could be seen that there was no multicollinearity among the variables to ensure the effectiveness of the following regression estimation results.

Table 3. Unit roots and multicollinearity test.

Variables	I (0)		I (1)	VIF
	LLC Test	IPS Test	IPS Test	
lnNE	−9.7787 ***	−2.1377	−9.3706 ***	—
lnnurb	−28.3692 ***	−4.7110 ***	−12.5630 ***	1.51
lnhagg	−9.1874 ***	−1.5977 *	−8.2932 ***	2.30
lnpgdp	−5.4468 ***	1.7051	−4.3022 ***	3.67
lnr	−11.3619 ***	−3.9842 ***	−8.6963 ***	1.23
lnr&d	−5.6201 ***	0.3098	−12.3932 ***	3.00
lnfdi	−9.6044 ***	−2.7313 ***	−9.0860 ***	4.84
lnis	−7.3855 ***	1.7466	−6.4407 ***	2.33
lnce	−3.3887 ***	2.0213	−5.4591 ***	5.71
lnhc	−5.6826 ***	1.0969	−7.6319 ***	4.65
lnes	−9.1010 ***	−1.8949 **	−5.4591 ***	2.34

Note: *, ** and *** indicate significance at the levels of 10%, 5% and 1%.

3.2. Regression of the Basic Model

Considering the robustness of the estimation results, this paper adopted the random effects model, fixed effects model and SYS-GMM model for estimation. From the regression

results in Columns 1–3, in Table 4, in addition to the estimated coefficient of $\ln fdi$, the influence coefficients of the dependent variables estimated by the random effects model, fixed effects model and SYS-GMM model on NOx emissions were consistent; that is, the robustness of the estimated results was verified. In the estimation of the SYS-GMM method, based on the research of Arellano and Bond [51] and Arellano and Bover [68], the Sargan test and Arellano bond test were applied to determine whether there was a second-order autocorrelation between the effectiveness of the instrumental variables and the error term or not. From the regression results in Table 4, it was shown that, in the Sargan test, the original hypothesis of the effectiveness of the instrumental variables was accepted, and in the statistics of AR (2) in Arellano bond test, the original assumption that the second-order sequence of residual terms had no autocorrelation showed that the model setting was effective.

Table 4. Baseline regression results.

Variables	Contains No Interaction Term		Contain Interaction Items	
	RE	FE	SYS-GMM	SYS-GMM
$\ln NE_{i,t-1}$	—	—	0.4075 *** (0.0176)	0.4633 *** (0.0242)
$\ln nurb$	−0.1273 * (0.0773)	−0.1750 ** (0.0799)	−0.4766 *** (0.0639)	−0.2929 *** (0.0992)
$\ln hagg$	0.1723 *** (0.0631)	0.2006 *** (0.0634)	0.1290 *** (0.0157)	0.0963 *** (0.0167)
$\ln nurb * \ln hagg$	—	—	—	−0.2818 *** (0.0665)
$\ln is$	2.5061 *** (0.2845)	2.8958 *** (0.3243)	2.1128 *** (0.2156)	1.6204 *** (0.3252)
$\ln fdi$	0.0361 (0.0321)	−0.0040 (0.0340)	0.1421 *** (0.0255)	0.1173 *** (0.0199)
$\ln er$	−0.1881 *** (0.0592)	−0.1486 ** (0.0608)	−0.4251 *** (0.0372)	−0.3833 *** (0.0350)
$\ln pgdp$	−0.3390 *** (0.0719)	−0.3235 *** (0.0768)	−0.6537 *** (0.0377)	−0.5941 *** (0.0638)
$\ln r\&d$	0.2245 *** (0.0622)	0.2060 *** (0.0630)	0.4274 *** (0.0463)	0.3560 *** (0.0736)
cons	9.6767 *** (0.9698)	10.6965 *** (1.0116)	11.6863 *** (0.7497)	9.6132 *** (0.9050)
AR (1)	—	—	−1.8979 (0.0577)	−2.0145 (0.0440)
AR (2)	—	—	1.0735 (0.2830)	1.074 (0.2828)
sargan	—	—	28.2426 (1.0000)	27.6578 (1.0000)

Note: *, ** and *** indicate significance at the levels of 10%, 5% and 1%, respectively; the values in parentheses for the variable and constant items represent the standard errors.

The regression coefficients in all the independent variables were significant at the 1% level, and the first-order coefficient in the early stage of the NOx emissions was positive; from this, it was indicated that China's NOx emissions had a cumulative effect, which means the increase of NOx emissions in the early stage will result in the increase of NOx emissions during the current period.

New urbanization, environmental regulation and economic development will promote to reduce NOx emissions. For every 1% increase in the level of new urbanization, the nitrogen oxides emissions can be reduced by 0.4766%, as, for every 1% increase in the environmental regulations, the NOx emissions will be reduced by 0.4251%. For every 1% increase in economic development, nitrogen oxides emissions will be reduced by 0.6537%.

The agglomeration of energy-intensive industries, industrial structure, technological innovation and foreign direct investment were positively correlated with the increase of

NOx emissions. For every 1% increase in the agglomeration of energy-intensive industries, NOx emissions will be increased by 0.1290%. The industrial structure is the biggest factor affecting NOx emissions, with the elasticity coefficient reaching 2.1128. Therefore, it is the key to realizing China's NOx emissions reduction to optimize the industrial structure. The elastic coefficient of technological innovation is 0.4274, which indicates that there is a positive correlation between technological innovation and NOx emissions. From this result, it is shown that China's technological innovation has not yet played its role in reducing emissions [69,70]. The coefficient of foreign direct investment is 0.1421, indicating that, for every 1% increase in foreign direct investment, the NOx emissions will increase by 0.1421%.

Furthermore, new urbanization will attract similar industries to gather in specific regions, and industrial agglomeration will drive population agglomeration, thereby promoting the development of new urbanization. Therefore, there may be an interaction between the new urbanization and agglomeration of energy-intensive industries. From the regression results in Column 4 in Table 4, it is shown that the new urbanization and agglomeration of energy-intensive industries mutually interact. After adding the interaction terms of the new urbanization and agglomeration of energy-intensive industries, the positive and negative affecting coefficients in each dependent variable on NOx emissions have not been changed and are significant at the level of 1%, which, once again, verifies the robustness of the regression results. The interaction coefficient between the new urbanization and agglomeration of energy-intensive industries is -0.2818 , showing that the promotion of NOx emissions by the agglomeration of high-energy-consuming industries decreases as the level of new urbanization increases. With the improvement development of new urbanization, the adverse impact of energy-intensive industries agglomeration on NOx emissions reduction will be weakened gradually.

3.3. Mechanism Analysis

Based on the benchmark study in Table 4, it is found that China's new urbanization has a strong inhibitory effect on NOx emissions; however, energy-intensive industries agglomeration has a strong promotion effect on NOx emissions. In this section, the transmission mechanism of new urbanization and energy-intensive industries agglomeration on NOx emissions is explored with the intermediary effect model.

During the period of exploring the transmission mechanism between new urbanization and NOx emissions, it should be considered whether new urbanization can affect NOx emissions with energy efficiency and human capital. It can be seen from Table 5 that, when energy efficiency was taken as the intermediary variable into the model, the absolute value of the estimated coefficient of the impact of new urbanization on NOx emissions in Equation (5) was less than Equation (3), the impact of new urbanization on the energy efficiency was positive and the impact of the energy efficiency on NOx was negative, which was significant at the level of 1%. At the same time, it showed that energy efficiency is the intermediary variable of new urbanization affecting NOx emissions. New urbanization will benefit the improvement of energy efficiency, which not only reduces the level of unit energy consumption but also produces additional economic benefits, leading to reduce NOx emissions. Therefore, new urbanization reduces NOx emissions by improving the energy efficiency. When human capital is introduced into the model as an intermediary variable, the estimation coefficient of new urbanization on NOx emissions in Equation (5) was less than Equation (3), the impact of new urbanization on human capital was positive and the impact of human capital on NOx was negative. It is shown that human capital is the intermediary variable of the new urbanization affecting NOx emissions. With the improvement of new urbanization, better educational opportunities will be provided for more people, in order to promote human capital. At the same time, as the human capital level improves, it contributes to the enhancement of residents' awareness of environmental protection, playing a positive role in pollutant emissions reduction [71,72], which means that the human capital in new urbanization will improve the reduction of NOx emissions.

Table 5. Research results on the mechanism of NOx emissions by new urbanization.

Variables	The Mediating Variable of Energy Efficiency			The Mediating Variable of Human Capital		
	lnNE	ln _{nee}	lnNE	lnNE	ln _h c	lnNE
	(3)	(4)	(5)	(3)	(4)	(5)
lnNE _{i,t-1}	0.4238 *** (0.0163)	—	0.4047 *** (0.0232)	0.4238 *** (0.0163)	—	0.4259 *** (0.0296)
ln _{nee} _{i,t-1}	—	0.8671 *** (0.0132)	—	—	—	—
ln _h c _{i,t-1}	—	—	—	—	0.9659 *** (0.0214)	—
ln _{nurb}	−0.4236 *** (0.0426)	0.0470 *** (0.0076)	−0.2199 *** (0.0489)	−0.4236 *** (0.0426)	0.0089 * (0.0048)	−0.3304 *** (0.0472)
ln _{nee}	—	—	−0.9432 *** (0.0785)	—	—	—
ln _h c	—	—	—	—	—	−0.3117 *** (0.0957)
ln _{pgdp}	−0.6330 *** (0.0351)	0.0361 * (0.0201)	−0.2535 *** (0.0791)	−0.6330 *** (0.0351)	−0.0330 *** (0.0078)	−0.6642 *** (0.0574)
ln _{er}	−0.3980 *** (0.0360)	0.0248 *** (0.0055)	−0.3486 *** (0.0308)	−0.3980 *** (0.0360)	0.0225 *** (0.0027)	−0.3433 *** (0.0381)
ln _{r&d}	0.4067 *** (0.0419)	−0.0022 (0.0111)	0.4190 *** (0.0444)	0.4067 *** (0.0419)	−0.0513 *** (0.0071)	0.4051 *** (0.0360)
ln _{fdi}	0.1307 *** (0.0231)	0.0300 *** (0.0043)	0.2554 *** (0.0277)	0.1307 *** (0.0231)	0.0133 *** (0.0021)	0.2363 *** (0.0368)
ln _{is}	2.2238 *** (0.1920)	0.1023 (0.0645)	1.7462 *** (0.2563)	2.2238 *** (0.1920)	0.1179 *** (0.0287)	2.5879 *** (0.3300)
Cons	11.3629 *** (0.5210)	−0.8930 *** (0.2597)	4.3882 *** (1.1342)	11.3629 *** (0.5210)	0.2036 ** (0.0950)	11.3177 *** (0.9964)
AR (1)	−1.8648 (0.0622)	−3.8826 (0.0001)	−2.0264 (0.0427)	−1.8648 (0.0622)	−1.9778 (0.0479)	−1.8819 (0.0599)
AR (2)	0.6226 (0.5336)	1.4088 (0.1589)	0.6659 (0.5055)	0.6226 (0.5336)	0.3007 (0.7636)	0.5858 (0.5580)
sargan	28.9093 (1.0000)	28.2143 (1.0000)	28.7847 (1.0000)	28.9093 (1.0000)	24.1725 (1.0000)	28.1055 (1.0000)

Note: *, ** and *** indicate significance at the levels of 10%, 5% and 1%, respectively; the values in parentheses for the variable and constant items represent the standard errors.

In the process of exploring the transmission mechanism between the agglomeration of energy-intensive industries and NOx emissions, it should be considered whether energy-intensive industries agglomerations can affect NOx emissions with the industrial structure and energy structure. It can be seen from Table 6 that, when the industrial structure is taken as the intermediary variable into the model, the estimation coefficient of the agglomeration of energy-intensive industries on NOx emissions was positive, and Equation (5) was less than Equation (3). The impact of agglomeration of energy-intensive industries on the industrial structure was positive, and the impact of the industrial structure on NOx was positive, which were significant at the confidence level of 1%. At the same time, it also showed that the industrial structure is an intermediary variable for the agglomeration of energy-intensive industries agglomeration to affect NOx emissions. The agglomeration of energy-intensive industries will intensify NOx emissions with the proportion of secondary industry increasing. When the energy structure is taken as the intermediary variable into the model, the estimated coefficient of agglomeration of energy-intensive industries on NOx in Equation (5) is greater than that in Equation (3), and the coefficient signs of the direct and indirect effects of agglomeration of energy-intensive industries on NOx emissions are different. It seemed that the energy structure showed the masking effect. At this time, agglomeration will benefit the upgrading of energy-saving technologies and the transformation of energy-saving equipment and the large-scale use of new energy fuels, so it greatly reduces the proportion of coal in the energy consumption, thus reducing the

pollutant emissions [73]. The agglomeration of energy-intensive industries has a positive impact on NO_x emissions; however, the agglomeration of energy-intensive industries will reduce this adverse impact by optimizing the energy structure.

Table 6. Research results on the mechanism of NO_x emissions by energy-intensive industries agglomeration.

Variables	The Mediating Variable of Industrial Structure			The Mediating Variable of Energy Structure		
	lnNE	lnis	lnNE	lnNE	lnes	lnNE
	(3)	(4)	(5)	(3)	(4)	(5)
lnNE _{i,t-1}	0.6317 *** (0.0166)	— —	0.4075 *** (0.0176)	0.6317 *** (0.0166)	— —	0.5943 *** (0.0193)
lnis _{i,t-1}	— —	0.8524 *** (0.0179)	— —	— —	— —	— —
lnes _{i,t-1}	— —	— —	— —	— —	1.1056 *** (0.0212)	— —
lnhagg	0.1830 *** (0.0125)	0.0067 *** (0.0007)	0.1290 *** (0.0157)	0.1830 *** (0.0125)	−0.0488 *** (0.0053)	0.2073 *** (0.0159)
lnis	— —	— —	2.1128 *** (0.2156)	— —	— —	— —
lnes	— —	— —	— —	— —	— —	0.2757 *** (0.0785)
lnnurb	−0.2588 *** (0.0707)	−0.0135 *** (0.0020)	−0.4766 *** (0.0639)	−0.2588 *** (0.0707)	0.0172 (0.0127)	−0.4228 *** (0.0407)
lnpgdp	−0.4778 *** (0.0363)	−0.0624 *** (0.0047)	−0.6537 *** (0.0377)	−0.4778 *** (0.0363)	−0.0781 *** (0.0083)	−0.5319 *** (0.0430)
lnr&d	0.3947 *** (0.0396)	0.0198 *** (0.0056)	0.4274 *** (0.0463)	0.3947 *** (0.0396)	0.0107 * (0.0065)	0.4480 *** (0.0369)
lnfdi	0.0635 *** (0.0123)	−0.0135 *** (0.0019)	0.1421 *** (0.0255)	0.0635 *** (0.0123)	0.0252 *** (0.0078)	0.1360 *** (0.0194)
lnrer	−0.3864 *** (0.0303)	−0.0094 *** (0.0024)	−0.4251 *** (0.0372)	−0.3864 *** (0.0303)	−0.0488 *** (0.0087)	−0.4717 *** (0.0368)
cons	7.4228 *** (0.7617)	1.0860 *** (0.0580)	11.6863 *** (0.7497)	7.4228 *** (0.7617)	0.2498 ** (0.0998)	8.0992 *** (0.5764)
AR(1)	−2.044 (0.0409)	−1.7381 (0.0822)	−1.8979 (0.0577)	−2.044 (0.0409)	−3.5169 (0.0004)	−1.9668 (0.0492)
AR(2)	1.2714 (0.2036)	−1.5556 (0.1198)	1.0735 (0.2830)	1.2714 (0.2036)	−0.9703 (0.3319)	1.2362 (0.2164)
sargan	28.8792 (1.0000)	26.8120 (1.0000)	28.2426 (1.0000)	28.8792 (1.0000)	23.6664 (1.0000)	29.3790 (1.0000)

Note: *, ** and *** indicate significance at the levels of 10%, 5% and 1%, respectively; the values in parentheses for the variable and constant items represent the standard errors.

From the above, the impact mechanism of new urbanization and agglomeration of energy-intensive industries on NO_x through intermediary variables is tested. It is found that the increase of the level of new urbanization not only directly promotes the reduction of NO_x but also reduces NO_x pollution by improving the energy efficiency and human capital. At present, the high proportion of China's secondary industry is still the key factor, leading to an increase in NO_x emissions. Although the agglomeration of energy-intensive industries can reduce NO_x emissions through the reduction of coal consumption, its masking effect is less than the direct effect of the agglomeration of energy-intensive industries on NO_x emissions. Therefore, the total effects of the agglomeration of energy-intensive industries on NO_x emissions still showed a positive correlation. In order to grasp the inspection results comprehensively, all the inspection results are summarized in Table 7.

Table 7. Summary of the mechanism analysis.

Variables	Object	Type of Effect	Mediating (Masking) Effect/The Total Effect
new urbanization	energy efficiency	mediating effect	0.1047
	human capital	mediating effect	0.0065
energy-intensive industries	industrial structure	mediating effect	0.0774
agglomeration	energy structure	masking effect	−0.0735

4. Conclusions and Policy Implications

From the provincial panel data from 2006 to 2017, this paper comprehensively measured and analyzed the impact of the new urbanization and agglomeration of energy-intensive industries on NO_x emissions in China; at the same time, the systematic GMM method was applied to empirically analyze the impact of China's new urbanization and agglomeration of energy-intensive industries on NO_x emissions; what was more, this paper also used the intermediary effect model to explore its impact mechanism.

From above, the conclusions were as follows: (1) There was a negative correlation between new urbanization and NO_x emissions. For every 1% increase in the level of new urbanization, the NO_x emissions will be reduced by 0.4766%. There was a positive correlation between the agglomeration of energy-intensive industries and NO_x emissions. For every 1% increase in the agglomeration of energy-intensive industries, NO_x emissions will be increased by 0.1290%. (2) The new urbanization and agglomeration of energy-intensive industries have a mutual impact on NO_x emissions. The agglomeration of energy-intensive industries' promotion of NO_x emissions weakens with the increase in the level of new urbanization. (3) From the research results of the transmission mechanism, it showed that the energy efficiency and human capital reflected the intermediary effect mechanism in the impact of new urbanization on NO_x. New urbanization reduces the NO_x emissions by improving the energy efficiency and human capital. There are two different mechanisms between the agglomeration of energy-intensive industries and NO_x emissions such as: the intermediary effect and masking effect. The industrial structure plays an intermediary role in the agglomeration of energy-intensive industries and NO_x emissions, while the mechanism of the energy structure in the agglomeration of the energy-intensive industries and NO_x emissions is the masking effect.

From the above conclusions, this paper lists the following suggestions: firstly, the emissions reduction effect of new urbanization shall be given attention to, high-level talent agglomeration is supported and the resource factors shall be invested. At the same time, there is no need in excessively pursuing the development speed of new urbanization, ensuring the quality of development, narrowing the economic and social gaps among regions and realizing urban sustainable development. Secondly, it is scientific and reasonable to guide the agglomeration of energy-intensive industries and optimize the industrial structure, as well as the energy structure. Thirdly, it is also significant to improve the level of scientific and technological governance, as well as give full attention to the ability of coordinated emission reduction.

With the energy transformation continuously promoted, carbon emission reduction, carbon emission peak and carbon neutralization have become the focus of global attention. Next, the research will focus on promoting the coordinated treatment of carbon dioxide and air pollution.

Author Contributions: Data curation, Y.Y., and writing—original draft preparation, Y.Y. and T.W. All authors have read and agreed to the published version of the manuscript.

Funding: This study was supported by funds from the First-class Discipline Construction of Beijing University of Chemical Technology (XK1802-5).

Institutional Review Board Statement: Not applicable.

Informed Consent Statement: Not applicable.

Data Availability Statement: The datasets used and/or analyzed in the current study are available from the corresponding author upon reasonable request.

Conflicts of Interest: The authors declare no conflict of interest.

References

- Rodriguez-Alvarez, A. Air pollution and life expectancy in Europe: Does investment in renewable energy matter? *Sci. Total Environ.* **2021**, *792*, 148480. [CrossRef]
- Ścibor, M.; Balcerzak, B.; Galbarczyk, A.; Jasienska, G. Quality of life of patients with bronchial asthma exposed to gaseous air pollution in the place of residence. *Sustain. Cities Soc.* **2021**, *64*, 102541. [CrossRef]
- Kanner, J.; Pollack, A.Z.; Ranasinghe, S.; Stevens, D.R.; Nobles, C.; Rohn, M.C.H.; Sherman, S.; Mendola, P. Chronic exposure to air pollution and risk of mental health disorders complicating pregnancy. *Environ. Res.* **2021**, *196*, 110937. [CrossRef] [PubMed]
- Bakolis, I.; Hammoud, R.; Stewart, R.; Beevers, S.; Dajnak, D.; MacCrimmon, S.; Broadbent, M.; Pritchard, M.; Shiode, N.; Fecht, D.; et al. Mental health consequences of urban air pollution: Prospective population-based longitudinal survey. *Soc. Psychiatry Psychiatr. Epidemiol.* **2020**, *56*, 1587–1599. [CrossRef]
- Gutiérrez-Delgado, R.I.; Barraza-Villarreal, A.; Escamilla-Núñez, M.C.; Hernández-Cadena, L.; Cortez-Lugo, M.; Sly, P.; Romieu, I. Prenatal exposure to VOCs and NOx and lung function in preschoolers. *Pediatr. Pulmonol.* **2020**, *55*, 2142–2149. [CrossRef] [PubMed]
- Ministry of Environmental Protection of the People's Republic of China. *Bulletin on the Second National Census of Pollution Sources*; Ministry of Environmental Protection of the People's Republic of China: Beijing, China, 2020.
- Gilbert, B.A.; McDougall, P.P.; Audretsch, D.B. Clusters, knowledge spillovers and new venture performance: An empirical examination. *J. Bus. Ventur.* **2008**, *23*, 405–422. [CrossRef]
- Iammarino, S.; McCann, P. The structure and evolution of industrial clusters: Transactions, technology and knowledge spillovers. *Res. Policy* **2006**, *35*, 1018–1036. [CrossRef]
- Chou, T.L.; Ching, C.H.; Fan, S.-M.; Chang, J.Y. Global linkages, the Chinese high-tech community and industrial cluster development: The semiconductor industry in Wuxi, Jiangsu. *Urban Stud.* **2011**, *48*, 3019–3042. [CrossRef]
- Ehrl, P. Agglomeration economies with consistent productivity estimates. *Reg. Sci. Urban Econ.* **2013**, *43*, 751–763. [CrossRef]
- Lin, X.; Lu, C.; Song, K.; Su, Y.; Lei, Y.; Zhong, L.; Gao, Y. Analysis of coupling coordination variance between urbanization quality and eco-environment pressure: A case study of the west Taiwan strait urban agglomeration, China. *Sustainability* **2020**, *12*, 2643. [CrossRef]
- Borrego, C.; Martins, H.; Tchepel, O.; Salmim, L.; Monteiro, A.; Miranda, A.I. How urban structure can affect city sustainability from an air quality perspective. *Environ. Model. Softw.* **2006**, *21*, 461–467. [CrossRef]
- Li, M.; Huang, Y.; Han, M. How to maintain a sustainable environment? A spatial evolution of urban atmospheric pollution and impact factors in China. *Sustainability* **2019**, *11*, 4376. [CrossRef]
- Han, F.; Lu, X.; Xiao, C.; Chang, M.; Huang, K. Estimation of health effects and economic losses from ambient air pollution in undeveloped areas: Evidence from Guangxi, China. *Int. J. Environ. Res. Public Health* **2019**, *16*, 2707. [CrossRef] [PubMed]
- Poumanyvong, P.; Kaneko, S. Does urbanization lead to less energy use and lower CO₂ emissions? A cross-country analysis. *Ecol. Econ.* **2010**, *70*, 434–444. [CrossRef]
- Zhao, Y.; Wang, S.; Zhou, C. Understanding the relation between urbanization and the eco-environment in China's Yangtze River Delta using an improved EKC model and coupling analysis. *Sci. Total Environ.* **2016**, *571*, 862–875. [CrossRef]
- Ge, X.; Zhou, Z.; Zhou, Y.; Ye, X.; Liu, S. A spatial panel data analysis of economic growth, urbanization, and NOx emissions in China. *Int. J. Environ. Res. Public Health* **2018**, *15*, 725. [CrossRef] [PubMed]
- Malthus, T.R. *An Essay on the Principle of Population*; J. Johnson: London, UK, 1798.
- Preston, S.H. The effect of population growth on environmental quality. *Popul. Res. Policy Rev.* **1996**, *15*, 95–108. [CrossRef]
- Dietz, T.; Rosa, E.A. Effects of population and affluence on CO₂ emissions. *Proc. Natl. Acad. Sci. USA* **1997**, *94*, 175–179. [CrossRef]
- Chalkley, K. Population growth and consumption. *Popul. Today* **1997**, *25*, 4. [PubMed]
- Cramer, J.C.; Cheney, R.P. Lost in the ozone: Population growth and ozone in California. *Popul. Environ.* **2000**, *21*, 315–338. [CrossRef]
- Hosoe, M.; Naito, T. Trans-boundary pollution transmission and regional agglomeration effects. *Pap. Reg. Sci.* **2006**, *85*, 99–120. [CrossRef]
- Li, K.; Chu, C.; Hung, D.; Chang, C.; Li, S. Industrial cluster, network and production value chain: A new framework for industrial development based on specialization and division of labour. *Pac. Econ. Rev.* **2010**, *15*, 596–619. [CrossRef]
- Ehrlich, M.V.; Seidel, T. More similar firms—More similar regions? On the role of firm heterogeneity for agglomeration. *Reg. Sci. Urban Econ.* **2013**, *43*, 539–548. [CrossRef]
- Virkanen, J. Effect of urbanization on metal deposition in the bay of Töölönlahti, Southern Finland. *Mar. Pollut. Bull.* **1998**, *36*, 729–738. [CrossRef]
- Li, X.; Xu, Y.; Yao, X. Effects of industrial agglomeration on haze pollution: A Chinese city-level study. *Energy Policy* **2021**, *148*, 111928. [CrossRef]
- Liu, S.; Zhu, Y.; Du, K. The impact of industrial agglomeration on industrial pollutant emission: Evidence from China under New Normal. *Clean Technol. Environ. Policy* **2017**, *19*, 2327–2334. [CrossRef]

29. Verhoef, E.T.; Nijkamp, P. Externalities in urban sustainability: Environmental versus localization-type agglomeration externalities in a general spatial equilibrium model of a single-sector monocentric industrial city. *Ecol. Econ.* **2002**, *40*, 157–179. [CrossRef]
30. Andersson, M.; Lööf, H. Agglomeration and productivity: Evidence from firm-level data. *SSRN Electron. J.* **2011**. [CrossRef]
31. Chen, C.; Sun, Y.; Lan, Q.; Jiang, F. Impacts of industrial agglomeration on pollution and ecological efficiency-A spatial econometric analysis based on a big panel dataset of China's 259 cities. *J. Clean. Prod.* **2020**, *258*, 120721. [CrossRef]
32. Shen, N.; Peng, H. Can industrial agglomeration achieve the emission-reduction effect? *Socioecon. Plann. Sci.* **2021**, *75*, 100867. [CrossRef]
33. Zhang, L.; Rong, P.; Qin, Y.; Ji, Y. Does Industrial agglomeration mitigate fossil CO₂ emissions? An empirical study with spatial panel regression model. *Energy Procedia* **2018**, *152*, 731–737. [CrossRef]
34. Gao, C.; Gao, W.; Song, K.; Na, H.; Tian, F.; Zhang, S. Spatial and temporal dynamics of air-pollutant emission inventory of steel industry in China: A bottom-up approach. *Resour. Conserv. Recycl.* **2019**, *143*, 184–200. [CrossRef]
35. Ye, P.; Xia, S.; Xiong, Y.; Liu, C.; Li, F.; Liang, J.; Zhang, H. Did an ultra-low emissions policy on coal-fueled thermal power reduce the harmful emissions? Evidence from three typical air pollutants abatement in China. *Int. J. Environ. Res. Public Health* **2020**, *17*, 8555. [CrossRef] [PubMed]
36. Zheng, C.; Zhang, H.; Cai, X.; Chen, L.; Liu, M.; Lin, H.; Wang, X. Characteristics of CO₂ and atmospheric pollutant emissions from China's cement industry: A life-cycle perspective. *J. Clean. Prod.* **2021**, *282*, 124533. [CrossRef]
37. Liu, R.C.; Jiang, F.Y.; Liu, Z.Q. Comments on NO_x emission abatement in cement industry. *Adv. Mater. Res.* **2012**, *422*, 509–513. [CrossRef]
38. Ialongo, I.; Stepanova, N.; Hakkarainen, J.; Virta, H.; Gritsenko, D. Satellite-based estimates of nitrogen oxide and methane emissions from gas flaring and oil production activities in Sakha Republic, Russia. *Atmos. Environ. X* **2021**, *11*, 100114. [CrossRef]
39. Shimada, K.; Mizoguchi, S.; Hibino, G.; Matsuo, Y. A Study on the Effects on Local Air Quality from the Greenhouse Gas Mitigation Measures. *Environ. Syst. Res.* **2000**, *28*, 77–84. [CrossRef]
40. Liu, L.J.; Liang, Q.M. Changes to pollutants and carbon emission multipliers in China 2007–2012: An input-output structural decomposition analysis. *J. Environ. Manag.* **2017**, *203*, 76–86. [CrossRef]
41. Hermoso-Orzáez, M.J.; García-Alguacil, M.; Terrados-Cepeda, J.; Brito, P. Measurement of environmental efficiency in the countries of the European Union with the enhanced data envelopment analysis method (DEA) during the period 2005–2012. *Environ. Sci. Pollut. Res.* **2020**, *27*, 15691–15715. [CrossRef]
42. Xu, F.; Shu, C.; Tian, J.; Chen, L. A decade advance in eco-efficiency and cost-benefits of emissions reduction targeting fine chemical manufacturers. *J. Environ. Manag.* **2021**, *298*, 113476. [CrossRef]
43. Guo, Y.; Liu, W.; Tian, J.; He, R.; Chen, L. Eco-efficiency assessment of coal-fired combined heat and power plants in Chinese eco-industrial parks. *J. Clean. Prod.* **2017**, *168*, 963–972. [CrossRef]
44. Hu, W.; Guo, Y.; Tian, J.; Chen, L. Eco-efficiency of centralized wastewater treatment plants in industrial parks: A slack-based data envelopment analysis. *Resour. Conserv. Recycl.* **2019**, *141*, 176–186. [CrossRef]
45. Zhu, Y.; Xia, Y. Industrial agglomeration and environmental pollution: Evidence from China under new urbanization. *Energy Environ.* **2019**, *30*, 1010–1026. [CrossRef]
46. Yu, Y.; Deng, Y.R.; Chen, F.F. Impact of population aging and industrial structure on CO₂ emissions and emissions trend prediction in China. *Atmos. Pollut. Res.* **2018**, *9*, 446–454. [CrossRef]
47. Wang, X.; Luo, Y. Has technological innovation capability addressed environmental pollution from the dual perspective of FDI quantity and quality? Evidence from China. *J. Clean. Prod.* **2020**, *258*, 120941. [CrossRef]
48. Yu, Y.; Xu, W. Impact of FDI and R&D on China's industrial CO₂ emissions reduction and trend prediction. *Atmos. Pollut. Res.* **2019**, *10*, 1627–1635. [CrossRef]
49. Ngo, T.Q. How do environmental regulations affect carbon emission and energy efficiency patterns? A provincial-level analysis of Chinese energy-intensive industries. *Environ. Sci. Pollut. Res.* **2021**, 1–17. [CrossRef]
50. Grossman, G.; Krueger, A.B. Environmental impacts of a North American Free Trade Agreement. *CEPR Discuss. Pap.* **1992**, *2*, 223–250. [CrossRef]
51. Arellano, M.; Bond, S. Some tests of specification for panel data: Monte Carlo evidence and an application to employment equations. *Rev. Econ. Stud.* **1991**, *58*, 277–297. [CrossRef]
52. Blundell, R.; Bond, S. Initial conditions and moment restrictions in dynamic panel data models. *J. Econom.* **1998**, *87*, 115–143. [CrossRef]
53. Roodman, D. How to do xtabond2: An introduction to “difference” and “system” GMM in Stata. work. *Stata J.* **2009**, *9*, 86–136. [CrossRef]
54. Judd, C.M.; Kenny, D.A. Process analysis: Estimating mediation in treatment evaluations. *Eval. Rev.* **2016**, *5*, 602–619. [CrossRef]
55. Baron, R.M.; Kenny, D.A. The Moderator-Mediator variable distinction in social psychological research: Conceptual, strategic, and statistical considerations. *J. Pers. Soc. Psychol.* **1986**, *51*, 1173–1182. [CrossRef]
56. Zhao, X.; Lynch, J.G.; Chen, Q. Reconsidering Baron and Kenny: Myths and truths about mediation analysis. *J. Consum. Res.* **2010**, *37*, 197–206. [CrossRef]
57. MacKinnon, D.P.; Krull, J.L.; Lockwood, C.M. Equivalence of the mediation, confounding and suppression effect. *Prev. Sci.* **2000**, *1*, 173–181. [CrossRef] [PubMed]

58. Yanna, Z.; Gang, H.; Guisheng, Z.; Keyu, B.; Chaoyu, Y.; Xiangqian, W. Research on coupling coordination and spatial differentiation of new-type urbanization and ecological environment in Wanjiang demonstration area. *Geojournal* **2020**, 1–13. [CrossRef]
59. Li, W.; Wang, Y.; Xie, S.; Cheng, X. Coupling coordination analysis and spatiotemporal heterogeneity between urbanization and ecosystem health in Chongqing municipality, China. *Sci. Total Environ.* **2021**, 791, 148311. [CrossRef] [PubMed]
60. Liao, S.; Wu, Y.; Wong, S.W.; Shen, L. Provincial perspective analysis on the coordination between urbanization growth and resource environment carrying capacity (RECC) in China. *Sci. Total Environ.* **2020**, 730, 138964. [CrossRef] [PubMed]
61. Fan, W.; Wang, H.; Liu, Y.; Liu, H. Spatio-temporal variation of the coupling relationship between urbanization and air quality: A case study of Shandong Province. *J. Clean. Prod.* **2020**, 272, 122812. [CrossRef]
62. National Bureau of Statistics of China 2007–2018. *China Statistical Yearbook*; China Statistics Press: Beijing, China, 2018.
63. Ministry of Ecology and Environment of the People's Republic of China 2006–2015. *Annual Report on Environmental Statistics*; Ministry of Ecology and Environment: Beijing, China, 2015.
64. Ministry of Environmental Protection of the People's Republic of China 2007–2018. *China Environment Yearbook*; Ministry of Environmental Protection of the People's Republic of China: Beijing, China, 2018.
65. Levin, A.; Lin, C.F.; Chu, C.S.J. Unit root tests in panel data: Asymptotic and finite-sample properties. *J. Econom.* **2002**, 108, 1–24. [CrossRef]
66. Levin, A.; Lin, C.F. Unit root tests in panel data: Asymptotic and finite-sample integrated systems. *Econometrica* **1992**, 61, 783–820.
67. Im, K.S.; Pesaran, M.H.; Shin, Y. Testing for unit roots in heterogeneous panels. *J. Econom.* **2003**, 115, 53–74. [CrossRef]
68. Arellano, M.; Bover, O. Another look at the instrumental variable estimation of error-components models. *J. Econom.* **1995**, 68, 29–51. [CrossRef]
69. Fisher-Vanden, K.; Sue Wing, I. Accounting for quality: Issues with modeling the impact of R&D on economic growth and carbon emissions in developing economies. *Energy Econ.* **2008**, 30, 2771–2784. [CrossRef]
70. Yu, Y.; Du, Y. Impact of technological innovation on CO₂ emissions and emissions trend prediction on 'New Normal' economy in China. *Atmos. Pollut. Res.* **2019**, 10, 152–161. [CrossRef]
71. Pata, U.K.; Caglar, A.E. Investigating the EKC hypothesis with renewable energy consumption, human capital, globalization and trade openness for China: Evidence from augmented ARDL approach with a structural break. *Energy* **2021**, 216, 119220. [CrossRef]
72. Ahmed, Z.; Asghar, M.M.; Malik, M.N.; Nawaz, K. Moving towards a sustainable environment: The dynamic linkage between natural resources, human capital, urbanization, economic growth, and ecological footprint in China. *Resour. Policy* **2020**, 67, 101677. [CrossRef]
73. Yang, H.Y. A note on the causal relationship between energy and GDP in Taiwan. *Energy Econ.* **2000**, 22, 309–317. [CrossRef]

Article

Pollution Characteristics and Health Risk Assessment of VOCs in Jinghong

Jianwu Shi ^{1,2}, Yuzhai Bao ^{1,2}, Feng Xiang ^{3,*}, Zhijun Wang ^{1,2}, Liang Ren ¹, Xiaochen Pang ^{1,2}, Jian Wang ³, Xinyu Han ^{1,4,*} and Ping Ning ^{1,2}

¹ Faculty of Environmental Science and Engineering, Kunming University of Science and Technology, Kunming 650500, China; shijianwu@kust.edu.cn (J.S.); 20192207012@stu.kust.edu.cn (Y.B.); 20202207027@stu.kust.edu.cn (Z.W.); renliang@stu.kust.edu.cn (L.R.); 20192207085@stu.kust.edu.cn (X.P.); ningping58@sina.com (P.N.)

² National-Regional Engineering Center for Recovery of Waste Gases from Metallurgical and Chemical Industries, Kunming University of Science and Technology, Kunming 650500, China

³ Yunnan Ecological Environmental Monitoring Center, Kunming 650034, China; 3491192@qq.com

⁴ Faculty of Civil Engineering and Mechanics, Kunming University of Science and Technology, Kunming 650500, China

* Correspondence: ynemcs@163.com (F.X.); 20110020@kust.edu.cn (X.H.); Tel.: +86-13608846304 (F.X.); +86-15087150201 (X.H.)

Abstract: In order to investigate the seasonal variation in chemical characteristics of VOCs in the urban and suburban areas of southwest China, we used SUMMA canister sampling in Jinghong city from October 2016 to June 2017. Forty-eight VOC species concentrations were analyzed using atmospheric preconcentration gas chromatography–mass spectrometry (GC–MS). Then, regional VOC pollution characteristics, ozone formation potentials (OFP), source identity, and health risk assessments were studied. The results showed that the average concentration of total mass was $144.34 \mu\text{g}\cdot\text{m}^{-3}$ in the urban area and $47.81 \mu\text{g}\cdot\text{m}^{-3}$ in the suburban area. Alkanes accounted for the highest proportion of VOC groups at 38.11%, followed by olefins (36.60%) and aromatic hydrocarbons (25.28%). Propane and isoprene were the species with the highest mass concentrations in urban and suburban sampling sites. The calculation of OFP showed that the contributions of olefins and aromatic hydrocarbons were higher than those of alkanes. Through the ratio of specific species, the VOCs were mainly affected by motor vehicle exhaust emissions, fuel volatilization, vegetation emissions, and biomass combustion. Combined with the analysis of the backward trajectory model, biomass burning activities in Myanmar influenced the concentration of VOCs in Jinghong. Health risk assessments have shown that the noncarcinogenic risk and hazard index of atmospheric VOCs in Jinghong were low (less than 1). However, the value of the benzene cancer risk to the human body was higher than the safety threshold of 1×10^{-6} , showing that benzene has carcinogenic risk. This study provides effective support for local governments formulating air pollution control policies.

Keywords: volatile organic compounds; Jinghong city; ozone formation potentials; source identity; health risk

Citation: Shi, J.; Bao, Y.; Xiang, F.; Wang, Z.; Ren, L.; Pang, X.; Wang, J.; Han, X.; Ning, P. Pollution Characteristics and Health Risk Assessment of VOCs in Jinghong. *Atmosphere* **2022**, *13*, 613. <https://doi.org/10.3390/atmos13040613>

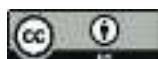
Academic Editors: Duanyang Liu, Honglei Wang and Kai Qin

Received: 3 March 2022

Accepted: 6 April 2022

Published: 11 April 2022

Publisher's Note: MDPI stays neutral with regard to jurisdictional claims in published maps and institutional affiliations.



Copyright: © 2022 by the authors. Licensee MDPI, Basel, Switzerland. This article is an open access article distributed under the terms and conditions of the Creative Commons Attribution (CC BY) license (<https://creativecommons.org/licenses/by/4.0/>).

1. Introduction

China's energy consumption has increased rapidly, and urban air environment problems have become increasingly prominent in recent years. Tropospheric ozone (O_3) has become one of the main pollutants affecting air quality. Volatile organic compounds (VOCs) have attracted widespread attention as important precursors of O_3 . VOCs refer to a class of organic gas compounds that exist in the air, including alkanes, aromatic hydrocarbons, olefins, halogenated hydrocarbons, and oxygenated hydrocarbons [1,2]. Extensive participation in atmospheric photochemical reactions leads to the formation of ozone and secondary organic aerosols (SOAs), which have a strong risk of carcinogenicity, which

is harmful to ambient air quality and human health [3,4]. Health brings threats such as respiratory damage, teratogenicity, and carcinogenicity [5,6].

Presently, various countries in the world have carried out VOCs-related research. China's research is mainly concentrated in the Beijing-Tianjin-Hebei and surrounding areas [7–10], Yangtze River Delta [11–13], Pearl River Delta [14–16], and other economically developed and densely populated areas of urban agglomerations, using offline or online monitoring analysis instruments and analysis methods to conduct related research. For example, Jay used proton transfer reaction time-of-flight mass spectrometry (PTR-TOF-MS) to perform highly time-resolved measurements in Beijing to study the characteristics and sources of volatile organic compounds (VOCs) [7]. Wei and Wang studied Handan, Hebei Province, a typical industrialized city in China; they conducted online measurements of VOCs and discussed their impact on PM_{2.5} in the atmosphere [8,9]. Gu analyzed the multiscale chemical characterization and source apportionment of volatile organic compounds (VOCs) in Tianjin, China, from 1 November 2018 to 15 March 2019 [10]. Wang conducted online measurements of VOCs in Nanjing during the epidemic and evaluated the impact of the COVID-19 lockdown on the mixing ratio and sources of VOCs [12]. Ma investigated the pollution characteristics of VOCs products from eight synthetic resin enterprises in Shanghai, China [13]. Wang conducted a field study on the specific VOC (including OVOC) emissions of six construction machinery and five inland ships in the Pearl River Delta (PRD) region [14].

Relatively less attention has been paid to the atmospheric environment in southwest China, especially in the border cities affected by Southeast and South Asia. Jinghong city is located in the south of Yunnan province, close to Myanmar, Laos, and other countries, with the characteristics of a tropical climate and dense vegetation. It is restricted by the natural geographical conditions of typical basin topography, less precipitation, high temperature, and more inversion weather in winter and low winds. Village units and residential edges have frequent straw and waste incineration, as well as downtown restaurants and barbecue stalls with no pollution control facilities. Surrounding the city, rubber and wood processing factories produce waste gases. Combined with this, vehicle use has risen in recent years; all of the above release emissions of nitrogen oxides (NO_x) and VOCs into the city and increase the production of ozone. Ozone is a secondary photochemical pollutant and greenhouse gas. It is formed by the reaction of NO_x and VOCs, and other precursors under high-intensity ultraviolet light. Favorable conditions for ozone generation are mainly found in suburban areas, where NO_x-rich air from windward urban agglomerations mix with VOCs emitted by trees and at high altitudes due to enhanced UV radiation [17]. Phytotoxic ozone has caused significant damage to terrestrial vegetation worldwide [18]. Dry deposition on plant surfaces (cuticle, bark), soil and stagnant water, and deposition through stomata into leaves leads to oxidative damage, which is the cause of carbon dioxide absorption in photosynthesis and decreased forest productivity [19,20].

In this study, VOCs, an important precursor of ozone, were taken as the research object, as well as VOC species concentration, ozone formation potentials, and health risks and sources. These were studied to provide a scientific basis for VOCs and ozone pollution control in this region.

2. Materials and Methods

2.1. VOCs Sampling

The atmospheric sampling sites of this study were the Municipal Environmental Protection Bureau and the Olive Dam Water Quality Automatic Monitoring Station of Jinghong. As shown in Figure 1, the Jinghong Municipal Environmental Protection Bureau is located in the city's urban center, where transportation is more frequent. The Olive Dam Water Quality Automatic Monitoring Station is located in the suburb, with relatively little human activity and transportation; it was taken as the suburban sampling control site. By sampling the urban and suburban areas, we can understand the difference in VOC species concentration in the suburban and urban areas of Jinghong City.

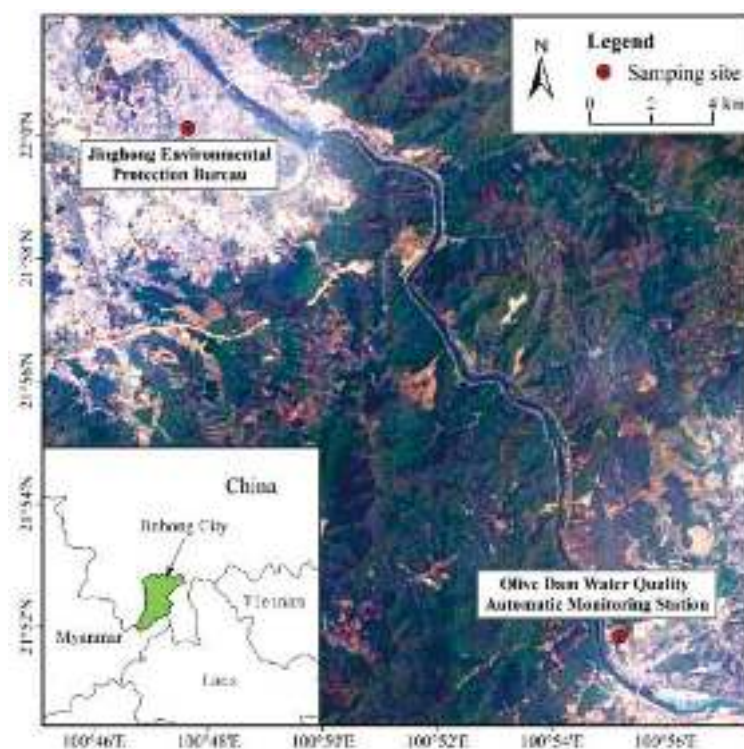


Figure 1. Sampling sites of VOCs in Jinghong.

2.2. Sample Collection and Component Analysis

According to the “Measuring Tank Sampling of Ambient Air Volatile Organic Compounds/Gas Chromatography-Mass Spectrometry (HJ759-2015)”, the air samples were collected using a 3.2 L stainless-steel sampling tank produced by Entech Corporation of the United States. The inner wall of the SUMMA canister was cut and silanized, a flow valve controlled the sampling inlet flow, and a SUMMA canister sample was collected every 2 h. Sampling occurred in October 2016 and March, April, May, and June 2017, with 5 consecutive days of sampling at the beginning of each month. Meteorological conditions such as air temperature, air pressure, and wind speed during the sampling period were monitored and recorded online at a height of 3 m through the Vantage Pro2™ wireless weather station (Davis Instruments, Hayward, CA, USA). The rainfall in Jinghong varies significantly from month to month (abundant rainfall from June to October each year), so this paper defines the samples collected in October 2016 and June 2017 as the rainy season samples, and the samples collected in March, April, and May 2017 as the dry season samples.

This study analyzed 58 VOC species (alkanes, olefins, and aromatic hydrocarbons) by atmospheric preconcentration gas-conjugated methods. The main instruments were the atmospheric preconcentrator (Entech 7100, Entech Instruments, Simi Valley, CA, USA)-GC (Agilent 6890N, Agilent Technologies, Roseville, CA, USA)-MS (Agilent 5973N, Agilent Technologies, Roseville, CA, USA), and the column was the GS-GASPRO with a size of 60 m × 0.32 μm. The SUMMA canister was first connected to the autosampler, and 400 mL of the sample was pumped into the preconcentrator. The sample was concentrated by dewatering and using carbon dioxide interferences such as a 3-stage cold trap; then, the sample was transferred to GC-MS for detection. The carrier gas was high-purity helium, and the heating procedure was: initial temperature of 35 °C, held for 15 min, heated to 150 °C at 5 °C·min^{−1}; held for 7 min; heated to 200 °C at 10 °C·min^{−1}, maintained for 4 min. The inlet temperature was 140 °C, the carrier gas velocity was 1.0 mL·min^{−1}, and the solvent delay time was 5.6 min. Mass spectrometry conditions: interface temperature, 250 °C; ion source temperature, 230 °C; mass spectrometry detector ion source type, electron bombardment ionization (EI), operated by full scan (SCAN), with scanning range of 35~300 u. Five standard curves of different concentration gradients were established using

a PAMS calibration gas mixture (Spectra Gases USA) with volume fractions of 0.25×10^{-9} , 0.5×10^{-9} , 1×10^{-9} , 2×10^{-9} , and 3×10^{-9} .

2.3. Quality Assurance and Control

The SUMMA canister was cleaned 3 times with high-purity nitrogen with an automatic de-tanker (Entech 3100) before each sampling and pumped to a vacuum state, so that the pressure in the tank was less than 50 millitorr, and was ready for later. A cleaned SUMMA canister was injected with high-purity nitrogen as a laboratory blank, and the laboratory blank test was performed before the analysis of each batch of samples.

In the sample analysis process, 1 parallel sample was analyzed for every 10 samples measured, and the relative deviation in the target in the parallel sample was $\leq 30\%$. The correlation coefficients of the target compounds in the standard curve were >0.995 . The retention time of the internal target in the sample deviated from the retention time of the internal standard in the continuous or recently drawn calibration curve of the day by no more than 20 s. Every 24 h, we analyzed the middle concentration point of the standard curve (1×10^{-9}); the measurement result was $\leq 30\%$ of the initial mass concentration value; otherwise, the cause should be found or redrawn. The results showed no contamination during sample handling and collection, as assured by the quality assurance and control (QC/QA) procedures.

2.4. Analytical Methods

2.4.1. Ozone Formation Potentials (OFP)

Ozone formation potentials can be used to evaluate the potential of VOCs emissions participating in the reaction to generate ozone, and they provided some guidance for the formulation of VOCs control measures. In this study, the maximum incremental reactivity method (MIR) was used to determine the contribution of active components and key species in VOCs to O_3 production [21,22], calculated as in Equation (1):

$$OFP_i = VOC_{si} \times MIR_i \quad (1)$$

where OFP_i represents the amount of ozone generation potential of species i in $\mu g \cdot m^{-3}$; VOC_{si} represents the mass concentration of species i in $\mu g \cdot m^{-3}$; and MIR_i represents the MIR coefficient of species i [23].

2.4.2. HYSPLIT Model

The HYSPLIT model (https://ready.arl.noaa.gov/HYSPLIT_traj.php, accessed on 1 July 2021) is a comprehensive model system developed by the National Oceanic and Atmospheric Centre (NOAA) and the Australian Meteorological Agency (BOM). It can be used to calculate and analyze processes such as airflow movement, sedimentation, air pollutant transport, and diffusion trajectory [24]. At present, it has been widely used to study the transmission routes and source analysis of air pollutants [25–28].

In this paper, TrajStat follow-up software [29] was used to analyze and study the backward trajectory of air masses in Jinghong. As the 500 m height wind field accurately reflects the average flow field characteristics of the boundary layer [27], the simulated height was chosen as 500 m. Jinghong ($100^\circ 47' 38''$ E, $22^\circ 00' 07''$ N) was the simulated receiving point, 8:00 (Beijing time) every day was the pushback start time, and the 72 h backward trajectory of the receiving point from July 2016 to June 2017 was calculated, to reflect the characteristics of the airflow.

2.4.3. Health Risk Assessment

In order to study the potential harm of VOCs to human health in Jinghong City, it is necessary to assess the health risk of VOCs. This study adopted a new health risk assessment method (EPA-540-R-070-002) proposed by the U.S. EPA in 2009 for inhaled route pollutants in specific places. The calculation formula is as follows:

$$EC = \frac{CA \times ET \times EF \times ED}{AT} \quad (2)$$

$$HQ = \frac{EC}{(RfC \times 1000)} \quad (3)$$

$$R = EC \times IUR \quad (4)$$

$$HI = \sum HQ_i \quad (5)$$

where EC is the exposure concentration in units of $\mu\text{g}\cdot\text{m}^{-3}$; CA is the ambient concentration of VOCs in $\mu\text{g}\cdot\text{m}^{-3}$; ET is the exposure time in $\text{h}\cdot\text{d}^{-1}$, with a value of 24; EF is the exposure frequency in $\text{d}\cdot\text{a}^{-1}$, with a value of 365; ED is the exposure time in a, with a value of 70; AT is the average time in h, with a value of $70 \times 365 \times 24$; HQ is the noncarcinogenic risk hazard quotient value; RfC is the reference concentration in $\mu\text{g}\cdot\text{m}^{-3}$; R is the lifetime risk value of carcinogenicity, IUR is the inhalation risk in $\mu\text{g}\cdot\text{m}^{-3}$; and HI is the hazard index. The RfC and IUR values are from the reference [30].

2.4.4. Data Sources

This study used daily averaged and hourly data on the concentrations of six atmospheric pollutants (SO_2 , NO_2 , CO, O_3 , $\text{PM}_{2.5}$, and PM_{10}) at two environmental monitoring stations in Jinghong from July 2016 to June 2017. Contaminant data were from the National Environmental Monitoring Center of China (<https://air.cnemc.cn:18007/>, accessed on 1 July 2021). The data used in the backward trajectory model were 2016–2017 Global Data Assimilation System (GDAS) data provided by the NCEP (National Center for Environmental Prediction). Meteorological data were derived from the National Meteorological Science Data Sharing Service Platform (<http://data.cma.cn/>, accessed on 1 July 2021).

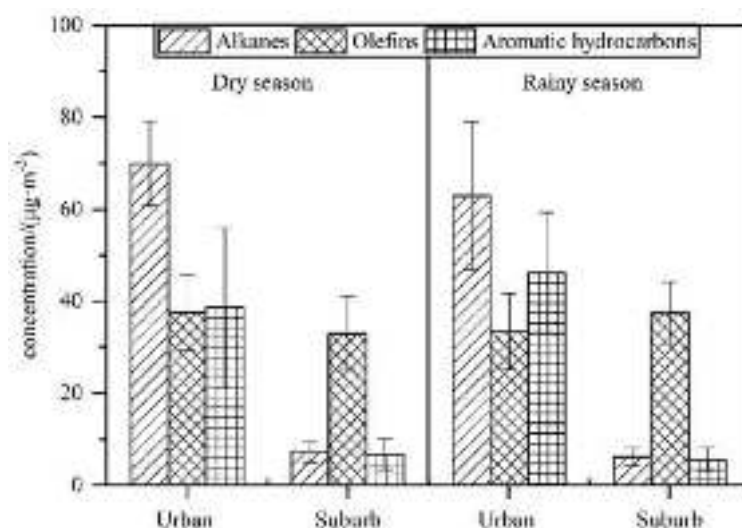
3. Results and Discussions

3.1. Species Composition Characteristics of VOCs

During the sampling period, 58 VOC compounds (alkanes, olefins, and aromatic hydrocarbons) were detected in the atmosphere at the urban and suburban monitoring sites in Jinghong, and a total of 48 VOC species were detected. As shown in Table 1, the total concentration of VOCs was $(144.34 \pm 36.15) \mu\text{g}\cdot\text{m}^{-3}$ at the urban sampling site, which was much higher than at the suburban sampling site ($48.21 \pm 12.55 \mu\text{g}\cdot\text{m}^{-3}$). Compared with the suburban sampling site, the urban sampling site in Jinghong was closer to various anthropogenic emission sources, which are susceptible to factors such as the emission of VOC sources of human activities. These emission sources have the characteristics of continuity, concentration, and high concentration, which make the concentration of VOCs in urban areas highly accumulated. As shown in Figure 2, in the dry season, the concentrations of alkanes, olefins, aromatic hydrocarbons, and TVOCs in the urban areas of Jinghong were $(69.94 \pm 9.25) \mu\text{g}\cdot\text{m}^{-3}$, $(37.53 \pm 8.22) \mu\text{g}\cdot\text{m}^{-3}$, $(38.72 \pm 17.32) \mu\text{g}\cdot\text{m}^{-3}$, and $146.19 \mu\text{g}\cdot\text{m}^{-3}$, respectively, with those in the suburban areas were $(7.40 \pm 2.34) \mu\text{g}\cdot\text{m}^{-3}$, $(32.22 \pm 7.99) \mu\text{g}\cdot\text{m}^{-3}$, $(6.74 \pm 3.43) \mu\text{g}\cdot\text{m}^{-3}$, and TVOCs $47.15 \mu\text{g}\cdot\text{m}^{-3}$, respectively. During the rainy season, the concentrations of alkanes, olefins, aromatic hydrocarbons, and TVOCs in urban areas were $(62.93 \pm 16.13) \mu\text{g}\cdot\text{m}^{-3}$, $(33.44 \pm 8.22) \mu\text{g}\cdot\text{m}^{-3}$, $(46.13 \pm 13.17) \mu\text{g}\cdot\text{m}^{-3}$, and $142.5 \mu\text{g}\cdot\text{m}^{-3}$, respectively, and those in suburban areas were $(6.21 \pm 1.99) \mu\text{g}\cdot\text{m}^{-3}$, $(37.48 \pm 6.69) \mu\text{g}\cdot\text{m}^{-3}$, $(5.58 \pm 2.65) \mu\text{g}\cdot\text{m}^{-3}$, and $49.27 \mu\text{g}\cdot\text{m}^{-3}$, respectively. The VOC groups at the urban sampling site were mainly alkanes, while the VOC groups at the suburban sampling site were mainly olefins. A nonparametric test (one-way analysis of variance, 95% confidence level) showed there were no significant differences in VOCs concentration and species composition between the dry season and rainy season ($p > 0.05$). The concentration of aromatic hydrocarbon groups in the urban sampling site was higher than that in the dry season, which may be related to the increase in benzene emissions due to the cooling of motor vehicle air conditioning and cooling in the rainy season.

Table 1. Concentration levels of atmospheric VOCs in different cities.

City	Period	Number of VOCs Species	Concentration of VOCs/($\mu\text{g}\cdot\text{m}^{-3}$)	Alkanes/(%)	Olefins/(%)	Aromatic Hydrocarbons/(%)	Reference
urban of Jinghong	2016~2017	48	144.35 ± 36.15	46.03	24.58	29.39	This study
suburbs of Jinghong			48.21 ± 12.55	14.12	73.11	12.78	
Kunming	2014	35	30.22	68.58	7.78	23.64	[31]
Guangzhou	2009	31	114.50	59.97	15.18	39.24	[32]
Beijing	2016	99	44.00	36.80	7.00	11.80	[33]
Chengdu	2012	59	108 ± 52.43	47.08	11.53	44.52	[34]
Monterrey (Mexico)	2011	29	80.14	62.88	9.55	24.67	[35]
Nagoya (Japan)	2003~2004	48	62.28	50.08	9.28	40.64	[36]

**Figure 2.** Concentration of alkanes, olefins, and aromatics in urban and suburban areas of Jinghong.

The comparison of VOC species concentrations in different atmospheric environments in Jinghong and other cities is shown in Table 1. The data sample collection equipment used a Suma tank with a volume of 6 L, and about 28 effective samples were in Kunming. The samples were collected with stainless-steel tubes, and about 12 effective samples were collected in Chengdu. VOC observations adopted syntech spectra gc955 online monitoring systems produced by synspec company in the Netherlands, and about 220 groups of effective data were from Guangzhou. The VOC sampling was conducted at the superstation for atmospheric environmental monitoring in Beijing Normal University, and the amount of valid data was not mentioned in Beijing. Samples were collected using ENTECH (Malvern, PA, USA) summa electro-polished stainless-steels container (6 L) following the United States Environmental Protection Agency analytical method (US EPA, 1999), and about 56 effective samples were collected in Monterey; an automatic measurement system for Non-methane Hydrocarbons (NMHCs) was constructed. The system was set-up at the Hydrospheric Atmospheric Research Center (HyARC) building in Nagoya University, and the amount of valid data was not mentioned in Nagoya (Japan). The sampling areas of the above cities were urban areas. Table 1 shows that there was a significant difference in the proportion of species between the urban and suburban area of Jinghong City. The concentration in the urban area was about three times that in the suburbs. The highest proportion of VOC species in the urban area was alkane, 46.03%, followed by olefin and aromatic hydrocarbon species, accounting for 24.58% and 29.39%, respectively. Its species composition was different from those of Kunming, Guangzhou, Beijing, Chengdu, Monterey, Nagoya, and other cities. The proportion of olefins in the suburbs of Jinghong was highest (73.11%), followed by alkanes and aromatic hydrocarbons (14.12% and 12.78%, respectively), which may be related to the dense vegetation in the suburbs monitored by this study. During the whole observation period, the average concentration of VOCs in the

urban area of Jinghong city reached $(144.35 \pm 36.15) \mu\text{g}\cdot\text{m}^{-3}$, which was higher than those in other comparison cities, showing a high concentration level.

Figure 3 shows the distribution of VOC species concentrations in the dry and rainy seasons of the urban and suburban sampling site in Jinghong during the sampling period. As shown in Figure 2, the propane concentrations at the urban sampling site were highest during the entire sampling period. Higher alkane concentrations included propane, n-butane, isobutane, and isoamylene; alkene concentrations included isoprene and propylene species. Higher aromatic hydrocarbon concentrations were mainly toluene, which was much higher than the concentration of suburban points, reflecting the more significant impact of urban motor vehicle exhaust on the concentration of atmospheric VOCs. The concentration of isoprene in the suburban monitoring points was more prominent, which is closely related to suburban monitoring sites moving away from anthropogenic sources and closer to natural sources such as dense forests. This was followed by propane, probably related to petrochemical emissions. The concentrations of other species were low. The spectral characteristics of VOCs at the two sampling sites in Jinghong urban and suburban areas had a large difference, indicating that there were certain differences in the sources of VOCs between the two sampling sites in the city and suburb.

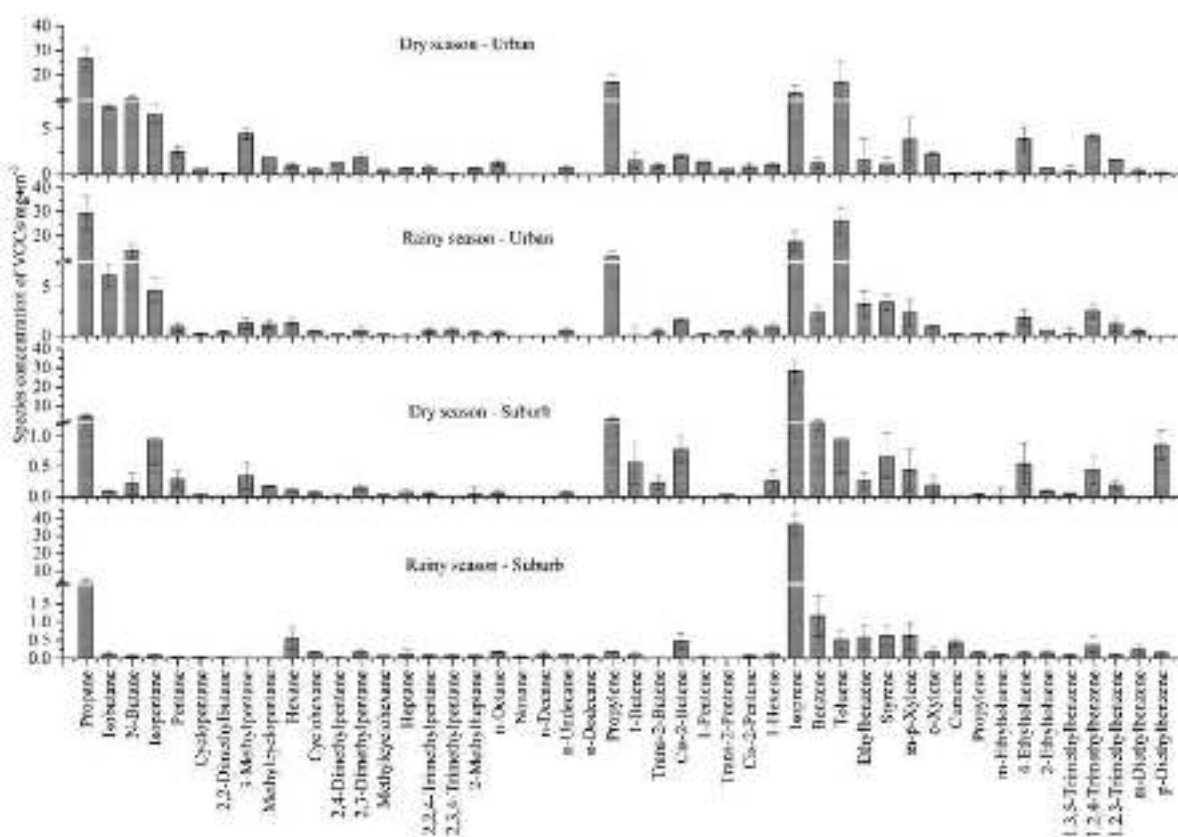


Figure 3. The level profiles of VOCs concentrations in Jinghong.

3.2. Ozone Formation Potentials (OFP) of VOCs

Table 2 lists the OFP values of VOCs species at urban and suburban sampling sites in Jinghong. The OFP of total VOCs in the atmosphere in the urban area of Jinghong was $588.07 \mu\text{g}\cdot\text{m}^{-3}$ and $535.38 \mu\text{g}\cdot\text{m}^{-3}$ in the dry season and $535.38 \mu\text{g}\cdot\text{m}^{-3}$, respectively, which was much higher than that of the suburb, indicating that the ozone generation capacity in the urban area of Jinghong was much higher than that in the suburban area. In the dry season, urban alkanes, olefins, and aromatic hydrocarbons accounted for 11.49%, 57.73%, and 30.78% of the OFP, respectively, and correspondingly accounted for 1.82%, 89.70%, and 8.48% of the OFP in the suburb. During the rainy season, alkanes, olefins, and aromatic hydrocarbons

accounted for 10.10%, 56.91%, and 32.99% of the OFP in the urban atmosphere, respectively, compared with 1.14%, 92.41%, and 6.45% in the suburb during the same period. Olefins are the key species of ozone formation potential in Jinghong, and the OFP ranking has always been manifested as: olefins > aromatic hydrocarbons > alkanes. The contribution of olefins to ozone generation in the suburban atmosphere is higher than that in urban areas, indicating that the suburban ozone generation is mainly affected by olefins.

Table 2. Potential Ozone Formation of VOCs in Jinghong.

Species	MIR Value	Ozone Formation Potential ($\mu\text{g}\cdot\text{m}^{-3}$)			
		DU	DS	RU	RS
Propane	0.48	12.75	2.21	14.18	1.92
Isobutane	1.21	8.99	0.11	7.47	0.14
N-Butane	1.02	10.64	0.22	14.03	0.06
Isopentane	1.38	9.17	1.31	6.45	0.11
Pentane	1.04	2.60	0.30	0.94	0.04
Cyclopentane	1.38	0.77	0.05	0.32	0.05
2,2-Dimethylbutane	0.82	0.10	0.01	0.3	0.02
3-Methylpentane	1.50	6.75	0.51	1.91	0.02
Methylcyclopentane	2.80	5.26	0.49	3.16	0.04
Hexane	0.98	0.94	0.11	1.27	0.54
Cyclohexane	1.28	0.72	0.09	0.58	0.20
2,4-Dimethylpentane	1.50	1.86	0.02	0.21	0.04
2,3-Dimethylpentane	1.31	2.40	0.20	0.71	0.22
Methylcyclohexane	2.80	1.48	0.10	0.38	0.20
Heptane	0.81	0.55	0.06	0.03	0.11
2,2,4-Trimethylpentane	0.93	0.71	0.05	0.4	0.07
2,3,4-Trimethylpentane	1.60	0.16	0.00	0.96	0.11
2-Methylheptane	0.96	0.63	0.04	0.34	0.06
n-Octane	0.60	0.74	0.04	0.22	0.11
Nonane	0.54	-	-	-	0.02
n-Decane	0.46	-	-	-	0.05
n-Undecane	0.42	0.31	0.03	0.22	0.05
n-Dodecane	0.38	-	-	-	0.02
Total alkanes		67.55	5.95	54.08	4.20
propylene	9.40	157.26	27.68	108.47	1.78
1-Butene	8.90	13.62	-	0.48	0.88
Trans-2-Butene	10.00	9.50	-	4	0.13
Cis-2-Butene	10.00	20.60	7.84	16.57	4.77
1-Pentene	6.20	8.68	0.00	0.89	0.16
Trans-2-Pentene	8.80	4.95	0.34	4.05	0.05
Cis-2-Pentene	8.80	7.88	0.00	5.78	0.59
1-Hexene	4.40	4.62	1.13	3.92	0.46
Isoprene	9.10	112.39	256.62	160.52	332.15
Total olefins		339.50	293.60	304.67	340.97
Benzene	0.42	0.52	0.82	0.98	0.49
Toluene	2.70	44.70	2.56	70.68	1.36
Ethylbenzene	2.70	4.24	0.72	8.74	1.55
Styrene	1.95	7.48	4.36	22.25	3.97
m-p-Xylene	7.40	7.45	0.87	4.6	1.20
o-Xylene	6.50	17.01	1.48	7.09	1.16
Cumene	2.20	0.90	0.09	1.56	2.85
Propylene	2.10	0.49	0.08	0.55	0.34
m-Ethyltoluene	7.20	0.61	0.04	0.55	0.20
4-Ethyltoluene	7.20	28.10	3.88	13.37	1.08
2-Ethyltoluene	7.20	4.86	0.67	4.15	1.08
1,3,5-Trimethylbenzene	10.10	2.99	0.39	1.8	0.67
1,2,4-Trimethylbenzene	8.87	42.20	4.50	25.86	3.83
1,2,3-Trimethylbenzene	8.90	14.63	1.76	10.38	0.96
m-Diethylbenzene	6.45	3.34	-	4.09	2.09
p-Diethylbenzene	6.45	1.51	5.51	-	0.98
Total aromatic hydrocarbons		181.01	27.75	176.64	23.81
Total VOCs		588.07	327.30	535.38	368.98

DU: Dry season—Urban; DS: Dry season—Suburb; RU: Rainy season—Urban; RS: Rainy season—Suburb.

From the analysis of specific VOCs compounds, in the dry season, the top 12 substances with the highest OFP in the atmosphere of Jinghong were propylene, isoprene, toluene,

1,2,4-trimethylbenzene, p-ethyltoluene, cis-2-butene, o-xylene, 1,2,3-trimethylbenzene, 1-butene, propane, n-butane, and trans-2-butene, and their mass concentration accounts for 67.86% of total volatile organic compounds (TVOCs). The top 12 substances in the suburban area regarding OFPs were isoprene, propylene, cis-2-butene, p-diethylbenzene, 1,2,4-trimethylbenzene, styrene, p-ethyltoluene, toluene, propane, 1,2,3-trimethylbenzene, o-xylene, and isopentane, which accounted for 88.75% of the TVOCs by mass. The ozone generation accounted for 97.28% of the total OFPs. In the rainy season, the top 12 substances of OFPs in the urban air were isoprene, propylene, toluene, 1,2,4-trimethylbenzene, styrene, cis-2-butene, propane, n-butane, p-ethyltoluene, 1,2,3-trimethylbenzene, ethylbenzene, and isobutane, which accounted for 83.34% of TVOCs by mass and 88.26% of total OFP by ozone generation. The top 12 substances of OFPs in the suburb were isoprene, cis-2-butene, styrene, 1,2,4-trimethylbenzene, isopropylbenzene, m-diethylbenzene, propane, propylene, ethylbenzene, toluene, p- and m-xylene, and o-xylene, which accounted for 90.69% of the TVOCs by mass and 97.20% of the total OFPs by ozone potential. Overall, isoprene accounted for the highest percentage of OFP in Jinghong, indicating that natural vegetation emission sources in Jinghong contributed prominently to ozone, followed by toluene, propylene, m-p-xylene, and other motor vehicle exhaust emissions that contributed significantly to ozone generation.

3.3. Source Analysis of VOCs

3.3.1. Ratio of Specific Species

The ratio of toluene to benzene is commonly used to determine the sources of traffic emissions, fuel combustion, and industrial and solvent use in the current regional atmospheric environment [37–40]. Isopentane and n-pentane have similar chemical reactions with free radicals, and their ratios can also be used to indicate different sources [38,41,42]. The ratio of m/p-xylene to ethylbenzene is often used to evaluate the degree of aging of gas clusters [42–44], and the length of photochemical age. Ethylbenzene is less reactive than m/p-xylene and the ratio decreases in atmospheric chemical reactions where m/p-xylene is consumed faster—the smaller the ratio, the higher the degree of aging of the gas cluster. Moreover, BTEX pollution may be affected by regional transmission [45]. Table 3 shows the degree of air mass aging for m- and p-xylene and ethylbenzene for the ranges of benzene to toluene and isopentane to n-pentane ratios, respectively, corresponding to the pollution sources. Benzene to toluene, isopentane to n-pentane, and m-p-xylene to ethylbenzene ratios were selected for the study; additionally, the emission share of isoprene was considered to study the emissions from natural sources, where a larger ratio indicates that the air mass is fresher, and a smaller ratio indicates that the air mass is aging.

Table 3. Ratio data of benzene to toluene and isopentane to n-pentane.

Characteristic Species Ratio	Value	Source	Reference
Benzene/Toluene	0.00–0.20	solvent usage	[39]
	0.50–0.60	vehicle emissions	
	1.05–2.20	coal emissions	
	2.50	biomass burning	
Isopentane/n-pentane	0.56–0.80	coal emissions	[41]
	1.50–3.00	liquid gasoline	
	1.84–4.60	fuel volatilization	
	2.93	motor vehicle exhaust	

Jinghong is located at the southern tail end of the longitudinal valley of the Hengduan Mountains, which has a tropical and subtropical humid monsoon climate with high precipitation and dense vegetation covering a wide area. As shown in Table 4, the concentration of isoprene in the suburban area (59.80% in the dry season and 74.10% in the rainy season) was higher than that in the urban area (8.45% in the dry season and 12.38% in the rainy season), indicating that the release of large amounts of VOCs from dense vegetation in

the suburb had an important impact on VOCs in the ambient air, and isoprene emission from vegetation exponentially increased with sunlight and temperature on rainy days. The benzene/toluene ratios of 2.42 and 2.70 in the dry and rainy seasons in the suburban area, respectively, showed that fresh emissions or exhaust emissions and biomass burning were the primary source. The ratios of 0.09 and 0.10 in the dry and rainy seasons in the urban area, respectively, which were less than 0.2, showed that solvent use was the primary source. From the ratios of isopentane/n-pentane, it shows that the ratios of 3.24 and 2.10 for the dry and rainy seasons in suburban areas, respectively, were mainly influenced by gasoline fuel volatilization, and the ratios of 2.66 and 5.19 for the dry and rainy seasons in urban areas, respectively, were mainly influenced by motor vehicle exhaust and fuel volatilization. The ratio of M-p-xylene/Ethylbenzene was small in the urban and suburban areas in the rainy season, which means that the air mass was relatively aging. In addition to local emissions, some of the benzene series pollution came from regional transmission. In the dry season, the ratio between urban and suburban areas was bigger, which means that the air mass was relatively fresh, and the pollution was mainly transmitted locally.

Table 4. Species ratio in dry and rainy seasons in urban and suburban areas of Jinghong.

Area	Benzene/Toluene	Isopentane/ n-Pentane	Isoprene/TVOCs	M-p-Xylene/Ethylbenzene
DU	0.09	2.66	8.45%	2.44
RU	0.10	5.19	12.38%	0.73
DS	2.42	3.24	59.80%	1.67
RS	2.70	2.10	74.10%	1.07

DU: Dry season—Urban; DS: Dry season—Suburb; RU: Rainy season—Urban; RS: Rainy season—Suburb; TVOCs: Total Volatile Organic Compounds.

3.3.2. The Long-Range Transport

As shown in Figure 4, the incoming air masses during the year of the sampling period were resolved using the HYSPLIT model to track the trajectories of air masses arriving in the region in the past 72 h. The air masses from the Southwest were the most abundant in the region. Almost all air masses originated from Southeast Asian countries, with the most air masses coming from Myanmar, accounting for the most southwestern air mass transport (Cluster 1 air masses, 48.09%) and the lowest transport altitude (pressure above 870 hPa).

The trajectory air masses in different directions may contain different levels of pollutants. The backward trajectory clustering and pollutant concentration information were combined to analyze the influence of each trajectory air mass on pollutants in the study area. The results are shown in Table 5. The pollutant concentrations in different trajectory air masses varied widely, with the largest values of pollutants being SO₂, NO₂, CO, O₃, PM_{2.5}, and PM₁₀ in cluster 2 and the second largest values in cluster 5, mainly from the central region of Myanmar, becoming the most important transport path affecting the atmospheric pollutant concentrations in Jinghong. The airflow near Thailand and Laos (clusters 1 and 4) had the lowest ozone concentration values, compared to the other airflow (from Myanmar) trajectories, which had higher ozone concentration values, probably related to the more frequent biomass burning activities in Myanmar. It can be speculated that the outbound transport of VOCs may be mainly influenced by the transport from Myanmar.

3.4. Health Risk Assessment of VOCs

Benzene, toluene, ethylbenzene, m/p-xylene, and o-xylene are the important VOCs species in the atmosphere of Jinghong, and the proportion of aromatic hydrocarbons was ~58.70%. Table 6 compares the noncarcinogenic and carcinogenic risks of BTEX (benzene, toluene, ethylbenzene, m/p-xylene, o-xylene) mass concentration in Jinghong with other cities. The results show that the noncarcinogenic risk values of benzene > m/p-xylene > o-xylene > ethylbenzene > toluene in both the dry and rainy season of suburban sampling

sites, and benzene > m/p-xylene > o-xylene > toluene > ethylbenzene in both the dry and rainy season of urban sampling sites, ranging from 1.01×10^{-4} to 7.75×10^{-2} , were within the safe range ($HQ < 1$) as determined by the US EPA. The lifetime carcinogenic risk value of benzene ranged from 9.02×10^{-6} to 1.82×10^{-5} , which is higher than the safety range ($R < 1.00 \times 10^{-6}$) as determined by the US EPA. These results indicate the existence of carcinogenic risk and the possibility of inducing lymphatic system immune diseases and leukemia in humans exposed to the environment for an extended time, which should be taken more seriously.

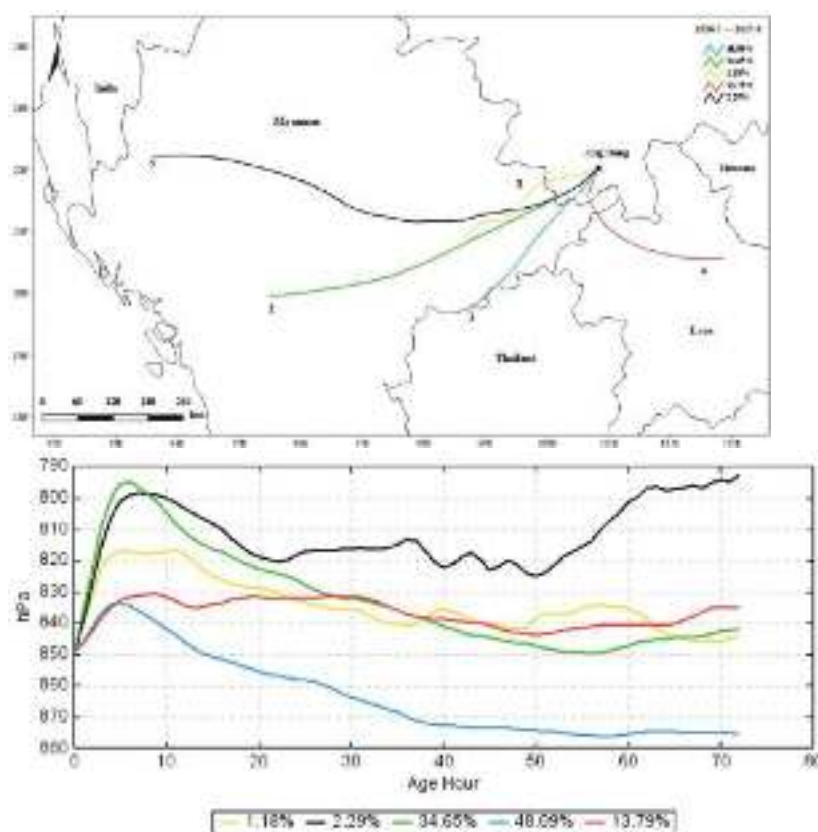


Figure 4. Trajectory clustering from July 2016 to June 2017.

Table 5. Statistical results of various trajectory pollutant concentrations from July 2016 to June 2017 in Jinghong.

Trajectory	Frequency of Occurrence/ (%)	SO ₂ / (μg·m ⁻³)	NO ₂ / (μg·m ⁻³)	CO/ (mg·m ⁻³)	O ₃ / (μg·m ⁻³)	PM _{2.5} / (μg·m ⁻³)	PM ₁₀ / (μg·m ⁻³)
1	48.09	6.83	13.85	0.70	36.21	20.01	39.45
2	34.65	8.90	20.08	0.81	50.84	34.65	61.78
3	1.18	6.56	14.38	0.72	40.85	22.06	42.71
4	13.79	6.38	13.48	0.73	29.85	19.14	37.27
5	2.29	7.89	20.82	0.78	49.65	34.45	57.64

The changing trend of the noncarcinogenic risk quotient in Jinghong shows that benzene and toluene had higher noncarcinogenic risk quotient values, which was the same as those of Guangzhou [32] and Beijing [46]. However, it was shown that benzene and xylene had higher noncarcinogenic risk quotients in Chengdu [34] and Xiamen [47], while xylene had higher quotients in Lanzhou [48], and benzene had a higher quotient in Port Moody (Canada), Burnaby South (Canada) [49], and Tabriz (Iran) [50]. In this study, HI values were higher in urban areas than in suburban areas, and lower in Jinghong than in other cities. The lifetime carcinogenic risk of benzene was low compared to other cities,

except for the dry season suburban area and rainy season urban area, which were higher than that of the residential sampling site in Xiamen (1.23×10^{-5}). Overall, it was shown that the health risk level in Jinghong was lower than its urban counterparts, However, it should be noted that the carcinogenic risk value of benzene in this region has exceeded the safety threshold. Therefore, it is necessary to increase the control of benzene emissions to reduce its carcinogenic risk.

Table 6. Comparison of noncarcinogenic and carcinogenic risks of BTEX in Jinghong with other cities.

Sampling Site	R (Benzene)	HQ					HI	Reference
		Benzene	Toluene	Ethylbenzene	m/p-Xylene	O-Xylene		
dry season in suburb of Jinghong	1.52×10^{-5}	6.48×10^{-2}	1.90×10^{-4}	2.68×10^{-4}	4.48×10^{-3}	2.00×10^{-3}	7.18×10^{-2}	This work
dry season in urban of Jinghong	9.62×10^{-6}	4.11×10^{-2}	3.31×10^{-3}	1.57×10^{-3}	3.82×10^{-2}	2.30×10^{-2}	1.07×10^{-1}	
rainy season in suburb of Jinghong	9.02×10^{-6}	3.85×10^{-2}	1.01×10^{-4}	5.74×10^{-4}	6.16×10^{-3}	1.57×10^{-3}	4.70×10^{-2}	
rainy season in urban of Jinghong	1.82×10^{-5}	7.75×10^{-2}	5.24×10^{-3}	3.24×10^{-3}	2.36×10^{-2}	9.57×10^{-3}	1.91×10^{-1}	
Guangzhou	5.34×10^{-5}	2.28×10^{-1}	3.95×10^{-1}	4.26×10^{-3}	3.06×10^{-2}	2.42×10^{-2}	2.91×10^{-1}	[32]
urban area of Chengdu	6.77×10^{-5}	2.89×10^{-1}	2.36×10^{-3}	3.34×10^{-3}	1.18×10^{-1}	3.38×10^{-2}	4.47×10^{-1}	[34]
traffic area of Chengdu	6.98×10^{-5}	2.98×10^{-1}	3.09×10^{-3}	3.19×10^{-3}	9.08×10^{-2}	3.38×10^{-2}	4.29×10^{-1}	
Beijing	4.19×10^{-5}	1.57×10^{-1}	2.39×10^{-1}	3.29×10^{-3}	8.06×10^{-3}	3.53×10^{-3}	1.96×10^{-1}	[46]
residential area of Xiamen	1.23×10^{-5}	5.25×10^{-2}	9.73×10^{-4}	2.37×10^{-3}	1.63×10^{-2}	1.13×10^{-2}	8.34×10^{-2}	[47]
industrial area of Xiamen	3.08×10^{-5}	1.32×10^{-1}	4.29×10^{-3}	7.98×10^{-3}	5.57×10^{-2}	4.36×10^{-2}	2.43×10^{-1}	
lanzhou	8.09×10^{-6}	3.46×10^{-2}	1.27×10^{-4}	4.07×10^{-4}	6.18×10^{-3}	2.76×10^{-3}	4.42×10^{-2}	[48]
Port Moody (Canada)	-	2.02×10^{-1}	9.17×10^{-3}	2.62×10^{-4}	-	-	2.02×10^{-1}	[49]
Burnaby South (Canada)	-	1.51×10^{-1}	6.29×10^{-3}	1.32×10^{-4}	-	-	1.51×10^{-1}	
Tabriz (Iran)	-	1.07×10^{-1}	1.29×10^{-3}	-	-	-	2.21×10^{-1}	[50]

“-” means that there are no such data in the references.

4. Conclusions

In this study, VOCs samples were collected in Jinghong and analyzed for their mass concentration, ozone formation potential, source identity, and health risk assessments in dry and rainy seasons. During the sampling period, a total of 48 VOC species were detected at the urban and suburban monitoring sites. In the dry season, the TVOCs concentration was $146.19 \mu\text{g}/\text{m}^3$ in the urban area and $47.15 \mu\text{g}/\text{m}^3$ in the suburban areas. In the rainy season, the TVOCs concentration was $142.5 \mu\text{g}/\text{m}^3$ in the urban area and $49.27 \mu\text{g}/\text{m}^3$ in the suburban area. TVOCs in urban areas were much higher than those in suburbs, which was related to human activities. The concentration of VOCs in the dry season at the urban sampling site was higher than in the rainy season, while at the suburban sampling sites, the concentration in the rainy season was higher than that in the dry season. These results may be related to the emission of more olefins in the rainy season when the vegetation is dense and grows vigorously.

The species with high concentrations of atmospheric VOCs in Jinghong were propane, toluene, propylene, and isoprene, and their OFPs were olefins > aromatic hydrocarbons > alkanes. The species with the highest OFP was isoprene, indicating that the surrounding dense vegetation contributes significantly to the generation of O_3 . The ratio of specific species was used to analyze

the primary sources of VOCs in the atmosphere of the main urban area of Jinghong: plant sources, motor vehicle exhaust, and oil and gas volatilization; combined with the study of air mass trajectories, the transmission of biomass combustion sources in the Myanmar region may influence VOCs in the study area. The health risk of VOCs in the main urban area of Jinghong was generally lower than those of other cities, and the noncarcinogenic risk was within the safety threshold. However, benzene's lifetime carcinogenic risk value in the atmosphere exceeded the safety range ($R < 1.00 \times 10^{-6}$), and there was a particular carcinogenic risk. The control of local VOC sources should be strengthened appropriately to reduce benzene emissions.

In this paper, chemical composition and source characteristics of VOCs in a plateau border city were first studied, and the main sources of VOCs in Jinghong were resolved. The results can provide scientific data to support VOCs pollution control in local and similar cities. In addition, due to high vegetation coverage, forest and vehicle exhaust emissions were prone to produce phytotoxic ozone, which reduced forest productivity and damaged terrestrial vegetation. Therefore, the local government needs to take corresponding measures. Biomass burning activities in Myanmar had an impact on VOCs concentration changes in Jinghong, and cross-border pollution issues also need attention, which has a certain guiding significance for our government to carry out international cooperation projects in Southeast Asia.

Author Contributions: Conceptualization, J.S. and X.H.; investigation, Z.W. and L.R.; resources, J.W. and F.X.; data curation, X.P.; writing—original draft preparation, Y.B.; writing—review and editing, J.S. and X.H.; supervision, P.N. All authors have read and agreed to the published version of the manuscript.

Funding: This research was partially supported by the National Natural Science Foundation of China (grant number 21966016), the National Key R&D Program of China (grant number 2019YFC0214405), and the Science and Technology Special Project of Demonstration Zone for National Sustainable Development in Yunnan (grant number. 202104AC100001-A14).

Institutional Review Board Statement: Not applicable.

Informed Consent Statement: Not applicable.

Data Availability Statement: The data used in this paper can be provided by Jianwu Shi (shijianwu@kust.edu.cn).

Acknowledgments: This work was partially supported by the National Natural Science Foundation of China, the National Key R&D Program of China (No. 2019YFC0214405), and the Science and Technology Special Project of Demonstration Zone for National Sustainable Development in Yunnan.

Conflicts of Interest: The authors declare that there are no competing financial interests that could inappropriately influence the contents of this manuscript.

References

1. Kamal, M.S.; Razzak, S.A.; Hossain, M. Catalytic oxidation of volatile organic compounds (VOCs)—A review. *Atmos. Environ.* **2016**, *140*, 117–134. [CrossRef]
2. Yang, C.T.; Miao, G.; Pi, Y.H.; Xia, Q.P.; Wu, J.L.; Li, Z.; Xiao, J. Abatement of various types of VOCs by adsorption/catalytic oxidation: A review. *Chem. Eng. J.* **2019**, *370*, 1128–1153. [CrossRef]
3. Huang, C.; Lou, D.; Hu, Z.Y.; Feng, Q.; Chen, Y.R.; Chen, Y.H.; Tan, P.J.; Yao, D. A PEMS study of the emissions of gaseous pollutants and ultrafine particles from gasoline- and diesel-fueled vehicles. *Atmos. Environ.* **2013**, *77*, 703–710. [CrossRef]
4. Sukul, P.; Schubert, J.K.; Oertel, P.; Kamysek, S.; Taunk, K.; Trefz, P.; Miekisch, W. FEV manoeuvre induced changes in breath VOC compositions: An unconventional view on lung function tests. *Sci. Rep.* **2016**, *17*, 28029. [CrossRef]
5. Zhao, Q.; Wang, Q.; Li, Y.; Ning, P.; Tian, S. Influence of volatile organic compounds (VOCs) on pulmonary surfactant monolayers at air-water interface: Implication for the pulmonary health. *Colloid. Surf.* **2019**, *562*, 402–408. [CrossRef]
6. Jiménez-Garza, O.; Guo, L.; Byun, H.M.; Carrieri, M.; Bartolucci, G.B.; Barrón-Vivanco, B.S.; Baccarelli, A.A. Aberrant promoter methylation in genes related to hematopoietic malignancy in workers exposed to a VOC mixture. *Toxicol. Appl. Pharmacol.* **2018**, *339*, 65–72. [CrossRef]
7. Wang, L.W.; Jay, G.S.; Tong, Y.D.; Duan, J.; Gu, Y.F.; Pragati, R.; Qi, L.; Giulia, S.; Urs, B.; Huang, R.J.; et al. Characteristics of wintertime VOCs in urban Beijing: Composition and source apportionment. *Atmos. Environ.* **2021**, *9*, 100100. [CrossRef]

8. Wei, W.; Chen, S.S.; Wang, Y.; Cheng, L.; Wang, X.Q.; Cheng, S.Y. The impacts of VOCs on PM_{2.5} increasing via their chemical losses estimates: A case study in a typical industrial city of China. *Atmos. Environ.* **2022**, *273*, 118978. [CrossRef]
9. Wang, Y.; Yang, G.; Wang, L.; Zhao, L.; Ji, S.; Qi, M.; Lu, X.; Liu, Z.; Tan, J.; Liu, Y.; et al. Characteristics and Source Apportionment of VOCs in a City with Complex Pollution in China. *Aerosol Air Qual. Res.* **2020**, *20*, 2196–2210. [CrossRef]
10. Gu, Y.; Liu, B.; Li, Y.; Zhang, Y.; Bi, X.; Wu, J.; Song, C.; Dai, Q.; Han, Y.; Ren, G.; et al. Multi-scale volatile organic compound (VOC) source apportionment in Tianjin, China, using a receptor model coupled with 1-hr resolution data. *Environ. Pollut.* **2020**, *265 Pt A*, 115023. [CrossRef]
11. Liu, Y.H.; Wang, H.L.; Jing, S.G.; Peng, Y.Y.; Gao, Y.P.; Yan, R.S.; Wang, Q.; Lou, S.R.; Cheng, T.T.; Huang, C. Strong regional transport of volatile organic compounds (VOCs) during wintertime in Shanghai megacity of China. *Atmos. Environ.* **2021**, *244*, 117940. [CrossRef]
12. Wang, M.; Lu, S.; Shao, M.; Zeng, L.; Zheng, J.; Xie, F.; Lin, H.; Hu, K.; Lu, X. Impact of COVID-19 lockdown on ambient levels and sources of volatile organic compounds (VOCs) in Nanjing, China. *Sci. Total Environ.* **2021**, *757*, 143823. [CrossRef] [PubMed]
13. Ma, Y.; Fu, S.; Gao, S.; Zhang, S.; Che, X.; Wang, Q.; Jiao, Z. Update on volatile organic compound (VOC) source profiles and ozone formation potential in synthetic resins industry in China. *Environ. Pollut.* **2021**, *291*, 118253. [CrossRef] [PubMed]
14. Wang, J.; Zhang, Y.L.; Wu, Z.Z.; Luo, S.L.; Song, W.; Wang, X.M. Ozone episodes during and after the 2018 Chinese National Day holidays in Guangzhou: Implications for the control of precursor VOCs. *J. Environ. Sci.* **2022**, in press. [CrossRef]
15. Wang, R.; Yuan, Z.; Zheng, J.; Li, C.; Huang, Z.; Li, W.; Xie, Y.; Wang, Y.; Yu, K.; Duan, L. Characterization of VOC emissions from construction machinery and river ships in the Pearl River Delta of China. *J. Environ. Sci.* **2020**, *96*, 138–150. [CrossRef] [PubMed]
16. Zhang, Y.; Wang, X.; Zhang, Z.; Lu, S.; Huang, Z.; Li, L. Sources of C₂–C₄ olefins, the most important ozone nonmethane hydrocarbon precursors in the Pearl River Delta region. *Sci. Total Environ.* **2015**, *502*, 236–245. [CrossRef]
17. Monks, P.S.; Granier, C.; Fuzzi, S.; Stohl, A.; Williams, M.L.; Akimoto, H.; Amann, M.; Baklanov, A.; Baltensperger, U.; Bey, I.; et al. Atmospheric composition change—global and regional air quality. *Atmos. Environ.* **2009**, *43*, 5268–5350. [CrossRef]
18. Tai, A.P.; Martin, M.V.; Heald, C.L. Threat to future global food security from climate change and ozone air pollution. *Nat. Clim. Chang.* **2014**, *4*, 817–821. [CrossRef]
19. Agyei, T.; Juráň, S.; Kwakye, K.O.; Šigut, L.; Urban, O.; Marek, M.V. The impact of drought on total ozone flux in a mountain Norway spruce forest. *J. For. Sci.* **2020**, *66*, 280–287. [CrossRef]
20. Agyei, T.; Juráň, S.; Edwards-Jonášová, M.; Fischer, M.; Švik, M.; Komínková, K.; Ofori-Amanfo, K.K.; Marek, M.V.; Grace, J.; Urban, O. The Influence of Ozone on Net Ecosystem Production of a Ryegrass–Clover Mixture under Field Conditions. *Atmosphere* **2021**, *12*, 1629. [CrossRef]
21. Guo, H.; Cheng, H.R.; Ling, Z.H.; Louie, P.K.; Ayoko, G.A. Which emission sources are responsible for the volatile organic compounds in the atmosphere of Pearl River Delta? *J. Hazard. Mater.* **2011**, *188*, 116–124. [CrossRef] [PubMed]
22. Zhang, Y.; Xue, L.; Carter, W.; Pei, C.; Chen, T.; Mu, J.; Wang, Y.; Zhang, Q.; Wang, W. Development of ozone reactivity scales for volatile organic compounds in a Chinese megacity. *Atmos. Chem. Phys.* **2021**, *21*, 11053–11068. [CrossRef]
23. Venecek, M.A.; Carter, W.P.L.; Kleeman, M.J. Updating the SAPRC Maximum Incremental Reactivity (MIR) scale for the United States from 1988 to 2010. *J. Air Waste Manag. Assoc.* **2018**, *68*, 1301–1316. [CrossRef] [PubMed]
24. Zhang, C.; Luo, S.; Zhao, W.; Wang, Y.; Zhang, Q.; Qu, C.; Liu, X.; Wen, X. Impacts of Meteorological Factors, VOCs Emissions and Inter-Regional Transport on Summer Ozone Pollution in Yuncheng. *Atmosphere* **2021**, *12*, 1661. [CrossRef]
25. Ma, Y.; Wang, M.; Wang, S.; Wang, Y.; Feng, L.; Wu, K. Air pollutant emission characteristics and HYSPLIT model analysis during heating period in Shenyang, China. *Environ. Monit. Assess.* **2020**, *193*, 9. [CrossRef]
26. Hosseini; Dehshiri, S.S.; Firoozabadi, B.; Afshin, H. A new application of multi-criteria decision making in identifying critical dust sources and comparing three common receptor-based models. *Sci. Total Environ.* **2022**, *808*, 152109. [CrossRef]
27. Gao, Y.Q.; Li, M.; Wan, X.; Zhao, X.W.; Wu, Y.; Liu, X.X.; Li, X. Important contributions of olefins and aromatics to VOCs emissions, chemistry and secondary pollutants formation at an industrial site of central eastern China. *Atmos. Environ.* **2021**, *244*, 117927. [CrossRef]
28. Zhong, Y.; Wang, X.; Cheng, S. Characteristics and Source Apportionment of PM_{2.5} and O₃ during Winter of 2013 and 2018 in Beijing. *Atmosphere* **2020**, *11*, 1324. [CrossRef]
29. Wang, Y.Q.; Zhang, X.Y.; Draxler, R.R. TrajStat: GIS-based software that uses various trajectory statistical analysis methods to identify potential sources from long-term air pollution measurement data. *Environ. Model. Softw.* **2009**, *24*, 938–939. [CrossRef]
30. Dai, H.; Jing, S.; Wang, H.; Ma, Y.; Li, L.; Song, W.; Kan, H. VOC characteristics and inhalation health risks in newly renovated residences in Shanghai, China. *Sci. Total Environ.* **2017**, *577*, 73–83. [CrossRef]
31. Liu, Y.; Xiang, F.; Han, X.Y.; Shi, Z.; Wang, C.H.; Huang, Y.; Shi, J.W.; Ning, P. On pollution characteristics and sources apportionment of ambient VOCs in summer and autumn in Kunming. *J. Yunnan Univ.* **2018**, *40*, 104–112. (In Chinese)
32. Li, L.; Li, H.; Wang, X.Z.; Zhang, X.M.; Wen, C. Pollution characteristics and health risk assessment of atmospheric VOCs in the downtown area of Guangzhou, China. *Environ. Sci.* **2013**, *34*, 4558–4564. (In Chinese)
33. Liu, Y.; Song, M.; Liu, X.; Zhang, Y.; Hui, L.; Kong, L.; Zhang, Y.; Zhang, C.; Qu, Y.; An, J.; et al. Characterization and sources of volatile organic compounds (VOCs) and their related changes during ozone pollution days in 2016 in Beijing, China. *Environ. Pollut.* **2020**, *257*, 113599. [CrossRef] [PubMed]
34. Li, Y.P.; Tang, Y.; Fan, Z.Y.; Pu, M.; Zhang, J.L.; Yang, Z.Z.; Wu, D.L. Pollution Characteristics and Health Risk Assessment of Atmospheric VOCs in Chengdu. *Environ. Sci.* **2018**, *39*, 576–584. (In Chinese)

35. Menchaca-Torre, H.L.; Mercado-Hernández, R.; Mendoza-Domínguez, A. Diurnal and seasonal variation of volatile organic compounds in the atmosphere of Monterrey, Mexico. *Atmos. Pollut. Res.* **2015**, *6*, 1073–1081. [CrossRef]
36. Shinji, S.; Ipppei, N.; Hiroshi, K. Characteristics of ambient C₂–C₁₁ non-methane hydrocarbons in metropolitan Nagoya, Japan. *Atmos. Environ.* **2009**, *43*, 4384–4395.
37. Kumar, A.; Singh, D.; Kumar, K.; Singh, B.B.; Jain, V.K. Distribution of VOCs in urban and rural atmospheres of subtropical India: Temporal variation, source attribution, ratios, OFP and risk assessment. *Sci. Total Environ.* **2018**, *613–614*, 492–501. [CrossRef]
38. Li, C.; Li, Q.; Tong, D.; Wang, Q.; Wu, M.; Sun, B.; Su, G.; Tan, L. Environmental impact and health risk assessment of volatile organic compound emissions during different seasons in Beijing. *J. Environ. Sci.* **2020**, *93*, 1–12. [CrossRef]
39. Zhang, L.; Li, H.; Wu, Z.; Zhang, W.; Liu, K.; Cheng, X.; Zhang, Y.; Li, B.; Chen, Y. Characteristics of atmospheric volatile organic compounds in urban area of Beijing: Variations, photochemical reactivity and source apportionment. *J. Environ. Sci.* **2020**, *95*, 190–200. [CrossRef]
40. Yang, S.; Li, X.; Song, M.; Liu, Y.; Yu, X.; Chen, S.; Lu, S.; Wang, W.; Yang, Y.; Zeng, L.; et al. Characteristics and sources of volatile organic compounds during pollution episodes and clean periods in the Beijing-Tianjin-Hebei region. *Sci. Total Environ.* **2021**, *799*, 149491. [CrossRef]
41. Zhang, Y.X.; Yin, S.S.; Yuan, M.H.; Zhang, R.Q.; Zhang, M.; Yu, S.J.; Li, Y.D. Characteristics and Source Apportionment of Ambient VOCs in Spring in Zhengzhou. *Environ. Sci.* **2019**, *40*, 4372–4381. (In Chinese)
42. Dehghani, M.; Fazlzadeh, M.; Sorooshian, A.; Tabatabaee, H.R.; Miri, M.; Baghani, A.N.; Delikhoon, M.; Mahvi, A.H.; Rashidi, M. Characteristics and health effects of BTEX in a hot spot for urban pollution. *Ecotoxicol. Environ. Saf.* **2018**, *155*, 133–143. [CrossRef]
43. Hamid, H.H.A.; Latif, M.T.; Uning, R.; Nadzir, M.S.M.; Khan, M.F.; Ta, G.C.; Kannan, N. Observations of BTEX in the ambient air of Kuala Lumpur by passive sampling. *Environ. Monit. Assess.* **2020**, *192*, 342. [CrossRef]
44. Lyon, D.R.; Alvarez, R.A.; Zavala-Araiza, D.; Brandt, A.R.; Jackson, R.B.; Hamburg, S.P. Aerial Surveys of Elevated Hydrocarbon Emissions from Oil and Gas Production Sites. *Environ. Sci. Technol.* **2016**, *50*, 4877–4886. [CrossRef] [PubMed]
45. Wang, Y.C.; Lin, C.; Lin, Y.K.; Wang, Y.F.; Weng, W.H.; Kuo, Y.M. Characteristics and determinants of ambient volatile organic compounds in primary schools. *Environ. Sci. Process. Impacts* **2016**, *18*, 1458–1468. [CrossRef] [PubMed]
46. Zhang, Y.; Mu, Y.; Liu, J.; Mellouki, A. Levels, sources and health risks of carbonyls and BTEX in the ambient air of Beijing, China. *J. Environ. Sci.* **2012**, *24*, 124–130. [CrossRef]
47. Xu, H.; Deng, J.J.; Xin, Z.Y.; Chen, J.S. Pollution characteristics and health risk assessment of VOCs in different functional zones of Xiamen. *Acta. Sci. Circum.* **2015**, *35*, 2701–2709. (In Chinese)
48. Jia, C.H.; Mao, X.X.; Huang, T.; Liang, X.X.; Wang, Y.N.; Shen, Y.J.; Jiang, W.Y.H.; Wang, H.Q.; Bai, Z.L.; Ma, M.Q. Non-methane Hydrocarbons (NMHCs) and Their Contribution to Ozone Formation Potential in a Petrochemical Industrialized City, Northwest China. *Atmos. Res.* **2016**, *169*, 225–236. [CrossRef]
49. Xiong, Y.; Bari, M.A.; Xing, Z.; Du, K. Ambient volatile organic compounds (VOCs) in two coastal cities in western Canada: Spatiotemporal variation, source apportionment, and health risk assessment. *Sci. Total Environ.* **2020**, *706*, 135970. [CrossRef]
50. Leila, T.; Zahra, S.; Parvin, S.; Khaled, Z.B.; Mohammad, S.; Yahya, R.; Raana, R.; Siamak, D. Spatiotemporal variation, ozone formation potential and health risk assessment of ambient air VOCs in an industrialized city in Iran. *Atmos. Pollut. Res.* **2019**, *10*, 556–563.

Article

Characteristics and Source Apportionment of Size-Fractionated Particulate Matter at Ground and above the Urban Canopy (380 m) in Nanjing, China

Hao Wu ¹, Pulong Chen ², Tijian Wang ^{3,*}, Min Xie ³, Bingliang Zhuang ³, Shu Li ³ and Mengmeng Li ³
¹ Key Laboratory of Transportation Meteorology of China Meteorological Administration, Nanjing Joint Institute for Atmospheric Sciences, Nanjing 210041, China; haowu@cma.gov.cn

² Jingling Era Jiangsu Environmental Technology Co., Ltd., Suzhou 215011, China; plchen@nju.edu.cn

³ School of Atmospheric Sciences, Nanjing University, Nanjing 210023, China; minxie@nju.edu.cn (M.X.); blzhuang@nju.edu.cn (B.Z.); lishu@nju.edu.cn (S.L.); mengmengli2015@nju.edu.cn (M.L.)

* Correspondence: tjwang@nju.edu.cn; Tel./Fax: +86-25-8968-3797

Citation: Wu, H.; Chen, P.; Wang, T.; Xie, M.; Zhuang, B.; Li, S.; Li, M. Characteristics and Source Apportionment of Size-Fractionated Particulate Matter at Ground and above the Urban Canopy (380 m) in Nanjing, China. *Atmosphere* **2022**, *13*, 883. <https://doi.org/10.3390/atmos13060883>

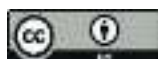
Academic Editors: Duanyang Liu, Kai Qin and Honglei Wang

Received: 8 May 2022

Accepted: 27 May 2022

Published: 29 May 2022

Publisher's Note: MDPI stays neutral with regard to jurisdictional claims in published maps and institutional affiliations.



Copyright: © 2022 by the authors. Licensee MDPI, Basel, Switzerland. This article is an open access article distributed under the terms and conditions of the Creative Commons Attribution (CC BY) license (<https://creativecommons.org/licenses/by/4.0/>).

Abstract: In this study, the concentrations and chemical components of size-fractionated particulate matter (PM) in Nanjing at the ground (Gulou, 20 m) and above the urban canopy (Zifeng, 380 m) were sampled and analyzed from 16 November to 12 December in 2016. Higher concentrations of PM₁₀, PM_{10-2.1}, and PM_{2.1} ($108.3 \pm 23.4 \mu\text{g m}^{-3}$, $47.3 \pm 10.6 \mu\text{g m}^{-3}$, and $61.0 \pm 18.8 \mu\text{g m}^{-3}$) were measured at Gulou than those ($88.1 \pm 21.1 \mu\text{g m}^{-3}$, $31.4 \pm 6.7 \mu\text{g m}^{-3}$, and $56.7 \pm 18.6 \mu\text{g m}^{-3}$) at Zifeng. The most abundant chemical components for size-fractionated PM were SO₄²⁻, NO₃⁻, organic carbon (OC), NH₄⁺, elemental carbon (EC), and crustal elements such as Al, Ca, Fe, and Mg, varying significantly on different particulate sizes. The concentrations of OC and EC were $7.46\text{--}19.60 \mu\text{g m}^{-3}$ and $3.44\text{--}5.96 \mu\text{g m}^{-3}$ at Gulou and were $8.34\text{--}18.62 \mu\text{g m}^{-3}$ and $2.86\text{--}4.11 \mu\text{g m}^{-3}$ at Zifeng, showing an equal importance in both fine and coarse particles. Nitrate, sulfate, and ammonium were more concentrated in PM_{2.1}, contributing $11.30\text{--}13.76 \mu\text{g m}^{-3}$, $8.91\text{--}9.40 \mu\text{g m}^{-3}$, and $5.78\text{--}6.81 \mu\text{g m}^{-3}$, which was more than in PM_{10-2.1}, which contributed $2.73\text{--}5.06 \mu\text{g m}^{-3}$, $2.16\text{--}3.81 \mu\text{g m}^{-3}$, and $0.85\text{--}0.87 \mu\text{g m}^{-3}$. In contrast, the crustal elements were larger in coarse particles and at the ground level, accounting for 18.6% and 15.3% of the total PM at Gulou and Zifeng. Source apportionment using the chemical mass balance (CMB) model EPA showed that the dominant three sources were secondary nitrate (18.2–24.9%), secondary sulfate (14.5–20.4%), and secondary organic aerosols (15.5–19.6%) for PM₁₀, PM_{2.1}, and PM_{1.1} at both Gulou and Zifeng during the entire sampling period. However, for PM_{10-2.1}, the largest three contributors were secondary organic aerosols (18.3%), the coal-fired power plant (15.6%), and fugitive dust (14.4%), indicating dusts including construction dust, fugitive dust, and soil dust would contribute more at the ground. The results also showed that the concentrations of PM₁₀, PM_{2.1}, and PM_{1.1} were lower than the work carried out in the winter of 2010 at the same sampling site by 41.4%, 26.3%, and 24.8%, confirming the improvement of the air quality and the efficient control of PM pollutants.

Keywords: size-fractionated PM; chemical characteristics; source apportionment; ground level (20 m); urban canopy (380 m)

1. Introduction

Nowadays, atmospheric particulate matter (PM) are receiving a lot of attention in atmospheric and environmental studies due to their complex and important impact on various problems, including human health [1,2], radiation balance and climate change [3–5], visibility degradation [6,7], and air pollution [8–10]. In recent decades, with increased economic and industrial development, PM have become the primary air pollutant in urban areas, and PM pollution, especially PM_{2.5} pollution (atmospheric particulate matter with an aerodynamic diameter less than 2.5 μm), has been found to be a severely impairing

issue in China. So, considerable attention from governments and scientific communities has been drawn [11–15] and lots of studies have been focused on the mass concentrations and chemical properties of particles [16,17]. The chemical compositions of atmospheric PM consist of numerous numbers of species (metals, ions, and carbonaceous matter) and come from complex sources, including anthropogenic and natural sources [18]. Meanwhile, the formation processes involve complicated multiphase formation pathways that are not well understood yet [19,20]. So, it is significant to understand the formation and contribution to PM mass in urban areas.

Many previous efforts have been conducted to evaluate the size distributions and chemical compositions at ground level (0~20 m), which is significantly influenced by local emission sources such as fugitive dust, construction dust, and vehicle exhaust. In comparison, an observation of size-fractionated particulate matter (PM) on a height of 300–400 m would be meaningful to understand the influences from a large scale of the sources, transportation, formation, and removal mechanisms to particulate matter [21–23]. Nanjing is a megacity located in the most developed region of the Yangtze River Delta in China with a huge population and a large urban center. It is a perfect target to carry out the ground level and high-height level observations. Characteristics and source contributions of atmospheric particles were discussed by previous studies in Nanjing [24,25], but the chemical compositions and sources of PM in different sizes at ground level and high-height level have not yet been conducted. As the nocturnal planetary boundary height during the winter is often about 300 m, we chose Zifeng Tower (380 m) in Nanjing to be the observation site of atmospheric particulate matter in the lower boundary layer [26].

Compared to developed countries, the emission sources of atmospheric particles in developing countries are much more complex. An explicit knowledge of the source contributions and probable source locations is the first step for understanding and planning management strategies of particulate matter [27]. The receptor model is used for quantitative analysis of PM source contributions, as there is no limitation on pollution discharge, weather conditions, or terrain factors. Based on chemical analysis, the receptor models that could be chosen are either the chemical mass balance (CMB) method or a multivariate factor analysis model such as the positive matrix factorization (PMF) method. Both methods have been widely applied to evaluate the particles' source contributions [28–31]. Source profiles are necessary in the former method but useless in the latter method. However, there is no limitation in the number of samples in the former method, but a minimum number of samples should be prescribed in the latter method. The source profiles in Nanjing were obtained in a previous work [18], and due to the limitation of sample numbers, the CMB model was used in this study. Additionally, backward trajectory clustering analysis could be used to trace the source locations of emissions [32]. Moreover, backward trajectory clustering analysis combined with the results of receptor models have been proved to be a beneficial tool for identifying the major source locations [33–35].

In this study, a synchronous and parallel observation was carried out at the ground level and the 380 m platform on Zifeng Tower in Nanjing from November to December in 2016. The mass concentrations of size-fractionated PM were obtained, and the chemical compositions including elements, water-soluble ions, and carbonaceous matter (elemental carbon (EC) and organic carbon (OC)) were analyzed. The size distribution of chemical components and variations between the ground level and the 380 m platform were investigated. The CMB model was applied to apportion the emission source contributions of PM in different sizes. The characteristics of source contributions at ground level and above the urban canopy (380 m) were evaluated. Combined with backward trajectory clustering analysis, the potential transport pathways were traced at the two heights. Finally, based on the results above, we explored reasonable control measures that may be helpful for policymakers.

2. Materials and Methods

2.1. Study Area and Sample Collection

Nanjing (118°22" and 119°14" E, 31°14" and 32°37" N) is the capital of Jiangsu province, the second largest city in the Yangtze River Delta. With rapid development in recent decades, vehicle exhaust, coal-fired power generation, and industrial activities have become the main anthropogenic sources of PM in Nanjing. The Gulou District is the urban center of Nanjing with huge population and heavy traffic. So, we chose the Gulou campus of Nanjing University and Zifeng Tower in this district to be the sampling sites. One of the sampling sites, Zifeng Tower, is a 450-meter skyscraper completed in 2010 in Nanjing, China. It is the tallest building in Jiangsu province, and the 10th tallest building in the world (as of August 2016). The observation instruments were located on the top platform at 380 m. Another set of observation instruments was located on the roof of a 20 m high building in Gulou campus, Nanjing University. The two observation points are close with a distance of less than 700 m. The locations of sampling sites are shown in Figure 1. The two sampling sites are represented as Gulou and Zifeng in the following text.



Figure 1. The locations of sampling sites.

The sampling campaign was carried out from 16 November to 12 December in 2016 at 20 m and 380 m height, except 28 November due to power failure at Gulou. During the experiment, size-fractionated ambient particulate matter (PM) were collected with an eight-stage Sierra-Andersen cascade impactor (Andersen Instruments, Inc., Atlanta, GA, USA), which can classify nine intervals in the following order: $<0.43\ \mu\text{m}$, $0.43\text{--}0.65\ \mu\text{m}$, $0.65\text{--}1.1\ \mu\text{m}$, $1.1\text{--}2.1\ \mu\text{m}$, $2.1\text{--}3.3\ \mu\text{m}$, $3.3\text{--}4.7\ \mu\text{m}$, $4.7\text{--}5.8\ \mu\text{m}$, $5.8\text{--}9.0\ \mu\text{m}$, and $9.0\text{--}10\ \mu\text{m}$ (aerodynamic diameter) [25,36]. Two parallel samplers with flow rate of $28.3\ \text{L min}^{-1}$ were placed at each height in order to obtain chemical compositions of particles with Teflon-membrane filters and quartz fiber filters (Diameter 81 mm). Forty-seven hours of sampling was performed every two days from 9 am to 8 am and on the third day to obtain adequate materials at high level.

2.2. Chemical Analysis

Elements (e.g., Al, As, Ba, Ca, Cd, Co, Cr, Cu, Fe, K, Mg, Mn, Ni, P, Pb, Sn, Sr, Ti, V, and Zn), ions (e.g., F^- , CH_3COO^- , HCOO^- , Cl^- , NO_3^- , SO_4^{2-} , $\text{C}_2\text{O}_4^{2-}$, Na^+ , NH_4^+ , K^+ , $(\text{CH}_3)_2\text{NH}_2^+$, Ca^{2+} , Mg^{2+}), and carbonaceous materials (organic carbon (OC) and elemental carbon (EC)) were analyzed for each sample.

2.2.1. Analysis of Elements

Elements obtained from Teflon filters were analyzed by an inductively coupled plasma mass spectrometer (ICP-MS, Agilent Technologies, Inc., Model 7500a, Santa Clara, CA, USA). Calibration with reference material (Environmental Calibration Standard, Part 5183-4688, Agilent Technologies) demonstrated good linearity and sensitivity for the instrument. The relative standard deviation for each measurement (repeated twice) was within 3%. The method detection limits (MDLs) were determined by adding 3 standard deviations of the blank readings to the average blank values [26].

2.2.2. Analysis of Water-Soluble Ions

Water-soluble ions obtained from half of the quartz fiber filters were analyzed by an ion chromatography (IC, DIONEX Corporation, Model ICS-90, Sunnyvale, CA, USA). The IC was periodically checked with standard reference materials. The relative standard deviation for each measurement (repeated twice) was within 3%. The method detection limit (MDL) was provided by the ion chromatography manufacturer. Determination of inorganic cations and ammonium in environmental waters was performed by ion chromatography with a high-capacity cation-exchange column. The MDLs of cations were 22, 20, 5, 48, 6, and 48 ng/mL for Na^+ , NH_4^+ , K^+ , Mg_2^+ , Ca_2^+ , and $(\text{CH}_3)_2\text{NH}_2^+$, respectively. The MDLs of anions were 2, 4, 11, 9, 66, 7, and 15 ng/mL for F^- , Cl^- , NO_3^- , SO_4^{2-} , CH_3COO^- , HCOO^- , and $\text{C}_2\text{O}_4^{2-}$, respectively.

2.2.3. Analysis of Carbonaceous Materials

Carbonaceous materials (OC and EC) obtained from another half of the quartz fiber filters were analyzed by a thermal/optical carbon analyzer (DRI, Model 2001, Desert Research Institute, Reno, NV, USA) with the thermal/optical reflectance (TOR) method [37,38]. A circle piece of 0.53 cm^2 was cut off from the filters and was sent into the thermal optical carbon analyzer. A blank sample was analyzed for blank subtraction. Quality control and quality assurance procedures were routinely applied for all the elemental, ion, and carbonaceous analyses.

2.3. CMB Model

The chemical mass balance (CMB) receptor model was used in this study to apportion the source contributions to the size-fractionated PM at different heights. The EPA CMB 8.2 version (US EPA, 2004) with the effective variance weighted least-squares fitting method was applied. CMB is a widely used method for source apportionment of particulate matter. It consists of a solution to a set of linear equations that expresses each receptor chemical concentration as a linear sum of products of source profile abundances and source contributions. Source samples were collected and analyzed, and then profiles were determined for local representative emissions [18,26]. The chemical abundances are normalized to values between 0% and 100%.

$$C_{it} = \sum_{i=1}^N F_{in} S_{nt} + E_{it} \quad (1)$$

In Equation (1), C_{it} represents the ambient concentration of the i -th chemical species measured at time t . It is equal to the sum of the contributions from N sources, in theory. F_{in} is the fractional abundance (source profile) of the i -th species in the n -th source type. S_{nt} is the mass contribution of n -th source at time t . E_{it} represents the difference between the measured and estimated ambient concentration [25].

2.4. Cluster Analysis of Back Trajectories

The three-dimensional (latitude, longitude, and altitude) cluster analysis of back trajectories shows us the dominant transport pathways of air mass, which could reflect the potential influence of sources from a large scale during the sampling campaign. Trajectories were generated with version 4.9 of the NOAA Air Resources Laboratory's Hybrid Single-

Particle Lagrangian Integrated Trajectory (HYSPPLIT) model [39]. Archived meteorological data from the National Centers for Environmental Prediction (NCEP)/National Center for Atmospheric Research (NCAR) reanalysis project data set with 6 h intervals and a spatial resolution of $2.5 \times 2.5^\circ$ in longitude and latitude were used as input data to calculate 36 h trajectories starting at 20 m and 380 m, separately. During the observation periods, back trajectories were computed every three hours for each sampling day (00 h, 03 h, 06 h, 09 h, 12 h, 15 h, 18 h, and 21 h in UTC). Then, all the trajectories were clustered with HYSPPLIT clustering algorithm. The clustering of back trajectories is based on the total spatial variance (TSV) method [40], which minimizes the inter-cluster differences among trajectories.

Hourly weather data such as temperature (T), relative humidity (RH), wind speed (WS), and wind direction (WD) were obtained from an automatic weather station on the roof of a 20 m high building in Gulou campus, Nanjing University.

3. Results and Discussion

3.1. Size-Fractionated PM Mass Characteristics

During the sampling period, the average PM_{10} concentration was $108.3 \pm 23.4 \mu\text{g m}^{-3}$ and $88.1 \pm 21.1 \mu\text{g m}^{-3}$ at Gulou and Zifeng, respectively. The mean mass concentration of the PM_{10} concentration at ground level was 22.9% higher than that at high height (380 m), and the PM_{10} concentration at Gulou was higher at every sampling day than at Zifeng. The average $PM_{2.1}$ concentration was $56.7 \pm 18.6 \mu\text{g m}^{-3}$ with the range from $34.6 \mu\text{g m}^{-3}$ to $89.7 \mu\text{g m}^{-3}$ at Zifeng. The average $PM_{2.1}$ concentration was $61.0 \pm 18.8 \mu\text{g m}^{-3}$, ranging from $32.4 \mu\text{g m}^{-3}$ to $87.5 \mu\text{g m}^{-3}$ at Gulou, which was 7.6% higher than that measured at Zifeng. At specific sampling days, the mass concentrations of $PM_{2.1}$ were higher at high height (380 m). In contrast, the averaged mass concentration of $PM_{1.1}$ at Zifeng was $44.8 \pm 15.8 \mu\text{g m}^{-3}$, which was 9.5% higher than $40.9 \pm 13.0 \mu\text{g m}^{-3}$ at Gulou.

The more active secondary formation processes of aerosols at the higher level or the long-distance transportation from other regions may have caused these results, which will be explored and discussed in the following text. The coarse particles showed the same feature as PM_{10} at different heights. The summary statistics of measured PM_{10} , $PM_{10-2.1}$, $PM_{2.1}$, and $PM_{1.1}$ are presented in Table 1. The mass concentrations of PM_{10} , $PM_{2.1}$, and $PM_{1.1}$ in this study were 41.4%, 26.3%, and 24.8% lower than those in previous study at Gulou, Nanjing during winter 2010 [24]. Meanwhile, compared with the similar research in a megacity of North China from December 2013 to January 2014 [41], the mass concentrations of PM_{10} and $PM_{2.1}$ in Tianjin were 107.5% and 73.6% higher than those in this study. Overall, the air quality in Nanjing is better for these years, and a decrease trend of size-fractionated PM mass concentrations with increasing height was shown, except for $PM_{1.1}$.

Table 1. Statistics of measured PM_{10} , $PM_{10-2.1}$, $PM_{2.1}$, and $PM_{1.1}$ at Gulou and Zifeng ($\mu\text{g m}^{-3}$).

Site	Type	Mean	SD ^a	Max	Min
Gulou	PM_{10}	108.3	23.4	145.6	62.7
	$PM_{10-2.1}$	47.3	10.6	66.1	36.1
	$PM_{2.1}$	61.0	18.8	87.5	32.5
	$PM_{1.1}$	40.9	13.0	72.7	25.3
Zifeng	PM_{10}	88.1	21.1	124.1	56.5
	$PM_{10-2.1}$	31.4	6.7	41.9	21.8
	$PM_{2.1}$	56.7	18.6	89.7	34.6
	$PM_{1.1}$	44.8	15.8	79.4	27.1

^a Standard deviation.

Figure 2 shows the time series of observed size-fractionated PM mass concentrations at Gulou and Zifeng, which indicates that the time-scale variation trend was consistent at two heights. The correlation coefficient of PM_{10} , $PM_{10-2.1}$, and $PM_{2.1}$ between Gulou and Zifeng was 0.79, 0.86, and 0.73, respectively. Further, in order to study the variations of particulate

concentrations and chemical compositions, the coefficient of divergence (CD) [42,43] could be used as follows:

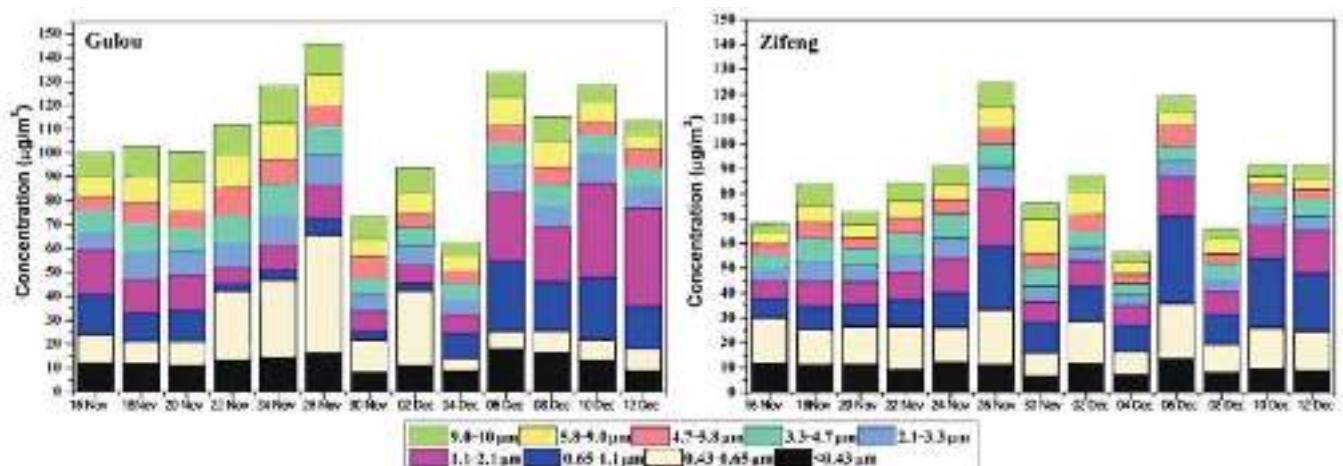


Figure 2. Time series of size-fractionated mass concentrations at Gulou (20 m) and Zifeng (380 m).

$$CD_{gz} = \sqrt{\frac{\sum_{n=1}^N \left(\frac{C_{ng} - C_{nz}}{C_{ng} + C_{nz}} \right)^2}{N}} \quad (2)$$

where g and z represent the two sampling sites, and N is the total number of sampling days. C_{ng} or C_{nz} means mass concentrations at different sites in the n th day. The value of CD shows the similarity of the mass concentrations of particulate matter at the two sites. The lower value represents the stronger similarity. When the value of CD is zero, it means the mass concentrations at the two sites are the same. [44]. In actual analysis, a CD value above 0.3 indicates a difference between each height, whereas a CD value less than 0.3 could be a sign of similarity between two heights [45]. To the mass concentrations, the values of CD for different particle sizes are shown in Table 2. All the CD values for PM_{10} , $PM_{10-2.1}$, $PM_{2.1}$, and $PM_{1.1}$ between Gulou and Zifeng are less than 0.3, which indicates that the mass concentrations of particles are similar at each height. The CD value of the $PM_{10-2.1}$ mass concentration is relatively higher than those of $PM_{2.1}$ and $PM_{1.1}$, which suggests that the coarse particulate matter presents a larger variation between 20 m and 380 m. This might imply that local and primary sources contributed more to coarse particles at the ground than high height.

Table 2. Coefficient of divergence (CD) of mass concentrations and main chemical compositions for size-fractionated PM between Gulou (20 m) and Zifeng (380 m).

Species	PM_{10}	$PM_{10-2.1}$	$PM_{2.1}$	$PM_{1.1}$
PM mass	0.139	0.220	0.097	0.096
Al	0.251	0.326	0.151	0.190
Ca	0.235	0.304	0.161	0.185
Fe	0.286	0.355	0.161	0.213
K	0.188	0.242	0.170	0.233
Mg	0.243	0.314	0.180	0.229
Cl	0.201	0.221	0.192	0.175
Na	0.172	0.185	0.290	0.324
NO_3^-	0.196	0.321	0.173	0.169
SO_4^{2-}	0.121	0.282	0.087	0.124
NH_4^+	0.195	0.405	0.130	0.117
OC	0.089	0.125	0.096	0.093
EC	0.245	0.424	0.212	0.210
CH_3COO^-	0.490	0.487	0.529	0.598
$HCOO^-$	0.206	0.230	0.126	0.165
$C_2O_4^{2-}$	0.278	0.117	0.425	0.464
$(CH_3)_2NH_2^+$	0.449	0.607	0.466	0.489

The sampling was conducted during November to December 2016, the most polluted time of the year. In this study, there is no 2.5 μm cut point, so 2.1 μm is defined as the threshold of fine particles, and the clear day standard for $\text{PM}_{2.5}$, which is less than $75 \mu\text{g m}^{-3}$ (Technical Regulation on Ambient Air Quality Index (HJ633-2012)), would be used for $\text{PM}_{2.1}$ here. During the whole sampling period, there were four samples exceeding $75 \mu\text{g m}^{-3}$ at the ground (26–27 November, 6–7 December, 10–11 December, and 12–13 December), and at Zifeng (380 m) there were two samples exceeding $75 \mu\text{g m}^{-3}$ (26–27 November and 6–7 December). According to previous work, the beginning, process, and dispersion of particulate pollution could be influenced or driven by meteorological conditions [46–48]. The weather data observed at Gulou (20 m) were discussed with the concentration level. The hourly series of meteorological conditions including temperature (T), relative humidity (RH), wind speed (WS), and wind direction (WD) were shown in Figure 3. Under the weather condition of low wind speed, the PM concentrations would increase. The concentrations of $\text{PM}_{2.1}$ at Gulou were higher than $75 \mu\text{g m}^{-3}$ in 26–27 November, 6–7 December, 10–11 December, and 12–13 December when the daily maximum wind speeds were 2.9 m/s, 2.8 m/s, 3.8 m/s, and 3.9 m/s, respectively. However, the lowest concentration of $\text{PM}_{2.1}$ was $32.5 \mu\text{g m}^{-3}$ in 4–5 December, with a much higher daily maximum wind speed (7 m/s). Additionally, the sampling day with low RH showed cleaner than the sampling day with high RH. The concentrations of $\text{PM}_{2.1}$ at Gulou in 26–27 November and 12–13 December with higher daily average RH (69.6% and 79.1%) were much larger than that in 4–5 December with lower daily average RH (60.0%).

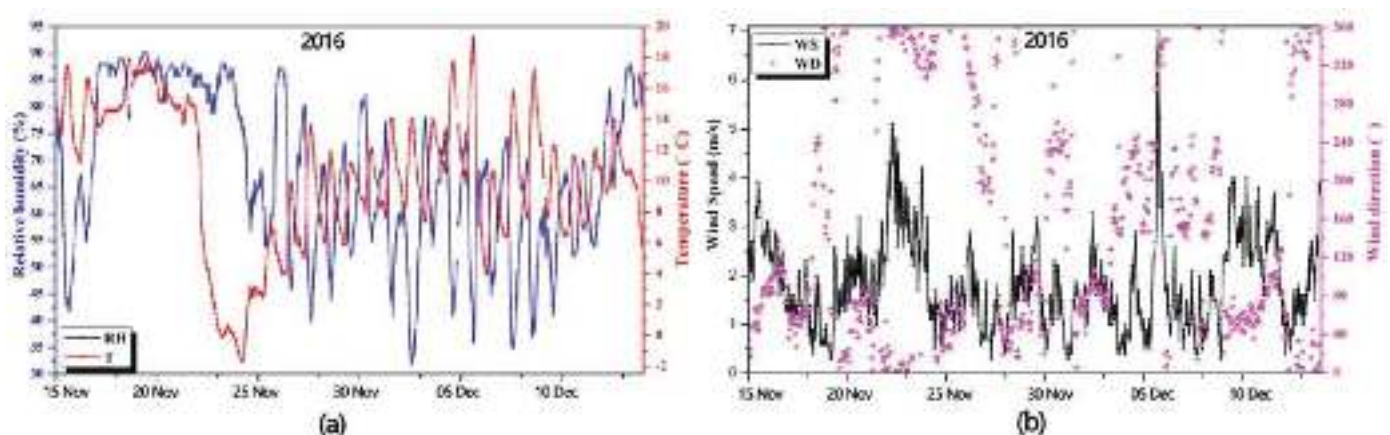


Figure 3. Time series of hourly (a) temperature and relative humidity and (b) wind speed and wind direction.

The average mass concentrations of size-fractionated PM manifested different features at different heights. The mass size distributions of PM with standard deviation at Gulou and Zifeng are shown in Figure 4. The distribution patterns of PM mass concentrations from $9.0\text{--}10 \mu\text{m}$ to $1.1\text{--}2.1 \mu\text{m}$ at two sites were similar, which showed an increasing trend with finer particulate size and the minimum concentration at $4.7\text{--}5.8 \mu\text{m}$. However, the distribution patterns of particles smaller than the size bin of $1.1\text{--}2.1 \mu\text{m}$ were different. A bimodal distribution pattern could be found at Gulou with higher concentrations in the size bin of $1.1\text{--}2.1 \mu\text{m}$ and $0.43\text{--}0.65 \mu\text{m}$. Otherwise, a unimodal distribution pattern could be found at Zifeng with a highest concentration in size bin of $0.43\text{--}0.65 \mu\text{m}$. Particles in different sizes showed generally larger concentrations at Gulou than those at Zifeng, except in size bins of $0.65\text{--}1.1 \mu\text{m}$ and $0.43\text{--}0.65 \mu\text{m}$, which caused the concentrations of $\text{PM}_{1.1}$ to be larger at 380 m than at the ground. The average ratios of $\text{PM}_{2.1}/\text{PM}_{10}$ at Gulou and Zifeng were 0.56 and 0.64, indicating that more fine particulate matter were contained in PM_{10} at high height. The average ratios of $\text{PM}_{1.1}/\text{PM}_{2.1}$ at Gulou and Zifeng were 0.67 and 0.79, indicating in wintertime that the fine particulate matter at the top of the boundary

layer were finer than those at the ground level. The ratios of $PM_{2.1}/PM_{10}$ and $PM_{1.1}/PM_{2.1}$ for each sampling day at Gulou and Zifeng are shown in Figure 4.

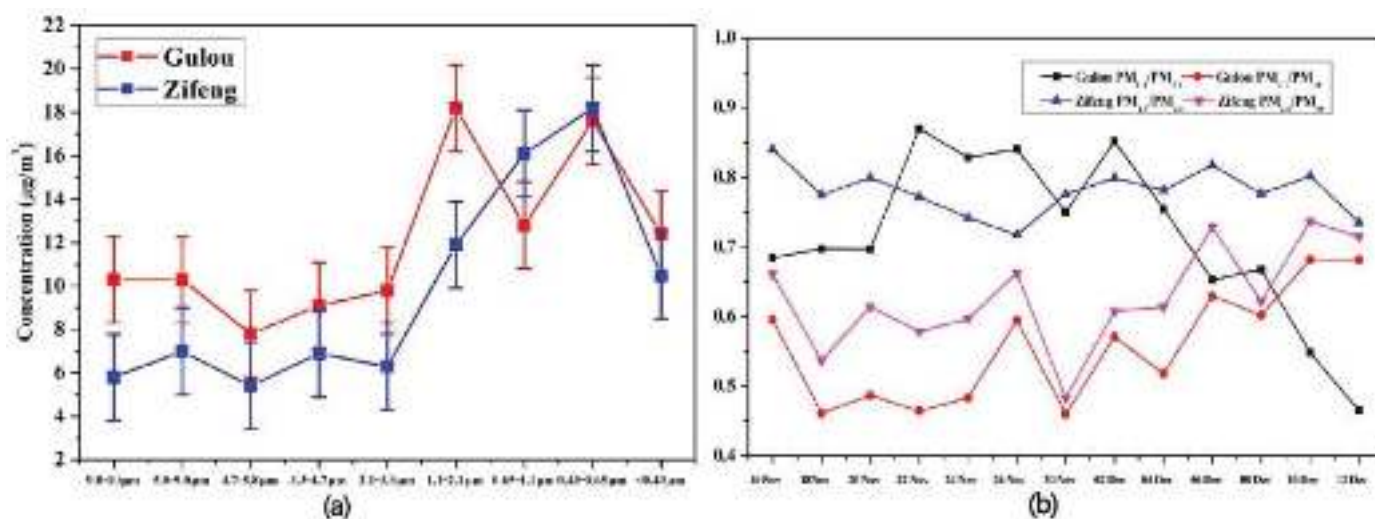


Figure 4. (a) The average mass size distributions of PM with standard deviation at Gulou (20 m) and Zifeng (30 m). (b) The ratios of $PM_{2.1}/PM_{10}$ and $PM_{1.1}/PM_{2.1}$ at Gulou and Zifeng.

3.2. Characteristics of Chemical Compositions

The size-fractionated PM are mainly composed of crustal elements, water-soluble ions, and carbonaceous matter. The average mass concentrations of the chemical components at each sampling height in PM_{10} , $PM_{10-2.1}$, $PM_{2.1}$, and $PM_{1.1}$ are shown in Table 3. The characteristics of chemical compositions are discussed in three sections containing elements, water-soluble ions, and carbonaceous matter.

3.2.1. Elements

Elements obtained from Teflon filters were analyzed by an inductively coupled plasma mass spectrometer (ICP-MS, Agilent Technologies, Inc., Model 7500a, Santa Clara, CA, USA). Calibration with reference material (Environmental Calibration Standard, Part 5183-4688, Agilent Technologies, Santa Clara, CA, USA) demonstrated good linearity and sensitivity for the instrument. The relative standard deviation for each measurement (repeated twice) was within 3%. The method detection limits (MDLs) were determined by adding three standard deviations of the blank readings to the average blank values [26]. The elemental species are classified into three categories: crustal elements such as Al, Ca, Fe, and Mg, heavy metal elements including As, Ba, Cr, Cu, Mn, Ni, Pb, Ti, and Zn, and trace elements including the rest of the elemental species such as Cd, Co, P, Sn, Sr, and V. The most important part of the elements was the crustal elements, which accounted for 85.3%, 79.9%, and 78.8 of all the elements at PM_{10} , $PM_{2.1}$, and $PM_{1.1}$, respectively. The crustal elements, heavy metal elements, and trace elements constituted relative fractions varied at different particulate sizes, with higher mass percentages of PM_{10} and coarse particles than that of fine particulate matter. The mass concentrations of most elements showed a decreasing trend with increasing sampling height, especially in coarse particles, implying that elements were mainly emitted from locally ground fugitive and construction dust. The percentages of chemical compositions in PM_{10} , $PM_{10-2.1}$, $PM_{2.1}$, and $PM_{1.1}$ at different sampling heights are shown in Figure 5. According to CD values of elements in Table 2, the CD values for crustal elements such as Al, Ca, Fe, and Mg were generally less than 0.3 in PM_{10} , $PM_{2.1}$, and $PM_{1.1}$ but more than 0.3 in $PM_{10-2.1}$, indicating larger differences of crustal elements between two heights in coarse particles.

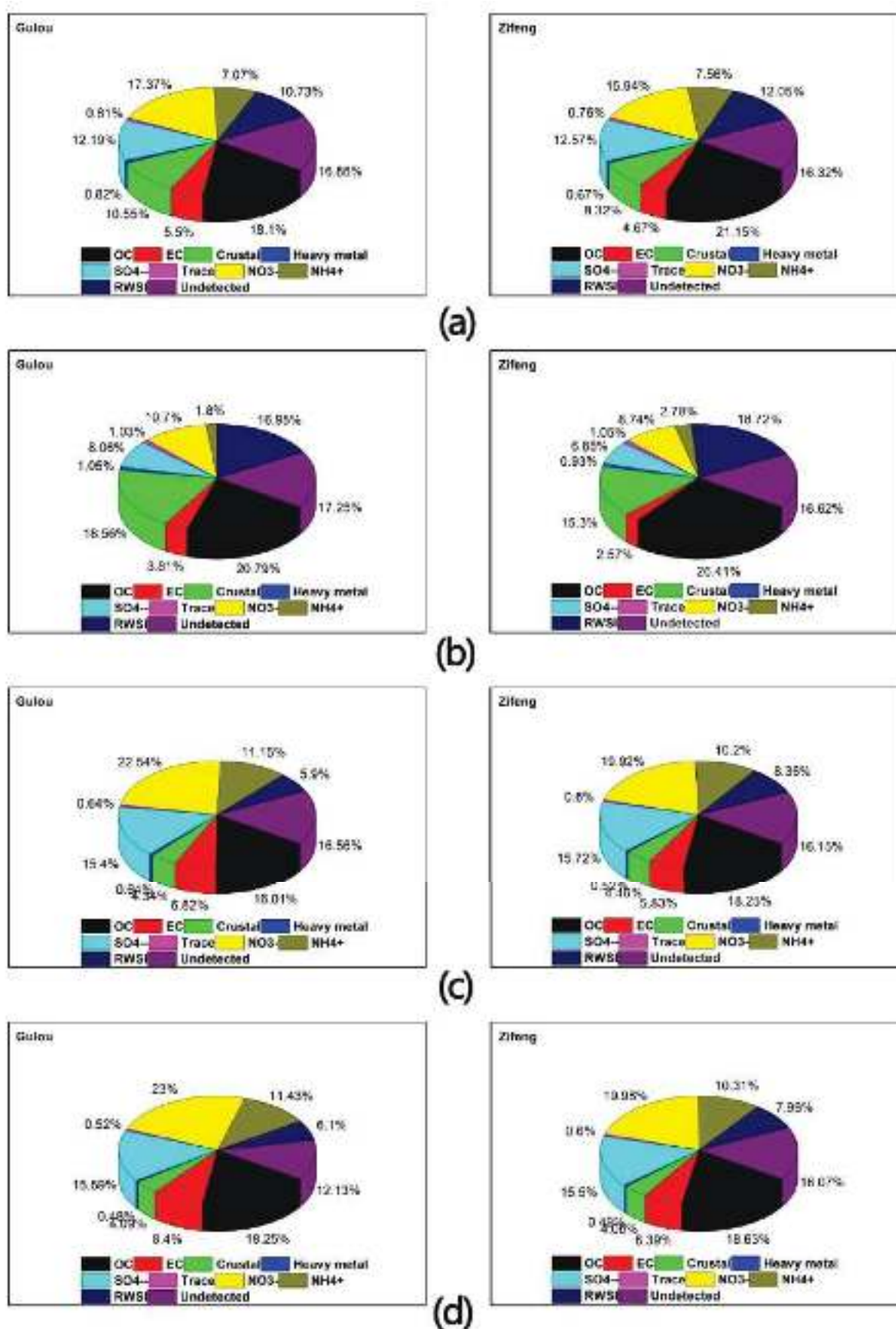


Figure 5. The percentages of chemical compositions in (a) PM₁₀, (b) PM_{10-2.1}, (c) PM_{2.1}, and (d) PM_{1.1} at Gulou and Zifeng.

3.2.2. Water-Soluble Ions

Water-soluble ions are indispensable components in PM, taking a percentage of about 40–50%, especially in fine particles, where there was the largest part of all the compositions. The sulfate, nitrate, ammonium, and the rest of the water-soluble ions (RWSI) accounted for varied from 8.1–15.6%, 10.7–23.0%, 1.8–11.4%, and 5.9–17.0%, respectively, in different particulate sizes at Gulou, and varied from 6.9–15.7%, 8.7–20.0%, 2.8–10.3%, and 8.0–18.7%, respectively, in different particulate sizes at Zifeng. Most of the water-soluble ions showed the characteristics of larger mass concentrations in finer particles, except Na^+ , Ca^{2+} , Mg^{2+} , and F^- , which showed the characteristics of higher mass concentrations in coarse particulate matter. As we know, sea salt was the major source of Na^+ and F^- in coarse particles [49,50]. Therefore, the abundant Na^+ and F^- in coarse particles were mainly from marine salt. However, the sum mass concentrations of Na^+ and F^- in coarse particles only accounted for about 2.56% of the $\text{PM}_{10-2.1}$ mass at the ground level, indicating less contribution from sea salt aerosols to the particulate matter. In total, 88.8% of Ca^{2+} and 76.2% of Mg^{2+} were concentrated in $\text{PM}_{10-2.1}$ at the ground, and the concentrations of Ca^{2+} and Mg^{2+} at Gulou (20 m) were about 100.5% and 52.4% larger than those at Zifeng (380 m), indicating that Ca^{2+} and Mg^{2+} were mainly from the sources of soil and construction dust [51,52] in coarse particles and local ground areas.

To evaluate the equivalence between cations and anions, the cations and anions were calculated based on the following equations, and the ratio of cations/anions (C/A) was applied to estimate the neutralizing level for size-fractionated PM at two heights. The average ratios of cations to anions at Gulou in nine particulate sizes ($<0.43 \mu\text{m}$, $0.43\text{--}0.65 \mu\text{m}$, $0.65\text{--}1.1 \mu\text{m}$, $1.1\text{--}2.1 \mu\text{m}$, $2.1\text{--}3.3 \mu\text{m}$, $3.3\text{--}4.7 \mu\text{m}$, $4.7\text{--}5.8 \mu\text{m}$, $5.8\text{--}9.0 \mu\text{m}$, and $9.0\text{--}10 \mu\text{m}$) were 0.99, 0.94, 0.93, 0.91, 0.98, 1.09, 1.35, 1.66, and 1.92, respectively. In addition, the ratios of C/A at Zifeng in nine particulate sizes from fine to coarse were 1.00, 0.87, 0.91, 0.92, 1.02, 1.05, 0.91, 1.84, and 1.47. Similar neutralizing relationships were shown at different height sites, which implied an acidic tendency of fine particles and an alkaline tendency of coarse particles. The loss of CO_3^{2-} and HCO_3^- , which were not analyzed, is a reason for the deficit of anions in the coarse particles.

$$\text{Cation} = \text{Na}^+ / 23 + \text{K}^+ / 39 + 2 \times \text{Mg}^{2+} / 24 + 2 \times \text{Ca}^{2+} / 40 + \text{NH}_4^+ / 18 + (\text{CH}_3)_2\text{NH}_2^+ / 46 \quad (3)$$

$$\text{Anion} = \text{Cl}^- / 35.5 + \text{F}^- / 19 + \text{NO}_3^- / 62 + 2 \times \text{SO}_4^{2-} / 96 + \text{HCOO}^- / 45 + \text{CH}_3\text{COO}^- / 59 + 2 \times \text{C}_2\text{O}_4^{2-} / 88 \quad (4)$$

In further analysis, the relative contribution of stationary sources such as industrial and powered coal fire to the mobile source for size-fractionated PM was indicated by the ratio of $\text{NO}_3^- / \text{SO}_4^{2-}$ [53,54]. As listed in Table 4, the average mass ratios of $\text{NO}_3^- / \text{SO}_4^{2-}$ were compared at different height levels in different particulate sizes: 1.42, 1.33, 1.46, and 1.48 at Gulou (20 m) and 1.27, 1.27, 1.28, and 1.29 at Zifeng (380 m) in PM_{10} , $\text{PM}_{10-2.1}$, $\text{PM}_{2.1}$, and $\text{PM}_{1.1}$, respectively. The calculated ratios of $\text{NO}_3^- / \text{SO}_4^{2-}$ at Gulou were higher than those at Zifeng, indicating that the mobile source played a relatively more important role to PM at the ground level than at 380 m. The average ratios of $\text{NO}_3^- / \text{SO}_4^{2-}$ at Gulou showed a feature with a larger value of finer particles, suggesting that more contributions from the mobile source were to fine particles than coarse particles, whereas the mean ratios of $\text{NO}_3^- / \text{SO}_4^{2-}$ at Zifeng were similar in PM_{10} , $\text{PM}_{10-2.1}$, $\text{PM}_{2.1}$, and $\text{PM}_{1.1}$, implying that the sources of nitrate and sulfate at higher heights were relatively fixed at different particulate sizes and would be dominantly driven by the secondary formation mechanisms. In addition, higher ratio values of $\text{NO}_3^- / \text{SO}_4^{2-}$ were also found during the pollutant days: 1.44, 1.34, 1.48, and 1.51 at Gulou (20 m) and 1.43, 1.15, 1.48, and 1.54 at Zifeng (380 m) in PM_{10} , $\text{PM}_{10-2.1}$, $\text{PM}_{2.1}$, and $\text{PM}_{1.1}$, respectively, which indicated that the formation of nitrate played an important role under pollutant conditions. Comparing with other studies, the $\text{NO}_3^- / \text{SO}_4^{2-}$ ratios were similar to the work (1.50–0.54) in Beijing at 260 m height before and during the APEC [24] and were higher than those works (0.65–0.86) in Tianjin from

10–220 m height [10,41,54,55], but they were lower than works in Southern California (5.0) and in Denver (2.09) due to the lower usage of sulfur-containing coal in the USA than in China [56–58].

3.2.3. Carbonaceous Components

Carbonaceous species are a very important part of particles. The mass concentrations of size-fractionated OC, EC, and the ratios of OC/EC are shown in Tables 3 and 4 and Figure 6. At ground level, the size distribution of OC was a trimodal mode with peaks at 0.43–0.65 μm , 1.1–2.1 μm , and 4.7–5.8 μm . EC had a bimodal distribution that peaked at <0.43 μm and 5.8–9.0 μm . At the 380 m level, the size distribution of OC was found to be a bimodal mode peaking at 0.43–0.65 μm and 3.3–4.7 μm , while EC only showed a single peak at 0.43–0.65 μm . It could be found that more carbonaceous components were concentrated in fine particulate matter at higher heights. To PM_{10} and $\text{PM}_{10-2.1}$, the mass concentrations of OC and EC were larger at Gulou than Zifeng, indicating a decreasing trend with increased height. Interestingly, in contrast to $\text{PM}_{2.1}$ and $\text{PM}_{1.1}$, the mass concentrations of OC and EC were larger at Zifeng than Gulou, especially the organic acids such as CH_3COO^- and $\text{C}_2\text{O}_4^{2-}$, which could reflect much more influences of the formation mechanism of secondary organic aerosols at the higher level than at the ground. The size-fractionated ratios of OC/EC showed similar trends at Gulou and Zifeng with unimodal distribution. The peak of the OC/EC ratio at Gulou was 3.3–4.7 μm , while at Zifeng the OC/EC ratio peaked at 4.7–5.8 μm . At both sites, the ratios were larger than two, indicating the formation of secondary organic particles [59,60].

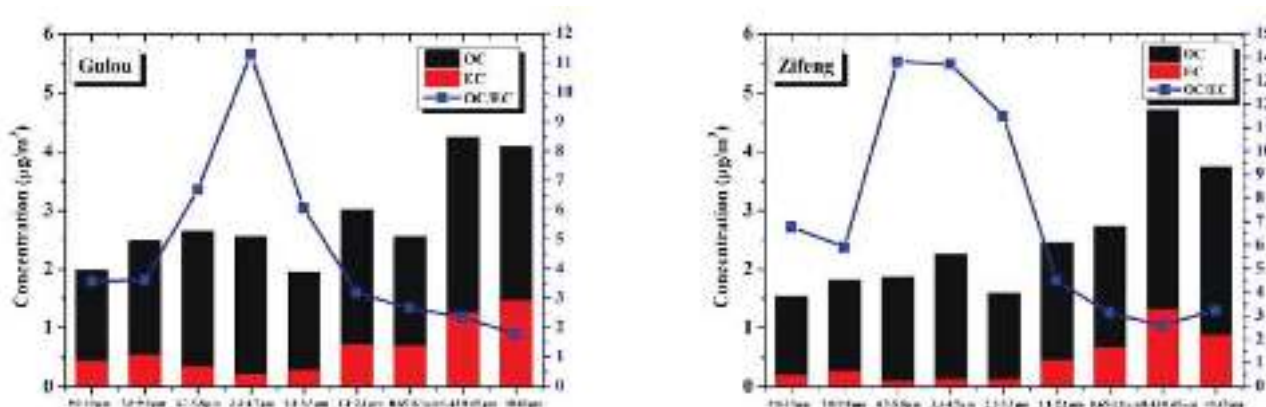


Figure 6. Carbonaceous species and ratios of OC/EC of size-fractionated PM at Gulou (20 m) and Zifeng (380 m).

In addition, the correlation between OC and EC was calculated, which could be a factor of common sources if the value was high. The correlation values (R^2) showed an increasing trend with the particulate size decreased at both sites: 0.80 (PM_{10}) < 0.81 ($\text{PM}_{2.1}$) < 0.91 ($\text{PM}_{1.1}$) at Gulou and 0.68 (PM_{10}) < 0.76 ($\text{PM}_{2.1}$) < 0.79 ($\text{PM}_{1.1}$) at Zifeng. This result suggested that there were common sources of OC and EC in fine particles, while the sources were inconsistent in coarse particles. The OC of coarse PM might be contributed from the hygroscopic growth of water-soluble OC during the transport or the emissions of industrial sources in the regional areas [61]. The EC in the coarse particles could be formed by the resuspension of soil dust and the friction loss of tires [61–63].

Table 3. The average mass concentrations of main chemical compositions at each sampling height in PM₁₀, PM_{10-2.1}, PM_{2.1}, and PM_{1.1} ($\mu\text{g m}^{-3}$).

	Gulou (20 m)				Zifeng (380 m)			
	PM ₁₀	PM _{10-2.1}	PM _{2.1}	PM _{1.1}	PM ₁₀	PM _{10-2.1}	PM _{2.1}	PM _{1.1}
Al	1.24	0.92	0.32	0.20	0.81	0.51	0.30	0.21
Ca	6.80	5.26	1.54	1.10	4.52	3.00	1.52	1.03
Cu	0.07	0.04	0.03	0.018	0.05	0.03	0.02	0.016
Fe	2.64	2.03	0.61	0.38	1.52	0.98	0.54	0.35
Mg	0.74	0.56	0.18	0.10	0.48	0.31	0.17	0.11
Pb	0.07	0.03	0.04	0.020	0.05	0.02	0.03	0.025
V	0.008	0.005	0.004	0.002	0.005	0.002	0.003	0.002
Zn	0.30	0.13	0.17	0.07	0.18	0.08	0.10	0.07
Na ⁺	1.25	0.88	0.37	0.27	1.12	0.64	0.49	0.34
K ⁺	0.94	0.31	0.63	0.46	0.99	0.30	0.69	0.34
Cl ⁻	2.30	1.13	1.17	0.78	1.66	0.80	0.86	0.64
NO ₃ ⁻	18.82	5.06	13.76	9.41	14.03	2.73	11.30	8.94
SO ₄ ²⁻	13.21	3.81	9.40	6.37	11.07	2.16	8.91	6.94
NH ₄ ⁺	7.66	0.85	6.81	4.67	6.66	0.87	5.78	4.61
OC	19.60	9.84	9.77	7.46	18.62	8.28	10.35	8.34
EC	5.96	1.80	4.16	3.44	4.11	0.81	3.30	2.86
CH ₃ COO ⁻	0.61	0.34	0.27	0.18	2.41	1.12	1.29	1.02
HCOO ⁻	0.61	0.43	0.18	0.13	0.42	0.23	0.19	0.15
C ₂ O ₄ ²⁻	0.25	0.15	0.10	0.07	0.43	0.18	0.25	0.20
(CH ₃) ₂ NH ₂ ⁺	0.12	0.06	0.06	0.04	0.09	0.05	0.04	0.03

Table 4. The average ratios of cations/anions, NO₃⁻/SO₄²⁻, and OC/EC for size-fractionated PM.

PM Size	Cations/Anions		NO ₃ /SO ₄ ²		OC/EC	
	GL ^a	ZF ^a	GL	ZF	GL	ZF
<0.43 μm	0.99	1.00	1.44	0.92	1.78	3.24
0.43–0.65 μm	0.94	0.87	1.35	1.42	2.35	2.60
0.65–1.1 μm	0.93	0.91	1.68	1.34	2.66	3.12
1.1–2.1 μm	0.91	0.92	1.44	1.19	3.18	4.50
2.1–3.3 μm	0.98	1.02	1.32	1.39	6.07	11.53
3.3–4.7 μm	1.09	1.05	1.55	1.54	11.30	13.77
4.7–5.8 μm	1.35	0.91	1.15	0.86	6.69	13.87
5.8–9.0 μm	1.66	1.84	1.52	1.34	3.62	5.92
9.0–10 μm	1.92	1.47	1.06	1.04	3.57	6.77
PM ₁₀	1.08	1.01	1.42	1.27	3.29	4.53
PM _{10-2.1}	1.36	1.27	1.33	1.27	5.46	10.28
PM _{2.1}	0.94	0.91	1.46	1.28	2.35	3.13
PM _{1.1}	0.95	0.91	1.48	1.29	2.17	2.92

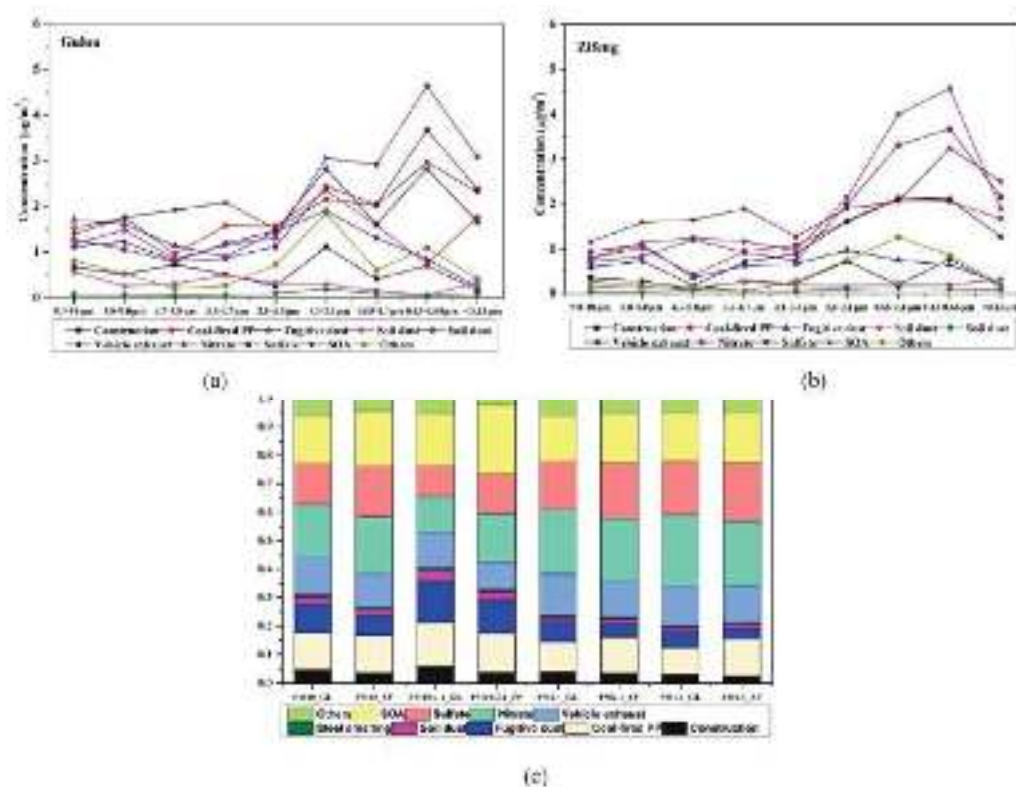
^a GL represents Gulou site (20 m), ZF represents Zifeng site (380 m).

3.3. Source Apportionment

The source contributions of size-fractionated PM were calculated with the CMB model, which has been widely used in previous studies [64–66]. The source profiles including soil dust, the coal-fired power plant, vehicle exhaust, steel smelting, construction dust, secondary sulfate, secondary nitrate, and fugitive dust were used as model input for the CMB model. These profiles were obtained by previous work in the Yangtze River Delta [18]. Twenty-two species (Al, As, Ba, Ca, Cd, Cr, Cu, Fe, Mg, Mn, Pb, Zn, Ti, V, Cl⁻, NO₃⁻, SO₄²⁻, NH₄⁺, K⁺, Na⁺, OC, and EC), as well as the mass concentrations of size-fractionated PM, were used as ambient data for the CMB calculations. The source contribution estimates (SCEs) of different particulate sizes at Gulou and Zifeng are summarized in Table 5 and are also shown in Figure 7.

Table 5. Source contribution estimates (SCEs) of PM₁₀, PM_{10-2.1}, PM_{2.1}, and PM_{1.1} mass concentrations with CMB model ($\mu\text{g m}^{-3}$).

	Gulou (20 m)				Zifeng (380 m)			
	PM ₁₀	PM _{10-2.1}	PM _{2.1}	PM _{1.1}	PM ₁₀	PM _{10-2.1}	PM _{2.1}	PM _{1.1}
Construction	5.09	2.69	2.41	1.28	3.05	1.22	1.84	1.11
Coal-fired PP	13.84	7.39	6.45	4.09	11.65	4.24	7.41	5.81
Fugitive dust	11.11	6.81	4.30	2.39	6.22	3.66	2.56	1.60
Soil dust	2.77	1.93	0.84	0.55	1.83	0.95	0.88	0.71
Steel smelting	0.79	0.37	0.41	0.22	0.70	0.28	0.42	0.32
Vehicle exhaust	14.74	5.81	8.93	6.10	10.17	3.06	7.12	5.50
Nitrate	19.69	5.98	13.70	10.65	17.88	5.27	12.61	10.47
Sulfate	15.65	5.11	10.54	8.11	15.51	4.38	11.12	9.14
SOA	18.14	8.68	9.47	7.31	17.23	7.54	9.69	7.79
Others	6.51	2.54	3.96	2.12	3.82	0.76	3.06	2.32

**Figure 7.** Source contributions of (a) size-fractionated PM at Gulou ($\mu\text{g}/\text{m}^3$), (b) size-fractionated PM at Zifeng ($\mu\text{g}/\text{m}^3$), and (c) PM₁₀, PM_{10-2.1}, PM_{2.1}, and PM_{1.1} at both sites (100%).

The contributions of total emission sources to the size-fractionated PM accounted for varied from 97.3% to 89.9% at Gulou and from 99.2% to 92.2% at Zifeng. The three highest contributors of PM₁₀ were found to keep consistent with nitrate, secondary organic aerosols, and sulfate arranging in order of contribution concentrations. To coarse particles, the three largest sources were secondary organic aerosols, the coal-fired power plant, and fugitive dust at Gulou, whereas the three largest sources were secondary organic aerosols, nitrate, and sulfate at Zifeng, indicating that the ground level would be more influenced by local sources such as fugitive dust, but at higher heights the formations of secondary inorganic and organic aerosols were more important. There was a similar contribution pattern in PM_{2.1} and PM_{1.1} at both heights, and the three largest emissions were nitrate, sulfate, and secondary organic aerosols. Interestingly, the fourth largest emission at Gulou was vehicle exhaust in PM₁₀, PM_{2.1}, and PM_{1.1}, whereas it was the coal-fired power plant

at Zifeng in PM_{10} , $PM_{2.1}$, and $PM_{1.1}$, also implying that the local source (vehicle exhaust) influenced more at the ground level.

As shown in Figure 7, the contributions to coarse and fine particulate matter were significantly different for specific sources. The construction dust (3.9–5.7% vs. 3.2–3.9%), fugitive dust (11.7–14.4% vs. 4.5–7.1%), and soil dust (3.0–4.1% vs. 1.4–1.6%) in coarse and fine particles showed larger contributions in the coarse size bin of PM, in which was found a similar tendency with the concentrations of crustal elements described in Section 3.2.1. The contributions of nitrate (12.7–16.8% vs. 22.2–22.5%) and sulfate (10.8–14.0% vs. 17.3–19.6%) in $PM_{10-2.1}$ and $PM_{2.1}$ indicated an increasing trend as the particulate size decreased. However, the source contributions of secondary organic aerosols were 18.3–24.1% of $PM_{10-2.1}$ and 15.5–17.1% of $PM_{2.1}$.

As shown in Table 5, the contribution estimates of each source for PM_{10} and $PM_{10-2.1}$ were larger at Gulou (20 m) than Zifeng (380 m), depending more on the higher concentrations of PM_{10} and $PM_{10-2.1}$ at Gulou than Zifeng. By contrast, the source contribution estimates for fine particles such as $PM_{2.1}$ and $PM_{1.1}$ showed different features. Dusts, such as construction dust, fugitive dust, and soil dust, contributed a larger amount and proportion at Gulou than Zifeng since these dust sources were from ground and local areas. Vehicle exhaust also contributed larger concentrations at Gulou than Zifeng, which could reflect the influence of heavy traffic at the ground near the sampling site. However, the contributions of sulfate and secondary organic aerosols become larger with higher height, illustrating that the formation mechanisms of secondary aerosols played an important role at the height above the urban canopy. Similarly, the coal-fired power plant and steel smelting also contributed larger concentrations at Zifeng than Gulou, which might be caused not only by the industrial areas in the north of Nanjing but also by the transportation from regional areas. Furthermore, 36 h back trajectories were calculated every three hours for the sampling periods at 20 m and 380 m in this study. A total of 440 trajectories were used for clustering analysis in order to identify common atmospheric transport patterns. All trajectories were categorized into seven and six clusters at 20 m and 380 m, respectively. The average trajectories were shown in Figure 8. It could be found that there were more local sources (clusters two, three, and five in Figure 8a) at 20 m with lower wind speed, while there was more long-distance transportation (clusters one, four, five, and six in Figure 8b) from north of Nanjing with greater wind speed at 380 m.

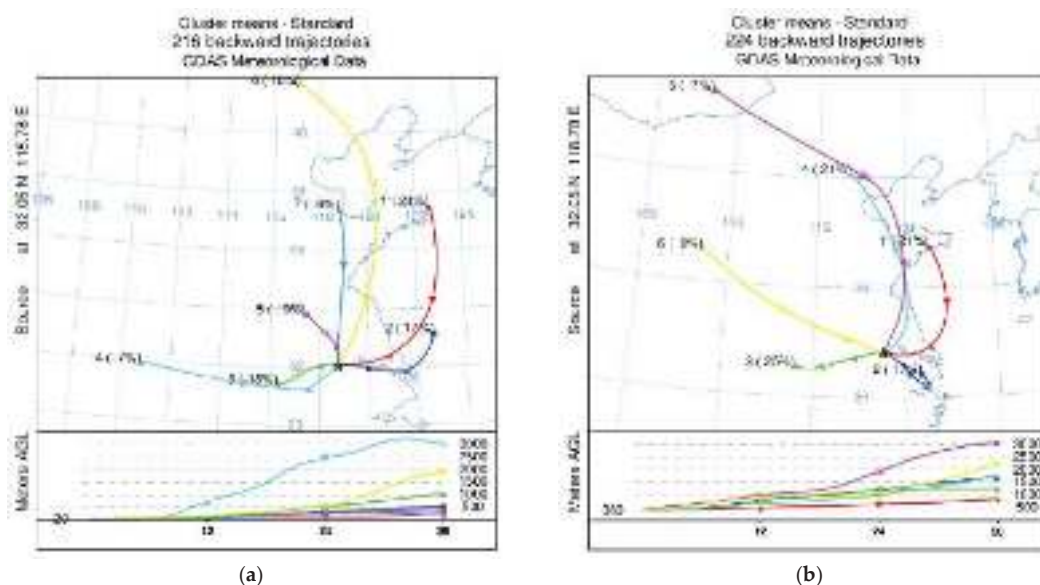


Figure 8. Clustering analysis every three hours for the sampling periods at (a) 20 m and (b) 380 m.

4. Conclusions

The concentrations and chemical compositions of size-fractionated PM were sampled and measured from 16 November to 12 December in 2016 at Gulou (20 m) and Zifeng (380 m) in Nanjing, China. The characteristics of size-fractionated PM mass concentrations at different heights were described and the chemical components including elements, water-soluble ions, and carbonaceous species were analyzed and compared for different particulate sizes and sites. Furthermore, the source apportionment was carried out with the CMB model, and the characteristics of contribution estimates were discussed in this study.

The concentrations of PM_{10} and $PM_{2.1}$ were $108.3 \pm 23.4 \mu\text{g m}^{-3}$ and $61.0 \pm 18.8 \mu\text{g m}^{-3}$ at Gulou and were $88.1 \pm 21.1 \mu\text{g m}^{-3}$ and $56.7 \pm 18.6 \mu\text{g m}^{-3}$ at Zifeng, which indicated a decreasing trend as the height increased. In contrast, the concentrations of $PM_{1.1}$ were $40.9 \pm 13.0 \mu\text{g m}^{-3}$ and $44.8 \pm 15.8 \mu\text{g m}^{-3}$ at Gulou and Zifeng, indicating particles congregating in a finer particulate size bin at the higher level. The PM pollutant days were relative to the weather conditions, especially when wind speed was low.

All the species of size-fractionated PM detected in this study accounted for 82.7–87.9% of the total PM mass concentrations at Gulou and accounted for 83.1–83.4% at Zifeng. The crustal elements were concentrated more in coarse particles, accounting for 18.6% and 15.3% at Gulou and Zifeng. The water-soluble ions, especially nitrate (8.7–23.0%), sulfate (6.9–15.6%), and ammonium (1.8–11.4%), were dominant components of size-fractionated PM. The concentrations of nitrate, sulfate, and ammonium showed an increasing tendency with decreasing particulate size. Organic carbon was another dominant component of size-fractionated PM, accounting for 16.0–20.8% and 18.3–26.4%, respectively, at Gulou and Zifeng, which indicated larger contributions at the higher level.

The source contribution estimates (SCEs) calculated by the CMB model showed that the secondary inorganic and organic aerosols were the largest three contributors of PM_{10} , $PM_{2.1}$, and $PM_{1.1}$ at both sites, but the fourth largest sources at Gulou and Zifeng were vehicle exhaust and the coal-fired power plant, respectively. To $PM_{10-2.1}$, the largest three contributors at Gulou were secondary organic aerosols, the coal-fired power plant, and fugitive dust, which was different with Zifeng. Zifeng showed secondary organic aerosols, nitrate, and sulfate as the largest sources of $PM_{10-2.1}$. These results illustrated that dusts including construction dust, fugitive dust, soil dust, and vehicle exhaust would contribute more at the ground level. In recent years, concentrations were decreased by 41.4%, 26.3%, and 24.8% of PM_{10} , $PM_{2.1}$, and $PM_{1.1}$ in this study compared to the winter of 2010 at the same sampling site. These results showed an encouraging improvement in the control of particulate matter in Nanjing.

Author Contributions: Conceptualization, T.W. and H.W.; data curation, P.C.; funding acquisition, T.W.; investigation, M.X. and B.Z.; methodology, S.L. and M.L.; supervision, H.W.; visualization, P.C. and H.W.; writing—original draft, H.W. All authors have read and agreed to the published version of the manuscript.

Funding: This work was supported by the National Natural Science Foundation of China (42077192, 41621005), the National Key Basic Research and Development Program of China (2020YFA0607802, 2019YFC0214603) and the Emory University-Nanjing University Collaborative Research Grant.

Institutional Review Board Statement: Not applicable.

Conflicts of Interest: The authors declare no conflict of interest.

References

1. Rohr, A.C.; Wyzga, R.E. Attributing health effects to individual particulate matter constituents. *Atmos. Environ.* **2012**, *62*, 130–152. [CrossRef]
2. Ma, J.; Chen, L.L.; Guo, Y.; Wu, Q.; Yang, M.; Wu, M.H. Phthalate diesters in Airborne $PM_{2.5}$ and PM_{10} in a suburban area of Shanghai: Seasonal distribution and risk assessment. *Sci. Total Environ.* **2014**, *497*, 467–474. [CrossRef] [PubMed]
3. Intergovernmental Panel on Climate Change (IPCC). 2006. Available online: <http://www.ipcc-nggip.iges.or.jp/public/2006gl/index.html> (accessed on 26 May 2022).

4. Isaksen, I.S.; Granier, C.; Myhre, G.; Berntsen, T.K.; Dalsøren, S.B.; Gauss, M.; Klimonth, Z.; Benestad, R.; Bousquet, P.; Collins, W.; et al. Atmospheric composition change: Climate—Chemistry interactions. *Atmos. Environ.* **2009**, *43*, 5138–5192. [CrossRef]
5. Ramachandran, S.; Kedia, S. Black carbon aerosols over an urban region: Radiative forcing and climate impact. *J. Geophys. Res. Atmos.* **2010**, *115*, D10202. [CrossRef]
6. Watson, J.G. Visibility: Science and regulation. *J. Air Waste Manag. Assoc.* **2002**, *52*, 628–713. [CrossRef] [PubMed]
7. Ying, Q.; Mysliwiec, M.; Kleeman, M.J. Source apportionment of visibility impairment using a three-dimensional source-oriented air quality model. *Environ. Sci. Technol.* **2014**, *38*, 1089–1101. [CrossRef]
8. Sun, Y.L.; Zhuang, G.; Tang, A.; Wang, Y.; An, Z. Chemical characteristics of PM_{2.5} and PM₁₀ in haze-fog episodes in Beijing. *Environ. Sci. Technol.* **2006**, *40*, 3148–3155. [CrossRef]
9. Zhao, X.J.; Zhao, P.S.; Xu, J.; Meng, W.; Pu, W.; Dong, F.; He, D.; Shi, Q. Analysis of a winter regional haze event and its formation mechanism in the North China Plain. *Atmos. Chem. Phys.* **2013**, *13*, 5685–5696. [CrossRef]
10. Wu, H.; Zhang, Y.; Han, S.; Wu, J.; Bi, X.; Shi, G.; Wang, J.; Yao, Q.; Cai, Z.; Liu, J.; et al. Vertical characteristics of PM_{2.5} during the heating season in Tianjin, China. *Sci. Total Environ.* **2015**, *523*, 152–160. [CrossRef]
11. Tie, X.; Cao, J. Aerosol pollution in China: Present and future impact on environment. *Particuology* **2009**, *7*, 426–431. [CrossRef]
12. Zheng, M.; Wang, F.; Hagler, G.; Hou, X.; Bergin, M.; Cheng, Y. Sources of excess urban carbonaceous aerosol in the Pearl River Delta Region, China. *Atmos. Environ.* **2011**, *45*, 1175–1182. [CrossRef]
13. Wang, L.T.; Wei, Z.; Yang, J.; Zhang, Y.; Zhang, F.; Su, J.; Meng, C.; Zhang, Q. The 2013 severe haze over the southern Hebei, China: Model evaluation, source apportionment, and policy implications. *Atmos. Chem. Phys.* **2014**, *14*, 3151–3173. [CrossRef]
14. Choi, K.; Chong, K. Modified Inverse Distance Weighting Interpolation for Particulate Matter Estimation and Mapping. *Atmosphere* **2022**, *13*, 846. [CrossRef]
15. Wu, H.; Wang, T.; Wang, Q.; Cao, Y.; Qu, Y.; Nie, D. Radiative effects and chemical compositions of fine particles modulating urban heat island in Nanjing, China. *Atmos. Environ.* **2021**, *247*, 118201. [CrossRef]
16. Zhang, Y.; Xu, H.; Tian, Y.; Shi, G.L.; Zeng, F.; Wu, J. The study on vertical variability of PM₁₀ and the possible sources on a 220 m tower, in Tianjin, China. *Atmos. Environ.* **2011**, *45*, 6133–6140. [CrossRef]
17. Quan, J.; Tie, X.; Zhang, Q.; Liu, Q.; Li, X.; Gao, Y. Characteristics of heavy aerosol pollution during the 2012–2013 winter in Beijing, China. *Atmos. Environ.* **2014**, *88*, 83–89. [CrossRef]
18. Chen, P.; Wang, T.; Dong, M.; Kasoar, M.; Han, Y.; Xie, M.; Li, S.; Zhuang, B.; Li, M.; Huang, T. Characterization of major natural and anthropogenic source profiles for size-fractionated PM in Yangtze River Delta. *Sci. Total Environ.* **2017**, *598*, 135–145. [CrossRef]
19. Kanakidou, M.; Seinfeld, J.H.; Pandis, S.N.; Barnes, I.; Dentener, F.J.; Facchini, M.C.; Van Dingenen, R.; Ervens, B.; Nenes, A.; Nielsen, C.J.; et al. Organic aerosol and global climate change modeling: A review. *Atmos. Chem. Phys.* **2005**, *5*, 1053–1123. [CrossRef]
20. Zhang, Q.; Jimenez, J.L.; Canagaratna, M.R.; Allan, J.D.; Coe, H.; Ulbrich, I.; Alfarra, M.R.; Takami, A.; Middlebrook, A.M.; Sun, Y.L.; et al. Ubiquity and dominance of oxygenated species in organic aerosols in anthropogenically influenced Northern Hemisphere midlatitudes. *Geophys. Res. Lett.* **2007**, *34*, L13801. [CrossRef]
21. Shi, G.; Tian, Y.; Han, S.; Zhang, Y.; Li, X.; Feng, Y.; Wu, J.; Zhu, T. Vertical characteristics of carbonaceous species and their source contributions in a Chinese mega city. *Atmos. Environ.* **2012**, *60*, 358–365. [CrossRef]
22. Han, S.; Zhang, Y.; Wu, J.; Zhang, X.; Tian, Y.; Wang, Y.; Ding, J.; Yan, W.; Bi, X.; Shi, G.; et al. Evaluation of regional background particulate matter concentration based on vertical distribution characteristics. *Atmos. Chem. Phys.* **2015**, *15*, 11165–11177. [CrossRef]
23. Sun, Y.; Chen, C.; Zhang, Y.; Xu, W.; Zhou, L.; Cheng, X.; Zheng, H.; Ji, D.; Li, J.; Tang, X.; et al. Rapid formation and evolution of an extreme haze episode in Northern China during winter 2015. *Sci. Rep.* **2016**, *6*, 27151. [CrossRef]
24. Chen, P.; Wang, T.; Hu, X.; Xie, M. Chemical mass balance source apportionment of size-fractionated particulate matter in Nanjing, China. *Aerosol Air Qual. Res.* **2015**, *15*, 1855–1867. [CrossRef]
25. Chen, P.; Wang, T.; Lu, X.; Yu, Y.; Kasoar, M.; Xie, M.; Zhuang, B. Source apportionment of size-fractionated particles during the 2013 Asian Youth Games and the 2014 Youth Olympic Games in Nanjing, China. *Sci. Total Environ.* **2017**, *579*, 860–870. [CrossRef]
26. Zhang, W.; Zhang, Y.; Lv, Y.; Li, K.; Li, Z. Observation of atmospheric boundary layer height by round-based LiDAR during haze days. *J. Remote Sens.* **2013**, *17*, 981–992.
27. Chow, J.; Watson, J. Review of PM_{2.5} and PM₁₀ apportionment for fossil fuel combustion and other sources by the chemical mass balance receptor model. *Energy Fuels* **2002**, *16*, 222–260. [CrossRef]
28. Deng, J.; Zhang, Y.; Qiu, Y.; Zhang, H.; Du, W.; Xu, L.; Hong, Y.; Chen, Y.; Chen, J. Source apportionment of PM_{2.5} at the Lin'an regional background site in China with three receptor models. *Atmos. Res.* **2018**, *202*, 23–32. [CrossRef]
29. Wang, H.; Zhuang, Y.; Wang, Y.; Sun, Y.; Yuan, H.; Zhuang, G. Long-term monitoring and source apportionment of PM_{2.5}/PM₁₀ in Beijing, China. *J. Environ. Sci.* **2008**, *20*, 1323–1327. [CrossRef]
30. Xie, S.; Liu, Z.; Chen, T.; Hua, L. Spatiotemporal variations of ambient PM₁₀ source contributions in Beijing in 2004 using positive matrix factorization. *Atmos. Chem. Phys.* **2008**, *8*, 2701–2716. [CrossRef]
31. Yao, L.; Yang, L.; Yuan, Q.; Yan, C.; Dong, C.; Meng, C. Source apportionment of PM_{2.5} in a background site in the North China Plain. *Sci. Total Environ.* **2016**, *541*, 590–598. [CrossRef]

32. Stohl, A. Trajectory statistics—A new method to establish source-receptor relationships of air pollutants and its application to the transport of particulate sulfate in Europe. *Atmos. Environ.* **1996**, *30*, 579–587. [CrossRef]
33. Hwang, I.; Hopke, P. Estimation of source apportionment and potential source locations of PM_{2.5} at a west coastal IMPROVE site. *Atmos. Environ.* **2007**, *41*, 506–518. [CrossRef]
34. Yang, Y.; Zheng, X.; Gao, Z.; Wang, H.; Wang, T.; Li, Y.; Lau, G.; Yim, S. Long-Term Trends of Persistent Synoptic Circulation Events in Planetary Boundary Layer and Their Relationships with Haze Pollution in Winter Half Year over Eastern China. *J. Geophys. Res. Atmos.* **2018**, *123*, 10991–11007. [CrossRef]
35. Yang, Y.; Yim, S.H.; Haywood, J.; Osborne, M.; Chan, J.C.; Zeng, Z.; Cheng, J.C. Characteristics of Heavy Particulate Matter Pollution Events over Hong Kong and Their Relationships with Vertical Wind Profiles Using High-Time-Resolution Doppler Lidar Measurements. *J. Geophys. Res. Atmos.* **2019**, *124*, 9609–9623. [CrossRef]
36. Xue, M.; Ma, J.; Yan, P.; Pan, X. Impacts of pollution and dust aerosols on the atmospheric optical properties over a polluted rural area near Beijing city. *Atmos. Res.* **2011**, *101*, 835–843. [CrossRef]
37. Chow, J.; Watson, J.; Pritchett, L.; Pierson, W.; Frazier, C.; Purcell, R. The dri thermal/optical reflectance carbon analysis system: Description, evaluation and applications in U.S. air quality studies. *Atmos. Environ.* **1993**, *27*, 1185–1201. [CrossRef]
38. Chow, J.; Watson, J.; Chen, L.; Arnott, W.; Moosmuller, H. Equivalence of elemental carbon by thermal/optical reflectance and transmittance with different temperature protocols. *Environ. Sci. Technol.* **2004**, *38*, 4414–4422. [CrossRef]
39. Draxler, R.; Rolph, G. *HYSPLIT (HYbrid Single-Particle Lagrangian Integrated Trajectory) Model*; Access via NOAA ARL READY Website; NOAA Air Resources Laboratory: Silver Spring, MD, USA, 2012, Available online: <http://ready.arl.noaa.gov/HYSPLIT.php> (accessed on 26 May 2022).
40. Draxler, R.; Stunder, B.; Rolph, G.; Stein, A.; Taylor, A. *HYSPLIT4 User's Guide*, version 4; Report; NOAA: Silver Spring, MD, USA, 2012.
41. Wang, J.; Zhou, M.; Liu, B.; Wu, J.; Peng, X.; Zhang, Y.; Han, S.; Feng, Y.; Zhu, T. Characterization and source apportionment of size-segregated atmospheric particulate matter collected at ground level and from the urban canopy in Tianjin. *Environ. Pollut.* **2016**, *219*, 982–992. [CrossRef]
42. Wongphatarakul, V.; Friedlander, S.; Pinto, J. A comparative study of PM_{2.5} ambient aerosol chemical databases. *Environ. Sci. Technol.* **1998**, *32*, 3926–3934. [CrossRef]
43. Wilson, J.; Kingham, S.; Sturman, A. Intraurban variations of PM₁₀ air pollution in Christchurch, New Zealand, Implications for epidemiological studies. *Sci. Total Environ.* **2006**, *367*, 2–3. [CrossRef]
44. Hwang, I.; Hopke, P.; Pinto, J. Source apportionment and spatial distributions of coarse particles during the regional air pollution study. *Environ. Sci. Technol.* **2008**, *42*, 3524–3530. [CrossRef] [PubMed]
45. Amato, F.; Alastuey, A.; Rosa, J.; Castanedo, Y.; Campa, A.; Pandolfi, M.; Lozano, A.; Gonzalez, J.; Querol, X. Trends of road dust emission contributions on ambient air particulate levels at rural, urban and industrial sites in southern Spain. *Atmos. Chem. Phys.* **2014**, *14*, 3533–3544. [CrossRef]
46. Jia, Y.; Rahn, K.; He, K.; Wen, T.; Wang, Y. A novel technique for quantifying the regional component of urban aerosol solely from its sawtooth cycles. *J. Geophys. Res.* **2008**, *113*, D21309. [CrossRef]
47. Guo, S.; Hu, M.; Zamora, M.; Peng, J.; Shang, D.; Zheng, J.; Du, Z.; Wu, Z.; Shao, M.; Zeng, L. Elucidating severe urban haze formation in China. *Proc. Natl. Acad. Sci. USA* **2014**, *111*, 17373–17378. [CrossRef]
48. Sun, Y.; Jiang, Q.; Wang, Z.; Fu, P.; Li, J.; Yang, T.; Yin, Y. Investigation of the sources and evolution processes of severe haze pollution in Beijing in January 2013. *J. Geophys. Res. Atmos.* **2014**, *119*, 4380–4398. [CrossRef]
49. Herner, J.; Ying, Q.; Aw, J.; Gao, O.; Chang, D.; Kleeman, M. Dominant mechanisms that shape the airborne particle size and composition in central California. *Aerosol Sci. Technol.* **2006**, *40*, 827–844. [CrossRef]
50. Kumar, A.; Sarin, M.M.; Sudheer, A.K. Mineral and anthropogenic aerosols in Arabian Sea-atmospheric boundary layer: Sources and spatial variability. *Atmos. Environ.* **2008**, *42*, 5169–5181. [CrossRef]
51. Arimoto, R.; Duce, R.; Savoie, D.; Prospero, J.; Talbot, R.; Cullen, J.; Tomza, U.; Lewis, N.; Ray, B. Relationships among aerosol compositions from Asia and the North Pacific during Pem-West. *J. Geophys. Res.* **1996**, *101*, 2011–2023. [CrossRef]
52. Wang, Y.; Zhuang, G.; Tang, A.; Yuan, H.; Sun, Y.; Chen, S.; Zheng, A. The ion chemistry and source of PM_{2.5} aerosol in Beijing. *Atmos. Environ.* **2005**, *39*, 3771–3784. [CrossRef]
53. Gao, X.; Yang, L.; Cheng, S.; Gao, R.; Zhou, Y.; Xue, L.; Shou, Y.; Wang, J.; Wang, X.; Nie, W.; et al. Semi-continuous measurement of water-soluble ions in PM_{2.5} in Jinan, China: Temporal variations and source apportionments. *Atmos. Environ.* **2011**, *45*, 6048–6056. [CrossRef]
54. Tian, Y.Z.; Shi, G.L.; Han, S.; Zhang, Y.; Feng, Y.; Liu, G.R.; Gao, L.; Wu, J.; Zhu, T. Vertical characteristics of levels and potential sources of water-soluble ions in PM₁₀ in a Chinese megacity. *Sci. Total Environ.* **2013**, *447*, 1–9. [CrossRef] [PubMed]
55. Zhang, T.; Cao, J.; Tie, X.; Shen, Z.; Liu, S.; Ding, H.; Han, Y.M.; Wang, G.H.; Ho, K.F.; Qiang, J.; et al. Water-soluble ions in atmospheric aerosols measured in Xi'an, China: Seasonal variations and sources. *Atmos. Res.* **2011**, *102*, 110–119. [CrossRef]
56. Kim, B.; Teffer, S.; Zeldin, M. Characterization of PM_{2.5} and PM₁₀ in the South Coast Air Basin of Southern California: Part 1—spatial variations. *J. Air. Waste Manag. Assoc.* **2000**, *50*, 2034–2044. [CrossRef] [PubMed]
57. Yao, X.; Chan, C.; Fang, M.; Cadle, S.; Chan, T.; Mulawa, P.; He, K.; Ye, B. The water-soluble ionic composition of PM_{2.5} in Shanghai and Beijing, China. *Atmos. Environ.* **2002**, *36*, 4223–4234. [CrossRef]

58. Ozturk, F.; Bahreini, R.; Wagner, N.; Dubé, W.P.; Young, C.J.; Brown, S.S.; Brock, C.A.; Ulbrich, I.M.; Jimenez, J.L.; Cooper, O.R.; et al. Vertically resolved chemical characteristics and sources of submicron aerosols measured on a Tall Tower in a suburban area near Denver, Colorado in winter. *J. Geophys. Res.* **2013**, *118*, 13591–13605. [CrossRef]
59. Turpin, B.; Cary, R.; Huntzicker, J. An in-situ, time-resolved analyzed for aerosol organic and elemental carbon. *Aerosp. Sci. Technol.* **1990**, *12*, 161–171. [CrossRef]
60. Castro, L.M.; Pio, C.A.; Harrison, R.; Smith, D. Carbonaceous aerosol in urban and rural European atmospheres, estimation of secondary organic carbon concentrations. *Atmos. Environ.* **1999**, *33*, 2771–2781. [CrossRef]
61. Wang, H.L.; Zhu, B.; An, J.L.; Duan, Q.; Zou, J.N.; Shen, L.J. Size distribution and characterization of OC and EC in atmospheric aerosols during the Asian youth games of Nanjing, China. *J. Environ. Sci.* **2014**, *35*, 3271–3279. (In Chinese)
62. Shah, S.; Cocker, D.; Miller, J.; Norbeck, J. Emission rates of particulate matter and elemental and organic carbon from In-use diesel engines. *Environ. Sci. Technol.* **2004**, *38*, 2544–2550. [CrossRef]
63. Lan, Z.; Chen, D.; Li, X.; Huang, X.; He, L.; Deng, Y.; Feng, N.; Hu, M. Modal characteristics of carbonaceous aerosol size distribution in an urban atmosphere of South China. *Atmos. Res.* **2011**, *100*, 51–60. [CrossRef]
64. Chow, J.C.; Watson, J.; Lowenthal, D. Sources and chemistry of PM₁₀ aerosol in Santa Barbara County, CA. *Atmos. Environ.* **1996**, *30*, 1489–1499. [CrossRef]
65. Feng, Y.; Bai, Z.; Zhu, T. The principle and application of improved-source-apportionment technique of atmospheric particulate matter Chinese. *J. Environ. Sci.* **2002**, *23*, 106–108.
66. Shi, G.; Feng, Y.; Zeng, F.; Li, X.; Zhang, Y.; Wang, Y. Use of a nonnegative constrained principal component regression chemical mass balance model to study the contributions of nearly collinear sources. *Environ. Sci. Technol.* **2009**, *43*, 8867–8873. [CrossRef] [PubMed]

Article

Impact of the Levels of COVID-19 Pandemic Prevention and Control Measures on Air Quality: A Case Study of Jiangsu Province, China

Wenwen Ai ¹, Xixi Yang ^{1,2,*} , Duanyang Liu ^{2,3} , Min Zhang ¹, Yan Sun ¹, Boni Wang ^{1,2} and Xiaochun Luo ¹

¹ Jiangsu Meteorological Service Center, Nanjing 210041, China; awwn@163.com (W.A.); z857188112@163.com (M.Z.); suen_2022@163.com (Y.S.); bnsmile@163.com (B.W.); ntlxc9@163.com (X.L.)

² Key Laboratory of Transportation Meteorology, China Meteorological Administration, Nanjing 210041, China; liuduanyang@cma.gov.cn

³ Nanjing Joint Institute for Atmospheric Sciences, Nanjing 210041, China

* Correspondence: yangqq2014@lzu.edu.cn

Abstract: In order to control the spread of the COVID-19 pandemic, the prevention and control measures of public health emergencies were initiated in all provinces of China in early 2020, which had a certain impact on air quality. In this study, taking Jiangsu Province in China as an example, the air pollution levels in different regions under different levels of pandemic prevention and control (PPC) measures are evaluated. The implementation of the prevention and control policies of COVID-19 pandemic directly affected the concentration of air pollutants. No matter what level of PPC measures was implemented, the air quality index (AQI) and pollutant concentrations of NO₂, CO, PM₁₀ and PM_{2.5} were all reduced by varied degrees. The higher the level of PPC measures, the greater the reduction was in air pollutant concentrations. Specifically, NO₂ was the most sensitive to PPC policies. The concentrations of CO and atmospheric particulate matter (PM₁₀ and PM_{2.5}) decreased most obviously under the first and second level of PPC. The response speed of air quality to different levels of PPC measures varied greatly among different cities. Southern Jiangsu, which has a higher level of economic development and is dominated by secondary and tertiary industries, had a faster response speed and a stronger responsiveness. The results of this study reflect the economic vitality of different cities in economically advanced regions (i.e., Jiangsu Province) in China. Furthermore, the results can provide references for the formulation of PPC policies and help the government make more scientific and reasonable strategies for air pollution prevention and control.

Keywords: COVID-19; pandemic prevention and control levels; air quality; PM_{2.5}; O₃

Citation: Ai, W.; Yang, X.; Liu, D.; Zhang, M.; Sun, Y.; Wang, B.; Luo, X. Impact of the Levels of COVID-19 Pandemic Prevention and Control Measures on Air Quality: A Case Study of Jiangsu Province, China. *Atmosphere* **2022**, *13*, 640. <https://doi.org/10.3390/atmos13050640>

Academic Editor: Célia Alves

Received: 16 March 2022

Accepted: 15 April 2022

Published: 19 April 2022

Publisher's Note: MDPI stays neutral with regard to jurisdictional claims in published maps and institutional affiliations.



Copyright: © 2022 by the authors. Licensee MDPI, Basel, Switzerland. This article is an open access article distributed under the terms and conditions of the Creative Commons Attribution (CC BY) license (<https://creativecommons.org/licenses/by/4.0/>).

1. Introduction

In early 2020, a sudden outbreak of the coronavirus disease 2019 (COVID-19) occurred in China. This virus is highly contagious, and has caused a high mortality rate in sensitive groups. So far, the COVID-19 has not yet been completely controlled. In order to curb the spread of COVID-19, the government has implemented a series of interventions since the outbreak, including lockdowns, quarantine, travel restrictions, temporary closures of businesses and public facilities, etc. These control and emergency measures have greatly affected the human activities, economic development, social relations and natural environment [1–4].

Compared with the temporary control during major events and meetings in recent years, the control of COVID-19 pandemic is the strictest in history in both time and space. Therefore, it is possible to systematically study the impact of strict control measures implemented by the government on air quality. In recent years, some scholars have studied the impact of temporary control measures on urban air quality during major events or conferences, such as the 22nd Asia-Pacific Economic Cooperation Economic Leaders' Meeting in Beijing [5],

the 2013 Asian Youth Games [6] and 2014 Summer Youth Olympic Games in Nanjing [7], and the 2016 G20 Hangzhou summit [8]. The variations of air quality during these events demonstrate that the control measures are highly effective in alleviating air pollution.

The COVID-19 pandemic has had a significant impact on the environment, which has been studied by scholars around the world. Several studies have shown that after the measures taken by the Chinese government against the COVID-19 pandemic, air pollution reduced significantly by 12.0–52.8% [1,9–15]. Similar situations appeared in other countries. Air pollution in northeastern United States dropped by 30% after pandemic prevention and control (PPC) measures were adopted [16]. The European Environment Agency found that air pollution also decreased significantly after taking PPC measures in European cities [17]. From 16–22 March 2020, NO₂ concentration in Bergamo of Italy and Barcelona of Spain respectively decreased by 47% and 55% compared with that during the same period of 2019. During the PPC period of COVID-19, NO₂ concentration dropped by 25.5% in the United States [2], while NO₂ and particulate matter (PM₁₀ and PM_{2.5}) concentrations dropped by nearly 50% in four Indian metropolises [18]. However, due to the complexity of PPC implementation, it has been found that in many countries, even in lockdown period a few pollutants' concentrations showed an increasing trend. The O₃ concentration in Singapore increased by 18% during the lockdown period [19]. During the lockdown, the SO₂ concentration in southern India increased slightly, and the O₃ concentration increased in the Indo Gangetic plain [20]. The concentration of O₃ increased greatly in Hubei and the Yangtze River Delta [21,22]. Since the start of the COVID-19 lockdown, the concentration of PM_{2.5} in Beijing was higher than that in the same period in history [23]. And the decline of the concentration of SO₂ in Wuhan was weaker than that in history [21]. These studies have confirmed that the change in air pollution is mainly related to the slower economic growth and travel restrictions during the pandemic [1,10].

Social production and operations as well as travel restrictions are closely related to the level of PPC measures released by the government. Although many studies have confirmed that the government's PPC measures have a significant impact on air quality, however, there is still a lack of specific information on the relationship between different PPC levels and air pollution. Furthermore, the impact of the PPC levels on air quality may vary in different regions under different levels of PPC. In addition, the speed of economic recovery after the slowdown of the pandemic reflects the economic vitality of a city. The changes in air quality in different cities after the implementation of PPC measures also reflect the differences in the economic vitality of different cities, which has rarely been discussed in previous studies. In this study, the variation characteristics of air quality in different response levels to PPC measures in Jiangsu Province is studied, and the impact of PPC measures of different levels on air quality is evaluated, especially the response speed of urban air quality to PPC measures in cities with different economic development levels. By revealing the relationship between government decision-making behavior and air pollution, this study can provide references for the formulation of government PPC policies and can also help the government to develop more scientific and reasonable strategies for air pollution prevention and control.

The remainder of this paper is organized as follows. Section 2 describes the data and methods. Section 3 presents results and related discussions. Finally, the main conclusions are given in Section 4.

2. Materials and Methods

2.1. Air Pollutants and Meteorological Elements

In this study, the air quality data are from the national air quality monitoring stations of Jiangsu Environmental Monitoring Center that are located in 13 prefecture-level cities of Jiangsu. The hourly mean of all national stations in each city is taken as the hourly monitoring value of this city, and the arithmetic mean of hourly monitoring values of 13 cities is taken as the hourly monitoring value of Jiangsu. The data mainly include hourly data of SO₂, NO₂, CO, O₃, PM₁₀ and PM_{2.5} pollutants. According to the Technical

Regulation on Ambient Air Quality (HJ 633—2012), we calculated the individual air quality index (IAQI) based on the arithmetic mean of each pollutant in the whole province each day, and furthermore, the daily AQI of the province was calculated. The meteorological data come from 71 national standard meteorological stations covering the whole Jiangsu Province, including hourly temperature, wind speed, precipitation, relative humidity and visibility from 2018 to 2020. The hourly means of the 71 stations were taken as the hourly monitoring values of the province. The administrative division of the study area is shown in Figure 1.

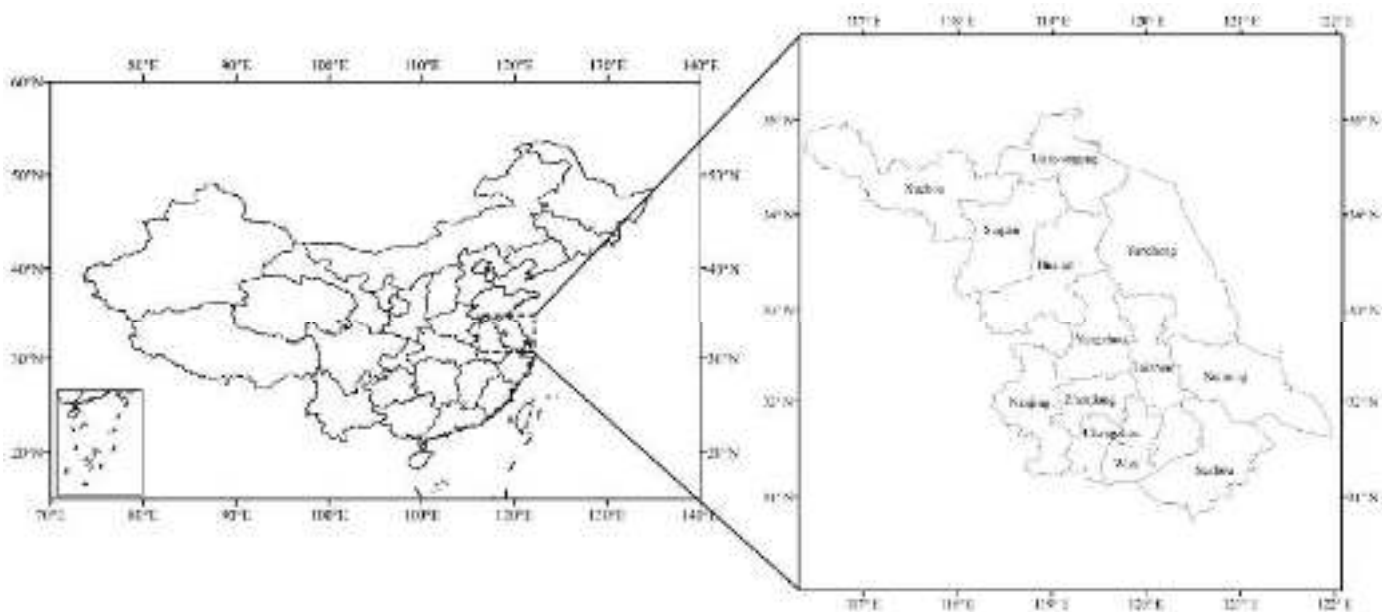


Figure 1. Administrative division of the study area.

2.2. Situations of Pandemic Prevention and Control

On 22 January 2020, the National Health Commission of the People's Republic of China confirmed a positive case of COVID-19 in Suzhou, which was the first case in Jiangsu Province. In order to control the spread of COVID-19, Jiangsu activated the first-level public health emergency response at 0000 CST (China Standard Time, the same below) on 25 January 2020. The interventions included travel restrictions, restrictions on public gatherings, and temporary closures of businesses and facilities. At 0000 CST on 25 February 2020, the response level was adjusted to the second level, which meant that all businesses could reopen scientifically and reasonably. That is, it was suggested that production and life could be recovered, while gathering and group activities were still restricted. As of 27 March 2020, there had been no newly confirmed local patients for 38 consecutive days. Therefore, since 0000 CST on 28 March, the level of PPC measures was adjusted to the third level, and the normal production and living of people gradually recovered, entering the stage of regular PPC. The same emergency response was implemented to the whole province at the same time by the Jiangsu provincial government, making it possible to study the impact of PPC measures of different levels on air pollution in the whole province, which is what this paper concerns.

2.3. Economic Development Data of Jiangsu Province

In this study, 13 prefecture-level cities in Jiangsu Province are taken as the research units. Data from the *Jiangsu Statistical Yearbook 2019 and 2020* (<http://tj.jiangsu.gov.cn/col/col80733/index.html>, accessed on 1 March 2022) and the website of the National Bureau of Statistics (<http://www.stats.gov.cn/>, accessed on 1 March 2022), and the statistical bulletins of national economic and social developments of cities in Jiangsu (<http://www.tjcn.org/tjgb/10js/>, accessed on 5 March 2022) are used in the study. The 13 prefecture-level

cities in Jiangsu are divided into three parts: southern Jiangsu (including Nanjing, Wuxi, Changzhou, Suzhou and Zhenjiang), central Jiangsu (Nantong, Yangzhou and Taizhou) and northern Jiangsu (Xuzhou, Lianyungang, Huai'an, Yancheng and Suqian).

2.4. Method of Analysis and Validation

The data collected were divided into two groups. One is the data in 2020 representing the pandemic period, and the other is data in 2018 and 2019 representing the historical period. Each group was divided into four subgroups according to the PPC level, that is, no PPC period, first-level PPC period, second-level PPC period and third-level PPC period. No PPC period is 1–21 January 2020. In order to reduce the impact of the first reported case on residents' lifestyles, the data from 22–24 January were excluded. The end of the statistical date for the third-level response was set to 30 April to ensure that the numbers of days in periods under different response levels are similar, so as to avoid the interference brought by the time length. Table 1 lists the time ranges for different response levels (http://www.nanjing.gov.cn/zt/yqfk/zccs/202001/t20200127_1782811.html, accessed on 1 March 2022).

Table 1. Time ranges for response levels of pandemic prevention and control of COVID-19 in Jiangsu Province.

	Non	L1	L2	L3
2020	1–21 January	25 January–24 February	25 February–27 March	28 March–30 April
2018–2019	Same period	Same period	Same period	Same period
Total Days	21	31	32	34

The daily average AQI value of the whole province was used to calculate the grade of daily air quality, and the grades I–VI correspond to the air quality of very good, good, slightly polluted, moderately polluted, heavily polluted and severely polluted. The days with air quality of grades I–II are good air days, and the days with air quality of grades III–VI are polluted air days.

Based on the time-series analysis method, the air quality and concentrations of six atmospheric pollutants in different PPC periods in 2020 were compared with those during the same periods in 2018–2019 to explore the variations of air quality under different PPC levels in Jiangsu. The rate of change (CR) in the period without PPC in 2020 over the same period in previous two years was regarded as the natural change rate (NCR) in 2020. During the periods in first-level (L1), second-level (L2) and third-level (L3) responses to PPC, CR minus the NCR was regarded as the change rate under the PPC conditions (PCR). The formulas of CR, NCR and PCR are as follows.

$$CR = \frac{X_{rec} - X_{his}}{X_{his}} \times 100\%,$$

$$NCR = CR, \text{ in the period without PPC,}$$

$$PCR = CR - NCR, \text{ in the period with PPC,}$$

where X_{rec} is the air quality or concentration of six atmospheric pollutants in 2020, and X_{his} is the air quality or concentration of six atmospheric pollutants during the same periods in 2018–2019. The PCR of the mean and extreme values were analyzed separately to study the impact of the implementation of PPC policies on air quality. The analysis of mean values used the daily mean values of AQI, pollutant concentrations and meteorological elements, and the analysis of extreme value used the maximum daily mean values of AQI, pollutant concentrations, the minimum daily mean value of visibility, and the maximum daily mean values of other meteorological elements. In order to verify the significance of the differences in air quality before and after the outbreak of COVID-19 pandemic and

among different levels of PPC measures, we first used the *F*-test to test the variance of samples in two different periods, and then carried out the Student's *t*-test of equal variance or heteroscedasticity according to the results of the *F*-test. If $p < 0.05$ in the two tailed *t*-test, it was regarded as a significant difference. The variations of air quality in 13 prefecture-level cities of Jiangsu under different PPC levels were compared, so as to explore the differences in the response of urban air quality variations to the PPC levels under different economic development levels.

3. Results

3.1. Differences in Air Quality in Different Scenarios

Figure 2 shows the number of days for each grade of air quality at the four PPC stages from 2018 to 2020. It can be seen that on the no PPC stage (Figure 2a), the number of days with air quality of grade I in 2020 increased over previous years, and the number of days with air quality of grade V decreased. Overall, there were few changes in the past 3 years. In the first-level PPC period (Figure 2b), the number of days with air quality of grades I and II in 2020 increased over the same period in the previous 2 years, and the number of days with air quality of grade III were significantly reduced, and there was no moderate or severe pollution. There were 9, 11 and 2 polluted days in 2018, 2019 and 2020, respectively, suggesting that the pollution time was significantly reduced. In the second-level PPC period (Figure 2c), the number of days with air quality of grades I and II in 2020 also increased over the previous 2 years, and there were no polluted days. In the third-level PPC period (Figure 2d), there were still no polluted days in 2020, and the number of good air days was the same as that in 2019. In general, the air quality in 2020 was significantly improved compared with the same period in previous years, which means the implementation of PPC policies had a certain impact on air quality. It is worth noting that whether the epidemic occurred or not, the number of polluted days was decreasing from January to April. This is due to the obvious cooling of ground radiation at night in winter, and the “temperature inversion layer” is easy to appear in the low altitude of the atmosphere, resulting in the accumulation of pollutants and thus the poor air quality. With the increase of temperature in spring, the atmospheric stability decreases and the diffusion conditions become better, so the air quality is improved.

Statistics of atmospheric pollutant data in 13 cities show that except for SO₂, the levels of pollutants and air quality indexes are significantly different during the periods before and after the implementation of PPC policies ($p < 0.05$, Table 2), indicating that the social restrictions implemented in the PPC period had a direct impact on atmospheric pollutants. As long as PPC measures are taken, the concentration of pollutants could be affected regardless of the level of PPC. From the perspective of the PPC levels, the concentrations of SO₂, NO₂ and CO were significantly different between the periods with the first- and second-level PPC measures, and the concentrations of SO₂, NO₂, CO and O₃ were significantly different between the periods with the first- and third-level PPC measures, while there was little difference in pollutant concentrations between the periods with the second- and third-level PPC measures.

3.2. Impacts of COVID-19 on Air Quality

Compared with the same period in 2018 and 2019, the values of AQI, SO₂, NO₂, CO, PM₁₀ and PM_{2.5} in 1–21 January of 2020 decreased by 9.75%, 45.36%, 21.01%, 13.00%, 19.29% and 9.33%, respectively (Table 3), which are the NCRs in air quality in 2020 as defined above. This indicates that without the influence of PPC, the concentrations of air pollutants were also gradually decreasing, which is consistent with the results in other parts of China. The change in air quality is mainly attributed to the “Three-Year Action Plan for Cleaner Air” to win the battle for a blue sky released by the State Council of China in 2018. This action plan aims at significantly reducing the total emissions of major air pollutants and greenhouse gases, further lowering the concentrations of fine particulate matter (PM_{2.5}), significantly reducing the number of heavily polluted days and thus improving the air quality.

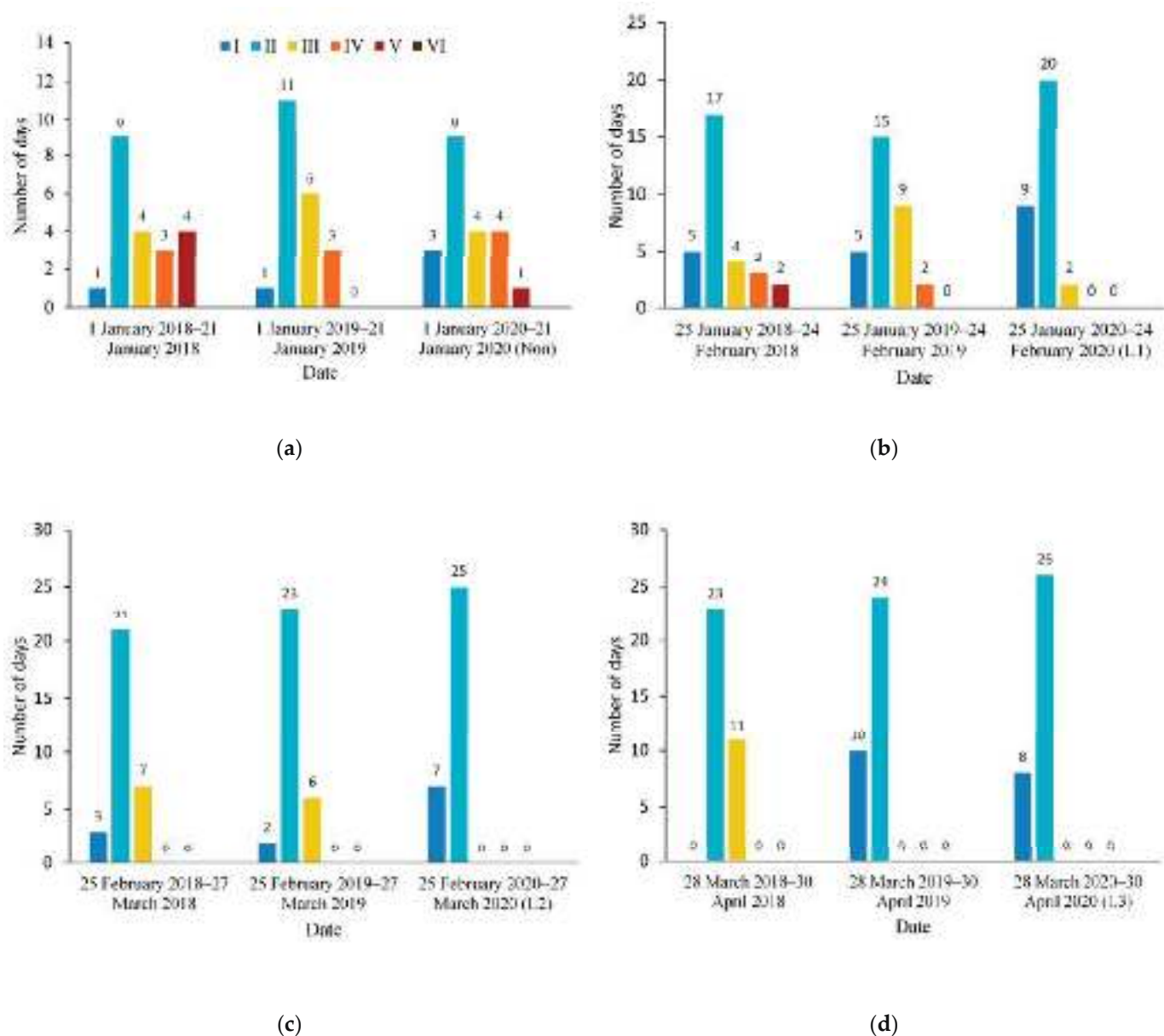


Figure 2. The number of days for each grade of air quality under different pandemic prevention and control levels in Jiangsu Province ((a), Non; (b), L1; (c), L2; (d), L3).

Table 2. Significance levels for periods with different levels of PPC measures by Student's *t*-test ($\alpha = 0.05$).

Scenes	AQI	SO ₂	NO ₂	CO	O ₃	PM ₁₀	PM _{2.5}
COVID-19 vs. Non	1.1×10^{-3}	0.22	4.3×10^{-8}	2.0×10^{-5}	2.4×10^{-16}	5.7×10^{-3}	5.4×10^{-4}
L1 vs. Non	2.1×10^{-3}	8.9×10^{-4}	5.2×10^{-12}	2.0×10^{-4}	2.03×10^{-11}	2.3×10^{-3}	2.3×10^{-3}
L2 vs. Non	8.9×10^{-4}	0.51	2.0×10^{-5}	8.5×10^{-6}	1.8×10^{-12}	7.2×10^{-3}	3.6×10^{-4}
L3 vs. Non	9.5×10^{-4}	0.59	1.8×10^{-3}	7.1×10^{-6}	8.4×10^{-17}	0.017	2.5×10^{-4}
L1 vs. L2	0.49	0.022	7.5×10^{-7}	0.049	0.23	0.31	0.12
L1 vs. L3	0.57	5.3×10^{-4}	8.4×10^{-10}	0.03	2.6×10^{-8}	0.08	0.064
L2 vs. L3	0.84	0.27	0.13	0.85	1.7×10^{-9}	0.42	0.72

Table 3. Variations of AQI, atmospheric pollutants and meteorological conditions during the pandemic period and the same period of previous years.

Air Pollutions or Weather Conditions	Period	Historical Mean	2020 Mean	Mean CR	Mean PCR	Historical Daily Extreme Values	2020 Daily Extreme Values	Daily Extreme CR	Daily Extreme PCR
AQI	Non	115.64	104.36	−9.75%	/	234.55	212.28	−9.49%	/
	Level 1	91.20	62.27	−31.72%	−21.97%	218.67	109.57	−49.89%	−40.40%
	Level 2	81.27	58.74	−27.72%	−17.97%	143.86	93.74	−34.84%	−25.34%
	Level 3	74.37	59.47	−20.04%	−10.29%	143.72	85.37	−40.60%	−31.11%
SO ₂ (µg/m ³)	Non	14.56	7.95	−45.36%	/	30.72	11.43	−62.79%	/
	Level 1	11.93	6.55	−45.10%	0.26%	26.72	9.30	−65.19%	−2.40%
	Level 2	12.26	7.62	−37.81%	7.55%	22.12	12.78	−42.22%	20.57%
	Level 3	12.13	8.21	−32.34%	13.02%	20.50	11.77	−42.59%	20.21%
NO ₂ (µg/m ³)	Non	52.05	41.11	−21.01%	/	94.25	60.22	−36.11%	/
	Level 1	35.33	17.68	−49.96%	−28.95%	86.46	33.20	−61.60%	−25.49%
	Level 2	43.05	28.91	−32.84%	−11.82%	75.17	51.29	−31.77%	4.34%
	Level 3	38.23	32.14	−15.93%	5.09%	60.93	53.54	−12.13%	23.98%
CO (mg/m ³)	Non	1.14	0.99	−13.00%	/	1.80	1.61	−10.56%	/
	Level 1	0.95	0.71	−24.99%	−12.00%	1.61	1.03	−36.02%	−25.47%
	Level 2	0.86	0.64	−25.30%	−12.30%	1.28	0.91	−28.91%	−18.35%
	Level 3	0.74	0.63	−14.70%	−1.70%	1.15	0.85	−26.09%	−15.53%
O ₃ (µg/m ³)	Non	32.69	36.78	12.50%	/	57.35	60.71	5.86%	/
	Level 1	53.66	64.82	20.80%	8.30%	74.03	86.16	16.39%	10.53%
	Level 2	66.71	68.48	2.66%	−9.84%	90.74	86.23	−4.97%	−10.83%
	Level 3	81.45	87.59	7.54%	−4.96%	139.44	123.65	−11.32%	−17.18%
PM ₁₀ (µg/m ³)	Non	118.27	95.46	−19.29%	/	250.50	188.75	−24.65%	/
	Level 1	94.30	57.24	−39.30%	−20.01%	208.46	103.74	−50.24%	−25.58%
	Level 2	89.97	62.97	−30.01%	−10.71%	154.41	99.38	−35.64%	−10.99%
	Level 3	91.10	67.22	−26.21%	−6.92%	207.62	119.69	−42.35%	−17.70%
PM _{2.5} (µg/m ³)	Non	85.70	77.70	−9.33%	/	184.55	162.28	−12.07%	/
	Level 1	66.10	44.72	−32.34%	−23.01%	168.67	82.65	−51.00%	−38.93%
	Level 2	58.38	38.02	−34.88%	−25.55%	110.09	69.99	−36.42%	−24.36%
	Level 3	48.77	36.91	−24.32%	−14.99%	109.98	63.29	−42.45%	−30.39%
Temperature (°C)	Non	2.83	4.56	61.06%	/	8.80	10.61	20.58%	/
	Level 1	2.66	6.09	129.07%	68.01%	10.30	13.32	29.29%	8.71%
	Level 2	10.14	11.28	11.28%	−49.77%	18.10	19.87	9.76%	−10.82%
	Level 3	15.93	13.93	−12.57%	−73.63%	24.70	24.37	−1.34%	−21.92%
precipitation (mm)	Non	1.92	2.67	39.42%	/	37.90	15.19	−59.92%	/
	Level 1	2.11	1.48	−29.88%	−69.30%	18.30	12.05	−34.13%	25.78%
	Level 2	1.99	2.05	3.02%	−36.40%	51.00	20.04	−60.72%	−0.80%
	Level 3	1.80	1.63	−9.66%	−49.08%	24.10	23.47	−2.62%	57.29%
relative humidity (%)	Non	78.10	82.76	5.97%	/	98.00	95.61	−2.44%	/
	Level 1	74.03	74.96	1.26%	−4.71%	98.00	97.20	−0.82%	1.62%
	Level 2	72.28	70.16	−2.94%	−8.91%	97.00	96.73	−0.28%	2.17%
	Level 3	71.67	64.36	−10.20%	−16.17%	98.00	91.15	−6.98%	−4.54%
wind speed (m/s)	Non	1.93	1.96	1.42%	/	4.40	3.91	−11.24%	/
	Level 1	2.22	2.33	5.11%	3.69%	4.90	4.18	−14.75%	−3.52%
	Level 2	2.47	2.60	5.53%	4.11%	5.40	4.45	−17.53%	−6.29%
	Level 3	2.47	2.32	−6.35%	−7.77%	5.90	4.35	−26.19%	−14.95%
visibility (km)	Non	6.16	5.60	−9.08%	/	1.34	1.88	40.74%	/
	Level 1	8.56	10.64	24.25%	33.33%	2.30	3.53	53.10%	12.36%
	Level 2	8.64	12.59	45.80%	54.88%	3.16	3.21	1.57%	−39.17%
	Level 3	10.13	15.06	48.60%	57.68%	4.49	7.93	76.36%	35.63%

After the outbreak of COVID-19, the AQI and concentrations of NO_2 , CO, PM_{10} and $\text{PM}_{2.5}$ decreased with a magnitude larger than those before the outbreak, displaying the characteristics of varied degrees of declines under different levels of PPC measures. Specifically, the AQI and pollutant concentrations decreased the most under the first- and second-level PPC, and decreased slightly under the third-level PPC. The NCR of SO_2 concentration in 2020 was -45.36% , which was significantly lower than the value in the same period in historical years, indicating that the control effect of SO_2 in Jiangsu Province is obvious. But the decreasing trend of SO_2 weakened after the outbreak of COVID-19, and similar results have been obtained in other parts of China [21]. We speculate that on one hand, it is related to the industrial production activities that have not been interrupted during the epidemic period, such as increasing the emission of coal-fired pollution from coal-fired power plants and coal-fired heating boilers. To some extent, epidemic control has increased the demand for household electricity, heating and cooking. From the perspective of provincial distribution, cities with a high proportion of secondary industry have a relatively high SO_2 PCR, such as Changzhou, Zhenjiang and Taizhou (data omitted). On the other hand, sulfur dioxide is easily soluble in water, and the reduction of precipitation during the epidemic increased the content of sulfur dioxide in the atmosphere. The O_3 concentration in 2020 increased. In particular, the O_3 concentration increased by 20.8% under the first-level PPC measures compared with that during the same period in previous years. This result is similar to the results of studies focusing on the Chinese mainland, the Guangdong–Hong Kong–Macao Greater Bay Area [9,24], Europe [25] and India [18]. This phenomenon is mainly due to the particularity and complexity of ozone formation and depletion mechanisms. Ozone is formed by photochemical reactions between nitrogen oxides and volatile organic compounds emitted from natural sources and human activities [26]. Air pollution is also somewhat related to meteorological conditions [27,28]. Generally speaking, high temperature, low relative humidity and high solar radiation are conducive to the formation of ozone [29–31]. During the period with first-level PPC measures, the daily average temperature in Jiangsu was $3.43\text{ }^\circ\text{C}$ higher than that in the same period of historical years, with an increase of 129.07% , while precipitation decreased by 29.88% . Brighter weather and lower concentrations of particulate matters allow more sunlight to pass through. Higher temperatures and stronger light, along with increased photochemical activity, lead to higher ozone concentrations. Changes in visibility also reflect changes in air quality to some extent [32]. During the periods in the first-, second- and third-level responses to PPC, the average values of atmospheric visibility respectively increased by 24.25% , 45.80% and 48.60% compared with those in the same period of previous years, and the daily minimum value of visibility also increased. This indicates that after the outbreak of COVID-19, the concentrations of atmospheric particulate matters decreased and thus the atmospheric transparency gradually increased.

3.3. Impact of Pandemic Prevention and Control on Air Quality

The reduction in air pollution is closely related to the PPC policy. During the period with first-level PPC measures, the PCRs of AQI and the concentrations of six air pollutants (SO_2 , NO_2 , CO, O_3 , PM_{10} and $\text{PM}_{2.5}$) were -21.97% , 0.26% , -28.95% , -12.00% , 8.30% , -20.01% and -23.01% , respectively. During the period with second-level PPC measures, the PCRs were -17.97% , 7.55% , -11.82% , -12.30% , -9.84% , -10.71% and -25.55% , respectively. During the period with third-level PPC measures, the PCRs were -10.29% , 13.02% , 5.09% , -1.70% , -4.96% , -6.92% and -14.99% , respectively (Table 3). It can be seen that, except for SO_2 and O_3 , the AQI and concentrations of other pollutants were significantly reduced under the PPC measures. In turn, the improvement of air quality could help reduce the spread of COVID-19 and play a positive role in PPC [33,34].

The first-level response was ordered by the State Council of the People's Republic of China, and the provincial government organized and coordinated the provincial emergency response under the unified leadership and command. The second-level response was deployed by the provincial government, and the third-level emergency plan in response

was formulated by the municipal and county governments. Therefore, the control force and restriction policies in different provinces may be different, resulting in different impacts of emergency responses on air quality in different provinces. Some studies have shown that due to travel restrictions during the pandemic, AQI and concentrations of NO_2 , CO, PM_{10} and $\text{PM}_{2.5}$ in cities of northern China decreased by 7.80%, 24.7%, 4.58%, 13.7% and 5.93%, respectively [1]. For cities in the Guangdong–Hong Kong–Macao Greater Bay Area, the AQI and concentrations of the above four pollutants were reduced by 37.4%, 47.0%, 24.1%, 44.8% and 40.5% during the period with first-level PPC measures and by 24.4%, 25.5%, 23.2%, 25.6% and 32.5% during the period with second-level PPC measures, which were 27.1%, 12.1%, 9.86%, 24.1% and 31.0% during the period with third-level PPC measures [24]. Therefore, the air quality in Jiangsu was more likely to be affected by the PPC policies compared with that in cities of northern China, but the sensitivity of air quality to restrictive policies was slightly lower than that in the Pearl River Delta.

NO_2 was the pollutant most sensitive to the PPC policies (Figure 3). The higher the PPC level, the higher was the reduction of NO_2 . The PCRs of NO_2 concentration under the first-, second- and third-level responses decreased by 28.95%, 11.82% and 5.09%, respectively. As the NO_2 in the atmosphere is mainly from fossil fuel combustion, vehicle exhaust and industrial production emissions, with the relaxation of PPC and the recovery of normal production and living, the concentration of NO_2 rose again.

The CO in the atmosphere is mainly from the incomplete combustion of fossil fuels and biofuels [11]. During the period in response to PPC measures, CO emissions from domestic boilers and power stations were significantly affected. The PCRs of CO concentrations in the first-, second- and third-level responses decreased by 12.00%, 12.30% and 1.70%, respectively. In the first- and second-level responses to PPC policies, CO was well-controlled. After the implementation of the third-level PPC policy, industrial production activities gradually recovered, and the CO concentration rebounded. For historical average (2018–2019), the CO concentration showed a declining trend from February to April, while there was no such obvious downward trend from February to April of 2020 due to the implementation of the PPC policy (Figure 3).

In addition, the concentration of atmospheric particulate matters (PM_{10} and $\text{PM}_{2.5}$) also decreased significantly during the period in response to PPC measures. The main sources of $\text{PM}_{2.5}$ are the residues emitted from combustion in the process of daily power generation, industrial production and vehicle exhaust emissions. PM_{10} comes from direct emissions from pollution sources, such as coal-burning flue gas, construction and transportation dust, smelting dust, building material dust and traffic powder. The PCRs of PM_{10} concentration in the first-, second- and third-level responses were reduced by 20.01%, 10.71% and 6.92%, respectively, while the reductions were 23.01%, 25.99% and 14.99% for $\text{PM}_{2.5}$, respectively. Thus, the concentrations of atmospheric particulate matters decreased most obviously under the first- and second-level responses. With the recovery of production and living activities, the concentrations of particulate matters gradually approached the average value in the same period of previous years (Figure 3).

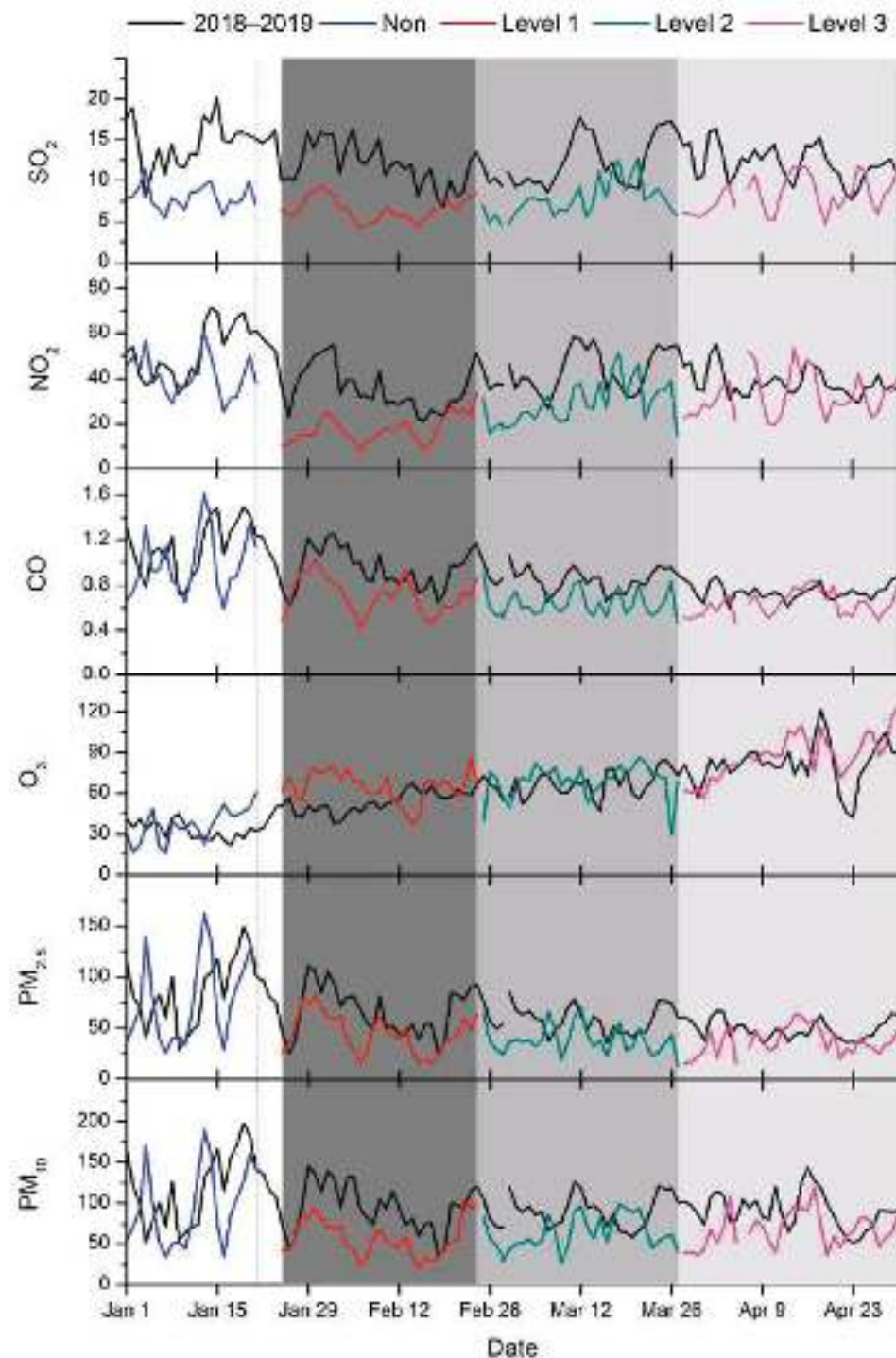


Figure 3. Daily variations of pollutant concentrations under different PPC levels. The shadows of dark grey, medium grey and light grey represent the L1, L2 and L3 period respectively.

3.4. Variations of Urban Air Quality in Response to Pandemic Protection and Control Measures under Different Economic Development Levels

Table 4 and Figure 4 show the year-on-year variations of AQI in 13 cities of Jiangsu under different levels of PPC measures. It can be seen that in 2018 and 2019, there were significant differences in air quality among 13 cities. Among them, the air quality in Xuzhou that has a large proportion of heavy industry was the worst. After the outbreak of COVID-19, the gaps in air quality among 13 cities decreased. During the period with no PPC measures, except for Nantong and Yangzhou, the AQI values in other cities all

declined, which means that the air quality generally improved in 2020. During the period with first-level PPC measures, the AQI values in all cities showed a larger magnitude of decline. Among them, Wuxi, Nanjing and Suzhou have the largest magnitudes of 40.4%, 39.7% and 38.3%, respectively, while Suqian, Huai'an and Lianyungang have the smallest magnitudes of 21.1%, 23.1% and 24.2%, respectively. During the period with second-level PPC measures, the magnitude of the AQI decline in each city was smaller than that during the period in first-level response. Among them, Yangzhou, Taizhou and Zhenjiang had the largest magnitudes of 34.3%, 32.8% and 32.4%, respectively, while Huai'an, Suqian and Lianyungang had the smallest magnitudes of 20.6%, 23.7% and 24.4%, respectively. During the period with third-level PPC measures, the decline of the AQI in each city was smaller than that during the period in second-level response. Specifically, Zhenjiang, Xuzhou, Yangzhou and Taizhou had larger magnitudes of 27.8%, 26.2%, 24.2% and 23.7%, respectively, while Lianyungang, Nantong, Huai'an and Suqian had smaller magnitudes of 11.9%, 14.0%, 15.2% and 17.8%, respectively.

The daily variations of AQI in Xuzhou, Suqian, Nanjing and Suzhou in 2020 are presented in Figure 5. It can be seen that before the outbreak of COVID-19, the air quality in southern Jiangsu (Nanjing and Suzhou) was relatively good, while the air quality in northern Jiangsu (Xuzhou and Suqian) was poor. After the implementation of the first-level PPC measures, the air quality improved significantly. After the resumption of production, the pollutant concentrations rebounded, and the differences in the air quality among different cities shrank. The cities in southern Jiangsu returned to the pre-pandemic situation more quickly.

The GDP of 13 cities from 2019 to 2020 is shown in Table 5. The GDP of cities in southern Jiangsu is relatively higher. For example, the GDPs of Suzhou and Nanjing in 2020 reached CNY 2017.05 billion and CNY 1481.795 billion, respectively, while the GDPs of cities in northern Jiangsu were relatively lower. Suqian, the city with the lowest GDP in the province, had a GDP of CNY 326.24 billion in 2020. From the perspective of industrial structure (Figure 6), the proportion of primary industry in northern Jiangsu is higher than the average level of the whole province, while the proportions of secondary and tertiary industry are lower. The situation is the opposite in southern Jiangsu [35]. Under the epidemic prevention and control measures, the industrial and vehicle emissions were limited, so the secondary industry represented by industry and the tertiary industry represented by service industry were greatly affected. Therefore, the southern Jiangsu, dominated by the secondary and tertiary industries, was more sensitive to the PPC measures.

Table 4. Variations of AQI in 13 prefecture-level cities of Jiangsu under different levels of pandemic prevention and control measures, and those in the same period of historical years (the data are consistent with Figure 4).

City	Non		L1		L2		L3	
	2018–2019	2020	2018–2019	2020	2018–2019	2020	2018–2019	2020
Changzhou	113	108	92	59	87	62	83	64
Huaian	128	115	94	72	83	66	77	65
Lianyungang	121	105	89	68	73	55	69	61
Nanjing	117	91	88	53	77	57	74	58
Nantong	87	90	76	54	72	53	67	57
Suzhou	100	94	84	52	75	55	75	59
Suqian	140	129	103	81	89	68	77	63
Taizhou	107	99	89	61	83	56	76	58
Wuxi	100	89	84	50	74	55	73	59
Xuzhou	167	146	126	85	112	77	91	67
Yancheng	108	94	89	59	81	57	71	59
Yangzhou	110	110	90	57	89	59	82	62
Zhenjiang	121	103	93	62	89	60	81	59

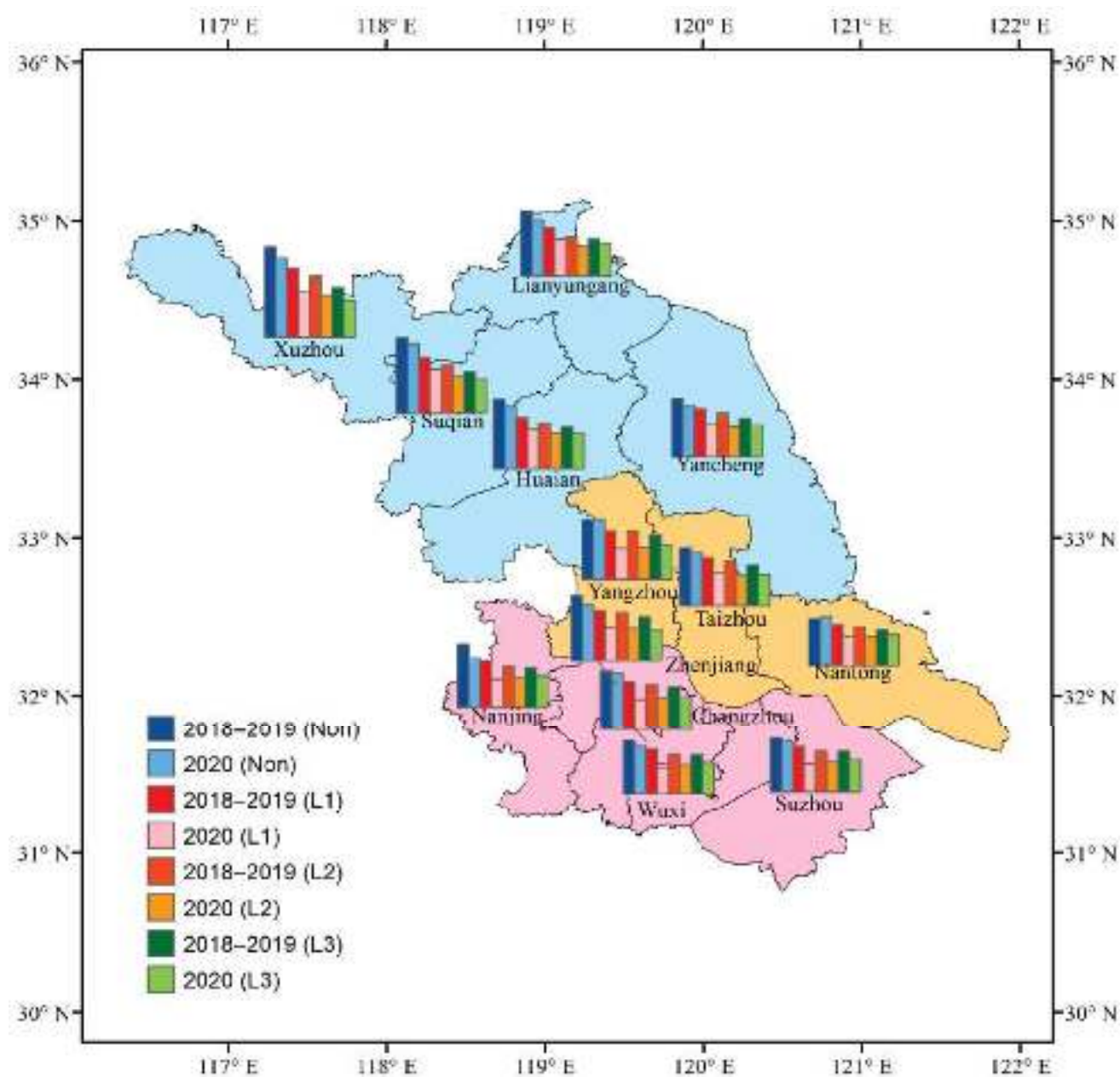


Figure 4. Variations of AQI in 13 prefecture-level cities of Jiangsu under different levels of pandemic prevention and control measures, and those in the same period of historical years (the data are consistent with Table 4). Three colors in the map: blue, northern Jiangsu region; orange, central Jiangsu region; pink, southern Jiangsu region.

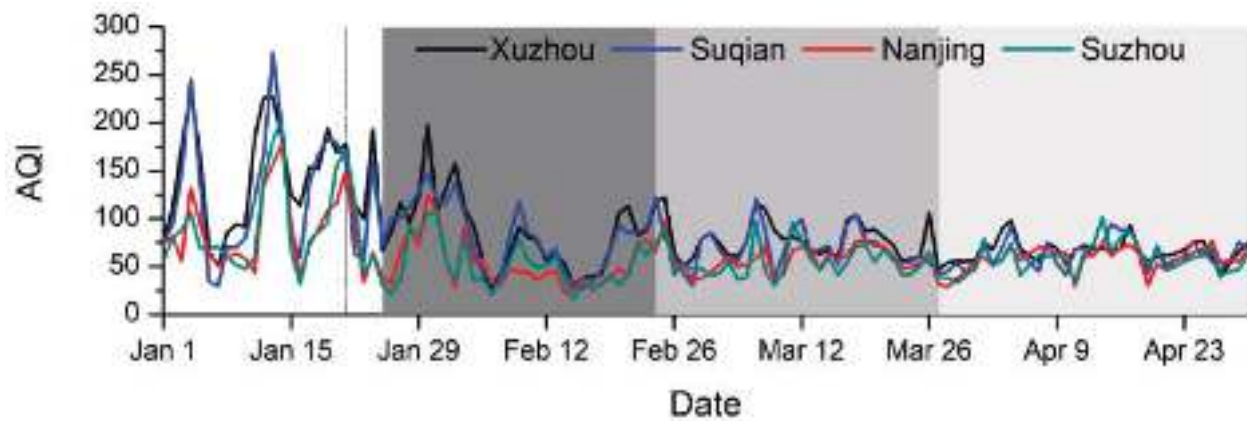


Figure 5. Daily variations of AQI in Xuzhou, Suqian, Nanjing and Suzhou in 2020. The shadows of dark grey, medium grey and light grey represent the L1, L2 and L3 period respectively.

Table 5. GDP rankings of 13 prefecture-level cities in Jiangsu Province (data from the National Bureau of Statistics of China, <http://www.stats.gov.cn/>, accessed on 10 March 2022).

Ranking	City	2020 GDP (Billion Yuan)	2019 GDP (Billion Yuan)
1	Suzhou	2017.05	1923.58
2	Nanjing	1481.795	1403.015
3	Wuxi	1237.048	1185.232
4	Nantong	1003.63	938.339
5	Changzhou	780.53	740.086
6	Xuzhou	731.977	715.135
7	Yangzhou	604.833	585.008
8	Yancheng	595.338	565.626
9	Taizhou	531.28	513.336
10	Zhenjiang	422.01	412.732
11	Huaian	402.537	387.121
12	Lianyungang	327.707	313.929
13	Suqian	326.24	309.923

Therefore, the response speed of urban air quality to the PPC level varied greatly under different economic development levels and industrial structure. The southern Jiangsu, which has a higher level of economic development and is dominated by secondary and tertiary industries, had a faster response speed and a stronger responsiveness. The pollutant concentration dropped rapidly during the period under first-level PPC, the economic production recovered quickly and the economic vitality was high during the periods under second- and third-level PPC. On the contrary, the northern Jiangsu, where the level of economic development is relatively backward and the proportion of primary industry is relatively high, had a slower response speed and a weaker responsiveness. The pollutant concentrations decreased slowly during the period under first-level PPC. After the relaxation of PPC measures, it takes a longer time for the economy to recover, and thus the economic vitality will be relatively weaker.

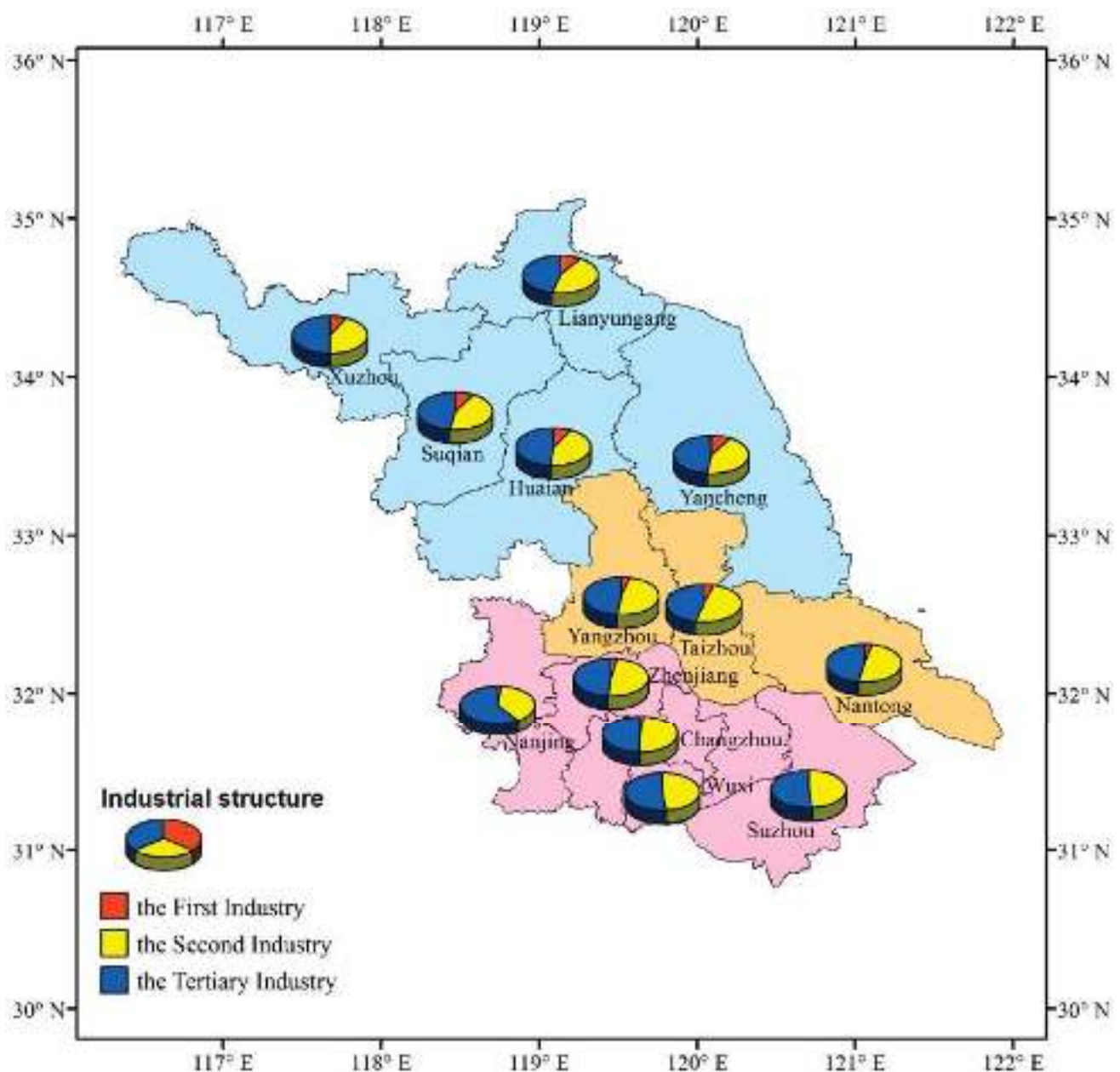


Figure 6. Industrial structure distribution map of 13 cities in Jiangsu Province. The data are from the *Jiangsu Statistical Yearbook 2020*, <http://tj.jiangsu.gov.cn/2020/nj20/nj2006.htm>, accessed on 10 March 2022.

4. Conclusions

In early 2020, the outbreak of the COVID-19 pandemic occurred. In order to control the spread of the pandemic, the Jiangsu provincial government took different levels of public health emergency responses. This paper studies the variations of air quality in response to different levels of PPC measures. In 2018, the Jiangsu provincial government issued the “Implementation Plan of Jiangsu Province’s Three-Year Action Plan for Cleaner Air”. Since then, the air quality has improved significantly. Therefore, this study focuses on analyzing the air quality during 2018–2020. By analyzing the relationships of air pollution data with PPC levels and meteorological conditions, the major conclusions are as follows.

The implementation of COVID-19 related PPC policies directly affected the concentrations of air pollutants. For AQI and pollutants of NO_2 , CO, PM_{10} and $\text{PM}_{2.5}$, as long as the countermeasures were taken, the AQI and pollutant concentrations were reduced by

varied degrees regardless of the levels of PPC. However, there was no significant decrease in SO₂ and O₃ concentration during the period in response to PPC measures.

The air pollution reduction was closely related to the levels of PPC. In general, the higher the level of PPC measures, the greater was the reduction of air pollutant concentrations. Compared with the cities in northern China, the air quality in Jiangsu was more likely to be affected by restrictive policies, but the sensitivity of air quality to restrictive policies was slightly lower than that in the Guangdong–Hong Kong–Macao Greater Bay Area. This may be related to urban development and industrial structure in different regions.

NO₂ was the pollutant most sensitive to PPC policies. The higher the level of PPC, the greater was the reduction of NO₂ concentration. The CO and atmospheric particulate matter concentrations were most significantly reduced during the periods with first- and second-level PPC measures. With the recovery of production and living order, the pollutant concentrations gradually approached the average value in the same period of previous years.

There were great differences in the response speeds of urban air quality to the levels of PPC among cities with different levels of economic development and industrial structures. Southern Jiangsu, which has a higher level of economic development and is dominated by secondary and tertiary industries, had a faster response speed and a stronger responsiveness, indicating its high economic vitality.

Due to the complexity of air pollution change, in which many factors may play a key role in this process, this paper still has some limitations, which need to be discovered in further investigation.

Author Contributions: Conceptualization, W.A. and X.Y.; methodology, X.Y.; software, X.Y. and M.Z.; validation, X.Y. and M.Z.; formal analysis, Y.S. and B.W.; investigation, X.Y. and D.L.; resources, W.A. and X.L.; data curation, X.Y.; writing—original draft preparation, X.Y.; writing—review and editing, D.L., X.Y. and W.A.; visualization, X.Y. and M.Z.; supervision, W.A. and X.L.; project administration, W.A.; funding acquisition, W.A. and X.Y. All authors have read and agreed to the published version of the manuscript.

Funding: This research was funded by the General Projects of Jiangsu Meteorological Bureau (KM202204), the Youth Fund of Jiangsu Meteorological Bureau (KQ202005), the Innovation Fund of the Public Meteorological Service Center of China Meteorological Administration (M2021010), the Open Research Fund of China Meteorological Administration Key Laboratory of Transportation Meteorology (BJG202206) and the East China Regional Meteorological Science and Technology Collaborative Innovation Fund Cooperation Project (QYHZ202109).

Institutional Review Board Statement: Not applicable.

Informed Consent Statement: Not applicable.

Data Availability Statement: The data presented in this study are available upon request from the corresponding author.

Acknowledgments: We thank Jiangsu Environmental Monitoring Center for the provision of air quality data. We are also very grateful to Shen Jinyou of Nanjing University of Science and Technology, Zhang Zhiwei of Jiangsu Meteorological Society and Chen Hao of Jiangsu Meteorological Observatory for their guidance and help to this paper.

Conflicts of Interest: The authors declare no conflict of interest.

References

1. Bao, R.; Zhang, A. Does lockdown reduce air pollution? Evidence from 44 cities in northern China. *Sci. Total Environ.* **2020**, *731*, 139052. [CrossRef]
2. Berman, J.D.; Ebisu, K. Changes in US air pollution during the COVID-19 pandemic. *Sci. Total Environ.* **2020**, *739*, 139864. [CrossRef]
3. Tian, H.; Liu, Y.; Li, Y.; Wu, C.-H.; Chen, B.; Kraemer, M.U.G.; Li, B.; Cai, J.; Xu, B.; Yang, Q.; et al. An investigation of transmission control measures during the first 50 days of the COVID-19 epidemic in China. *Science* **2020**, *368*, 638–642. [CrossRef] [PubMed]
4. Venter, Z.S.; Aunan, K.; Chowdhury, S.; Lelieveld, J. COVID-19 lockdowns cause global air pollution declines. *Proc. Natl. Acad. Sci. USA* **2020**, *117*, 18984–18990. [CrossRef]

5. Wang, Z.S.; Li, Y.T.; Zhang, D.W.; Chen, T.; Sun, F.; Li, L.J.; Li, J.X.; Sun, N.D.; Chen, C.; Wang, B.Y. Analysis on air quality in Beijing during the 2014 APEC conference. *Acta Sci. Circumst.* **2016**, *36*, 675–683.
6. Li, X.; Kong, S.; Yin, Y.; Li, L.; Yuan, L.; Li, Q.; Xiao, H.; Chen, K. Polycyclic aromatic hydrocarbons (PAHs) in atmospheric PM_{2.5} around 2013 Asian Youth Games period in Nanjing. *Atmos. Res.* **2016**, *174*, 85–96. [CrossRef]
7. Huang, Q.; Wang, T.; Chen, P.; Huang, X.; Zhu, J.; Zhuang, B. Impacts of emission reduction and meteorological conditions on air quality improvement during the 2014 Youth Olympic Games in Nanjing, China. *Atmos. Chem. Phys.* **2017**, *17*, 13457–13471. [CrossRef]
8. Zhao, J.; Luo, L.; Zheng, Y.; Liu, H. Analysis on air quality characteristics and meteorological conditions in Hangzhou during the G20 summit. *Acta Sci. Circumst.* **2017**, *37*, 3885–3893.
9. Chen, Q.X.; Huang, C.L.; Yuan, Y.; Tan, H.-P. Influence of COVID-19 event on air quality and their association in Mainland China. *Aerosol Air Qual. Res.* **2020**, *20*, 1541–1551. [CrossRef]
10. Filonchyk, M.; Hurynovich, V.; Yan, H.; Gusev, A.; Shpilevskaya, N. Impact assessment of COVID-19 on variations of SO₂, NO₂, CO and AOD over East China. *Aerosol Air Qual. Res.* **2020**, *20*, 1530–1540. [CrossRef]
11. Wan, S.; Cui, K.; Wang, Y.F.; Wu, J.-L.; Huang, W.-S.; Xu, K.; Zhang, J. Impact of the COVID-19 event on trip intensity and air quality in southern China. *Aerosol Air Qual. Res.* **2020**, *20*, 1727–1747. [CrossRef]
12. Xu, K.; Cui, K.; Young, L.H.; Wang, Y.-F.; Hsieh, Y.-K.; Wan, S.; Zhang, J. Air quality index, indicator air pollutants and impact of COVID-19 event on the air quality near central China. *Aerosol Air Qual. Res.* **2020**, *20*, 1204–1221. [CrossRef]
13. Zhang, J.; Cui, K.; Wang, Y.-F.; Wu, J.-L.; Huang, W.-S.; Wan, S.; Xu, K. Temporal variations in the air quality index and the impact of the COVID-19 event on air quality in Western China. *Aerosol Air Qual. Res.* **2020**, *20*, 1552–1568. [CrossRef]
14. Zhang, L.; Yang, L.; Zhou, Q.; Zhang, X.; Xing, W.; Zhang, H.; Toriba, A.; Hayakawa, K.; Tang, N. Impact of the COVID-19 outbreak on the long-range transport of particulate PAHs in East Asia. *Aerosol Air Qual. Res.* **2020**, *20*, 2035–2046. [CrossRef]
15. Jiaxin, C.; Hui, H.; Feifei, W.; Mi, Z.; Ting, Z.; Shicheng, Y.; Ruoqiao, B.; Nan, C.; Ke, X.; Hao, H. Air quality characteristics in Wuhan (China) during the 2020 COVID-19 pandemic. *Environ. Res.* **2021**, *195*, 110879. [CrossRef] [PubMed]
16. Blumberg, S. Data Shows 30 Percent Drop in Air Pollution over Northeast U.S. NASA. 2020. Available online: <https://www.nasa.gov/feature/goddard/2020/drop-in-air-pollution-over-northeast> (accessed on 4 April 2020).
17. EEA. Air Pollution Goes Down as Europe Takes Hard Measures to Combat Coronavirus. 2020. Available online: <https://www.eea.europa.eu/highlights/air-pollution-goes-down-as> (accessed on 25 March 2020).
18. Bedi, J.S.; Dhaka, P.; Vijay, D.; Aulakh, R.S.; Gill, J.P.S. Assessment of air quality changes in the four metropolitan cities of India during COVID-19 pandemic lockdown. *Aerosol Air Qual. Res.* **2020**, *20*, 2062–2070. [CrossRef]
19. Li, J.; Tartarini, F. Changes in air quality during the COVID-19 lockdown in Singapore and associations with human mobility trends. *Aerosol Air Qual. Res.* **2020**, *20*, 1748–1758. [CrossRef]
20. Singh, V.; Singh, S.; Biswal, A.; Kesarkar, A.P.; Mor, S.; Ravindra, K. Diurnal and temporal changes in air pollution during COVID-19 strict lockdown over different regions of India. *Environ. Pollut.* **2020**, *266*, 115368. [CrossRef] [PubMed]
21. Almond, D.; Du, X.; Zhang, S. *Ambiguous Pollution Response to COVID-19 in China*; National Bureau of Economic Research: Cambridge, MA, USA, 2020. [CrossRef]
22. Li, L.; Li, Q.; Huang, L.; Wang, Q.; Zhu, A.; Xu, J.; Liu, Z.; Li, H.; Shi, L.; Li, R.; et al. Air quality changes during the COVID-19 lockdown over the Yangtze River Delta Region: An insight into the impact of human activity pattern changes on air pollution variation. *Sci. Total Environ.* **2020**, *732*, 139282. [CrossRef]
23. Pei, Z.; Han, G.; Ma, X.; Su, H.; Gong, W. Response of major air pollutants to COVID-19 lockdowns in China. *Sci. Total Environ.* **2020**, *743*, 140879. [CrossRef]
24. Li, J.; Yang, H.; Zha, S.; Yu, N.; Liu, X.; Sun, R. Effects of COVID-19 emergency response levels on air quality in the Guangdong-Hong Kong-Macao greater bay area, China. *Aerosol Air Qual. Res.* **2021**, *21*, 200416. [CrossRef]
25. Sicard, P.; De Marco, A.; Agathokleous, E.; Feng, Z.; Xu, X.; Paoletti, E.; Rodriguez, J.J.D.; Calatayud, V. Amplified ozone pollution in cities during the COVID-19 lockdown. *Sci. Total Environ.* **2020**, *735*, 139542. [CrossRef] [PubMed]
26. Pyrgou, A.; Hadjinicolaou, P.; Santamouris, M. Enhanced near-surface ozone under heatwave conditions in a Mediterranean island. *Sci. Rep.* **2018**, *8*, 1–10. [CrossRef] [PubMed]
27. Wu, Z.; Liu, D.; Zhao, T.; Su, Y.; Zhou, B. Size Distributions of Water-Soluble Inorganic Ions in Atmospheric Aerosols during the Meiyu Period in the Yangtze River Delta, China. *Front. Environ. Sci.* **2021**, *515*. [CrossRef]
28. Zhou, B.; Liu, D.; Yan, W. A Simple new method for calculating precipitation scavenging effect on particulate matter: Based on five-year data in Eastern China. *Atmosphere* **2021**, *12*, 759. [CrossRef]
29. Lee, Y.C.; Shindell, D.T.; Faluvegi, G.; Wenig, M.; Lam, Y.F.; Ning, Z.; Hao, S.; Lai, C.S. Increase of ozone concentrations, its temperature sensitivity and the precursor factor in South China. *Tellus B Chem. Phys. Meteorol.* **2014**, *66*, 23455. [CrossRef]
30. Li, K.; Jacob, D.J.; Liao, H.; Bates, K.H. Anthropogenic drivers of 2013–2017 trends in summer surface ozone in China. *Proc. Natl. Acad. Sci. USA* **2019**, *116*, 422–427. [CrossRef]
31. Tan, Z.; Hofzumahaus, A.; Lu, K.; Brown, S.S.; Holland, F.; Huey, L.G.; Kiendler-Scharr, A.; Li, X.; Liu, X.; Ma, N.; et al. No evidence for a significant impact of heterogeneous chemistry on radical concentrations in the North China Plain in summer 2014. *Environ. Sci. Technol.* **2020**, *54*, 5973–5979. [CrossRef]
32. Liu, D.; Yan, W.; Qian, J.; Liu, M.; Wang, Z.; Cheng, M.; Peng, H. A Movable Fog-Haze Boundary Layer Conceptual Model Over Jianghuai Area, China. *Front. Environ. Sci.* **2021**, *591*. [CrossRef]

33. Wang, P.; Chen, K.; Zhu, S.; Wang, P.; Zhang, H. Severe air pollution events not avoided by reduced anthropogenic activities during COVID-19 outbreak. *Resour. Conserv. Recycl.* **2020**, *158*, 104814. [CrossRef]
34. Zhu, Y.; Xie, J.; Huang, F.; Cao, L. Association between short-term exposure to air pollution and COVID-19 infection: Evidence from China. *Sci. Total Environ.* **2020**, *727*, 138704. [CrossRef] [PubMed]
35. Lu, Y.; Li, X.; Ni, H.; Chen, X.; Xia, C.; Jiang, D.; Fan, H. Temporal-spatial evolution of the urban ecological footprint based on net primary productivity: A case study of Xuzhou Central Area, China. *Sustainability* **2019**, *11*, 199. [CrossRef]

Article

Effect of Combustion Boundary Conditions and n-Butanol on Surrogate Diesel Fuel HCCI Combustion and Emission Based on Two-Stroke Diesel Engine

Shiye Wang ¹, Jundong Zhang ^{1,*} and Li Yao ^{2,*}

¹ Marine Engineering College, Dalian Maritime University, Dalian 116026, China; wangshiye@dlmu.edu.cn

² Merchant Marine College, Shanghai Maritime University, Shanghai 201306, China

* Correspondence: zhjundong@dlmu.edu.cn (J.Z.); yaoli@dicp.ac.cn (L.Y.)

Abstract: The combustion and emission characteristics of surrogate diesel fuel homogeneous charge compression ignition (HCCI) with different combustion boundary conditions and n-butanol (NB) mixing ratios are studied in this work. Engine data of a two-stroke low-speed direct-injection marine diesel engine were selected for the reactor. HCCI combustion was achieved by compressing a completely homogeneous mixture of fuel and air. The results show that NO emissions decrease slightly with the increase of initial boundary pressure at a constant equivalence ratio and initial temperature. In addition, the different initial boundary temperature has little effect on NO emission. The results also indicate that the ignition delay time of the mixed fuel rises with the increase of n-butanol mixing ratio. The emissions and reaction rate of NO_x reduce significantly with the increase of n-butanol percentage in surrogate diesel fuel and n-butanol mixing combustion at a constant equivalence ratio and total mole fraction. Meanwhile, CO₂ emissions also decrease significantly with the increase of n-butanol mixing ratio.

Keywords: homogeneous charge compression ignition; surrogate diesel fuel; ignition delay; n-butanol; NO_x emission

Citation: Wang, S.; Zhang, J.; Yao, L. Effect of Combustion Boundary Conditions and n-Butanol on Surrogate Diesel Fuel HCCI Combustion and Emission Based on Two-Stroke Diesel Engine. *Atmosphere* **2022**, *13*, 303. <https://doi.org/10.3390/atmos13020303>

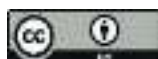
Academic Editors: Duanyang Liu, Kai Qin and Honglei Wang

Received: 11 January 2022

Accepted: 8 February 2022

Published: 10 February 2022

Publisher's Note: MDPI stays neutral with regard to jurisdictional claims in published maps and institutional affiliations.



Copyright: © 2022 by the authors. Licensee MDPI, Basel, Switzerland. This article is an open access article distributed under the terms and conditions of the Creative Commons Attribution (CC BY) license (<https://creativecommons.org/licenses/by/4.0/>).

1. Introduction

The development of society and the economy is inseparable from energy. The demand for energy is increasing constantly in the current society, and the rapid consumption of fossil fuels has caused people to face a serious energy crisis. Therefore, people develop and explore new renewable and efficient fossil fuel alternative energy sources to deal with the increasingly severe energy problem [1–3]. At the same time, the massive burning of fossil fuels has also brought serious pollution problems. Large amounts of CO₂ and thermal NO_x are produced when the engine burns fossil fuels. NO and NO₂ are the two most important harmful pollutants in thermal NO_x produced by combustion [4–6]. In order to alleviate the serious environmental damage caused by fossil fuels combustion, various countries have formulated different measures to control the exhaust emissions of diesel engines strictly. The European Parliament plans to limit greenhouse gas emissions to deal with the serious problem of global warming and strive to achieve the goal of reducing more than 80% in 2050 [7]. The British Parliament passed an amendment in 2019 to achieve a net zero emission target by 2050. The French National Assembly had already incorporated a net zero target into law in June 2019. Therefore, the development and utilization of new renewable clean energy is receiving more and more attention.

N-heptane is often selected as a surrogate diesel fuel in previous simulations of diesel engines [8–10]. However, the carbon chain of actual diesel fuel is longer than that of n-heptane fuel, and the number of carbon atoms is about 10 to 25 [11]. The composition of diesel is complicated, and it is difficult to reproduce the combustion chemistry characteristics of diesel under low-temperature combustion through a single component

represented by n-heptane. N-dodecane is considered to be a closer alternative fuel to diesel than n-heptane. Earlier, Luo et al. developed a simplified one-component diesel substitute (pure n-dodecane) to simulate diesel engines [12]. However, the mechanism of n-dodecane lacks alkylbenzene, which is an important component in diesel. It cannot reflect the real combustion of diesel well. Then, Pei et al. developed a diesel substitution mechanism (consisting of 77% n-dodecane and 23% m-xylene) on this basis and compared it with the experimental data of shock tube. Research has found that the mixture of m-xylene and n-dodecane can represent the combustion and emission characteristics of diesel fuel better than pure n-dodecane [13].

Oxygenated fuel can reduce PM and soot emissions significantly in diesel engine combustion [14–19]. At the same time, some oxygenated fuels are renewable. Oxygenated fuel can be used as a single fuel or mixed with diesel in a certain proportion. Therefore, oxyfuel is an ideal substitute for fossil energy. As a representative of the new generation of oxygenated fuel, the development and application of n-butanol ($C_4H_{10}O$) have attracted the extensive attention of scholars [20,21]. N-butanol has less corrosiveness and high safety. As an oxygenated fuel, burning n-butanol can reduce soot emissions effectively. The viscosity of n-butanol is lower than that of diesel, and it has better mutual solubility with diesel. The mixed combustion of n-butanol and diesel can be realized on the diesel engine with small changes to the engine [22–25]. In terms of environmental protection, n-butanol can be produced by biological methods, which can solve the problem of large fossil fuel consumption effectively. The renewability of n-butanol has high research value and wide application prospects.

As a new type of combustion concept, HCCI combustion has low NO_x emissions and high combustion heat efficiency compared to traditional gasoline and diesel engines [26–28]. Analyzing the fuel combustion reaction rate through chemical reaction kinetics and controlling the ignition strategy of the engine are the most important contents in HCCI combustion [29]. A single fuel or fuel mixture can be used to control the ignition of different types of engines and the chemical reaction rates of the fuel in HCCI combustion process [30–32]. At present, a variety of fuels including biodiesel, n-butanol and n-heptane have been used in HCCI engines for research [33–37].

Therefore, the purpose of the study is to apply the HCCI combustion method to a marine diesel engine and reduce engine emissions of diesel. The method of reducing engine emissions in diesel surrogate fuel (77% n-dodecane and 23% m-xylene mixture) HCCI combustion by mixing with n-butanol in a two-stroke diesel engine is first proposed in the research.

2. Kinetic Models and Methods

The IC engine module in the CHEMKIN-PRO software is used to simulate a low-speed two-stroke diesel engine HCCI combustion. The selected model is the B&W 6S70MC engine produced by MAN. This research combines the parameters of this engine model with closed internal combustion on engine simulator and applies the HCCI combustion method to a marine diesel engine to study the effects of n-butanol on diesel surrogate fuel HCCI combustion and emission characteristics. The fuel is completely homogeneously mixed with the air during the intake and compression strokes to form a lean, homogeneous mixture. When the piston is compressed to the vicinity of the TDC, the combustion of the mixed gas in the cylinder is realized by the self-ignition of the air-fuel mixture. Table 1 shows the main technical parameters of the diesel engine [38].

Table 1. Test engine parameters and specifications.

Item	Data
Engine speed	85 rpm
Effective power	13,364 kW
Mean effective pressure	15.27 bar
Stroke	3674 mm
Number of cylinders	6
Connecting rod length	3066 mm
Cylinder diameter	700 mm

The diesel surrogate fuel (77% n-dodecane and 23% m-xylene) reaction mechanism model came from the Lawrence Livermore National Laboratory [13], which is defined as DX in this study. The n-butanol combustion reaction mechanism came from the National University of Ireland [39]. The NO_x combustion reaction mechanism came from the C0-C1 NO_x mechanism of the National University of Ireland [40]. These mechanisms were combined through ANSYS Workbench to eliminate duplicate reactions and redundant species. Then, a detailed mixed fuel combustion reaction kinetics mechanism was constructed to study the HCCI combustion and emission characteristics of two-stroke diesel engines. Table 2 shows the comparison of the properties of n-butanol, DX [41] and actual diesel [41]. The cetane number of DX is much higher than that of actual diesel, while the cetane number of n-butanol is lower. Therefore, the cetane number of mixed fuel can be reduced to close to the cetane number of actual diesel by mixing with n-butanol.

Table 2. Properties of fuels.

Property	Diesel	DX	n-Butanol
C/H mass ratio	6.53	5.96	4.80
Lower heating value (MJ/kg)	42.98	43.33	35.10
Oxygen content (weight %)	0	0	21.6
Cetane number	46	70	12

The actual equivalence ratio of the low-speed two-stroke diesel engine is generally 0.45 to 0.5. In this study, the equivalence ratio is 0.5. Four different initial intake pressures of 0.8, 1.0, 1.2, and 1.4 atm are selected as the pressure boundary conditions of the two-stroke diesel engine HCCI combustion. Four different initial intake temperatures of 380, 400, 420, and 440 K are selected as the temperature boundary conditions for DX HCCI combustion. At a certain total mole fraction, DX and n-butanol are mixed in different proportions, and the mixing ratio of n-butanol increases gradually. Table 3 shows the mole fraction and cetane number of mixed fuel and air. Argon is used as the filling gas and does not participate in the actual reaction.

Table 3. Species composition ratio and cetane number of DX-NB mixtures.

Mole Fraction of DX	Mole Fraction of NB	Mole Fraction of O ₂	Mole Fraction of N ₂	Mole Fraction of Ar	Cetane Number
1.0	0	33.32	125.35	0	70.0
0.9	0.1	31.19	117.33	10.15	64.2
0.8	0.2	29.06	109.32	20.29	58.4
0.7	0.3	26.92	101.27	30.48	52.6
0.6	0.4	24.79	93.26	40.62	46.8

3. Results and Discussion

This article first verifies the reliability of the skeleton mechanism by comparing the ignition delay with the experiment. Then, the effects of different initial conditions and

n-butanol blending ratio on two-stroke diesel engine DX HCCI combustion are researched in the study.

3.1. Ignition Delay Verification of DX-NB-NO_x Skeleton Mechanism

The ignition delay data come from the simulation results of fuel in CHEMKIN closed internal combustion on engine simulator under different equivalence ratios. Figures 1–3 show the comparison of n-dodecane ignition delay time between the mixed fuel skeleton mechanism and the experimental value [42]. It can be seen that the study selects three different equivalence ratios (0.5, 1.0 and 1.5) for comparison at 8 atm and 15 atm respectively. The simulation results are in good agreement with the experimental values in the high-temperature stage, and there are some differences in the low-temperature stage. This is because the experimental data of fuel ignition delay are obtained from the shock tube experiment, while the simulated ignition delay results come from diesel engine combustion. There are some differences in the working mode between two styles. Therefore, there is a certain difference between the diesel engine combustion simulation results and the shock tube experimental data. The overall trend of two modes is consistent, and the error is within a reasonable range. So, the reliability of the combustion simulation of n-dodecane in the newly constructed combustion reaction mechanism can be guaranteed.

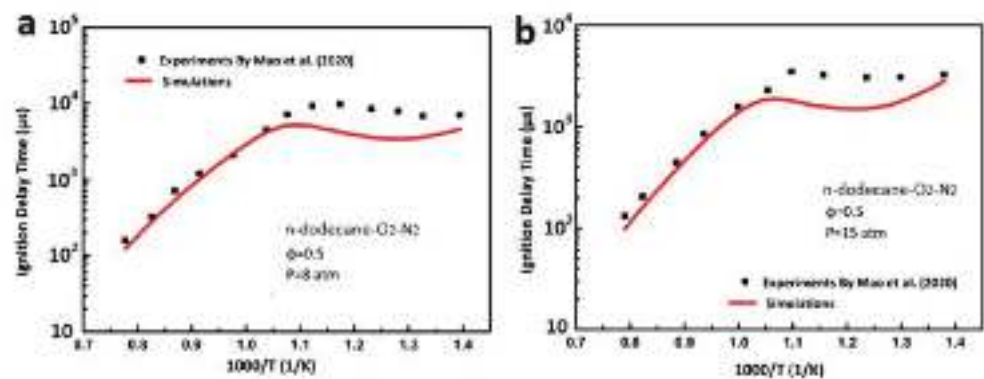


Figure 1. (a) Comparison of simulated and experimental ignition delay time of n-dodecane at $\Phi = 0.5$, 8 atm; (b) Comparison of simulated and experimental ignition delay time of n-dodecane at $\Phi = 0.5$, 15 atm.

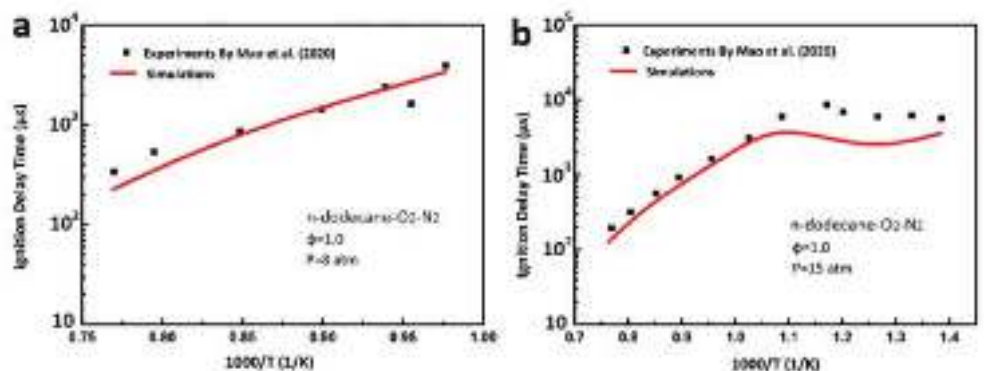


Figure 2. (a) Comparison of simulated and experimental ignition delay time of n-dodecane at $\Phi = 1.0$, 8 atm; (b) Comparison of simulated and experimental ignition delay time of n-dodecane at $\Phi = 1.0$, 15 atm.

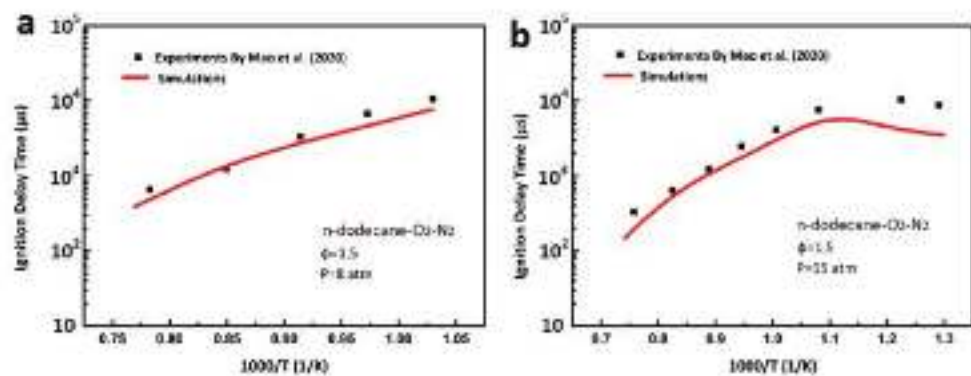


Figure 3. (a) Comparison of simulated and experimental ignition delay time of n-dodecane at $\Phi = 1.5$, 8 atm; (b) Comparison of simulated and experimental ignition delay time of n-dodecane at $\Phi = 1.5$, 15 atm.

Figure 4 shows the comparison of n-butanol ignition delay time between the newly constructed fuel mechanism and the experimental value [43]. It can be seen that the ignition delay times of n-butanol at three different pressures of 1.5, 3, and 42 atm are compared with the experimental values at the equivalent ratio of 1.0. The results show that the ignition delay time of n-butanol in the newly constructed mechanism was consistent with the experimental value, which ensured the reliability of the combustion simulation of n-butanol in the newly constructed combustion reaction mechanism.

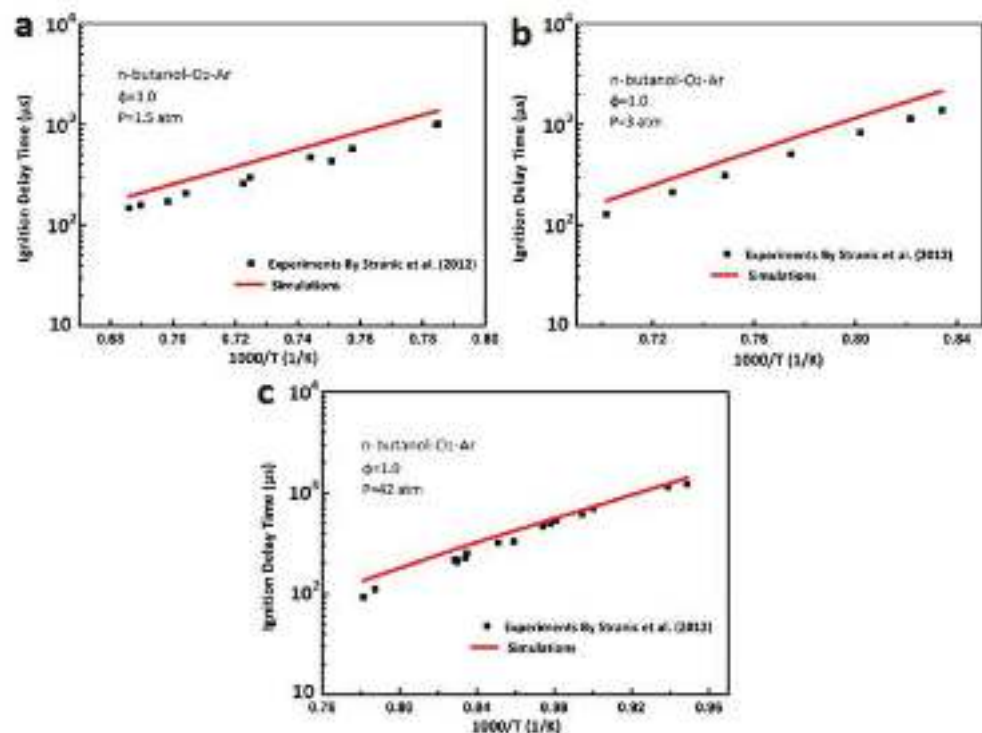


Figure 4. (a) Comparison of simulated and experimental ignition delay time of n-butanol at $\Phi = 1.0$, 1.5 atm; (b) Comparison of simulated and experimental ignition delay time of n-butanol at $\Phi = 1.0$, 3 atm; (c) Comparison of simulated and experimental ignition delay time of n-butanol at $\Phi = 1.0$, 42 atm.

3.2. Effect of Initial Pressure on DX HCCI Combustion and NO Emissions

In order to keep the combustion pressure consistent with the actual two-stroke diesel engine in the cylinder, at an equivalence ratio of 0.5 and an initial temperature of 400 K,

four different pressures of 0.8, 1.0, 1.2, and 1.4 atm are selected as the initial pressure of the two-stroke diesel engine HCCI combustion. Figure 5 shows the effect of different initial pressures on the in-cylinder pressure in the DX HCCI combustion. It can be seen that the peak combustion pressure increases with an increase of initial pressure. When the initial pressure is 1.4 atm, the DX HCCI combustion pressure is consistent with the experimental pressure [38]. The actual combustion pressure in the cylinder rises to the highest point after the top dead center (TDC) compared with HCCI combustion. The reason is that HCCI is an ideal combustion mode, multiple ignition points are distributed in the cylinder. When the fuel reaches ignition conditions, all the fuel is combusted at the same time in the cylinder, and the pressure rises to the highest point instantly in the cylinder. The fuel combustion reaction needs some time to progress gradually in the actual diesel engine, the fuel is completely burned after the TDC, and the cylinder pressure reaches the maximum. Therefore, the study selects 1.4 atm as the initial combustion pressure of the two-stroke engine without affecting the engine efficiency.

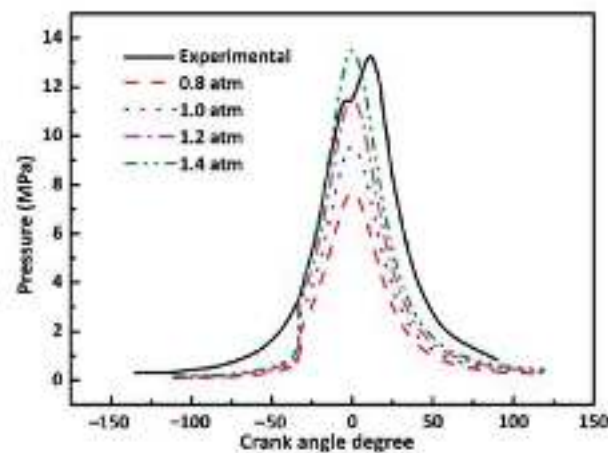


Figure 5. Comparison of different initial pressures and experimental pressure.

Figure 6 shows the effect of different initial combustion pressures on NO emissions. NO increases very slightly with the increase of initial intake pressure at a 0 crank angle degree. This is because the increase of pressure leads to an increase in the reaction rate of NO formation at the TDC, which increases the production of NO. It can be seen that the NO emission decreases slightly with the increase of initial pressure at a 50–119 crank angle degree. The reason is that the increase in combustion pressure accelerates the disturbance of the gas in the cylinder, speeds up the destruction of NO, and reduces the final production of NO. Therefore, the increase of initial combustion pressure can help to reduce NO emissions.

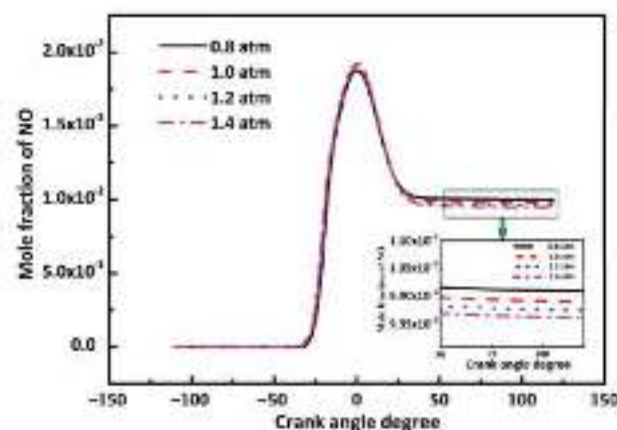


Figure 6. Effect of initial combustion pressures on NO emissions.

3.3. Effect of Initial Combustion Temperature on DX HCCI Combustion and NO Emissions

At a constant initial combustion pressure of 1.4 atm, equivalence ratio of 0.5. The study selects 380, 400, 420, and 440 K as the initial combustion temperatures for DX HCCI combustion. Figure 7 shows that when the initial temperatures are 400 K and 420 K, the combustion peak pressures in the cylinder are close to the actual combustion pressure [38]. At the same time, the fuel ignition delay time at 420 K is shorter than that at 400 K, so DX HCCI combustion can be synchronized with the actual combustion pressure curve earlier at the initial temperature of 420 K.

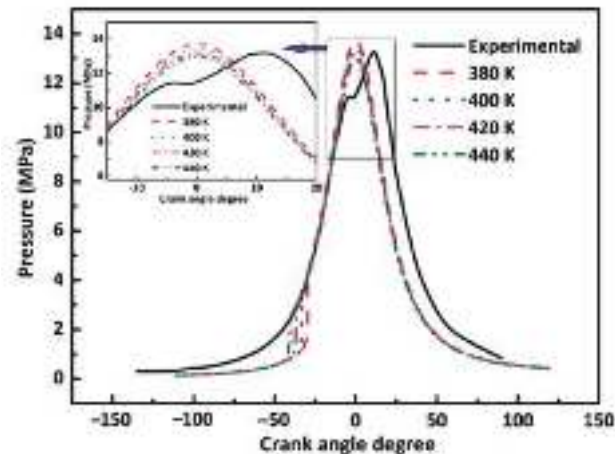


Figure 7. Effect of initial combustion temperatures on in-cylinder pressure.

Figure 8 shows the effect of different initial combustion temperatures on NO emissions. It can be seen that the NO emissions at the TDC increase significantly with an increase of initial temperature, which is because the maximum in-cylinder combustion temperatures rise with the increase of the initial temperature. The final emissions of NO at the exhaust port increase slightly at different initial temperatures.

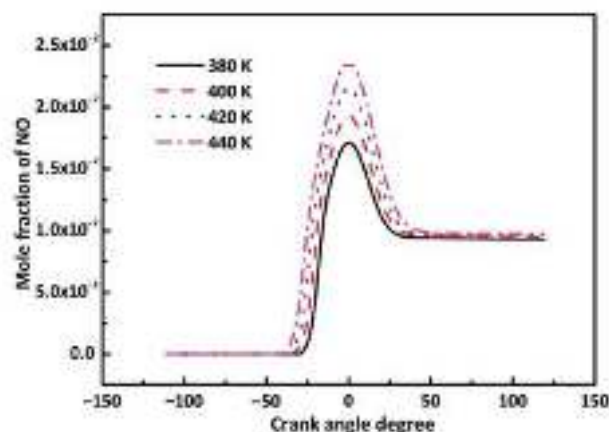


Figure 8. Effect of initial combustion temperatures on NO emissions.

Therefore, the DX HCCI combustion will not increase significantly at the initial combustion temperature of 420 K. The simulated combustion pressure can maintain a good consistency with the actual diesel engine combustion pressure in the cylinder.

3.4. Effect of n-Butanol on DX HCCI Combustion and Emission Characteristics

3.4.1. Effect of n-Butanol Blending Ratio on the Ignition Delay Time

At a constant engine speed of 85 rpm, equivalence ratio of 0.5, the total mole fraction of the mixed fuel is fixed. Figure 9a shows the effect of n-butanol blending ratio on the ignition delay time of the high-temperature part. It can be seen that when the temperature is higher than 1100 K, the ignition delay time of the mixed fuel rises with the increase of n-butanol blending ratio. The same trend also appears in the low-temperature stage (Figure 9b). The ignition delay time increases significantly with the increase of n-butanol blending ratio when the temperature is lower than 830 K. This is because the cetane number of n-butanol is lower than that of DX (Table 2). With the increase of n-butanol mixing ratio, the cetane number of the mixed fuel decreases. As a result, the ignition delay time of the mixed fuel becomes longer. The fuel and air have more time to mix fully and uniformly before the combustion starts, which can improve the fuel combustion efficiency effectively. The cetane number of DX is higher than that of diesel, and the cetane number of n-butanol is lower than that of diesel (Table 2). Therefore, adding a certain proportion of n-butanol to DX can make the cetane number of the mixed fuel closer to real diesel. It can be seen that when the blending ratio of n-butanol is 40%, the cetane number of the mixed fuel is closest to real diesel (Table 3).

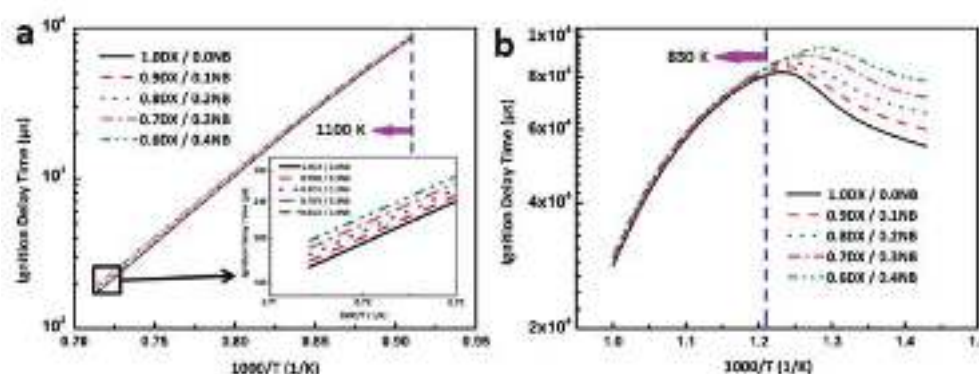


Figure 9. (a) Effect of DX and n-butanol blending ratio on high-temperature ignition delay; (b) Effect of DX and n-butanol blending ratio on low-temperature ignition delay.

3.4.2. Effect of n-Butanol Blending Ratio on Combustion Temperature and Pressure

Figure 10 shows that the combustion temperature decreases with an increase of n-butanol percentage at a constant equivalence ratio of 0.5. This is because the lower heating value of n-butanol is lower than that of DX, the total heating value of fuel reduces with the increase of n-butanol percentage at the constant total mole fraction. The difference between the heating value of DX and n-butanol is not very large, it will not cause a significant decrease in the temperature of the main combustion process. However, the lower heating value will shorten the combustion process time. When the fuel is completely burned, the lower the heating value, the faster the combustion temperature decreases. The reduction of combustion temperature helps to reduce the production of thermal NO_x. Therefore, the combustion temperature can be adjusted in an appropriate range by regulating the mixing ratios of DX and n-butanol to decrease NO_x emissions

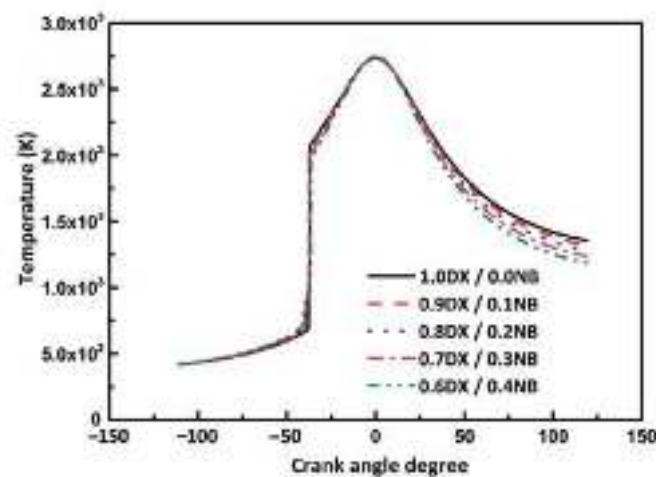


Figure 10. Effect of DX and n-butanol mixing ratio on combustion temperature in cylinder.

Figure 11 shows the effect of n-butanol mixing ratio on in-cylinder combustion pressure. It can be seen that the combustion pressure has not obvious change with the increase of n-butanol mixing ratio in a two-stroke diesel engine. Therefore, adding n-butanol to DX HCCI combustion will not cause a major change to the engine combustion pressure, which ensures the working efficiency of the engine.

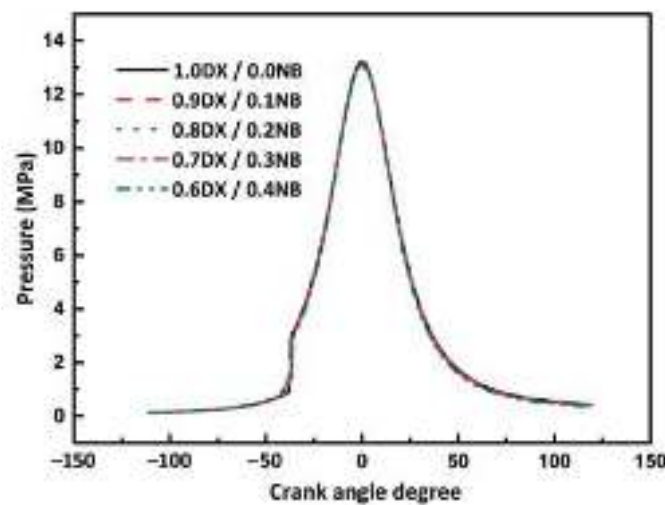


Figure 11. Effect of DX and n-butanol mixing ratio on combustion pressure in cylinder.

3.4.3. Effect of n-Butanol Blending Ratio on NO_x Emissions

Figure 12a shows the effect of DX and n-butanol blending ratio on NO emissions. It can be seen that NO emissions decrease significantly with the increase of n-butanol mixing ratio. When the blending ratio of n-butanol increases from 0% to 40%, the final NO emissions decreased by 21.9% (Figure 12b). Therefore, NO emissions can be reduced effectively by adding the n-butanol mixing ratio.

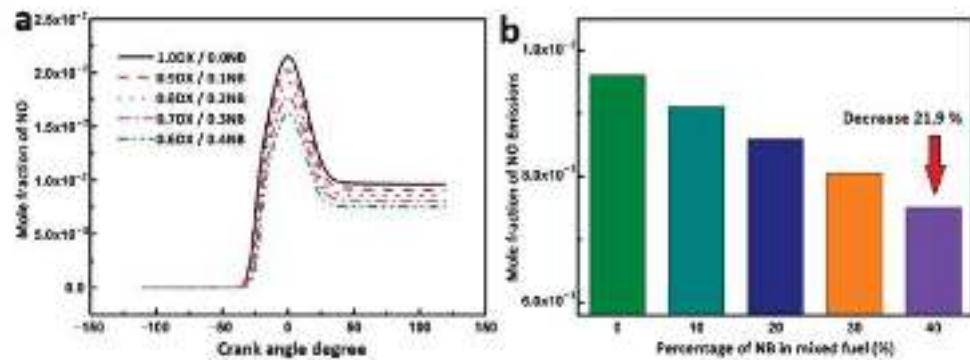


Figure 12. (a) Effect of DX and n-butanol blending ratio on NO emissions; (b) Effect of n-butanol percentage on final NO emissions.

The same trend also appears in NO₂ emissions (Figure 13a). It can be seen that the final emission of NO₂ shows a downward trend with the increase of n-butanol mixing ratio. It can be clearly seen that with the blending ratio of n-butanol increases from 0% to 40%, the final NO₂ emissions decrease by 7.8% from Figure 13b. Therefore, NO₂ emissions can be reduced effectively by adding n-butanol in DX HCCI combustion.

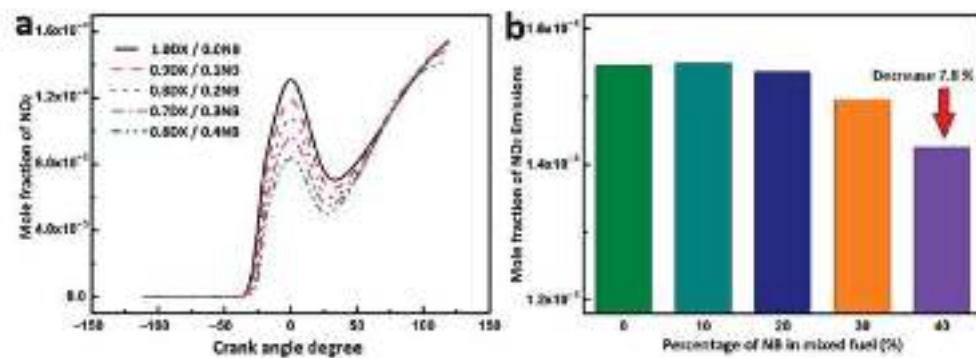


Figure 13. (a) Effect of DX and n-butanol mixing ratio blending ratio on NO₂ emissions; (b) Effect of n-butanol percentage on final NO₂ emissions.

NO_x emissions show an obvious downward trend with the increase of n-butanol blending ratio. The main reason is that the lower heating value of DX is higher than that of n-butanol. The total heating value of fuel decreases with the increase of n-butanol blending ratio, causing the combustion temperature in the cylinder to decrease, which leads to a decrease in NO_x emissions. At the same time, the increase of n-butanol blending ratio leads to a lower cetane number of the mixed fuel and increases the ignition delay time. The fuel has sufficient time for uniform mixing and shortens the combustion process. Since long-time combustion is also an important factor that causes the increase of NO_x emissions. Therefore, the NO_x emissions can be reduced by shortening the combustion process.

3.4.4. Effect of n-Butanol Blending Ratio on NO_x Reaction Rate

Figure 14 shows the effect of n-butanol blending ratio on the chemical reaction rate of NO produced at the maximum combustion temperature in the cylinder. The main reaction paths of NO generation at the in-cylinder combustion peak temperature are indicated by the following chemical equations:



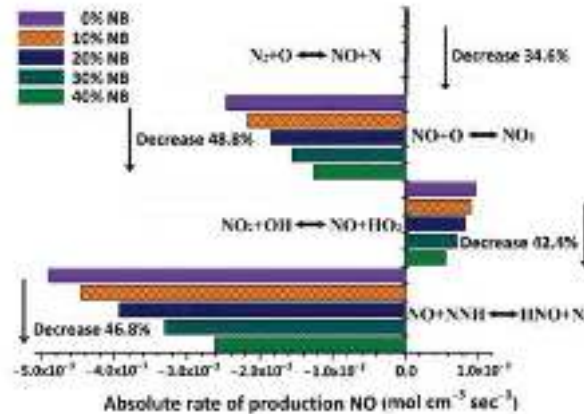


Figure 14. Effect of n-butanol mixing ratio on NO formation rate.

It can be seen that the reaction rate of NO decreases significantly with the increase of n-butanol mixing ratio. The maximum reduction of NO production rate can reach about 48.8%. The main reason is that the increase of n-butanol mixing ratio leads to a decrease in the total heating value of the mixed fuel, which reduces the in-cylinder combustion temperature. The lower combustion temperature suppresses the perturbation of the gas in the cylinder. Therefore, the production rate and emissions of NO are reduced effectively.

Figure 15 shows the effect of n-butanol blending ratio on the chemical reaction rate of NO₂ produced at the maximum combustion temperature in the cylinder. The main reaction paths of NO₂ generation at the in-cylinder combustion peak temperature are indicated by the following chemical equations:

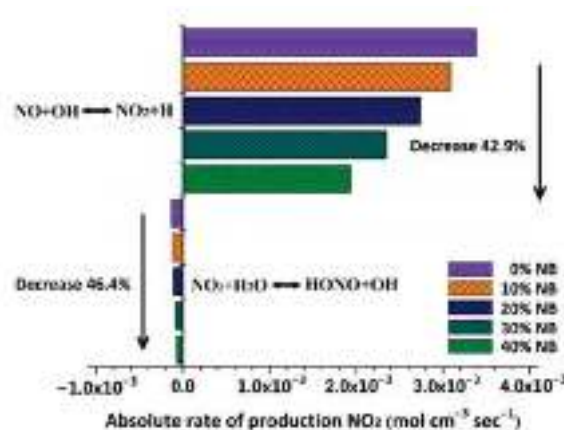


Figure 15. Effect of n-butanol mixing ratio on NO₂ formation rate.

It's the same as the decrease of NO reaction rate, the total heating value of the mixed fuel decreases with the increase of n-butanol blending ratio, which reduces the combustion temperature in the cylinder. The lower combustion temperature suppresses the perturbation of the gas in the cylinder, the combustion reaction rate of NO₂ decreases, which leads

to a reduction in NO_2 emissions. The NO_2 generation rate can be reduced by about 46.4% at most.

It can be seen that the combustion reaction rate and emissions of NO_x reduces significantly with the increase of n-butanol mixing ratio. When the blending ratio of n-butanol reaches 40%, the production rate of NO and NO_2 can be reduced by more than 40%. Therefore, NO_x emissions can be reduced effectively by increasing n-butanol mixing ratio in a suitable range.

3.4.5. Effect of n-Butanol Blending Ratio on CO_2 Emissions

Figure 16 shows the effect of DX and n-butanol mixing ratio on CO_2 emissions at an equivalence ratio of 0.5. It can be seen that the CO_2 emissions decrease significantly with the increase of n-butanol blending ratio. The reason for the decrease in CO_2 production is that the C/H ratio of n-butanol is lower than that of DX. The C/H ratio of the mixed fuel decreases with the increase of n-butanol. Therefore, it can be known that CO_2 emissions in two-stroke diesel engine HCCI combustion reduce significantly with an increase of n-butanol mixing ratio.

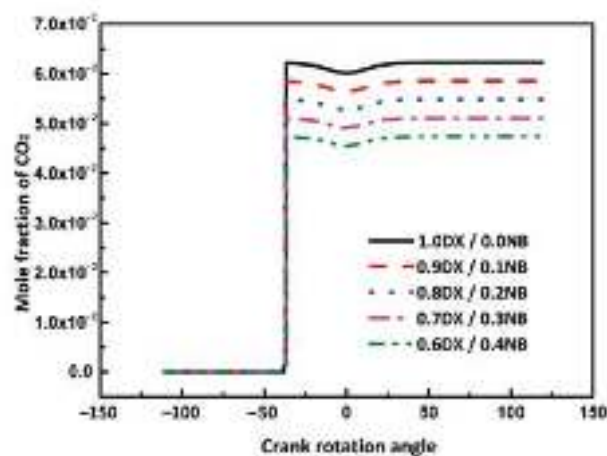


Figure 16. Effect of DX and n-butanol blending ratio on CO_2 emissions.

Figure 17 shows the effect of n-butanol blending ratio on the C/H mass ratio and the final CO_2 emissions of the mixed fuel. It can be clearly seen that the C/H mass ratio of the mixed fuel decreases significantly with the increase of n-butanol mixing ratio. The decrease of the C/H mass ratio leads to the reduction of the final CO_2 emissions. The final CO_2 emission decreases by about 23.9% when the blending ratio of n-butanol reaches 40%. Therefore, C/H mass ratio and CO_2 emissions of the two-stroke diesel engine HCCI combustion can be reduced effectively by increasing the n-butanol mixing ratio in a suitable range.

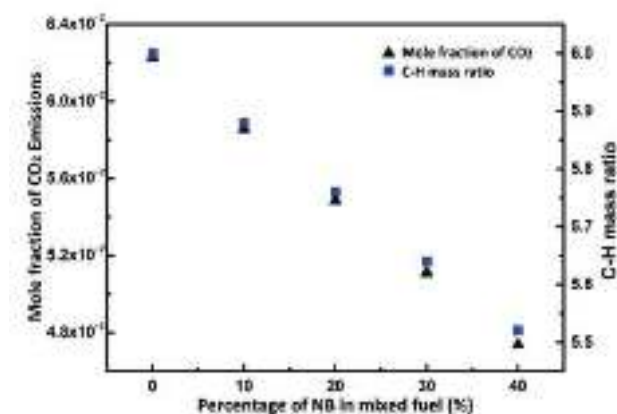


Figure 17. Effect of n-butanol percentage on C-H mass ratio and final CO₂ emissions.

4. Conclusions

A mixture of n-dodecane and m-xylene was used as an alternative fuel for diesel. The complete combustion reaction mechanism of diesel (DX), n-butanol and NO_x was established for two-stroke diesel engine HCCI combustion. Through the sensitivity analysis, ignition delay time, combustion temperature, in-cylinder pressure, NO_x and CO₂ emissions were obtained for different n-butanol mixture ratios during the diesel alternative fuel DX HCCI combustion. Through the analysis of reaction paths, the main formation path and chemical reaction rate of NO_x were observed accurately. The main findings from this research are as follows:

The peak combustion pressure increased with an increase of initial intake pressure from 0.8 to 1.4 atm on low-speed two-stroke diesel engines HCCI combustion. The combustion pressure of the model used at 1.4 atm in the cylinder was consistent with the actual combustion pressure. The final NO emissions decreased slightly with the increase of initial intake pressure.

The ignition time advances with the increase of initial intake temperature from 380 to 440 K. The combustion pressure of the model used at initial temperature of 420 K was consistent with the actual combustion pressure. The final NO emissions increased slightly with the increase of initial intake temperature.

Different DX and n-butanol mixing ratios were used at a constant total mole fraction. The ignition delay time increased with an increase of n-butanol ratio. The combustion temperature decreased rapidly with the increase of the n-butanol blending ratio after the TDC. The reaction rate and emissions of NO_x reduced significantly with the increase of n-butanol mixing ratio. When the blending ratio of n-butanol reaches 40%, the production rate of NO and NO₂ could be reduced by more than 40%. The NO_x reaction rates decreased rapidly with the increase of n-butanol mixing ratio at the TDC. At the same time, C/H mass ratio and the CO₂ emissions decreased significantly with the increase of n-butanol percentage. Therefore, the combustion and emission of DX HCCI combustion can be improved by increasing the n-butanol mixing ratio at the same engine load.

Author Contributions: Writing—original draft preparation, S.W.; project administration, J.Z.; writing—review and editing, L.Y. All authors have read and agreed to the published version of the manuscript.

Funding: This work was supported by Research on Intelligent Ship Testing and Verification ([2018]473). The Major Research plan of the National Natural Science Foundation of China (Grant No. 91441132).

Institutional Review Board Statement: Not applicable.

Informed Consent Statement: Not applicable.

Data Availability Statement: The data presented in this study are available on request from the first author.

Acknowledgments: All authors are very grateful to the editors and anonymous reviewers for their great contributions on the manuscript reviewing and constructive comments.

Conflicts of Interest: The authors declare no conflict of interest.

Nomenclature

HCCI	homogeneous charge compression ignition
DX	n-dodecane and m-xylene
NB	n-butanol
rpm	revolutions per minute
Ar	argon
TDC	top dead center

References

- Demirbas, A. Importance of biodiesel as transportation fuel. *Energy Policy* **2007**, *35*, 4661–4670. [CrossRef]
- Pienkos, P.T.; Darzins, A. The promise and challenges of microalgal-derived biofuels. *Biofuels Bioprod. Biorefining* **2009**, *3*, 431–440. [CrossRef]
- Blasio, G.D.; Ianniello, R.; Beatrice, C. Hydrotreated Vegetable Oil as Enabler for High-Efficient and Ultra-Low Emission Vehicles in the View of 2030 Targets. *Fuel* **2022**, *310*, 122206. [CrossRef]
- Cho, C.P.; Pyo, Y.D.; Jang, J.Y.; Kim, G.C.; Shin, Y.J. NO_x Reduction and N₂O Emissions in A Diesel Engine Exhaust Using Fe–Zeolite and Vanadium based SCR Catalysts. *Appl. Therm. Eng.* **2017**, *110*, 18–24. [CrossRef]
- Geng, P.; Tan, Q.; Zhang, C.; Wei, L.; He, X.; Cao, E.; Jiang, K. Experimental investigation on NO_x and green house gas emissions from a marine auxiliary diesel engine using ultralow sulfur light fuel. *Sci. Total Environ.* **2016**, *572*, 467–475. [CrossRef] [PubMed]
- Jeon, J.; Lee, J.T.; Park, S. Nitrogen Compounds (NO, NO₂, N₂O, and NH₃) in NO_x Emissions from Commercial EURO VI Type Heavy-Duty Diesel Engines with a Urea-Selective Catalytic Reduction System. *Energy Fuels* **2016**, *30*, 6828–6834. [CrossRef]
- European Parliament of 4 February 2009 on 2050: The Future Begins Today-Recommendations for the EU's Future Integrated Policy on Climate Change. Available online: https://www.europarl.europa.eu/doceo/document/TA-6-2009-0042_EN.html (accessed on 10 January 2022).
- Kong, S.-C.; Sun, Y.; Rietz, R.D. Modeling Diesel Spray Flame Liftoff, Sooting Tendency, and NO_x Emissions Using Detailed Chemistry with Phenomenological Soot Model. *J. Eng. Gas Turbines Power* **2005**, *129*, 245–251. [CrossRef]
- Senecal, P.K.; Richards, K.J.; Pomraning, E.; Yang, T.; Dai, M.Z.; McDavid, R.M.; Patterson, M.A.; Hou, S.; Shethaji, T. A New Parallel Cut-Cell Cartesian CFD Code for Rapid Grid Generation Applied to In-Cylinder Diesel Engine Simulations. In Proceedings of the SAE World Congress & Exhibition, Detroit, MI, USA, 16–19 April 2007.
- Som, S.; Aggarwal, S.K. Effects of Primary Breakup Modeling on Spray and Combustion Characteristics of Compression Ignition Engines. *Combust. Flame* **2010**, *157*, 1179–1193. [CrossRef]
- Pitz, W.J.; Cernansky, N.P.; Dryer, F.L.; Egolfopoulos, F.N.; Farrell, J.T.; Friend, D.G.; Pitsch, H. Development of an Experimental Database and Kinetic Models for Surrogate Diesel Fuels. In Proceedings of the SAE World Congress & Exhibition, Detroit, MI, USA, 16–19 April 2007.
- Luo, Z.; Som, S.K.; Sarathy, S.M.; Plomer, M.; Pitz, W.J.; Longman, D.E.; Lu, T. Development and validation of an n-dodecane skeletal mechanism for spray combustion applications. *Combust. Theory Model.* **2014**, *18*, 187–203. [CrossRef]
- Pei, Y.; Mehl, M.; Liu, W.; Lu, T.; Pitz, W.J.; Som, S. A Multi-Component Blend as A Diesel Fuel Surrogate for Compression Ignition Engine Applications. In Proceedings of the ASME 2014 Internal Combustion Engine Division Fall Technical Conference, ICEF2014-5625, Columbus, IN, USA, 19 October 2014.
- Bowman, C.T.; Golden, D.M.; Hanson, R.K.; Pitsch, H.; Wang, L. *Optimization of Synthetic Oxygenated Fuels for Diesel Engines*; GCEP Technical Report; Global Climate and Energy Project (GCEP) at Stanford University: Stanford, CA, USA, 2006.
- Ren, Y.; Huang, Z.; Miao, H.; Di, Y.; Jiang, D.; Zeng, K.; Liu, B.; Wang, X. Combustion and emissions of a DI diesel engine fuelled with diesel-oxygenate blends. *Fuel* **2008**, *87*, 2691–2697. [CrossRef]
- Cheng, A.S.; Dibble, R.W.; Buchholz, B.A. The Effect of Oxygenates on Diesel Engine Particulate Matter. *SAE Pap.* **2002**, *1*, 1705.
- Flower, W.L. An investigation of Soot Formation in Axisymmetric Turbulent Diffusion Flames at Elevated Pressure. *Symp. Combust.* **1989**, *22*, 425–435. [CrossRef]
- Zannis, T.; Hountalas, D.T.; Kouremenos, D.A. Experimental Investigation to Specify the Effect of Oxygenated Addition Content and Type on DI Diesel Engine Performance and Emissions. *SAE Trans.* **2004**, *113*, 166–179.
- Yeh, L.I.; Rieckard, D.J.; Duff, J.L.C.; Bateman, J.R.; Schlosberg, R.H.; Caers, R.F. Oxygenates: An Evaluation of their Effects on Diesel Emissions. *SAE Trans.* **2001**, *110*, 1482–1498.
- Yao, M.; Wang, H.; Zheng, Z.; Yue, Y. Experimental study of n-butanol additive and multi-injection on HD diesel engine performance and emissions. *Fuel* **2010**, *89*, 2191–2201. [CrossRef]

21. Rakopoulos, C.D.; Dimaratos, A.M.; Giakoumis, E.G. Study of Turbocharged Diesel Engine Operation, Pollutant Emissions and Combustion Noise Radiation During Starting with Bio-diesel or N-butanol Diesel Fuel Blends. *Appl. Energy* **2011**, *88*, 3905–3916. [CrossRef]
22. Siwale, L.; Kristóf, L.; Adam, T.; Bereczky, A.; Mbarawa, M.; Penninger, A.; Kolesnikov, A. Combustion and Emission Characteristics of n-Butanol/Diesel Fuel Blend in A Turbo-Charged Compression Ignition Engine. *Fuel* **2013**, *107*, 409–418. [CrossRef]
23. Chen, G.; Shen, Y.; Zhang, Q.; Yao, M.; Zheng, Z.; Liu, H. Experimental study on combustion and emission characteristics of a diesel engine fueled with 2,5-dimethylfuran–diesel, n-butanol–diesel and gasoline–diesel blends. *Energy* **2013**, *54*, 333–342. [CrossRef]
24. Jin, C.; Yao, M.; Liu, H.; Lee, C.-F.F.; Ji, J. Progress in the production and application of n-butanol as a biofuel. *Renew. Sustain. Energy Rev.* **2011**, *15*, 4080–4106. [CrossRef]
25. Doğan, O. The Influence of n-Butanol/Diesel Fuel Blends Utilization on A Small Diesel Engine Performance and Emissions. *Fuel* **2011**, *90*, 2467–2472. [CrossRef]
26. Kumar, P.; Rehman, A. Bio-diesel in homogeneous charge compression ignition (HCCI) combustion. *Renew Sustain. Energy Rev.* **2016**, *56*, 536–550. [CrossRef]
27. Ma, J.; Lü, X.; Ji, L.; Huang, Z. An experimental study of HCCI-DI combustion and emissions in a diesel engine with dual fuel. *Int. J. Therm. Sci.* **2008**, *47*, 1235–1242. [CrossRef]
28. Dempsey, A.B.; Curran, S.J.; Wagner, R.M. A Perspective on the Range of Gasoline Compression Ignition Combustion Strategies for High Engine Efficiency and Low NO_x and Soot Emissions: Effects of In-Cylinder Fuel Stratification. *Int. J. Engine. Res.* **2016**, *17*, 897–917. [CrossRef]
29. Yao, M.; Zheng, Z.; Liu, H. Progress and recent trends in homogeneous charge compression ignition (HCCI) engines. *Prog. Energy Combust. Sci.* **2009**, *35*, 398–437. [CrossRef]
30. Lu, X.C.; Han, D.; Huang, Z. Fuel Design and Management for the Control of Advanced Compression-ignition Combustion Modes. *Prog. Energy Combust.* **2011**, *37*, 741–783. [CrossRef]
31. Olsson, J.-O.; Tunestål, P.; Johansson, B. Closed-Loop Control of an HCCI Engine. *SAE Trans.* **2001**, *110*, 1076–1185. [CrossRef]
32. Wang, S.Y.; Yao, L. Effect of Engine Speeds and Dimethyl Ether on Methyl Decanoate HCCI Combustion and Emission Characteristics Based on Low-Speed Two-Stroke Diesel Engine. *Pol. Marit. Res.* **2020**, *27*, 85–95. [CrossRef]
33. Jothi, N.M.; Nagarajan, G.; Renganarayanan, S. Experimental studies on homogeneous charge CI engine fueled with LPG using DEE as an ignition enhancer. *Renew. Energy* **2007**, *32*, 1581–1593. [CrossRef]
34. Szybist, J.P.; McFarlane, J.; Bunting, B.G. Comparison of Simulated and Experimental Combustion of Biodiesel Blends in a Single Cylinder Diesel HCCI Engine. *SAE Trans.* **2007**, *116*, 1250–1260.
35. He, B.-Q.; Yuan, J.; Liu, M.-B.; Zhao, H. Combustion and emission characteristics of a n-butanol HCCI engine. *Fuel* **2014**, *115*, 758–764. [CrossRef]
36. Maurya, R.K.; Agarwal, A.K. Combustion and Emission Characterization of n-Butanol Fueled HCCI Engine. *J. Energy Resour. Technol.* **2014**, *137*, 011101. [CrossRef]
37. Zheng, M.; Han, X.; Asad, U.; Wang, J. Investigation of butanol-fuelled HCCI combustion on a high efficiency diesel engine. *Energy Convers. Manag.* **2015**, *98*, 215–224. [CrossRef]
38. Radica, G.; AntoniĆ, R.; Račić, N. Engine Working Cycle Analysis for Diagnostic and Optimisation Purposes. *Brodogradnja* **2009**, *60*, 378–387.
39. Black, G.; Curran, H.; Pichon, S.; Simmie, J.; Zhukov, V. Bio-butanol: Combustion properties and detailed chemical kinetic model. *Combust. Flame* **2010**, *157*, 363–373. [CrossRef]
40. Zhang, Y.; Mathieu, O.; Petersen, E.L.; Bourque, G.; Curran, H.J. Assessing the Predictions of A NO_x Kinetic Mechanism on Recent Hydrogen and Syngas Experimental Data. *Combust. Flame* **2017**, *182*, 122–141. [CrossRef]
41. Kook, S.; Pickett, L.M. Liquid length and vapor penetration of conventional, Fischer–Tropsch, coal-derived, and surrogate fuel sprays at high-temperature and high-pressure ambient conditions. *Fuel* **2012**, *93*, 539–548. [CrossRef]
42. Mao, Y.; Raza, M.; Wu, Z.; Zhu, J.; Yu, L.; Wang, S.; Zhu, L.; Lu, X. An experimental study of n-dodecane and the development of an improved kinetic model. *Combust. Flame* **2020**, *212*, 388–402. [CrossRef]
43. Stranic, I.; Chase, D.P.; Harmon, J.T.; Yang, S.; Davidson, D.F.; Hanson, R.K. Shock Tube Measurements of Ignition Delay Times for the Butanol Isomers. *Combust. Flame* **2012**, *159*, 516–527. [CrossRef]

Article

How Sensitive Morphological Parameters Influence on the PM_{2.5} Diffusion: An Empirical Study of Two Neighborhoods in Central Beijing

Peihao Zhang ¹, Haomiao Cheng ^{1,*} , Zhiwen Jiang ² and Fanding Xiang ¹

¹ College of Architecture and Urban Planning, Beijing University of Technology, Beijing 100121, China; zhangpeih@outlook.com (P.Z.); xiangfandel@outlook.com (F.X.)

² Key Laboratory of Beijing on Regional Air Pollution Control, Faculty of Environment and Life, Beijing University of Technology, Beijing 100121, China; jiangzw@foxmail.com

* Correspondence: chenghaomiao@bjut.edu.cn

Abstract: Air quality is highly related to the health of a human being. Urban morphology has a significant influence on air quality; however, the specific relationship between urban morphology characteristics and air quality at the neighborhood scale has yet to be investigated, especially the vegetation effect on PM_{2.5} concentration and diffusion. The relevant morphological parameters based on the affected pathways of urban morphology on air quality were selected, and the sensitivity degree and laws of the selected morphological parameters to PM_{2.5} were quantified by numerical simulation, bivariate correlation analysis, and regression analysis. The results showed that Building Density (BD), Block Envelope Degree (BED), Average Building Volume (ABV), Average Building Floors (ABF), Standard Deviation of Building Height (SDH) and Greenbelt Coverage Rate (GCR) were Sensitive Morphological Parameters (SMPs). A positive and cosine curve trend of BD and BED with PM_{2.5} was observed. GCR was significant to dust retention along with vertical canopy height. When ABV = 40,000 m³ and ABF = 20F, the lowest PM_{2.5} concentration was examined, while increased SDH could promote airflow and enhance the capacity of PM_{2.5} diffusion. Finally, morphology-optimization strategies were proposed at the neighborhood scale: (1) Decreasing the BED along the street; (2) considering the species of vegetation with the appropriate height and increasing the GCR; (3) increasing the ABF of neighborhoods appropriately while controlling the ABV and distinguishing the internal SDH of neighborhoods. The study could apply the scientific basis for the planning and design of healthy and livable cities.

Citation: Zhang, P.; Cheng, H.; Jiang, Z.; Xiang, F. How Sensitive Morphological Parameters Influence on the PM_{2.5} Diffusion: An Empirical Study of Two Neighborhoods in Central Beijing. *Atmosphere* **2022**, *13*, 921. <https://doi.org/10.3390/atmos13060921>

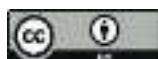
Academic Editors: Duanyang Liu, Kai Qin and Honglei Wang

Received: 12 May 2022

Accepted: 5 June 2022

Published: 6 June 2022

Publisher's Note: MDPI stays neutral with regard to jurisdictional claims in published maps and institutional affiliations.



Copyright: © 2022 by the authors. Licensee MDPI, Basel, Switzerland. This article is an open access article distributed under the terms and conditions of the Creative Commons Attribution (CC BY) license (<https://creativecommons.org/licenses/by/4.0/>).

Keywords: sensitive morphological parameters; PM_{2.5}; CFD; neighborhoods; Beijing

1. Introduction

Rapid urbanization has resulted in air pollution issues that had a negative impact on many sectors of human lives. According to the Beijing State of the Environment Bulletin 2020 [1], the number of days that met air quality standards in 2020 was 276 days, accounting for 75.4%. Although the overall air quality has improved compared to the previous period, the distribution of pollution still showed north–south differences, and the concentration of pollutants such as PM_{2.5} and PM₁₀ in ecological zones in the north and northwest is significantly lower than that in the southern high-density built-up areas and high-density population areas, which showed a “Low-Northwest while High-Southeast” situation. As urban planning became a more essential component of the development of livable cities, how to enhance air quality by optimizing urban morphology evolved into a focus of investigation in relevant disciplines [2,3].

Based on the foregoing, studies on urban morphology and air quality were steadily established [4]. Studies mainly involve two scales: regional-urban [5] and neighborhoods [6]. At the regional-urban scale, most scholars had focused on exploring the intrinsic effects

of different urban morphological features on air quality. Research elements included physical spatial characteristics such as city size and urban shape, [7] vegetation cover [8], and non-physical characteristics such as population density and employment density [9]. In addition, studies have also been conducted to analyze the correlation between urban morphology and air quality from a spatial and temporal perspective [10].

At the neighborhood scale, most studies had conducted comparative studies of neighborhoods with different morphological characteristics for the correlation between urban morphology and pollutants [11,12] with air pollutant monitoring data from urban observatories. However, the specific relationship between urban morphological parameters and PM_{2.5} concentration as well as diffusion has not been investigated clearly. In addition, the generalization of urban morphological characteristics needed a systematic and comprehensive framework. Since the selection of vegetation and non-physical morphological indicators is relatively weak in existing studies, they are unable to provide universal laws.

In recent years, the development of simulation techniques such as Computational Fluid Dynamics (CFD) has provided the technical support to establish the correlation between urban morphology and pollutant dispersion at the neighborhood scale with the Fluent simulation software being the most widely utilized. Studies could be divided into two categories. First, ideal-neighborhood simulation based on traditional settlement patterns [13] was constructed (lineal type, point group type, etc.). Different building combinations [14] or vegetation layouts [15] were explored individually, and the effect of different morphological features on the dispersion of pollutants based on simulation results was qualitative or quantitative analyzed. Secondly, a simulation based on actual cases was constructed. Different urban design schemes for the same neighborhoods [16] or comparisons of different neighborhoods [17] have been studied to promote the air quality. In general, the correlation between urban morphology and air quality had been gradually established; however, the quantitative guidance was limited. The simulation studies of ideal neighborhoods were separated from the complicated morphology of the building arrangement in the actual environment, and the simulation data were based on empirical data. In addition, in terms of modeling, the impact of the integrated neighborhood environment of buildings and vegetation on pollution dispersion has not been considered in previous studies, while the simulation studies of actual cases were aimed at promoting the air quality of specific public spaces and neighborhoods, which lacked the general application.

The study, which focused on two typical residential neighborhoods with different features in central Beijing, explored the quantitative rules of affection between urban morphology and air quality. We devised an urban morphology and air quality mechanism for selecting morphological parameters. Through the neighborhood-scale CFD simulation, which includes the calibration of vegetation factors and multi-source data, the Sensitive Morphological Parameters (SMPs) impacting air quality (PM_{2.5}, for example) at the neighborhood scale were filtrated before statistical models. Therefore, the quantitative rules of the influence of SMPs on the “pollutant-wind environment” could be estimated.

2. Data and Methods

2.1. Study Area

Taking a traditional residential area in central Beijing as the study area, the study selected a low-rise residential neighborhood (Neighborhood A) and a high-rise residential neighborhood (Neighborhood B) as the core study area based on the street network, buildings' layout, and its group form (Figure 1a). Neighborhood A, which was built in the 1990s, is dominated by enclosed low-medium-rise residential buildings with schools and underlying retail; Neighborhood B, which was built in the early twenty-first century, is dominated by row-slab high-rise residential buildings with a few underlying retails. The aforementioned two neighborhoods differ in terms of building periods, functional placement, and spatial arrangement, which might illustrate the main features of Beijing's residential neighborhood morphology.



Figure 1. The study area: (a) the study area; (b) core study area, A refer to Neighborhood A, B refer to Neighborhood B.

2.2. Wind Environment and Pollutant Monitoring

The objective of the field monitoring is to count the concentration levels of pollutants in the neighborhoods as well as the characteristics of the wind environment and to conduct a preliminary analysis of the differences in pollutant concentrations and wind environment between neighborhoods, which serves as a foundation for testing and validating simulation results. The XL68 intelligent environmental monitoring equipment is chosen to monitor $PM_{2.5}$ concentration (resolution: $1 \mu g/m^3$, range: $0\sim1000 \mu g/m^3$) and wind speed (resolution: $0.1 m/s$, range: $0\sim60 m/s$) of the neighborhoods at monitoring points P1 and P2 ($z = 3 m$, $z = 2 m$) (Figure 1b). Details of equipment are shown in Table S1.

2.3. “Pollutant-Wind Environment” Model Setting

Micro-scale CFD numerical simulations have been widely used in the simulation of outdoor wind environments and pollutant dispersion [17]. ANSYS FLUENT 21.0 based on the finite volume method was adopted for numerical simulations, and the governing equation was the Reynolds-averaged Navier–Stokes equation. The standard K- ϵ turbulence model was adopted to simulate the airflow [18]. Pollutants and air were considered as continuous phases, and the pollutant concentrations were solved with the component transport model [19,20].

2.3.1. Computational Domain and Grid Generation

The calculation domain was constructed according to the method specified by the European Cooperation in the Field of Scientific and Technical Research (COST) [21], keeping a minimum of $5H$ for vertical distances (H —the maximum building height) and $5H$ for horizontal and horizontal distances (Figure 2). At the same time, an unstructured meshing method based on a hexahedron was adopted to save computational costs. Three sets of coarse–medium–fine meshes were divided, and grid irrelevance was tested. The final grid was 2.4×10^8 for Neighborhood A and 2.6×10^8 for Neighborhood B.

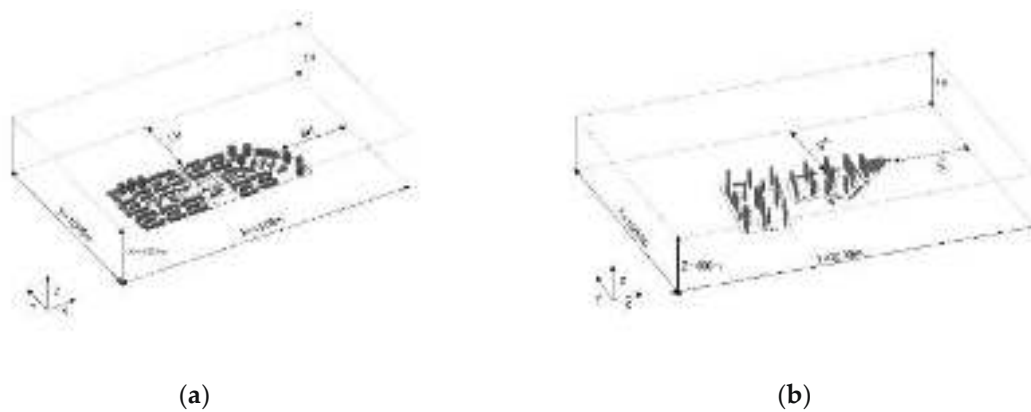


Figure 2. Computing domain construction of neighborhoods: (a) Neighborhood A; (b) Neighborhood B.

2.3.2. Boundary Condition

The incoming wind speed is exponentially distributed with height [22]. For the simulation, the calculation domain entry was set as the velocity-inlet boundary condition and adopted a user-defined function:

$$U = \frac{U_*}{\kappa} \ln\left(\frac{z + z_0}{z_0}\right) \quad (1)$$

U —horizontal wind speed at height z (m), m/s

U_* —ground friction speed, m/s

κ —Von·Karman constant, $\kappa = 0.42$

z_0 —surface roughness, $z_0 = 0.25$

$PM_{2.5}$ was mainly emitted from traffic emissions and was relatively stable by default. Pollutants were emitted vertically upwards at 0.5 m/s, and the source intensity was from the nearest urban monitoring station on the simulation day. The zero static gauge pressure outlet was used for the downstream boundary condition, and the standard wall functions with roughness modification were used for the building surface and the bottom of the computational domain. The roughness height was 0.0025–0.003 m, and the roughness constant was 0.75. Symmetry boundary conditions were served to the side-face computational domain and the upper-face computational domain [23]. Detailed boundary conditions are shown in Figure 3.

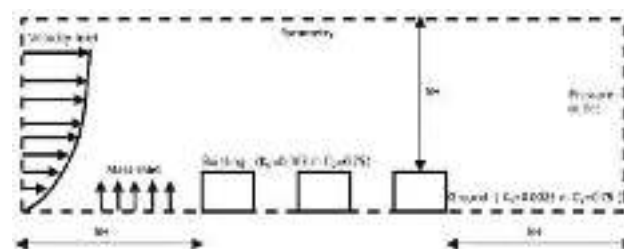


Figure 3. Calculation of domain boundary condition settings.

The study treated the canopy section of the tree with a porous medium due to the influence of trees on the surrounding flow field in reducing wind speed and increasing flow disturbance. According to the relevant literature [24], the modeling of the influence of tree canopy on the flow field was accomplished by adding source terms to the momentum equation, the K equation and the ε equation, respectively. The porosity was 0.7, the inertial resistance was 0.18, and the viscous resistance was 1.67. Meanwhile, pollutant sorption

and deposition by trees were adjusted to a constant value, and the rate of deposition was determined by wind speed and pollutant concentration [25]:

$$Y_{PM_{2.5}} = v \cdot d \cdot LAD \cdot t \quad (2)$$

$Y_{PM_{2.5}}$ —Pollutant adsorption capacity per unit area ($\mu\text{g}/\text{m}^2$)

v —Adsorption rate (m/s)

d —Pollutant concentration ($\mu\text{g}/\text{m}^3$)

LAD —leaf area density; (m^2/m^3)

t —Adsorption time (s)

2.3.3. Solution Settings

The finite volume method was used to discretize the control equation, solved by the SIMPLE algorithm, and the second-order upwind algorithm was adopted. In the initial condition setting, the ground observation data of the Beijing meteorological station on typical dates (Table 1) were used as the initial conditions for the simulation. $PM_{2.5}$ monitoring concentrations close to those of national control stations were used as the basis for selecting typical dates, and four typical dates with typical meteorological characteristics during the monitoring period were selected to establish the CFD numerical model.

Table 1. Meteorological data of national control stations on simulation dates.

Date	Wind Direction	Wind Speed (m/s)	$PM_{2.5}$ ($\mu\text{g}/\text{m}^3$)	Temperature ($^{\circ}\text{C}$)
7.10	E	2.0	44	24.6
7.13	SE	1.7	55	28.6
10.14	N	1.8	9	9.2
10.26	NW	1.6	30	8.8

2.4. Selection and Extraction of Urban Morphological Parameters

2.4.1. Selection of Urban Morphological Parameters

Based on the research framework of urban morphology influencing air pollutant transport (Figure 4) and the generalization of existing studies, a system of six categories of urban morphological characteristics, including size, density, function, structure, shape and immaterial morphological characteristics, were constructed.

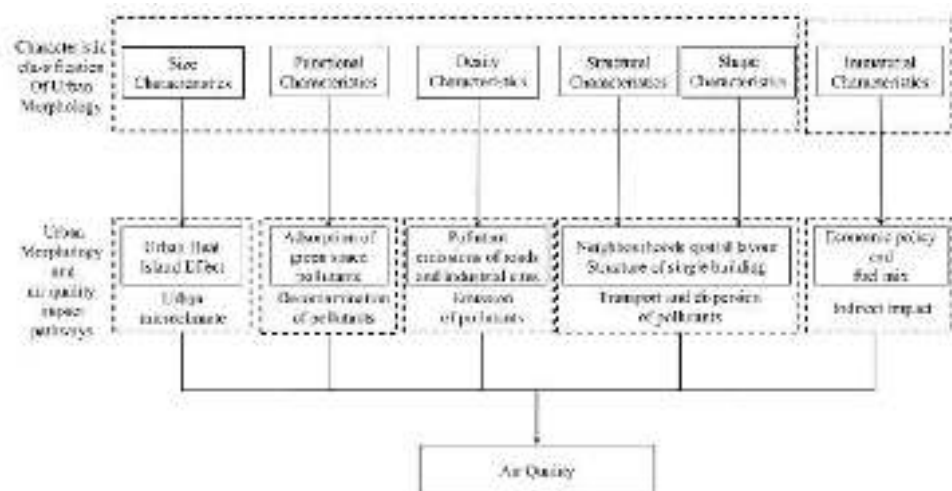


Figure 4. Framework of interaction mechanism between urban morphology and air quality.

The six morphological characteristics stated above have been proved to have a direct or indirect impact on air quality and the urban microclimate. In particular, urban size

affects the urban microclimate, pollutant emissions, and dispersion transport, and pollutant concentrations increase significantly as urban size increases [26]. The association between land use and air pollutants is more obvious, and air pollution is severe in industrial sites and commercial districts with greater emission sources [27]. In contrast, green spaces and water bodies can improve the local microclimate [28] and reduce the concentration of PM_{2.5} in the region [29]. Different density characteristics demonstrate a broad range of heterogeneity in the routes of effect on air quality, such as the impact of building density on the alteration of local wind fields, which influences pollution dispersion [30,31], and the impact of road density on traffic pollutants [9]. Urban layout structure is a major factor affecting the wind environment, and a large number of scholars have conducted detailed studies on the elements of layout structure with wind environment and pollutant levels [32,33]. Most of the studies on shape features have focused on investigating the effects of different building shapes and combinations of building morphologies on the wind environment and pollutant dispersion [34]. Furthermore, since physical urban morphology is the spatial projection of non-physical urban morphology on land use [35], the adoption of the immaterial morphological indicator is highly relevant to the overall morphology of the neighborhoods.

Thus, ten morphological parameters were selected for investigation based on the principles of neighborhood scale, potential impact on pollutant levels, ease of implementation at the control and design stages, and the interaction mechanisms between the preceding morphological features and air quality, as well as the research progress of relevant literature (Table 2).

Table 2. Selection of characteristic morphological parameters of neighborhoods.

Morphological Characteristics	Morphological Parameters	Calculation Method
Size Characteristics	Total building area, TBA	$TBA = \sum_{i=1}^n S_i * F_i$ S _i —Building single-story area F _i —buildings Floors
	Floor area ratio, FAR	$FAR = TBA/SA$ SA—Neighborhoods area
Functional Characteristics	Greenbelt coverage rate, GCR	$GCR = TGA/SA$ TGA—Area of horizontal vegetation projection
Density Characteristics	Building density, BD	$BD = BBA/SA$ BBA—Building footprint
Structural Characteristics	Block envelope degree, BED	$BED = TBP/TSP$ TBP—Building envelope perimeter TSP—Neighborhood perimeter
	Space openness, SO	$SO = (1 - BD)/FAR$
Shape Characteristics	Average building volume, ABV	$ABV = \frac{\sum_{i=1}^n V_i}{n}$ V _i —Building volume
	Average building floors, ABF	$ABF = FAR/BD$
	The standard deviation of building height, SDH	$SDH = \sqrt{\frac{\sum_{i=1}^n (h_i - \bar{h})^2}{n}}$ \bar{h} —Average building height
Immaterial Characteristics	Population density, PD	$PD = TP/SA$ TP—Neighborhoods population

2.4.2. Extraction of Urban Morphological Parameters

The subject area's similarities and differences can be quantitatively investigated by the division of calculating units. The neighborhoods were divided into 20 units according to road boundaries, spatial structure divisions and the size of typical urban neighborhoods by a 200 × 200 m grid (Figure 5). The Beijing Institute of Surveying and Mapping was used to obtain the 3D environmental data of the neighborhoods, while the sociological data were

obtained from the field survey. The selected morphological parameters were calculated separately in ArcGIS 10.5.

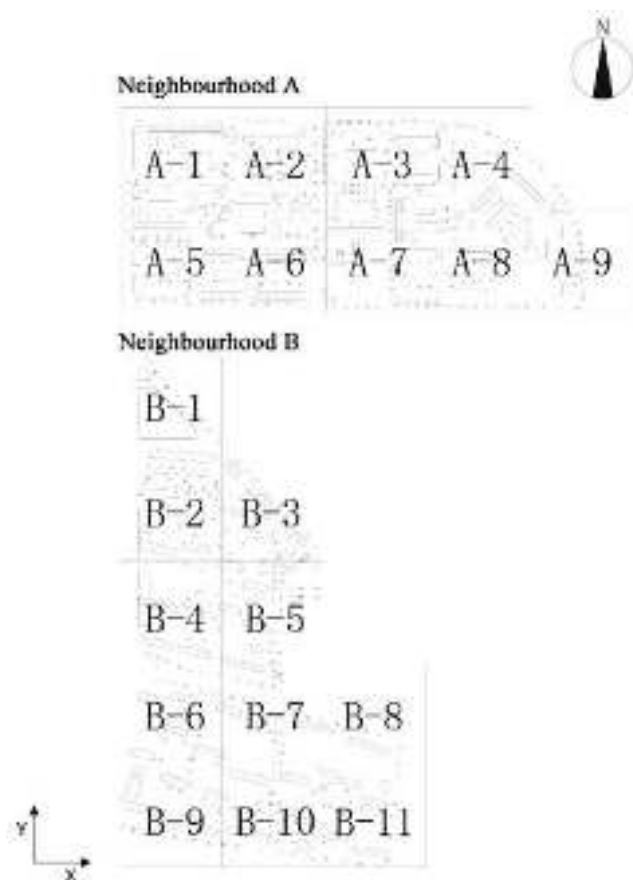


Figure 5. Grid division of neighborhoods.

2.5. Selection of Indicators for the Evaluation of “Pollutants–Wind Environment”

The “wind speed ratio” [23] evaluation index refers to the ratio of the wind speed at the actual selected location to the incoming wind speed on that day, which is often used to reflect the degree of influence of different areas or buildings on the wind speed, as a way to evaluate the condition of the wind environment in the region. “Pollutant concentration ratio” means the ratio of the concentration of pollutants in different areas to the concentration of incoming pollutants, which is used to quantify the relative level of pollution in a local area.

$$VR_w = \frac{V_p}{V_\infty} \quad (3)$$

$$CR_p = \frac{C_p}{C_\infty} \quad (4)$$

In Equations (3) and (4), VR_w is the wind speed ratio; V_p is the wind speed value at a certain height in a region (m/s); CR_p is the pollutant concentration ratio; V_p is the average concentration of pollutants at a certain height in a region ($\mu\text{g}/\text{m}^3$); V_∞ is the average concentration of incoming pollutants in a region ($\mu\text{g}/\text{m}^3$).

2.6. Statistic Analysis Model

The Pearson bivariate correlation analysis was used to filtrate the Sensitive Morphological Parameters (SMPs) with a high correlation to $\text{PM}_{2.5}$ and wind speed. To avoid the effect of excessive differences in the morphology of different neighborhoods, a correlation analysis was used between the GCR (A) in Neighborhood A and the GCR (B) in Neighborhood B separately.

The Curvilinear Regression was used to estimate the influence pattern of SMPs with $PM_{2.5}$ and wind speed. SMPs in 20 calculation units are used as independent variables, and the simulation results of the CR_p and VR_w at 1.5 m height are used as dependent variables.

3. Results

3.1. Monitoring Results

Field monitoring is shown in Figure 6. Overall, trends in pollutant concentrations within neighborhoods are influenced by overall urban background concentrations, and the two neighborhoods are relatively close but again show part of the local variability.

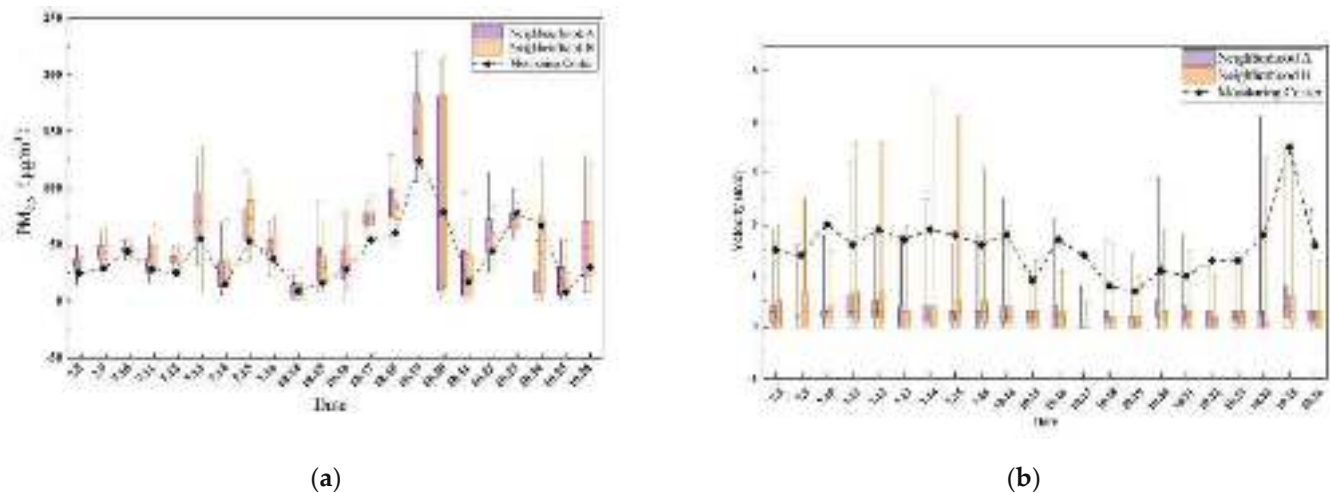


Figure 6. Monitoring data: (a) $PM_{2.5}$ monitoring data; (b) wind speed monitoring data.

3.2. Simulation Results and Error Analysis

In the correlation test (Figure 7), the two data sets showed a high correlation ($R^2 = 0.82, 0.77$). In the paired t -test (Table 3), the data significance (P) was greater than 0.05 for both groups at 95% confidence, which means that there was no significant difference before and after the simulation.

As a result, the CFD numerical model developed can predict the neighborhoods' $PM_{2.5}$ concentration and wind environment more accurately. It can be used to predict a neighborhoods' $PM_{2.5}$ concentration and wind environment under different morphological parameters.

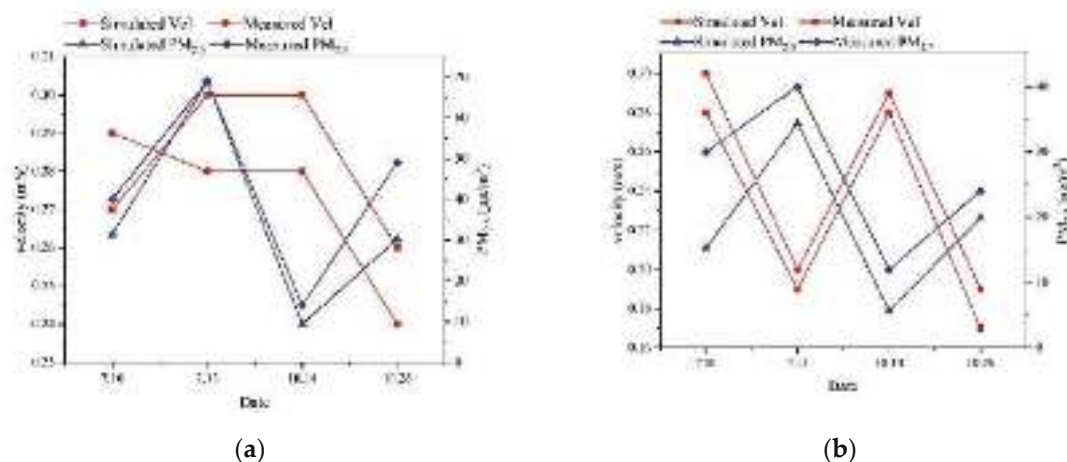


Figure 7. Correlation test before and after simulation of: (a) Neighborhood A; (b) Neighborhood B.

Table 3. P1 and P2 simulated data were paired with measured data for the sample test.

Comparing Criteria	Paired Differences					t	sig. (2-Tailed)
	Means	Std. Deviation	Std. Error Mean	95% Confidence Interval of the Difference			
				Lower	Upper		
Velocity	0.00875	0.026424	0.009342	−0.013341	0.030841	0.937	0.380
PM _{2,5}	8.27500	13.066615	4.619746	−2.648964	19.198964	1.79	0.116

3.3. Sensitive Morphological Parameters Filtrating

Table 4 shows the results of the correlation analysis between morphological parameters and the CR_p and VR_w of different neighborhoods. Among the 10 morphological parameters, BD, BED, ABV, ABF, SDH and GCR showed strong sensitivity ($p < 0.05$) to CR_p and VR_w with correlation coefficients between 0.4 and 0.8. It is suggested that there is a slight interaction between morphological parameters and pollutant concentrations and wind speeds, and alterations in these morphological parameters can result in more sensitive responses in PM_{2.5} concentrations and wind conditions, which are Sensitive Morphological Parameters (SMPs). In contrast, the four parameters TBA, FAR, SO and PD were less sensitive ($p > 0.05$) to the PM_{2.5} concentration ratio and wind speed ratio, with correlation coefficients below 0.3. It is suggested that alterations in these morphological features do not appear to produce more sensitive changes in PM_{2.5} concentration and wind environment response.

Table 4. Correlation analysis of morphological parameters with PM_{2.5} and wind speed.

Analysis of Variables	CR_p		VR_w	
	R	P	R	P
TBA	−0.246	0.325	0.114	0.268
FAR	−0.246	0.325	0.114	0.268
BD	0.443	0.025	−0.709 **	0.000
SO	0.221	0.379	−0.217	0.388
BED	0.401	0.035	−0.636 **	0.001
ABV	−0.564 **	0.005	0.505 *	0.012
ABF	−0.628 **	0.002	0.684 **	0.000
SDH	−0.612 **	0.001	0.573 **	0.004
GCR (A)	−0.912 **	0.001	−0.818 **	0.007
GCR (B)	−0.726 **	0.001	−0.810 **	0.003
PD	0.162	0.520	−0.128	0.296

** The correlation is significant at the 0.01 level (two-tailed). * The correlation is significant at the 0.05 level (two-tailed).

Furthermore, the correlation coefficient R suggests that each SMP demonstrates an inverse trend of association between wind speed and PM_{2.5}. Among them, BD, BED and GCR show a positive correlation with PM_{2.5} and a significant negative correlation with wind speed. ABV, ABF and SDH show part of negative correlation with PM_{2.5} and a significant positive correlation with wind speed. Therefore, the SMPs influence the transport and dispersion of air pollutants primarily via altering the wind environment in the surrounding area: increased wind speed enhances the transport and dispersion of air pollutants, resulting in reduced air pollutant concentrations. In general, the wind environment is still the main factor influencing the dispersion of pollutants. In the case of identical neighborhoods' land uses, the different morphological parameters affect the dispersion of pollutants mainly indirectly by influencing the wind environment.

4. Discussion

4.1. Trend Analysis of the Influence of SMPs

Figure 8 shows the interaction curves of the six SMPs with $PM_{2.5}$ and wind speed. It also demonstrates that the effect of each SMP on $PM_{2.5}$ concentration and wind speed has an inverse connection within a particular interval, but the outcomes of other intervals on $PM_{2.5}$ concentration and wind speed are different.

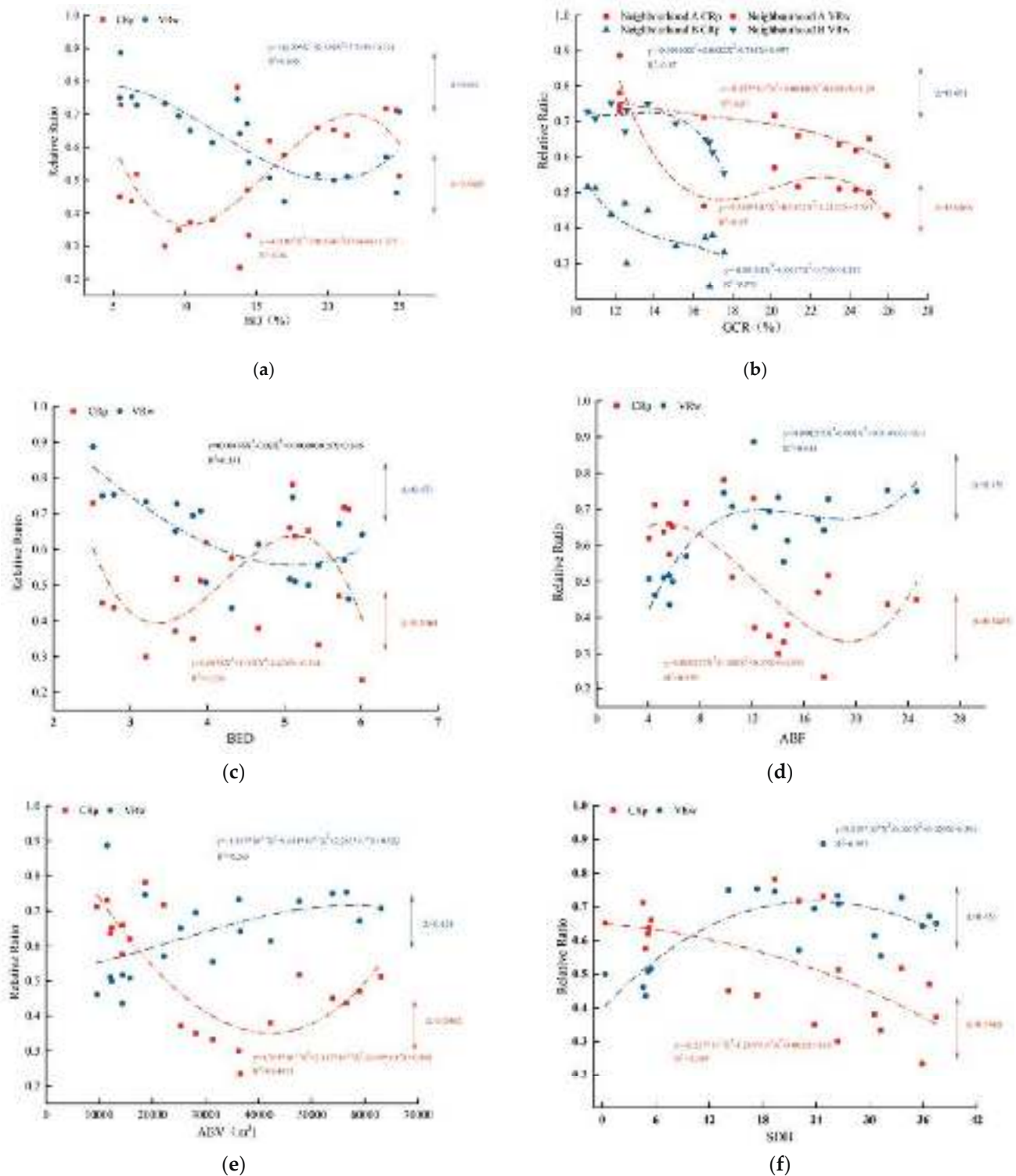


Figure 8. Curve fitting of different morphological parameters with $PM_{2.5}$ and wind speed: (a) BD; (b) GCR; (c) BED; (d) ABF; (e) ABV; (f) SDH.

According to Figure 8, wind speed is the most important element influencing $PM_{2.5}$ dispersion, and high wind speeds promote pollution transport and dispersion. The spatial morphological characteristics of distinct neighborhoods define their internal wind environment under the same incoming wind speed conditions, which has an impact on the transport dispersion and concentration distribution of air pollutants. Furthermore, the different impact results are exhibited by the morphological parameters in different intervals. It is claimed that there are parameter intervals for each morphological parameter that are more positive (or less positive) to the transmission and dispersion of air contaminants.

4.1.1. BD and BED

The relationship between BD, BED and $PM_{2.5}$ and wind speed all show a trend of sine and cosine curves (Figure 8a,c). As BD or BED rises, $PM_{2.5}$ shows a trend of decreasing, while wind speeds show a decrease followed by an increase, then increasing and then decreasing. In particular, $PM_{2.5}$ is lowest when BD is around 10% and continues to rise above 10%, reaching a maximum of $PM_{2.5}$ at around 20%. $PM_{2.5}$ is lowest at a BED of around 3 and highest at 5. When BD = 20% or BED = 5, the corresponding wind speed is at its minimum. The effect of BD and BED on the wind environment can be further seen by comparing the local area wind speed vectors for Neighborhood A and Neighborhood B (Figure 9): BD and BED of Neighborhood A with the relatively smooth internal wind environment is higher than Neighborhood B. This is because when the BD and BED are within a specific range, the transport of pollutants from outside is considerably restricted. However, when the BD and BED rise to a certain level, the neighborhood's wind environment tends to stabilize, which is not conducive to the migration and dispersion of atmospheric pollutants and creates a cumulative effect. Therefore, keeping the building density and block envelope degree of neighborhoods within a reasonable range can assist in enhancing air quality.

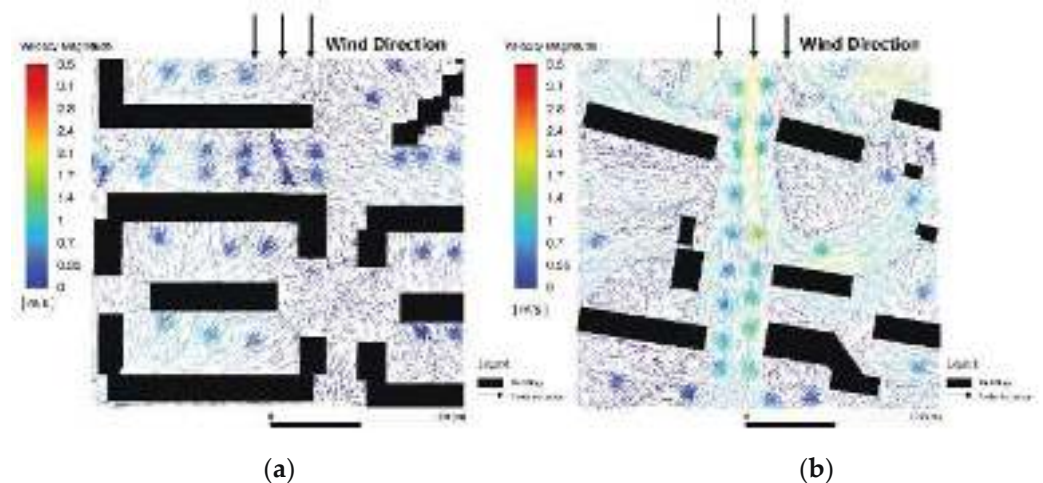


Figure 9. Vector diagram of local wind speed in: (a) Neighborhood A; (b) Neighborhood B.

4.1.2. GCR

As the GCR increases, $PM_{2.5}$ concentration and wind speed all showed a decreasing trend (Figure 8b). This is because wind speed is reduced and dust is suppressed by vegetation in the vertical zone beneath the canopy, with a progressive decrease in the zone above the canopy. As an example, Figure 10 illustrates the local vegetation XZ plane wind speed and $PM_{2.5}$ distribution in Neighborhood A, which suggests that the influence of vegetation on pollutant concentrations and wind speed is related to the height of the vegetation and its dust retention effect is most noticeable in the vertical zone beneath the canopy, with a progressive decrease in the zone above the canopy.

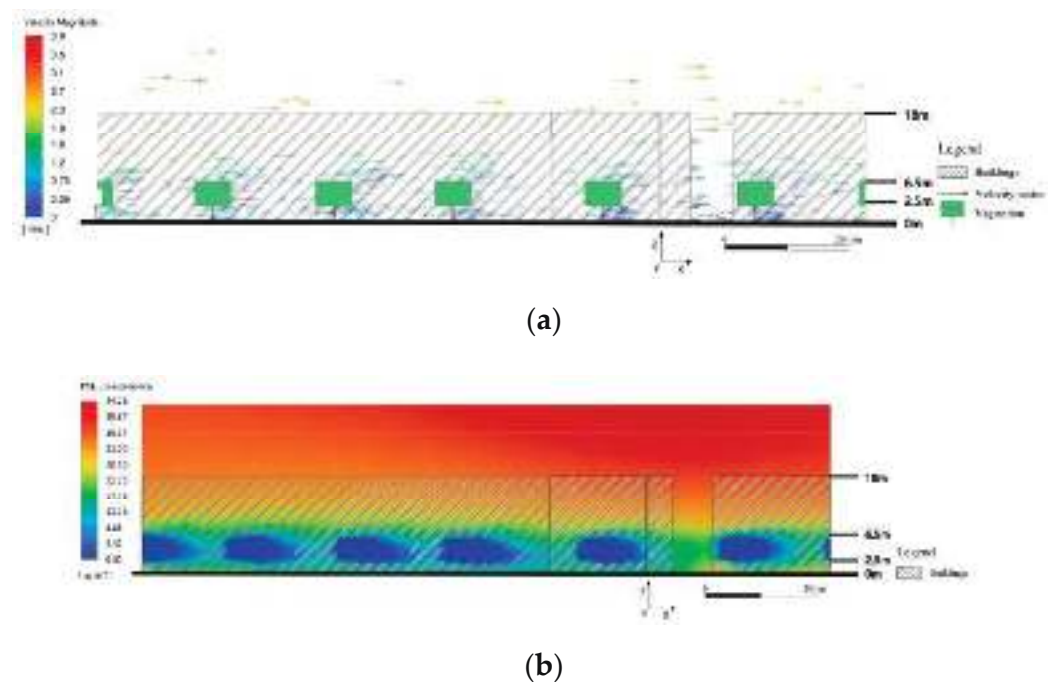


Figure 10. XZ plane in the local area of Neighborhood A of: (a) velocity vector; (b) PM_{2.5} concentration distribution.

4.1.3. ABF, ABV and SDH

ABF, ABV and SDH demonstrated varying degrees of positive and negative correlations with PM_{2.5} and wind speed, respectively. When ABV = 40,000 m³ and ABF = 20F, the lowest PM_{2.5} concentration was observed. The rise in ABF indirectly increases the building separation and enhances the air circulation within and outside the neighborhoods. When ABF exceeds 20, wind speed is further increased, but the static wind zone is formed on the leeward side of the building, which hinders the diffusion of pollutants (Figure 8d). As the ABV increases, PM_{2.5} concentration shows a tendency to decrease and then increase (Figure 8e). This is because, within a certain volume range, increasing ABV helps to increase the open space and reduces the weakening effect on wind speed due to a large number of buildings. However, excessive ABV might increase the static wind area in the neighborhood and limit the effect of wind on pollution transmission.

The results reveal that the difference in height between buildings on the windward and leeward sides of the neighborhoods affects wind speed in the direction of incoming airflow differently (Figure 8f). Taking the example of four street valleys in the typical YZ plane of two neighborhoods (Figure 11), rising valley 1 and valley 4 are more effective in diffusing PM_{2.5} in vertical space than falling valley 2 and valley 3. Therefore, reasonable SDH regulation promotes airflow rising, establishing a pleasant neighborhood wind environment, and boosting pollutant dispersion in vertical space. Moreover, angular flow zones are created with building heights up to a certain level, which enhances the dispersion of pollutants to the leeward side.

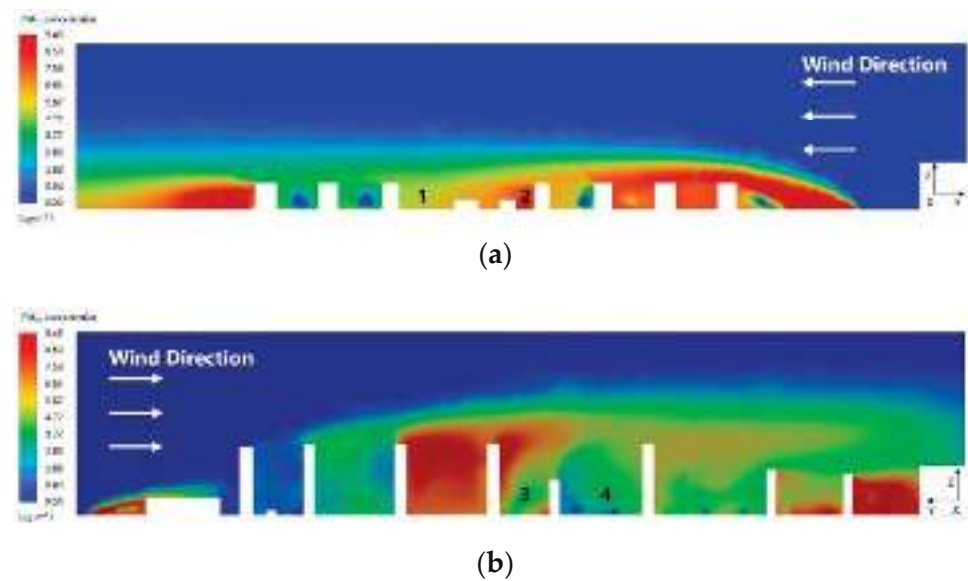


Figure 11. $PM_{2.5}$ diffusion distribution of typical Y-Z section in: (a) Neighborhood A; (b) Neighborhood B.

4.2. Morphology-Optimization Strategies for Pollutant Dispersion at Neighborhood-Scale

Based on the findings of the preceding investigation, strategies for optimizing neighborhood morphology based on air quality improvements were proposed. First, the relationship between BD, BED and $PM_{2.5}$ show a trend of sine and cosine curves. Therefore, BD should be reasonably controlled in the neighborhoods, and the BED of residential buildings along the street should be reduced while increasing the commercial buildings along the street (Figure 12a). Second, in terms of functional morphological characteristics, GCR showed a reduced influence on wind speed and $PM_{2.5}$ below the canopy, and the reducing effect decreases as the vertical height above the canopy increases. Therefore, it is critical to plant a diverse variety of vegetation species of varying heights (Figure 12b). Furthermore, it is important to increase the GCR while ensuring the functional integrity of the neighborhoods. Third, in terms of the shape morphological characteristics, ABF and ABV showed a trend of increasing and then decreasing with $PM_{2.5}$ values. Therefore, when the intensity of development is identified, specific buildings' heights should be increased, and the individual building's masses and number of total buildings in the neighborhood should be limited (Figure 12c). Additionally, the difference of building heights should be reasonably delineated (Figure 12d), according to the SDH curve fitting, to promote the climbing of incoming winds.

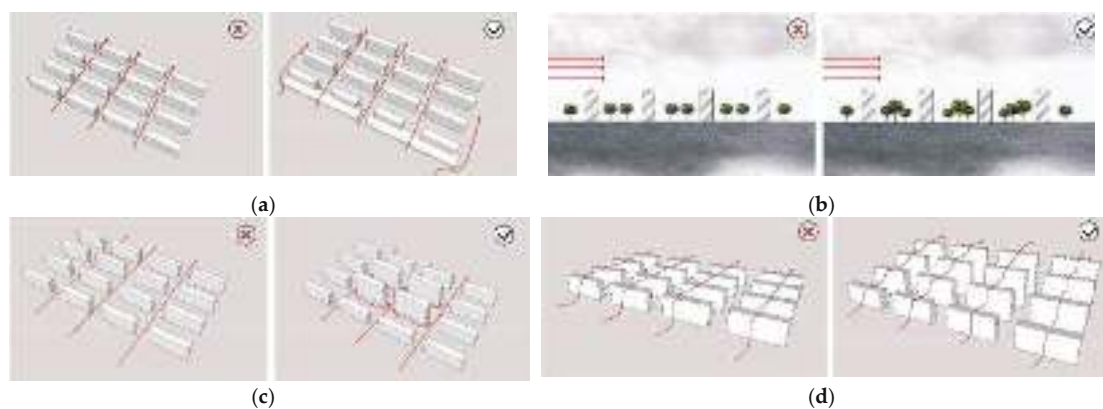


Figure 12. Morphology-optimization strategies for pollutant dispersion: (a) BED solution; (b) GCR solution; (c) ABV solution; (d) SDH solution.

5. Conclusions

This study aims to investigate the mechanisms underlying the correlation between urban form and atmospheric pollutants ($PM_{2.5}$, for example), and two types of typical residential neighborhoods in Beijing were selected as the study area. Morphological parameters were selected according to the research pathway of urban morphology affecting air quality, and a sensitivity analysis of morphological parameters with $PM_{2.5}$ and wind speed was carried out through field monitoring and CFD numerical simulation.

In the sensitivity filtering, six morphological parameters, such as BD, BED, etc., showed high sensitivity to $PM_{2.5}$ concentrations and wind speed within the neighborhood, which are called the Sensitive Morphological Parameters (SMPs). The different correlations of SMPs between $PM_{2.5}$ and wind speed were observed. This demonstrates the existence of a tripartite relationship between morphological characteristics, wind environment, and pollutant dispersion.

The SMPs showed different influential rules on the $PM_{2.5}$ diffusion. It revealed a positive and cosine curve trend of BD and BED with $PM_{2.5}$. $PM_{2.5}$ is lowest when BD is around 10% and BED around 3 and continues to rise when BD is above 10%, reaching a maximum of $PM_{2.5}$ when BD is at around 20% and BED is at 5. GCR was significant to dust retention along with vertical canopy height, with a most noticeable effect in the vertical zone beneath the canopy and a progressive decrease in the zone above the canopy. When $ABV = 40,000 \text{ m}^3$ and $ABF = 20F$, the lowest $PM_{2.5}$ concentration was observed. Increased SDH could promote airflow and enhance the capacity of $PM_{2.5}$ diffusion.

To optimize the circumstances of pollutant dispersion, three residential planning strategies were proposed. First, the BED of residential buildings along the street should be minimized while commercial buildings along the street should be expanded, and BD should be reasonably managed. Second, vegetation species of appropriate height should be considered, and GCR should be increased. Third, building height should be increased appropriately, as should a proper division of building height disparities in neighborhoods. Furthermore, acceptable control of individual building mass and the total number of buildings in the neighborhood should be considered.

Supplementary Materials: The following supporting information can be downloaded at: <https://www.mdpi.com/article/10.3390/atmos13060921/s1>, Table S1: The Details of XL68 Equipment.

Author Contributions: Conceptualization, H.C. and P.Z.; methodology, H.C., P.Z. and Z.J.; software, P.Z. and Z.J.; validation, P.Z.; formal analysis, P.Z. and H.C.; investigation, P.Z.; data curation, P.Z. and F.X.; writing—original draft preparation, P.Z.; writing—review and editing, H.C. and F.X.; supervision and funding acquisition, H.C. All authors have read and agreed to the published version of the manuscript.

Funding: This research was funded by the National Natural Science Foundation of China, grant numbers 52170174 and 51808009.

Institutional Review Board Statement: Not applicable.

Informed Consent Statement: Not applicable.

Data Availability Statement: The data that support the findings of this study are available from the Beijing Municipal Ecological and Environmental Monitoring Center, <http://www.bjmemc.com.cn> (accessed on 1 January 2020).

Conflicts of Interest: The authors declare no conflict of interest.

References

1. *Beijing Ecological and Environmental Status Bulletin 2020*; Beijing Municipal Bureau of Ecology and Environment: Beijing, China, 2020.
2. Tao, Y.; Zhang, Z.; Ou, W. How does urban form influence $PM_{2.5}$ concentrations: Insights from 350 different-sized cities in the rapidly urbanizing Yangtze River Delta region of China, 1998–2015. *Cities* **2020**, *98*, 102581. [CrossRef]
3. McCarty, J.; Kaza, N. Urban form and air quality in the United States. *Landsc. Urban Plan.* **2015**, *139*, 168–179. [CrossRef]
4. Ding, W.; Hu, Y.; Dou, P. Study on the correlation between urban form and urban microclimate. *J. Archit.* **2012**, *7*, 16–21.

5. Chen, M.; Dai, F. PCA-Based Identification of Built Environment Factors Reducing PM_{2.5} Pollution in Neighborhoods of Five Chinese Megacities. *Atmosphere* **2022**, *13*, 115.
6. Viecco, M.; Jorquera, H.; Sharma, A. Green roofs and green walls layouts for improved urban air quality by mitigating particulate matter. *Build. Environ.* **2021**, *204*, 108–120. [CrossRef]
7. Wang, S.; Wang, J.; Fang, C. Estimating the impacts of urban form on CO₂ emission efficiency in the Pearl River Delta, China. *Cities* **2019**, *85*, 117–129. [CrossRef]
8. Moradpour, M.; Hosseini, V. An investigation into the effects of green space on air quality of an urban area using CFD modeling. *Urban Clim.* **2020**, *34*, 100686. [CrossRef]
9. Lee, C. Impacts of multi-scale urban form on PM_{2.5} concentrations using continuous surface estimates with high-resolution in U.S. metropolitan areas. *Landsc. Urban Plan.* **2020**, *204*, 103935. [CrossRef]
10. Hx, A.; Hong, C. Impact of urban morphology on the spatial and temporal distribution of PM_{2.5} concentration: A numerical simulation with WRF/CMAQ model in Wuhan, China. *J. Environ. Manag.* **2021**, *290*, 112427.
11. Dai, F.; Chen, M.; Wang, M.; Zhu, S.; Fu, F. Effect of Urban Block Form on Reducing Particulate Matter: A Case Study of Wuhan. *Chin. Landsc. Archit.* **2020**, *36*, 109–114.
12. Cao, Q.; Luan, Q.; Liu, Y. The effects of 2D and 3D building morphology on urban environments: A multi-scale analysis in the Beijing metropolitan region. *Build. Environ.* **2021**, *192*, 107635. [CrossRef]
13. Silva, F.; Reis, N.C.; Santos, J.M. Influence of urban form on air quality: The combined effect of block typology and urban planning indices on city breathability. *Sci. Total Environ.* **2022**, *814*, 152670. [CrossRef]
14. Chao, Y.; Ng, E.; Norford, L.K. Improving air quality in high-density cities by understanding the relationship between air pollutant dispersion and urban morphologies. *Build. Environ.* **2014**, *71*, 245–258.
15. Opa, B.; Pm, A.; Cc, A. Impact of morphological parameters on urban ventilation in compact cities: The case of the Tuscolano-Don Bosco district in Rome. *Sci. Total Environ.* **2022**, *807*, 150490.
16. Yan, L.; Hu, W.; Gu, L. Correlation analysis between air quality in squares and spatial design elements: A case study on six design schemes of Urumqi diamond city square. *Urban Plan.* **2020**, *44*, 61–70.
17. Hassan, A.M.; ELMokadem, A.A.; Megahed, N.A.; Eleinen, O.M.A. Urban morphology as a passive strategy in promoting outdoor air quality. *J. Build. Eng.* **2020**, *29*, 101204. [CrossRef]
18. Li, Q.; Cai, X.; Kang, L. CFD simulations of flow and dispersion under construction disturbance conditions. *Res. Environ. Sci.* **2013**, *26*, 829–837.
19. Wang, J.; Mu, Y. Study on spatial strategy responding to automobile exhaust pollution in urban street cantons. *Urban Plan.* **2013**, *37*, 54–60.
20. Li, S.; Shi, T.; Zhou, S.; Gong, J.; Zhu, L.; Zhou, Y. Diffusion effects of atmospheric pollutants on the three dimensional landscape pattern of urban block. *J. Shenyang Jianzhu Univ. Nat. Sci.* **2016**, *32*, 1111–1121.
21. Franke, J.; Hellsten, A.; Schlunzen, K.H. The COST 732 Best Practice Guideline for CFD simulation of flows in the urban environment: A summary. *Int. J. Environ. Pollut.* **2011**, *44*, 419–427. [CrossRef]
22. Richards, P.J.; Norris, S.E. Appropriate boundary conditions for computational wind engineering models revisited. *J. Wind Eng. Ind. Aerodyn.* **2011**, *99*, 257–266. [CrossRef]
23. Jiang, Z.; Cheng, H.; Zhang, P.; Kang, T. Influence of urban morphological parameters on the distribution and diffusion of air pollutants: A case study in China. *J. Environ. Sci.* **2021**, *105*, 163–172. [CrossRef] [PubMed]
24. Li, L.; Li, X.; Lin, B.; Zhu, Y. Simulation of canopy flows using k-ε two-equation turbulence model with source/sink terms. *J. Qing Hua Univ. Nat. Sci.* **2006**, *4*, 753–756.
25. Liu, W.; Yu, Z. Simulation on PM_{2.5} detention service of green space in Haidian District, Beijing, China. *Chin. J. Appl. Ecol.* **2016**, *27*, 2580–2586.
26. Zhang, S.; Han, L.; Zhou, W.; Li, W. Impact of urban population on concentrations of nitrogen dioxide (NO₂) and fine particles (PM_{2.5}) in China. *Acta Ecol. Sin.* **2016**, *36*, 5049–5057.
27. Gao, Y.; Wang, Z.; Liu, C.; Peng, Z. Assessing neighborhood air pollution exposure and its relationship with the urban form. *Build. Environ.* **2019**, *155*, 15–24. [CrossRef]
28. Wang, Y.; Akbari, H. A simulation study of the effects of street tree planting on Urban Heat Island mitigation in Montreal. In Proceedings of the 21st Canadian Connective Tissue Conference 2015, Quebec, QC, Canada, 28–30 May 2015.
29. Dai, F.; Deng, Y.; Chen, M.; Guo, X. Effects of Green Space Layout on PM_{2.5} in Different Types of Residential Areas Based on ENVI-met Simulation. *Landsc. Archit.* **2021**, *28*, 70–76.
30. Yang, J.; Shi, B.; Shi, Y. Air pollution dispersal in high-density urban areas: Research on the triadic relation of wind, air pollution, and urban form. *Sustain. Cities Soc.* **2019**, *54*, 101941. [CrossRef]
31. Aldegunde, J.A.Á.; Sánchez, A.F.; Saba, M.; Bolaños, E.Q.; Palenque, J.Ú. Analysis of PM_{2.5} and Meteorological Variables Using Enhanced Geospatial Techniques in Developing Countries: A Case Study of Cartagena de Indias City (Colombia). *Atmosphere* **2022**, *13*, 506. [CrossRef]
32. Adolphe, L. A simplified model of urban morphology: Application to an analysis of the environmental performance of cities. *Environ. Plan. B Plan. Des.* **2001**, *28*, 183–200. [CrossRef]
33. Yang, J.; Zhang, T.; Fu, X. *Coupling Mechanism between Wind Environment and Space form and Optimization Design in City Center*, 1st ed.; Southeast University Press: Nanjing, China, 2016; pp. 126–151.

34. Cheng, H.; Jiang, Z.; Zhang, P.; Kang, T. The influence of urban form parameters on the diffusion of air pollutant in residential area based on the CFD simulation. *J. Beijing Univ. Technol.* **2021**, *47*, 1377–1387.
35. Zhuang, Y.; Lu, J.; Chen, J. Exploring the “Morphological Structure” in contemporary urban design practices. *Archit. J.* **2021**, *5*, 91–98.

Article

PCA-Based Identification of Built Environment Factors Reducing PM_{2.5} Pollution in Neighborhoods of Five Chinese Megacities

Ming Chen and Fei Dai *

School of Architecture & Urban Planning, Huazhong University of Science and Technology, Wuhan 430074, China; chen_m@hust.edu.cn

* Correspondence: daifei@hust.edu.cn; Tel.: +86-139-8620-3411

Abstract: Air pollution, especially PM_{2.5} pollution, still seriously endangers the health of urban residents in China. The built environment is an important factor affecting PM_{2.5}; however, the key factors remain unclear. Based on 37 neighborhoods located in five Chinese megacities, three relative indicators (the range, duration, and rate of change in PM_{2.5} concentration) at four pollution levels were calculated as dependent variables to exclude the background levels of PM_{2.5} in different cities. Nineteen built environment factors extracted from green space and gray space and three meteorological factors were used as independent variables. Principal component analysis was adopted to reveal the relationship between built environment factors, meteorological factors, and PM_{2.5}. Accordingly, 24 models were built using 32 training neighborhood samples. The results showed that the adj- R^2 of most models was between 0.6 and 0.8, and the highest adj- R^2 was 0.813. Four principal factors were the most important factors that significantly affected the growth and reduction of PM_{2.5}, reflecting the differences in green and gray spaces, building height and its differences, relative humidity, openness, and other characteristics of the neighborhood. Furthermore, the relative error was used to test the error of the predicted values of five verification neighborhood samples, finding that these models had a high fitting degree and can better predict the growth and reduction of PM_{2.5} based on these built environment factors.

Keywords: PM_{2.5}; principal component analysis; green space; gray space; neighborhood

Citation: Chen, M.; Dai, F. PCA-Based Identification of Built Environment Factors Reducing PM_{2.5} Pollution in Neighborhoods of Five Chinese Megacities. *Atmosphere* **2022**, *13*, 115. <https://doi.org/10.3390/atmos13010115>

Academic Editors: Duanyang Liu, Honglei Wang and Kai Qin

Received: 29 November 2021

Accepted: 10 January 2022

Published: 12 January 2022

Publisher's Note: MDPI stays neutral with regard to jurisdictional claims in published maps and institutional affiliations.



Copyright: © 2022 by the authors. Licensee MDPI, Basel, Switzerland. This article is an open access article distributed under the terms and conditions of the Creative Commons Attribution (CC BY) license (<https://creativecommons.org/licenses/by/4.0/>).

1. Introduction

Air pollution, especially PM_{2.5} pollution, still seriously endangers the health of urban residents in China. According to the 2020 World Air Quality Report published by IQAir, China is 14th in the rankings for poor air quality among the 106 countries that have been given air quality monitoring stations by the WHO. In particular, the middle and lower reaches of the Yangtze River are among of the most polluted areas in China, where a large number of residents live. Serious PM_{2.5} pollution has resulted in respiratory issues, asthma, and even death [1]. To maintain the basic requirement of respiratory health, it is urgent to improve air quality.

Spatial-temporal variations in PM_{2.5} and the impact factors on PM_{2.5} have attracted much attention in recent years; among these studies, PM_{2.5} levels were mainly affected by socioeconomic environments [2], climatic conditions [3], and urban physical environments [4]. Human activities, such as traffic emissions, industrial activities, and coal consumption, cause severe PM_{2.5} pollution [5,6]. At the same time, the loss of natural land and increase in artificial ground cover exacerbate the problem [7]. In addition, the change in urban land cover and its spatial pattern leads to environmental problems, especially urban heat island effects that always contribute to gathering atmospheric pollutants or forming secondary pollutants, thereby strengthening PM_{2.5} pollution [8]. Investigating the

temporal variations in $PM_{2.5}$ and its mitigation approach is essential to improve the human settlement environment.

The built environment, usually measured by factors from various perspectives including land cover type, land use, urban form at the urban scale and public space, layout of buildings and roads at the neighborhood scale [9], is one of the important factors affecting $PM_{2.5}$; however, the key factors remain unclear. Obvious differences in $PM_{2.5}$ levels are found across urban land cover patterns [10]. In addition, urban landscape patterns or structures, including the composition and configuration of built environments, have aroused interest by using a series of relevant metrics to investigate their effects on $PM_{2.5}$ [11–14], although the influence of individual metrics may differ among studies. Moreover, urban morphology has attracted increasing attention because of its strong impacts on $PM_{2.5}$. At the city scale, the spatial format of urban built-up areas, such as the size, compactness, fragmentation, and complexity of the morphology of urban areas, influences the city's average $PM_{2.5}$ level [15–17]. At the local scale, the $PM_{2.5}$ concentration varies from neighborhood to neighborhood [18]. The difference in street canyon characteristics, building layout, and spatial form is one of the important factors that significantly influence $PM_{2.5}$ levels [19–21]. Local climate zones (LCZs), a concept aimed at classifying local built environment features, have been widely used in urban climate studies [22–24]. Ten built-up LCZs and seven land cover LCZs can be provided for measuring different built environments and natural environments, respectively. Indicators, such as the sky view factor, aspect ratio, impervious surface fraction, pervious surface fraction, and height of roughness elements, are frequently used for determining these LCZs [25–27]. However, they are rarely involved in the $PM_{2.5}$ field. Neighborhood-level $PM_{2.5}$ pollution should be a main concern because it is closely related to people's daily lives. In a high-density neighborhood environment, densely constructed buildings block air ventilation and consequently impede pollutant dispersion [28]. Particular attention should be given to the mitigation of $PM_{2.5}$ by optimizing the neighborhood-level built environment, which constitutes the basic fabric in a city.

Previous studies have explored the relationship between the urban built environment and $PM_{2.5}$ from different aspects, yet there are still shortcomings. First, the lack of systematic investigation of the built environment may result in the unclear key factors that significantly influence $PM_{2.5}$. Second, most studies focus on individual cities instead of regions, which may limit the applicability of the research findings. Considering the complexity of the built environment in a neighborhood, traditional stepwise regression analysis has some limitations, including the potential collinearity among multiple variables and the possibility of removal of some predictive variables significantly related to dependent variables [29]. Principal component analysis (PCA) has been adopted to convert complex variables into new variables that contain most of the original information and are independent of each other, thereby reducing the predictors' collinearity in $PM_{2.5}$ simulation [30].

For this, this study explored key built environment factors influencing $PM_{2.5}$ in common neighborhoods that are abundant in cities. We focused on 37 neighborhoods located in five megacities in the middle and lower reaches of the Yangtze River to better understand the influence mechanism of the built environment on $PM_{2.5}$ pollution. Principal component analysis (PCA) was conducted before regression analysis to increase its performance. All principal component variables were retained for regression analysis to establish the optimal influencing factors. Therefore, key factors can be obtained.

2. Materials and Methods

2.1. Study Area and Neighborhoods

Five megacities (Wuhan, Hefei, Nanjing, Shanghai, and Hangzhou) in the middle and lower reaches of the Yangtze River were selected as the study area (Figure 1); they have the same climate conditions. Due to the extreme high-density construction, these cities experience more serious $PM_{2.5}$ pollution than other cities in this region [31]. The similar

features of the five cities provide sufficient comparability for this study, including urban form, landform, population, and PM_{2.5} pollution characteristics.



Figure 1. Location of five megacities and distribution of monitoring stations [32].

On average, each city has 10 national PM_{2.5} monitoring stations that present a relatively uniform distribution throughout the constructed areas. A neighborhood was then defined as a square domain with an area of 1 km² (1 km × 1 km) centered at a monitoring station because 1 km is a common size for a *neighborhood* division in China and was frequently used in previous studies [32,33]. In addition, the air environment within this size plays an important role in people's quality of daily life [34]. In consideration of the unique locations of 13 neighborhoods and subsequent special land use, such as close to pollution sources (construction sites) and natural land (urban parks or scenic regions), 37 neighborhoods were selected for analysis in this study. Detailed information on the 37 cities is shown in Table S1.

2.2. PM_{2.5} Data Source and Processing

Our previous studies examined the influences of neighborhood green space and urban morphology on PM_{2.5} separately, providing evidence for the effects of urban green space coverage and morphological patterns and gray space forms on PM_{2.5} [18,32,35]. As a series of studies, hourly PM_{2.5} concentrations from 2016 to 2017 were collected from monitoring stations to ensure the consistency of PM_{2.5} data. These data in different cities were monitored with the same standard. Because of the different locations of 37 neighborhoods, the uncontrolled factors (such as weather conditions, PM_{2.5} background concentration of five cities) were kept at similar levels to remove the external impact factors as much as possible and to greatly minimize evident differences, thereby performing an intercomparison. Consistent with our previous studies [32,35], three relative indicators, the range (C_{in} and C_{de}), duration (Δt_{in} and Δt_{de}), and rate (C_{in}' and C_{de}'), of the increase and decrease in PM_{2.5} concentration were calculated. To investigate pollution-level differences in the effect of the neighborhood-level built environment on PM_{2.5}, four pollution levels, including slight (PM_{2.5} level ranging from 75 µg/m³ to 114 µg/m³), moderate (PM_{2.5} level ranging from 115 µg/m³ to 150 µg/m³), heavy (PM_{2.5} level greater than 150 µg/m³), and overall pollution, were analyzed based on Chinese ambient air quality standards. The average of slight, moderate, and heavy pollution levels of observations was defined as the overall pollution level. The process of PM_{2.5} data is shown in Figure 2. Consequently, PM_{2.5} data of eight, three, and two days in 2016, and eight, two, and one day in 2017 were used for slight, moderate, and heavy pollution, respectively (Table S2).

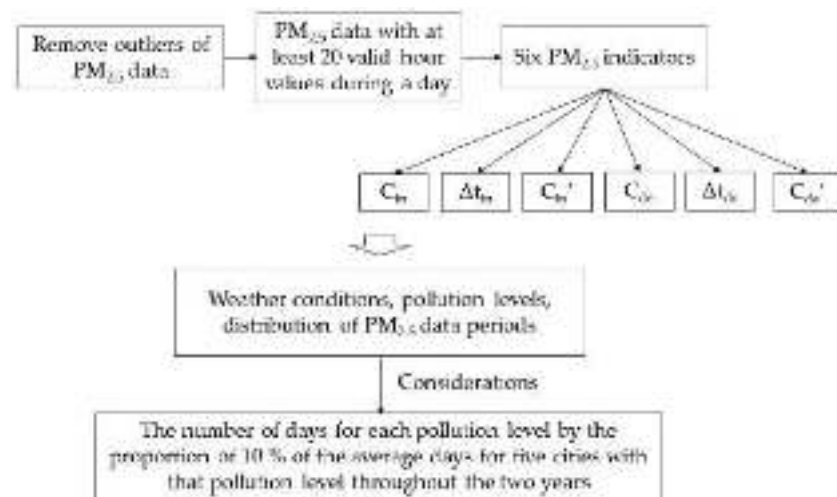


Figure 2. The process of PM_{2.5} data.

2.3. Built Environment Variables and Meteorological Factors

Built environment factors, including green space and gray space, were included in this study, as well as three important meteorological factors: atmospheric temperature (T_a), relative humidity (RH), and wind velocity (V). A total of 22 variables were selected for analysis based on the quantity and spatial pattern of green and gray spaces (Table 1). Detailed information on the 22 variables is shown in Tables S3–S5. The determination of these variables also took into account their potential impacts on PM_{2.5} and the representativeness of built environment characteristics in neighborhoods.

Table 1. Indicators for model building.

Dimension	Independent Variables			Dependent Variables
	Green Space	Gray Space	Meteorological Factors	
Quantity	TCR (x_1), GCR (x_2)	HSCR (x_{10})		
Spatial Pattern	Core (x_3), Islet (x_4), Perforation (x_5), Edge (x_6), Loop (x_7), Bridge (x_8), Branch (x_9)	BD_1 (x_{11}), BD_2 (x_{12}), BD_3 (x_{13}), FAR (x_{14}), H (x_{15}), H_σ (x_{16}), BEI (x_{17}), SVF (x_{18}), RD (x_{19})	T_a (x_{20}), RH (x_{21}), V (x_{22})	C_{in} (y_1), Δt_{in} (y_2), $C_{in'}$ (y_3), C_{de} (y_4), Δt_{de} (y_5), $C_{de'}$ (y_6)

The measurements and computations of built environment factors were based on a GIS vector dataset generated with a high-precision digital map (Google Earth, 2017) of each city, which ensured high accuracy of the calculation. On the one hand, the neighborhood green space cover ratio (GCR) and tree cover ratio (TCR) were two variables measuring the quantity of green space in the neighborhoods. The spatial pattern of green space was measured by morphological spatial pattern analysis (MSPA), which can provide seven types of green space patterns, including the core, islet, perforation, edge, loop, bridge, and branch [32].

On the other hand, the neighborhood hard space cover ratio (HSCR) was used as the quantity variable for gray space. Spatial pattern variables of the gray space were selected with a consideration of the density, vertical morphology, and spatial layout of gray spaces in neighborhoods. First, building density was considered one of the most important density variables, which was further classified into three categories, including building densities of one to three floors (BD_1), four to nine floors (BD_2), and more than nine floors (BD_3) [35]. In addition, as one of the major pollutant sources in neighborhoods, roads are a special kind of gray space, which may reflect the degree of traffic emissions. Road density (RD) was calculated as in many previous studies [36,37]. Second, the floor area ratio (FAR), mean building height (H), and standard deviation of building height (H_σ) were adopted to measure the vertical morphology of gray space in neighborhoods. FAR reflects the development intensity of the neighborhood. The larger the FAR is, the

greater the development intensity and the higher the height of buildings. A neighborhood with a higher building height usually has a lower wind velocity near the ground, which results in better ventilation conditions [38]. H_σ represents the variation of building height. The higher the H_σ , the dispersion of the building height is greater. Third, the building evenness index (BEI) and sky view factor (SVF) were chosen to represent the layout of buildings in the neighborhood. BEI is a reflection of the difference in buildings' flat form. A neighborhood with a higher BEI value implies a more uneven flat form of buildings. SVF is an important index reflecting built environment geometry [39]. A lower value of SVF indicates a more closed neighborhood space. The 3D building models were adopted for the calculation of SVF based on ArcGIS software according to the method of Gal' et al. [40].

2.4. Analytical Methods

2.4.1. PCA Analysis

PCA was performed before establishing a regression model to involve all built environment factors and meteorological factors in the models as much as possible. The method can also remove the collinearity of independent variables to a certain extent. The principle of PCA is to convert a large number of factors into new principal factors through certain calculation methods and retain most of the information contained in the initial factors [41]. The principal factors are independent of each other and have no correlation, thereby eliminating the collinearity between factors when performing regression analysis. The relationship between the principal factors and the initial factors is as follows:

$$P_i = \sum_{j=1}^n l_{ji} x_j \quad (1)$$

$$l_{ji} = A_{ji} / \sqrt{\lambda_i} \quad (2)$$

where P_i is the i -th principal factor, n is the number of principal factors, equal to 22, l_{ji} refers to a principal component loading of x_j , and λ_i denotes an eigenvalue of the i -th principal factor.

Before PCA, it is necessary to carry out standardization due to the various dimensions of each factor in green space, gray space, and meteorology. The Kaiser–Meyer–Olkin (KMO) test and Bartlett sphere test were performed for 22 factors. PCA can be carried out only when the KMO value is greater than 0.5 and the Bartlett sphere test is significant (p -value < 0.01). PCA was then carried out using standardized factors. According to the number of independent variables, a total of 22 principal factors can be obtained. The variance and eigenvalue of the principal factor reflect their contribution to the initial factor. The greater the value, the greater the contribution and the information containing the initial factor.

2.4.2. Regression Models and Evaluation

As Zhai et al. [29] suggested, there may be some problems that the contributions of the predictors truly driving $PM_{2.5}$ variations were unclear when using anterior principal components as explanatory variables without explicit rules and standards. To better understand the relationship between the built environment and $PM_{2.5}$ and establish regression models, this study carried out stepwise regression analysis involving all principal factors, which can have a screening process for the principal factors and obtain the principal factors that have a significant impact on the dependent variables [29]. The verification of regression models was in accordance with the common methods used in relevant research fields in which the neighborhood samples were divided into test samples and verification samples [35]. The selection of two types of samples should not only consider that there are enough test samples to establish the regression model but also take a certain number of verification samples for validation. Therefore, one neighborhood sample in each city was randomly selected for validation, including WH4, HF5, NJ3, SH4, and HZ4. The remaining 32 neighborhood samples were test samples for the construction of the regression model.

The accuracy of the regression model was measured by comparing the difference between predicted values and actual values of the dependent variable. The relative error (RE) was used to evaluate the accuracy of the predicted values of the PM_{2.5} indicators of the five validation samples.

$$RE_i = \frac{|y_i' - y_i|}{y_i} \times 100\% \quad (3)$$

where RE_i is the relative error of the i -th validation sample and y_i' and y_i are the predicted value and actual value of a PM_{2.5} indicator of the i -th validation sample, respectively.

3. Results and Discussion

3.1. Results of PCA

3.1.1. Overall Characteristics of PCA

PCA had pollution level differences due to the difference in meteorological factors included at the different pollution levels. At the overall pollution level, the KMO value of 22 standardized factors was 0.630, and the significance of the Bartlett spherical test was 0.000, which met the requirements of PCA. As shown in Figure 3a, with the increase in the number of principal factors, the eigenvalues and variance showed a downwards trend. The eigenvalue of principal factors reflects their contribution. The eigenvalues of the first six main factors were greater than 1, and the cumulative contribution of these six principal factors was 85.7%, which can explain most of the information of the initial factors. When the number of principal factors reached 12, it could basically contain 98% of the information of the initial factors. The contribution of the first principal factor (P_1) to the total variance was 35.2%. There was little difference between the loadings of P_1 , most of which were between 0.2 and 0.3. P_1 was negatively correlated with the green space factor and positively correlated with the gray space factor. Therefore, P_1 reflects the great difference between the green space and the gray space of the neighborhood. The contribution of P_2 to the total variance was 18.7%. The higher loading of P_2 was higher than 0.3, which was mainly positively correlated with TCR (x_1) and the Edge (x_6), reflecting the large-scale green space of the neighborhood. The contribution of P_3 to the total variance was 11.2%. The higher loading of P_3 was more than 0.4, which was significantly positively correlated with H (x_{15}) and H_σ (x_{16}), reflecting the higher building height in the neighborhood and their greater height differences. P_4 contributed 9.2% to the total variance. Relative humidity (x_{21}) and wind speed (x_{22}) were two principal factors for P_4 , representing meteorological factors. P_5 and P_6 contributed 6.4% and 5% to the total variance, respectively, and GCR (x_2) and Loop (x_7) were principal factors.

The variance and eigenvalue showed similar trends at different pollution levels, which were similar to those of the overall pollution (Figure 3b). The KMO values of 22 standardized factors were 0.621, 0.615, and 0.612 for slight, moderate, and heavy pollution, respectively, and the significance of the Bartlett spherical test was 0.000. The eigenvalues of the first six principal factors were greater than 1, and the cumulative contributions of these six main factors were 85.3%, 86.0%, and 83.9%. When the number of principal factors reached 12, they could contain 98% of the information of the initial factors.

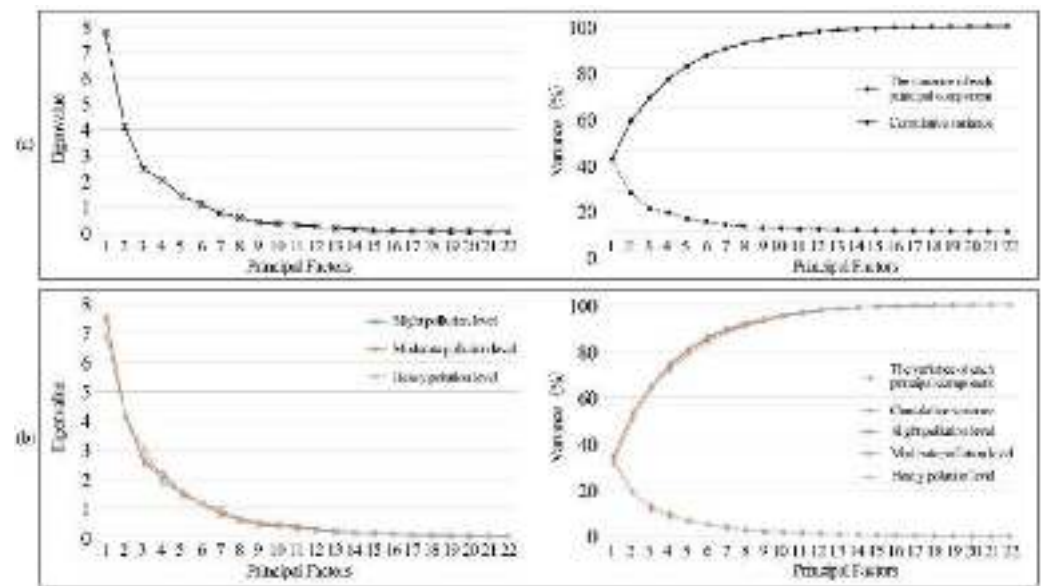


Figure 3. Variance and eigenvalue of principal factors at: (a) Overall pollution level; (b) Slight, moderate, and heavy pollution level.

3.1.2. Principal Factors Composition

The principal factor (P_i) is composed of 22 initial factors (x_i) with a certain proportion coefficient (principal component loading l). The absolute value of the loading represents the contribution of the initial factor to a P_i , and the positive and negative values represent the influence mode of the initial factor on a P_i . Therefore, the principal component of a P_i is reflected by the initial factor with relatively high loadings. There were certain differences in the higher loading between different principal factors. Taking P_1 as an example, the relationship between it and the initial factor at the overall pollution level is as follows:

$$P_1 = -0.209x_1 - 0.18x_2 - 0.293x_3 + 0.216x_4 - 0.248x_5 - 0.053x_6 - 0.131x_7 + 0.116x_8 + 0.176x_9 + 0.285x_{10} + 0.012x_{11} + 0.235x_{12} + 0.238x_{13} + 0.315x_{14} + 0.111x_{15} + 0.083x_{16} + 0.125x_{17} - 0.325x_{18} + 0.252x_{19} - 0.281x_{20} - 0.195x_{21} + 0.23x_{22} \quad (4)$$

where $x_1, x_2, x_3, \dots, x_{22}$ are the standardization values of the initial factor.

P_i reflects the relationship between each principal factor and its main initial factors. The composition characteristics of each P_i can be sorted and summarized according to the corresponding loading. At the overall pollution level, the loading of 22 principal factors was between -1 and 1 . The maximum absolute value was 0.685 and the minimum value was 0.0004 . The loading of each principal factor at different pollution levels was basically consistent with this, indicating that the composition characteristics of each principal factor were similar.

3.2. Construction and Verification of Models

Based on 22 principal factors, 24 regression models of six $PM_{2.5}$ relative indicators were carried out for four pollution levels, which included principal factors that significantly influenced $PM_{2.5}$. Regression models of six $PM_{2.5}$ relative indicators at the overall pollution level passed the test of significance (Table 2). However, the principal factors included in the six models were different, indicating the complex impacts of different principal factors on the range, duration, and rate of $PM_{2.5}$ increase or decrease. The number of principal factors included in the regression model was 3–11. The more principal factors were included in the regression model, the adj_R^2 value was relatively higher. In these models, P_3, P_4, P_{13} , and P_{17} were the four principal factors that appeared more frequently, indicating their significant effects on the increase/decrease in $PM_{2.5}$. Overall, these principal factors can

explain approximately 60.6~81.3% of the PM_{2.5} reduction indicators but only approximately 23.2~67.9% of the PM_{2.5} increase indicators.

Table 2. Regression model of principal factors at the overall pollution level.

Dependent Variable	Principal Factors	Constant	p-Value	F-Value	Adj_R ²
C _{in}	P ₃ (0.058,0.429) ***, P ₄ (0.060,0.361) **, P ₂₀ (−0.521,−0.340) **	1.424 ***	0.002	6.492	0.347
Δt _{in}	P ₁ (−0.037,−0.182) *, P ₃ (0.142,0.391) ***, P ₄ (0.089,0.199) *, P ₅ (−0.146,−0.283) **, P ₇ (−0.118,−0.189) *, P ₁₃ (−0.367,−0.251) **, P ₁₅ (0.353,0.191) *, P ₁₆ (−0.586,−0.284) **, P ₁₇ (0.654,0.246) **, P ₁₈ (−0.729,−0.227) **, P ₂₂ (3.749,0.295) **	7.725 ***	0.000	6.962	0.679
C _{in} '	P ₁₁ (−0.021,−0.416) **, P ₁₆ (0.027,0.298) *, P ₁₈ (0.041,0.286) *	0.199 ***	0.015	4.128	0.232
C _{de}	P ₄ (−0.010,−0.354) ***, P ₅ (0.017,0.532) ***, P ₁₂ (0.020,0.287) **, P ₁₆ (0.045,0.346) ***, P ₂₁ (−0.118,−0.256) **	0.539 ***	0.000	10.520	0.606
Δt _{de}	P ₁ (−0.053,−0.269) ***, P ₂ (−0.069,−0.253) ***, P ₃ (0.079,0.222) **, P ₄ (0.200,0.457) ***, P ₅ (−0.154,−0.302) ***, P ₁₀ (0.150,0.153) *, P ₁₃ (0.430,0.299) ***, P ₁₅ (0.713,0.393) ***, P ₁₇ (0.788,0.301) ***, P ₁₈ (0.449,0.142) *, P ₂₀ (−0.692,−0.172) **	6.508 ***	0.000	13.228	0.813
C _{de} '	P ₃ (−0.002,−0.265) ***, P ₄ (−0.003,−0.374) **, P ₅ (0.004,0.415) ***, P ₁₀ (−0.004,−0.194) **, P ₁₃ (−0.010,−0.327) ***, P ₁₅ (−0.012,−0.326) ***, P ₁₆ (0.008,0.176) *, P ₁₇ (−0.021,−0.385) ***, P ₁₈ (−0.017,−0.251) **	0.100 ***	0.000	12.783	0.774

Note: ***, **, and * indicate that the factors passed the test of significance at 1%, 5%, and 10%, respectively, and the numbers in brackets indicate the regression coefficient and standardization coefficient, respectively.

PM_{2.5} indicator regression models at different pollution levels also passed the test of significance (Table S6). First, although there were great differences in the principal factors included in the different models, some principal factors had a high frequency and great impacts on PM_{2.5}. However, these principal factors varied based on pollution levels. For example, P₃, P₁, and P₁₆ were important principal factors affecting the relative indicators of PM_{2.5} at slight, moderate, and heavy pollution levels, respectively. Second, the explanation degree of these principal factors for different PM_{2.5} indicators showed a similar trend at different pollution levels. The explanation degree of C_{in} was higher than that of C_{in}', and Δt_{in} was generally between them. The explanation degree of C_{de} was lower than that of C_{de}', and Δt_{de} was often in between. Nonetheless, the explanations of these principal factors for PM_{2.5} increase and decrease indicators were different. At the slight pollution level, these principal factors explained relatively more (approximately 52~81%) of the PM_{2.5} decrease indicators and less (approximately 16~49%) of the PM_{2.5} increase indicators. At the moderate pollution level, the principal factors had a higher explanation for PM_{2.5} increase indicators (approximately 70~84%), while the explanation for PM_{2.5} decrease indicators was lower (approximately 60~62%). At the heavy pollution level, the difference in the explanation of PM_{2.5} increase and decrease indicators by principal factors narrowed, focusing on 60~75%.

The prediction accuracy of the verification neighborhood samples was calculated for validation. Figure 4 shows the comparison between the predicted value and the actual value of PM_{2.5} indicators. Generally, the predicted value and actual value of each PM_{2.5} indicator were similar. There were individual samples with great differences between the predicted value and the actual value, which were mainly at heavy pollution, followed by moderate pollution. Furthermore, the accuracy of different PM_{2.5} indicators of five verification samples was compared through the RE value via Equation (3). At the overall pollution level, the RE of the six PM_{2.5} indicators of each verification sample was mostly less than 10%. The prediction error of different verification samples had great randomness. The maximum prediction error was C_{in} (33.3%) of sample HZ4, and the minimum was Δt_{de} in WH4, whose RE was 0.3%. At different pollution levels, the trend of prediction error of verification samples increased with the increase in pollution level, and the prediction error of each verification sample varied greatly.

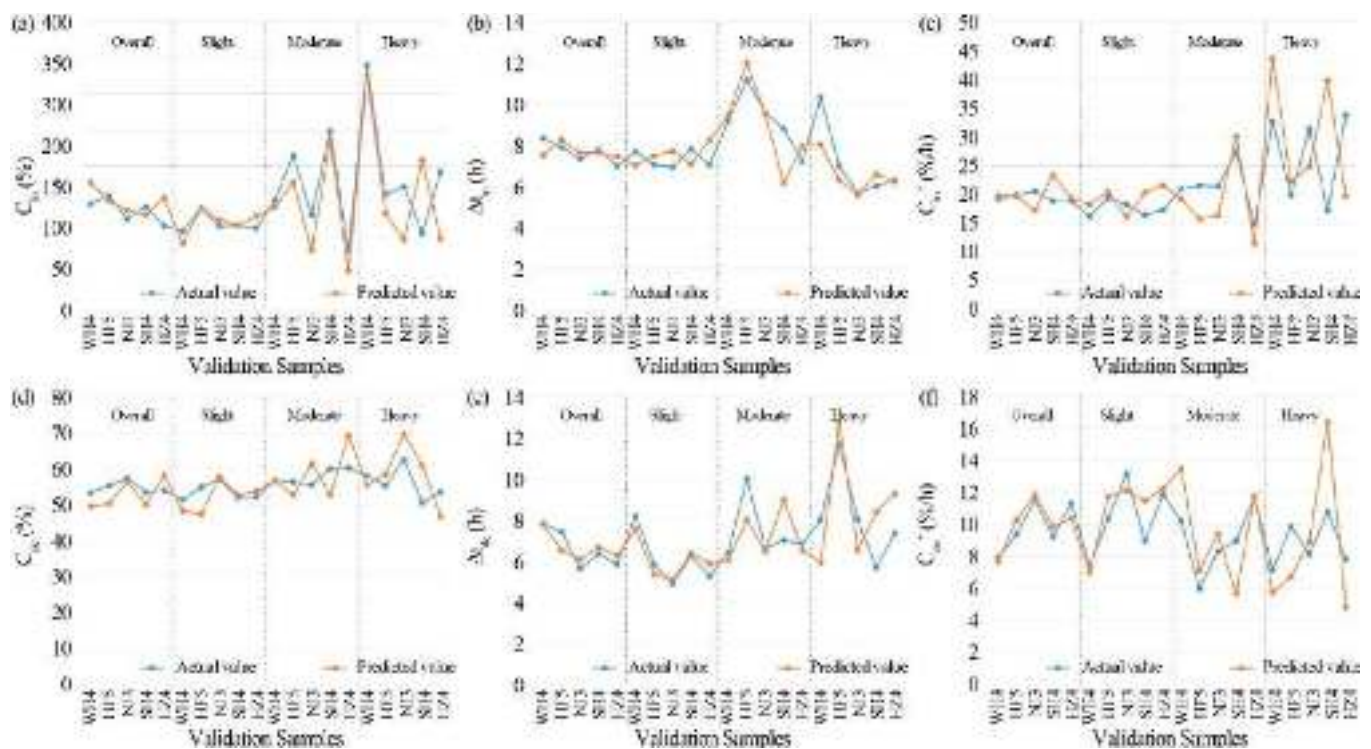


Figure 4. Validation for regression models of six PM_{2.5} indicators at the different pollution levels. (a) C_{in} ; (b) Δt_{in} ; (c) C_{in}' ; (d) C_{de} ; (e) Δt_{de} ; (f) C_{de}' .

The prediction error was relatively low at the overall pollution level because more days of data (24 days) were used for testing. With the increase in pollution level, the number of days used for verification was less, which is vulnerable to accidental or sudden factors outside the built environment, resulting in an increase in prediction error. Based on these models, although the short-term prediction error is unstable, it can still achieve high prediction accuracy for the long-term PM_{2.5} change trend of the block. Therefore, it has high application value.

Data with fewer days used in the analysis usually lead to a lower R^2 and a greater RE. In this study, due to the limited number of heavy pollution days, only 3 days of data were used for analysis at this pollution level. However, 4-day PM_{2.5} data and 3-day data monitored by instruments were used to analyze the effects of urban lake wetlands, neighboring urban greenery, and plant communities on PM_{2.5}, respectively [42,43]. There may be some accidental factors influencing the results by limited data, but it is enough for analysis.

3.3. The Influence of Built Environment on PM_{2.5}

Because the included principal factors varied from model to model (Table 2 and Table S6), the most important factors influencing PM_{2.5} were obtained by counting the times of principal factors that significantly influenced PM_{2.5} in 24 models of four pollution levels. As Figure 5 shows, the darker the color, the greater the frequency of a principal factor. First, C_{in} , Δt_{in} , and C_{in}' were synthesized as the increase change of PM_{2.5}. The decrease change of PM_{2.5} included C_{de} , Δt_{de} , and C_{de}' . The principal factors that had the most significant impact on the increase change of PM_{2.5} were P_1 and P_3 , which occurred seven times, followed by P_4 , P_6 , P_{16} , and P_{17} , which occurred six times. P_7 , P_{12} , and P_{18} occurred five times. The most significant principal factor affecting the decrease change of PM_{2.5} was P_5 , which occurred 10 times, followed by P_3 and P_4 , which occurred eight times. The frequency of P_1 , P_{12} , P_{13} , P_{15} , and P_{16} was six times. Overall, P_1 , P_3 , P_4 , and P_{16} were important factors that significantly affected the growth and reduction of PM_{2.5} at the same time. These principal factors reflect the differences in green and gray space,

building height and its differences, relative humidity, openness, and other characteristics of the neighborhood. In addition, these principal factors with high frequency were the factors that contributed the most to the corresponding dependent variable in the model. This further indicated their important role in $PM_{2.5}$.

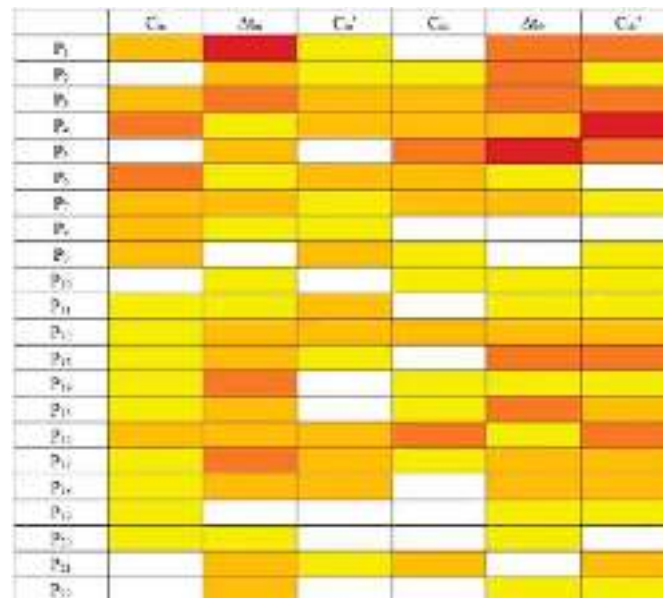


Figure 5. Frequency of principal factors that significantly influence $PM_{2.5}$.

Second, each $PM_{2.5}$ indicator was analyzed separately to find the differences in their principal factors. For C_{in} , P_4 and P_6 had the most contributions, indicating that meteorological factors and the green corridor connecting green space internally would greatly influence $PM_{2.5}$ increase change. P_1 contributed the most to Δt_{in} . However, there were no obvious principal factors for C_{in}' compared with C_{in} and Δt_{in} . As for C_{de} , P_5 and P_{16} had the most contribution to it. Moreover, P_5 showed a more important role in Δt_{de} than C_{de} . Therefore, attention should be given to green space coverage and openness of neighborhood for $PM_{2.5}$ reduction. P_4 was the most important principal factor for C_{de}' .

To strengthen the application of the regression model based on the built environment of the neighborhood and provide a reference for the optimization strategy of the built environment, we selected several neighborhoods from five cities with strong and weak $PM_{2.5}$ reduction effects. A neighborhood with strong $PM_{2.5}$ reduction effects is characterized by a high value of C_{de} and C_{de}' or a low value of Δt_{de} . Their effects on the increase and decrease of $PM_{2.5}$ were analyzed through the analysis of the scale and spatial form of green and gray spaces in the neighborhood.

Neighborhoods with strong $PM_{2.5}$ reduction capacity included WH6, HF5, NJ4, SH7, and HZ7 (Figure 6a). On the one hand, WH6 and NJ4 have large-scale green spaces, which play a great role in promoting the adsorption and reduction of $PM_{2.5}$ [44]. Meanwhile, the lower building density contributes to the diffusion of $PM_{2.5}$ in the neighborhood and promotes the decrease in $PM_{2.5}$ [45]. HZ7 has a stable regulatory effect on $PM_{2.5}$. It can both inhibit the increase in $PM_{2.5}$ and promote the decrease in $PM_{2.5}$. Although the building density of HF5 and SH7 is higher than that of other neighborhoods, the almost determinant building layout and height arrangement of HF5 are conducive to the formation of a ventilation corridor. The large building height difference and building shape uniformity index of SH7 promote the decline of $PM_{2.5}$.

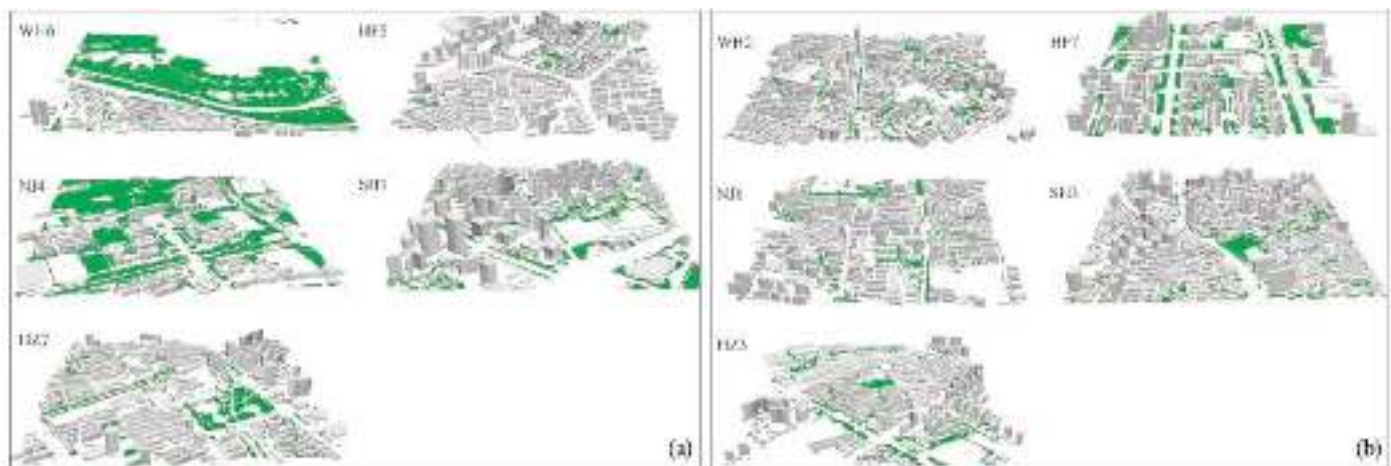


Figure 6. Neighborhoods with (a) strong and (b) weak $PM_{2.5}$ reduction capacity.

Neighborhoods with weak $PM_{2.5}$ reduction capacity included WH2, HF7, NJ1, SH3, and HZ3 (Figure 6b). Among these neighborhoods, WH2, NJ1, and HZ3 have a common feature of low-rise and high-density, which is not conducive to ventilation in the neighborhood. The building density of SH3 is high, and there are some high-rise buildings. However, the scale of green space in these neighborhoods is generally small, which reduces the active adsorption of $PM_{2.5}$ by green space. HF7 is a high-rise, low-density neighborhood. Too many high-rise buildings aggravate the pollution of $PM_{2.5}$ in the neighborhood and are difficult to evacuate.

4. Conclusions

This paper constructed a prediction model of $PM_{2.5}$ increase and decrease dynamic changes in neighborhoods based on 22 factors of green space, gray space, and meteorological factors, revealing the comprehensive impact mechanism of neighborhood-level built environments on $PM_{2.5}$ and laying a foundation for proposing specific optimization strategies. The adj_R^2 of these models was concentrated in 0.6–0.8, with the highest value of 0.836, indicating that it can better fit the existing indicators. P_1 , P_3 , P_4 , and P_{16} were the most important factors that significantly affected the increase and decrease in $PM_{2.5}$ at the same time, which reflected the characteristics of the green–gray space difference, building height and its difference, relative humidity, and openness, respectively. Among the many indicators of green space, green space coverage was significantly conducive to $PM_{2.5}$ reduction. The green corridor connecting green space internally would greatly influence the change of $PM_{2.5}$ increase. For gray space, the openness of the neighborhood was important to $PM_{2.5}$ reduction. In addition, relative humidity and wind speed contributed more to the change of both the decrease and increase of $PM_{2.5}$ than temperature.

There are some issues that need to be further explored. This study used $PM_{2.5}$ monitoring data for analysis, lacking exploration of $PM_{2.5}$ sources. Further study requires discussion on the emissions in the urban zones because of the different pollution sources in the five cities [46]. Data from more days, especially heavy pollution levels, can be included for more accurate research.

Supplementary Materials: The following are available online at <https://www.mdpi.com/article/10.3390/atmos13010115/s1>, Table S1: Detailed information for 37 neighborhoods, Table S2: The date of different pollution level in 2016 and 2017 for the five cities, Table S3: Statistical of green space indicators, Table S4: Statistical of gray space indicators, Table S5: Statistical of meteorological factors, Table S6: Regression models of principal factors at different pollution levels.

Author Contributions: Conceptualization, methodology, software, validation, formal analysis, investigation, writing—original draft preparation, visualization, M.C.; writing—review and editing,

supervision, project administration, funding acquisition, F.D. All authors have read and agreed to the published version of the manuscript.

Funding: This research was funded by the Fundamental Research Funds for the Central Universities (grant number 2020kfyXJJS104) and the National Natural Science Foundation of China (grant number 51778254).

Institutional Review Board Statement: Not applicable.

Informed Consent Statement: Not applicable.

Data Availability Statement: The data used in this study are not currently publicly available.

Acknowledgments: The authors would like to thank all the participants for their time and effort to participate in this study.

Conflicts of Interest: The authors declare no conflict of interest.

References

1. Sundell, J.; Levin, H.; Nazaroff, W.W.; Cain, W.S.; Fisk, W.J.; Grimsrud, D.T.; Gyntelberg, F.; Li, Y.; Persily, A.K.; Pickering, A.C.; et al. Ventilation rates and health: Multidisciplinary review of the scientific literature. *Indoor Air* **2011**, *21*, 191–204. [CrossRef] [PubMed]
2. Liu, Y.; Wu, J.; Yu, D. Disentangling the complex effects of socioeconomic, climatic, and urban form factors on air pollution: A case study of China. *Sustainability* **2018**, *10*, 776. [CrossRef]
3. Tecer, L.H.; Süren, P.; Alagha, O.; Karaca, F.; Tuncel, G. Effect of meteorological parameters on fine and coarse particulate matter mass concentration in a coal-mining area in Zonguldak, Turkey. *J. Air Waste Manage. Assoc.* **2008**, *58*, 543–552. [CrossRef]
4. Cheng, Z.; Li, L.; Liu, J. Identifying the spatial effects and driving factors of urban PM_{2.5} pollution in China. *Ecol. Indic.* **2017**, *82*, 61–75. [CrossRef]
5. Huang, Y.; Shen, H.; Chen, H.; Wang, R.; Zhang, Y.; Su, S.; Chen, Y.; Lin, N.; Zhuo, S.; Zhong, Q.; et al. Quantification of global primary emissions of PM_{2.5}, PM₁₀, and TSP from combustion and industrial process sources. *Environ. Sci. Technol.* **2014**, *48*, 13834–13843. [CrossRef]
6. Liu, Z.; Wang, Y.; Hu, B.; Ji, D.; Zhang, J.; Wu, F.; Wan, X.; Wang, Y. Source appointment of fine particle number and volume concentration during severe haze pollution in Beijing in January 2013. *Environ. Sci. Pollut. Res.* **2016**, *23*, 6845–6860. [CrossRef] [PubMed]
7. Romero, H.; Ihl, M.; Rivera, A.; Zalazar, P.; Azocar, P. Rapid urban growth, land-use changes and air pollution in Santiago, Chile. *Atmos. Environ.* **1999**, *33*, 4039–4047. [CrossRef]
8. Aslam, M.Y.; Krishna, K.R.; Beig, G.; Tinmaker, M.I.R.; Chate, D.M. Diurnal evolution of urban heat island and its impact on air quality by using ground observations (SAFAR) over New Delhi. *Open J. Air Pollut.* **2017**, *6*, 52–64. [CrossRef]
9. Yuan, M.; Song, Y.; Huang, Y.; Shen, H.; Li, T. Exploring the association between the built environment and remotely sensed PM_{2.5} concentrations in urban areas. *J. Clean Prod.* **2019**, *220*, 1014–1023. [CrossRef]
10. Yang, H.; Chen, W.; Liang, Z. Impact of land use on PM_{2.5} pollution in a representative city of middle China. *Int. J. Environ. Res. Public Health* **2017**, *14*, 462. [CrossRef]
11. Łowicki, D. Landscape pattern as an indicator of urban air pollution of particulate matter in Poland. *Ecol. Indic.* **2019**, *97*, 17–24. [CrossRef]
12. Lu, D.; Mao, W.; Yang, D.; Zhao, J.; Xu, J. Effects of land use and landscape pattern on PM_{2.5} in Yangtze River Delta, China. *Atmos. Pollut. Res.* **2018**, *9*, 705–713. [CrossRef]
13. Wu, J.; Xie, W.; Li, W.; Li, J. Effects of urban landscape pattern on PM_{2.5} pollution-A Beijing case study. *PLoS ONE* **2015**, *10*, e0142449. [CrossRef]
14. Yang, S.; Wu, H.; Chen, J.; Lin, X.; Lu, T. Optimization of PM_{2.5} estimation using landscape pattern information and land use regression model in Zhejiang, China. *Atmosphere* **2018**, *9*, 47. [CrossRef]
15. Fan, C.; Tian, L.; Zhou, L.; Hou, D.; Song, Y.; Qiao, X.; Li, J. Examining the impacts of urban form on air pollutant emissions: Evidence from China. *J. Environ. Manag.* **2018**, *212*, 405–414. [CrossRef] [PubMed]
16. Lee, C. Impacts of multi-scale urban form on PM_{2.5} concentrations using continuous surface estimates with high-resolution in U.S. metropolitan areas. *Landsc. Urban Plann.* **2020**, *204*, 103935. [CrossRef]
17. Liu, Y.; Wu, J.; Yu, D.; Ma, Q. The relationship between urban form and air pollution depends on seasonality and city size. *Environ. Sci. Pollut. Res.* **2018**, *25*, 15554–15567. [CrossRef]
18. Chen, M.; Dai, F.; Yang, B.; Zhu, S. Effects of neighborhood green space on PM_{2.5} mitigation: Evidence from five megacities in China. *Build. Environ.* **2019**, *156*, 33–45. [CrossRef]
19. Hu, H.; Chen, Q.; Qian, Q.; Lin, C.; Chen, Y.; Tian, W. Impacts of traffic and street characteristics on the exposure of cycling commuters to PM_{2.5} and PM₁₀ in urban street environments. *Build. Environ.* **2021**, *188*, 107476. [CrossRef]
20. Yang, J.; Shi, B.; Shi, Y.; Marvin, S.; Zheng, Y.; Xia, G. Air pollution dispersal in high density urban areas: Research on the triadic relation of wind, air pollution, and urban form. *Sustain. Cities Soc.* **2020**, *54*, 101941. [CrossRef]

21. Edussuriya, R.; Chan, A.; Ye, A. Urban morphology and air quality in dense residential environments in Hong Kong. Part I: District-level analysis. *Atmos. Environ.* **2011**, *45*, 4789–4803. [CrossRef]
22. Das, M.; Das, A. Assessing the relationship between local climatic zones (LCZs) and land surface temperature (LST)—A case study of Sriniketan-Santiniketan Planning Area (SSPA), West Bengal, India. *Urban Clim.* **2020**, *32*, 100591. [CrossRef]
23. Kotharkar, R.; Bagade, A.; Singh, P.R. A systematic approach for urban heat island mitigation strategies in critical local climate zones of an Indian city. *Urban Clim.* **2020**, *34*, 100701. [CrossRef]
24. Johnson, S.; Ross, Z.; Kheirbek, I.; Ito, K. Characterization of intra-urban spatial variation in observed summer ambient temperature from the New York City Community Air Survey. *Urban Clim.* **2020**, *31*, 100583. [CrossRef]
25. Perera, N.G.R.; Emmanuel, R. A “Local Climate Zone” based approach to urban planning in Colombo, Sri Lanka. *Urban Clim.* **2018**, *23*, 188–203. [CrossRef]
26. Ziaul, S.; Pal, S. Analyzing control of respiratory particulate matter on Land Surface Temperature in local climatic zones of English Bazar Municipality and Surroundings. *Urban Clim.* **2018**, *24*, 34–50. [CrossRef]
27. Zhou, X.; Okaze, T.; Ren, C.; Cai, M.; Ishida, Y.; Watanabe, H.; Mochida, A. Evaluation of urban heat islands using local climate zones and the influence of sea-land breeze. *Sust. Cities Soc.* **2020**, *55*, 102060. [CrossRef]
28. Ng, E. Policies and technical guidelines for urban planning of high-density cities-air ventilation assessment (AVA) of Hong Kong. *Build. Environ.* **2009**, *44*, 1478–1488. [CrossRef]
29. Zhai, L.; Li, S.; Zhou, B.; Sang, H.; Fang, X.; Xu, S. An improved geographically weighted regression model for PM_{2.5} concentration estimation in large areas. *Atmos. Environ.* **2018**, *181*, 145–154. [CrossRef]
30. Han, R.Y.; Chen, J.; Wang, B.; Wu, D.; Tang, M. LUR models for simulating the spatial distribution of PM_{2.5} concentration in Zhejiang Province. *Bull. Sci. Technol.* **2016**, *32*, 215–220.
31. Zhang, M.; Ma, Y.; Wang, L.; Gong, W.; Hu, B.; Shi, Y. Spatial-temporal characteristics of aerosol loading over the Yangtze River Basin during 2001–2015. *Int. J. Climatol.* **2017**, *38*, 2138–2152. [CrossRef]
32. Chen, M.; Dai, F.; Yang, B.; Zhu, S. Effects of urban green space morphological pattern on variation of PM_{2.5} concentration in neighborhoods of five Chinese megacities. *Build. Environ.* **2019**, *158*, 1–15. [CrossRef]
33. Lei, Y.; Duan, Y.; He, D. Effects of urban greenspace patterns on particulate matter pollution in metropolitan Zhengzhou in Henan, China. *Atmosphere* **2018**, *9*, 199. [CrossRef]
34. Zhao, C.; Fu, G.; Liu, X.; Fu, F. Urban planning indicators, morphology and climate indicators: A case study for a north-south transect of Beijing, China. *Build. Environ.* **2011**, *46*, 1174–1183. [CrossRef]
35. Chen, M.; Bai, J.; Zhu, S.; Yang, B.; Dai, F. The influence of neighborhood-level urban morphology on PM_{2.5} variation based on random forest regression. *Atmos. Pollut. Res.* **2021**, *12*, 101147. [CrossRef]
36. Clark, L.P.; Millet, D.B.; Marshall, J.D. Air quality and urban form in US urban areas: Evidence from regulatory monitors. *Environ. Sci. Technol.* **2011**, *45*, 7028–7035. [CrossRef]
37. Wang, F.; Peng, Y.; Jiang, C. Influence of road patterns on PM_{2.5} concentrations and the available solutions: The case of Beijing city, China. *Sustainability* **2017**, *9*, 217. [CrossRef]
38. Mei, D.; Deng, Q.; Wen, M.; Fang, Z. Evaluating dust particle transport performance within urban street canyons with different building heights. *Aerosol Air Qual. Res.* **2016**, *16*, 1483–1496. [CrossRef]
39. Svensson, M.K. Sky viewfactor analysis-implications for urban air temperature differences. *Meteorol. Appl.* **2004**, *11*, 201–211. [CrossRef]
40. G’al, T.; Lindberg, F.; Unger, J. Computing continuous sky view factors using 3D urban raster and vector databases: Comparison and application to urban climate. *Theor. Appl. Climatol.* **2009**, *95*, 111–123. [CrossRef]
41. Olvera, H.A.; Garcia, M.; Li, W.W.; Yang, H.; Amaya, M.A.; Myers, O.; Burchiel, S.W.; Berwick, M.; Pingitore, N.E. Principal component analysis optimization of a PM_{2.5} land use regression model with small monitoring network. *Sci. Total Environ.* **2012**, *425*, 27–34. [CrossRef] [PubMed]
42. Zhao, L.; Li, T.; Przybysz, A.; Guan, Y.; Ji, P.; Ren, B.; Zhu, C. Effect of urban lake wetlands and neighboring urban greenery on air PM₁₀ and PM_{2.5} mitigation. *Build. Environ.* **2021**, *206*, 108291. [CrossRef]
43. Zhu, C.; Przybysz, A.; Chen, Y.; Guo, H.; Chen, Y.; Zeng, Y. Effect of spatial heterogeneity of plant communities on air PM₁₀ and PM_{2.5} in an urban forest park in Wuhan, China. *Urban For. Urban Gree.* **2019**, *46*, 126487. [CrossRef]
44. McDonald, A.G.; Bealey, W.J.; Fowler, D.; Dragosits, U.; Skiba, U.; Smith, R.I.; Donovan, R.G.; Brett, H.E.; Hewitt, C.N.; Nemitz, E. Quantifying the effect of urban tree planting on concentrations and depositions of PM₁₀ in two UK conurbations. *Atmos. Environ.* **2007**, *41*, 8455–8467. [CrossRef]
45. Shi, Y.; Xie, X.; Fung, J.C.H.; Ng, E. Identifying critical building morphological design factors of street-level air pollution dispersion in high-density built environment using mobile monitoring. *Build. Environ.* **2018**, *128*, 248–259. [CrossRef]
46. Dai, F.; Chen, M.; Yang, B. Spatiotemporal variations of PM_{2.5} concentration at the neighborhood level in five Chinese megacities. *Atmos. Pollut. Res.* **2020**, *11*, 190–202. [CrossRef]

Article

The Impact of Air Pollution (PM_{2.5}) on Atherogenesis in Modernizing Southern versus Northern China

Kamsang Woo ^{1,*}, Changqing Lin ², Yuehui Yin ³, Dongshuang Guo ⁴, Ping Chook ¹, Timothy C. Y. Kwok ¹ and David S. Celermajer ⁵

¹ Department of Medicine and Therapeutics, The Chinese University of Hong Kong, Hong Kong, China; pingchook2@cuhk.edu.hk (P.C.); tkwok@cuhk.edu.hk (T.C.Y.K.)

² Division of Environment and Sustainability, The Hong Kong University of Science and Technology, Hong Kong, China; cqlin@ust.hk

³ Second Hospital of Chongqing Medical University, Chongqing 400010, China; yinyh@hospital.cqmu.edu.cn

⁴ Department of Medicine, Yu County Provincial Hospital, Yangquan 045100, China; guods8008@163.com

⁵ Faculty of Medical and Health Science, The University of Sydney, Sydney, NSW 2006, Australia; David.Celermajer@health.nsw.gov.au

* Correspondence: kamsangwoo@cuhk.edu.hk; Tel./Fax: +852-2647-4966

Abstract: To evaluate the impact of PM_{2.5} air pollution on atherogenic processes in modernizing Southern versus Northern China, we studied 1323 asymptomatic Chinese in Southern and Northern China in 1996–2007. PM_{2.5} exposure and metabolic syndrome (MS) were noted. Brachial flow-mediated dilation (endothelial function FMD) and carotid intima-media thickness (IMT) were measured by ultrasound. Although age and gender were similar, PM_{2.5} was higher in Northern China than in Southern China. The Northern Chinese were characterized by lower lipids, folate and vitamin B12, but higher age, blood pressures, MS and homocysteine (HC) ($p = 0.0015$). Brachial FMD was significantly lower and carotid IMT was significantly greater (0.68 ± 0.13) in Northern Chinese, compared with FMD and IMT (0.57 ± 0.13 , $p < 0.0001$) in Southern Chinese. On multivariate regression, for the overall cohort, carotid IMT was significantly related to PM_{2.5}, independent of location and traditional risk factors (Model $R^2 = 0.352$, $F = 27.1$, $p < 0.0001$), while FMD was inversely related to gender, age, and northern location, but not to PM_{2.5}. In Southern Chinese, brachial FMD was inversely correlated to PM_{2.5}, independent of age, whereas carotid IMT was significantly related to PM_{2.5}, independent of age and gender. In Northern Chinese, brachial FMD was inversely related to gender only, but not to PM_{2.5}, while carotid IMT was related to traditional risk factors. Despite a higher PM_{2.5} pollution in Northern China, PM_{2.5} pollution was more significantly associated with atherogenic surrogates in Southern compared to Northern Chinese. This has potential implications for atherosclerosis prevention.

Keywords: atherogenesis; flow-mediated dilation; carotid intima-media thickness; air-pollution (PM_{2.5}); modernizing China

Citation: Woo, K.; Lin, C.; Yin, Y.; Guo, D.; Chook, P.; Kwok, T.C.Y.; Celermajer, D.S. The Impact of Air Pollution (PM_{2.5}) on Atherogenesis in Modernizing Southern versus Northern China. *Atmosphere* **2021**, *12*, 1552. <https://doi.org/10.3390/atmos12121552>

Academic Editors: Duanyang Liu, Kai Qin and Honglei Wang

Received: 29 September 2021

Accepted: 8 November 2021

Published: 24 November 2021

Publisher's Note: MDPI stays neutral with regard to jurisdictional claims in published maps and institutional affiliations.



Copyright: © 2021 by the authors. Licensee MDPI, Basel, Switzerland. This article is an open access article distributed under the terms and conditions of the Creative Commons Attribution (CC BY) license (<https://creativecommons.org/licenses/by/4.0/>).

1. Introduction

Atherosclerotic diseases (stroke and heart attack CVS) are currently the most important global health hazard, including for mainland China, which is now in a rapid phase of modernization [1,2]. Traditional atherosclerosis risk factors, including smoking, hypertension, diabetes mellitus, hyperlipidemia, obesity and physical inactivity, have been implicated [3]. Recently the detrimental association of air pollution (AP) with CVS in modernized society has been realized. In particular, small particulate matter less than 2.5 μm in diameter (PM_{2.5}) has been associated with cardiovascular morbidity and mortality [4–6]. Of the 7 million premature deaths each year linked to air pollution (PM_{2.5}), 34% were related to ischemic heart disease, 26% to respiratory disease and 20% were due to stroke [7].

The pathobiology of PM_{2.5}-related atherosclerotic disease may involve direct effects of PM_{2.5} on cardiovascular system and/ or indirect effects of PM_{2.5} mediated by oxidative

stress and vascular inflammation [8,9]. In other words, PM_{2.5} can act as a trigger in susceptible persons, or it can contribute to long-term atherogenic processes. On this issue, we and others have previously documented the negative impact of long-term PM_{2.5} exposure on atherosclerosis surrogates (brachial endothelial dysfunction FMD and carotid intima-media thickening IMT), which are closely linked to cardiovascular and stroke outcome [10–12].

In the past three decades, China has been undertaking a process of rapid economic development and modernization [13]. This started from the Southern seashore region and the greater Pearl Delta Bay area, and later moved to the Northern parts of the country, with different PM_{2.5} pollution exposure. The present study aimed to evaluate the impact of PM_{2.5} pollution on atherogenic process in Southern compared with Northern China.

2. Subjects and Methods

A total of 1323 asymptomatic Chinese adults (mean age 47.1 ± 11.7 years and 47.5% male) in Southern China (Hong Kong, Macau, Pan Yu, $n = 395$) and Northern China (Yu County in Shanxi and Three Gorges Territories of Yangtze River, $n = 928$) were studied in 1996–2007, as part of the international collaborative Chinese Atherosclerosis in the Aged and Young Project (CATHAY Study). The study protocol and some related findings have been reported previously [14–18].

All recruited subjects were apparently healthy. They were not known to have hypertension, diabetes mellitus or metabolic syndrome, had no major vascular, hepatic or renal disease, and were not taking any regular medications, including vitamin supplementation. Nearly all subjects (>95%) were local born residents and the other migrated to the county for over 10 years. After fasting for 14 h and signing written informed consent, their cardiovascular risk profiles, including smoking, body mass index (BMI), waist circumference, waist hip ratio (WHR), systolic and diastolic blood pressure (SBP, DBP) were measured. On recruitment, blood was taken once for fasting lipid profile (total, high and low lipoprotein cholesterol, TC, HDL-C, LDL-C and triglycerides TG), creatinine, vitamin B12, folate, and fasting total homocysteine (HC). Fasting glucose was measured by haemstix and HC was evaluated on stored frozen sample by enzymatic immune assay (Abbott IMX analyses, Abbott Peak, IL, USA). Blood was assayed in batches at the The Hospital Central Corde de Januarie, Macau, and The Prince of Wales Hospital, Hong Kong, currently accredited by the USA laboratory centres. MTHFR genotypes were evaluated by PCR technique at the Li Hysan research laboratory of the Chinese University of Hong Kong. Metabolic Syndrome (MS) was diagnosed according to International Diabetes Federation (IDF) criteria [19,20].

Our research study and informed consent form were reviewed and approved by our institutional research ethics committee of The Chinese University of Hong Kong (CREC 2000-108). This study complied with the 1995 and 2003 Helsinki Declaration for human studies.

2.1. PM_{2.5} Air Pollution Exposure

The yearly mean PM_{2.5} concentration over China was assessed by using the satellite remote sensing technology. Firstly, spectral data from the two moderate resolution imaging spectroradiometer (MODIS) instruments aboard the Terra and Aqua satellites were used to build aerosol optical depth (AOD) data at a resolution of $0.01^\circ \times 0.01^\circ$, over China [21]. Secondly, an observational data-driven algorithm, which took the ground-observed visibility and relative humidity data as inputs, was developed to derive the yearly mean ground-level PM_{2.5} concentration from the AOD [22]. Evaluation of the long-term satellite-derived PM_{2.5} concentration against the ground observations demonstrated a correlation coefficient of >0.9 and a mean absolute percentage error within $\pm 20\%$ [23]. The mean concentration of PM_{2.5} over a single year was registered, corresponding to the study year of each subject.

2.2. Arterial Ultrasound Studies

Atherosclerotic surrogate markers, flow-mediated dilation (FMD) of brachial artery, and carotid intima-media thickness (IMT), were studied once on recruitment using high resolution ultrasound as reported previously [24,25]. Briefly, forearm tourniquet cuff placement was applied to induce reactive hyperemia on deflation, and percentage of dilation in vessel diameter (from baseline) was computed, as indicator of endothelium-dependent dilation, in comparison with dilation after sublingual glyceryltrinitrate (endothelium-independent dilation GTN). Similarly carotid IMT was measured by using a standard scanning protocol for both carotid arteries as described by Salonen and Salonen, Bots and Touboul et al. [26–28]. Images of the far wall of the distal 10 mm of the common carotid artery were used. All scans were evaluated off-line by a verified automatic edge-detecting software device. The intra-observer variability for mean IMT was 0.03 ± 0.01 mm (coefficient of variation 1%, $R = 0.99$).

2.3. Statistical Analyses

The group mean values, standard deviation and 95% confidence intervals (CI) when appropriate were computed. Standard testing of normality of distribution was used for the assessment of normal distribution. Possible intergroup differences were identified with independent samples Students' test and a one-way ANCOVA model. The primary study endpoints were carotid IMT and brachial FMD, whereas other outcome variables were compared after Bonferroni adjustment for multiple comparisons. On the assumption of mean carotid IMT being 0.61 ± 0.14 mm and brachial FMD being $8\% \pm 1\%$ in the subjects, we estimated that enrolment of 350 subjects in Southern China and 600 subjects in Northern China would result in adequate power (80%) to detect a 18% difference in carotid IMT and an 8% difference in brachial FMD, between the two location groups at $2p < 0.05$ significance level [29]. Linear multivariate regressions were performed to assess the major determinants of IMT and FMD, including age, gender, smoking status, BMI, metabolic syndrome, LDL-C, PM2.5, southern and northern locations. The variables with significant standardized beta coefficients (beta value with $2p < 0.05$) as an indicator of the contribution to the model, were identified, and insignificant variables ($2p > 0.05$) were removed subsequently. Group differences with an error probability of 5% ($2p < 0.05$) were considered statistically significant. Analyses were performed with SPSS version 25.

3. Results

The demographic and clinical characteristics of the southern/ northern groups were tabulated (Table 1). While their gender, mean age, BMI and fasting glucose were similar, smoking status, SBP, DBP, metabolic syndrome and homocysteine were significantly lower, but their LDL-C, vitamin B12 and folate were significantly higher in Southern Chinese compared with the Northern Chinese ($p < 0.0015$). PM2.5 exposure in Southern China ($44.0 \pm 6.8 \mu\text{g}/\text{m}^3$) (Figure 1A,B) was significantly lower than in Northern China ($71.1 \pm 15.8 \mu\text{g}/\text{m}^3$), $p < 0.0015$. (Figure 2A,B).



Figure 1. (A) Far view of residential estates and Mount Ma On along the Shing Moon River of Shatin, Hong Kong on clear day with PM_{2.5} concentration of 14 $\mu\text{g}/\text{m}^3$, and (B) on foggy polluted day with PM_{2.5} concentration of 45 $\mu\text{g}/\text{m}^3$ (Woo et al. [18]).



Figure 2. (A) Sky view of Chongqing Garden on clear day with PM_{2.5} concentration of 45 $\mu\text{g}/\text{m}^3$, and (B) Chongqing residence estate near riverside on a foggy day with PM_{2.5} concentration of 79 $\mu\text{g}/\text{m}^3$ (Courtesy of Prof. YH Yin).

Table 1. Demographic Characteristics of Southern–Northern China.

	Southern China (n = 395)	Northern China (n = 928)	p-Value (Bonferroni Adjusted)
Male Gender (%)	48	47	0.719 (>0.99)
Age (yr)	46.8 \pm 12.8	47.4 \pm 9.5	0.340 (>0.99)
Smoking Status (%)	15	35	<0.0001 (0.0015)
BMI	23.0 \pm 4.0	23.4 \pm 3.4	<0.203 (>0.99)
SBP (mmHg)	119.0 \pm 15.7	123.7 \pm 17.6	<0.0001 (0.0015)
DBP (mmHg)	75.9 \pm 9.3	80.2 \pm 11.0	<0.0001 (0.0015)
PM _{2.5} ($\mu\text{g}/\text{m}^3$)	44.0 \pm 6.8	71.1 \pm 15.8	<0.0001 (0.0015)
Creatinine ($\mu\text{mol}/\text{L}$)	81.7 \pm 16.1	63.2 \pm 16.7	<0.0001 (0.0015)
Glucose (mmol/L)	5.6 \pm 1.2	5.4 \pm 6.0	0.004 (0.06)
LDL-C	3.4 \pm 1.0	2.56 \pm 0.82	<0.0001 (0.0015)
Metabolic Syndrome (%)	15.0	24.5	<0.0001 (0.0015)
B12 (pmol/L)	411.7 \pm 249.4	156.5 \pm 90.6	<0.0001 (0.0015)
Folate (nmol/L)	31.1 \pm 15.6	13.1 \pm 5.6	<0.0001 (0.0015)
Homocysteine ($\mu\text{mol}/\text{L}$)	9.6 \pm 4.5	25.0 \pm 21.0	<0.0001

B12: Vitamin B12. BMI: Body Mass Index. DBP: Diastolic Blood Pressure. LDL-C: Low Density Lipoprotein Cholesterol. PM_{2.5}: Particulate Matter <2.5 μm in Diameter.

3.1. Vascular Parameters

Brachial FMD and carotid IMT were normally distributed. Brachial FMD was significantly lower (7.5 ± 1.8 , 95% CI 7.3–7.7%, $p < 0.001$), but carotid IMT was significantly greater (0.68 ± 0.13 , 95% CI 0.67–0.69 mm, $p < 0.0001$) in Northern Chinese, compared with their Southern counterparts (8.1 ± 3.0 , 95% CI 7.8–8.5% and 0.57 ± 0.13 , 95% CI 0.56–0.58 mm, respectively) (Table 2). The GTN responses of the two groups were similar.

Table 2. Vascular Parameters in Northern–Southern China Locations.

	Location		<i>p</i> -Value
	Southern	Northern	
Hyperemia (%)	655 ± 289	715 ± 217	0.006
(95% CI)	(623–686)	(687–743)	
GTN (%)	18.1 ± 4.8	18.2 ± 3.0	0.912
(95% CI)	(17.6–18.7)	(17.8–18.6)	
FMD (%)	8.1 ± 3.0	$7.5 \pm 1.8^{\dagger}$	0.001
(95% CI)	(7.8–8.5)	(7.3–7.7)	
Carotid IMT (mm)	0.57 ± 0.13	$0.68 \pm 0.13^{\dagger\dagger}$	0.0001
(95% CI)	(0.56–0.58)	(0.67–0.69)	

Compared with Southern China $\dagger p < 0.0001$; $\dagger\dagger p = 0.01$. FMD: Flow-mediated Dilation. GTN: Glyceryltrinitrate Dilation. IMT: Intima-media Thickness.

3.2. Determinants of Risk Factors for Impaired Brachial FMD

On multivariate regression analyses, in Southern Chinese, brachial FMD was inversely related to PM2.5 (beta = -0.274 , $p = 0.001$), age (beta = -0.238 , $p < 0.005$), but not to gender, smoking status, BMI, MS, homocysteine, LDL-C or MTHFR. (Model $R^2 = 0.202$, $F = 4.026$, $p < 0.0001$) (Table 3). In Northern Chinese, brachial FMD was related to gender (beta = -0.329 , $p = 0.009$), but not to other traditional risk factors (Model $R^2 = 0.211$, $F = 3.802$, $p < 0.0001$). In the overall 1323 Chinese cohort, lower brachial FMD was related to older age, male gender and northern location, but not to PM2.5 (Model $R^2 = 0.190$, $F = 7.802$, $p < 0.0001$).

Table 3. Determinants of Risk Factors for Brachial FMD *.

Risk Factors	Southern Chinese *		Northern Chinese **		Overall Cohort ***	
	Beta Value	<i>p</i> -Value	Beta Value	<i>p</i> -Value	Beta-Value	<i>p</i> -Value
Age (yr)	-0.238	0.005	-0.163	0.062	-0.210	<0.0001
Gender	-0.174	0.050	-0.329	0.009	-0.163	0.013
Smoking status	-0.154	0.077	0.029	0.802	-0.118	0.075
BMI	-0.036	0.674	-0.040	0.415	0.005	0.938
MS	-0.067	0.436	-0.032	0.741	-0.051	0.403
Homocysteine	0.076	0.374	-0.196	0.066	-0.025	0.725
LDL-C	-0.058	0.473	-0.057	0.502	-0.090	0.206
MTHFR	-0.097	0.201	0.158	0.114	-0.014	0.822
PM2.5	-0.274	0.001	0.011	0.892	-0.022	0.862
Location	-	-	-	-	-0.325	0.005

* Model $R^2 = 0.202$; F -value = 4.026; $p < 0.0001$. ** Model $R^2 = 0.211$; F -value = 3.802; $p < 0.0001$. *** Model $R^2 = 0.190$; F -value = 7.802; $p < 0.0001$. BMI: Body Mass Index. FMD: Flow-mediated Dilation. LDL-C: Low Density Lipoprotein Cholesterol. MTHFR: Methylenetetrahydrofolate Reductase Gene Polymorphisms. PM2.5: Particulate Matters $< 2.5 \mu\text{m}$ in Diameter.

On multivariate regression analyses, carotid IMT in Southern Chinese was significantly related to PM2.5 (beta = 0.334 , $p < 0.0001$), independent of age (beta = 0.393 , $p < 0.0001$) and gender (beta = 0.146 , $p = 0.043$) (Model $R^2 = 0.451$, $F = 13.3$, $p < 0.0001$) (Table 4). In Northern Chinese, carotid IMT was related to age (beta = 0.385 , $p < 0.0001$), smoking status (beta = 0.157 , $p = 0.01$), MS (beta = 0.110 , $p = 0.039$), homocysteine (beta = 0.137 , $p = 0.014$) and LDL-C (beta = 0.145 , $p = 0.0003$), but not to PM2.5 (beta = 0.033 , $p = 0.471$). For the overall cohort, carotid IMT was related to PM2.5 (beta = 0.368 , $p < 0.0001$), independent

of other atherosclerotic risk factors including age, male gender, BMI, MS, HC, LDL-C and northern location (beta = 0.206, $p = 0.002$) (Model $R^2 = 0.362$, $F = 27.1$, $p < 0.0001$). No PM2.5 and age (beta = 0.305, $p = 0.125$), or PM2.5 and location (beta = 0.093, $p = 0.056$) interactions were identified.

Table 4. Determinants of Risk Factors for Carotid IMT.

Risk Factors	Southern Chinese *		Northern Chinese **		Overall Cohort ***	
	Beta Value	<i>p</i> -Value	Beta Value	<i>p</i> -Value	Beta-Value	<i>p</i> -Value
Age (yr)	0.393	<0.0001	0.385	<0.0001	0.396	<0.0001
Gender	0.146	0.043	0.058	0.357	0.127	0.006
Smoking status	0.061	0.388	0.157	0.010	0.091	0.053
BMI	0.074	0.299	0.088	0.103	0.121	0.005
MS	0.119	0.095	0.110	0.039	0.099	0.019
Homocysteine	0.048	0.501	0.137	0.014	0.121	0.010
LDL-C	0.084	0.204	0.145	0.003	0.136	0.004
MTHFR	0.046	0.463	−0.065	0.223	−0.026	0.554
PM2.5	0.334	<0.0001	0.033	0.471	0.368	<0.0001
Location	−	−	−	−	−0.206	0.002

* Model $R^2 = 0.451$; F -value = 13.3; $p < 0.0001$. ** Model $R^2 = 0.335$; F -value = 7.67; $p < 0.0001$. *** Model $R^2 = 0.362$; F -value = 27.1; $p < 0.0001$. BMI: Body Mass Index. IMT: Intima-media thickness. LDL-C: Low Density Lipoprotein Cholesterol. MS: Metabolic Syndrome. MTHFR: Methylenetetrahydrofolate Reductase Gene Polymorphisms. PM2.5: Particulate Matters < 2.5 μ m in Diameter.

4. Discussion

The present report further confirms the detrimental impact of PM2.5 air pollution on atherogenic processes in modernizing China, independent of traditional atherosclerotic risk factors [12,18,30]. Specifically, Northern Chinese were more prone to higher carotid IMT and worse arterial endothelial dysfunction, compared with Southern Chinese. This may be attributed to more smoking, higher SBP, DBP, homocysteine, PM2.5 exposure and metabolic syndrome rates, and lower (unfavorable) vitamin B12 and folate levels. Metabolic syndrome includes the impact of several atherosclerotic risk factors i.e., blood pressure, waist circumference, HDL and LDL-cholesterol and fasting glucose. We and others have documented its detrimental impact on atherogenesis, independent of PM2.5 [18,31].

Multivariate regression of the overall cohort suggested that PM2.5 exposure and location were important determinants of carotid IMT, independent of homocysteine and other traditional vascular risk factors. Higher homocysteine presumably could be related to unique Northern dietary pattern of low folate and vitamin B12 intakes, the formal documentation of which is awaited with interest. On this issue, we have previously confirmed the beneficial effects of vitamin B12 and folate supplementations on atherogenic process (FMD and IMT) in 207 Northern Chinese adult subjects with subnormal nutritional status [32].

Greater carotid IMT is an important prognostic atherosclerosis surrogate related to later risk of stroke and cardiovascular diseases [33]. We have previously shown that increased carotid IMT is a marker of subclinical atherosclerosis in westernized as compared with rural Southern Chinese [15]. To contextualize the magnitude of the IMT difference (19.3%, 0.11 mm), a 0.16 mm increase in carotid IMT has been associated with 41% increase in stroke and 43% increase in acute myocardial infarction over a follow up period of 2–7 years [33]. The 19.3% difference in carotid IMT in the present study was far greater than the kind of difference between diabetic and non-diabetic Chinese adults [17].

4.1. Limitations

We acknowledge some limitations in our present study. Firstly, we have not explored inflammatory markers, such as fibrinogen, C-reactive protein or cytokine family, in the Northern compared with Southern Chinese. This will be valuable for confirming the hypothesis of generalized vascular inflammation in AP-induced atherogenic process. Secondly, the concentration and LDL-C happened (by chance) to be lower, but hyperemia

(by ultrasound) to be higher in Northern Chinese. These, however, have not contributed to the worse FMD and IMT results, since these two factors would have been associated with better rather than worse FMD and IMT levels in the Northern Chinese. Thirdly, we have identified FMD, an early atherosclerotic surrogate, is lower in Northern Chinese on univariate analyses, but its relationship with PM_{2.5} concentration is borderline only on multivariate analyses. FMD is more labile and dynamic compared with carotid IMT measurement, subjected to daily fluctuation of PM_{2.5} concentration. This was measured once only during the study period. Perhaps more FMD measurements for individual subject over the study period may illuminate the real impact of PM_{2.5} on FMD. Fourthly, realtime long term PM_{2.5} measurement is more informative and better than yearly mean PM_{2.5} estimation for studying its relationship with more labile FMD measurement. This, however, has logistic and economic implications which may not be readily resolved.

4.2. General Remarks

We propose carotid IMT and brachial FMD as two surrogate targets for measuring the success of possible prevention of PM_{2.5}-related atherogenesis in Chinese. While the nationwide adoption of PM_{2.5}-reduction policies will be welcomed in both Northern and Southern Chinese, our present study would suggest the possible importance of micronutrient (folate and vitamin B12) deficiencies in some areas of Northern China, apart from control of vascular risk factor [31]. In addition, strategies on a more personal approach may be advisable particularly in southern China, including face-mask and filtering devices for indoor air pollution [34–37], as well as exploration of potential medical therapies to reduce the impact of atherosclerosis.

5. Conclusions

PM_{2.5} air pollution in China, in particular in Southern Chinese, is related to atherogenic surrogates, independent of traditional risk factors, with potential implications in both dietary and air pollution reduction strategies for atherosclerosis prevention.

Author Contributions: K.W.: Project conception and design, research administration, statistical analysis and interpretation of data, drafting and revision of the article and final approval of the version to be published. C.L.: Provision and interpretation of PM_{2.5} data in China, revision of the article and final approval of the version to be published. Y.Y.: Project conception, interpretation of data, revision of the article and final approval of the version to be published. D.G.: project conception and design, co-administration of the field work at Yu County, revision of the articles and final approval of the version to be published. P.C.: Project conception and design, performance of ultrasonography analysis and interpretation of data, drafting, revision of the article and final approval of the version to be published. T.C.Y.K.: Design of project, interpretation of data, revision of the article and final approval of the version to be published. D.S.C.: Project conception and design, interpretation of data, drafting and revision of the article, and final approval of the version to be published. All authors have read and agreed to the published version of the manuscript.

Funding: This work was supported by The Chinese Atherosclerosis Trust, Madam Leung Kit Wah Project Fund, Dr Stanley Ho Medical Development Foundation (grant and donation), Star Industrial Company and Dr Thomas HC Cheung Trust. They provided unrestricted sponsorships for the present study, without any involvement in study design, data collection, analysis or interpretation, nor in the writing of this report or the decision to submit the paper for publication.

Institutional Review Board Statement: The study was conducted according to the guidelines of the Declaration of Helsinki, and approved by the Institutional Review Board.

Informed Consent Statement: Informed consent was obtained from all subjects involved in the study.

Data Availability Statement: The research data will be available from the corresponding author to the editor and Atmosphere readers on reasonable request.

Acknowledgments: We wish to acknowledge the valuable support of the Chinese Atherosclerosis Trust, Leung Kit Wah Project Fund, Stanley Ho Medical Development Foundation Trust, The Star Industrial Company Fund of The Chinese University of Hong Kong and Thomas HC Cheung Trust

in sponsoring the study. We also acknowledge The Macau Heart Foundation, for helping recruitment of subjects, and the Pathology Department of Centro Hospitalar Conde de Sao Januario in Macau for the blood assays. We acknowledge the superb statistical analyses and clerical work of Guo Cui of the School of Public Health, Mikki Wong and Chu Pui Yan, Daphne, of The Chinese University of Hong Kong.

Conflicts of Interest: The authors declare no conflict of interest.

References

1. Lloyd-Jones, D.; Adams, R.; Carnethon, M.; de Simone, G.; Ferguson, T.B.; Flegal, K.; Ford, E.; Furie, K.; Go, A.; Greenlund, K.; et al. American Heart Association Statistics Committee and Stroke Statistics Subcommittee. Heart disease and stroke statistics—2009 update: A report from the American Heart Association Statistics Committee and Stroke Statistics Subcommittee. *Circulation* **2009**, *119*, 480–486. [PubMed]
2. Roth, G.A.; Johnson, C.; Abajobir, A.; Abd-Allah, F.; Abera, S.F.; Abyu, G.; Ahmed, M.; Aksut, B.; Alam, T.; Alam, K.; et al. Global regional and national burden of cardiovascular diseases for 10 causes, 1990–2015. *J. Am. Coll. Cardiol.* **2017**, *70*, 1–25. [CrossRef] [PubMed]
3. Danaei, G.; Ding, E.L.; Mozaffarian, D.; Taylor, B.; Rehm, J.; Murray, C.J.L.; Ezzati, M. The preventable causes of death in the United States: Comparative risk assessment of dietary, lifestyle, and metabolic risk factors. *PLoS Med.* **2009**, *6*, e1000058. [CrossRef] [PubMed]
4. Rajagopalan, S.; Al-Kini, S.G.; Brook, R.D. Air pollution and cardiovascular disease. *J. Am. Coll. Cardiol.* **2018**, *72*, 2054–2070. [CrossRef] [PubMed]
5. Liang, F.; Liu, F.; Huang, K.; Yang, X.; Li, J.; Xiao, Q.; Chen, J.; Liu, X.; Cao, J.; Shen, C.; et al. Longterm exposure to fine particulate matter and cardiovascular disease in China. *J. Am. Coll. Cardiol.* **2020**, *75*, 707–717. [CrossRef]
6. Brook, R.D.; Rajagopalan, S.; Pope, C.A., 3rd; Brook, J.R.; Bhatnagar, A.; Diez-Roux, A.V.; Holguin, F.; Hong, Y.; Luepker, R.V.; Mittleman, M.A.; et al. American Heart Association Council on Epidemiology and Prevention, Council on the Kidney in Cardiovascular Disease, and Council on Nutrition, Physical Activity and Metabolism. Particulate matter air pollution and cardiovascular disease: An update to the scientific statement from the American Heart Association. *Circulation* **2010**, *121*, 2331–2378.
7. Jasarevic, T.; Thomas, G.; Osseiran, N. 7 Million Premature Deaths Annually Lined to Air Pollution. WHO Media Centre 2014. Available online: <https://www.who.int/mediacentre/news/releases/2014/air-pollution/en/> (accessed on 25 March 2014).
8. Arden Pope, C., 3rd; Burnett, R.T.; Thurston, G.D.; Thun, M.J.; Calle, E.E.; Krewski, D.; Godleski, J.J. Cardiovascular mortality and long-term exposure to particular air pollution – Epidemiological evidence of general pathophysiological pathways of disease. *Circulation* **2004**, *109*, 71–77. [CrossRef]
9. Pepine, C.J. The effects of angiotensin-converting enzyme inhibition on endothelial dysfunction: Potential role in myocardial ischemia. *Am. J. Cardiol.* **1998**, *82*, 23S–27S. [CrossRef]
10. Roux, A.V.D.; Auchincloss, A.H.; Franklin, T.G.; Raghunathan, T.; Barr, R.G.; Kaufman, J.; Astor, B.; Keeler, J. Long-term exposure to ambient particulate matter and prevalence of subclinical atherosclerosis in the Multi-Ethnic Study of Atherosclerosis. *Am. J. Epidemiol.* **2008**, *167*, 667–675. [CrossRef]
11. Bauer, M.; Moebus, S.; Möhlenkamp, S.; Dragano, N.; Nonnemacher, M.; Fuchsluger, M.; Kessler, C.; Jakobs, H.; Memmesheimer, M.; Erbel, R.; et al. HNR Study Investigative Group. Urban particulate matter air pollution is associated with subclinical atherosclerosis: Results from the HNR (Heinz Nixdorf Recall) study. *J. Am. Coll. Cardiol.* **2010**, *56*, 1803–1808. [CrossRef]
12. Woo, K.S.; Chook, P.; Hu, Y.J.; Lao, X.Q.; Lin, C.Q.; Lee, P.; Kwok, C.; Wei, A.N.; Guo, D.S.; Yin, Y.H.; et al. The Impact of Particulate Matter Air Pollution (PM_{2.5}) on Atherosclerosis in Modernizing China: The report from CATHAY Study. *Int. J. Epidemiol.* **2020**, *50*, 1–11. [CrossRef]
13. Yang, J.; Siri, J.G.; Remais, J.V.; Cheng, Q.; Zhang, H.; Chan, K.K.Y.; Sun, Z.; Zhao, Y.; Cong, N.; Li, X.; et al. The Tsinghua-lancet commission on healthy cities in China: Unlocking the power of cities for a healthy China. *Lancet* **2018**, *391*, 2140–2184. [CrossRef]
14. Woo, K.S.; Robinson, J.T.; Chook, P.; Adams, M.R.; Yip, G.; Mai, Z.J.; Lam, C.W.; Sorensen, K.E.; Deanfield, J.E.; Celermajer, S.D. Differences in the effect of cigarette smoking on endothelial function in Chinese and white adults. *Ann. Int. Med.* **1997**, *127*, 372–375. [CrossRef]
15. Woo, K.S.; Chook, P.; Raitakari, O.T.; McQuillan, B.; Feng, J.Z.; Celermajer, D.S. Westernization of Chinese adults and increased subclinical atherosclerosis. *Arter. Thromb. Vasc. Biol.* **1999**, *19*, 2487–2493. [CrossRef]
16. Thomas, G.N.; Chook, P.; Qiao, M.; Huang, X.S.; Leong, H.C.; Celermajer, D.S.; Woo, K.S. Deleterious impact of “high normal” glucose levels and other metabolic syndrome components on arterial endothelial function and intima-media thickness in apparently healthy Chinese subject: The CATHAY study. *Arterioscler. Thromb. Vasc. Biol.* **2004**, *24*, 739–743. [CrossRef]
17. Woo, K.S.; Chook, P.; Yu, C.W.; Sung, R.Y.T.; Qiao, M.; Leung, S.S.F.; Lam, C.W.K.; Metreweli, C.; Celermajer, D.S. Effects of diet and exercise on obesity-related vascular dysfunction in children. *Circulation* **2004**, *109*, 1981–1986. [CrossRef] [PubMed]
18. Woo, K.S.; Timothy, K.C.Y.; Chook, P.; Hu, Y.J.; Yin, Y.H.; Lin, C.Q.; Lau, K.H.A.; Lee, P.W.A.; Celermajer, D.S. Independent Effects of Metabolic Syndrome and Air Pollution (PM_{2.5}) on Atherosclerosis in Modernizing China. *Austin J. Public Health Epidemiol.* **2021**, *8*, 1097.

19. Zimmet, P.; Alberti, K.; George, M.M.; Rios, M.S. A new International Diabetes Federation (IDF) worldwide definition of the metabolic syndrome: The rationale and the results. *Rev. Esp. Cardiol.* **2005**, *58*, 1371–1376. [CrossRef]
20. Woo, K.S.; Hu, Y.J.; Chook, P.; Wei, A.N.; Chan, R.; Yin, Y.H.; Celermajer, D.S. A Tale of Three Gorges in the Yangtze River: Comparing the Prevalence of Metabolic Syndrome According to ATP III, WHO, and IDF Criteria and the Association with Vascular Health in Modernizing China. *Metab. Syndr. Relat. Disord.* **2019**, *17*, 137–142. [CrossRef]
21. Li, C.; Lau, A.K.H.; Mao, J.; Chu, D.A. Retrieval, validation, and application of the 1-km aerosol optical depth from MODIS measurements over Hong Kong. *IEEE Trans. Geosci. Remote Sens.* **2005**, *43*, 2650–2658.
22. Lin, C.Q.; Li, Y.; Yuan, Z.B.; Lau, A.K.H.; Li, C.C.; Fung, J.C.H. Using satellite remote sensing data to estimate the high-resolution distribution of ground-level PM_{2.5}. *Remote Sens. Environ.* **2015**, *156*, 117–128. [CrossRef]
23. Lin, C.Q.; Liu, G.; Lau, A.K.H.; Li, Y.; Li, C.C.; Fung, J.C.H.; Lao, X.Q. High-resolution satellite remote sensing of provincial PM_{2.5} trends in China from 2001 to 2015. *Atmos. Environ.* **2018**, *180*, 110–116. [CrossRef]
24. Celermajer, D.S.; Sorensen, K.; Gooch, V.; Spiegelhalter, D.J.; Miller, O.I.; Sullivan, I.D.; Lloyd, J.K.; Deanfield, J.E. Non-invasive detection of endothelial dysfunction in children and adults at risk of atherosclerosis. *Lancet* **1992**, *340*, 1111–1115. [CrossRef]
25. Woo, K.S.; Chook, P.; Yu, C.W.; Sung, R.Y.T.; Qiao, M.; Leung, S.S.F.; Lam, C.W.K.; Metreweli, C.; Celermajer, D.S. Overweight in children is associated with arterial endothelial dysfunction and intima-media thickening. *Int. J. Obes.* **2004**, *28*, 852–857. [CrossRef]
26. Salonen, J.T.; Salonen, R. Ultrasonographically assessed carotid morphology and the risk of coronary heart disease. *Arterioscler. Thromb. Vasc. Biol.* **1991**, *11*, 1245–1249. [CrossRef] [PubMed]
27. Bots, M.L.; Hoes, A.W.; Koudstaal, P.J.; Hofman, A.; Grobbee, D.E. Common carotid intima-media thickness and risk of stroke and myocardial infarction: The Rotterdam Study. *Circulation* **1997**, *96*, 1432–1437. [CrossRef]
28. Touboul, P.J.; Hennerici, M.G.; Meairs, S.; Adams, H.; Amarenco, P.; Desvarieux, M.; Ebrahim, S.; Fatar, M.; Hernandez Hernandez, R.; Kownator, S.; et al. Advisory Board of the 3rd Watching the Risk Symposium 2004, 13th European Stroke Conference. Mannheim intima-media thickness consensus. *Cereb. Dis.* **2004**, *18*, 346–349. [CrossRef] [PubMed]
29. Schulz, K.F.; Grimes, D.A. Sample size calculations in randomised trials: Mandatory and mystical. *Lancet* **2005**, *365*, 1348–1353. [CrossRef]
30. Li, H.; Cai, J.; Chen, R.; Zhao, Z.; Ying, Z.; Wang, L.; Chen, J.; Hao, K.; Kinney, P.L.; Chen, H.; et al. Particulate matter exposure and stress hormone levels: A randomized, double-blind, crossover trial of air purification. *Circulation* **2017**, *136*, 618–627. [CrossRef] [PubMed]
31. Maloberti, A.; Bombelli, M.; Vallerio, P.; Milani, M.; Cartella, I.; Tavecchia, G.; Tognola, C.; Grasso, E.; Sun, J.; de Chiara, B.; et al. Metabolic syndrome is related to vascular structural alterations but not to functional ones both in hypertensives and healthy subjects. *Nutr. Metab. Cardiovas. Dis.* **2021**, *31*, 1044–1052. [CrossRef]
32. Woo, K.S.; Kwok, T.C.Y.; Celermajer, D.S. Vegan diet, subnormal vitamin B-12 status and cardiovascular health. *Nutrients* **2014**, *6*, 3259–3273. [CrossRef] [PubMed]
33. O'Leary, D.H.; Polak, J.F.; Kronmal, R.A.; Manolio, T.A.; Burke, G.L.; Wolfson, S.K., Jr. Carotid-artery intima and media thickness as a risk factor for myocardial infarction and stroke in older adults. *N. Engl. J. Med.* **1999**, *340*, 14–22. [CrossRef]
34. Baumgartner, J.; Smith, K.R.; Chockalingam, A. Reducing CVD through improvements in household energy - Implications for policy-relevant research. *Global. Heart* **2012**, *7*, 243–247. [CrossRef] [PubMed]
35. Langrish, J.; Mills, N.; Chan, J.; Leseman, D.; Aitken, R.; Fokkens, P.; Cassee, F.; Li, J.; Donaldson, K.; Newby, D.; et al. Beneficial cardiovascular effects of reducing exposure to particulate air pollution with a simple facemask. *Part. Fibre Toxicol.* **2009**, *6*, 8. [CrossRef]
36. Allen, R.W.; Carlsten, C.; Karlen, B.; Leckie, S.; van Eeden, S.; Vedal, S.; Wong, I.; Brauer, M. An air filter intervention study of endothelial function among healthy adults in a woodsmoke-impacted community. *Am. J. Respir. Crit. Care Med.* **2011**, *183*, 1222–1230. [CrossRef] [PubMed]
37. Rajagopalan, S.; Brook, R.D. Indoor-outdoor air pollution continuum and CVD burden—An opportunity for improving global health. *Glob. Heart* **2012**, *7*, 207–213. [CrossRef]

Article

Mass Concentration, Chemical Composition, and Source Characteristics of PM_{2.5} in a Plateau Slope City in Southwest China

Jianwu Shi ¹, Yinchuan Feng ¹, Liang Ren ¹, Xiuqing Lu ², Yaoqian Zhong ¹, Xinyu Han ^{1,2,*} and Ping Ning ¹

¹ Faculty of Environmental Science and Engineering, Kunming University of Science and Technology, Kunming 650500, China; Shijianwu@kust.edu.cn (J.S.); 20182207073@stu.kust.edu.cn (Y.F.); renliang@stu.kust.edu.cn (L.R.); zhong@kust.edu.cn (Y.Z.); ningping58@sina.com (P.N.)

² Architectural Engineering Institute, Kunming University of Science and Technology, Kunming 650500, China; Lxq058258@126.com

* Correspondence: 20110020@kust.edu.cn; Tel.: +86-15912128009

Citation: Shi, J.; Feng, Y.; Ren, L.; Lu, X.; Zhong, Y.; Han, X.; Ning, P. Mass Concentration, Chemical Composition, and Source Characteristics of PM_{2.5} in a Plateau Slope City in Southwest China. *Atmosphere* **2021**, *12*, 611. <https://doi.org/10.3390/atmos12050611>

Academic Editors: Duanyang Liu, Kai Qin and Honglei Wang

Received: 22 April 2021

Accepted: 5 May 2021

Published: 8 May 2021

Publisher's Note: MDPI stays neutral with regard to jurisdictional claims in published maps and institutional affiliations.



Copyright: © 2021 by the authors. Licensee MDPI, Basel, Switzerland. This article is an open access article distributed under the terms and conditions of the Creative Commons Attribution (CC BY) license (<https://creativecommons.org/licenses/by/4.0/>).

Abstract: In order to investigate the seasonal variations in the chemical characteristics of PM_{2.5} at the plateau slope of a mountain city in southwest China, 178 PM_{2.5} filters (89 quartz and 89 Teflon samples for PM_{2.5}) were collected to sample the urban air of Wenshan in spring and autumn 2016 at three sites. The mass concentrations, water-soluble inorganic ions, organic and inorganic carbon concentrations, and inorganic elements constituting PM_{2.5} were determined, principal component analysis was used to identify potential sources of PM_{2.5}, and the backward trajectory model was used to calculate the contribution of the long-distance transmission of air particles to the Wenshan area. The average concentration of PM_{2.5} in spring and autumn was $44.85 \pm 10.99 \mu\text{g}/\text{m}^3$. Secondary inorganic aerosols contributed 21.82% and 16.50% of the total PM_{2.5} in spring and autumn, respectively. The daily mean value of OC/EC indicated that the measured SOC content was generated by the photochemical processes active during the sampling days. However, elements from anthropogenic sources (Ti, Si, Ca, Fe, Al, K, Mg, Na, Sb, Zn, P, Pb, Mn, As and Cu) accounted for 99.38% and 99.24% of the total inorganic elements in spring and autumn, respectively. Finally, source apportionment showed that SIA, dust, industry, biomass burning, motor vehicle emissions and copper smelting emissions constituted the major components in Wenshan. This study is the first to investigate the chemical characterizations and sources of PM_{2.5} in Wenshan, and it provides effective support for local governments formulating air pollution control policies.

Keywords: PM_{2.5}; PCA; backward trajectories; chemical composition; source

1. Introduction

In recent decades, with rapid economic development, industrialization and urbanization in China, the number of motor vehicles and the total energy consumption have increased, and atmospheric particulate matter (PM) has become one of the most significant air contaminants [1–3]. PM, particularly PM_{2.5} (aerodynamic diameter $\leq 2.5 \mu\text{m}$), can exist in the atmosphere for a long time, which is conducive to its long-distance transport through the atmosphere and deposition towards remote areas. During long-range transport, PM_{2.5} carries abundant anthropogenic pollutants and has a serious impact on the global and regional climate, the visibility and composition of the atmosphere, the global biogeochemical cycle and the activation of cloud condensation nuclei (CCN) [4–6].

PM_{2.5} has been widely studied in recent years in China due to its potential impacts on air quality and human health. Water-soluble inorganic ions (WSIIs), organic carbon (OC) particles, inorganic carbon (EC) particles, and inorganic elements (IEs), as the main chemical components of PM_{2.5}, have been extensively studied in China [7–9]. WSIIs are dominated by secondary inorganic aerosols (SIAs), including NH_4^+ , NO_3^- , and SO_4^{2-} .

OC is composed of thousands of organic compounds and contains many toxic substances. Heavy metals are an important part of the inorganic elements comprising $PM_{2.5}$, such as Fe, Zn, Cu and Pb [10–12].

Whether worldwide or only in China, it is essential to reduce $PM_{2.5}$ concentrations to control their sources. The key point in formulating policies for the government to control $PM_{2.5}$ pollution is the result of source apportionment and reliable source quantification [13,14]. In fact, $PM_{2.5}$ is usually sourced by the emission of pollutants, and its classification is very complex, including its anthropogenic and natural sources and gas and particle phases [15,16]. In addition, $PM_{2.5}$ forms secondary pollutants from primary emissions through photochemical reactions after being released from pollution sources, making it difficult to quantify its impacts [17–19]. The contribution levels of different sources in the air can be quantitatively estimated by using the receptor model. Generally, researchers have identified the possible sources of $PM_{2.5}$ as traffic and industrial, coal combustion, biomass burning and secondary inorganic aerosol sources [20,21].

In recent years, most studies have generally focused on the Jing-Jin-Ji region and its coastal areas with severely degraded atmospheric environments in China [22–24]. Only a few researchers have investigated $PM_{2.5}$ pollution in Yunnan Province, which is a remote southwestern region. More research has been conducted in areas such as Kunming and Yuxi [25–27]. Despite the economic backwardness of the remote southwestern mountains, there are still cases of $PM_{2.5}$ exceeding the standard every year [28–30]. Therefore, we should pay more attention to these areas to improve their air quality.

Wenshan, a developing industrialized city in southwest China, has a high degree of air pollution, mainly resulting from the presence of $PM_{2.5}$ in the atmosphere. Furthermore, Wenshan is located in the basin valley on the plateau, and the urban area is surrounded by high mountains, which aggravate particulate pollution. Wenshan is chosen as the study area to conduct $PM_{2.5}$ sampling during the spring and autumn seasons at three monitoring sites. The concentrations of $PM_{2.5}$, WSIs, OC, EC and IEs are analyzed and discussed in the current study. Principal component analysis (PCA) is used for $PM_{2.5}$ source apportionment to analyze the pollution sources. Potential major contributors were identified on the basis of PCA and local environmental background information. The details of the pollution characteristics and the results of $PM_{2.5}$ source apportionment in this study can provide the local government with reasonable and effective measures to slow down atmospheric pollution with $PM_{2.5}$.

2. Methods

2.1. Sampling Site and Sample Collection

Wenshan is a developing industrialized city with half a million inhabitants in an urban area of 75 km². With a longitude of 103°43′–104°27′ E and a latitude of 23°06′–23°44′ N, Wenshan lies in southwest China (Figure 1), which is the transition zone of the Yunnan-Guizhou Plateau and Vietnam Basin.

Wenshan lies in a small basin valley on the plateau and is surrounded by mountains on three sides. The terrain inclines from northwest to southeast, and the mountain range runs almost from north to south. Therefore, a corridor topography consisting of high points on both sides and low points in the middle is formed. The relative altitude difference is 1751.2 m, with the highest altitude of 2991.2 m in Bozhu Mountain and the lowest of 1240 m in the urban area. Wenshan is dominated by a subtropical monsoon climate, which is characterized by a long spring and autumn, no bitter cold in winter, no brutal heat in summer and delightful weather in all seasons. Airflow near the ground can only enter the urban area from the southeast. The cold air in Siberia from the north is obstructed by mountains, and the monsoon of the Beibu Gulf and the Bay of Bengal traveling from the southeast flows right into the urban area, which forms comfortable temperatures, low wind speeds and high ultraviolet (UV) light conditions throughout the year. Strong ultraviolet light is conducive to the formation of photochemical atmospheric effects, and the conditions of low pressure and low oxygen can lead to the incomplete combustion of fuel and can

increase the resulting pollution emissions. The conditions of low wind speed (<3 m/s) and the large diurnal temperature variation readily form an inversion layer, hindering the diffusion of pollutants.

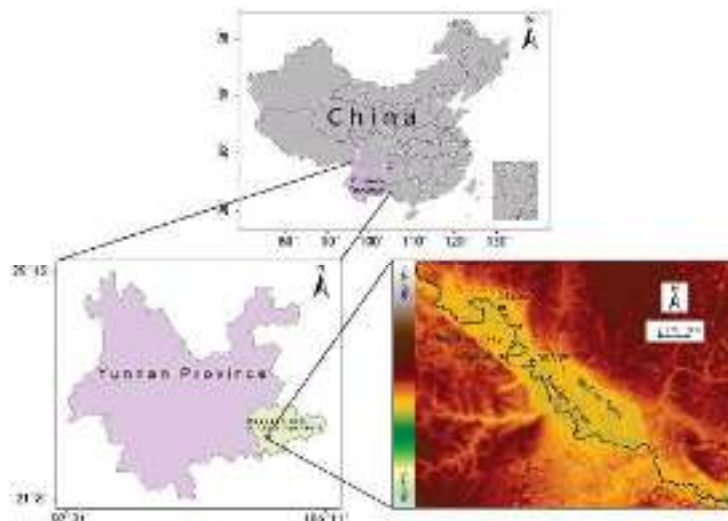


Figure 1. Location of the sampling site in Wenshan, China.

Measurement campaigns of $PM_{2.5}$ sampling at three sites at the Convenience Service Center of Wenshan (CSCW), Water Authority of Wenshan (WAW) and Environmental Monitoring Station of Wenshan (EMSW) in Wenshan city (Figure 1), were carried out in two periods in 2016, i.e., 19 April to 3 May and 12 October to 26 October. Daily measurements of 22 ± 1 h with an intelligent mid-volume atmospheric particulate sampler (TH-150F, Tianhong, China) were conducted at a 100 L/min sample flow. Teflon filters (China, 90 mm) were used to analyze IEs, and quartz filters (PALL Inc., USA, 90 mm) were used to analyze OC particles, EC components and WSIs. A total of 178 $PM_{2.5}$ samples and 12 blank samples were collected. After sampling, the filters were individually placed into plastic boxes and put into a freezer at -20°C until transport and subsequent analysis.

2.2. Chemical Analysis and Quality Control

2.2.1. WSII Analysis

The anion (i.e., F^{-} , Cl^{-} , SO_4^{2-} and NO_3^{-}) and cation (i.e., K^{+} , Ca^{2+} , Mg^{2+} and NH_4^{+}) concentrations were measured by ion chromatography (DX-600, Dionex, USA). This system was outfitted with a separation column (Dionex AS-14A for anions and CS-12A for cations) and a guard column (Dionex AG14A for anions and CG12A for cations). A gradient weak base eluent (3.5 mmol/L Na_2CO_3 ; 1 mmol/L $NaHCO_3$) was used for anion detection, while a weak acid eluent (18 mmol/L methanesulfonic acid) was used for cation detection. The measurement error of each ion in a standard solution is within 10%, and the average relative standard deviations of anions and cations are 3.0% and 4.0%, respectively. For quality assurance, two blank spaces were detected in each batch of samples, and the test was carried out at 10%. At least six standard solution concentrations needed to be mixed for each ion component.

2.2.2. Elements Analysis

Li, Be, P, Cr, Mn, Bi, Co, Ni, Cu, Sr, Mo, Cs, Cd, Tl, Pb, Th, Sc, V, As, Rb, Y, Zr, Sn, Sb, La, Ce, U, Sm and W were analyzed by inductively coupled plasma-mass spectrometry (ICP-MS). Mg, Ca, K, Fe, Al, Ba, Zn, Na and Si were analyzed by inductively coupled plasma-atomic emission spectrometry (ICP-AES).

2.2.3. OC and EC Analysis

The concentrations of OC and EC were analyzed by DRI Model 2001 OC/EC Analyser, which was developed by the American Desert Institute (DRI). The main testing principle of this method is as follows: the sample is heated and converted into CO₂ under different temperature gradients and gas environments. CO₂ is reduced to CH₄ by catalyzing MnO₂ and is detected by using a flame ion detector (FID). Then, using a 633 nm helium/neon laser to detect the anti-light intensity of filter paper to detect the production of organic pyrolysis carbon (OPC), eight different carbon components (OC1, OC2, OC3, OC4, OPC, EC1, EC2, and EC3) were obtained. IMPROVE (Interagency Monitoring of Protected Visual Environments) defines OC as OC1+OC2+OC3+OC4+OCPyro and EC as EC1+EC2+EC3+OCPyro. The detection limits were 0.82 (OC), 0.19 (EC) and 0.93 (TC) µg/cm², and the measuring range was 0.2~750 µg/cm².

2.2.4. Principal Component Analysis (PCA) Modeling

PCA is an important multivariate statistical tool that can reduce the dimensionality of large datasets and extract the number of principal components needed to explain all the variance of such datasets, which is much less than the original number of variables [31,32]. PCA extracts new variables by the correlation between all variables, which contain most of the information about the data, called principal components. Each variable has the same significance, and each topic has the same weight. The first component extracted explains the maximum amount of data variance. The maximum amount of remaining data variance will be further explained by successive components [33–35]. This process sets up the orthogonal distribution of components to each other, and the result of the regression adjustment of factors is simple and stable, regardless of how large a dataset is and how many variables are included in the study [36].

2.2.5. HYSPLIT4 Model

The HYSPLIT4 model is a professional model jointly developed by the National Oceanic and Atmospheric Administration (NOAA) Air Resources Laboratory (ARL) and the Australian Bureau of Meteorology (BOM) in the past 20 years to calculate and analyze the transport and diffusion trajectories of atmospheric pollutants. The model has a relatively complete transport, diffusion and sedimentation model that can handle multiple meteorological element input fields, multiple physical processes, and different types of pollutant emission sources. It is widely used in the study of the transmission and diffusion of multiple pollutants in various regions. In this study, the independent version of the backward trajectory model was used, the auxiliary software package was used (GUI; Ghostscript; ImageMagick), and the meteorological data were obtained through NCEP (National Centers for Environmental Prediction) and GDAS (Global Data Assimilation System).

2.2.6. Quality Control

The quartz filters were baked at 450 °C for 5 h in a muffle furnace before sampling to identify the possible presence of organics. All filters were placed in a clean room (temperature of 25 °C ± 5; relative humidity of 50 ± 5%) for 48 h and weighed by a high-precision electronic balance (EX125ZH) with an accuracy of 10 mg before and after sampling. Each filter was weighed twice, with the difference between the two results not exceeding 0.2 mg for quartz filters and 0.02 mg for Teflon filters, to guarantee the precision of the weighting results. All filters were stored in a freezer at −20 °C before analysis to prevent the loss of volatile components.

In the sample analysis process, the instrument was calibrated with standard gas before and after the sample analysis. Then, one sample was randomly selected from every 10 samples for parallel analysis, and the standard sample was measured twice a week. The recovery rate of the standard sample was 98%~102%. Finally, the system blank of the instrument and the blank of the laboratory system were measured every week. The results

showed no contamination during sample handling and collection, as assured by the quality assurance and control (QC/QA) procedures.

3. Results and Analyses

3.1. Concentration Characteristics of PM_{2.5}

During the two sampling campaigns, the mass concentrations (from Telfon filters) of PM_{2.5} ranged from 29.11 µg/m³ to 62.03 µg/m³ in spring and from 24.46 µg/m³ to 60.08 µg/m³ in autumn (Figure 2). The overall concentration of PM_{2.5} is higher in spring than that in autumn. The concentration on individual days in autumn is higher than that in spring, which may be related to changes in meteorological conditions. The daily concentration levels of PM_{2.5} were all within Chinese National Ambient Air Quality Standards II (75 µg/m³). In addition, the total average concentration of PM_{2.5} in spring and autumn (44.85 ± 10.99 µg/m³) was higher than Standard II (35.00 µg/m³) (GB3095-2012), and was 3.0 times higher than the annual standard concentration in the USA (15 µg/m³). These values are lower than those of developed cities in the plains of China, such as Beijing, Tianjing and Shanghai [37,38]. Furthermore, the concentration of PM_{2.5} in Wenshan was lower than that in some plateau cities, such as Guiyang and Kunming [39]. In our previous research, we found that the dust emission volume of Wenshan was 1164 t, accounting for 52.9% of the total emissions. PM_{2.5} pollution may be associated with city construction, and the floor space of buildings under construction was 5.48×10^6 m² during 2016 in Wenshan. The mean concentrations of PM_{2.5} decreased from spring (48.00 ± 11.01 µg/m³) to autumn (41.64 ± 10.10 µg/m³). There were 10 and 5 days in spring and autumn, respectively, that exceeded the total average concentration, which means that were 62.5% of the days in spring exceeded the total average concentration, and it was twice that in autumn. This seasonal mean concentration variation is attributed to the primary influence of meteorological characteristics and source emissions.

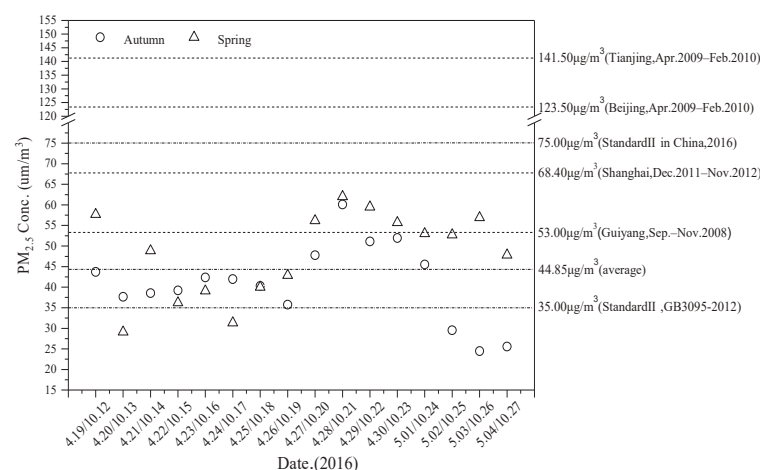


Figure 2. The daily mass concentration of PM_{2.5} during sampling.

3.2. Chemical Composition Characteristic of PM_{2.5}

3.2.1. WSIs Levels

The concentrations of WSIs were 11.75 ± 3.25 and 12.50 ± 3.40 µg/m³ in spring and autumn, respectively. In PM_{2.5}, the concentrations of K⁺, NH₄⁺, Ca²⁺, Mg²⁺, Cl[−], F[−], NO₃[−] and SO₄^{2−} were 0.67, 2.54, 1.28, 0.07, 0.24, 0.16, 1.25 and 5.53 µg/m³ in spring and 0.59, 3.17, 0.78, 0.07, 0.38, 0.22, 0.77 and 6.53 µg/m³ in autumn, respectively. The annual concentration of WSIs was 12.15 µg/m³ and occupied 26.91% of the total PM_{2.5}. This result indicated that WSIs were one of the main components of PM_{2.5}. The mass concentrations of sulfate occupied 49.67% of the total WSIs, followed by NH₄⁺ (23.50%), Ca²⁺ (8.60%), NO₃[−] (8.37%), K⁺ (5.21%), Cl[−] (2.52%), F[−] (1.56%), and Mg²⁺ (0.57%). The dominant compounds were secondary inorganic aerosols (SIAs, including NO₃[−], SO₄^{2−}

and NH_4^+), with concentrations accounting for more than 80% of the total WSII mass of $\text{PM}_{2.5}$. The concentrations of WSII in Wenshan are shown in Table 1 and compared to other typical cities, such as Kunming [30] and Guiyang [40] on the plateau and Beijing [41] and Nanjing [42] on the plain. Compared to other Chinese studies, most of the ionic species identified in research are found to be on the lower side. Compared with Kunming and Guiyang, the concentration of SO_4^{2-} was lowest, which is consistent with the lagged industrial development of Wenshan. These results show that the WSII concentrations at Wenshan were impacted more by local pollution sources (e.g., biomass burning, agricultural dust, construction dust, etc.) [43].

Table 1. Mean concentrations of WSII sampled in Wenshan in 2016 compared with data from other sites ($\mu\text{g}/\text{m}^3$).

Ion	Wenshan	Kunming [30]	Guiyang [40]	Beijing [41]	Nanjing [42]
K^+	0.63 ± 0.24	0.77	0.41	1.90	1.2
Ca^{2+}	1.04 ± 0.5	2.83	1.77	3.92	0.7
Mg^{2+}	0.07 ± 0.02	0.30	0.20	0.76	0.2
NH_4^+	2.81 ± 1.16	0.52	4.29	12.47	4.5
Cl^-	0.31 ± 0.19	0.72	1.30	6.76	1.9
F^-	0.19 ± 0.07	0.54	0.03	-	0.2
SO_4^{2-}	5.98 ± 2.07	9.72	17.43	21.60	5.1
NO_3^-	1.00 ± 0.40	0.51	1.34	20.552	9.1

SIAs were the dominant ions in the $\text{PM}_{2.5}$ component in both autumn and spring. The spring and autumn concentrations of SIAs follow the order $\text{SO}_4^{2-} > \text{NH}_4^+ > \text{NO}_3^-$ (Figure 3). One of the reasons is that industrial production leads to the incomplete combustion of fossil fuels, which increases the emission of the gaseous precursor SO_2 [44,45]. Moreover, the geographical structure of urban areas is not favorable to pollutant diffusion in the atmosphere. Another reason is the high conversion rate of SO_2 to $\text{PM}_{2.5}$, which may be due to the relatively high humidity in autumn [46,47]. In addition, NH_4^+ was the most dominant cation in $\text{PM}_{2.5}$ in the two seasons, and the emission of NH_4^+ originated from the nitrogen fertilizers used in agriculture [48,49]. The observed NO_3^- levels were related to the synthetic action of various influencing factors, i.e., precursor NO_x emissions, complex photochemical and heterogeneous reactions and gas-aerosol equilibrium [50,51].

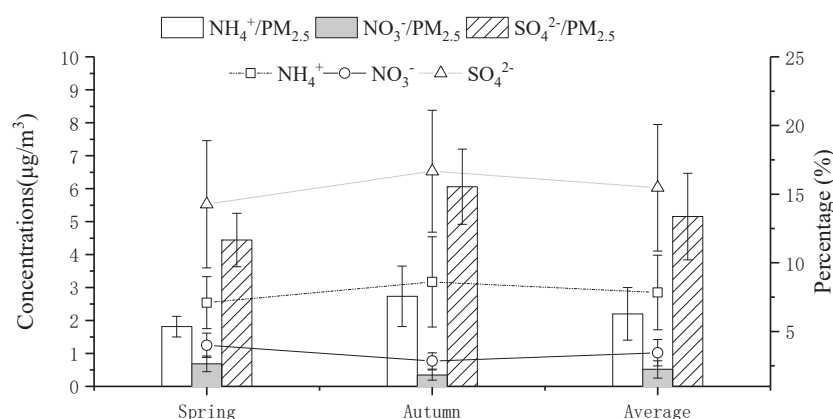


Figure 3. Seasonal variations in SIAs and their ratios in $\text{PM}_{2.5}$ in Wenshan.

To discuss the relative importance of mobile and stationary sources of SO_2 and NO_x , the mass concentration ratio of $\text{NO}_3^-/\text{SO}_4^{2-}$ was used as an indicator [52]. The seasonal variation in $\text{NO}_3^-/\text{SO}_4^{2-}$ in $\text{PM}_{2.5}$ ranged from 0.16 to 0.32 and from 0.09 to 0.18 in spring and autumn, respectively, with an annual mean of 0.18 ± 0.07 , which was lower than the values measured in Shanghai (0.43) [53], Qingdao (0.35) [54] and Taiwan (0.20) [55].

Therefore, with the increasing number of motor vehicles, the contribution of mobile sources is more important than before.

Ion balance calculations are frequently used to investigate the acid base balance of ions in $PM_{2.5}$. The correlation of CE and AE and the variation in CE/AE in the two seasons were calculated. According to the electroneutrality of solutions, AE must be equal to CE [56]. The correlation coefficient between CE and AE for spring ($R^2 = 0.92$) was higher than that for autumn ($R^2 = 0.85$), showing that cations and anions maintained better equilibrium during neutralization in spring. The average CE/AE ratios for autumn (1.72) were higher than those for spring (1.54), which indicates the basic nature of aerosols in which $PM_{2.5}$ is alkaline in the two seasons in Wenshan [57,58].

3.2.2. IEs Levels

The concentrations of IEs in $PM_{2.5}$ in the two seasons are shown in Figure 4. The concentrations of IEs in $PM_{2.5}$ were $4.82 \mu\text{g}/\text{m}^3$ and $4.10 \mu\text{g}/\text{m}^3$ in spring and autumn, respectively. Fifteen main elements, Ti, Si, Ca, Fe, Al, K, Mg, Na, Sb, Zn, P, Pb, Mn, As and Cu, account for 99.38% and 99.24% of the total inorganic elements in spring and autumn, respectively. These fifteen elements play a key role in the estimation of emission sources and are associated with human activity (such as industrial processes, residential activities, and traffic patterns).

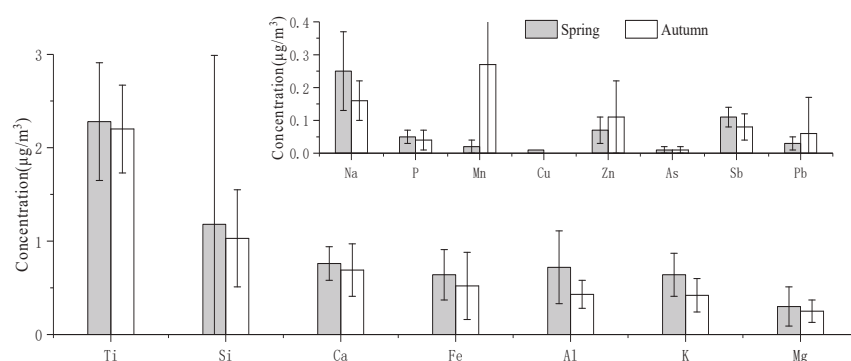


Figure 4. Mean concentrations of inorganic elements in $PM_{2.5}$ sampled at Wenshan.

In the $PM_{2.5}$ samples, the relatively high concentrations of elements are in the order of $\text{Ti} > \text{Si} > \text{Ca} > \text{Al} > \text{Fe} > \text{K} > \text{Mg} > \text{Na} > \text{Sb} > \text{Zn} > \text{P} > \text{Pb} > \text{Mn} > \text{As} > \text{Cu}$ (spring) and $\text{Ti} > \text{Si} > \text{Ca} > \text{Fe} > \text{Al} > \text{K} > \text{Mn} > \text{Mg} > \text{Na} > \text{Zn} > \text{Sb} > \text{Pb} > \text{P} > \text{As} > \text{Cu}$ (autumn). The fifteen main IE concentrations accounted for 14.88% of the total $PM_{2.5}$ in spring and 14.89% in autumn. The concentrations of the identified elements of soil dust (Ti, Si, Al, Ca, Mg) were $5.24 \mu\text{g}/\text{m}^3$ in spring and $4.29 \mu\text{g}/\text{m}^3$ in autumn, which showed that surface dust was the main source of $PM_{2.5}$. The concentrations of the industrial discharge elements (As, Zn, and Mn) were $0.10 \mu\text{g}/\text{m}^3$ in spring and $0.38 \mu\text{g}/\text{m}^3$ in autumn. The concentration of Pb was $0.03 \mu\text{g}/\text{m}^3$ in spring and $0.06 \mu\text{g}/\text{m}^3$ in autumn, and it may be due to motor vehicle exhaust emissions. The concentrations of K accounted for 1.35% of $PM_{2.5}$ in spring and 0.99% in autumn, which may be due to biomass burning [59–61].

3.2.3. OC and EC Levels

The mean concentrations of OC were $12.03 \pm 2.24 \mu\text{g}/\text{m}^3$ and $9.32 \pm 2.13 \mu\text{g}/\text{m}^3$ in spring and autumn, respectively (Figure 5). The mean EC concentrations were $3.66 \pm 0.47 \mu\text{g}/\text{m}^3$ and $2.88 \pm 0.61 \mu\text{g}/\text{m}^3$ in spring and autumn, respectively. Wenshan is located in the basin valley on the plateau, with wind speeds that are too low to be conducive to pollutant spreading during the two seasons. During the two sampling campaigns, the daily mean value of OC/EC was 2.64–4.17 in spring and 2.74–3.65 in autumn, all of which exceeded 2.0, which indicated that Wenshan experienced secondary organic carbon (SOC) pollution in both seasons. Moreover, OC and EC in Wenshan had a better correlation in autumn ($R = 0.86$) than in spring ($R = 0.69$), which showed that the measured OC and

EC were derived from similar sources during autumn and from complex sources during spring. The possible reason is that the spring is affected by the long-distance transmission of biomass combustion sources in Southeast Asia due to climatic conditions.

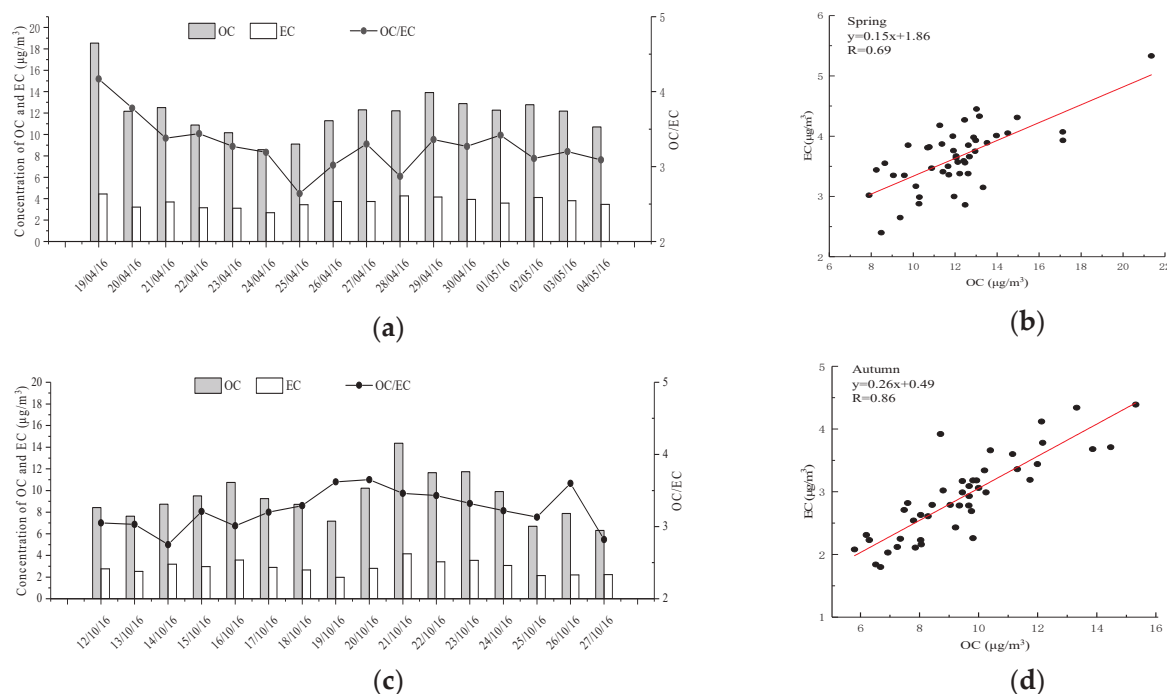


Figure 5. Concentrations of OC and EC, the value of OC/EC and the relevance of OC and EC in $\text{PM}_{2.5}$ during the sampling period. (a) Concentrations of OC and EC in spring. (b) Concentrations of OC and EC in autumn. (c) The value of OC/EC and the relevance of OC and EC in $\text{PM}_{2.5}$ during the spring sampling period. (d) The value of OC/EC and the relevance of OC and EC in $\text{PM}_{2.5}$ during the autumn sampling period.

Since there is no simple and direct calculation method for SOC, this study estimates the content of SOC considering the lowest value of the OC/EC ratio in the two seasons [62–64]. The principle of this method is the use of the lowest value of OC/EC rather than that of the OC/EC of the primary pollutant in every season. $\text{SOC} = \text{TOC} \times \text{EC} \times (\text{OC}/\text{EC})_{\min}$, and TOC and EC are the concentrations of OC and EC in $\text{PM}_{2.5}$, respectively [65,66]. The average values of SOC in $\text{PM}_{2.5}$ are $2.36 \pm 1.00 \mu\text{g}/\text{m}^3$ and $1.41 \pm 0.46 \mu\text{g}/\text{m}^3$ in spring and autumn, respectively. The values of SOC/OC in the two seasons are 19.65% and 15.14% in spring and autumn, respectively. The radiation and temperature in autumn were higher than those in spring, which represented more favorable photochemical conditions for the formation of SOC in autumn. However, there was more rain in autumn in Wenshan, which could limit the formation of SOC. The order of OC, SOC and SOC/EC was the same pattern as spring > autumn, which meant that the impact of radiation and temperature was less than that of rainfall, and rainfall was the main influencing factor and had a greater impact on SOC [67,68].

3.3. Source Apportionment of $\text{PM}_{2.5}$

3.3.1. Principal Component Analysis (PCA)

The sample quantity is crucial for good PCA. The PCA of the study was performed considering the chemical constituents of 90 $\text{PM}_{2.5}$ samples. The outliers (those beyond 2SD) were removed, and the dataset was normalized prior to the operation [69]. When the value of KMO is close to 1, it indicates that there is a strong correlation between these variables (KMO indicates the amount of variance shared among the items designed to measure a latent variable when compared to that shared with the error), and these variables are more suitable for PCA [70]. In this study, the SPSS software package (IBM, version 24.0) was used to conduct PCA research on substances in $\text{PM}_{2.5}$ to obtain the emission characteristics

of its pollution sources. For this study, the species of Li, Na, K, Mn, Cu, Zn, As, Pb, Al, Mg, Ca, Fe, Ba, Si, Ti, NH_4^+ , NO_3^- , SO_4^{2-} , OC and EC had strong correlations in the two seasons, and the PCA results are listed in Table 2.

Table 2. Matrix of loading factors of PCA in spring and autumn.

Element	Spring						Autumn				
	F1	F2	F3	F4	F5	F6	F1	F2	F3	F4	F5
Li			0.52				0.86				
Na					0.80					0.52	
K				0.56			0.83				
Mn			0.93				0.94				
Cu					0.77		0.76				
Zn			0.71				0.88				
Pb			0.94				0.96				
Al		0.62							0.68		
Mg						0.91			0.79		
Ca						0.64	0.55				0.56
Ba		0.95									
Fe		0.56				0.55			0.82		
Si		0.93								0.78	
Ti		0.62									0.76
NH_4^+	0.90							0.90			
NO_3^-	0.87							0.92			
SO_4^{2-}	0.90							0.83			
OC				0.82				0.74			
EC				0.70				0.65			
Eigenvalue	3.40	3.09	2.69	2.19	2.06	1.82	5.59	3.56	2.34	1.77	1.69
Variance contribution %	18.15	16.28	14.15	11.55	10.83	9.58	29.40	18.73	12.33	9.30	8.91

From Table 2, we know that PCA resolved six components explaining 80.5% of the variance in spring.

Factor 1: The first factor contributes 18.15% to the total factor contributions and is characterized by a high concentration of SIAs, which indicates that Wenshan was greatly affected by secondary inorganic aerosol pollution in spring. SIAs are mainly generated by the photochemical reactions of precursor gases (SO_2 , NH_3 , and NO_x), which are emitted from specific identified sources of human activity (coal combustion, vehicle exhaust emission, and biomass burning). Therefore, the strict control of precursor gases is conducive to reducing $\text{PM}_{2.5}$ levels.

Factor 2: The second factor contributed 16.28% of the total $\text{PM}_{2.5}$, and mostly originated from natural sources, such as the lifting of dust or mechanical abrasion processes, which was identified by high concentrations of Al, Fe, Si and Ti, indicating the leading contribution of dust [71]. Si and Ti are the key tracers of soil dust caused by winds. The extra Ba is emitted from brake linings and tire tread wear. These results can be explained as a consequence of dust persisting in the atmosphere longer because of calm and low-speed winds.

Factor 3: The third factor resolved 14.15%, and represents the factor contribution from industrial emissions. The elements are related to the industrial metal smelting process and represent anthropogenic emissions from various industries near the sampling site [72].

Factor 4: This source provided 11.55% of $\text{PM}_{2.5}$. OC and EC are considered to be tracers of motor vehicle emissions, and EC is an indicator of primary emissions of OC [73]. The presence of K also deserved our attention, directly indicating emissions from biomass burning.

Factor 5: Cu and Na were apportioned to this factor, which suggests that the effect of this factor was manifold, such as copper smelting and sea salt [74]. The contribution of this factor towards $\text{PM}_{2.5}$ was 10.83%, as revealed by PCA. In addition, Na might travel long

distances from the Indian Ocean, and Cu could have come from the nearby industrial area in Honghe Prefecture.

Factor 6: This factor is construction cement dust, which is represented by high concentrations of Ca and Mg [75]. This finding indicates that construction and demolition activities were prevalent in the urban areas in Wenshan during the sampling period, without effective measures for dust control. More precise and effective policies are needed for the local government to improve PM_{2.5} pollution.

In addition, PCA resolved five components explaining 78.7% of the variance in autumn. Different from spring, Factor 1 represent biomass burning and industry sources, contributing 29.40% of PM_{2.5}. Factor 2 includes secondary inorganic aerosols and motor vehicle exhaust emissions, which resolved 18.73% of the factor contribution. Factor 3 represents metal smelting, with remarkable representative Al, Fe and Mg features, which can be attributed to the smelting production activities around the site. Factor 4 and Factor 5 are soil dust and construction dust, which resolved 9.30% and 8.91% of the factor contributions, respectively.

3.3.2. The Long-Range Transport

To better understand the transport of airborne particles from distant sources, the 72 h backward trajectories starting at a height of 100 m at the sampling site were calculated using the Hybrid Single Particle Lagrangian Integrated Trajectory 4.0 (HYSPLIT4) model with a 12 h period (meteorological data from the Global Data Assimilation System (GDAS)). The back trajectories were classified into three clusters using TrajStat in this study.

In spring, the trajectories were grouped into three clusters (Figure 6). Cluster 1 (blue line), from the southwestern direction, was associated with slower and lower air mass trajectories and accounted for 57%. The other two trajectory clusters (green line and red line) came from the north and southwestern directions, accounting for 24% and 19%, respectively. Cluster 1 came from central Myanmar and passed through during spring sampling in northern Vietnam and the Honghe Prefecture in Yunnan Province, China, which explains the effect of Factor 3. At the same time, Cluster 2 (green line) came from the industrial region in Chongqing, which explained the source of biomass burning in Factor 1 and the industrial impact in Factor 3. Figure 6b shows that wind mainly originated from the south during the sampling period, which prevented the diffusion and great accumulation of NO_x and SO₂. Then, they formed secondary pollution through photochemical reaction transformation, which conforms to the SIA pollution in Factor 1. The higher wind speeds were also consistent with the contribution of Factor 2.

In autumn, the trajectories were grouped into three clusters from the southeastern direction (Figure 7). Cluster 1 (red line) came from Guangxi Province and passed through the industrial region in Baise, which explains the presence of industrial elements in Factor 1. The other two trajectory clusters (blue line and green line) accounted for 33% and 8%, respectively. Figure 7b also shows that the wind mainly originated from the south during the sampling period and resulted in the impossibility of the diffusion and dilution of pollutants, which was also the reason for the SIA pollution in Factor 2.

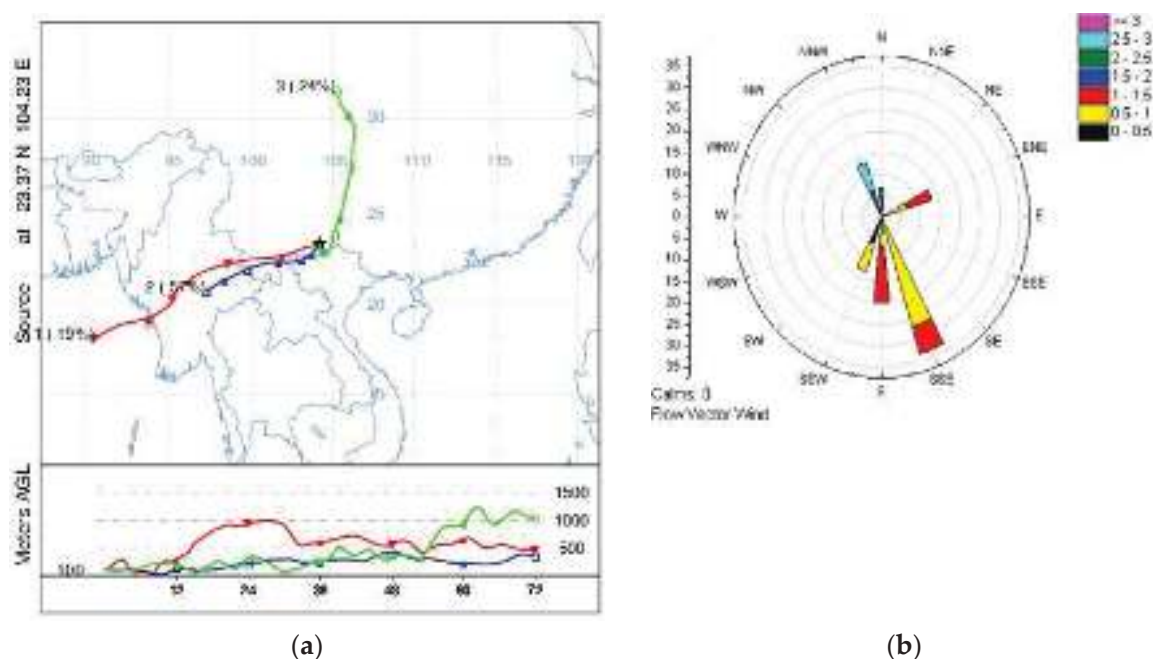


Figure 6. (a) Mean 72 h backward trajectories of each trajectory cluster during spring and the percentage of allocation to each cluster. (b) Wind roses of Wenshan during spring sampling.

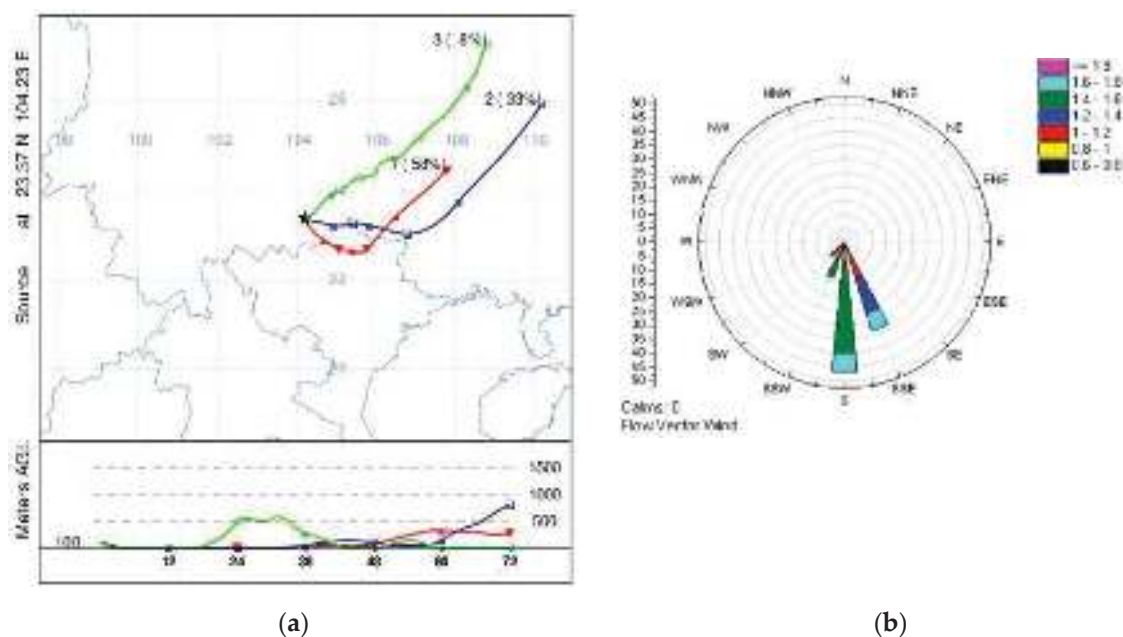


Figure 7. (a) The mean 72 h backward trajectories of each trajectory cluster during autumn and the percentage of allocation to each cluster. (b) Wind roses of Wenshan during autumn sampling.

4. Conclusions

In this study, PM_{2.5} samples were collected in Wenshan, and their mass concentration, chemical composition and source apportionment characteristics were analyzed in spring and autumn. The mean concentrations of PM_{2.5} were $48.00 \pm 11.01 \mu\text{g}/\text{m}^3$ and $41.64 \pm 10.10 \mu\text{g}/\text{m}^3$ in spring (sampled on 19 April–3 May) and autumn (sampled on 12 October–26 October). The annual mean concentration of PM_{2.5} at the three sites was $44.85 \pm 10.99 \mu\text{g}/\text{m}^3$, which was lower than that in Standard II ($75.00 \mu\text{g}/\text{m}^3$) and higher

than that in Standard II ($35.00 \mu\text{g}/\text{m}^3$). This means that the air quality in Wenshan is better than that in most cities in China.

WSIIs and OC were the main components of $\text{PM}_{2.5}$, accounting for 26.91% and 23.80% of $\text{PM}_{2.5}$, respectively. SIAs were the major contributors to WSIIs, due to the incomplete combustion of fossil fuels and the slathering of nitrogen fertilizers in agriculture. Wenshan was greatly affected by secondary inorganic aerosol pollution in the two seasons, which contributed 21.82% and 16.50% to the total factor contributions in spring and autumn, respectively. The ratio of $\text{NO}_3^-/\text{SO}_4^{2-}$ implied that the contribution of mobile sources was not significantly different from that of other developed areas. The daily mean value of OC/EC was 2.64–4.17 in spring and 2.74–3.65 in autumn, which indicates that the SOC was generated by the photochemical process during the sampling days in Wenshan. Moreover, the OC and EC concentrations in Wenshan had a better correlation in autumn ($R = 0.86$) than in spring ($R = 0.69$), which shows that OC and EC were derived from similar sources during autumn and from complex sources during spring. However, elements from anthropogenic sources (Ti, Si, Ca, Fe, Al, K, Mg, Na, Sb, Zn, P, Pb, Mn, As and Cu) accounted for 99.38% and 99.24% of the total inorganic element concentration in spring and autumn, respectively.

Source apportionment showed that SIAs (18.15%), the lifting of dust or mechanical abrasion processes (16.28%), industrial sources (14.15%), motor vehicle emissions (11.55%), copper smelting and sea salt pathways (10.83%), and construction cement dust emissions (9.58%) were the main pollution sources in $\text{PM}_{2.5}$ in spring. Furthermore, source apportionment showed that biomass burning and industry (29.40%), SIAs and motor vehicle exhaust (18.73%), metal smelting (12.33%), soil dust (9.30%) and construction dust (8.91%) emissions were the main pollution sources of $\text{PM}_{2.5}$ in autumn. Different source contributions were found in spring and autumn. According to the research results, the pollution prevention and control suggestions are as follows: (1) Exert related effective management for artificial sources, such as industry and construction sites, to accelerate industrial transformation and upgrading. (2) Adopt emission control measures, such as motor vehicle restrictions and the promotion of new energy transportation methods.

The results of cluster analysis indicate that the long-range transport of air pollutants has a profound effect on local air quality in Wenshan. Wenshan is mainly affected by long-distance atmospheric transmission from the southwest and the northeast in spring and autumn, respectively.

In this paper, chemical composition and source characteristics of $\text{PM}_{2.5}$ in a plateau slope city were first studied, and the main sources of $\text{PM}_{2.5}$ in Wenshan City are resolved. The results can provide scientific data to support $\text{PM}_{2.5}$ pollution control in local and similar cities.

Author Contributions: Conceptualization, J.S. and X.H.; investigation, Y.Z. and L.R.; resources, X.H.; data curation, Y.F.; writing—original draft preparation, X.L.; writing—review and editing, J.S. and X.H.; supervision, P.N. All authors have read and agreed to the published version of the manuscript.

Funding: This research was funded by the National Key R&D Projects of China (grant number 2019YFC0214405) and the National Natural Science Foundation of China (grant number 21966016 and 21667014).

Institutional Review Board Statement: Not applicable.

Informed Consent Statement: Not applicable.

Data Availability Statement: The data used in this paper can be provided by Jianwu Shi (Shijianwu@kust.edu.cn).

Acknowledgments: This work was supported by the National Key R&D Projects of China (No. 2019YFC0214405), and the National Natural Science Foundation of China (No. 21966016, 21667014).

Conflicts of Interest: The authors declare that there are no competing financial interests that could inappropriately influence the contents of this manuscript.

Nomenclature

PM _{2.5}	Particulate matter with aerodynamic equivalent diameter less than or equal to 2.5 microns in ambient air
NO _x	Refers to the sum of NO and NO ₂
CCN	cloud condensation nuclei
WSIIs	Water-soluble inorganic ions
OC	organic carbon
EC	inorganic carbon
IEs	inorganic elements
PCA	Principal component analysis
UV	Ultraviolet
CSCW	Convenience Service Center of Wenshan
WAW	Water Authority of Wenshan
EMSW	Environmental Monitoring Station of Wenshan
ICP-AES	inductively coupled plasma-atomic emission spectrometry
DRI	Desert Institute
FID	Flame ion detector
OPC	Organic pyrolysis carbon
IMPROVE	Interagency Monitoring of Protected Visual Environments
SIAs	Secondary inorganic aerosols (including NO ₃ [−] , SO ₄ ^{2−} and NH ₄ ⁺)
CE/AE	Cation/Anion concentration ratio
NCEP	National Centers for Environmental Prediction
GDAS	Global Data Assimilation System
QC/QA	Quality control and Quality assurance

References

1. Zong, Z.; Wang, X.; Tian, C.; Chen, Y.; Qu, L.; Ji, L.; Zhi, G.; Li, J.; Zhang, G. Source apportionment of PM_{2.5} at a regional background site in North China using PMF linked with radiocarbon analysis: Insight into the contribution of biomass burning. *Atmos. Chem. Phys.* **2016**, *16*, 11249–11265. [CrossRef]
2. Li, L.; Wu, W.; Feng, J.; Zhang, D.; Li, H.; Gu, Z.; Wang, B.; Sheng, G.; Fu, J. Composition source mass closure of PM_{2.5} aerosols for four forests in eastern China. *J. Environ. Sci.* **2010**, *22*, 405–412. [CrossRef]
3. Lu, D.; Xu, J.; Yang, D.; Zhao, J. Spatio-temporal variation and influence factors of PM_{2.5} concentrations in China from 1998 to 2014. *Atmos. Pollut. Res.* **2017**, *8*, 1151–1159. [CrossRef]
4. Samresh, K.; Ramya, S.R. Inorganic ions in ambient fine particles over a National Park in central India: Seasonality, dependencies between SO₄^{2−}, NO₃[−] and NH₄⁺, and neutralization of aerosol acidity. *Atmos. Environ.* **2016**, *143*, 152–163.
5. Andreae, M.O.; Rosenfeld, D. Aerosol–cloud–precipitation interactions. Part 1. The nature and sources of cloud-active aerosols. *Earth Sci. Rev.* **2008**, *89*, 13–41. [CrossRef]
6. Turap, Y.; Talifu, D.; Wang, X.; Abulizi, A.; Maihemuti, M.; Tursun, Y.; Ding, X.; Aierken, T.; Rekefu, S. Temporal distribution and source apportionment of PM_{2.5} chemical composition in Xinjiang, NW-China. *Atmos. Res.* **2019**, *218*, 257–268. [CrossRef]
7. Qiao, B.; Chen, Y.; Tian, M.; Wang, H.; Yang, F.; Shi, G.; Zhang, L.; Peng, C.; Luo, Q.; Ding, S. Characterization of water soluble inorganic ions and their evolution processes during PM_{2.5} pollution episodes in a small city in southwest China. *Sci. Total Environ.* **2019**, *650*, 2605–2613. [CrossRef] [PubMed]
8. Tian, S.; Liu, Y.; Wang, J.; Hou, L.; Lv, B.; Wang, X.; Zhao, X.; Yang, W.; Geng, C.; Han, B. Chemical Compositions and Source Analysis of PM_{2.5} during Autumn and Winter in a Heavily Polluted City in China. *Atmosphere* **2020**, *11*, 336. [CrossRef]
9. Guo, W.; Long, C.; Zhang, Z.; Zheng, N.; Xiao, H.; Xiao, H. Seasonal Control of Water-Soluble Inorganic Ions in PM_{2.5} from Nanning, a Subtropical Monsoon Climate City in Southwestern China. *Atmosphere* **2019**, *11*, 5. [CrossRef]
10. Zhang, J.; Tong, L.; Huang, Z.; Zhang, H.; He, M.; Dai, X.; Zheng, J.; Xiao, H. Seasonal variation and size distributions of water-soluble inorganic ions and carbonaceous aerosols at a coastal site in Ningbo, China. *Sci. Total Environ.* **2018**, *639*, 793–803. [CrossRef]
11. Dong, Z.; Su, F.; Zhang, Z.; Wang, S. Observation of chemical components of PM_{2.5} and secondary inorganic aerosol formation during haze and sandy haze days in Zhengzhou, China. *J. Environ. Sci.* **2020**, *88*, 316–325. [CrossRef]
12. Golly, B.; Waked, A.; Weber, S.; Samake, A.; Jacob, V.; Conil, S.; Rangognio, J.; Chrétien, E.; Vagnot, M.-P.; Robic, P.-Y.; et al. Organic markers and OC source apportionment for seasonal variations of PM_{2.5} at 5 rural sites in France. *Atmos. Environ.* **2019**, *198*, 142–157. [CrossRef]
13. Jin, Q.; Fang, X.; Wen, B.; Shan, A. Spatio-temporal variations of PM_{2.5} emission in China from 2005 to 2014. *Chemosphere* **2017**, *183*, 429–436. [CrossRef]
14. Siudek, P.; Frankowski, M. Atmospheric deposition of trace elements at urban and forest sites in central Poland—Insight into seasonal variability and sources. *Atmos. Res.* **2017**, *198*, 123–131. [CrossRef]

15. Guan, Q.; Liu, Z.; Yang, L.; Luo, H.; Yang, Y.; Zhao, R.; Wang, F. Variation in PM_{2.5} source over megacities on the ancient Silk Road, northwestern China. *J. Clean. Prod.* **2019**, *208*, 897–903. [CrossRef]
16. Pineda-Martínez, L.F.; Carbajal, N.; Campos-Ramos, A.; Aragón-Piña, A.; García, A.R. Dispersion of atmospheric coarse particulate matter in the San Luis Potosí, Mexico, urban area. *Atmósfera* **2014**, *27*, 5–19. [CrossRef]
17. Dai, Q.; Bi, X.; Liu, B.; Li, L.; Ding, J.; Song, W.; Bi, S.; Schulze, B.C.; Song, C.; Wu, J.; et al. Chemical nature of PM_{2.5} and PM₁₀ in Xi'an, China: Insights into primary emissions and secondary particle formation. *Environ. Pollut.* **2018**, *240*, 155–166. [CrossRef]
18. Wang, S.; Yu, R.; Shen, H.; Wang, S.; Hu, Q.; Cui, J.; Yan, Y.; Huang, H.; Hu, G. Chemical characteristics, sources, and formation mechanisms of PM_{2.5} before and during the Spring Festival in a coastal city in Southeast China. *Environ. Pollut.* **2019**, *251*, 442–452. [CrossRef] [PubMed]
19. Xie, Y.; Liu, Z.; Wen, T.; Huang, X.; Liu, J.; Tang, G.; Yang, Y.; Li, X.; Shen, R.; Hu, B.; et al. Characteristics of chemical composition and seasonal variations of PM_{2.5} in Shijiazhuang, China: Impact of primary emissions and secondary formation. *Sci. Total Environ.* **2019**, *677*, 215–229. [CrossRef] [PubMed]
20. Souto-Oliveira, C.E.; Babinski, M.; Araújo, D.F.; Weiss, D.J.; Ruiz, I.R. Multi-isotope approach of Pb, Cu and Zn in urban aerosols and anthropogenic sources improves tracing of the atmospheric pollutant sources in megacities. *Atmos. Environ.* **2019**, *198*, 427–437. [CrossRef]
21. Li, R.; Hardy, R.; Zhang, W.; Reinbold, G.L.; Strachan, S.M. Chemical Characterization and Source Apportionment of PM_{2.5} in a Nonattainment Rocky Mountain Valley. *J. Environ. Qual.* **2018**, *47*, 238–245. [CrossRef] [PubMed]
22. Wang, H.L.; Qiao, L.P.; Lou, S.R.; Zhou, M.; Ding, A.J.; Huang, H.Y.; Chen, J.M.; Wang, Q.; Tao, S.K.; Chen, C.H.; et al. Chemical composition of PM_{2.5} and meteorological impact among three years in urban Shanghai, China. *J. Clean. Prod.* **2016**, *112*, 1302–1311. [CrossRef]
23. Cao, L.; Zhu, Q.; Huang, X.; Deng, J.; Chen, J.; Hong, Y.; Xu, L.; He, L. Chemical characterization and source apportionment of atmospheric submicron particles on the western coast of Taiwan Strait, China. *J. Environ. Sci.* **2017**, *52*, 293–304. [CrossRef]
24. Zhu, W.; Xu, X.; Zheng, J.; Yan, P.; Wang, Y.; Cai, W. The characteristics of abnormal wintertime pollution events in the Jing-Jin-Ji region and its relationships with meteorological factors. *Sci. Total Environ.* **2018**, *626*, 887–898. [CrossRef]
25. Li, J.; Bi, L.; Han, X.; Shi, J.; Yang, J.; Shi, Z.; Ning, P. Characteristics and source apportionment of the water soluble inorganic ions in PM_{2.5} of Kunming. *J. Yunnan Univ.* **2017**, *39*, 63–70. (In Chinese)
26. Bi, L.; Hao, J.; Ning, P.; Shi, J.; Shi, Z.; Xu, X. Characteristics and sources apportionment of PM_{2.5}-bound PAHs in Kunming. *China Environ. Sci.* **2015**, *35*, 659–667. (In Chinese)
27. Wang, C.H.; Yan, K.; Han, X.Y.; Shi, Z.; Bi, L.M.; Xiang, F.; Ning, P.; Shi, J.W. Physico-chemical Characteristic Analysis of PM_{2.5} in the Highway Tunnel in the Plateau City of Kunming. *Environ. Sci.* **2017**, *38*, 4968–4975. (In Chinese)
28. Han, L.; Huang, J.; Han, X.; Yang, J.; Shi, J.; Zhang, C.; Ning, P. Characteristics and Sources of Heavy Metals in Atmospheric PM_{2.5} Research during the Dry Season in Kunming. *J. Kunming Univ. Sci. Technol. Nat. Sci.* **2019**, *44*, 99–110. (In Chinese)
29. Sun, Z.-R.; Ji, Z.-Y.; Han, X.-Y.; Shi, J.-W.; Zhang, J.; Zhang, C.-N.; Ning, P. Spatial and temporal characteristics of atmospheric VOCs and other pollutants concentrations in urban air of Yuxi City. *J. Yunnan Univ.* **2018**, *40*, 705–715. (In Chinese)
30. Shi, Z.; Bi, L.; Shi, J.; Xiang, F.; Qian, L.; Ning, P. Characterization and Source Identification of PM_{2.5} in Ambient Air of Kunming in Windy Spring. *Environ. Sci. Technol.* **2014**, *37*, 143–147, 153. (In Chinese)
31. Jain, S.; Sharma, S.; Mandal, T.; Saxena, M. Source apportionment of PM₁₀ in Delhi, India using PCA/APCS, UNMIX and PMF. *Particuology* **2018**, *37*, 107–118. [CrossRef]
32. Dallarosa, J.; Teixeira, E.C.; Meira, L.; Wiegand, F. Study of the chemical elements and polycyclic aromatic hydrocarbons in atmospheric particles of PM₁₀ and PM_{2.5} in the urban and rural areas of South Brazil. *Atmos. Res.* **2008**, *89*, 76–92. [CrossRef]
33. Lara, L.; Artaxo, P.; Martinelli, L.; Victoria, R.; Camargo, P.; Krusche, A.; Ayers, G.; Ferraz, E.; Ballester, M. Chemical composition of rainwater and anthropogenic influences in the Piracicaba River Basin, Southeast Brazil. *Atmos. Environ.* **2001**, *35*, 4937–4945. [CrossRef]
34. Lee, B.K.; Hong, S.H.; Lee, N.S. Chemical composition of precipitation and wet deposition of major ions on the Korean peninsula. *Atmos. Environ.* **2000**, *34*, 563–575.
35. Chan, T.W.; Mozurkewich, M. Application of absolute principal component analysis to size distribution data: Identification of particle origins. *Atmos. Chem. Phys. Discuss.* **2007**, *7*, 887–897. [CrossRef]
36. Gupta, S.; Gadi, R.; Sharma, S.; Mandal, T. Characterization and source apportionment of organic compounds in PM₁₀ using PCA and PMF at a traffic hotspot of Delhi. *Sustain. Cities Soc.* **2018**, *39*, 52–67. [CrossRef]
37. Zhao, P.S.; Dong, F.; He, D.; Zhao, X.J.; Zhang, X.L.; Zhang, W.Z.; Yao, Q.; Liu, H.Y. Characteristics of concentrations and chemical compositions for PM_{2.5} in the region of Beijing, Tianjin, and Hebei, China. *Atmos. Chem. Phys.* **2013**, *13*, 4631–4644. [CrossRef]
38. Zhao, M.; Huang, Z.; Qiao, T.; Zhang, Y.; Xiu, G.; Yu, J. Chemical characterization, the transport pathways and potential sources of PM_{2.5} in Shanghai: Seasonal variations. *Atmos. Res.* **2015**, *158*, 66–78. [CrossRef]
39. Liu, N.; Feng, X.; Matthew, L.; Chen, Z.; Qiu, G. Pollution Characteristics of PM_{2.5} in Guiyang and Its Influence on Meteorological Parameters. *Earth Environ.* **2014**, *42*, 311–315. (In Chinese)
40. Xiao, J.; Tang, X.; Hu, Y. Initial interpretation on the source of atmospheric PM_{2.5} in Guiyang city. *Environ. Prot. Technol.* **2014**, *5*, 1–18. (In Chinese)
41. Yang, Y.; Zhou, R.; Wu, J.; Yu, Y.; Ma, Z.; Zhang, L. Seasonal variations and size distributions of water-soluble ions in atmospheric aerosols in Beijing, 2012. *J. Environ. Sci.* **2015**, *34*, 197–205. [CrossRef]

42. Xue, G.Q.; Zhu, B.; Wang, H.L. Size Distributions and Source Apportionment of Soluble Ions in Aerosol in Nanjing. *Environ. Sci.* **2014**, *5*, 1633–1643. (In Chinese)
43. Li, W.; Wang, X.; Zhang, Y. Influence of PRD Industrial Emission Variation on Concentrations of SO₂, NO_x and their Secondary Pollutants. *Res. Environ. Sci.* **2009**, *22*, 207–214. (In Chinese)
44. Wang, H.; An, J.; Cheng, M.; Shen, L.; Zhu, B.; Li, Y.; Wang, Y.; Duan, Q.; Sullivan, A.; Xia, L. One year online measurements of water-soluble ions at the industrially polluted town of Nanjing, China: Sources, seasonal and diurnal variations. *Chemosphere* **2016**, *148*, 526–536. [CrossRef]
45. Wang, Y.; Zhuang, G.; Zhang, X.; Huang, K.; Xu, C.; Tang, A.; Chen, J.; An, Z. The ion chemistry, seasonal cycle, and sources of PM_{2.5} and TSP aerosol in Shanghai. *Atmos. Environ.* **2006**, *40*, 2935–2952. [CrossRef]
46. He, Q.; Yan, Y.; Guo, L.; Zhang, Y.; Zhang, G.; Wang, X. Characterization and source analysis of water-soluble inorganic ionic species in PM_{2.5} in Taiyuan city, China. *Atmos. Res.* **2017**, *184*, 48–55. [CrossRef]
47. Rengarajan, R.; Sudheer, A.K.; Sarin, M.M. Wintertime PM_{2.5} and PM₁₀ carbonaceous and inorganic constituents from urban site in western India. *Atmos. Res.* **2011**, *102*, 420–431. [CrossRef]
48. Favez, O.; Cachier, H.; Sciare, J.; Alfaro, S.C.; El-Araby, T.M.; Harhash, M.A.; Abdelwahab, M.M. Seasonality of major aerosol species and their transformations in Cairo megacity. *Atmos. Environ.* **2008**, *42*, 1503–1516. [CrossRef]
49. Qiu, T.; Zhou, J.; Xiao, J.; Guo, H.; Yu, W. Characteristics and sources apportionment of water-soluble ions in PM_{2.5} in autumn and winter of Wuhan. *Environ. Pollut. Prev.* **2015**, *37*, 17–20. (In Chinese)
50. Sun, Y.; Zhuang, G.; Wang, Y.; Han, L.; Guo, J.; Dan, M.; Zhang, W.; Wang, Z.; Hao, Z. The air-borne particulate pollution in Beijing—concentration, composition, distribution and sources. *Atmos. Environ.* **2004**, *38*, 5991–6004. [CrossRef]
51. Zhang, T.; Cao, J.; Tie, X.; Shen, Z.; Liu, S.; Ding, H.; Han, Y.; Wang, G.; Ho, K.; Qiang, J.; et al. Water-soluble ions in atmospheric aerosols measured in Xi'an, China: Seasonal variations and sources. *Atmos. Res.* **2011**, *102*, 110–119. [CrossRef]
52. Wang, P.; Cao, J.-J.; Shen, Z.-X.; Han, Y.-M.; Lee, S.-C.; Huang, Y.; Zhu, C.-S.; Wang, Q.-Y.; Xu, H.-M.; Huang, R.-J. Spatial and seasonal variations of PM_{2.5} mass and species during 2010 in Xi'an, China. *Sci. Total Environ.* **2015**, *508*, 477–487. [CrossRef]
53. Yao, X.; Chan, C.K.; Fang, M.; Cadle, S.; Chan, T.; Mulawa, P.; He, K.; Ye, B. The water-soluble ionic composition of PM_{2.5} in Shanghai and Beijing, China. *Atmos. Environ.* **2002**, *36*, 4223–4234. [CrossRef]
54. Hu, M.; He, L.-Y.; Zhang, Y.-H.; Wang, M.; Kim, Y.P.; Moon, K. Seasonal variation of ionic species in fine particles at Qingdao, China. *Atmos. Environ.* **2002**, *36*, 5853–5859. [CrossRef]
55. Fang, G.-C.; Chang, C.-N.; Wu, Y.-S.; Fu, P.P.-C.; Yang, C.-J.; Chen, C.-D.; Chang, S.-C. Ambient suspended particulate matters and related chemical species study in central Taiwan, Taichung during 1998–2001. *Atmos. Environ.* **2002**, *36*, 1921–1928. [CrossRef]
56. Bhuyan, P.; Deka, P.; Prakash, A.; Balachandran, S.; Hoque, R.R. Chemical characterization and source apportionment of aerosol over mid Brahmaputra Valley, India. *Environ. Pollut.* **2018**, *234*, 997–1010. [CrossRef]
57. Meng, C.; Wang, L.; Zhang, F.; Wei, Z.; Ma, S.; Ma, X.; Yang, J. Characteristics of concentrations and water-soluble inorganic ions in PM_{2.5} in Handan City, Hebei province, China. *Atmos. Res.* **2016**, *171*, 133–146. [CrossRef]
58. Yang, Y.; Zhou, R.; Yu, Y.; Yan, Y.; Liu, Y.; Wu, D.; Zhang, W. Size-resolved aerosol water-soluble ions at a regional background station of Beijing, Tianjin, and Hebei, North China. *J. Environ. Sci.* **2017**, *55*, 146–156. [CrossRef]
59. Huang, L.; Wang, G. Chemical characteristics and source apportionment of atmospheric particles during heating period in Harbin, China. *J. Environ. Sci.* **2014**, *26*, 2475–2483. [CrossRef] [PubMed]
60. Lv, S.; Shao, L.; Wu, M. Characteristics of Chemical Elements in Beijing PM₁₀ and Their Source Apportionment. *J. China Univ. Min. Technol.* **2006**, *35*, 685–688. (In Chinese)
61. Pakkanen, T.A.; Loukkola, K.; Korhonen, C.H.; Aurela, M.; Mäkelä, T.; Hillamo, R.E.; Aarnio, P.; Koskentalo, T.; Kousa, A.; Maenhaut, W. Sources and chemical composition of atmospheric fine and coarse particles in the Helsinki area. *Atmos. Environ.* **2001**, *35*, 5381–5391. [CrossRef]
62. Chu, S.H. Stable estimate of primary OC/EC ratios in the EC tracer method. *Atmos. Environ.* **2005**, *39*, 1383–1392. [CrossRef]
63. Wang, T.; Nie, W.; Gao, J.; Xue, L.K.; Gao, X.M.; Wang, X.F.; Qiu, J.; Poon, C.N.; Meinardi, S.; Blake, D.; et al. Air quality during the 2008 Beijing Olympics: Secondary pollutants and regional impact. *Atmos. Chem. Phys.* **2010**, *10*, 7603–7615. [CrossRef]
64. Rotivitt, L.; Jacobsen, D. Temperature increase and respiratory performance of macroinvertebrates with different tolerances to organic pollution. *Limnologia* **2013**, *43*, 510–515. [CrossRef]
65. Cheng, S.-Y.; Liu, C.; Han, L.-H.; Li, Y.; Wang, Z.; Tian, C. Characteristics and Source Apportionment of Organic Carbon and Elemental Carbon in PM_{2.5} During the Heating Season in Beijing. *J. Beijing Univ. Technol.* **2014**, *40*, 586–591. (In Chinese)
66. Tan, J.; Duan, J.; He, K.; Ma, Y.; Duan, F.; Chen, Y.; Fu, J. Chemical characteristics of PM_{2.5} during a typical haze episode in Guangzhou. *J. Environ. Sci.* **2009**, *21*, 774–781. [CrossRef]
67. Zhang, C.; Lu, X.; Zhai, J.; Chen, H.; Yang, X.; Zhang, Q.; Zhao, Q.; Fu, Q.; Sha, F.; Jin, J. Insights into the formation of secondary organic carbon in the summertime in urban Shanghai. *J. Environ. Sci.* **2018**, *72*, 118–132. [CrossRef]
68. Zhang, Q.; Sarkar, S.; Wang, X.; Zhang, J.; Mao, J.; Yang, L.; Shi, Y.; Jia, S. Evaluation of factors influencing secondary organic carbon (SOC) estimation by CO and EC tracer methods. *Sci. Total Environ.* **2019**, *686*, 915–930. [CrossRef] [PubMed]
69. Cusack, M.; Perez, N.; Pey, J.; Alastuey, A.; Querol, X. Source apportionment of fine PM and sub-micron particle number concentrations at a regional background site in the western Mediterranean: A 2.5 year study. *Atmos. Chem. Phys. Discuss.* **2013**, *13*, 5173–5187. [CrossRef]

70. Song, Y.; Xie, S.; Zhang, Y.; Zeng, L.; Salmon, L.G.; Zheng, M. Source apportionment of PM_{2.5} in Beijing using principal component analysis/absolute principal component scores and UNMIX. *Sci. Total Environ.* **2006**, *372*, 278–286. [CrossRef] [PubMed]
71. Morera-Gómez, Y.; Elustondo, D.; Lasheras, E.; Alonso-Hernández, C.M.; Santamaría, J.M. Chemical characterization of PM₁₀ samples collected simultaneously at a rural and an urban site in the Caribbean coast: Local and long-range source apportionment. *Atmos. Environ.* **2018**, *192*, 182–192. [CrossRef]
72. Qiu, X.; Duan, L.; Gao, J.; Wang, S.; Chai, F.; Hu, J.; Zhang, J.; Yun, Y. Chemical composition and source apportionment of PM₁₀ and PM_{2.5} in different functional areas of Lanzhou, China. *J. Environ. Sci.* **2016**, *40*, 75–83. [CrossRef]
73. Jiang, N.; Yin, S.; Guo, Y.; Li, J.; Kang, P.; Zhang, R.; Tang, X. Characteristics of mass concentration, chemical composition, source apportionment of PM_{2.5} and PM₁₀ and health risk assessment in the emerging megacity in China. *Atmos. Pollut. Res.* **2018**, *9*, 309–321. [CrossRef]
74. Maenhaut, W.; Karnieli, A.; Andreae, M.O. Ten-year study of fine aerosol at Sde Boker, Israel, using PIXE: Time trends, seasonal variation, correlations, and source areas for anthropogenic elements. *Nucl. Instrum. Methods Phys. Res.* **2014**, *318*, 119–124. [CrossRef]
75. Li, X.; Wang, L.; Ji, D.; Wen, T.; Pan, Y.; Sun, Y.; Wang, Y. Characterization of the size-segregated water-soluble inorganic ions in the Jing-Jin-Ji urban agglomeration: Spatial/temporal variability, size distribution and sources. *Atmos. Environ.* **2013**, *77*, 250–259. [CrossRef]

Article

Research on the Temporal and Spatial Characteristics of Air Pollutants in Sichuan Basin

Chunsheng Fang, Xiaodong Tan, Yue Zhong and Ju Wang *

College of New Energy and Environment, Jilin University, Changchun 130012, China; fangcs@jlu.edu.cn (C.F.); tanxd19@mails.jlu.edu.cn (X.T.); zhongyue20@mails.jlu.edu.cn (Y.Z.)

* Correspondence: wangju@jlu.edu.cn

Abstract: Sichuan Basin is one of the most densely populated areas in China and the world. Human activities have great impact on the air quality. In order to understand the characteristics of overall air pollutants in Sichuan Basin in recent years, we analyzed the concentrations of six air pollutants monitored in 22 cities during the period from January 2015 to December 2020. During the study period, the annual average concentrations of CO, NO₂, SO₂, PM_{2.5} and PM₁₀ all showed a clear downward trend, while the ozone concentration was slowly increasing. The spatial patterns of CO and SO₂ were similar. High-concentration areas were mainly located in the western plateau of Sichuan Basin, while the concentrations of NO₂ and particulate matter were more prominent in the urban agglomerations inside the basin. During the study period, changes of the monthly average concentrations for pollutants (except for O₃) conformed to the U-shaped pattern, with the highest in winter and the lowest in summer. In the southern cities of the basin, secondary sources had a higher contribution to the generation of fine particulate matter, while in large cities inside the basin, such as Chengdu and Chongqing, air pollution had a strong correlation with automobile exhaust emissions. The heavy pollution incidents observed in the winter of 2017 were mainly caused by the surrounding plateau terrain with typical stagnant weather conditions. This finding was also supported by the backward trajectory analysis, which showed that the air masses arrived in Chengdu were mainly from the western plateau area of the basin. The results of this study will provide a basis for the government to take measures to improve the air quality in Sichuan Basin.

Citation: Fang, C.; Tan, X.; Zhong, Y.; Wang, J. Research on the Temporal and Spatial Characteristics of Air Pollutants in Sichuan Basin. *Atmosphere* **2021**, *12*, 1504. <https://doi.org/10.3390/atmos12111504>

Academic Editors: Duanyang Liu, Kai Qin and Honglei Wang

Received: 15 September 2021
Accepted: 13 November 2021
Published: 15 November 2021

Publisher's Note: MDPI stays neutral with regard to jurisdictional claims in published maps and institutional affiliations.



Copyright: © 2021 by the authors. Licensee MDPI, Basel, Switzerland. This article is an open access article distributed under the terms and conditions of the Creative Commons Attribution (CC BY) license (<https://creativecommons.org/licenses/by/4.0/>).

Keywords: air pollution; spatio-temporal variations; Sichuan Basin; back-trajectory

1. Introduction

In the past 20 years, China has experienced severe air pollution due to rapid economic development and increasing urbanization [1]. Studies showed that exposure to ambient air pollution has been associated with increased risks of mortality and morbidity worldwide [2,3]. According the Global Burden of Disease (GBD) project, air pollution was responsible for 1.6 million deaths in China and 4.2 million deaths worldwide in 2015 [4]. The continuous and serious air pollution has caused an immense burden for China's medical and economic [5]. In order to cope with serious air quality problems, China has taken a series of measures in recent years [6,7].

In 2005 and 2011, China implemented the installation of desulphurization and selective catalytic reduction (SCR) systems for coal-fired power plants [8]. At the same time, the strategies of upgrading vehicle fuel and prohibiting polluting old vehicles were introduced at the city level [9]. The Ministry of Environmental Protection of China issued the revised "Ambient Air Quality Standards" (CAAQS, GB3095-2012) in February 2012, adding PM_{2.5} and O₃ to CAAQS for the first time [10]. In 10 September 2013, the Chinese government promulgated the Air Pollution Prevention and Control Action Plan. The plan aimed to reduce the number of severely polluted days drastically and improve the national air quality significantly through long-term efforts [11]. Despite these efforts, there were still many cities that have not yet reached the current CAAQS [12]. According to the "2020

Reports on the State of Environment of China”, there were still 135 cities whose ambient air quality exceeded the standard, accounting for 40.1% of the total number of cities. In the days exceeding the standard, the proportions of PM_{2.5}, O₃, and PM₁₀ as the primary pollutants were 51%, 37.1%, and 11.7%, respectively.

Previous studies showed that Beijing-Tianjin-Hebei area (BTH), Yangtze River Delta (YRD), Pearl River Delta (PRD) and Sichuan Basin were the four main regions with severe air pollution in China [13,14]. In Beijing, YRD and PRD, some scholars have carried out a lot of research to understand the basic characteristics, chemical mechanisms, main components and transmission sources of air pollution [15–19]. Since 2000, the air quality in Sichuan Basin has further deteriorated due to increased anthropogenic emissions. However, only a few studies have focused on Sichuan Basin [20,21]. And in the past, related studies on Sichuan Basin were mainly concentrated in the two megacities of Chongqing and Chengdu, and there were few studies on the overall air quality for the whole of large-scale valley terrain [22,23]. The characteristics and source of air pollution for Sichuan Basin in recent years are still unclear [24]. In this study, we analyzed air quality data collected from Sichuan Basin for six years (January 2015 to December 2020) to fill this gap. The main goal is to investigate (1) the temporal and spatial characteristics of the overall air pollution in Sichuan Basin, (2) the industry contribution reflected by the ratio of different pollutants, and (3) a regional-scale air pollution episode that influenced multiple cities in the region. The knowledge gained in this study provides a scientific basis for formulating future emission control policies aimed at reducing severe PM_{2.5} pollution in this unique watershed

2. Materials and Methods

2.1. Air Quality Monitoring Sites

The air quality was monitored at 127 stations spread over 22 cities across Sichuan Basin, covering an area of over 260,000 square kilometers. Located in the central and southern part of the Asian continent, with a total population of more than 100 million, Sichuan Basin is one of the most densely populated areas in China and the world. Completely surrounded by high mountains and plateaus, it is a vast subtropical low hills and plains. The west is surrounded by the high-altitude Qinghai-Tibet Plateau, the south is the Yunnan-Guizhou Plateau, the east is Wushan, and the north is Dabashan. Due to low wind speed and high relative humidity, it was one of the four traditional areas with acidic rain and frequent haze events [25]. Figure 1 showed the locations of the 22 cities that collected the air quality data used in this study.

Considering the completeness of the data, this study collected the socio-economic data of each city in Sichuan Basin during 2018 (source: http://tjj.cq.gov.cn/zw/gk_233/tjnj/2019/zk/indexce.htm (accessed on 15 September 2021)). Table 1 listed the city’s abbreviations, number of vehicles, population, and GDP (Gross Domestic Product). In 2018, Chongqing’s total population was 31.01 million, the total number of vehicles was 6.31 million, and the GDP was 20363 billion yuan, ranking first among the cities. As another megacity in Sichuan Basin, Chengdu has a total population of 16.33 million, a total of 4.87 million vehicles, and a GDP of 1.5342 billion yuan, second only to Chongqing.

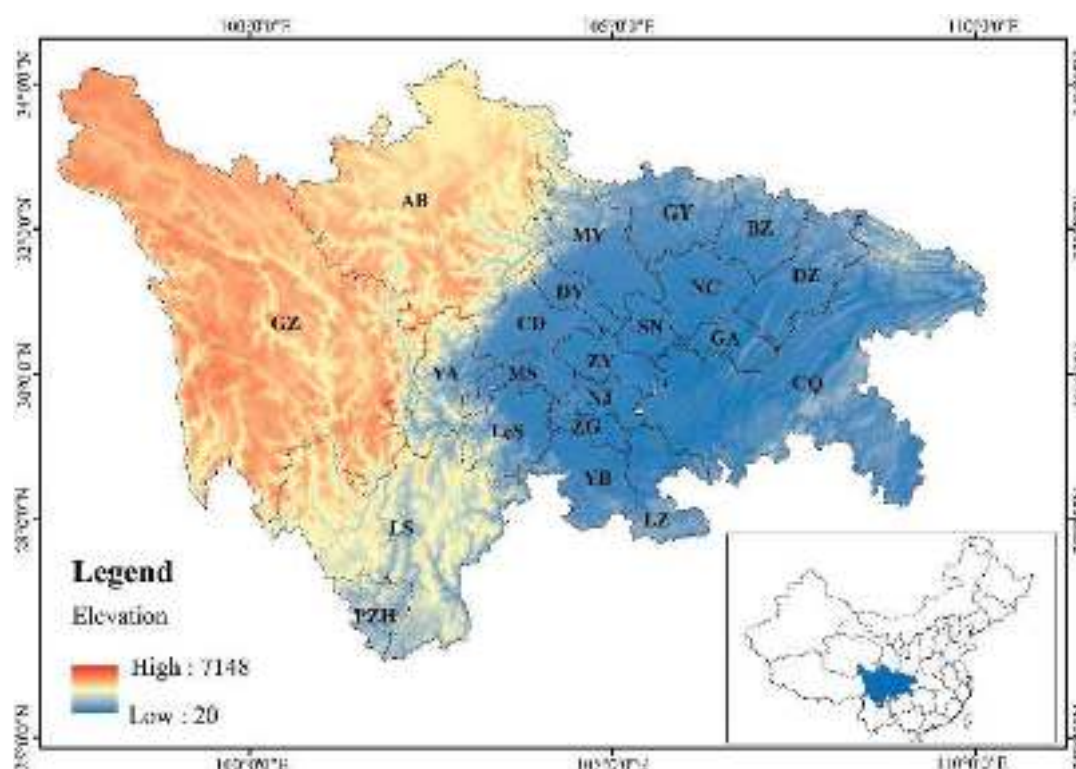


Figure 1. The map of Sichuan Basin and the locations of 22 city stations.

Table 1. Urban areas, population, number of vehicles, and GDP of each city in the Sichuan Basin in 2018.

City	Population (10,000 Persons)	GDP (Billion Yuan)	Primary Industry (Billion Yuan)	Secondary Industry (Billion Yuan)	Tertiary Industry (Billion Yuan)	Vehicle Numbers (10,000 Units)
Chengdu (CD)	1633	15,342.77	522.59	6516.19	8303.99	487.7169
Mianyang (MY)	485.7	2303.82	301.27	929.4	1073.15	49.9193
Deyang (DY)	354.5	2213.87	243.31	1071.13	899.43	40.5155
Leshan (LeS)	326.7	1615.09	165.92	721.78	727.39	39.2793
Meishan (MS)	298.4	1256.02	186.5	554.46	515.06	37.9811
Yaan (YA)	154	646.1	85.83	303	257.27	11.1461
Ziyang (ZY)	251.2	1066.53	166.79	507.61	392.13	31.0002
Zigong (ZG)	292	1406.71	151.55	653.71	601.45	66.1452
Yibin (YB)	455.6	2026.37	248.57	1006.73	771.07	51.8162
Luzhou (LZ)	432.4	1694.97	190.58	882.97	621.42	18.2872
Neijiang (NJ)	369.9	1411.75	219.31	610.8	581.64	25.1536
Chongqing (CQ)	3101.79	20,363.19	1378.27	8328.79	10,656.13	631.7233
Guang'an (GA)	324.1	1250.24	173.52	575.23	501.49	35.733
Nanchong (NC)	644	2006.03	381.87	824.05	800.11	17.9184
Suining (SN)	320.2	1221.39	165.64	565.22	490.53	25.2796
Guangyuan (GY)	266.7	801.85	118.1	358.56	325.19	24.403
Dazhou (DZ)	572	1690.17	326.24	603.91	760.02	18.0632
Bazhong (BZ)	332.2	645.88	98.27	316.39	231.22	9.0715
Aba (AB)	94.4	306.67	49.55	139.53	117.59	24.2416
Ganzi (GZ)	119.6	291.2	65.47	121.78	103.95	23.3053
Liangshan (LS)	490.8	1533.19	307.61	613.13	612.45	35.1002
Panzhihua (PZH)	123.6	1173.52	39.74	731.13	402.65	25.5248

2.2. Air Quality Data

The concentrations of six pollutants, SO_2 , NO_2 , CO , O_3 , $\text{PM}_{2.5}$ and PM_{10} , were monitored hourly over 22 cities across Sichuan Basin from January 2015 to December 2020. The data were made available by the China National Environmental Monitoring Center (<http://www.cnemc.cn/> (accessed on 15 September 2021)).

The instruments for air quality monitoring were deployed according to the China Environmental Protection Standard HJ 664-2013. The equipment came from Shenzhen Aosen Purification Technology Co., Ltd., China. The gaseous pollutant and PM concentrations were measured following the Specifications and Test Procedures for Ambient Air Quality Continuous Automated Monitoring System HJ 654-2013 for SO_2 , NO_2 , O_3 and CO , and HJ

653–2013 for PM_{2.5} and PM₁₀, as stipulated in the National Environmental Protection Standards of the People's Republic of China. The air quality monitoring stations were located at least 50 m away from any notable stationary pollution sources, and the inlets for the instruments were placed at least 1 m higher than the roof of the building or wall [26]. Data quality assurance and quality control (QA/QC) were conducted following the technical guidelines on environmental monitoring quality management (HJ 630-2011) established in the National Environmental Protection Standards of the People's Republic of China. The validity of the data was checked following the national ambient air quality standards specified in the National Standards of the People's Republic of China (GB 3095-2012), as used in earlier studies [27,28]. The daily, monthly, and annual means of the data were calculated from the hourly concentrations (with ~80% of the available data to be considered as valid for calculating the mean).

2.3. Back-Trajectory Analysis

Backward trajectory analysis essentially follows a parcel of air backward in hourly time steps for a specified length of time [29]. The HYbrid-Single Particle Lagrangian Integrated Trajectory (HYSPLIT) model developed by the National Oceanic and Atmospheric Administration (NOAA) was used to identify the potential source area of air pollution in a specific city and capture the vertical movement of the air masses from the sources to the receptor inside planetary boundary layer [30].

The HYSPLIT model was used to investigate the movement of air masses during a heavy particulate pollution observed in winter 2017. In order to understand the impact of the regional transmission process, three-dimensional 48 h backward trajectories arriving at 500 m above ground level (AGL) of the receptor sites were also calculated using $1^\circ \times 1^\circ$ Global Data Assimilation System (GDAS) data from National Centers for Environmental Prediction (NCEP). Based on the Euclidean distance between the motion trajectories, the Ward layering method was used to assign the motion trajectories to different clusters according to their moving speed and direction. The hour with the highest PM concentration of coarse particles in Chengdu was selected as the start time of the trajectory, and the backward trajectory at a height of 500 m from 3 January to 6 January 2017 was calculated. The main transportation routes that caused severe air pollution in the winter of 2017 were identified by combining the trajectory with the corresponding average concentration of pollutants [31].

3. Results

3.1. Spatio-Temporal Characteristics of the Air Quality

The annual average concentrations of the pollutants in Sichuan Basin were determined by averaging the effective data from all stations. Their values are shown in Figure 2. The annual mean concentrations of CO, NO₂, SO₂, O₃, PM_{2.5} and PM₁₀ in the entire basin area ranged from 0.67–0.90 mg/m³, 24.33–30.4 µg/m³, 8.41–17.76 µg/m³, 80.08–91.4 µg/m³, 31.2–46.56 µg/m³ and 47.87–75.19 µg/m³, respectively. During the same period, in Chengdu and Chongqing, two megacities of Sichuan Basin, the annual average concentrations of the six pollutants ranged from 0.69–1.08 (0.79–1.1) mg/m³, 33.75–49.46 (37.18–45.5) µg/m³, 6.56–15.75 (7.49–16.17) µg/m³, 87.86–101.56 (68.98–81.54) µg/m³, 39.23–61.85 (32.27–54.42) µg/m³, 61.27–103.83 (51.85–84.12) µg/m³, respectively.

The annual average SO₂ concentration was the lowest in Bazhong, with a value of 4.71 µg/m³, and the highest in Panzhihua, with a value of 33.69 µg/m³. The lowest NO₂ concentration of 9.21 µg/m³ was observed in Aba Prefecture, and the highest in Chengdu, reached 43.73 µg/m³. The highest annual average CO concentration observed at 1.49 mg/m³ in Panzhihua, and the lowest of 0.48 mg/m³ was observed in Ganzi. The lowest annual average concentration of O₃ was observed in Ya'an during 2015, which was 53.2 µg/m³. The highest annual average concentration of O₃ was observed in Zigong during 2018, with a value of 105.19 µg/m³. The annual average concentration of PM_{2.5} and PM₁₀ in Aba Prefecture was the lowest, 15.12 µg/m³ and 26.38 µg/m³, respectively. The

highest values of $84.94 \mu\text{g}/\text{m}^3$ and $109.6 \mu\text{g}/\text{m}^3$ was observed in Zigong, both of which appeared in 2015.

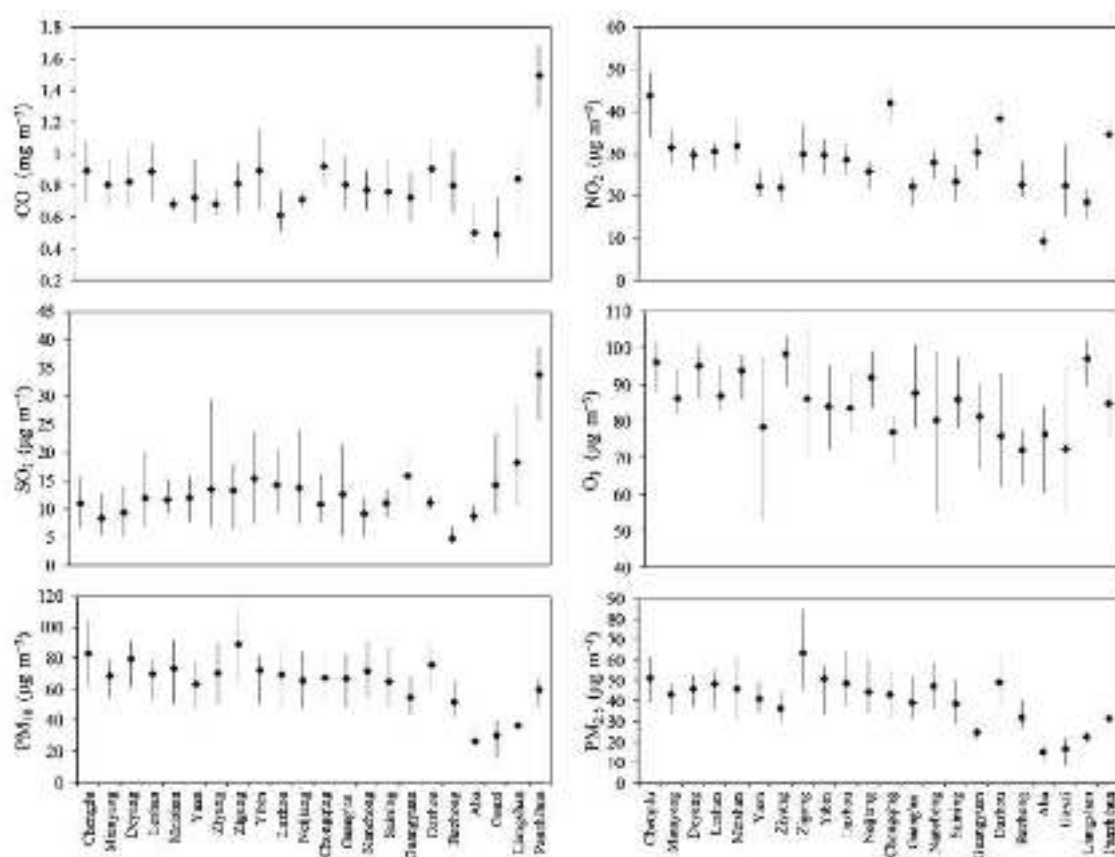


Figure 2. The annual average concentrations of pollutants in Sichuan Basin. The filled circle represents the mean concentration whereas the error bar denotes the range of the annual concentration. The data used in each city comes from every station during 2015–2020.

As shown in Figure 3, the concentrations of five pollutants other than O_3 all showed a downward trend from 2015 to 2020 in Sichuan Basin. The concentration of NO_2 was the highest in 2017, at $30.4 \mu\text{g}/\text{m}^3$, and the lowest in 2020, at $24.33 \mu\text{g}/\text{m}^3$, with an average annual decline rate of 2.72%. The highest concentrations of CO , SO_2 , $\text{PM}_{2.5}$ and PM_{10} all appeared in 2015 with the value of $0.9 \text{ mg}/\text{m}^3$, $17.76 \mu\text{g}/\text{m}^3$, $46.56 \mu\text{g}/\text{m}^3$ and $75.19 \mu\text{g}/\text{m}^3$, respectively. The lowest concentrations all appeared in 2020 with the value of $0.67 \text{ mg}/\text{m}^3$, $8.41 \mu\text{g}/\text{m}^3$, $31.2 \mu\text{g}/\text{m}^3$, $47.87 \mu\text{g}/\text{m}^3$, and the average annual decline rates were 5.14%, 10.52%, 6.59%, and 7.27%, respectively.

At present, the environmental concentration of most air pollutants in China is declining, but the concentration of secondary pollutants such as O_3 is increasing at both provincial and capital city levels [32,33]. Previous studies showed that the rising rate of O_3 in China's 2 + 26 urban areas was almost 14 times that of the global O_3 [34]. The lowest ozone concentration of $80.08 \mu\text{g}/\text{m}^3$ in Sichuan Basin was observed in 2015, and reached the highest in 2018, with the value of $91.4 \mu\text{g}/\text{m}^3$. It declined slightly in the following two years, but still showed an upward trend during the overall study period. The annual growth rate was about 0.76%.

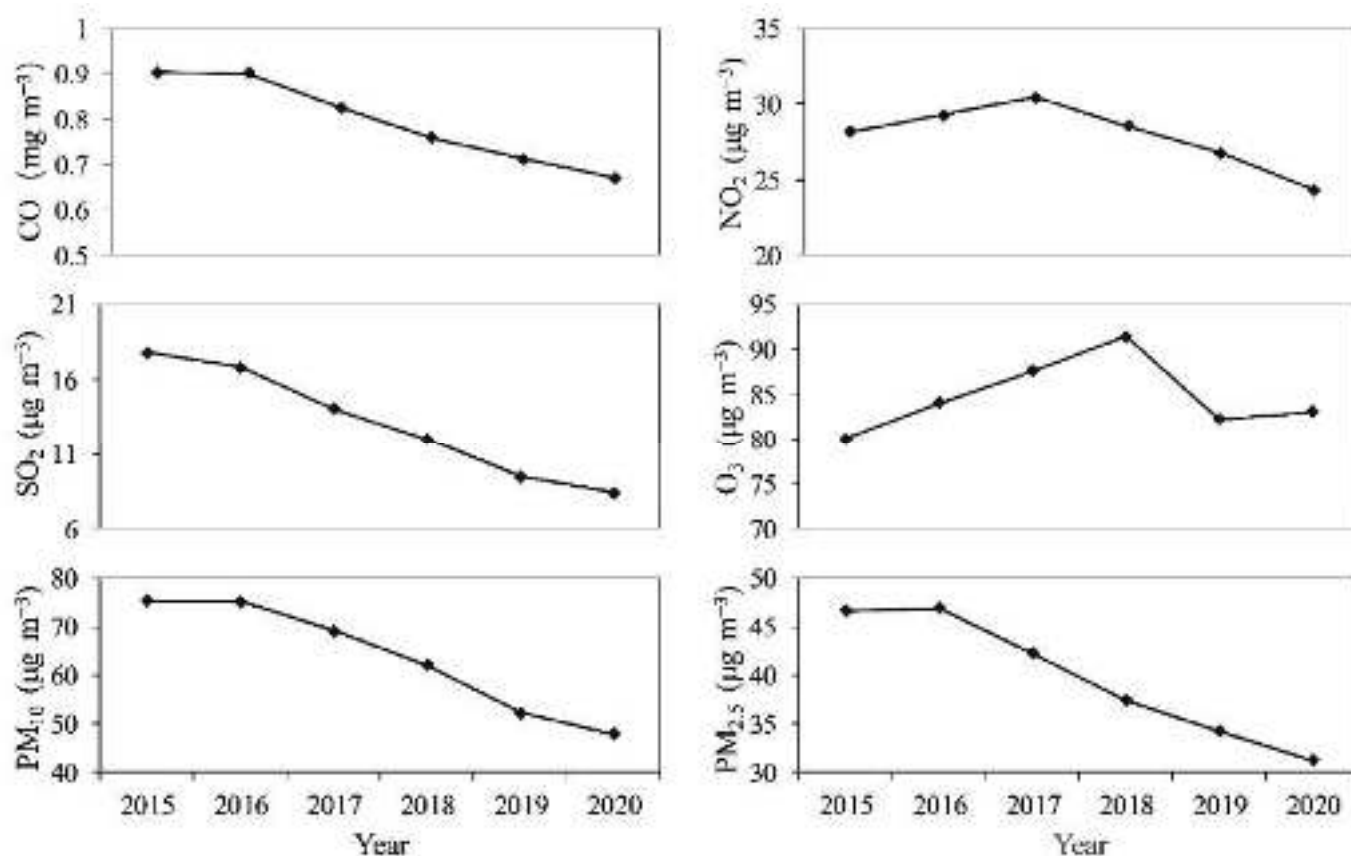


Figure 3. Annual average concentration trend of the six pollutants.

Ozone is not directly emitted by pollution sources in the environment [35]. It is a secondary pollutant generated by chemical reactions of nitrogen oxides and volatile organic compounds under strong ultraviolet light irradiation [36]. Although China has adopted strict control measures in recent years, which has made PM, NO₂, SO₂ and other atmospheric pollutants show a clear downward trend, the ozone concentration is still slowly increasing [37]. The main reason for this phenomenon is that emissions of NO_x and VOCs (main precursors of O₃) remain high in China [38]. And the meteorological conditions of high temperature and low rainfall are conducive to the generation of O₃ in recent years [39]. At the same time, the global O₃ background value has been continuously increasing, which also makes a certain promoting effect on China's ozone concentration [40].

3.2. Seasonal Variations of Pollutants

Figure 4 shows the seasonal variations of the six pollutants in each city. For almost all pollutants (except O₃), the highest concentrations were observed in winter and the lowest in summer. It is speculated that the continuous adverse weather conditions in winter include smaller wind speed and rainfall, lower temperature and atmospheric boundary height, which are not conducive to the diffusion of pollutants. And compared with other seasons, the consumption of coal and biomass fuel for heating in winter is higher [41,42]. On the contrary, in summer, the wind speed and planetary boundary layer is higher, the rainfall is abundant, the rain removal effect is obvious, and the pollutant concentration is lower [43,44].

Since NO₂ is the main man-made pollutant emitted from vehicles and transportation facilities and fuel combustion, these activities are more frequent in the two megacities of Chengdu and Chongqing than in other places [45]. In 2018, the total number of motor vehicles in Chengdu and Chongqing accounted for 28.2% and 36.5% of the entire basin area respectively. Therefore, the highest NO₂ concentration was observed in these two

cities. The average concentration of NO_2 in winter was between $111.87 \mu\text{g}/\text{m}^3$ (Chengdu) and $50.93 \mu\text{g}/\text{m}^3$ (Aba Prefecture). Similar characteristics were observed for CO, namely the highest and lowest concentrations were observed in winter and summer, respectively. The opposite trend of ozone occurred. The highest concentration happened in spring and summer, and the lowest concentration occurred in winter. This is related to the formation mechanism of ozone. Many studies showed that under sufficient light, volatile organic compounds (VOCs) and nitrogen oxides (NO_x) underwent a photochemical reaction to generate O_3 and at the same time produced secondary pollutants in the atmosphere [46–48]. High temperature, strong ultraviolet and high photochemical reaction rate were common phenomena in Sichuan Basin during spring and summer. The weaker solar radiation in winter inhibited the photochemical reaction, which was not conducive to the production of O_3 . Therefore, the O_3 concentration in the Sichuan Basin had the highest trend in spring and summer.

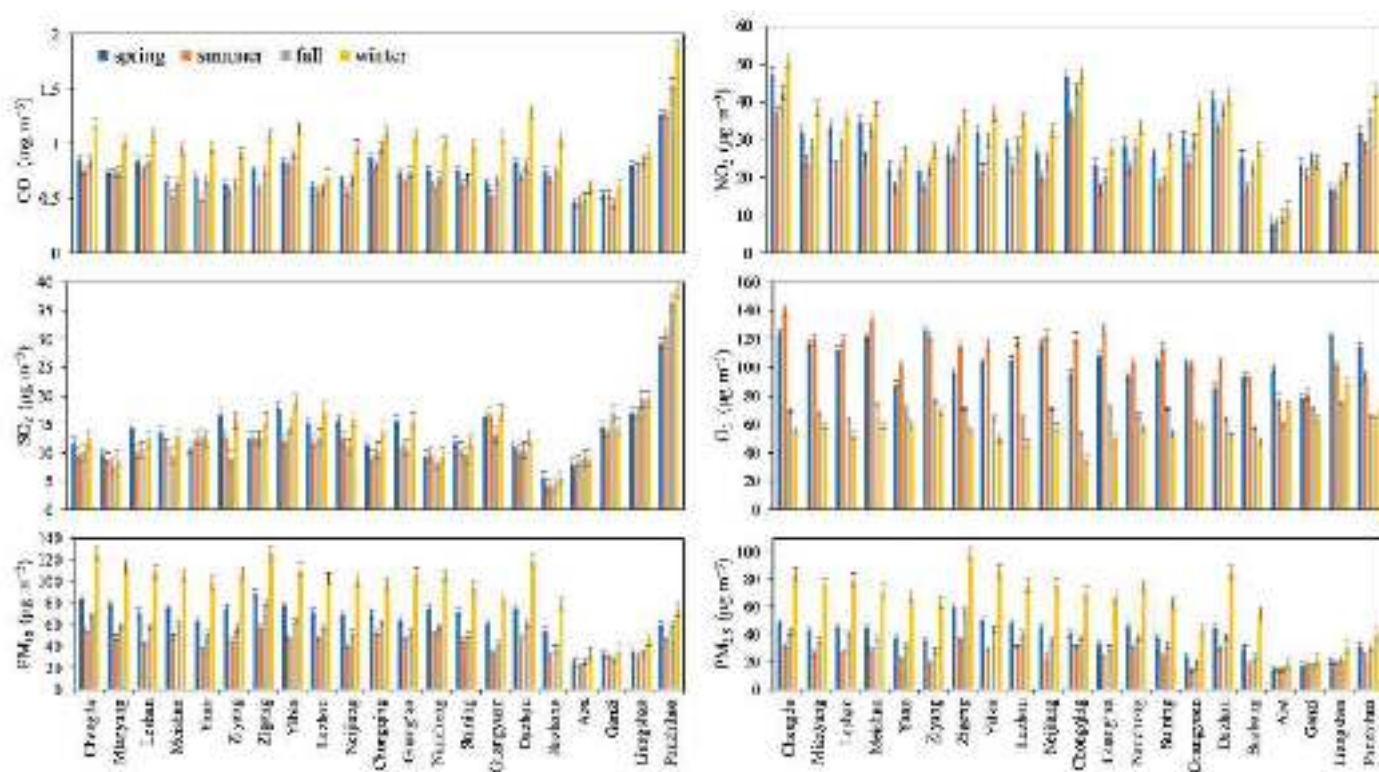


Figure 4. Seasonal variation in concentrations of air pollutants in Sichuan Basin. The vertical error bars represent the standard deviation values. Spring (March to March), Summer (June to August), Autumn (September to November), Winter (December to February of the following year).

Regions with high SO_2 concentrations were mainly located in the plateau areas of the western Sichuan Basin, such as Panzhihua, Liangshan, Ganzi and other cities. Far more than the cities such as Chengdu and Mianyang in the basin, the winter SO_2 concentration of Panzhihua was $38.7 \mu\text{g}/\text{m}^3$, about 3 times of the average SO_2 concentration in whole Sichuan Basin ($12.8 \mu\text{g}/\text{m}^3$). On the one hand, the SO_2 of cities in the basin such as Chengdu was mainly derived from industrial emissions. In these areas, the government took strict desulfurization measures, which greatly reduced the concentration of SO_2 . On the other hand, coal combustion for household heating due to low temperature in high altitude regions, led to more SO_2 emissions, and the implementation of desulfurization measures in these areas were not yet fully completed.

Different with northern China, due to the warm temperature in Sichuan Basin (about 10°C on average), there was no widespread coal or wood burning for household heating in winter; therefore, atmospheric processes and meteorological conditions played an

important role in the seasonal changes of particulate matter effect [49]. Almost all regions had the highest concentration of particulate matter in winter, about 1.8–2.5 times that of the other three seasons. The concentration was similar in spring and autumn, and the lowest concentration occurred in summer.

3.3. Analysis of City's Pollutant Ratio

The average $PM_{2.5}/PM_{10}$ ratio of all cities in Sichuan Basin was 0.61, and the monthly ratio was between 0.43 and 0.69, appeared in April and January respectively. The average ratio in Chengdu and Chongqing was 0.60 and 0.63, respectively. In 2017, a study reported the average ratio of 0.58 for 31 provincial capital cities, and Zhang (2015) reported an average ratio of 0.56 for 190 cities in China [7,50]. However, in Beijing (0.80), Shanghai (0.70) and Guangzhou (0.72), the ratio was much higher than that observed in this study [51]. These findings indicated that, compared to developed cities in China, the air quality in Sichuan Basin was more affected by coarse particles. Figure 5 showed the monthly average ratios of different cities in Sichuan Basin during the study period. The lowest average ratio was found to be 0.43 (in Guangyuan), while the highest average ratio (0.69) was observed in Zigong and Luzhou.

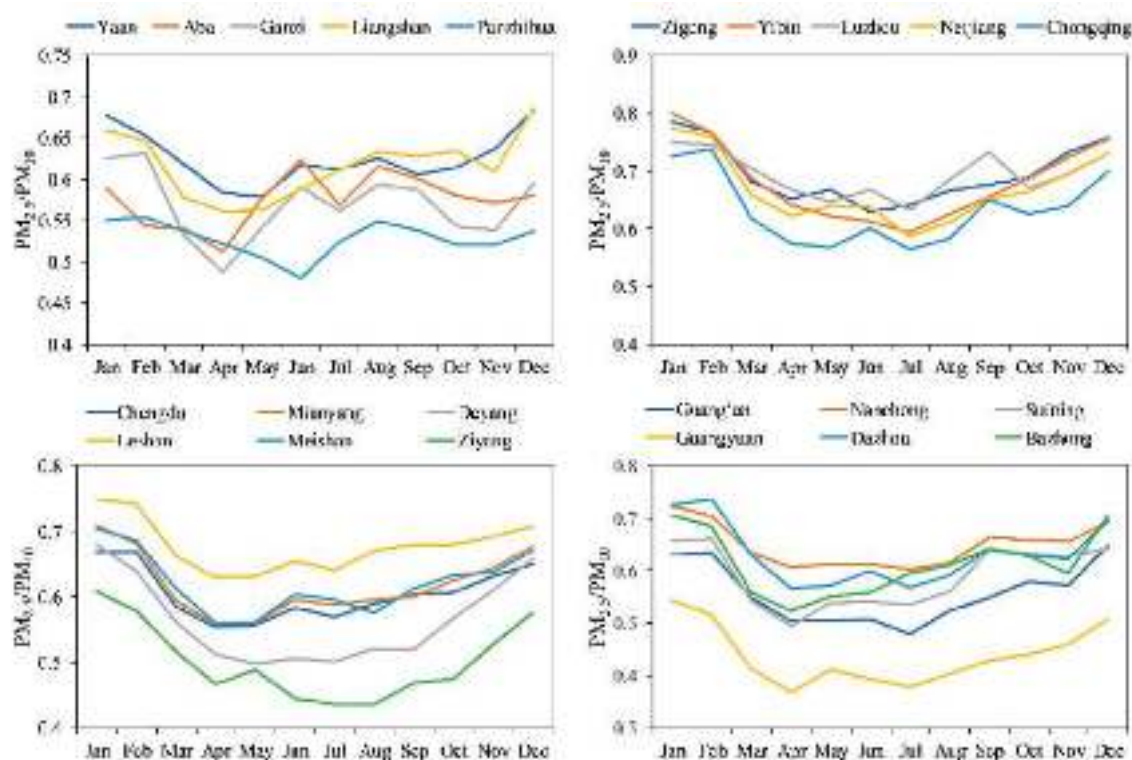


Figure 5. The monthly average $PM_{2.5}/PM_{10}$ ratio of each city.

In winter, all cities had the highest $PM_{2.5}/PM_{10}$ ratio, while in spring and summer, the ratio decreased rapidly. This was due to the high emissions of coarse particulate matter from sand and soil during the spring when it is very dry, windy, and dusty in Sichuan Basin [52]. Dust emitted from desert areas in Xinjiang (such as Taklimakan) may be transported towards the Qinghai-Tibet Plateau in the northwest of Sichuan Basin, thereby affecting the atmosphere and ecosystems of the basin area.

SO_2 can be used to normalize $PM_{2.5}$ to exclude the effects of coal combustion and meteorological conditions. It can be seen from Figure 6 that during the study period, among the cities in Sichuan Basin, the city with the highest $PM_{2.5}/SO_2$ was Bazhong (6.39), followed by Deyang (5.19) and Nanchong (5.18), which reflected the contribution of non-industrial source to $PM_{2.5}$. The average ratio in Sichuan Basin is 3.45, which was close to

the national average (2.92) in the previous study [53]. It is worth noting that in Panzhihua, Aba, Liangshan and other areas, the value of $PM_{2.5}/SO_2$ has always remained at a low level throughout the year, which may be because the industry in Sichuan Basin is mainly concentrated in the western region, and industrial sources contribute more to fine particles.

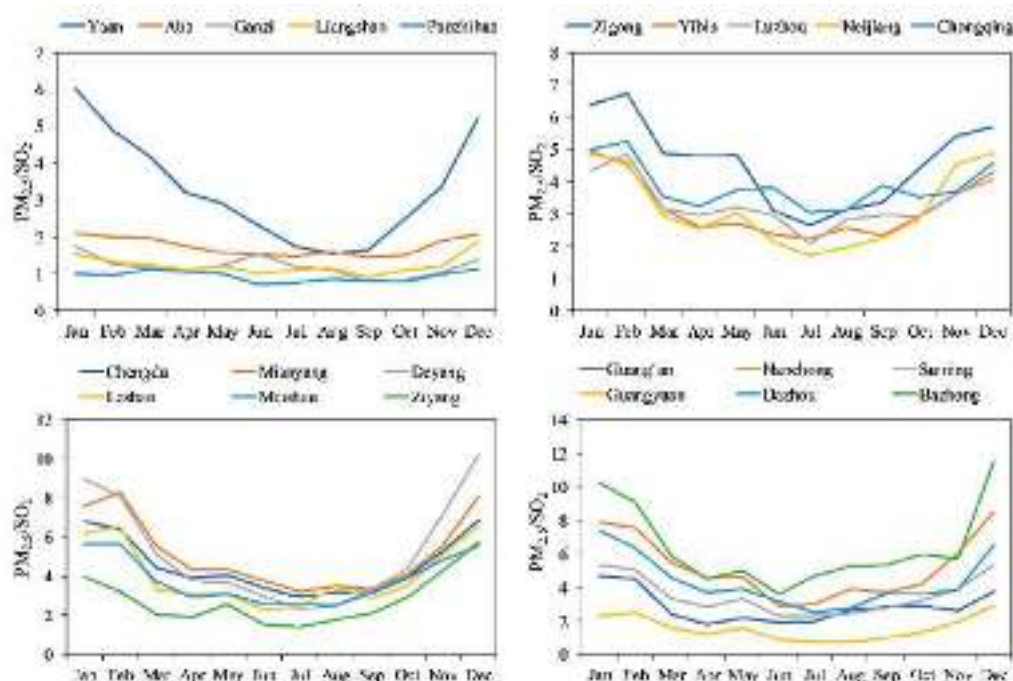


Figure 6. The monthly average $PM_{2.5}/SO_2$ ratio of each city.

$PM_{2.5}/SO_2$ also exhibited a U-shaped mode in most cities, which reflected that non-industrial sources such as power and residential contributed more to $PM_{2.5}$ in winter. Multi-resolution Emission Inventory for China (MEIC) was often used to estimate emissions from various sectors in China [54]. In order to determine the relationship between this dynamic change and the emission trends of key sectors involved in the air pollution process, we collected $PM_{2.5}$ emission information from key sectors in the 2017 MEIC inventory of Sichuan Basin (Figure A1). Among them, non-industrial source emissions showed a similar U-shaped trend, which was consistent with the previous conclusions.

CO is an indicator of the primary combustion source. The secondary formation of fine particles in the basin can be studied by calculating the ratio of $PM_{2.5}$ to CO [55]. From 2015 to 2020, the value of $PM_{2.5}/CO$ was higher in the southern areas such as Luzhou and Zigong, and the lowest in the western plateau areas such as Panzhihua (Figure 7). This indicated that the secondary sources in the southern cities of the basin had a higher contribution to the generation of fine particles.

Previous research reported that the sulfur dioxide emissions were much lower than the emissions of nitrogen oxides for motor vehicles in China, and the ratio of $[SO_2]/[NO_2]$ in motor vehicles was usually between 0.0084 and 0.042. Both NO_x and SO_2 were emitted from stationary sources, but the emissions of SO_2 was relatively more. The ratio of $[SO_2]/[NO_2]$ in fixed sources was usually between 1.25 and 5 [56]. Therefore, the SO_2/NO_2 ratio was often used as an indicator of air pollution caused by stationary sources and mobile sources [57]. Figure 8 showed the monthly average ratio of SO_2/NO_2 in each city. In study area, Liangshan and Panzhihua had the highest SO_2/NO_2 ratios, indicating that the air pollution in these western plateau cities mainly came from local industrial sources and coal combustion. Bazhong was the lowest (0.21), followed by Chengdu (0.24) and Chongqing (0.26). These results confirmed that there was a strong correlation between air pollution and automobile exhaust emissions in Chengdu and Chongqing.

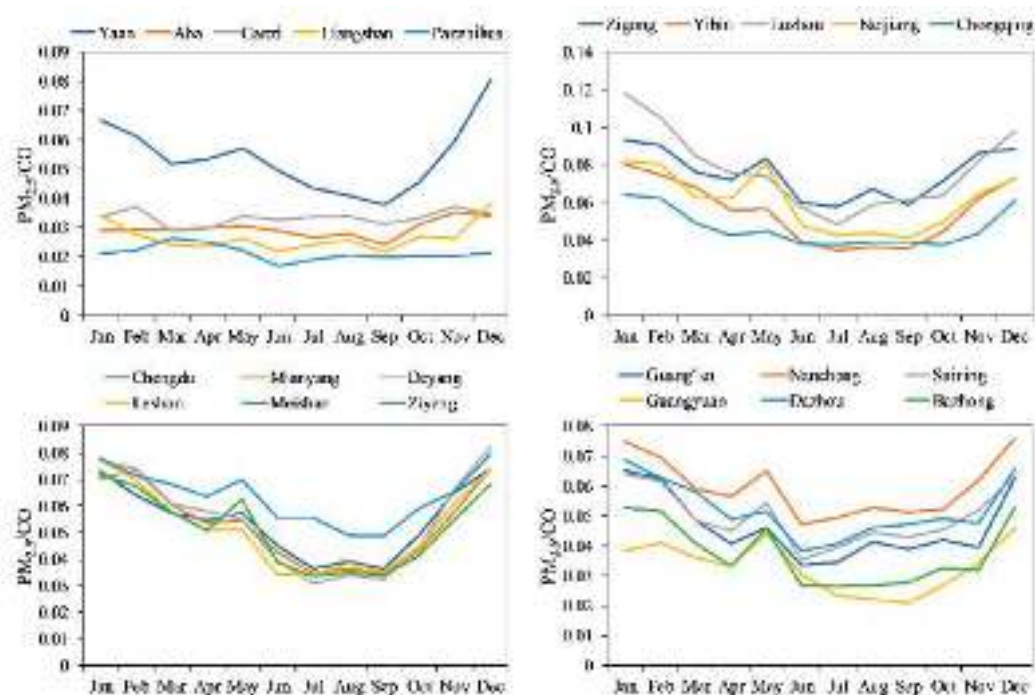


Figure 7. The monthly average $PM_{2.5}/CO$ ratio of each city.

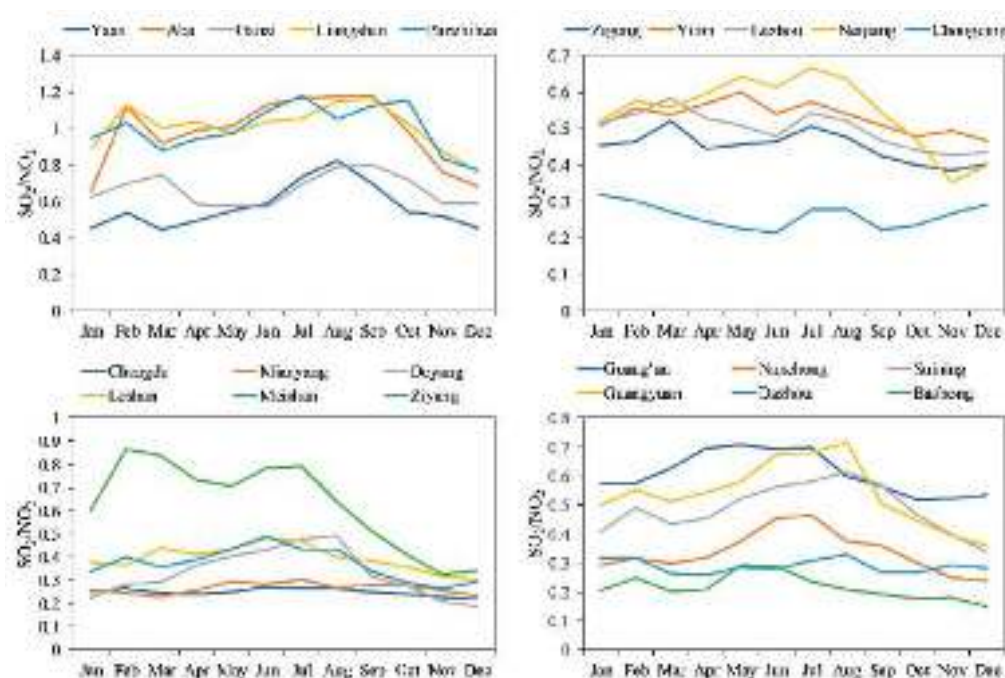


Figure 8. The monthly average SO_2/NO_2 ratio of each city.

From 2015 to 2020, the ratio of $PM_{2.5}/SO_2$ in Sichuan Basin had shown a continuous upward trend, and the ratio of SO_2/NO_x had shown a continuous downward trend (Figure A2). It showed that the contribution of industrial sources to fine particulate matter continued to decline. This was related to the pollutant emission reduction measures that the government had introduced. $PM_{2.5}/CO$ also showed a downward trend, reflecting the decline in the contribution of secondary sources to fine particulate matter, which was related to the decrease in the concentration of SO_2 and NO_x in the regional atmosphere. In 2015, the executive meeting of the State Council of China decided to implement ultra-low emission and energy-saving retrofits for coal-fired power plants before 2020. Sichuan

Province had successively formulated the implementation rules for the Air Pollution Prevention and Control Action Plan from 2014 to 2017, and proposed a series of measures to improve the atmosphere environmental quality, including the elimination of coal-fired boilers below 10 tons per hour and the prohibition of new coal-fired boilers below 20 tons per hour. At the same time, we also noticed that during the study period, the ratio of $PM_{2.5}/PM_{10}$ showed an overall upward trend. This reflected the effectiveness of current dust removal measures to a certain extent, because the existing dust removal measures had far greater removal effects on coarse particles than fine particles.

3.4. Characterization of an Air Pollution Episode in Winter 2017

During this research period, the particulate pollution incident that caused a wide range of impacts was identified in the winter of 2017. Figure 9 showed the hourly average PM_{10} concentration of four cities affected by air pollution incidents (3–6 January 2017), during which the hourly average PM_{10} concentration of all cities exceeded $120 \mu g/m^3$. The average daily concentrations from 3–6 January in Chengdu, Deyang, Ya'an and Meishan were $366 \mu g/m^3$, $245 \mu g/m^3$, $232 \mu g/m^3$ and $225 \mu g/m^3$, respectively. The average daily PM_{10} concentration in these cities was about 10–18 times higher than the WHO guidelines. During the period of heavy pollution, the average ratio of $PM_{2.5}/PM_{10}$ increased over Chengdu, Deyang, Ya'an and Meishan to 0.65, 0.68, 0.69 and 0.74, respectively. The ratio of the four cities is greater than 0.65, much higher than the annual average value of 2017 (0.59), indicating the dominance of fine particulate matter during the event.

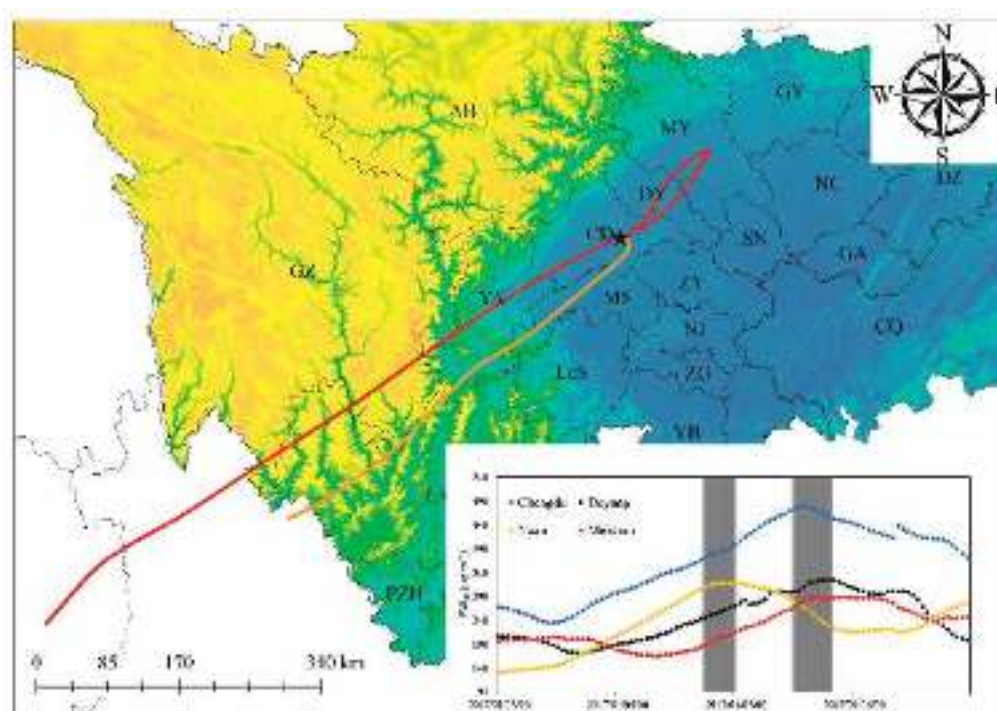


Figure 9. Air transport clustering trajectory in Chengdu during heavy pollution period, and the color of red and orange represent two different trajectories. The right picture shows the hourly average PM_{10} concentration of the four cities during the event. The shaded part represents the arrival time of the peak concentration.

After clustering the downloaded backward trajectories, it was found that they mainly originated over the plateau area of the southwestern part in the basin. The air mass reached Ya'an first from the southwest. The concentration of particulate matter in Ya'an reached a peak with the value of $316 \mu g/m^3$ at 20 o'clock on 4 January, and then the air mass continued to move northeastward. When the air mass moved to Chengdu, the concentration of particulate matter increased. Moreover, the highest concentration was

observed in the Chengdu area, and the highest concentration may occurred over Chengdu and Deyang. Chengdu and Meishan peaked at around 15:00 on 5 January, with PM₁₀ concentrations of 478 µg/m³ and 288 µg/m³, respectively. Deyang reached the maximum concentration of 324 µg/m³ during the pollution period at around 20 o'clock on 5 January.

It is worth noting that the backward trajectory changed the direction in DY and MY before arriving in CD. The further enrichment of particulate matter concentration from DY to MY and CD may be affected by climatic conditions. The adverse meteorological conditions in heavy pollution days, including high pressure, weak wind (0.7 m/s in average) and low temperature (10.5 °C in average), make the pollution track not easy to spread and can only flow inside the basin.

Southwest region is the industrial concentration area of Sichuan Basin, with developed secondary industry. In these cities of Southwest region, PZH is one of the four major iron ore areas in China. In 2018, the economic proportion of the secondary industry in PZH was 62.3%, the highest among all cities in Sichuan Basin. Previous studies have shown that there is a strong positive correlation between the secondary industry and PM_{2.5} concentration [58]. Dense industrial sources in southwest region and adverse meteorological conditions may be the main causes of heavy pollution events in the selected cities.

3.5. Comparison of Air Quality with Standards and Guidelines

In this section, we compared the mean concentration of the pollutants with the available national and WHO guidelines to determine the impacts of current air quality on human health in Sichuan Basin. China revised the National Ambient Air Quality Standard in February 2012. The WHO standards were more stringent than China. Table 2 compared the annual average concentrations of the four pollutants in the basin with different standards, such as the United States Environmental Protection Agency (USEPA), European Union (EU), Australia and Indian standards. The situation regarding pollutants in Sichuan Basin was severe. The WHO guideline for PM_{2.5}(PM₁₀) was exceeded by a factor of approximately 4 (3.8), indicating that the health of the residents will be affected. And the concentrations of PM_{2.5} and PM₁₀ are approximately 2 and 1.8 times higher than the national Grade-I standards, respectively.

Table 2. Comparison of the annual average concentration of the four pollutants with the available standards.

Species	China		WHO	USEPA	EU	Australia	India	Sichuan Basin (This Study)
	Grade-I	Grade-II						
PM _{2.5}	15	35	10	15	25	8	40	39.75
PM ₁₀	40	70	20	-	40	25	60	75.19
SO ₂	20	60	-	-	-	20 *	50	17.76
NO ₂	40	40	40	53 *	40	30 *	40	28.17

Values are in µg m⁻³, * Values in ppb (parts per billion).

In Figure 10, the annual average concentration was compared with WHO standards and national Grade-I and II standards. During the study period, the average annual SO₂ concentration of all cities in Sichuan Basin reached the national Grade-II standard. All cities except Panzhihua reached the national Grade-I standard in 2020. The high concentration of SO₂ in Panzhihua may be due to the burning of coal and biomass and the work of power plants. Moreover, the annual average concentration in Panzhihua declined rapidly since 2018, and it was only slightly higher than the national Grade-I standard in 2020.

During the study period, the annual NO₂ concentration in almost all cities was lower than the WHO and national Grade-I standard. As the two megacities in the basin, Chengdu and Chongqing have the largest anthropogenic activities and emissions, so their annual average concentration of NO₂ was the highest. In 2015–2018, the annual average level was 1.04–1.23 times higher than the WHO guidelines. However, in 2019–2020, its concentration dropped rapidly, mainly due to the strict implementation of the government's environmental protection policy.

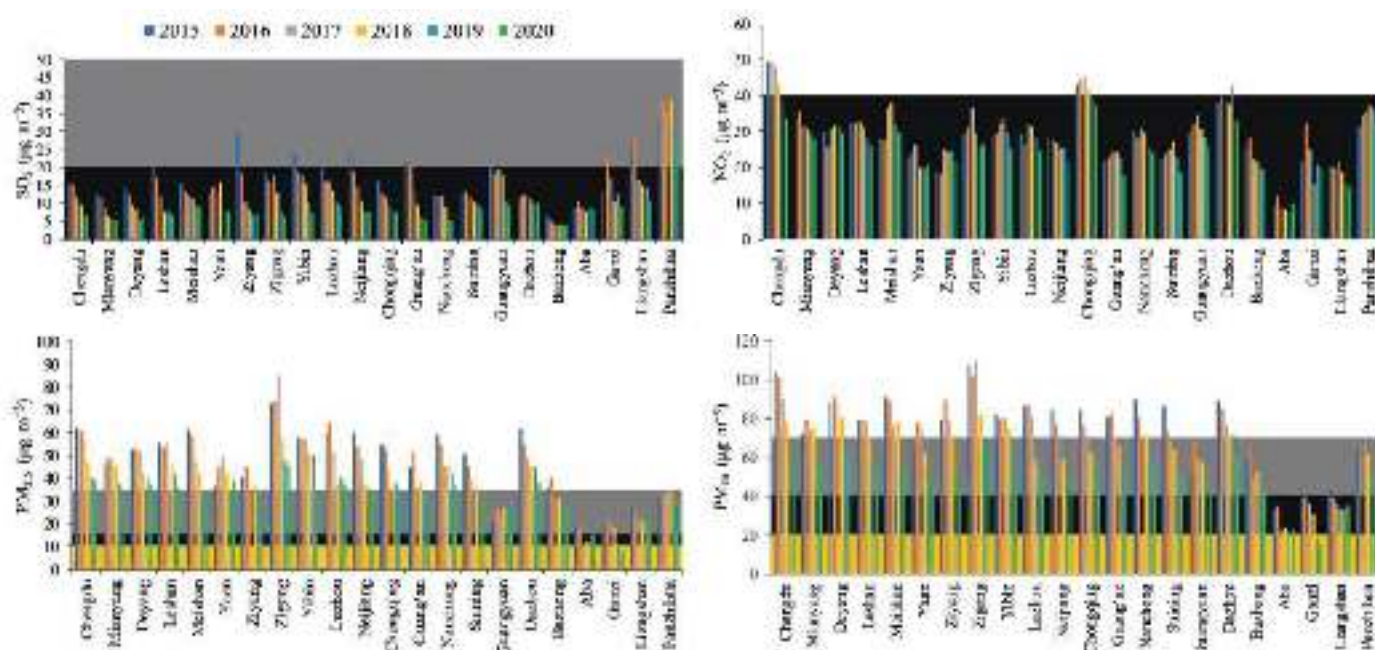


Figure 10. Annual mean concentrations of the pollutants at each site and comparison with the WHO guideline values (yellow shading) and National Grade-I (black shading) and Grade-II (dark gray shading) standards for air quality.

In 2020, the concentration of fine particulate matter in almost all cities in the basin exceeded the WHO regulations. Among these 22 cities, only the average PM_{2.5} concentration of Ganzi was within the WHO standard in 2020. The PM_{2.5} concentration in Aba Prefecture in the past two years was only 0.37 µg/m³ higher than the national Grade-I standard. In Chengdu, Deyang, Zigong and other cities, although the concentration of particulate matter has been declining in recent years, it was still higher than the national Grade-II standard, about 3.5–3.9 times higher than the WHO standard. Compared with PM_{2.5}, the situation of PM₁₀ is slightly better. In 2020, the PM₁₀ concentration of all cities reached the national Grade-II standard. Both Aba and Liangshan reached the national Grade-I standard, and only Ganzi reached the WHO standard in 2019–2020.

4. Conclusions

This study used air quality monitoring data to present the overall air quality status of 22 cities in Sichuan Basin from January 2015 to December 2020. The annual average concentrations of CO, NO₂, SO₂, O₃, PM_{2.5} and PM₁₀ in the entire basin were 0.79 mg/m³, 28.17 µg/m³, 13.08 µg/m³, 84.76 µg/m³, 39.75 µg/m³ and 63.56 µg/m³, respectively. Except for O₃, the annual average concentration of the other five pollutants showed a clear downward trend. CO, NO₂, SO₂, PM_{2.5} and PM₁₀ decreased by 25.7%, 13.6%, 52.6%, 32.9%, and 36.3% respectively during the study period. And O₃ was slowly increasing at an average annual rate of 0.6 µg/m³. The spatial patterns of CO and SO₂ were similar. High-concentration areas were mainly located in the western plateau of Sichuan Basin, while the concentrations of NO₂ and particulate matter were more prominent in the urban agglomerations inside the basin.

The annual average value of PM_{2.5}/SO₂ has been maintained at a low level in Panzhihua (0.9), Liangshan (1.2) and other regions for many years, indicating that industrial sources in the western Sichuan Basin have made a greater contribution to fine particulate matter. Non-industrial sources such as electricity and housing contribute more to fine particulate matter in winter. PM_{2.5}/CO is higher in the southern Sichuan Basin, such as Luzhou (0.077) and Zigong (0.075), indicating that secondary sources have a greater impact on the generation of fine particles. The low SO₂/NO₂ values in megacities such as

Chengdu (0.24) and Chongqing (0.26) indicate that there is a strong correlation between air pollution and automobile exhaust emissions.

During the heavy pollution incident in the winter of 2017, the average daily concentrations from 3–6 January in Chengdu, Deyang, Ya'an and Meishan were $366 \mu\text{g}/\text{m}^3$, $245 \mu\text{g}/\text{m}^3$, $232 \mu\text{g}/\text{m}^3$ and $225 \mu\text{g}/\text{m}^3$, respectively, which were mainly caused by the surrounding plateau terrain under typical stagnant weather conditions. This finding is also supported by backward trajectory analysis, indicating that the air masses arriving in Chengdu are mainly from the plateau area in the western part of the basin. During the study period, the annual average concentration of $\text{PM}_{2.5}$ (PM_{10}) exceeded the WHO guidelines by as much as 4 (3) times. This shows that PM is still the main air pollutant of concern in the region. Therefore, reducing PM should become an integral part of the strategy, policy and action plan of the air pollution management plan. This paper conducts an in-depth study on the temporal and spatial distribution characteristics of six standard air pollutants in the Sichuan Basin, hoping to provide a strong scientific basis for effective air pollution control planning in this area and similar urban agglomerations.

Author Contributions: Data curation and methodology, C.F.; supervisors and directors, J.W.; conceptualization, original draft writing, review and editing, X.T.; field sampling and formal analysis, Y.Z. All authors have read and agreed to the published version of the manuscript.

Funding: This research was funded by Ecology and Environment Department of Jilin Province. The project numbers are 2018-19 and 2019-08.

Institutional Review Board Statement: Not applicable.

Informed Consent Statement: Not applicable.

Data Availability Statement: Publicly available datasets were analyzed in this study. This data can be found here: [<http://www.cnemc.cn/>].

Acknowledgments: The author would like to thank Xin Siyu for her encouragement and company, as well as the group members of Laboratory 537 and 142 in Jilin University.

Conflicts of Interest: The authors declare no conflict of interest.

Appendix A

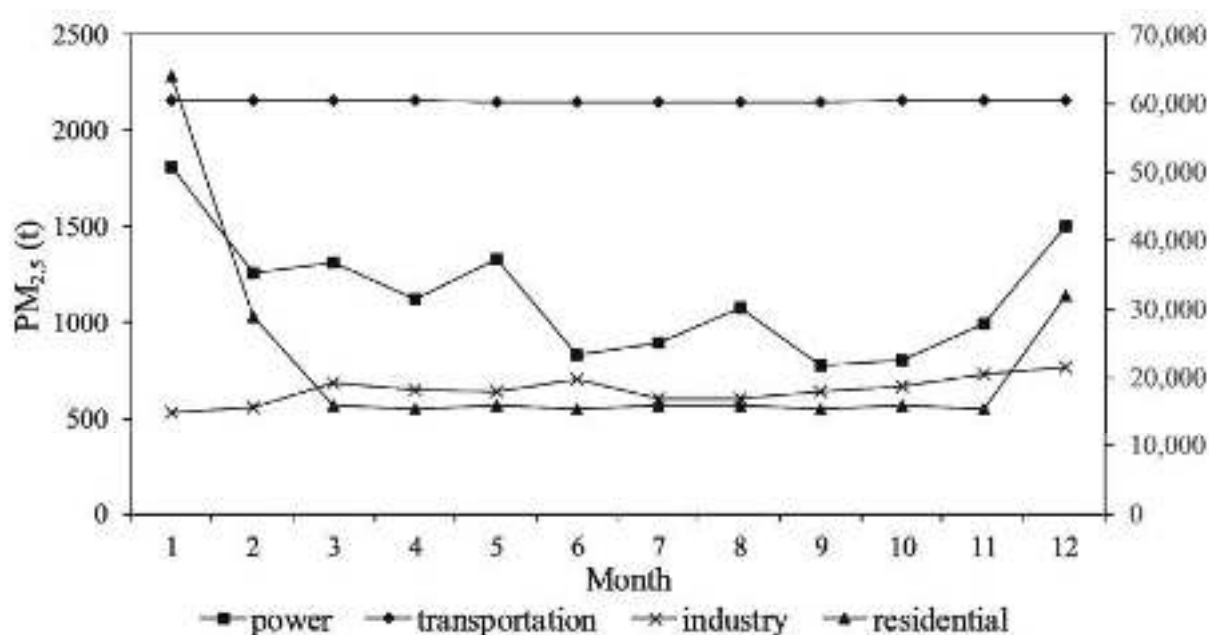


Figure A1. $\text{PM}_{2.5}$ emissions of various departments in Sichuan Basin based on 2017 MEIC inventory statistics. The transportation department corresponds to the left axis, and the other departments correspond to the right axis.

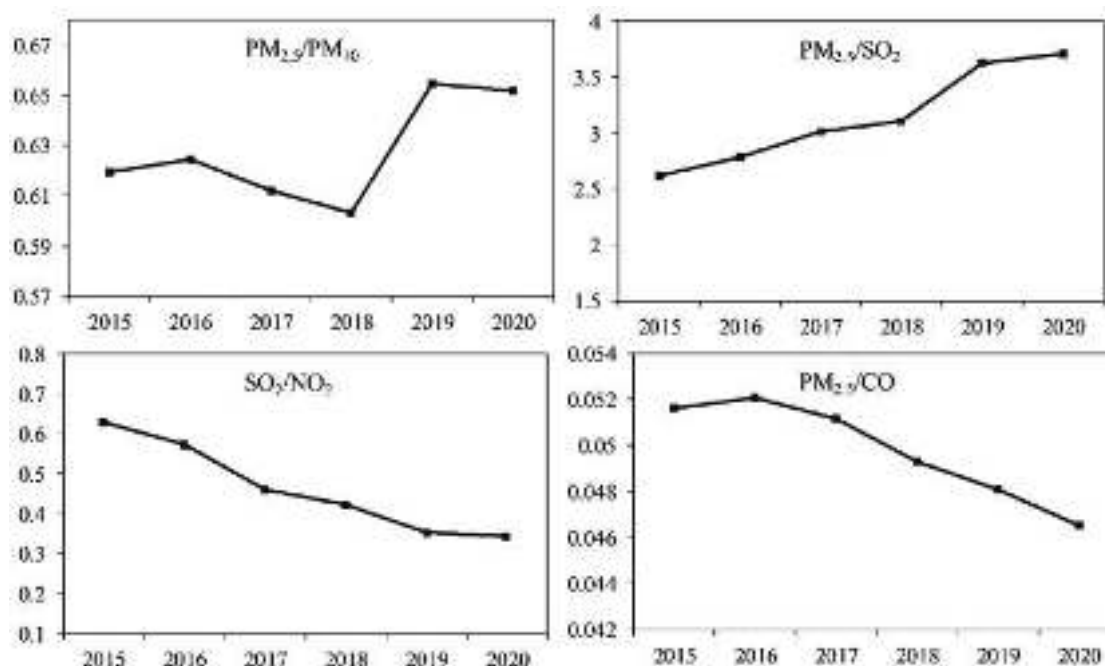


Figure A2. Annual change in the proportion of pollutants.

References

1. Tie, X.; Cao, J. Aerosol pollution in China: Present and future impact on environment. *Particuology* **2009**, *7*, 426–431. [CrossRef]
2. West, J.J.; Cohen, A.; Dentener, F.; Brunekreef, B.; Zhu, T.; Armstrong, B.; Bell, M.L.; Brauer, M.; Carmichael, G.; Costa, D.L.; et al. What We Breathe Impacts Our Health: Improving Understanding of the Link between Air Pollution and Health. *Environ. Sci. Technol.* **2016**, *50*, 4895–4904. [CrossRef] [PubMed]
3. Cao, J.; Yang, C.; Li, J.; Chen, R.; Chen, B.; Gu, D.; Kan, H. Association between long-term exposure to outdoor air pollution and mortality in China: A cohort study. *J. Hazard. Mater.* **2011**, *186*, 1594–1600. [CrossRef] [PubMed]
4. Forouzanfar, M.H.; Afshin, A.; Alexander, L.T.; Anderson, H.R.; Bhutta, Z.A.; Biryukov, S.; Brauer, M.; Burnett, R.; Cercy, K.; Charlson, F.J.; et al. Global, regional, and national comparative risk assessment of 79 behavioural, environmental and occupational, and metabolic risks or clusters of risks, 1990–2015: A systematic analysis for the Global Burden of Disease Study 2015. *Lancet* **2016**, *388*, 1659–1724. [CrossRef]
5. Burnett, R.; Chen, H.; Szyszkowicz, M.; Fann, N.; Hubbell, B.; Pope, C.A., 3rd; Apte, J.S.; Brauer, M.; Cohen, A.; Weichenthal, S.; et al. Global estimates of mortality associated with long-term exposure to outdoor fine particulate matter. *Proc. Natl. Acad. Sci. USA* **2018**, *115*, 9592–9597. [CrossRef]
6. Han, S.; Bian, H.; Feng, Y.; Liu, A.; Li, X.; Zeng, F.; Zhang, X. Analysis of the Relationship between O₃, NO and NO₂ in Tianjin, China. *Aerosol. Air Qual. Res.* **2011**, *11*, 128–139. [CrossRef]
7. He, J.; Gong, S.; Yu, Y.; Yu, L.; Wu, L.; Mao, H.; Song, C.; Zhao, S.; Liu, H.; Li, X.; et al. Air pollution characteristics and their relation to meteorological conditions during 2014–2015 in major Chinese cities. *Environ. Pollut.* **2017**, *223*, 484–496. [CrossRef]
8. Zhang, Q.; Zheng, Y.; Tong, D.; Shao, M.; Wang, S.; Zhang, Y.; Xu, X.; Wang, J.; He, H.; Liu, W.; et al. Drivers of improved PM_{2.5} air quality in China from 2013 to 2017. *Proc. Natl. Acad. Sci. USA* **2019**, *116*, 24463–24469. [CrossRef]
9. Wu, Y.; Zhang, S.; Hao, J.; Liu, H.; Wu, X.; Hu, J.; Walsh, M.P.; Wallington, T.J.; Zhang, K.M.; Stevanovic, S. On-road vehicle emissions and their control in China: A review and outlook. *Sci. Total Environ.* **2017**, *574*, 332–349. [CrossRef]
10. Li, R.; Mao, H.; Wu, L.; He, J.; Ren, P.; Li, X. The evaluation of emission control to PM concentration during Beijing APEC in 2014. *Atmos. Pollut. Res.* **2016**, *7*, 363–369. [CrossRef]
11. Song, C.; Wu, L.; Xie, Y.; He, J.; Chen, X.; Wang, T.; Lin, Y.; Jin, T.; Wang, A.; Liu, Y.; et al. Air pollution in China: Status and spatiotemporal variations. *Environ. Pollut.* **2017**, *227*, 334–347. [CrossRef]
12. Maji, K.J.; Sarkar, C. Spatio-temporal variations and trends of major air pollutants in China during 2015–2018. *Environ. Sci. Pollut. Res. Int.* **2020**, *27*, 33792–33808. [CrossRef]
13. Tao, J.; Zhang, L.; Cao, J.; Zhang, R. A review of current knowledge concerning PM_{2.5} chemical composition, aerosol optical properties and their relationships across China. *Atmos. Chem. Phys.* **2017**, *17*, 9485–9518. [CrossRef]
14. Xie, Y.; Zhao, B.; Zhang, L.; Luo, R. Spatiotemporal variations of PM_{2.5} and PM₁₀ concentrations between 31 Chinese cities and their relationships with SO₂, NO₂, CO and O₃. *Particuology* **2015**, *20*, 141–149. [CrossRef]
15. Gao, J.; Wang, K.; Wang, Y.; Liu, S.; Zhu, C.; Hao, J.; Liu, H.; Hua, S.; Tian, H. Temporal-spatial characteristics and source apportionment of PM_{2.5} as well as its associated chemical species in the Beijing-Tianjin-Hebei region of China. *Environ. Pollut.* **2018**, *233*, 714–724. [CrossRef]

16. Ma, T.; Duan, F.; He, K.; Qin, Y.; Tong, D.; Geng, G.; Liu, X.; Li, H.; Yang, S.; Ye, S.; et al. Air pollution characteristics and their relationship with emissions and meteorology in the Yangtze River Delta region during 2014–2016. *J. Environ. Sci.* **2019**, *83*, 8–20. [CrossRef]
17. Shen, Y.; Zhang, L.; Fang, X.; Ji, H.; Li, X.; Zhao, Z. Spatiotemporal patterns of recent PM_{2.5} concentrations over typical urban agglomerations in China. *Sci. Total Environ.* **2019**, *655*, 13–26. [CrossRef]
18. Xiao, C.; Chang, M.; Guo, P.; Gu, M.; Li, Y. Analysis of air quality characteristics of Beijing-Tianjin-Hebei and its surrounding air pollution transport channel cities in China. *J. Environ. Sci.* **2020**, *87*, 213–227. [CrossRef]
19. Dong, Z.; Wang, S.; Xing, J.; Chang, X.; Ding, D.; Zheng, H. Regional transport in Beijing-Tianjin-Hebei region and its changes during 2014–2017: The impacts of meteorology and emission reduction. *Sci. Total Environ.* **2020**, *737*, 139792. [CrossRef]
20. Zhao, S.; Yu, Y.; Qin, D.; Yin, D.; Dong, L.; He, J. Analyses of regional pollution and transportation of PM_{2.5} and ozone in the city clusters of Sichuan Basin, China. *Atmos. Pollut. Res.* **2019**, *10*, 374–385. [CrossRef]
21. Zhao, S.; Yu, Y.; Yin, D.; Qin, D.; He, J.; Dong, L. Spatial patterns and temporal variations of six criteria air pollutants during 2015 to 2017 in the city clusters of Sichuan Basin, China. *Sci. Total Environ.* **2018**, *624*, 540–557. [CrossRef]
22. Wang, H.; Tian, M.; Chen, Y.; Shi, G.; Liu, Y.; Yang, F.; Zhang, L.; Deng, L.; Yu, J.; Peng, C.; et al. Seasonal characteristics, formation mechanisms and source origins of PM_{2.5} in two megacities in Sichuan Basin, China. *Atmos. Chem. Phys.* **2018**, *18*, 865–881. [CrossRef]
23. Hu, W.; Hu, M.; Hu, W.-W.; Niu, H.; Zheng, J.; Wu, Y.; Chen, W.; Chen, C.; Li, L.; Shao, M.; et al. Characterization of submicron aerosols influenced by biomass burning at site in the Sichuan Basin, southwestern China. *Atmos. Chem. Phys.* **2016**, *16*, 13213–13230. [CrossRef]
24. Zeng, S.; Zheng, Y. Analysis of a Severe Pollution Episode in December 2017 in Sichuan Province. *Atmosphere* **2019**, *10*, 156. [CrossRef]
25. Chen, Y.; Xie, S.D. Long-term trends and characteristics of visibility in two megacities in southwest China: Chengdu and Chongqing. *J. Air Waste Manag. Assoc.* **2013**, *63*, 1058–1069. [CrossRef]
26. Zhang, W.; Liu, B.; Zhang, Y.; Li, Y.; Sun, X.; Gu, Y.; Dai, C.; Li, N.; Song, C.; Dai, Q.; et al. A refined source apportionment study of atmospheric PM_{2.5} during winter heating period in Shijiazhuang, China, using a receptor model coupled with a source-oriented model. *Atmos. Environ.* **2020**, *222*, 117157. [CrossRef]
27. Fu, S.; Guo, M.; Fan, L.; Deng, Q.; Han, D.; Wei, Y.; Luo, J.; Qin, G.; Cheng, J. Ozone pollution mitigation in Guangxi (south China) driven by meteorology and anthropogenic emissions during the COVID-19 lockdown. *Environ. Pollut.* **2021**, *272*, 115927. [CrossRef]
28. Gao, S.; Cong, Z.; Yu, H.; Sun, Y.; Mao, J.; Zhang, H.; Ma, Z.; Azzi, M.; Yang, W.; Jiang, Y.; et al. Estimation of background concentration of PM in Beijing using a statistical integrated approach. *Atmos. Pollut. Res.* **2019**, *10*, 858–867. [CrossRef]
29. Escudero, M.; Stein, A.; Draxler, R.R.; Querol, X.; Alastuey, A.; Castillo, S.; Avila, A. Determination of the contribution of northern Africa dust source areas to PM₁₀ concentrations over the central Iberian Peninsula using the Hybrid Single-Particle Lagrangian Integrated Trajectory model (HYSPLIT) model. *J. Geophys. Res.* **2006**, *111*. [CrossRef]
30. Urlea, A.D.; Barbu, N.; Andrei, S.; Ștefan, S. Simulation of Vesuvius volcanic ash hazards within Romanian airspace using the Hybrid Single-Particle Lagrangian Integrated Trajectory Volcanic Ash numerical model. *Meteorol. Appl.* **2021**, *28*. [CrossRef]
31. Meng, F.; Wang, J.; Li, T.; Fang, C. Pollution Characteristics, Transport Pathways, and Potential Source Regions of PM_{2.5} and PM₁₀ in Changchun City in 2018. *Int. J. Environ. Res. Public Health* **2020**, *17*, 6585. [CrossRef] [PubMed]
32. Yao, Y.; He, C.; Li, S.; Ma, W.; Li, S.; Yu, Q.; Mi, N.; Yu, J.; Wang, W.; Yin, L.; et al. Properties of particulate matter and gaseous pollutants in Shandong, China: Daily fluctuation, influencing factors, and spatiotemporal distribution. *Sci. Total Environ.* **2019**, *660*, 384–394. [CrossRef] [PubMed]
33. Li, B.; Shi, X.F.; Liu, Y.P.; Lu, L.; Wang, G.L.; Thapa, S.; Sun, X.Z.; Fu, D.L.; Wang, K.; Qi, H. Long-term characteristics of criteria air pollutants in megacities of Harbin-Changchun megalopolis, Northeast China: Spatiotemporal variations, source analysis, and meteorological effects. *Environ. Pollut.* **2020**, *267*, 115441. [CrossRef] [PubMed]
34. Fan, Y.; Ding, X.; Hang, J.; Ge, J. Characteristics of urban air pollution in different regions of China between 2015 and 2019. *Build. Environ.* **2020**, *180*, 107048. [CrossRef]
35. Pusede, S.E.; Steiner, A.L.; Cohen, R.C. Temperature and recent trends in the chemistry of continental surface ozone. *Chem. Rev.* **2015**, *115*, 3898–3918. [CrossRef]
36. Monks, P.S.; Archibald, A.T.; Colette, A.; Cooper, O.; Coyle, M.; Derwent, R.; Fowler, D.; Granier, C.; Law, K.S.; Mills, G.E.; et al. Tropospheric ozone and its precursors from the urban to the global scale from air quality to short-lived climate forcer. *Atmos. Chem. Phys.* **2015**, *15*, 8889–8973. [CrossRef]
37. Wang, T.; Xue, L.; Brimblecombe, P.; Lam, Y.F.; Li, L.; Zhang, L. Ozone pollution in China: A review of concentrations, meteorological influences, chemical precursors, and effects. *Sci. Total Environ.* **2017**, *575*, 1582–1596. [CrossRef]
38. Zhang, Q.; Yuan, B.; Shao, M.; Wang, X.; Lu, S.; Lu, K.; Wang, M.; Chen, L.; Chang, C.C.; Liu, S.C. Variations of ground-level O₃ and its precursors in Beijing in summertime between 2005 and 2011. *Atmos. Chem. Phys.* **2014**, *14*, 6089–6101. [CrossRef]
39. Liu, Z.; Wang, Y.; Gu, D.; Zhao, C.; Huey, L.G.; Stickel, R.; Liao, J.; Shao, M.; Zhu, T.; Zeng, L.; et al. Summertime photochemistry during CAREBeijing-2007: ROx budgets and O₃ formation. *Atmos. Chem. Phys.* **2012**, *12*, 7737–7752. [CrossRef]

40. Cooper, O.R.; Parrish, D.D.; Ziemke, J.; Balashov, N.V.; Cupeiro, M.; Galbally, I.E.; Gilge, S.; Horowitz, L.; Jensen, N.R.; Lamarque, J.F.; et al. Global distribution and trends of tropospheric ozone: An observation-based review. *Elem. Sci. Anthr.* **2014**, *2*, 000029. [CrossRef]
41. Xu, Z.; Huang, X.; Nie, W.; Chi, X.; Xu, Z.; Zheng, L.; Sun, P.; Ding, A. Influence of synoptic condition and holiday effects on VOCs and ozone production in the Yangtze River Delta region, China. *Atmos. Environ.* **2017**, *168*, 112–124. [CrossRef]
42. Chen, J.; Shen, H.; Li, T.; Peng, X.; Cheng, H.; Ma, A.C. Temporal and Spatial Features of the Correlation between PM_{2.5} and O₃ Concentrations in China. *Int. J. Environ. Res. Public Health* **2019**, *16*, 4824. [CrossRef]
43. Chen, Z.; Chen, D.; Zhao, C.; Kwan, M.P.; Cai, J.; Zhuang, Y.; Zhao, B.; Wang, X.; Chen, B.; Yang, J.; et al. Influence of meteorological conditions on PM_{2.5} concentrations across China: A review of methodology and mechanism. *Environ. Int.* **2020**, *139*, 105558. [CrossRef]
44. Yu, H.; Yang, W.; Wang, X.; Yin, B.; Zhang, X.; Wang, J.; Gu, C.; Ming, J.; Geng, C.; Bai, Z. A seriously sand storm mixed air-polluted area in the margin of Tarim Basin: Temporal-spatial distribution and potential sources. *Sci. Total Environ.* **2019**, *676*, 436–446. [CrossRef]
45. Casquero-Vera, J.A.; Lyamani, H.; Titos, G.; Borrás, E.; Olmo, F.J.; Alados-Arboledas, L. Impact of primary NO₂ emissions at different urban sites exceeding the European NO₂ standard limit. *Sci. Total Environ.* **2019**, *646*, 1117–1125. [CrossRef]
46. Guo, H.; Chen, K.; Wang, P.; Hu, J.; Ying, Q.; Gao, A.; Zhang, H. Simulation of summer ozone and its sensitivity to emission changes in China. *Atmos. Pollut. Res.* **2019**, *10*, 1543–1552. [CrossRef]
47. Su, Y.; Lu, C.; Lin, X.; Zhong, L.; Gao, Y.; Lei, Y. Analysis of Spatio-temporal Characteristics and Driving Forces of Air Quality in the Northern Coastal Comprehensive Economic Zone, China. *Sustainability* **2020**, *12*, 536. [CrossRef]
48. Duan, Z.; Yang, Y.; Wang, L.; Liu, C.; Fan, S.; Chen, C.; Tong, Y.; Lin, X.; Gao, Z. Temporal characteristics of carbon dioxide and ozone over a rural-cropland area in the Yangtze River Delta of eastern China. *Sci. Total Environ.* **2021**, *757*, 143750. [CrossRef]
49. Jia, B.; Wang, Y.; Wang, C.; Zhang, Q.; Gao, M.; Yung, K.K.L. Sensitivity of PM_{2.5} to NO_x emissions and meteorology in North China based on observations. *Sci. Total Environ.* **2021**, *766*, 142275. [CrossRef]
50. Zhang, Y.L.; Cao, F. Fine particulate matter (PM_{2.5}) in China at a city level. *Sci. Rep.* **2015**, *5*, 14884. [CrossRef]
51. Wang, Y.; Ying, Q.; Hu, J.; Zhang, H. Spatial and temporal variations of six criteria air pollutants in 31 provincial capital cities in China during 2013–2014. *Environ. Int.* **2014**, *73*, 413–422. [CrossRef]
52. Wang, J.; Xie, X.; Fang, C. Temporal and Spatial Distribution Characteristics of Atmospheric Particulate Matter (PM₁₀ and PM_{2.5}) in Changchun and Analysis of Its Influencing Factors. *Atmosphere* **2019**, *10*, 651. [CrossRef]
53. Jing, B.; Wu, L.; Mao, H.; Gong, S.; He, J.; Zou, C.; Song, G.; Li, X.; Wu, Z. Development of a vehicle emission inventory with high temporal–spatial resolution based on NRT traffic data and its impact on air pollution in Beijing—Part 1: Development and evaluation of vehicle emission inventory. *Atmos. Chem. Phys.* **2016**, *16*, 3161–3170. [CrossRef]
54. Li, M.; Liu, H.; Geng, G.; Hong, C.; Liu, F.; Song, Y.; Tong, D.; Zheng, B.; Cui, H.; Man, H.; et al. Anthropogenic emission inventories in China: A review. *Natl. Sci. Rev.* **2017**, *4*, 834–866. [CrossRef]
55. Hu, J.; Wang, P.; Ying, Q.; Zhang, H.; Chen, J.; Ge, X.; Li, X.; Jiang, J.; Wang, S.; Zhang, J.; et al. Modeling biogenic and anthropogenic secondary organic aerosol in China. *Atmos. Chem. Phys.* **2017**, *17*, 77–92. [CrossRef]
56. Fiedler, V.; Nau, R.; Ludmann, S.; Arnold, F.; Schlager, H.; Stohl, A. East Asian SO₂ pollution plume over Europe—Part 1: Airborne trace gas measurements and source identification by particle dispersion model simulations. *Atmos. Chem. Phys.* **2009**, *9*, 4717–4728. [CrossRef]
57. Lian, X.; Huang, J.; Huang, R.; Liu, C.; Wang, L.; Zhang, T. Impact of city lockdown on the air quality of COVID-19-hit of Wuhan city. *Sci. Total Environ.* **2020**, *742*, 140556. [CrossRef]
58. Wang, Y.; Yao, L.; Xu, Y.; Sun, S.; Li, T. Potential heterogeneity in the relationship between urbanization and air pollution, from the perspective of urban agglomeration. *J. Clean. Prod.* **2021**, *298*. [CrossRef]

Article

Effects of Carbon Emission Trading on Companies' Market Value: Evidence from Listed Companies in China

Maogang Tang ^{1,*}, Silu Cheng ^{1,*}, Wenqing Guo ¹, Weibiao Ma ^{1,*} and Fengxia Hu ²

¹ School of Business, East China University of Science and Technology, Shanghai 200237, China; tangmaogang@ecust.edu.cn (M.T.); 19002842@mail.ecust.edu.cn (W.G.)

² School of Statistics and Mathematics, Shanghai Lixin University of Accounting and Finance, Shanghai 201209, China; hufengxia@lixin.edu.cn

* Correspondence: 19002805@mail.ecust.edu.cn (S.C.); weibiao.ma@mail.ecust.edu.cn (W.M.)

Abstract: Emissions trading schemes (ETs) are effective measures that facilitate economic growth and carbon mitigation, especially for developing countries such as China. These schemes can further affect the cash flow, production, and investment decisions of regulated companies. However, few empirical studies have explored how ETs promote companies' market value. We systematically evaluate the influence of the carbon emission trading (CET) policy on companies' market value and explore the influential mechanism. We use the data of listed companies from the Chinese stock "A" markets and employ the difference-in-difference method to account for the unobserved cause of the CET policy regarding companies' market value. Robust benchmark regression results reveal that the CET policy promotes companies' market value significantly. The mechanism analysis reveals that the CET policy can improve the market value of listed companies by influencing the carbon price, innovative activities, and carbon disclosure. The results of the heterogeneity analysis show that the CET policy's impact on companies' market value is heterogeneous in terms of marketization degree, industry, firm ownership, and different regions. We suggest that the carbon pricing mechanism, degree of market perfection, carbon disclosure policy, and carbon finance should be optimized to improve the efficiency of ETs.

Keywords: carbon emission trading schemes; carbon price; China; difference-in-difference; market value

Citation: Tang, M.; Cheng, S.; Guo, W.; Ma, W.; Hu, F. Effects of Carbon Emission Trading on Companies' Market Value: Evidence from Listed Companies in China. *Atmosphere* **2022**, *13*, 240. <https://doi.org/10.3390/atmos13020240>

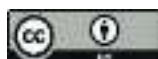
Academic Editors: Duanyang Liu, Kai Qin, Honglei Wang and Célia Alves

Received: 23 December 2021

Accepted: 28 January 2022

Published: 30 January 2022

Publisher's Note: MDPI stays neutral with regard to jurisdictional claims in published maps and institutional affiliations.



Copyright: © 2022 by the authors. Licensee MDPI, Basel, Switzerland. This article is an open access article distributed under the terms and conditions of the Creative Commons Attribution (CC BY) license (<https://creativecommons.org/licenses/by/4.0/>).

1. Introduction

As a market-oriented environmental regulation policy, the carbon emission trading (CET) policy internalizes the cost of carbon emission reduction of enterprises, which will be transmitted to the securities market and may affect the market value of enterprises. Based on the outcomes of some previous studies, a CET policy will lead to a reduction in an enterprise's market value [1–3]. Implementing a CET policy increases the production and operation costs of enterprises, which would crowd out their investment expenditure. This cost information is exposed to the capital market via corporate financial reports. This results in a reduction in the market value of enterprises. For example, Liu et al. (2021) showed that the implementation of carbon emission trading reduced the value of the current capital market. However, other studies have shown that the CET policy will enhance an enterprise's market value [4]. As carbon emission permits are freely allocated, the sale of the remaining permits could be accounted for by higher cash flows due to free permits, which would increase the market value of enterprises [5,6]. According to the price signals of carbon emission permits, some enterprises will adapt to the new direction of industrial development policy, increase investment in innovative activities, and conform to environmental legitimacy to improve their sustainable development ability, thereby enhancing their market value. In addition, certain companies with better carbon emission abatement performance and comparative advantages in terms of abatement cost

will provide detailed information disclosures to attract the attention of investors, thereby exerting a positive impact on the corporation's market value. As the effect of emission trading schemes (ETSs) on a company's market value is difficult to determine accurately, it is necessary to evaluate this effect thoroughly at the micro-level, especially for developing countries such as China.

After implementing a CET policy, a carbon emission permits market is established, wherein the equilibrium of supply and demand determines the price of carbon emission permits. The carbon emission permit price provides companies with a signal to choose between investing in emissions reduction or purchasing emission allowances on the carbon trading market. Accordingly, companies will invest in abatement until the marginal cost equals the CET permit price [7,8]. On the one hand, CET prices may affect enterprises' investment behaviors and expectations of investors, and these influences would be reflected in the stock market [9]. On the other hand, many companies involved in carbon emission trading can shift the carbon emission permit price to their product prices, thus influencing the return rate of their stock prices [10]. Accordingly, there is a strong link between the stock market and the carbon emission trading market [11]. Based on this price signal and its productivity, a company will decide whether to purchase carbon emission rights to meet the government's emission reduction requirements or reduce emissions per unit of output through innovation. First, companies with low productivity can only purchase carbon emission rights to meet the government's emission reduction requirements, which will bring compliance costs to the company and reduce its profits [12]. Carbon emission trading restricts the carbon emissions of these companies and increases the costs of emission reduction, compliance, and technology updates, thereby reducing the company's market value [13,14]. Second, companies with higher productivity can carry out innovative activities that meet the government's emission reduction requirements, and enhance product competitiveness and profits, thereby increasing the company's market value [12,13]. Therefore, there are many mechanisms by which EST affects the market value of companies, and it has a heterogeneous impact on companies with different productivities, which needs to be deeply explored.

As the world's largest carbon emitter, China actively seeks to promote carbon emission reduction through a carbon ETS. Since the European Union introduced the ETS in 2005, this policy has been widely adopted in the US, New Zealand, Australia, Japan, South Korea, and China [15,16]. The development and history of the international and Chinese CET markets are shown in Table 1. At the end of 2011, the Chinese National Development and Reform Commission (NDRC) issued a notice and authorized seven administrative areas at different levels of economic growth and industrial structure to pilot and build projects incorporating carbon emission trading [17]. The pilots cover all four province-level municipalities (Beijing, Shanghai, Tianjin, and Chongqing), two provinces (Guangdong and Hubei), and one special economic zone (Shenzhen) [18]. The preparation and launch of the seven ETS pilots were set to take place within three years (2011–2014) [19]. The seven ETS pilot projects were independently designed and operated, featuring a wide heterogeneity in economic and energy conditions in terms of population, income, the share of manufacturing, and energy consumption [18,20]. Thus, China's CET pilot initiatives offer an excellent opportunity for policy evaluation to investigate the impact of ETS on companies' market value.

Previous studies have extensively investigated the relationship between CET policies and the market value of enterprises. Many studies have investigated the impact of CET policy on enterprises' market value from the perspective of cost and innovation effects, but they obtained contradicting results. Studies from the perspective of the cost effect showed that the impact of CET policy on enterprises' market value is negative. On the contrary, studies from the perspective of innovation effects showed that the impact of CET policy on enterprises' market value is positive [5,10,21]. Furthermore, many studies have explored this effect from the perspective of the transmission effect of the carbon emission permit price. Flora and Vargiolu (2020) confirmed that the carbon price stability mechanism in

the European Union (EU) ETS significantly affects the timing of investment decisions and helps reduce investment related to carbon emissions [18]. Brouwers et al. (2016) found that following the EU's carbon verification, the capital market had a significantly negative response to companies whose carbon emissions exceeded their quotas [22]. Some studies showed that EU allowances price changes and stock returns of the most important European electricity corporations are positively related [1,2]. In addition, many other studies have examined the relationship between the carbon price and the stock returns of the electricity market. Ji et al. (2017) believed that there is strong information interdependence between carbon price returns and electricity stock returns, evidenced by a high total connected index [23]. Veith et al. (2009) measured the economic consequences of ETS using investors' expectations regarding the regulatory impact of firm value. They showed that returns on the common stock of the power generation industry are positively correlated with rising prices for emission rights [2]. However, little is known about the internal mechanism by which the ETS influences companies' market value. To address this research gap, we explore the influence mechanism of ETS on companies' market value by taking the CET pilot policy as a natural experiment.

Table 1. The development of history of international and China's CET market.

Time	Actions or Regulations
1 January 2005	The European Union Emission Trading Scheme (EU ETS) introduced EU allowances, which is the first phase of the EU ETS (2005–2007).
February 2007	Seven U.S. states and four Canadian provinces have joined together to create a regional greenhouse gas emissions trading system.
1 January 2008	The second phase of the EU ETS (2008–2012) started.
September 2008	The New Zealand ETS was enacted.
April 2010	Japan's Kyoto Cap-and-trade system was officially launched.
1 July 2010	The Australian government announced the introduction of its Carbon Pollution Reduction Scheme.
November 2011	The Chinese NDRC issued a notice on carrying out pilot emissions trading, approved seven provinces and cities to carry out pilot programs.
December 2011	The Chinese State Council issued the 12th Five-Year Work Plan on Controlling GHGs.
June 2012	The Chinese NDRC issued the Interim Procedures for the Management of Voluntary Greenhouse Gas Emissions Trading. The voluntary emissions trading mechanism was established, and China Certification Emission Reduction (CCER) trading was put forward.
18 June 2013	The first Chinese ETS pilot was launched in Shenzhen.
August 2013	The Chinese State Council issued the Opinions on Speeding up the Development of Energy Conservation and Environmental Protection Industries. The pilot emission trading schemes was regarded as a means to promote market-oriented mechanism.
26 November 2013	The second Chinese ETS pilot was launched in Shanghai
28 November 2013	Chinese Beijing ETS was launched
19 December 2013	Chinese Guangdong ETS was launched
26 December 2013	Chinese Tianjin ETS was launched
4 April 2014	Chinese Hubei ETS was launched
19 June 2014	Chinese Chongqing ETS was launched
1 January 2015	South Korea launched a carbon trading scheme
19 December 2017	The Chinese NDRC issued the National Carbon Emission Trading Market Construction Scheme to control greenhouse gas emissions.
16 July 2021	China's national CET market launched online trading, making the power generation industry the first to be included in the national carbon market.

This study aims to investigate the effect of the CET policy on companies' market value and explore the influential mechanism. Exploring this influence effect and mechanism is conducive to realizing the synergistic effect of economic growth and carbon mitigation for policymakers in China and potentially other developing countries. Our study's contributions are the following: (1) we systematically evaluate the CET policy's influence on companies' market value and explore the influential mechanism; (2) we employ the difference-in-difference (DID) method to account for unobserved trends in the CET policy's effect on companies' market value across pilot and non-pilot regions. In addition,

we select the study sample from listed companies on China's Shanghai and Shenzhen stock exchanges.

The remainder of this paper is organized as follows: the Section 2 provides a theoretical foundation. The Section 3 presents the empirical model and data. The Section 4 describes the benchmark results and a robustness check. The Section 5 presents the mechanism analysis. The Section 6 presents the heterogeneity analysis. Finally, the conclusions and policy recommendations are derived from the empirical outcomes.

2. Theoretical Foundation

2.1. Carbon Price

CET permits are traded as commodities in the exchange market to form an equilibrium carbon price. The carbon price signals emission reduction costs for enterprises [24]. The carbon price and its changes have a major impact on enterprises' investment decision-making [25].

First—the effect of the carbon price on a company's market value because the trading scheme puts compliance costs on the companies subject to it [2,26]. Carbon prices can influence companies' cash flows, as they can incorporate their carbon emission reduction costs in their sale offers [27]. If companies can pass on any additional costs arising from the trading scheme to their customers, then carbon prices have almost no effect on companies' cash flows [28]. The CET scheme will likely lead to additional costs for regulated companies when they cannot completely pass on the costs to their customers. Such circumstances will affect the companies' cash flows and their cost structure and production decision-making behaviors [3]. Companies need to arrange some part of their cash flows to purchase the CET permits, or to invest in emissions abatement equipment and measures, reducing their output [29]. Accordingly, capital market participants expect decreasing profits of regulated firms due to a rising carbon price for CET permits [1,2].

Second, the CET policy may provide appropriate carbon price signals to industrial operators who can select a strategy of capital investments in clean technology rather than operational practices, such as installing abatement equipment to minimize the sum of abatement costs and permit expenses [24]. When a company's productivity and competitiveness are relatively high, a rising carbon price in emission permits could encourage the company to invest in clean technology to meet emissions abatement requirements by the government [30]. This further results in an increase in the company's investors' expectations of future profits, leading to a higher market value for the company.

Finally, price fluctuations may affect investors' expectations, thereby affecting companies' market value. A variation in carbon prices is reflected in companies' output prices as well as in their costs [31]. Carbon price fluctuations can alter the preferred input combination that companies use in their production processes, thereby affecting their profitability and market value. In addition, according to some studies, a price floor for CET permits reduces uncertainty over companies' future profitability and influences the long-term price signal distribution, while a minimum carbon price creates incentives to invest in new low-carbon technologies [32,33]. Some studies have suggested that the effect of carbon price variations on companies' market value could be asymmetric [34,35].

2.2. Innovative Activities

The CET policy is an environmental instrument that gives individual firms flexibility how they achieve compliance [36]. This policy is expected to generate dynamic incentives to increase companies' innovative activities, mainly in terms of research, development, and demonstration (RD&D) and the adoption and diffusion of abatement technologies or low-carbon technologies [37,38]. Some companies with high abatement costs would purchase permits or conduct innovative activities to meet regulatory requirements. When regulated companies are not able to pass on the additional costs arising from the CET policy to their customers, while at the same time the imposed regulatory costs could even be overcompensated by the buyers, companies could be incentivized to undertake

innovative activities [2,39]. In this setting, companies are inclined to increase investment in emission reduction technologies and low-carbon technologies to achieve emission reduction targets [40]. This increases companies' fixed assets and technology levels, and enhances the value of their products, thereby promoting an increase in their market value [41].

Furthermore, improving companies' emission reduction performance will improve their image and help adjust the expectations of investors and other stakeholders, which will further increase the value of their products and the return in the stock market. Consequently, we can draw a research hypothesis that the CET policy could incentivize some companies to carry out innovative emissions abatement, clean, or low-carbon technologies, thereby enhancing their market value [42]. However, it is worth noting that the innovation effect of the CET policy also depends on market participants, networks, institutions, cumulative learning processes between users and producers, and companies' technology levels [36,40]. Accordingly, the government should improve the degree of marketization by improving laws and regulations related to the CET policy and formulating relevant implementation rules to reduce the impact of institutional uncertainty and institutional transaction costs [43]. Concurrently, the government can subsidize the innovation activities of companies, particularly costly innovation, which requires promotion from the government.

2.3. Carbon Disclosure

Carbon disclosure is a tool that describes companies' carbon-related activities and information to stakeholders. There are generally two types of theories regarding the impact of carbon disclosure on the market value of companies: legitimacy theory and voluntary disclosure theory. According to the legitimacy theory, the cost of environmental information collection, management, and disclosure may outweigh the benefits. To meet various stakeholders' requirements, companies with inferior carbon performance would make soft and unverifiable qualitative disclosure about their performance to maintain legitimacy [44,45]. When the legitimacy of a company is threatened, stakeholders may perceive the company as unsustainable.

Furthermore, information about process inefficiency and environmental initiatives accessible to competitors may weaken firm competition and financial performance, while misleading information or errors in reports can also increase litigation costs significantly [46,47]. Conversely, the voluntary disclosure theory posits that carbon disclosure is positively associated with market value [48]. Under the CET scheme, mandatory carbon reporting [regarding corporate social responsibility (CSR)] helps companies communicate their carbon emissions information and increase information transparency [10]. The improved transparency of high-quality disclosure reduces the information gap to stakeholders, thereby resulting in financial consequences through lower risk [49]. Consequently, carbon disclosure can help stakeholders, such as shareholders and creditors, to make better investment decisions.

Finally, carbon disclosure can also help stakeholders, such as regulatory agencies, institutional investors, and the public, to better monitor and regulate a company's carbon emissions [42,50]. A company's high-quality carbon disclosure often leads to high carbon performance, thus affecting its market value. Therefore, we can hypothesize that the relationship between the CET policy and companies' market value by enhancing carbon disclosure seems to be mixed and inconsistent.

3. Data, Variables, and the Empirical Model

3.1. Data Source

The research sample is obtained from the Chinese Stock "A" markets (Shanghai Stock Exchange and Shenzhen Stock Exchange). The sample period ranges from 2000 to 2019. Data to measure companies' market value (denoted by "MV") and control variables are obtained from the WIND system and the China Stock Market & Accounting Research (CSMAR) system. We consider 2013 the start date of China's CET policy, as Liu et al. (2015) did [51]. We take Beijing, Shanghai, Tianjin, Chongqing, Hubei Province, Guangdong

Province, and Shenzhen as trading pilots. The carbon price data are obtained by initially crawling the daily transaction price data of the carbon market from the exchange websites of each pilot region and then taking the annual average value. The patent and green patent data of listed companies used to measure their innovative activities come from the Chinese Research Data Service (CNRDS) platform, containing multiple sub-databases. The ones used in this study are the China Innovation Research Database (CIRD) and the Green Patent Research Database (GPRD). We derive the patent data of the listed companies from the CIRD. The green patent data of listed companies conform to the GPRD. We use the evaluation data of listed companies' social responsibility reports by Hexun index to represent companies' carbon disclosure [52]. Finally, we eliminate the sample data of listed companies in the financial industry, as their businesses do not involve substantial carbon emissions [42,53]. Listed companies marked with ST, *ST, or PT are deleted from the sample. Additionally, we exclude the sample data of listed companies whose asset-liability ratio is greater than one and eliminate incomplete or omitted sample data, such as company registration location [47]. Ultimately, the final sample consists of 3283 firms.

3.2. Variables

This study uses a series of financial variables, such as financial leverage, return, and profitability, as control variables, owing to their potential impact on companies' market value. Simultaneously, characteristic variables of individual companies, such as age, size, and management shareholding ratio, are used to control their impact on companies' market value. Variables and data descriptions are shown in Table 2.

- (1) SIZE. Large-scale companies have greater resource allocation capabilities and are more capable of conducting innovative activities, enhancing their market value [14].
- (2) BM. The book-to-market ratio is calculated by the total assets divided by the market value, denoted by BM [54].
- (3) ROE. The firm's equity return is measured by the net profit divided by total assets, denoted by ROE [55].
- (4) DAR. Financial leverage is a symbol of financial risk in firms and affects the decision-making of important stakeholders [56]. Accordingly, companies with high financial leverage face greater financial pressures and higher risks, and they are prone to losing investment opportunities, which could reduce their market value. Financial leverage is measured by liabilities divided by total assets and is denoted by DAR in our study.
- (5) fix. Fixed assets are the core assets of companies that can resist market risks; thus, their proportion in total assets affects companies' market value. In this study, we control for the ratio of fixed assets, which is measured by companies' fixed assets to their total assets and is denoted as "fix".
- (6) ROA. Return on assets (ROA) reflects the profitability of companies' total assets. ROA identifies how a company's market value is influenced by improving its operational efficiency [57]. We measure ROA using net income before preferred dividends divided by total assets.
- (7) MSR. Corporate governance factors affect a company's merger and acquisition (M&A) decisions. The proportion of management holdings positively correlates with the probability of M&A. A company with a higher management shareholding ratio has a stronger motivation for external mergers, affecting the company's investment and market value [58,59]. It is measured by the number of shares owned by the management divided by the total number of shares (denoted as "MSR").
- (8) Inage. Older companies have greater motivation and capacity to participate in more carbon emissions abatement activities as they have adequate resources at a relatively lower cost [12,14,60]. Hence, we use the natural logarithm of company age to measure enterprise maturity, denoted by Inage.
- (9) cash and subsidy. Finally, we control companies' operating cash flow (cash) and subsidies obtained from the government (subsidy).

Table 2. Variables and data descriptions.

Variables	Definition	Variable Notation	Unit	Description or Calculation Method
Explained variable	Companies' market value	MV	million yuan	Data were obtained from the database of listed companies.
Explanatory variable	The pilot of the CET policy	did	none	If the city in which company i is located has already launched the pilot CET policy in year t , we define did_{irt} as 1; otherwise, we define it as 0.
Control variable	Companies' scale	SIZE	yuan	It is measured by the following formula: $SIZE = \ln(\text{total assets}/10,000/\text{invest.index2000} + 1)$, where invest.index2000 is the price index of fixed asset investment (last year = 100).
	The book-to-market ratio	BM	none	It is calculated by the total assets divided by the market value.
	The return on a firm's equity	ROE	none	It is measured by the net profit divided by total assets.
	Financial leverage	DAR	none	It is measured by liabilities divided by total assets.
	The ratio of companies' fixed assets	fix	none	It is measured by the ratio of companies' fixed assets to their total assets.
	Return on assets	ROA	none	It is measured by using net income before preferred dividends divided by total assets.
	Management's shareholding ratio	MSR	none	It is measured by the number of shares owned by the management divided by the total number of shares.
	Companies' age	lnage	year	It is measured by the natural logarithm of company age.
	Companies' operating cash flow	cash	none	Data were obtained from the database of listed companies.
	Companies' subsidies obtained from the government	subsidy	yuan	Data were obtained from the database of listed companies.

3.3. Descriptive Statistics

Figure 1 shows the market value of listed companies for the pilot and non-pilot ETS regions. As shown in Figure 1, the market value of listed companies between pilot and non-pilot regions has been presented since 2011, while the trend is parallel before 2011. Although the pilot of the CET policy was only completed in 2013–2014, the Chinese NDRC proposed this policy officially at the end of 2011. Companies in the pilot regions would have behaved rationally and adopted forward-looking decision-making processes to reduce their emissions costs or taking innovative activities such as investing in abatement technologies [61]. Accordingly, the companies' market value difference between the pilot and non-pilot regions shows no significant change after 2013. Nevertheless, these results demonstrate that the parallel trend hypothesis of the DID model can be roughly confirmed graphically.

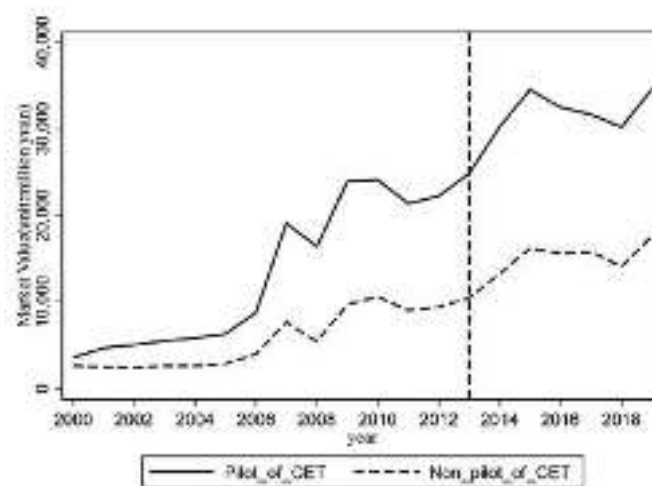
**Figure 1.** The market value of listed companies for pilot and non-pilot regions of ETS.

Table 3 presents the descriptive statistics of the dependent variable (MV) and control variables for the treatment and control groups. The results indicate that the average market value of companies in the treatment group is significantly higher than that in the control group. However, the differences in control variables, such as SIZE, BM, ROE, DAR, fix, ROA, MSR, lnage, cash, and subsidy, between the treatment and control group are not significant.

Table 3. Summary descriptive statistics of the main variables.

Variables	Mean	Standard Deviation	Min	Max	N
Panel A: The sample of treatment group					
MV	24,100	111,000	190	2,990,000	13,200
SIZE	12.5058	1.3636	10.0515	16.3809	13,500
BM	0.6359	0.2357	0.1376	1.1170	13,200
ROE	0.0736	0.1303	−0.7657	0.3796	13,500
DAR	0.4286	0.2056	0.0525	0.8822	13,500
fix	0.2036	0.1699	0.0025	0.7188	13,500
ROA	0.0416	0.0539	−0.1980	0.1947	13,500
MSR	0.1265	0.2054	0.0000	0.6860	13,100
lnage	2.6879	0.4739	1.0986	3.4965	13,500
cash	0.0463	0.0737	−0.1630	0.2552	13,500
subsidy	17,300	140,000	0	1,400,000	13,500
Panel B: The sample of control group					
MV	10,900	26,400	243	1,530,000	21,000
SIZE	12.2870	1.1724	10.0515	16.3809	21,600
BM	0.6512	0.2326	0.1376	1.1170	21,000
ROE	0.0651	0.1427	−0.7657	0.3796	21,600
DAR	0.4372	0.2015	0.0525	0.8822	21,600
fix	0.2573	0.1666	0.0025	0.7188	21,600
ROA	0.0393	0.0558	−0.1980	0.1947	21,600
MSR	0.1047	0.1848	0.0000	0.6860	21,000
lnage	2.5909	0.4834	1.0986	3.4965	21,600
cash	0.0503	0.0712	−0.1630	0.2552	21,600
subsidy	17,500	142,000	0	1,400,000	21,600

3.4. Empirical Model

An effective method to explore the net effect of a policy using the DID model is by comparing treatment and control groups before and after implementing the policy. In this study, the following DID model is constructed to analyze the heterogeneous effect of the market value of listed companies in pilot regions (i.e., treatment group) and non-pilot regions (i.e., control group) before and after the implementation of the CET policy:

$$\ln(MV)_{it} = \beta_0 + \beta_1 treat_i \times time_t + \beta_2 \times X_{it} + \mu_i + \gamma_t + \varepsilon_{it} \quad (1)$$

where i , r , and t denote the listed companies, city, and time, respectively. $\ln(MV)_{it}$ is the natural logarithm of market value of the company i at period t . $treat_i$ is equal to 1 if a company is located in one of the seven pilot provinces and cities; otherwise, it is 0. $time_t$ equals one for every year after 2013; otherwise, it equals 0. X_{it} represents all the control variables, including SIZE, BM, ROE, DAR, fix, ROA, MSR, lnage, cash, and subsidy. β_0 is the constant term and β_1 is the core explanatory variable that indicates the net causal impact of the CET policy on companies' market value. β_2 represents the coefficients of all control variables. μ_i denotes the fixed effects of listed companies, γ_t is the time fixed effect, and ε_{it} is the standard error term.

4. Empirical Results

4.1. Benchmark Regression Results

Table 4 shows the benchmark regression results of the effect of the pilot CET policy on companies' market value according to the empirical model shown in Equation (1).

Column (1) shows the estimation results without controlling for any variable and by controlling for the fixed effects of the firm, while column (2) displays the outcomes without controlling for any variables, while the fixed effects of the firm and year are controlled. Column (3) presents the results with all control variables, and the fixed effects of firm and year are controlled. Column (4) outlines the results by controlling for the fixed effects of firm and industry. Column (5) displays the results by controlling for the fixed effects of the firm, year, and industry [14]. The coefficient of the core explanatory variable is significantly positive after adding control variables and fixing various effects, indicating that the result is relatively robust.

The benchmark regression results show that the market value of listed companies in the pilot regions is significantly higher than that of listed companies in the non-pilot regions. The market-oriented trading mechanism provides the price signals of carbon emissions permits to encourage companies to increase their investment in innovative activities and conform to the carbon emissions abatement requirements, thereby improving companies' market value. Additionally, the free allocation of carbon emissions permits could be accounted for by higher cash flows, which would also increase the market value of companies. These findings are in accordance with those of previous studies, such as those of Oberndorfer (2009), Veith et al. (2009), Oestreich and Tsiakas (2015), and Bui et al. (2019), who stated that the ETS scheme is positively related to companies' market value [1,2,5,6].

Table 4. The regression results of the effect of the pilot CET policy on companies' market value.

Variables	(1)	(2)	(3)	(4)	(5)
	Ln (MV)	Ln (MV)	Ln (MV)	Ln (MV)	Ln (MV)
did	1.263 *** (0.023)	0.067 ** (0.031)	0.016 ** (0.008)	0.046 *** (0.008)	0.017 ** (0.008)
SIZE			0.984 *** (0.006)	0.988 *** (0.005)	0.983 *** (0.006)
BM			−1.832 *** (0.012)	−1.767 *** (0.010)	−1.832 *** (0.013)
ROE			0.026 (0.020)	−0.010 (0.021)	0.023 (0.020)
DAR			0.048 *** (0.015)	0.021 (0.015)	0.051 *** (0.015)
fix			0.034 ** (0.014)	−0.021 (0.016)	0.032 ** (0.014)
ROA			0.054 (0.068)	0.152 ** (0.072)	0.061 (0.068)
MSR			−0.016 (0.015)	−0.001 (0.017)	−0.013 (0.015)
lnage			0.000 (0.018)	0.326 *** (0.007)	0.009 (0.018)
cash			0.006 (0.017)	0.019 (0.018)	0.007 (0.017)
subsidy			0.000 (0.000)	0.000 (0.000)	0.000 (0.000)
_cons	22.147 *** (0.005)	22.400 *** (0.007)	11.366 *** (0.077)	10.432 *** (0.050)	11.355 *** (0.075)
R ²	0.649	0.867	0.990	0.989	0.990
Observations	34,097	34,097	32,980	32,980	32,980
Firm FE	Yes	Yes	Yes	Yes	Yes
Year FE	No	Yes	Yes	No	Yes
Ind FE	No	No	No	Yes	Yes

Note: Standard errors are in parentheses, and they are clustered at firm level. ** and *** indicate statistical significance at the 5% and 1% levels, respectively.

4.2. Robustness Test

4.2.1. Parallel Trend Test and Dynamic Effect

To ensure the effectiveness of the DID model, it is essential to prove that the common trend assumption is satisfied between the treatment and control groups. To test whether the parallel hypothesis was satisfied, we replace the dummy variable in Equation (1) with one corresponding to several years before and after implementing the CET policy [12,61,62]. The regression model is estimated as follows:

$$\ln(MV)_{it} = \beta_0 + \sum_{k=-13}^6 \beta_k (treat_i \times time_t)^k + \beta_2 \times X_{it} + \mu_i + \delta_r + \gamma_t + \varepsilon_{it} \quad (2)$$

where $(treat_i \times time_t)^k$ is 1 when in the k -th year before the implementation of the pilot CET policy ($k < 0$) or in the k -th year after the implementation of the pilot CET policy ($k > 0$) for treatment groups, and 0 otherwise. Since the number of periods before 2013 is very large in our sample, the effects of the 9 to 13 years before 2013 are combined in a single group. If the coefficients of did_{irt}^k are insignificant before 2013 and significant after 2013, then the parallel trend hypothesis is satisfied. Figure 2 shows the test results of the parallel trend hypothesis and the dynamic trend of the pilot CET policy and companies' market value. The results indicate no significant difference between the treatment and control groups before the policy is implemented, while it implies a significant increase in companies' market value after implementing the pilot CET policy. The results confirm the parallel trend hypothesis.

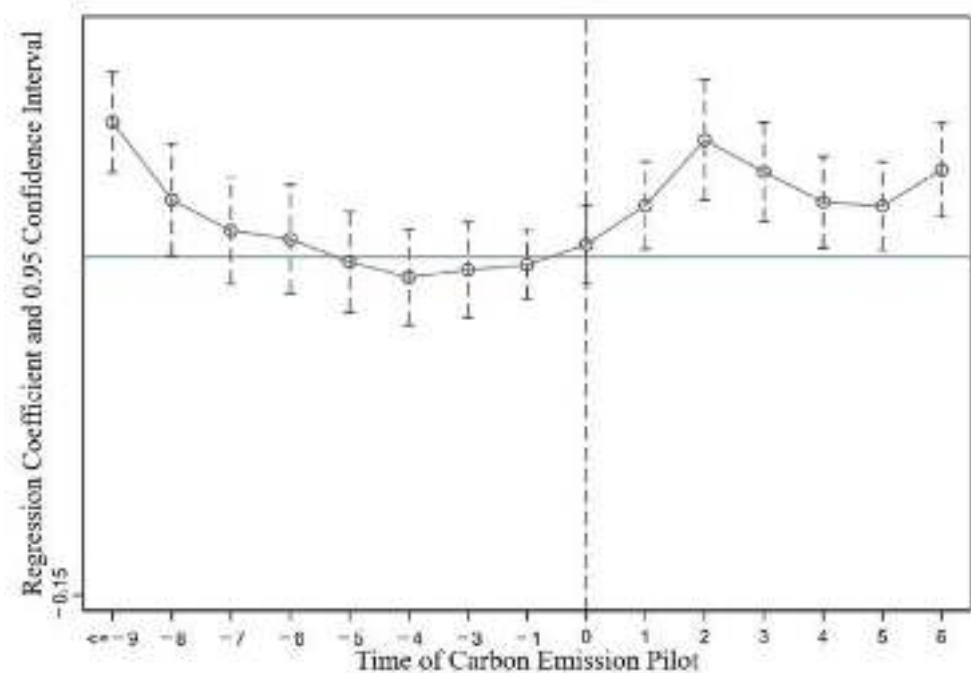


Figure 2. The test of parallel trend hypothesis and the dynamic trend of the pilot CET policy and companies' market value.

4.2.2. Placebo Test

We further perform a placebo test to exclude the effect of the pilot CET policy on a firm's market value from the interference of other non-observable omitted variables. This involved random selection of certain regions as virtual "pilot regions" to enable the comparison of the differences of the effects between the real treatment group and the randomly generated group [61]. More specifically, if there are n firms in 2013 located in the area where the pilot CET policy is launched, keeping the time of the pilot CET policy constant, we randomly select n sample firms from the entire sample of firms as the

treatment group to conduct a counterfactual test. We repeat 500 estimates based on the benchmark regression results in column (3) of Table 4. Figure 3 illustrates the probability density distribution of the regression coefficients for the placebo test. Based on random samples, the estimated coefficients are distributed centrally around 0, while the benchmark regression result (0.016) falls almost outside the possible range estimated from the virtual pilot regions shown in Figure 3. Hence, the results indicate that the pilot CET policy has no policy effect when randomly set up. Therefore, the placebo test reveals that the benchmark regression results of the DID method are reliable.

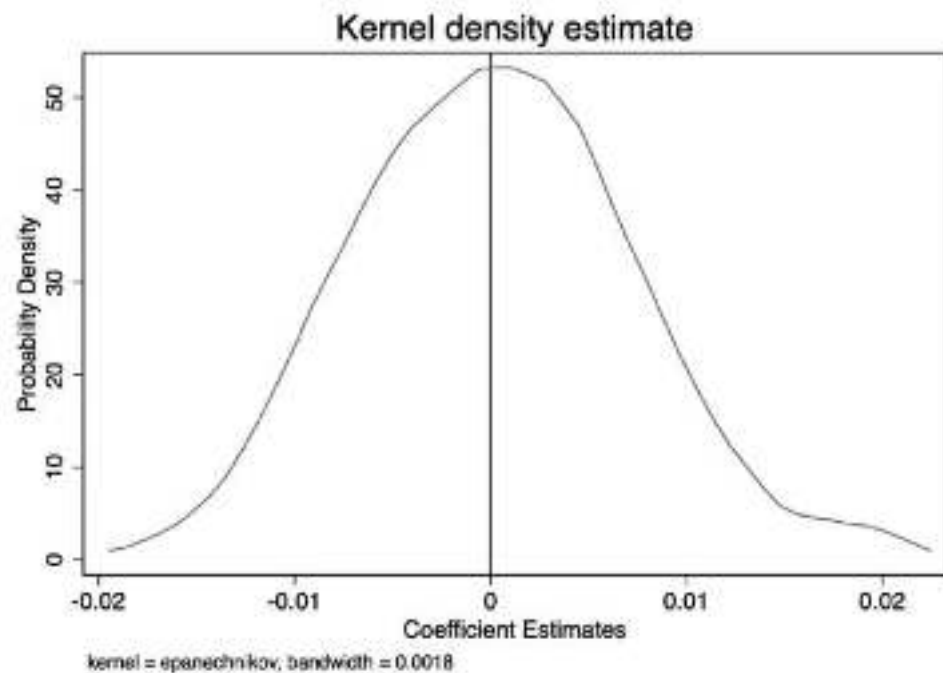


Figure 3. Results of the distribution of the DID estimator for the placebo test.

4.2.3. Other Robustness Tests

Next, we conduct a series of robustness tests to enhance the reliability of the benchmark results.

- (1) Time-lag analysis of companies' market value. To prevent the lag effect of the CET policy, we further examine the effect of the CET policy on companies' market value with a lag of one year [14]. As is shown in column (1) of Table 5, the results indicate that the coefficient of "did" is also significant, implying that the CET policy has a significant lagging effect on promoting companies' market value.
- (2) Policy shocks under changes at the pilot time point. After the CET mechanism is implemented, a certain process and cycle will be required to affect the companies' market value [14]. Hence, we move the treatment year to 2014 (the variable *did* is changed to *did1*) to conduct a robustness check. We find the regression results to be similar to our benchmark results, as reported in column (3) of Table 4, indicating robust benchmark results.
- (3) Changes in the sample period. As the sample period before implementing the pilot policy is too long, we restrict the sample period from 2009 to 2019 and perform a DID regression for robustness checks [14]. Column (3) of Table 5 displays the regression outcomes, suggesting that the estimated conclusions are still robust.

Table 5. Regression results of the other robustness check.

Variables	(1)	(2)	(3)
	L. Ln (MV)	Ln (MV)	Ln (MV)
did	0.020 * (0.011)		0.036 *** (0.007)
SIZE	0.850 *** (0.008)	0.984 *** (0.006)	0.966 *** (0.007)
BM	−1.078 *** (0.019)	−1.832 *** (0.012)	−1.857 *** (0.013)
ROE	−0.151 *** (0.035)	0.025 (0.020)	0.023 (0.026)
DAR	−0.159 *** (0.023)	0.047 *** (0.015)	0.059 *** (0.016)
fix	0.165 *** (0.027)	0.034 ** (0.014)	0.039 ** (0.018)
ROA	−0.557 *** (0.109)	0.056 (0.068)	0.097 (0.080)
MSR	−0.273 *** (0.035)	−0.015 (0.015)	−0.004 (0.016)
lnage	0.107 *** (0.026)	0.001 (0.018)	0.032 (0.039)
cash	0.210 *** (0.033)	0.007 (0.017)	0.021 (0.020)
subsidy	0.000 (0.000)	0.000 (0.000)	0.000 (0.000)
did1		0.021 *** (0.008)	
_cons	12.262 *** (0.114)	11.363 *** (0.077)	11.581 *** (0.123)
R ²	0.958	0.990	0.990
Observations	28,962	32,980	24,420
Firm FE	Yes	Yes	Yes
Year FE	Yes	Yes	Yes

Note: Standard errors are in parentheses, and they are clustered at firm level. *, **, *** indicate statistical significance at the 10%, 5%, and 1% levels, respectively. Column (1) shows the regression results for time-lag analysis of companies' market value. Column (2) shows the regression results by moving the treatment year to 2014. Column (3) shows the regression results by restricting the sample period from 2009 to 2019.

5. Mechanism Analysis

5.1. Carbon Price

Implementing the CET policy has created a carbon trading market in which a carbon price is formed when the supply and demand of permits are balanced. As a signal of the carbon emission reduction cost, the carbon price may positively or negatively impact the market value of companies. Therefore, we empirically analyze the mechanism by which the CET policy affects companies' market value from the perspective of carbon prices. The empirical model used in the mechanism analysis is as follows:

$$m_price_{it} = \beta_0 + \beta_1 treat_i \times time_t + \beta_2 \times X_{it} + \mu_i + \gamma_t + \varepsilon_{it} \quad (3)$$

$$Ln(MV)_{it} = \beta_0 + \beta_1 treat_i \times time_t + \beta_2 \times X_{it} + \delta \times m_price_{it} + \mu_i + \gamma_t + \varepsilon_{it} \quad (4)$$

where m_price is obtained by aggregating daily carbon prices to yearly averages for pilot regions, and the data are collected from China Carbon Information Technology Research Institute.

The regression results of the mediation mechanism analysis are presented in Table 6. The regression results in columns (1) and (2) of Table 6 indicate that the carbon price has a negative mediation effect in the CET policy process, affecting the market value of listed companies. This is mainly because the CET policy will likely lead to additional

compliance costs for regulated companies. To achieve carbon mitigation targets, regulated companies must arrange some part of their cash flows to purchase the CET permits or invest in emission abatement equipment and measures, reducing companies' output. This does not only affect companies' cash flows but also their cost structure and decision-making behaviors of production and R&D investment. A rising carbon price for CET permits lowers investors' expectations of profits, which results in a decrease in companies' market value. These results are consistent with those of previous studies, such as those of Oberndorfer (2009), Veith et al. (2009), Keppler and Cruciani (2010), Mo et al. (2012), and Chan et al. (2013), who found that carbon price variations are negatively correlated with companies' stock market value, returns, or revenue [1,2,35,63,64].

Table 6. Regression results of mediation mechanism analysis based on carbon price.

Variables	(1)	(2)	(3)	(4)
	m_price	Ln (MV)	Ln (MV)	Ln (MV)
did	20.262 *** (0.784)	0.030 *** (0.009)	−0.000 (0.016)	0.031 *** (0.010)
SIZE	0.175 (0.224)	0.984 *** (0.006)	0.982 *** (0.011)	0.984 *** (0.006)
BM	1.215 ** (0.606)	−1.831 *** (0.012)	−1.709 *** (0.023)	−1.854 *** (0.014)
ROE	−0.713 (0.731)	0.025 (0.020)	−0.013 (0.029)	0.041 * (0.025)
DAR	−2.246 *** (0.789)	0.046 *** (0.015)	0.056 (0.038)	0.035 ** (0.016)
fix	−0.206 (0.827)	0.033 ** (0.014)	0.032 (0.021)	0.029 (0.018)
ROA	−0.217 (2.493)	0.054 (0.068)	0.169 (0.123)	0.018 (0.079)
MSR	2.872 ** (1.357)	−0.014 (0.015)	0.020 (0.025)	−0.020 (0.017)
lnage	6.727 *** (0.957)	0.005 (0.018)	−0.005 (0.032)	0.007 (0.021)
cash	−1.126 (0.796)	0.005 (0.017)	−0.041 (0.031)	0.021 (0.020)
subsidy	−0.000 (0.000)	0.000 (0.000)	−0.000 (0.000)	0.000 (0.000)
m_price		−0.001 *** (0.000)	0.001 (0.001)	−0.001 *** (0.000)
_cons	−20.026 *** (3.360)	11.352 *** (0.077)	11.309 *** (0.177)	11.376 *** (0.086)
R ²	0.778	0.990	0.995	0.989
Observations	32,980	32,980	6012	26,938
Firm FE	Yes	Yes	Yes	Yes
Year FE	Yes	Yes	Yes	Yes

Note: Standard errors are in parentheses, and they are clustered at firm level. *, **, *** indicate statistical significance at the 10%, 5%, and 1% levels, respectively. Columns (1) and (2) show the results of the mediation mechanism analysis based on the carbon price. Column (3) shows the regression results for the high-carbon industries. Column (4) shows the regression results for the low-carbon industries.

Companies in regulated high-carbon industries are more affected by CET policies than those in low-carbon industries. To this end, we compare the impact of the CET policy on the market value of companies in high-carbon and low-carbon industries. We regard the eight industries, including the petrochemical sector (C25), chemical industry (C26), construction materials (C30), steel (C31), non-ferrous metals (C32), papermaking (C22), electricity (D44, D45), and aviation (G56) as high-carbon industries; the rest are regarded as low-carbon industries according to Chen et al. (2021) [14]. Columns (3) and (4) of Table 6 show the regression results for the high-carbon and low-carbon industries, respectively. It can be observed that the coefficient of “did” for high-carbon industries is negative

and insignificant, while that for low-carbon industries is significantly positive. This is because companies in high-carbon industries face stronger carbon constraints and bear more compliance costs under the CET policy, compared with the low-carbon industries. Accordingly, the CET policy has a negative impact on the market value of companies in high-carbon industries, while it has a positive effect on the market value of companies in low-carbon industries. These results are in accordance with those of previous studies, such as those of Veith et al. (2009), da Silva et al. (2016), and Wen et al. (2020), which revealed that the effect of carbon price change on the stock market returns in the power industry was asymmetric [2,9,27].

5.2. Innovative Activities

Implementing the CET policy has brought flexible arrangements to achieve carbon emission reductions for relevant listed companies. Companies can maintain their carbon emissions within the designated limits by installing abatement equipment or purchasing carbon permits. However, the cost of such emission reduction will increase with the increase in the carbon price and the reduction of carbon permits, which will reduce companies' profits [65,66]. In this regard, if the cost of investing in cleaner technology is relatively low for some competitive companies, these will choose to invest in innovative activities to minimize carbon emission reduction costs [67]. Implementing the CET policy is conducive to incentivizing companies to increase their innovative activities in cleaner technologies or low-carbon technologies, thereby enhancing companies' market value. Thus, we should investigate the influential mechanism by which innovation affects the CET policy's effect on companies' market value. The empirical model used in the mechanism analysis is as follows:

$$innovation_{it} = \beta_0 + \beta_1 treat_i \times time_t + \beta_2 \times X_{it} + \mu_i + \gamma_t + \varepsilon_{it} \quad (5)$$

$$Ln(MV)_{it} = \beta_0 + \beta_1 treat_i \times time_t + \beta_2 \times X_{it} + innovation_{it} + \mu_i + \gamma_t + \varepsilon_{it} \quad (6)$$

where the mediation variable *innovation* represents the number of green patent applications (denoted as *innovation1*) and green patents granted (denoted as *innovation2*). It is used to measure the innovative activities of companies.

The regression results are shown in Table 7. The results indicate that ETS has significantly promoted green innovation, and the improvement of green innovation can significantly increase companies' market value. The CET policy could enhance the market value of listed companies by promoting green innovation. These results are in line with those of previous studies, such as those of Weber and Neuhoﬀ (2010), Brauneis et al. (2013), and Gersbach and Riekhof (2021), who found that the carbon price signal creates incentives to invest in cleaner, low-carbon, or green technologies under the CET policy, thus enhancing companies' stock market value or returns [30,32,43].

Table 7. Regression results of mediation mechanism analysis based on technological innovation.

Variables	(1)	(2)	(3)	(4)
	Innovation1	Ln (MV)	Innovation2	Ln (MV)
did	0.182 *** (0.056)	0.042 *** (0.012)	0.200 *** (0.057)	0.043 *** (0.013)
SIZE	0.148 *** (0.038)	0.967 *** (0.009)	0.102 *** (0.038)	0.962 *** (0.011)
BM	0.185 *** (0.069)	−1.759 *** (0.020)	0.238 *** (0.069)	−1.764 *** (0.022)
ROE	0.191 (0.140)	−0.015 (0.030)	0.161 (0.143)	0.021 (0.031)
DAR	−0.006 (0.126)	0.037 (0.024)	−0.014 (0.126)	0.021 (0.027)

Table 7. Cont.

Variables	(1)	(2)	(3)	(4)
	Innovation1	Ln (MV)	Innovation2	Ln (MV)
fix	0.262 * (0.143)	0.031 (0.029)	0.137 (0.151)	0.026 (0.030)
ROA	−0.295 (0.393)	0.175 ** (0.086)	−0.317 (0.385)	0.029 (0.092)
MSR	0.358 ** (0.144)	0.018 (0.024)	0.364 *** (0.134)	−0.010 (0.024)
lnage	0.043 (0.182)	0.108 * (0.063)	0.248 (0.207)	0.114 (0.071)
cash	−0.046 (0.138)	0.032 (0.030)	0.014 (0.131)	0.005 (0.031)
subsidy	0.000 (0.000)	0.000 (0.000)	0.000 (0.000)	0.000 (0.000)
innovation1		0.011 *** (0.004)		
innovation2				0.019 *** (0.006)
_cons	−1.829 *** (0.640)	11.297 *** (0.163)	−1.882 *** (0.652)	11.369 *** (0.204)
R ²	0.668	0.994	0.693	0.994
Observations	10,583	10,583	9367	9367
Firm FE	Yes	Yes	Yes	Yes
Year FE	Yes	Yes	Yes	Yes

Note: Standard errors are in parentheses, and they are clustered at firm level. *, **, *** indicate statistical significance at the 10%, 5%, and 1% levels, respectively. Columns (1) and (2) show the results of the mediation mechanism analysis based on green patent applications (*innovation1*). Columns (3) and (4) show the results of the mediation mechanism analysis based on green patents granted (*innovation2*).

5.3. Carbon Disclosure

In recent years, listed companies have been obliged to disclose carbon information related to their production and operation processes and their products to satisfy the concerns of relevant stakeholders, such as shareholders, consumers, and regulatory authorities [68,69]. According to the legitimacy and voluntary disclosure theories, the relationship between carbon disclosure and companies' market value presents two conflicting results. Specifically, we should empirically identify how carbon disclosure affects companies' market value for Chinese CET policies. The empirical model of mechanism model is as follows:

$$disclosure_{it} = \beta_0 + \beta_1 treat_i \times time_t + \beta_2 \times X_{it} + \mu_i + \gamma_t + \varepsilon_{it} \quad (7)$$

$$Ln(MV)_{it} = \beta_0 + \beta_1 treat_i \times time_t + \beta_2 \times X_{it} + disclosure_{it} + \mu_i + \gamma_t + \varepsilon_{it} \quad (8)$$

where disclosure represents the degree of companies' carbon disclosure. We used the evaluation data of listed companies' social responsibility reports by Hexun index to represent the degree of companies' carbon disclosure.

The regression results are shown in Table 8. The results indicate that carbon disclosure plays a negative role in the mechanism by which the CET policy affects companies' market value. According to the legitimacy theory, there is an invisible contract between companies and society, which makes listed companies increase carbon disclosure to meet investors' expectations, thereby maintaining legitimacy. However, the cost of environmental information collection and disclosure is likely to be greater than the benefits obtained by enterprises, especially when enterprises increase costs and improve carbon performance to meet relevant stakeholders' needs. Obviously, a large increase in enterprise costs will reduce companies' market value. These results are consistent with those of previous studies, such as those of Aragon-Correa et al. (2016) and Liu and Zhang (2017), who stated that carbon disclosure enhances cost legitimation and reduces companies' market value [44,45].

Columns (3) and (4) of Table 8 show the regression results after dividing the sample into high-carbon and low-carbon industries. The results indicate that carbon disclosure has a significantly negative correlation with companies' market value for low-carbon industries, while the reduction effect in the market value of high-carbon industries is insignificant.

Table 8. Regression results of mediation mechanism analysis based on carbon disclosure.

Variables	(1)	(2)	(3)	(4)
	Discosco	Ln (MV)	Ln (MV)	Ln (MV)
did	−0.610 (0.538)	0.035 *** (0.006)		
SIZE	4.565 *** (0.325)	0.969 *** (0.007)	0.969 *** (0.016)	0.966 *** (0.008)
BM	−3.890 *** (0.850)	−1.856 *** (0.013)	−1.733 *** (0.024)	−1.881 *** (0.014)
ROE	13.037 *** (1.561)	0.038 * (0.023)	0.014 (0.044)	0.050 * (0.027)
DAR	−4.582 *** (1.109)	0.056 *** (0.017)	0.079 * (0.044)	0.057 *** (0.019)
fix	−2.765 * (1.427)	0.035 * (0.020)	0.049 (0.034)	0.022 (0.025)
ROA	60.686 *** (4.316)	0.063 (0.074)	0.092 (0.136)	0.056 (0.087)
MSR	−5.583 *** (1.356)	−0.005 (0.016)	0.015 (0.027)	−0.018 (0.018)
lnage	−2.674 (2.440)	0.018 (0.036)	−0.020 (0.053)	0.013 (0.041)
cash	1.376 (1.430)	0.032 (0.021)	−0.036 (0.032)	0.047 ** (0.024)
subsidy	−0.000 (0.000)	0.000 (0.000)	−0.000 (0.000)	0.000 (0.000)
discosco		−0.000 *** (0.000)	−0.000 (0.000)	−0.000 *** (0.000)
_cons	−22.327 *** (7.177)	11.598 *** (0.117)	11.621 *** (0.224)	11.680 *** (0.134)
R ²	0.619	0.990	0.995	0.989
Observations	23,172	23,172	3862	19,269
Firm FE	Yes	Yes	Yes	Yes
Year FE	Yes	Yes	Yes	Yes

Note: Standard errors are in parentheses, and they are clustered at firm level. *, **, *** indicate statistical significance at the 10%, 5%, and 1% levels, respectively. Columns (1) and (2) show the results of the mediation mechanism analysis based on carbon disclosure. Column (3) shows the regression results for the high-carbon industries. Column (4) shows the regression results for the low-carbon industries.

6. Heterogeneity Analysis

6.1. The Impact of Firm Ownership

It is generally believed that non-state-owned firms are more flexible in their production, operation, and investment decisions than state-owned firms [70]. Therefore, non-state-owned firms are likely to enhance their market value by implementing a CET policy [14,71]. To this end, we conduct a heterogeneity analysis of the impact of firm ownership on the relationship between CET policy and companies' market value. The regression results are listed in Table 9. The results show that the implementation of the CET policy has a positive and significant impact on the market value of non-state-owned enterprises, while it has an insignificant positive impact on the market value of state-owned enterprises. This is because companies face greater pressure on emission reduction costs, incentivizing them to invest in more advanced cleaner technologies or low-carbon technologies. Non-state-owned companies that are encouraged to invest in clean technologies often convey information to investors that they are more productive and competitive, increasing investors' expectations of the company's future profits, leading to an increase in their market value. By contrast,

state-owned enterprises enjoy more government subsidies, financial support, and more free carbon permits, making them lose their motivation to innovate. Thus, the effect of the CET policy on the market value of state-owned enterprises is insignificant.

Table 9. Heterogeneous analysis of the impact of firm ownership.

Variables	(1)	(2)
	Ln (MV)	Ln (MV)
did	0.018 (0.012)	0.018 ** (0.009)
SIZE	0.993 *** (0.008)	0.981 *** (0.008)
BM	−1.729 *** (0.021)	−1.929 *** (0.015)
DAR	0.034 * (0.020)	0.037 * (0.020)
fix	0.031 ** (0.016)	0.020 (0.025)
MSR	−0.196 (0.123)	−0.025 (0.016)
lnage	0.021 (0.026)	−0.022 (0.023)
cash	0.015 (0.027)	0.043 * (0.025)
subsidy	−0.000 (0.000)	0.000 (0.000)
_cons	11.105 *** (0.099)	11.560 *** (0.117)
R ²	0.993	0.987
Observations	15,148	17,464
Firm FE	Yes	Yes
Year FE	Yes	Yes

Note: Standard errors are in parentheses, and they are clustered at firm level. *, **, *** indicate statistical significance at the 10%, 5%, and 1% levels, respectively. Column (1) shows the regression results for SOEs. Column (2) shows the regression results for non-state-owned firms.

6.2. Heterogeneity Analysis of Different Regions

Chinese provinces are categorized into three regions according to their locations and economic development: eastern, central, and western. The eastern region includes the provinces of Beijing, Tianjin, Hebei, Shanghai, Jiangsu, Zhejiang, Fujian, Shandong, Guangdong, and Hainan. The central region encompasses the provinces of Jilin, Heilongjiang, Shanxi, Henan, Anhui, Hubei, Jiangxi, and Hunan. The western region includes the remaining provinces. Therefore, we conduct a heterogeneity analysis of different regions by dividing the entire sample into eastern, central, and western regions according to the companies' locations. The results are presented in Table 10. The results indicate that the implementation of the CET policy has the most significant effect on enhancing the market value of companies in the eastern and central regions of China, while this effect is not significant in the western region of China. This may be because the economic development, technological level, and marketization degree of the eastern and central regions are higher than those of the western region. Thus, companies in the eastern and central regions are more inclined to conduct innovative activities to achieve carbon emission reduction targets than those in the western region, enhancing their market value. Conversely, companies in the western region are more dependent on natural resources and produce more carbon emissions, thus the impact of the CET policy on companies' market value is negative.

Table 10. Heterogeneous analysis of the different regions.

Variables	(1)	(2)	(3)
	Ln (MV)	Ln (MV)	Ln (MV)
did	0.026 *** (0.009)	0.057 *** (0.019)	0.004 (0.022)
SIZE	0.991 *** (0.007)	0.965 *** (0.013)	0.981 *** (0.011)
BM	−1.831 *** (0.016)	−1.814 *** (0.024)	−1.842 *** (0.026)
ROE	0.058 ** (0.029)	−0.030 (0.029)	0.024 (0.040)
DAR	0.035 ** (0.017)	0.027 (0.035)	0.081 ** (0.041)
fix	0.021 (0.016)	0.006 (0.035)	0.049 (0.033)
ROA	−0.049 (0.091)	0.207 * (0.111)	0.062 (0.151)
MSR	−0.013 (0.017)	−0.092 ** (0.044)	−0.011 (0.054)
lnage	0.002 (0.026)	0.017 (0.029)	−0.078 *** (0.029)
cash	0.034 (0.021)	−0.051 (0.038)	−0.073 * (0.044)
subsidy	0.000 (0.000)	0.000 (0.000)	−0.000 (0.000)
_cons	11.274 *** (0.100)	11.584 *** (0.170)	11.599 *** (0.172)
R ²	0.990	0.989	0.992
Observations	22,672	5240	5057
Firm FE	Yes	Yes	Yes
Year FE	Yes	Yes	Yes

Note: Standard errors are in parentheses, and they are clustered at firm level. *, **, *** indicate statistical significance at the 10%, 5%, and 1% levels, respectively. Column (1) shows the regression results for the eastern region. Column (2) shows the regression results for the central region. Column (3) shows the regression results for the western region.

6.3. The Impact of Different Industries

Companies in the manufacturing industries are mainly regulated by the CET policy, which makes it necessary to invest a large number of funds to purchase carbon permits or install emissions abatement equipment. This could squeeze out companies' original production investments, reducing their market value. Accordingly, we identify the impact of the CET policy on the market value of companies in manufacturing and non-manufacturing industries by using the difference-in-difference-in-difference (DDD) model. We multiply *did* by *industry* to obtain the dummy variable *ddd* of the DDD model for the manufacturing and non-manufacturing industries. The dummy variable *industry* is 1 if the company belongs to high-carbon industries (including the eight industries, C25, C26, C30, C31, C32, C22, D44, D45, and G56), and 0 otherwise. The regression results are listed in Table 11. The results indicate that the estimated coefficients of both the manufacturing and non-manufacturing companies are significantly negative, and the suppression effect of the manufacturing companies is greater than that of the non-manufacturing companies; the CET policy has a significantly negative impact on companies' market value for high-carbon industries. China's ETS pilot policy mainly involves manufacturing and supply industries, including transportation. Manufacturing companies face greater carbon constraints, and the implementation of the CET policy brings about a great cost effect for them, thereby reducing their market value even more.

Table 11. Heterogeneous analysis of the different industries.

Variables	(1) Ln (MV)	(2) Ln (MV)
ddd	−0.041 *** (0.006)	−0.038 *** (0.010)
SIZE	0.992 *** (0.001)	0.994 *** (0.001)
BM	−1.806 *** (0.006)	−1.825 *** (0.009)
ROE	0.000 (0.000)	0.001 (0.001)
DAR	0.004 (0.006)	0.035 *** (0.008)
fix	0.061 *** (0.007)	0.052 *** (0.008)
ROA	0.131 *** (0.014)	0.096 *** (0.021)
MSR	−0.109 *** (0.006)	−0.133 *** (0.010)
lnage	0.012 *** (0.003)	0.009 ** (0.004)
cash	−0.031 ** (0.013)	0.002 (0.018)
subsidy	0.000 (0.000)	0.000 (0.000)
_cons	11.244 *** (0.015)	11.228 *** (0.019)
R^2	0.982	0.987
Observations	21,265	11,812
Firm FE	Yes	Yes
Year FE	Yes	Yes

Note: Standard errors are in parentheses, and they are clustered at firm level. **, *** indicate statistical significance at the 5% and 1% levels, respectively. Column (1) shows the regression results for manufacturing companies. Column (2) shows the regression results for non-manufacturing companies.

6.4. Heterogeneity Analysis of the Marketization Degree

The enhancement of companies' market value by the market-oriented mechanism is affected by the perfection of the market system. When market transaction costs, market power, and information asymmetry exist, the role of market-oriented mechanisms is weakened [72]. Accordingly, we evaluate the heterogeneity analysis of the marketization degree using the DDD model. We use data from the "Marketization Index for China's Provinces of Gang Fan for 2000–2017" to measure the degree of marketization in a certain region [73]. We divide the sample into two groups depending on whether the marketization index score in the region where the company is located is higher or lower than the median of all regions, then conduct a heterogeneity analysis. The regression results are listed in Table 12. These results indicate that the CET policy significantly affects companies' market value when the marketization degree is high. Conversely, the CET policy has a negative and insignificant impact on companies' market value when the marketization degree is low. These findings are in line with those of Jaraitė–Kažukauskė and Kažukauskas (2015), Hu et al. (2020), and Ren et al. (2020) [74–76]. Companies in a region with a high degree of marketization demonstrate increased flexibility in response to market changes and the ability to profit from the carbon emission trading market. When the market system is not perfect, it affects the price of carbon emissions trading and the company's costs, benefits, and expectations. Hence, the degree of marketization influences companies' investment decisions on carbon emission reduction and innovative activities, and in turn, their market value.

Table 12. Heterogeneous analysis of marketization degree.

Variables	(1) Ln (MV)	(2) Ln (MV)
did	0.031 ** (0.015)	−0.005 (0.013)
SIZE	1.006 *** (0.013)	0.982 *** (0.009)
BM	−1.807 *** (0.029)	−1.816 *** (0.020)
ROE	0.069 (0.052)	0.025 (0.029)
DAR	0.022 (0.031)	0.010 (0.025)
fix	0.032 (0.037)	0.020 (0.025)
ROA	−0.068 (0.150)	−0.020 (0.118)
MSR	−0.007 (0.028)	−0.009 (0.053)
lnage	−0.038 (0.058)	−0.048 * (0.027)
cash	0.061 (0.042)	−0.034 (0.029)
subsidy	−0.000 (0.000)	0.000 (0.000)
_cons	11.234 *** (0.199)	11.469 *** (0.152)
R ²	0.991	0.992
Observations	8044	7983
Firm FE	Yes	Yes
Year FE	Yes	Yes

Note: Standard errors are in parentheses, and they are clustered at firm level. *, **, *** indicate statistical significance at the 10%, 5%, and 1% levels, respectively. Column (1) shows the regression results for companies with a high degree of marketization. Column (2) shows the regression results for companies with a low degree of marketization.

6.5. Heterogeneity Analysis of Financial Constraints

Under the carbon emission reduction pressure, companies have had to install carbon abatement equipment or upgrade their production progress by investing in low-carbon technologies, which undoubtedly aggravates their financial constraints [77]. Companies suffering from tight financial constraints cannot obtain sufficient financial resources to respond flexibly to the requirements of the CET policy. At the same time, this also affects the carbon emission reduction, production, and innovative activities of companies, thereby affecting their market value. We use the size-age (SA) index to measure the financing constraints of companies and divide the sample into two groups according to whether the SA index is higher than or lower than the median value for heterogeneity analysis. Companies with an SA index greater than the median value face loose financial constraints, while those with an SA index less than the median value face tight financial constraints. The SA index is calculated according to the formula: $SA = 0.043 \times \text{size} \times \text{size} - 0.737 \times \text{size} - 0.04 \times \text{age}$, where size is the logarithm of companies' total assets [74]. The regression results are listed in Table 13. The results indicate that the CET policy has a significantly positive impact on the market value of companies with an SA index greater than the median. Conversely, the CET policy has no significant effect on the market value of companies with an SA index less than the median. Companies with loose financial constraints have more flexibility and better financial resources, they can optimize their decisions and strategies to enhance their market value in the CET market.

Table 13. Heterogeneous analysis of financial constraints.

Variables	(1)	(2)
	Ln (MV)	Ln (MV)
did	0.038 *** (0.011)	0.007 (0.012)
SIZE	1.010 *** (0.010)	0.951 *** (0.011)
BM	−1.609 *** (0.017)	−2.019 *** (0.018)
ROE	0.009 (0.029)	0.008 (0.024)
DAR	0.055 *** (0.018)	0.043 * (0.024)
fix	0.008 (0.014)	0.016 (0.023)
ROA	0.145 (0.089)	0.086 (0.083)
MSR	0.071 *** (0.020)	−0.042 * (0.022)
lnage	0.044 (0.041)	−0.003 (0.020)
cash	0.035 (0.022)	−0.012 (0.024)
subsidy	−0.000 (0.000)	0.000 (0.000)
_cons	10.773 *** (0.121)	11.826 *** (0.149)
R ²	0.992	0.967
Observations	16,437	16,278
Firm FE	Yes	Yes
Year FE	Yes	Yes

Note: Standard errors are in parentheses, and they are clustered at firm level. *, *** indicate statistical significance at the 10% and 1% levels, respectively. Column (1) shows the regression results for companies with loose financial constraints (companies with an SA index greater than the median). Column (2) shows the regression results for companies with tight financial constraints (companies with an SA index less than the median).

7. Discussions, Conclusions, and Policy Recommendations

Using China's CET policy as a quasi-natural experiment, we innovatively explore the effect of this policy on companies' market value. We investigate how the ETS scheme promotes companies' market value from the carbon price, technological innovation, and carbon disclosure angle. Additionally, we conduct a heterogeneity analysis of the marketization degree, industries, firm ownership, and different regions. We use the data of listed companies from the Chinese stock "A" markets and match the data with patent and green patent data from the CNRDS platform. We employ the DID method to account for the unobserved cause of the CET policy regarding companies' market value. Understanding this mechanism is important for advancing the performance of the carbon markets in China and potentially those in other developing countries that consider emission trading in their policy mix. The results of our study will help policymakers take full account of matching and coordinating existing laws, rules, and various policy instruments to create synergies. In addition, the findings of this study may be important for investors to optimize their decision-making and enhance their market value under the ETS mechanism.

Through theoretical and empirical analysis, we drew a series of conclusions:

1. The benchmark regression results reveal that the CET policy promoted companies' market value significantly. A series of robustness tests (e.g., parallel trend, dynamic effects, and placebo tests) show robust outcomes.
2. The mechanism analysis of carbon price indicate that the CET policy could improve the market value of listed companies by influencing carbon price signals, and that

carbon prices have a greater impact on the market value of companies in high-carbon industries. The mechanism analysis of technological innovation reveals that the CET policy has promoted green innovation considerably, and the improvement of green innovation can significantly increase companies' market value. The mechanism analysis of carbon disclosure shows that carbon disclosure plays a negative role in the mechanism by which the CET policy affects companies' market value, and that the reduction effect in the market value of high-carbon industries is less than that of low-carbon industries.

3. The heterogeneity analysis of the marketization degree demonstrates that the CET policy significantly affects companies' market value when the market system is perfect.
4. The CET policy's impact on companies' market value is heterogeneous in industry, firm ownership, and different regions.

Our findings have important implications for regulators, policymakers, investors, and managers.

First, China's CET market's carbon pricing mechanism needs to be further improved to form a reasonable and effective carbon price. For the carbon market, a reasonable carbon price mechanism is of great significance to give full play to the role of the carbon market in energy saving and emission reduction. It is useful to set up a mechanism wherein the carbon prices are determined by the market and regulated by government. It is necessary to form a reasonable carbon price to reflect the scarcity of carbon permits and form effective incentives for companies. A carbon price that is too low cannot form a compelling incentive for companies, while a carbon price that is too high will increase the cost of companies.

Second, the government should improve the degree of market perfection and reduce market transaction costs. Perfecting the market rules of ETSs, including the carbon discharge permit system and monitoring system, is critical for improving their efficiency. It is also necessary for the government to set up and improve ETSs implementing policy and system development. The government should improve the information quality of carbon trading, which in turn will provide accurate supply and demand information and lower the costs of collecting information.

Third, regulators may consider the adverse impact of carbon disclosure on stakeholders and devise a carbon disclosure policy to encourage companies to disclose carbon emissions voluntarily. The government should strengthen and optimize the corporate social responsibility disclosure systems or utilize external institutions, such as media and public attention, to magnify the potential value losses of companies' socially irresponsible behaviors.

Fourth, the government should further improve policies and regulations that encourage investors and companies to participate in cleaner and low-carbon innovative activities. The government is committed to establishing an incentive mechanism and strengthening the support of innovative capital, market systems, talents, and other elements to promote sustainable economic development effectively.

Finally, we propose that the Chinese government further improve carbon trading regulations and incorporate carbon finance into the carbon trading policy system. The role of tools such as carbon forwards and carbon futures should be further used to assist the carbon market in generating timely, true, and effective carbon price signals.

Author Contributions: Conceptualization, M.T.; methodology, W.M. and S.C.; software, S.C. and W.G.; validation, S.C.; formal analysis, S.C., W.M. and W.G.; investigation, S.C.; resources, M.T.; data curation, S.C.; writing—original draft preparation, M.T.; writing—review and editing, M.T.; visualization, W.M.; supervision, F.H.; project administration, F.H.; funding acquisition, M.T. All authors have read and agreed to the published version of the manuscript.

Funding: This research was funded by the Major Project of the Chinese National Social Science Fund "Research on improving the development mechanism of urban-rural integration" (21AZD036), the General Project of the Chinese National Social Science Fund "Land development right transaction,

land resource allocation mechanism and high-quality economic development” (21FJYB052), and the National Natural Science Foundation of China (72073045).

Institutional Review Board Statement: Not applicable.

Informed Consent Statement: Not applicable.

Data Availability Statement: The data presented in this study are available on request from the corresponding author.

Conflicts of Interest: The authors declare no conflict of interest in this article.

References

1. Oberndorfer, U. EU Emission Allowances and the stock market: Evidence from the electricity industry. *Ecol. Econ.* **2009**, *68*, 1116–1126. [CrossRef]
2. Veith, S.; Werner, J.R.; Zimmermann, J. Capital market response to emission rights returns: Evidence from the European power sector. *Energy Econ.* **2009**, *31*, 605–613. [CrossRef]
3. Fabra, N.; Reguant, M. Pass-Through of Emissions Costs in Electricity Markets. *Am. Econ. Rev.* **2014**, *104*, 2872–2899. [CrossRef]
4. Liu, M.; Zhou, C.; Lu, F.; Hu, X. Impact of the implementation of carbon emission trading on corporate financial performance: Evidence from listed companies in China. *PLoS ONE* **2021**, *16*, e0253460. [CrossRef]
5. Bui, B.; Moses, O.; Houqe, M.N. Carbon disclosure, emission intensity and cost of equity capital: Multi-country evidence. *Account. Financ.* **2020**, *60*, 47–71. [CrossRef]
6. Oestreich, A.M.; Tsiakas, I. Carbon emissions and stock returns: Evidence from the EU Emissions Trading Scheme. *J. Bank. Financ.* **2015**, *58*, 294–308. [CrossRef]
7. Clarkson, P.M.; Li, Y.; Pinnuck, M.; Richardson, G.D. The Valuation Relevance of Greenhouse Gas Emissions under the European Union Carbon Emissions Trading Scheme. *Eur. Account. Rev.* **2015**, *24*, 551–580. [CrossRef]
8. Matisoff, D.C. The Adoption of State Climate Change Policies and Renewable Portfolio Standards: Regional Diffusion or Internal Determinants? *Rev. Policy Res.* **2008**, *25*, 527–546. [CrossRef]
9. Wen, F.; Zhao, L.; He, S.; Yang, G. Asymmetric relationship between carbon emission trading market and stock market: Evidences from China. *Energy Econ.* **2020**, *91*, 104850. [CrossRef]
10. Velte, P.; Stawinoga, M.; Lueg, R. Carbon performance and disclosure: A systematic review of governance-related determinants and financial consequences. *J. Clean. Prod.* **2020**, *254*, 120063. [CrossRef]
11. Jiménez-Rodríguez, R. What happens to the relationship between EU allowances prices and stock market indices in Europe? *Energy Econ.* **2019**, *81*, 13–24. [CrossRef]
12. Tang, M.; Li, Z.; Hu, F.; Wu, B.; Zhang, R. Market failure, tradable discharge permit, and pollution reduction: Evidence from industrial firms in China. *Ecol. Econ.* **2021**, *189*, 107180. [CrossRef]
13. Liu, C.; Ma, C.; Xie, R. Structural, Innovation and Efficiency Effects of Environmental Regulation: Evidence from China’s Carbon Emissions Trading Pilot. *Environ. Resour. Econ.* **2020**, *75*, 741–768. [CrossRef]
14. Chen, Z.; Zhang, X.; Chen, F. Do carbon emission trading schemes stimulate green innovation in enterprises? Evidence from China. *Technol. Forecast. Soc. Chang.* **2021**, *168*, 120744. [CrossRef]
15. Martin, R.; Muuls, M.; Wagner, U.J. The Impact of the European Union Emissions Trading Scheme on Regulated Firms: What Is the Evidence after Ten Years? *Rev. Environ. Econ. Policy* **2016**, *10*, 129–148. [CrossRef]
16. Zhu, J.; Fan, Y.; Deng, X.; Xue, L. Low-carbon innovation induced by emissions trading in China. *Nat. Commun.* **2019**, *10*, 4088. [CrossRef]
17. Liu, L.; Wang, Y.; Wu, C.; Wu, W. Disentangling the determinants of real oil prices. *Energy Econ.* **2016**, *56*, 363–373. [CrossRef]
18. Zhang, J.; Wang, Z.; Du, X. Lessons learned from China’s regional carbon market pilots. *Econ. Energy Environ. Policy* **2017**, *6*, 19–38. [CrossRef]
19. Zhang, D.; Karplus, V.J.; Cassisa, C.; Zhang, X. Emissions trading in China: Progress and prospects. *Energy Policy* **2014**, *75*, 9–16. [CrossRef]
20. Descheemaeker, K.; Oosting, S.J.; Tui, S.H.-K.; Masikati, P.; Falconnier, G.N.; Giller, K.E. Climate change adaptation and mitigation in smallholder crop–livestock systems in sub-Saharan Africa: A call for integrated impact assessments. *Reg. Environ. Chang.* **2016**, *16*, 2331–2343. [CrossRef]
21. Flora, M.; Vargiolu, T. Price dynamics in the European Union Emissions Trading System and evaluation of its ability to boost emission-related investment decisions. *Eur. J. Oper. Res.* **2020**, *280*, 383–394. [CrossRef]
22. Brouwers, R.; Schoubben, F.; Van Hulle, C.; Van Uytbergen, S. The initial impact of EU ETS verification events on stock prices. *Energy Policy* **2016**, *94*, 138–149. [CrossRef]
23. Ji, J.; Zhang, Z.; Yang, L. Carbon emission reduction decisions in the retail-/dual-channel supply chain with consumers’ preference. *J. Clean. Prod.* **2017**, *141*, 852–867. [CrossRef]
24. Stigler, G.J.; Friedland, C. What Can Regulators Regulate? The Case of Electricity. *J. Law Econ.* **1962**, *5*, 1–16. [CrossRef]
25. Cui, J.; Zhang, J.; Zheng, Y. Carbon Pricing Induces Innovation: Evidence from China’s Regional Carbon Market Pilots. *AEA Pap. Proc.* **2018**, *108*, 453–457. [CrossRef]

26. Da Silva, P.P.; Moreno, B.; Figueiredo, N.C. Firm-specific impacts of CO₂ prices on the stock market value of the Spanish power industry. *Energy Policy* **2016**, *94*, 492–501. [CrossRef]
27. Abrell, J.; Cludius, J.; Lehmann, S.; Schleich, J.; Betz, R. Corporate Emissions-Trading Behaviour During the First Decade of the EU ETS. *Environ. Resour. Econ.* **2021**, 1–37. [CrossRef]
28. Montgomery, W.D. Markets in licenses and efficient pollution control programs. *J. Econ. Theory* **1972**, *5*, 395–418. [CrossRef]
29. Brauneis, A.; Mestel, R.; Palan, S. Inducing low-carbon investment in the electric power industry through a price floor for emissions trading. *Energy Policy* **2013**, *53*, 190–204. [CrossRef]
30. Boersen, A.; Scholtens, B. The relationship between European electricity markets and emission allowance futures prices in phase II of the EU (European Union) emission trading scheme. *Energy* **2014**, *74*, 585–594. [CrossRef]
31. Weber, T.A.; Neuhoﬀ, K. Carbon markets and technological innovation. *J. Environ. Econ. Manag.* **2010**, *60*, 115–132. [CrossRef]
32. Gröll, G.; Taschini, L. Cap-and-trade properties under different hybrid scheme designs. *J. Environ. Econ. Manag.* **2011**, *61*, 107–118. [CrossRef]
33. Zachmann, G.; von Hirschhausen, C. First evidence of asymmetric cost pass-through of EU emissions allowances: Examining wholesale electricity prices in Germany. *Econ. Lett.* **2008**, *99*, 465–469. [CrossRef]
34. Mo, J.-L.; Zhu, L.; Fan, Y. The impact of the EU ETS on the corporate value of European electricity corporations. *Energy* **2012**, *45*, 3–11. [CrossRef]
35. Rogge, K.S.; Hoffmann, V.H. The impact of the EU ETS on the sectoral innovation system for power generation technologies—Findings for Germany. *Energy Policy* **2010**, *38*, 7639–7652. [CrossRef]
36. Fischer, C.; Parry, I.W.H.; Pizer, W.A. Instrument choice for environmental protection when technological innovation is endogenous. *J. Environ. Econ. Manag.* **2003**, *45*, 523–545. [CrossRef]
37. Rogge, K.S.; Schneider, M.; Hoffmann, V.H. The innovation impact of the EU Emission Trading System—Findings of company case studies in the German power sector. *Ecol. Econ.* **2011**, *70*, 513–523. [CrossRef]
38. Golombek, R.; Hoel, M. Endogenous technology and tradable emission quotas. *Resour. Energy Econ.* **2008**, *30*, 197–208. [CrossRef]
39. Greaker, M.; Hagem, C. Strategic Investment in Climate Friendly Technologies: The Impact of Global Emissions Trading. *Environ. Resour. Econ.* **2014**, *59*, 65–85. [CrossRef]
40. Kemp, R.; Pontoglio, S. The innovation effects of environmental policy instruments—A typical case of the blind men and the elephant? *Ecol. Econ.* **2011**, *72*, 28–36. [CrossRef]
41. Siddique, M.A.; Akhtaruzzaman, M.; Rashid, A.; Hammami, H. Carbon disclosure, carbon performance and financial performance: International evidence. *Int. Rev. Financ. Anal.* **2021**, *75*, 101734. [CrossRef]
42. Gersbach, H.; Riekhof, M.-C. Permit markets, carbon prices and the creation of innovation clusters. *Resour. Energy Econ.* **2021**, *65*, 101229. [CrossRef]
43. Aragón-Correa, J.A.; Marcus, A.; Hurtado-Torres, N. The Natural Environmental Strategies of International Firms: Old Controversies and New Evidence on Performance and Disclosure. *Acad. Manag. Perspect.* **2016**, *30*, 24–39. [CrossRef]
44. Liu, X.; Zhang, C. Corporate governance, social responsibility information disclosure, and enterprise value in China. *J. Clean. Prod.* **2017**, *142*, 1075–1084. [CrossRef]
45. Matsumura, E.M.; Prakash, R.; Vera-Muñoz, S.C. Firm-Value Effects of Carbon Emissions and Carbon Disclosures. *Account. Rev.* **2013**, *89*, 695–724. [CrossRef]
46. Wang, S.; Wang, H.; Wang, J.; Yang, F. Does environmental information disclosure contribute to improve firm financial performance? An examination of the underlying mechanism. *Sci. Total Environ.* **2020**, *714*, 136855. [CrossRef]
47. Khlif, H.; Chalmers, K. A review of meta-analytic research in accounting. *J. Account. Lit.* **2015**, *35*, 1–27. [CrossRef]
48. Lueg, K.; Krastev, B.; Lueg, R. Bidirectional effects between organizational sustainability disclosure and risk. *J. Clean. Prod.* **2019**, *229*, 268–277. [CrossRef]
49. Shen, F.; Ma, Y.; Wang, R.; Pan, N.; Meng, Z. Does environmental performance affect financial performance? Evidence from Chinese listed companies in heavily polluting industries. *Qual. Quant.* **2019**, *53*, 1941–1958. [CrossRef]
50. Liu, L.; Chen, C.; Zhao, Y.; Zhao, E. China’s carbon-emissions trading: Overview, challenges and future. *Renew. Sustain. Energy Rev.* **2015**, *49*, 254–266. [CrossRef]
51. Luo, L. The influence of institutional contexts on the relationship between voluntary carbon disclosure and carbon emission performance. *Account. Financ.* **2019**, *59*, 1235–1264. [CrossRef]
52. Yi, Y.; Zhang, Z.; Yan, Y. Kindness is rewarded! The impact of corporate social responsibility on Chinese market reactions to the COVID-19 pandemic. *Econ. Lett.* **2021**, *208*, 110066. [CrossRef]
53. Lv, M.; Bai, M. Evaluation of China’s carbon emission trading policy from corporate innovation. *Financ. Res. Lett.* **2021**, *39*, 101565. [CrossRef]
54. Zhang, Y.-J.; Wang, W. How does China’s carbon emissions trading (CET) policy affect the investment of CET-covered enterprises? *Energy Econ.* **2021**, *98*, 105224. [CrossRef]
55. Xu, X.D.; Zeng, S.X.; Zou, H.L.; Shi, J.J. The Impact of Corporate Environmental Violation on Shareholders’ Wealth: A Perspective Taken from Media Coverage. *Bus. Strat. Environ.* **2016**, *25*, 73–91. [CrossRef]
56. Busch, T.; Hoffmann, V.H. How Hot Is Your Bottom Line? Linking Carbon and Financial Performance. *Bus. Soc.* **2011**, *50*, 233–265. [CrossRef]

57. Malmendier, U.; Tate, G.; Yan, J. Overconfidence and Early-Life Experiences: The Effect of Managerial Traits on Corporate Financial Policies. *J. Financ.* **2011**, *66*, 1687–1733. [CrossRef]
58. Malmendier, U.; Tate, G. Who makes acquisitions? CEO overconfidence and the market's reaction. *J. Financ. Econ.* **2008**, *89*, 20–43. [CrossRef]
59. Huergo, E.; Jaumandreu, J. Firms' age, process innovation and productivity growth. *Int. J. Ind. Organ.* **2004**, *22*, 541–559. [CrossRef]
60. Gao, Y.; Li, M.; Xue, J.; Liu, Y. Evaluation of effectiveness of China's carbon emissions trading scheme in carbon mitigation. *Energy Econ.* **2020**, *90*, 104872. [CrossRef]
61. Li, P.; Lu, Y.; Wang, J. Does flattening government improve economic performance? Evidence from China. *J. Dev. Econ.* **2016**, *123*, 18–37. [CrossRef]
62. Keppler, J.H.; Cruciani, M. Rents in the European power sector due to carbon trading. *Energy Policy* **2010**, *38*, 4280–4290. [CrossRef]
63. Chan, R.; Li, S.; Zhang, F. Firm competitiveness and the European Union emissions trading scheme. *Energy Policy* **2013**, *63*, 1056–1064. [CrossRef]
64. Popp, D. Induced Innovation and Energy Prices. *Am. Econ. Rev.* **2002**, *92*, 160–180. [CrossRef]
65. Zeng, S.; Nan, X.; Liu, C.; Chen, J. The response of the Beijing carbon emissions allowance price (BJC) to macroeconomic and energy price indices. *Energy Policy* **2017**, *106*, 111–121. [CrossRef]
66. Popp, D. Innovation and Climate Policy. *Annu. Rev. Resour. Econ.* **2010**, *2*, 275–298. [CrossRef]
67. Meng, X.; Zeng, S.; Shi, J.J.; Qi, G.; Zhang, Z. The relationship between corporate environmental performance and environmental disclosure: An empirical study in China. *J. Environ. Manag.* **2014**, *145*, 357–367. [CrossRef] [PubMed]
68. Li, D.; Huang, M.; Ren, S.; Chen, X.; Ning, L. Environmental Legitimacy, Green Innovation, and Corporate Carbon Disclosure: Evidence from CDP China 100. *J. Bus. Ethics* **2018**, *150*, 1089–1104. [CrossRef]
69. Brandt, L.; Van Biesebroeck, J.; Zhang, Y. Challenges of working with the Chinese NBS firm-level data. *China Econ. Rev.* **2014**, *30*, 339–352. [CrossRef]
70. Hahn, R.W. Market Power and Transferable Property Rights. *Q. J. Econ.* **1984**, *99*, 753–765. [CrossRef]
71. Jaffe, A.B.; Newell, R.G.; Stavins, R.N. A tale of two market failures: Technology and environmental policy. *Ecol. Econ.* **2005**, *54*, 164–174. [CrossRef]
72. Wang, K.; Wei, Y.-M.; Huang, Z. Potential gains from carbon emissions trading in China: A DEA based estimation on abatement cost savings. *Omega* **2016**, *63*, 48–59. [CrossRef]
73. Jaraitė-Kažukauskė, J.; Kažukauskas, A. Do Transaction Costs Influence Firm Trading Behaviour in the European Emissions Trading System? *Environ. Resour. Econ.* **2014**, *62*, 583–613. [CrossRef]
74. Hu, Y.; Ren, S.; Wang, Y.; Chen, X. Can carbon emission trading scheme achieve energy conservation and emission reduction? Evidence from the industrial sector in China. *Energy Econ.* **2020**, *85*, 104590. [CrossRef]
75. Ren, S.; Hu, Y.; Zheng, J.; Wang, Y. Emissions trading and firm innovation: Evidence from a natural experiment in China. *Technol. Forecast. Soc. Chang.* **2020**, *155*, 119989. [CrossRef]
76. An, S.; Li, B.; Song, D.; Chen, X. Green credit financing versus trade credit financing in a supply chain with carbon emission limits. *Eur. J. Oper. Res.* **2021**, *292*, 125–142. [CrossRef]
77. Hadlock, C.J.; Pierce, J.R. New Evidence on Measuring Financial Constraints: Moving Beyond the KZ Index. *Rev. Financ. Stud.* **2010**, *23*, 1909–1940. [CrossRef]

MDPI
St. Alban-Anlage 66
4052 Basel
Switzerland
Tel. +41 61 683 77 34
Fax +41 61 302 89 18
www.mdpi.com

Atmosphere Editorial Office
E-mail: atmosphere@mdpi.com
www.mdpi.com/journal/atmosphere



MDPI
St. Alban-Anlage 66
4052 Basel
Switzerland
Tel: +41 61 683 77 34
www.mdpi.com



ISBN 978-3-0365-6604-7